Woodhead Publishing Series in Electronic and Optical Materials

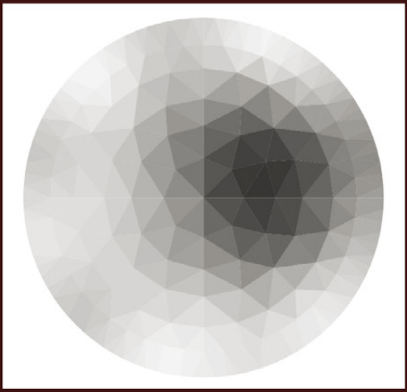

Industrial Tomography

Systems and Applications

Edited by Mi Wang

WP
WOODHEAD PUBLISHING

Industrial Tomography

Related titles

Laser spectroscopy and sensing
(ISBN 978-0-85709-273-1)

Terahertz technology for imaging and sensing
(ISBN 978-0-85709-235-9)

In-situ characterisation of film deposition
(ISBN 978-1-84569-934-5)

Woodhead Publishing Series in Electronic and Optical Materials: Number 71

Industrial Tomography

Systems and Applications

Edited by

Mi Wang

AMSTERDAM • BOSTON • CAMBRIDGE • HEIDELBERG
LONDON • NEW YORK • OXFORD • PARIS • SAN DIEGO
SAN FRANCISCO • SINGAPORE • SYDNEY • TOKYO
Woodhead Publishing is an imprint of Elsevier

Woodhead Publishing is an imprint of Elsevier
80 High Street, Sawston, Cambridge, CB22 3HJ, UK
225 Wyman Street, Waltham, MA 02451, USA
Langford Lane, Kidlington, OX5 1GB, UK

Copyright © 2015 Elsevier Ltd. All rights reserved.

No part of this publication may be reproduced, stored in a retrieval system or transmitted in any form or by any means electronic, mechanical, photocopying, recording or otherwise without the prior written permission of the publisher.

Permissions may be sought directly from Elsevier's Science & Technology Rights Department in Oxford, UK: phone (+44) (0) 1865 843830; fax (+44) (0) 1865 853333; email: permissions@elsevier.com. Alternatively you can submit your request online by visiting the Elsevier website at http://elsevier.com/locate/permissions, and selecting Obtaining permission to use Elsevier material.

Notice
No responsibility is assumed by the publisher for any injury and/or damage to persons or property as a matter of products liability, negligence or otherwise, or from any use or operation of any methods, products, instructions or ideas contained in the material herein. Because of rapid advances in the medical sciences, in particular, independent verification of diagnoses and drug dosages should be made.

British Library Cataloguing in Publication Data
A catalogue record for this book is available from the British Library

Library of Congress Control Number: 2014957597

ISBN 978-1-78242-118-4 (print)
ISBN 978-1-78242-123-8 (online)

For information on all Woodhead Publishing publications visit our website at http://store.elsevier.com/

Typeset by TNQ Books and Journals
www.tnq.co.in
Printed and bound in the United Kingdom

ELSEVIER
Book Aid International
Working together to grow libraries in developing countries
www.elsevier.com • www.bookaid.org

Contents

List of contributors **xiii**

Woodhead Publishing Series in Electronic and Optical Materials **xv**

Introduction – an overview of process applications of tomographic techniques **xix**

Part One Tomographic modalities 1

1 Electrical capacitance tomography **3**

Q. Marashdeh, F.L. Teixeira, L.-S. Fan

1.1 Introduction **3**
1.2 Principle of operation **4**
1.3 Image reconstruction algorithms **6**
1.4 Data acquisition system **9**
1.5 Electrical capacitance volume tomography **10**
1.6 Illustrative examples and discussion **15**
1.7 Conclusions **19**
1.8 Future trends **19**
Acknowledgement **20**
References **20**

2 Electrical impedance tomography **23**

M. Wang

2.1 Introduction **23**
2.2 EIT sensor **25**
2.3 Electrode modelling **28**
2.4 Signal sources **33**
2.5 Sensing strategies **36**
2.6 Sensor electronics and demodulation **40**
2.7 Data acquisition systems **45**
2.8 Imaging capability **47**
2.9 EIT data for process application **49**
2.10 Future trends **51**
2.11 Sources of further information **52**
References **52**

3 Electromagnetic induction tomography **61**
A.J. Peyton
3.1 Introduction **61**
3.2 Principle of operation and governing equations **65**
3.3 Solution to the forward problem **72**
3.4 Solution to the inverse problem **82**
3.5 System hardware **89**
3.6 Applications **101**
3.7 Conclusions and outlook **103**
References **104**

4 Magnetic resonance imaging **109**
A.J. Sederman
4.1 Introduction to MRI and NMR **109**
4.2 MRI: basic imaging principles **110**
4.3 Image contrast **116**
4.4 Basic imaging techniques **121**
4.5 Fast imaging approaches **123**
4.6 Applications in engineering **128**
4.7 Conclusions **130**
4.8 Sources of further information and advice **132**
References **132**

5 Chemical species tomography **135**
H. McCann, P. Wright, K. Daun
5.1 Introduction **135**
5.2 Absorption spectroscopy for chemical species tomography **136**
5.3 Image reconstruction for low beam-count systems **143**
5.4 Beam array design and optimization **150**
5.5 Design of CST systems **151**
5.6 Case studies **162**
5.7 Future trends **168**
References **170**

6 X-ray computed tomography **175**
U. Hampel
6.1 Introduction **175**
6.2 Variants of X-ray computed tomography for process applications **177**
6.3 X-ray sources for process tomography **178**
6.4 X-ray detectors **183**
6.5 Attenuation measurement with X-rays **185**
6.6 Beam hardening and radiation scattering **188**
6.7 Cone-beam X-ray computed tomography for gas holdup measurements **190**

6.8 Static mixer studies with ultrafast electron beam X-ray tomography **193**
6.9 Future trends **194**
6.10 Sources of further information and advice **195**
References **195**

7 Gamma-ray tomography **197**

G.A. Johansen

7.1 Introduction **197**
7.2 Radioisotope sources and gamma-ray emission **199**
7.3 Gamma-ray attenuation in matter **201**
7.4 Detector and read-out systems **206**
7.5 System engineering and geometry **209**
7.6 Case studies **212**
7.7 Future trends **220**
References **221**

8 Radioisotope tracer techniques **223**

D. Parker

8.1 Nuclear medicine imaging **223**
8.2 Industrial applications **227**
8.3 Particle tracking **230**
References **233**

9 Ultrasound tomography **235**

N.J. Watson

9.1 Introduction **235**
9.2 Ultrasound theory **236**
9.3 Equipment and techniques **244**
9.4 Industrial applications **253**
9.5 Future trends **254**
9.6 Sources of further information and advice **256**
9.7 Summary **256**
References **257**

10 Spectro-tomography **263**

B.S. Hoyle

10.1 Multidimensional process measurement requirements **263**
10.2 Multidimensional process sensing **266**
10.3 Spectral energy sensing dimension **268**
10.4 Spectro-tomography principles **271**
10.5 Spectro-tomography system implementation **274**
10.6 Demonstration and implementation **278**
10.7 Spectro-tomography application review **283**
References **284**

11 Tomographic imaging in sensor networks 285

G. Kamath, W.-Z. Song

11.1 Introduction 285
11.2 Seismic tomography 286
11.3 Sensor networks for volcano monitoring 288
11.4 In-network tomographic imaging 290
11.5 In-network tomography imaging applications 296
11.6 Future trends in in-network tomography imaging 298
11.7 Other sources and advice 299
References 300

Part Two Tomographic image reconstruction 303

12 Mathematical concepts for image reconstruction in tomography 305

S. Kim, A.K. Khambampati

12.1 Introduction 305
12.2 Transmission tomography 306
12.3 Electrical tomography 314
12.4 Diffraction tomography 331
12.5 Future trends 341
12.6 Further useful information 341
References 342

13 Image reconstruction for hard field tomography 347

U. Hampel

13.1 Introduction and basic considerations 347
13.2 The forward problem: projections and the Radon space 351
13.3 The inverse problem and two-dimensional analytic image reconstruction with parallel beams 352
13.4 The central slice theorem 356
13.5 Implementation 362
13.6 Algebraic image reconstruction 366
13.7 3D analytic image reconstruction 370
13.8 Local tomography, limited-angle tomography, and limited-data tomography 372
13.9 Future trends 373
13.10 Sources of further information and advice 374
Appendix A.1: proof of rotational invariance of the 2D Fourier transform 374
References 375

14 Direct methods for image reconstruction in electrical capacitance tomography 377

Z. Cao, L. Xu

14.1 Introduction 377
14.2 Three typical direct algorithms for ECT 379

14.3 Constructions of the Dirichlet-to-Neumann/ Neumann-to-Dirichlet maps **385**
14.4 Calculation of the scattering transforms **388**
14.5 Reconstructed results and discussion **390**
14.6 Conclusions **394**
14.7 Future trends **396**
14.8 Further information **396**
References **396**

15 Statistical image reconstruction 401
R.G. Aykroyd
15.1 Introduction **401**
15.2 Background **401**
15.3 Bayesian paradigm **405**
15.4 Data models **408**
15.5 Pixel-based continuous prior models **409**
15.6 Other pixel-based prior models **413**
15.7 Feature-based prior models **413**
15.8 Estimation methodology **415**
15.9 Estimation examples **420**
15.10 Discussion and future trends **421**
References **424**

Part Three Tomography applications 429

16 Applications of tomography in mineral transportation 431
C. Tan, F. Dong
16.1 Introduction **431**
16.2 Flow pattern and flow pattern identification with industrial process tomography **432**
16.3 Mineral transportation process measurement and monitoring with industrial process tomography **434**
16.4 Industrial process tomography in multiphase-flow measurement with multisensory fusion **445**
16.5 Conclusions **448**
Acknowledgements **448**
References **448**

17 X-ray tomography of fluidized beds 451
A. Kantzas
17.1 Introduction **451**
17.2 Imaging of fluid beds **453**
17.3 Computational models and their experimental validation **455**
17.4 Experimental studies **455**
17.5 Data evaluation **459**

17.6 Validation experiments for narrow and wide particle size distribution **462**
17.7 Comparison between different validation approaches **463**
17.8 Validation for reactor scale-up **464**
17.9 Ultrafast X-ray computer tomography **467**
17.10 Future trends **469**
Acknowledgements **469**
References **470**

18 Applications of tomography in bubble column and trickle bed reactors **477**
D.J. Holland
18.1 Introduction **477**
18.2 Bubble column reactors **478**
18.3 Trickle bed reactors **488**
18.4 Future trends **494**
18.5 Sources of further information **496**
References **497**

19 Applications of tomography in reaction engineering (mixing process) **509**
V. Mosorov
19.1 Introduction **509**
19.2 Review of tomographic techniques utilized for different kinds of mixing processes **511**
19.3 How to extract information about mixing from tomographic images **512**
19.4 Application of one-plane tomography in mixing processes **513**
19.5 Mixing process monitoring by twin-plane tomographic system **515**
19.6 Other applications of tomography for mixing processes **521**
19.7 Future trends **526**
Acknowledgement **527**
References **527**

20 Applications of capacitance tomography in gas–solid fluidized bed systems **529**
A. Wang, Q. Marashdeh, F.L. Teixeira, L.-S. Fan
20.1 Introduction to fluidized bed systems **529**
20.2 Electrical capacitance characterization of gas–solid fluidized beds **532**
20.3 Examples and discussion for electrical capacitance tomography applications in conventional fluidized beds **536**
20.4 Applications of capacitance tomography in the pharmaceutical industry **542**

20.5 Effective permittivities of mixtures and phase distributions **546**
20.6 Future trends and conclusion **548**
References **548**

21 Process tomography and estimation of velocity fields 551
J.P. Kaipio, A. Seppänen, M. Vauhkonen, A. Lipponen, A. Voutilainen, A. Lehikoinen, V. Rimpiläinen
21.1 Introduction **551**
21.2 Nonstationary inverse problems and state estimation **557**
21.3 Approximate nonlinear and non-Gaussian state estimation and handling modelling errors **563**
21.4 Approaches with auxiliary parameters **565**
21.5 Tomographic state space estimation of velocity fields **567**
21.6 Computational case studies **574**
21.7 Discussion **581**
21.8 Sources of further information and advice **582**
Acknowledgement **583**
References **583**

22 Applications of tomography in oil-gas industry – Part 1 591
C.-G. Xie
22.1 Introduction **591**
22.2 Seismic tomography in hydrocarbon exploration and reservoir characterization **591**
22.3 Multicomponent seismic data for reservoir characterization **608**
22.4 Simultaneous inversion of time-lapse seismic surveys for reservoir monitoring **615**
22.5 Borehole seismic surveys **619**
22.6 Future trends **626**
22.7 Sources of further information and advice **629**
Acknowledgements **630**
References **630**

23 Applications of tomography in the oil-gas industry – Part 2 633
C.-G. Xie, M. Wilt
23.1 Introduction **633**
23.2 Cross-well electromagnetic tomography in hydrocarbon reservoir monitoring **633**
23.3 Potential of tomography in hydrocarbon production monitoring **644**
23.4 Future trends **656**
23.5 Sources of further information and advice **658**
Acknowledgements **658**
References **659**

24 Application of tomography in microreactors 667
N. Ali Othman, M. Takei
24.1 Introduction **667**
24.2 X-ray and γ-ray tomography **668**
24.3 X-ray and γ-ray absorption/radiography tomography **675**
24.4 Nuclear magnetic resonance imaging **677**
24.5 Positron emission tomography **678**
24.6 Electrical impedance tomography **682**
24.7 Future trends **688**
References **690**

25 Applications of tomography in food inspection 693
M.A. Del Nobile, J. Laverse, V. Lampignano, B. Cafarelli, A. Spada
25.1 Introduction **693**
25.2 Description of testing method used in X-ray microtomography **693**
25.3 To date: food products studied **695**
25.4 Case studies of food products studied to date **696**
25.5 Future trends **709**
25.6 Further information **710**
References **710**

26 Application of process tomography in nuclear waste processing 713
K. Primrose
26.1 Introduction **713**
26.2 Applications of resistance tomography **715**
26.3 Applications of other tomographic modalities **723**
26.4 Future trends **724**
26.5 Sources of further information and advice **724**
Acknowledgement **725**
References **725**

Index 727

List of contributors

N. Ali Othman Universiti Kebangsaan Malaysia, Bangi, Selangor, Malaysia; Chiba University, Inage, Chiba, Japan

R.G. Aykroyd University of Leeds, Leeds, UK

B. Cafarelli University of Foggia, Foggia, Italy

Z. Cao Beihang University, Beijing, China

K. Daun University of Waterloo, Waterloo, Ontario, Canada

M.A. Del Nobile University of Foggia, Foggia, Italy

F. Dong Tianjin University, Tianjin, China

L.-S. Fan The Ohio State University, Columbus, OH, USA

U. Hampel Helmholtz-Zentrum Dresden-Rossendorf, Dresden, Germany; Technische Universität Dresden, Dresden, Germany

D.J. Holland University of Canterbury, Christchurch, New Zealand

B.S. Hoyle University of Leeds, Leeds, UK

G.A. Johansen Faculty of Engineering and Business Administration, Bergen University College, Bergen, Norway

J.P. Kaipio The University of Auckland, Auckland, New Zealand; University of Eastern Finland, Kuopio, Finland; Rocsole Ltd, Kuopio, Finland

G. Kamath Georgia State University, Atlanta, GA, USA

A. Kantzas University of Calgary, Calgary, AB, Canada

A.K. Khambampati Institute for Nuclear Science and Technology, Jeju National University, Jeju, South Korea

S. Kim School of Energy Systems Engineering, Chung-Ang University, Seoul, South Korea

V. Lampignano University of Foggia, Foggia, Italy

J. Laverse University of Foggia, Foggia, Italy

A. Lehikoinen University of Eastern Finland, Kuopio, Finland; Rocsole Ltd, Kuopio, Finland

A. Lipponen University of Eastern Finland, Kuopio, Finland

Q. Marashdeh Tech4Imaging LLC, Columbus, OH, USA

H. McCann University of Edinburgh, Edinburgh, Scotland, UK

V. Mosorov Institute of Applied Computer Science, Lodz University of Technology, Lodz, Poland

D. Parker University of Birmingham, Birmingham, UK

A.J. Peyton University of Manchester, Manchester, UK

K. Primrose Industrial Tomography Systems plc, Manchester, UK

V. Rimpiläinen The University of Auckland, Auckland, New Zealand

A.J. Sederman Department of Chemical Engineering and Biotechnology, University of Cambridge, Cambridge, UK

A. Seppänen University of Eastern Finland; Kuopio, Finland

W.-Z. Song Georgia State University, Atlanta, GA, USA

A. Spada University of Foggia, Foggia, Italy

M. Takei Chiba University, Inage, Chiba, Japan

C. Tan Tianjin University, Tianjin, China

F.L. Teixeira The Ohio State University, Columbus, OH, USA

M. Vauhkonen University of Eastern Finland, Kuopio, Finland; Rocsole Ltd, Kuopio, Finland

A. Voutilainen Rocsole Ltd, Kuopio, Finland

A. Wang The Ohio State University, Columbus, OH, USA

M. Wang University of Leeds, Leeds, West Yorkshire, UK

N.J. Watson University of Nottingham, Nottingham, UK

M. Wilt Schlumberger Gould Research Centre, Cambridge, UK; Schlumberger Oilfield PetroTechnical Services, Richmond, CA, USA

P. Wright University of Manchester, Manchester UK

C.-G. Xie Singapore Well Testing Centre (SWTC), Schlumberger Oilfield (S) Pte Ltd, Singapore; Schlumberger Gould Research Centre, Cambridge, UK; Schlumberger Oilfield PetroTechnical Services, Richmond, CA, USA

L. Xu Beihang University, Beijing, China

Woodhead Publishing Series in Electronic and Optical Materials

1 **Circuit analysis**
J. E. Whitehouse
2 **Signal processing in electronic communications: For engineers and mathematicians**
M. J. Chapman, D. P. Goodall and N. C. Steele
3 **Pattern recognition and image processing**
D. Luo
4 **Digital filters and signal processing in electronic engineering: Theory, applications, architecture, code**
S. M. Bozic and R. J. Chance
5 **Cable engineering for local area networks**
B. J. Elliott
6 **Designing a structured cabling system to ISO 11801: Cross-referenced to European CENELEC and American Standards**
Second edition
B. J. Elliott
7 **Microscopy techniques for materials science**
A. Clarke and C. Eberhardt
8 **Materials for energy conversion devices**
Edited by C. C. Sorrell, J. Nowotny and S. Sugihara
9 **Digital image processing: Mathematical and computational methods**
Second edition
J. M. Blackledge
10 **Nanolithography and patterning techniques in microelectronics**
Edited by D. Bucknall
11 **Digital signal processing: Mathematical and computational methods, software development and applications**
Second edition
J. M. Blackledge
12 **Handbook of advanced dielectric, piezoelectric and ferroelectric materials: Synthesis, properties and applications**
Edited by Z.-G. Ye
13 **Materials for fuel cells**
Edited by M. Gasik
14 **Solid-state hydrogen storage: Materials and chemistry**
Edited by G. Walker
15 **Laser cooling of solids**
S. V. Petrushkin and V. V. Samartsev

16 **Polymer electrolytes: Fundamentals and applications**
Edited by C. A. C. Sequeira and D. A. F. Santos
17 **Advanced piezoelectric materials: Science and technology**
Edited by K. Uchino
18 **Optical switches: Materials and design**
Edited by S. J. Chua and B. Li
19 **Advanced adhesives in electronics: Materials, properties and applications**
Edited by M. O. Alam and C. Bailey
20 **Thin film growth: Physics, materials science and applications**
Edited by Z. Cao
21 **Electromigration in thin films and electronic devices: Materials and reliability**
Edited by C.-U. Kim
22 ***In situ* characterization of thin film growth**
Edited by G. Koster and G. Rijnders
23 **Silicon-germanium (SiGe) nanostructures: Production, properties and applications in electronics**
Edited by Y. Shiraki and N. Usami
24 **High-temperature superconductors**
Edited by X. G. Qiu
25 **Introduction to the physics of nanoelectronics**
S. G. Tan and M. B. A. Jalil
26 **Printed films: Materials science and applications in sensors, electronics and photonics**
Edited by M. Prudenziati and J. Hormadaly
27 **Laser growth and processing of photonic devices**
Edited by N. A. Vainos
28 **Quantum optics with semiconductor nanostructures**
Edited by F. Jahnke
29 **Ultrasonic transducers: Materials and design for sensors, actuators and medical applications**
Edited by K. Nakamura
30 **Waste electrical and electronic equipment (WEEE) handbook**
Edited by V. Goodship and A. Stevels
31 **Applications of ATILA FEM software to smart materials: Case studies in designing devices**
Edited by K. Uchino and J.-C. Debus
32 **MEMS for automotive and aerospace applications**
Edited by M. Kraft and N. M. White
33 **Semiconductor lasers: Fundamentals and applications**
Edited by A. Baranov and E. Tournie
34 **Handbook of terahertz technology for imaging, sensing and communications**
Edited by D. Saeedkia
35 **Handbook of solid-state lasers: Materials, systems and applications**
Edited by B. Denker and E. Shklovsky
36 **Organic light-emitting diodes (OLEDs): Materials, devices and applications**
Edited by A. Buckley
37 **Lasers for medical applications: Diagnostics, therapy and surgery**
Edited by H. Jelínková
38 **Semiconductor gas sensors**
Edited by R. Jaaniso and O. K. Tan

39 **Handbook of organic materials for optical and (opto)electronic devices: Properties and applications**
Edited by O. Ostroverkhova
40 **Metallic films for electronic, optical and magnetic applications: Structure, processing and properties**
Edited by K. Barmak and K. Coffey
41 **Handbook of laser welding technologies**
Edited by S. Katayama
42 **Nanolithography: The art of fabricating nanoelectronic and nanophotonic devices and systems**
Edited by M. Feldman
43 **Laser spectroscopy for sensing: Fundamentals, techniques and applications**
Edited by M. Baudelet
44 **Chalcogenide glasses: Preparation, properties and applications**
Edited by J.-L. Adam and X. Zhang
45 **Handbook of MEMS for wireless and mobile applications**
Edited by D. Uttamchandani
46 **Subsea optics and imaging**
Edited by J. Watson and O. Zielinski
47 **Carbon nanotubes and graphene for photonic applications**
Edited by S. Yamashita, Y. Saito and J. H. Choi
48 **Optical biomimetics: Materials and applications**
Edited by M. Large
49 **Optical thin films and coatings**
Edited by A. Piegari and F. Flory
50 **Computer design of diffractive optics**
Edited by V. A. Soifer
51 **Smart sensors and MEMS: Intelligent devices and microsystems for industrial applications**
Edited by S. Nihtianov and A. Luque
52 **Fundamentals of femtosecond optics**
S. A. Kozlov and V. V. Samartsev
53 **Nanostructured semiconductor oxides for the next generation of electronics and functional devices: Properties and applications**
S. Zhuiykov
54 **Nitride semiconductor light-emitting diodes (LEDs): Materials, technologies and applications**
Edited by J. J. Huang, H. C. Kuo and S. C. Shen
55 **Sensor technologies for civil infrastructures**
Volume 1: Sensing hardware and data collection methods for performance assessment
Edited by M. Wang, J. Lynch and H. Sohn
56 **Sensor technologies for civil infrastructures**
Volume 2: Applications in structural health monitoring
Edited by M. Wang, J. Lynch and H. Sohn
57 **Graphene: Properties, preparation, characterisation and devices**
Edited by V. Skákalová and A. B. Kaiser
58 **Silicon-on-insulator (SOI) technology**
Edited by O. Kononchuk and B.-Y. Nguyen

59 **Biological identification: DNA amplification and sequencing, optical sensing, lab-on-chip and portable systems**
Edited by R. P. Schaudies
60 **High performance silicon imaging: Fundamentals and applications of CMOS and CCD sensors**
Edited by D. Durini
61 **Nanosensors for chemical and biological applications: Sensing with nanotubes, nanowires and nanoparticles**
Edited by K. C. Honeychurch
62 **Composite magnetoelectrics: Materials, structures, and applications**
G. Srinivasan, S. Priya and N. Sun
63 **Quantum information processing with diamond: Principles and applications**
Edited by S. Prawer and I. Aharonovich
64 **Advances in non-volatile memory and storage technology**
Edited by Y. Nishi
65 **Laser surface engineering: Processes and applications**
Edited by J. Lawrence, C. Dowding, D. Waugh and J. Griffiths
66 **Power ultrasonics: Applications of high-intensity ultrasound**
Edited by J. A. Gallego-Juárez and K. F. Graff
67 **Advances in delay-tolerant networks (DTNs): Architectures, routing and challenges**
Edited by J. J. P. C. Rodrigues
68 **Handbook of flexible organic electronics: Materials, manufacturing and applications**
Edited by S. Logothetidis
69 **Machine-to-machine (M2M) communications: Architecture, performance and applications**
Edited by C. Anton-Haro and M. Dohler
70 **Ecological design of smart home networks: Technologies, social impact and sustainability**
Edited by N. Saito and D. Menga
71 **Industrial tomography: Systems and applications**
Edited by M. Wang
72 **Vehicular communications and networks: Architectures, protocols, operation and deployment**
Edited by W. Chen
73 **Modeling, characterization, and production of nanomaterials: Electronics, photonics and energy applications**
Edited by V. Tewary and Y. Zhang
74 **Reliability characterisation of electrical and electronic systems**
Edited by J. Swingler
75 **Handbook of industrial wireless sensor networks: Monitoring, control and automation**
Edited by R. Budampati S. Kolavennu
76 **Epitaxial growth of complex metal oxides: Techniques, properties and applications**
Edited by G. Koster, G. Rijnders and M. Huijben
77 **Semiconductor nanowires: Materials, synthesis, characterization and applications**
Edited by J. Arbiol and Q. Xiong

Introduction – an overview of process applications of tomographic techniques

1. Historical development

Since its inception the goal of process tomography has been to sense and interpret complex data in order to extract qualitative and quantitative information of the behaviour of fluids moving within processes. These processes may be reactors, pipelines or measurements focused on the properties of materials being manufactured. At one extreme, we have the classical physics of nondestructive testing (a parlance reserved for testing of static products undergoing routine characterisation) and at the other extreme are attempts to quantitate multiphase fluids under chaotic flow regimes. In all cases, there is trade-off between spatial and component resolution and the dynamic (or temporal) resolution. The roots of the discipline lie in medical tomography in which a static (literal) body was investigated using now well-known medical tomographic sensors based on radiation and electromagnetic sensing. Process tomography sought to extend the principles applied to static and steady-state objects to industrial applications (Beck & Williams, 1995, p. 550; Chaouki, Larachi, & Duduković, 1997; Williams, 2010). The journey of this book takes a sensor-perspective, introducing the capabilities of different sensors (often called modalities) and then examining their application for specific measurement tasks.

The process engineer starts at the process. The physicist and instrument engineer may often start with the sensors. Process tomography requires integration at both ends, but invariably the practicalities of the purpose of the measurement should be used to drive the design of the overall process. Whilst there is a natural desire to want to know everything about the process, in reality this is beyond reach. The approach must focus not on the quality of an image but on the specification of measurements from which judgments can be made for specific purposes. We see this dilemma in the early works on Process Tomography in the World Congress conference series commencing in 1999 (see Bibliography [B10]). Here, sensors were normally evaluated in static tests using phantom objects against different conditions – far removed from real processes. These were necessary tests, but they were not sufficient for the realities of process measurement.

More sophisticated computational and modeling methods were needed to extract information of interest – and this information was often not an image. Nevertheless, preoccupation with images has persisted for obvious reasons. Figure 1 illustrates

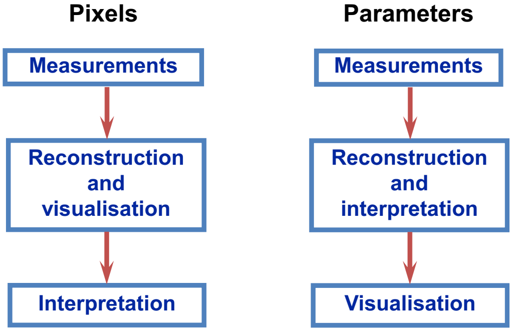

Figure 1 Approaches to reconstruction.
West, Jia, and Williams (2000).

two very different approaches to how information derived from tomographic measurements might be used. In the case of the left-hand column, measurements are reconstructed (using some assumptions that need to be justified) to produce a visualisation. The resultant image is then interpreted. The errors are often undefined and frequently undefinable! This is the classical medical tomography approach. In the second case, the right-hand column of Figure 1, measurements are made through proxies or parameters that can be measured and known. These parameters are reconstructed and interpreted. Then, if desired, a visualisation of the parameters can be displayed, but the interpretation has already occurred. Here, the errors involved in the inversion can be defined and can be expressed statistically. An example is given later in the chapter, but the point is that it illustrates the need for a distinctly different approach to complex and unknown processes compared with well-defined medical or nondestructive testing environments.

The World Congress community has continued to evolve with biannual conferences coupled with related annual community workshops on a global basis. There have also been numerous specialist conferences embedded within academic disciplines and industrial sectors, some of which are reflected in special volumes of established periodicals [B11–15].

2. Industrial measurement needs

Measurement of the flow and position of fast-moving components in industrial mixture and processes takes us to the extremes of science and engineering. The subject is intellectually demanding due to the complexity of the measurement science and modeling. The subject area is also intriguing due to the alluring nature of its imagery. Deployment is invariably technically challenging because the realities of materials, safety and cost define envelopes for operation that are narrow, requiring great ingenuity. Nevertheless, significant advances have brought process tomography into the mainstream as a discovery tool and an industrially deployable technique. This chapter indicates the navigation pathways around challenges that have resulted in a range of proven

Table 1 **A hierarchy of process tomographic measurement applications**

1. Gaining experimental understanding (Chapters 6, 17, 18, 19)
2. Sub-process modeling (Chapters 19, 24)
3. Process design and optimization (Chapters 20, 26)
4. Component flow measurement (Chapters 5, 21)
5. Process measurement and control (Chapters 7, 16, 21, 23)
6. Process audit and safety (Chapters 5, 23)
7. Product quality assurance (Chapter 25)
8. Product functionality testing (Chapter 4)

applications for process tomography. Some key works are indicated in the bibliography along with selected specific references, which cite some landmark works in the development of the subject.

Tomographic approaches aim to derive data taken from a multiplicity of sensors observing different attributes of a process. The end purpose is to obtain a rich data set of measurements that detail the spatial dependence of particular properties of the mixture within the process. Dynamic behaviour is commonly sought from which temporal properties of the process can be deduced. Not surprisingly, this gives rise to many different tomography applications of interest both at a fundamental experimental and applied industrial scale. The diversity of applications is not readily systematised. But by way of introduction, some principal examples of the types of applications will be mentioned in this chapter, setting the scene for some further detailed expositions elsewhere in the book.

Table 1 gives an overview in the form of a hierarchy of applications for process tomographic methods. Each of these eight stages draws on tomographic measurements in different ways. In practice, such applications are often augmented using other non-tomographic measurements. These might include additional single-point measurements relating to chemical/pressure/optical sensors, gravimetric information and hybrid or interlaced mathematical models. The purpose of this chapter is, therefore, also to provide a background to the ethos around the development of process tomography.

3. Key developments in linking modelling and measurement

A key and obvious statement is the fact that increasingly advanced computing speeds and cellular hardware structures have driven a thirst for simulating complex multiphase processes at increasing levels of detail. Such approaches require experimental data relating to key assumptions in the models within the simulation calculation and then verification of all or some of the key properties predicted from the simulation. The evolution of tomographic measurements has occurred alongside these changes but only recently have the two been implicitly connected as a matter of routine. Fusion of experimental measurements with simulated solutions of the process model and, if used, the reconstruction model is at the core of future developments of the subject.

Pre-1990s complex systems and structures defied prediction and were represented by simple so-called black box models that express the properties of the systems empirically. In such models, the connection between inputs and output measurements are fitted using parameters that do not bear a relation to an understanding of the underlying process because the underlying process was not understood or incapable of being measured directly through experiment. The nature of the empirical model was, of course, set by the limits of what input and output properties (or proxies) could be measured.

Subsequently, greater computational ability and process understanding fostered the development of phenomenological models. In these, the essence of the science underlying the mechanisms being observed was guessed or known and represented by models that had a clear, intuitive sense. In this way, quantitative parameters could be abstracted from fitting, as mentioned earlier in the chapter. An example in chemical and process engineering is the concentration profile of solids in a separating device that is known to follow a certain functional form, and tomographic data are used to derive the parameters of this functional form (West, Jia, & Williams, 2000). Other features such as the dimensions of the air-core present in the device can be deduced. Such methods can be used to verify outcome predictions of computational fluid simulations (Cullivan, Williams, & Cross, 2003; Rakesh, Vakamalla, Reddy, & Narasimha, 2014). Figure 2 shows the concept of fitting three parameters to describe the radial concentration of solids, expressed by the local slurry conductivity, $\sigma(r)$, across the diameter of a separator. The device has a central air core (no solids, no liquid and no conductivity) with a varying concentration across from the air core boundary to the wall of the separator (conductivity rises to a maximum then drops off at the external wall). The figure shows the 2D plot of conductivity in a slice through the cyclone (left-hand top) and the conductivity profile beneath (left-hand bottom). The resultant parametric-derived plot

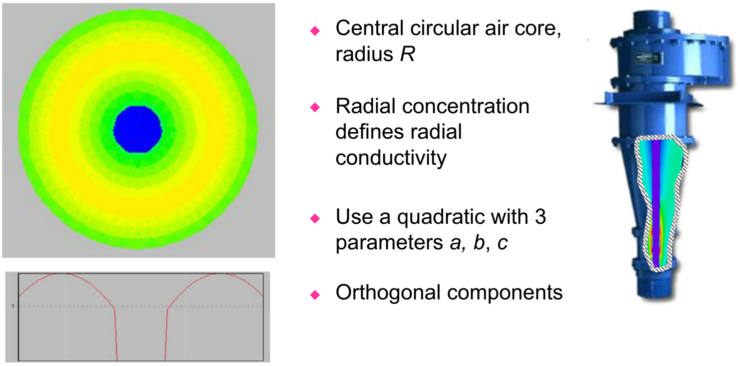
◆ Central circular air core, radius R
◆ Radial concentration defines radial conductivity
◆ Use a quadratic with 3 parameters a, b, c
◆ Orthogonal components

$$\sigma(r) = a + b\,(3r - 2) + c\,(10r^2 - 12r + 3)$$

Figure 2 Parametric reconstruction of specific process features in a hydrocyclone separator. Williams et al. (1999).

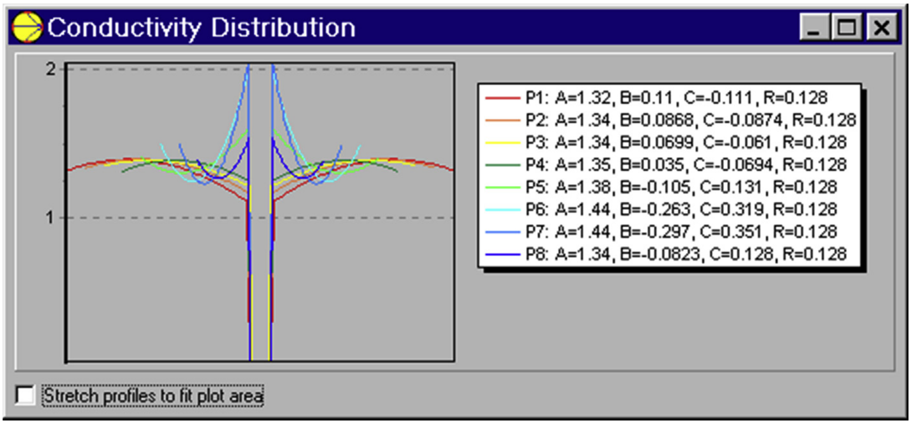

☐ Stretch profiles to fit plot area

Figure 3 Radial concentration profiles in a clay/silica hydrocyclone defined by parametric reconstruction of conductivity at different eight different axial positions in the separator.

of conductivity is shown in Figure 3 at different axial positions along the cyclone (West & Williams, 2000; Williams et al., 1999).

In some cases, separate (simpler) experiments or observations could be used to obtain values of parameters for some of the sub-models. In some cases, spatial effects could be recreated by developing a spatial network of interconnected models, such as in cellular mixing modelling (Mann, Williams, Dyakowski, Dickin, & Edwards, 1997). In this way, complex effects in a process reactor could be mapped with time, from which kinetic rates expressions and mixing could be derived, but without recourse to full computational fluids dynamics modelling. This method provided a sense of practical utility and enabled extraction of fit statistics. These techniques led to the need for 3D measurements because cellular assemblies were so dimensioned. Early work described 3D measurements and reconstruction of data. Later, Finnish researchers demonstrated dynamic state–space methods interlacing reconstruction with fluid simulation in a dynamic simulation to predict single-phase flow. This had significant computational demand (e.g. Kaipio & Somarsali, 2005) but was a step change. An example of the scope for direct interlacing of tomographic methods with modelling as part of the reconstruction is given later in this volume (see Chapter 21, Kaipio).

Other approaches to solutions of ill-posed inversion problems of tomographic reconstruction used statistical logic for predicting likely outcomes of processes, and from these, expected images could be rendered. An example is the use of Bayesian methods applied to powder flow (Grudzien, Romanowski, & Williams, 2005).

The next genre of models were essentially multiscale and multiphase, in which a plethora of models describing the behaviour of different components in a system (types of liquid, gas, solid) were used. Such intermeshed models demand significant computational assets. The length scale of resolution of system properties may require one or more techniques to be used. Commonly, this has been most common in the area of product analysis using magnetic resonance imaging (NMR) or X-ray microtomography. Three examples, of different complexity, will be considered next by way of illustration.

First, the admission of fluid through a porous structure had first been defined using X-ray tomography. The digitised spatial environment defined by the X-ray analysis sets the environment for the fluid modelling that may be a combination of classical computational fluid flow and molecular level modeling emulated through lattice Boltzmann methods, Figure 4. The methodology of this approach is described by Selomulya et al. (2005). Consideration of errors that arise in fusing tomographic measurements with simulations is an area of future development and real need. Some concepts around image registration and approaches to defining regional errors have been described by Zeidan, Jia, and Williams (2007) and Moreno-Atanasio, Williams, and Jia (2010).

A second example comes from the domain of product quality and assurance assessment (Table 1). In formulating complex structured products, there is a desire to control the use properties – often around mechanisms of controlled release. In other cases, the dissolution of the materials or specific components within are critical to the application and need to be measured and simulated. A grand example of this is the need to predict mineral leaching behaviour in metallic minerals, which is an emerging example of linking mineralogical analysis (in 3D from X-ray digital mapping) to system behaviour estimated through flow simulation and chemistry modelling. Examples of the approach have been given for pharmaceutical tablets and products (Jia & Williams, 2007), from which dissolution rates and tablet disintegration can be estimated. The principle can be seen in Figure 5 where tomographically derived images of a tablet (in this case an aspirin) reveal atomic number contrasts between the different granular components and their distribution. From the digital maps created, it is possible to run fluid contact and chemical reactions models in a digitised simulation, from which dissolution profiles can be estimated. Further, by remapping the consequences of the

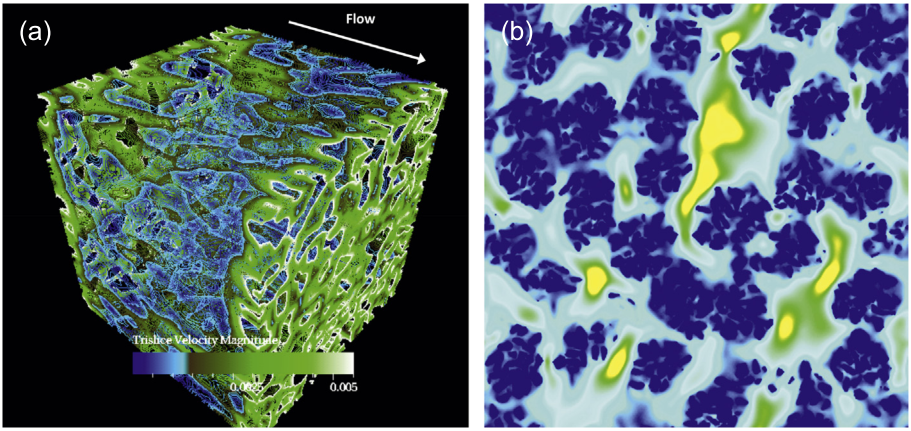

Figure 4 (a) Flow through an X-ray microtomography-determined mapping of solids forming a sediment of aggregates using lattice Boltzmann (LBM) simulation applied to the digital voxel free-space. This is used to develop the concept of desktop virtual permeametry. (b) LBM flow simulation around digitised aggregates of mineral particles, here shown in 2D.

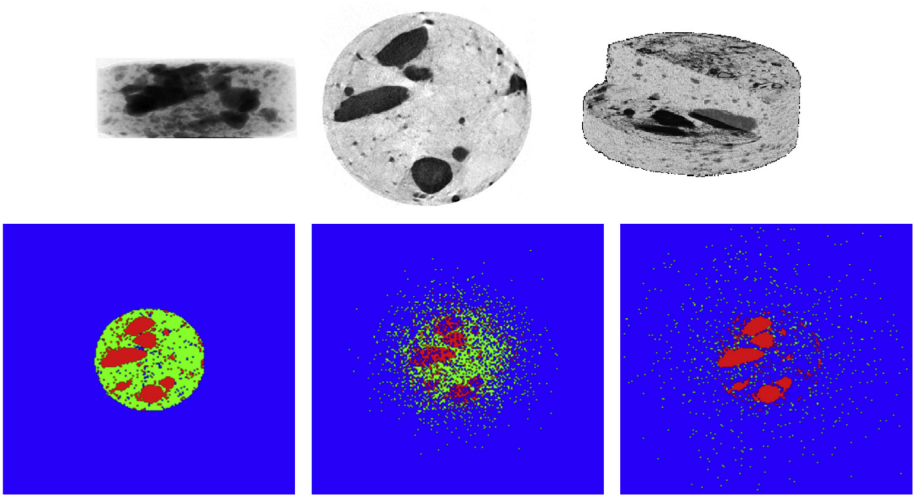

Figure 5 X-ray tomographically derived digital structure and composition analysis (top views) and simulation of tablet dissolution and disintegration with time (bottom views). After Jia and Williams (2007).

solid phases digestion and applying micromechanical modelling the way on which the tablet disintegrates can be simulated.

A third example is the real-time computation and measurement of a fluidised bed column in which fluid flow and distinct elements methods are computed using a graphical processor – and central processor – based scheme in a supercomputer (Li et al., 2013). These systems represent the worlds of virtual engineering in which complex phenomena are used to emulate the complex behaviours, and tomography is deployed to affirm the simulations. Note that the scale of modelling is changed continuously according to the model physics, and commensurate with this, the computational scales are also flexed continuously, hence, the term multiscale computational simulation. This is the ultimate destination in linking tomographically derived data with systems modelling.

The fusion of tomographically derived data and its use with fluid dynamic and chemical reaction models is a prime area for future development.

R.A. Williams
University of Birmingham, Birmingham, UK

References

Beck, M. S., & Williams, R. A. (1995). *Process tomography – Principles, techniques and applications*. Oxford: Butterworth-Heinemann. ISBN: 0-7506-0743-2.

Chaouki, J., Larachi, F., & Duduković, M. P. (Eds.). (1997). *B3. Non-invasive monitoring of multiphase flows*. Elsevier. ISBN: 978-0-82521-6.

Cullivan, J. C., Williams, R. A., & Cross, C. R. (2003). Understanding the hydrocyclone separator through computational fluid dynamics. *Transactions of IChemE, 81*(Part A4), 455–466. ISSN: 0263-8762.

Grudzien, K., Romanowski, A., & Williams, R. A. (2005). Application of a Bayesian approach to the tomographic analysis of hopper flow. *Particle & Particle Systems Characterisation, 22*, 246–253. ISSN: 0934-0866.

Jia, X., & Williams, R. A. (2007). A hybrid mesoscale modeling approach to dissolution of granules and tablets. *Chemical Engineering Research & Design, 85*, A7. ISSN: 0263-8762 (Electronic ISSN: 1744-3563).

Kaipio, J., & Somersalo, E. (2005). Statistical and computational inverse problems. *Applied Mathematical Sciences, 160*(XVI), 340.

Li, J., Ge, W., Wei, W., Yang, N., Liu, X., Wang, L., et al. (2013). *From multiscale modeling to meso-science: A chemical engineering perspective*. Springer. ISBN-13: 978-3642351884.

Mann, R., Williams, R. A., Dyakowski, T., Dickin, F. J., & Edwards, R. B. (1997). Development of mixing models using electrical resistance tomography. *Chemical Engineering Science, 52*(13), 2073–2085. ISSN: 0009-2509.

Moreno-Atanasio, R., Williams, R. A., & Jia, X. (2010). Combining X-ray microtomography with computer simulation for analysis of granular and porous materials. *Particuology, 8*(2), 81–99. ISSN: 1674-2001.

Rakesh, A., Vakamalla, T. S. R., Reddy, K., & Narasimha, M. (2014). Air-core size measurement of operating hydrocyclone by electrical resistance tomography. *Chemical Engineering and Technology, 37*(5), 1–12.

Selomulya, C., Jia, X., & Williams, R. A. (2005). Direct prediction of structure and permeability of flocculated structures and sediments using 3D tomographic imaging. *Chemical Engineering Research and Design, 83*(A7), 844–852. ISSN: 0263-8762.

West, R. M., Jia, X., & Williams, R. A. (2000). Parametric modeling in industrial process tomography. *Chemical Engineering Journal, 77*(1–2), 31–36. ISSN: 1385-8947.

Williams, R. A. (2010). Landmarks in the application of electrical tomography in particle science and technology. *Particuology, 8*(6), 493–497. http://dx.doi.org/10.1016/j.partic.2010.07.017. ISSN:1674-2001.

Williams, R. A., Jia, X., West, R. M., Wang, M., Cullivan, J. C., Bond, J., et al. (1999). Industrial monitoring of hydrocyclone operation using electrical resistance tomography. *Minerals Engineering, 12*(10), 1245–1252. ISSN: 0892-6875.

Zeidan, M., Jia, X., & Williams, R. A. (2007). Errors implicit in digital particle characterisation. *Chemical Engineering Science, 62*(7), 1905–1914. ISSN: 0009-2509.

Bibliography

General texts on applications and principles

B1. Scott, D. M., & Williams, R. A. (Eds.). (1995). *Frontiers in industrial process tomography*. New York: AIChE and Engineering Foundation. ISBN: 0-939204-52-5.

B2. Williams, R. A., & Beck, M. S. (Eds.). (1995). *Process tomography – Principles, techniques and applications* (p. 550). Oxford: Butterworth-Heinemann. ISBN: 0-7506-0743-2.

B3. Chaouki, J., Larachi, F., & Duduković, M. P. (Eds.). (1997). *Non-invasive monitoring of multiphase flows*. Elsevier. ISBN: 978-0-82521-6.

B4. Electrical impedance tomography: methods, history and applications. Holder, D. S. (Ed.). (2004), *Series in medical physics and biomedical engineering* (p. 456). CRC Press.

B5. Scott, D. M., & McCann, H. (Eds.). (2005). *Process imaging for automatic control*. Boca Raton: CRC Press. ISBN: 0-8247-5920-6.

Specialist texts on research developments

B6. Beck, M. S., Campogrande, E., Morris, M. A., Williams, R. A., & Waterfall, R. C. (Eds.). (1993). *Tomographic techniques for process design and operation* (p. 490). Southampton: Computational Mechanics Publications. ISBN: 1-85312-256-7/1-56252-170-5.

B7. Beck, M. S., Campogrande, E., Morris, M. A., Williams, R. A., & Waterfall, R. C. (Eds.). (1994). *Process tomography – A strategy for industrial exploitation 1993* (p. 374). Manchester: University of Manchester Institute of Science & Technology. ISBN: 0-9523165-01.

B8. Beck, M. S., Campogrande, E., Hammer, E., Morris, M. A., Williams, R. A., & Waterfall, R. C. (Eds.). (1994). *Process tomography – A strategy for industrial exploitation 1994* (p. 512). Manchester: University of Manchester Institute of Science & Technology. ISBN: 0-9523165-1X.

B9. Williams, R. A., Beck, M. S., Hoyle, B. S., Morris, M. A., & Waterfall, R. C. (Eds.). (1995), *Process tomography – Implementation for industrial processes* (p. 521). Manchester: University of Manchester Institute of Science & Technology. ISBN: 0-9523165-2-8.

B10. Process tomography world congress (series): 1st:14th–17th April 1999, Buxton, United Kingdom, ISBN: 978-0-853-16317-6; 2nd: 9th–31st August 2001, Hannover, Germany, ISBN: 978-0-853-16318-3; 3rd: 2nd–5th September 2003, Banff, Canada, ISBN: 978-0-853-16319-0; 4th: 5th–5th September 2005, Aizu, Japan, ISBN: 978-0-853-16320-6; 5th: 3rd–6th September 2007, Bergen, Norway, ISBN: 978-0-853-16321-3; 6th: 6th–9th September 2010, Beijing, China, ISBN: 978-0-853-16322-0; 7th: 2nd–5th September 2013, Krakow, Poland, ISBN: 978-0-853-16323-7.

B11. *Chemical Engineering Journal, 77*(Issues 1–2) (2000), 142 (Special Issue).

B12. *Measurement Science and Technology, 15*(7) (July 2004) (Special Issue).

B13. *IEEE Sensors Journal, 5*(2) (April 2005) (Special Issue).

B14. *Chemical Engineering Journal, 130*(2–3) (June 1, 2007) (Special Issue).

B15. *Advances in Chemical Engineering, 37* (2009). ISBN: 978-0-12-374738-9.

This page intentionally left blank

Part One

Tomographic modalities

This page intentionally left blank

Electrical capacitance tomography

1

Q. Marashdeh[1], *F.L. Teixeira*[2], *L.-S. Fan*[2]
[1]Tech4Imaging LLC, Columbus, OH, USA; [2]The Ohio State University, Columbus, OH, USA

1.1 Introduction

Multiphase flow systems are a critical element of many industrial processes as they constitute the medium through which basic ingredients are processed to yield the final product(s). Examples of their use include energy generating processes, food processing, and drug manufacturing, among others. The ability to image multiphase flow interactions in real time has always been a highly desirable capability to further understand the complex dynamics among interacting phases in any flow system. Such understanding is critical, for example, to effectively model, optimize, and scale up the reactors that host the process. From early on, electrical sensing techniques have attracted much attention as a noninvasive means for imaging of multiphase flow systems. In addition, the rates in which phase interactions occur often demand fast imaging modalities, again making electric sensing techniques a natural choice.

Electrical capacitance tomography (ECT) is an electric sensing modality that easily meets the high-speed demands of multiphase flow real-time imaging. ECT has also a noninvasive characteristic, a feature much desired in industrial applications as noted. Interest in using ECT can be traced back to the early 1980s at the U.S. Department of Energy and at the University of Manchester in the United Kingdom. Both institutions deployed capacitance plates around a process column and reconstructed images of phase flow distributions from the measured mutual capacitances obtained from different plate pairs (Huang, Xie, Beck, Thorn, & Snowden, 1992; Xie et al., 1992). The basic system components used for ECT then, and still used today, are a set of capacitance plates constituting the ECT sensor, data acquisition system (DAS) for measuring the mutual capacitance between different plate pairs, and a processing device for image reconstruction and visualization. Each of these individual components has been further developed over the years in terms of both hardware and software capabilities. Most notable are the efforts aimed at developing new imaging reconstruction techniques to extract better images from the limited set of capacitance data (Lionheart, 2001; Marashdeh, Warsito, Fan, & Teixeira, 2006a, 2006b; Yang & Peng, 2003).

Specific applications of ECT include fluidized beds, circulating fluidized beds, pneumatic conveying systems, bubbling beds, trickle beds, and combustion. Favorable features of ECT sensors for these applications are the low profile and, as mentioned before, the noninvasive nature of the sensing apparatus, the fast imaging speed, safety, ease of use, sensor flexibility for fitting around virtually any vessel geometry

Industrial Tomography. http://dx.doi.org/10.1016/B978-1-78242-118-4.00001-0
Copyright © 2015 Elsevier Ltd. All rights reserved.

(including nonstraight cylindrical vessels, T-junctions, L-junctions, etc.), applicability to scale up units, and relatively low complexity and low cost. A present limitation of ECT is the relatively low spatial resolution of the final images compared to some alternative imaging techniques such as MRI or X-rays. ECT is most successful for imaging of low conductivity media. ECT systems operate typically with excitation frequencies below around 10 MHz. This means that for typical industrial size, the field inside the vessels is quasi static and the system is scale invariant in the sense that the field distribution inside a vessel is a solution of Laplace's equation and scales directly with the vessel and sensor size. At these frequencies or lower, ECT sensors can be employed in actual industrial scales for columns up to several meters in diameter or likewise for miniature device applications (Quek, Mohr, Goddard, Fielden, & York, 2010).

In this chapter, the basic operating principles of ECT systems will be discussed and a brief description of available electronic measuring techniques will be presented. Sensor design and its impact on imaging reconstruction will also be reviewed. Finally, some sample results and discussions will be provided to better illustrate ECT value and potential in process applications. The main objective of this chapter is to outline the capabilities and strengths of ECT, and to motivate its use in industrial settings. As such, the technical discussion is kept mostly at an introductory level. Further technical details can be found in the list of references appended to this chapter.

1.2 Principle of operation

The ECT sensing problem corresponds to the reconstruction of the dielectric distribution in an imaging domain from a set of capacitance measurements taken at the domain boundary, that is, from between a set of electrode plates placed around the domain. Figure 1.1 shows a schematic view of the basic components of an ECT, consisting of capacitance sensors, data acquisition electronics, and image reconstruction/visualization software. The capacitive sensors are used here to blanket the region to be imaged with a static electric field, from which sensitivity maps indicate the regions in the imaging domain from where the changes on the mutual capacitances are being affected. The data acquisition electronics measure the capacitance variations as changes in dielectric material distribution that take place inside the imaging domain. The set of mutual capacitance data measured by the acquisition system is one dimensional (1D). Nevertheless, imbedded in such data is the spatial information per the sensor design and relative spatial arrangement among the electrode plates. The reconstruction algorithm essentially aims at decoding such two-dimensional (2D) or three-dimensional (3D) spatial information from the 1D capacitance measurements.

Capacitance sensors can be distributed in one plane for 2D imaging. Such 2D arrangement comprises the majority of ECT systems. In this case, the flow is imaged at a particular cross-section inside a vessel. For 3D or volumetric imaging, variations in

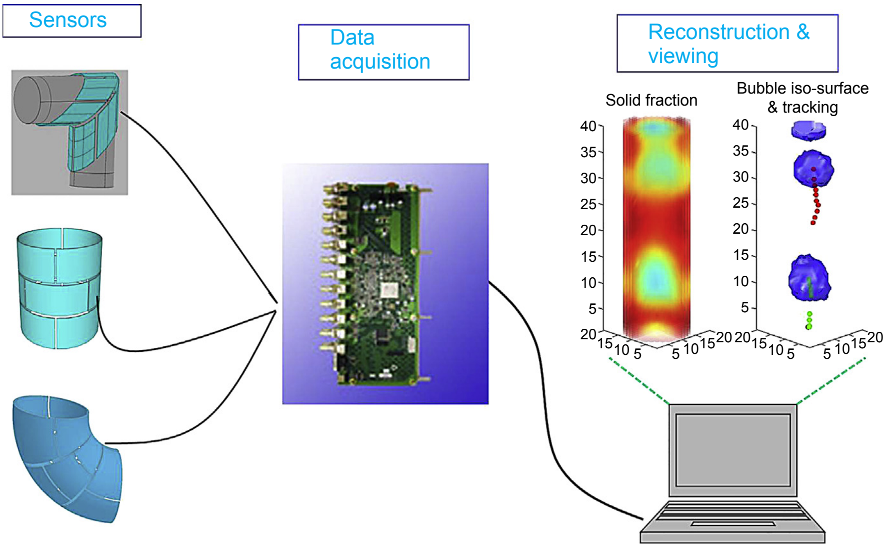

Figure 1.1 Illustration of the basic electrical capacitance tomography (ECT) system components.

sensor sensitivity along the axial direction are introduced either by arranging the plates in multiple planes or by varying plate shapes axially to provide 3D sensitivity. Although a time-varying signal is used for measuring the capacitance between sensor plates, a spatial distribution of the electric field can be assumed to follow that of an electrostatic field. This assumption is valid as long as the employed signal is in the order of a few MHz or less and the characteristic dimensions (e.g., diameter) of the cross-section to be imaged are much smaller than the excitation wavelength. These conditions are met in industrial applications. Following the electrostatic approximation, the dielectric constant distribution and electric field distribution inside the sensor domain are governed by the Laplace equation, which relates the dielectric distribution in the imaging domain to the resulting electric field distribution from a given set of boundary conditions.

The electrical capacitance between a pair of electrode plates is defined as the ratio of increase in stored charge relative to an increase in the voltage difference between said plate pair. The measurement acquisition electronics or the DAS normally employs a fixed-amplitude voltage signal square or sinusoidal in shape, and measures the mutual capacitance through current integration or by directly measuring the current amplitude. The ECT problem then becomes how to determine the dielectric distribution (or, equivalently, the spatial distribution of the various phases in the flow) within the imaging domain given the measured capacitance between all combinations of plate pairs. Plate pairs are considered independent as long as the sensitivity maps they provide are distinct. As will be shown below, the sensitivity maps are directly related to the electric field distribution produced by any pair of plates.

In an ECT sensor, the number of available independent capacitance measurements M is a function of the total number of plates n according to the formula

$$M = \frac{n(n-1)}{2} \tag{1.1}$$

The electric field produced by each plate blankets the imaging domain differently. All capacitance measurements are normalized with respect to the cross-sectional area (or volume) they cover so that they can be used simultaneously for image reconstruction. Different normalization techniques have been developed and described in scientific literature; however, the most accepted are the parallel and series normalization schemes. The parallel scheme assumes that the total capacitance between a pair of plates is the sum of many smaller banks of different dielectric "tubular regions" running in parallel from plate to plate. The normalization in this case is implemented by subtracting the empty cell measurement from the measured capacitance and dividing by the dynamic range between a full and an empty cell. On the other hand, the series normalization scheme assumes a series connection and performs normalization by using the reciprocal of the capacitances.

1.3 Image reconstruction algorithms

In ECT, even though the electric field in the imaging domain obeys the Laplace equation, which is a linear partial differential equation, the inverse problem (i.e., image reconstruction) is inherently nonlinear. The nonlinearity here is a result of the how the quantity to be determined (i.e., the spatial dielectric distribution) enters as a local coefficient in the Laplace equation. In other words, a change in such local coefficient produces a change on the underlying field solution (for a given set of boundary conditions) that does not follow a linear relationship with said coefficient. The accuracy of the final solution for the estimated permittivity distribution is determined by the degree of such nonlinear effects (often referred to as the "soft-field effect" inherent in ECT systems, and absent in "hard-field" tomography techniques such as X-ray), the number of independent capacitance measurements available, and the level of ill-posedness of the inverse problem (i.e., the fact that the number of capacitance measurements is typically much smaller than the number of pixels to be determined). The ill-posedness of the problem also affects how noise and small perturbations on the measured data influence the final solution.

Imaging reconstruction algorithms for ECT can be roughly classified into two main types: algebraic and optimization techniques (Lionheart, 2001; Marashdeh et al., 2006a, 2006b; Yang & Peng, 2003). Both types start first by characterizing the sensor response under small perturbations of dielectric material. This essentially provides an "impulse response" of the capacitance measurements' "sensor output signal" to the dielectric distribution "input signal" under a linear approximation of the problem. For this purpose, the imaging domain is initially divided into small pixels (voxels in the 3D case). Next, the electric field is computed inside the imaging domain when one single plate is excited with a unit potential while the others are grounded (set to zero potential). This process is repeated for all combinations of plate pairs. The "impulse response" or sensitivity matrix is then calculated with elements:

$$\boldsymbol{S}_{ij} = V_{0j}\boldsymbol{E}_{\mathrm{s}i}(x,y,z)\cdot\boldsymbol{E}_{\mathrm{d}i}(x,y,z) \tag{1.2}$$

where $\boldsymbol{E}_{\mathrm{s}i}$ is electrical field distribution at the voxel j location when source plate in pair i is activated with unit voltage and other plates are grounded. Similarly, $\boldsymbol{E}_{\mathrm{d}i}$ is the electrical field distribution produced at voxel j location by the detector plate of pair i activated with unit voltage and when other plates are grounded. V_{0j} is the volume of voxel j.

In summary, Eqn (1.2) provides a linearization of the relationship between the mutual capacitance response to a perturbation on any given pixel permittivity. This is only an approximation because it ignores the nonlinearity caused by the interaction between multiple pixel perturbations at different locations, which also affects the resulting electric field and hence the measured capacitance values. Mathematically, the approximation incurred by the sensitivity matrix in Eqn (1.2) is somewhat akin to that of applying a first-order Born approximation in scattering theory. Results produced by applying the sensitivity matrix in Eqn (1.2) can be accurate as long as the contrast between the permittivity of the different phases is not too high and/or if the fractional volume of the perturbed pixel regions is small.

The sensor response to dielectric distribution can also be considered linear with respect to sensitivity matrix as a first-order approximation. This is equivalent to the solution obtained using linear back projection (LPB):

$$\widehat{\boldsymbol{g}} = \boldsymbol{S}^{\boldsymbol{T}}\boldsymbol{\lambda} \tag{1.3}$$

where $\widehat{\boldsymbol{g}}$ is the image vector (pixel values), $\boldsymbol{S}^{\boldsymbol{T}}$ is the transpose of the sensitivity matrix, and λ is the measured (mutual) capacitance vector. LBP provides a very fast solution, but because it is a linear approximation, it suffers from visible artifacts. Those artifacts are direct results of the "soft-field" (nonlinear) nature of the ECT problem. To reduce such artifacts, iterative algebraic approaches, for example, can be applied to the ECT problem. In those approaches, the resulting image from the LPB solution is solved for the capacitance values of different plate combinations (i.e., forward solution). The discrepancy between the original measured data and the forward solution is then minimized iteratively. This approach yields significant improvements to the image quality. The Landweber algorithm is perhaps the most common type of iterative algebraic reconstruction utilized in ECT. The iteration can be expressed as

$$\widehat{\boldsymbol{g}}_{\boldsymbol{k}+1} = \widehat{\boldsymbol{g}}_{\boldsymbol{k}} - \alpha\boldsymbol{S}^{\boldsymbol{T}}(\boldsymbol{S}_{\widehat{\boldsymbol{g}}\boldsymbol{k}} - \boldsymbol{\lambda}) \tag{1.4}$$

which converges to a stable solution for the image vector if the parameter α is set according to the following constraint:

$$0 < \alpha < \frac{2}{||\boldsymbol{S}^{\boldsymbol{T}}(\boldsymbol{S}_{\widehat{\boldsymbol{gk}}} - \boldsymbol{\lambda})||^2} \tag{1.5}$$

The most straightforward way to solve the forward problem in iterative algebraic techniques is to forward project the resulting image form the last iteration onto the sensitivity matrix. While this method is very fast and convenient (since it utilizes the same sensitivity matrix calculated in advance), it is also limited by the linearization error from representing the soft-field ECT problem using linear superposition of individual perturbation responses (sensitivity matrix). It is possible to increase the accuracy of iterative reconstruction approaches by solving the forward problem using more exact methods such as the finite element methods. However, this strategy incurs significant computational costs that often render it impractical for use in connection with fast acquisitions and real-time imaging applications.

In addition to LBP and iterative algebraic approaches, other image reconstruction approaches are used in ECT, most prominently optimization approaches that combine into an objective function expected image properties such as entropy as a criterion for image reconstruction, in addition to minimizing the iterative error as in iterative algebraic technique. Those techniques assume that there is an inherit limit in reconstructing the ECT image, which can be supplemented by some a priori information about the nature of the desired image. For example, the neural-network multicriteria-optimization image reconstruction technique assumes the desired image as the one that provides the maximum entropy (i.e., image information), least noise (i.e., the objective function includes a smoothness indicator), and also fulfills the iterative minimization of linearized error (Marashdeh et al., 2006b). The difference between these two approaches—optimization and algebraic—is better illustrated through the following example. Considering an ECT sensor with n electrode plates, the signal-to-noise ratio (SNR) and sensitivity of different plate combinations depend on their geometrical arrangement. Since the sensitivity matrix is ill-posed, noise contamination in certain channels will introduce disproportionate artifacts in the final image. Using algebraic techniques, the reconstruction algorithm will show this artifact as it resolves the final image to best match the measured set of capacitances. On the other hand, optimization algorithms would weight this artifact and attempt to assign a degree of likelihood to it. For example, a single pixel with high dielectric value in a surrounding background of low dielectric value would most likely be interpreted as noise, and the algorithm would either ignore it or dilute it. This is implemented in optimization algorithms through the additional set of terms in the objective function that depend on the nature of the final image, in addition to minimizing the error between the measured data and forward solution of the final image. Finally, we note that even for algebraic algorithms it is important to implement regularization techniques to address the ill-posedness of the reconstruction problem. In ECT, this has been achieved with various degrees of success.

1.4 Data acquisition system

As explained above, ECT is concerned with determining dielectric distribution maps in the imaging domain from variations in capacitance signals measured at its boundary. This variation is measured between different pairs of capacitance plates. The DAS is required to record those variations in the presence of parasitic capacitances, which can be many orders of magnitude larger. Parasitic capacitance is the (static) underlying capacitance that exist between the plates used for measurement, or between each plate and its surroundings (ground), and which does not contribute to the varying component being measured. Stray capacitance, on the other hand, is inherent capacitance in the ECT system that is not related to the domain of geometry between the capacitance sensor plates. Stray capacitance is related to coupling between sender/receiver plate paths to the ground. This coupling includes capacitance of cables that connect the DAS to the sensor plates and capacitance between plates and grounded shield. Stray capacitances can also be many orders of magnitude higher than the capacitance variations being measured.

A basic requirement of any good DAS design is the automatic rejection of stray capacitances. Two basic circuit configurations are typically adopted for ECT sensor systems: charge−discharge and AC-based designs (Huang et al., 1992; Yang & York, 1999). Both DAS designs rely on amplifying the current through the capacitance sensor plates while automatically rejecting stray capacitance. From the sender plate side, the stray capacitance is in parallel to the capacitance-measuring circuit, and, as a result, the current it pulls is diverted from passing through the interplate (desired) capacitive path. Similarly, the stray capacitance on the receiver side is in parallel to the input port of the operational amplifier (op-amp) used to amplify the output current coming out of the detector plate. The op-amp has an input voltage difference of virtual zero. The shunt connection of stray capacitance before and after the targeted interplate capacitance makes the current passing to the op-amp a function of interplate capacitance only. For the charge/discharge design, the relation between output of the op-amp voltage and interplate capacitance can be written as

$$V_{\mathrm{out}} = 2KfV_{\mathrm{c}}C_{\mathrm{x}}R_{\mathrm{f}} \tag{1.6}$$

where K is a gain factor, f is operating frequency, V_{c} is source voltage, C_{x} is capacitance to be measured, and R_{f} is the value of the feedback resistor. The main disadvantage of the charge−discharge circuit is that it relies on CMOS switches for switching, which have large capacitance values compared to C_{x}.

As for the AC-based circuit, the interplate capacitance is found from

$$V_{\mathrm{out}} = -\frac{C_{\mathrm{x}}}{C_{\mathrm{f}}}V_{\mathrm{i}} \tag{1.7}$$

where C_{f} is a feedback capacitor for the op-amp and V_{i} is the input excitation voltage. This equation is an approximation that assumes a high-frequency excitation in the

1−10 MHz range and appropriately selected values for the feedback capacitor and resistor. AC-based circuit designs provide higher SNR compared to charge−discharge at the expense of increased circuit complexity.

The output voltage from both types of circuits varies depending on the flow dynamics between plates and the consequent change in dielectric distribution. The output signal is commonly amplified using programmable gain amplifiers (PGAs) and digitized using analog-to-digital (ADC) converters. Those two steps usually happen in sequence. The PGAs amplify the weak signals to boost their SNR while keeping them within the range of ADCs. PGA values are determined experimentally by a calibration process where the sensor is examined in its full and empty domain states. The full state represents the highest anticipated readings from the sensor inter-plate combinations and is used to set the PGAs to their maximum gain within the range of ADC. The empty state is used as a floor reference for a later normalization process.

In any ECT sensor, the sensitivity map produced by different pairs of electrode plates depends on the relative distance and angular positioning between the pair. For image reconstruction purposes, the intensity of all plate combinations are "normalized" with respect to overall sensor response so they can be used more uniformly across different sensor deployments. Some normalization strategies have been discussed in Section 1.2 above in relation to the capacitance measurements, and, similarly, different normalization approaches are applied to aid in the image reconstruction process. All these normalization strategies require a measurement of all sensor plate combinations when the sensor is full with dielectric material and when it is empty. The simplest and most commonly used capacitance normalization is

$$\tilde{C}_{ij} = \frac{C_{ij} - C_{ij}^{(\mathrm{e})}}{C_{ij}^{(\mathrm{f})} - C_{ij}^{(\mathrm{e})}} \tag{1.8}$$

where the tilded (normalized) capacitance value refers to the variable actually employed in the reconstruction algorithm, and the superscripts (e) and (f) refer to capacitance values with empty and full vessels, respectively.

1.5 Electrical capacitance volume tomography

In conventional ECT applications, the capacitance sensors are designed to surround the 2D imaging domain (vessel cross-section) by means of electrode plates that are symmetrically distributed and equally spaced. The electrode plates are also desired to be of substantial axial length to acquire data with high SNR and reduce the asymmetry of the electric field distribution along the axial direction. The axial asymmetry arises from fringing field effects at the upper and lower edges of activated plates. Since conventional ECT is used for 2D imaging, such fringing effect is viewed as distortion to the desired sensor sensitivity distribution and efforts are made to minimize it. Because of this, elongating the electrode plates along the axial direction is the simplest and most widely used technique to reduce fringing effect.

ECT sensors can also be used to produce quasi-3D images by placing two rows of ECT sensors vertically above each other to acquire two simultaneous 2D images. The quasi-3D image is then formed by interpolating the 2D images into one continuous 3D image. Another technique uses time division of a single sensor to achieve the same goal. In such arrangements, successive 2D images acquired by an ECT sensor over a period of time are interpolated to again form a quasi-3D image (Banasiak, Wajman, Betiuk, & Soleimani, 2009). Similar strategies have been successfully used in other hard field imaging modalities as well. However, those techniques pose a challenge in ECT due both to the considerably longer electrodes (and hence the longer 2D "image averaging lengths") and soft-field nature of capacitance measurements.

A technique for capacitance electrode design was devised recently that, instead of attempting to mitigate fringing field effects, *exploits* such effects between capacitance plates and volumetric arrangements thereof to construct sensitivity maps that yield inherent 3D features (Warsito, Marashdeh, & Fan, 2007; Li & Holland, 2013). The overall sensor in this case is designed with electrode plates of various shapes, ensuring that the aggregate sensitivity map covers a volume and at the same time exhibits sufficient sensitivity variations along the x-, y-, and z-axes. Since the term *3D capacitance tomography* is normally used to refer to 3D or quasi-3D imaging by interpolating successive 2D images as discussed above, the term *electrical capacitance volume tomography* (ECVT) is used to refer to such direct 3D imaging using 3D capacitance sensors. Figure 1.2 depicts various sensor designs that exhibit 3D features.

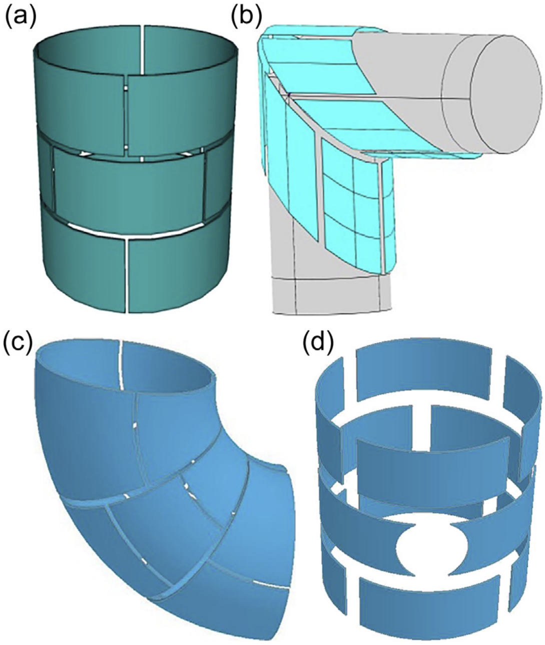

Figure 1.2 Various electrical capacitance volume tomography (ECVT) sensor designs: (a) cylinder, (b) sharp bend, (c) duct, and (d) side injection.

Case A provides 3D sensitivity distribution by arranging the plates in a staggered fashion across successive planes. Cases B and C use irregular column shapes to provide sensitivity distributions with exploitable 3D features. Note that these cases also use plates of different shapes and sizes. Case D has a geometrical arrangement similar to Case A, but with an inserted circular hole at one side to accommodate a side flow injection, as opposed to a predominant axial flow. As it can be easily surmised from this figure, ECVT sensors provide substantially more flexibility in plate arrangements, plate shape, and geometric conformality to more general column (vessel) shapes and topologies such as L-junctions and T-junctions.

ECVT sensors also natural allow for more independent capacitance channels to be used and hence yield higher spatial resolution. For example, in 2D ECT it is observed that the use of more than 12 capacitance plates around the cylindrical cross-section provides diminishing returns for imaging resolution. This is due in part to the restriction on capacitance plate shapes on the circular boundary and on the decrease on the SNR for each channel when more plates are used (more plates require less area and hence smaller overall capacitances and output signals). In contrast, there is considerably more flexibility in the geometrical distribution of the plates of an ECVT sensor as well as on the ability to choose plates with virtually any 2D shape. It was indeed verified experimentally that this added flexibility provided room for obtaining substantial resolution improvements in ECVT when using more than 12 channels (Wang, Marashdeh, Teixeira, & Fan, 2014). Figure 1.3 depicts an experimental result illustrating the improvement in resolution that can be obtained in ECVT by increasing the number of channels from 12 to 24. The design depicted in Figure 1.2, Case A, corresponds to a 12-channels ECVT sensor. A similar design can be adopted for a 24-channel sensor by building the sensor with four planes having six plates in each plane. Both 12-channel and 24-channel sensors were designed to cover the same volume, and two spheres filled with sand were used to test the resolution capability of each sensor. Figure 1.3(a) is a schematic of the objects under imaging, that is, two adjacent balls of different size in a uniform background. Figure 1.3(b) shows the imaging result when using the 12-channel sensor, while Figure 1.3(c) shows the result for the 24-channel sensors. It is clear from these results that using a 24-channel ECVT sensor provides better spatial resolution versus a 12-channel ECVT sensor. Similar experiments were conducted using both sensors and arrived at a similar conclusion (Wang et al., 2014).

Figure 1.4 depicts sensitivity map distributions for two pairs of plates in 12-channel and 24-channel ECVT sensors. The sensitivity maps in Figure 1.4(a) and (b) correspond to pairs of plates in the same plane for the 12-channel and 24-channel cases, respectively. On the other hand, the sensitivity maps in Figure 1.4(c) and (d) correspond to pairs of plates between the first and third rows of the 12-channel and 24-channel sensors, respectively. Both sets of figures provide a qualitative assessment of the increase in resolution due to the increase in number of plates in ECVT sensors. In particular, this can be seen from Figure 1.4 as the volume encapsulated by the isosurfaces becomes narrower in the case of a 24-channel sensor. This narrowing of the sensitivity maps reflects the ability to provide more independent channels and hence an overall better resolution irrespective of the reconstruction algorithm to be utilized.

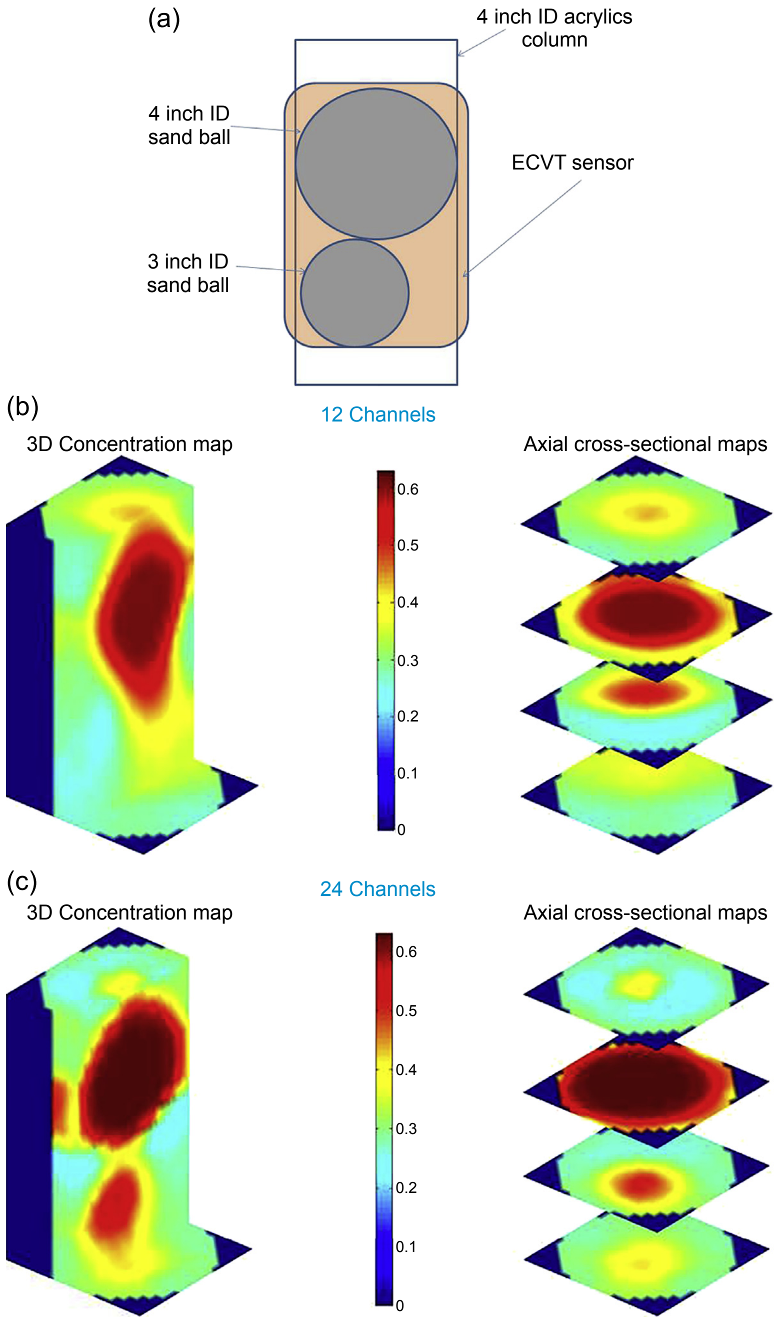

Figure 1.3 Comparison of resolution quality for (a) two balls of different sizes in a uniform background, using electrical capacitance volume tomography (ECVT) sensors with (b) 12 and (c) 24 channels (plate electrodes) (Wang et al., 2014).

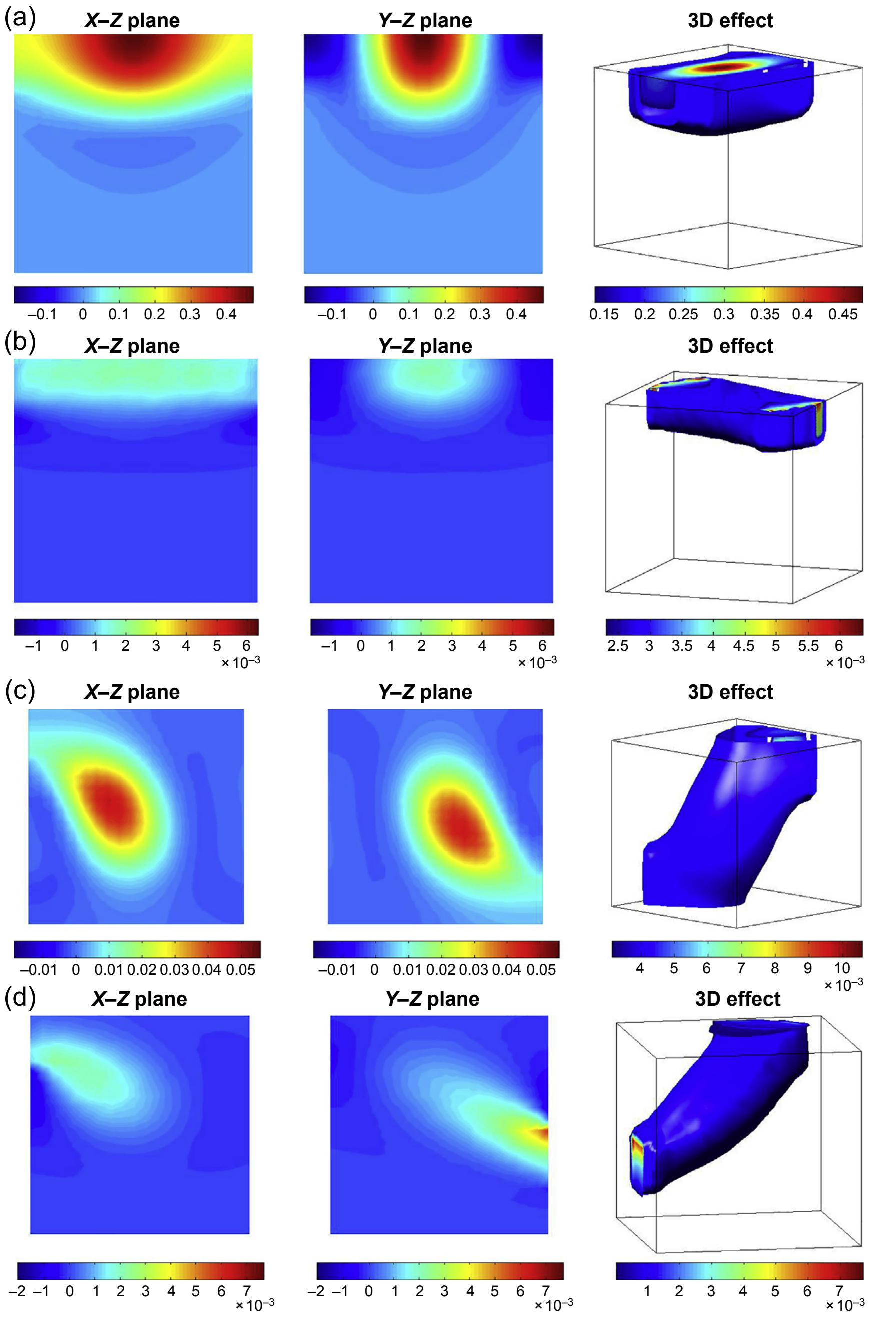

Figure 1.4 Isosurface volume images of sensitivity distribution between selected electrical capacitance volume tomography (ECVT) sensor plates for the 12-channel sensor (a, c) and the 24-channel (b, d) sensor (Wang et al., 2014).

1.6 Illustrative examples and discussion

The value of ECT in process tomography is better illustrated through examples that demonstrate feasibility of the technology in real applications. This section will present some results obtained from ECVT sensors as they correspond to state-of-the-art applied ECT technologies.

The first example is taken from Weber, Layfield, Essendelft Van, & Mei (2013) and provides a comparison between results obtained from computational fluid dynamics (CFD) simulations versus those from ECVT imaging for a 4″ ID column of glass bead particles. The CPFD™ software *Barracuda version 15.0.3* was used to carry the CFD simulations; in this case (Snider, 2007; O'Rourke & Snider, 2012) ECVT sensors were used on a column with the same dimensions as the simulated case (Weber et al., 2013). Figure 1.5 depicts solid fraction results using different simulation models. The last column in this figure presents the ECVT results. More details on the experiment, as well as further discussions and results, are found in Weber et al. (2013). This experiment shows that ECVT can be a valuable guiding tool to selecting/using the proper simulation model for a given set of experimental conditions.

Figure 1.6 builds on results from the previous figure to determine the appropriate simulation model for comparing real-time results of void fraction and bubble formations using ECVT. This figure shows that ECVT results are able to capture the bubble formation process and the amount of void fraction around the bubbles with very good agreement against the simulation results.

CFD simulations are carried out based on assumptions related to the process under investigation. They can provide invaluable information if executed properly, however, using them for validation can only be justified when the experimental

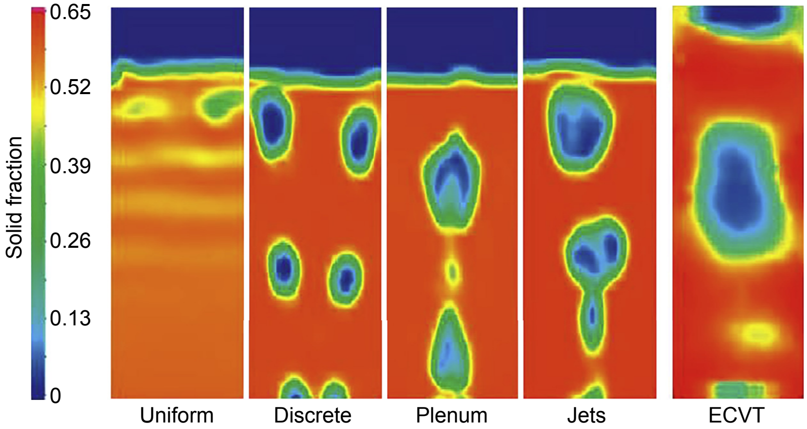

Figure 1.5 Comparison between various computational fluid dynamics (CFD) simulation models and electrical capacitance volume tomography (ECVT) for a solid fraction snapshot inside a cylindrical vessel with gas flow.

Figure reproduced from Weber et al. (2013), with permission from Elsevier.

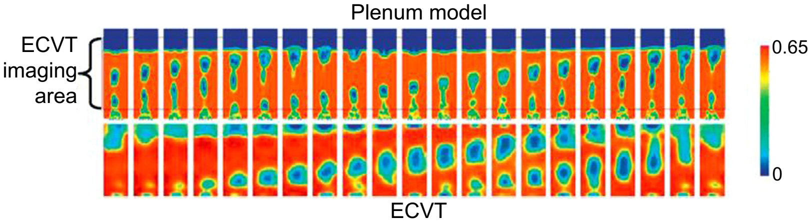

Figure 1.6 Plenum computational fluid dynamics (CFD) simulation model compared to electrical capacitance volume tomography (ECVT) imaging results.
Figure reproduced from Weber et al. (2013), with permission from Elsevier.

conditions are well matched to the assumptions made in the simulation model. An alternative approach for assessing ECVT results is to use another, established imaging technology that has a quantifiable resolution. Magnetic resonance imaging (MRI) in particular has been used extensively in the medical field and has demonstrated an impressive capability to resolve fine details. Recently, MRI has found applications in process tomography in laboratory settings as well (Holland et al., 2009), although some of the important disadvantages of MRI in this case are the relatively high cost and much bulkier equipment, as well as less suitability for high-speed, real-time applications. Nevertheless, the high resolution of MRI makes it an ideal candidate for ECVT validation. A recent study compared fluidized bed results of a 2″ ID column using ECVT and MRI (Holland et al., 2009). The experiments were conducted using each imaging technology independently, but under similar operating conditions. As noted before, ECVT sensors are mostly made of conductive metallic plates. This is a limitation in MRI as metals should be commonly avoided around high intensity magnets. Figure 1.7 is reproduced from Holland et al. (2009) and depicts the ECVT sensor design used in this experiment. Figure 1.7(b) shows a direct qualitative comparison between ECVT and MRI results through a vertical cross-section of the volume image obtained using each technology. This figure shows clearly that while ECVT can detect voids (bubbles), their location, and size, it has less spatial resolution compared to MRI. Recalling the results presented in Figure 1.3, one would expect that ECVT can provide better resolution if a 24-channel sensor were to be used instead of the 12-channel sensor actually utilized in this study. However, it is expected that ECVT still would fall short compared to MRI in capturing the very fine details of the flow structure. For example, the MRI result was able to detect the wake of the bubble rising in the surrounding solid phase, a feature that cannot be well captured by ECVT even when utilizing a 24-channel sensor. A more quantitative comparison is provided in Figure 1.7(c). Here, the void fraction, as measured by each of the two imaging techniques, is plotted across the diameter of the sensing region. One can see clearly that while both technologies predict accurately the void fraction amplitude, the ECVT results (dashed lines) are a smoothed version of the MRI results (solid lines).

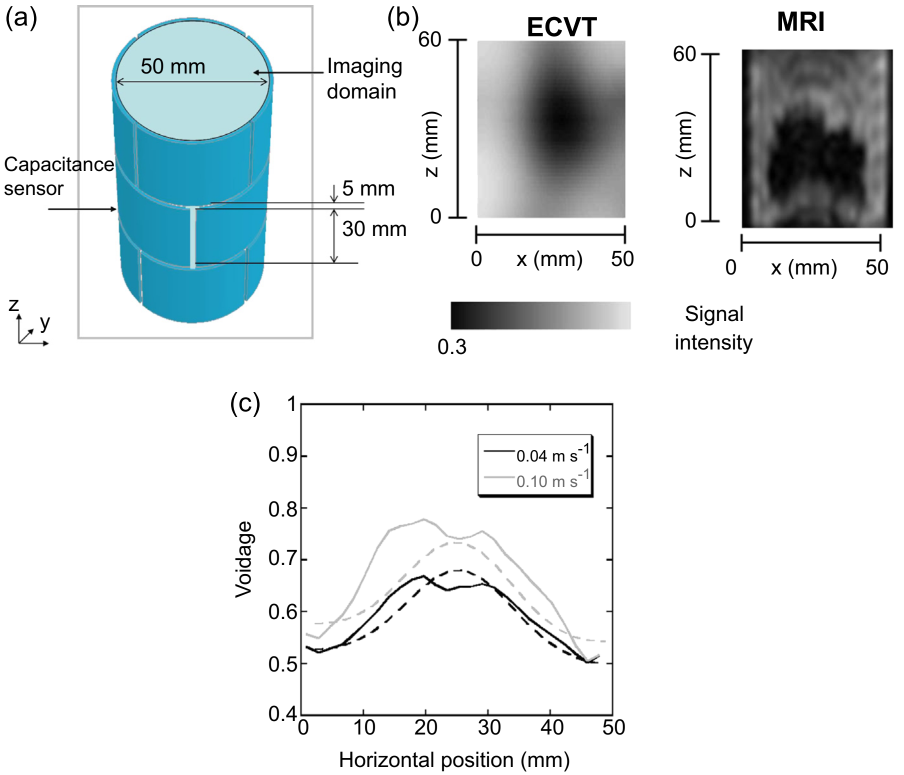

Figure 1.7 A comparison between electrical capacitance volume tomography (ECVT) and MRI results. (a) ECVT sensor design. (b) Vertical cross-section of imaged bubble. (c) Voidage distribution across imaging domain for ECVT and MRI results, for two flow speeds. The dashed lines refer to ECVT results and the solid lines to MRI results.
Reprinted (adapted) with permission from Holland et al. (2009), Copyright (2009) American Chemical Society.

The results illustrated here highlight some of the attractive features of ECT that make it suitable for many industrial applications. To summarize, the main attractive features of ECT sensor technology include:

- It operates by noninvasive means.
- It can produce imaging (frame) rates in the hundreds of frames per second, thus enabling high-speed real-time measurements of fast reactions and physical flow processes.
- It is safe and nonionizing.
- It is scale invariant, so that the same basic sensor arrangements and imaging reconstruction algorithms can be used equally well in scale-up or scale-down applications.
- It is geometrically flexible, and ECVT sensors in particular can be designed to fit around virtually any shape.
- It can be installed and operated at a relatively low cost compared to other imaging technologies.

However, one major disadvantage of ECT/ECVT is its low spatial resolution versus some other modalities such as MRI, as illustrated in Figure 1.7. Recall that the limitation in the spatial resolution of ECT stems from two basic reasons. First, ECT sensors provide only a limited number of independent measurements, far below the number of unknown variables (i.e., pixels) necessary for high-resolution imaging. This makes the ECT/ECVT problem highly ill-conditioned if higher resolution is required. Secondly, ECT belongs to the "soft-field" category of tomography modalities, wherein the field solution is a nonlinear function on dielectric distribution in the imaging domain, and the inverse problem (of determining the dielectric distribution from the capacitance measurements) is also inherently nonlinear.

As discussed before, a basic factor that limits the number of independent capacitance measurements in ECT and ECVT is the fact that measured capacitance variations in flow systems are typically very small, and there is a need for a minimum electrode plate area to provide sufficient SNR for the output signal. This minimum area requirement sets up a limit on the maximum number of plates for any given vessel size. A recent advancement in ECVT sensor design geared toward mitigating the limited number of independent measurements from a capacitance sensor has been the development of adaptive electrical capacitance volume tomography (AECVT), which lifts the limitation on the number of independent measurements by creating synthetic shapes from very small, individual plate segments (Marashdeh, Teixeira, & Fan, 2014). In other words, in AECVT each conventional capacitance plate is replaced by an adaptive plate composed of many smaller segments each with a separate signal acquisition circuitry. Such segments can each be activated with different voltage levels. The aggregate voltages on all activated segments form a synthetic plate with a voltage envelope based on activation chosen for each segment. New independent measurements can thus be obtained by changing the synthetic plate activation, that is, either the voltage envelope or the choice of activated segments, while keeping the minimum area requirement in place for any (synthetic) plate. It is clear that many different choices exist for yielding synthetic plate with a multitude of geometries, including noncontiguous shapes. The principle of AECVT is illustrated in Figure 1.8, where Figure 1.8(a) depicts a conventional ECVT sensor and Figure 1.8(b) depicts an adaptive ECVT sensor made of many small segments (Marashdeh, Teixeira, et al., 2014). The different colors in the selected segments of the adaptive sensor reflect different voltage activation levels.

AECVT requires an acquisition circuit that can accommodate an increased number of segment electrodes and the overall increase in complexity in the sensor design. In AECVT, the aggregate current from the receiver plate is a summation of intercapacitance interaction between each of the selected (activated) segments and receiver plate. Consequently, the current measured at the receiver plate side using a current-to-voltage amplifier is equivalent to the current produced by the mutual capacitance interaction from a conventional capacitance plate of equivalent shape but with a (spatial) weight provided by the given voltage envelope distribution. Further details on the AECVT technique can be found in (Marashdeh, Teixeira, et al., 2014).

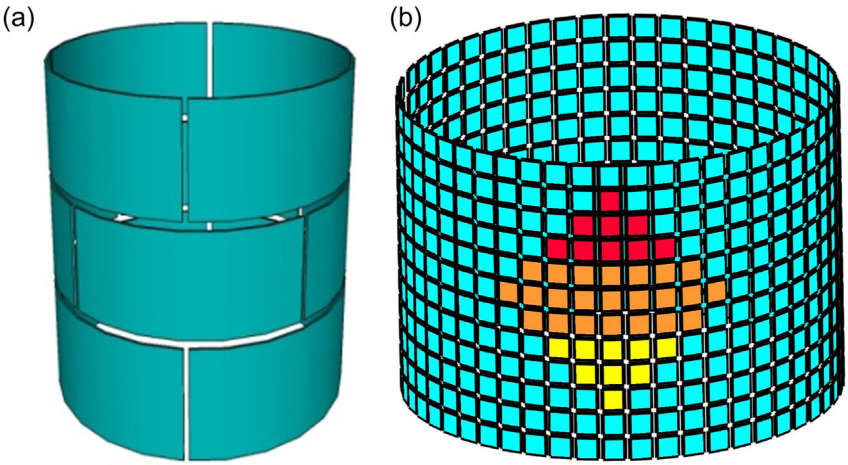

Figure 1.8 Schematic representations of (a) conventional electrical capacitance volume tomography (ECVT) sensor and (b) adaptive ECVT sensor. Copyright 2014 IEEE. Reprinted, with permission, from Marashdeh, Teixeira et al. (2014).

1.7 Conclusions

In this chapter, we have discussed the basic principles of ECT and described the favorable features that make it suitable for flow process tomography applications, including the industrial setting. The basic architecture of an ECT system can be broken down into three main components: the sensing electrodes composed of capacitive plates placed around the domain to be sensed, the data acquisition system and the image reconstruction software. Recent advances in sensor design have enabled direct volume imaging through the suitable distribution of the capacitance plates around a 3D domain, embodied in ECVT systems. Currently, AC-based data acquisition constitutes the most common type of circuit used for capacitance measurements due to its superior performance compared to the more traditional charge–discharge model. We have also discussed practical examples of the application of ECT in industrial settings and its most recent developments, embodied in ECVT and AECVT systems.

1.8 Future trends

Image reconstruction techniques represent an active area of research in ECT, and different algorithms have been introduced over the years with varying degrees of success. Ongoing research is aimed at improving reconstruction techniques for ECT, ECVT, and AECVT.

In practice, ECT systems are primarily applied for imaging of permittivity distributions in flow systems involving low conductive materials, but in principle they can also be exploited for conductivity imaging in dual-modality systems (Marashdeh, Warsito, Fan, & Teixeira, 2008).

AECVT is a recently introduced advance in ECT aimed at improving the resolution obtained in conventional ECT and ECVT by allowing for much larger independent channel measurements to be produced (and hence reduce the ill-posedness of the image reconstruction problem in ECT) through the use of electronically configured, synthetic plates. It is likely that the capabilities opened up by AECVT will lead to new research venues in terms of tailored reconstruction techniques to obtain better images with increased resolution. Finally, AECVT also opens up new capabilities in terms of dual-use electrode plates that may act either as sender/receiver plates for the capacitance signals or as active control guards to modify the sensitivity pattern inside the imaging domain and increase the ultimate resolution capabilities (Marashdeh, Fan, Teixeira, & Zeeshan, 2014).

Acknowledgement

Support from the U.S. Department of Energy is gratefully acknowledged.

References

Banasiak, R., Wajman, R., Betiuk, J., & Soleimani, M. (2009). A new application area for 3D ECT in non-destructive evaluation of dielectric materials. In *3rd International Workshop on Process Tomography, 2009-04-17-2009-04-19, Tokyo*.

Holland, D. J., Marashdeh, Q., Muller, C. R., Wang, F., Dennis, J. S., Fan, L.-S., et al. (2009). Comparison of ECVT and MRI measurements of voidage in a gas-fluidized bed. *Industrial & Engineering Chemistry Research, 48*, 172−181.

Huang, S. M., Xie, C. G., Beck, M. S., Thorn, R., & Snowden, D. (1992). Design of sensor electronics for electrical capacitance tomography. *IEE Proceedings G Circuits, Devices and Systems, 139*(1), 83−88.

Li, Y., & Holland, D. J. (2013). Fast and robust 3D electrical capacitance tomography. *Measurement Science and Technology, 24*, 105406.

Lionheart, W. R. B. (2001). Reconstruction algorithms for permittivity and conductivity imaging. In *Proc. 2nd World Congress Industrial Process Tomography, Hannover, Germany* (pp. 4−11).

Marashdeh, Q., Fan, L.-S., Teixeira, F. L., & Zeeshan, Z. (2014). *Active control guards and rationometric calibration and reconstruction for use with electrical capacitance volume tomography*. International Patent Application PCT/US14/38032.

Marashdeh, Q., Teixeira, F. L., & Fan, L.-S. (2014). Adaptive electrical capacitance volume tomography. *IEEE Sensors Journal, 14*(4), 1253−1259.

Marashdeh, Q., Warsito, W., Fan, L.-S., & Teixeira, F. L. (2006a). Nonlinear forward problem solution for electrical capacitance tomography using feed-forward neural network. *IEEE Sensors Journal, 6*(2), 441−449.

Marashdeh, Q., Warsito, W., Fan, L.-S., & Teixeira, F. L. (2006b). Nonlinear image reconstruction technique for ECT using a combined neural network approach. *Measurement Science and Technology, 17*(8), 2097−2103.

Marashdeh, Q., Warsito, W., Fan, L.-S., & Teixeira, F. L. (2008). Dual imaging modality of granular flow based on ECT sensors. *Granular Matter, 10*, 75−80.

O'Rourke, P. J., & Snider, D. M. (2012). Inclusion of collisional return-to-isotropy in the MP-PIC method. *Chemical Engineering Science, 80*, 39−54.

Quek, S., Mohr, S., Goddard, N., Fielden, P., & York, T. (2010). Miniature electrical tomography for micro-fluidic systems. In *Proc. 6th World Congr. Ind. Process Tomography, Beijing, China* (pp. 1320−1326).

Snider, D. M. (2007). Three fundamental granular flow experiments and CPFD predictions. *Powder Technology, 176*(1), 36−46.

Wang, A., Marashdeh, Q., Teixeira, F. L., & Fan, L-S. (2014). Electrical capacitance volume tomography: a comparison between 12- and 24-channels sensor systems, submitted for publication.

Warsito, W., Marashdeh, Q., & Fan, L.-S. (2007). Electrical capacitance volume tomography. *IEEE Sensors Journal, 7*(4), 527−528.

Weber, J. M., Layfield, K. J., Essendelft, Van, D. T., & Mei, J. S. (2013). Fluid bed characterization using electrical capacitance volume tomography (ECVT), compared to CPFD software's barracuda. *Powder Technology, 250*, 138−146.

Xie, C. G., Huang, S. M., Hoyle, B. S., Thorn, R., Lenn, C., & Snowden, D. (1992). Electrical capacitance tomography for flow imaging: system model for development of image reconstruction algorithms and design of primary sensor. *IEE Proceedings G Circuits, Devices Systems, 139*(1), 89−98.

Yang, W. Q., & Peng, L. (2003). Image reconstruction algorithms for electrical capacitance tomography. *Measurement Science and Technology, 14*, 4−7.

Yang, W. Q., & York, T. A. (1999). New AC-based capacitance tomography system. *IEE Proceedings - Science, Measurement and Technology, 146*(1), 47−53.

This page intentionally left blank

Electrical impedance tomography

2

M. Wang
University of Leeds, Leeds, West Yorkshire, UK

2.1 Introduction

A variety of types of electrical tomography have evolved since the late 1980s (Bates, McKinnon, & Seagar, 1980; Dines & Lytle, 1981; Lytle & Dines, 1978) to provide alternative, low-cost solutions for clinical, geophysical and industrial process applications. Sensing techniques based on, for example, electrical impedance acquired from the boundaries of process equipment enable the possibility of a low-cost, safe and fast imaging (1000 images per second) instrumentation (Wang et al., 2005; Wilkinson et al., 2005). The first clinical frontal plane electrical impedance imaging technique was proposed by Swanson in 1976 (Swanson, 1976). Henderson, Webster, and Swanson (1976) and Henderson and Webster (1978) designed an 'impedance camera' based on the principle of X-ray transmission imaging. In operation, a large electrode was placed on the chest, which resulted in varying currents being collected through a 100-electrode array on the back (Webster, 1990). However, the spatial resolution from the camera was lower than that in X-ray transmission since the current flow in body tissues is not confined to a direct path between the transmitter and the receiver (Brown, Barber, & Freeston, 1983). Brown et al. proposed a tetrapolar-based measurement strategy for electrical impedance tomography in 1983 and refined it in 1985 (Brown et al., 1983; Brown & Barber, 1985). This strategy is well known in electrical impedance tomography (EIT) and is referred to as the adjacent electrode or neighbouring pair's strategy. The first commercial EIT for medical research was reported in 1987 and was referred to as the Sheffield APT (applied potential tomography) system (Brown & Seagar, 1987), and then the first commercial EIT for process application was launched in 1997 and was referred to as the Manchester system (Boone, Barber, & Brown, 1997; Wang, Dickin, & Beck, 1993). It was also called electrical resistance tomography (ERT) in process tomography since the early work only measured the resistance components. A number of EIT systems in various forms were developed over the past three decades. Some of them are given in Table 2.1, showing the development of EIT at its early stage in biomedical research and for process engineering in the past (Boone et al., 1997).

The goal of EIT is to obtain the impedance distribution in the domain of interest. The impedance distribution can be obtained by injecting currents or applying voltages to the domain and measuring voltages or currents via a number of electrodes that are mounted nonintrusively but invasively on the boundary of the domain. An accurate and stable data acquisition system (DAS) used for this purpose is a basic necessity, which incorporates signal sources, two multiplexer arrays for applying current

Industrial Tomography. http://dx.doi.org/10.1016/B978-1-78242-118-4.00002-2
Copyright © 2015 Elsevier Ltd. All rights reserved.

Table 2.1 **Electrical impedance tomography (EIT) at its early stage for biomedical research and development for process engineering**

Authors	Institution	System name	Applied areas	Design frequency	Frame speed	Excitation
Brown and Seagar (1987)	University of Sheffield	Mark I	Biomedical	50 kHz		Floating current
Brown et al. (1994)	University of Sheffield	Mark III	Biomedical	9.6 kHz−1.2 MHz		Dual currents
Wilson et al. (2001)	University of Sheffield	Mark III.5	Biomedical	2 kHz−1.6 MHz	25 fps	Floating current
Lidgey et al. (1992)	Oxford Brookes University	OXPACT-II	Biomedical	9.6 kHz		Constant voltage
Zhu, McLeod, Denyer, Lidgey, and Lionheart (1994)	Oxford Brookes University	OXBACT-III	Biomedical	10−160 kHz		Multiple currents
Newell et al. (1988), Gisser et al. (1991), Cook et al. (1994)	Rensselaer Polytechnic Institute	ACT-III	Biomedical	30 kHz	480 fps	Multiple currents
Wang et al. (1993)	University of Manchester	MARK I-b	Process engineering	1.2−72.8 kHz	20 fps	Dual currents
Ma et al. (2003), Wang et al. (2005), Schlaberg, Jia, Qiu, Wang, and Li (2008)	University of Leeds	FICA	Process engineering	10−320 kHz	1000 dfps	Dual currents
Jia et al. (2010)	University of Leeds	Voltage-applied ERT	Process engineering	10 kHz	300 dfps	Dual voltages
Cilliers et al. (2001), Wilkinson et al. (2005)	University of Manchester, University of Cape Town		Process engineering	12 µs pulse/64 µs circle	1000 fps	Bipolar DC current pulse

or voltage and measure voltage or current, respectively, voltmeters or signal demodulators, and a system controller. Such complexity is necessary due to the low amplitude of measurements at the boundary, which are in the order of mV; the small responses of the dynamic change, which are in the order of μV; the large number of electrode channel operations − a minimum of 104 times for sequential measurements from 16 electrodes; and the high common voltages, which are in the order of V. This chapter will address the basic principles and elementary functions of EIT systems, providing inside knowledge of EIT.

2.2 EIT sensor

A typical EIT sensor consists of a set of equally spaced electrodes mounted around the periphery of a circular process vessel, in contact with the process fluids inside the vessel. In principle, electrodes could be spread out to any distance and the process vessel could be in any shape depending on the processing domain and imaging sensitivity of interests. The sequence and combination of the measuring electrodes depend on the kind of measurement protocol used, for example, the adjacent electrode pair strategy (Brown & Barber, 1985; Seagar, Barber, & the Brown, 1987). In the adjacent electrode pair strategy, the mutual impedance of the measuring electrode pair is obtained by injecting current to a pair of electrodes and taking voltage measurement from other pairs of electrodes. To adapt the specific conditions in process application, the geometric locations of electrodes and the strategy of sensing should be carefully selected. Figure 2.1 gives an overview of specific sensors for various applications (Wang, 2005a). Figure 2.1(a) shows an eight-plane sensing array for visualisation of a large-scale mixing process (Mann et al., 1996a; Wang, Mann, & Dickin, 1996). A total of 128 stainless steel electrodes of 4 × 10 cm in size were installed on the nonconductive inner wall of a 3-m^3 mixing tank with a diameter of 1.5 m. Figure 2.1(b) shows a sensor for metal-walled containers or pipeline (Wang, Dickin, & Williams, 1994, 1995), which has been proved to be a very fruitful approach (Aw, Rahim, Rahiman, Yunus, & Goh, 2014; Yuen, Mann, York, & Grieveet, 2001). A ‘single-electrode’ sensor (such as a conductive ceramic ring shown in Figure 2.1(c)) was invented to replace the multiplicity of discrete electrodes used in conventional EIT sensors for measurement of stratified flows in horizontal pipelines (Wang & Yin, 2002; Wang, Yin, & Holliday, 2002). The significance of this sensor development is that for the first time a simple electrode can sense complex flows including multiphase mixtures containing stratified gas−water (Wu, Li, Wang, & Williams, 2005) or oil−water flows (Li, Wang, Wu, Ma, & Williams, 2005). Sensor designs suited to the various specific applications are demonstrated in Figure 2.1(d)−(f), including the miniature sensor (Figure 2.1(d)) for the measurement of flow dynamics in an upwards slurry flow and the linear electrode array (Figure 2.1(e)) for the visualisation of mixing process in a pharmaceutical process based on a linear sensor developed for the measurement of sub-seabed porosity (Qiu, Dickin, James, & Wang, 1994). A similar sensor layout has also been used for the measurement of sediment and sedimentation in a storage

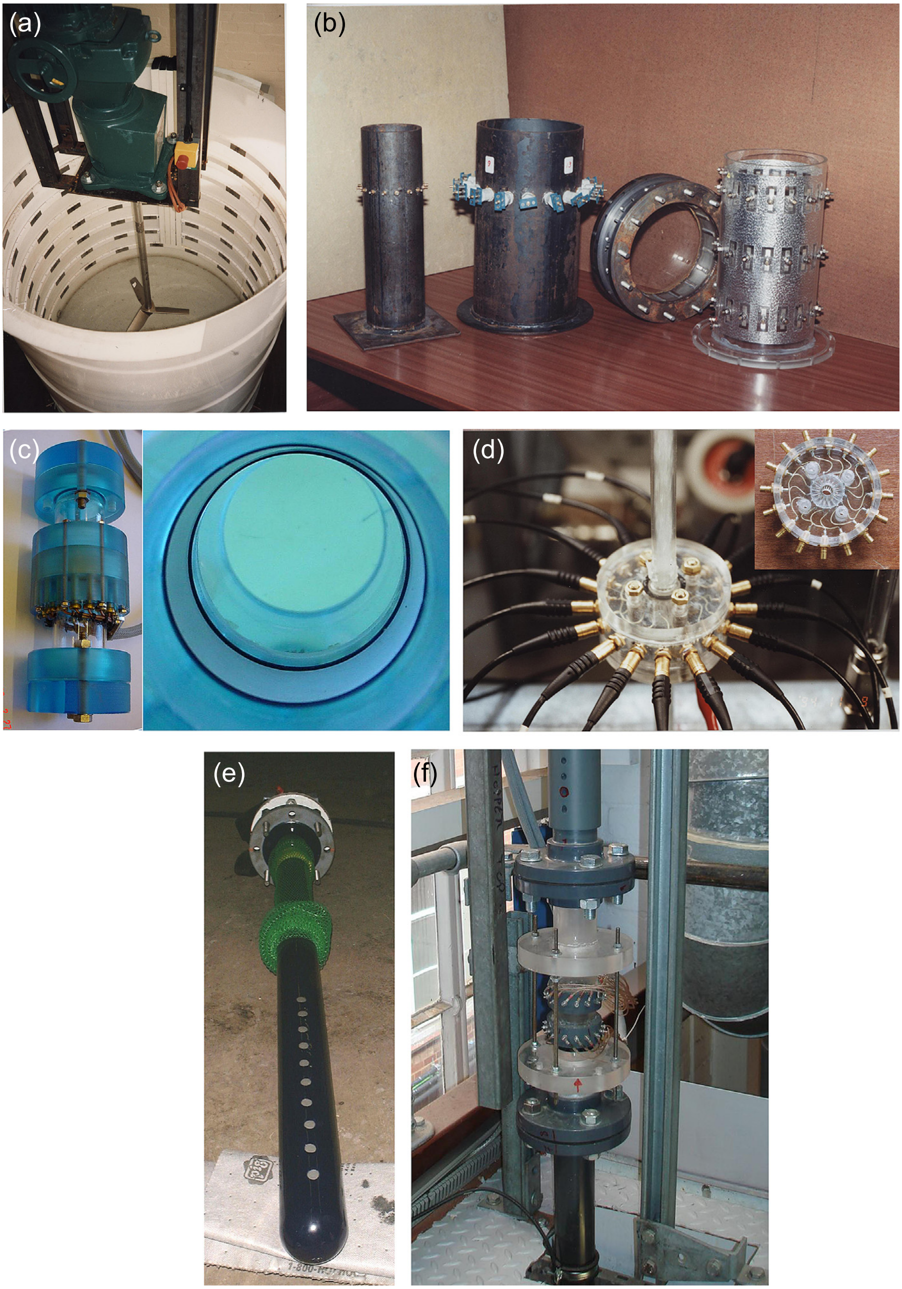

Figure 2.1 Electrical impedance tomography (EIT) sensors in various applications: (a) large-scale mixing (ϕ1500 mm), (b) metal-walled vessels and pipeline (ϕ155 mm), (c) conductive ring sensor (diam. ϕ50 mm), (d) miniature slurry pipeline (ϕ6 mm), (e) linear probe for mixing process (provided courtesy of ITS) and (f) solid−water flow pipeline (ϕ50 mm).

tank (Cullivan et al., 2005). Figure 2.1(f) shows a dual-plane sensor for measurement of both flow concentration and velocity distributions (Faraj & Wang, 2012; Wang, Jones, & Williams, 2003). Other specific sensors were also reported, e.g. the cross-plane sensor combined with both perpendicular and axial sensing planes for characterisation and control of bubble columns (Vijayan, Schlaberg, & Wang, 2007), the U-shaped sensor for the measurement of the transit dynamics in an open channel flow (Schlaberg et al., 2006) and the parallel-bar linear sensor developed for the visualisation of fluid passage in a heap leaching process (Hurry, Wang, Williams, Cross, & Esdaile, 2004). The variety of EIT sensor configurations has demonstrated its excellent adaptability and applicability for process application (Kaipio, Seppänen, & Somersalo, 2005; Ruzinsky & Bennington, 2007; Schlaberg, Wang, Qiu, & Shirhatti, 2005).

The most important issues in EIT sensor design are the materials and the size of electrodes. Other important factors in the selection of materials for electrodes in an EIT sensor are the electrical conductivity, effect of electrochemical polarisation, capability of anticorrosion and erosion, hygiene rate and capabilities for fabrication, depending on the specific requirements in applications. The effect of the overpotential presented at the electrode—electrolyte interface due to different materials is less important in an EIT sensor since alternating current (AC) coupling circuits are used in most process EIT systems. Stainless steel is the most available material for electrode fabrication, but other metallic materials, such as gold, silver, platinum and silver palladium, can also be used (Dickin & Wang, 1996). In a specific case, conductive ceramic, rubber or plastic materials can be considered. Electrodes in an EIT sensor have two functions, injecting current and measuring voltage. The size of electrode is more important in the function of current injection than it is in measurement, mainly as the common voltage created in measurement is inversely proportional to the size of electrodes used for current injection. Equation (2.1) provides a simple relationship between the bulk resistance and the size of electrode, which can be used to estimate the common voltage drop on the electrode simply following Ohm's law. Supposing the surface of a metal electrode in contact with the conductive medium is hemispherically shaped and the radius of the process vessel is far larger than that of the hemisphere, the bulk resistance can be estimated as (Weinman & Mahler, 1964)

$$R_{\mathrm{b}} = \frac{1}{2\pi\sigma\, ap}\ (\Omega) \tag{2.1}$$

where a denotes the radius of a hemispherically shaped electrode in contact with a conductive medium, and the bulk resistance, R_{b}, is bulk resistance derived based on Ohm's law. Equation (2.1) can be extended to encompass other shapes of electrode by employing a shape and surface-texture multiplication factor p ($p = 2$ for a metal sphere, 1 for a hemisphere and 0.6 for a flat-cut disk-shaped electrode) (Weinman & Mahler, 1964). It should be particularly noticed that the change ratio of the bulk resistance is proportional to the change ratio of the dimension (not to the area), and, therefore, a current change in proportion to the dimension will produce the same potential at the electrode after change (not to the current density).

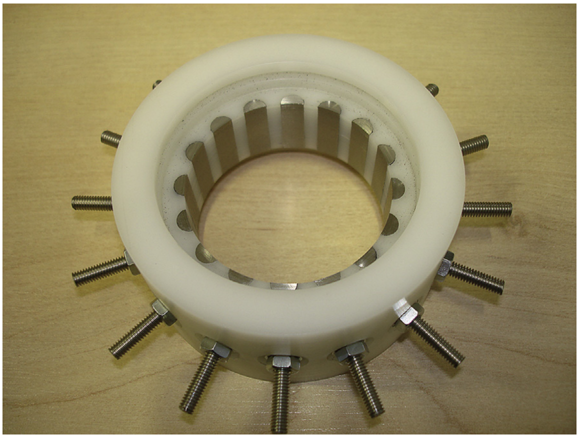

Figure 2.2 An electrical impedance tomography (EIT) sensor for flow measurement.

Due to the limited common voltage rejection ratio of sensor electronic circuit (60—80 dB), a large common voltage may greatly affect the measurement sensitivity. Therefore, it is expected that the size of the current injection electrode should be sufficiently large to reduce the voltage drop between the electrode and electrolyte. In contrast, the current absorbed by modern sensor electronics via a measurement electrode is very tiny and thus the voltage drop between the measurement electrode and electrolyte can be ignored. Therefore, measurement electrodes can be made as small as a needle to enhance their spatial sensitivity. Ideally, the electrodes in an EIT sensor could be in the form of either 'compounded' — a measurement electrode with insulation in the centre of a current injection electrode — or 'interleaved' — both electrodes in an interleave arrangement (Hua, Woo, Webster, & Tompkins, 1993; Paulson, Breckon, & Pidcock, 1992). Dickin and Wang (1996) summarised the variety of electrode designs and commonly acceptable electrode configurations with the same electrode for both functions in most EIT sensors in process engineering applications. As an example, a well-designed and manufactured EIT sensor for pipeline flow measurement is given in Figure 2.2.

2.3 Electrode modelling

The electrode used in EIT is a transducer that converts the electronic current in a wire to an ionic current in an electrolyte. The behaviour at the electrode—electrolyte interface is a predominantly electrochemical reaction. A metal electrode immersed in an electrolyte is polarised when its potential is different from its open-circuit potential (Weinman & Mahler, 1964). The difference between the open-circuit potential V_e (equilibrium potential) and the actual potential V is the overpotential, η, relating the net current density, j, of the electrochemical reaction to the overpotential of the

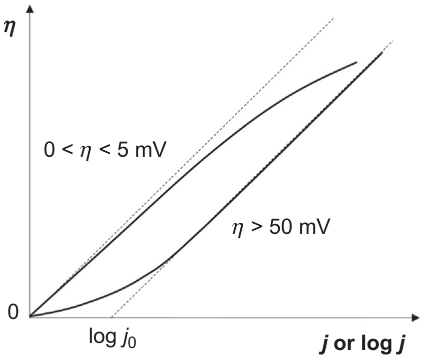

Figure 2.3 The relation between overpotential and current density. According to Bockris and Drazic (1972).

Butler—Volmer equation as described by Eqn (2.2) and illustrated in Figure 2.3 (Bockris & Drazic, 1972):

$$j = j_0\{\exp[(1-\beta)F\eta/GT] - \exp[(-\beta F\eta/GT)]\} \ (\mathrm{A/cm^2}) \tag{2.2}$$

where j_0 is the exchange current density and a function of the electrode—electrolyte system and, to a limited extent, of the surface structure of the metal. As an example, for a platinum electrode immersed in 75 Ω cm resistivity saline, j_0 is in the order of 5×10^{-5}A/cm^2 (Pollak, 1974b), F is the Faraday constant (96,500 C/mol), G is the gas constant (8.317 J/K/mol), T is the temperature in Kelvin (298 K at room temperature) and β is a factor close to 0.5 related to the electrical energy in the passage of the ion across the electrode—electrolyte interface (Bockris & Drazic, 1972).

For small overpotentials (-5 mV $< \eta <$ 5 mV) the relation between overpotential and current density is linear as given by Eqn (2.3) and illustrated in Figure 2.3. The limits of linearity in Eqn (2.2) are typically reached at current density levels of up to 1 mA/cm^2 when a direct current is applied (Schwan & Ferris, 1968; Weinman & Mahler, 1964). When overpotentials are greater than 50 mV or less than -50 mV, the relation to current density is described by Eqn (2.4) as shown in Figure 2.3:

$$\eta = \frac{GT}{j_0 F} j \ [\mathrm{V}] \tag{2.3}$$

$$\eta = a + b \ln j \ \ (\mathrm{V}) \tag{2.4}$$

where $a = -\frac{GTj_0}{(1-\beta)F}; \ \ b = \frac{GT}{(1-\beta)F}.$

By analogy with Ohm's law ($V = IR$) the gradient of the η—j line in Figure 2.3 can be interpreted as the equivalent resistance per unit area, R_C, of the charge-transfer process on the electrode as given in Eqn (2.5) and which is called the charge-transfer resistance for small overpotentials:

$$R_C = \frac{\partial\eta}{\partial j} = \frac{GT}{j_0 F} = \frac{E_T}{j_0} = \frac{0.026}{j_0} \quad \left(\Omega\ \mathrm{cm}^2\right) \tag{2.5}$$

where E_T is called the temperature voltage. Its value at room temperature is approximately 0.026 V.

Geddes, Costa, and Wise (1971) reported that when current density was increased up to 25 mA/cm^2, a definite nonlinear behaviour was observed during his experiments at frequencies from 20 Hz to 10 kHz, which resulted in considerable distortion of the applied sine wave.

Both theory and experiment confirm that the amount of charge stored in the region where the metal electrode is in contact with the electrolyte varies as a function of the potential difference across it (Bockris & Drazic, 1972; Crow, 1974). A simple model of the double layer was suggested by Helmholtz and Perrin at the end of the nineteenth century (Bockris & Conway, 1969; Bockris & Reddy, 1970). This represents the double layer in terms of the simple plates of a capacitor's point of view. The metal electrode, with its excess charge, forms one side of the double layer, and the electrolyte, with its excess countercharge, forms the other side of the double layer. Of course, there is no real plate on the electrolyte side, but it is imagined that the excess charges in the electrolyte make up a layer of charge just as if they were attached to a plate there (Bockris & Drazic, 1972). The Helmholtz double-layer capacitance, C_H, is given by

$$C_H = \frac{dq_m}{dV} = \frac{\varepsilon_r\varepsilon_0}{\delta^H} \quad \left(\mu\mathrm{F/cm}^2\right) \tag{2.6}$$

In Eqn (2.6), q_m is the excess charge on the metal electrode, V is the potential across the double layer, ε_0 is the permittivity of a vacuum (8.85×10^{-8} μF/cm), ε_r is the relative permittivity of the material between the plates and δ^H is the effective distance between the plates (e.g. δ^H in water is around $2.8\ \mathrm{E} \times 10^{-8}$ cm) (Bockris & Drazic, 1972). In reality, however, the double-layer capacitance is not constant with potential, and, for most electrode systems of practical importance, the capacitance in the absence of larger externally applied potential differences can be estimated as about 10 μF/cm^2 (Pollak, 1974a) or 15.9 μF/cm^2 (Bockris & Drazic, 1972) irrespective of the ratio of the ions (Bockris & Reddy, 1970).

The Gouy–Chapman diffuse model (Bockris & Drazic, 1972) may present a better description of the double-layer structure, in which it was assumed that there would be no 'sticking' of ions to the electrode and no contact adsorption, and suggested a diffuse charge model as an addition to the Helmholtz theory. The diffuse capacitance is given in Eqn (2.7) by Crow (1974).

$$C_G = \varepsilon_r\varepsilon_0\kappa = \frac{\varepsilon_r\varepsilon_0}{\delta^G} \quad \left(\mu\mathrm{F/cm}^2\right) \tag{2.7}$$

where $1/\kappa$ is the effective radius of the ion atmosphere, here it is identified with δ^{G} the diffuse length of double layer.

The total capacitance of the double layer, C, is made up of C_{H} from the inner (adsorption) layer and C_{G} from the diffuse layer. It is assumed that these capacitances are connected in series:

$$\frac{1}{C}=\frac{1}{C_{\mathrm{H}}}+\frac{1}{C_{\mathrm{G}}} \quad \text{or} \quad C=\frac{C_{\mathrm{H}}C_{\mathrm{G}}}{C_{\mathrm{H}}+C_{\mathrm{G}}} \tag{2.8}$$

Consequently, if the electrolyte solution is very dilute, $C_{\mathrm{G}} \ll C_{\mathrm{H}}$, then $C \approx C_{\mathrm{G}}$. The double layer is now essentially all diffuse, which is the Gouy—Chapman diffuse model. On the other hand, when the solution is very concentrated, $C_{\mathrm{G}} \gg C_{\mathrm{H}}$, then $C \approx C_{\mathrm{H}}$, which satisfies Helmholtz's earliest model of the double layer.

An equivalent circuit of the electrode—electrolyte given by Pollak (1974b) is shown in Figure 2.4. The total impedance is made up of the interface, the diffusion and the inner resistance, which are connected in series.

The response of the diffusion layer to an AC current injection was given as (Cobbold, 1974)

$$|Z_{\mathrm{D}}| \approx \frac{E_T}{z^2 c_0 F\sqrt{2\pi D}}\,\frac{1}{\sqrt{f}}\ \ (\Omega\ \mathrm{cm}^2) \tag{2.9}$$

where E_T is the temperature voltage (0.026 V), F the Faraday constant (96,500 C/mol), D the diffusion coefficient (cm^2/s), z the charge-transfer number and c_0 the concentration of the electrolyte under equilibrium conditions (mol/cm^3).

For typical electrolyte in process applications, e.g. NaCl solution, the diffusion coefficient is in the order of 1.5×10^{-5} cm^2/s and a charge-transfer number in the order

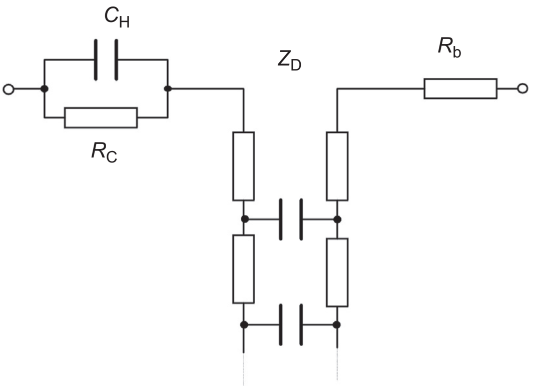

Figure 2.4 Equivalent circuit of the electrode—electrolyte impedance. R_{C} is the charge-transfer resistance, C_{H} is the Helmhotz double-layer capacitance, Z_{D} is the diffusion-layer impedance and R_{b} is the bulk resistance of the electrolyte.
According to Pollak (1974b).

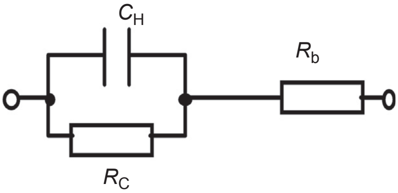

Figure 2.5 Equivalent circuit of the electrode–electrolyte impedance ignoring the diffusion effect.

of 0.4 as concentration is below 0.2 mol/L (Conway, 1952). With these parameters the equation yields

$$|Z_D| \approx \frac{7 \times 10^{-5}}{c_0\sqrt{f}} \quad \left(\Omega\ \text{cm}^2\right) \tag{2.10}$$

The expression given by Eqn (2.1) can be employed down to frequencies where the diffusion length δ^G becomes comparable with the electrode diameter d (Pollak, 1974a):

$$\delta^G = \sqrt{\frac{D}{2\pi f}} < d \quad (\text{cm}) \tag{2.11}$$

$$f > \frac{D}{2\pi d^2} \approx \frac{8 \times 10^{-6}}{d^2} \quad (\text{Hz})\ (d \text{ in units of cm}) \tag{2.12}$$

For the instance of a concentration 1×10^{-5} mol/cm^3 at a frequency 100 Hz, $|Z_D| = 0.7\ \Omega\ \text{cm}^2$ obtained from Eqn (2.10).

Combining all of the above analyses, the total impedance, Z, of the electrode–electrolyte, at very low frequencies, is approximately equal to the diffusion-layer impedance Z_D (Cobbold, 1974; Pollak, 1974b):

$$Z \approx Z_D \propto \frac{1}{\sqrt{f}} \quad \left(\Omega\ \text{cm}^2\right) \tag{2.13}$$

and at very high frequency:

$$Z \approx R_b + \frac{1}{j\omega C_H} \quad \left(\Omega\ \text{cm}^2\right) \tag{2.14}$$

In the majority of applications, the effect of the diffusion layer can be ignored in order to simplify the solution (Cobbold, 1974; Pollak, 1974a). The simplified equivalent circuit is given as in Figure 2.5.

Only electrode modelling with respect to electrochemistry was discussed in the section. Electrode modelling with respect to electrode size and its relation to the electrical field and boundary voltage as well as to common voltage were also discussed (Wang, 2005b).

2.4 Signal sources

Excitation signals in alternative waveforms (AC) have great advantages in reducing the effect of electrode polarisation, isolating the direct current (DC) offset potential (e.g. the overpotential), which are used in most current EIT systems. Signals in sinusoidal waveform provide an access to full electrical impedance demodulation and, further, a capability to carry out spectroscopic measurement.

The bidirectional DC pulse excitation was initially used in geophysical tomography (Ronald et al., 1993), where a high voltage (about 100 V) and slow measurement speed (in minutes per frame) are normally used. Recently, a number of bidirectional pulse excitation-based systems for both medical and process applications were developed (Cilliers, Xie, Neethling, Randall, & Wilkinson, 2001) due to the advantage of its simple electronic construction. A recent report indicates it has achieved 1000 frames per second of data acquisition rate (Wilkinson et al., 2005). The system has been demonstrated to work well with a pair of narrow (12 μs) bidirectional current pulses when the medium is assumed to be purely resistive. However, it may not be able to measure, in its current form, both real and imaginary components. With regard to EIT instrumentation simplification, a bipolar DC pulse method would greatly simplify instrumentation as compared to sinusoidal waveform techniques if the targeted fluids of interest can be considered to be a resistive medium, where phase angles do not have to be considered (van Weereld, Collie, & Player, 2001; Wilkinson et al., 2005).

Monolithic function generators were initially used to generate a sinusoidal waveform but were soon replaced by digital forms of ‘staircase’ sinusoidal function in EPROM-based look-up tables, which also provide synchronous sampling signals for demodulation. A quartz-crystal-driver counter is used to clock a stored staircase waveform out of the table repetitively, then convert it to an analogue signal and subsequently filter to remove unwanted harmonics (Brown & Seagar, 1985; Dickin & Wang, 1996; Wang, 1994). More capable monolithic function generators based on direct digital synthesis (DDS) of a sinusoidal waveform were used (Ma & Wang, 2004) when specific waveform generators were widely commercially available (Analogue Device, 1995).

There is a long-standing use of current sources as the excitation source in EIT (Brown & Seagar, 1985; Dickin & Wang, 1996). The simplest form of current source is shown in Figure 2.6. The single operational amplifier (op-amp) is arranged in an inverting configuration with the load in the feedback path. Since the gain of an ideal op-amp is considered to be infinite, the inverting input is at virtual earth potential, and, because very little current enters this input, the load current is simply the input voltage divided by the input resistor (Etuke, 1994). The major drawback of this circuit is that it cannot be used in applications with an earthed load or for systems with more than one current source since the output current may not be the same as the input current. In addition, a single current source will generate a high common voltage. Consequently, various designs for float current sources or balanced bipolar current sources were developed to overcome this inherent problem and also to maintain a constant output amplitude over a wide range of load impedances

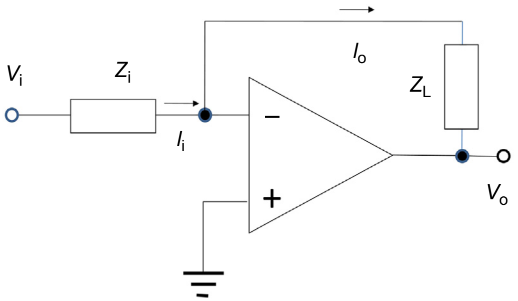

Figure 2.6 One amplifier negative feedback current source.
Dickin, F. J., & Wang, M. (1996). Electrical resistance tomography for process applications. Measurement Science and Technology IOP, 7, 247–260, IOP.

encountered in different process applications. The dual op-amp design developed and shown in Figure 2.7 (Dickin & Wang, 1996; Wang et al., 1993) was based on a positive feedback architecture of Howland's circuit. The bandwidth and current amplitude of the voltage controlled current source (VCCS) extends linearly from 75 Hz to 153.6 kHz and the adjustable peak-to-peak current amplitude from 0 to 30 mA, respectively. In addition, the output impedance of the VCCS stage is 2.5 MΩ at 76.8 kHz, falling to 1.74 MΩ at 153.6 kHz.

The output admittance and load current of the circuit in Figure 2.7 are given by Eqns (2.15) and (2.16):

$$G_{\text{out}} = \frac{1 - [1 + (Z_2/Z_1)]/[1 + (Z_3/Z_4)]}{R} \tag{2.15}$$

$$I_L = \frac{V_1 Z_2}{R Z_1} \tag{2.16}$$

Bragos, Rosell, and Riu (1994) described a wide-band AC coupled current source that overcomes the problem of saturation at the output DC blocking capacitor. Their solution employs a DC feedback loop in conjunction with a current-sensing VCCS

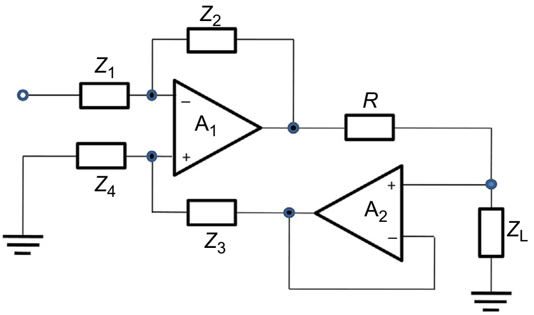

Figure 2.7 The dual operational amplifier positive feedback VCCS.

built around a commercially available current feedback amplifier (AD844). The reported output current up to ±10 mA and impedances of their circuit are 6.9 M at 100 kHz, falling to 0.3 M at 1 MHz. To increase the output current, a parallel structure consisting of eight AD844 to constitute four pairs of a bi-direction VCCS was developed and is shown in Figure 2.8 (Wang et al., 2005). Two inverting inputs of each pair of AD844s are cascaded together with a current-setting resistor *R*. The positive and negative current outputs of each pair are summed together to form larger current outputs. Two inverse-phased sine-wave voltage inputs are buffered and then connected to the noninverting input of each AD844, where two capacitances *C* and two resistances *r* with time constant *RC* can restore the DC components generated in the circuit and then cancel the DC offset at the current outputs. The total output currents can be estimated using Eqn (2.17). The $\pm I_{\text{out}}$ have an ideal 180° phase difference with negligible DC biasing, and their amplitudes can be easily balanced with the potentiometer, Rp. The maximum output current amplitude of this circuit is 40 mA. Its output impedance was approximated as 0.75 MΩ//18 pF (Wang et al., 2005):

$$\pm I_{\text{OUT}} = \pm 8 \times V_{\text{SIN}}/(2 \times R_{\text{IN}} + R) \tag{2.17}$$

To implement a high specification current source, particularly with high output impedance and large current at high frequency, is still challenging. In contrast, a precise voltage source is generally easier and also less complicated and lower cost in its implementation (Hartov, Demidenko, Soni, Markova, & Paulsen, 2002). The key issue is that the actual current must be known in order to obtain the impedance being measured. Jia, Wang, Schlaberg, and Li (2010) developed a voltage-drive EIT system, in which two power amplifiers (OPA549) are used to deliver a stable bipolar voltage excitation and a current-sensing transform is connected to the voltage output in series for sensing the actual current flow. At the time of applying the voltage source, the current and differential response voltages from electrodes are simultaneously measured to calculate the trans-impedance

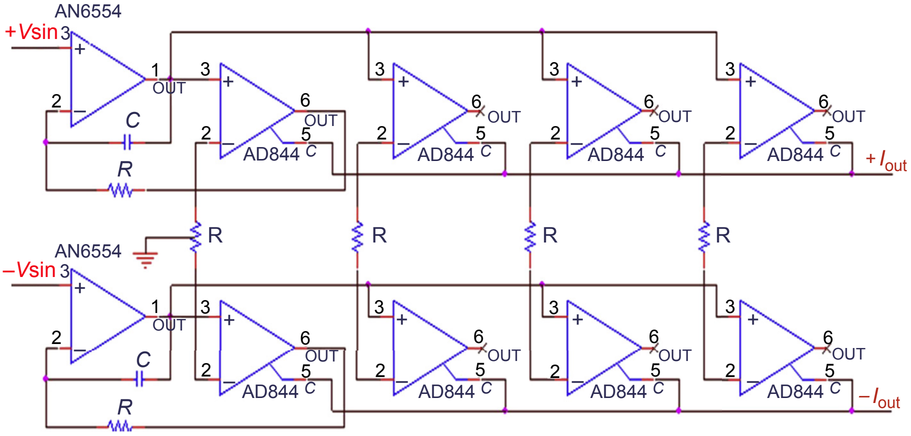

Figure 2.8 Voltage-controlled bipolar current source.

across the whole sensing domain. The voltage excitation can supply bipolar current up to ±320 mA at a frequency of 10 kHz. It has far fewer requirements for a high specification of the amplifiers in comparison with a constant current source since both the voltage and current on the load are measured at the same time and the resultant measurement is in trans-impedance.

2.5 Sensing strategies

In EIT, the boundary conditions required to determine the impedance distribution in a domain of interest comprise the injected currents via electrodes and subsequently measured voltages, also via boundary electrodes. A number of excitation and measurement methods or sensing strategies have been reported since the late 1980s. In 1976, Henderson and Webster applied a constant 100 kHz voltage to a large electrode on a patient's chest, which resulted in varying currents collected through a 100-electrode array on the back. All electrodes, except for the measuring electrode, were maintained at 0 V, which directly resulted in an impedance map. This was an early attempt to produce an impedance image of the human chest, however, not the tomography in theory (Webster, 1990). Lytle and Dines (1978) applied stepped voltages to all electrodes that would produce a uniform current distribution in a homogeneous media. They measured the resulting currents at all electrodes and repeated the procedure from several angular directions, which was the first attempt to utilise the tomography technique for electrical impedance imaging. The adjacent electrode pair strategy for EIT was proposed in 1983 (Brown et al., 1983) and refined in 1985 (Brown & Barber, 1985; Brown & Seagar, 1985). With the adjacent pair strategy, current was applied between adjacent electrode pairs and voltages measured between every other pair of adjacent electrodes (Figure 2.9(a)). The adjacent electrode pair strategy is now widely used due to the high signal-to-common voltage ratio, high number of independent measurements and simplicity of hardware and software implementation. Hua, Webster, and Tompkins (1987) used the opposite method of data collection as shown in Figure 2.9(b). The main difference between the adjacent electrode pair strategy and the opposite electrode pair strategy is that, in the latter, currents are injected between diametrically opposite electrode pairs rather than between adjacent electrode pairs. They expressed the reason for this simple modification was to enable a relatively higher current density to flow through the centre of the vessel and, therefore, expected the imaging sensitivity at the centre could be improved. Gisser (1987) proposed the adaptive current strategy where almost any desired current distribution can be obtained by injecting current of appropriate magnitude through all the electrodes simultaneously and measuring voltages between these electrodes and a single grounded electrode (see Figure 2.9(c)). It was expressed that this method yields the optimal distinguishability and is the most versatile method of data collection (Webster, 1990). Applying a conventional approach to a conducting walled vessel would result in the excitation currents being of limited use due to both the shunting effect of the conducting wall and the distortion of the electric field distribution. The key step to

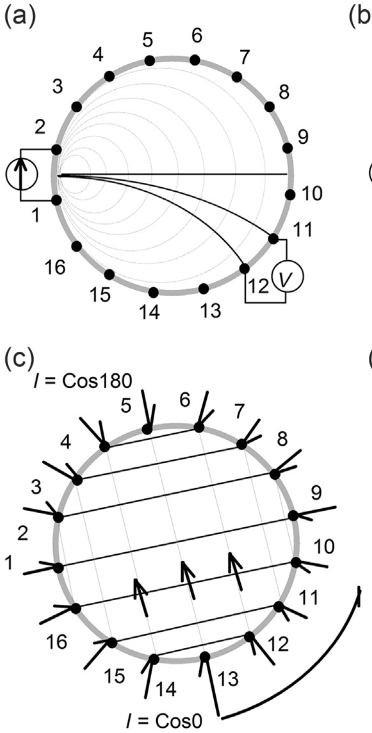

Figure 2.9 A variety of sensing strategies (the dotted line denotes current stream lines and the solid line denotes equal potential lines): (a) adjacent electrode pair strategy, (b) opposite electrode pair strategy, (c) adaptive current strategy and (d) metal wall strategy.

developing a sensing strategy for a metal-walled vessel was based on the concept of utilising the shunting effect of the metal wall for the measurement (Wang et al., 1994, 1995). In the strategy, the current is injected from one electrode and withdrawn from the whole metal wall. An example of the sensor utilising this concept is given in Figure 2.9(d).

The principle of measuring electrical impedance is simply based on Ohm's law by applying a known voltage or current and measuring the response of current through, or voltage across, two points (or via two electrodes) of the target, respectively. The response voltages or currents are also measured from other pairs of electrodes of an EIT sensor. The resultant impedance is called mutual impedance as the different electrode pairs are used for the excitation and measurement. Geselowitz (1971) and Lehr (1972) derived the lead theorem from the divergence theorem and stated that the mutual impedance change ΔZ for a four-electrode system is the same as expressed by Eqn (2.18) for connections illustrated in Figure 2.9, where V_{CD} and V_{AB} are voltages at two ports (C–D and A–B) in response to the presence of currents I_{AB} or I_{CD} at two ports (A–B and C–D), respectively. The lead theorem was later linearised by Murai and Kagawa

(1985) and utilised by Wang (2002) for tomographic imaging. Equation (2.18) is also known as the reciprocity theorem:

$$\Delta Z = \frac{V_{CD}}{I_{AB}} = \frac{V_{AB}}{I_{CD}} \tag{2.18}$$

Based on the reciprocity theorem, for a two-port/four-terminal static impedance system as given in Figure 2.10, the voltage measurements, V_{CD} and V_{AB}, are the same if the values of the currents remain the same in both Figure 2.10(a) and (b), which can be expressed by Eqn (2.19) and leads to identifying the independent data sets from a measurement system with multiple electrodes:

$$\text{If } I_{AB} = I_{CD} \text{ then } V_{CD} \equiv V_{AB} \tag{2.19}$$

Applying the reciprocity theorem as given by Eqn (2.19), the number of independent measurements from an EIT sensor with 16 electrodes in the use of the adjacent electrode pair method is given by Eqns (2.20) or (2.21), which are 120 or 104, depending on those measurements from electrodes involved with or without current excitation. Ignoring the measurements from current drive electrodes, the number of independent measurements is 104, 96 and 120, with respect to Figure 2.10(a), (b) and (d):

$$N_{\text{meas}} = \frac{N_{\text{electrode}}(N_{\text{electrode}} - 1)}{2} \tag{2.20}$$

$$N_{\text{meas}} = \frac{N_{\text{electrode}}(N_{\text{electrode}} - 3)}{2} \tag{2.21}$$

where N_{meas} refers to the number of independent measurements and $N_{\text{electrode}}$ denotes the number of electrodes in the sensor. Equation (2.21) is employed in most systems to avoid measurements affected by the electrode—electrolyte interface.

A typical measurement data set captured from a miscible liquid mixing process with the P2 + EIT system (Industrial Tomography Systems) is given in Figure 2.11, which well illustrates the format of the 104 independent measurements, where the horizontal index indicates the pair of electrodes for measurement and the vertical index indicates the pair of electrodes for current injection. A graphic plot of the data set is shown in Figure 2.12, which reveals the high dynamic range feature of these measurements.

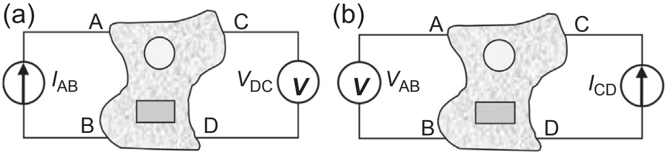

Figure 2.10 Two-port impedance system with the exchange of excitation and measurement positions: (a) original connection (b) with the exchange.

Current injection pairs	Voltage measurement pairs														Measurement set
	02–03	03–04	04–05	05–06	06–07	07–08	08–09	09–10	10–11	11–12	12–13	13–14	14–15	15–16	
16–01	4.741e+002	1.606e+002	8.008e+001	4.688e+001	3.359e+001	2.769e+001	2.573e+001	2.822e+001	3.418e+001	4.761e+001	7.617e+001	1.543e+002	4.619e+002		1
01–02		4.985e+002	1.689e+002	7.813e+001	4.741e+001	3.438e+001	2.842e+001	2.739e+001	2.920e+001	3.589e+001	4.863e+001	8.057e+001	1.650e+002	5.063e+002	2
02–03			4.834e+002	1.538e+002	7.617e+001	4.629e+001	3.340e+001	2.866e+001	2.656e+001	2.837e+001	3.438e+001	4.805e+001	7.910e+001	1.650e+002	3
03–04				4.678e+002	1.606e+002	7.764e+001	4.761e+001	3.545e+001	2.896e+001	2.725e+001	2.876e+001	3.501e+001	4.878e+001	8.154e+001	4
04–05					4.912e+002	1.655e+002	8.057e+001	5.112e+001	3.564e+001	3.022e+001	2.798e+001	2.949e+001	3.594e+001	5.137e+001	5
05–06						4.839e+002	1.621e+002	8.301e+001	4.902e+001	3.545e+001	2.837e+001	2.729e+001	2.886e+001	3.516e+001	6
06–07							4.907e+002	1.719e+002	8.154e+001	5.000e+001	3.467e+001	2.974e+001	2.744e+001	2.944e+001	7
07–08								5.044e+002	1.626e+002	8.008e+001	4.766e+001	3.477e+001	2.822e+001	2.671e+001	8
08–09									4.814e+002	1.621e+002	7.813e+001	4.824e+001	3.462e+001	2.866e+001	9
09–10										4.956e+002	1.621e+002	8.154e+001	5.137e+001	3.755e+001	10
10–11											4.814e+002	1.655e+002	8.105e+001	5.112e+001	11
11–12												4.985e+002	1.646e+002	8.252e+001	12
12–13													4.912e+002	1.660e+002	13
13–14														4.902e+002	14

Figure 2.11 Format of 104 independent measurements from a 16-electrode sensor with the adjacent electrode pair sensing strategy.

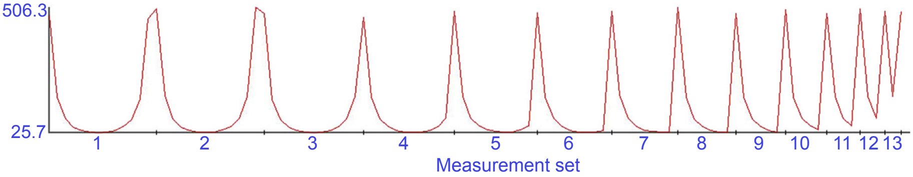

Figure 2.12 A typical measurement profile from a 16-electrode sensor with the adjacent electrode pair sensing strategy.

2.6 Sensor electronics and demodulation

Due to the large number of ON–OFF multiplexer channel operations in the DAS, the transient time has to be taken into account and becomes a key issue for maintaining the data's accuracy, particularly at a fast data collection rate. To analyse the effects of transient time of the sensing interface, an equivalent circuit for one conductivity measurement channel in EIT (Figure 2.13) was proposed (Wang, Ma, Dai, & Holliday, 2007). The left side of the figure is for modelling the current excitation and the right side for modelling the voltage measurement. In the figure, $i(t)$ is a sinusoidal current source, S the switch, C_{d1}, R_{t1} the double-layer capacitance and transfer resistance of the electrode–electrolyte interface at the current injection electrode, C_{d2} and R_{t2} the double-layer capacitance and transfer resistance of the electrode–electrolyte interface at the measurement electrode, Amp a voltage buffer with high input impedance and Gain = 1, C and R the AC coupling circuit, R_b the bulk resistance of the process and ku_1 the transformed voltage at the measured electrode. To simplify the discussion, perfect sinusoidal current source and voltage

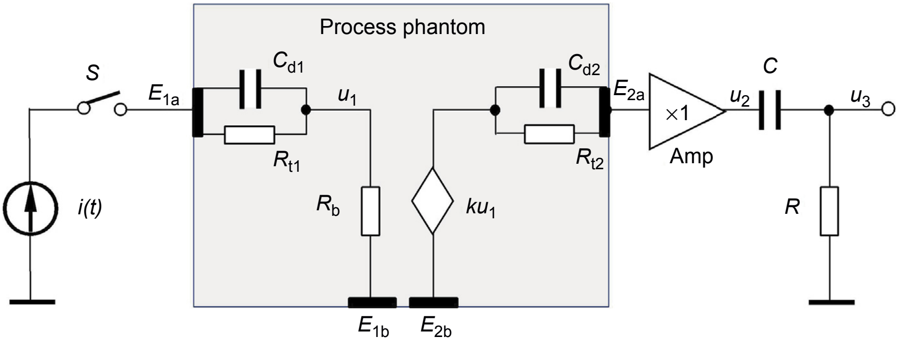

Figure 2.13 The equivalent circuit for one excitation and measurement channel (Wang & Ma, 2006).
Wang, M., & Ma, Y. (2006). Over-zero switching scheme for fast data collection operation in electrical impedance tomography. Measurement Science and Technology IOP, 17(8), 2078–2082, IOP.

buffer with infinite output and input impedances, respectively, are assumed in the model. All stray capacitances in circuits and distribution capacitances in aqueous-based processes are also ignored.

Wang and Ma (2006) described the details of the transient process and reported that the response of a sensing system using switched sinusoidal current excitation is approximately the sum of an exponential term and a sinusoidal term (Eqn (2.22)). The exponential term is due to the discharging process of the residual potential across C_{d2}, which was charged during the previous switch operation. The value of the residual potential will be uncertain if the switch is operated randomly. The attenuation speed of the charged electrode–electrolyte interface is relatively slow (for example, $\tau_2 = 5$ ms) compared with the fast frame collection rate ($\Delta t_f < 1$ ms) and sampling rate of measurement ($\Delta t_s < 12.5$ µs) (Wang et al., 2005). Therefore, the residual potential (the first term in Eqn (2.22)) could produce significant error from a fast data acquisition rate:

$$u_3(t) \approx V_{C_{d2}} e^{-t/\tau_2} + kI_m R_b \cos(\omega t + \theta_1) \tag{2.22}$$

where $\theta_1 = \arctan(\omega\tau)$, $\tau_1 = RC$, $\tau_2 = R_{t2}C_{d2}$, $V_{C_{d2}}$ is the charged residual voltage due to the previous switch operation and I_m is the amplitude of $i(t)$.

To eliminate the charged potential, an over-zero switching (OZS) scheme was developed by controlling the switching phase angle of the sinusoidal current injection (Jia, Wang, Schlaberg, & Li, 2012; Ma, Lai, Wang, & Jia, 2009; Wang & Ma, 2006; Wang et al., 2005). Both analyses and simulations revealed that the coupling time could be dramatically reduced by the employment of the OZS scheme used now in the Leeds FICA electrical impedance camera to achieve a data acquisition speed of 1164 dual-frames (2.383 million data points) per second with a root-mean-square error of less than 0.6% at 80 kHz in static test application (Ma & Wang, 2004).

One of the most problematic measurement errors arises from common mode voltage (CMV) of the differential measurement because of the limited common mode voltage rejection ratio (CMRR) of the op-amps. The voltage on each measurement electrode is determined from a combination of the injecting current value, the electrode impedance and the conductivity of the conductive region. The differential voltage between electrode pairs, e.g. in the adjacent electrode pair strategy, is the difference between two voltages on the electrode pair, which is normally much smaller than the common voltage (to the ground) on the electrodes. The error caused by the CMV is mainly due to the limited CMRR of the op-amps, which results in partial transferring of CMV to the output of the op-amps. Besides selecting op-amps with high CMRR and reducing the mismatched impedance of circuits to get a 'good' measurement, the better approach is to reduce the CMV. A method used by Brown and Seagar (1985) is the common mode voltage feedback (CMFB). However, because of the phase delay of the feedback circuit, it may cause a phase error in the demodulation and possible feedback oscillation (Murphy & Rolfe, 1988) at high frequency. In most process engineering applications, the potential reference can be obtained by directly grounding an electrical contact to the conductive medium in the process since

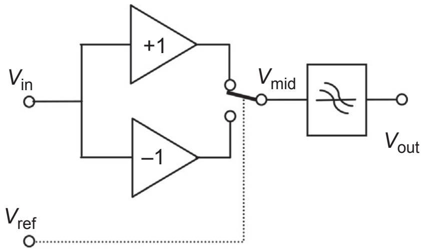

Figure 2.14 Operation principle of PSD.

electrical isolation of the instrument's ground is no longer necessary in most industrial applications, which is referred to as the grounded floating measurement (GFM) (Wang et al., 1993). The feedback path of the CMFB and GFM methods is generally through any unused electrode in contact with the conductive region.

The AC signals must be 'readable' by a specific measurement device. The use of the conventional rectification method to convert a weak AC signal to DC is not suitable since its minimum threshold value, e.g. 0.7 V in the use of a diode, is much higher than the signals and also it cannot provide the phase information. Phase-sensitive demodulators (PSDs) in both analogue and digital forms, such as switching demodulators, multipliers and digital matched filters, are widely used in EIT DASs (Brown & Seagar, 1987; Cook, Saulnier, & Goble, 1991; Goovaerts et al., 1988; Smith, Freeston, Brown, & Sinton, 1992; Webster, 1978). The simplest PSD is illustrated in Figure 2.14, which includes a positive buffer, a negative buffer, a switch and a low-pass filter. In operation, it just effectively flips the input signal based on the polarity unity level of a function, e.g. a sequence of square pulses, which equals $V_{mid} = V_{in} \times V_{ref}$. The signal conditions are illustrated in Figure 2.15, where the input is a sinusoidal signal, $V_{in} = V_m \sin(\omega_0 t + \varphi)$, $\omega_0 = 2\pi f_0$ and the reference is a square wave with a unit amplitude and the same angular frequency, ω_0.

With Fourier series expansion, V_{mid} can be presented as (Wang et al., 1993)

$$V_{mid}(\omega_0 t, \varphi) = \frac{2}{\pi} V_m \cos\varphi + \frac{4}{\pi} V_m \sum_{n=1}^{\infty} \frac{1}{4n^2 - 1} \{2n \sin(2n\omega_0 t) \sin\varphi - \cos(2n\omega_0 t)\cos\varphi\} \tag{2.23}$$

Then in-phase output of the switch-based PSD after the low-pass filter can be expressed as

$$V_{out}(\varphi) = \frac{2}{\pi} V_m \cos\varphi \tag{2.24}$$

The quadrature output can be obtained with the same principle when the reference has a phase shift of $\pi/2$.

Using a similar principle but replacing the switch by two multipliers with two sinusoidal references having in-phase and π/2 phase shift angles, respectively, outputs of the multiplication-based PSD after the low-pass filter are expressed as Eqns (2.25) and (2.26):

$$V_{\text{out}}(\varphi)\big|_{\text{in-phase}} = \frac{V_{\text{r}}V_{\text{m}}}{2}\cos\varphi \tag{2.25}$$

$$V_{\text{out}}(\varphi)\big|_{\text{quadrature}} = \frac{V_{\text{r}}V_{\text{m}}}{2}\sin\varphi \tag{2.26}$$

Smith et al. (1992) proposed a phase-sensitive detector based on matched filter theory to extract the amplitude and phase of a periodic measurement, which showed that the SNR improvement is equal to its analogue counterpart.

The sampled input, $V_{\text{in}}[n]$ at a frequency f_{s}, can be presented as

$$V_{\text{in}}[n] = A\sin(2\pi R_f n + \varphi) \tag{2.27}$$

where $R_f = f_0/f_{\text{s}}$, $n = 0, 1, 2, \ldots, N-1$ and $N = T_{\text{m}} f_{\text{s}}$ is the number of samples.

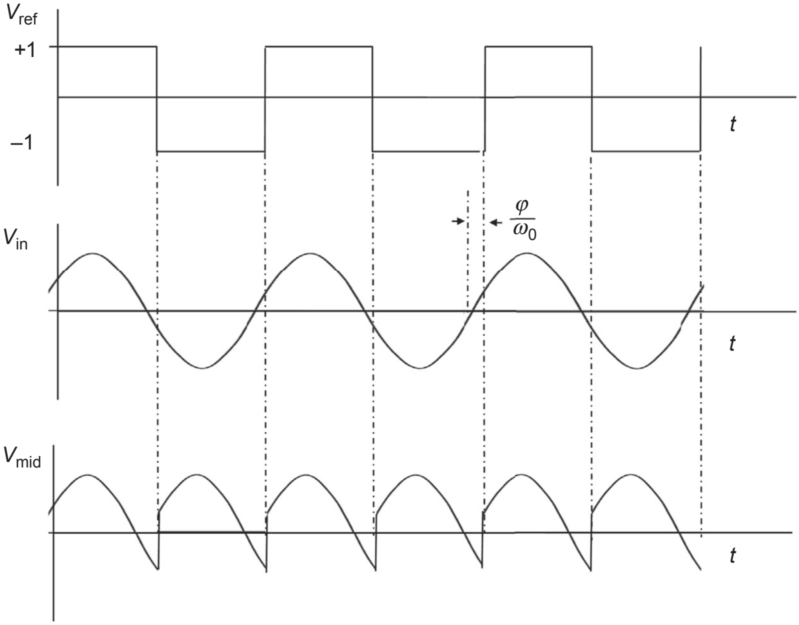

Figure 2.15 Illustration of input and output signals of a PSD.
According to Smith et al. (1992).

The reference sequences, $h[n]$ and $g[h]$, are two sine waveforms with the same frequency as V_{in} but with unit amplitude zero (in-phase) and $\pi/2$ phase shifts, respectively:

$$h[n] = A \sin\left(2\pi R_f n\right) \tag{2.28}$$

$$g[n] = A \cos\left(2\pi R_f n\right) \tag{2.29}$$

Taking the sums of products from sampled measurements and reference sequences as expressed by Eqns (2.30) and (2.31),

$$V_{\text{out}}^{h} = \sum_{n=0}^{N-1} V_{\text{in}}[n] \cdot h[n] \tag{2.30}$$

$$V_{\text{out}}^{g} = \sum_{n=0}^{N-1} V_{\text{in}}[n] \cdot g[n] \tag{2.31}$$

Provided that T_{m} is a multiple of $1/f_0$ and that $f_{\text{s}} > 2f_0$, outputs in Eqns (2.30) and (2.31) can be expressed as

$$V_{\text{out}}^{h} = \frac{AT_{\text{m}} f_{\text{s}} \cos\varphi}{2} \tag{2.32}$$

$$V_{\text{out}}^{g} = \frac{AT_{\text{m}} f_{\text{s}} \sin\varphi}{2} \tag{2.33}$$

The phase shift of the input signal is derived from

$$\varphi = \operatorname{arctg} \frac{V_{\text{out}}^{g}}{V_{\text{out}}^{h}} \tag{2.34}$$

In the above equations, φ is the phase shift between the demodulated signal and the reference signal, T_{m} is the measurement time of a multiple of the demodulated signal period ($1/f_0$) and f_{s} is the sample frequency ($f_{\text{s}} > 2f_0$).

The major drawback of analogue PSD is its time cost due to the low-pass filter. It would also cause the complex circuitry and associated cost for demodulation of the signal from a multifrequency excitation. Using digital demodulation, its SNR can be much closer to the theoretical value (Smith et al., 1992) and it has a potential to be further implemented for demodulation of the multifrequency signal in various waveforms.

2.7 Data acquisition systems

Various EIT DASs have been developed with specific features and application areas (Brown & Seagar, 1987; Cook et al., 1994; Dong, Xu, Zhang, & Ren, 2012; Gisser et al., 1991; Jia, Wang, Schlaberg, & Li, 2010; Lidgey, Zhu, McLeod, & Breckon, 1992; Ma et al., 2003; Newell, Gisser, & Isaacson, 1988; Wang et al., 1993; Wilkinson et al., 2005; Wilson, Milnes, Waterworth, Smallwood, & Brown, 2001). A typical EIT DAS is made up of six functional parts: voltage generator, current or voltage generator, electrode controller, voltmeter, operation controller and power supply. Figure 2.16 shows the block diagram of a DAS (Dickin & Wang, 1996; Wang et al., 1993). A single-chip microprocessor, the Intel i8052AH, was employed to manage the operation of the system, which controlled the sine wave generator, the electrode (channel) operation and analogue-to-digital conversion (ADC). Current or voltage was applied to electrodes in the EIT sensor via a multiplexer in a specific scheme. Signals from the EIT sensor were firstly isolated with voltage buffers and then provided to an instrument amplifier. Then, the output of the instrument amplifier was demodulated by either an analogue or digital PSD. These functional parts were built on five EURO cards plugged into a 64-way backplane utilised for digital signal transfer and control between each board and the microcontroller. The system can accommodate up to 128 electrodes to form different sensing strategies using a programmable combination.

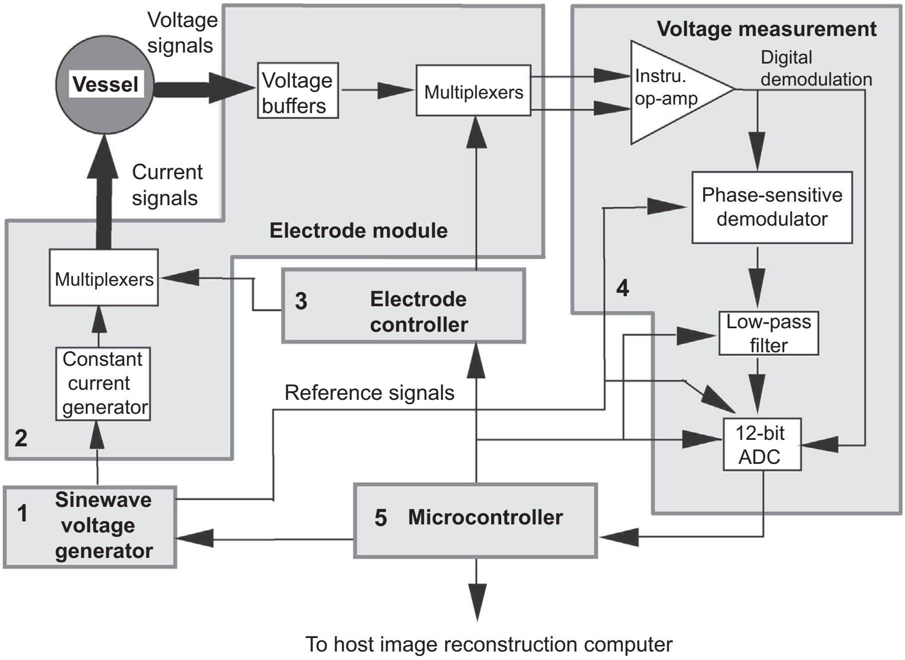
Voltage signals
Vessel
Voltage buffers
Multiplexers
Voltage measurement
Digital demodulation
Instru. op-amp
Current signals
Electrode module
Phase-sensitive demodulator
Multiplexers
3 Electrode controller
4
Low-pass filter
Constant current generator
Reference signals
2
12-bit ADC
1 Sinewave voltage generator
5 Microcontroller
To host image reconstruction computer

Figure 2.16 Block diagram of the UMIST MK.1b EIT data acquisition system (Wang et al., 1993).

The diagram of a more sophisticated EIT system (Wang et al., 2007), known as the Leeds FICA system, is shown in Figure 2.17, which was developed for online measurement of two-phase flows with axial velocities up to 10 m/s (Ma et al., 2003; Wang et al., 2005). The system was designed in a modular fashion and can consist of several data acquisition modules and computing modules. The data acquisition module includes a voltage-controlled current source, a waveform generator and a parallel measurement module with arrays of programmable gain amplifiers (PGAs), analogue-to-digital convertors (A/D) and first-in—first-out (FIFO) memories. The processes (from sampling to digital data output) in parallel measurement are fully logically operated. Both the excitation and measurement are synchronised by the synchronisation unit. Two identical data acquisition subsystems are connected to two electrode arrays. A data acquisition speed of 1164 dual-frames (2.383 million data points) per second was achieved with a root-mean-square error of less than 0.6% at 80 kHz in a static set-up (Ma & Wang, 2004). The measurement system, as shown in Figure 2.17, can consist of up to four digital signal processor (DSP) modules. The third DAS collects data from conductivity, pressure, temperature and other auxiliary sensors. All three DASs are controlled by one DSP module through a common interface. Each DSP module can be configured to communicate with a remote PC via a fast interface of IEEE1394 but only one at a time (Dai, Ma, & Wang, 2003; Holliday, Ma, Wang, & Williams, 2003; Ma et al., 2003).

To overcome the limits of the current source for use in process applications involved with high conductive solution, e.g. seawater in 5 S/m conductivity or the 3.5 M nitric acid in nuclear fuel process (Bolton et al., 2007), an EIT system with a bipolar voltage source and current sensing was developed (Jia et al., 2010; Wang & Jia, 2009). The amplitude of the current output can reach more than 300 mA. Figure 2.18 illustrates a brief block diagram of the system: a voltage excitation was applied to a pair of electrodes via the first multiplexer and its corresponding current though the target was sensed by a current sensor. voltage drops between electrode pairs

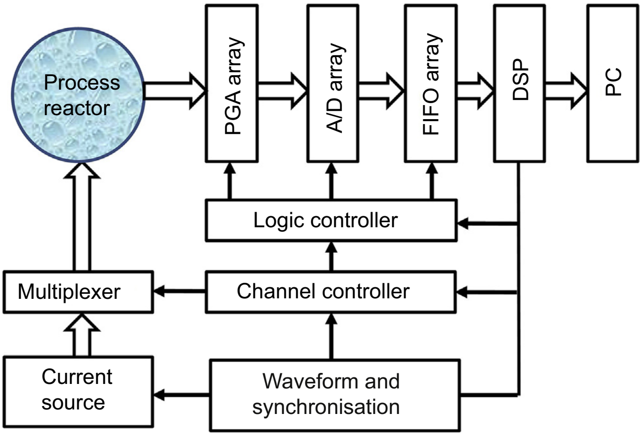

Figure 2.17 Diagram of the Leeds FICA EIT data acquisition system with parallel measurement.

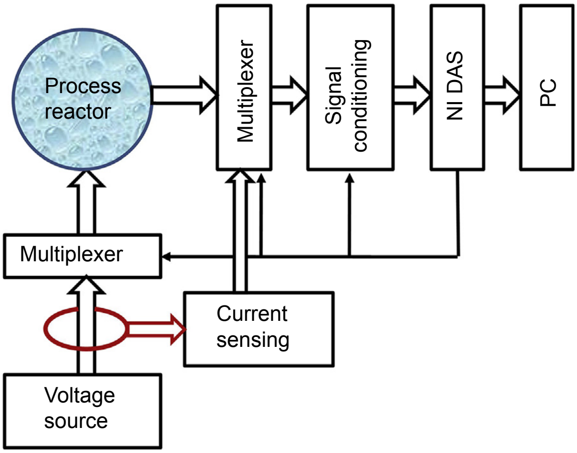

Figure 2.18 Diagram of a voltage-drive EIT system.

were sampled via the second multiplexer and demodulated by a National Instrument (NI) data acquisition board, which transmitted the acquired data to a PC via a USB 2.0 communication interface for image reconstruction and data fusion.

2.8 Imaging capability

Seagar et al. (1987) have proposed definitions of spatial resolution, conductivity contrast, conductivity resolution and visibility of the reconstructed image for assessment of accuracy in EIT. These definitions cover the major performance in practice. Four major specifications for assessing the accuracy of imaging are defined as below.

Spatial resolution: the smallest region of a medium into which the conductivity can be independently determined:

$$\text{spatial resolution} = \frac{r_{\mathrm{a}}}{r_{\mathrm{b}}} \tag{2.35}$$

Conductivity contrast: the ratio between the conductivity of an anomaly to that of its surrounding region:

$$\text{conductivity contrast} = \alpha = \frac{\sigma_{\mathrm{a}}}{\sigma_{\mathrm{b}}} \tag{2.36}$$

Conductivity resolution: the fractional change in conductivity contrast:

$$\text{conductivity contrast} = \frac{\delta\alpha}{\alpha} \tag{2.37}$$

Distinguishability: the minimum distance between two objects with the same conductivity contrast to their surrounding region:

$$\text{distinguishability (at } \alpha) = \frac{t_{\text{distinguishable distance}}}{D_{\text{vessel diameter}}} \tag{2.38}$$

To have a close view of EIT performance, assessments based on the above definition were carried out (Wang, Mann, & Dickin, 1999). The assessments on imaging capability of EIT were limited to the data simulated with a two-dimensional finite element model in the use of the adjacent electrode pair strategy with 16 electrodes and the images reconstructed using a conjugate gradient method—based algorithm (Wang, 2002). Random errors were added to the simulated measurements. The test set-up is shown in Figure 2.19, where an object with conductivity σ_a and radius r_a is positioned at the centre of the two-dimensional domain with conductivity σ_b and radius r_b.

The pre-error (or measurement error) presented at precondition is defined as the error between the boundary voltages obtained from measurement and that simulated from forward solution. The post-error (or conductivity error) presented at the post-condition is defined as the error between the conductivity set-up and that reconstructed from inverse solution (Wang et al., 1999). In most applications, only the pre-error can be obtained. Figure 2.20 shows how the error in measurement influences the image (a series of pre-errors related to post-errors) by set-ups of different sizes of an object with the same conductivity ratio 1.36:1 (Figure 2.20(a)) and different conductivity values of an object with a fixed radius ratio 0.24:1 (Figure 2.20(b)), which reveals that for a system with a pre-error of 1%, the spatial resolution and the conductivity resolution could achieve 5% and 10% (2.4% of the mean change), respectively. The distinguishability was tested by setting two objects both with area ratio (1/253):1 and conductivity ratio 1.36:1 near the centre of the disk domain, which revealed from the simulated results shown in Figure 2.20(c) that the imaging distinguishability of the given image in a 16-division of the view scale is around 20%.

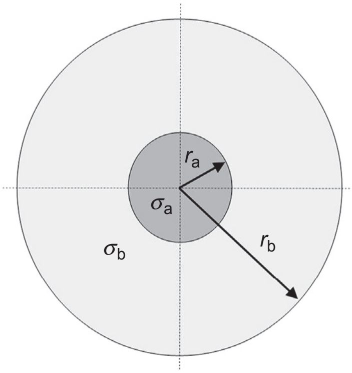

Figure 2.19 The set-up for the assessment of EIT performance.

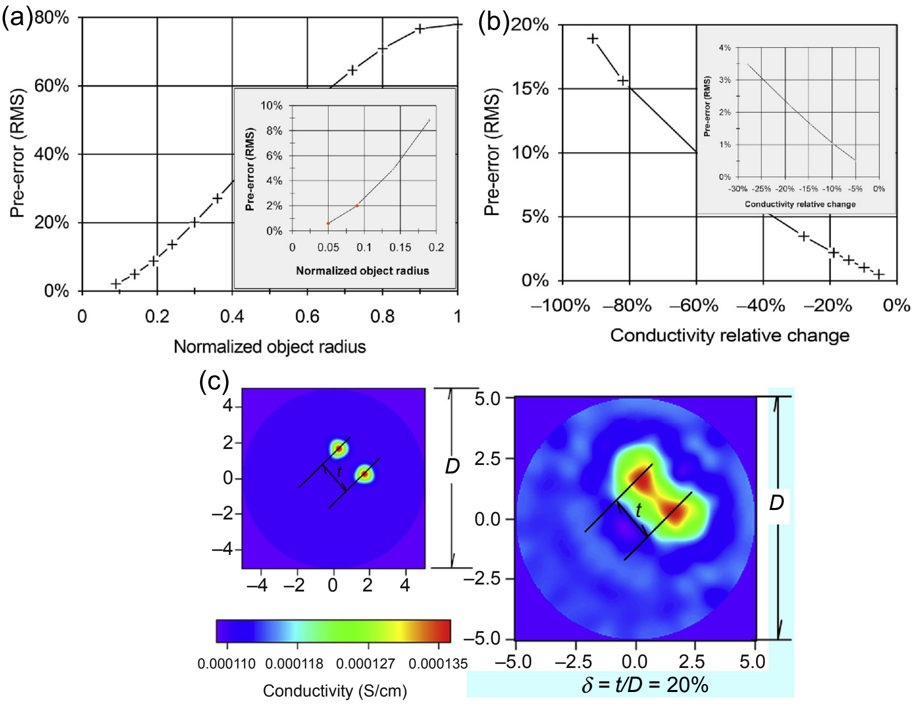

Figure 2.20 Performance of an EIT: (a) spatial resolution, (b) conductivity resolution and (c) distinguishability (the left: set-up; the right: reconstructed).

2.9 EIT data for process application

Since EIT can detect local changes in electrical conductivity, the technique is used to study unsteady mixing or fluid dynamics of flow mixtures, such as gas–liquid and solid–liquid mixtures, where the dispersed phase of fluids or solids has different conductivities from the aqueous continuous phase. EIT may, therefore, be suitable for numerous aqueous-based processes. However, EIT only produces electrical conductivity distribution or maps. For most process applications, relevant engineering data have to be implemented from conductivity-based information. A few of the typical relationships are introduced here.

A number of correlations have been proposed to convert electrical conductivity of a particulate system to volumetric fraction of a dispersed phase (Table 2.2, Shirhatti, 2007). Among them, the Maxwell relationship is the most widely used in EIT application in process engineering applications (Sharifi & Young, 2013).

In research on miscible liquid mixing, the liquids under investigation can be labelled with sufficient conductivity contrast to enhance the imaging performance (Wang et al., 1999). High-concentration saline solution can also be used as a tracer

Table 2.2 Correlation functions of conductivity and dispersed phase volumetric fraction (Shirhatti, 2007)

Reference	Correlation
Maxwell (1873)	$C_v = \dfrac{2\sigma_f + \sigma_s - 2\sigma_m - \frac{\sigma_m\sigma_s}{\sigma_f}}{2\sigma_f + \sigma_m - 2\sigma_s - \frac{\sigma_m\sigma_s}{\sigma_f}}$ for conductive solid $C_v = \dfrac{2\sigma_f - 2\sigma_m}{2\sigma_f + \sigma_m}$ for nonconductive solid or liquid
Bruggeman (1935) for particles of different sizes (Mactaggart, Nasr-El-Din, & Masliyah, 1993)	$\dfrac{\sigma_m}{\sigma_f} = (1 - C_v)^{1.5}$(for insulating solid) $\dfrac{\sigma_m}{\sigma_f} = (1 - C_v)^3$ (for conductive solid)
Meredith and Tobias (1962)	$\dfrac{\sigma_m}{\sigma_f} = 8\dfrac{(2 - C_v)(1 - C_v)}{(4 + C_v)(4 - C_v)}$ (for insulating solid) $\dfrac{\sigma_m}{\sigma_f} = \dfrac{(1 - C_v)(2 + C_v)}{(1 - C_v)(2 - C_v)}$ (for conductive solid)
Maxwell–Wagner equation or Maxwell–Garnett equation or Wiener's rule (Fricke, 1953)	$\dfrac{\sigma_m - \sigma_f}{\sigma_m + 2\sigma_f} = \left(\dfrac{\sigma_s - \sigma_f}{\sigma_s + 2\sigma_f}\right)C_v$
Rayleigh (Mactaggart et al., 1993)	$\sigma_m = \sigma_f\left[1 + \dfrac{3C_v}{(0.394C_v^{10/3} - C_v - 2)}\right]$
De la Rue and Tobias (Mactaggart et al., 1993)	$\sigma_m = \sigma_f(1 - C_v)^m$; $m = 1.5$ for $0.45 \le C_v \le 0.75$
Prager (1963)	$\sigma_m = \dfrac{\sigma_f(1 - C_v)(3 - C_v)}{3}$
Weissberg (1963)	$\sigma_m = \sigma_f\left(2\dfrac{(1 - C_v)}{2 - \ln(1 - C_v)}\right)$

Notes: σ_f is the conductivity of the aqueous continuous phase, σ_s is the conductivity of the dispersed phase and σ_m is the mixture conductivity. If the dispersed phase is nonconductive, σ_s equals zero, C_v is the volumetric fraction.
Shirhatti, V. S. (2007). Characterisation and visualisation of particulate solid–liquid mixing using electrical resistance tomography (Ph.D. thesis). University of Leeds.

to track the dynamic trajectory of the mixing process (Holden, Wang, Mann, Dickin, & Edwards, 1999). In an instance of single-phase miscible liquid mixing, the conductivity of mixture, σ_m, provides a linear relation to the concentration C_w of salt (Holden, Wang, Mann, Dickin, & Edwards, 1998; Mann et al., 1996b; Wang et al., 1999):

$$\sigma_m = 1.728636 \times C_w + \sigma_f \tag{2.39}$$

$$C_w = 0.5785 \times (\sigma_{mc} - \sigma_f) \tag{2.40}$$

where σ_m and σ_f are the mixture's and aqueous conductivity in units of mS/cm, respectively; the concentration C_w is in g/L, the range of C_w: $0 \le C_w \le 10$.

Qiu et al. (1994) and Qui, Dickin, James, and Wang (1997) also used Archie's law to convert the conductivity value of a laboratory sub-seabed set-up to porosity. The conversion is given as (Archie, 1942)

$$\phi = \left(\frac{\sigma_m}{\sigma_f}\right)^k \tag{2.41}$$

where ϕ is the porosity (%), σ_m the conductivity of the formation (S/m), σ_f the water conductivity (S/m) and k the cementation index dependent on the shape and packing of the particles ($k = 1.5$ for spherical glass beads).

The principle of cross-correlation method has been widely used to derive the velocity component of moving objects from two sets of measurements or images taken with a known time interval, e.g. the car speeding detector of police road camera or the velocity distribution derived by particle image velocimetry (PIV). Unlike the speeding camera, each velocity vector in PIV is statistically derived from many seeds' images over an interrogation region due to the unsteady nature of turbulent flow. It is also possible to derive a velocity map of the dispersed-phase-flow component in the use of tomograms obtained from a dual-plane EIT sensor with a known distance between the two sensing planes (Li, Wang, Wu, & Lucas, 2009, pp. 81−93; Lucas, Cory, Waterfall, Loh, & Dickin, 1999). The concept of cross-correlation method and its application in process tomography are extensively discussed in the later chapter of the book.

2.10 Future trends

EIT is based on measurements of electrical properties of materials by applying a low-frequency (from DC up to a few MHz) electric field (e.g. current or voltage). They are inexpensive and relatively straightforward to implement with the potential for sub-millisecond temporal resolution. Due to the limited number of measurements and the propagation nature of low-frequency electromagnetic waves, they normally provide images with a spatial resolution around 5% (the diameter of the object to the diameter of the vessel) and a homogeneity resolution better than 1% (e.g. the mean concentration of gas in water) for an EIT system having 1% measurement error. The use of the high-rank DSP and field-programmable gate array technique has brought remarkable performance improvement to EIT with high speed and/or high flexibility for onboard control and management of various sensing strategies and measurement protocols (Dong et al., 2012; Wang et al., 2005). However, in the consideration of financial, time and maintenance costs for new development, EIT systems with a commercially available DAS with well-supported software, e.g. Labview, have become more popular (Jia et al., 2010). To break the limitation of EIT in process application due to the request of electrodes to be invasive, an EIT system based on capacitively coupled contactless conductivity detection (C4D) was developed (Wang, Hu, Ji, Huang, & Li, 2012). The system uses metallic electrodes installed on the outside wall of a nonconductive pipe, which forms coupling capacitances between the metal electrodes and electrolyte inside the pipe and therefore allows excitation signal penetration into the process. Most of the current EIT techniques in process engineering only use the resistance part or magnitude of electrical impedance to implement engineering data, e.g. the concentration of a dispersed phase in a mixing process. Electrical impedance tomography spectroscopy (EITS) was proposed for imaging the human thorax (Brown, Leathard, Lu, Wang, & Hampshire, 1995) and received serious attention from many other researchers (Gary et al., 2007; McEwan, Tapson, Schaik, & Holder, 2009; Oh et al., 2008; Saulnier et al., 2007). The impedance spectrum can provide not only the electric but also the dielectric property distributions of the object under investigation, which will be particularly important in colloid-based process engineering since the surface charges of particles present a significant contribution to the imaginary part of impedance (Zhao, Wang, & Hammond, 2011, 2013). EITS is extending the boundary of information from time domain to frequency domain. It is expected that significant new knowledge will be revealed with EITS in a completely different direction.

2.11 Sources of further information

An early book edited by Webster (1990) provided a systematic view of electrical impedance tomography in medical applications, and has been a significant influence for the development of EIT for process engineering applications. The book edited by Williams and Beck (1995), which included EIT as part of its contents, discussed the principle and application of process tomography at its early stage. Boone et al. (1997) presented an excellent review and summary on EIT in medical research and diagnoses. It may be a good starting point for beginners to read several of these articles. Brown (2001) addressed a brief review of development and specific features of EIT in both medicine and process engineering. Articles by Dickin and Wang (1996), York (2001) and Wang (2005a) provided specific focus on EIT techniques for process engineering. Dyakowski, Jeanmeure, and Jaworski (2000) presented a good review on electrical tomography for gas—solids and liquid—solids flows, and the most recent review paper by Sharifi and Young (2013) extensively reviewed and summarised the applications of EIT in chemical engineering. Readers can also review specific techniques and featured applications from books edited by Holder (2005), Sikora and Wojtowicz (2010) and Kak and Slaney (2001).

References

Analog devices datasheet. (1995). *AD7008/PCB DDS evaluation board.*

Archie, G. E. (1942). The electrical resistivity log as an aid in determining some reservoir characteristics. *Transactions of American Institute of Minning Metallurgical Engineers, 146*, 54—62.

Aw, S. R., Rahim, R. A., Rahiman, M. H. F., Yunus, F. R. M., & Goh, C. L. (2014). Electrical resistance tomography: a review of the application of conducting vessel walls. *Powder Technology, 254*, 256–264.

Bates, R. H. T., McKinnon, G. C., & Seagar, A. D. (1980). A limitation on systems for imaging electrical conductivity distributions. *IEEE Transactions on Biomedical Engineering, BME-27*, 418–420.

Bockris, J. O.'M., & Conway, B. E. (1969). *Modern aspects of electrochemistry*. New York: Plenum Press.

Bockris, J. O.'M., & Drazic, D. M. (1972). *Electro-chemical science*. Taylor and Francis Ltd.

Bockris, J. O.'M., & Reddy, A. K. N. (1970). *Modern electrochemistry*. London: Macdonald.

Bolton, G., Bennett, M. A., Wang, M., Qiu, C., Wright, M., Primrose, K., et al. (2007). Development of an electrical tomographic system for operation in a remote, acidic and radioactive environment. *Chemical Engineering Journal, 130*, 165–169.

Boone, R., Barber, D., & Brown, B. R. (1997). Review: imaging with electricity: report of the European concerted action on impedance tomography. *Journal of Medical Engineering & Technology, 21*(6), 201–232.

Bragos, R., Rosell, I., & Riu, P. (1994). A wide-band a.c.-coupled current source for electrical impedance tomography. *Physiological Measurement*, (Suppl. 2a), A91–99.

Brown, B. H. (2001). Medical impedance tomography and process impedance tomography: a brief review. *Measurement Science and Technology, 12*, 991–996.

Brown, B. H., Barbar, D. C., Wang, W., Lu, L., Leathard, A. D., Smallwood, R. H., et al. (1994). Multi-frequency imaging and modelling of respiratory related electrical impedance changes. *Physiological Measurement, 15*(Suppl. 2A), A1–A12.

Brown, B. H., & Barber, D. C. (1985). *Tomography*, UK Patent No. GB2160323A.

Brown, B. H., Barber, D. C., & Freeston, I. L. (1983). *Tomography*, UK Patent No. GB2119520A, 1983.

Brown, B. H., Leathard, A. D., Lu, L., Wang, W., & Hampshire, A. (1995). Measured and expected cole parameters from electrical impedance tomographic spectroscopy images of the human thorax. *Physiological Measurement, 16*, A57–A67.

Brown, B. H., & Seagar, A. D. (1985). Applied potential tomography: data collection problems. *IEE International Conference on Electric and Magnetic fields in Medicine and Biology*. London, Dec. 79–82.

Brown, B. H., & Seagar, A. D. (1987). The Sheffield data collection system. *Clinical Physics and Physiological Measurement, 8*(Suppl. A), 91–97.

Bruggeman, D. A. G. (1935). Calculation of various physical constants of heterogeneous substances, part 1, constant and conductivity of mixtures of isotropic substances. *Annual Physics, Leipzig, 24*, 636.

Cilliers, J. J., Xie, W., Neethling, S. J., Randall, E. W., & Wilkinson, A. J. (2001). Electrical resistance tomography using a bi-directional current pulse technique. *Measurement Science and Technology, 12*(8), 997–1001.

Cobbold, R. S. C. (1974). *Transducers for biomedical measurements: Principles and applications*. John Wiley & Sons.

Conway, B. E. (1952). *Electrochemical data*. Elsevier Publishing Company.

Cook, R. D., Saulnier, G. J., Gisser, D. G., Goble, J. C., Newell, J. C., & Isaacson, D. (1994). Act3-a high-speed, high-precision electrical-impedance tomograph. *IEEE Transactions on Biomedical Engineering, 41*(8), 713–722.

Cook, R. D., Saulnier, G. J., & Goble, J. C. (1991). A phase sensitive voltmeter for a high-speed, high-precision electrical impedance tomography. *Annual International Conference of the IEEE Engineering in Medicine and Biology Society, 13*(1), 22−23.

Crow, D. R. (1974). *Principles and applications of electrochemistry*. London: Chapman and Hall.

Cullivan, J. C., Wang, M., Bolton, G., Baker, G., Clarke, W., & Williams, R. A. (2005). Linear EIT for sedimentation and sediment bed characterization. In: *Proceedings of 4th World Congress on Industrial Process Tomography* (pp. 910−915). VCIPT, Aizu.

Dai, Y., Ma, Y., & Wang, M. (2003). A specific signal conditioner for electrical impedance tomography. In: *Proceedings of the 3rd World Congress on Industrial Process Tomography* (pp. 45−49). Banff, VCIPT.

Dickin, F. J., & Wang, M. (1996). Electrical resistance tomography for process applications. *Measurement Science and Technology IOP, 7*, 247−260.

Dines, K. A., & Lytle, R. J. (1981). Analysis of electrical conductivity imaging. *Geophysics, 46*, 1025−1036.

Dong, F., Xu, C., Zhang, Z., & Ren, S. (2012). Design of parallel electrical resistance tomography system for measuring multiphase flow. *Chinese Journal of Chemical Engineering, 20*(2), 368−379.

Dyakowski, T., Jeanmeure, L. F. C., & Jaworski, A. J. (2000). Applications of electrical tomography for gas−solids and liquid−solids flows — a review. *Powder Technology, 112*.

Etuke, E. O. (1994). *Impedance spectroscopy form component specificity in tomography imaging* (Ph.D. thesis). UMIST (now University of Manchester).

Faraj, Y., & Wang, M. (2012). ERT investigation on horizontal and vertical counter-gravity slurry flow in pipelines. In: *20th International Congress of Chemical and Process Engineering CHISA 2012*. Procedia Engineering, Elsevier.

Fricke, H. (1953). The Maxwell−Wagner dispersion in a suspension of ellipsoids. *The Journal of Physical Chemistry, 57*(9), 934−937. http://dx.doi.org/10.1021/j150510a018. Publication Date: September 1953.

Gary, J., Liu, S. N., Tamma, C., Xia, H., Kao, T. J., Newell, J. C., et al. (2007). An electrical impedance spectroscopy system for breast cancer detection. In: *Proceedings of the 29th Annual International Conference of the IEEE EMBS* (pp. 4154−4157). France: CitéInternationale, Lyon.

Geddes, L. A., Costa, C. P. D., & Wise, G. (1971). The impedance of stainless-steel electrodes. *Medical & Biological Engineering, 9*, 511−521.

Geselowitz, D. B. (1971). An application of electrocardiographic lead theory to impedance plethysmography. *IEEE Transactions on Biomedical Engineering, 18*, 38−41.

Gisser, D. G. (1987). Current topics in impedance imaging. *Clinical Physics and Physiological Measurement, 8*(Suppl. A), 39−46.

Gisser, D. G., Newell, J. C., Salunier, G., Hochgraf, C., Cook, R. D., & Goble, J. C. (1991). Analog electronics for a high-speed high-precision electrical impedance tomography. *Proceedings of the Annual International Conference of the IEEE EMBS (Engineering in Medicine and Biology Society), 13*, 23−24.

Goovaerts, H. G., de Vries, F. R., Meijer, J. H., de Vries, P. M. J. M., Donker, A. J. M., & Schneider, H. (1988). Microprocessor-based system for measurement of electrical impedances during haemodialysis and in postoperative care. *Medical & Biological Engineering & Computing, 26*, 75−80.

Hartov, A., Demidenko, E., Soni, N., Markova, M., & Paulsen, K. (2002). Using voltage sources as current drivers for electrical impedance tomography. *Measurement Science and Technology, 13*, 1425–1430.

Henderson, P. R., & Webster, J. G. (1978). An impedance camera for spatial specific measurements of the thorax. *IEEE Transactions on Biomedical Engineering, BME-25*, 250–254.

Henderson, P. R., Webster, J. G., & Swanson, D. K. (1976). A thoracic electrical impedance camera. *Proceedings of the 29th Annual Conference on Engineering in Medicine and Biology,* Nov. 6–10, Boston*, 18*, 322.

Holden, P. J., Wang, M., Mann, R., Dickin, F. J., & Edwards, R. B. (1998). Imaging stirred-vessel macromixing using electrical resistance tomography. *AIChE Journal*, 780–790.

Holden, P. J., Wang, M., Mann, R., Dickin, F. J., & Edwards, R. B. (1999). On detecting mixing pathologies inside a stirred vessel using electrical resistance tomography. *Transactions of IChemE, 77*(A), 709–712. IChemE.

Holder, D. S. (Ed.). (2005). *Electrical impedance tomography, methods, history and applications*. Bristol: IOP Publishing.

Holliday, N. T., Ma, Y., Wang, M., & Williams, R. A. (2003). A powerful computational DSP module for multiphase flow measurement. In: *Proceedings of the 3rd World Congress on Industrial Process Tomography* (pp. 62–67). Banff, VCIPT.

Hua, P., Webster, J. G., & Tompkins, W. J. (1987). Effect of the measurement method on noise handling and image quality of EIT imaging. *Proceedings of the Annual International Conference of the IEEE Engineering in Medicine and Biology Society, 9*, 1429–1430.

Hua, P., Woo, E. J., Webster, J. G., & Tompkins, W. J. (1993). Using compound electrodes in electrical impedance tomography. *IEEE Transactions on Biomedical Engineering, 40*, 29–34.

Hurry, R., Wang, M., Williams, R. A., Cross, C., & Esdaile, L. (2004). Development and application of industrial process tomography to monitoring liquid distribution in heap and column leaching. In: *JKMRC, International Student Conference, Brisbane, Australia. Industrial Tomography Systems*. Sunlight House, Quay Street, Manchester, M3 3JZ, UK.

Jia, J., Wang, M., Schlaberg, H. I., & Li, H. (2010). A novel tomographic sensing system for high electrically conductive multiphase flow measurement. *Flow Measurement and Instrumentation, 21*, 184–190.

Jia, J., Wang, M., Schlaberg, H. I., & Li, H. (2012). An optimisation method for the overzero switching scheme. *Flow Measurement and Instrumentation, 27*, 47–52.

Kaipio, J. P., Seppänen, A., & Somersalo, E. (2005). Inference of velocity fields with tomographic measurements. In: *Proceedings of 4th World Congress on Industrial Process Tomography* (pp. 625–630). Japan: Aizu, ISBN 0 85316 2557.

Kak, A. C., & Slaney, M. (2001). *Principles of computerized tomographic imaging*. Philadelphia, USA: The Society for Industrial and Applied Mathematics (SIAM).

Lehr, J. (1972). A vector derivation useful in impedance plethysmographic field calculations. *IEEE Transactions on Biomedical Engineering, 19*, 156–157.

Lidgey, F. J., Zhu, Q. S., McLeod, C. N., & Breckon, W. R. (1992). Electrical impedance tomography. Electrode current determination from programmable voltage sources. *Clinical Physics and Physiological Measurement, 13*(Suppl. A), 43–46.

Li, H., Wang, M., Wu, Y., & Lucas, G. P. (2009). *Volume flow rate measurement in vertical oil-in-water pipe flow using electrical impedance tomography and a local probe*, 81–93. http://dx.doi.org/10.1615/MultScienTechn.v21.i1–2.70.

Li, H., Wang, M., Wu, Y., Ma, Y., & Williams, R. (2005). Measurement of oil volume fraction and velocity distributions in vertical oil-in-water flows using electrical resistance tomography and a local probe. *Journal of Zhejiang University Science, 6A*(12), 1412–1415.

Lucas, G. P., Cory, J., Waterfall, R., Loh, W. W., & Dickin, F. J. (1999). Measurement of the solids volume fraction and velocity distributions in solid-liquid flows using dual-plane electrical resistance tomography. *Journal of Flow Measurement and Instrumentation, 10*, 249−258.

Lytle, R. J., & Dines, K. A. (1978). *An impedance camera: A system for determining the spatial variation of electrical conductivity*. UCPL-52413. Livermore, CA: Lawrence Livermore Lab, 94550.

Mactaggart, Nasr-El-Din, & Masliyah. (1993). A conductivity probe for measuring local solids concentration in a slurry mixing vessel. *Separations Technology, 3*, 151−160.

Ma, Y., Holliday, N., Dai, Y., Wang, M., Williams, R. A., & Lucas, G. (2003). A high performance online data processing EIT system. In: *Proceedings of the 3rd World Congress on Industrial Process Tomography* (pp. 27−32). Banff, VCIPT, ISBN 0853162409.

Ma, Y., Lai, Y., Wang, M., & Jia, J. (2009). Experimental validation of over-zero switching method. In: *What where when multi-dimensional advances for industrial process monitoring, Leeds, UK, June 23−24* (pp. 408−416), ISBN 978-0-85316-278-0.

Mann, R., Wang, M., Dickin, F. J., Dyakowski, T., Holden, P. J., Forrest, A. E., et al. (1996a). Resistance tomography imaging of stirred vessel mixing at plant scale. In HadjBenkreira (Ed.), *Fluid mixing Vol. 5,* (pp. 155−166). Bradford: IChemE, ISBN 0852953763.

Mann, R., Wang, M., Dickin, F. J., Dyakowski, T., Holden, P. J., Forrest, A. E., et al. (1996b). Resistance tomography imaging of stirred vessel mixing at plant scale. In: *IChemE Symp., Series: Vol. 140. Fluid mixing 5* (pp. 155−166).

Ma, Y., & Wang, M. (2004). Performance of a high-speed impedance camera for flow informatics. In: *Proceedings of EDSA04*. Manchester: ASME.

Maxwell, J. C. A. (1873). *Treatise on electricity and magnetism* (Vol. 1). New York: Dover Publications Inc, 1954.

McEwan, A., Tapson, J., van Schaik, A., & Holder, D. S. (2009). Code-division-multiplexed electrical impedance tomography spectroscopy. *IEEE Transactions on Biomedical Circuits and Systems, 3*(5), 332−338.

Meredith, R. E., & Tobias, C. W. (1962). *Advances in electrochemistry and electrochemical engineering* (2nd ed.). New York: Interscience.

Murai, T., & Kagawa, Y. (1985). Electrical impedance computed tomography based on a finite element model. *IEEE Transactions on Biomedical Engineering, 32*, 177−184.

Murphy, D., & Rolfe, P. (1988). Aspects of instrumentation design for impedance imaging. *Clinical Physics and Physiological Measurement, 9A*, 5−14.

Newell, J. C., Gisser, D. G., & Isaacson, D. (1988). An electric current tomography. *IEEE Transactions on Biomedical Engineering, 35*, 828−833.

Oh, T. I., Koo, H., Lee, K. H., Kim, S. M., Lee, J., Kim, S. W., et al. (2008). Validation of a multi-frequency electrical impedance tomography (mfEIT) system KHU Mark1: impedance spectroscopy and time-difference imaging. *Physiological Measurement, 29*, 295−307.

Paulson, K. S., Breckon, W. R., & Pidcock, M. K. (1992). A hybrid phantom for electrical impedance tomography. *Clinical Physics and Physiological Measurement, A13*, 155−161.

Pollak, V. (1974a). An equivalent diagram for the interface impedance of metal needle electrodes. *Medical and Biological Engineering*, 454−459.

Pollak, V. (1974b). Computation of the impedance characteristics of metal electrodes for biological investigations. *Medical and Biological Engineering*, 460−464.

Prager, S. (1963). Diffusion and viscous flow in concentrated suspensions. *Physica, 29*, 129−139.

Qiu, C. H., Dickin, F. J., James, A. E., & Wang, M. (1994). Electrical resistance tomography for imaging sub-seabed sediment porosity: initial findings from laboratory-scale experiments using spherical glass beads. In M. S. Beck, E. Campogrande, M. Morris, R. A. Williams, & R. C. Waterfall (Eds.), *Process tomography—a strategy for industrial exploitation* (pp. 33—41). Oporto: UMIST, ISBN 095231651X.

Qui, C., Dickin, F., James, A., & Wang, M. (1997). Electrical resistance tomography for imaging sub-seabed sediment porosity. *Proceedings of ICEMI '97, Beijing*, 666—669.

Ronald, S. B., et al. (1993). Geopulse — a modular resistivity meter for electrical imaging (tomography). In: *Proceedings of the symposium on the application of geophysics to engineering and environmental problems, enviromental and engineering geophysical society, 1, San Diego, California, USA*.

Ruzinsky, F., & Bennington, C. P. J. (2007). Aspects of liquor flow in a model digester measured using electrical resistance tomography. *Chemical Engineering Journal, 130*(2—3), 67—74.

Saulnier, G. J., Liu, N., Tamma, C., Xia, H., Kao, T., Newell, J. C., & Isaacson, D. (2007). An electrical impedance spectroscopy system for breast cancer detection. In: *Proceedings of the 29th Annual International Conference of the IEEE EMBS CitéInternationale, Lyon, France, August 23—26*.

Schlaberg, H. I., Baas, J. H., Wang, M., Best, J. L., Williams, R. A., & Peakall, J. (2006). Electrical resistance tomography for suspended sediment measurement in open channel flows using a novel sensor design. *Particles & Particle Systems Characterization, 23*(3/4), 78.

Schlaberg, H. I., Jia, J., Qiu, C., Wang, M., & Li, H. (2008). Development and application of the fast impedance camera - a high performance dual-plane electrical impedance tomography system. In: *Proceedings of 5th International Symposium on Process Tomography, Zakopane, Poland August*.

Schlaberg, H. I., Wang, M., Qiu, C., & Shirhatti, V. (2005). Parallel array sensors for process visualisation. In: *Proceedings of 4th World Congress on Industrial Process Tomography* (pp. 177—182). Aizu, ISBN 0 85316 2557.

Schwan, H. P., & Ferris, C. D. (1968). Four-electrode null techniques for impedance measurement with high resolution. *The Review of Scientific Instruments, 39*(4), 481—485.

Seagar, A., Barber, D. C., & Brown, B. H. (1987). Theoretical limits to sensitivity and resolution in impedance imaging. *Clinical Physics and Physiological Measurement, 8*(Suppl. A), 13—31.

Sharifi, M., & Young, B. (2013). Electrical resistance tomography (ERT) applications to chemical engineering. *Chemical Engineering Research and Design, 91*(9), 1625—1645.

Shirhatti, V. S. (2007). *Characterisation and visualisation of particulate solid-liquid mixing using electrical resistance tomography* (Ph.D. thesis). University of Leeds.

Sikora, J., & Wojtowicz, S. (Eds.). (2010). *Industrial and biological tomography —theoretical basis and applications*. Warszawa: Electrotechnical Institute.

Smith, R. W. M., Freeston, I. L., Brown, B. H., & Sinton, A. M. (1992). Design of a phase-sensitive detector to maximize signal-to-noise ratio in the presence of Gaussian wide-band noise. *Measurement Science and Technology, 3*, 1054—1062.

Swanson, D. K. (1976). *Measurement errors and the origin of electrical impedance changes in the limb* (Ph.D. thesis). Dept. Electrical and Computer Eng. Univ. Wisconsin, Madison, WI 53706.

vanWeereld, J. J. A., Collie, D. A. L., & Player, M. A. (2001). A fast resistance measurement system for impedance tomography using a bipolar DC pulse method. *Measurement Science and Technology, 12*, 1002—1011.

Vijayan, M., Schlaberg, H. I., & Wang, M. (2007). Effects of sparger geometry on the mechanism of flow pattern transition in a bubble column. *Chemical Engineering Journal, 130*, 171−178.

Wang, M. (1994). *Electrical impedance tomography on conducting walled vessels* (Ph.D. thesis). UMIST (now University of Manchester), U.K.

Wang, M. (2002). Inverse solutions for electrical impedance tomography based on conjugate gradients methods. *Measurement Science and Technology IOP, 13*, 101−117.

Wang, M. (2005a). Seeing a new dimension − the past decade's developments on electrical impedance tomography. *Progress in Natural Science, 15*(13), 1−13.

Wang, M. (2005b). Electrode models in electrical impedance tomography. *Journal of Zhejiang University Science, 6A*(12), 1386−1389.

Wang, M., & Jia, J. B. (2009). *EIT system for highly conductive medium*. PCT/GB2010/051035, GB0910704.6, Publication number CA2803667 (A1).

Wang, M., Dickin, F. J., & Beck, M. S. (1993). Improved electrical impedance tomography data collection system and measurement protocols. In M. S. Beck, E. Campogrande, M. Morris, R. A. Williams, & R. C. Waterfall (Eds.), *Tomography technique and process design and operation* (pp. 75−88). Manchester: Computational Mechanics Publications, ISBN 1853122467.

Wang, M., Dickin, F. J., & Williams, R. A. (1994). Electrical resistance tomography of metal walled vessels and pipelines. *Electronics Letters, 30*(10), 771−773.

Wang, M., Dickin, F., & Williams, R. (1995). *Electrical impedance tomography*. PCT/GB95/00520, GB2300927, AU18570/95, EP749285,US5807251, Publication number WO 95/24155.

Wang, B., Hu, Y., Ji, H., Huang, Z., & Li, H. (2012). A novel electrical resistance tomography system based on C4DTechnique. *Proceedings of 17th IEEE Instrumentation and Measurement Technology. Conf. 1929−32, 62*(5), 1017−1024.

Wang, M., Jones, T. F., & Williams, R. A. (2003). Visualisation of asymmetric solids distribution in horizontal swirling flows using electrical resistance tomography. *Transactions on IChemE, 81*(Part A), 854−861.

Wang, M., & Ma, Y. (2006). Over-zero switching scheme for fast data collection operation in electrical impedance tomography. *Measurement Science and Technology IOP, 17*(8), 2078−2082.

Wang, M., Ma, Y., Dai, Y., & Holliday, N. (2007). *EIT data processing system & methods*. PCT/GB04/003670, GB2422676, US 10/570,054.

Wang, M., Ma, Y., Holliday, N., Dai, Y., Williams, R. A., & Lucas, G. (2005). A high performance EIT system. *IEEE Sensors Journal, 5*(2), 289−299.

Wang, M., Mann, R., & Dickin, F. J. (1996). A large scale tomographic sensing system for mixing processes. In: *Proceedings for IWISP'96 (the 3rd Int. Workshop on Image and Signal Processing Advances in Computational Intelligence in Manchester)* (pp. 647−650). Manchester: Elsevier Science B.V., ISBN 0444825878

Wang, M., Mann, R., & Dickin, F. J. (1999). Electrical resistance tomographic sensing systems for industrial applications. *Chemical Engineering Communications, 175*, 49−70. OPA (Overseas Publishers Association).

Wang, M., & Yin, W. (2002). *Electrical impedance tomography*. PCT/GB01/05636, GB0129772.9, EP1347706, US 6940286, Publication number WO 02/053029.

Wang, M., Yin, W., & Holliday, N. (2002). A highly adaptive electrical impedance sensing system for flow measurement. *Measurement Science and Technology IOP, 13*, 1884−1889.

Webster, J. G. (1978). Amplifiers and signal processing. In J. G. Webster (Ed.), *Medical instrumentation: Application and design*. Boston: Houghton Mifflin.

Webster, J. G. (Ed.). (1990). *Electrical impedance tomography*. Bristol: Adam Hilger.

Weinman, J., & Mahler, J. (1964). An analysis of electrical properties of metal electrodes. *Medical Electronics and Biological Engineering, 2*, 299–310.

Weissberg, H. L. (1963). Effective diffusion coefficient in porous media. *Journal of Applied Physics, 34*, 2636–2639.

Wilkinson, A. J., Randall, E. W., Cilliers, J. J., Durrett, D. R., Naidoo, T., & Long, T. (2005). A 1000-measurement frames/second ERT data capture system with real-time visualization. *IEEE Sensors Journal, 5*(2), 300–307.

Williams, R. A., & Beck, M. S. (Eds.). (1995). *Process tomography- principles, techniques and applications*. Amsterdam: Butterworth-Heinemann.

Wilson, A. J., Milnes, P., Waterworth, A. R., Smallwood, R. H., & Brown, B. H. (2001). Mk3.5: a modular, multi-frequency successor to the Mk3a EIS/EIT system. *Physiological Measurement, 22*(1), 49–54.

Wu, Y., Li, H., Wang, M., & Williams, R. A. (2005). Characterization of air-water two-phase vertical flow by using electrical resistance imaging. *Canadian Journal of Chemical Engineering, 83*(1), 37–41.

York, T. (2001). Status of electrical tomography in industrial applications. *Journal of Electronic Imaging, 10*(3), 608–619.

Yuen, E. L., Mann, R., York, T. A., & Grieveet, B. D. (2001). Electrical resistance tomography imaging of a metal walled solid-liquid filter. In: *Proceedings of 2nd World Congress on Industrial Process Tomography: Hanover: VCIPT* (pp. 183–190).

Zhao, Y., Wang, M., & Hammond, R. B. (2011). Characterisation of crystallisation processes with electrical impedance spectroscopy. *Nuclear Engineering & Design Journal, 241*, 1938–1944.

Zhao, Y., Wang, M., & Hammond, R. B. (2013). Characterisation of nano-particles in colloids: relationship between particle size and electrical impedance spectra. *Journal of Nanoscience and Nanotechnology, 13*(2), 808–812.

Zhu, Q. S., McLeod, C. N., Denyer, C. W., Lidgey, F. J., & Lionheart, W. R. (1994). Development of a real-time adaptive current tomograph. *Physiological Measurement, 15*(Suppl. 2a), A37–A43.

This page intentionally left blank

Electromagnetic induction tomography

3

A.J. Peyton
University of Manchester, Manchester, UK

3.1 Introduction

Electromagnetic induction tomography is similar in terms of operation to the other electrical tomography methods and complements electrical resistance tomography (ERT) and electrical capacitance tomography (ECT) in completing a set of techniques based on the measurement of electrical impedance (be it resistance, capacitance or inductance). The technique is known loosely as electromagnetic tomography, but may be better referred to as magnetic induction tomography (MIT) or eddy current tomography by different workers in the field (Griffith, 2001; Norton & Bowler, 1993). Electromagnetic induction tomography operates by exciting the region of interest with an alternating magnetic field, whereas ECT and ERT both use electric field excitation. MIT exploits the principle of Faraday induction and is sensitive to magnetically permeable material due to the polarisation of magnetic dipoles or electrically conductive material resulting from the flow of magnetically induced eddy currents. A comparison of ECT, ERT and MIT is given in Table 3.1, showing their principal material sensitivities, nature of their sensing element and examples of applications.

The operation of an MIT system can be split into four generic functions:

1. The excitation of the region of interest with an energising magnetic field using alternating current flowing through a coil (or coils).
2. Modification of this field resulting from the action of the material distribution within the object space.
3. Boundary measurement of the resulting modified field distribution. The transmitters and receivers are usually placed on the external boundary based on accessibility to the process and not necessarily in a circular configuration.
4. Image reconstruction, often termed the inverse problem or inversion, which involves converting the measurements back into an image or measurements of the original material distribution.

In many cases, the system output will not be in the form of an image but may be a parameter or profile of interest. This output may be either calculated directly by the inversion process without an image or may be obtained indirectly via an intermediary step involving image reconstruction.

Referring to the twin coil example shown in Figure 3.1, a sinusoidal current is applied to the transmitter (the energising coil) to generate the magnetic field within the object space. We can assume a background condition with a relative permeability

Industrial Tomography. http://dx.doi.org/10.1016/B978-1-78242-118-4.00003-4
Copyright © 2015 Elsevier Ltd. All rights reserved.

Table 3.1 **A comparison of ECT, ERT and MIT**

Method	**Sensor elements**	**Typical arrangement**	**Measure values**	**Typical material properties**	**Typical material**
ECT	Capacitive plates	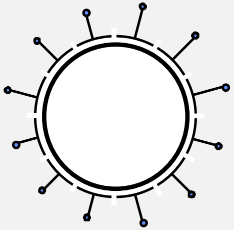	Capacitance C	ε_{r}, 1−100 σ, <0.1 S/m low	Oil, water, non-metallic powders, polymers, burning gasses
ERT (EIT)	Electrodes	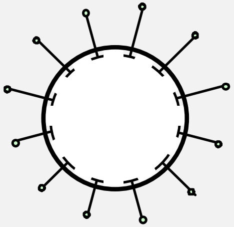	Resistance/ Impedance R/Z	σ, 0.001−10^7 S/m wide − determined by drive and detection circuitry ε_{r}, 1−100	Water/saline, biological tissue, rock/geological materials, semiconductors, e.g. silicon
MIT	Coils	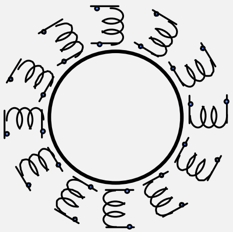	Self/Mutual inductance L/M	σ, 0.01−107 S/m depends on size and frequency range μ_{r}, 1−10,000	Metals, some minerals, magnetic materials, biological tissue, graphite.

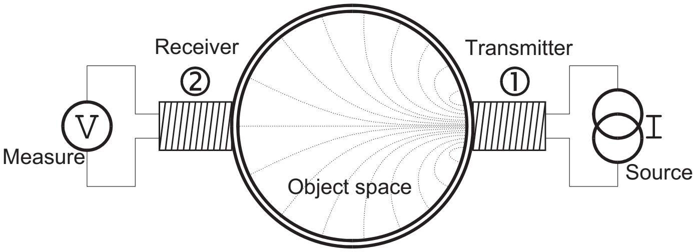

Figure 3.1 Simple concept of an electromagnetic induction tomography system.

of unity when the object space is empty (filled with air). In this condition, a measurable voltage will be induced in the receiver coil, corresponding to a background or empty space measurement. The relationship between the received voltage v and the transmitter current i is given by

$$v = j\omega Mi \tag{3.1}$$

where M is the mutual inductance between the transmitter and receiver coils.

The spatial distribution of the magnetic field and, hence, the mutual coupling between the coils is altered by the introduction of magnetic (relative permeability > 1) and/or metallic (high conductivity) items inside the object space. This gives rise to a change in the signal, Δv, in the receiver coil caused by the change in mutual inductance, ΔM, as given by the following:

$$\Delta v = j\omega \, \Delta M \, i \tag{3.2}$$

Magnetic material generally increases the mutual coupling between the coils, resulting in an increased measurement, whereas conducting objects generally attenuate the measurement due to eddy current losses in the material itself. Note ΔM is the usual complex representing both reactive and resistive coupling. These effects will be described in more detail shortly in Section 3.2. In order to acquire sufficient data for image reconstruction, several impendent excitation profiles, loosely termed projections, should be applied to the object space. For each projection, a number of receiver measurements should be made. This can be achieved by using a single transmitter–receiver pair. Indeed, one of the earliest reports of MIT (Al-Zeibak and Saunders, 1993) described an experimental system in which the object was physically moved through a transmitter–receiver coil pair to obtain one projection; then the object was rotated, and the process was repeated for another projection. This step was repeated several times to obtain the multiple projections for image reconstruction. Clearly, this mechanical procedure is time-consuming and only suited for a limited number of laboratory applications. Virtually all practical systems use multiple transmitters and receivers and multiplex electronically to acquire the measures of the mutual coupling between receiver and transmitter elements in real time.

Figure 3.2 shows the main elements of an MIT system. The system is split into three main subsystems (sensor array, conditioning electronics and host computer).

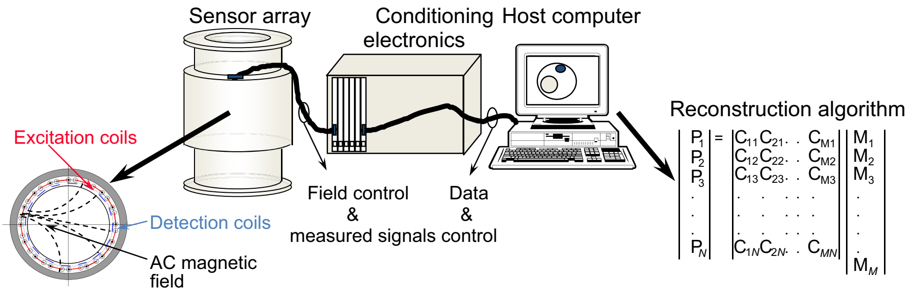

Figure 3.2 Block diagram of a typical electromagnetic induction tomography system.

The sensor array is energised with an AC magnetic field created by one or more of the excitation coils. Electrically conductive or ferromagnetic objects within the space cause the distribution of the applied magnetic field to be modified, and the resultant field changes are measured on the periphery of the space with an array of detection coils. These measurements are fed into a host computer. A set of such measurements is taken for a variety of flux injection patterns. From the acquired data, the host computer is able to produce an image of the material distribution by using suitable reconstruction software, which is shown in a much simplified form in the diagram as a matrix multiplication relating measured data values to pixel values. In practice, more sophisticated algorithms are used, as described later in Section 3.4.

In the context of this chapter, MIT generally refers to systems with excitation coils as the transmitters and detection coils as the receivers. So, in effect, the MIT system exploits the changes in the complex mutual induction between the transmitter and receiver coils. In some systems, the coils may perform both transmit and receive functions (Ma, Peyton, Higson, Lyons, & Dickinson, 2006), although in general, separate coils are preferred as this avoids the need for circuitry to perform the switching function. Coils are also relatively easy to wind, and coils can often be wound on top of each other. Virtually all applications use coils as opposed to permanent magnets for excitation simply because coils can be electronically controlled and operated at high frequencies (MHz) if necessary. Coils are also widely used as receivers and are generally preferred over other forms of magnetometers such as flux gates, magnetoresistors and hall sensors because most MIT systems operate in the range of tens of kHz to tens of MHz, where induction coils have benefits in terms of signal to noise performance (Tumanski, 2007).

MIT, ERT and ECT are often seen as distinct techniques, with ERT and ECT using plates or electrodes and MIT employing coils or magnetometers. However, there are reports of hybrid systems, where the excitation is achieved by induction and the detection is accomplished using contact electrodes. One such example is induced current ERT where AC magnetic fields are used to induce eddy currents in the object, and ERT is performed using contact electrodes as detectors (Tanguay, Gagnon, & Guardo, 2007). An alternative example (Resagk, Men, Ziolkowski, Kuilekov, & Brauer, 2006) employed direct current injection for excitation and magnetometers to detect the resulting magnetic field caused by the current flow. In this study, two conducting fluids were contained in a cylindrical cell, and the tomographic reconstruction problem was to determine the shape of the 2D interface between the two fluids.

In addition to AC induction, the motion of the object material through the sensor array can also create a measureable secondary magnetic field as a result of Faraday's law of induction. This approach is particularly appropriate for measuring velocity flow in conducting fluids. The excitation field is typically applied with a DC or very low-frequency electromagnet, and the resulting secondary field can be measured using either (i) contract electrodes or (ii) very sensitive magnetometers, such as flux gates. An example of case (i) is the measurement of flow rate through pipes. In particular, conventional electromagnetic flow meters consisting of a perpendicular arrangement of flow, magnetic field and measurement electrodes have been widely used. Unfortunately, conventional flow meters are sensitive to the flow profile within the liquid and, consequently, must be installed away from bends. The tomographic approach has been reported (Horner, Mesch, & Trächtler, 1996) to improve the response of these measurement devices. Recently, this approach has been extended to allow single- and dual-phase flow profiles to be imaged (Zhao, Lucas, Leeungculsatien, & Zhang, 2102). An example of (ii) is contactless inductive flow tomography (CIFT), and in one report (Stefani, Gundrum, & Gerbeth, 2004), the 3D velocity profile of a room-temperature liquid metal, InGaSn, has been demonstrated when the liquid InGaSn is driven by an impeller. The CIFT technique has also been applied to models of continuous casting of the type commonly used in the steel industry (Timmel, Eckert, Gerbeth, Stefani, & Wondrak, 2010).

The noncontacting and noninvasive nature of inductive tomography systems have made these systems attractive to research in a number of applications where conductive or magnetic materials are involved. The ability to vary the excitation frequency, which in turn determines the depth of penetration of the field into a conducting object, allows frequency to be used for depth profiling and, hence, to provide additional depth information. Examples of applications include nondestructive testing (NDT), such as imaging cracks in metallic components and depth profiling of conducting coatings; imaging the flow of conducting fluids and in particular the flow of liquid metals; security applications such as characterising metal objects in walk-through metal detectors; biomedical applications; and inspection of nuclear graphite. These are described in more detail later in Section 3.6.

3.2 Principle of operation and governing equations

A formal description of this measuring system can be derived from Maxwell's equations, as follows:

$$\nabla \times \boldsymbol{E} = -\frac{\partial \boldsymbol{B}}{\partial t} \tag{3.3a}$$

$$\nabla \times \boldsymbol{H} = \boldsymbol{J} + \frac{\partial \boldsymbol{D}}{\partial t} \tag{3.3b}$$

$$\nabla \cdot \boldsymbol{D} = \rho \tag{3.3c}$$

$$\nabla \cdot \boldsymbol{B} = 0 \tag{3.3d}$$

where $\boldsymbol{B}$ is the magnetic flux density vector, $\boldsymbol{H}$ is the magnetic field strength vector, $\boldsymbol{D}$ is the electrical displacement, $\boldsymbol{E}$ is the electric field strength, $\boldsymbol{J}$ is the current density and ρ the charge density at position $\boldsymbol{r}$ in space. If we assume the materials have linear and isotropic electrical and magnetic properties, then the following are true:

$$\boldsymbol{B} = \mu_0 \mu_\mathrm{r} \boldsymbol{H} \tag{3.4a}$$

$$\boldsymbol{D} = \varepsilon_0 \varepsilon_\mathrm{r} \boldsymbol{E} \tag{3.4b}$$

$$\boldsymbol{J} = \sigma \cdot \boldsymbol{E} \tag{3.4c}$$

where μ and ε represent permeability and permittivity, respectively, with subscripts 0 and r in turn describing free space and relative values, and σ is the electrical conductivity. For many practical applications, several fundamental simplifications can be made, such as (i) ignoring the effects of the displacement current, which may be negligible for the materials and signal frequencies of interest, that is $\sigma >> j\omega \ \ \varepsilon_0 \varepsilon_\mathrm{r}$ and (ii) ignoring the velocity terms, which are mainly of interest to CIFT. So Maxwell's equations for the induction problem can be rewritten as follows:

$$\nabla \times \left[\left(\nabla \times \frac{\boldsymbol{B}}{\mu} \right) \Big/ \sigma \right] = -\mathrm{j}\omega \boldsymbol{B} \tag{3.5a}$$

$$\nabla \cdot \boldsymbol{B} = 0 \tag{3.5b}$$

$$\nabla \cdot \boldsymbol{D} = \rho \tag{3.5c}$$

These sets of simultaneous partial differential equations describe the general forward MIT problem and should be solved with the appropriate boundary conditions, which express the particular MIT application and sensor geometry, and an outer boundary condition that ensures that the magnetic field tends to zero, as $|\boldsymbol{r}| \to \infty$. The Maxwell expression $\nabla \cdot \boldsymbol{B} = 0$ is a statement of the continuity of the magnetic field. The electrostatic conditions represented Gauss's Law, that is $\nabla \cdot \boldsymbol{D} = \rho$, must also be solved together with the induction effect described by Eqn (3.5a). The free charge, ρ, builds up on the surface between conductors and insulators to ensure that current flow is parallel to the surface. In some special cases that have 2D symmetry, there may be no accumulation of surface charge (the magnetically induced electric field is tangential to the surface), and then electrostatic effects can be ignored. However, in general, a full 3D solution to the field problem is essential.

The vector field expressions are often stated in terms of vector magnetic potential, $\boldsymbol{A}$, and scalar electric potential, V, defined as follows:

$$\boldsymbol{B} = \nabla \times \boldsymbol{A} \tag{3.6a}$$

$$\boldsymbol{E} = -\nabla V - \mathrm{j}\omega \boldsymbol{A} \tag{3.6b}$$

Considering individual regions in the object space with constant electrical conductivity and magnetic permeability, then Eqn (3.5) can be expressed as follows:

$$\nabla^2 \boldsymbol{A} + \mathrm{j}\omega\mu\sigma \boldsymbol{A} = \mu \boldsymbol{J} \tag{3.7a}$$

$$\nabla^2 V = -\frac{\rho}{\varepsilon} \tag{3.7b}$$

Consideration of Eqn (3.7) reveals the scaling relations for the ECT, ERT and MIT modalities. For ERT and ECT, which obey the Laplace/Poisson equation (3.7b), a simple scaling relation exists, and the geometry of the sensor can be scaled to suit the application as long as all the dimensions are scaled in proportion. For MIT, the scaling relationship is different. Considering Eqn (3.7a), and assuming as dimensional scaling such that the following results:

$$\boldsymbol{r} = k\,\boldsymbol{r}' \tag{3.8}$$

and letting $\boldsymbol{A}'(\boldsymbol{r}')$ be a solution to Eqn (3.7) and defining $\boldsymbol{A}'(\boldsymbol{r}') = \boldsymbol{A}(k\boldsymbol{r}')$. Because$\nabla^2 \boldsymbol{A} = \frac{1}{k^2}\nabla^2 \boldsymbol{A}'$, Eqn (3.7a) becomes the following:

$$\nabla^2 \boldsymbol{A}' - \mathrm{j}\omega\mu\sigma k^2 \boldsymbol{A}' = -k^2 \mu \boldsymbol{J} \tag{3.9}$$

which is a diffusion equation. Equation (3.9) indicates that if the current density $\boldsymbol{J}$ and the frequency increase by k^2 times, then the magnetic potential in the new system is just a geometrically scaled version of the original system. For an inflated system ($k < 1$), if the current density reduces by $\frac{1}{k^2}$ times, then the current remains the same considering the area increases by $\frac{1}{k^2}$ times. From $\boldsymbol{B}' = \nabla \times \boldsymbol{A}' = k\nabla \times \boldsymbol{A} = k\boldsymbol{B}$, it can be seen that the magnetic flux density reduces by $\frac{1}{k}$ times. However, the area the flux flows through increases by $\frac{1}{k^2}$ times; hence, the inductance increases. The induced voltage and inductance can also be expressed in terms of a line integration of $\boldsymbol{A}$, where an inflated system increases the integral line length and results in an increase in inductance. These conclusions are true for 3D cases. In a 2D situation, the induced voltage and the inductance are expressed as the difference of $\boldsymbol{A}$ at the two ends of the coil, and therefore, the inductance remains the same irrespective of any geometrical scaling.

In general eddy current problems, the depth of penetration, also termed the skin depth, is expressed as follows:

$$\delta = \sqrt{\frac{1}{f\mu\sigma\pi}} \tag{3.10}$$

Therefore, $\frac{1}{k^2}$ times increase in frequency corresponds to k times decrease in the skin depth, which essentially is a geometrical quantity. Therefore, by scaling the frequency with a square term of the geometrical scale, a simple relation in terms of its primary quantities (magnetic field intensity, flux density, etc.) and secondary quantities (inductance, coupling coefficient) can also be found. These relations provide useful guidelines in process scaling up and scaling down (Yin & Peyton, 2010a).

The depth of penetration, δ, is an important parameter in MIT because it describes the distance that the applied electromagnetic field can penetrate into electrically conducting material. Equation (3.10) shows that δ is inversely proportional to the square root of frequency. For the plane geometry case, the field will fall away exponentially from the surface of the material such that by a distance of δ from the surface, the field will be $1/e$ (36.79%) times the surface value. Clearly, this effect dictates the required range of frequencies for an MIT system. Normally, the depth of penetration is chosen either to be comparable with the dimensions of the largest conducting objects in the object space, or if the space is completely filled with conductive material, to be comparable with the largest dimension of the object space. In the limiting case when δ is much smaller than the object dimensions, then the field penetration is limited to just the very surfaces of the objects, and the received signals contain only information on the shape and surface impedance of the conductive material in the object space. On the other hand, when δ is much larger than the object dimensions, then the field may completely penetrate the object. But, the field interactions will be relatively small, and therefore, the signals caused by the object will also be very small. This is the case for lower conductivity material, for instance, biological tissues. Figure 3.3 shows a plot of penetration depth versus frequency for a range of nonmagnetic materials of different conductivities. As can be seen, metals (with conductivities in the MS/m range) require low excitation frequencies, kHz or less, whereas biological tissues and aqueous objects (with conductivities of the order of 1 S/m) require frequencies in the MHz range. It is important to note that Figure 3.3 represents the situation for a nonmagnetic material. For magnetic materials with $\mu_r \gg 1$, such as ferritic steel, then δ will be much smaller than the values in the graph due to the permeability term in Eqn (3.10).

The basic interactions of magnetic and conducting materials with an AC magnetic field that are relevant to MIT are summarised in Figures 3.4–3.6. There are two fundamental physical processes in play, namely polarisation and induced eddy currents.

Magnetic materials ($\mu_r > 1$) can polarise due to the interaction of the applied field with the magnetic dipoles at the electronic and atomic scales within the material. Depending on the nature of the dipole interactions, the response of the material may be generally classed as either ferrimagnetic or ferromagnetic. In both cases, the material tends to concentrate the magnetic flux, and a simple illustration is given in

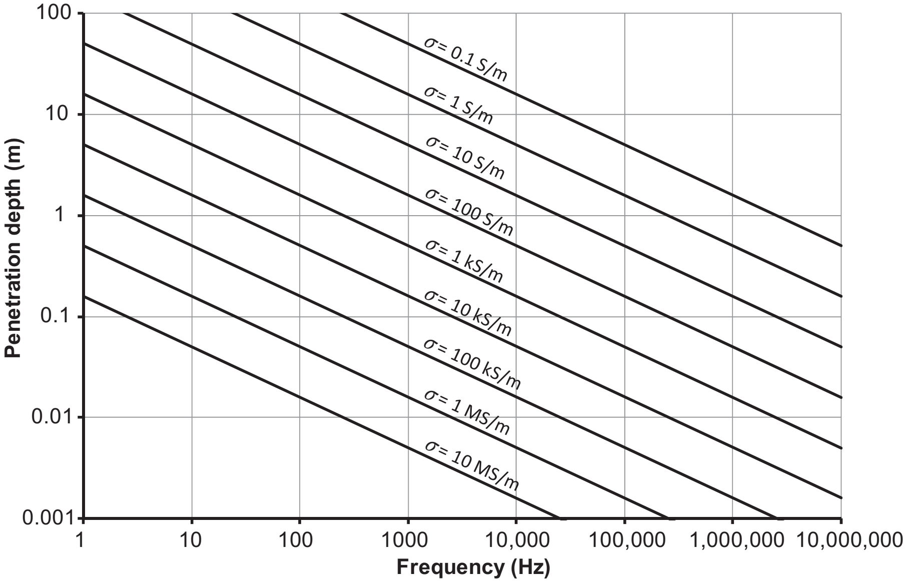

Figure 3.3 Depth of penetration versus frequency for nonmagnetic materials of different electrical conductivity.

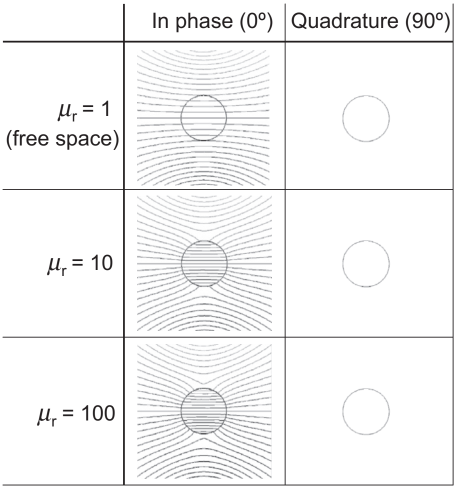
In phase (0°)
Quadrature (90°)
μr = 1
(free space)
μr = 10
μr = 100

Figure 3.4 The effects of magnetic permeability for a nonconducting spherical object placed in a magnetic field.

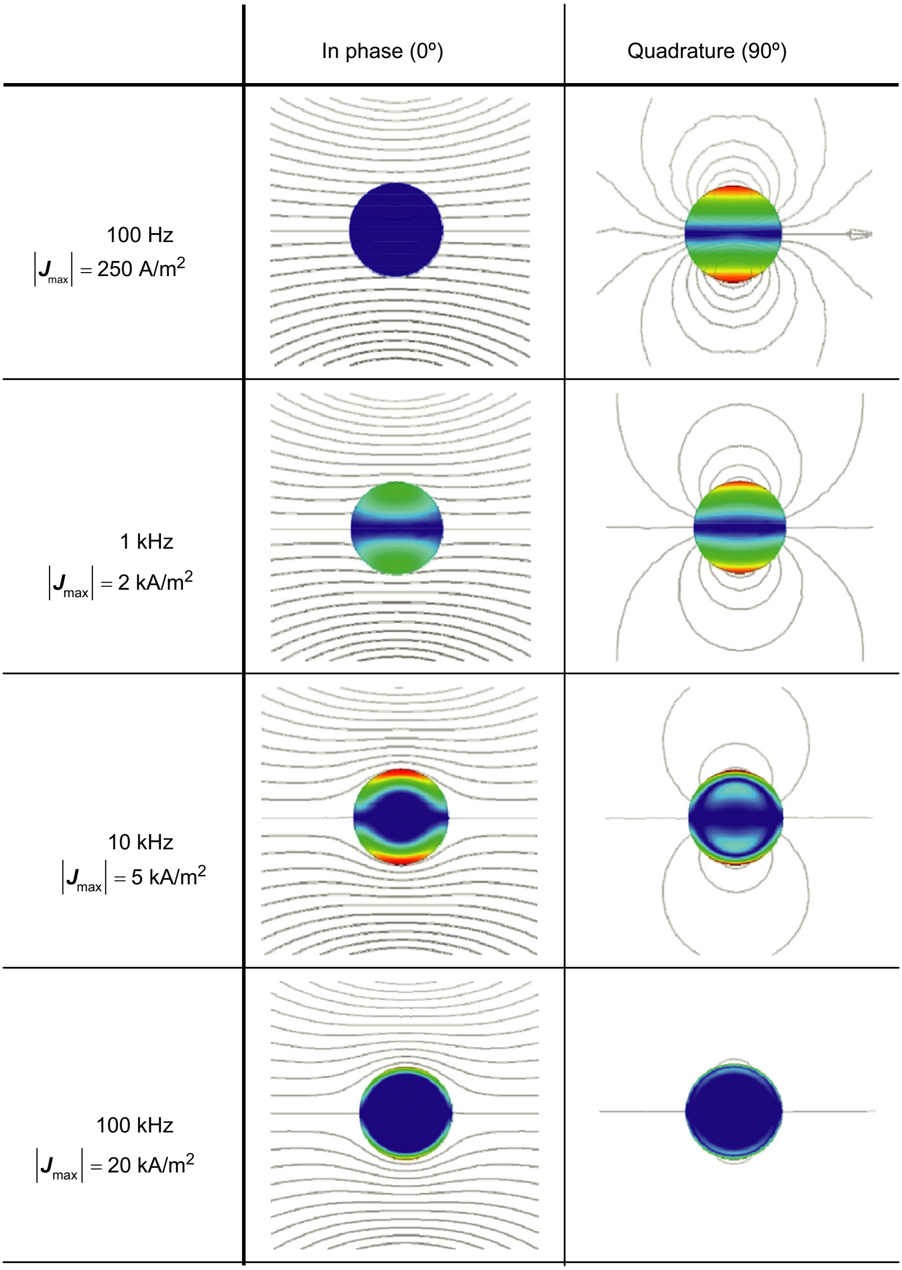
In phase (0º)
Quadrature (90º)
100 Hz
$|\boldsymbol{J}_{\max}| = 250\ \mathrm{A/m^2}$
1 kHz
$|\boldsymbol{J}_{\max}| = 2\ \mathrm{kA/m^2}$
10 kHz
$|\boldsymbol{J}_{\max}| = 5\ \mathrm{kA/m^2}$
100 kHz
$|\boldsymbol{J}_{\max}| = 20\ \mathrm{kA/m^2}$

Figure 3.5 The effects of diffusion with frequency for a conducting, nonmagnetic spherical object placed in an AC magnetic field.

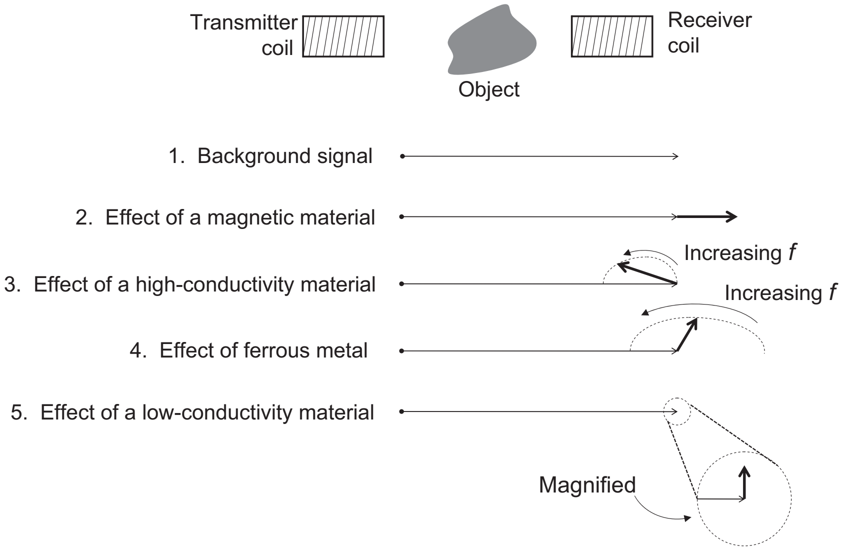
Transmitter coil
Object
Receiver coil
1. Background signal
2. Effect of a magnetic material
3. Effect of a high-conductivity material
Increasing *f*
4. Effect of ferrous metal
Increasing *f*
5. Effect of a low-conductivity material
Magnified

Figure 3.6 Phasor response of different objects in MIT.

Figure 3.4. Here, a nonconducting sphere is shown in an applied AC magnetic field, and the effects of three different values of μ_r are shown on the distribution of the lines of magnetic flux for both the in-phase and quadrature components of the field. The free space condition, that is when $\mu_r = 1$ for the sphere, shows the situation if the sphere was not present. As μ_r increases, the magnetic flux becomes more concentrated within the sphere, as shown for the cases with $\mu_r = 10$ and $\mu_r = 100$ where the sphere offers an easier path for the flux to circulate through. Note that the majority of the flux concentration occurs for $1 < \mu_r > 10$. Note also the quadrature component of the field remains zero.

Eddy currents are induced in electrically conducting materials when an AC magnetic field is applied. The eddy currents flow as to oppose the field that has produced them, resulting in a net energy loss in the system. A simple illusion of the effects of the induced eddy currents in a conducting, nonmagnetic sphere is given in Figure 3.5. Here, the sphere is aluminium and has a diameter of 2 cm. The magnitude of the induced eddy currents within the sphere is shown as a colour scale. The colour scale is light spectra coded, where blue represents zero, green represents middle values and red represents maximum. The maximum eddy current magnitudes, $|\boldsymbol{J}_{\max}|$, are also given for each example. At low frequencies (100 Hz), the in-phase component of the field is virtually the same as for the free space case, but there is a small quadrature component to the field caused by the induced eddy currents. The induced eddy currents are also the smallest of the four cases shown. As frequency increases, the eddy currents also increase in magnitude, but they are distributed closer to the upper and lower surfaces of the sphere as shown in this cross-section, which illustrates the diffusion effect associated with induced fields. Also, as frequency increases, the eddy currents become stronger for the in-phase compared to the quadrature component. At the highest frequency, 100 kHz, the eddy currents flow on the outer skin of the sphere, and there is virtually no penetration of the magnetic flux inside the sphere; all the magnetic flux circulates around the object.

Figure 3.6 shows the effect of a magnetic and/or conducting object on the measured signal as represented by a complex phasor. The diagram shows an idealised situation with the coupling between a transmitter and a receiver and the object positioned in between. Five situations are shown:

1. When there is no object, there is only the background signal resulting from the magnetic flux that directly couples the two coils.
2. For a magnetic, nonconducting object, there is an additional phasor, known as the object signal, which is in-phase with the background signal. Here, the object signal is caused by the increased flux passing thought the object. This was also shown earlier in Figure 3.4.
3. For a conducting, nonmagnetic material, the phasor caused by the object has both in-phase and quadrature components. This situation was also shown earlier in Figure 3.5. Note the phase angle between the object signal and background signal is approximately 90°at zero frequency and 180° as the frequency approaches infinity.
4. The effect of a magnetic and conducting material such as a ferrous metal is the combination of the two cases above. Note the phase angle between the object signal and background signal is approximately 0° at zero frequency and 180° as frequency approaches infinity.
5. This is a special case for low-conducting material, typical of biological tissues. Here, there is only a weak interaction between the applied field and the object. The resulting object signal is approximately 90° out of phase with the background. Note that this illustration is idealised and ignores the effects of any diamagnetic or paramagnetic properties and also the flow of capacitive (displacement) current, which will produce a small (and potentially measureable) in-phase signal.

The discussion so far in this section has only covered the two coil case with a single transmitter and receiver. The tomographic problem for MIT is, therefore, to excite the object space with a number of spatially distinct magnetic field patterns that can be measured at accessible positions on the boundary of the object space. A sufficient number of independent field patterns and field measurements must be used to provide an adequate measurement set to enable images of an acceptable quality to be produced. To achieve this objective, the object space is surrounded by an array of coils. It is usual in MIT to use dedicated excitation and detection coils/channels; however, it is possible to operate coils in both modes using suitable switching circuitry. To obtain the maximum amount of information from the object space measurements, the in-phase (or real) and quadrature (or imaginary) components of both the radial and two tangential field components should be acquired. However, most practical systems ignore the tangential field components and only use coils facing in a radial direction.

3.3 Solution to the forward problem

MIT involves the solution of both the forward and inverse problems. The forward problem is to calculate the received signals for all relevant transmitter/receiver coil combinations if the distribution and electrical properties of the object material are known. This is usually a well-defined problem with a unique solution based on the description of physical laws, as may be expressed by Maxwell's equations. The inverse problem is the converse and involves estimating the object distribution from the measured mutual inductances between the coils, which is both an ill-posed and ill-conditioned problem.

Often the object space is divided into pixel (2D) or voxel (3D) elements, and the purpose of the image reconstruction or inversion algorithm is to determine the electrical properties, μ or σ, of each element to produce a 2D image or 3D representation of the object space. However, the use of pixels or voxels is just one way of representing the object, and in many cases, the end user is interested in particular parameters such as a conductivity gradient or the position of a boundary between two phases or the position and size of a crack in a metallic component. In these cases, it may be more efficient and accurate to represent the object material in a parameterised form and develop a forward solution specifically for that particular description of the problem.

The key requirements of the forward solution are to be accurate and computationally efficient. Unfortunately, these are usually conflicting requirements, and since the 1990s, there have been reports of several different methods, including the following:

1. Linear approximations
2. Analytical approach
3. Finite element method (FEM)
4. Boundary element method (BEM)
5. Full wave solutions
6. Impedance method
7. Dipole approximation

These will be described briefly in the following sections.

A crucial task in the formulation and implementation of the forward problem is to validate and calibrate the model against measurements from the real system. One example of this process for an inductive sensor is described by Johnstone and Peyton (2001). For MIT, a calibration process is often needed to fine-tune parameters such as the exact position of the coils between measurements and model (Gürsoy and Sharfettter, 2011) and also to account for simplifications assumed in the analysis.

3.3.1 Linear approximation

The linear approximation may be applied only to very small perturbations in voxel values, and a linear response is assumed between changes in the values of the pixels (or voxels) and the consequential changes in the measured mutual inductances between the coils. If there are k pixels each of value p_i, which represents a required electromagnetic property of the pixel, then the pixel values can be arranged into a vector $\mathbf{P}$. Similarly, if there are n measured coil combinations, each with a measured mutual inductance of m_j, then the measured values can be arranged into a vector, $\mathbf{M}$. The linear approximation simply relates small changes in **M**, that is $\delta\mathbf{M}$, to the change in **P**, that is $\delta\mathbf{P}$ via a sensitivity matrix, **S**, as follows:

$$\delta\mathbf{M} = \mathbf{S}\cdot\delta\mathbf{P} \tag{3.11}$$

S is also the Jacobian matrix of the MIT system, where **M**, **S** and **P** are given by the following:

$$\delta\mathbf{P} = \begin{vmatrix} \delta p_1 \\ \vdots \\ \delta p_i \\ \vdots \\ \delta p_k \end{vmatrix} \quad \delta\mathbf{M} = \begin{vmatrix} \delta m_1 \\ \vdots \\ \delta m_j \\ \vdots \\ \delta m_n \end{vmatrix} \quad \mathbf{S} = \begin{vmatrix} \frac{\partial m_1}{\partial p_1} & \cdots & \frac{\partial m_1}{\partial p_k} \\ \vdots & \ddots & \vdots \\ \frac{\partial m_n}{\partial p_1} & \cdots & \frac{\partial m_n}{\partial p_k} \end{vmatrix} \tag{3.12}$$

Often the δ notation is omitted as the signal changes with respect to the background, and $\delta\mathbf{P}$ and $\delta\mathbf{M}$ are simply referred to as **P** and **M**, respectively. The coefficients in **S** can be obtained experimentally by sweeping a small test object, which represents a perturbation, over the object space and measuring the resulting response of each relevant coil combination. This is a laborious process unless automated. So, the usual approach is to compute the $\frac{\partial m_j}{\partial p_k}$ coefficients either by perturbing each pixel in turn using, for instance, an FEM model, which is very computationally intensive, or by using the vector fields from a full field solution as described in Section 3.4.

Each row in **S** can be rearranged into its original 2D or 3D pixel structure to represent a sensitivity map of the response of a particular transmitter—receiver coil combination to the spatial position of material in the object space. Figure 3.7 shows an example of a sensitivity map for a circular 16-pole MIT array in which each pole contained both a transmitter and a receiver coil. In this example, the empty space sensitivity map between poles 1 (12 o'clock position) and 3 (2 o'clock position) is shown. As can be seen, the response is very high for the pixel positions directly in front of the poles.

The advantages of the linear approximation method are the ease of implementation and computational simplicity; it one of the simplest forward models for MIT. Although the linear approximation may be satisfactory for other forms of electrical tomography, such as ECT, where the changes of material properties are relatively small, it does not describe the physics of eddy current induction particular well. Consequently, the disadvantages are manifold. The method is inaccurate, especially for material with a high conductivity or permeability because the object material significantly changes the applied field distribution. Overall, the linear forward model does tend to produce qualitative images showing roughly where the material is within the object space. It performs better for identifying isolated regions of high-conductibility material against

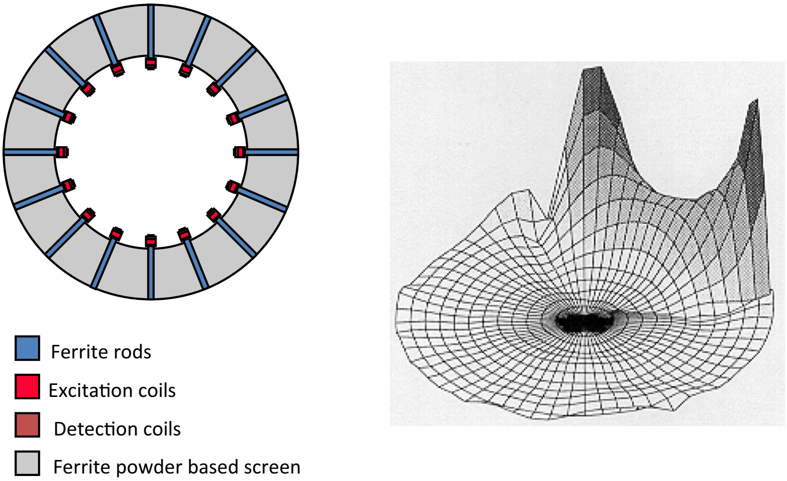

Figure 3.7 Example of a sensitivity map in MIT.

an empty space background. For imaging inside conducting regions, the sensitivity matrix should be calculated for a nominal baseline object distribution, which assumes that the external shape of the conducting object is known.

3.3.2 Analytical approach

In cases where the application has a high degree of symmetry or a simple geometry, such as a circular coil positioned in parallel above a large conducting plate or a coaxial coil placed inside a circular pipe, analytical solutions may exist. These can be used either to solve the forward problem directly or to validate the solutions from other computational models by providing examples of known solutions. One popular example is the solution by Dodd and Deeds (1968). This has been extended (Cheng, Dodd, & Deeds, 1971) for a circular coil above a layered metal, which is illustrated in schematic form in Figure 3.8 and can form a basis for tomographic inversion for depth profiling (Yin, Dickinson, & Peyton, 2005).

An advantage of the analytical approach can be computation speed. Unfortunately, the approach can only be used for simple geometries, and the method has the disadvantages of having to deal with complicated algebraic solutions that typically involve integrating sums of Bessel functions.

3.3.3 Finite element method

FEM has been widely reported in MIT research, both as a tool to assist sensor design and also as a forward solver as part of an iterative reconstruction algorithm (Hollaus, Magele, Merwa, & Scharfetter, 2004a; Soleimani, Lionheart, Peyton, Ma, & Higson, 2006). There is a considerable amount of literature on the FEM; one good text is Silvester and Ferrari (1996). There are also many commercial suppliers of FEM

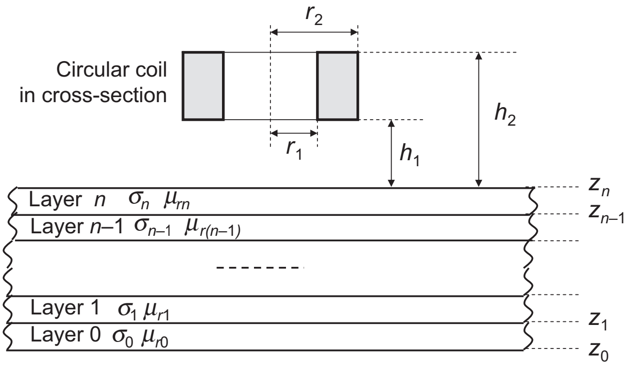
r_2
Circular coil
in cross-section
h_2
r_1
h_1
Layer n σ_n μ_{rn}
Layer n–1 σ_{n-1} $\mu_{r(n-1)}$

Layer 1 σ_1 μ_{r1}
Layer 0 σ_0 μ_{r0}
z_n
z_{n-1}
z_1
z_0

Figure 3.8 A schematic of the solution of Deeds and Dodd for a circular coil above an infinite flat plate.

software, so it is unusual for the worker to construct FEM code from first principles. Commercial software packages vary in terms of their features; however, of particular importance for tomography is ability to access solution data at the mesh level, which is vital for the image reconstruction or inversion process.

The FEM involves discretising the problem space into discrete elements, usually triangles for 2D applications and tetrahedra for 3D geometries. The FEM describes the field solution for each element with simple linear or quadratic equations, which are solved simultaneously for the complete system. In MIT, the complete sensor geometry, the material in the object space and, if the sensor array is not shielded, sufficient external space to account for the field distribution must be included in the model. Eddy current phenomena also present particular difficulties for FEM modelling as the field penetration should be well represented. Typically, the tetrahedra should be smaller than the penetration depth described earlier in Eqn (3.10). Regions where the skin depth is small, for example metal components, and especially ferritic steel, may require a large number of tetrahedra to accurately describe the diffusion of the field, which can result in a problem with a very large number of tetrahedra. In addition, the tetrahedral elements in the skin region may be very small (e.g. <0.1 mm), whereas the elements elsewhere in free space regions may be large >100 mm. This large factor in element size can also lead to numerical instabilities in the FEM computational processes.

A good example of an FEM mesh applied to a biomedical problem is shown in Figure 3.9. In this case, the FEM mesh was used in the study of MIT for imaging cerebral haemorrhage. The image on the left shows an enlarged view of the tetrahedral elements on the surface of the head and internal tissues, whereas the right-hand image shows the complete mesh (Zolgharni, Ledger, Armitage, Holder, & Griffiths, 2009).

The advantages of FEM are the widespread availability of commercial and research codes, and the method can give a physically accurate description of most problem geometries. Unfortunately, the computation demands from FEM can be significant, and there is usually a trade-off between accuracy and computational speed. On the one hand, the forward problem should be represented with a large number of elements

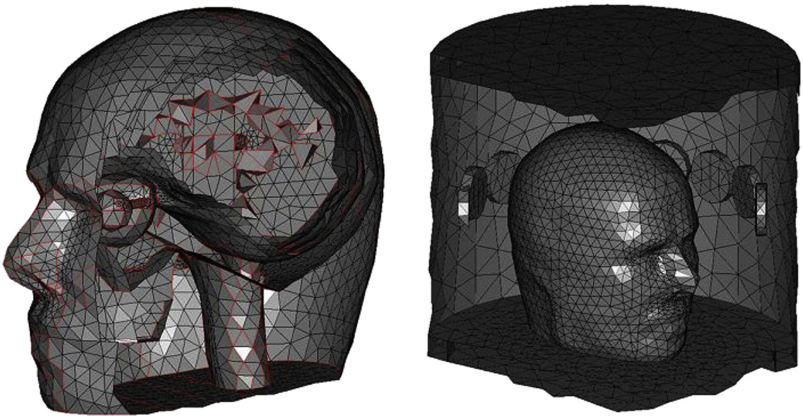

Figure 3.9 Example of an FEM mesh used in the study of MIT for imaging a cerebral haemorrhage. Left: enlarged view of the boundary elements on the surface of the head and internal tissues. Right: the complete mesh.
Reproduced courtesy Zolgharni et al. (2009).

in the finite element mesh to ensure adequate accuracy. Normally this involves a study of mesh convergence, whereby meshes of different sizes and distributions are tested to determine the point at which the solution converges to a common value within error limits. On the other hand, computation time increases markedly with mesh size. At present, FEM cannot offer real-time operation (e.g. video rate) on mid-performance workstations; models with >100 K tetrahedra are often required with computational times per model in the minutes to tens of minutes range. Specialist hardware and optimisation of the algorithms and coding can bring these timescales down significantly.

3.3.4 Boundary element method

Boundary methods can offer a more efficient approach for applications where there are a small number of distinct regions and the tomographic problem is to determine either the boundary or the electromagnetic properties of the material. The approach now is to use surface integrals and Green functions for the particular geometry and solve the fields on the boundaries between the different regions. Once the fields on the boundary are known, the fields everywhere can be determined from the Green functions.

A good example of this approach was reported (Pham, Hua, & Gray, 2000a) for imaging solidification of molten metal inside a metal pipe. This is of particular interest to the metal production industry of furnace tapping and molten metal flow control. Figure 3.10 shows a schematic of the measurement system which contains a solenoid carrying AC current placed around the pipe. The impedances of the solenoids are sensitive to the electrical conductivity of the metal pipe, the solidified metal and the liquid metal. The tomographic problem is to determine the position of the boundary between the liquid and solid metals inside the pipe. To achieve this, the sensing technique exploits the difference in electrical conductivity between the solid and liquid metals.

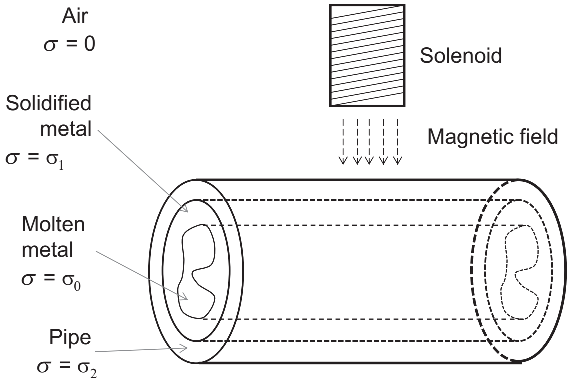

Figure 3.10 Schematic of the measurement system that contains a solenoid carrying AC current placed around the pipe, as used by Pham et al. (2000b).

The boundary approach can offer an efficient, bespoke solution for applications where the geometry can be split into well-defined regions and the tomographic inversion problem can be specified in these terms. Of course, the solution is tailored to the needs of the application and, therefore, requires a high investment of effort to formulate and prove the electromagnetic formulations and the detailed the implementation of the model. As a final comment, it is possible to combine BEM/FEM approaches, so that boundary methods are used for large regions of uniform properties, and FEM is used to describe regions with internal detail.

3.3.5 Full wave solutions

There are a variety of techniques for solving the full set of Maxwell's equations, which include, for example, both frequency and time domain methods. FEM is popular for frequency domain solutions where the fields are calculated for a defined frequency. Time domain techniques directly model the propagation of electromagnetic waves. Here, the problem space is typically divided into a Cartesian grid of cubic elements, and the solution involves calculating the propagation of the electric and magnetic fields between neighbouring elements in discrete time steps. Popular methods include the finite difference time domain (FDTD) technique and the transmission line matrix (TLM) method.

Generally, full wave solvers are very inefficient for MIT because the eddy current and magnetic polarisation effects occur at much lower frequencies than wave propagation phenomena, and consequently, the solution process must continue until all transients have dissipated and the model settles to near DC conditions. Nevertheless, full wave solvers do offer the potential to account for parasitic coupling due to electric fields (important for electrostatic screening) and also the effects of displacement current (important because MIT is used for increasingly higher frequencies). Full wave solvers also provide an independent means of validating other forward models, as reported by Zolgharni et al. (2009).

3.3.6 Impedance method

For applications where the skin depth, δ, is much larger than the object dimensions, such as low conductivity applications in biology and processing aqueous solutions, then the field changes caused by the object may be very small compared to the applied field. This is also known as the 'weakly coupled' case. Here, the excitation field can be assumed to be unaffected by the object and, therefore, can be computed a priori. The object field resulting from this excitation can be computed independently, and it typically acts with a phase angle in quadrature to the applied field, as illustrated earlier in Figure 3.5 (top row) and Figure 3.6, example 5.

The weakly coupled approximation is used by a number of researchers working on medical MIT applications (Morris, Griffiths, & Gough, 2001; Ktistis, Armitage, & Peyton, 2008; Dekdouk, Wuliang Yin, Ktistis, Armitage, & Peyton, 2010) to reduce the computation load of the forward problem. The impedance method is an alternative to edge FEM for solving the induced field inside the object. The method involves dividing the problem space into cubic voxels, with the nodes of the impedance mesh at the voxel centres. The voxels are represented as an electrical network consisting of six admittances and six induced voltages, as shown in Figure 3.11. Thus, the forward problem is reduced to an electrical network equivalent that is solved accordingly. More details on the impedance method are given in Armitage, Le Veen, and Pethig (1983) and Gandhi, DeFord, and Kanai (1984).

Figure 3.12 shows an example of the impedance method applied to a study of head imaging (Dekdouk et al., 2010). Figure 3.12(a) shows the head model with coronal cutaway plane showing the conductivity distribution for a normal head with the electrical conductivity of the tissues labelled using gray scale. Figure 3.12(b) contains a

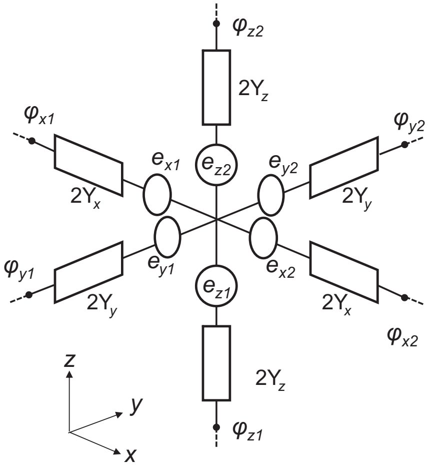

Figure 3.11 Method for dividing the problem space into cubic voxels, with the nodes of the impedance mesh at the voxel centres. The voxels are represented as an electrical network consisting of six admittances and six induced voltages.

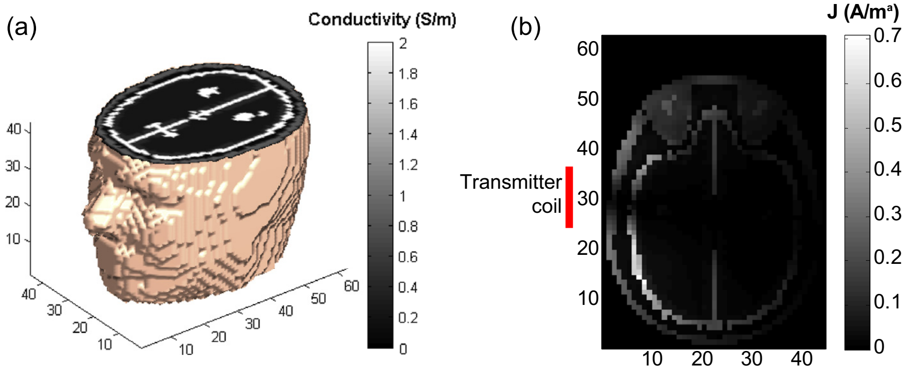

Figure 3.12 Example of the impedance method applied to a study of head imaging *(courtesy Dekdouk et al., 2010)*. (a) Head model with coronal cutaway plane showing conductivity distribution for a normal head; (b) contains a plot of the current density on the sagittal sectional.

plot of the current density on the sagittal sectional plane of the head. As expected, the current flow is highest in regions with relatively high conductivities, notably in the cerebrospinal fluid (CSF) as well as near the excitation coil where the flux density is strong. The eddy currents also tend to circulate in loops parallel to the current flow in the excitation coil and tend to zero on the axis of the coil, which is also indicated on the plot.

3.3.7 Dipole approximation

The dipole approximation offers a very efficient solution to the forward problem in special situations where the location and characterisation of a metallic or magnetic object is required and the object is relatively small (i.e. < factor of 10) compared to the dimensions of the sensor array. These situations are typical of metal detection, for instance, in walk-through metal detectors (WRMDs) and systems for explosive remnants of war (ERW) such as landmines.

In the time harmonic regime, the projection of a conducting target with an alternating primary magnetic field by an MIT sensor generates, according to Faraday's induction law, a flow of eddy currents inside the volume of the target. These currents, in turn, produce a perturbation secondary field that is sensed by the inductive sensor. In theory, the eddy currents can be expanded into a series of multipole moments of currents, and a similar representation also applies to the associated secondary field. For a magnetic multipole expansion series of order n, the field terms will have strengths falling off as $1/r^{n+2}$, at distances r away from the currents. The lowest order term in this series is called the dipole moment. If the target is placed far enough from the sensor, the secondary field can be approximated by an induced dipole moment. Figure 3.13 shows an illustration of this approximation with the field from the target being generated by a dipole moment.

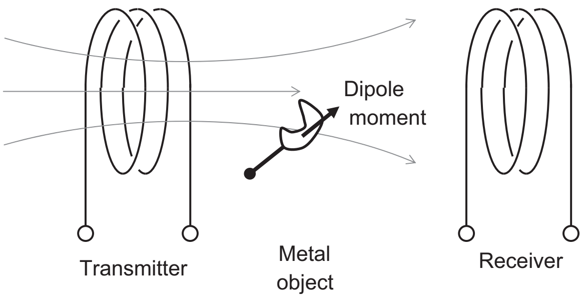

Figure 3.13 Schematic illustration of the dipole approximation with the field from the target being generated by an equivalent magnetic dipole moment.

For a sensor with co-located excitation and receiver coils, the well-known Lorentz reciprocity principle, which states that the sensor response is invariant when the excitation and receiver coils are interchanged (Dyck, Lowther, & Freeman, 1994), can be used to express the induced impedance due to the presence of the target as follows:

$$Z(\boldsymbol{r}_1,\omega) = \frac{\mathrm{j}\omega\mu_0}{I_T I_\mathrm{R}} \boldsymbol{H}_\mathrm{R}(\boldsymbol{r}_1)\cdot\mathbf{M}(\omega)\cdot\boldsymbol{H}_\mathrm{T}(\boldsymbol{r}_1) \tag{3.13}$$

where $Z(r,\omega)$ is the complex mutual impedance between the transmitter and receiver coils, $\boldsymbol{H}_\mathrm{T}$ and $\boldsymbol{H}_\mathrm{R}$ are the background magnetic field strengths generated by the transmitter and the receiver coils, respectively, at the centre of the target location, $\boldsymbol{r}_1$, relative to the sensor and I_R and I_T are the currents through the receiver and transmitter coils respectively. Note that the background terminology refers to the fields being evaluated in space in the absence of the target. In Eqn (3.13), $\mathbf{M}(\mathrm{j}\omega)$ is a 3×3 symmetric matrix that denotes the magnetic polarisability tensor characterising the target. It should be noted that the engineering adoption of this tensor structure as described by nine elements is a scope of the current investigation in applied mathematics. Recent progress in the area (Ledger & Lionheart, submitted for publication) examined the derivation of an asymptotic formula for the perturbed secondary field due to the presence of a target and suggested that an earlier derivation of tensor represented as a rank four tensor (Ammari, Chen, Chen, Garnier, & Volkov, 2014) with 81 coefficients can reduce to a rank two tensor with only nine coefficients, which provides a solid foundation for the current configuration. These coefficients forming the matrix $\mathbf{M}$ are complex valued and frequency dependent. As a result, a frequency dependent phase shift between the incident field and the induced impedance is introduced. The fields $\boldsymbol{H}_\mathrm{T}$ and $\boldsymbol{H}_\mathrm{R}$, however, are virtually frequency independent given the electric size in the medium in which the target is buried is usually long compared to the target's depth, which is usually valid for typical MIT frequencies ($\leq$1 MHz). Therefore, using the dipole model, the frequency and target positional dependences in the MIT response are separated between the polarisability tensor and the fields respectively, where $\mathbf{M}(\mathrm{j}\omega)$ is invariant with target position but contains its spectral behaviour, and the fields are only a function of target position. This has the advantage of helping in the estimation of the target's tensor and location.

Examples of the use of the dipole approximation for WTMDs have been reported by Marsh, Ktistis, Järvi, Armitage, and Peyton (2013, 2014) for single and multiple objects, respectively, and by Makkonen et al. (2013) using classification techniques. Several workers have investigated the dipole model for identification of buried ERW notably (Norton & Won, 2001).

3.4 Solution to the inverse problem

The previous section considered several key techniques used to describe the physics of the MIT sensing process. Of course, tomography requires this process to be inverted. In general, the MIT inverse problem shares similarities with the inversion problems from other so-called soft field tomographic techniques, especially the electrical methods; it is usually ill-posed, ill-conditioned and nonlinear. The aim of this section is to give a summary of the main approaches used for inversion in MIT.

3.4.1 *Linear case*

The linear case has limited application for many MIT problems as described earlier in Section 3.3.1, and this should be used with caution. However, the method can give crude qualitative images showing rough approximations of the material distribution. The method works best for small perturbations in the material properties against a known background for which the sensitivity matrix can be calculated. Assuming the linear case for small changes in the pixel values, then the system can be described as $\delta\mathbf{M} = \mathbf{S}\cdot\delta\mathbf{P}$. Normally, the δ notation is omitted as it is implicit that the measurement and pixel values are derived with respect to a fixed background value, so $\mathbf{M} = \mathbf{S}\cdot\mathbf{P}$. For inversion, it is necessary to determine $\mathbf{P}$ from the measurements, $\mathbf{M}$. Unfortunately, the sensitivity matrix $\mathbf{S}$ cannot be directly inverted. A natural solution, $\mathbf{S}^\dagger$, would be to choose the Moore–Penrose generalised inverse:

$$\mathbf{S}^\dagger = \left(\mathbf{S}^\mathbf{T}\cdot\mathbf{S}\right)^{-1}\cdot\mathbf{S}^\mathbf{T} \tag{3.14}$$

where $\mathbf{P} = \mathbf{S}^\dagger\cdot\mathbf{M}$ is the least squares solution to $\mathbf{M} = \mathbf{S}\cdot\mathbf{P}$, that is $\min\ \|\mathbf{M}-\mathbf{S}\cdot\mathbf{P}\|^2$. Many MIT applications are underdetermined ($k > n$), so the problem is usually extremely ill-posed and the calculation of $(\mathbf{S}^\mathbf{T}\cdot\mathbf{S})^{-1}$ or $(\mathbf{S}\cdot\mathbf{S}^\mathbf{T})^{-1}$ is normally swamped by numerical error. Consequently, regularisation is required, which not only seeks to minimise the least squares error but also to penalise large pixel/parameter values in $\mathbf{P}$, stated as follows:

$$\min\ \left\{\|\mathbf{M}-\mathbf{S}\cdot\mathbf{P}\|^2 + \alpha^2\|\mathbf{P}\|^2\right\} \tag{3.15}$$

The coefficient α^2 controls a compromise between fitting the data and controlling the magnitude of the solution. The choice of α^2 represents the introduction of a degree of a priori knowledge relating to the magnitude of the solution. The result is the commonly used Tikhonov regularisation:

$$\mathbf{P} = \left(\mathbf{S}^{\mathbf{T}} \cdot \mathbf{S} + \alpha^2 \mathbf{I}\right)^{-1} \mathbf{S}^{\mathbf{T}} \mathbf{M} \tag{3.16}$$

Other forms of regularisation are also popular in MIT and electrical tomography such as truncated singular value decomposition, which are well covered in the literature.

3.4.2 Iterative solutions

For many MIT applications, the simple linear solutions described in the previous section cannot accurately express the problem. In these cases, an iterative solution is sought that seeks to minimise an objective function. The objective function, also known as a cost function, describes the fit between the actual measured data and the simulated data produced from the forward problem. This procedure is summarised by the block diagram in Figure 3.14.

The algorithm is initiated with a first guess of the pixel or parameter values in **P**, which may be either the background (baseline) values or, for a temporally continuous application, the previously converged solution from the last set of measured data. Typically some form of constraining is applied to limit or cap extreme values in **P**, such as excluding non-physical values, for instance, negative electrical conductivities. The previous estimate is then updated to produce the $K + 1$ estimate. This estimate of **P** is subsequently input to the forward model. The calculated measurements are then subtracted from the actual measurements to produce an error vector that is applied to the approximate inverse solution, which is usually based on a piecewise linear approximation, similar to the methods described in Section 3.4.1. The next estimate of **P** is then made, and the iterative process continues. A regularisation parameter λ is introduced to stabilise the iterative scheme to convergence, and usually, the value of λ is also adaptively controlled.

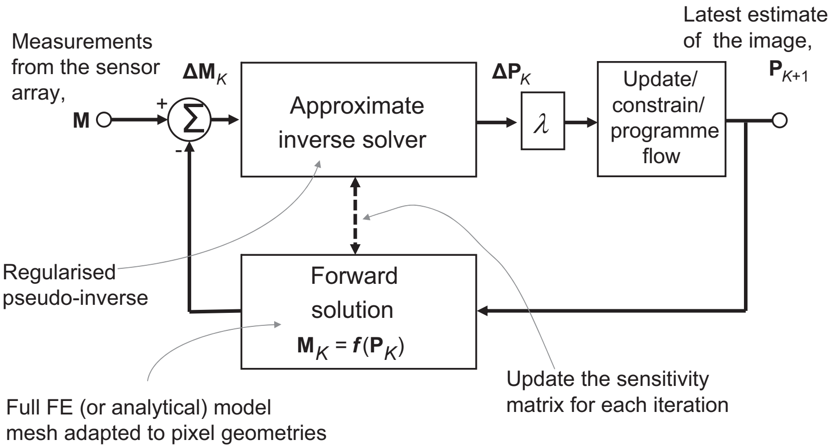
Measurements from the sensor array,
M
ΔM_K
+
-
Σ
Approximate inverse solver
ΔP_K
λ
Update/ constrain/ programme flow
Latest estimate of the image,
P_{K+1}
Forward solution
M_K = f(P_K)
Regularised pseudo-inverse
Full FE (or analytical) model mesh adapted to pixel geometries
Update the sensitivity matrix for each iteration

Figure 3.14 Block diagram of a typical MIT inversion algorithm.

The inverse problem requires sensitivity values, such as, the sensitivity of a particular measurement to a change in the conductivity of a particular voxel. The sensitivity values are affected by the distribution of the material in the object space and, therefore, may need to be recalculated regularly and, possibly, during each iteration because the material distribution changes as the algorithm converges to a solution.

The block diagram essentially describes a minimisation problem, which can be stated as follows:

$$\mathbf{P}^* = \underset{\mathbf{P}}{\operatorname{argmin}} \left\{ \|f(\mathbf{P}) - \mathbf{M}\|^2 \right\} \tag{3.17}$$

The inverse problem is solved by generating a sequence of $\mathbf{P}$ vectors, that is, $\mathbf{P}_0$, $\mathbf{P}_1$, $\mathbf{P}_2$, ... $\mathbf{P}^*$, which converge toward the values that minimise the least squares error between $f(\mathbf{P})$ and $\mathbf{M}$. Each iteration of this process requires a new evaluation of the forward problem, which for MIT is generally where the main computational cost of this method occurs. Depending on the algorithm used, $\mathbf{S}$ may also be updated during each iteration, which has an additional computational cost. The choice as to whether the Jacobian $\mathbf{S}$ is updated is based on how linear the problem is expected to be, with more highly nonlinear problems requiring a method that incorporates updates to the Jacobian.

All iterative algorithms of this type require an initial estimate to the solution $\mathbf{P}_0$ and then generate a series of vectors that estimate the solution. These estimates are constructed so as to iteratively approach an overall minimum ($\mathbf{P}^*$) of the objective function, $\|f(\mathbf{P}) - \mathbf{M}\|^2$. Ideally, a global minimum is required; however, very few algorithms are capable of guaranteeing global convergence, so a (sufficiently small) local minimum must often suffice. Which local minimum, or possibly a global minimum, is reached may depend upon the choice of the initial solution.

A new output solution vector is determined by calculating an update to the current output solution:

$$\mathbf{P}_{K+1} = \mathbf{P}_K + \lambda \Delta \mathbf{P}_K \tag{3.18}$$

where $\Delta\mathbf{P}_K$ is the output solution update at iteration K, and λ is a relaxation parameter used to control the step size and, hence, the convergence of the iterative procedure. Most MIT algorithms use methods in which the objective function must decrease after each iteration. These methods are known as descent methods; that is:

$$\|f(\mathbf{P}_{K+1}) - \mathbf{M}\|^2 < \|f(\mathbf{P}_K) - \mathbf{M}\|^2 \tag{3.19}$$

The value of $\Delta\mathbf{P}_K$ can be obtained by making a linear approximation for each iteration using techniques, for instance:

$$\Delta\mathbf{P}_K = \left\{ \left(\mathbf{S}_K^{\mathbf{T}} \cdot \mathbf{S}_K + \alpha^2\,\mathbf{I} \right)^{-1} \mathbf{S}_K^{\mathbf{T}} \right\} \Delta\mathbf{M}_K \tag{3.20}$$

There are a number of well-established algorithms for achieving stable inversion of nonlinear problems such as MIT. One common approach is the regularised Gauss–Newton method:

$$\Delta\mathbf{P}_K = \left(\mathbf{S}_K^{\mathbf{T}}\mathbf{S}_K + \alpha^2\,\mathbf{R}^{\mathbf{T}}\mathbf{R}\right)^{-1}\left\{\mathbf{S}_K^{\mathbf{T}}\left(\Delta\mathbf{M}_K - \alpha^2\,\mathbf{R}^{\mathbf{T}}\mathbf{R}\,\mathbf{P}_K\right)\right\} \tag{3.21}$$

with α being a regularisation parameter, and **R** is a regularisation operator chosen to provide particular types of smoothing.

3.4.3 Sensitivity formulations

The calculation of the sensitivity matrix is fundamental to inversion. As discussed earlier in Section 3.3.1, the coefficients in the sensitivity matrix represent the change caused in a measured parameter, which for MIT is typically the trans-impedance between a defined transmitter–receiver coil pair, to the change in the a material parameter or pixel value in the object space. Consequently, the sensitivity of a measurement to changes in permeability, conductivity or velocity at a particular point in space is essential to the inversion process. The sensitivity values are dependent on the material distribution in the object space and, therefore, may need to be recalculated during each iteration of the inversion algorithm. The sensitivity values can be calculated directly from the field values as follows.

Considering a typical setup, a number of coils (normally 8 or 16) are used as transmitters and receivers in MIT. When a particular coil is used as a transmitter, it is fed by currents of certain values to produce alternating magnetic fields; other coils are used to measure the secondary field due to the velocity-induced magnetic field and the magnetic field produced by the eddy currents in the objects. Several authors (Norton & Bowler, 1993; Dyck, et al., 1994; Hollaus, Magele, Merwa, & Scharfetter, 2004b; Soleimani & Lionheart, 2006; Yin & Peyton, 2010b) have reported derivations for the sensitivity matrix for a range of electromagnetic problems. These typically follow the approach of defining an adjoint problem to which the reciprocity theorem is then applied. This allows the change in electromagnetic fields to be calculated for a given change in material properties. Following the approach by Dyck et al. (1994), normally, the measured variable can be expressed in the following form:

$$\boldsymbol{F} = \int_V f(\boldsymbol{E},\boldsymbol{H})\,\mathrm{d}V \tag{3.22}$$

where $\boldsymbol{F}$ is a function of the electric and magnetic fields at a point. In the MIT case, the receiver voltage, V_{R}, measured when a particular excitation coil is activated can be expressed as follows:

$$V_{\mathrm{R}} = \int_V \boldsymbol{E}_{\mathrm{T}}\cdot\frac{\boldsymbol{J}_{\mathrm{R}}}{I_{\mathrm{R}}}\,\mathrm{d}V \tag{3.23}$$

where $\boldsymbol{E}_{\mathrm{T}}$ is the electric field produced by the current flows when one transmitter is activated, and $\boldsymbol{J}_{\mathrm{R}}$ is the current flowing in the receiver coil with a current value of I_{R}. Note that $\frac{\boldsymbol{J}_{\mathrm{R}}}{I_{\mathrm{R}}}$ is a unit vector following the strands of the receiver coil. Parameter changes such as conductivity, permittivity, permeability and velocity cause a change in $\boldsymbol{E}$, $\boldsymbol{H}$ which in turn results in a change of $\boldsymbol{F}$. A variation of $\boldsymbol{F}$ can be expressed as follows:

$$\delta \boldsymbol{F} = \int_V (\nabla_{\mathbf{E}} f(\boldsymbol{E},\boldsymbol{H})\cdot\delta\boldsymbol{E} + \nabla_{\mathbf{H}} f(\boldsymbol{E},\boldsymbol{H})\cdot\delta\boldsymbol{H})\mathrm{d}V \tag{3.24}$$

which expressed in terms of the functions of the parameters gives the following:

$$\delta \mathrm{F} = \int_V \left(S_\sigma \delta\sigma + S_\mu \delta\mu + S_\varepsilon \delta\varepsilon + S_\upsilon \cdot \delta\boldsymbol{\upsilon}\right)\mathrm{d}V \tag{3.25}$$

where S is the sensitivity of $\boldsymbol{F}$ in response to the concerned parameters, respectively. Defining a quasi-Poynting vector, $\mathbf{S}_{12} = \boldsymbol{E}_1 \times \boldsymbol{H}_2$, where the two field $\boldsymbol{E}_1$ and $\boldsymbol{H}_2$ are taken from two separate systems (1 and 2) with possibly different material parameters, different source currents and/or different boundary conditions. Taking the volume integral of the divergence of this quasi-Poynting vector, and applying the divergence theorem yields the following:

$$\int_V \nabla\cdot\mathbf{S}_{12}\,\mathrm{d}V = \int_V \nabla\cdot(\boldsymbol{E}_1 \times \boldsymbol{H}_2)\,\mathrm{d}V = \oint_S \boldsymbol{E}_1 \times \boldsymbol{H}_2\cdot\,\boldsymbol{n}\,\mathrm{d}S \tag{3.26}$$

where S is the surface bounding V, and $\boldsymbol{n}$ is the unit vector normal to the surface and directed outward. Applying the vector identity $\nabla(\boldsymbol{a}\times\boldsymbol{b}) = \boldsymbol{b}\cdot\nabla\times\boldsymbol{a} - \boldsymbol{a}\cdot\nabla\times\boldsymbol{b}$, we have the following:

$$\int_V (\boldsymbol{H}_2\cdot\nabla\times\boldsymbol{E}_1 - \boldsymbol{E}_1\cdot\nabla\times\boldsymbol{H}_2)\,\mathrm{d}V = \oint_S \boldsymbol{E}_1\times\boldsymbol{H}_2\cdot\boldsymbol{n}\,\mathrm{d}S \tag{3.27}$$

Substituting the linear time harmonic Maxwell's equation (3.3) into (3.26) gives the following Eqn (3.28a), and the same is true is when we simply exchange systems 1 and 2 in (3.28b).

$$\begin{aligned}&\int_V \left\{\begin{aligned}&\boldsymbol{E}_1\cdot((\sigma_2 + \mathrm{j}\omega_2\varepsilon_2)\boldsymbol{E}_2 + \boldsymbol{J}_{\mathrm{EX2}} + \sigma_2(\boldsymbol{\upsilon}_2\times\boldsymbol{B}_2))\\ &\quad + \mathrm{j}\omega_1\mu_1\boldsymbol{H}_1\cdot\boldsymbol{H}_2\end{aligned}\right\}\mathrm{d}V\\ &\quad = -\oint_S \boldsymbol{E}_1\times\boldsymbol{H}_2\cdot\boldsymbol{n}\,\mathrm{d}S\end{aligned} \tag{3.28a}$$

$$\int\limits_V \left\{ \begin{aligned} &\boldsymbol{E}_2 \cdot ((\sigma_1 + \mathrm{j}\omega_1\varepsilon_1)\boldsymbol{E}_1 + \boldsymbol{J}_{\mathrm{EX1}} + \sigma_1(\boldsymbol{\upsilon}_1 \times \mathbf{B}_1)) \\ &\quad + \mathrm{j}\omega_2\mu_2\boldsymbol{H}_2 \cdot \boldsymbol{H}_1 \end{aligned} \right\} \mathrm{d}V = -\oint\limits_S \boldsymbol{E}_2 \times \boldsymbol{H}_1 \cdot \boldsymbol{n}\,\mathrm{d}S \tag{3.28b}$$

The derivation of the sensitivity formulas now follows from a series of substitutions. First, we replace system 1 with a system containing a small variation of the parameters as follows:

$$\begin{aligned} &\mu_1 \rightarrow \mu + \delta\mu, \quad \sigma_1 \rightarrow \sigma + \delta\sigma, \\ &\varepsilon_1 \rightarrow \varepsilon + \delta\varepsilon, \quad \boldsymbol{v}_1 = \boldsymbol{v} + \delta\boldsymbol{v}, \end{aligned} \tag{3.29a}$$

which causes a small change in the field vectors,

$$\boldsymbol{E}_1 \rightarrow \boldsymbol{E}_{\mathrm{A}} + \delta\boldsymbol{E}_{\mathrm{A}} \quad \boldsymbol{H}_1 \rightarrow \boldsymbol{H}_{\mathrm{A}} + \delta\boldsymbol{H}_{\mathrm{A}} \tag{3.29b}$$

Then, set the material properties for system 2 as follows:

$$\mu_2 \rightarrow \mu, \quad \sigma_2 \rightarrow \sigma, \quad \varepsilon_2 \rightarrow \varepsilon, \quad \boldsymbol{v}_{\mathbf{2}} = 0 \tag{3.29c}$$

with both systems having a common frequency, ω. Making this substitution into Eqn (3.28), we have the following:

$$\int\limits_V \left\{ \begin{aligned} &(\boldsymbol{E}_{\mathrm{A}} + \delta\boldsymbol{E}_{\mathrm{A}}) \cdot ((\sigma + \mathrm{j}\omega\varepsilon)\boldsymbol{E}_{\mathrm{B}} + \boldsymbol{J}_{\mathrm{EXB}}) \\ &\quad + \mathrm{j}\omega(\mu + \delta\mu)(\boldsymbol{H}_{\mathrm{A}} + \delta\boldsymbol{H}_{\mathrm{A}}) \cdot \boldsymbol{H}_{\mathrm{B}} \end{aligned} \right\} \mathrm{d}V = -\oint\limits_S (\boldsymbol{E}_{\mathrm{A}} + \delta\boldsymbol{E}_{\mathrm{A}}) \times \boldsymbol{H}_{\mathrm{B}} \cdot \boldsymbol{n}\,\mathrm{d}S \tag{3.30a}$$

$$\int\limits_V \left\{ \begin{aligned} &\boldsymbol{E}_{\mathrm{B}} \cdot \begin{pmatrix} (\sigma + \delta\sigma + \mathrm{j}\omega\varepsilon + \mathrm{j}\omega\,\delta\varepsilon)(\boldsymbol{E}_{\mathrm{A}} + \delta\boldsymbol{E}_{\mathrm{A}}) \\ + \boldsymbol{J}_{\mathrm{EXA}} + (\sigma + \delta\sigma)((\boldsymbol{\upsilon} + \delta\boldsymbol{\upsilon}) \times (\boldsymbol{B}_{\mathrm{A}} + \delta\boldsymbol{B}_{\mathrm{A}})) \end{pmatrix} \\ &\quad + \mathrm{j}\omega\mu(\boldsymbol{H}_A + \delta\boldsymbol{H}_A) \cdot \boldsymbol{H}_{\mathrm{B}} \end{aligned} \right\} \mathrm{d}V = -\oint\limits_S \boldsymbol{E}_{\mathrm{B}} \times (\boldsymbol{H}_{\mathrm{A}} + \delta\boldsymbol{H}_{\mathrm{A}}) \cdot \boldsymbol{n}\,\mathrm{d}S \tag{3.30b}$$

If we now set the perturbations to zero and subtract this result from Eqn (3.30), then two expressions for the perturbations follow. Furthermore, in the limit as of small perturbations, terms containing the product of more than one δ quantity will vanish. So, neglecting these higher order terms results in the following:

$$\begin{aligned}
&\int_V \left\{ \begin{aligned} &\delta\boldsymbol{E}_{\mathrm{A}}\cdot((\sigma+\mathrm{j}\omega\varepsilon)\boldsymbol{E}_{\mathrm{B}}+\boldsymbol{J}_{\mathrm{EXB}}) \\ &\quad+\ \mathrm{j}\omega(\mu\ \delta\boldsymbol{H}_{\mathrm{A}}+\boldsymbol{H}_{\mathrm{A}}\ \delta\mu)\cdot\boldsymbol{H}_{\mathrm{B}} \end{aligned} \right\} \mathrm{d}V \\
&\quad = \ -\oint_S \delta\boldsymbol{E}_{\mathrm{A}}\times\boldsymbol{H}_{\mathrm{B}}\cdot\boldsymbol{n}\,\mathrm{d}S
\end{aligned} \tag{3.31a}$$

$$\begin{aligned}
&\int_V \left\{ \begin{aligned} &\boldsymbol{E}_{\mathrm{B}}\cdot\left(\begin{aligned} &(\delta\sigma+\mathrm{j}\omega\ \delta\varepsilon)\boldsymbol{E}_{\mathrm{A}}+(\sigma+\mathrm{j}\omega\ \varepsilon)\ \delta\boldsymbol{E}_{\mathrm{A}} \\ &+\sigma(\delta\boldsymbol{\upsilon}\times\boldsymbol{B}_{\mathrm{A}})+\sigma(\boldsymbol{\upsilon}\times\delta\boldsymbol{B}_{\mathrm{A}})+\delta\sigma(\boldsymbol{\upsilon}\times\boldsymbol{B}_{\mathrm{A}}) \end{aligned} \right) \\ &\quad+\ \mathrm{j}\omega\mu\ \boldsymbol{H}_{\mathrm{B}}\cdot\delta\boldsymbol{H}_{\mathrm{A}} \end{aligned} \right\} \mathrm{d}V \\
&\quad = \ -\oint_S \boldsymbol{E}_{\mathrm{B}}\times\delta\boldsymbol{H}_{\mathrm{A}}\cdot\boldsymbol{n}\,\mathrm{d}S
\end{aligned} \tag{3.31b}$$

Finally, subtracting (b) from (a) in the above equations yields the following:

$$\begin{aligned}
&\int_V \boldsymbol{J}_{\mathrm{EXB}}\cdot\delta\boldsymbol{E}_{\mathrm{A}}\mathrm{d}V \\
&\quad = \int_V (\boldsymbol{E}_{\mathrm{A}}\cdot\boldsymbol{E}_{\mathrm{B}}\delta\sigma+\mathrm{j}\omega\ \boldsymbol{E}_{\mathrm{A}}\cdot\boldsymbol{E}_{\mathrm{B}}\delta\varepsilon-\mathrm{j}\omega\ \boldsymbol{H}_{\mathrm{A}}\cdot\boldsymbol{H}_{\mathrm{B}}\delta\mu)\mathrm{d}V \\
&\qquad + \int_V \{\boldsymbol{E}_{\mathrm{B}}\cdot(\sigma(\delta\boldsymbol{\upsilon}\times\boldsymbol{B}_{\mathrm{A}})+\sigma(\boldsymbol{\upsilon}\times\delta\boldsymbol{B}_{\mathrm{A}})+\delta\sigma(\boldsymbol{\upsilon}\times\boldsymbol{B}_{\mathrm{A}}))\}\mathrm{d}V \\
&\qquad + \oint_S (\boldsymbol{E}_{\mathrm{B}}\times\delta\boldsymbol{H}_{\mathrm{A}}+\ \ \boldsymbol{E}_{\mathrm{B}}\times\delta\boldsymbol{H}_{\mathrm{A}})\cdot\boldsymbol{n}\,\mathrm{d}S
\end{aligned} \tag{3.32}$$

In the case of an inductively coupled system, where system A is considered to be the transmitter coil and system B the receiver coils, then $\boldsymbol{J}_{\mathrm{E}}\times\boldsymbol{B}$ equals $\frac{\boldsymbol{J}_{\mathrm{R}}}{I_{\mathrm{R}}}$, and $\int_V \boldsymbol{J}_{\mathrm{EXB}}\cdot\delta\boldsymbol{E}_{\mathrm{B}}\mathrm{d}V$ is the change in receiver voltage cause by the perturbations. In addition, if we take the boundary far enough away such that the fields are completed encompassed, then the surface integral on the right-hand of Eqn (3.32) can be neglected.

By identifying the correspondence with Eqn (3.25), the following equalities hold using the vector identity $\boldsymbol{A}\cdot(\boldsymbol{B}\times\boldsymbol{C}) = (\boldsymbol{C}\times\boldsymbol{A})\cdot\boldsymbol{B}$ for Sv:

$$\begin{aligned}
S_\sigma &= \boldsymbol{E}_{\mathbf{A}}\cdot\boldsymbol{E}_{\mathbf{B}}+(\boldsymbol{\upsilon}\times\boldsymbol{B}_{\mathbf{A}})\cdot\boldsymbol{E}_{\mathbf{B}} \\
S_\varepsilon &= \mathrm{j}\omega\,\boldsymbol{E}_{\mathbf{A}}\cdot\boldsymbol{E}_{\mathbf{B}} \\
S_\mu &= -\mathrm{j}\omega\boldsymbol{H}_{\mathbf{A}}\cdot\boldsymbol{H}_{\mathbf{B}} \\
S_v &= \sigma\,\boldsymbol{B}_{\mathbf{A}}\times\boldsymbol{E}_{\mathbf{B}}
\end{aligned} \tag{3.33}$$

Note, the first three terms are widely used in electrical tomography; the S_σ sensitivity now includes the effects of Faraday induction caused by the movement of conducting material in the magnetic field. Note the sensitivity to magnetically permeable material is of the form $\boldsymbol{H}\cdot\boldsymbol{H}$, which is determined by the magnetic fields. In contrast, the sensitivity to electrically conductive material is of the form $\boldsymbol{E}\cdot\boldsymbol{E}$, which is determined by the induced field and the flow eddy currents within the conductive object.

3.5 System hardware

MIT systems can be configured in a number of ways depending on the number of transmitter and receiver coils, size and geometry of the equipment being instrumented and the frequency range. There is considerable scope for design customisation, and implementation details can vary significantly from application to application. This section reviews the main considerations and options in the design of an MIT system.

3.5.1 System configurations

MIT systems can use either dual-function transmitter and receivers coils or have dedicated transmit only and receive only coils. Of course, system configurations with dual-function coils require additional electronic circuitry to switch between transmit and receive modes, and the switching circuitry must be designed to minimise any unwanted coupling from the transmitter to the receiver when the coil is in receiver mode. Coils are usually relatively easy and inexpensive to fabricate and also can be readily overlaid on top of each other. Consequently, dedicated transmitter and receiver coils are preferred over dual-function configurations, eliminating the need for the switching circuitry. For circular coil arrays, transmitter and receiver coils can be interleaved or wound on the same formers, as shown in Figure 3.15.

A block diagram of a typical transmitter channel is shown in Figure 3.16 and consists of the following main blocks:

- Digital to analogue converter (DAC)
- Buffer amplifier
- Excitation on/off switch
- Current sense circuitry

A DAC or dedicated waveform generator, such as a direct digital synthesiser (DDS), generates the waveform required by the transmitter coil. This signal is amplified/buffered to the required voltage and current levels for the transmitter coil. For dual-function coils, an on/off switch provides the necessary isolation when the coil is used in receive mode, which requires a very low off capacitance. The on/off switch must be able to operate with the full transmitter current, which in some cases can be several amps. A current sense facility is also shown, which can be achieved with a current sense resistor and a current sense amplifier. The output of the current sense amplifier can be digitised and de-modulated in the same way as the signal from the receiver

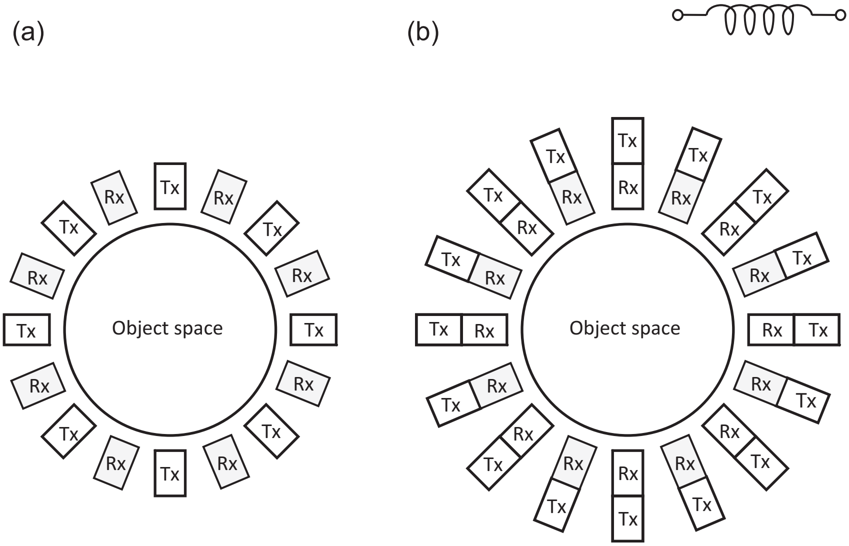
(a)
(b)
Object space
Tx
Rx
Object space
Tx
Rx

Figure 3.15 Circular MIT arrays with separate transmitter, Tx, and receiver, Rx, coils. (a) Interleaved coils. (b) Transmitter and receiver coils sharing the same former.

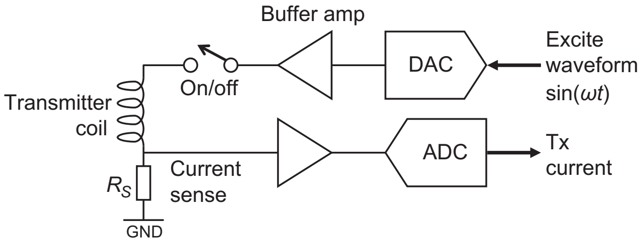
Buffer amp
DAC
Excite waveform sin(ωt)
On/off
Transmitter coil
ADC
Tx current
Current sense
R_S
GND

Figure 3.16 A block diagram of a typical MIT transmitter channel that contains a current sense facility.

coil, as explained in the following paragraphs. The current sense facility is required to implement a proper trans-impedance, Z_T, measurement between each receiver and transmitter coil, as given by the complex division:

$$Z_{\mathrm{T}} = \frac{v_{\mathrm{r}}}{i_{\mathrm{t}}} \tag{3.34}$$

where, v_r is the voltage detected by the receiver coil, and i_t is the current following the transmitter coil. Naturally, the resistance of the sensor resistor, R_S in Figure 3.16, should be much less than the reactance of the transmitter coil. A current transformer can be used as an alternative to the current sense resistor. MIT systems can operate without the current sense facility but will then be sensitive to any temperature variations and ageing affects in the transmitter coils.

A block diagram of a typical receiver channel is shown in Figure 3.17 and consists of the following main blocks:

- Front-end amplifier
- Programmable gain amplifier
- Analogue to digital converter (ADC)
- In-phase (real) and quadrature (imaginary) demodulation

The front-end amplifier is usually positioned relatively close to the receiver to minimise the effects of either EM interference or parasitic capacitance in the connecting leads. The capacitance of the connecting leads can introduce an unwanted resonance in the frequency response of the coil if not properly managed. A programmable gain amplifier (PGA) is needed to accommodate the difference in the dynamic range of the signal between different coil positions. For instance, the adjacent transmitter/receiver coils in Figure 3.15(a) or the transmitter/receiver coils sharing the same former in Figure 3.15(b) will have a large signal, whereas diametrically opposite transmitter/receiver coils will have a much smaller signal. Typically, this can require a gain range of 0 to 40 dB.

Since 2005, there has been a trend toward digital signal processing systems, in which case the PGA will be followed by a high-speed ADC. The resolution of the ADC is usually 14 or 16 bit. The minimum number of samples per cycle of transmitter waveform is 4 (Smith, Freeston, Brown, & Sinton, 1992), but generally, MIT systems employ more than this, exploiting oversampling to increase signal to noise ratio (SNR). Typically, 8 or 16 samples per cycle are employed, and integer values are preferred to avoid spectral leakage. In-phase and quadrature demodulation consists of a multiplier and low-pass filter for both the real and imaginary phases, which are implemented on a digital signal processor (DSP) or field programmable gate array (FPGA). Earlier MIT systems used analogue demodulation, with the analogue to digital conversion being performed after the demodulation. In this analogue case, the outputs of the demodulators can often be multiplexed into a smaller number of ADCs. The analogue scheme is still preferred in some cases as the expense of high-speed ADCs and the cost and time associated with implementing the signal processing on DSPs or FPGAs can be decisive factors.

An important consideration for optimising the SNR performance of an MIT system is to share a common reference voltage between all the channels so any variations in the primary reference will affect the channels equally in proportion and, therefore, can

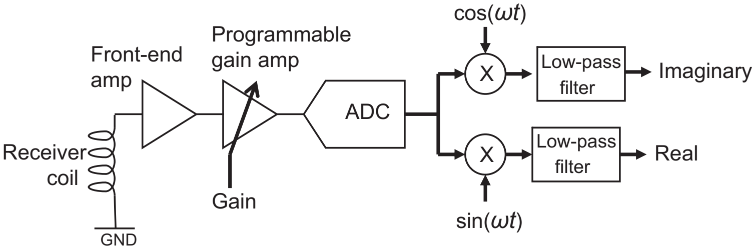

Figure 3.17 A block diagram of a typical MIT receiver channel.

be cancelled in the impedance division of Eqn (3.34). Similarly, it is also important with the digital architecture, shown in Figures 3.17 and 3.18, that all sampling processes are synchronised to a common clock to minimise noise related to unwanted phase jitter or spectral leakage introduced during demodulation.

A block diagram of a 16 transmitter and 16 receiver channel MIT system is shown in Figure 3.18 (Peyton et al., 1999). This system uses an analogue demodulation scheme and indicates some of the complexity required to configure a complete MIT system. Here, the circuit functions are split onto different PCBs, and the signal to the ADCs is multiplexed to make best use of the sampling rate of the ADCs. A controller, in this case an embedded PC, is used to control the measurement procedure with complete flexibility over the sequencing of excite and receive channels. Communication of the data and top-level control of the acquisition process is achieved over an Ethernet link, which allows the host computer to be positioned anywhere with suitable internet access.

There are several examples of MIT systems reported in the literature, for example, an 8-channel system used for imaging molten steel (Ma, Peyton, Higson, Lyons, & Dickinson, 2006) and a 16-channel system for biomedical research (Watson, Williams, Gough, & Griffiths, 2008), which was amongst the first capable of imaging conductivities below 10 S/m and was built for research on brain oedema. A system was reported based on a similar coil array (Vauhkonen, Hamsch, & Igney, 2008). A single-channel system based on gradiometers as receivers and capable of multifrequency operation was reported (Scharfetter, Lackner, & Rosell, 2001) and further advanced to an array later (Scharfetter, Köstinger, & Issa, 2008).

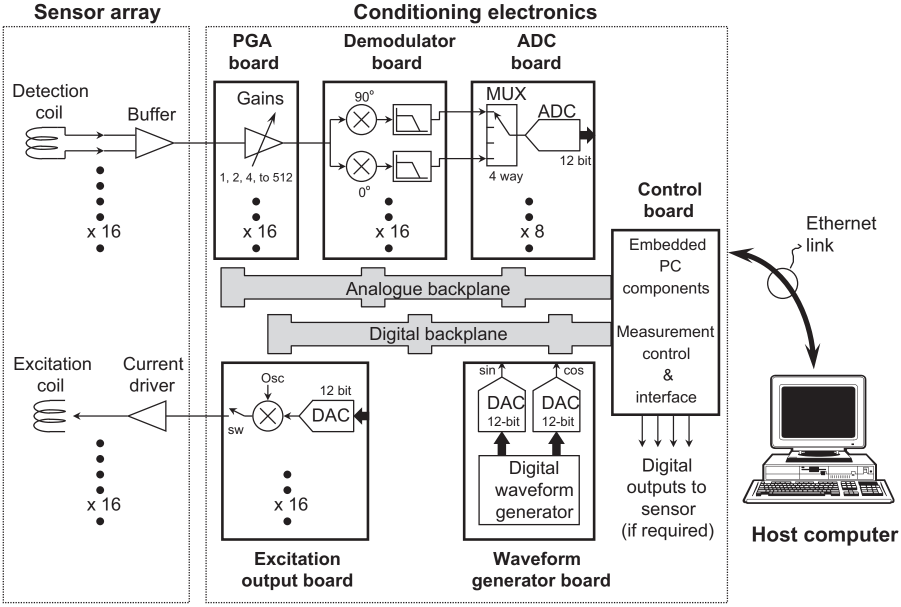
Sensor array
Conditioning electronics
PGA board
Demodulator board
ADC board
Detection coil
Buffer
Gains
1, 2, 4, to 512
x 16
90°
0°
x 16
MUX
ADC
12 bit
4 way
x 8
Control board
Embedded PC components
Measurement control & interface
Ethernet link
Analogue backplane
Digital backplane
Excitation coil
Current driver
x 16
Osc
12 bit
DAC
sw
x 16
sin
cos
DAC 12-bit
DAC 12-bit
Digital waveform generator
Digital outputs to sensor (if required)
Host computer
Excitation output board
Waveform generator board

Figure 3.18 A block diagram of a 16 Tx channel – 16 RX channel MIT system.

There is considerable variety in the geometry of MIT arrays depending on the opportunity to position the coils next to the object space as afforded by the physical access allowed by the application. In general, the MIT array geometry may be split into three broad categories, as shown schematically in Figure 3.19:

1. Circular/cylindrical
2. Planar
3. Dual-sided

Circular arrays were amongst the first to be researched and are favoured for pipeline and many of the biomedical studies. The majority of publications address the 2D circular case; the 3D cylindrical case has received little attention to date. Access is restricted to one surface, which is typical for some NDT applications, geophysical/geological surveying and detection/characterisation of buried land mines and other ERW. In some cases, access is available from two surfaces, a very common example of this type of coil array can be found in WTMDs used for security screening of personnel. Other possible examples include plate and conveyor belt applications.

The majority of publication in MIT research on the arrays described relate to systems that operate at a single frequency, with very few studies on multifrequency, multicoil arrays. This is partly due to the complexity of the electronic hardware required for full spectral and spatial interrogation of the object space and partly due to the added computational complexity of solving the forward and inverse problems for multiple excitation frequencies. The use of multiple frequencies is also referred to as magnetic induction spectroscopy. One example of a single-channel

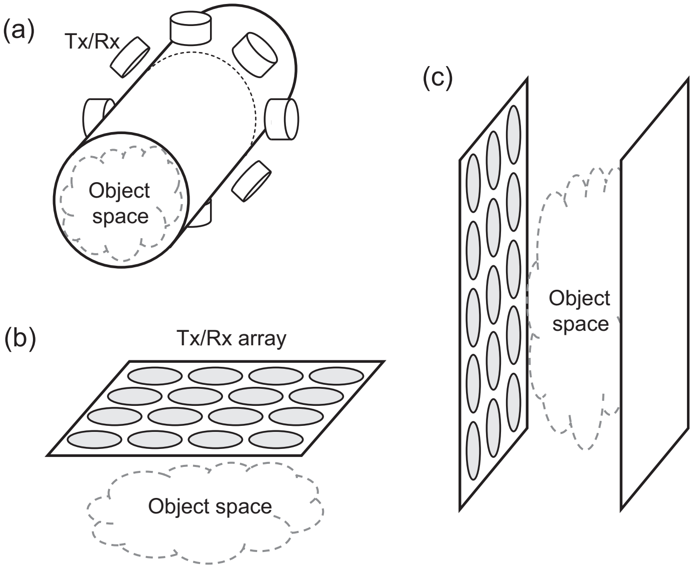

Figure 3.19 Three typical MIT sensor array configurations. (a) Circular configuration with coils surrounding the object space; (b) planar configuration with coils on just one side of the object space; and (c) dual-sided configuration with coil panels on opposite sides of the object space.

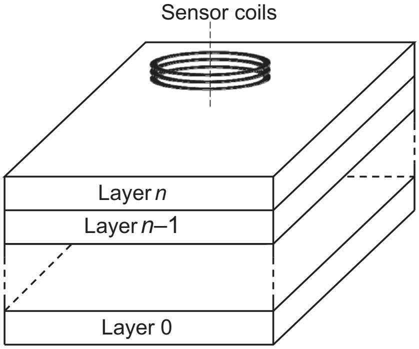

Figure 3.20 Depth profiling using multiple-frequency excitation.

multifrequency problem is depth profiling, where the material properties or thicknesses of subsurface layers are required, as depicted in Figure 3.20, for applications monitoring the thickness of protective metal coatings or noncontact thickness measurement of metal sheeting. Here, different excitation frequencies are used to provide different depths of penetration of the EM field and, hence, probe the depth profile of the conducting layers underneath the coil.

3.5.2 Practical considerations

This section considers a number of practical considerations associated with designing and implementing MIT systems, including coil design, electrostatic screening, resonance and input stage considerations.

3.5.2.1 Coil design

Coils are either wound on a former or realised using printed circuit board (PCB) techniques. PCBs are attractive because the geometry of the coils can be precisely controlled, and the coils can be fabricated in a very repeatable manner. There are a number of PCB substrates available, offering different degrees of mechanical stability. However, if used, the standard FR4 is most common. Thin and flexible substrates are also available, which can be attached directly to standard rigid PCBs in a flexi-rigid process. However, PCBs have their disadvantages; they are limited in size (typically less than 30 cm); the number of turns is limited, and the resistance of the tracks is high. Track resistance is a particular limitation for larger coils and at lower frequencies (below around 100 kHz) where higher excitation currents are needed (typically > 100 mA). Wound coils offer flexibility in the choice of conductor, insulation and geometry. Coils can be designed to survive extreme environments, very high temperatures (e.g. up to 1000 °C), very high radiation fluxes and can extremely rugged. Custom designed and machined or even 3D-printed formers can be used to increase the repeatability and precision to which the coils can be built. For very high mechanical stability, coils can be encapsulated in a variety of potting compounds, such as polyurethane, epoxy or ceramic and even concrete-based grouts. Hybrid constructions can be used, typically where the transmitter coils are wire wound for high current capacity and receiver coils are printed.

A key design parameter for the coils is the number of turns, and there are different considerations for the transmitter and receiver coils. In general, the receiver coils are designed to have as many turns as possible because the detected voltage, v_r, is approximately directly proportional to the number of turns:

$$v_r = -\frac{\mathrm{d}\lambda}{\mathrm{d}t} \approx -\frac{\mathrm{d}(N\varphi)}{\mathrm{d}t} = N\frac{\mathrm{d}}{\mathrm{d}t}\int\limits_{S_\mathrm{A}} \boldsymbol{B}\cdot\mathrm{d}S \tag{3.35}$$

where λ is the flux linkage to the receiver coil, φ is the magnetic flux and S_A is the surface bounded by each turn. The upper limit on the number of turns is dictated by electromagnetic, space, and cost constraints because winding coils with many thousands of turns can be expensive unless automated. The self-resonant frequency of the coil is the main electromagnetic constraint; increasing the number of turns increases both the self-inductance and self-capacitance of the coil, which in turn reduces the self-resonant frequency. Resonance issues in MIT will be described in more detail shortly. The number of turns on the transmitters is generally chosen to maximise the applied magneto-motive force (MMF) or ampere-turns applied to the object space. This is a case of matching the impedance of each transmitter to the voltage and current drive available from the drive circuitry. High-frequency MIT systems (above a few MHz) may be designed to have an impedance close to 50 Ω for maximum power transfer from radio frequency power amplifiers.

There is considerable scope for variety in the geometry of the coils, with dozens of patents claiming inventive coil configurations for inductive applications dating back over many decades. Often, the coils are simple circular or rectangular arrangements, sized to maximise the magnetic flux coupling. Ferrite flux concentrators can also be used, as well as an external magnetic screen (Yu, Worthington, Stone, & Peyton, 1995); however, the extra weight, cost and concerns over temperature drift often do not justify this choice. An external electrostatic shield is important to reduce external electromagnetic interference and to help minimise the capacitive coupling between the coils in the array (Peyton, Watson, Williams, Griffiths, & Gough, 2003).

Gradiometers offer a means of reducing the background coupling between the transmitter and receiver coils to near zero. The subject of background and object signals was discussed earlier in Section 3.2 and illustrated in Figure 3.6. Reducing the background signal to effectively zero allows the full dynamic range of the system to be used for the object signal and, hence, to increase the SNR of the system. This benefit is not without penalty because gradiometer configurations offer no net DC spatial response, which means that material must be passing through the MIT array in transient bursts or known to occupy a specific volume within the object space, for instance, positioned on one side of the array. Planar and axial gradiometer configurations are shown in Figure 3.21. The receiver is wound in two halves, Rx 1.1 and Rx 1.2, which are connected in series opposition so that the induced voltages from the transmitter in

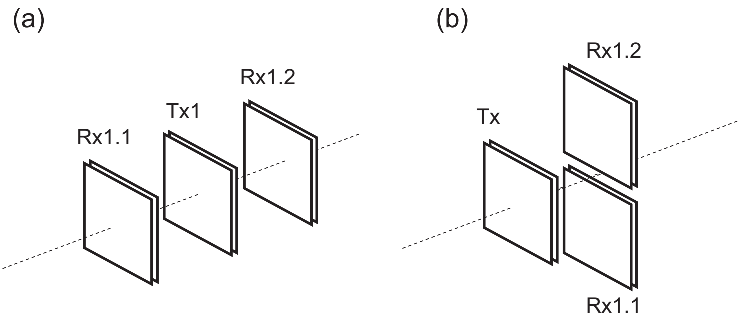

Figure 3.21 Schematic diagram of an axial gradiometer (a) and planar gradiometer (b).

each half subtract. Of course, all transmitter and receiver coil combinations should benefit from the background cancellation property of the gradiometer. Consequently, axial gradiometers are suitable for planar arrays and planar gradiometers for circular arrays.

Coils can also be positioned to reduce the background signal. For example, with phased arrays in nuclear magnetic resonance (NMR), the coils can be overlapped to give zero mutual coupling and, hence, avoid problematic interactions between nearby coils (Roemer, Edelstein, Hayes, Souza, & Mueller, 1990). Overlapping coils for zero mutual inductance can also be used in MIT to reduce the large background measurements that can occur when excitation and detection coils are positioned close together. Figure 3.22 illustrates this idea using the planar coil array described earlier. In part (a), the measured output of a detection coil is plotted against the angular position as the coil is moved with respect to the excitation coil that is shown in the cross-sectional view. At 0°, the coils are coincident, and the output is a maximum. At the opposite extreme, when the coils are furthest apart with an angle of 180°, the output is approximately 50 times smaller. At two points in between these extremes, when the coils are partially overlapping, the output is virtually zero. These are null points where there is no net flux passing through the detection coil, as shown in an idealised form and with no magnetic screen in Figure 3.22(b). With careful sensor array design, it is possible to ensure that all the detector coils are positioned in the null points of their two neighbouring excitation coils. This helps to reduce the variations in signal size that must be processed by the conditioning electronics.

3.5.2.2 Electrostatic screening

For higher frequency (typically over 100 kHz) MIT systems, the effects of parasitic capacitive coupling between the coils become increasingly significant. Electrostatic screening can minimise these effects. Three examples of different types of screen are shown in Figure 3.23. Foil envelopes may be used to screen solenoids, see Figure 3.23(a). Coils are screened both underneath and on top of the winding, to provide a complete Faraday cage around the coil. The screen offers a larger conductive area to its surrounding and, as a result, may increase the parasitic coupling, particularly for source coils and coils with few turns. The screen also acts as a single turn

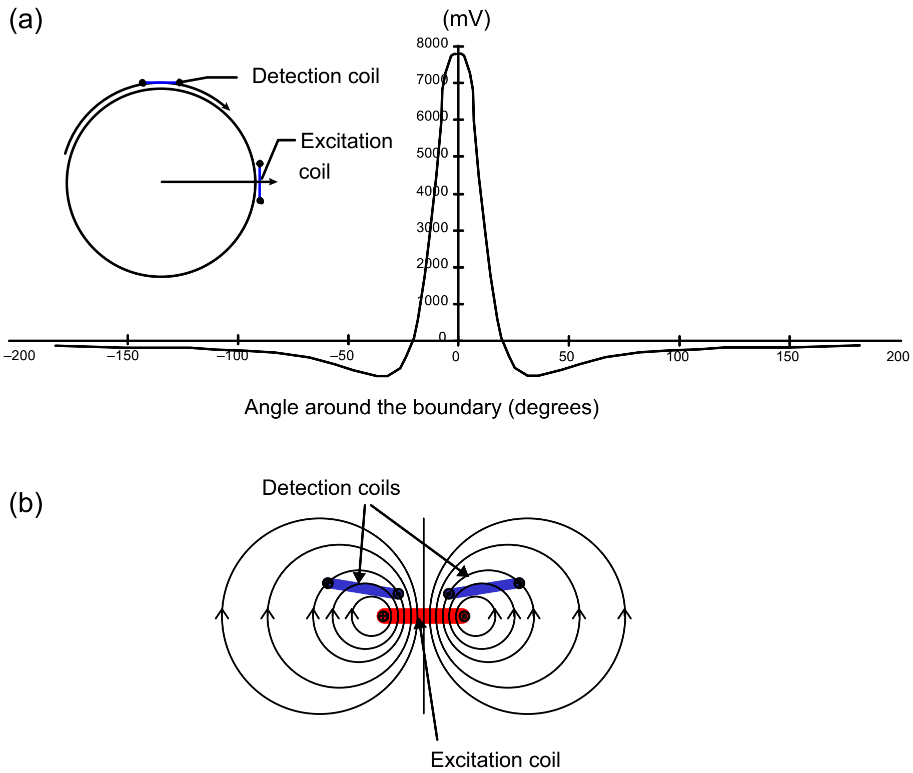

Figure 3.22 Overlapping transmitter and receiver coils to minimise background coupling. (a) Signal response versus angular position showing two zero crossover positions. (b) Coils positioned on lines of magnetic flux.

inductor; therefore, the induced EMF between one end of the screen and the other will be 1/*N* times the source voltage, where *N* is the number of turns. Consideration should also be given to which end of the coil is connected to ground, as this first turn can also act as a screen. Combs of various configurations, see Figure 3.23(b), have been used to screen the electric fields produced by the source coil. The thickness and pitch of the tracks must be sufficient to ensure effective screening of the electric field, but must have minimal effect on the magnetic coupling. Ground planes have two roles, as an electromagnetic shield (Yu et al., 1995) and as a defined capacitive route to ground, see Figure 3.23(c). It will, however, also reduce the magnetic coupling, especially between opposite coils. The screen—coils separation is, therefore, a compromise between minimising the capacitive coupling between coils and maximising the magnetic field within the sensor. Ground planes have been used to control capacitive coupling in medical MIT systems, and its influence on the spatial sensitivity has been simulated (Peyton et al., 2003).

Electrostatic shields constructed from resistive materials are popular for some inductive sensor systems, especially conveyor-based metal detectors. Materials such

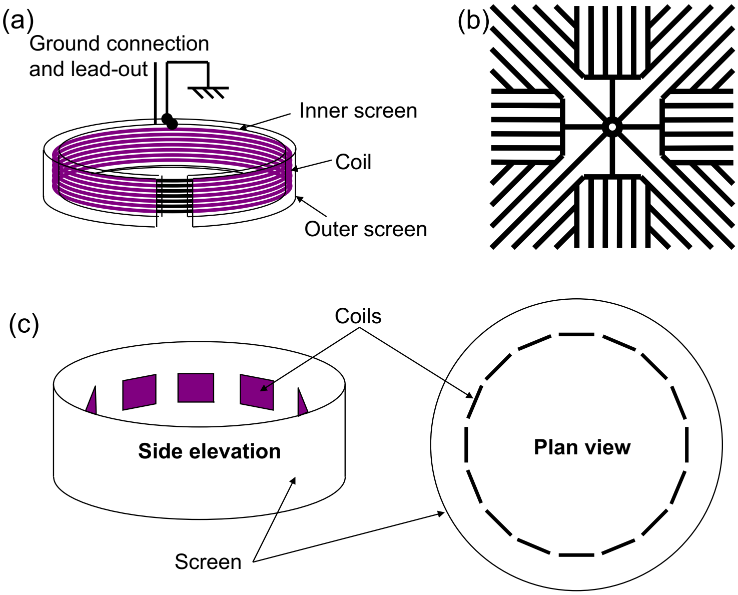

Figure 3.23 Electrostatic screen designs: (a) solenoid, (b) printed and (c) outer case.

as conducting graphite paint, conducting polymer sheet and fabrics with woven conducting wires are used in these instruments. It is important to ensure the resistive shield has a sufficiently high surface resistivity (Ω/square) so that it does not affect an applied AC magnetic field, but the surface resistivity is low enough to attenuate the electrostatic field.

3.5.2.3 Resonance

As with many other inductive sensors, coil resonance is also a fundamental concern for MIT. Resonance can be either purposely employed or, alternatively, avoided as much as possible. The main issues regarding the use of resonance for MIT are summarised in Table 3.2. As can be seen, resonance offers higher signal levels with greater SNR due to the band pass filtering action that resonance provides. However, the resonant interactions are difficult to manage. The effects of multiple resonances in MIT interactions are illustrated in Figure 3.24. The result is that the detected signals are averaged spatially, which makes the reconstruction problem more difficult to solve. Only the magnitudes of the signals are sketched in the diagram. However, resonance also introduces significant phase variations.

The detection coils must be connected to a high-impedance input stage. Low input capacitance is essential to maximise the resonant frequencies. For connecting leads

Table 3.2 **Resonant versus nonresonant detection schemes**

	Non-resonant	**Resonant**
Signal quality	Smaller signal	Larger signals, multiplied by the coil Q-factor
	Wider bandwidth presented to noise and interference	Narrow noise window
	Susceptibility to interference increases linearly with frequency due to the differential action of the detector coils	Susceptibility to interference is low, governed by the narrow band pass resonant response.
	Lower signal to noise ratio	Higher SNRs
Physical principle	Sensor array outputs (e.g. 0° and 90°) are a direct function of the object material and the detected signals can be derived directly from Maxwell's equations using e.g. FE analysis.	Outputs are dependent on both Maxwell's equations and on the transfer function(s) of the detector coil(s). For one resonant coil alone, the transfer function can be readily established. However, if several coupled coils are resonant simultaneously at the same frequency, then the outputs are very difficult to predict theoretically.
		Significant phase changes in the signals can be introduced by the coil transfer functions.
Hardware issues	Simple parallel data acquisition schemes can be employed (i.e. with measurements taken from all coils simultaneously) because interactions between the individual measurement coils are negligible	Parallel acquisition schemes can be employed, but the interactions between the coils would present a significant problem for image reconstruction, especially for high Q factors.

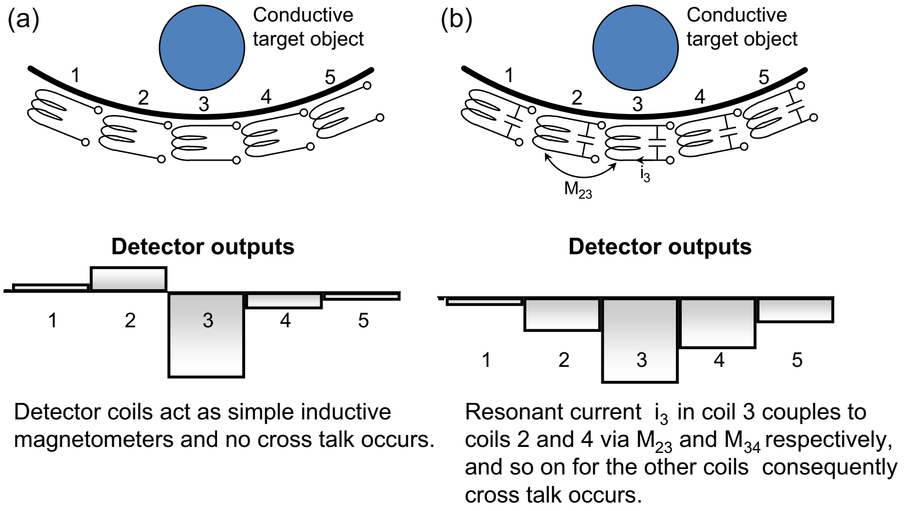
(a)
Conductive target object
1
2
3
4
5
Detector outputs
1
2
3
4
5
Detector coils act as simple inductive magnetometers and no cross talk occurs.
(b)
Conductive target object
1
2
3
4
5
M_{23}
i_3
Detector outputs
1
2
3
4
5
Resonant current i_3 in coil 3 couples to coils 2 and 4 via M_{23} and M_{34} respectively, and so on for the other coils consequently cross talk occurs.

Figure 3.24 The effects of multiple interacting resonances on an MIT sensor: (a) no resonance, (b) resonant case.

greater than 10 cm and operating frequencies above 100 kHz, the lead capacitance can have a significant parasitic effect, see Figure 3.25(a). The resonant frequency, f_r is given by the following:

$$f_r = \frac{1}{2\pi\sqrt{L.C_{TOT}}} \tag{3.36}$$

Consequently, the buffer amplifier must often be connected as close as possible to the detector coils. For similar reasons, the driver circuits should also be connected directly to the excitation coils. Differential input configurations, such as shown in Figure 3.25(b), are often used to minimise interference. Note radio frequency filtering and a DC bias path are important practical additions, as is the use of screened twisted pair cables for the interconnections.

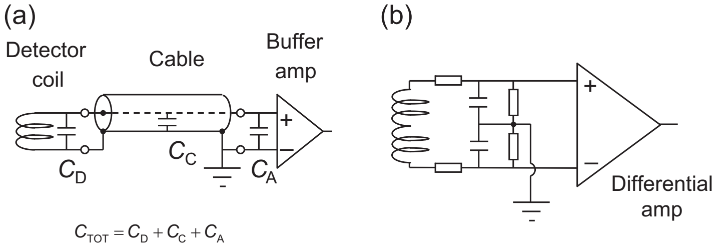
(a)
Detector coil
Cable
Buffer amp
+
−
C_D
C_C
C_A
$C_{TOT} = C_D + C_C + C_A$
(b)
+
−
Differential amp

Figure 3.25 Receiver coil input connections: (a) input capacitances, (b) differential input connections.

3.6 Applications

Electromagnetic sensors are used on a wide variety of materials including metals, aqueous fluids and biological tissues, and consequently, MIT applications are reflected across this base. Examples of these include the following:

1. Liquid metal processing
2. Nondestructive testing (crack imaging and coating thickness)
3. Conductivity profiling
4. Biomedical
5. Oil industry processes
6. Metal detection
7. Geophysical surveying

A full review of all these application areas is beyond the scope of this chapter; however, selected areas are covered in the following sections to give an indication of the diversity of the use of induction techniques.

3.6.1 Hot metal processing

There are a number of reports of electromagnetic imaging and inversion techniques being applied to high-temperature metal process applications due to the robust and simple nature of the sensor arrays. Examples include continuous casting, tapping and controlled cooling.

Continuous casting is widely used in the steel industry in the production of billets, blooms and slabs, which are subsequently processed into a variety of products. Increasing demand for tighter manufacturing tolerances, improved steel quality (i.e. cleanliness and surface quality) and more complex compositions has required constant improvements to the entire steel production process. Continuous casting is a critical process as any defects introduced during solidification are difficult to remove in later processes. MIT has been used to study two-phase molten steel—argon flows that occur in the submerged entry nozzle, which is used to transport liquid steel into the mould. Laboratory (Ma, Peyton, Binns, & Higson, 2005) and plant (Higson, Drake, Lyons, Peyton, & Lionheart, 2006) studies have shown that cross-section images of the phase fraction can be obtained under the harsh operating conditions with very high temperatures. CIFT has been demonstrated in a laboratory environment on a tenth-scale laboratory model of the continuous casting process using the room-temperature liquid metal, InGaSn (Stefani et al., 2004). Recently, experiments on these laboratory models have shown the potential of combining the MIT technique for monitoring the liquid gas fractions within the submerged entry nozzle (SEN) with CIFT for imaging the flow within the mould (Wondrak et al., 2012), revealing oscillatory or pulsating behaviour of the flow under certain conditions.

The imaging of the solidification of liquid metal in a pipe has been studied (Pham et al., 2000a) with the aim of realising a sensor to form part of an electronic flow control system for liquid metal delivery by thermally controlling the degree of solidification inside the refractory pipe. The sensing technique exploits the difference in electrical conductivity of molten metal to solid metal. A later study (Coveney, Gray, & Kyllo, 2005) considered the application of this method to tapping of copper smelters.

Following casting in the production route is hot rolling to form the metal into a strip, plate or a desired section. In the case of steel, hot rolling is also associated with controlled cooling. For some steel grades, such as high-strength strip steel used in the automobile industry, the correct cooling process is vital to obtained the required microstructure and, hence, the required mechanical properties in the final steel product. Magnetic induction spectroscopy has been considered for this application and applied online (Peyton et al., 2010). The use of an array of electromagnetic sensors to monitor the changes of the steel properties as it cools has been reported by imaging the paramagnetic to ferromagnetic phase transition as strip steel cools below the Curie point (Sharif et al., 2001).

3.6.2 Conductivity profiling

Conductivity profiling applications are typically one-dimension inversion problems in which the inductance or eddy current spectrum of a single coil or coil pair is used as the source data for the reconstruction algorithm. Typical applications are conducting coatings or depth profiling. Conducting coatings are used as a protective barrier against corrosion or thermal degradation in a number of engineering applications. One of the first reports (Norton, Kahn, & Mester, 1989) of the use of multifrequency or spectroscopic eddy current methods studied the feasibility of coating measurements on cylindrical geometries such as rods, the so-called pin in sleeve. Later, Yin et al. (2005) studied the feasibility of profiling an arbitrary conductivity profile using induction spectroscopy. There are important practical applications for this technique in the power generation industry in particular, for instance, the inspection of the thermal barrier coating MCrAlZ, on gas turbine blades (Randazzo & Pignone, 2007; Antonelli, Ruzzier, & Necci, 1998) and the inspection of the electrical conductivity profile within graphite bricks inside advanced gas cooled nuclear reactors to monitor their density changes (Dekdouk, Chapman, Brown, & Peyton, 2012).

3.6.3 Biomedical

The electrical conductivity and permittivity of biological tissues, typically in the range 0.01−1 S/m, can vary significantly depending on the tissue type. The electrical bioimpedance of tissues has been extensively reported; Gabriel, Gabriel, and Corhout (1996) provided a relatively comprehensive and well-cited review. Tissues have finite ionic conductivities commensurate with the nature and extent of their ionic content and ionic mobility, and their dielectric properties also vary significantly with frequency showing distinct bands of dispersion. The low-frequency α-dispersion is associated with ionic diffusion processes at the site of the cellular membrane. The β-dispersion, in the tens to hundreds of kilohertz region, is due mainly to the polarisation of cellular membranes that act as barriers to the flow of ions between the intra- and extra-cellular media. Other contributions to the β-dispersion come from the polarisation of protein and other organic macromolecules. Finally, the γ-dispersion, in the gigahertz region, is due to the polarisation of water molecules.

A number of researchers have tried to exploit the variations in electrical conductivity for biomedical monitoring or tomographic imaging. Applications include life signs monitoring (Tarjan & McFee, 1968), body composition and brain oedema. A good review of MIT within the context of medical EIT is given by Griffiths (2005).

3.6.4 Metal detection

Walk-through metal detection (WTMD) has proven to be a fundamental part of the screening of large numbers of personnel for potential threat objects, and WTMD use is widespread in locations such as airports, prisons, embassies, ports and government buildings. Rather than imaging the metal in the plane of the detector, Marsh et al. (2013) constructed a forward problem based of the dipole approximation, representing the metal target as an equivalent electromagnetic polarisability tensor. The inversion problem was to determine the tensor components and the 3D coordinate sequence of the metal object as it was carried through the portal. A subsequent report (Marsh, Ktistis, Järvi, Armitage, & Peyton, 2014) showed that multiple metal objects could be characterised and positioned simultaneously in this manner.

3.7 Conclusions and outlook

This chapter has attempted to summarise the current state-of-the-art in MIT technology, covering the key issues including the underlying theory, solutions to the forward and inverse problems, system implementations and applications. The first reports of MIT date back to the early 1990s with relatively simple systems and crude image reconstruction techniques. There has been considerable progress in the subject over the past two decades, and unfortunately, the available space in this chapter does not permit a completely exhaustive review, citing all the relevant MIT literature.

Forward and inverse solutions for MIT are now relatively well understood; however, accurate quantitative forward models are currently very computer intensive. It is likely that progress in computer technology will shorten inversion times, but nevertheless, more progress is needed to formulate algorithms that are more efficient.

As regards hardware platforms, the past decade has seen a slow migration from systems with a high degree of analogue processing, especially demodulation, to digital systems where the ADC is placed as soon in the signal processing chain as possible. It is likely that this trend toward more digital systems will continue. The majority of MIT systems are either multiple channel, single frequency or single channel, multiple frequency. Some of the single-channel, multiple-frequency systems also employ simultaneous multifrequency operation with spectrally rich excitation waveforms. A future direction for MIT hardware innovations is likely to be toward simultaneous multifrequency and multichannel systems, with all the additional complexity. The majority of MIT research has been based on 2D arrays; clearly, 3D arrays offer more potential as the forward problem is inherently three-dimensional.

The number of applications has increased since the 1990's with the early work being laboratory-based and speculative. Later publications became more application focused. No MIT system is likely to offer a global solution, and each application likely involves a bespoke solution with a dedicated coil array, data acquisitions scheme and inversion. Many applications do not require images, but particular parameters. Often, a similar inversion process can be used for these cases. This requires a broader interpretation of the term tomography in the case of MIT, as imagery is not necessarily the required output.

Finally, the number of researchers that have gained Ph.D.'s from MIT research is increasing. Some of these are have found employment in industry and scientific institutes, which will help the growth for the subject. However, it is crucial that the research become increasingly application-led for solving problems of high value to industry.

References

Al-Zeibak, S., & Saunders, N. H. (1993). A feasibility study of in vivo electromagnetic imaging. *Physics in Medicine and Biology, 38*, 151–160.

Ammari, H., Chen, J., Chen, Z., Garnier, J., & Volkov, D. (2014). Target detection and characterization from electromagnetic induction data. *Journal de Mathématiques Pures et Appliquées, 101*, 54–75.

Antonelli, G., Ruzzier, M., & Necci, F. (1998). Thickness measurement of MCrAlY high-temperature coatings by frequency scanning eddy current technique. *Journal of Engineering for Gas Turbines and Power, 120*, 537–542.

Armitage, D. W., Le Veen, H. H., & Pethig, R. (1983). Radiofrequency-induced hyperthermia: computer simulation of specific absorption rate distribution using realistic anatomic models. *Physics in Medicine and Biology, 28*, 31–42.

Cheng, C. C., Dodd, C. V., & Deeds, W. E. (1971). General analysis of probe coils near stratified conductors. *International Journal of Nondestructive Testing, 3*, 109–130.

Coveney, J. A., Gray, N. B., & Kyllo, A. K. (2005). Applications in the metals production industry. In D. M. Scott & H. McCann (Eds.), *Process imaging for automatic control. Book series: Electrical and computer engineering: a series of reference books and textbooks* (pp. 401–433). CRC press-Taylor & Francis.

Dekdouk, B., Chapman, R., Brown, M., & Peyton, A. J. (2012). Evaluating the conductivity distribution in isotropic polycrystalline graphite using spectroscopic eddy current technique for monitoring weight loss in advanced gas cooled reactors. *NDT&E International, 51*, 150–159.

Dekdouk, B., Wuliang Yin, W., Ktistis, C., Armitage, D. W., & Peyton, A. J. (2010). A method to solve the forward problem in magnetic induction tomography based on the weakly coupled field approximation. *IEEE Transactions on Biomedical Engineering, 57*, 914–921.

Dodd, C. V., & Deeds, W. E. (1968). Analytical solutions to eddy-current probe-coil problem. *Journal of Applied Physics, 39*, 2829–2839.

Dyck, D. N., Lowther, D. A., & Freeman, E. M. (1994). A method of computing the sensitivity of electromagnetic quantities to changes in materials and sources. *IEEE Transactions on Magnetics, 30*, 3415–3418.

Gabriel, C., Gabriel, S., & Corhout, E. (1996). The dielectric properties of biological tissues. *Physics in Medicine and Biology, 41*, 2231−2249.

Gandhi, O. P., DeFord, J. F., & Kanai, H. (1984). Impedance method for calculation of power deposition patterns in magnetically induced hyperthermia. *IEEE Transactions on Biomedical Engineering, 31*, 644−651.

Griffiths, H. (2001). Magnetic induction tomography. *Measurement Science and Technology, 12*, 1126−1131.

Griffiths, H. (2005). Magnetic induction tomography. In D. S. Holder (Ed.), *Electrical impedance tomography: Methods, history and applications*. IOP Publishing.

Gürsoy, D., & Scharfetter, H. (2011). Imaging artefacts in magnetic induction tomography caused by the structural incorrectness of the sensor model. *Measurement Science and Technology, 22*(015502), 10.

Higson, S. R., Drake, P., Lyons, A., Peyton, A., & Lionheart, B. (2006). Electromagnetic visualisation of steel flow in continuous casting nozzles. *Ironmaking and Steelmaking, 33*, 357−361.

Hollaus, K., Magele, C., Merwa, R., & Scharfetter, H. (2004a). Numerical simulation of the eddy current problem in magnetic induction tomography for biomedical applications by edge elements. *IEEE Transactions on Magnetics, 40*, 623−626.

Hollaus, K., Magele, C., Merwa, R., & Scharfetter, H. (2004b). Fast calculation of the sensitivity matrix in magnetic induction tomography by tetrahedral edge finite elements and the reciprocity theorem. *Physiological Measurement, 25*, 159−165.

Horner, B., Mesch, F., & Trächtler, A. (1996). A multi-sensor induction flowmeter reducing errors due to non-axisymmetric flow profiles. *Measurement Science and Technology, 7*, 354−360.

Johnstone, S., & Peyton, A. J. (2001). The application of parametric 3D finite element modelling techniques to evaluate the performance of a magnetic sensor system. *Sensors and Actuators A:Physical, 93*, 109−116.

Ktistis, C., Armitage, D. W., & Peyton, A. J. (2008). Calculation of the forward problem for absolute image reconstruction in MIT. *Physiological Measurement, 29*, S455−S464.

Ledger, P.D. and Lionheart, W.R.B. Characterising the shape and material properties of hidden targets from magnetic induction data. *IEEE Transactions on Magnetics* (submitted for publication).

Ma, X., Peyton, A. J., Binns, R., & Higson, S. R. (2005). Electromagnetic techniques for imaging the cross-section distribution of molten steel flow in the continuous casting nozzle. *IEEE Sensors Journal, 5*, 224−232.

Ma, X., Peyton, A. J., Higson, S. R., Lyons, A., & Dickinson, S. J. (2006). Hardware and software design for an electromagnetic induction tomography (EMT) system for high contrast metal process applications. *Measurement Science and Technology, 17*, 111−118.

Makkonen, J., Marsh, L. A., Vihonen, J., Järvi, A., Armitage, D. W., Visa, A., et al. (2013). KNN classification of metallic targets using the magnetic polarizability tensor. *Measurement Science and Technology, 25*(055105), 9.

Marsh, L. A., Ktistis, C., Järvi, A., Armitage, D. W., & Peyton, A. J. (2013). Three-dimensional object location and inversion of the magnetic polarizability tensor at a single frequency using a walk-through metal detector. *Measurement Science and Technology, 24*(045102), 13.

Marsh, L. A., Ktistis, C., Järvi, A., Armitage, D. W., & Peyton, A. J. (2014). Determination of the magnetic polarizability tensor and three dimensional object location for multiple objects using a walk-through metal detector. *Measurement Science and Technology, 25*(055107), 12.

Morris, A., Griffiths, H., & Gough, W. (2001). A numerical model for magnetic induction tomographic measurements in biological tissues. *Physiological Measurement, 22*, 113−119.

Norton, S. J., & Bowler, J. R. (1993). Theory of eddy current inversion. *Journal of Applied Physics, 73*, 501−510.

Norton, S. J., & Won, I. J. (2001). Identification of buried unexploded ordnance from broadband electromagnetic induction data. *IEEE Transaction Geoscience and Remote Sensing, 39*, 2253−2261.

Norton, S. J., Kahn, A. H., & Mester, M. L. (1989). Reconstructing electrical conductivity profiles from variable-frequency eddy current measurements. *Research in Nondestructive Evaluation, 1*, 167−179.

Peyton, A. J., Beck, M. S., Borges, A. R., de Oliveira, J. D., Lyon, G. M., Yu, Z. Z., et al. (1999). Development of electromagnetic tomography (EMT) for industrial applications. In *Part 1: Sensor design and instrumentation, first world congress on industrial process tomography, Buxton, Greater Manchester, April 14−17* (pp. 306−312).

Peyton, A. J., Watson, S., Williams, R. J., Griffiths, H., & Gough, W. (2003). *Characterising the effects of the external electromagnetic shield on a magnetic induction tomography sensor 3rd world congress on industrial process tomography*. Banff, Canada, 352−357.

Peyton, A. J., Yin, W., Dickinson, S. J., Davis, C. L., Strangwood, M., Hao, X., et al. (2010). Monitoring microstructure changes in rod online by using induction spectroscopy. *Ironmaking and Steelmaking, 37*, 135−139.

Pham, M. H., Hua, Y., & Gray, N. B. (2000a). Imaging the solidification of molten metal by eddy currents: I. *Inverse Problems, 16*, 469−482.

Pham, M. H., Hua, Y., & Gray, N. B. (2000b). Imaging the solidification of molten metal by eddy currents: II. *Inverse Problems, 16*, 483−494.

Randazzo, A., & Pignone, E. (2007). A blade coating inspection method based on an electromagnetic inverse scattering approach. In *IEEE international workshop on imaging systems and techniques - IST 2007, Krakow, Poland.*

Resagk, C., Men, S., Ziolkowski, M., Kuilekov, M., & Brauer, H. (2006). Magnetic field tomography on two electrically conducting fluids. *Measurement Science and Technology, 17*, 2136−2140.

Roemer, P. B., Edelstein, W. A., Hayes, C. E., Souza, S. P., & Mueller, O. M. (1990). The NMR phased array. *Magnetic Resonance in Medicine, 16*, 192−225.

Scharfetter, H., Köstinger, A., & Issa, S. (2008). Hardware for quasi-single-shot multifrequency magnetic induction tomography (MIT): the Graz Mk2 system. *Physiological Measurement, 29*, 431−443.

Scharfetter, H., Lackner, H.k, & Rosell, J. (2001). Magnetic induction tomography: hardware for multi-frequency measurements in biological tissues. *Physiological Measurement, 22*, 131−146.

Sharif, E., Bell, C., Morris, P. F., & Peyton, A. J. (2001). Imaging the transformation of hot strip steel using magnetic techniques, SPIE. *Journal of Electronic Imaging, 10*, 669−678. http://dx.doi.org/10.1117/1.1380386.

Silvester, P. P., & Ferrari, R. L. (1996). *Finite elements for electrical engineers*. Cambridge: Cambridge University Press.

Smith, R. W. M., Freeston, I., Brown, B. H., & Sinton, A. M. (1992). Design of a phase-sensitive detector to maximise signal-to-noise ratio in the presence of Gaussian wideband noise. *Measurement Science and Technology, 3*, 1054−1062.

Soleimani, M., & Lionheart, W. R. B. (2006). Absolute conductivity reconstruction in magnetic induction tomography using a nonlinear method. *IEEE Transactions on Medical Imaging, 25*, 1521−1530.

Soleimani, M., Lionheart, W. R. B., Peyton, A. J., Ma, X., & Higson, S. R. (2006). A three-dimensional inverse finite-element method applied to experimental eddy-current imaging data. *IEEE Transactions on Magnetics, 42*, 1560−1567.

Stefani, F., Gundrum, T., & Gerbeth, G. (2004). Contactless inductive flow tomography. *Physical Review E, 70*, 056306.

Tanguay, L.-F., Gagnon, H., & Guardo, R. (2007). Comparison of applied and induced current electrical impedance tomography. *IEEE Transactions on Biomedical Engineering, 54*, 1643−1649.

Tarjan, P. R., & McFee, R. (1968). Electrodeless measurement of the effective resistivity of the human torso and head by magnetic induction. *IEEE Transactions on Biomedical Engineering, 15*, 266−278.

Timmel, K., Eckert, S., Gerbeth, G., Stefani, F., & Wondrak, T. (2010). Experimental modeling of the continuous casting process of steel using low melting point metal alloys—the LIMMCAST program. *ISIJ International, 50*, 1134−1141.

Tumanski, S. (2007). Induction coil sensors—a review. *Measurement Science and Technology, 18*, R31−R46.

Vauhkonen, M., Hamsch, M., & Igney, C. H. (2008). A measurement system and image reconstruction in magnetic induction tomography. *Physiological Measurement, 29*, S445−S454.

Watson, S., Williams, R. J., Gough, W., & Griffiths, H. (2008). A magnetic induction tomography system for samples with conductivities below 10 S m^{-1}. *Measurement Science and Technology, 19*(045501), 11.

Wondrak, Th, Eckert, S., Galindo, V., Gerbeth, G., Stefani, F., Timmel, K., et al. (2012). Liquid metal experiments with swirling flow submerged entry nozzle. *Ironmaking and Steelmaking, 39*, 1−9.

Yin, W., Dickinson, S. J., & Peyton, A. J. (2005). Imaging the continuous conductivity profile within layered metal structures using inductance spectroscopy. *IEEE Sensors, 5*, 161−166.

Yin, W., & Peyton, A. J. (2010a). Dimensional scaling relationships in electrical tomography. In *Sixth world congress on Industrial Process Tomography, Beijing, China*.

Yin, W., & Peyton, A. J. (2010b). Sensitivity formulation including velocity effects for electromagnetic induction systems. *IEEE Transactions on Magnetics, 46*, 1172−1176.

Yu, Z. Z., Worthington, P. F., Stone, S., & Peyton, A. J. (1995). Electromagnetic screening of inductive tomography sensors. In *European concerted action on process tomography conference, Bergen, Norway* (pp. 300−310).

Zhao, Y. Y., Lucas, G., Leeungculsatien, T., & Zhang, T. (2012). Measurement system design of an imaging electromagnetic flow meter. *AIP Conference Proceedings, 1428*, 258.

Zolgharni, M., Ledger, P. D., Armitage, D. W., Holder, D. S., & Griffiths, H. (2009). Imaging cerebral haemorrhage with magnetic induction tomography: numerical modelling. *Physiological Measurements, 30*, S187−S200.

This page intentionally left blank

Magnetic resonance imaging

4

A.J. Sederman
Department of Chemical Engineering and Biotechnology, University of Cambridge, Cambridge, UK

4.1 Introduction to MRI and NMR

Magnetic resonance imaging (MRI) is now ubiquitous as a diagnostic tool in clinical medicine to the extent that it is recognised by the general public; however, its use in engineering and the physical sciences is much less well known. Despite this, it has many attributes that make it an exceptionally powerful tomography technique due to the different types of contrast and information that it can be used to measure. These include but are not limited to chemical concentration, molecular diffusion and velocity, all of which can be measured locally in an image of the sample. MRI is also an inherently quantitative measurement tool with well-defined and well-understood physical principles underpinning it. This chapter is aimed principally as a pedagogical introduction to MRI for engineers and will include the basic principles of data acquisition and image reconstruction. It will also consider some of the practicalities and limitations along with its benefits and a few examples of applications to engineering systems.

MRI is, in fact, just a subset of the nuclear magnetic resonance (NMR) technique. NMR encompasses all magnetic resonance (MR) methods, both spatially unresolved and spatially resolved, and many readers will be familiar with NMR as a useful analytical tool for spectroscopy in chemistry or for determining the structure of proteins. In general, MR measurements can be divided into two classes — those which do not require any spatial resolution within the data and those that do. Where spatial encoding information is required, then, in addition to a basic MR equipment, which is typically performed in a large magnetic field, additional smaller constant gradients in the magnetic field will also be used at some point during the experiment. Here, we generally consider spatially resolved MR measurements and how to acquire them, but it is useful to note that any information that can be extracted from an NMR experiment can, in theory, be obtained in a spatially resolved form of an image, where signal-to-noise (SNR) and acquisition time are sufficient.

This chapter first explains the basic principles of MRI before looking at specific imaging techniques and how these techniques can be modified to get different image contrast and how to speed up acquisition to enable real-time image collection. The chapter will finish off with some examples of applications of MRI in engineering and some final conclusions.

Industrial Tomography. http://dx.doi.org/10.1016/B978-1-78242-118-4.00004-6
Copyright © 2015 Elsevier Ltd. All rights reserved.

4.2 MRI: basic imaging principles

In this section, there is a brief exposition on the fundamentals of NMR, MRI and the measurement of diffusion and flow. Where suitable, practical advice on sequence selection and implementation and other aspects of MRI will also be included. There are a number of excellent texts treating the subject in greater detail, and the interested reader in the fundamentals of NMR and MRI may find the following texts of interest: Levitt (2002) for an introduction to NMR, and Callaghan (1991, 2011) for imaging and, in particular, translational motion. Sodickson and Cory (1998) approach the theory of imaging from a slightly different perspective, and for an alternative medical perspective on MRI physics and pulse sequence selection and design, the reader is referred to the text by Haacke (1999) and others.

4.2.1 The precessing magnetisation vector

Before considering how we get spatial information from the MRI experiment, it is necessary to introduce the basics of the spatially unresolved NMR experiments. This is often taken to suggest a spectroscopy experiment, although other bulk properties such as diffusion and relaxation times may also be measured. The spatially unresolved spectroscopy experiment is the simplest type of MR experiment, and the principles upon which this measurement is based underpin all types of MR measurement and so are of relevance here.

All NMR experiments must be performed on nuclei of nonzero nuclear spin, most commonly ^{1}H, and in the presence of a magnetic field. At equilibrium, a greater proportion of the nuclear spins align with the magnetic field (with the overpopulation defined by the Boltzmann distribution), as a result of which there exists a net magnetisation vector aligned parallel to the direction of the magnetic field. This magnetisation vector can be manipulated by the application of electromagnetic energy of appropriate frequency. The frequency at which this manipulation occurs is called the resonance frequency, ω_0, and is given by the following:

$$\omega_0 = \gamma B_0 \tag{4.1}$$

where γ is the (nuclei-specific) gyromagnetic ratio, and B_0 is the magnetic field strength. All NMR sequences have an excitation pulse that is used to perturb the magnetisation away from parallel to the magnetic field. After the magnetisation vector has been perturbed, it will precess about the direction of the magnetic field, B_0, at the resonance frequency ω_0 as it returns to its equilibrium magnetisation. This precession emits electromagnetic energy that can be detected and forms the basis of the MR measurement. In a standard NMR spectroscopy measurement, the magnetic field observed is slightly modified by the electronic environment of the nucleus under study, thus ω_0 is also modified and the distribution of frequencies, or spectrum, becomes a fingerprint of the molecular species under investigation.

4.2.2 Magnetic field gradients and imaging

Performing spatially resolved experiments (imaging) requires the additional effect of spatial variations in the magnetic field or magnetic field gradients. So far, we have assumed that B_0 was homogeneous over all experimental space or at least that inhomogeneities were small. Magnetic field gradients are designed such that they add a relatively small magnetic field that varies linearly with position to the main field such that the resultant field, $B(\boldsymbol{r})$, at position $\boldsymbol{r}$ varies according to the following:

$$B(\boldsymbol{r}) = B_0 + \boldsymbol{G}\cdot\boldsymbol{r} \tag{4.2}$$

where $\boldsymbol{G}$ is the strength of the applied gradient. Practically, the gradient can be applied in any direction, with a known strength and duration. Substituting this into Eqn (4.1), we now see that the frequency is a function of the sample position:

$$\omega(\boldsymbol{r}) = \gamma(B_0 + \boldsymbol{G}\cdot\boldsymbol{r}) \tag{4.3}$$

If we measure the frequency relative to the resonance frequency, ω_0, also known as the rotating frame, we observe that the frequency is directly proportional to the position, and this relationship underpins all MRI experiments. If we consider a local volume element $\mathrm{d}V$ within our sample, the local spin density, $\rho(\boldsymbol{r})$, for spins within the volume element $\mathrm{d}V$ is then $\rho(\boldsymbol{r})\mathrm{d}V$. The NMR signal as a function of time, $\mathrm{d}S(t)$, from this element may then be written as follows:

$$\mathrm{d}S(t) \propto \rho(\boldsymbol{r})\exp[\mathrm{i}\omega(\boldsymbol{r})t]\mathrm{d}V \tag{4.4}$$

Inserting Eqn (4.3) into (4.4) we obtain

$$\mathrm{d}S(t) \propto \rho(\boldsymbol{r})\exp[\mathrm{i}\gamma(B_0 + \boldsymbol{G}\cdot\boldsymbol{r})t]\mathrm{d}V \tag{4.5}$$

A transformation into the rotating frame of reference followed by integration over all the sample allows us to write Eqn (4.5) in terms of the overall observed signal $S(t)$ and becomes the following:

$$S(t) = \iiint \rho(\boldsymbol{r})\exp[\mathrm{i}\gamma\boldsymbol{G}\cdot\boldsymbol{r}t]\mathrm{d}\boldsymbol{r} \tag{4.6}$$

where $\mathrm{d}\boldsymbol{r}$ represents integration over all space. Mansfield and Grannell (1973) realised that this equation could be simplified by the introduction of the concept of $\boldsymbol{k}$-space defined as follows:

$$\boldsymbol{k} = \frac{\gamma\boldsymbol{G}t}{2\pi} \tag{4.7}$$

where $\boldsymbol{k}$ is known as the reciprocal space vector and has units of m^{-1}. More generally, it can be written as the first moment of the gradient with time:

$$\boldsymbol{k}(t) = \frac{\gamma}{2\pi}\int_0^t \boldsymbol{G}(t)\mathrm{d}t \tag{4.8}$$

Substituting Eqn (4.7) into (4.6) gives an expression that describes how the measured signal, S, varies as a function of $\boldsymbol{k}$:

$$S(\boldsymbol{k}) = \iiint \rho(\boldsymbol{r})\exp[\mathrm{i}2\pi\boldsymbol{k}\cdot\boldsymbol{r}]\mathrm{d}\boldsymbol{r} \tag{4.9}$$

And the Fourier transformation of Eqn (4.9) gives the following:

$$\rho(\boldsymbol{r}) = \iiint S(\boldsymbol{k})\exp[-\mathrm{i}2\pi\boldsymbol{k}\cdot\boldsymbol{r}]\mathrm{d}\boldsymbol{k} \tag{4.10}$$

Taken together, Eqns (4.9) and (4.10) tell us that $S(\boldsymbol{k})$ and $\rho(\boldsymbol{r})$ form a mutually conjugate Fourier transform pair. It, therefore, follows that if we acquire our signal over a suitable range of $\boldsymbol{k}$ and then perform a Fourier transform, we will recover ρ, the spin density or nuclei concentration as a function of the position, $\boldsymbol{r}$, that is our concentration image.

This relationship shows that we acquire our image data in the frequency space of the image itself – a fact that can be useful when trying to identify specific repeating features in an image that may show up more clearly in the directly acquired data (Holland, Blake, Tayler, Sederman, & Gladden, 2011). To produce an image of the required resolution and field-of-view (FOV), data must be acquired over a suitable range and increment of $\boldsymbol{k}$. From Fourier theory, it follows that the range of $\boldsymbol{k}$ defines the image resolution and an increment in $\boldsymbol{k}$ defines the FOV such that:

$$\mathrm{FOV} = \frac{1}{\Delta\boldsymbol{k}}, \quad \Delta l = \frac{1}{\boldsymbol{k}_{\mathbf{range}}} \tag{4.11}$$

where $\Delta\boldsymbol{k}$ is the increment in $\boldsymbol{k}$, Δl is the image resolution and $\boldsymbol{k}_{\mathbf{range}}$ is the total range of $\boldsymbol{k}$ sampled from $-\boldsymbol{k}$ to $\boldsymbol{k}$. Although the majority of MRI measurement is done by fully sampling $\boldsymbol{k}$-space followed by a Fourier transform as described, there has recently been great interest in utilising other image reconstruction methods such as compressed sensing (Candes, Romberg, & Tao, 2006; Donoho, 2006) where data sampling, and therefore, imaging time is reduced. These will be discussed in more detail in Section 5.2.1.

4.2.3 Frequency and phase encoding

From the previous section, we see that it is sufficient to acquire a signal over the correct range of $\boldsymbol{k}$ to produce an image of the desired FOV and resolution. The range of $\boldsymbol{k}$ values that we wish to acquire is termed $\boldsymbol{k}$-space, and experimentally, there are a number of different ways to traverse through $\boldsymbol{k}$-space. In a typical experiment, an excitation pulse will be followed by data acquisition and the application of magnetic field gradients of known magnitude and duration. In conventional imaging, all points in $\boldsymbol{k}$-space must be acquired to produce a fully resolved image, and these points would be acquired in the 'read' direction and the 'phase' direction. In the read (or readout) direction, the gradient is kept constant during the acquisition, and $\boldsymbol{k}$-space is traversed with successive points being acquired at constant time increments. From Eqn (4.7), we see that different values of $\boldsymbol{k}$ are achieved by keeping $\boldsymbol{G}$ constant as the value of t increases in this method. This is also known as the *frequency encode* direction; the spins will have a position-dependent frequency during the readout, as defined by Eqn (4.3). This method assumes that the time evolution of the signal is only due to the position of the nuclei and the applied gradients, which may not always be valid. But, it provides a very cheap way to acquire points quickly as the time increment between points is typically of the order of a few μs, and a whole line of $\boldsymbol{k}$-space of several 100 points can be acquired in less than 1 ms. In conventional imaging, the other spatial dimension would be the *phase encode* direction in which a gradient is applied for a fixed duration at some time between excitation and acquisition, thus imparting a position-dependent phase (angle) as can be seen from a time integral of Eqn (4.3), where $\omega(\boldsymbol{r})$ is the rate of change of phase angle with time. In the phase direction, the gradient is off during the acquisition and usually subsequent $\boldsymbol{k}$-space points in the phase direction are acquired in successive excitations by changing the strength of the applied gradient. The delay between successive excitations is determined by the relaxation of the magnetisation back to equilibrium (T_1 relaxation) and is typically of the order of seconds.

4.2.4 Simple 1D and 2D imaging sequences

A conceptually simple imaging sequence is a one-dimensional (1D) image or profile with frequency encoding for position in one direction, as shown in Figure 4.1. In a

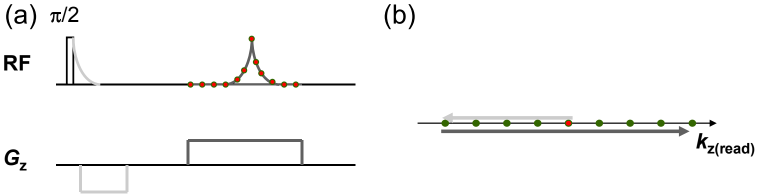

Figure 4.1 (a) Schematic of a simple 1D profile image and (b) the corresponding trajectory through $\boldsymbol{k}$-space.

1D profile in the x-direction, the intensity at each x position corresponds to the integration over y and z at that x position. In $\boldsymbol{k}$-space, we just need to acquire a single line of points in the k_x direction, as shown in Figure 4.1(a), where $\Delta \boldsymbol{k}$ and $\boldsymbol{k}_{\mathbf{range}}$ are determined from Eqn (4.11). Initially, the magnetisation lies along the direction of the magnetic field (z direction), but after perturbation by a 90° excitation pulse, it is in the transverse (x—y) plane and will precess as described by Eqn (4.1). After excitation, the value of $\boldsymbol{k}$ is initialised to zero, so a negative de-phasing gradient is applied to move the system to -$\boldsymbol{k}_{\mathbf{max}}$. At this point, the polarity of the gradient is switched, and as the system moves from $-\boldsymbol{k}_{\mathbf{max}}$ to $\boldsymbol{k}_{\mathbf{max}}$, the digitiser is open to acquire data at fixed time increments that correspond to $\Delta \boldsymbol{k}$. Following Fourier transformation of the data, a 1D profile of the sample is obtained. Timescales for this image are short, and excitation, de-phasing gradient and data acquisition can take < 1 ms.

More often, we are interested in a 2D image, and using convention imaging, this would be done with a frequency encoding direction and a phase direction. A simple 2D imaging sequence and associated 2D $\boldsymbol{k}$-space raster are shown in Figure 4.2. In this sequence, acquisition of $\boldsymbol{k}$-space in one direction follows in exactly the same way as in the 1D sequence, that is, a de-phasing gradient is first applied, followed by a frequency encoding gradient during data acquisition. In the other imaging dimension, the phase direction, a gradient will be applied before acquisition to move the system to the desired $\boldsymbol{k}_{\mathbf{phase}}$ position before acquisition. In this method, a single line of $\boldsymbol{k}$-space is acquired after excitation with the position of that line determined by the strength and duration of the phase gradient (Eqn (4.7)). To acquire all points on the $\boldsymbol{k}$-space raster, multiple excitations must be done with the delay between excitations characterised by T_1 (typically of the order of seconds), so the total image acquisition time will often be several minutes. The 2D image is obtained by 2D Fourier transformation of all points in the 2D $\boldsymbol{k}$-space raster.

Here, a practical difference between the read and phase directions is seen where points in the read direction may be acquired every few μs, but points in the phase direction are acquired every few seconds, which would suggest that we want to acquire points in the read direction wherever possible. This is often the case, but the number of read points that can be acquired from a single excitation is

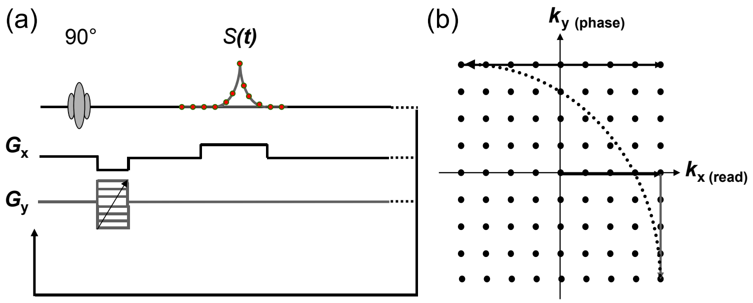

Figure 4.2 (a) Schematic of a simple 2D imaging pulse sequence. (b) The corresponding $\boldsymbol{k}$-space raster used to show how we may interpret the pulse sequence. Following a sufficient T_1 relaxation period, the whole sequence is repeated N times to produce the full $\boldsymbol{k}$-space data set.

determined by adherence to the previous statement that 'the time evolution of the signal is only due to the position of the nuclei and the applied gradients'. To understand this and other image acquisition time issues, we must consider signal relaxation (Section 3.1).

4.2.5 Slice selection

Although we have seen how to acquire a 2D image in Section 2.4, this would correspond to a projection of all material in the direction perpendicular to the imaging plane. To obtain a 2D slice image, we must use a pulse sequence that includes slice selection. Slice selection is obtained by applying an excitation or refocusing pulse that has a narrow excitation band and the application of a gradient field, $\boldsymbol{G}$, simultaneously; the effect of this is shown schematically in Figure 4.3 where the gradient is in the z direction. Figure 4.3(a) shows the amplitude of the pulse field plotted against the sample frequency. At the same time, the resonance frequencies of the spins along the gradient direction are spread out by the gradient, as shown in Figure 4.3(b). Therefore, the only spins that will be excited are those that resonate within the excitation frequency, $\Delta\omega$, of the pulse, and consequently, only those spins that lie within the slice defined by Δz are observed. The adjustable parameters $\Delta\omega$ and $\boldsymbol{G}$ control the width of the selected slice, and thin slice selection is obtained by either narrow-band radio frequency (RF) irradiation or a strong gradient $\boldsymbol{G}$. The shape of the slice to be excited is the same as the frequency profile of the pulse, which is related via a Fourier relationship to the modulation of the pulse in time. In most cases, the preferred slice shape would be a perfect rectangle or Heaviside Hat function. Unfortunately, the Fourier pair of the Hat function is the sinc function $\left(\frac{\sin(x)}{x}\right)$, which has signal intensity extending to infinite time; so, it must be truncated to some extent (often severely), as the pulse must be of finite length. This truncation induces artefacts in the frequency domain, which is unsuitable if good slice definition is required. An often used alternative, the Gaussian pulse, gives rise to a Gaussian response. The truncation for this is less severe, and the artefacts are

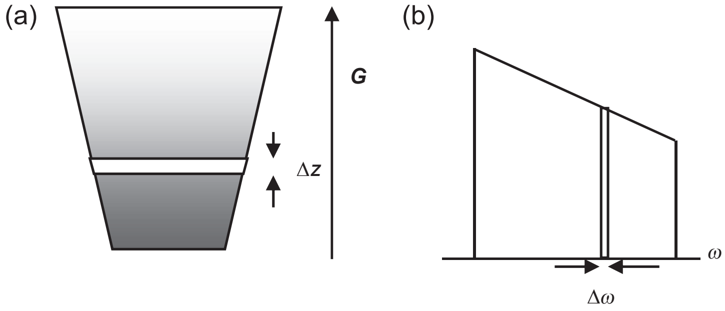

Figure 4.3 Slice selection by selective excitation. When a gradient, $\boldsymbol{G}$, is applied across a sample, the precession frequency is dependent on the position. A slice may be selected by a pulse with a narrow excitation frequency, $\Delta\omega$.

almost completely eliminated. It can be seen that soft pulses will be used to form the basis of many experiments. Used alone, they can excite specific regions of the chemical spectrum, and used concurrently with a magnetic gradient, they can be used to excite a localised slice at any place or direction within a sample without the need to reposition the sample.

4.3 Image contrast

4.3.1 Signal relaxation

Following the application of an excitation pulse, the system has excess energy. To return to thermal equilibrium, the system has to redistribute this excess energy — a process known as relaxation. These relaxation times are important in imaging as they will strongly influence how fast images can be acquired and the contrast/quantification in those images. The most important relaxation times for imaging experiments are the spin—lattice relaxation (T_1) and spin—spin relaxation (T_2) time constants along with the magnetic field inhomogeneity modified spin—spin relaxation (T_2^*). T_1 characterises the energy exchange between the excited nuclear spin and the surrounding physical environment (i.e. the lattice), whereas T_2 and T_2^* characterise the loss of phase angle coherence between nuclear spins. In practical imaging experiments, T_1 effects how fast repeated excitations can be made, and T_2/T_2^* effects how long after excitation a measurable signal remains. We, therefore, want a short T_1 for fast repetition but a long T_2 so that many points can be acquired after excitation. Because $T_2 \leq T_1$, systems where $T_2 \approx T_1$ offer the best possibilities for fast image acquisition. If a system is characterised by a very small T_2 (e.g. many solids) the coherent signal may decay too fast for it to be possible to perform imaging experiments, whereas a system with very long T_1 will require a long time to come to equilibrium between successive excitations. So, imaging may become prohibitively long. Each system and even species within a system will have its own T_1 and T_2 relaxation times from which contrast may be produced. Further in-depth discussion on the theories of relaxation can be found elsewhere (Abragam, 1961).

T_1 relaxation: At thermal equilibrium, before the system is perturbed with an excitation pulse, the net magnetisation vector is aligned along the direction of the static magnetic field (z). It is the magnitude of this vector that provides the quantitative measurement of the number of nuclear spins excited within the sample. After a 90° excitation pulse, the magnetisation vector is rotated through 90° to lie in the x—y plane. As soon as the excitation stops, the magnitude of the magnetisation vector increases back along z direction as it returns to equilibrium. This relaxation process back to its equilibrium magnetisation, M_0, can be described by an exponential recovery:

$$\frac{dM_z}{dt} = -\frac{M_z - M_0}{T_1} \tag{4.12}$$

where M_z refers to the z-component of the magnetisation, and T_1 is the time constant of the recovery. For the 90° excitation described above, the solution at some time, t, after excitation for Eqn (4.12) is as follows:

$$M_z(t) = M_0\left[1 - \exp\left(-\frac{t}{T_1}\right)\right] \tag{4.13}$$

From this, it follows that if we wait a short time between excitations, only a fraction of the magnetisation will have been reestablished along z. If we wait ~5–7 times longer than T_1, the system will have recovered to equilibrium, and M_z will have recovered to M_0. In a sequence with repeated excitation pulses such as that shown in Figure 4.2, the total magnetisation available for excitation and, therefore, detection can be calculated from Eqn (4.13), where t is the delay time between excitation pulses. Thus, if we have two species with different T_1 characteristics, by careful selection of the delay time between excitations, a signal can be acquired with contrast between the components. This is termed T_1 contrast.

T_2 and T_2^* relaxation: On shorter time scales than T_1, spin–spin relaxation (T_2) occurs. T_2 characterises the loss of phase angle coherence between spins. During the period following excitation, the individual spins will lose phase coherence with each other as a result of spin–spin interactions and local variations in B_0 causing a decay in the measureable magnetisation. This decay of magnetisation in the x–y plane due to spin–spin interactions is characterised by the time constant T_2 and is an irreversible decay.

$$M_{xy}(t) = M_0 \exp\left(-\frac{t}{T_2}\right) \tag{4.14}$$

where $M_{xy}(t)$ is the magnetisation in the x–y plane at a time t after excitation.

In addition to this decay is the effect of magnetic field heterogeneities – different regions of the sample will have small differences in the magnetic field strength, possibly due to materials with different magnetic susceptibilities and, therefore, frequency (Eqn (4.1). This will lead to a loss of phase coherence in addition to T_2 – the decay constant used to model this component of the decay is termed T_2', and the combined decay constant, T_2^*, is given by the following:

$$\frac{1}{T_2^*} = \frac{1}{T_2} + \frac{1}{T_2'} \tag{4.15}$$

Thus, the decay of the signal after an excitation pulse, in the presence of spin–spin interactions and magnetic field variations, will decay with an envelope of T_2^* time constant. The component due to magnetic field variations (T_2') is recoverable in some imaging sequences, usually using a spin echo. As T_2^* may be much less than T_2 in engineering samples, this is an important consideration when choosing or designing an imaging sequence. As with T_1, it is also possible to obtain T_2 contrast in an image

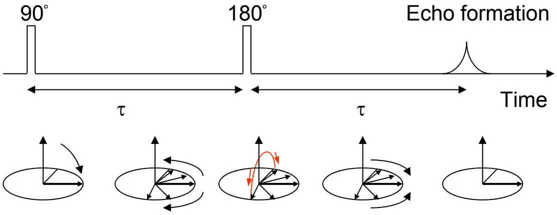

Figure 4.4 The spin echo. The spins are rotated into the transverse plane and de-phased due to B_0 inhomogeneities. After time, τ, a 180° pulse is applied, and the spins begin to refocus. At time 2τ, a spin echo is formed.

where different components have different T_2. To obtain T_2 or T_2^* contrast, the delay allowed for de-phasing between the excitation pulse and data acquisition are adjusted.

4.3.1.1 The spin echo

When a heterogeneous sample is placed in a uniform magnetic field, local magnetic field distortions are created near material boundaries. These field distortions will affect the local frequency, as seen from Eqn (4.1), and so T_2^* may be much shorter than T_2 — in such cases it is beneficial to use the spin echo to refocus de-phasing due to these field distortions, so the signal decays only with T_2. A schematic of the spin echo is shown in Figure 4.4. The 180° refocusing pulse acts to reverse the de-phasing effects due to the local heterogeneities in $B_{0,}$ such that the final acquired signal (the echo) suffers attenuation resulting from spin—spin interactions only. In short, by using an echo sequence, instead of exciting the system and then allowing the magnetisation to decay to zero, the majority of the magnetisation can be recovered for use in subsequent measurements. This makes the simple echo sequence shown in Figure 4.4 a common feature of MRI pulse sequences.

4.3.2 Flow and diffusion

One of the powerful features of MR is the ability to measure incoherent motion (diffusion) and coherent motion (flow). There have been a number of reviews on the use of MRI as a tool to study flow and translational motion in nonmedical research areas (Callaghan, 2011; Elkins & Alley, 2007; Fukushima, 1999; Mantle & Sederman, 2003), and more details and examples can be found in those. Here we introduce time-of-flight (TOF) and phase-shift velocity measurement methods. The diffusion measurement method, also referred to as PFG or PGSE in the literature has a close association with the phase-shift measurement and is not discussed in detail here, but an in-depth treatise can be found in Chapter 6 of Callaghan's book (Callaghan, 1991).

4.3.2.1 Time-of-flight velocity imaging

TOF or spin tagging methods were first reported in 1959, and their use has been widespread since then. At their simplest, they may just consist of an imaging sequence

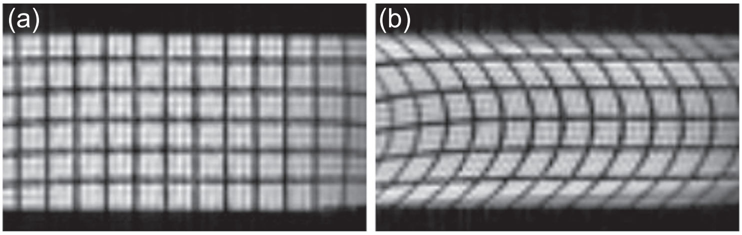

Figure 4.5 Example of a TOF velocity image. Proton image of a longitudinal slice through a pipe: (a) stationary and (b) with flow.

where the time delay between excitation and acquisition has been increased, and only spins that remain within a selected slice will contribute to signal intensity. Therefore, high velocity areas, where fewer spins have remained in the slice will appear as darker areas in the final image. If the slice thickness and sequence timings are known, then an estimate of the velocity may be made. Although this method is good for identifying flowing regions, accurate quantification can be difficult. Another form of spin tagging, which can aid quantification and provide a very intuitive visualisation of the motion, is where the imaging plane is perpendicular to the tagging. An example of this is when a grid of spins are tagged by a specially tailored pulse. An example of such a TOF image of pipe flow is shown in Figure 4.5, where laminar flow in a pipe has been imaged with a time delay between the tagging and the imaging sequence without flow (Figure 4.5(a)) and with flow (Figure 4.5(b)).

4.3.2.2 Phase-shift velocity imaging

Phase-shift or phase-contrast displacement measurement probably offers the most robust and quantitative way of measuring flow by NMR. Whilst spin tagging methods are adequate for flow visualisations, their velocity resolution is often limited by the overall spatial imaging resolution. The dynamic range of phase-shift velocity imaging can be adjusted from as little as a few μm s^{-1} up to 10–100 m s^{-1}. It is limited at lower velocities to displacements due to self-diffusion and at higher velocities to residence time in the measurement volume.

The principle of phase-shift velocity imaging can be understood by considering the effects of the applied gradient $\boldsymbol{G}(t)$ on the phase of moving spins. Equation (4.3) describes the precession frequency at position $\boldsymbol{r}$. Consider this to be time-dependent, $\boldsymbol{r}(t)$; then, the phase shift $\phi(t)$ is given by the following:

$$\phi(t) = \gamma \int_0^t \boldsymbol{G}(t)\boldsymbol{r}(t)\mathrm{d}t \tag{4.16}$$

If the time-dependent position of this spin set is expanded as follows,

$$\boldsymbol{r}(t) = \boldsymbol{r}_0 + \boldsymbol{v}_0 t + \frac{1}{2}\boldsymbol{a}_0 t^2 + \cdots \tag{4.17}$$

then the time-dependent phase accrued by the spins will be the following:

$$\phi(t) = \gamma\left[\boldsymbol{r}_0\int_0^t \boldsymbol{G}(t)\mathrm{d}t + \boldsymbol{v}_0\int_0^t \boldsymbol{G}(t)t\mathrm{d}t + \boldsymbol{a}_0\int_0^t \boldsymbol{G}(t)t^2\mathrm{d}t + \cdots\right] \tag{4.18}$$

The integrals are the successive moments ($\boldsymbol{M}_0$, $\boldsymbol{M}_1$, $\boldsymbol{M}_2$ ...) of the gradient with time:

$$\text{Zeroth moment,}\quad \boldsymbol{M}_0 = \int_0^t \boldsymbol{G}(t)\mathrm{d}t \tag{4.19a}$$

$$\text{First moment,}\quad \boldsymbol{M}_1 = \int_0^t \boldsymbol{G}(t)t\mathrm{d}t \tag{4.19b}$$

$$\text{Second moment,}\quad \boldsymbol{M}_2 = \int_0^t \boldsymbol{G}(t)t^2\mathrm{d}t \tag{4.19c}$$

The zeroth moment, $\boldsymbol{M}_0$, causes a phase shift proportional to position $\boldsymbol{r}_0$, and the first moment, $\boldsymbol{M}_1$, causes a phase shift proportional to velocity $\boldsymbol{v}_0$, etc. Therefore, gradient waveforms can be designed that have a nonzero $\boldsymbol{M}_1$ (but zero $\boldsymbol{M}_0$), and the phase, which can be measured, will be proportional to the velocity. Often, a bipolar pair as shown in Figure 4.6 will be used, and the velocity can be calculated from the measured phase because $\boldsymbol{M}_1$ is known. Experimentally, this is often done by acquiring the image twice with two values of $\boldsymbol{M}_1$, and a velocity is calculated from the difference in phase. The component of the velocity in the direction of the applied gradients is encoded for, and a full velocity vector can be measured by repeating the experiment with velocity gradients applied in three orthogonal directions. Figure 4.7 shows a phase-shift velocity image of parabolic flow in a pipe and a comparison to the analytical velocity distribution; the measurement technique is seen to be highly quantitative.

It should be noted that velocity-induced phase can also cause image artefacts that are undesirable. A detailed discussion of these is beyond the scope of this chapter, but one approach to mitigate against artefacts is to 'velocity compensate' the gradient waveforms such that $\boldsymbol{M}_1$ is zero. Several practical methods are well described by Pope and Yao (1993).

4.3.2.3 Diffusion

A very similar experimental approach to phase-shift velocity imaging can be used to measure local diffusion coefficients. A bipolar pair of gradients similar to those shown

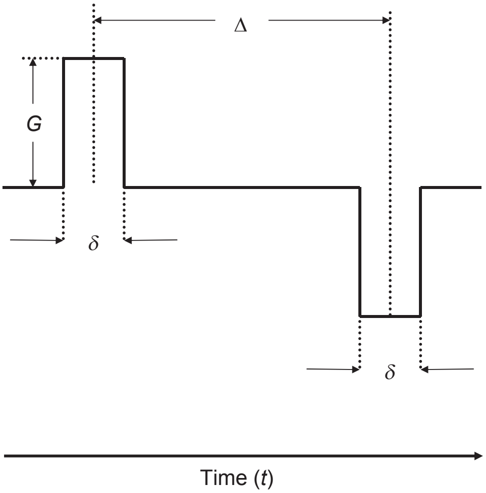

Figure 4.6 A bipolar gradient pulse sequence that has no zero moment with time but a nonzero first moment.

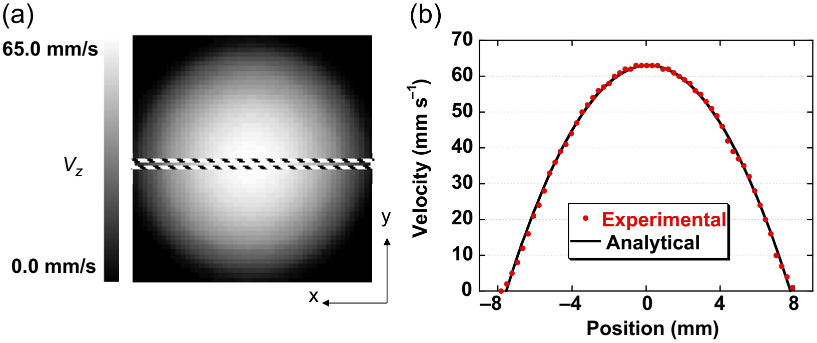

Figure 4.7 Example of a phase-shift velocity image. (a) Transverse slice where the intensity is proportional to the signal phase and, therefore, to the velocity. (b) Comparison of a slice extracted from (a) with the analytical result for laminar flow in a pipe.

in Figure 4.6 is again used, but instead of imparting a phase shift, diffusion will reduce, or attenuate, the signal. The diffusion coefficient can be calculated from this attenuation and where coherent flows are also present; the velocity can also be calculated from the phase shift as described above.

4.4 Basic imaging techniques

There are a great variety of possible imaging techniques that are used and that can be designed according to the type of information that is required in the image (concentration, velocity, diffusion, T_1, etc.). To obtain an image, it is sufficient to acquire all points on the $\boldsymbol{k}$-space raster followed by Fourier transformation. The user can then build up the sequence to add contrast, such as including a velocity weighting gradient (nonzero $\boldsymbol{M}_1$) to obtain velocity information. In this section, we show some of the basic sequences and how they can be extended to include velocity information.

4.4.1 Gradient echo and spin echo imaging sequences

Most imaging sequences can broadly be described as either gradient echo or spin echo sequences. In gradient echo sequences, the spins are refocused by the gradient alone; an example is shown in Figure 4.8(a). This is very similar to the sequence shown in Figure 4.2, which is also a gradient echo sequence but has the addition of a slice-selective excitation pulse. In this sequence, the spins are de-phased (due to different locations in the applied gradient) when the negative gradient is applied and will then start to rephrase when the gradient polarity is switched. When the total gradient time integral is zero, $\boldsymbol{k} = 0$ (Eqn (4.8)), the spins will be refocused, and a 'gradient echo' is formed. Throughout this time, de-phasing of the spins will also occur due to T_2^* such that the acquired points will be T_2^* weighted. As described previously, one direction of $\boldsymbol{k}$-space is acquired in the frequency encode direction with the gradient on during signal detection, whilst the other is acquired in the phase direction with a gradient applied before acquisition.

An alternative to the gradient echo sequence is the spin echo sequence shown in Figure 4.8(b). In this case, a 180° refocusing pulse is inserted at time, τ, so that de-phasing due to magnetic field inhomogeneities, T_2', is refocused at 2τ, and a spin echo is formed; the signal at this point is T_2 weighted. Another difference is the polarity of the de-phasing gradient; the 180° refocusing pulse inverts the phase of the spins and, therefore, the effective polarity of the gradient. In this case, the de-phasing gradient must have the same polarity as the re-phasing gradient because they are separated by the 180° refocusing pulse. Although this is termed a spin echo experiment, two echoes are formed — the spin echo at 2τ and the gradient echo at $\boldsymbol{k} = 0$ — and these

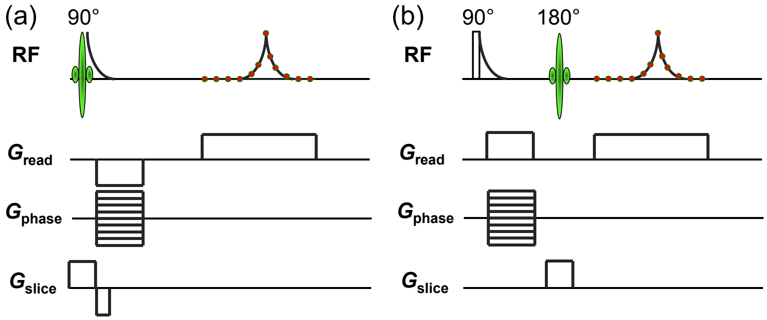

Figure 4.8 Schematic of a simple, slice selective, 2D (a) gradient echo and (b) spin echo pulse sequence.

are usually chosen to coincide. In this sequence, the data will be T_2 weighted, compared to T_2^* for the gradient echo sequence. In engineering samples with several material boundaries, T_2 can be much greater than T_2^*, so a spin echo sequence will be used for quantitative images with minimal contrast in them. Whereas, a gradient echo sequence may be used to highlight heterogeneities in the sample.

4.4.2 Signal relaxation measurement

All MRI images will have some relaxation weighting — signal loss from the effects of relaxation — which will change the image intensity. The most important of these in the spin echo sequence is due to T_2, and the signal will decay according to Eqn (4.14), where t is the time between excitation and data acquisition. Here M_{xy} is the measured signal intensity, and M_0 is proportional to the absolute material density. Any signal loss can be minimised by making $\frac{t}{T_2} \ll 1$ such that $M_{xy} \simeq M_0$, but this may not be possible in some situations where T_2 is particularly small. In such systems, a series of images can be acquired with increasing values of t and then the pixel measured intensities, M_{xy}, fitted to Eqn (4.14) with M_0 and T_2 as fitted parameters. The final image of material concentration or spin density is proportional to M_0, whilst the image of T_2 contains information on local molecular mobility (Chen, Hughes, Gladden, & Mantle, 2010).

4.4.3 Velocity imaging

To obtain a quantitative phase-shift velocity image, it is necessary to acquire all points in $\boldsymbol{k}$-space as described in the previous section but also to add a gradient waveform that has a nonzero $\boldsymbol{M}_1$, such as that shown in Figure 4.6. An example of a simple velocity imaging sequence is shown in Figure 4.9. This is a spin echo imaging sequence with the addition of a velocity encoding pair of gradients, similar to the bipolar pair shown in Figure 4.6. But now, both have the same polarity because they are separated by the 180° refocusing pulse. The phase of the signal from this sequence will be proportional to the local velocity and the experimental parameter $\boldsymbol{M}_1$. Although the velocity can, in theory, be calculated directly from the phase in the image, it is much more usual to acquire two images with an increment in $\boldsymbol{M}_1$ and use the increment in measured phase to calculate the velocity. The example in Figure 4.9 illustrates how a velocity encoding pair of gradients can be added to a standard imaging sequence, and this method can be used more generally in much more complicated imaging sequences where adding velocity encoding gradients enables velocity measurements to be made.

4.5 Fast imaging approaches

Acquiring images using the simple methodologies described previously will typically take several minutes or longer to acquire, but we are often interested in imaging systems that change over timescales shorter than that. There are a number of families of fast imaging techniques, and this section will introduce the most important of these.

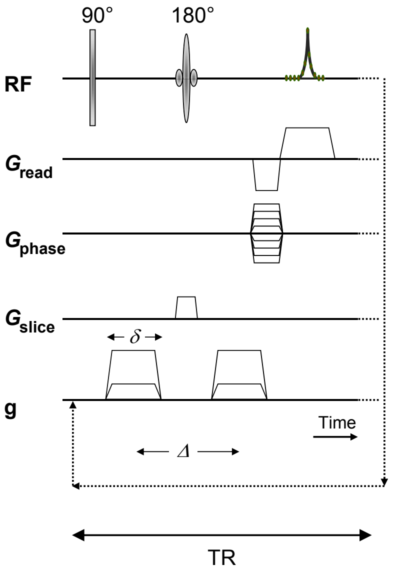

Figure 4.9 A schematic of a simple velocity imaging pulse sequence.

All of these methods aim to acquire the same points in $\boldsymbol{k}$-space that were being acquired in Section 2.4 but to utilise the magnetisation in a more efficient way to maximise the temporal resolution of the images. The goal is fast or ultra-fast imaging to acquire the entire 2D $\boldsymbol{k}$-space raster from a single excitation. Echo planar imaging (EPI) and rapid acquisition with relaxation enhancement (RARE) are two such methods and will be discussed further, as will fast low-angle shot imaging (FLASH), which still uses multiple excitations but with a very short time between excitations. The chapter will also briefly discuss the use of sparse sampling methods in which the $\boldsymbol{k}$-space raster is undersampled and innovative image reconstruction techniques are used.

4.5.1 Full k-space fast sampling

4.5.1.1 Echo planar techniques

The fastest possible imaging techniques are echo planar or EPI-based schemes that were proposed by Mansfield (1977), who realised that the complete 2D $\boldsymbol{k}$-space raster could be acquired following a single excitation pulse. After an initial line in $\boldsymbol{k}$-space has been acquired in the presence of a read gradient, the gradient polarity is switched at the same time as a blip in the phase direction is applied. With successive phase blips, the whole of 2D $\boldsymbol{k}$-space is traversed. There are many variations of the EPI technique, and one is shown in Figure 4.10. In the EPI sequence, the digitiser is kept open for the entire image acquisition and is, therefore, a very efficient method for fast imaging with images often acquired in 5−50 m. Since there are no 180° refocusing pulses during the acquisition, the signal decays with T_2^* during this period, making this method

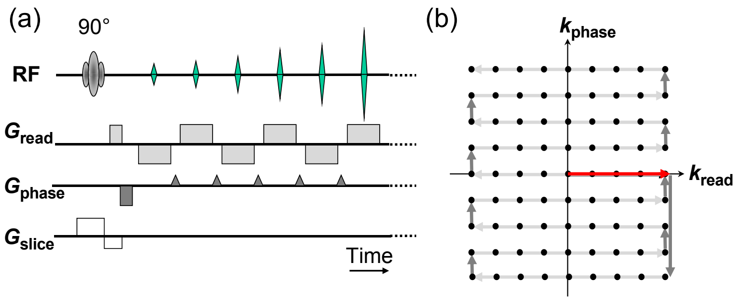

Figure 4.10 EPI (a) slice selective pulse sequence and (b) corresponding ***k***-space raster. Although the two dimensions have been designated as read and phase here, they are sometimes both considered as read directions and referred to as the first and second read directions.

unsuitable when the sample has a short T_2^* as is the case for many engineering systems. Despite this, the spiral variant that has very short acquisition times has been successfully used for rapid velocity imaging in two-phase flows (Tayler, Holland, Sederman, & Gladden, 2012b).

4.5.1.2 RARE

Like EPI, the RARE technique (Hennig, Nauerth, & Friedburg, 1986) can acquire a whole 2D image from a single excitation. Unlike EPI, there is a 180° refocusing pulse used between each line of ***k***-space to form successive spin echoes. The pulse sequence is shown in Figure 4.11. This pulse sequence is much more robust to local field heterogeneities as the magnetisation is continually refocused, so the signal decays with T_2 rather than T_2^*. Although slightly longer than EPI techniques because of the time required for the 180° refocusing pulse between lines of ***k***-space, this is a more robust technique and well suited to engineering samples where fluid velocities are low. Imaging times for 64 × 64 acquired points are likely to be 100−200 m.

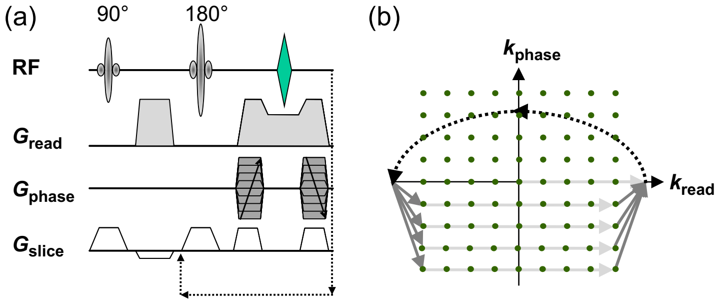

Figure 4.11 RARE (a) schematic of the pulse sequence with (b) ***k***-space raster.

4.5.1.3 FLASH

Haase, Frahm, Matthaei, Hanicke, and Merboldt (1986) have shown how a fast 2D image may be acquired using the simple gradient echo imaging sequence shown in Figure 4.8(a). In this imaging sequence, a single line of $\boldsymbol{k}$-space is acquired after each excitation. But in the FLASH implementation, the repetition (recycle) time between excitations is reduced to a few ms, and an excitation angle much below 90° is used. At this rate, a 64 × 64 image would take 192 ms to acquire. Because of the small excitation angle, sometimes only a few degrees, FLASH uses only a small amount of the longitudinal magnetisation, and SNR is lower than either EPI or RARE. Despite the low SNR of this technique, it is very robust to image artefacts, and thus, it provides a very useful tool, particularly for low-resolution imaging where SNR is less likely to be a problem.

4.5.2 Sparse and nonlinear sampling

Acquiring all points on the k-space raster is time-consuming and may be unnecessary when there is only a limited amount of data in the reconstructed image. If the $\boldsymbol{k}$-space data can be undersampled, faster imaging techniques can be developed and employed, but from Nyquist sampling theorem, we then expect that linear recovery methods will lead to image artefacts and a lossy recovery. It is important to note, however, that not all of the Fourier coefficients are equally important for the reconstruction of the image, and several methods have been suggested as ways to reconstruct images from undersampled data. The most successful and promising of these is compressed sensing, which is briefly discussed below, though more details can be found in Holland and Gladden (in press) and references within. Note that compressed sensing has been found to be useful in many areas of image reconstruction including electrical tomography, radio-astronomy, electron micro-tomography and X-ray tomography.

4.5.2.1 Compressed sensing

Compressed sensing (Candes et al., 2006; Donoho, 2006; Lustig, Donoho, & Pauly, 2007) has recently attracted much interest in image reconstruction and MRI in particular. This reconstruction method utilises the sparsity of the reconstructed image and can produce good reconstructions from significantly undersampled $\boldsymbol{k}$-space data. An image is said to be sparse if it can be accurately represented by fewer points in some transform domain of the image, such as a wavelet or Fourier transform. Lustig et al. (2007) showed that the sparsity of MR images in a transform domain could be exploited. Many natural images exhibit sparsity in terms of their Fourier or wavelet coefficients or in terms of discrete gradients. In the same way that photographs can be compressed significantly with minimal loss of information, for example, with JPEG compression, so can many MR images.

Since MR images are compressible, compressed sensing theory (Candes et al., 2006; Donoho, 2006) suggests that taking fewer acquisition samples (undersampling), combined with prior knowledge that the image is sparse in some transform domain, may allow for an accurate image reconstruction. This is achieved using a nonlinear reconstruction method based on optimising a convex function involving l_1-norms, more details of which can be found elsewhere (Donoho, 2006; Lustig et al., 2007).

When implementing compressed sensing, we must choose which points that we are going to sample. Compressed sensing requires that undersampling causes incoherent artefacts, so pseudo-random sampling schemes or radial/spiral sampling schemes are often used.

The principle of the compressed sensing reconstruction is to transform the image into the sparse domain and then, by optimisation, maximise the sparsity (minimise the number of nonzero points) of this sparse domain data whilst ensuring the image retains fidelity with the acquired data. Thus, if an image that we wish to reconstruct is represented as a stacked vector $\mathbf{x}$, Ψ is the operator that transforms the image to a sparse representation (e.g. the wavelet transform), F is the Fourier transform mapping the image to $\boldsymbol{k}$-space and $\mathbf{y}$ is a vector containing all the (undersampled) measured $\boldsymbol{k}$-space data. The reconstruction is then obtained by solving the following constrained optimisation problem:

$$\begin{aligned} &\min \|\Psi \mathbf{x}\|_1 \\ &\text{subject to } \|F\mathbf{x} - \mathbf{y}\|_2 \leq \in \end{aligned} \tag{4.20}$$

where $\in$ is a threshold that can be set based on the expected noise level in the data. The l_1-norm,

$$\|x\|_1 = \Sigma_i |x_i| \tag{4.21}$$

acts as a proxy for sparsity — that is the minimisation produces an image that has, in the transform domain, the sparsest representation subject to remaining consistent with the acquired data. There are a variety of methods used to solve the optimisation (Eqn (4.20)). The amount of data sampled is typically reduced by a factor of 2—10 without significant reduction in the quality of the image. A real strength of compressed sensing is that it can be combined with most MRI techniques including the ultrafast single-shot imaging described previously, reducing 2D imaging times to just a few milliseconds with 3D images being acquired in 30—50 m. An example of such use in engineering applications is shown later in the chapter.

4.5.3 Practicalities and limitations

In principle, MR techniques have many advantages; however, there are a number of practical limitations that must be considered when choosing such a methodology. Advantages of MR include the following:

- The measurement is quantitative. Following calibration, we know exactly how much of each chemical species is present.

- The measurement can be made sensitive to a large range of different physical parameters, which can then be measured or used to provide image contrast. These include velocity, diffusion, molecular mobility (via relaxation) and chemical shift.
- 2D slice images via slice selection or fully resolved 3D images can be acquired.
- It is a noninvasive measurement with no need for tracers.
- It uses low-power, non-ionising radiation.

Despite these many advantages, it is not a widely used technique in industrial settings for which there may be a number of reasons as detailed below.

Complexity of measurement: The large range of parameters MR can be sensitive to and the countless number of pulse sequences means this is a complex technique to fully understand. Although MR is used in some push-button applications, it often requires skilled operators to fully utilise the technique.

Cost of equipment: Although a number of permanent magnet systems are now available in the price range £30,000−100,000, high-field superconducting magnets that are used for high-resolution imaging are typically an order of magnitude more expensive (£300,000−£1,000,000).

Sample environment and material restriction: All samples must be placed in a strong magnetic field, which means ferromagnetic materials cannot be used. In addition, the spin manipulation and detection are done with electromagnetic radiation, usually in the RF range, and samples must be transparent to these frequency electromagnetic waves. In practice, this means that whilst stainless steel or other nonferromagnetic metals can be used in the strong magnetic fields, the sample itself usually cannot as it will be invisible to the electromagnetic radiation. Although single-sided magnets, which allow unrestricted access from one direction, are available, most sample environments will have a significant geometric restriction such as a maximum sample diameter that can be passed through the bore of the magnet.

SNR and resolution: There are many things that will affect the resolution and SNR of the image, but typical spatial resolutions may go up to a few tens of microns and 2D images may be acquired in as little as 5 ms. However, there is usually a trade-off between time resolution, spatial resolution and SNR.

4.6 Applications in engineering

There are a great number of applications of MR in engineering, and this chapter does not attempt to review them all here. Instead, three recent examples are given of the application to gas−liquid bubbly flows, and the interested reader may wish to consult more extensive reviews (Fukushima, 1999; Mantle & Sederman, 2003).

Gas−liquid bubbly flows pose a significant problem to many measurement techniques, and MRI is no exception. They are highly dynamic both in geometry and velocity with many moving phase boundaries.

4.6.1 Non-spatially resolved measurement

Although this chapter has been about the imaging aspects of MR techniques, useful information can often be acquired from an acquisition that does produce a full image.

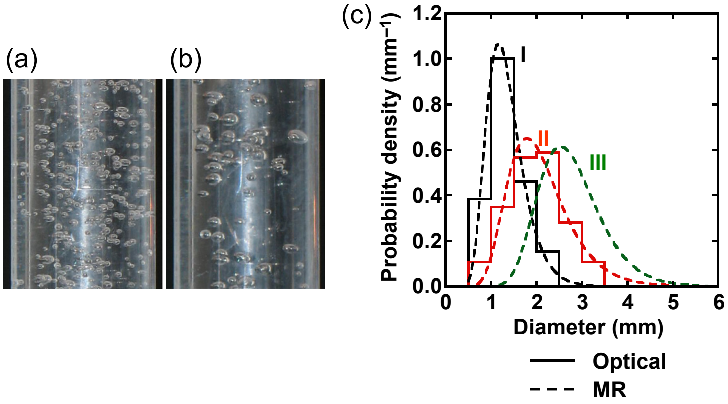

Figure 4.12 Photographs of a swarm of gas bubbles obtained using (a) distributor 1 and (b) distributor 2. The gas flow rate was 100 ml min^{-1}, giving a total voidage of 2% in each case. Note the larger bubble size obtained from distributor 2. (c) Comparison of the size distribution obtained in these systems using distributor 1 (black) and distributor 2 (red) from both the optical (solid lines) and MR (dashed lines) techniques. At a gas velocity of 1000 ml min^{-1} using distributor 2 (dotted line), the gas voidage was 15%, and the optical technique could not be used. Adapted and reproduced with permission from Holland et al. (2011).

MR methods using gradients are routinely used in industrial applications such as emulsion droplet sizing and oil well logging. Recently, Holland et al. (2011) have developed a method of directly analysing the acquired data with Bayesian statistics to extract bubble sizes and rock core grain sizes. The hardware requirements for this measurement are much simpler than for many imaging applications, and this technique has been demonstrated both on a low-field permanent magnet system and even a system using the earth's magnetic field. Figure 4.12 shows how this technique has been applied to gas—liquid bubbly flows in a vertical column. Despite this being a highly dynamic system, the Bayesian analysis can be used to extract a probability distribution of the bubble size, and the distribution is seen to alter as the gas distributor is changed or the gas flow rate is changed.

4.6.2 MRI and time-of-flight

Sederman and Gladden (2001) used a variant of the RARE imaging sequence to investigate bubbly flows in ceramic monoliths. In this system, there are three phases making field heterogeneities worse, and the use of a spin echo technique necessary. In the channels, the bubble velocities are reduced to a single direction — parallel to the monolith channels. In this application, the position of the bubbles in the monolith are imaged, and by repeated image acquisition, all from the same excitation pulse, the bubbles can be tracked. So, bubble velocities are recorded. This can, therefore, be used as a time-of-flight velocity imaging technique. Two images from a single excitation are shown in Figure 4.13 where each image was acquired in 160 ms.

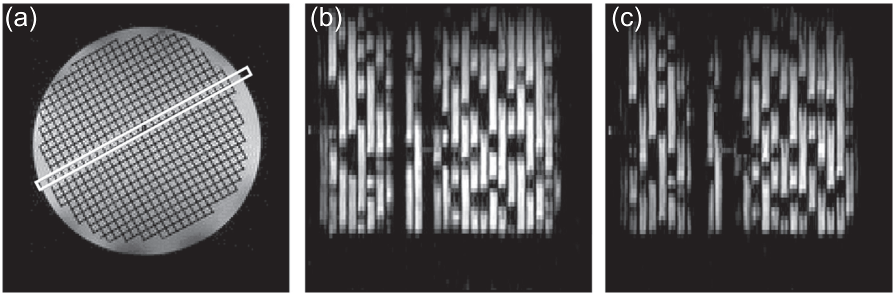

Figure 4.13 MRI of two-phase flow within a ceramic monolith. A cross-sectional *xy* image of the fully water-saturated monolith (a) shows the internal structure of the monolith; each channel has a side length of 1.2 mm. The highlighted region shows the position of the image slice in the *xz* direction for which the visualisations of gas—liquid distribution during two-phase flow is shown in (b) and (c). Data acquisition time for each image was 160 ms; there was a time period of 160 ms between the start of acquisition of each of the images shown in (b) and (c). In all images, the presence of water is indicated by high intensity (white); gas and ceramic are identified by zero intensity (black).
Reproduced with permission from Mantle and Sederman (2003).

4.6.3 Phase-shift velocity imaging

Phase-shift velocity imaging techniques, when allied to an EPI-based sequence, are probably the fastest method of MR velocimetry, with 2D images being acquired in under 5 ms and a frame rate of 188 frames per second. The spiral EPI-based technique has been applied to turbulent flow in pipes and has also been successfully applied to a single gas bubble (Tayler et al., 2012b) and to gas—liquid bubbly flows (Tayler, Holland, Sederman, & Gladden, 2012a). Quantitative velocity images of gas—liquid distributions during bubbly flow and velocity images of the liquid phase are shown in Figure 4.14. The high-resolution image of liquid velocities around a single bubble in Figure 4.14(a) shows three orthogonal velocity components, and each image was acquired in 5 ms using sparse sampling. The compressed sensing reconstruction technique was then used to reconstruct each velocity component, and the three velocity component images were combined to show a full description of the local liquid velocity.

4.7 Conclusions

MRI is an extremely powerful tomography technique that is capable of noninvasively and quantitatively measuring many parameters including flow, chemical composition and concentration within an image. These benefits have made it ubiquitous in the medical field as a diagnostic tool, but they also make it particularly useful as a research tool in engineering and the physical sciences. Despite this, its use has been restricted due to the costs and complexity required to make full use of its capabilities. It is routinely used in some industries such as oil well characterisation where a subset of measurements is made on more restricted hardware.

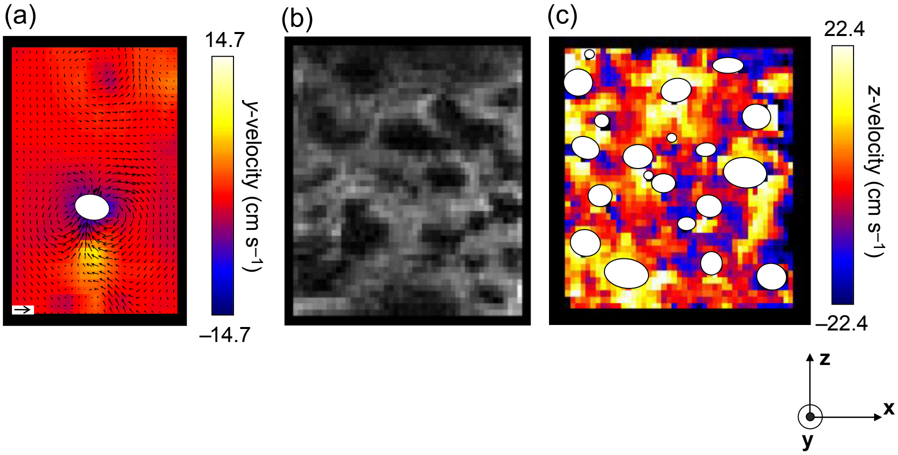

Figure 4.14 (a) Longitudinal image of three orthogonal liquid velocity components for a single bubble rising through water. The vector scale bar on the image corresponds to 15 cm s^{-1}, and the three components of the velocity were acquired in a total of 15.9 ms. The approximate location of the bubble is highlighted by the filled white ellipses. Longitudinal (b) magnitude image and (c) velocity image of gas–liquid bubbly flow at a voidage of 28.3%.
Adapted and reproduced with permission from Tayler et al. (2012a,b).

By understanding the physics underpinning MRI, the user can begin to identify how it can be used and find suitable applications. This chapter aims to provide such a basic understanding of the MRI method and what techniques can be used to speed up acquisition. With this knowledge, the reader can better identify where MRI may provide useful data.

4.7.1 Future trends

There are a number of very exciting developments in MR and data analysis that are set to make MR methods more widely used in engineering applications. High-field MRI with superconducting magnets is likely to remain predominantly in the research environment due to the significant costs and user expertise required to make developments. But with new data analysis techniques such as compressed sensing and probabilistic information extraction methods, new time scales and length scales can now be accessed with MRI. This will expand the range of applications that can be investigated. In particular, with imaging timescales of a few milliseconds, many more multiphase transient processes can be explored.

There are also exciting developments in permanent magnets and low-field MR. Permanent magnets offer MR at significantly lower capital costs and are virtually maintenance-free, so they can be placed where no cryogens or other services are available. They can also be designed with virtually no external magnetic field, and therefore, they can be placed on site without safety concerns. Whilst these systems will not have the full capability of high-field systems, they can be designed to do specific experiments with minimal user input making them useful as monitoring equipment. It is, therefore, likely that we will see a number of new devices come into the engineering workplace that are all optimised to specific applications.

4.8 Sources of further information and advice

There are a number of excellent books on both the theory of MRI and its application in the engineering and physical sciences. Some further texts for the interested reader are the following: Bluemich (2003), Callaghan (1991), Callaghan (2011), Haacke (1999), Levitt (2002).

References

Abragam, A. (1961). *Principles of nuclear magnetism*. Oxford: Oxford University Press.

Bluemich, B. (2003). *NMR imaging of materials*. Clarendon Press.

Callaghan, P. T. (1991). *Principles of nuclear magnetic resonance microscopy*. New York: Oxford University Press.

Callaghan, P. T. (2011). *Translational dynamics and magnetic resonance*. New York: Oxford University Press.

Candes, E. J., Romberg, J. K., & Tao, T. (2006). Stable signal recovery from incomplete and inaccurate measurements. *Communications on Pure and Applied Mathematics, 59*(8), 1207−1223.

Chen, Y. Y., Hughes, L. P., Gladden, L. F., & Mantle, M. D. (2010). Quantitative ultra-fast MRI of HPMC swelling and dissolution. *Journal of Pharmaceutical Sciences, 99*(8), 3462−3472.

Donoho, D. L. (2006). Compressed sensing. *IEEE Transactions on Information Theory, 52*(4), 1289−1306.

Elkins, C. J., & Alley, M. T. (2007). Magnetic resonance velocimetry: applications of magnetic resonance imaging in the measurement of fluid motion. *Experiments in Fluids, 43*(6), 823−858.

Fukushima, E. (1999). Nuclear magnetic resonance as a tool to study flow. *Annual Review of Fluid Mechanics, 31*, 95−123.

Haacke, E. M. (1999). *Magnetic resonance imaging: Physical principles and sequence design*. John Wiley and Sons.

Haase, A., Frahm, J., Matthaei, D., Hanicke, W., & Merboldt, K. D. (1986). Flash imaging - rapid NMR imaging using low flip-angle pulses. *Journal of Magnetic Resonance, 67*(2), 258−266.

Hennig, J., Nauerth, A., & Friedburg, H. (1986). Rare imaging - a fast imaging method for clinical MR. *Magnetic Resonance in Medicine, 3*(6), 823−833.

Holland, D. J., Blake, A., Tayler, A. B., Sederman, A. J., & Gladden, L. F. (2011). A Bayesian approach to characterising multi-phase flows using magnetic resonance: application to bubble flows. *Journal of Magnetic Resonance, 209*(1), 83−87.

Holland, D. J., & Gladden, L. F. (2014). Less is more: how ‘compressed sensing’ is transforming metrology in chemistry. *Angewandte Chemie, 53*(49), 13330−13340. http://dx.doi.org/10.1002/anie.201400535.

Levitt, M. H. (2002). *Spin dynamics*. England: John Wiley and Sons, Ltd.

Lustig, M., Donoho, D., & Pauly, J. M. (2007). Sparse MRI: the application of compressed sensing for rapid MR imaging. *Magnetic Resonance in Medicine, 58*(6), 1182−1195.

Mansfield, P. (1977). Multi-planar image-formation using NMR spin echoes. *Journal of Physics C, 10*(3), L55−L58.

Mansfield, P., & Grannell, P. K. (1973). NMR diffraction in solids. *Journal of Physics C, 6*, L422−L426.

Mantle, M. D., & Sederman, A. J. (2003). Dynamic MRI in chemical process and reaction engineering. *Progress in Nuclear Magnetic Resonance Spectroscopy, 43*(1−2), 3−60.

Pope, J. M., & Yao, S. (1993). Quantitative NMR imaging of flow. *Concepts in Magnetic Resonance, 5*, 281−302.

Sederman, A. J., & Gladden, L. F. (2001). Magnetic resonance visualisation of single- and two-phase flow in porous media. *Magnetic Resonance Imaging, 19*(3−4), 339−343.

Sodickson, A., & Cory, D. G. (1998). A generalized k-space formalism for treating the spatial aspects of a variety of NMR experiments. *Progress in Nuclear Magnetic Resonance Spectroscopy, 33*, 77−108.

Tayler, A. B., Holland, D. J., Sederman, A. J., & Gladden, L. F. (2012a). Applications of ultra-fast MRI to high voidage bubbly flow: measurement of bubble size distributions, interfacial area and hydrodynamics. *Chemical Engineering Science, 71*, 468−483.

Tayler, A. B., Holland, D. J., Sederman, A. J., & Gladden, L. F. (2012b). Exploring the origins of turbulence in multiphase flow using compressed sensing MRI. *Physical Review Letters, 108*(26), 264505.

This page intentionally left blank

Chemical species tomography

5

H. McCann[1], *P. Wright*[2], *K. Daun*[3]
[1]University of Edinburgh, Edinburgh, Scotland, UK; [2]University of Manchester, Manchester UK; [3]University of Waterloo, Waterloo, Ontario, Canada

5.1 Introduction

It has been appreciated since at least 1980 (Santoro, Semerjian, Emmerman, & Goulard, 1981) that the principles of X-ray tomographic imaging can be readily adapted to the case where photon absorption or emission depends on the chemical species of the absorbing/emitting atom or molecule, opening up the possibility of resolving the distribution of a particular chemical species in gas phase. If many path-integrated measurements can be made through the measurement subject, images may subsequently be reconstructed showing the concentration distribution of the species of interest. Chemical species tomography (CST) has advanced gradually over the intervening period, stimulated not only by the needs of process engineers but also by technological advances in optoelectronics. The last 10–15 years have witnessed the most substantial advances in their application to process engineering problems, see e.g. York, McCann, & Ozanyan (2011).

In this chapter, we aim to describe the state-of-the-art in CST, where electronic or vibrational–rotational transitions of the target atomic or molecular species are used to achieve chemical specificity and steps are taken to eliminate the contribution of scattered photons to the path-integral measurements. Our focus is on absorption-based CST, although we present an example of emission (chemiluminescence)-based CST in Case Study 2 at the end of the chapter. Several other tomographic modalities offering some form of chemical specificity are considered to lie beyond the scope of this chapter. Radio-frequency CST, using transitions of nuclear spin alignment, is generally called magnetic resonance imaging and is described in Chapter 4. There has also been substantial development in optical CST for medical application, where the signal that is measured arises substantially from scattering within the subject, possibly in combination with spectral absorption, and the technique is generally called diffuse optical tomography (Gibson, Hebden, & Arridge, 2005). This technique is a *soft-field* modality, with image reconstruction issues akin to those discussed in Chapters 12 and 14. In this chapter, our focus is on applications of optical tomography to process engineering systems, in particular, gaseous flows. These systems often exhibit negligible contribution of scattered photons to the measured path-integrals, placing their study firmly in the *hard-field* category of tomography, as discussed in Chapter 13. Haisch has presented a recent review of optical tomography (Haisch, 2012), considering examples of both low-scattering (atmospheric monitoring) and high-scattering (medical imaging) applications.

Industrial Tomography. http://dx.doi.org/10.1016/B978-1-78242-118-4.00005-8
Copyright © 2015 Elsevier Ltd. All rights reserved.

Section 5.2 briefly describes the spectroscopic issues involved, ranging from fundamental absorption spectroscopy to the thermodynamic condition of the measured subject. Since practical implementations of these systems typically have small beam count (a few tens), Section 5.3 discusses in detail the related problems of image reconstruction, and Section 5.4 presents methods to optimize the beam arrangement. The potential for significant scattering in process engineering subjects means that its elimination from the measured signals is a primary objective, as discussed in Section 5.5, which also considers the crucial issue of optical access to the subject and the optoelectronic methods used to obtain appropriate measurements. Two case studies are presented in Section 5.6, followed by a discussion of future trends in Section 5.7.

5.2 Absorption spectroscopy for chemical species tomography

The fundamentals of molecular absorption spectroscopy are discussed at length in many textbooks, a good example being Banwell and McCash (1994). At its simplest, Figure 5.1 shows a schematic of the absorption of light incident of wave number η at intensity $I_{0,\eta}$ on a gaseous absorbing medium containing the target absorbing species at mole fraction χ_{abs}, where η has been chosen to correspond to a particular spectroscopic transition of the target species, yielding received light intensity $I_{\text{r},\eta}$. (Wave number, in vacuo wavelength λ, and frequency ν are related by $\eta = 1/\lambda_0 = \nu/c_0$, where c_0 is the speed of light in a vacuum.) For the case shown in Figure 5.1, neglecting attenuation by out-scattering or contributions due to blackbody emission or in-scattering,[1] the drop in intensity is governed by the Beer–Lambert law:

$$I_{\text{r},\eta} = I_{0,\eta} \exp\left\{ -\int_0^L k_\eta[\mathbf{r}(u)]\,\mathrm{d}u \right\} = I_{0,\eta} \exp(-\alpha_\eta) \tag{5.1}$$

where L (cm) is the path length through the medium, $\alpha_\eta = -\ln(I_{\text{r},\eta}/I_{0,\eta})$ is the spectral absorbance (or optical density)[2], $\mathbf{r}$ is the position vector corresponding to a parametric location u along the beam, and the spectral absorption coefficient k_η (cm^{-1}) is given by Liu, Zhou, Jeffries, and Hanson (2007):

$$k_\eta = P\,\chi_{\text{abs}} S(T)\phi(T,P,\eta) \tag{5.2}$$

---

[1] These assumptions are almost always reasonable for molecular gases, since absorption dominates scattering at the wavelengths used for CST, which are also much shorter than wavelengths important to blackbody emission.

[2] Spectral transmittance and spectral absorptance are often defined as the fractions of intensity transmitted through and absorbed by a gas layer, i.e. $\tau_\eta = I_{r,\eta}/I_{0,\eta}$ and $\alpha_\eta = 1 - I_{r,\eta}/I_{0,\eta}$, but the definition in Eqn (5.1) is more prevalent in the tunable diode laser absorption spectroscopy (TDLAS) community.

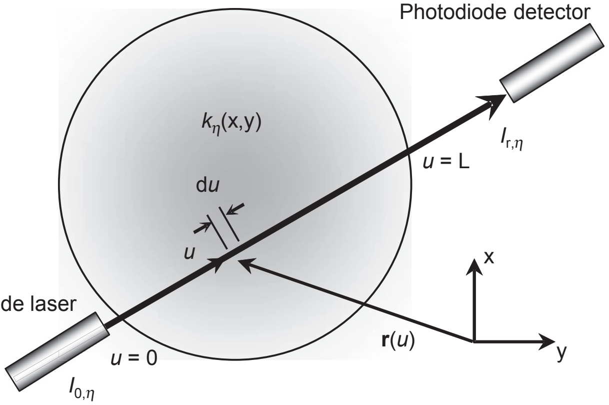

Figure 5.1 A schematic depicting the absorption of spectral intensity $I_{0,\eta}$ by an absorbing medium containing the target species.

where $S(T)$ ($\text{cm}^{-2}\cdot\ \text{atm}^{-1}$) is the absorption line strength of the chosen spectroscopic transition, $\phi(T,P,\eta)$ (cm) is its line shape function, and P (atm) and T (K) are the pressure and temperature of the absorbing medium, respectively. Figure 5.1 also indicates the use of a diode laser as the light source and a photodiode as the detector, which is a commonly used approach in gas sensing; the ability of diode lasers to be tuned across target absorption features gives rise to the technique's name, TDLAS, which is developed and practised by many groups (Liu et al., 2007; Sonnenfroh & Allen, 1997; Mihalcea, Baer, & Hanson, 1997; Bakowski et al., 2002; Fawcett, Parkes, Shallcross, & Orr-Ewing, 2002; Teichert, Fernholz, & Ebert, 2003; Duffin, McGettrick, Johnstone, Stewary, & Moodie, 2007; Kosterev et al., 2008). The path integral in the exponent in Eqn (5.1) is the key measurement obtained from a CST system to enable image reconstruction, and it is often termed the path concentration integral (PCI) in the literature, e.g. York et al. (2011), where temperature effects are neglected.

For most molecular species of engineering interest, the practically useful spectroscopies for TDLAS and CST lie in the following regions:

- Mid-infrared (MIR), with wave numbers in the range $4000 \leq \eta \leq 400\ \text{cm}^{-1}$ (i.e. $2500 \leq \lambda_0 \leq 25{,}000$ nm), typically corresponding to fundamental vibrational–rotational transitions, or
- Near-infrared (NIR), with wave numbers in the range $14{,}000 \leq \eta \leq 4000\ \text{cm}^{-1}$ (i.e. $700 < \lambda_0 < 2500$ nm), resulting from overtones and combinations of the fundamental transitions.

Rapid development of low-cost, robust light sources, detectors and fibres for the NIR region, driven by applications in telecommunications and consumer electronics, has resulted in technologies more amenable to engineering application than their MIR counterparts. Hence, the great majority of CST activity to date has been in the NIR, despite the fact that the transition line strengths are typically 1000 times larger in the MIR, as illustrated in Figure 5.2 for the case of carbon dioxide (CO_2) at a typical combustion exhaust temperature.

Databases of line strengths and broadening parameters, such as HITRAN (Rothman et al., 2009), are commonly used to identify candidate absorption lines for a particular species measurement, prior to experimental verification. As indicated by Eqn (5.2), the detailed shape of the absorption feature is a function of both temperature and pressure, which we illustrate here by continuing to focus on the case of small absorbing molecules. Within a given spectrum, for a chosen target species j, the line strength, $S_{i,j}$, of a particular molecular rotational–vibrational transition i varies with temperature according to Liu et al. (2007):

$$S_{i,j}(T) = S_{i,j}(T_0)\frac{Q_j(T_0)}{Q_j(T)}\left(\frac{T_0}{T}\right)\frac{1-\exp\left(-\frac{hc_o\eta_{ij}}{k_B T}\right)}{1-\exp\left(-\frac{hc_o\eta_{ij}}{k_B T_0}\right)}\exp\left[-\frac{hc_0 E''_{i,j}}{k_B}\left(\frac{1}{T}-\frac{1}{T_0}\right)\right] \tag{5.3}$$

where h is Planck's constant (J s), $\eta_{i,j}$ is the centre wave number of the transition i for species j, k_B is Boltzmann's constant (J/K), $Q_j(T)$ is the population partition function between the available initial states of the rotational–vibrational transition of the absorbing molecule j, E'' is the lower state energy (cm^{-1}) of the transition, and T_0 is a reference temperature.

Each transition line has a small natural line width, typically 10^{-5} cm^{-1}, associated with Heisenberg's uncertainty principle. This line width is increased through the influence of (a) broadening due to molecular collisions, yielding a Lorentzian line shape;

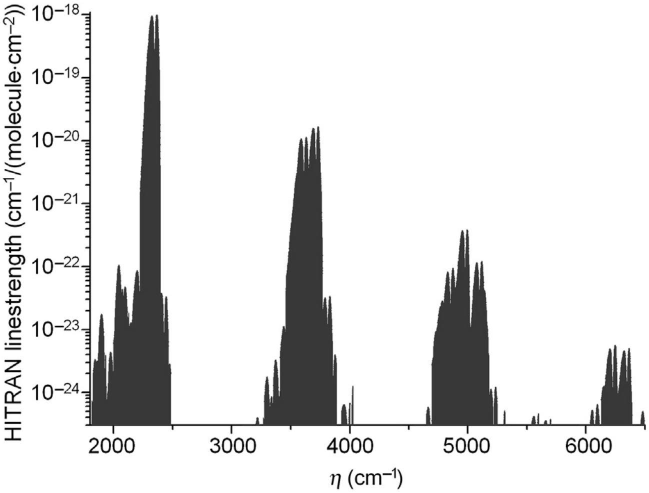

Figure 5.2 CO_2 line strengths at 800 K based on HITRAN 2008 (Rothman et al., 2009), using the directly related quantity 'intensity', as tabulated in HITRAN.

and (b) Doppler broadening, due to the random thermal motion of the molecules, yielding a Gaussian line shape. The convolution of these two effects results in a Voigt profile (Linne, 2002). Temperature dependence is harder to generalize as increasing temperature may either increase or decrease the population of the lower state, with a corresponding impact on the likelihood of absorption. For the case of water absorption spectroscopy, at around 1385 nm, the combined effects of temperature and pressure variation are illustrated in Figure 5.3.

At the atmospheric or elevated pressures found in the majority of engineering processes, the absorption at any given wavelength is likely to include contributions attributable to several absorption lines. This is evident in Figure 5.3, where a shoulder to the right of the 1385.12-nm feature at 1 atm reveals the presence of an additional line, unresolved in the higher pressure traces. As pressure and temperature then increase further, the two absorption features at shorter wavelengths begin to merge, whilst the highest-wavelength feature disappears altogether. Although the 1385.12-nm feature remains distinct at elevated pressures, which is desirable from a measurement perspective (Karagiannopoulos, Cheadle, Wright, & McCann, 2012), it clearly arises from more than one molecular state transition, resulting in a particularly complex variation of the spectral absorption coefficient with pressure, temperature and absorber concentration.

For CST imaging of a given target species in a measurement subject, several criteria can be identified for the selection of suitable absorption features for effective isolation

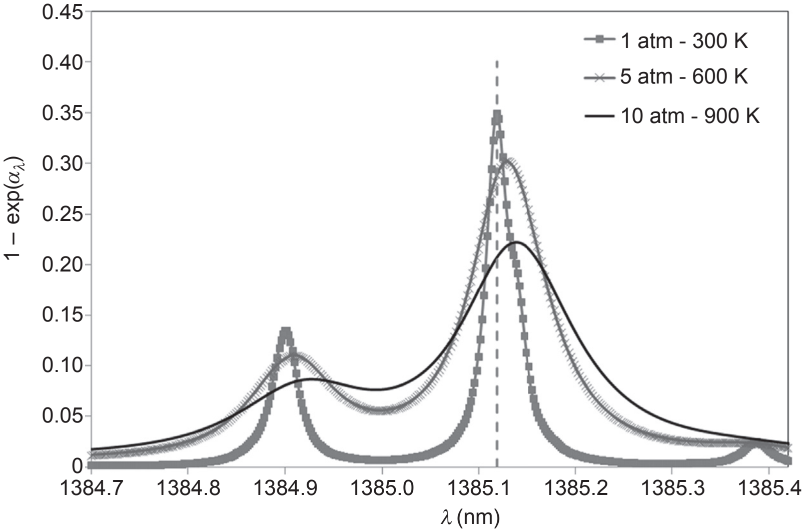

Figure 5.3 Simulated H_2O absorption spectra near a chosen laser wavelength (dashed line) at 1385.12 nm, for 10% mole fraction water vapour and 8-cm path length, at a series of temperatures and pressures relevant to automotive engine in-cylinder conditions (Karagiannopoulos et al., 2012).

of PCI data, but some of them are inevitably case dependent. In general, suitable absorption features should:

1. give rise to an appropriate range of measured transmittance values, enabling adequate sensitivity, even once the noise properties of the measurement system are considered;
2. be free from absorption by nontarget species; and
3. have well-characterized pressure and temperature variation that is consistent with measurement needs.

The line selection process typically requires considerable effort in spectroscopic modelling of both the target and interfering species, combined with experimental validation/calibration. Auxiliary measurements of the subject may be indispensable in a case where a criterion is unable to be met, e.g. in-cylinder pressure measurement during hydrocarbon fuel CST in the cylinder of an operating engine (Terzija et al., 2008; Wright et al., 2010). Temperature sensitivity may be non-monotonic and can necessitate sophisticated multiwavelength measurement, e.g. Karagiannopoulos et al. (2012), but also suggests the possibility of simultaneous temperature and concentration imaging.

Having identified a suitable absorption feature, an appropriate measurement method must be selected. If the feature is sufficiently broad and stable against varying thermodynamic conditions, it is attractive to carry out a simple direct absorption measurement at an essentially fixed wave number, typically the peak of the absorption curve. This direct absorption approach has been applied to the measurement of iso-octane (2,2,4-trimethylpentane, $(CH_3)_3CCH_2CH(CH_3)_2$), unleaded gasoline and propane (Terzija et al., 2008; Wright et al., 2010; Hindle et al., 2001). This work utilized an overtone band of the fundamental (2960 cm^{-1}) C—H stretch vibration. The spectrum of this fundamental absorption, itself relatively smooth due to the varied environment of each C—H bond within the molecule (Klingbeil, Jefferies, & Hanson, 2007), is further smoothed in the overtone band, yielding the broad, relatively unstructured absorption feature shown in Figure 5.4. Intensity modulation may be used within direct absorption schemes, to aid low-noise detection, but any associated wavelength modulation is incidental to the measurement. Scattering or other nonspecific attenuation effects can be accounted for in direct absorption schemes by making a simultaneous measurement at a nonresonant wavelength, using the so-called dual wavelength ratio (DWR) technique (Wright et al., 2010).

The situation is somewhat different when targeting species of low molecular weight, such as CO_2 or H_2O. Except at elevated pressures, the individual transitions within the absorption spectra of these molecules are often well resolved, as seen in Figure 5.3. Without the stabilising influence of many blended transitions, a direct absorption measurement may exhibit high sensitivity to changes in pressure and temperature, reflecting the properties of just a few underlying absorption lines. Similarly, it will show acute sensitivity to the exact wave number of the probe radiation, due to the sharpness of the absorption features. Direct absorption spectroscopy (DAS) exploits this to obtain additional information using a limited spectral scan,

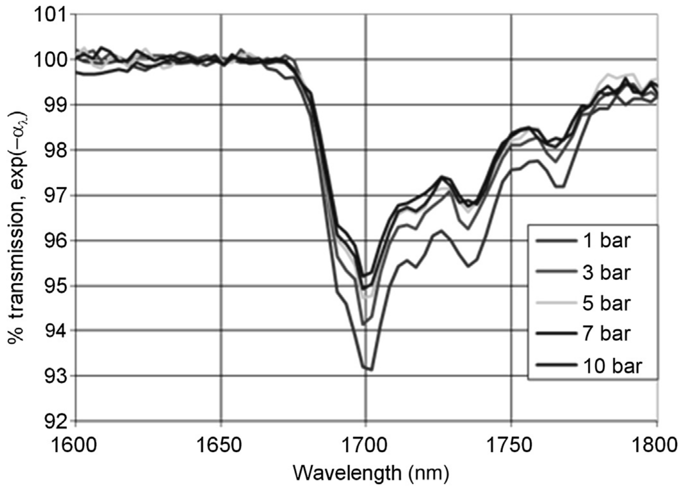

Figure 5.4 Measured transmission spectrum of iso-octane/air mixture at combustion stoichiometry (at 10 bar), for path length 85 mm.

but its sensitivity is limited by the need to detect small changes in a high baseline transmittance. Various techniques have been developed to enhance detection sensitivity. Typically, a small-amplitude, high-frequency (f) intensity *and* wave number modulation is superimposed on the relatively slow modulation used for spectral scanning, enabling baseline-free synchronous signal recovery at this frequency ($1f$) or its overtones ($2f$, $3f$, etc.). This process is illustrated schematically in Figure 5.5, and a full analytical treatment is provided in a series of papers by Kluczynski and co-workers (Kluczynski & Axner, 1999; Kluczynski, Gustafsson, Lindberg, & Axner, 2001; Kluczynskki, Lindberg, & Axner, 2001a; Kluczynski, Lindberg, & Axner, 2001b).

For the case of shallow high-frequency modulation:

- the $1f$ signal is sensitive principally to the *gradients* of the absorption feature and yields *zero* signal at its peak;
- the $2f$ signal approximates the second *derivative* of the shape of the absorption feature, resulting in a *maximum* signal at its peak.

A detailed discussion of these techniques is beyond the scope of this chapter, and the reader is directed to the TDLAS literature, particularly that regarding wavelength modulation spectroscopy (WMS). The implications of the spectroscopic measurement method adopted for the electronic implementation of a CST system are, however, discussed further in Section 5.5.3.

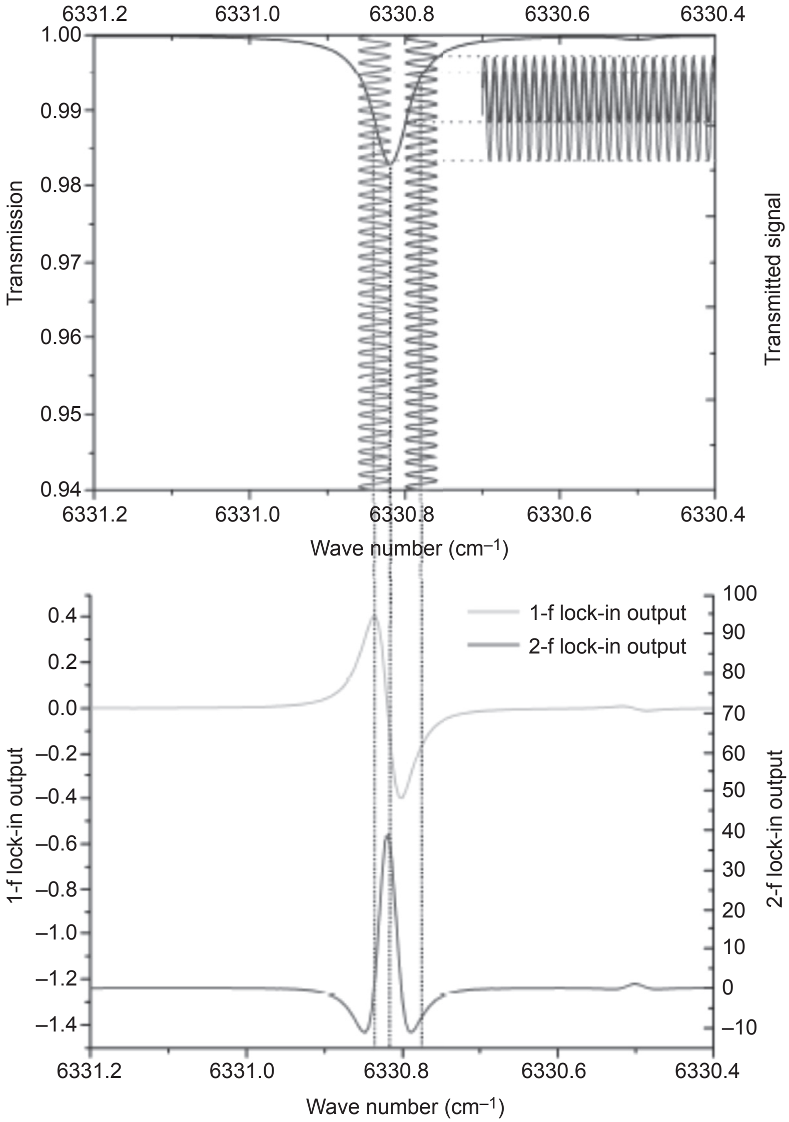

Figure 5.5 Schematic of wavelength modulation spectroscopy (WMS). The selected absorption feature is shown in the upper plot (ranging from about 6331.0 to 6330.6 wave numbers), with the effect of WM (at frequency *f*) illustrated at two points in the sweep through the plot: the absorption signal at the low η side is shown as the lighter sinusoid on the right, and the absorption signal at the high η side is shown as the darker sinusoid on the right. The resulting signals recovered from lock-in detection at *f* and 2*f* are indicated in the lower plot.

5.3 Image reconstruction for low beam-count systems

Chemical species tomography systems based on absorption spectroscopy are governed by Eqn (5.1), which can be rewritten as a Fredholm integral equation of the first kind (IFK):

$$b_i = b(s_i,\theta_i) = \alpha_{h,i} = \int_0^\infty k_\eta[\mathbf{r}_{(s_i,\theta_i)}(u)]\mathrm{d}u \tag{5.4}$$

where b_i is the absorbance of the ith beam and (s_i,θ_i) specify the position of the ith beam; s_i is the perpendicular distance between the beam and the origin, and θ_i is the angle formed between the beam and the y-axis. These quantities are shown in Figure 5.6. Deconvolving Eqn (5.4) is an *ill-posed* problem, since it does not satisfy all requirements for a *well-posed* problem, i.e. one that: (1) has a solution; (2) that is unique; and (3) that is stable to small perturbations in the input data (Hadamard, 1923). In the limiting case in which only one beam transects the tomography plane, the deconvolution problem clearly violates the second (uniqueness) criterion since an infinite set of candidate distributions f exist that, when substituted into the integral of Eqn (5.4), would explain the data.

This ambiguity is reduced by increasing the number of beams transecting the measurement subject. In the limiting case in which $b(s,\theta)$ is known as a continuous function over the domain $R_{s,\theta} = \{(s,\theta)|s \in (-R,R),\ \theta \in (0,\pi)\}$, the field variable can be reconstructed through an inverse Fourier transform via the Radon transform and the projection slice theorem (Bertero & Boccacci, 1998):

$$f(x,y) = \frac{1}{4\pi^2}\int_0^\pi \mathrm{d}\theta \int_{-\infty}^{\infty} b(\omega,\theta)|\omega|e^{i\omega(x\cos\theta + y\sin\theta)}\mathrm{d}\omega \tag{5.5}$$

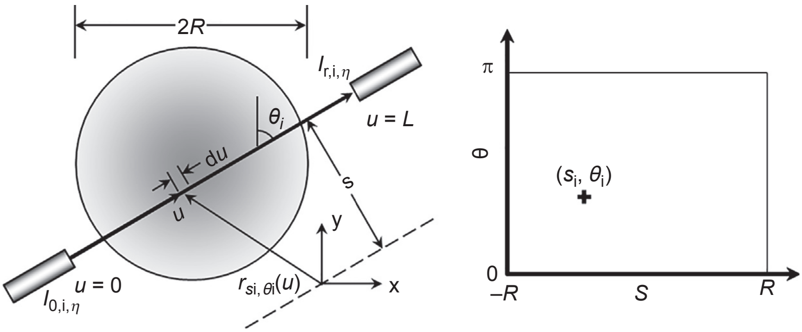

Figure 5.6 Each beam transecting the tomography space is identified by its (s,θ) coordinates in sinogram space.

where

$$b(\omega, \theta) = \int_{-\infty}^{\infty} b\left(s, \theta\right) e^{-i\omega s} \mathrm{d}s \tag{5.6}$$

In practice, however, $b(s,\theta)$ is not often known as a continuous function; instead, a related technique called *filtered back-projection* works on a discrete set $\{b_i\}$, usually sampled at uniformly spaced coordinates on $R_{(s,\theta)}$, as shown in Figure 5.7, and incorporates a filter that removes high-frequency components caused by the discrete data from the reconstruction. This algorithm is the mainstay of medical tomography scanners and was used extensively in early CST experiments (Santoro et al., 1981; Beiting, 1992).

The main drawback of Fourier transform-based reconstruction algorithms, in the context of CST, is that they require a dense and regular sampling of the projection data over $R_{(s,\theta)}$, which in turn demands a regular beam arrangement (parallel-beam or fan-beam arrangements). This presents several problems: first, in lab-scale

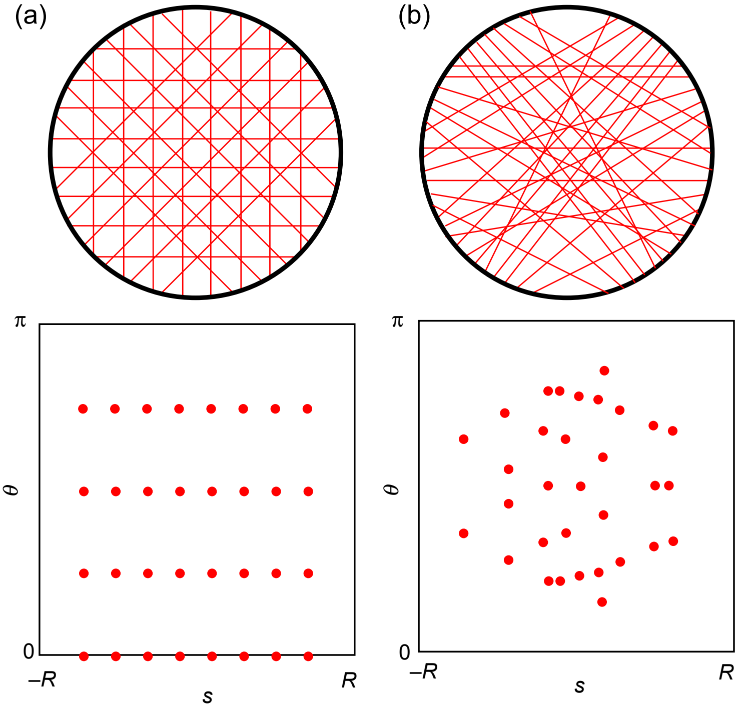

Figure 5.7 Beam arrangements and corresponding coordinates on $R_{(s,\theta)}$: (a) a regular beam arrangement suitable for a Fourier transform-based reconstruction; (b) an irregular beam array suitable for the algebraic reconstruction technique (ART).
Adapted from Terzija et al. (2008).

absorption spectroscopy tomography, uniform sampling of $R_{(s,\theta)}$ is usually obtained by traversing the optics through the flow field or vice versa. While this treatment only requires one sensor and detector, it disallows time-resolved tomographic reconstructions. Otherwise, the experimental apparatus needed to carry out a large number of simultaneous measurements at regular locations on the $s{-}\theta$ plane becomes extremely costly and complex. Moreover, CST experiments in the field (e.g. gas turbines (Ma et al., 2013) and internal combustion cylinders (Wright et al., 2010)) rarely permit the high degree of optical access needed to produce a dense or regular beam array.

For these reasons, an alternative approach called the *algebraic reconstruction technique* (ART) has gained favour among CST practitioners. In ART the tomography plane is discretized into a set of n pixels, and most often the species concentration is assumed to be uniform within each pixel. The integral in Eqn (5.4) is then approximated as a 'ray sum':

$$b_i = \sum_{j=1}^{n} A_{ij} x_j \tag{5.7}$$

where x_j is the species concentration in the jth pixel and A_{ij} is the chord length of the ith beam subtended by that pixel. Writing Eqn (5.7) for all m beams results in an $(m \times n)$ matrix equation, $\mathbf{Ax} = \mathbf{b}$, which, in principle, can be solved for the unknown concentration distribution in $\mathbf{x}$. The main advantage of ART versus Fourier transform-based reconstruction is that it does not require a regular sampling of $R_{(s,\theta)}$ space, as shown in Figure 5.7(b), thereby permitting much more flexibility in beam arrangements and numbers.

ART was originally conceived as a tool for electron and X-ray tomography (Gordon, Bender, & Herman, 1970). In these and many other types of *full data tomography* problems, the axial and angular projection dimensions are densely sampled and the resulting $\mathbf{A}$ matrix is full-rank but ill-conditioned; more generally, these types of inverse problems are *discrete ill-posed* (Hansen, 1999). In this scenario, small perturbations in the data are amplified into large variations in the recovered solution, violating the third (stability) criterion for well-posed problems. An ill-conditioned matrix can be diagnosed through a singular value decomposition, $\mathbf{A} = \mathbf{U}\Sigma\mathbf{V}^{\mathrm{T}}$, where $\mathbf{U} \in \Re^{m \times n}$ and $\mathbf{V} \in \Re^{n \times n}$ are orthonormal matrices and $\Sigma \in \Re^{(n \times n)}$ is a diagonal matrix containing the singular values arranged in decreasing order, $\{\sigma_1, \sigma_2, \sigma_3, \ldots, \sigma_n\}$. The orthonormality of U and V is then exploited to recover the solution:

$$\mathbf{x} = \sum_{j=1}^{n} \frac{\mathbf{u}_j^T \mathbf{b}}{\sigma_j} \mathbf{v}_j \tag{5.8}$$

An ill-conditioned $\mathbf{A}$ matrix has singular values that decay continuously over several orders of magnitude, as shown in Figure 5.8(a). In this scenario $\mathbf{x}$ can be found using Eqn (5.8) provided the 'exact' projection data are known, but in an experimental setting the data are invariably contaminated with measurement noise, in which case $\mathbf{b} = \mathbf{b}^{\text{exact}} + \boldsymbol{\delta}\mathbf{b}$, where $\mathbf{b}^{\text{exact}} = \mathbf{A}\mathbf{x}^{\text{exact}}$. (Even in the absence of

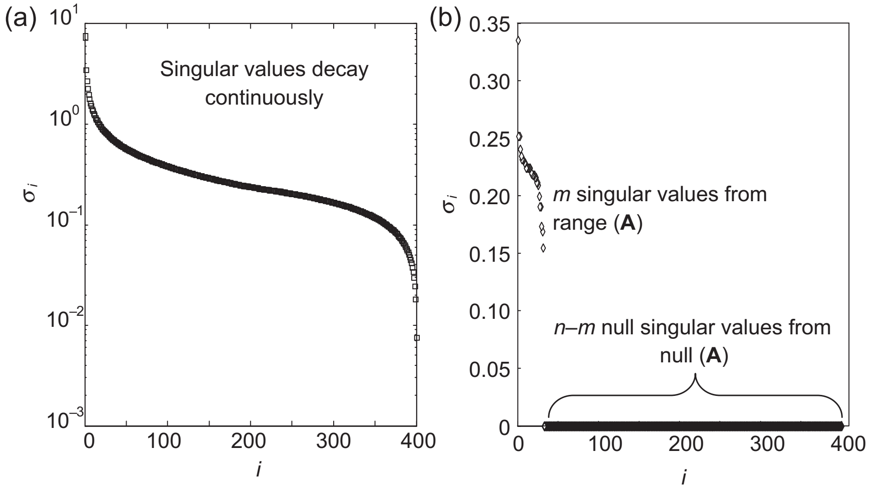

Figure 5.8 Singular values from: (a) a full-rank but discrete ill-posed problem (axisymmetric CST) that violates Hadamard's stability criterion; and (b) a rank-deficient problem (2D CST) that violates Hadamard's uniqueness criterion.

measurement noise there is a perturbation vector associated with the incompatibility of **b** due to discretization of the tomography domain.) Substituting into Eqn (5.8) results in

$$\mathbf{x} = \mathbf{x}^{\text{exact}} + \boldsymbol{\delta}\mathbf{x} = \sum_{j=1}^{n} \frac{\mathbf{u}_j^T \mathbf{b}^{\text{exact}}}{\sigma_j} \mathbf{v}_j + \sum_{j=1}^{n} \frac{\mathbf{u}_j^T \boldsymbol{\delta}\mathbf{b}}{\sigma_j} \mathbf{v}_j \tag{5.9}$$

Small singular values amplify the $\mathbf{u}_j^T \boldsymbol{\delta}\mathbf{b}$ terms, resulting in a large perturbation vector, $\boldsymbol{\delta}\mathbf{x}$, in the solution. In the original ART implementations, error amplification was suppressed through iterative regularization (Gordon, Bender, & Herman, 1970; Hansen, 1999). Axisymmetric deconvolution, a special one-dimensional case of CST, also involves the solution of an ill-conditioned matrix equation formed by discretizing Abel's integral equation, an IFK derived from the Beer–Lambert equation (Åkesson & Daun, 2008). In these problems noise amplification caused by small singular values can be suppressed through Abel three-point inversion (Dasch, 1992) or Tikhonov regularization (Åkesson & Daun, 2008; Tikhonov & Arsenin, 1977).

In the majority of multidimensional 'hard-field' CST experiments, however, the underlying tomography problem is not discrete ill-posed but rather *rank-deficient* because the number of pixels greatly exceeds the number of absorbance measurements; for example, in Wright et al. (2010), 27 (or fewer) laser beams transect a tomography domain discretized into 1844 elements, and the rank-nullity theorem states that Rank(**A**) $\leq m$. (Provided each beam path is unique, Rank(**A**) $= m$.) Indeed, carrying out a singular value decomposition on **A** reveals that the last

$n-m$ singular values in $\boldsymbol{\Sigma}$ are zero, and the set of solutions $\{\mathbf{x}\}$ that satisfy $\mathbf{Ax}=\mathbf{b}$ is given by

$$\mathbf{x}=\mathbf{x}_{\mathrm{LS}}+\mathbf{x}_n=\underbrace{\sum_{j=1}^{m}\frac{\mathbf{u}_j^T\mathbf{b}}{\sigma_j}\mathbf{v}_j}_{\mathbf{x}_{\mathrm{LS}}}+\underbrace{\sum_{j=m+1}^{n}C_j\mathbf{v}_j}_{\mathbf{x}_n} \tag{5.10}$$

where $\{C_j\}$ are any set of real numbers. Consequently, these problems violate the second (uniqueness) criterion of well-posed problems. Equation (5.10) shows that the solution has two components: $\mathbf{x}_{\mathrm{LS}}$, the (unique) solution belonging to the range of $\mathbf{A}$ that has the smallest Euclidean norm that satisfies $\mathbf{Ax}=\mathbf{b}$, and an infinite set of solutions from the null space of A, $\{\mathbf{x}_n|\mathbf{Ax}_n=0\}$. Figure 5.8(b) shows the singular values for the beam arrangement in Figure 5.9(a), and the corresponding $\mathbf{x}_{\mathrm{LS}}$ component found through the first summation in Eqn (5.10) is plotted in Figure 5.9(b). While this solution fully explains the observed attenuation data in $\mathbf{b}$, it is obviously not the true ‘physical’ solution.

Consequently, in these types of limited data tomography problems the measurement data in $\mathbf{b}$ must be supplemented with additional information about the presumed physical attributes of the species concentration field; in the context of Bayesian inference these are called ‘priors’ since they are based entirely on knowledge of the measurement subject available prior to the measurements being carried out. In CST the most common priors ensure that the species concentration distribution is nonnegative and promote a degree of spatial smoothness consistent with diffusion-dominated transport. The Industrial Process Tomography group at the University of Manchester has favoured a modified Landweber iteration (e.g. Wright et al., 2010; Garcia-Stewart, Polydorides, Ozanyan, & McCann, 2003; Terzija et al., 2008; Pal, Ozanyan, & McCann, 2008) for carrying out CST. In its original form, Landweber iteration (Landweber, 1951; Hansen, 1999) is used to regularize discrete ill-posed problems (i.e. suppress noise amplification associated with small singular values) and is closely related to ART

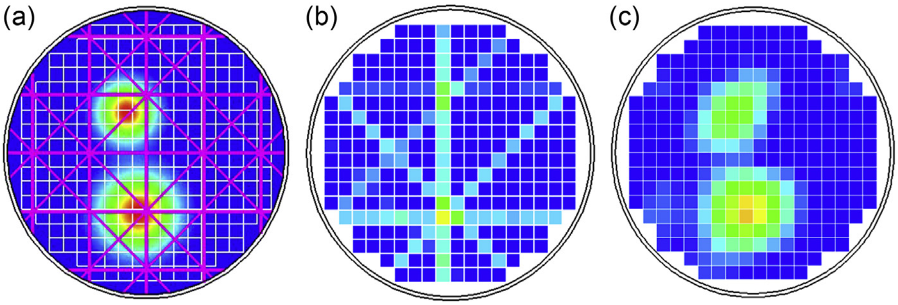

Figure 5.9 (a) Beam arrangement corresponding to a rank-deficient CST problem, with singular values shown in Figure 5.8(b); (b) $\mathbf{x}_{\mathrm{LS}}$ found from the first summation term in Eqn (5.10) explains $\mathbf{Ax}=\mathbf{b}$ but is not the physical solution; and (c) the solution found using first-order Tikhonov, Eqn (5.12).

regularization. Since **A** is rank-deficient, however, the algorithm must be modified to 'span' the null space of **A**; otherwise Landweber iteration will only affect the portion of **x** belonging to the range of **A**. This can be done by passing the solution through nonnegativity and mean, median, or wavelet filters between successive Landweber iterations to 'smear' the solution onto pixels that are not transected by beams.

Other CST practitioners (e.g. Ma et al., 2013; Cai, Ewing, & Ma, 2008; Daun, 2010) have favoured variations of first-order Tikhonov regularization (Tikhonov & Arsenin, 1977), coupled with a nonnegativity constraint. In this technique, the rank-deficient set of equations, $\mathbf{Ax} = \mathbf{b}$, is augmented with a second set of equations, $\lambda\mathbf{Lx} = 0$, where the smoothing matrix, **L**, is a discrete approximation of the directional derivative, e.g. for the case where the mth pixel is surrounded by k neighbouring pixels (e.g. $k = 4$, if one considers an interior pixel on a Cartesian grid)

$$L_{mn} = \begin{cases} 1 & \text{if } n = m \\ -1/k & \text{if } n \text{ neighbours } m \\ 0 & \text{otherwise} \end{cases} \tag{5.11}$$

and $\mathbf{Lx} = 0$ is satisfied by any uniform **x**. The species concentration distribution is found by solving

$$\mathbf{x}_\lambda = \operatorname{argmin} \left\| \begin{bmatrix} \mathbf{A} \\ \lambda\mathbf{L} \end{bmatrix} \mathbf{x} - \begin{bmatrix} \mathbf{b} \\ 0 \end{bmatrix} \right\|_2^2, \quad s.t. \ \mathbf{x} \geq 0 \tag{5.12}$$

where the parameter λ determines the influence of the additional smoothing equations, $\mathbf{Lx} = 0$, relative to the measurement data, $\mathbf{Ax} = \mathbf{b}$. When Tikhonov regularization is applied to discrete ill-posed problems, λ can be chosen using a parameter-selection technique, such as L-curve curvature (Hansen & O'Leary, 1993), or the discrepancy principle (Morozov, 1966; Hansen, 1999). It is important to note that these techniques presume that $\mathbf{x}_{\mathrm{LS}}$ is the correct solution in the absence of noise, however, and are thus *inappropriate for rank-deficient problems*. Instead, Daun presented a method for choosing λ based on a singular value decomposition of the augmented matrix $[\mathbf{A}; \lambda\mathbf{L}]$ (Daun, 2010). Figure 5.9(c) shows a reconstruction obtained through this technique.

Other, more elaborate, reconstruction techniques have been developed for limited data CST problems. Drescher et al. conceived the smooth basis function minimization (SBFM) method (Drescher, Gadgil, Price, & Nazaroff, 1996), in which the concentration distribution is represented by the sum of Gaussian basis functions, and the unknown weights are found by minimizing the least-squares residual between measured and modelled data. This approach was later refined by Fischer et al. (2001), who used it to reconstruct the evolving concentration of methane within an enclosure. More recently, Twynstra, Daun, and Waslander (2014) applied the level set method (LSM) to solve limited data CST problems. In most LSM implementations, a 2D boundary between discrete phases is defined by projecting a 3D dynamic implicit surface (the level set function) onto a plane; this is particularly useful for challenging and dynamically changing topologies, since it avoids a parameterized representation of the interface (Osher & Sethian, 1988). The level set function is initialized as a signed distance function and then progressively deformed by forces that scale with the difference between the modelled and measured data. Twynstra et al. extended the LSM to represent a continuously varying scalar field (Twynstra et al., 2014), and incorporated a first-order Tikhonov prior to promote a spatially smooth concentration distribution. The main advantage of the LSM over other reconstruction techniques is that it incorporates an explicit interface between the species of interest and surrounding gases into the solution priors, which is more consistent with the concentration distributions expected in advection-dominated flows. This technique provided superior reconstructions compared to first-order Tikhonov in a simulated CST experiment on a large-eddy simulation of a mixed-buoyant methane plume but was also more computationally expensive (Twynstra et al., 2014).

The above reconstruction methods span the null space of **A** by incorporating prior knowledge of the instantaneous spatial distribution (nonnegativity, spatial smoothness and, in the case of the LSM, an explicit phase boundary). If time-resolved measurements are made on a transient flow field, reconstruction accuracy can also be improved by incorporating assumptions about the time evolution of the concentration distribution. The discrete time Kalman filter is ideal for combining instantaneous optical measurements, spatial priors and temporal priors to obtain an estimate for the species concentration distribution. In this approach the inverse problem is transformed into a state estimation problem in which the state is predicted at each time step using a linearized model of the system dynamics (temporal prior) and then corrected with a measurement model. The relative influence of the state evolution model and measurement model on the predicted state is weighted by state transition and measurement covariance matrices to deliver an optimal (minimal covariance) estimate. In limited data tomography problems the measurement model must also be augmented with spatial priors, e.g. the Tikhonov smoothness prior. Reconstruction accuracy depends strongly on the fidelity of the state evolution model.

The simplest, and least-informative, state evolution model is the random walk model, in which the species concentration is assumed to remain unchanged between subsequent time steps. Daun, Waslander, and Tulloch (2011) tested this approach for a simulated optical CST experiment on a mixed-buoyant methane plume in a duct; they found an improvement in reconstruction accuracy when the measurements had low signal-to-noise ratios. Moreover, they showed that the Kalman filter allows ‘multiplexing’ of sequential measurements, which could simplify data acquisition in experiments involving large numbers of sensors.

A considerable improvement in reconstruction accuracy can be obtained by incorporating a more informative and realistic state transition model into the Kalman filter. Professor Kaipio’s research team derived a state transition model from a stationary estimate of the velocity profile to carry out electrical impedance tomography on single-phase and two-phase laminar duct flows (Seppänen, Vauhkonen, Vauhkonen, Somersalo, & Kaipio, 2001; Seppänen et al., 2007), and subsequently extended their technique to problems in which the velocity field is unknown (Seppänen, Voutilainen, & Kaipio, 2009; Lipponen, Seppänen, Hämäläinen, & Kaipio, 2010; Lipponen, Seppänen, & Kaipio, 2010; Lipponen, Seppänen, & Kaipio, 2011). These techniques are described in greater detail in Chapter 21.

5.4 Beam array design and optimization

Experimental (Terzija et al., 2008; Wright et al., 2010) and numerical (Daun, 2010; Verhoeven, 1993; Ibrahim et al., 1999) CST experiments have shown that reconstruction accuracy depends strongly on the arrangement of light sources and detectors. The cost and complexity of the laser and detection optics demand that these components be used to their maximum potential. Nevertheless, only a handful of studies have addressed the issue of how to optimize sensor layout in CST experiments.

Terzija et al. (2008) propose several heuristics for predicting the quality of a beam arrangement in laser line-of-sight-attenuation tomography experiments. In particular, since Fourier transform-based reconstruction techniques involve an integration of the projected data over $0 \leq \theta \leq \pi$ and $-R \leq s \leq R$, i.e. Eqns (5.5) and (5.6), they argue that the (s,θ) coordinates of a 'good' beam array should provide a low-discrepancy sampling of $R_{(s,\theta)}$, in the same way that Monte Carlo integration accuracy improves with increasing discrepancy of quadrature points. Following this argument, one would expect the beam arrangement shown in Figure 5.7(b) to provide more accurate reconstructions compared to Figure 5.7(a).

Twynstra and Daun (2013) provide a more systematic technique based on resolution matrices (Menke, 1989), in the context of unconstrained first-order Tikhonov regularization. The resolution matrix is derived from the regularized inverse:

$$\mathbf{A}^{\#} = \left(\mathbf{A}^{\mathrm{T}}\mathbf{A} + \lambda^2\mathbf{L}^{\mathrm{T}}\mathbf{L}\right)^{-1}\mathbf{A}^{\mathrm{T}} \tag{5.13}$$

Defined in this way, $\mathbf{x}_\lambda = \mathbf{A}^{\#}\mathbf{b}$ provides the same solution as Eqn (5.12) for a given λ if the bound constraints were relaxed. If the data vector is separated into the 'exact' and 'noise' components, $\mathbf{b} = \mathbf{b}^{\mathrm{exact}} + \boldsymbol{\delta}\mathbf{b} = \mathbf{A}\mathbf{x}^{\mathrm{exact}} + \boldsymbol{\delta}\mathbf{b}$ and $\mathbf{A}$ were full rank,

$$\mathbf{x}_\lambda = \mathbf{A}^{\#}\mathbf{A}\mathbf{x}^{\mathrm{exact}} + \mathbf{A}^{\#}\boldsymbol{\delta}\mathbf{b} = \mathbf{R}\mathbf{x}^{\mathrm{exact}} + \mathbf{A}^{\#}\boldsymbol{\delta}\mathbf{b} \tag{5.14}$$

where $\mathbf{R} = \mathbf{A}^{\#}\mathbf{A}$ is the resolution matrix. The reconstruction error is then defined by

$$\boldsymbol{\delta}\mathbf{x} = \mathbf{x}_\lambda - \mathbf{x}^{\mathrm{exact}} = (\mathbf{R} - \mathbf{I})\mathbf{x}^{\mathrm{exact}} + \mathbf{A}^{\#}\boldsymbol{\delta}\mathbf{b} \tag{5.15}$$

where $\mathbf{I}$ is the identity matrix. Equation (5.15) reveals two error components in $\boldsymbol{\delta}\mathbf{x}$: regularization error, $(\mathbf{R} - \mathbf{I})\mathbf{x}^{\mathrm{exact}}$, arises from the inconsistency between the smoothing prior, $\mathbf{L}\mathbf{x} = 0$, and the measurement equations, $\mathbf{A}\mathbf{x} = \mathbf{b}$; and $\mathbf{A}^{\#}\boldsymbol{\delta}\mathbf{b}$ is the error caused by perturbations in the data, which are amplified by the small singular values in $\mathbf{A}$. In discrete ill-posed problems (e.g. soft-field tomography problems) $\lambda\mathbf{L}\mathbf{x} = 0$ filters out noise amplifications by small singular values, and parameter-selection techniques provide a regularization parameter that gives a good trade-off between regularization and perturbation error (Hansen, 1999). In limited data tomography problems, on the other hand, $\mathbf{Ax} = \mathbf{b}$ provides an incomplete picture of the problem space, and $\mathbf{Lx} = 0$ fills in the missing pieces. In this case the nontrivial singular values of the rank-deficient A matrix are large, and Daun (2010) showed that $\mathbf{x}_\lambda$ is robust to perturbation error over a wide range of λ. Consequently, $\boldsymbol{\delta}\mathbf{x}$ is instead dominated by regularization error, $(\mathbf{R} - \mathbf{I})\mathbf{x}^{\text{exact}}$.

In an ideal tomography experiment $\mathbf{R} = \mathbf{I}$, which implies that the concentration within each pixel can be resolved from the measurement data, $\mathbf{b}$. This is not possible in rank-deficient problems: the addition of $\lambda\mathbf{Lx} = 0$ forces the off-diagonal terms in $\mathbf{R}$ to be nonzero, making the estimated concentration profile of each pixel a weighted average of the concentration of the surrounding pixels; this is unavoidable in low beam-count systems. Nevertheless, the beams should be arranged to maximize the information content of the laser attenuation measurements relative to the role of the prior information, so the Frobenius distance between $\mathbf{R}$ and $\mathbf{I}$ is a good figure of merit for a beam array. If $\boldsymbol{\Phi}$ contains the (s, θ) coordinates of the beams, this figure of merit can be written as

$$F(\boldsymbol{\Phi}) = \|\mathbf{R}(\boldsymbol{\Phi}) - \mathbf{I}\|_F^2 \tag{5.16}$$

Figure 5.10 shows that $F(\boldsymbol{\Phi})$ tracks the reconstruction error, $\varepsilon = \|\mathbf{x}_\lambda - \mathbf{x}^{\text{exact}}\|/\|\mathbf{x}^{\text{exact}}\|$, for an orthogonal beam array with varying beam spacing, and a fan-beam array with varying spread angle. Twynstra and Daun (2013) then show that the beam arrangement can be optimized by solving

$$\boldsymbol{\Phi}^* = \arg\min\,[F(\boldsymbol{\Phi})] \tag{5.17}$$

using a genetic algorithm. Numerical CST experiments on a large-eddy simulation of a mixed-buoyant methane plume showed that optimized beam arrangements provided superior reconstruction accuracy compared to other beam arrangements presented in the literature.

5.5 Design of CST systems

Implementations of CST systems vary widely in form, according to their intended application. Nevertheless, general comments can be made regarding scattering and optical access issues that influence CST system design, as well as various optoelectronic considerations. Figure 5.11 shows a hypothetical CST system architecture, intended to illustrate several commonly used design features. One or more optical sources (S1—SM), most often semiconductor diode lasers, are operated under tightly controlled current (I) and temperature (T) conditions, to provide optical radiation of the desired wavelength and intensity (both of which are typically time-varying). These sources are multiplexed across a set of launch optics (TX1—TXN), from where the

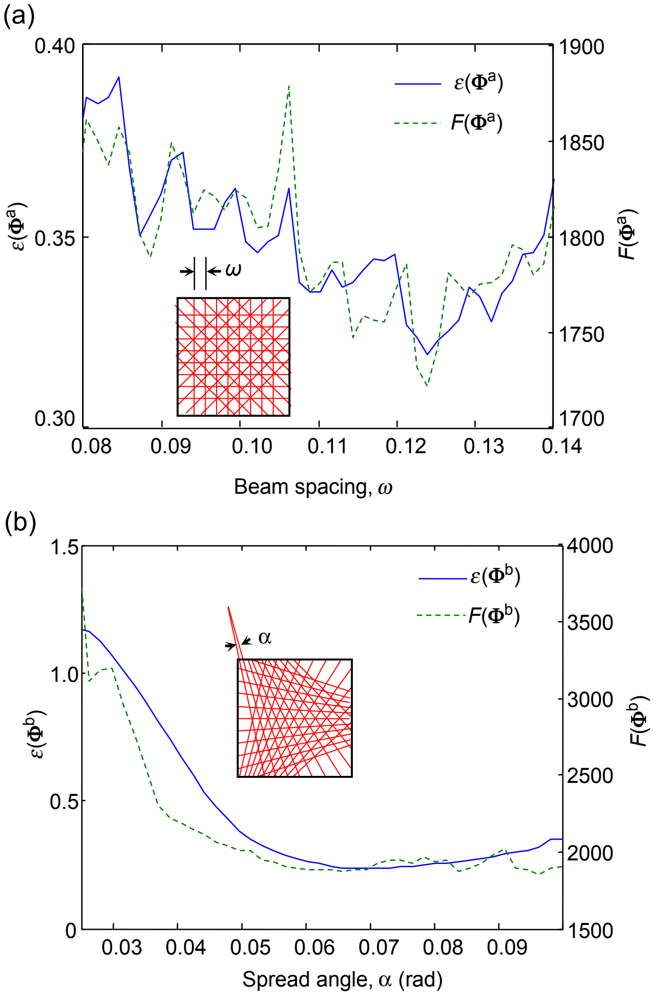

Figure 5.10 Figure-of-merit and reconstruction errors for: (a) orthogonal-beam arrays having various beam spacings; and (b) fan-beam arrays having various spread angles (Twynstra & Daun, 2013).

optical radiation transects the measurement space, before arriving at a corresponding set of collection optics (RX1—RXN) and associated photodetectors (PD1—PDN). The output from these photodetectors must then be amplified and the necessary signals, typically representing the transmittance of each beam path at one or more wavelengths, recovered. Many variations of source multiplexing are possible, in terms of both architecture and implementation technology, including the introduction of additional components to enable intensity modulation of individual beams or groups thereof. The corresponding demodulation process is typically the primary function of the signal recovery electronics.

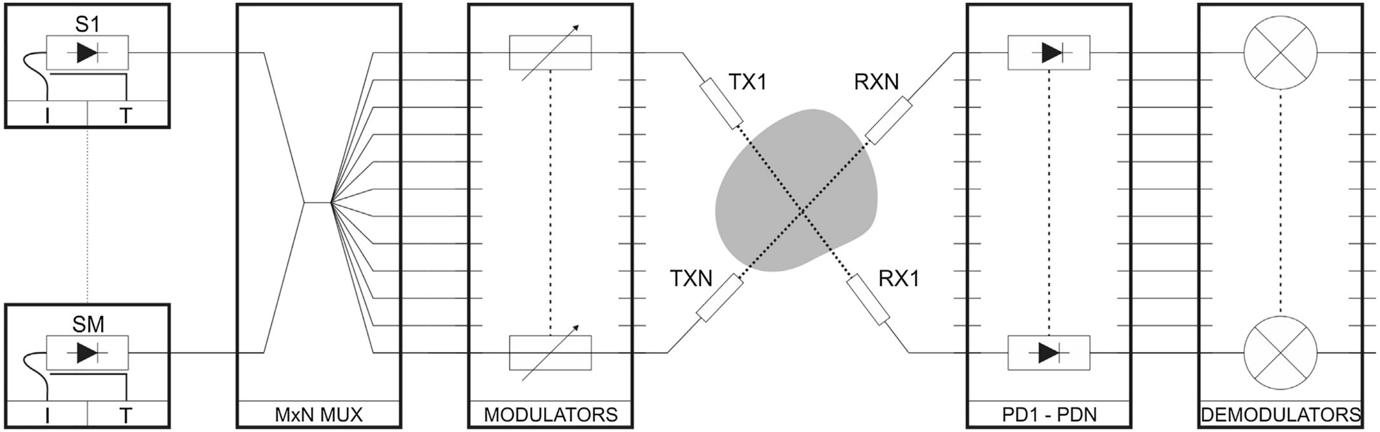
S1
I
T
SM
I
T
MxN MUX
MODULATORS
TX1
RXN
TXN
RX1
PD1 - PDN
DEMODULATORS

Figure 5.11 One possible CST system architecture.

The properties of the received optical signals depend upon the propagation characteristics of the medium and the design of the launch and receive optics, so next we shall consider these topics before examining optoelectronic issues.

5.5.1 Optical propagation and the importance of scattering

While scattering plays an important role in other tomography modalities (e.g. medical applications (Beiting, 1992)), as noted in Section 5.2 for CST experiments on molecular gases, scattering is, in principle, negligible. In reality, however, some scattering may occur, either due to contaminants in the tomography domain (e.g. particles, droplets) or spatial variations in the refractive index that arise from species or temperature inhomogeneity, which may spread or redirect the beam. Laser scattering within a CST system is problematic, complicating source-to-detector coupling and increasing the likelihood of crosstalk. The degree of scattering present in the measurement subject, and the value attached to its quantification, have profound implications for both the optical access arrangement and the preferred measurement approach. Two limiting cases can be identified:

Case (1): High scattering. When high levels of scattering are present, a considerable fraction of the light incident on a given detector is due to light scattered from paths other than the path between the detector and its intended source, and consequently each source will couple with many detectors, and a diffuse (soft-field) tomography approach is necessary. Soft-field techniques are generally preferred in medical applications (Haisch, 2012), in which their increased implementation complexity is offset by the additional information obtained from the distribution of the scattering coefficient, and the increase in computational processing needed to analyse radiation propagation through a scattering medium is often a secondary consideration.

Case (2): Negligible scattering. When scattering is insignificant, the attenuation of light between a source−detector pair is governed by Eqn (5.1). In this case, the receivers are coupled directly and exclusively to the corresponding (line-of-sight) sources.

Many industrial applications of optical tomography fall between the above extremes, and three further cases can be defined in which scattering can be treated as a modest perturbation of an otherwise hard-field problem:

Case (3): Scattering just above negligible levels. In this case, although a given source will not illuminate receivers other than its line-of-sight counterpart, out-scattering is nonnegligible, so the extinction coefficient must account for both absorption and scattering.

Case (4): Scattering with the potential for crosstalk. Here, sufficient scattering is present for a source to illuminate additional receivers but without the potential imaging utility present in case (1).

Case (5): Scattering only at the boundary. Scattering occurs only at the bounding optical surfaces.

Cases (3) and (4) can be regarded as the progressive breakdown of the true hard-field situation described in case (2). Considering Figure 5.12, a number of sources, S_N, and receivers, R_N, are distributed along a boundary B, within which

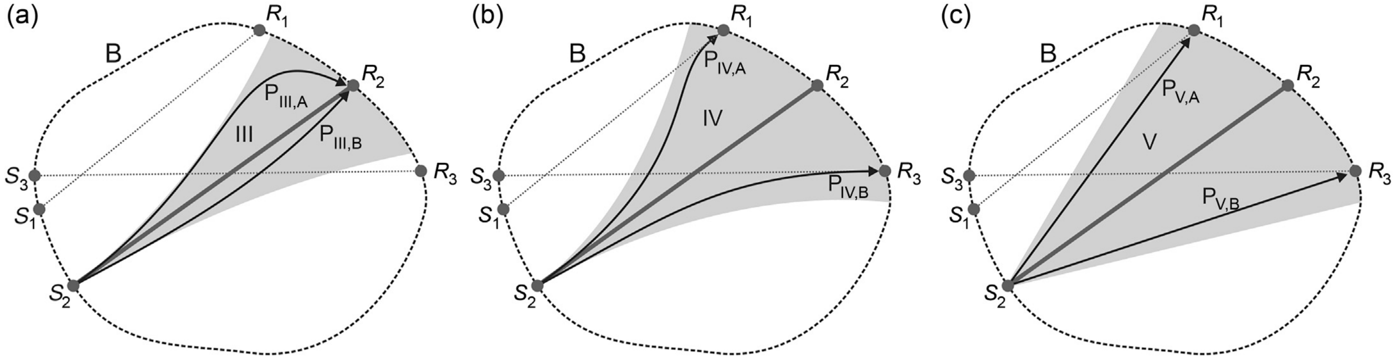
(a)
B
R_1
R_2
R_3
S_1
S_2
S_3
$P_{III,A}$
$P_{III,B}$
III
(b)
B
R_1
R_2
R_3
S_1
S_2
S_3
$P_{IV,A}$
$P_{IV,B}$
IV
(c)
B
R_1
R_2
R_3
S_1
S_2
S_3
$P_{V,A}$
$P_{V,B}$
V

Figure 5.12 Light paths between sensors and detectors for: (a) scattering just above negligible levels; (b) scattering with the potential for crosstalk; and (c) scattering at the boundary, corresponding to cases (3), (4) and (5) in the text, respectively.

scattering occurs. The line-of-sight path S_2—R_2, typifying case (2), is shown as a solid line.

In Figure 5.12 (a), corresponding to case (3), region III indicates locations reachable by significant levels of illumination from S_2. Case (3) requires, as a minimum, the separation of the absorption and scattering components of the observed attenuation. This can be accomplished using additional wavelengths having a different balance of these two components, ideally including regions of negligible absorption. Depending on the absorption feature under consideration, this may be implemented by chirping a single source, in the manner typical of TDLAS measurements (Bain et al., 2011), or it may require multiple sources, as in the DWR approach used in Wright et al. (2010). It is, however, apparent from example path $P_{\mathrm{III,A}}$ that this approach does nothing to restrict the spatial origin of the measured absorption signal, with the relative weighting of the various paths within the envelope being determined by the source properties and the subsequent scattering and absorption processes. Although not essential, increasing the directionality of the receivers by the inclusion of lenses or collimating apertures will constrain sensitivity closer to the line-of-sight path. Paths lying outside of $P_{\mathrm{III,B}}$ are then unlikely to make a significant contribution, enhancing the hard-field character of the measured data. Excessive collimation, however, will increase link losses and complicate alignment of the launch and receive optics.

Receiver collimation is also helpful in limiting the potential for crosstalk in case (4) but, as can be seen from the extent of region IV in Figure 5.12(b), cannot be 100% effective as crosstalk paths meeting the direction criteria, such as $P_{\mathrm{IV,A}}$, do exist. In some cases, alternating the direction of source—receive pairs within a projection, effectively doubling the beam pitch for crosstalk purposes, may be adequate but this does not address inter-projection crosstalk, exemplified by $P_{\mathrm{IV,B}}$. Situations where additional suppression of crosstalk is necessary can be addressed using multiplexing techniques that enable identification of the individual source contributions at a given receiver as discussed later in this chapter. Note that neither of the preceding approaches to crosstalk suppression is effective in constraining the spatial origin of the absorption signal. Moderate focussing of the launch has also been shown to reduce the post-scattering spot size in some cases.

Case (5) is subtly distinct from cases (3) and (4) in that, although straight-line propagation occurs within the measurement space, the reduced receiver directionality limits the scope for unwanted path rejection. Depending on the level of scattering at the source end, a situation analogous to either case (3) or case (4) will arise.

Time-of-flight (‘ballistic photon’) techniques merit passing mention as they offer an alternative to the use of launch and receive collimation in obtaining near-hard-field measurement data. Strictly, these systems offer filtering on the basis of optical path delay, but they can be effective in rejecting the contribution of indirect paths, especially in relatively homogeneous media. Cost and complexity have limited their application to demonstrations involving sequential translation and rotation of the measurement subject about a single measurement path (Ozanyan, Wright, Stringer, & Miles, 2011).

In view of the preceding issues, systems requiring data amenable to hard-field reconstruction from simultaneous multipath measurements in media in which scattering is nonnegligible usually employ some combination of:

1. multiple wavelengths to separate scattering and absorption;
2. source and receiver collimation for control of the spatial origin of the absorption signal; and
3. alternate (or equivalent) orientation of send-receive paths and/or orthogonal modulation of potentially interfering beams for crosstalk suppression.

The degree of scattering may be time-varying, either randomly or in response to process variation. In some cases, such as fuel injection in IC engines, the high-scattering regime is short-lived, and adopting a 'worst case' approach yields a system that is suboptimal during the majority of its operating cycle. Dynamic modification of the measurement approach, in this case between imaging of absorption and scattering, may offer a better compromise in such scenarios.

It is also worth noting that enhancing the spatial resolution of a CST system is not simply a matter of reducing the beam pitch or increasing the number of projections, since these changes sensitize the reconstruction to scattering effects. In some situations, increasing the density of the sampling grid will *require* a diffuse approach, which would complicate the experimental set-up, since some multiplexing or orthogonal coding would be necessary to separate contributions from each source, and would also demand considerably more computational effort to carry out the reconstructions.

5.5.2 Achieving optical access

Although most nonmedical applications of CST share a hard-field approach to measurements drawn from a thin slice of subject space, the physical form of this slice varies enormously. In studies of atmospheric composition (Price, Fischer, Gadgil, & Sextro, 2001), the path integrals may be measured over tens of metres, with their end points located to achieve coverage of some arbitrary region of interest, with pressure and temperature at ambient levels. In contrast, industrial applications may need to gain optical access to processes at nonambient pressure and/or temperature, often across some physical boundary such as a reactor wall. The path lengths involved range from tens of millimetres to several metres. In this section, we will examine how the factors discussed in Section 5.5.1 influence the design of optical access arrangements.

In the absence of significant attenuation by the object, an ideal optical access arrangement would deliver efficient transmission of light along each measurement path, with negligible crosstalk. Collimation lenses are readily available for such coupling tasks and, in situations where scattering within the object can be neglected (case (2)), they offer a convenient solution to the measurement of path-integrated absorption. As noted above, many cases of practical interest feature thermally or species-derived refractive index gradients, particulates or droplets that give rise to nonnegligible scattering. In such cases, the properties of the measurement subject are paramount in selecting an optical arrangement, an approach made explicit by Kranendonk and Sanders (2005) in determining the requirements for in-cylinder path-integral measurements in combustion engines. Their empirical scattering models led them to adopt a small-diameter collimating launch lens in combination with a larger receive lens, combining optical collection efficiency with receiver directionality, as can be appreciated from Figure 5.9(a).

Numerous lens options exist, including conventional spherical and ball lenses, aspherics and gradient-index (GRIN) rod lenses; the latter are particularly suited to fibre optics. Where multiple wavelengths are used for the separation of scattering and absorption, an achromatic launch condition is clearly desirable. This is relatively straightforward in TDLAS implementations, thanks to the narrow chirp range, but challenging in the DWR case due to the limited availability of small achromatic lenses and the difficulty of achieving a correspondingly achromatic source distribution. Fan-beam arrangements, having multiple receivers per source, are attractive in space-constrained applications. True fan implementations, using line generation optics at each launch, are very wasteful of optical power as much falls between receivers, but relatively efficient embodiments can be constructed using diffractive optical elements to produce a ‘fan of beams’.

In situations where the optical paths must cross a physical boundary, a key decision is whether the relevant elements will function purely as optical access ‘windows’ or also act as lenses. In the latter case, the reduced degrees of freedom within the optical design may make it impossible for the optical elements to have the same form as the internal boundary they replace. In some applications, most obviously food and pharmaceuticals, the resulting crevices may be unacceptable and the use of dedicated windows may be necessary. This increase in design freedom comes at the expense of increased cost, complexity and susceptibility to interferometric noise.

Of particular note is the case in which the measurement subject is contained within a transparent annulus, such as glass pipework, as shown in Figure 5.13. It is tempting to regard the annulus as a single continuous window, suitable for use with external collimation lenses. This approach has significant limitations, however: the annulus acts as a weak meniscal cylindrical lens, which introduces significant astigmatism, making receiver coupling more difficult; additional corrective optics or increased detector area are necessary to avoid increased insertion loss; and the annulus’s varying tilt with respect to a given optical path means that the required correction is also position dependent. Practical demonstrations of this approach (e.g. Hindle et al., 2001) have tolerated increased insertion losses, particularly in chord beams, in preference to implementing these corrections. The inclusion of cylindrical elements also requires greater care in the avoidance of polarisation-related issues, especially in systems incorporating optical fibres, which may contribute spontaneous polarisation drift, leading to significant low-frequency noise in systems with polarisation dependence.

The development of affordable fibre optics compatible with the near-IR absorption features of molecular gases has greatly extended the scope for industrial CST. They allow beam delivery and collection arrangements impossible using free space optics, particularly in confined or dirty environments. The ready availability of 1:*N* fibre couplers is particularly useful in systems that share a light source across several launch

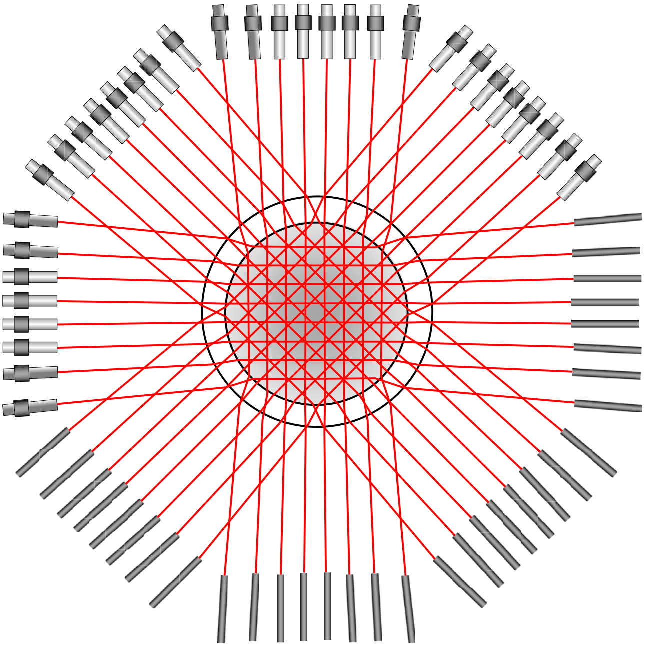

Figure 5.13 When the measurement subject is contained within an annulus, it is essential to adjust the beam arrangement to compensate for the effect of the cylindrical element. In some instances, this may have to include astigmatic correction.
Adapted from Hindle et al. (2001).

positions. The use of fibreoptics is, however, not without drawbacks: polarisation and bend loss effects must be considered; multimode fibres are susceptible to modal noise; and fibre performance drops off rapidly in the mid-IR. The short fibre lengths and, in receiver applications, poorly controlled launch conditions typical of CST systems mean that cladding mode propagation may be significant. The weakly guided nature of such propagation gives it the potential to become a significant source of amplitude noise in high vibration environments.

The availability of suitable window and lens materials is another important consideration, especially in mid-IR or harsh environment applications. Fused silica and sapphire both perform well at high temperatures and pressures. Silica-based optical glasses are typically preferred up to their transmission cut-off at around 2 μm. Sapphire remains semitransparent beyond 5 μm but is difficult to polish, and its high refractive index implies high levels of surface reflection loss. Alternative mid-IR materials, such as CaF_2, cannot match the mechanical and chemical robustness of sapphire but are easier to work and offer lower refractive indices and, in some cases, dispersion. Other mechanical factors, such as the achievable beam positioning, packing density and the ability of particular elements to withstand the pressures and/or temperatures present within the measurement subject, also influence the selection of optical materials.

5.5.3 Optoelectronic considerations

Semiconductor diode lasers have been the preferred light source in many gas sensing and CST applications since they became widely available in the 1990s. They are compact, rugged and possess a spectral width and tuning range appropriate to many gas spectroscopy needs. Various measurement schemes, such as DAS and WMS, have been developed that exploit the controllability of these devices. In the NIR region, output powers of 1–50 mW are typically available. For single-path measurements, this is usually sufficient to ensure that measurement performance is not limited by the available optical power but rather by interferometric noise or other optical considerations. However, in CST systems a source may have to be shared among several beam paths, and the performance of the receiver electronics then assumes much greater importance (Wright, Ozanyan, Carey, & McCann, 2005), unless a means to increase the available optical power can be included. Semiconductor optical amplifiers (SOAs) are an obvious candidate and offer chirp-free modulation if desired (Karagiannopoulos et al., 2012), but modest gain and limited availability outside of key telecommunications wavelengths limit their utility. Fibre lasers also show great promise for amplification of diode laser seeds, with at least one such system in development (FLITES). The increasing availability of widely tunable sources has enabled hyperspectral approaches, utilising more absorption features than would be possible with conventional TDLAS techniques, e.g. An et al. (2011). In the MIR region, source costs are appreciably higher, especially in per-unit-power terms. Quantum cascade lasers (QCLs), offering relatively high output power and non-cryogenic operation, have largely replaced lead salt lasers in this spectral region.

Where fibre optics are used, they will typically be single mode (SM), which are readily coupled to laser sources and free from the modal noise problems associated with multimode (MM) fibres. Passive distribution of a single source across all paths is a cost-effective architecture, requiring only the source, with associated current and temperature control, and a 1:*N* coupler to supply all launch lenses. DWR implementation requires the addition of a second source and a WDM coupler to provide the necessary 2:*N* functionality. The addition of a layer of modulators before the launch lenses would enable full source multiplexing control but the high cost of suitable modulators makes this attractive only in fully diffuse, case (1), systems. Where modulation control is needed only for crosstalk suppression, case (4), architectures offering a small number of modulation subgroups mitigate the cost implications of individual modulators. Depending on source and modulator costs at the wavelengths in question, and the optical power required, the use of multiple sources may be preferable. At certain wavelengths, mass market application has driven down the cost of diode lasers to the point where the use of a dedicated source per beam path can be contemplated. It must be appreciated, however, that the cost of the necessary individual temperature and drive current control within such a scheme may still be prohibitive, so some degree of source multiplexing is likely to feature in the majority of CST systems.

Single-point detection at visible and NIR wavelengths is dominated by photodiodes, with silicon, germanium and InGaAs most prevalent. Moving to the MIR and then to long-wavelength IR, a progressive shift first to photoconductive (e.g. PbS) and eventually thermal detection is typical. All of these detectors exhibit sensitivity over a wide range of angle of incidence, so receiver directionality must be implemented by supplementary collimation. This often also serves to focus the available light onto a relatively small detector, whose reduced capacitance enables improved speed and noise performance. Direct illumination of detectors is therefore relatively rare, with the majority of systems including some means to control the receiver numerical aperture (NA). Possible receiver architectures, shown in Figure 5.14, include: a lens—detector combination; a lensed fibre with butt-coupled detector; and an unlensed fibre with ball lens coupling to detector. For the lens—detector combination, the NA is defined by the diameter and location of the aperture stop (AS), with the optical field of view (FOV) being set by a dedicated field stop (FS). Where the latter stop is omitted, the FOV is dictated by the extent of the detector. For a lensed fibre with butt-coupled detector, due to the absence of a limiting aperture or vignetting in the lens, the input NA is defined by that of the fibre, as modified by the lens. The use of MM fibre is typical here, principally due to the difficulties of coupling into SM fibre from a poorly defined source. Care is required to avoid modal noise as equilibrium mode distributions are unlikely in the relatively short fibres and vibration levels typical of CST systems. As a minimum, the detector should capture the entire output of the fibre, either by butt coupling of a large detector or via a suitable coupling lens. In the third scenario, the receiver NA is simply that of the fibre.

As discussed in Section 5.2, the optical signal at the detector is typically modulated, not only by absorption and scattering within the measurement space but additionally by source modulation, introduced on optoelectronic performance grounds. This combined modulation determines several of the CST system's electronic requirements. In DAS, a relatively low-frequency drive current ramp is used to generate the required wavelength chirp so the bandwidth requirements are modest. However, the signal must be separated from residual amplitude modulation (RAM), as described in Kluczynskki et al. (2001), and the low sensitivity of the technique leads to challenging noise performance and dynamic range requirements. In WMS, the signal must be demodulated at the much higher frequency f or its overtones ($2f$, $3f$, ...), necessitating high bandwidth and, in most cases, high sampling rates. Even in applications where wavelength chirp is either absent or inconsequential, e.g. direct absorption

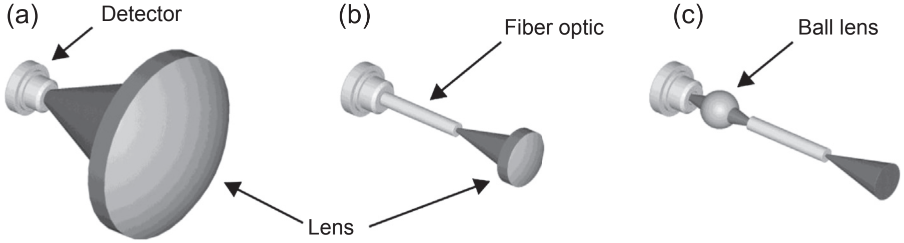

Figure 5.14 (a) lens—detector combination; (b) lensed fibre with butt-coupled detector; (c) unlensed fibre with ball lens coupling to detector.

measurements, source modulation has significant benefits. High-frequency operation is always advantageous, to avoid so-called "flicker" or "1/*f*" noise, and in some cases the modulation frequency may target a region of known low noise. In DWR, or other multi-wavenumber schemes, modulation enables the use of time- or frequency-division multiplexing to isolate the individual source contributions within the detected signal. The essentially electronic nature of these multiplexing approaches makes them substantially cheaper than schemes based on wavelength-division multiplexing, which require additional detectors and wavelength-selective elements. The associated electronic complexities should not, however, be overlooked; e.g. the use of frequency-division multiplexing in the system described in Case Study 1 enables a high frame rate but at the cost of a greatly increased detection bandwidth.

5.6 Case studies

The following case studies are intended to illustrate practical application of CST to process measurement problems. Case Study 1 exemplifies absorption-based hard-field CST, whereas Case Study 2 describes an alternative approach, based on chemiluminescence.

5.6.1 Case study 1: automotive in-cylinder hydrocarbon imaging

Internal combustion (IC) engines used in automotive applications must be optimized to deliver performance and efficiency over a wide range of speed and load conditions. This problem involves a vast parameter space, with many possible variations of engine geometry, fuel quantity and timing, ignition and valve timing, yet few tools exist to aid this optimisation. CFD-based simulations are used to model in-cylinder gas dynamics, but experimental measurements commonly available for their validation, such as pressure-volume ($P-V$) curves and exhaust gas analysis, are aggregated across one or more cylinders and therefore offer only limited insight into the underlying in-cylinder gas distributions. Air–fuel mixing is critical to efficient combustion, but its quantification in production engines is problematic, necessitating the use of indirect methods, such as planar laser-induced fluorescence (PLIF) studies in 'glass-walled' research engines of similar geometry (Richter, Li, & Alden, 2007) or post-ignition flame-front measures (e.g. AVL's Visioknock product (Heiss, Bobicic, Lauer, Geringer, & Schmuck-Soldan, 2012)).

The IMAGER project demonstrated *pre-ignition* hydrocarbon imaging by NIR CST within a cylinder of a minimally modified multicylinder gasoline engine (Wright et al., 2010). Fibre optics were used to gain access to the combustion chamber, via a 6-mm-thick OPtical Access Layer (OPAL) replacing the uppermost portion of the cylinder wall, shown in Figure 5.15. Twenty-seven transmission paths were implemented on an irregular grid designed to minimize disruption of the engine's thermal and mechanical characteristics. Individual microlenses were used to collimate the source and receive elements, ensuring a substantively hard-field character in the data.

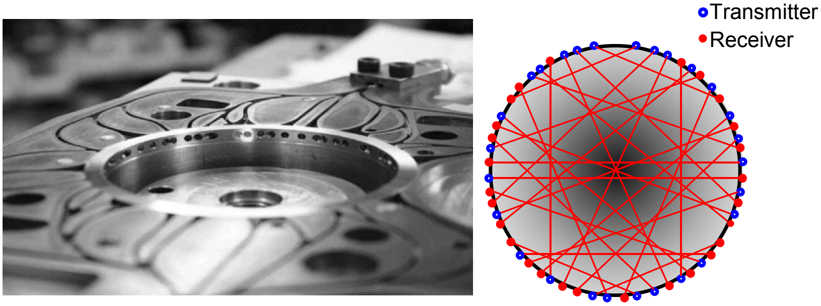

Figure 5.15 Optical access layer (OPAL) and beam configuration used in the IMAGER project.

A DWR approach allowed separation of attenuation due to nonresonant scattering, for example by soot particles, from that attributable to hydrocarbon absorption at 1700 nm. At this wavelength, the measurement is sensitive to almost all C—H bonds in all hydrocarbon molecules, from propane (C_3) upwards in C-number. A reference wavelength of 1651 nm maximized the differential absorption without introducing unnecessary chromatic aberration, to fully exploit the DWR method to obtain PCI data for the target species. Operation in the NIR, at the margin of the telecommunications bands, offers ready availability of fibres, detectors and sources at far lower costs than MIR equivalents. Electronically, the system used frequency division multiplexing, at 300 kHz and 500 kHz, to enable separation of the resonant and nonresonant contributions. This allowed a sample rate of 10^5 frames per second (fps), enabling imaging of transient in-cylinder phenomena, such as direct injection events as discussed below. The high required bandwidth and low received power at each detector ($\sim 1\ \mu W$) demanded high-performance signal recovery electronics, comprising low-noise preamplification (Wright et al., 2005) followed by lock-in detection.

The OPAL necessarily provides an irregular and sparse sampling of $R_{(s,\theta)}$. The resulting image reconstructions (Terzija et al., 2008; Wright et al., 2010), believed to be the first from data of this type, were obtained using an iterative median-filtered Landweber method. As noted in Section 5.4, ongoing research is focused on improving reconstruction algorithms by explicitly incorporating prior knowledge about the measurement subject into the reconstruction (Terzija et al., 2008; Daun et al., 2011; Twynstra et al., 2014; Terzija, 2011) and also on developing new techniques for optimizing beam layout (Twynstra & Daun, 2013). Measurements were made with the IMAGER system in one cylinder of a four-cylinder in-line Ford Duratec 2.0 L port fuel-injected engine operating at moderate speed and load conditions and running on retail gasoline (which is a mixture of many hydrocarbon species). At 1500 revolutions per minute (rpm) and moderate load, with fuel injection conditions thought to yield a homogeneous charge, CST images showed a relatively flat distribution of hydrocarbon-related absorption, as shown in Figure 5.16(a), where localized artefacts are associated with the loss of some beams (6 out of 27) to lens contamination. Laboratory tests with steady-state gaseous phantoms yielded good-quality data as shown in Figure 5.16(b) where 25 beams were used. The system exhibited surprisingly good spatial resolution, given its small number of beams.

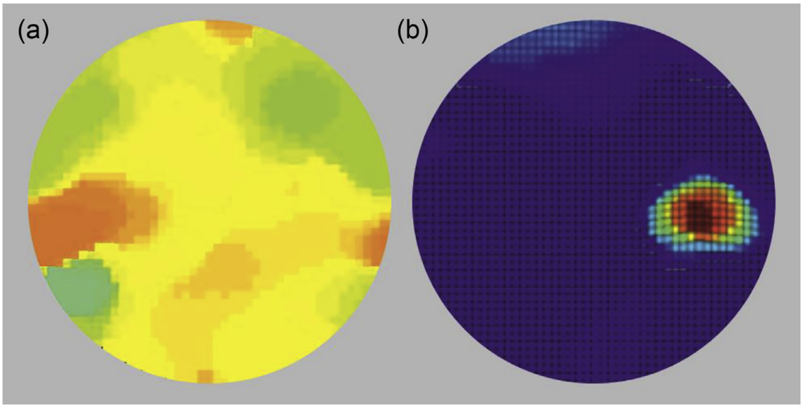

Figure 5.16 CST images of (a) in-cylinder gasoline distribution in an operating engine, *adapted from Wright et al. (2010)*, and (b) a single propane plume, of diameter 18 mm, one-fifth that of the sensing field, *taken from Terzija et al. (2008)*.

In further work to study in-cylinder HC fuel distribution in a gasoline direct injection engine, Terzija et al. (2014) applied the optoelectronics of the above IMAGER system to a single-cylinder Ricardo Hydra research engine where a 10-mm-high section of the cylinder liner consisted of a fused silica annulus. Light was launched and received along 32 paths through the cylinder via fibres terminated at the engine using GRIN lenses, each GRIN—fibre interface being fixed within a finished ferrule assembly supplied by Grintech GmbH (Jena, Germany). In a novel approach, the launch and receive assemblies were laid into accurately machined V-grooves in a flat metal plate to achieve a robust and cost-effective system. To overcome some of the effects of the optical liner, as discussed in Section 5.5.2, the groove positions were calculated using ray-tracing software. It was found that a tolerance of 50 μm on the optical liner geometry was necessary in order to achieve acceptable optical alignment of launch and receive; such liners were readily manufactured by Gooch and Housego Ltd (Ilminster, Somerset, UK). The 32 beam paths within the cylinder were arranged in four projections, each with eight parallel beams. The engine was motored at 1200 rpm on a dynamometer, i.e. no combustion took place in these experiments, unlike the multi-cylinder engine study discussed above. The fuel used was a mixture of iso-octane (90% by volume) and 3-pentanone (10%).

In all such engine studies, robust assessment of beam data quality is critically important, and the process described in Terzija et al. (2014) uses a wavelet denoising (WD) step, applied to the time-series data stream of each individual beam. Beams yielding high-quality data are not significantly affected, but WD enables robust assessment of the temporal (i.e. crank angle, CA) variation of the signals from poor-quality beams, enabling their retention in the data analysis whenever possible. In other respects, the data analysis and image reconstruction applied in Terzija et al. (2014) are equivalent to that in the multi-cylinder case (Wright et al., 2010).

In the work reported in Terzija et al. (2014), the distribution of spray droplets during the intake stroke was imaged at 7200 fps (one frame per degree crank angle, °CA) by tomographic reconstruction of the reference beam attenuation (reaching values of 60% or more) due to scattering, i.e. using nonspecies-specific tomography. The droplet distribution showed very rapid variations that were consistent from one engine cycle to the next. During the compression stroke, the DWR method was applied to obtain PCI data, which showed peak attenuation of the 1700-nm wavelength, due specifically to HC fuel, to be about 5%. Moreover, the PCI data behaved very smoothly and reliably, showing marked improvements upon the equivalent data obtained in the multi-cylinder study (Wright et al., 2010). Typically, 30 beams were found to provide robust data for image reconstruction. After averaging the PCI data over periods of 3 °CA during the compression stroke, CST images of HC fuel vapour distribution were produced, and examples are shown in Figure 5.17 — each row shows the evolution of fuel vapour distribution during a single compression stroke at 2400 fps, and each column shows the distribution at a fixed crank angle in consecutive engine cycles. The absence of the two poor-quality beams made only a minor contribution to the observed inhomogeneity in fuel distribution.

The temporal and spatial behaviours of images such as those in Figure 5.17 are discussed in detail in Terzija et al. (2014). This was the first engine demonstration of the imaging of both the spray distribution during the intake stroke and the subsequent vapour distribution during the compression stroke, for individual engine cycles.

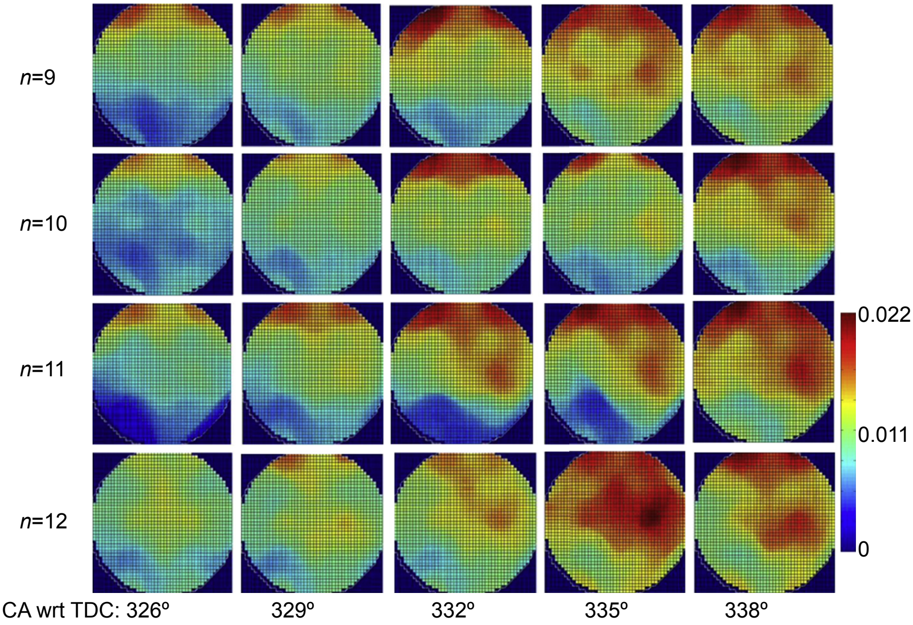

Figure 5.17 CST images of in-cylinder HC fuel vapour distribution, at intervals of 3 °CA, during the latter stage of each compression stroke of four consecutive engine cycles, numbered 9—12 in a burst of 16 fuelled cycles. The concentration scale (arbitrary units) for all images is shown at the right. The top and bottom of each image correspond, respectively, to the exhaust and inlet sides of the cylinder. The same 30 beams were used for all images.
Taken from Terzija et al. (2014).

5.6.2 Case study 2: laboratory combustion studies

Operating gas turbines toward the fuel-lean limit of stable combustion improves fuel efficiency but occasionally leads to unstable operation characterized by high-frequency fluctuations in localized volumetric heat release, resulting in excessive noise, increased NOx emissions, and high mechanical loading on the engine components that shortens service life and, in extreme cases, can lead to catastrophic failure. Understanding the underlying cause of these instabilities, and ways to avoid them, motivates much of present-day research into turbulent combustion.

Researchers at Universität Karlsruhe recently developed a new tomography tool for investigating instantaneous heat release rates in lab-scale turbulent flames. Rather than use absorption spectroscopy, which is the main focus of this chapter, these researchers performed tomographic imaging of chemiluminescence from OH* radicals (Anikin, Suntz, & Bockhorn, 2010). Although the modality is slightly different, the observed chemiluminescence measurement is related to OH* radical concentration distribution by a Fredholm IFK similar to Eqn (5.4). Their apparatus, shown in Figure 5.18, consists of 10 Kepler telescopes arranged in a semicircle surrounding the flame, with a capacity for nine additional telescopes if necessary. Each telescope projects the collimated flame image onto a corresponding strip of 90 optical fibres, which are then projected onto a linear array of an ICCD camera. The OH* chemiluminescence distributions are then reconstructed from the projections.

The telescopes provide a dense and uniform sampling of $R_{(s,\theta)}$ space, and consequently this full data tomography problem can be solved using either Fourier transform-based techniques or regularization methods. Anikin et al. (2010) compare the performance of filtered back-projection to Tikhonov regularization. The first-order Tikhonov smoothing described above is inappropriate in this case since the OH* radicals are concentrated within thin, spatially discontinuous turbulent flame fronts. Instead, the authors use standard (zeroth-order) Tikhonov.

$$\mathbf{x}_\lambda = \arg\min\left[\|\mathbf{Ax}-\mathbf{b}\|_2^2 + \lambda^2\|\mathbf{x}\|_2^2\right] \tag{5.18}$$

which promotes a solution with a small Euclidean norm. The regularization parameter, λ, is chosen using the L-curve curvature technique (Hansen & O’Leary, 1993; Hansen, 1999).

Due to the short exposure times needed to capture the transient turbulent phenomena of interest (100–200 μs), the signal-to-noise ratio in the projected data is low, so the prior information is crucial for suppressing noise amplification due to the ill-posedness of the deconvolution problem. Anikin et al. (2010) carried out simulated and actual tomographic reconstructions on laminar flat flames and showed that standard Tikhonov provided superior reconstructions compared to filtered back-projection.

The authors subsequently used their technique to image instantaneous OH* chemiluminescence within turbulent diffusion flames (Anikin, Häber, Schwamberger, Suntz, & Bockhorn, 2013), specifically a mildly turbulent cylindrical flame and a highly turbulent conical flame. A sample reconstruction for the latter case is shown in Figure 5.19. The authors note some confusion as to whether short-wave features in

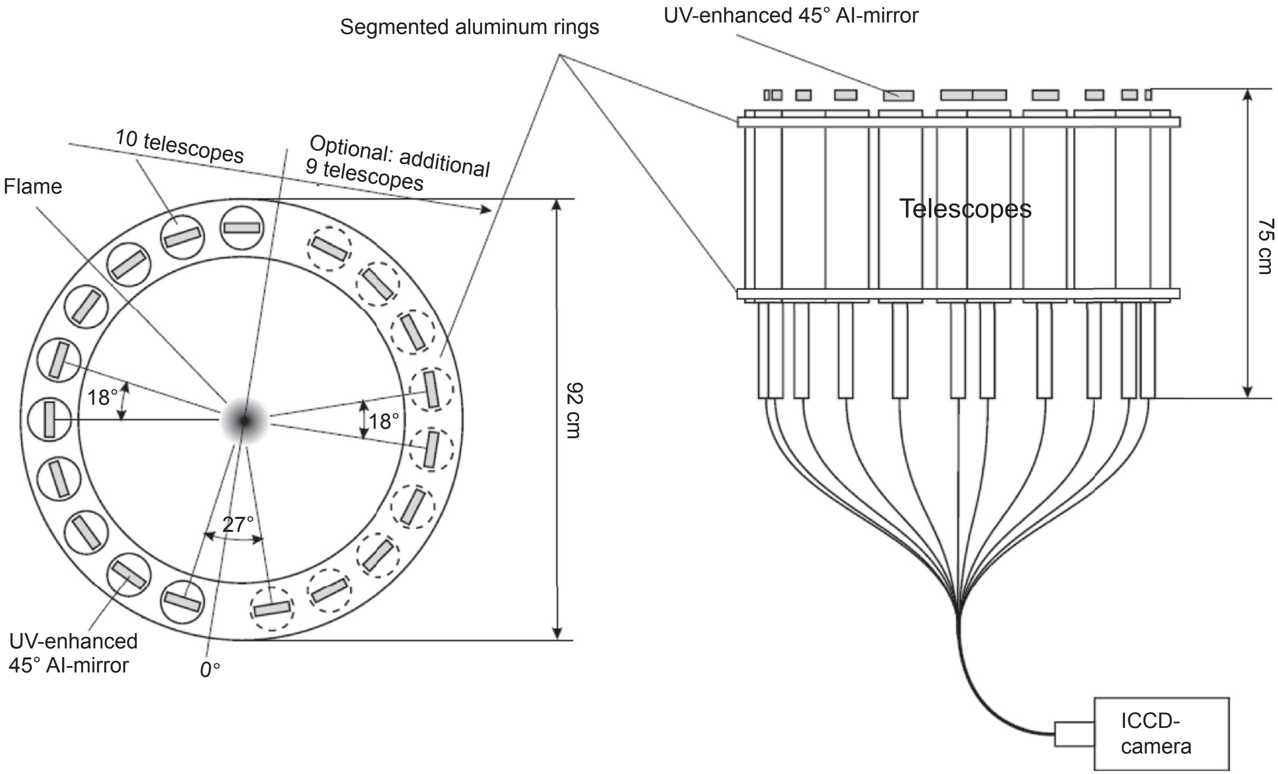
Segmented aluminum rings
UV-enhanced 45° Al-mirror
10 telescopes
Optional: additional 9 telescopes
Flame
18°
18°
27°
0°
UV-enhanced 45° Al-mirror
92 cm
Telescopes
75 cm
ICCD-camera

Figure 5.18 Schematic of the tomography apparatus used to reconstruct OH* chemiluminescence in laboratory-scale laminar and turbulent flames (Anikin et al., 2010; Anikin et al., 2013; Anikin et al., 2012).

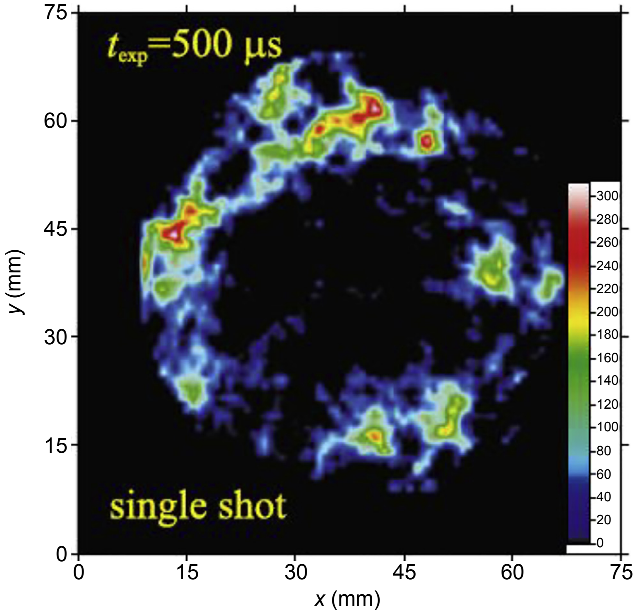

Figure 5.19 Sample reconstruction of OH* chemiluminescence from a lab-scale turbulent diffusion flame (Anikin et al., 2013). The authors note some difficulty distinguishing reconstruction artefacts from short-wavelength turbulent structures.

their reconstructions are authentic turbulent structures or artefacts caused by amplified measurement noise. Most recently, the authors have extended their technique to the simultaneous detection of OH* chemiluminescence and soot incandescence in laminar diffusion flames (Anikin, Suntz, & Bockhorn, 2012).

5.7 Future trends

For more than 50 years, due to health and environmental concerns, there has been continuous legislative pressure on the owners of chemical processes, and on associated equipment manufacturers, to achieve greater control of chemical emissions and their reduction, e.g. in the automotive industry (Official Journal of the European Union, 2009). This has been a major motivating factor for the development of many techniques aimed at imaging the spatial distribution of chemical species in a variety of situations, e.g. Sick (2013). Over the last 20 years, great advances in commercially available photonics and electronics hardware, initially facilitated by the manufacturing technology of the optical communication industry, have stimulated the development of optical CST, as described in the preceding sections. In parallel, the growth and commercialization of several modalities of tomography, e.g. as described in Chapters 1, 2 and 6, and applied in situ to a wide range of engineering problems with associated physical limitations of the measurement arrays deployed, have driven fundamental research in tomographic reconstruction methods and practical algorithms. These advances in the constituent technologies have been used to synthesize substantial improvements in CST, evidenced by the fact that, between 2000 and 2010, CST has gone from a specialty diagnostic in mainly experimental and academic settings to widespread deployment in a diverse range of engineering applications. With many regions of the globe striving for and achieving rapid industrialization, the above legislative pressures will increase and will encompass further industrial sectors, suggesting that CST technology will be exploited further. Moreover, the ongoing development of photonic and electronic hardware is opening up new options, such as the development of all-electronic optical switching systems (Karagiannopoulos et al., 2012) and improvements in MIR systems (Sick, 2013), and confidence in robust CST system development is enhanced greatly by the emergence of rational methods for beam array optimization, as discussed in Section 5.4. Hence, the potential for continuing development of CST methodology and technology is substantial.

To address this range of opportunities, and to focus on key obstacles in the field, a dedicated 1-week workshop on CST took place in Manchester, UK, in November 2012, attended by 43 experts in the field, and their proceedings are now publicly available (MIRAN). In particular, the workshop identified the key opportunities and challenges for a range of chemical reaction systems, with emphasis on combustion plant, and the critical steps for CST technology. The opportunities in front of the CST community, in terms of both ‘applications pull’ and ‘technology push’ are immense: the potential is very clear for CST to make a huge impact on issues such as improved plant design for efficiency and reduced emissions; as a youthful technique, CST clearly stands to gain enormously from exploitation of a huge range of new technologies and methods that have been emerging in other fields. In the following, we present a distilled overview of the findings of the workshop:

- Critical scientific and technological challenges are the driving force for innovation in CST. These challenges range from validation of theoretical models and simulation codes for processes, through the design of process plant, to its optimal control, e.g. for environmental compliance (Scott & McCann, 2005). An example of the last category is the imaging of NH_3 and NO distributions for de-NOx optimization in various fossil fuel combustors (Deguchi, Kamimoto, Kiyota, Choi, & Shim, 2013), which would yield great societal and commercial benefit if successful.
- For many practical applications, it is imperative to extend systems to enable measurement in large vessels, 1-m diameter and larger, such as coal incinerators. Development of robust methods for optical access by many beams (>100) is also a key goal, perhaps exploiting new technologies such as fibre microprocessing and microelectromechanical systems.
- Many new parts of the e.m. spectrum are being opened up for CST by continuing developments in lasers and other light sources, e.g. enabling the exploitation of mid-IR and THz spectroscopy of target species. Hyperspectral methods that probe many species transitions simultaneously, using light sources with inherently broad spectral range, have recently been reported (An et al., 2011; Ma et al., 2013). A fundamental issue that faces the CST community is to achieve the disentanglement of the spatial distribution of temperature from that of target species concentration.

- Challenges in the optoelectronic area include the development of sensitivity to enable CST of species at minor concentrations (<1000 ppm) (e.g. Pal, Ozanyan, & McCann, 2008; Pal & McCann, 2011), or weak absorbers, an example of the latter being O_2, with obvious relevance to combustion systems.
- Progress in inverse mathematics still has much to offer, such as the further use of Bayesian methods, which can ameliorate the underlying ill-posedness of tomographic image reconstruction. This area also has great scope to help establish systematic methods for beam array design. Furthermore, it is important to develop methods to enable robust quantitative determination of spatial resolution, taking account of the sparse beam arrays used.

In addition to the other references cited in this chapter, the proceedings of the above workshop (MIRAN), and references therein, constitute a valuable source of further information. We hope that in this chapter we have demonstrated the excitement and challenges of CST, and strong progress in its development. We have attempted to set out the concepts and the basic technology that will enable substantial further progress in the near future. Given the growing community in CST, we are confident that a similar review in 10 years' time will present an array of achievements that are unimaginable at the present time.

References

Åkesson, E. O., & Daun, K. J. (2008). Parameter selection methods for axisymmetric flame tomography through Tikhonov regularization. *Applied Optics, 47*, 407–416.

Anikin, N. B., Häber, T., Schwamberger, D., Suntz, R., & Bockhorn, H. (2013). Tomographic detection of the 2-dimensional distributions of the OH*-chemiluminescence and the thermal radiation of soot in laminar diffusion flames. *8th Mediterranean combustion symposium, Çeşme, Turkey*.

Anikin, N., Suntz, R., & Bockhorn, H. (2010). Tomographic reconstruction of the OH*-chemiluminescence distribution in premixed and diffusion flames. *Applied Physics B, 100*, 675–694.

Anikin, N. B., Suntz, R., & Bockhorn, H. (2012). Tomographic reconstruction of 2D OH*-chemiluminesence distributions in turbulent diffusion flames. *Applied Physics B, 107*, 591–602.

An, X., Kraetschmer, T., Takami, K., Sanders, S. T., Ma, L., Cai, W., et al. (2011). Validation of temperature imaging by H_2O absorption spectroscopy using hyperspectral tomography in controlled experiments. *Applied Optics, 50*, A29–A37.

Bain, J. R. B., Johnstone, W., Ruxton, K., Stewart, G., Lengden, M., & Duffin, K. (2011). Recovery of absolute gas absorption line shapes using tunable diode laser spectroscopy with wavelength modulation—part 2: experimental investigation. *IEEE Journal of Lightwave Technology, 29*, 987–996.

Bakowski, B., Corner, L., Hancock, G., Kotchie, R., Peverall, R., & Ritchie, G. A. D. (2002). Cavity-enhanced absorption spectroscopy with a rapidly swept diode laser. *Applied Physics B, 75*, 745–750.

Banwell, C. N., & McCash, E. M. (1994). *Fundamentals of molecular spectroscopy* (4th ed.). London: McGraw Hill.

Beiting, E. J. (1992). Fiber-optic fan-beam absorption tomography. *Applied Optics, 31*, 1328–1343.

Bertero, M., & Boccacci, P. (1998). *Introduction to inverse problems in imaging*. Boca Raton, FL: CRC Press.

Cai, W., Ewing, D. J., & Ma, L. (2008). Application of simulated annealing for multispectral tomography. *Computer Physics Communications, 179*, 250−255.

Dasch, C. (1992). One-dimensional tomography: a comparison of abel, onion-peeling, and filtered backprojection methods. *Applied Optics, 31*, 1146−1152.

Daun, K. J. (2010). Infrared species limited data tomography through Tikhonov reconstruction. *Journal of Quantitative Spectroscopy and Radiative Transfer, 111*, 105−115.

Daun, K. J., Waslander, S. L., & Tulloch, B. B. (2011). Infrared species tomography of a transient flow field using kalman filtering. *Applied Optics, 50*, 891−900.

Deguchi, Y., Kamimoto, T., Kiyota, Y., Choi, D., & Shim, J. (2013). Real-time 2D concentration and temperature measurement method using CT tunable diode laser absorption spectroscopy. In *7th world congress on industrial process tomography, WCIPT7, Krakow, Poland*.

Drescher, A. C., Gadgil, A. J., Price, P. N., & Nazaroff, W. W. (1996). Novel approach for tomographic reconstruction of gas concentration distributions in air: use of smooth basis functions and simulated annealing. *Atmospheric Environment, 30*, 929−940.

Duffin, K., McGettrick, A. J., Johnstone, W., Stewart, G., & Moodie, D. G. (2007). Tunable diode laser spectroscopy with wavelength modulation: a calibration-free approach to the recovery of absolute gas absorption line shapes. *Journal of Lightwave Technology, 25*, 3114−3125.

Fawcett, B. L., Parkes, A. M., Shallcross, D. E., & Orr-Ewing, A. J. (2002). Trace detection of methane using continuous wave cavity ring-down spectroscopy at 1.65 micrometers. *Physical Chemistry Chemical Physics, 4*, 5960−5965.

Fischer, M. L., Price, P. N., Thatcher, T. L., Schwalbe, C. A., Craig, M. J., Wood, E. E., et al. (2001). Rapid measurements and mapping of tracer gas concentrations in a large indoor space. *Atmospheric Environment, 35*, 2837−2844.

FLITES: Fibre-laser imaging of gas turbine exhaust species (Online). Available at http://flites.eu.

Garcia-Stewart, C. A., Polydorides, N., Ozanyan, K. B., & McCann, H. (2003). Image reconstruction algorithms for high-speed chemical species tomography. In *3rd world congress on industrial process tomography, Baniff, AB*.

Gibson, A. P., Hebden, J. C., & Arridge, S. R. (2005). Recent advances in diffuse optical imaging. *Physics in Medicine and Biology, 50*, R1−R43.

Gordon, R., Bender, R., & Herman, T. G. (1970). Algebraic reconstruction techniques (ART) for three-dimensional electron microscopy and X-ray photography. *Journal of Theoretical Biology, 29*, 471−481.

Hadamard, J. S. (1923). *Lectures on Cauchy's problem in linear partial differential equations* (Lectures Given at Yale University). New Haven, CT: Yale University Press.

Haisch, C. (2012). Optical tomography. *Annual Review of Analytical Chemistry, 5*, 57−77.

Hansen, P. C. (1999). *Rank deficient and discrete ill-posed problems: numerical aspects of linear inversion*. Philadelphia, PA: SIAM.

Hansen, P. C., & O'Leary, D. P. (1993). The use of the L-curve in the regularization of discrete ill-posed problems. *SIAM Journal of Scientific Computing, 14*, 1487−1503.

Heiss, M., Bobicic, N., Lauer, T., Geringer, B., & Schmuck-Soldan, S. (2012). A detailed analysis of the initiation of abnormal combustion with reaction kinetics and multi-cycle simulation In *Proceedings of the FISITA 2012 world automotive congress (Lecture notes in electrical engineering volume 190)* (pp. 1007−1018). Berlin: Springer.

Hindle, F. P., Carey, S. J., Ozanyan, K., Winterbone, D. E., Clough, E., & McCann, H. (2001). Measurement of gaseous hydrocarbon distribution by a near-infrared absorption tomography system. *Journal of Electronic Imaging, 10*, 593−600.

Ibrahim, S., Green, R. G., Dutton, K., Evans, K., Abdul Rahim, R., & Goude, A. (1999). Optical sensor configurations for process tomography. *Measurement Science and Technology, 10*, 1079−1086.

Karagiannopoulos, S., Cheadle, E. M., Wright, P., & McCann, H. (2012). Multiwavelength diode-laser absorption spectroscopy using external intensity modulation by semiconductor optical amplifiers. *Applied Optics, 51*, 8057−8067.

Klingbeil, A. E., Jefferies, J. B., & Hanson, R. K. (2007). Temperature-dependent mid-IR absorption spectra of gaseous hydrocarbons. *Journal of Quantitative Spectroscopy and Radiative Transfer, 107*, 407−420.

Kluczynski, P., & Axner, O. (1999). Theoretical description based on Fourier analysis of wavelength modulation spectrometry in terms of analytical and background signals. *Applied Optics, 38*, 5803−5815.

Kluczynski, P., Gustafsson, J., Lindberg, A., & Axner, O. (2001). Wavelength modulation absorption spectrometry — an extensive scrutiny of the generation of signals. *Spectrochimica Acta Part B, 56*, 1277−1354.

Kluczynski, P., Lindberg, A., & Axner, O. (2001). Background signals in wavelength-modulation spectrometry by use of frequency-doubled diode-laser light. II. Experiment. *Applied Optics, 40*, 794−805.

Kluczynskki, P., Lindberg, A., & Axner, O. (2001). Background signals in wavelength modulation spectrometry with frequency-doubled diode-laser light I. theory. *Applied Optics, 40*, 783−793.

Kosterev, A., Wysocki, G., Bakhirkin, Y., So, S., Lewicki, R., Fraser, M., et al. (2008). Application of quantum cascade lasers to trace gas analysis. *Applied Physics B, 90*, 165−176.

Kranendonk, L. A., & Sanders, S. T. (2005). Optical design in beam steering environments with emphasis on laser transmission measurements. *Applied Optics, 44*, 6762−6772.

Landweber, L. (1951). An iterative formula for Fredholm integral equations of the first kind. *American Journal of Mathematics, 73*, 615−624.

Linne, M. A. (2002). *Spectroscopic measurement: An introduction to the fundamentals*. London: Academic Press.

Lipponen, A., Seppänen, A., Hämäläinen, J., & Kaipio, J. P. (2010). Nonstationary inversion of convection−diffusion problems—recovery from unknown nonstationary velocity fields. *Inverse Problems and Imaging, 4*, 463−483.

Lipponen, A., Seppänen, A., & Kaipio, J. P. (2010). Reduced-order estimation of nonstationary flows with electrical impedance tomography. *Inverse Problems, 26*, 074010 (20 pages).

Lipponen, A., Seppänen, A., & Kaipio, J. P. (2011). Nonstationary approximation error approach to imaging of three-dimensional pipe flow: experimental evaluation. *Measurement Science and Technology, 22*, 104013.

Liu, X., Zhou, X., Jeffries, J. B., & Hanson, R. K. (2007). Experimental study of H_2O spectroscopic parameters in the near-IR (6940−7440 cm^{-1}) for gas sensing applications at elevated temperature. *Journal of Quantitative Spectroscopy and Radiative Transfer, 103*, 565−577.

Ma, L., Li, X., Sanders, S. T., Caswell, A. W., Roy, S., Plemmons, D. H., et al. (2013). 50-kHz-rate 2D imaging of temperature and H_2O concentration at the exhaust plane of a J85 engine using hyperspectral tomography. *Optics Express, 21*, 1152−1162.

Menke, W. (1989). *Geophysical data analysis: Discrete inverse theory*. San Diego, CA: Academic Press.

Mihalcea, R. M., Baer, D. S., & Hanson, R. K. (1997). Diode laser sensor for measurements of CO, CO_2, and CH_4 in combustion flows. *Applied Optics, 36*, 8745−8752.

MIRAN (Manchester image reconstruction and analysis) chemical species tomography workshop (Online). Available at http://www.mims.manchester.ac.uk/CSTworkshop/programme.php.

Morozov, A. V. (1966). On the solution of functional equations by the method of regularization. *Soviet Math. Dokl., 7*, 414−417.

Official Journal of the European Union. (2009). Regulation (EC) no 443/2009 of the European parliament and of the council of 23 April 2009: setting emission performance standards for new passenger cars as part of the community's integrated approach to reduce CO_2 emissions from light-duty vehicles.

Osher, S., & Sethian, J. A. (1988). Fronts propagating with curvature-dependent speed: algorithms. *Journal of Computational Physics, 79*, 12–49.

Ozanyan, K. B., Wright, P., Stringer, M. R., & Miles, R. E. (2011). Hard-field THz tomography. *IEEE Sensors Journal, 11*, 2507–2513.

Pal, S., Ozanyan, K. B., & McCann, H. (2008). A computational study of tomographic measurement of carbon monoxide at minor concentrations. *Measurement Science and Technology, 19*, 094018.

Pal, S., & McCann, H. (2011). Auto-Digital Gain Balancing: A New Detection Scheme for High-Speed Chemical Species Tomography of Minor Constituents. *Measurement Science and Technology, 22*, 115304.

Price, P. N., Fischer, M. L., Gadgil, A. J., & Sextro, R. G. (2001). An algorithm for real-time tomography of gas concentrations using prior information about spatial derivatives. *Atmospheric Environment, 35*, 2827–2835.

Richter, M., Li, Z., & Alden, M. (2007). Application of two-phonon laser-induced fluoresence for single shot visualization of carbon monoxide in a spark-ignited engine. *Applied Spectroscopy, 61*, 1–5.

Rothman, L., Gordon, I., Barbe, A., Benner, D., Bernath, P., Birk, M., et al. (2009). The HITRAN 2008 molecular spectroscopic database. *Journal of Quantitative Spectroscopy and Radiative Transfer, 110*, 533–572.

Santoro, R. J., Semerjian, H. G., Emmerman, P. J., & Goulard, R. (1981). Optical tomography for flow field diagnostics. *IJHMT, 24*, 1139–1150.

Scott, D. M., & McCann, H. (2005). *Process imaging for automatic control.* Boca Raton: CRC Press.

Seppänen, A., Heikkinen, L., Savolainen, T., Voutilainen, A., Somersalo, E., & Kaipio, J. P. (2007). An experimental evaluation of state estimation with fluid dynamical models in process tomography. *Chemical Engineering Journal, 127*, 23–30.

Seppänen, A., Vauhkonen, M., Vauhkonen, P. J., Somersalo, E., & Kaipio, J. P. (2001). State estimation with fluid dynamical evolution models in process tomography. *Inverse Problems, 17*, 467–483.

Seppänen, A., Voutilainen, A., & Kaipio, J. P. (2009). State estimation in process tomography-reconstruction of velocity fields using EIT. *Inverse Problems, 25*, 085009.

Sick, V. (2013). High speed imaging in fundamental and applied combustion research. *Proceedings of the Combustion Institute, 34*, 3509–3530.

Sonnenfroh, D. M., & Allen, M. G. (1997). Observations of CO and CO_2 absorption near 1.57 micrometers with an external-cavity diode laser. *Applied Optics, 36*, 3298–3300.

Teichert, H., Fernholz, T., & Ebert, V. (2003). Simultaneous in situ measurement of CO, H_2O and gas temperatures in a full-sized coal-fired power plant by near-infrared diode lasers. *Applied Optics, 42*, 2043–2051.

Terzija, N. (2011). Wavelet-based image reconstruction for hard-field tomography with severely limited data. *IEEE Sensors Journal, 11*, 1885–1893.

Terzija, N., Davidson, J. L., Garcia-Stewart, C. A., Wright, P., Ozanyan, K. B., Pegrum, S., et al. (2008). Image optimization for chemical species tomography with an irregular and sparse beam array. *Measurement Science and Technology, 19*, 094007.

Terzija, N., Karagiannopoulos, S., Begg, S., Wright, P., Ozanyan, K., & McCann, H. (2014). Tomographic imaging of the liquid and vapour fuel distributions in a single-cylinder direct injection gasoline engine. *International Journal of Engine Research*. http://dx.doi.org/10.1177/1468087414544178 (in press).

Tikhonov, A. N., & Arsenin, V. Y. (1977). *Solution of ill-posed problems*. Washington DC: Winston and Sons.

Twynstra, M. G., & Daun, K. J. (2013). Laser-absorption tomography beam arrangement optimization using resolution matrices. *Applied Optics, 51*, 7059−7068.

Twynstra, M. J., Daun, K. J., & Waslander, S. W. (2014). Line-of-sight-attenuation chemical species tomography through the level set method. *Journal of Quantitative Spectroscopy and Radiative Transfer, 143*, 25−34.

Verhoeven, D. (1993). Limited data computed tomography algorithms for the physical sciences. *Applied Optics, 32*, 3736−3754.

Wright, P., Ozanyan, K. B., Carey, S. J., & McCann, H. (2005). Design of high-performance photodiode receivers. *IEEE Sensors Journal, 5*, 281−288.

Wright, P., Terzija, N., Davidson, J. L., Garcia-Castillo, S., Pegrum, S., Colbourne, S., et al. (2010). High speed chemical species tomography in a Multi-cylinder automotive engine. *Chemical Engineering Journal, 158*, 2−10.

York, T. A., McCann, H., & Ozanyan, K. B. (2011). Agile sensing systems for tomography. *IEEE Sensors Journal, 11*, 3086−3105.

X-ray computed tomography

6

U. Hampel
Helmholtz-Zentrum Dresden-Rossendorf, Dresden, Germany; Technische Universität Dresden, Dresden, Germany

6.1 Introduction

The discovery of X-rays by Wilhelm Conrad Röntgen in 1895 was the starting point of an enormously successful development of medical and technical imaging technologies, which has continued through the present day. Röntgen found by chance, in his experimental studies with cathode rays, a new type of electromagnetic radiation. He found that this heretofore unknown radiation penetrates most materials, which are otherwise opaque for visible light, and that its attenuation is rather linear. The new X-rays were found to excite light emission in inorganic crystals and to expose photography plates and films as visible light does. The new radiation appeared particularly attractive for imaging of internal body structures. Röntgen's discovery rapidly led to the development of the first X-ray imaging devices, including X-ray tubes, X-ray films, and, later, X-ray detectors. With the advancements in computer technology in the 1960s and 1970s came another quantum leap in X-ray imaging technology. Computed tomography (CT) for the first time provided physicians with superposition-free cross-sectional images of internal body structures. Again this technique was pioneered by the use of X-rays.

Today X-ray CT is the most widely used imaging technique in medicine and nondestructive testing. In recent years it has also found its way into process diagnostics. One particular driver is the continuing interest of scientists and engineers to study multiphase flows in energy and process engineering applications (Heindel, 2011). Such flows of gases, liquids, and solids occur in chemical reactors, in coolant circuits of power plants, in heat exchangers and hydrodynamic machines, and also in pipelines and process equipment of the petroleum industry. However, process engineering is a field and market with needs and demands that hardly coincide with those of medicine and nondestructive testing. The main commonality is the need for a nonintrusive spatially resolving measurement technique that gives insight into otherwise nonaccessible and nondetectable structures and processes. While in medicine the key requirement is good contrast for tissue structures in the millimeter and submillimeter range at as low an energy dose as possible, in nondestructive testing the major focus is on highest spatial resolution, which may be compromised by long scanning times. The permissible energy dose here has almost no limitation. Process tomography poses completely different challenges. Industrial process conditions are often hostile and hazardous. Typical are high pressures and temperatures as well as aggressive fluids. Process vessels are commonly large, have thick metallic

Industrial Tomography. http://dx.doi.org/10.1016/B978-1-78242-118-4.00006-X
Copyright © 2015 Elsevier Ltd. All rights reserved.

walls, and often have complex internal structures, which limits the accessibility for instrumentation. Moreover, transient flow conditions in processes make fast imaging capabilities desirable. Radiation protection measures must be provided at the place of installation, which is often difficult and expensive, especially when hard X-rays are being used. Yet the costs of process measurement techniques are in general required to be low. Here, radiation-based measurement techniques have clear disadvantages. X-ray equipment is often bulky and expensive, and radiation protection efforts additionally increase complexity and costs. However, with respect to spatial and temporal resolution as well as capability to penetrate denser construction materials, X-rays are superior to any other type of signal carrier. Therefore, continued progress has been made in the recent past to develop this technology for laboratory and industrial applications.

X-ray attenuation in a material depends on the material's density and atomic number. Hence, X-rays can discriminate structures via their different attenuation, which mostly comes from different densities. Therefore X-ray imaging is well applicable for the visualization of phase distributions in gas—liquid two-phase flow, for instance in chemical multiphase reactors, or for particle flows in a fluidized bed. Another example is the measurement of three-phase gas—water—oil flow in a pipeline, for example, in mineral oil processing. In some rare cases, X-rays may disclose properties other than attenuation. Phase-contrast imaging with coherent X-rays enhances boundaries between areas of minute refractive index differences and is of great value in X-ray microscopy and microtomography (Waelchli, von Rohr, Stampanoni, 2005). On the other hand, high-energy X-rays may be used to excite secondary particles or radiation, which can be used to image certain other material properties than density and atomic number. As in medicine, for process diagnostics one therefore needs to critically assess if X-rays are an appropriate means to obtain the required information from the process. In multiphase flows X-rays are helpful to discriminate phases as long as they possess sufficient radiological contrast. For the discrimination between gas, liquid, and solid content of a flow, X-rays are superiorly suited. Discriminating solid phases and liquid phases is also possible. When density differences between the flow constituents are low, it might be helpful to consider lower X-ray energies and even multienergy techniques. For lower X-ray energies the photoabsorption becomes the dominant process of radiation—matter interaction; this is, unlike Compton scattering for higher energies, strongly dependent on atomic number and therefore on elementary species composition. However, since lower X-ray energies have less overall penetration capability, there are also physical limits to this approach. In cases where contrast of species is too low, addition of contrast agents containing chemical elements of high atomic number, such as barium or iodine, is an option. Moreover, such contrast agents can be deliberately used as flow tracers, for instance to study dispersion effects in multiphase flows. Limiting factors here are the stability and solubility of the tracer substances under given thermodynamic and chemical conditions. Also, as a matter of course particles of higher attenuation may be added to particulate flows to gain contrast (Seeger, Kertzscher, Affeld, & Wellnhofer, 2003). Wherever there is no variation in the attenuation properties of the process constituents, X-rays are of no use. This applies, for instance, to pure single-phase flows, gas mixture flows, and very dilute multiphase flows with dispersed particles, droplets, or bubbles. There, as in medicine, complementary methods must be considered. Such methods may be emission tomography, electrical tomography, magnetic tomography, optical tomography, or magnetic resonance imaging, introduced in other chapters of this book.

6.2 Variants of X-ray computed tomography for process applications

Originally, CT imaging was understood as the reconstruction of a parameter distribution within a thin slice of an object from a set of line integrals of this very parameter. Theoretically, all possible line integral values are needed for an accurate reconstruction. But as with any frequency resolution-limited technical sampling process, a subset of line integrals with a homogeneous distribution is sufficient for an approximate reconstruction. In X-ray tomography the line integrals are obtained by linear attenuation measurements with a set of narrow X-ray beams (Kak & Slaney, 1988). Practically, such beams are formed by the emission area of a focal spot in an X-ray tube and the active area of a radiation detector on the other side of the object. To obtain a "full set" of line integrals, the X-ray tube and detector must be subsequently placed into different positions in space. This can be achieved in multiple ways. Figure 6.1 shows different scanning principles of increasing complexity. Historically, the configurations were classified as different generations of X-ray tomography scanners (Kalender, 2005). The simplest arrangement is the one with a single beam, for which it is necessary to compile the line integrals sequentially by a combination of rotational and translational movements of the source–detector compound. An improvement in scanning speed can be achieved by using multiple

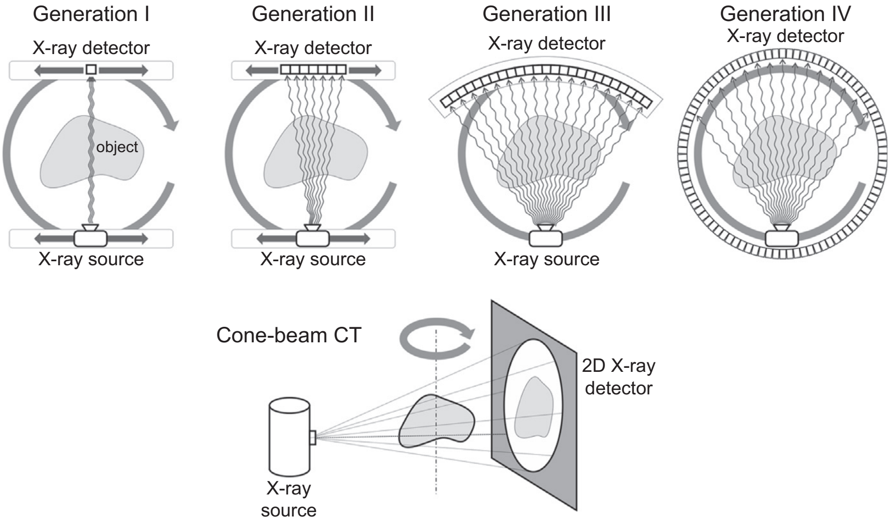

Figure 6.1 X-ray tomography scanning principles.

sources and detectors. This gives a large number of potential spatial—temporal scanning modes. Usually, multiple detectors are more affordable than multiple sources. In generation II scanners more detectors are used but still the translation-rotation scanning has to be sustained. A rotating single source and multiple detector arrangement of generation III is the most common scanner configuration in X-ray CT today. Here, a single X-ray source and an arc detector, made of many small detector elements, are used. The radiation fan fully encloses the object, such that only rotation of the source—detector compound, or alternatively the object, is required. In principle this setup can be extended toward incorporation of a second or even more X-ray sources, for instance sources with different X-ray energy. Generation III scanners have been widely used in multiphase flow studies, for example, to measure gas holdups in gas—liquid contactors (Toye, Marchot, Crine, Pelsser, & L'Homme, 1998), solids distributions in fluidized beds (Deza, Franka, Battaglia, & Heindel, 2009), or void distributions in heated rod bundle assemblies (Inoue et al., 1995). The generation IV arrangement foresees a rotating source and a fixed circular detector arrangement. For mechanically moving X-ray sources this concept has no particular advantage, so it did not find its way into existing technical solutions. However, it is inherently required for electron beam X-ray tomography, as will be shown further below.

So far, the discussed arrangements allow a two-dimensional (2D) reconstruction of the linear attenuation values in exactly the plane where source and detector are operated. Commonly, this is referred to as transversal scanning. 3D imaging would mathematically require a full set of line integrals in 3D space, which is technically very difficult to achieve (Grangeat, 1991). It can be shown, however, that very good approximation of this ideal sampling scheme can be made by using a rotating compound of a point X-ray source and a 2D X-ray detector, as is also shown in Figure 6.1. Since the detector records X-ray attenuation along lines within a radiation cone, this type of tomography is frequently referred to as cone-beam tomography. Because of its approximate nature, reconstruction will produce some deviations from the physical parameter distribution, especially in the off-plane regions of the image cube. This has to be considered when using the data for further analysis.

The above classification of tomography arrangements shall serve as a guide to what principle arrangements and scanning schemes are currently used in X-ray process tomography. As we will see in the further course of this chapter, both generation III and IV scanning principles as well as transversal and cone-beam tomography do exist. The salt in the soup, of course, are the details of existing and innovative technical solutions for X-ray generation, X-ray detection, and scanning principles. Hence the following sections will be devoted to the basic physical and technical principles involved in X-ray process tomography.

6.3 X-ray sources for process tomography

Physically, X-rays emerge whenever charged particles of energy larger than about 1 keV are stopped in a material. In technical X-ray tubes, electrons are accelerated by an electrostatic field over a short distance of a few centimeters and are then shot into the anode material. On a microscopic scale, deceleration of electrons in the Coulomb field of the target nuclei leads to emission of Bremsstrahlung with a continuous-emission energy spectrum between zero and the maximum electron energy $E_{\max} = eU_{\text{acc}}$, which is the product of unit charge and acceleration voltage. In X-ray tubes the lower part of the spectrum is damped due to absorption of low-energy photons in the anode and in the wall of the tube. Within this energy spectrum additional emission lines from characteristic radiation appear. This characteristic radiation arises when impinging electrons knock out bound inner shell electrons of target atoms and outer shell electrons refill the inner shell vacancies under emission of fluorescent X-ray photons, whose energy corresponds to the energy gap between the respective electron orbitals. In many process tomography applications conventional X-ray tubes with such a polyenergetic spectrum are used (Figure 6.2).

Figure 6.3 shows schematic drawings of a fixed anode and a rotating anode X-ray tube along with photographs of two technical X-ray tube assemblies. At the cathode side of an X-ray tube free electrons are generated by thermionic emission from a heated tungsten filament. Filament current control allows adjustment of the electron current and hence X-ray power. The electrical field in front of the cathode is shaped by a Wehnelt cylinder in such a way that the electrons are focused into a small spot on the opposite anode. For tubes with smaller loss power, that is, up to 10 kW, a fixed anode configuration is commonly used. There, the anode is a composite, consisting of a heavy metal conversion target embedded in a bulk copper block for good conductive heat transfer to the environment. In rotating anode tubes, which are made for higher power dissipation, the anode is a round plate-like composite body. Its upper layer is a rhenium–tungsten–molybdenum alloy with a high melting point. Underneath is a pure molybdenum layer, which gives the compound good thermomechanical strength, and further below is a graphite layer, which provides high temporary heat storage capacity. Radial slits in the anode plate provide increased thermomechanical resistance under the high centrifugal loads, which occur when the anode is rotating. During

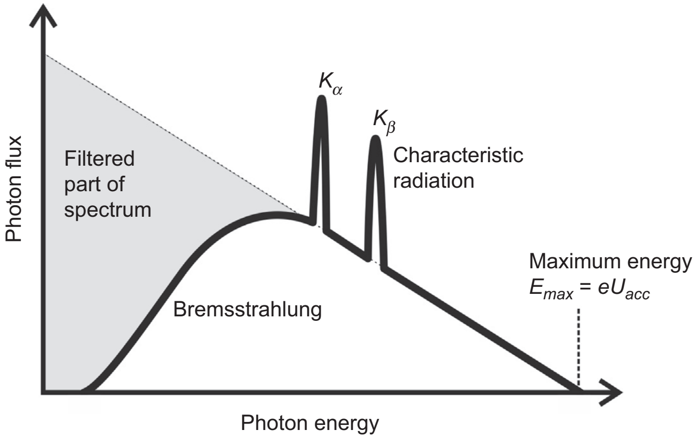

Figure 6.2 Energy spectrum of an X-ray tube.

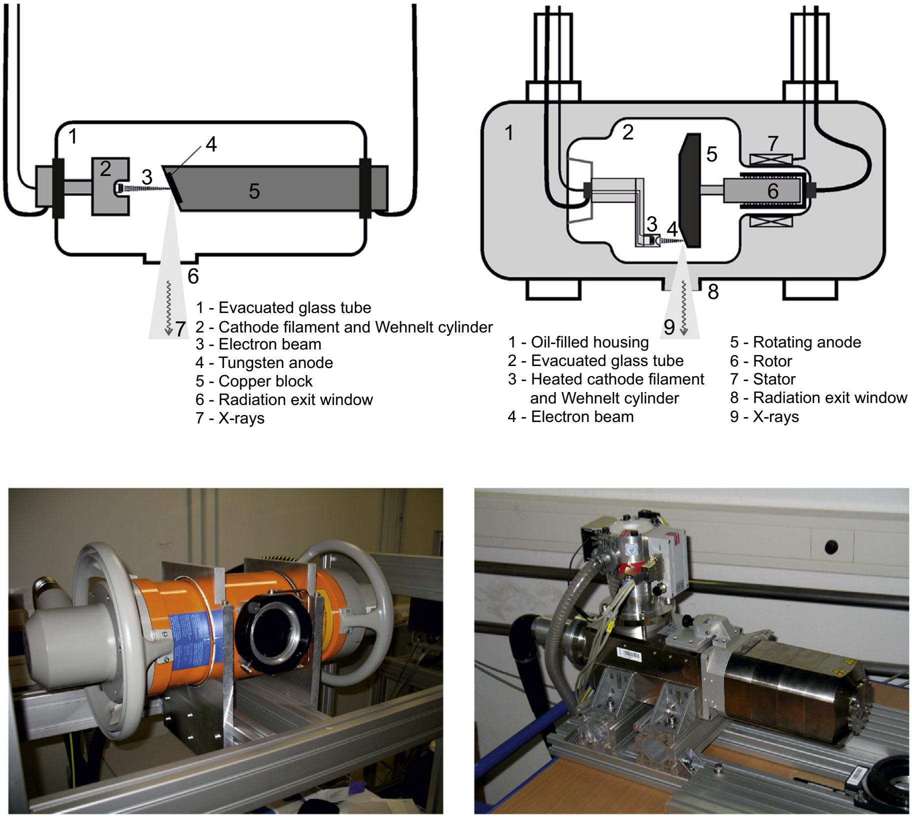
1
4
2
3
5
6
7
1 - Evacuated glass tube
2 - Cathode filament and Wehnelt cylinder
3 - Electron beam
4 - Tungsten anode
5 - Copper block
6 - Radiation exit window
7 - X-rays
1
2
5
7
6
3
4
8
9
1 - Oil-filled housing
2 - Evacuated glass tube
3 - Heated cathode filament and Wehnelt cylinder
4 - Electron beam
5 - Rotating anode
6 - Rotor
7 - Stator
8 - Radiation exit window
9 - X-rays

Figure 6.3 X-ray tubes: the top row shows schematics of a fixed anode and a rotating anode X-ray assembly. The bottom row depicts an industrial 450 kV X-ray radiator (left) and a 140 kV/400 W microfocus X-ray tube (right).

operation the anode plate is rotated at high speed of up to 9000 rpm (in some tubes even higher). It is driven by an electromotor whose stator is outside the tube housing behind the anode. Anode and cathode are supplied with power from a high-voltage generator. To ease electrical isolation, tubes are typically operated in a bipolar mode with $\pm\frac{1}{2}U_{\mathrm{acc}}$ at both terminals. The focal spot of an X-ray tube has the demagnified bar-like shape of the cathode filament. In the direction of the X-ray window this focal spot appears reduced in length due to the oblique face of the anode plate. The typical physical size of the spot in industrial X-ray tubes is between $0.5 \times 6\,\mathrm{mm}^2$ and $1.2 \times 12\,\mathrm{mm}^2$. The tube's electrical loss power, which can be up to more than 100 kW, is dissipated mainly as heat in this area. To cope with the high power density, different heat transfer and storage mechanisms cooperate inside the tube. By rotating the anode the heat produced in the focal spot is distributed across a ring. Heat conduction into the anode metal and subsequently into the graphite support serves to reduce thermal power density on the anode surface. The main heat removal mechanism is radiative heat transfer into a cooling oil bath outside the glass envelope of the tube, which improves with the fourth power of temperature (Stefan–Boltzmann law). A smaller part is conductively removed via the anode shaft. Technical X-ray tubes are moreover enclosed by a protective lead housing with an aluminum window for X-ray extraction. X-ray tube supply electronics allow adjustment and control of tube power, tube voltage, and total exposure time. In addition, it should be noted that modern medical X-ray CT scanners utilize rotating envelope tubes. In such tubes the anode is firmly connected with the metallic tube envelope such that heat is transferred efficiently by conductance to the outer oil bath. There, not only the anode but the whole envelope is rotated. The cathode in this arrangement is on the tube axis and a magnetic coil arrangement deflects the electrons into the focal spot on the anode plate (for more details see Schard et al., 2004).

Using industrial X-ray tubes for X-ray inspection and process tomography is quite common. Those types of radiators are well developed and optimized for many applications. The energy range of such tubes is from a few kV up to 450 kV tube voltage. The upper limit is mainly given by increasing technical complexity and effort for high-voltage isolation. High-power X-ray tubes are available with powers above 100 kW and special thermal designs. For high-resolution imaging tubes have to achieve small focal spot sizes. Such microfocus tubes are available with focal spot sizes down to 1 μm. Because of limited power dissipation capacity in the anode material, the average X-ray power of such tubes is accordingly small, between a few μW and a few hundred watts. Therefore, high-resolution CT imaging with X-ray tubes is always connected with long scanning times, which in turn means that only time-averaged phase fraction distributions of flows can be obtained (Moreno-Atanasio, Williams, & Jia, 2010).

Using a commercial X-ray tube for tomography applications inevitably requires that either the tube or the object of investigation has to be mechanically manipulated to generate the projection data required for reconstruction. Fast tomography, as will be discussed further below, has to abandon this principle, since fast mechanical motion of a heavy X-ray tube or an object has strict physical limits. In principle, there exist three options to avoid mechanical motion (Johansen, Hampel, & Hjertaker, 2010). One way is to use multiple switched X-ray tubes, which requires special nonconventional tube designs. Such solutions were, for instance, proposed by Hori (Hori, Fujimoto, Kawanishi, & Nishikawa, 1998). Another choice is to arrange a limited number of collimated X-ray tubes in such a way that they form disjointed X-ray fans in space (Mudde, 2011). This assures that the detectors placed in the same plane receive radiation from only one source and hence the sources can be operated simultaneously. However, the severe undersampling of projections in this case leads to images with rather low resolution.

Another option to realize a fast-moving X-ray source is to use a steered electron beam (Fischer et al., 2008). This, however, requires a technically different concept of an X-ray source, namely an electron beam generator coupled with a suitable X-ray target. Such a scanner is shown in Figure 6.4. As in conventional X-ray tubes, the electron current is produced by a heated cathode. A Wehnelt modulator is used to shape the electrostatic field to form the electron beam in front of the anode. Moreover, the Wehnelt electrode is additionally used to adjust the electron current by a negative counter-field that controls the electron penetration to the anode. It can be used either to adjust the beam current or to

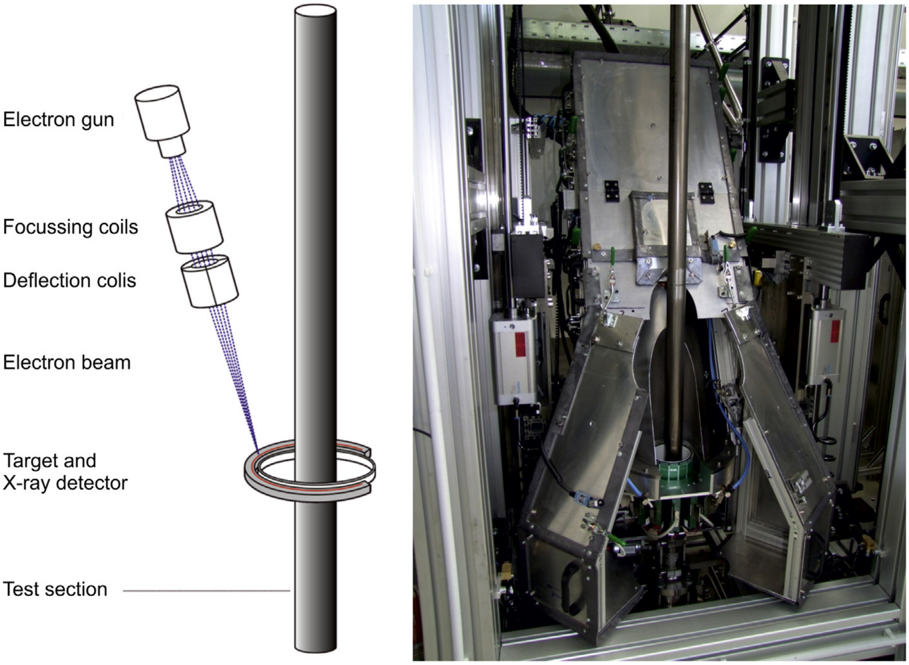

Figure 6.4 Ultrafast scanned electron beam X-ray tomograph ROFEX (Fischer et al., 2008).

switch the beam current quickly on and off. The anode, unlike in X-ray tubes, has a penetration hole, which allows the electrons to pass the anode and travel through the field-free space behind it. Here the electrons are no longer accelerated but move toward a target in the tomograph head at constant near-relativistic speed $v_{\mathrm{el}} = \sqrt{2eU_{\mathrm{acc}}/m_e}$. Behind the anode an electromagnetic lens system is arranged. This system comprises various electron optics elements, which are required for forming, focusing, and deflecting the beam. Among them is an astigmator to remove beam shape asymmetries, a static focusing coil, lenses for dynamic beam refocusing, and an x−y deflection system for beam steering. The target is a circular tungsten body located at the very bottom of the scanner head. By means of the electron beam optics the beam is periodically run across the target. Though simple in principle, this concept requires numerous additional technical features, such as beam diagnostics, vacuum system, target cooling, advanced temperature control, safety beam dump, and X-ray power reference measurements, whose description are beyond the scope of this book.

For reasons of completeness, it should be mentioned that higher X-ray powers can be achieved with other types of electron accelerators. For X-ray energies up to 10 MeV electrostatic accelerators of dynamitron type, traveling wave tube accelerators, microtrons, or betatrons may be employed (Hampel et al., 2012). For highest photon flux, coherent synchrotron radiation sources are of special importance (Berg et al., 2013). However, such X-ray sources are today rarely used for process tomography applications, mainly due to their complexity, immobility, and costs.

6.4 X-ray detectors

For X-ray detection in imaging applications, either scintillator-based detectors or room-temperature semiconductor detectors are being used (Shefer et al., 2013; van Eijk, 2002; Del Sordo et al., 2009). The physical conversion principles are illustrated in Figure 6.5. In an inorganic scintillator detector, interacting X-ray photons excite electrons in the valence band of the scintillation crystal lattice toward the conduction band or form excitons (loosely coupled electron—hole pairs). After some time of existence these electrons or excitons recombine. Activators, which are brought into the lattice in small quantities, deliver intermediate electron state levels at which recombination results in emission of fluorescent light. Examples for technically used scintillator materials are sodium iodine [NaI(Tl)] or cesium iodine [CsI(Tl)] (doped with thallium as activator), bismuth germanium oxide (BGO), cadmium tungstate ($CdWO_4$), or polycrystalline ceramic rare-earth scintillators. In pixel detectors each scintillator crystal is coupled to a photodiode, which converts the light into an electrical charge.

A direct way of converting X-ray photons into electrical charge is realized in room-temperature semiconductor detectors, such as cadmium telluride (CdTe) or cadmium

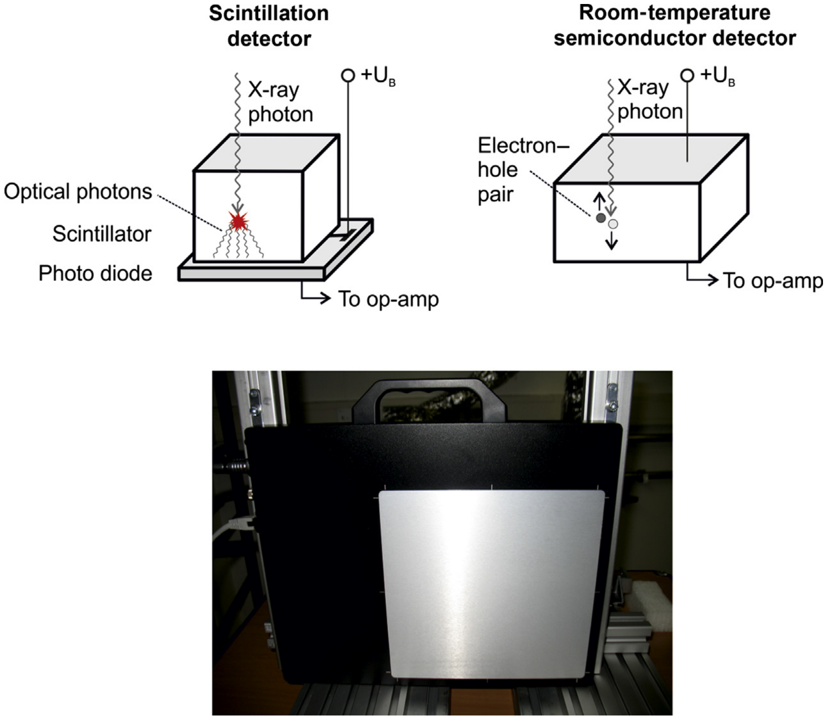
Scintillation detector
X-ray photon
+U$_B$
Optical photons
Scintillator
Photo diode
To op-amp
Room-temperature semiconductor detector
X-ray photon
+U$_B$
Electron–hole pair
To op-amp

Figure 6.5 X-ray detector principles (left) and photography of a 2D X-ray flat panel imager with active area 20 × 20 cm, 1024 × 1024 pixels, pixel size 200 × 200 µm, and 25 Hz/16 bit read-out.

zinc telluride (CdZnTe) detectors. They are wide (1.44–1.57 eV) band-gap semiconductors with high atomic number and density and thus good quantum efficiency, that is, capability to convert X-ray photons within a given detector volume. In such semiconductor detectors electron–hole pairs are directly produced from interacting X-rays. While room-temperature semiconductor detectors generally have better overall quantum efficiency compared to scintillation detectors, they have some disadvantages with respect to stability, especially in high-flux conditions, due to polarization effects induced by charge-trapping. In X-ray imaging applications, especially for fast imaging techniques, the X-ray photon flux is often rather high. Therefore X-ray detectors are commonly operated in current mode. That is, the charge delivered by the detector is immediately converted by a transimpedance amplifier into a continuous voltage signal. The bandwidth of this preamplifier is set to a value that fulfills the antialiasing requirements of the subsequent sampling stages. In some particular applications with low photon flux and longer measurement times, pulse processing might be more appropriate. There the detector's preamplifier is operated as a charge-sensitive amplifier, which generates an electrical pulse signal for each converted X-ray photon. X-ray intensities are then measured by counting pulses (Figure 6.6).

Whereas for transversal 2D tomography applications detector pixel arrangements in the form of custom-made linear, arched, or circular arrays are used, in cone-beam tomography often commercial planar imaging detectors are utilized (Figure 6.5). Such 2D flat-panel detectors consist of a plate scintillator for X-ray to optical photon conversion, which is coupled to a photodiode matrix with a special read-out circuitry. Such detector arrays were originally developed for digital radiography in medicine. They have a high spatial resolution and size (detector panels with 4 megapixels with 0.2 mm pitch are available) but are rather slow regarding imaging speed. Other options for 2D detectors are digital X-ray image intensifiers.

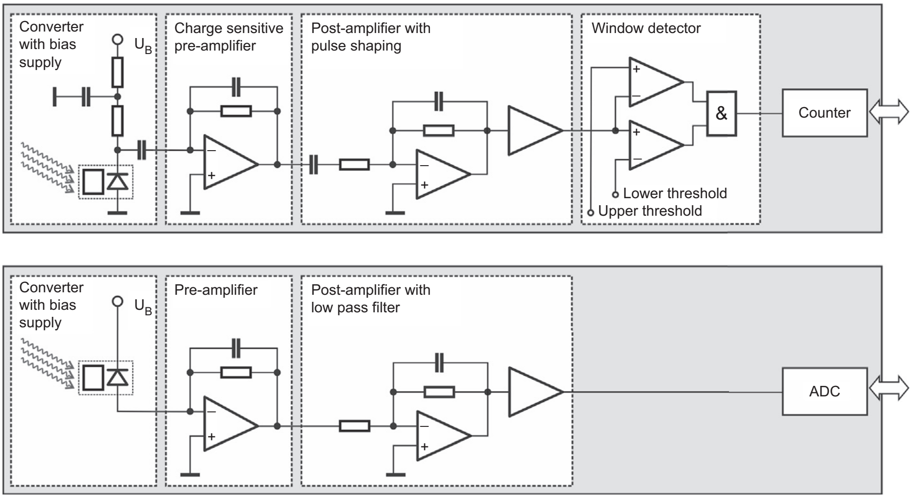
Converter with bias supply
U_B
Charge sensitive pre-amplifier
Post-amplifier with pulse shaping
Window detector
&
Counter
Lower threshold
Upper threshold
Converter with bias supply
U_B
Pre-amplifier
Post-amplifier with low pass filter
ADC

Figure 6.6 X-ray detector electronics for pulse mode (top) and current mode (bottom) detection.

Particularly for fast X-ray imaging and tomography, there are superior requirements for time response, sampling speed, and storage capacity of the X-ray detectors. For example, HZDR's ultrafast ROFEX scanner operates with a dual plane detector of 576 detector pixels total with 1 MHz sampling speed. The digital interface has to manage data rates of about 1 GB/s. One minute of scanning requires 60 GB memory. With a focal spot speed of up to 3000 m/s at 5000 frame/s, full-scale attenuation signal changes on the detector may be as short as 1 μs.

6.5 Attenuation measurement with X-rays

When X-rays penetrate material the beam intensity decreases along the beam path. As schematically shown in Figure 6.7, this is due to different physical effects. X-ray photons can be absorbed or elastically and nonelastically scattered at atoms and molecules. At photon energies much higher than twice the rest energy of electrons (1022 keV), there is additional pair creation in the Coulomb field of nuclei. The latter contribution becomes significant only for rather high photon energies, well above 2 MeV, so it is often not considered further in diagnostic X-ray imaging techniques. Also, on the other side of the energy spectrum, the contribution of elastic or Rayleigh scattering can

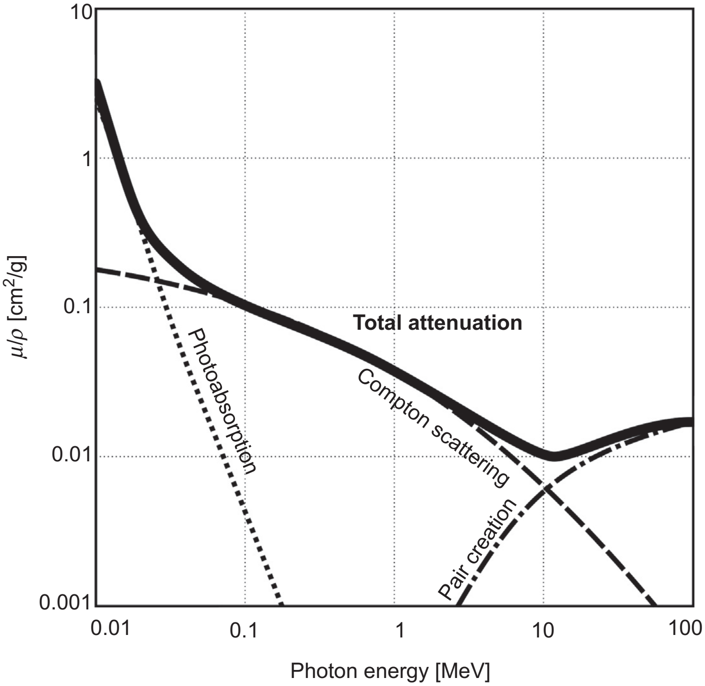

Figure 6.7 Mass attenuation coefficient of water as a function of X-ray energy.

be neglected for typical X-ray transmission measurements. So eventually X-ray absorption and Compton scattering are the dominating effects of X-ray attenuation in diagnostic imaging techniques (Figure 6.7).

The most fundamental concept to derive a quantitative description of X-ray attenuation in a material is the concept of the interaction cross-section. Assume that a single atom of a given chemical element is placed in a unidirectional dense flow of monoenergetic X-ray photons. No matter how complicated the details of the physical interaction between atom and electromagnetic radiation field are, one can simply assume that each atom has an effective cross-sectional target area, called microscopic cross-section, and whenever an X-ray photon propagates through this area it certainly interacts with the atom. For photoabsorption we denote the microscopic cross-section as σ_A and for Compton scattering as σ_C. Neglecting Rayleigh scattering and pair creation, the total microscopic cross-section is then $\sigma = \sigma_A + \sigma_C$. Applying more advanced physical analysis, one would find that $\sigma_A \sim Z^4$ and $\sigma_C \sim Z$. Thus, photoabsorption strongly increases with atomic number and hence electron density, while Compton scattering is linearly related to electron density. Further, we assume in the following that Compton scattering decreases the X-ray photon flux. This is not quite correct, since scattered X-rays with lower energy are produced. However, since the radiation is mainly scattered out of the original propagation direction, it can be considered as lost, for example, for a collimated beam. However, the more radiation is scattered, the higher the probability that scattered photons impinge on a detector. This effect is discussed later on.

With the microscopic cross-sections given above, one easily finds that a material slab of a thickness Δx [m], area A [m^2], a density of atoms n [m^{-3}], a molar mass M [$\mathrm{kg\,mol}^{-1}$], density ρ [$\mathrm{kg\,m}^{-3}$], and the Avogadro constant N_A [mol^{-1}] has a total cross-section of

$$S = n\sigma A\Delta x = A\sigma\frac{\rho N_A}{M}\Delta x. \tag{6.1}$$

Let us consider an X-ray beam propagating along the direction of x (Figure 6.8). At the left slab face it has intensity $I(x)$. Within the thin slab it loses as much intensity as given by the ratio S/A. Hence we may write for the small loss ΔI

$$\Delta I = -I(x)\frac{S}{A} = -I(x)\frac{\sigma\rho N_A}{M}\Delta x. \tag{6.2}$$

This holds only for very small Δx, hence one has to go to the limit $\Delta x \to 0$, giving

$$\mathrm{d}I = -I(x)\frac{\sigma\rho N_A}{M}\mathrm{d}x = -\mu I(x)\mathrm{d}x. \tag{6.3}$$

With $\mu = \sigma\rho N_A/M$ we define the macroscopic cross-section or linear attenuation coefficient, which uniquely defines the ratio $\mathrm{d}I/\mathrm{d}x$ for a material of certain elementary composition (σ, M) and density (ρ). Since density of a material is not a unique

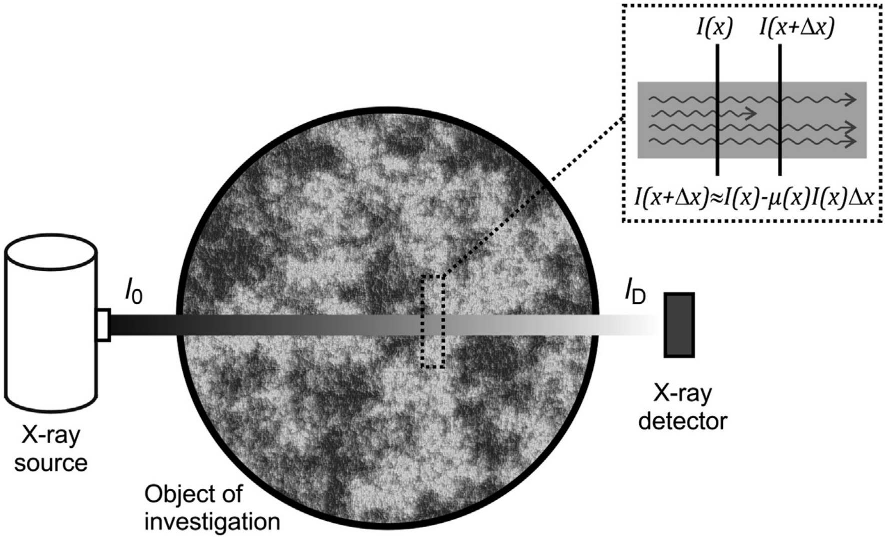

Figure 6.8 Derivation of the attenuation law for X-rays.

parameter (e.g., depending on temperature, pressure, porosity, etc.) the attenuation is often given as the mass attenuation coefficient, that is, the linear attenuation normalized by density $\mu_\rho = \mu/\rho = \sigma N_A/M$.

Now we consider the case that an X-ray passes an object with a locally changing attenuation coefficient, for instance a chemical reactor with internals and different gaseous and liquid reactants and products inside. At each position x Eqn (6.3) holds, but now with μ being dependent on x, hence

$$\mathrm{d}I = -I(x)\mu(x)\mathrm{d}x. \tag{6.4}$$

This is an ordinary first-order linear and inhomogeneous differential equation. If we solve it for the arrangement shown in Figure 6.8, with $I(0) = I_0$ being the beam intensity at the source and $I(x_D) = I_D$ the beam intensity at the detector, the solution is

$$I_D = I_0 \exp\left(-\int_0^{x_D} \mu(x)\mathrm{d}x\right). \tag{6.5}$$

For further analysis it is convenient to introduce a new parameter, the extinction E, which is the negative logarithm of the transmission $T = I_D/I_0$, that is

$$E = -\log(T) = -\log\frac{I_D}{I_0} = \int_0^{x_D} \mu(x)\,\mathrm{d}x. \tag{6.6}$$

The indirectly measurable quantity E (which is in fact a function of the directly measurable quantities I_0 and I_D) is simply the integral over the linear attenuation coefficient distribution along the ray. This linearity allows one to elegantly reconstruct 2D or 3D distributions of the linear attenuation coefficient from projections, as will be shown in Chapter 13. However, it should be noted that Eqn (6.6) is a strong simplification of the real physics. At least, there are two phenomena that spoil the linearity, namely beam hardening and radiation scattering. Both phenomena will be discussed briefly in the following section. An example of how to deal with them is given in Section 6.7.

6.6 Beam hardening and radiation scattering

Radiation from a technical X-ray source is, with the exception of synchrotron radiation, polyenergetic. That is, there is a continuous distribution of X-ray energies in the radiation spectrum. The microscopic and macroscopic interaction cross-sections are energy-dependent and this complicates the situation. Typically, the X-ray detector provides an energy-integral response, that is, Eqn (6.5) becomes

$$I_D = I_0 \int\limits_{\nu_{\min}}^{\nu_{\max}} P(\nu) \exp\left(\int\limits_{0}^{x_D} -\mu(x,\nu)\mathrm{d}x \right) \mathrm{d}\nu, \tag{6.7}$$

with ν being the photon frequency and $P(\nu)$ being the normalized X-ray power spectrum of the source (in other words, the probability distribution of the X-ray energies). Furthermore, the detector itself has an energy-dependent response function, defined among others by the quantum efficiency of radiation conversion. Thus the detector signal U is in fact given by

$$U_D = I_0 \int\limits_{\nu_{\min}}^{\nu_{\max}} h(\nu)P(\nu) \exp\left(\int\limits_{0}^{x_D} -\mu(x,\nu)\mathrm{d}x \right) \mathrm{d}\nu, \tag{6.8}$$

where $h(\nu)$ is the spectral sensitivity of the detector. To circumvent the complications associated with these complex expressions it is common practice to assume an energy-independent effective attenuation coefficient

$$\mu_{\mathrm{eff}}(x) = \int\limits_{\nu_{\min}}^{\nu_{\max}} h(\nu)P(\nu)\mu(x,\nu)\mathrm{d}\nu, \tag{6.9}$$

which then gives

$$I_D \approx I_0 \exp \int\limits_{0}^{x_D} -\mu_{\mathrm{eff}}(x)\mathrm{d}x. \tag{6.10}$$

Equations (6.9) and (6.10) tell us that this effective attenuation coefficient depends on the overall attenuation coefficient distribution $\mu(x,\nu)$ along the rays. Typically the attenuation decreases with energy: the more material in the ray path, the lower μ_{eff}. Or, said with other words, the more material is penetrated, the more low-energy radiation is absorbed and the harder is the remaining X-ray spectrum. In X-ray tomography this nonlinearity results in typical image artifacts, such as streaks along edges of high-attenuating solids (Duerinckx & Macovski, 1978) and overestimated attenuation values in the centroids of continuous phases, the so-called cupping artifacts. A common method for correcting these artifacts is the insertion of a variable c, such that

$$I_{\mathrm{D}}/I_0 + c = \int_{\nu_{\min}}^{\nu_{\max}} h(\nu)P(\nu)\mu(x,\nu)\mathrm{d}\nu. \tag{6.11}$$

c is determined by phantom measurements with material distributions close to those of the actual measurements. This method demands preliminary knowledge about the distribution of $\mu(x,\nu)$ (Joseph & Spital, 1978, Nalcioglu & Lou, 1979). The quality of the correction depends on the segmentation of the phases in the initial image. Further, the tomography system property $h(\nu)P(\nu)$ must be known. In (Herman, 1979) a method based on polynomial approximation for estimating c is given. The iteration of correcting projection data and image reconstruction converges to a highly artifact-reduced image. More advanced methods (Yan, Whalen, Beaupré, Yen, & Napel, 2000) are based not on the information of the material distribution, but on knowledge of the attenuation values of the present materials. For a two-phase system, it is assumed that every image voxel contains a mixture of phases, so that

$$\mu(x,\nu) = \varepsilon(x)\mu_1(x,\nu) + (1-\varepsilon(x))\mu_2(x,\nu), \quad \varepsilon(x) \in [0,1]. \tag{6.12}$$

Here, the volume fraction function $\varepsilon(x)$ is calculated by an iterative algorithm. Again, for every iteration step, a new image reconstruction has to be performed.

A correction of beam hardening without any knowledge about the present materials can be realized with multienergy tomography. In this case, the iteration process is controlled by the difference values of $\mu(x,\nu_i)$ reconstructed from the difference projection data.

Besides beam hardening, the linearity of integral attenuation and hence quality of reconstructed X-ray CT images depends on scattered radiation. Part of radiation scattered by Compton interactions may accidentally fall into the detector and create an intensity offset. For a rough qualitative analysis we may denote with m_{SD} the total material mass in the spatial channel between the source and a detector and with m_{Exp} the material mass exposed by X-rays. Then it turns out that scattering increases with the ratio $m_{\mathrm{Exp}}/m_{\mathrm{SD}}$. While the exact quantitative dependency is complex, this simple finding makes clear that limiting the radiation bundle to the available source—detector channels by spatial collimation is useful. Moreover directional collimation of detectors toward the source is helpful. Energetic collimation, as used in emission or gamma ray tomography, is not applicable for polyenergetic X-ray sources. While transversal scanning allows for effective in-plane collimation, in cone-beam CT only directional collimation can be applied. But the latter is technically highly challenging. Hence, for high-quality imaging software-based scattering correction algorithms are frequently being used. They are based on a proper subtraction of the scattered radiation offset, which has to be determined either by separate measurements or by radiation transport simulations. An example for such a correction scheme is given in the next section.

6.7 Cone-beam X-ray computed tomography for gas holdup measurements

One frequently emerging question in process engineering is that of the spatial distribution of the phases within a chemical reaction device. Carefully conducted analysis of the phase distribution enables a critical assessment of the reaction process with respect to process efficiency and discloses the possibilities for further optimization. The aerated continuous stirred-tank reactor is a prominent example for which the knowledge of spatial gas holdup distribution is of essential interest to determine local interfacial area density and, thus, local mass transfer and reaction rate. The following example describes the gas holdup measurement with X-ray tomography in a laboratory scale cylindrical autoclave reactor vessel with hemispherical bottom (Boden, Bieberle, & Hampel, 2008). Aeration and distribution of the disperse gas phase within the liquid inventory of the reactor is achieved by a multiblade gas-inducing impeller mounted on a hollow shaft, which acts as the inlet for the gaseous phase. The hollow shaft is open to the gas reservoir above the liquid and has holes between the stirrer blades. When the stirrer rotates, centrifugal forces in the liquid result in a pressure drop that sucks gas through the stirrer shaft to the outlets in the impeller region. Due to the high shear stresses in the impeller region the gas is dispersed and further distributed within the continuous phase by the turbulent liquid flow as well as by buoyancy forces. A “good mixing” means homogeneous distribution of the disperse gas bubbles within the reactor volume with reasonable residence times to enable proper mass transfer from the gas into the liquid phase.

Gas holdup in the reactor can effectively and accurately be measured by X-ray cone-beam CT. The setup consists of a rotating-anode X-ray tube and a digital X-ray flat panel detector. The stirred tank reactor vessel is between the two. Since only the gas holdup is of interest, a differential measurement approach is applied. That is, the reactor is scanned with liquid filling at very low stirrer speeds (no gas dispersed in the liquid) as well as in full operation. Then difference images are computed from both measurements, which give the local gas holdup. Special correction steps were implemented to account for beam hardening and radiation scattering, which is described in the following.

Scatter correction: To resolve small gas fractions reliably, radiation scattering must be corrected. As shown in Figure 6.9, a movable slit mask is arranged in front of the X-ray tube. This slit mask can be moved in a vertical direction and depending on its position only a thin X-ray fan radiographs the object. In this scenario most of the

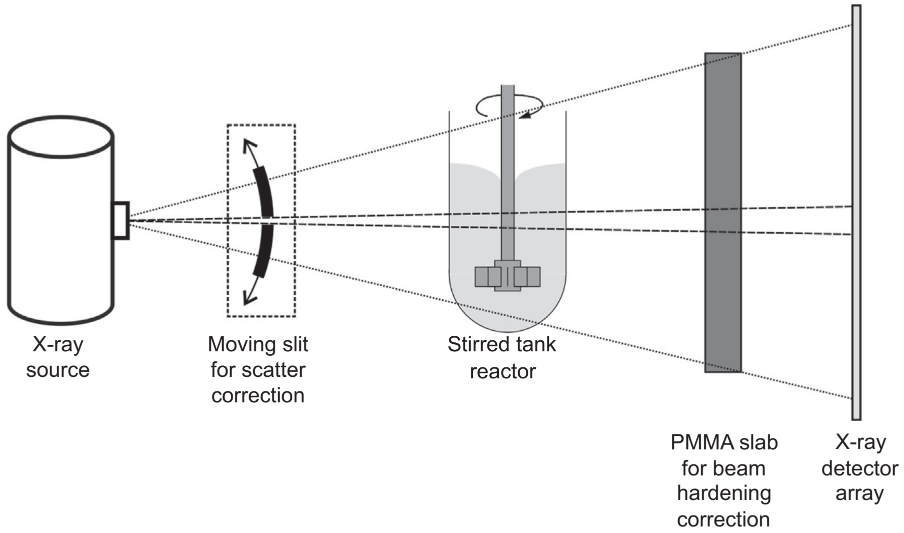
X-ray source
Moving slit for scatter correction
Stirred tank reactor
PMMA slab for beam hardening correction
X-ray detector array

Figure 6.9 Schematic illustration of the X-ray tomography setup to measure the gas holdup in an aerated stirred tank reactor (for further explanation see text).

scattered radiation is blocked off and only in-plane scattering with a much smaller contribution occurs. If scanning time is not a critical factor one can subsequently scan slices of the object by moving the slit mask and synthesize scatter-free projections from the scans. If scanning time is an issue this synthetic scanning can be done once for a reference state (e.g., the filled reactor) and repeated without the slit (full cone illumination). With $I_D^{(\text{slit})}$ and $I_D^{(\text{no slit})}$ denoting the X-ray intensities at a detector pixel D for both configurations, a scattering offset

$$I_D^{(\text{scat})} = I_D^{(\text{no slit})} - I_D^{(\text{slit})} \tag{6.13}$$

can be determined for each detector pixel, which is then subtracted from all other cone-illumination measurements later on. Note that this approach is twofold approximate. First, there is some minor remaining scattering fraction within the collimated fan. Secondly, changes in the object distribution, such as different total gas fractions, also change the scattering background. The appropriateness of these approximations must therefore be checked for each application. In this case, with a large source−detector distance and only small deviations of the object distribution from the reference state, these approximations are fully sufficient to reduce the overall error from scattered radiation to below 1%.

Beam hardening: An X-ray that propagates straight through the reactor is attenuated along its path by both reactor materials and the liquid. Also, each ray in the X-ray cone penetrates different lengths of these materials. Consequently, due to the beam hardening, for each ray there is a different effective attenuation coefficient $\mu_{\text{eff},D}^{(\text{liq})}$ for the liquid. Now considering that we have made two measurements, one for the gas-free reference state $I_D^{(\varepsilon=0)}$ and one for the aerated reactor $I_D^{(\varepsilon)}$, it follows that

$$\frac{I_D^{(\varepsilon)}}{I_D^{(\varepsilon=0)}} = \exp\left(\mu_{\text{eff},D}^{(\text{liq})} \int_{\text{ray}} \varepsilon(x)\mathrm{d}x\right). \tag{16.14}$$

Isolating the line integral of the gas fraction ε, which is input to the image reconstruction, gives

$$\int_{\text{ray}} \varepsilon(x)\mathrm{d}x = \frac{1}{\mu_{\text{eff},D}^{(\text{liq})}} \log \frac{I_D^{(\varepsilon)}}{I_D^{(\varepsilon=0)}}. \tag{6.15}$$

As shown in Figure 6.9, the missing values $\mu_{\text{eff},D}^{(\text{liq})}$ (one for each detector pixel) can be determined by one additional measurement. Therefore we insert a slab of a material with effective attenuation $\mu_{\text{eff},D}^{(\text{slab})}$ close to the liquid in the reactor between the reactor and the detector. From a calibration measurement $I_D^{(\text{cal})}$ with nonaerated reactor and the slab in the beam we get

$$\mu_{\text{eff},D}^{(\text{slab})} = \frac{\cos\alpha}{D} \log \frac{I_D^{(\text{cal})}}{I_D^{(\varepsilon=0)}}. \tag{6.16}$$

Here D denotes the slab thickness and α the angle between X-ray and slab normal. For materials with similar atomic number and density, such as liquid and plastics, the ratio $C = \mu_{\text{eff},D}^{(\text{liq})} \big/ \mu_{\text{eff},D}^{(\text{slab})}$ is rather constant over a wide energy range. Hence, having measured $\mu_{\text{eff},D}^{(\text{slab})}$ for each detector pixel with the plate methods and knowing C from either measurement or database values, we can compute the required line integral values of the gas fraction as

$$\int_{\text{ray}} \varepsilon(x)\mathrm{d}x = \frac{1}{C\mu_{\text{eff},D}^{(\text{slab})}} \log \frac{I_D^{(\varepsilon)}}{I_D^{(\varepsilon=0)}}. \tag{6.17}$$

Reconstruction in this experimental work was done with the generalized filtered back-projection algorithm for the 3D cone-beam tomography with circular source trajectory (Feldkamp, Davis, & Kress, 1984). By carefully accounting for beam hardening and radiation scattering effects as described above, gas holdup distribution profiles in the stirred tank reactor were obtained under different operating conditions at and above the critical stirrer speed (Figure 6.10). As can be seen, cone-beam X-ray tomography resolves well the central vortex around the stirrer shaft in the center of the reactor, as well as the concentration of the gas in the radial region between the

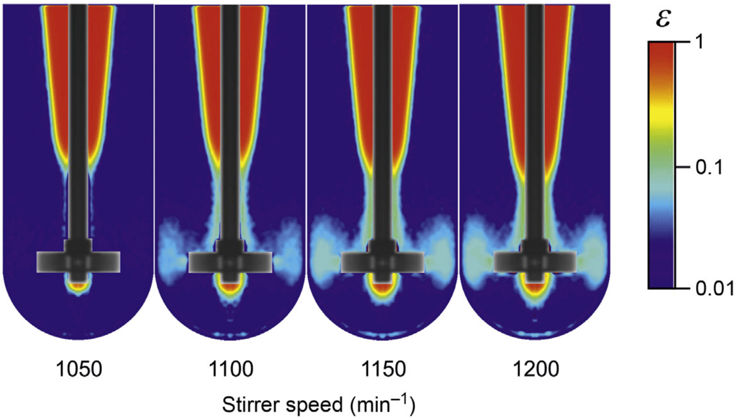

Figure 6.10 Results of the tomographic gas holdup measurement in an aerated stirred tank reactor for different stirrer speeds.

stirrer blades and the reactor wall, where the gas holdup is confined by the turbulent flow field. Critical evaluation of the tomographic method shows maximum quantitative errors of the measurements within about 3.5% absolute local gas holdup.

6.8 Static mixer studies with ultrafast electron beam X-ray tomography

Static mixers are an attractive alternative to mechanically stirred vessels (Thakur, Vial, Nigam, Nauman, & Djelveh, 2013). The small space requirement, low equipment cost, good mixing at low shear rates, self-cleaning, sharp residence time distribution, improved selectivity, and byproduct reduction are the main features of static mixers. Over the years, a large number of companies have designed and produced static mixers, including helical mixers, corrugated plate mixers, cross-bar mixers, and others. Static mixers are based on the principles of flow splitting and radial mixing by a series of baffles. Despite its increasing popularity, a detailed quantitative assessment of the mixing mechanism (particularly for gas–liquid systems) and, based on that, an optimal design was so far not possible due to lack of suitable measurement techniques.

Ultrafast X-ray tomography has been applied to study gas–liquid flow in a helical static mixer. The mixer was built-in in a vertical pipe of 80 mm inner diameter. The objective of the study was to elucidate the flow conditions and develop appropriate scale-up guidelines to ensure proper mixing by increasing the interfacial area and liquid turbulence at economically justifiable energy input. The helical static mixer (Figure 6.11) consists of segments of twisted blades with alternate clockwise and counterclockwise orientations, which are connected orthogonally with each other. The ultrafast electron beam X-ray tomography scanner ROFEX (Figure 6.4) was used for this study. It operates at 150 kV acceleration voltage and a maximum beam power of 10 kW. It comprises a dual detector ring with 2 × 288 room-temperature

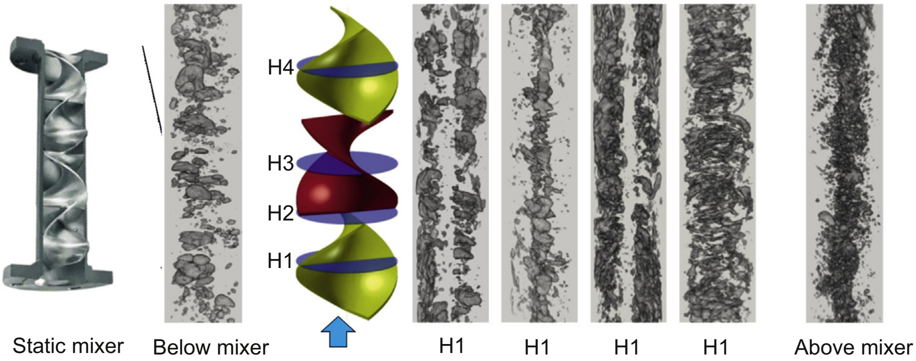

Figure 6.11 View of a helical static mixer (left) and 3D views of the gas distribution in the inlet section, in the outlet section, and within the mixer.

semiconductor pixels, which can be sampled with 1 MSamples per second fully parallel. The scanning speed here was 1000 frames per second in each of the two imaging planes and the plane distance is 11 mm. Figure 6.11 shows selected results of the static mixer study. Shown are the 3D representations of the interfacial area at different axial locations upstream of, within, and downstream of the static mixer. In this particular case the mixer was operated at 0.6 m/s liquid superficial velocity and 0.11 m/s gas superficial velocity. The 3D views were created by stacking subsequent cross-sectional images of one scanning plane together and extracting the gas phase, and thus the interfacial area, via a 3D image segmentation algorithm. The interfacial area calculated from the measured gas holdup and bubble diameters was found to increase significantly with the addition of the helical static mixer elements and to decrease with the increase of fluid velocity ratio. The results allowed providing the designer with fluid-dynamic data to optimize the mixer design. Furthermore, such data forms a sound basis for modeling of gas–liquid flows with computational fluid dynamics codes.

6.9 Future trends

X-ray tomography is a very desirable tool for process tomography and multiphase flow analysis. Recent developments have proven that it is a superior tool with respect to achievable spatial and temporal resolution in flow scanning. Nonetheless, expensiveness and efforts for radiation protection make X-ray CT methods less easily applicable, especially as a monitoring instrument in the field. Hence one of the future trends will be to provide technical solutions for fast X-ray CT that are applicable in real industrial applications, such as in the oil and gas industries. This requires numerous advances, such as high-power, cheap, compact, and robust multisource or moving-source X-ray generators; fully integrated data analysis software; and inherent radiation protection designs. For laboratory applications, where radiation protection and cost issues are somewhat less critical, a future trend is to achieve 3D scanning and increase penetration capability by going to higher X-ray energies. Moreover, interesting developments are to be expected in improving spatial resolution by fast fine-focus sources, multienergy full CT imaging (e.g., for three-phase flow studies), and combination of X-ray CT with other imaging modalities, such as electrical tomography or ultrasound scanning. Last, it should be noted that fast high-resolution tomography and its data processing, image reconstruction, and data analysis require ever increasing computer power as well as intelligent software solutions. Here parallel computing, for example, on graphics processing unit systems, will certainly evolve its potentials in the future.

6.10 Sources of further information and advice

For the fundamentals of X-ray CT, especially in medicine, there are many good textbooks. Particularly for its application in multiphase flow studies, the comprehensive review (Heindel, 2011) is to be recommended. The author and his group have extensively worked on X-ray CT application in multiphase flow analysis and particularly pioneered fast electron beam X-ray CT for process applications. Hence further information may be found in the various publications of the group and the internet presentation of Helmholtz-Zentrum Dresden-Rossendorf.

References

Berg, S., Ott, H., Klapp, S. A., Schwing, A., Neiteler, R., Brussee, N., et al. (2013). Real-time 3D imaging of Haines jumps in porous media flow. *PNAS, 110*, 3755–3759.

Boden, S., Bieberle, M., & Hampel, U. (2008). Quantitative measurement of gas holdup distribution in a stirred chemical reactor using X-ray cone-beam computed tomography. *Chemical Engineering Journal, 139*, 351–362.

Del Sordo, S., Abbene, L., Caroli, E., Mancini, A. M., Zappettini, A., & Ubertini, P. (2009). Progress in the development of CdTe and CdZnTe semiconductor radiation detectors for astrophysical and medical applications. *Sensors, 9*, 3491–3526.

Deza, M., Franka, N. P., Battaglia, F., & Heindel, T. J. (2009). CFD modeling and X-ray imaging of biomass in a fluidized bed. *Journal of Fluids Engineering, 131*, 111303.

Duerinckx, A. J., & Macovski, A. (1978). Polychromatic streak artifacts in computed tomography images. *Journal of Computer Assisted Tomography, 2*, 481–487.

Feldkamp, L. A., Davis, L. C., & Kress, J. W. (1984). Practical cone-beam algorithm. *Journal of Optical Society America, A 1*, 612–691.

Fischer, F., Hoppe, D., Schleicher, E., Mattausch, G., Flaske, H., Bartel, R., et al. (2008). An ultra fast electron beam x-ray tomography scanner. *Measurement of Science and Technology, 19*, 094002.

Grangeat, P. (1991). Mathematical framework of cone beam 3D reconstruction via the first derivative of the Radon transform. *Lecture Notes in Mathematics, 1497*, 66–97.

Hampel, U., Bärtling, Y., Hoppe, D., Kuksanov, N., Fadeev, S., & Salimov, R. (2012). Feasibility study for MeV electron beam tomography. *Review of Scientific Instruments, 83*, 093707.

Heindel, T. J. (2011). A review of X-ray flow visualization with applications to multiphase flows. *Journal of Fluids Engineering, 133*, 074001.

Herman, G. T. (1979). Correction for beam hardening in computed tomography. *Physics in Medicine and Biology, 24*, 81−106.

Hori, K., Fujimoto, T., Kawanishi, K., & Nishikawa, H. (1998). Development of an ultrafast X-ray computed tomography scanner system. *IEEE Transactions on Nuclear Science, 45*, 2089−2094.

Inoue, A., Kurosu, T., Aoki, T., Yagi, M., Mitsutake, T., & Morooka, S. (1995). Void fraction distribution in BWR fuel assembly and evaluation of subchannel code. *Journal of Nuclear Science and Technology, 32*, 629−640.

Johansen, G. A., Hampel, U., & Hjertaker, B. T. (2010). Flow imaging by high speed transmission tomography. *Applied Radiation and Isotopes, 68*, 518−524.

Joseph, P. M., & Spital, R. D. (1978). A method for correcting bone induced artifacts in computed tomography scanners. *Journal of Computer Assisted Tomography, 2*, 100−108.

Kak, A. C., & Slaney, M. (1988). *Principles of computerized tomographic imaging*. New York: IEEE Press.

Kalender, W. A. (2005). *Computed tomography. Fundamentals, system technology, image quality, applications* (2nd ed.). Erlangen: Publicis Corporate Publishing.

Moreno-Atanasio, R., Williams, R. A., & Jia, X. (2010). Combining X-ray microtomography with computer simulations for analysis of granular and porous materials. *Particuology, 8*, 81−99.

Mudde, R. F. (2011). Bubbles in a fluidized bed: a fast X-ray scanner. *AIChE Journal, 57*, 2684−2690.

Nalcioglu, O., & Lou, R. Y. (1979). Post-reconstruction method for beam hardening in computed tomography. *Physics in Medicine and Biology, 24*, 330−340.

Schard, P., Deuringer, J., Freudenberger, J., Hell, E., Knüpfer, W., Mattern, D., et al. (2004). New X-ray tube performance in computed tomography by introducing the rotating envelope tube technology. *Medical Physics, 31*, 2699−2706.

Seeger, A., Kertzscher, U., Affeld, K., & Wellnhofer, E. (2003). Measurement of the local velocity of the solid phase and the local solid holdup in a three-phase flow by X-ray based particle tracking velocimetry (XPTV). *Chemical Engineering Science, 58*, 1721−1729.

Shefer, E., Altman, A., Behling, R., Goshen, R., Gregorian, L., Roterman, Y., et al. (2013). State of the art of CT detectors and sources: a literature review. *Current Radiology Reports, 1*, 76−91.

Thakur, R. K., Vial, C., Nigam, K. D. P., Nauman, E. B., & Djelveh, G. (2013). Static mixers in the process industries - a review. *Chemical Engineering Research and Design, 81*, 787−826.

Toye, D., Marchot, P., Crine, M., Pelsser, A.-M., & L'Homme, G. L. (1998). Local measurement of void fraction and liquid holdup in packed columns using X-ray computed tomography. *Chemical Engineering and Proceedings, 37*, 511−520.

van Eijk, C. W. E. (2002). Inorganic scintillators in medical imaging. *Physics in Medical Biology, 47*, R85−R106.

Waelchli, S., von Rohr, R., & Stampanoni, M. (2005). Multiphase flow visualization in microchannels using X-ray tomographic microscopy (XTM). *Journal of Flow Visualization Image Processing, 12*, 1−13.

Yan, C. H., Whalen, R. T., Beaupré, G. S., Yen, S. Y., & Napel, S. (2000). Reconstruction algorithm for polychromatic CT imaging: application to beam hardening correction. *IEEE Transactions on Medical Imaging, 19*, 1−11.

Gamma-ray tomography

7

G.A. Johansen
Faculty of Engineering and Business Administration, Bergen University College,
Bergen, Norway

7.1 Introduction

The potential of using ionising radiation for imaging purposes was discovered by William Conrad Röntgen in 1895 at the same time as the ionising radiation itself. The imaging modality first applied was X-ray radiography, and this is still important, for instance, for nondestructive testing applications and in medicine. The application of tomographic imaging techniques to industrial problem solving has been around ever since the first commercial X-ray scanner was introduced by EMI in 1972, and even before.

Gamma radiation, also known as gamma-rays or γ-rays, was discovered by Paul Villard in 1900 while he was studying radiation emitted from radium. Gamma-rays are produced when an atomic nucleus decays from a high-energy state after, for instance, a disintegration. Gamma-rays and X-rays are photons with sufficient energy to ionise matter. They differ in their origin and the fact that gamma-ray photons, being nuclear radiation, classically have higher energy than X-ray photons originating from the atom. However, linear accelerators may produce X-rays with very high energy. The photon energy is expressed in terms of electronvolts (eV) and is typically in the range of about 10 keV to a few MeV for most tomography applications. Higher energy implies higher penetron capability and thus the possibility to study, for instance, processes inside vessels with thick stainless steel walls.

7.1.1 The fundamental principle of gamma-ray tomography

The foundation of all gamma-ray tomography systems is shown in Figure 7.1. In transmission mode a radioisotope source and a detector are positioned on opposite sides of the object under investigation. In scatter mode the detector is positioned somewhere outside direct view of the source so that it only measures radiation scattered from interactions generated by the incident beam. The beam intensity, which is the number of photons per second, depends on the number of interactions taking place inside the object and is measured continuously in the detector. As a first approximation one may say that the average density in the volume defined by the view of the detector may be derived by such measurements.

A tomography system comprises multiple measurements of this type in different directions through the cross-section of the object. For transmission tomography one or several fan beam collimated sources are typically used, each with an array of detectors on the opposite side defining as many projections as detectors. Based on the

Industrial Tomography. http://dx.doi.org/10.1016/B978-1-78242-118-4.00007-1
Copyright © 2015 Elsevier Ltd. All rights reserved.

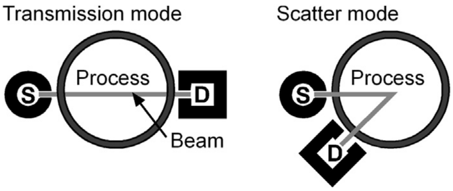
Transmission mode
Process
S
D
Beam
Scatter mode
Process
S
D

Figure 7.1 Measurement modes used in industrial gamma-ray systems. The radiation source (S) is shielded to reduce radiation dose to the environment and collimated to define the beam geometry and measurement volume. For the same reason, the detector(s) (D) are collimated and shielded to reduce background radiation.

geometry of the system and these measurements, a cross-sectional image of the object can be reconstructed.

7.1.2 Gamma-ray scatter tomography

Gamma-ray scatter tomography is often applied when there is access to only one side of the object to be inspected or when its dimensions are so large there is no transmission through it. The most common approach is to use one or several arrays of narrowly collimated detectors, each defining voxels in the intersections with the incident beam, the so-called point-by-point approach. There is no need for image reconstruction since the data from each voxel is directly available. This chapter focuses on transmission tomography; for a more complete treatment of gamma scatter tomography the review article of Harding and Harding (2010) is recommended, or, alternatively, recent articles on methods and applications (Achmad & Hussein, 2004; Evans, Martin, Burggraf, Roggeman, & Hangartner, 2002).

7.1.3 Computed tomography generations and categories

There has been a continuous development of computed tomography since the first X-ray scanner in 1972. Figure 7.2 shows the first- and third-generation scanning

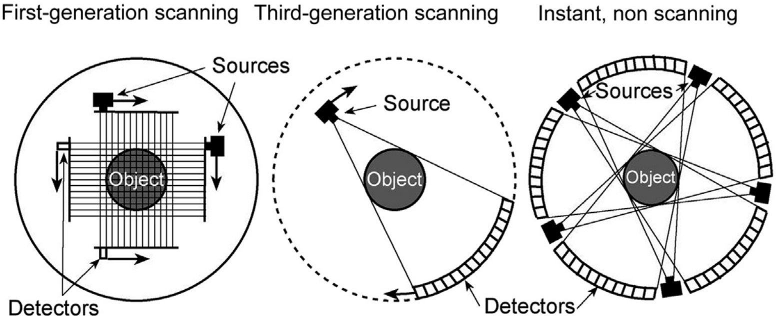
First-generation scanning
Third-generation scanning
Instant, non scanning
Sources
Object
Detectors
Source
Object
Detectors
Sources
Object

Figure 7.2 Measurement geometries used for medical X-ray tomography scanners of first and third generations. Also shown is the instant configuration, in which all projection measurements are carried out simultaneously.

geometries that are used for gamma-ray transmission tomography today, particularly the third-generation. The use of one source, a few detectors and mechanical scanning to obtain multiple projections keeps the costs low. This is an attractive alternative for imaging of fairly static objects or processes, or where temporal averaging of their dynamics is satisfactory. However, instant imaging, also shown in Figure 7.2, has to be used on dynamic objects or processes to avoid projection inconsistency in the measurement cross-section. Typical examples of dynamic processes with time constants in the subsecond region are multiphase flows and processes involving separation, sedimentation, filtration, mixing, etc. Instant imaging is also needed for imaging of objects carried on production lines such as conveyer belts.

Unlike X-ray tubes that are capable of producing very high-intensity beams, the intensity from radioisotope sources is limited. As a consequence of this and the fact the emission of gamma-ray photons from the source is a random process, the radiation intensity measurements are subject to measurement errors caused by counting statistics. This so-called counting or statistical error decreases with $\sqrt{n}$, where n is the number of counts. To reduce this error long counting (integration) times are preferred; however, that will be at the cost of the speed of response.

In summary, this implies a trade-off between three conflicting requirements: the measurement resolution of time, space and matter. In contrast to medical tomography, where the patient is kept still for the time it takes to acquire the data for one image, for some industrial tomography applications the data acquisition time has to be short to avoid inconsistency, as discussed above. This means there is a compromise between statistical error and measurement time. Likewise, the spatial resolution for a given system is basically improved by reducing the size of the detectors. This in turn means fewer counts in each detector and thus a higher statistical error in each projection measurement. In industrial tomography the solution is often, but not always, to relax the spatial resolution requirement compared to medical tomography, in order to obtain faster speed of response.

7.2 Radioisotope sources and gamma-ray emission

When a radioactive element decays the daughter nucleus often has some residual energy and is left in an excited state. The change to the ground state often involves the emission of a gamma-ray, i.e. a photon, with a discrete energy. A gamma-ray source is a sealed stainless steel capsule containing a gamma-ray-emitting material. It is so designed as to allow the radiation to escape whilst securely containing the radioactive material. Sealed sources only emit the ionising radiation through the capsule wall with no release of the radioactive material itself.

7.2.1 Gamma-ray sources

Gamma-ray sources are available in different shapes; however, spherical point sources and disc sources are most commonly used for tomography. Typical dimensions for these are 2–8 mm diameter for point sources and 8–40 mm for disc sources.

Table 7.1 **The most commonly used sealed gamma-ray source radioisotopes for industrial tomography and their main emissions**

Isotope	Half-life (years)	γ-ray emissions (keV)	X-ray emissions (keV)
^{241}Am	433	60	13.9, 17.8
^{133}Ba	10.5	82, 303, 356	30, 36
^{137}Cs	30.2	662	32.1
^{60}Co	5.27	1173, 1333	None

The most important source properties to consider are gamma-ray emission energy, activity and half-life. The activity, A, defines the beam intensity and is expressed in Bq (Becquerel; emissions per second) or the old unit Ci (Curie; 1 Ci = 3.7×10^{10} Bq). The half-life, $T_{½}$, is the time it takes for the amount of radioactive nuclei in the source to be halved. Some radioisotope sources have multiple emission energies or lines, and some also have X-ray emissions caused by the daughter atom being left in an excited state. Emission energy is an important criterion when selecting source; however, a relatively long half-life is also preferred to avoid continuous replacement of the source. Table 7.1 lists the most popular gamma-ray emitters (Johansen & Jackson, 2004, p. 25).

7.2.2 Safety and regulations

Selecting the right radiation source for the application is not only a technical question. The International Commission on Radiological Protection (ICRP, 1991) recommends that all use of nuclear radiation should follow the ALARA (as low as reasonably achievable) philosophy (Johansen & Jackson, 2004, p. 183). This implies a cost-benefit analysis aiming at lower dose levels in all applications. Firstly, the use of nuclear methods has to be justified to any other measurement principle. If so, the next step is to keep the dose as low as possible and always less than the recommended limits set by national bodies. The Radiation Protection Institutes in the Nordic countries recommend that the annual equivalent dose from nucleonic instrumentation should be kept below 0.1 mSv for the general public and below 5 mSv for workers operating such gauges. The risks in industries using radioisotope gauges are often found to be lower than those in other industries. This is due to effective safety precautions, and the basic policy of ICRP (1991) is to always keep this difference. This policy is the reason why the recommended dose limits have been lowered in recent years.

All industrial gamma-ray sources must be placed in source containers with lockable shutters. As will be explained in the next section, materials with high density and atomic number are the most efficient gamma-ray absorbers and, thus, shielding materials. Lead, with density of about 11 g/cm^3, is the most applied material because of the relatively low cost. Tungsten, with a density of about 17 g/cm^3, or a variety of tungsten alloys are applied in cases where the weight or dimensions of the container are critical. A typical source container is shaped as a sphere with the source in the centre and with an emission opening that can be closed and secured. The whole arrangement is placed inside a stainless steel capsule that is marked with the trefoil symbol and information about the source. Figure 7.10 shows the estimated absorbed dose rate of the four radioisotopes listed in Table 7.1, as a function of shielding thickness.

7.2.3 Collimation

Shielding materials are also used to define the beam or beams on the source output and, likewise, in front of the gamma-ray detectors. This is referred to as collimation, which in essence defines the volume in the object to be illuminated by the source and, likewise, the volumes viewed by the detectors. In its simplest form this may be a cylindrical hole in the shielding material in front of the source and the detector. As will be shown in examples later in this chapter, a very common design is to use a fan beam collimation in front of the source and a so-called focussed collimator set comprising multiple lead blades in front of an array of detectors. In this approach multiple beams and measurement volumes are defined and the influence of radiation scattered outside the defined beams into the corresponding detectors is reduced.

The latter is often referred to as the hard-field property, which is an important advantage with gamma-ray transmission tomography: The sensitivity of the measurement to the measured parameter is uniform and independent of the component distribution in the measurement volume. Nor is the measurement sensitive to anything outside this volume, provided that efficient collimation is applied. This facilitates the use of very powerful image reconstruction techniques known from medical X-ray tomography and, consequently, high-quality images with less distortion.

7.3 Gamma-ray attenuation in matter

7.3.1 Gamma-ray transmission

A Gamma-ray photon may travel a long distance in a material without being affected at all, but its history is terminated once it interacts. Therefore we need to consider the number of photons removed from a beam penetrating an absorber, as illustrated in Figure 7.3.

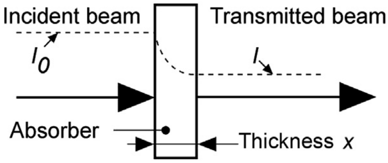

Figure 7.3 The attenuation of a parallel beam of gamma-ray photons in an absorber.

The attenuation of a narrow and parallel beam of monoenergetic photons penetrating a thin slab of homogeneous material follows Lambert—Beer's exponential decay law:

$$I = I_0 e^{-\mu x} \tag{7.1}$$

Here I_0 is the incident or initial intensity (number of photons/second); x the thickness of the absorber; μ its linear attenuation coefficient, often in unit cm^{-1}; and I the remaining beam intensity. The linear attenuation coefficient expresses the photon interaction probability per unit path length. It is strongly dependent on the radiation energy and the density and the atomic number of the absorber. It is composed additively of contributions from several independent interaction mechanisms, where the photoelectric effect (μ_τ) and Compton scattering (μ_σ) are the most important in the energy range used for industrial tomography (Johansen & Jackson, 2004, p. 45).

In the photoelectric effect a gamma photon collides or interacts with an orbital electron in the material, being the object under investigation, the radiation detector, or the surrounding material. The electron is ejected with a certain energy transferred from the photon. Gamma photons have sufficient energy to interact with one of the inner atomic electrons. The atom is left in an excited state and will, within a short time (typically less than 10 ns), return to a stable state through electron rearrangement. This may happen in one of two ways. The energy released in rearranging the electron structure is used to free an electron from the atom as a whole. This is the so-called Auger effect. The alternative to the Auger effect is fluorescence, where a characteristic X-ray is emitted (line emission) when the atom de-excites to a stable state. This X-ray photon may travel some distance before it interacts.

Compton scattering is an inelastic or incoherent scattering process where the incident gamma photon interacts with one of the outer and loosely bound atomic electrons. The incident photon is scattered at an angle θ to its original direction. A fraction of its energy is transferred to the so-called recoil electron.

For absorbers with low atomic numbers μ_σ is approximately proportional to the density, whereas μ_τ is approximately proportional to the atomic number in the power of 4—5, dependent on the energy. This can be seen from Figure 7.4, where the linear attenuation coefficient is plotted as a function of energy for oil, water and brine. In the Compton-dominant region the difference scales approximately with the density, whereas in the photoelectric-dominant region the difference is much higher due to the higher sensitivity to the atomic number.

In gamma-ray transmission measurements, radiation energies in the Compton region are often used, such as the 662 keV line from the ^{137}Cs isotope. In this region Compton scattering is the dominant attenuation mechanism and μ is approximately proportional to the density of the absorber. This is also the reason why this type of radioisotope gauge is referred to as a gamma-ray densitometer. However, energies in the photoelectric region, such as 60 keV from the ^{241}Am isotope, are increasingly being used because μ exhibits a strong dependence on the atomic number (Z^4 to Z^5) in this region. This facilitates better measurement contrast between components in

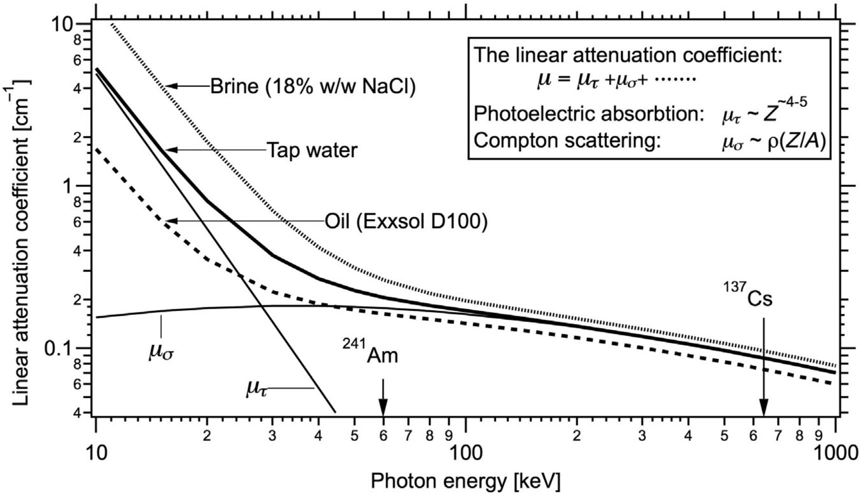

Figure 7.4 The linear attenuation coefficients of oil, tap water and brine as functions of photon energy. The effect of Rayleigh scattering is not shown, since its contribution is inferior to photoelectric absorption (μ_τ) and Compton scattering (μ_σ). At several MeV energies pair production also becomes significant.

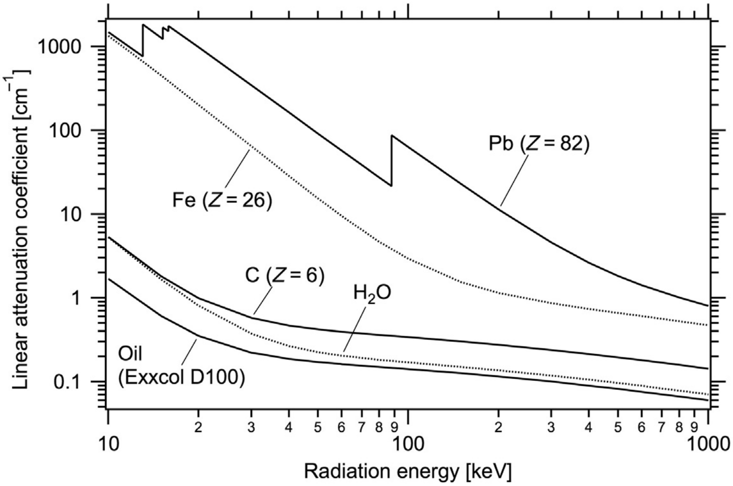

Figure 7.5 The energy dependence of the linear attenuation coefficients (μ) of water (H_2O), oil (Exxsol D100), carbon ($Z = 6$), iron ($Z = 26$) and lead ($Z = 82$).

many multiphase systems. The linear attenuation coefficient is plotted versus radiation energy in Figure 7.5 for typical low, intermediate and high Z elements.

Most often and particularly for high energies, the energy carried by an initial incident gamma photon is deposited through a chain of multiple interactions. These may be combinations of photoelectric and Compton interactions. Often the initial interactions are Compton scattering, followed by one or several more probable photoelectric interactions as the secondary photon energy decreases.

The energy of the initial incident gamma photon need not, as a consequence, be deposited on the spot of the initial interaction. Because electrons have a short range in matter, full energy deposition will take place with photoelectric interaction followed by the emission of an Auger electron. A photoelectric interaction followed by fluorescence or a Compton interaction result in an X-ray or a scattered gamma-ray, respectively, which may travel some distance before they interact. Through a series of multiple interactions the initial photon's energy thus may be deposited at multiple locations. There is thus a difference between gamma-ray (energy) absorption and gamma-ray attenuation. The latter refers to the initial interactions of the gamma photons emitted from the radioisotope source. That is, once a gamma photon in the incident beam with intensity I_0 has interacted, it is considered not to contribute to the transmitted beam I. This may not be true, as it may undergo an interaction where a secondary photon (X-ray fluorescence or Compton scatter) continues in approximately the same direction. To cope with this effect in transmission measurements, the build-up factor is introduced.

7.3.2 Build-up

Attenuation of gamma-rays obeys the Lambert—Beers law, as stated in Eqn (7.1), but only for a narrow or well-collimated beam. In reality there will always be some contribution to the transmitted beam from photons that have interacted and produced forward scatter. This is known as build-up, and may be accounted for by introducing the build-up factor, $B(\mu,x)$, into Eqn (7.1) (Johansen & Jackson, 2004, p. 54):

$$I = B(\mu, x) I_0 \mathrm{e}^{-\mu x} \tag{7.2}$$

The build-up factor is thus unity for a narrow parallel beam. Generally, $B(\mu,x)$ depends on the linear attenuation coefficient and its composition, and the thickness and geometry of the material in which the scatter is generated. This may be the collimation of the source and the detector, the measurement object itself, or even the source and detector encapsulation. The build-up factor cannot be calculated analytically; it has to be determined from experiments, simulations or models thereof.

The most common approach for handling build-up is to define the effective linear attenuation coefficient μ_{eff} so that:

$$I = BI_0^{-\mu x} = I_0 \mathrm{e}^{-\mu_{\mathrm{eff}} x} \tag{7.3}$$

This means that tabulated values for μ cannot be used, but rather values determined from calibration measurements. Gamma-ray tomography is all about determining the component distribution or mixing of multicomponent systems. Calibration measurements are typically carried out with the object or vessel under investigation in turn filled with the first component and then the second.

7.3.3 Counting statistics and measurement errors

The interaction of gamma-ray photons can be measured with high accuracy in a radiation detector, both the time of interaction and the deposited energy. Measurement of the transmitted intensity of a gamma-ray beam is as introduced in Section 7.1, burdened with counting statistics errors, which cannot be handled any other way than designing the system to meet the required accuracy. Now, the variable to be measured in gamma-ray tomography is the attenuation coefficient, which is derived from Eqn (7.1) or Eqn (7.3):

$$\mu = \frac{1}{x}\ln\left(\frac{I_0}{I}\right) \tag{7.4}$$

The relative counting error can be derived and expressed in terms of the relative standard deviation as (Johansen & Jackson, 2004, p. 141):

$$\frac{\sigma_\mu}{\mu} = \frac{1}{\mu x}\sqrt{\frac{e^{\mu x}}{I_0 \tau_I}} \tag{7.5}$$

where the error in the incident beam intensity, I_0, is negligible, since this can be measured with high accuracy through initial calibration measurements of longer duration (τ_0). The relative error given in Eqn (7.5) is plotted as a function of the product μx and the total number of incident photons or photons ($I_0 \tau_I$) in Figure 7.6.

This plot reveals two very important properties for pulse counting transmission measurements, which is important to consider when designing a system:

- The relative error has its minimum when $\mu x = 2.0$.
- Increasing the total number of incident photons ($I_0 \tau_I$), by increasing I_0, τ_I or both, reduces the error and increases the width of the valley of minimal error.

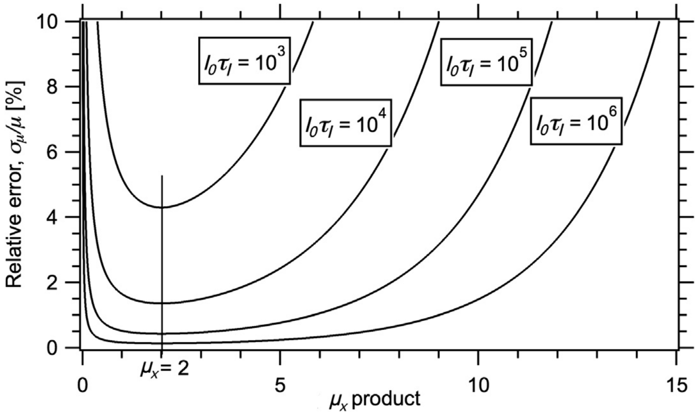

Figure 7.6 Relative error (standard deviation) in the measured average linear attenuation coefficient or thickness due to statistical fluctuations in the measured beam intensity, assuming the error in the incident intensity, I_0, is negligible.

7.4 Detector and read-out systems

The sensors for measurement of ionising radiation are commonly referred to as detectors. The purpose of these is to convert radiation energy into an electronic signal, and the detector thus requires to:

1. stop gamma photons in its active volume,
2. convert the energy of each of these photons to energy of secondary electrons, and finally
3. collect or sense the charge generated by these electrons.

The first stage in quantified by the stopping efficiency, expressing how large the fraction of the incident beam that is attenuated by the detector. For a given energy this depends on the dimensions of the detector, particularly the thickness in the direction of the incident beam, and the density and atomic number of its material.

As for the second stage, all energy of an interacting gamma photon ideally should be deposited in the active volume of the detector. However, photons resulting from one or several subsequent interactions may escape this volume and not contribute to the deposited energy for that initial event. Consequently even when a beam of monochromatic photons is incident to an ideal noiseless detector, multiple energies normally are detected. As for the stopping efficiency, density, atomic number and particularly the volume of the detector are important for efficient energy detection (Johansen & Jackson, 2004, p. 61).

When a gamma photon undergoes a photoelectric or Compton interaction in a detector, energetic electrons are produced as explained in Section 7.3. Photoelectrons, Auger electrons and Compton recoil electrons all ionise and excite the absorber, producing a large number of secondary electrons, of which the total energy ideally should be collected or sensed by the read-out electronics. The third stage takes into account that this is not always the case. Some of the energy generated in the detector volume may be lost before it is sensed by the read-out electronics.

7.4.1 Radiation detector technologies

There are two categories of radiation detectors, as illustrated in Figure 7.7: those sensing the ionisation by the interacting gamma photons directly in the active volume, and scintillation detectors in which scintillation light is generated by the ionisation and then measured with a sensitive light detector. The latter is most commonly a photo

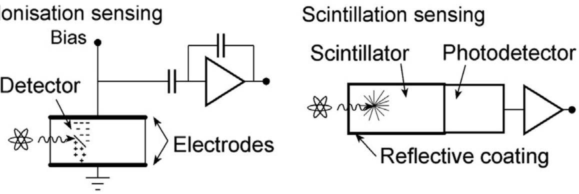

Figure 7.7 The two main radiation detector categories used for gamma-ray measurements. Both detector categories apply a preamplifier to interface the read-out electronics shown in Figure 7.8.

multiplier tube (PMT) where the signal also is amplified, or a photodiode that may or may not have internal gain. In both cases the signal is fed to a preamplifier, most often a charge-sensitive one. The latter is required in particular for photodiodes or semiconductor detectors without internal gain in order to optimise the signal-to-noise ratio (SNR).

The most commonly used ionisation sensing detectors for gamma-ray tomography are semiconductor detectors. Of these, cadmium zinc telluride (CZT) is a very popular material because it can be operated without cooling at room temperature combined with favourable stopping efficiency up to a few hundred keV. The drawback with this and other semiconductor materials is the steep increase in noise with temperature, which makes them less attractive in harsh applications outside laboratories (Johansen & Jackson, 2004, p. 87). For higher energies and harsh operation, scintillation crystal detectors are the preferred solution. Because the signal transmission in these is by light photons, they can be made with larger volumes than semiconductor detectors where the charge collection then would drop significantly. This means that scintillation detectors are the best candidates when it comes to stopping efficiency. The most popular scintillation crystal material is NaI(Tl) with PMT read-out, even though there are many new attractive crystals with higher stopping efficiency and better properties for high-speed counting. The popularity of NaI(Tl) can be explained by long experience, large volume production and thus relatively low cost. BGO ($Bi_4Ge_3O_{12}$) is another crystal that has been used in several imaging systems. It has higher stopping efficiency than NaI(Tl) and can more easily be stacked into arrays, which is an advantage for tomography applications. There are also compact PMTs available, and there are alternative compact scintillation light read-out detectors, such as silicon detectors with and without gain. The latter is not ideal because of the very small signal levels of the scintillation flashes.

7.4.2 Read-out electronics

The output of the preamplifier is fed to a combined band-pass filter and amplifier to further optimise the SNR, as shown schematically in Figure 7.8. In radiation detector terminology this is often referred to as the shaper amplifier. Gamma-ray detection systems are operated in pulse mode, meaning the total energy deposited in the detector volume from each and individual gamma-ray photon in the incident beam can be

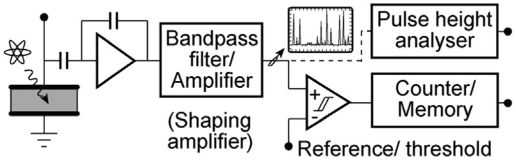

Figure 7.8 A typical read-out system for gamma-ray detectors comprising a preamplifier and a combined amplifier and band-pass filter, of which a typical output pulse train is shown. The discriminator and counter are required for intensity measurements, whereas the pulse height analyser, also shown, is applied when energy information on each event is required.

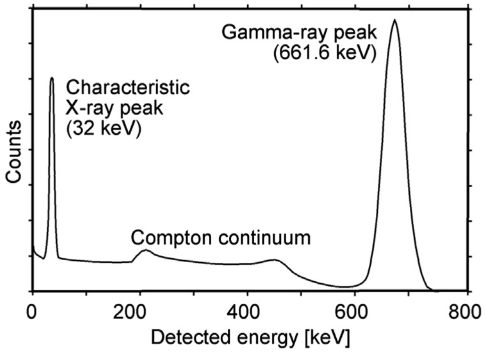

Figure 7.9 A typical pulse height spectrum of a ^{137}Cs source acquired with a NaI(Tl) scintillation detector.

measured. This is illustrated by the oscilloscope display on the output of the amplifier in Figure 7.8 showing a pulse train from subsequent interacting gamma photons of the incident beam. The height of each pulse is proportional to energy that a particular initial photon deposits in the active detector volume (Johansen & Jackson, 2004, p. 135). This signal may be fed to a pulse height analyser that produces a pulse height and thus an energy spectrum where the number of detected events is displayed as a function of their energy. Figure 7.9 shows a typical spectrum from a ^{137}Cs source that emits 661.2 keV gamma-rays and 32 keV X-rays. The peaks in the spectrum are smeared out by incomplete charge collection and noise in the read-out system. The energy continuum between these peaks and the two smaller peaks represent events where part of the energy of the initial gamma photon has escaped the active volume of the detector.

The pulse height analyser is very useful in the design and optimisation of radiation detection systems; however, it is seldom used for gamma-ray tomography or gamma-ray densitometry in general. To measure the intensity of a beam it is sufficient to use a discriminator and counter, also shown in Figure 7.8. The output of the amplifier is then fed to a comparator with built-in hysteresis to avoid multiple output signals from one and the same input signal. The reference voltage is carefully set so that the system does not trigger on noise. For a scintillation detector system used to produce the spectrum in Figure 7.9, the trigger level could be set to 100 keV so that all events above this energy are counted. All read-out systems are subject to drift in gain, and for this reason it is advantageous to use a low-energy trigger level where the influence of such gain shift is less. The trigger level should for the same reason not be set at or near the rising or falling edges of spectral peaks.

7.4.3 Intensity measurement

The intensity is determined by counting the number of events above the threshold for a predefined time, τ, the so-called integration time. For a given system and application the integration time is carefully selected, as discussed in Section 7.1. Measurements of dynamic variations in processes such as flow would typically imply that the integration time should be less than the flow rate with a margin. On the other hand, if temporal averaging of the process is sufficient, a longer integration time may be selected to obtain better resolution of the measured parameter (μ) or better spatial resolution in the case of tomography.

7.5 System engineering and geometry

Gamma-ray tomography applied to industrial processes and equipment has proven to be a rugged and reliable method to unravel information otherwise not available. The complexity of these systems varies, from a simple system based on one source and one detector that is moved around a object manually, for instance for column scanning, to rather complex systems with automated mechanical scanning and/or multiple sources and beams. Gamma-ray tomography systems are most often tailor-made, although important system components such as detector arrays may be available off the shelf.

7.5.1 System design

The system design should always start by answering these questions:

1. Is there any other measurement method that will perform equally well as gamma-ray tomography in this application?
2. What are the dimensions of the object and what is its composition?
3. Is the object encapsulated, for instance by vessel walls; and if so, what are the dimensions and composition?
4. Is there sufficient space available for the tomography system or any other restraints that must be considered?
5. What are requirements to the measurement resolutions of space, matter and time?

If the answer to the first question is yes, the ALARA principle states that the other method should be evaluated and chosen, if no other circumstances dictate otherwise. The latter could be cost issues or the possibility to measure high-pressure processes behind stainless steel walls. If the only option with sufficient performance is gamma-ray tomography, then the specifications defined through the remaining four questions are used to determine:

- Energy and isotope
- Source activity
- System geometry
- Shielding and collimation
- Detector technology
- Read-out electronics and computer interface
- Image reconstruction algorithms and software

These are interrelated, implying that the design and engineering phase often requires an iterative approach before the best solution is found. In such processes the following design principles are strongly recommended (Johansen & Jackson, 2004, p. 247):

- Once the energy is selected, carry out simple initial transmission measurements on the object in question or a phantom representing it, with a single source and detector connected to some general, laboratory electronics.
- If possible, develop Monte Carlo models benchmarked with measurements using single channel systems, and then carry out simulations of the full tomography system before building it.
- Always understand and test a single-beam version of the detector and read-out electronics using one source and one detector before building the full multichannel system.

7.5.2 Energy and isotope

The radiation energy determines the gamma-ray penetration capability and is initially defined so that the average product μx for the application is closest possible to two, as presented in Figure 7.6. The counting error is then at or close to its minimum. If the object in question is inside a vessel, the vessel wall attenuation also needs to be considered. Since there are limited isotopes and, consequently, energies to select between, this often comes down to using ^{241}Am and ^{137}Cs as low- and high-energy isotopes, respectively. These also have the advantage of fairly pure emission spectra (monochromatic), which is an advantage for image reconstruction. For even higher energies ^{60}Co is commonly used. The ALARA principle must be kept in mind in these considerations. The main justification for using a high-energy source is the capability to image, for instance, processes inside steel walls, where low attenuation radiation windows may be applied.

7.5.3 Source activity

Source activity is also a question of measurement accuracy, as can be seen from Figure 7.6, where I_0 is directly proportional to the activity of the source. The main question here is the requirement for temporal measurement resolution. If this can be relaxed, a low activity and longer integration time can be used. If high speed of response is required higher activity must be applied, but again the ALARA principle must be considered.

7.5.4 System geometry

The choice of geometry is very much a question of cost, since a multiple source and detector array system is far more expensive than one with a single source and a detector array, even taking the cost of a mechanical scanning system into consideration. It also depends on the energy selection, since higher energies, as described below, require more shielding and collimation and thus are heavier and more complex to operate. A system made for clamp-on installation will inevitably require more flexibility and be more complex than one designed for in-line installation. Normally, trade-offs must be made in the design geometry. Ideally, efficient collimation is desirable in front of the detectors to avoid scattered radiation and reduced image quality; however, this

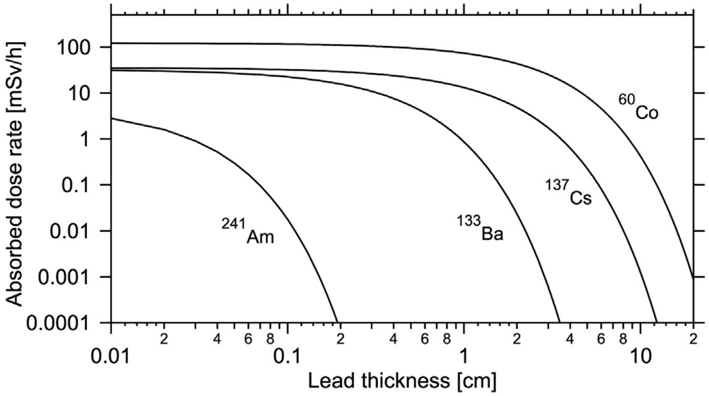

Figure 7.10 Estimated absorbed dose rates at 1 m distance as function of shielding lead thickness for four typical gamma-ray point sources with 3.7 × 10^5 MBq (10 Ci) activity (Johansen & Jackson, 2004, p. 188).

effect can to some extent also be reduced using scatter reduction algorithms (Maad, Hjertaker, & Johansen, 2008; Wagner, Bieberle, & Hampel, 2013).

7.5.5 Shielding and collimation

A low-energy source is much easier to shield than a high-energy one, as can be seen from the plot in Figure 7.10. The requirement of a larger radius for a spherical lead container for a high-energy source also has dramatic impact on its mass. When the latter becomes a problem tungsten alloys should be considered, although these are more expensive.

7.5.6 Detector technology

Selecting detector technology is primarily a question of gamma-ray energy, required speed of response and demands to the environment. A detector technology that works perfectly in a laboratory or at a test site with a controlled environment may be useless for operation at an industrial site. On the other side, there seems to be limited demand for full tomography systems for permanent installation at industrial sites. For laboratories and test sites CZT detectors are recommended for low-energy systems and BGO systems for higher energies. These have been on the market for many years and are available from several manufacturers, also pixelated in arrays.

7.5.7 Read-out electronics and computer interface

The development of customised read-out electronics is time consuming and demanding, particularly for high-count-rate applications where very fast response and low noise are required. It is therefore recommended to purchase compact and very large-scale integration electronics rather than developing dedicated electronics for the particular application. Several manufacturers offer complete detector and readout systems based on modules than can be stacked together (Wang et al., 2009). The cost may be higher in the short term, but in the long term it may pay off.

7.5.8 Image reconstruction algorithms and software

The hard-field property makes image reconstruction of gamma tomography data less of a challenge. There are a large number of reconstruction algorithms available, as is dealt with in Chapter 13; however, iterative algorithms produce best results (Maad & Johansen, 2008). Reconstruction time is not an issue for mechanical scanning systems, and real-time image reconstruction is rarely required for high-speed imaging systems where data streaming to disk and post-reconstruction is most often sufficient. For multisource systems semi-empirical algorithms should also be considered for scatter rejection.

7.6 Case studies

There are generally three categories of tomographic systems: laboratory systems, field equipment for diagnostics and mapping purposes, and permanently installed systems. Most developments are within the first category and are very often for research purposes. The selection of case studies presented here cover all categories, with main attention to the latter two, which often is referred to as agile tomography: tomography sensors and systems that can be deployed in situ, whether for permanent installation or for sporadic diagnostics or reference applications (York, McCann, & Ozanyan, 2011). The case studies also represent the different measurement geometries presented in Figure 7.2: first- and third-generation scanning geometries, instant nonscanning geometry and, in addition, a tomometry system for in situ operation using only one source and three detectors. Most of the recently developed gamma-ray tomography systems are based on the third-generation scanning geometry; see for instance Boyer and Fanget (2002) and Bieberle et al. (2013).

7.6.1 The Tracerco discovery pipe integrity scanner

Tracerco has developed and patented Discovery™, a novel nonintrusive inspection tool for pipeline visualisation. The development has been a market-driven process originating in the demand for better understanding of integrity and contents of subsea pipelines. Traditionally, pigging is applied for intrusive pipeline inspection and/or cleaning by sending gauges or ‘pigs’ through the pipelines. Discovery™ enables real-time inspection of pipelines that are not piggable (for instance because of valves or other obstacles), and can be applied without interfering with the production or process.

Discovery™ is a third-generation gamma-ray scanner utilising one ^{137}Cs source opposite a multiple array of scintillation detectors. It is designed for remotely operated vehicle clamp-on deployment onto pipes with diameters (including coatings) up to 27 inches; see Figure 7.11. The spatial resolution is about 2 mm and the scanning or data acquisition time is typically 1–2 min. The performance of the system is evident

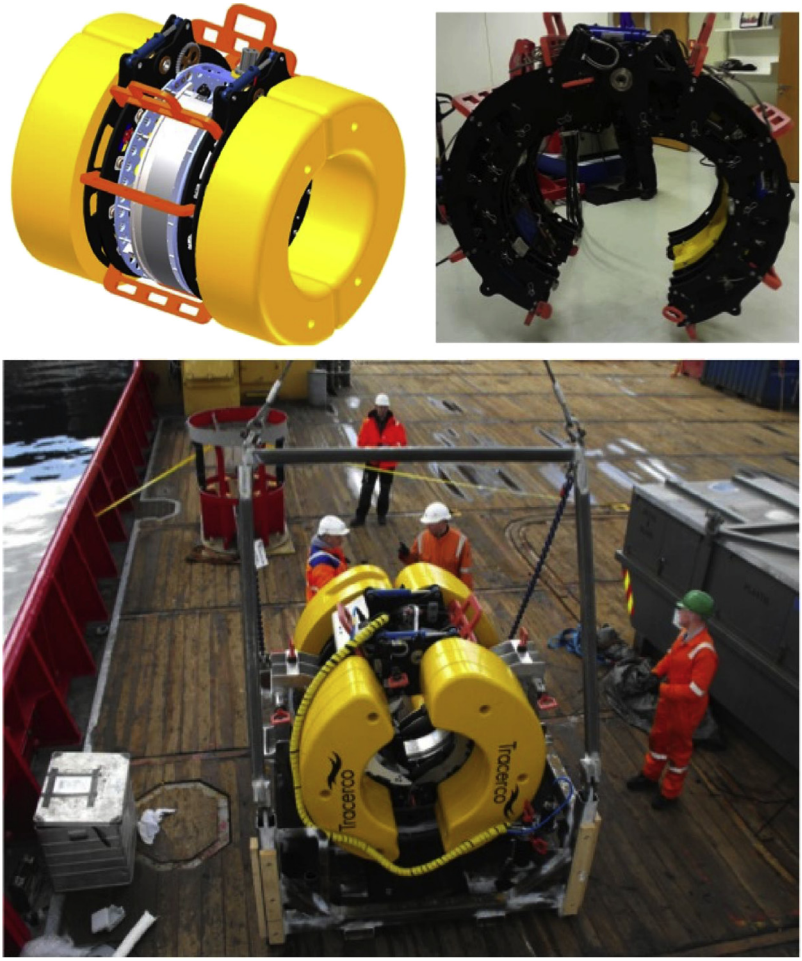

Figure 7.11 The Tracerco Discovery™ tool with floaters (yellow) and clamp-on installation. Courtesy of Tracerco.

from the test case shown in Figure 7.12. The dimensions of the tool are 1.2 m × Ø = 1.2 m and the weight is about 1300 kg on land and 30 kg in water, floaters included. Design details of this patented scanner cannot be revealed due to protection of Tracerco's proprietary rights.

7.6.2 The GammaScorpion

A transportable system for early detection of basal stem rot of oil palms due to Ganoderma disease has been developed at the Malaysian Nuclear Agency in Kajang. The system applies a first-generation scanner with a C-frame design on wheels so that it can be rolled into position surrounding the palm tree stem and clamped onto it. It

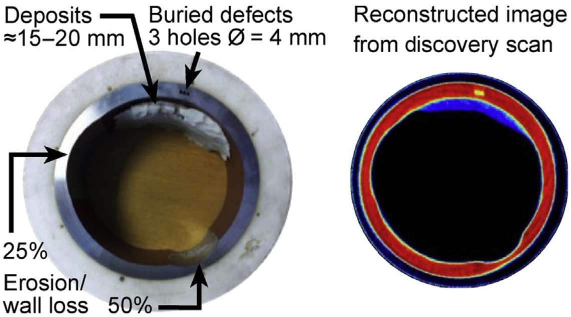

Figure 7.12 Results using Tracerco Discovery™ tool on a phantom imitating insulation, pipe erosion, deposits and defects, which all can be seen on the reconstructed image. Courtesy of Tracerco.

applies one 50 mCi ^{137}Cs source and one collimated 1-inch-diameter NaI(Tl) PMT scintillation detector. It produces good-quality tomographic images with sufficient contrast to differentiate Ganoderma-infected oil palm stems form healthy ones; see Figure 7.13. It has been successfully tested and used to detect the extent of basal stem rot damage on a number of stems in oil palm plantations in Malaysia without the need to cut down the trees. The method offers great advantages for in situ inspection and early detection of oil palm stem diseases as compared to the available conventional methods (Abdullah, Hassan, & Mohamad, 2013).

7.6.3 The University of Bergen's high-speed gamma-ray tomography for pipe flow imaging

Multiphase flow meters (MPFM) for measurements of gas, oil and water operate by combining instantaneous velocity and cross-sectional fraction measurements of the flow components. The major error source in these measurements is temporal variations in the distribution of gas and liquid in the measurement cross-section of the pipe. The flow regime-induced problems associated with monitoring of hydrocarbon multiphase flow can be significant. For example, the flow regime at the wellhead can have slugging, gas break-out and severe turbulence, varying from nearly pure oil to gas, or in any combination at high or low pressures or at high or low temperatures during the lifetime of the well (Thorn, Johansen, & Hjertaker, 2013).

Consequently, the development of MPFM hardware and software always involves tests in flow loop facilities where the flow composition and flow rate can be preset. The instantaneous flow pattern in the measurement volume of the flow meter under test, however, can only be determined by tomographic imaging measurements obtained close to the flow meter location. This measurement scenario was the objective of the development of the nonscanning high-speed gamma-ray tomograph at the University of Bergen (UiB). The objective is not to image small details of the flow, but rather to image gas bubbles with size of about 10% of the pipe diameter or bigger. Flow regime distributions with smaller gas bubbles will be interpreted as homogeneous mixtures and introduce only insignificant measurement errors in the MPFMs. The UiB

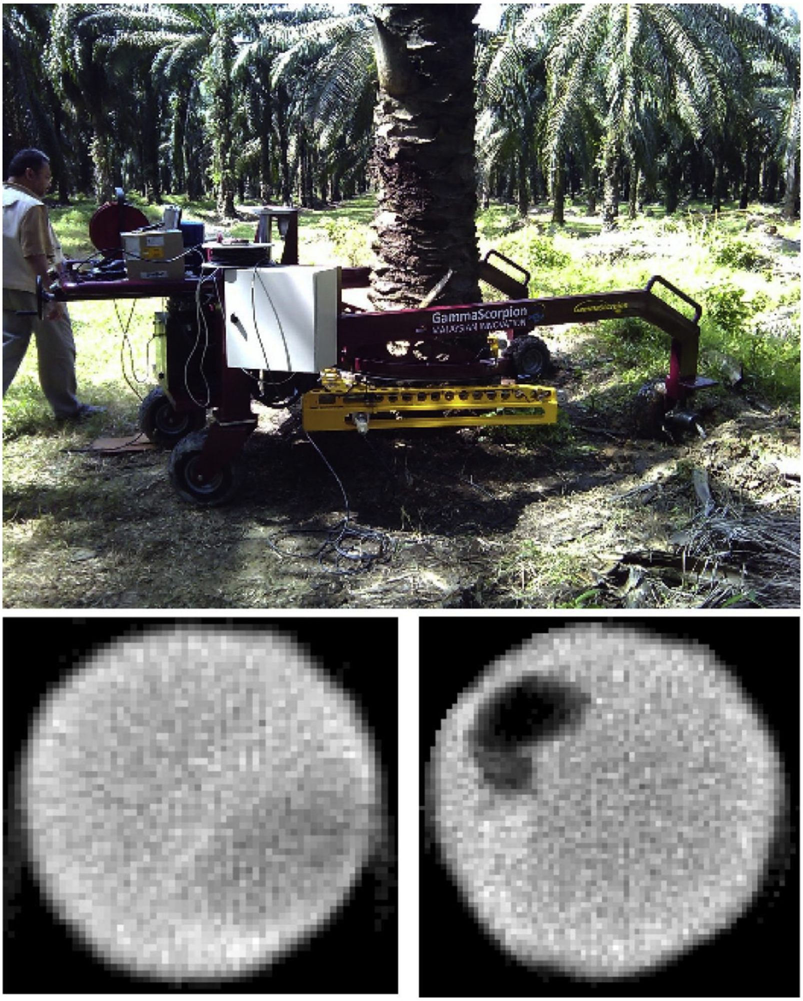

Figure 7.13 The GammaScorpion; a first-generation scanner developed by the Malaysian Nuclear Agency. Also shown is a tomogram of a healthy palm and one of a Ganoderma-infected palm, where the void caused by the disease is easily seen.
Courtesy of Malaysian Nuclear Agency.

high-speed gamma-ray tomograph is therefore designed with a focus on high temporal resolution rather than high spatial resolution.

The system is shown in Figure 7.14 and comprises a sensor head equipped with five 500 mCi ^{241}Am sources emitting gamma-rays with energy of 59.5 keV (Johansen, Frøystein, Hjertaker, & Olsen, 1996). Each of the five fan-beam collimated radiation sources faces detector modules with focussed grid collimation. Each detector module contains a linear array of 17 CdZnTe detectors operated in pulse counting mode with read-out electronics optimised for high-speed counting rather than energy resolution.

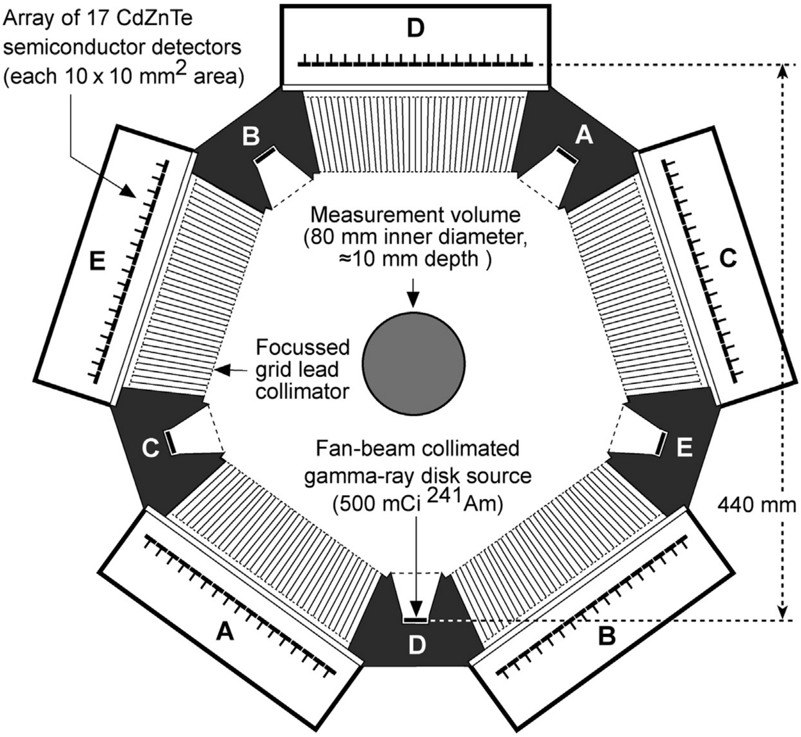
Array of 17 CdZnTe semiconductor detectors (each 10 x 10 mm^2 area)
D
B
A
E
C
Measurement volume (80 mm inner diameter, ≈10 mm depth)
Focussed grid lead collimator
C
E
Fan-beam collimated gamma-ray disk source (500 mCi ^{241}Am)
440 mm
A
D
B

Figure 7.14 Cross-sectional view of the University of Bergen (UiB) high-speed gamma-ray tomograph with five views and a total of 85 projections (Johansen et al., 1996).

The gamma-ray sensor head therefore has a total of 85 gamma-ray detectors. It is designed for a maximum pipe diameter of 80 mm.

The read-out electronics of the high-speed gamma-ray tomograph comprise charge-sensitive preamplifiers, amplifiers and filter electronics. Short-output pulses with 250 ns peaking time are accomplished by implementation of delay-line shaping and this ensures high-count-rate capability. The data acquisition and control system is based on microcontrollers providing a USB- or Ethernet-based communication interface to the computer. The data acquisition system utilises pipeline architecture where data from the 85 detector channels are fed into the microcontrollers, allowing a new data integration period to be started immediately.

The measurement and imaging characteristics of the system are determined in experiments using polypropylene phantoms with holes emulating gas bubbles in liquid. The true attenuation coefficient distribution of the discretised image is expressed by the true pixel values $\mu_{\text{true},i}$. The root mean square error (RMSE) of each reconstructed image is defined as:

$$\text{RMSE} = \frac{\sqrt{\sum_{i=1}^{N} \left(\mu_{\text{true},i} - \mu_{\text{reconstructed},i}\right)^2}}{N} \tag{7.6}$$

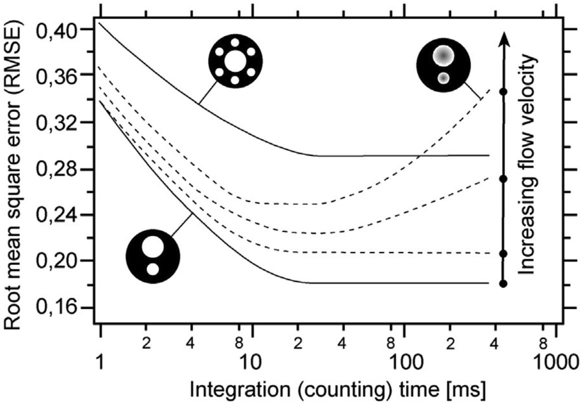

Figure 7.15 The solid lines are experimental data revealing the increasing dominance of counting errors at short integration times using static phantoms (Hjertaker, Maad, Schuster, Almås, & Johansen, 2008). Also shown is the strong dependency of the RMSE on the complexity of the flow pattern, here represented by two polypropylene (black) phantoms with cylindrical holes (white). In another experiment a polypropylene phantom with two spherical gas bubbles inside is used to study the error caused by the movement of the flow through the measurement cross-section (Maad, Hjertaker, Johansen, & Olsen, 2010). The dashed lines indicate the increase in the RMSE as the flow velocity increases, even though these data cannot be directly compared to the static phantom experiment. Iterative least square reconstruction on a 32 × 32 grid is used for all these experiments.

Here $\mu_{\text{reconstructed},i}$ is the reconstructed pixel values and N is the number of pixels in the reconstruction grid. The RMSE is an overall image quality indicator that encompasses counting errors, reconstruction errors and errors caused by the flow dynamics. Several experiments have been carried out to determine the dependence of the RMSE on integration time, reconstruction method and flow pattern. Some of these are summarised in Figure 7.15, where the RMSE is plotted as a function of integration time for different conditions.

The error depends strongly on the complexity of the flow pattern, as can be seen from the plots. However, the most important observation from Figure 7.15 is that for this particular system there will be a noise minimum in the area of 10−20 ms integration time in real flow operation. This corresponds to image rates of 50−100 frames per second. Longer integration times are not advisable because the data set collected then no longer produces an instant image, but rather the average of a longer flow section as the fluid passes through the measurement cross-section. This is analogous to photography, where the exposure (integration) time has to be much shorter than any moving object to produce a sharp image. On the other hand, it is possible to reduce the integration time below the noise valley at the cost of higher contribution of counting errors. The results presented in Figure 7.14 is produced iterative least square reconstruction; however, the system has also been tested with other reconstruction algorithms, such as the alternating minimisation technique, with similar results (Maad & Johansen, 2008). Scatter correction algorithms have also been applied (Maad et al., 2008). However,

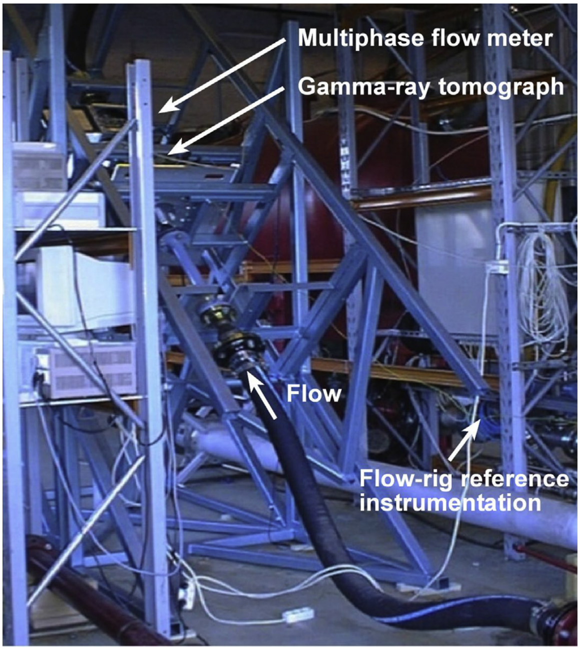

Figure 7.16 The tilt section of the multiphase flow loop facility at Christian Michelsen Research in Bergen, Norway. The Multiphase flow meters (MPFM) under test is mounted next to the gamma tomograph and data from both units are synchronised and streamed to disk for postprocessing. The flow loop computer controls the flow composition and flow rate. Here MPFMs can be tested at different inclination angles from 0° (horizontal flow) to 90° (vertical flow).

since the focused grid collimator efficiently reduces scatter, these provide limited error reduction except in cases with very low gas volume fractions (GVF).

In operation as a reference instrument in flow loop testing of MPFMs (see Figure 7.16), the data from the gamma tomograph are streamed to disk and synchronised with the MPFM data acquisition. By using post-image reconstruction and analysis, otherwise time-consuming iterative reconstruction methods do not pose any restrictions on the image capture rate. Even though the RMSE increases and the image quality drops, the gamma tomograph is capable of imaging the gas—liquid distribution at several hundred frames per second. Roxar Flow Measurement has applied the UiB gamma tomograph regularly in flow loop tests of their MPFMs and uses the tomographic information to enhance the models the flow computer uses to calculate the flow of gas, oil and water (Tjugum, Sætre, & Johansen, 2011).

7.6.4 The Roxar down-hole multibeam gamma sensor

By means of the UiB high-speed gamma-ray tomograph, the algorithms of the MPFM computer can be tuned to provide more accurate flow measurements in top-side as well as subsea installations where the flow meter also measures vertical upward flow.

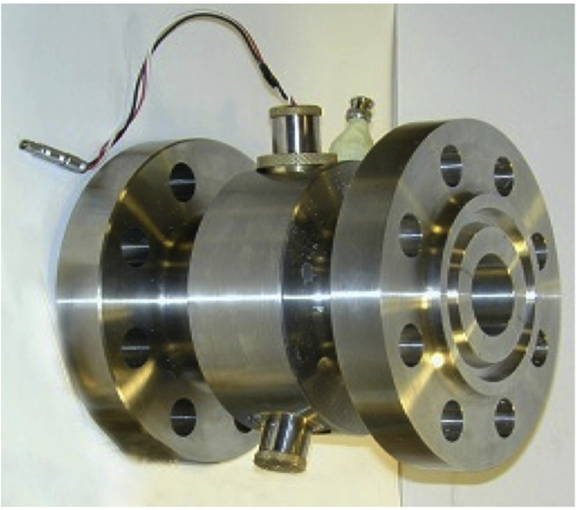

Figure 7.17 The MiniGamma, the first spool piece prototype of the multiple gamma-ray beam system with a ^{241}Am source and detectors embedded in the pipe wall.

In-well measurements are a lot more demanding, since variations in the flow regime are far less predictable. A feasible approach, therefore, is to continuously monitor the flow pattern in the measurement cross-section of the flow meter. Needless to say, a full tomography system is not feasible here, and actually is not required either. The solution is a system using just one gamma-ray source and two or three detectors defining as many beams at different angles through the cross-section. It is then possible to identify whether the instantaneous pattern is type stratified or annular, and to use this information to correct the measured gas fraction. This does not involve any image reconstruction and is often referred to as tomometry. Such a system has been developed in a collaboration of Roxar Flow Measurement, and the first laboratory prototype was named MiniGamma (Tjugum, Frieling, & Johansen, 2002); see Figure 7.17. This system, which has been further developed, comprises one ^{241}Am source and two detectors embedded in the pipe wall so that one detector measures transmission through the pipe centre and the other along the pipe wall.

The corrected GVF for stratified (α_S) and annular (α_A) flow relative to the measurement carried out by the centre beam can be calculated according to Eqn (7.6) (Sætre, Johansen, & Tjugum, 2010). For other flow patterns similar expressions are available.

$$\begin{aligned}\alpha_S &= 1-\frac{1}{\pi}\left[\cos^{-1}(2\alpha-1)-2(2\alpha-1)\cdot\sqrt{\alpha(1-\alpha)}\right]\\ \alpha_A &= \alpha^2\end{aligned} \tag{7.7}$$

The approach is to apply flow segmentation where the flow is split into small segments of a few to some tens of milliseconds, and to identify the flow pattern in

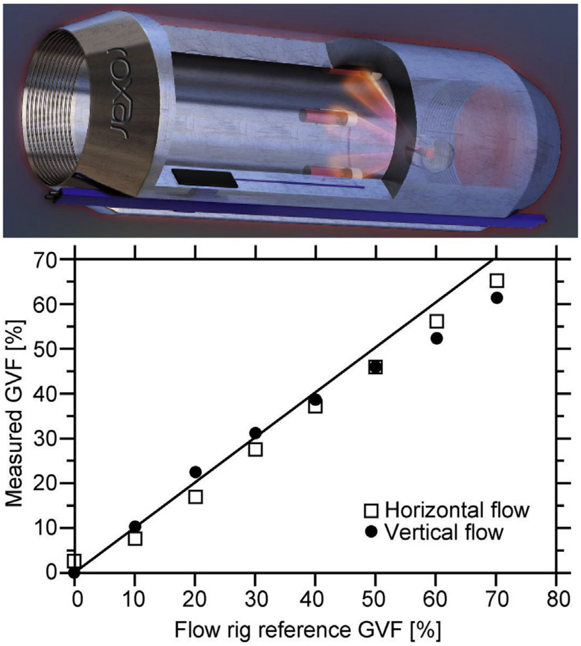

Figure 7.18 The Roxar down-hole multibeam gamma sensor launched in 2011 *(Courtesy of Roxar Flow Measurement)*. The results are from tests at the Christian Michelsen Research flow loop with the measured versus the rig reference gas fraction in horizontal and vertical flow (Tjugum et al., 2011).

each before the GVF is calculated. Running averaging is then applied on the final data to reduce counting statistics errors. The feasibility of this approach was proven using the high-speed gamma-ray tomograph as reference in flow loop tests. Increasing the running average time strongly improves the correlation with the tomograph reference data (Sætre et al., 2014).

Roxar Flow Measurement launched their first down-hole multibeam gamma sensor for gas fraction measurements in 2011. It uses a ^{137}Cs source with a 662 keV emission line and three detectors; see Figure 7.18. The results of the first flow loop test, also shown in Figure 7.18, confirm flow regime-independent measurements of the GVF. The deviation at high gas fractions is caused by slip between the gas and liquid phases (Tjugum et al., 2011). This is corrected for in field operation using data from subsequent flow velocity sensors (ΔP or X-correlation) on the production string.

7.7 Future trends

There has always been some scepticism of gamma-ray measurement systems; however, these have advantages that stimulate further developments also when the ALARA principle is considered. Gamma-rays respond to the fundamental physical properties of matter, the density of elemental particles, and is often less susceptible to variations in other parameters compared to other methods. Gamma-rays allow design of noncontact and clamp-on systems, they can be measured with high accuracy, and there are detectors available for operation and proven in harsh environments, such as in well logging. The most important trends are not specific to gamma-ray methods, but are common within industrial tomography:

- Multiple modality systems: The need for more information in different applications demands simultaneous operation of several measurement methods that are complementary with respect to what physical property they are sensitive to in a multiphase system.
- Tomometry: Tomographic imaging will still be important for laboratory applications and to some extent for process diagnostics carried out at plants on a regular basis. Tomographic methods will also play an important role in permanent in situ measurements, but then with fewer, but sufficient, measurements to extract the required information rather than full imaging. This is also caused by the fact that simple and cost-effective systems are preferred to more sophisticated ones because reliability in many cases is more important than measurement accuracy.
- Process and equipment tomography: There is an increasing interest in condition and integrity monitoring of process equipment such as pipes and vessels. This may involve tomographic measurements, as is the case with the Tracerco Discovery presented in Section 7.6.1; however, here also tomometry may be applied.
- Data reduction: Applications such as surveillance and condition monitoring of subsea process plants where a large number sensors produces large amounts of data, will require sophisticated algorithms for data analysis and rejection so that only the crucial information is left behind. For tomographic measurements this could for instance imply automatic interpretation or parameterisation of tomograms.

References

Abdullah, J., Hassan, H., & Mohamad, R. Shari (2013). GammaScorpion: mobile gamma-ray tomography system for early detection of basal stem rot in oil palm plantations. *Optical Engineering, 52*(3), 036502.

Achmad, B., & Hussein, E. M. A. (2004). An X-ray Compton scatter method for density measurement at a point within an object. *Applied Radiation and Isotopes, 60*, 805−814.

Bieberle, A., Nehring, H., Berger, R., Arlit, M., Härting, H.-U., Schubert, M., et al. (2013). Compact high-resolution gamma-ray computed tomography system for multiphase flow studies. *Review of Scientific Instruments, 84*, 033106.

Boyer, C., & Fanget, B. (2002). Measurement of liquid flow distribution in trickle bed reactor of large diameter with a new gamma-ray tomographic system. *Chemical Engineering Science, 57*, 1079−1089.

Evans, B., Martin, J. B., Burggraf, L. W., Roggeman, M. C., & Hangartner, T. N. (2002). Demonstration of energy-coded Compton scatter tomography with fan beams for one-sided inspection. *Nuclear Instruments and Methods, A480*, 797−806.

Harding, G., & Harding, E. (2010). Compton scatter imaging: a tool for historical exploration. *Applied Radiation and Isotopes, 68*, 993−1005.

Hjertaker, B. T., Maad, R., Schuster, E., Almås, O. A., & Johansen, G. A. (2008). A data acquisition and control system for high-speed gamma-ray tomography. *Measurement Science and Technology, 19*(9), 094012.

ICRP. (1991) (ICRP publication 60). *Radiation protection − 1990 recommendations of the ICRP annals of the international commission on radiological protection* (Vol. 21). Pergamon Press. pp. 1−3.

Johansen, G. A., Frøystein, T., Hjertaker, B. T., & Olsen, Ø. (1996). A dual sensor flow imaging tomographic system. *Measurement Science and Technology, 7*(3), 297−307.

Johansen, G. A., & Jackson, P. (2004). *Radioisotope gauges for industrial process measurements*. Chichester: John Wiley & Sons Ltd.

Maad, R., Hjertaker, B. T., & Johansen, G. A. (2008). Semi-empirical scatter correction model for high-speed gamma-ray tomography. *Measurement Science and Technology, 19*(9), 094016.

Maad, R., Hjertaker, B. T., Johansen, G. A., & Olsen, Ø. (2010). Dynamic characterization of a high speed gamma-ray tomograph. *Flow Measurement and Instrumentation, 21*(4), 538−545.

Maad, R., & Johansen, G. A. (2008). Experimental analysis of high-speed gamma-ray tomography performance. *Measurement Science and Technology, 19*(8), 085502.

Sætre, C., Johansen, G. A., & Tjugum, S.-A. (2010). Salinity and flow regime independent multiphase flow measurements. *Flow Measurement and Instrumentation, 21*(4), 454−461.

Sætre, C., Johansen, G. A., & Tjugum, S.-A. (2014). Tomographic segmentation in multiphase flow measurement. *Radiation Physics and Chemistry, 95*, 420−423.

Thorn, R., Johansen, G. A., & Hjertaker, B. T. (2013). Three-phase flow measurement in the petroleum industry. *Measurement Science and Technology, 24*, 012003.

Tjugum, S.-A., Frieling, J., & Johansen, G. A. (2002). A compact low-energy multibeam gamma-ray densitometer for pipe-flow measurements. *Nuclear Instruments and Methods, B197*, 301−309.

Tjugum, S.-A., Sætre, C., & Johansen, G. A. (2011). Multibeam gamma-ray measurements and electrical tomography for improved multiphase flow metering. In *Proceedings of the north sea flow measurement workshop,* Tønsberg, Norway, 25−28 October.

Wagner, M., Bieberle, A., & Hampel, U. (2013). Study on a simulation-based scatter correction for high-resolution gamma-ray tomography. In *Proceedings of the 7th world congress on industrial process tomography, international society for industrial process tomography*. www.isipt.org. Krakow, Poland, 2−5 September.

Wang, X., Meier, D., Sundal, B. M., Oya, P., Maehlum, G. E., Wagenaar, D. J., et al. (2009). A digital line-camera for energy resolved X-ray photon counting. *IEEE Nuclear Science Symposium Conference Record, 1−5*, 3453−3457.

York, T., McCann, H., & Ozanyan, K. B. (2011). Agile sensing systems for tomography. *IEEE Sensor Journal, 11*(12), 3086−3105.

Radioisotope tracer techniques

8

D. Parker
University of Birmingham, Birmingham, UK

8.1 Nuclear medicine imaging

8.1.1 Single photon emission computed tomography

In medicine, imaging the way in which a biologically interesting molecular species, labelled with a radioactive tracer, distributes through the human body provides one of the most powerful ways of studying normal physiology and identifying pathologies. Since Anger first invented the gamma camera in 1957 (Anger, 1964), the field of diagnostic nuclear medicine has developed into a major international industry.

A gamma camera (Figure 8.1) forms a two-dimensional (2D) image of the radioisotope distribution within the body by detecting emitted gamma-rays using a sheet of the scintillator sodium iodide (typically around 10 mm thick and 50 cm in

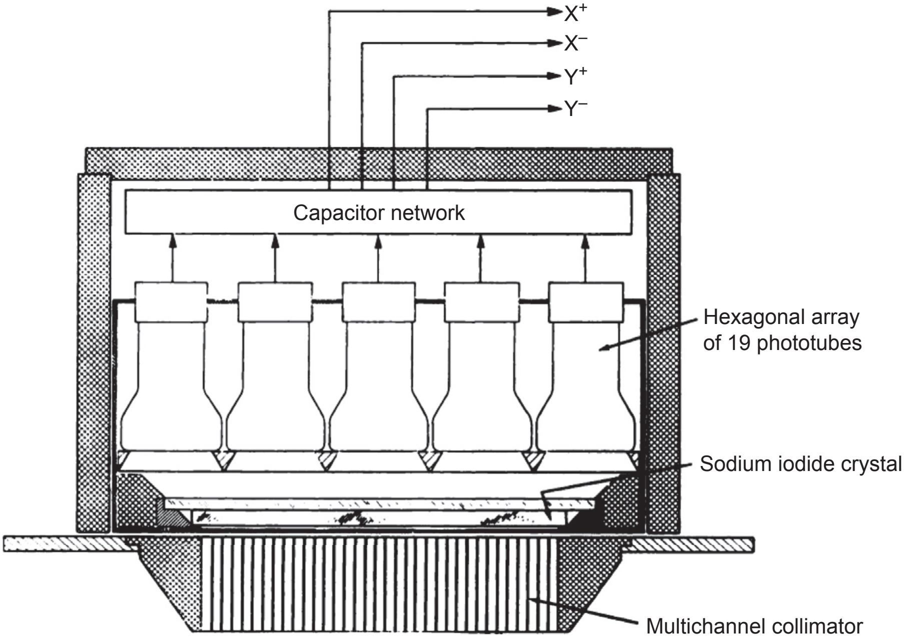

Figure 8.1 Schematic of gamma camera.
Taken from Anger (1964).

Industrial Tomography. http://dx.doi.org/10.1016/B978-1-78242-118-4.00008-3
Copyright © 2015 Elsevier Ltd. All rights reserved.

diameter) backed by an array of around 50 photomultiplier tubes (PMTs). Each gamma-ray interacting in the scintillator produces a flash of light, which spreads over several PMTs; by comparing the light intensities measured in the different PMTs the coordinates of the interaction can be determined to within a few mm.

Since it is not possible to focus gamma-rays, a collimator is used to define the direction from which each detected gamma has reached the detector. Although use of a pinhole collimator is possible, generally a parallel-hole collimator is used, consisting of a block of lead between 2.5 and 5 cm thick, through which are drilled a large number of parallel holes designed to transmit only gamma-rays close to normal incidence. In practice the collimator transmits a cone of gamma-rays, limited by the aspect ratio of the holes, so that the spatial resolution of the resulting image degrades linearly with distance to the source. A typical high-resolution collimator might have holes of 2 mm diameter × 50 mm long, resulting in a spatial resolution of around 12 mm for imaging a source at a distance of 30 cm. The thickness of the lead septa separating the holes is dictated by the need to attenuate non-normal gamma-rays by a sufficient factor, which becomes progressively harder as the gamma-ray energy increases. The majority of gamma camera imaging is performed using the radionuclide ^{99m}Tc, which emits 140 keV gamma-rays — this is an ideal energy for medical imaging: high enough to escape the body but low enough to be easily collimated. ^{99m}Tc is also popular because of its convenient half-life (6 h), absence of more damaging emissions and availability from decay of the radioactive parent ^{99}Mo (half-life 66 h) — this is supplied in the form of a *technetium generator* from which a solution of ^{99m}Tc can be eluted when required.

A static gamma camera measures a 2D projected view of the activity distribution within a 3D region. A tomographic image of the 3D volume can be obtained by rotating the camera around the patient, measuring projections at all angles and using a technique such as filtered back-projection or iterative reconstruction to reconstruct the activity within each voxel. This imaging modality is referred to as single photon emission computed tomography (SPECT) to distinguish it from the dual photon imaging used in positron emission tomography (PET) (see below). A complication of SPECT imaging is the need to correct for the attenuation of the gamma-rays within the body: the extent of this attenuation depends on the depth of the source and properties of the intervening material, information on which may be provided by complementary imaging techniques. The need to perform a depth-dependent correction for attenuation poses problems for a simple reconstruction technique like filtered back-projection, and with the increased availability of computing power iterative reconstruction techniques are increasingly popular.

8.1.2 Positron emission tomography

PET is a separate branch of nuclear medicine based on the use of positron-emitting radionuclides. These proton-rich nuclides decay by β^+ decay in which a positron (the positively charged anti-particle of the normal electron) is emitted. After slowing down to rest, the positron annihilates with a normal electron producing a pair of 511 keV photons,[1] which are emitted almost exactly back-to-back due to conservation of momentum. If the positron–electron pair had zero momentum prior to annihilation, then the pair of photons would be emitted exactly 180° apart; in practice the residual momentum of the electron results in an acollinearity of up to about 0.5°.

Simultaneous *coincidence* detection of the two annihilation photons using detectors on either side of the patient defines a *line of response* passing close to the site of the radioactive decay without the need for a physical collimator. For this reason the coincidence is said to provide *electronic collimation.* Major advantages of PET compared to SPECT include the much higher sensitivity (a typical parallel hole collimator blocks over 99.9% of gamma-rays, which would otherwise be detected) and geometric invariance – as noted above, the blurring caused by a parallel hole collimator increases linearly with distance, but the spatial resolution in a PET measurement is approximately independent of depth. Just as in SPECT, it is necessary to correct for attenuation of the 511 keV photons, but, because what matters is the overall probability of either of the two photons being attenuated, for a given line through the body the attenuation correction is independent of the depth of the source and can be accurately determined using an external transmission source.

A PET scanner (Figure 8.2) generally consists of one or more rings of blocks of thick, high-Z scintillator – 20-mm-thick bismuth germanate (BGO) is typical – giving high efficiency for detecting 511 keV photons. Each block is subdivided into smaller elements by cuts that penetrate part-way down, leaving an intact base to which are coupled four PMTs. Comparing the light intensities in the different PMTs allows the individual element in which the photon interacted to be uniquely identified.

Ultimately the spatial resolution of a PET study would be limited by the basic physics: the emitted positron travels some distance before annihilation, and the two photons are not emitted exactly back-to-back. The magnitude of these effects depends on the radioisotope used, the density of the material and the detector separation, but in a typical study they could be expected to contribute a positional uncertainty of 1–2 mm. In practice, the resolution is usually limited by the size of the detector elements. A typical clinical PET scanner might have blocks around $50 \times 50\ \text{mm}^2$ cut into an 8×8 array of elements, each approximately $6.5 \times 6.5\ \text{mm}^2$, but high-resolution scanners use $4 \times 4\ \text{mm}^2$ elements, and dedicated small animal scanners (intended for drug trials) have elements as small as $1.5 \times 1.5\ \text{mm}^2$.

A coincident pair of 511 keV photons is recognised by their near-simultaneous detection in opposing detector blocks. Because of variations in the time taken for a gamma-ray interaction to generate a pulse, and to allow for variations in time of arrival of the two photons due to the finite speed of light, some tolerance in timing

---

[1] These 511 keV photons are often referred to as gamma-rays. Strictly speaking this is incorrect, as the term gamma-ray is used to denote photons emitted by an excited nucleus.

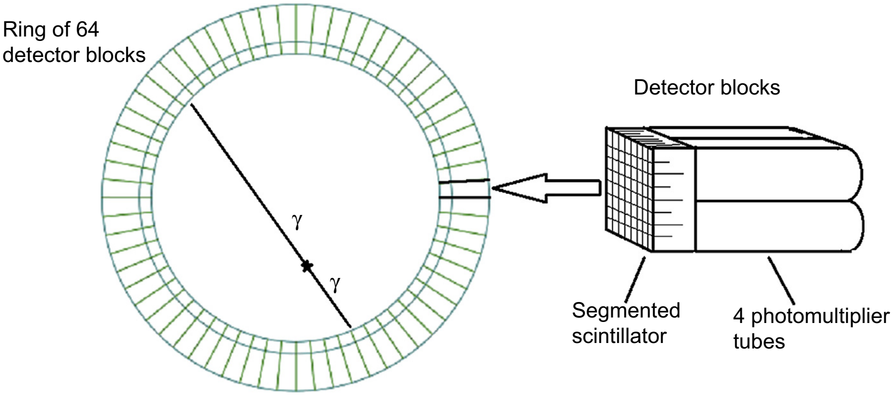

Figure 8.2 Schematic of a positron emission tomography scanner.

must be allowed. In practice, two pulses are considered coincident if they occur within a time interval less than a specified value τ, the *resolving time* of the system. For a PET scanner the resolving time is typically around 10 ns. If two unrelated pulses happen to occur within this time interval they will also be recorded — such events are described as *random coincidences*. Random coincidences add background to an image; although for any individual event it is not possible to identify it as *true* or *random*, the contribution of random coincidences to a study can be accurately estimated by repeating the same measurement with a delay ($\gg \tau$) introduced into one side of the coincidence circuit — this eliminates true coincidences but does not alter the rate or distribution of random coincidences. Many PET scanners continuously record both *prompt* and *delayed* coincidences and then reconstruct their images from the difference between the two datasets.

A more intractable problem is the background due to detection of a significant contribution of events where one or both of the photons has scattered prior to detection. For all but very high-Z materials, Compton scattering is the principal interaction mechanism for 511 keV photons. The energy resolution of the detector blocks is generally too poor to discriminate against photons that have scattered through a small angle. In an attempt to reduce the proportion of scattered events in the detected data, some early PET scanners incorporated collimating septa, which essentially subdivided the 3D imaging problem into a stack of separate 2D slices; this design improved the quality of the data, but at the cost of greatly reduced sensitivity, and is no longer popular.

Most clinical PET studies use the nuclide ^{18}F, which has to be produced using a cyclotron. The half-life of ^{18}F is 110 min, long enough to allow transport over extended distances, and a number of cyclotrons supply ^{18}F in the form of fluorode-oxyglucose. Where a local cyclotron is available the shorter lived isotopes ^{11}C (20 min), ^{13}N (10 min) and ^{15}O (2 min) can also be used.

8.2 Industrial applications

8.2.1 Single photon imaging

Given the widespread availability of gamma cameras in nuclear medicine, it is perhaps surprising that rather few industrial applications of gamma camera imaging have been reported. This may partly be attributed to the relatively low penetration of the low-energy gamma-rays for which parallel hole collimators are usually designed (1 cm steel attenuates the 140 keV gamma-rays from ^{99m}Tc by a factor of 5). Collimators designed to be used with ^{99m}Tc are generally unsuitable for imaging higher-energy gamma-rays.

The low data rates and consequent long imaging times are also a problem, meaning that SPECT has generally been confined to imaging steady-state or slow flows. For example, Perret et al. (2000) (Calgary) reported the use of SPECT to study breakthrough curves in saturated soil cores. Cores of 77 mm diameter were imaged over a 40 cm length using a rotating gamma camera fitted with a high-resolution collimator. ^{99m}Tc was injected into the flow, and images were acquired. Since each SPECT image took 6 min to acquire, imaging was performed in stop/start mode, with the flow halted during acquisition, and 2 min flow between each image. Images with a spatial resolution of around 4 mm were obtained and clearly showed the flow proceeding through macropore structures.

There have also been some efforts to develop dedicated industrial SPECT systems, suitable for use with higher-energy gamma-rays. Legoupil et al. (1997) at Saclay reported an experimental SPECT system for industrial imaging, comprising 36 collimated NaI detectors (6 banks, each of six detectors) in a single plane. This system was demonstrated by imaging flow, labelled by injection of ^{99m}Tc, in a 24-cm-diameter vessel. Full-width half-maximum spatial resolutions of approximately 10% of the vessel diameter were reported. More recently Park et al. (2014) report that they are developing a similar system at KAERI in Korea.

8.2.2 Positron emission tomography

In principle, PET is well suited to studying engineering systems, as the 511 keV photons are reasonably penetrating (50% are transmitted through 11 mm steel). Just as for SPECT, imaging is slow, so PET is most suited for studying steady-state or slow flows.

Positron-emitting nuclides are less widely available (and more expensive) than ^{99m}Tc. The positron emitter ^{68}Ga (half-life 68 min) can be obtained from a generator containing the parent ^{68}Ge (271 days). ^{64}Cu (12.4 h) can be produced by neutron activation of copper in a nuclear reactor. All other positron emitters are cyclotron produced.

Industrial application of PET was pioneered by the Birmingham group in the 1980s. In contrast to the ring scanners now standard in medical PET, the Birmingham work used a ‘positron camera’ consisting of two rectangular detectors (multi-wire proportional chambers) operating in coincidence. For 3D tomographic imaging it was necessary to rotate the camera about the field of view, measuring projected views at all angles, but useful information could also be obtained using 2D projection imaging. For example, Figure 8.3 shows a sequence of 10 min images of brine flow through a specimen of oil-reservoir sandstone (observing the passage of a bolus of ^{18}F fluoride), while Figure 8.4 shows a sequence of 1 min images of labelled dough being extruded into a metal mould.

More recently the Birmingham group has performed some PET imaging using a standard medical PET scanner. For example, Figure 8.5 shows the dispersion of a bolus of labelled powder within a pharmaceutical blender (Parker et al., 2008). Acquiring the data for each image took 20 min, so this study was performed in stop/start mode with the blender being tumbled for five revolutions between each image acquisition.

A few other groups have reported using PET to study industrial processes. For example, Barth et al. (2014) (Dresden) have recently reported the use of a small

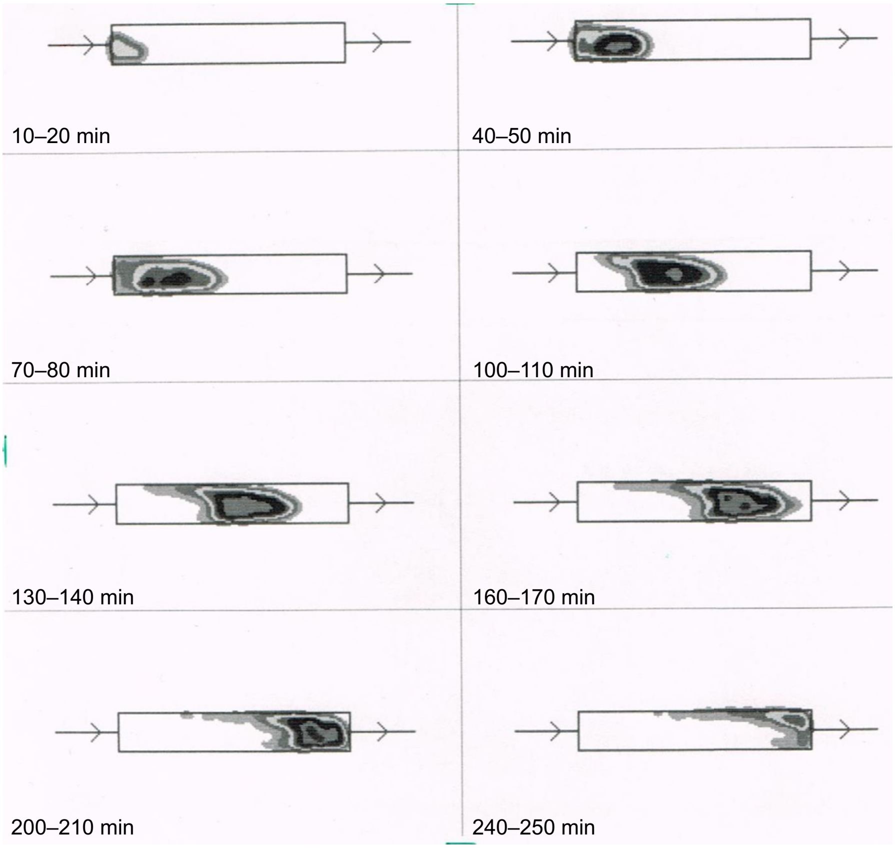

Figure 8.3 Sequence of 10 min positron projection images showing passage of a bolus of ^{18}F brine through a specimen of oil-reservoir sandstone ($30 \times 5 \times 5$ cm^3).
From Hawkesworth et al. (1991).

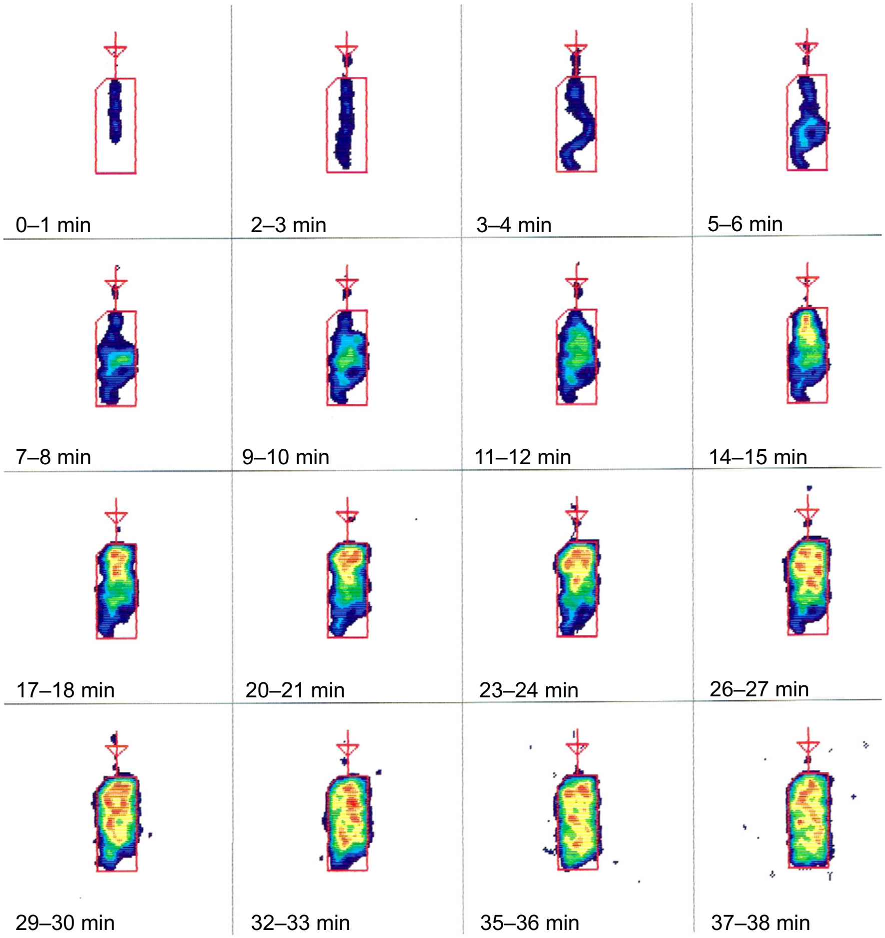
0–1 min
2–3 min
3–4 min
5–6 min
7–8 min
9–10 min
11–12 min
14–15 min
17–18 min
20–21 min
23–24 min
26–27 min
29–30 min
32–33 min
35–36 min
37–38 min

Figure 8.4 Selected 1 min images showing extrusion of labelled flour dough into a metal mould.

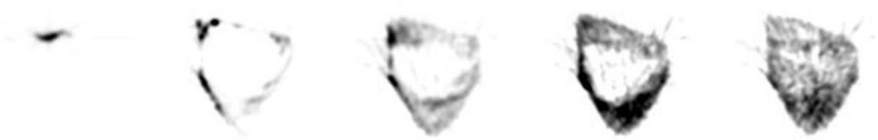

Figure 8.5 Sequence of images (central slice through 3D positron emission tomography image) showing mixing of a small amount of labelled powder with the unlabelled bulk powder in a pharmaceutical blender.
From Parker et al. (2008).

animal PET scanner to study the dynamics of deposition and resuspension of graphite dust, labelled with ^{18}F, within a working model of a pebble bed reactor.

8.3 Particle tracking

For studying rapid industrial flows, both SPECT and PET are of limited use due to the time required to acquire sufficient counts to enable reconstruction of a 3D tomographic image. Instead, valuable dynamic information can often be obtained by tracking a single radioactively labelled particle. If only a single radioactive source is present its location can be determined very rapidly, and by repeating this measurement at regular intervals the track of the particle can be observed. This is a powerful way of studying the behaviour of granular systems (if a representative grain is labelled and tracked) or viscous fluids (if a neutrally buoyant flow follower is tracked). In a closed system, where material recirculates, by tracking a single particle over an extended period (Lagrangian measurements) one can build up Eulerian time-averaged density and velocity maps for the labelled species along with information on dispersion.

Two separate techniques for tracking radioactive particles have been developed. Radioactive particle tracking (RPT) determines the source position by comparing count rates of high-energy gamma-rays detected by different detectors within an array of individual detectors, whereas positron emission particle tracking (PEPT) uses triangulation of the pairs of back-to-back annihilation photons from positron—electron annihilation. These two techniques are described below.

8.3.1 Radioactive particle tracking

In RPT the location of the tracer is found by comparing the gamma-ray intensities (count rates) measured in a number of small detectors, which are strategically positioned around the system under study. The intensity falls off with distance from the tracer according to the inverse square law, modified by the effects of gamma-ray attenuation and scattering within the system. For a particular geometry and material layout the actual relationships must be determined via a calibration procedure; for a given set of count rates, least-squares fitting then provides an estimate of tracer position. The technique has mainly been used with sources that emit high-energy gamma-rays (above about 1 MeV) so as to minimise attenuation. For practical reasons, sources with long half-lives are also preferred: examples include ^{46}Sc (84 days, 889 and 1121 keV gamma-rays) and ^{60}Co (5.3 years, 1173 and 1332 keV) and source activity is typically 100 μCi.

The concept of tracking a radioactive particle can be traced back at least to the 1960s. The first modern RPT system was developed by Lin et al. at Illinois (Lin et al., 1985). They used 12 2-inch NaI(Tl) scintillator detectors, mounted in three staggered rings, to track a 0.5 mm encapsulated particle of ^{46}Sc moving in a gas-fluidised bed of 0.5 mm glass beads, and obtained detailed velocity fields and autocorrelation functions.

This technique was refined by Dudukovic's group at St Louis, who reported a computer automated radioactive particle tracking (CARPT) facility (Moslemian et al., 1992) comprising 16 detectors operating at a sampling rate of 33 Hz. Over a vertical range of 60 cm in a 30 cm-diameter fluidised bed, this system determined the tracer location with a mean error of 9 mm. This system was extensively used to study gas–solid fluidised beds and the behaviour of the liquid phase in bubble columns.

The original CARPT technique assumed that for each detector the count rate depended only on the distance from the source to the centre of the detector, and not on direction or varying material content. Subsequently in Montreal Larachi, Chaouki and co-workers developed an improved approach: the volume of interest is divided into a fine grid and the expected count rates are determined for each grid location using Monte Carlo modelling which incorporates effects such as detector geometry and attenuation in the rig. During subsequent tracking, the experimental count rates in the various detectors are compared to the modelled rates, searching for the location that best matches the measured values (Larachi et al., 1995). A neural network approach has also been used (Godfroy et al., 1997). A problem with all these methods is that they are unable to correct for temporal variations in attenuation due to moving parts or changes in bed holdup.

Variants on the RPT technique have been used by a number of groups to study particle or fluid motion especially in fluidised beds and bubble columns.

8.3.2 Positron emission particle tracking

The technique PEPT was conceived and first developed at the University of Birmingham, UK, in the late 1980s. Since positron–electron annihilation generates pairs of almost back-to-back photons, if a single positron-emitting source is present in the field of view of a PET scanner then in principle it should be possible to estimate its location by triangulation using just two pairs of photons whose lines of response both pass close to this location (Figure 8.6). In practice the data contain a significant number of corrupt events – random coincidences or events where one or both photons has scattered prior

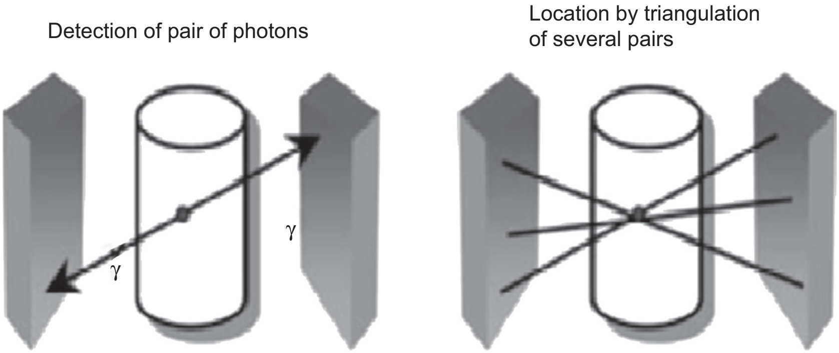
Detection of pair of photons
Location by triangulation of several pairs
γ
γ

Figure 8.6 Principle of positron emission particle tracking.

to detection – so that it is necessary to start with a larger dataset, typically 100 pairs. It should then be possible to distinguish the cluster of genuine events, which converge on the tracer location, from the broad background of corrupt events.

The standard PEPT algorithm (Parker et al., 1993) uses an iterative approach. Given a set of coincidence events, each of which defines a line of response, the algorithm calculates a centroid, defined as the point that minimises the sum of distances to all the lines of response. The lines furthest from the point are then discarded, and the centroid is recalculated using the remaining set of events. Iteration continues until only a specified fraction f of the original events remains; these are considered genuine events. The optimum value of f depends on the geometry and on the amount of scattering material through which the 511 keV photons have to pass. In contrast to RPT, calibration is not required, and because the PEPT algorithm efficiently removes scattered events accurate location is possible even when over 95% of the detected data is corrupt.

PEPT was first developed at Birmingham using the positron camera already mentioned, which consisted of a pair of rectangular gas-filled multi-wire proportional chambers, $60 \times 30\ \text{cm}^2$ in area. The efficiency of each chamber for detecting an incident 511 keV photon was just 7%, meaning that the overall efficiency for detecting a pair of photons, both of which struck the chambers, was just 0.5% (0.07^2). This low efficiency meant that the true coincidence data were always accompanied by a significant contribution of random coincidences, and in practice the useful data rate was limited to 3000 coincidence events per second. In 1999 this positron camera was replaced by one comprising a pair of sodium iodide gamma camera heads (Forte, manufactured by ADAC Laboratories, Milpitas, CA, USA), giving an order of magnitude improvement in efficiency (Parker et al., 2002). Using a tracer of optimum activity, the Forte can detect 10^5 coincidence events per second. If it takes 100 events to locate the tracer accurately, then this can be achieved every millisecond. For a slow-moving tracer, the location accuracy obtained using an initial sample of N events can be estimated as $\frac{w}{\sqrt{fN}}$, where w represents the spatial resolution of the positron camera (around 8 mm). Taking $N = 100$ and $f = 0.25$, this formula predicts a location accuracy of around 1.6 mm. The location accuracy deteriorates if the tracer moves significantly during the location interval; for the example cited this occurs at speeds above a few m/s. At lower speeds, more accurate location can be achieved by increasing the sampling interval.

PEPT has been used at Birmingham to study a very wide range of systems including stirred tanks, rotary kilns, gas-fluidised beds and vibrofluidised granular gases. The ADAC Forte positron camera is still used for many of these studies, and is popular due to its open geometry. To complement this system, a series of modular positron cameras have been developed, using the detector blocks and electronics from redundant medical PET scanners. As well as giving greater geometrical flexibility, these modular cameras have the advantage of being transportable, so that PEPT studies can be performed ‘in the field.’ For example, during 2006 a modular camera was used to perform a PEPT study of a large fluidised bed at BP’s Hull site (Ingram et al., 2007). Modular cameras have also been used to follow the motion of small

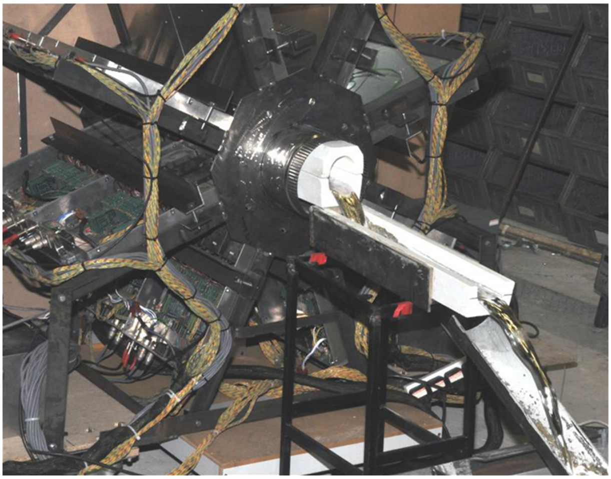

Figure 8.7 Modular positron camera being used to study flow of molten aluminium along a channel containing a weir.

refractory inclusions during the casting of liquid metals (molten steel or aluminium). Figure 8.7 shows a camera consisting of 64 BGO blocks (eight banks, each of eight detector blocks) being used to study flow of molten aluminium along a channel containing a weir: tracking was possible over a length of 600 mm. In some cases these modular cameras can generate data rates of over 1 MHz, enabling very accurate high-speed tracking.

PEPT has also been performed by Hoffman's group using a ring scanner: in 2011 they reported tracking of 500 μm particles in a hydrocyclone (Chang et al., 2011) located every millisecond with an accuracy of better than 200 μm. In 2009 the University of Cape Town established a PEPT facility at iThemba Labs in South Africa. PEPT Cape Town is equipped with a ring scanner (ECAT EXACT3D with an axial field of view of 23.4 cm) and more recently with an ADAC Vertex positron camera (similar to the ADAC Forte but with a slightly different gantry), and specialises in applications of PEPT in minerals processing.

References

Anger, H. O. (1964). Scintillation camera with multichannel collimators. *Journal of Nuclear Medicine, 5*, 515−531.

Barth, T., Ludwig, M., Kulenkampff, J., Gründig, M., Franke, K., Lippmann-Pipke, J., et al. (2014). Positron emission tomography in pebble beds. Part 1: Liquid particle deposition. *Nuclear Engineering and Design, 267*, 218−226.

Chang, Y.-F., Ilea, C. G., Aasen, O. L., & Hoffmann, A. C. (2011). Particle flow in a hydrocyclone investigated by positron emission particle tracking. *Chemical Engineering Science, 66*, 4203−4211.

Godfroy, L., Larachi, F., Kennedy, G., Grandjean, B. P. A., & Chaouki, J. (1997). On-line flow visualization in multiphase reactorsusing neural networks. *Appllied Radiation and Isotopes, 48*, 225−235.

Hawkesworth, M. R., Parker, D. J., Fowles, P., Crilly, J. F., Jefferies, N. L., & Jonkers, G. (1991). Nonmedical applications of a positron camera. *Nuclear Instruments and Methods in Physics Research Section A, 310*, 423−434.

Ingram, A., Hausard, M., Fan, X., Parker, D. J., Seville, J. P. K., Finn, N., et al. (2007). Portable positron emission particle tracking (PEPT) for industrial use. In F. Berruti, X. Bi, & T. Pugsley (Eds.), *The 12th international conference on fluidization − new horizons in fluidization engineering*. ECI Symposium Series (Vol. RP4) http://dc.engconfintl.org/fluidization_xii/60.

Larachi, F., Chaouki, J., & Kennedy, G. (1995). 3-D mapping of solids flow fields in multiphase reactors with RPT. *AIChE Journal, 41*, 439−443.

Legoupil, S., Pascal, G., Chambellan, D., & Bloyet, D. (1997). An experimental single photon emission computed tomograph method for dynamic 2D fluid flow analysis. *Appllied Radiation and Isotopes, 48*, 1507−1514.

Lin, J. S., Chen, M. M., & Chao, B. T. (1985). A novel radioactive particle tracking facility for measurement of solids motion in gas fluidized beds. *AIChE Journal, 31*, 465−473.

Moslemian, D., Devanathan, N., & Dudukovic, M. P. (1992). Radioactive particle tracking technique for investigation of phase recirculation and turbulence in multiphase systems. *Review of Scientific Instruments, 63*, 4361−4372.

Park, J. G., Jung, S.-H., Kim, J. B., Moon, J., Han, M. C., & Kim, C. H. (2014). Development of advanced industrial SPECT system with 12-gonal diverging-collimator. *Appllied Radiation and Isotopes, 89*, 159−166.

Parker, D. J., Broadbent, C. J., Fowles, P., Hawkesworth, M. R., & McNeil, P. A. (1993). Positron emission particle tracking − a technique for studying flow within engineering equipment. *Nuclear Instruments and Methods in Physics Research Section A, 326*, 592−607.

Parker, D. J., Forster, R. N., Fowles, P., & Takhar, P. S. (2002). Positron emission particle tracking using the new Birmingham positron camera. *Nuclear Instruments and Methods in Physics Research Section A, 477*, 540−545.

Parker, D. J., Leadbeater, T. W., Fan, X., Hausard, M. N., Ingram, A., & Yang, Z. (2008). Positron imaging techniques for process engineering: recent developments at Birmingham. *Measurement Science and Technology, 19*, 094004.

Perret, J., Prasher, S. O., Kantzas, A., Hamilton, K., & Langford, C. (2000). Preferential solute flow in intact soil columns measured by SPECT scanning. *Soil Science Society of America Journal, 64*, 469−477.

Ultrasound tomography

9

N.J. Watson
University of Nottingham, Nottingham, UK

9.1 Introduction

Ultrasound is a branch of acoustics that utilises mechanical pressure waves above 20 KHz. This frequency relates to the approximate uppermost frequency detected by humans. Acoustic waves are oscillations of pressure that elastically propagate through a medium. These pressure oscillations generate density and small thermal variations. The origins of study into acoustic waves date back to Pythagoras in Greek times and the theory has advanced thanks to the aid of distinguished scientists such as Helmholtz, Newton, Raleigh and Stokes. Acoustics now has applications in a wide range of disciplines such as medical imaging, detecting fatigue and flaws in mechanical components and mapping the ocean floors. There are many different classifications of acoustic and ultrasound techniques and these will briefly be presented before discussing the techniques relevant to industrial tomography.

The first classification is whether a system is passive or active. A passive system is defined as one that only detects acoustic waves, such as human hearing or microphones used to detect gas leaking from a pipe. In comparison, an active system is defined as one that transmits and receives acoustic waves through a medium. The second common classification of ultrasound is low power or high power. Low-power ultrasound generally has an intensity below 100 mW/cm^2 whereas high-power is between 10 and 10,000 W/cm^2 (Martini, 2013). Low-power waves are elastic in nature and make no changes to the medium in which they are propagating. Low-power ultrasound can be used to measure material properties of a substance, detects flaws or inhomogeneities and images samples. In contrast, high-power ultrasound is nonelastic and is used to disrupt and change a system. High-power ultrasound can be used to mix or homogenise fluid samples, modify the crystallisation process, and sterilise and degas samples and has numerous additional processing applications (Awad, Moharram, Shaltout, Asker, & Youssef, 2012).

As ultrasound tomography is used to monitor and image processes, it is classified as a low-power active system. For these types of ultrasound systems there are three necessary components: a transmitter, a medium for the wave to propagate through and a receiver. Often the transmitter can act as the receiver if the acoustic wave is reflected from an interface within the system. Tomography is defined as the two- or three-dimensional (2D or 3D) imaging of a sample or process; therefore, ultrasound tomography is imaging using ultrasonic waves. Ultrasound tomography was initially developed for medical applications in the 1970s (Greenleaf, 1970) and in the early 1980s the first systems were developed to study industrial processes such as

Industrial Tomography. http://dx.doi.org/10.1016/B978-1-78242-118-4.00009-5
Copyright © 2015 Elsevier Ltd. All rights reserved.

two-phase flows (Fincke, 1980) and identify solid objects in a fluid (Satti & Szilard, 1983). Ultrasound tomography systems have also been developed to operate in solid materials and have been used to image material loss in aircraft components (Hay, Royer, Gao, Zhao, & Rose, 2006), image stress fields in sandstone (Scott & Roegiers, 1994) and detect decay in trees (Liang, Wang, Wiedenbeck, Cai, & Fu, 2007).

The key benefits of using ultrasound for a tomography system include:

- Nondestructive
- Noninvasive
- Can operate online
- Can operate in near real time
- Can be used on opaque systems
- Operates on a wide range of length scales
- No moving parts
- No radioactive or other dangerous components
- Often less expensive than other techniques

Although these benefits make ultrasound appear to be an ideal topographic technique, there are challenges that must be overcome, such as transmitting the waves through heterogeneous samples and interpreting the received signals. An additional issue that must always be considered when using ultrasound is the wave propagation speed. For water at ambient temperature sound waves travel at approximately 1500 m/s; this is significantly slower than electromagnetic waves, which travel at around 300,000,000 m/s in the same medium (Hoyle, 1996). This relatively slow propagation speed can result in a major issue if the area to be imaged is large or the process is changing in a short period of time.

The remainder of this chapter will be structured as follows. Section 9.2 will present fundamental ultrasound/acoustic theory; this will include how acoustic waves are characterised and what happens when they interact with boundaries and changing physical properties within a system. This theory can then be used to explain what can be measured and imaged using ultrasound techniques. As well as covering all of the techniques currently used in ultrasound tomography systems, a more extensive explanation of the uses of ultrasound in process monitoring will be included. This is to enable the reader to imagine what additional uses ultrasound could have in future process tomography applications. Section 9.3 will present the different components required for an ultrasound tomography system and discuss image reconstruction techniques and how the specifications of the system can be calculated. Section 9.4 will discuss the applications of ultrasound tomography in process monitoring, and the chapter will end with sections on future trends, further reading and a summary.

9.2 Ultrasound theory

There are different types of ultrasound waves that can propagate in a medium; these are longitudinal, shear, surface (Rayleigh) and plate (Lamb). Generally speaking, only longitudinal waves propagate in fluids due to their densities being too low to support shear waves and no solid boundaries for surface or plate waves. The focus of this chapter is ultrasound tomography for process monitoring, which is generally a pipe-bound fluid system, so the theory will only be presented for longitudinal waves. For more details of acoustic propagation in solids the reader can refer to the books of Rose (1999) and Krautkrämer and Krautkrämer (1990). Ultrasound tomography systems have been developed utilising surface and plate waves, with an example being the imaging of defects in the floor of a fuel tank (Mazeika, Kazys, Raisutis, Demcenko, & Sliteris, 2006).

This theoretical section will first present the theory for a propagating longitudinal pressure wave and then discuss how it interacts with the material it propagates through and any interface or inhomogeneities within it. It is important to understand these interactions as they are what make an ultrasound system capable of delivering information on a sample or process. For further information on acoustic and ultrasound theory in fluid systems the reader should refer to Povey (1997), Dukhin and Goetz (2002), Challis, Povey, Mather, and Holmes (2005) and Cheeke (2002).

9.2.1 Acoustic propagation wave theory

Longitudinal or compression waves are defined as waves where the particle motion is in the same direction in which the wave is propagating. The oscillations in pressure are sinusoidal in nature and are characterised by their frequency, amplitude and wavelength (Figure 9.1).

The frequency (f) of a wave is related to the period (T) of a single cycle by the following equation:

$$f = \frac{1}{T}$$

with the unit of frequency being the Hz (per second). This frequency can be described as an angular or radial frequency (ω):

$$\omega = 2\pi f$$

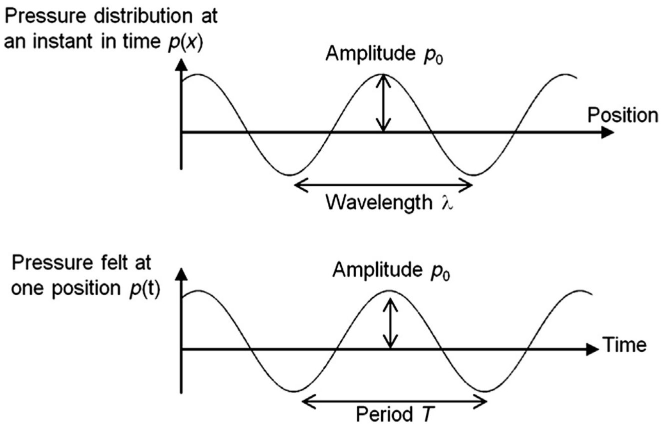
Pressure distribution at an instant in time $p(x)$
Amplitude p_0
Position
Wavelength λ
Pressure felt at one position $p(t)$
Amplitude p_0
Time
Period T

Figure 9.1 Descriptors of an acoustic wave.

In addition we must define the phase (ζ) of the wave, which is always relative to a specified point.

$$\zeta = k_c' x,$$

k_c' is the real part of the acoustic wave number

$$k_c' = \frac{2\pi}{\lambda} = \frac{\omega}{v_p} = \frac{2\pi f}{v_p},$$

$$\boldsymbol{k}_c = k_c' + ik_c'' = k_c' + i\alpha$$

Using these equations we can express the propagating pressure wave as:

$$\Delta p = \Delta p_0 \exp\{\mathrm{i}(\omega t - \zeta + \mathrm{i}\alpha x)\}$$

where Δp is the instantaneous pressure and Δp_0 is the maximum pressure deviation, respectively; $\mathrm{i} = \sqrt{-1}$; k' and k'' are the real and imaginary parts of the complex wave vector **k**; v_p is the phase velocity of the wave, λ is wavelength and α is the attenuation coefficient.

Often an acoustic wave will travel as a pulse consisting of multiple frequency components. The group velocity v of a pulse is the velocity of the envelope of the wave. This contains all cycles in the pulse and is given by:

$$v = \frac{\mathrm{d}\omega}{\mathrm{d}k}$$

The velocity of the different frequencies contained within the pulse are each given a phase velocity v_p given by:

$$v_p = \frac{\omega}{k} = f\lambda$$

where λ is the wavelength at the specific frequency. Pressure is related to amplitude or displacement ξ through:

$$p \sim \xi^2$$

The attenuation of the wave can then be defined in terms of measurable pressure differences as:

$$-\propto = \frac{1}{x} \ln \frac{\xi}{\xi_0} \text{ Neper m}^{-1}$$

or

$$-\propto \;=\; \frac{1}{x} 20 \log \frac{\xi}{\xi_0} \text{ dB m}^{-1}$$

The decibel (dB) and Neper (N) are called dimensionless units, because they are ratios. The attenuation is normally expressed in terms of pressure rather than displacement and, in this case

$$-\alpha\left[\text{dBm}^{-1}\right] \;=\; \frac{1}{x} 10 \log \frac{p}{p_0} \;=\; \frac{1}{x} 20 \log \frac{\xi}{\xi_0}.$$

9.2.2 Acoustic impedance

An acoustic wave will continue to propagate through a medium until it encounters an interface in the elastic distribution. These interfaces are parameterised through the characteristic acoustic impedance:

$$Z \;=\; \rho v$$

where ρ is the density. Consider plane sound waves in medium 1 (Z_1, v_1 and ρ_1) at normal incidence to an interface with medium 2 (Z_2, v_2 and ρ_2). The reflection coefficient R, the ratio of the reflected pressure amplitude (p_R) to the incidence pressure amplitude (p_I) (Krautkrämer & Krautkrämer, 1990) is given by the equation:

$$R \;=\; \frac{Z_2 - Z_1}{Z_2 + Z_1}$$

The above equation indicates that reflection increases with the size of the impedance mismatch. However, strictly, R is a function of incident angle θ and can change markedly with θ, for example, due to critical angles at which complete internal reflection or surface wave generation can occur. Broadly speaking, the interaction is a reflection of when the length scale of the boundary/bounded object l is much greater than the sound wavelength λ. Meanwhile, when $l \leq \lambda$, the feature acts as an inhomogeneity and scatters the sound. Scattering itself has a spectrum of behaviour, ranging from the mid-frequency regime ($l \sim \lambda$), where the scattering is sensitive to shape and size resonances (Uberall, 1992), up to the far limit of Rayleigh scattering, where the scattering becomes insensitive to shape ($l \gg \lambda$) (Morse & Ingard, 1968). To determine whether reflection or scattering will dominate when an incident wave hits the interface of a spherical object, we define the value ka:

$$ka \;=\; k_c' a \;=\; \frac{2\pi a}{\lambda}$$

where a is the radius of the sphere. When $ka \gg 1$ reflection will dominate and when $ka \ll 1$ scattering will dominate (Figure 9.2).

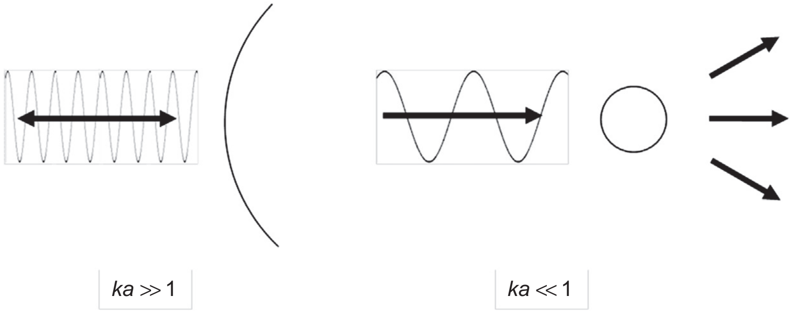

Figure 9.2 When an incident wave reaches an interface either reflection ($ka \gg 1$) or scattering ($ka \ll 1$) dominates.

9.2.3 Speed of sound

The frequency and amplitude of the propagating pulse are governed by the transducer and excitation source and these can be selected depending on the measurements required. However, the speed v at which the pulse propagates in a fluid is a function of the material's adiabatic compressibility (Woods, 1941):

$$v = \frac{1}{\sqrt{\kappa\rho}}$$

where κ is the adiabatic compressibility of the material and ρ is the materials density. The fact that the speed of sound is dependent on the material properties of the medium within which it propagates can be used to gain information on this medium. The speed of sound varies for different materials and is fastest in solids and slowest in gases. Table 9.1 indicates the speed of sound for some common materials:

Table 9.1 Speed of sound in some common materials

Material	Speed of sound (v) (m/s)
Iron	5170
Lead	2160
Water	1464
Oxygen	316
Air	331
Ethanol	1207
Methanol	1103
Castor oil	1477

Adapted from Dukhin and Goetz (2002).

9.2.4 What can ultrasound measure in an industrial process?

Acoustic waves can be used to gain information on a system in which they are propagating by measuring:

1. How the waves propagate in a single-phase system
2. What happens at an interface in a multiphase system

It is these two principles that are the focus of all ultrasound tomography systems. Therefore, the following section will discuss what information can be gained from each of them.

9.2.4.1 Wave propagation in a single phase

For a single-phase homogeneous fluid the speed of sound in its simplest form is a function of the density and the compressibility of the medium. Therefore, any changes in these material properties will affect the speed at which the wave propagates through the medium, and by regularly measuring the speed of sound any spatial or temporal changes in material properties such as density can be measured. The speed of a wave in a medium is recorded by sending an acoustic pulse through the medium from one transducer to another. If the distance (d) between the transducers is known and the time of flight (tof) of the pulse is recorded, v can be calculated from:

$$v = \frac{d}{\text{tof}}$$

The temperature of a fluid is known to have a significant effect on the speed of sound and attenuation of a wave propagating through it. This makes ultrasound techniques an ideal tool for monitoring temperature changes in a fluid, although prior knowledge of the speed of sound across the temperature range to be monitored must be known. Figure 9.3 displays the speed of sound and attenuation of water

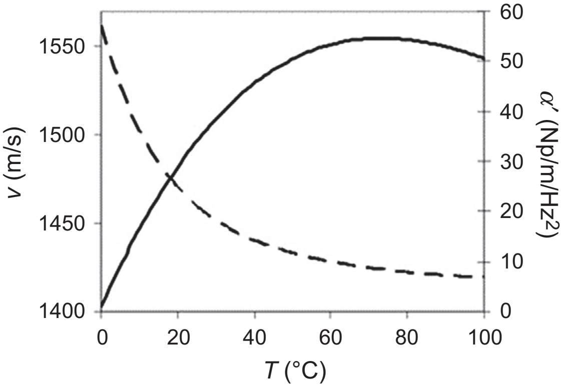

Figure 9.3 Speed of sound and attenuation of water as a function of temperature. Adapted from Povey (1997).

from 0 to 100 °C. Temperature fluctuations due to process or environmental factors can be one of the biggest challenges when using ultrasound techniques to monitor industrial processes. It is important to constantly monitor the temperature where the measurements are being made and ensure that an understanding of the temperature effects on the particular fluid or system exists.

The velocity of sound is also sensitive to the pressure of the fluid, and for water can be calculated from the following equation (Pierce, 1981):

$$\begin{aligned} v = {} & 1402.39 + 5.03711T - 0.0580852T^2 + 3.33420 \times 10^{-4}T^3 - 1.47800 \\ & \times 10^{-6}T^4 + 3.14643 \times 10^{-9}T^5 + 1.6 \times 10^{-6}\left(p_0 - 10^5\right) \end{aligned}$$

where T is the temperature in degrees Celsius and p_0 is the absolute pressure in Pascals. The concentration of mixtures can be determined from the sound velocity within them. In the simplest form the speed of sound of two miscible fluids is a function of the volume-averaged densities and compressibilities of the two fluids:

$$\begin{aligned} v &= \frac{1}{\sqrt{k_{VA}\rho_{VA}}} \\ k_{VA} &= \phi k_2 + (1 - \phi)k_1 \\ \rho_{VA} &= \phi\rho_2 + (1 - \phi)\rho_1 \end{aligned}$$

where ϕ is the volume fraction of fluid 2 in fluid 1. These equations have been adapted further to measure concentrations of particular substances in water, such as sugar (Contreras montes de Oca, Fairley, McClements, & Povey, 1992) and alcohol (Povey, 1997).

Phase transitions can be monitored using ultrasound techniques in emulsions, dispersions and homogeneous fluids. Accurate measurements of the temperature can be made at which the phase transition occurs. In a solid/liquid or liquid/solid phase transition a large change in compressibility occurs and this has an effect on the speed of sound (recall that speed of sound is largest in solids) An example of using speed of sound to detect phase changes is presented in Figure 9.4, where an oil in water emulsion goes from a liquid dispersed phase to a solid dispersed phase. Note the crystallisation temperature of 2.5 °C and the melting temperature of 15 °C and the associated changes on the speed of sound.

9.2.4.2 What happens at an interface in a multiphase system?

When a propagating acoustic wave reaches an interface characterised by a difference in acoustic impedance, reflection and/or scattering occurs. Whether reflection or scattering dominates depends on the size and shape of the scattering object in relation to the wavelength of the incoming wave. The majority of current ultrasound tomography systems operate on the premise that the system is operating in the short-wavelength

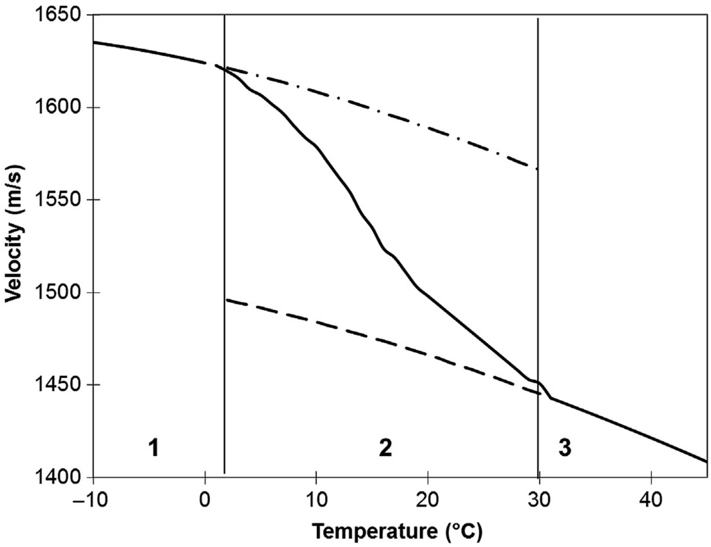

Figure 9.4 Ultrasound velocity of an oil in water margarine as a function of temperature. In region 1 the margarine is solid, in region 3 it is liquid and in region 2 it is a mixture of solid and liquid.
Adapted from McClements and Povey (1992).

limit ($ka \gg 1$), that is that the scatterers are significantly larger than the wavelength of the incident wave. These techniques assume that the majority of the incident wave is reflected at this interface and the location of the interface can be found by measuring the time it takes the transmitted ultrasound pulse to travel to the interface, be reflected and then propagate to the receiving transducers.

When ka is equal to or less than 1, acoustic scattering will occur. There are different techniques available to measure the size distribution of scattering particles in a fluid using ultrasound techniques, such as ultrasound spectroscopy (Alba, 1992). This technique measures the velocity and/or attenuation of the ultrasound as a function of frequency and acoustic path length and uses mathematical inversion models such as ECAH (Allegra & Hawley, 1972), Foldy (1945), Lloyd and Berry (1967) to calculate the particle size distribution. Ultrasound spectroscopy requires several measurements at one position so would not be suited to ultrasound tomography due to the many measurements required to construct tomographs. However, other more simple models such as the modified Urick equation (Pinfield, Povey, & Dickinson, 1995) exist which can calculate size from a single measurement but do assume a monodispersed size distribution where the wavelength is much larger than the radius of the spherical scattering objects. When using ultrasound to measure particle size it is important to understand the size distribution and localised concentrations of the scatterers, as often the systems may be outside the operating realms of the inversion models, an example being where simultaneous multiple scattering occurs.

Care should always be taken when using ultrasound techniques to measure bubble size distributions, as the incident wave will cause the bubbles to oscillate and resonate at a frequency dependent upon their radii (Leighton, Phelps, Ramble, & Sharpe, 1996). Although sizing the bubbles is possible, this resonance can cause complications in the interpretation of the acoustic signals and make data interpretation more difficult.

9.2.5 Limitations on ultrasound systems

Although ultrasound appears to be an attractive process monitoring tool, it does have several limitations. These must always be considered before deciding if it is the most suitable process tomography system to use. These limitations include:

- slow propagation velocity of sound waves
- difficult to understand signals in complex systems (e.g. large range of inhomogeneity size and concentration)
- temperature must remain constant or constantly be monitored
- inversion techniques must improve

9.3 Equipment and techniques

So far this chapter has focussed on the theory of ultrasound propagation and discussed what information can be gained from a measurement in a single position with an individual or pair of transducers. Tomography requires measurements to be made from multiple positions (projections) so that 2D and 3D spatial images can be constructed where the image contrast is governed by the property of a system under investigation (for example, density or void fraction). This section will introduce the main components required for an ultrasound tomography system and discuss the different setups that can be used.

9.3.1 Equipment setups

Ultrasound tomography instruments consist of various different hardware components and software to control the hardware and reconstruct the image from the many recorded projections. Although numerous different instrument setups exist, the primary components are acoustic transducers, pulser receiver device, control and signal processing hardware and a PC to control and generate the images.

9.3.1.1 Transducers

The ultrasound transducer is one of the most critical components of the tomography systems, as it is responsible for transmitting and receiving the pulse and has a significant effect of the performance parameters of the systems. The most common types of transducers are piezoelectric ones. These transducers utilise the piezoelectric effect, which is when a piezoelectric material deforms when an electrical voltage is applied across it. By applying an oscillating voltage the material will vibrate and emit a pressure wave. The inverse of this occurs when a pressure wave hits a piezoelectric material and a voltage is produced. Design and construction of piezoelectric transducers is a well-documented area and the reader can refer to Silk (1984) for more details. Piezoelectric transducers are not the only transducers available; other types include capacitance transducers (Wright, Schindel, Hutchins, Carpenter, & Jansen, 1998) and hydrophones (Martin, Beesle, & Myers, 1995).

How the acoustic wave propagates from the transducer face is an important property of the ultrasound tomography system, and transducers can be built that emit relatively straight waves, focussing waves and waves that spread out like a fan. As ultrasound tomography systems wish to construct a 2D image of a flowing process, transducers with a fan beam are often used as these cover the most area in two dimensions and so can generate the most spatial information for a single transmitted pulse. The beam spread of the fan-based transducer is characterised by the beam angle (α) at which the waves propagate (Figure 9.5). The selection of beam angle should be considered carefully, as although a wider angle will cover a greater area this will have a negative effect on the spatial resolution of the system (Schlaberg, Yang, & Hoyle, 1998). A fan-shaped beam can be produced by careful design of the size and shape of the transducer face or by adding a cylindrical lens (Steiner & Podd, 2006).

Ultrasound transducers are characterised by their frequency and bandwidth and it should always be remembered that the frequency of a propagating wave is a characteristic of the emitting transducer. The selection of suitable frequency is critical in any ultrasound system, as the frequency affects the propagation distance of the wave and the spatial resolution of the system. Acoustic attenuation increases with the frequency squared of the propagating wave, so lower frequencies would be more desirable in highly attenuating systems, although lower frequencies have lower spatial resolution. It is obvious that a tradeoff exists, so the selection of operating frequency should be made based on the requirements of the system and the medium the wave will

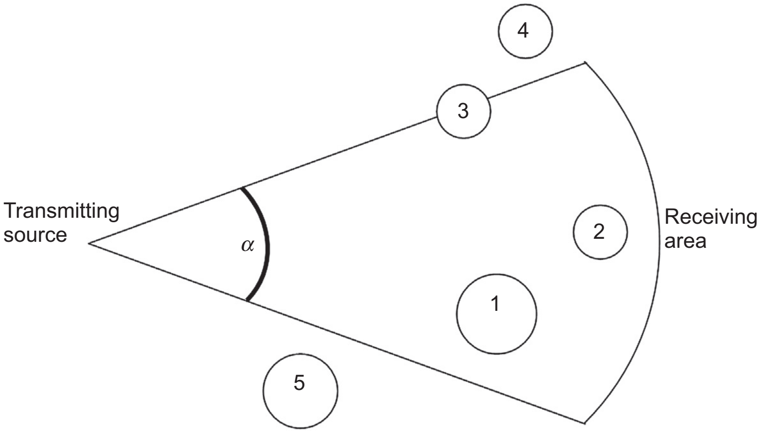

Figure 9.5 Wave propagation from a fan-based transducer. For the beam spread angle α the scatterers 1, 2 and 3 will have an effect on the propagating wave.

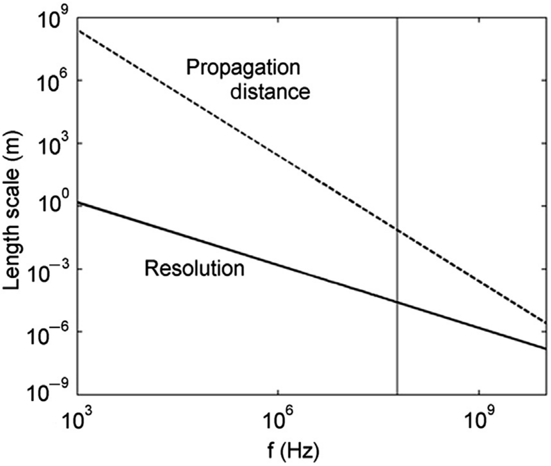

Figure 9.6 Tradeoff between frequency and operating distance for a focussed transducer in water.
Adapted from Parker and Povey (2009).

be propagating in. Figure 9.6 displays the tradeoff in spatial resolution and attenuation as a function of frequency for a transducer with a focussed beam. In general ultrasound tomography systems operate between 18 KHz and 20 MHz (Fazalul Rahiman, Abdul Rahim, Abdul Rahim, & Ayob, 2012), with the most commonly used transducer being around 2 MHz (Abdul Rahim, Fazalul Rahiman, & Mohd Taib, 2005).

The bandwidth of the transducer is a description of the frequency range over which it is capable of emitting waves. This is usually characterised by a central frequency and the frequency range at which the frequency-dependent output reduces by 6 dB. In most ultrasound tomography systems each transducer will emit at a single frequency to minimise difficulties in deconvoluting received signals. However, it may be desirable to transmit across a range of frequencies for applications such as particle sizing. As well as transducer frequency and bandwidth, other properties need to be considered, such as the operating temperature and physical size of the transducers.

The different transducer configurations used for ultrasound tomography can be categorised as:

- Single or pair of transducers attached to a mechanical system and rotated around pipe
- An array of emitting or receiving transducers
- An array of transmitting and receiving transducer

Generally multiple transducers will be equally spaced around the domain to be imaged, which is usually a circular pipe cross-section. The ultrasound tomography instrument begins by pulsing the first transmitting transducer and recording the detected signal at each receiving transducer. After all propagation from this transmitter has faded beyond a detectable level the next transducer will be excited. This process continues until a pulse has been transmitted from all transmitting transducers. It may seem ideal to have as many transducers as possible, as the more projections recorded, the greater the level of detail in the reconstructed image. However, the number of transducers and projections per image affects the time required to construct an image (Yang, Schlaberg, Hoyle, Beck, & Lenn, 1999).

How the transducers are attached to the system under investigation also requires thought. Some systems use transducers placed in the flowing system; these would benefit from a simpler propagation problem but could interfere with the flow and so were not classified as noninvasive, and transducers could suffer damage from the flowing medium. Other ultrasound tomography systems attach the transducers to the outside of the pipe, removing these issues (Steiner & Podd, 2006). When coupling transducers to the outside of the pipe, it should be considered that the waves must propagate through the pipe wall (which may not have uniform thickness) and a coupling medium is required between the transducer and the outside of the wall due to the large acoustic impedance mismatch between air and solid materials.

9.3.1.2 Pulser, receiver and signal processing

For an ultrasound transducer to generate an acoustic wave it must be excited by some form of electrical voltage. These can be provided by standalone pulsing devices or by USB-operated signal generators. Pulsers operate by either applying a high-voltage spike of known voltage, a square wave of known duration and voltage or a sinusoidal pulse of known voltage, frequency and duration. The excited voltage is selected as one that will result in a pulse that can propagate through the system under inspection and be detected by the receiving transducers. High-voltage excitations are required for highly attenuating systems, although the downside of high-voltage excitations is that they can distort the transmitted wave, introducing error into the signal analysis and image reconstruction process.

The signal received at the transducers must be saved before being processed and used to generate a tomograph. For earlier systems this would have been performed using an oscilloscope, but more recently this would be integrated into the software system. It is important that the excitation pulse is synchronised with the data acquisition process, as often time-of-flight measurements are required to calculate speed of sound in the system or to locate inhomogeneities or boundaries in space.

For airborne ultrasound or systems operating on processes with high attenuation it may be necessary to have some form of signal amplification for the transmitted and/or received signals. Other devices often utilised in an ultrasound tomography system include transducer positioning equipment and temperature monitoring or controlling equipment.

9.3.2 Different types of systems

The two most popular techniques are transmission and reflection ultrasound tomography systems. Transmission systems work by propagating a sound wave through a material and gaining information on the systems by the time and amplitude at which the pulse is received by transducers at different radial locations. Reflection devices

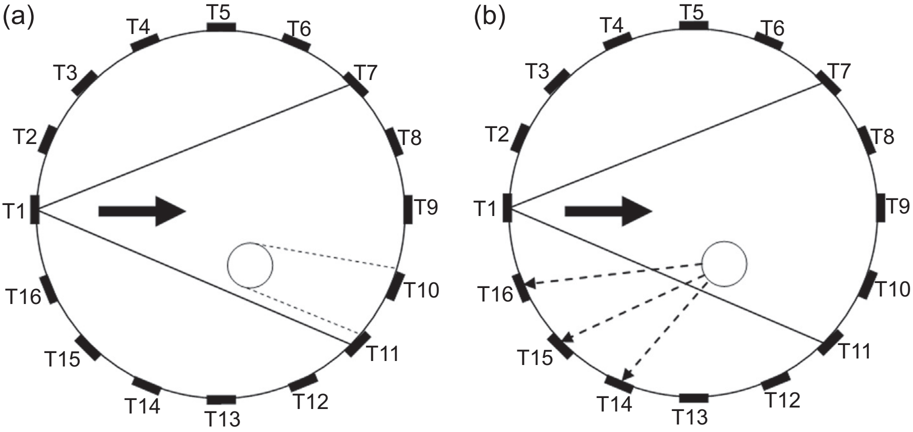

Figure 9.7 Operation of (a) transmission and (b) reflection ultrasound tomography systems.

operate by sending a pulse that is reflected at an interface with a different acoustic impedence before being detected by the transducers. Figure 9.7 highlights the difference in operation between a transmission and a reflection system. Reflection systems are generally used to study multiphase flows where a liquid and gas exist, as the acoustic impedance is large between liquids and gases. Transmission systems are more suited to detecting localised changes in material properties such as density or temperature but can also be used to detect inhomogeneities, as these will block the transmitted waves. Examples of transmission systems include the work of Fazalul Rahiman, Abdul Rahim, Fazalul Rahiman, and Tajjudin (2006) and Holstein et al. (2004), whereas examples of reflection systems include the work of Chen and Sanderson (1996) and Schlaberg et al. (1998).

It should be noted that often ultrasound tomography systems operate by utilising the transmission and reflection of acoustic waves. These systems have the benefit of acquiring more process information for each transmitted pulse but add additional complexity to the signal processing and inversion processes. Ultrasound tomography can also be performed on nonfluid pipe flows, for example acoustic microscopy inspection of electronic components and airborne ultrasound for foreign body detection in foods. In these systems a single or pair of transducers is used. The transducers will be scanned over the sample under inspection and a two- or three-dimensional picture can be constructed where each pixel represents a single pulse through a sample. A single transducer setup would be operating in reflection mode, whereas two transducers placed on either side of the sample are required for transmission mode.

9.3.3 Image reconstruction

Efficient and accurate image reconstruction algorithms are required to accurately produce images of the system property under investigation from the recorded ultrasound data. The majority of image reconstruction work for ultrasound tomography is focussed on medical applications (Lasaygues, Mensah, Guillermin, Rouyer, & Franceshini, 2012; Steiner & Watzenig, 2008). The requirements of medical ultrasound tomography systems are often different to those in industrial processes, which include flowing fluids with rapidly changing properties (Gai, Li, Plaskowski, & Beck, 1989). These flows will also often include gas or solid inhomogeneities. The image reconstruction algorithms used for industrial ultrasound tomography do not differ dramatically from the ones used for X-ray, electrical resistance tomography (ERT) or electrical capacitance tomography (ECT) techniques, with the most popular method being the linear back-projection method (Wright & O'Sullivan, 2003). This is used primarily due to the low computational cost (Fazalul Rahiman et al., 2012). The linear back-projection method can be split into the following stages:

1. Split the domain into a determined number of pixels. For a 2D image this could be, for example, a 64 by 64 array giving 4096 pixels
2. Create a sensitivity map, which is the expected response at each receiver from a given transmitter
3. Measure the desired property at the receiving transducer (amplitude or time of flight)
4. Back-project each measured value
5. Calculate the concentration map for each pixel using a suitable method
6. Represent each pixel as a colour level

For example, where the recorded value is the received voltage, the voltage distribution for a pixel with coordinates x and y can be found using (Fazalul Rahiman et al., 2012):

$$V_{\mathrm{LBP}}(x,y) = \sum_{Tx=1}^{m} \sum_{Rx=1}^{n} S_{Tx,Rx} \times \overline{M}_{Tx,Rx}(x,y)$$

where $V_{\mathrm{LBP}}(x,y)$ is the voltage distribution from the LBP algorithm in the concentration matrix and $S_{Tx,Rx}$ is the sensor loss voltage for the corresponding projection from Tx to Rx and $\overline{M}_{Tx,Rx}(x,y)$ is the normalised sensitivity matrices.

Fazalul Rahiman et al. (2012) reported that the LBP method is not the most accurate reconstruction method, as it can smear out details and lose definition at interface boundaries. These and other researchers have adapted the back-projection technique to include thresholding methods (Fazalul Rahiman et al., 2006; Opielinski & Gudra, 2006). This is where a pixel is given one of two values based on the value of the pixel relative to some predetermined threshold. These thresholding methods have been found to give an improvement in the classification of two phase flows (Abdul Rahim, Fazalul Rahiman, Chan, & Nawawi, 2007; Yang et al., 1999).

To identify the location of interfaces or reflectors in a system the following equation can be used:

$$\mathrm{tof} = \frac{1}{v}(s_1 + s_2) = \frac{1}{v}\left(\sqrt{(x_i - x_t)^2 + (y_i - y_t)^2} + \sqrt{(x_r - x_i)^2 + (y_r - y_i)^2}\right.$$

where tof is the time of flight between the transmit and received pulse, s_1 is the distance from the transmitter to the interface and s_2 is the distance from the interface to the receiver and v is ultrasonic velocity in the fluid. x and y are the coordinates in Cartesian space of the transmitter (t), receiver (r) and interface (i) respectively. These equations do of course assume that the acoustic pulse follows a straight line.

Other techniques used to reconstruct the image include parameterised contour model (Steiner & Watzenig, 2008), Fourier techniques (Mensah & Franceschini, 2006), sparse signal representation (Jovanovic, Hormati, Sbaiz, & Vetterli, 2007) and wave-based reconstruction (Roy, Jovanovic, Hormati, Parhizkar, & Vetterli, 2010). For further information on different reconstruction techniques for ultrasound tomography the reader can refer to the thesis of Jovanovic (2008). To aid the understanding of the accuracy and effect of different image reconstruction algorithms, often computer simulations are performed to access their effectiveness for a particular application. Examples of such simulations include those of Chen and Sanderson (1996), Li and Hoyle (1997), Norton and Linzer (1979) and Fazalul Rahiman, Abdul Rahim, and Zakaria (2008) (Figure 9.8).

9.3.4 Ultrasound tomography linked with additional techniques

Ultrasound tomographic techniques have also being linked with other modalities to increase the sensing capability of a system. Hoyle et al. (2001) describe a system that combines ERT, ECT and ultrasound tomography. They discuss the challenges in relation to hardware and data processing. Deinhammer, Steiner, Sommer, and Watzenig (2008) combine ultrasound and electrical capacitance techniques to monitor multiphase flows. They conclude that ultrasound techniques are more suited to detecting interfaces between materials, whereas the ECT are better at characterising the individual phases. Liu et al. (2011) combine ultrasound spectroscopy and ERT tomography to monitor an emulsification process. The combination of techniques is used to monitor the droplet size distribution in the emulsion. One issue with using ultrasound spectroscopy is the number of inputs required in the inversion model, so ERT is used to image the concentration profile and remove this unknown from the ultrasound inversion problem.

It should be remembered when using multiple sensing technologies that any propagating radiation does not interact with any other in an undesirable way and that the effect of additional measurements on the system specifications (such as temporal resolution) is known.

9.3.5 Calculating system resolution

For any industrial monitoring or imaging system it is important to be able to understand and have methods to calculate the operating specification of the system. For tomography systems the two most crucial are spatial and temporal resolution.

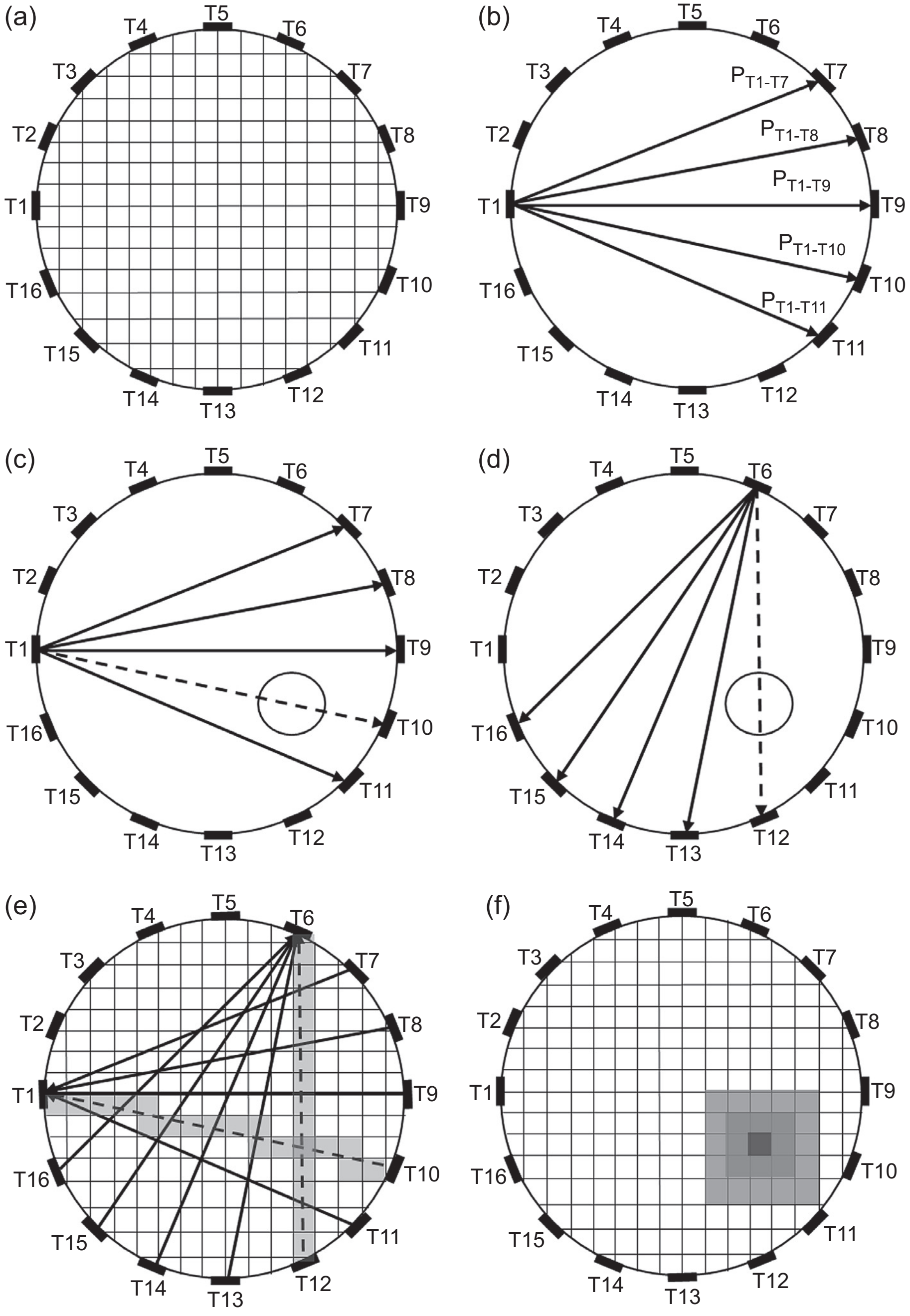
(a)
T1
T2
T3
T4
T5
T6
T7
T8
T9
T10
T11
T12
T13
T14
T15
T16
(b)
T1
T2
T3
T4
T5
T6
T7
T8
T9
T10
T11
T12
T13
T14
T15
T16
$P_{T1\text{-}T7}$
$P_{T1\text{-}T8}$
$P_{T1\text{-}T9}$
$P_{T1\text{-}T10}$
$P_{T1\text{-}T11}$
(c)
T1
T2
T3
T4
T5
T6
T7
T8
T9
T10
T11
T12
T13
T14
T15
T16
(d)
T1
T2
T3
T4
T5
T6
T7
T8
T9
T10
T11
T12
T13
T14
T15
T16
(e)
T1
T2
T3
T4
T5
T6
T7
T8
T9
T10
T11
T12
T13
T14
T15
T16
(f)
T1
T2
T3
T4
T5
T6
T7
T8
T9
T10
T11
T12
T13
T14
T15
T16

Figure 9.8 Image reconstruction for a transmission system utilising a back-projection method. (a) The cross-sectional area is split into pixels. (b) Sensitivity map created for each possible projection. (c) Projections from transducer 1; note how projection T_1–T_{10} is affected by the circular inhomogeneity. (d) Projection from transducer 6; note how the projection T_6–T_{12} is affected by the circular inhomogeneity. (e) Back-projection method. (f) Pixel intensity value.

9.3.5.1 Spatial resolution

Spatial resolution is defined by the size of inhomogeneities that can be detected and the accuracy of spatial results in the reconstructed pixelated image. As ultrasound tomography systems operate on the premise that reflection dominates at an interface ($ka \gg 1$) it is possible to calculate the size of the smallest scattering object that can be detected. Assuming that the transmitted pulse is 2 MHz and the fluid is water at 25 °C, the wavelength of the acoustic wave will be approximately 0.75 mm. To operate in the long-wavelength limit the scattering objects must have a radius of approximately 1 mm or larger. Increasing the transmitted frequency will result in the ability to detect smaller inhomogeneities without having to consider scattering, but it does come at the cost of increased signal attenuation.

For further discussion and methods for calculating spatial resolution of ultrasound tomography systems the reader can refer to Xu and Xu (1998) and Yang et al. (1999). Xu and Xu (1998) found that their ultrasound tomography system had a spatial resolution equal to 1% of the cross-sectional area and highlighted the fact that spatial resolution was not the same at different radial locations in this circular area.

9.3.5.2 Temporal resolution

Temporal resolution is the time to take the multiple measurements of the cross-section and then reconstruct the image. This time is important for process tomography systems, as often changes can occur within the system in a space of time that is shorter than the one required to record the measurements. This is further hampered by the fact that acoustic waves have a relatively slow propagation speed. For example, acoustic waves propagate as approximately 1500 m/s in water at 25 °C compared to 300,000,000 m/s for electromagnetic waves. Abdul Rahim et al. (2007) developed a system capable of making measurements at 300 frames per second but found that the image reconstruction process limited them to an imaging capability of 10 frames per second. The time to acquire a single 2D image for a reflection system in a pipe can be calculated from (Yang et al., 1999):

$$t = n\frac{2d}{v}(1+p)$$

where n is the number of transducers, d is the diameter of the pipe, c is the speed of sound in the medium and p is an additional percentage of time for the ultrasonic wave to attenuate below a detectable level. For a transmission system the 2 is removed from the equation. For a system with 32 transducers in a pipe of diameter 100 mm, assuming a fluid with $v = 1500$ m/s and $p = 0.3$, typical acquisition times are around 6.2 ms. However, the time to reconstruct an image is much longer, as each pulse from a transducer will be detected by multiple receivers, resulting in many projections. Image reconstruction can be improved by more efficient algorithms, more powerful computers and parallel processing.

9.4 Industrial applications

Section 9.2.4 described the different properties of a system in which information can be gained by utilising ultrasound techniques. This section will focus on reviewing the ultrasound tomography systems presented in the literature and will be split into two sections. The first will focus on single-phase systems and the second will focus on multi-phase systems.

9.4.1 Characterisation of single-phase systems

One of the earliest reported uses of ultrasound tomography to monitor single-phase systems was the work of Martin et al. (1995). In this work temperature variations were imaged in a fluid using multiple hydrophones. Wright and co-workers have imaged the flow velocity and spatial temperature differences in air using electrostatic ultrasound transducers (Figure 9.9) (Ingleby & Wright, 2002; Wright & O'Sullivan, 2003; Wright et al., 1998). During this work they have used different transducer configurations. Some work involved transducers that were moved to record the different projections, whereas other work had transducers fastened around a pipe section. All of their systems operated in the transmission mode and they recorded time of flight and received voltage amplitude data. Ingleby and Wright (2002) were also able to identify solid objects in the air flows using their ultrasound tomography system. Holstein et al. (2004) imaged air flow velocity and spatial temperature distribution using a transmission system, as did Jovanovic (2008). Li and Zhou (2006) used an ultrasound tomography system based on speed-of-sound measurements to monitor single-phase gas flow in a furnace.

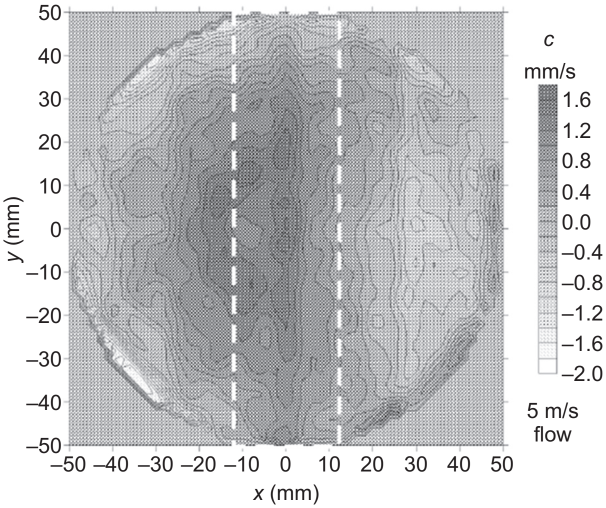

Figure 9.9 Reconstructed image of variation in the static speed of sound c at a flow speed of 5 m/s. The dashed white line indicates where a bluff body was located downstream of the flow. Wright and O'Sullivan (2003) Reproduced with permission.

9.4.2 Characterisation of multiphase flows

The majority of published work in the literature using process ultrasound tomography systems is for imaging multiphase flows. Some of the first work in the 1980s was by Kolbe, Turko, and Leskovar (1986), who used 20 transducers in a reflection system to detect bubbles in a liquid flow, and Wolf (1988), who used a transmission system to also image bubbles in a liquid flow.

In the 1990s research using ultrasound tomography systems continued. Brown, Reilly, and Mills (1996) used a transmission system with 18 transducers to detect solid objects in a gas system. Chen and Sanderson (1996) used a reflection system and imaged air bubbles in water using a fixed transmitter and a positionable receiver. Brown and Reilly (1996) also used repositionable transducers, but in a transmission system, and they were capable of imaging solid objects in air. Xu and co-workers (Xu, Han, Xu, & Yang, 1997) used a transmission system to detect bubbles in a liquid flow and were able to use their ultrasound tomography system to classify different types of two-phase flows such as bubble, slug, annular and stratified flow. Yang et al. (1999) used a reflection-based ultrasound tomography system to image bubbles and solid objects in a liquid flow. Warsito, Ohkawa, Kawata, and Uchida (1999) developed a transmission system with six moveable transducers to image gas and particle holdups in a slurry bubble common using ultrasonic velocity and attenuation measurements. Utomo, Warsito, Sakai, and Uchida (2001) used the same system to then image gas and TiO_2 holdups in a liquid flow.

Research using ultrasound tomography systems continued into the 2000s. West, Jia, and Williams (2000) and Schlaberg, Podd, and Hoyle (2000) were able to use a reflection ultrasound tomography system to study air liquid flows in a hydrocyclone. Deinhammer et al. (2008) coupled reflection ultrasound tomography with electrical capacitance tomography to detect air regions in a flowing liquid. Opielinski and Gudra (2006) used a transmission system with two pairs of moveable transmitters and receivers to detect multiple solid objects of varying shapes in a gas system. The Malaysia researchers Abdul Rahim and Fazalul Rahiman have many published articles on a transmission ultrasound tomography system using a fan-beamed transducer to image bubbles in flow and classify different types of liquid gas flows such as plug, stratified and annular (Figure 9.10) (Abdul Rahim et al., 2005, 2007; Abdul Wahab, Abdul Rahim, Fazalul Rahiman, & Ahmad, 2011; Fazalul Rahiman et al., 2006, 2012; Fazalul Rahiman, Abdul Rahim, Abdul Rahim, Muji, & Mohamad, 2012). This ultrasound tomography system was also capable of imaging gas and solids in the same fluid continuum (Abdul Wahad et al., 2011) and was used to image the quantity of oil and water flowing in a pipe by measuring the received signal voltage (Abdul Rahim, Nyap, Fazalul Rahiman, & San, 2007).

9.5 Future trends

There was a large body of work performed by various different research groups in the 1990s developing ultrasound tomography systems mainly with the purpose to monitor

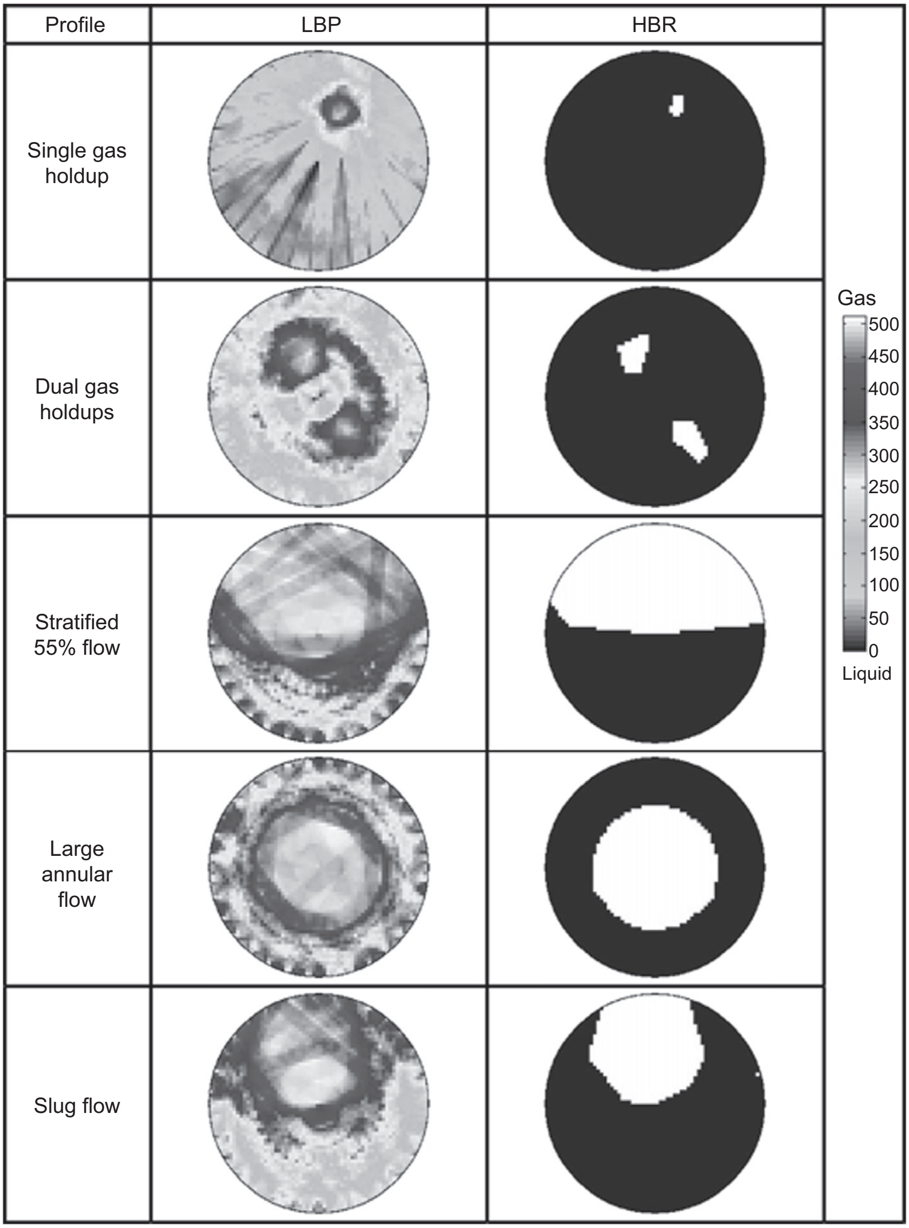

Figure 9.10 Image reconstruction of liquid gas flows using the linear back-projection and hybrid binary reconstruction techniques.
Abdul Rahim et al. (2007) Reproduced with permission.

flow or temperature profiles or characterise multiphase flows in pipes. However, since that time there does not appear to have been many significant advances or a large increase in publication volume in this area. This could be a result of the advances being incorporated into commercial systems or scientists and engineers focussing on other process tomography techniques. Despite this, non-tomography ultrasound techniques are still commonplace and growing in use in industrial processes. This is primarily due to the constant development of new transducers and electronics coupled with signal process algorithms. The list below summarises some trends in ultrasound techniques that should have a positive benefit on future ultrasound tomography systems for industrial processes.

- Constant improvement in design of ultrasound transducers
- Novel design and construction of airborne ultrasound transducers
- Reduction in cost and size of ultrasound transducers and other hardware components
- New methodologies developed using ultrasound techniques, for example, monitoring crystallisation
- Improvement in image reconstruction techniques
- Improvements in computer technologies, for example, parallel processing
- Development of process tomography systems using ultrasound and other imaging modalities

9.6 Sources of further information and advice

For detailed reading on acoustic theory in solids the reader should refer to the textbooks of Rose (1999) and Krautkrämer and Krautkrämer (1990). These books also include techniques for surface waves and waves in thin plates that have applications in ultrasound tomography. For ultrasound theory and techniques in fluid and colloidal systems the reader can refer to the books of Povey (1997) and Dukhin and Goetz (2002). For an overview of ultrasound techniques in industrial processes the reader can refer to Chapter 10 in *Ultrasonics: Fundamentals, technologies, and applications* (Ensminger & Bond, 2012). For further reading specifically on ultrasound process tomography the reader can refer to specific references within this chapter or Chapter 8 of *Process tomography: Principles, techniques and applications* (Williams & Beck, 1995).Ultrasound microscopy generates 2D and 3D images using ultrasound technology. These techniques may also be relevant to ultrasound process tomography, so for further information the reader should refer to the books of Briggs and Kolosov (2010) and Maev (2008).

9.7 Summary

This chapter has focussed on ultrasound process tomography instruments. Section 9.2 introduced the basic ultrasound theory and described what happens when an acoustic wave interacts with an interface. As the majority of industrial processes are fluid based, the theory was only presented for ultrasound and acoustics in fluids. This chapter has included what measurements are made using ultrasound methods so the reader can understand what can be imaged using the technique. This section not only included what measurements are made currently with ultrasound process tomography systems, but included an overview of all applications of ultrasound for process monitoring so the reader may understand the technique's full potential. Section 9.3 described the main components for an ultrasound tomography system and discussed the different types of systems and how the images are reconstructed and system specifications calculated. Section 9.4 presented the different systems used for ultrasound process tomography systems and was split into two sections, the first for imaging single-phase flows and the second for imaging multiphase flows. This chapter should have given the reader a detailed insight into how ultrasound techniques can be used for process imaging. Although ultrasound is a powerful technique with many applications and significant potential in the future of process imaging, the original limitations such as slow wave propagation speed will always remain. These issues should always be considered when deciding if it is the most suitable process imaging technique to use.

References

Abdul Rahim, R., Fazalul Rahiman, M. H., Chan, K. S., & Nawawi, S. W. (2007). Non-invasive imaging of liquid/gas flow using ultrasonic transmission-mode tomography. *Sensors and Actuators A, 135*, 337–345.

Abdul Rahim, R., Fazalul Rahiman, M. H., & Mohd Taib, M. N. (2005). Non-invasive ultrasonic tomography: liquid/gas flow visualization. In: *1st International conference on computers, communications, & signal processing with special track on biomedical engineering. Kuala Lumpur, Malaysia, November 14–16.*

Abdul Rahim, R., Nyap, N. W., Fazalul Rahiman, M. H., & San, C. K. (2007). Determination of water and oil flow composition using ultrasound tomography. *Elektrika, 9*(1), 19–23.

Abdul Wahab, Y., Abdul Rahim, R., Fazalul Rahiman, M. H., & Ahmad, M. A. (2011). Application of transmission-mode ultrasonic tomography to identify multiphase flow regime. In: *International conference on electrical, control and computer engineering, June 21–22.*

Alba, F. 1992. Method and apparatus for determining particle size distribution and concentration in a suspension using ultrasonics. U.S. Patent no. 5121629.

Allegra, J. R., & Hawley, S. A. (1972). Attenuation of sound in suspensions and emulsions theory and experiments. *Journal of the Acoustical Society of America, 51*, 1545–1564.

Awad, T. S., Moharram, H. A., Shaltout, O. E., Asker, D., & Youssef, M. M. (2012). Applications of ultrasound in analysis, processing and quality control of food: a review. *Food Research International, 48*, 410–427.

Briggs, G. A. D., & Kolosov, O. (2010). *Acoustic microscopy*. New York: Oxford Science Publications.

Brown, G. J., & Reilly, D. (1996). Ultrasonic tomographic imaging of solid objects in air using an array of fan-shaped-beam electrostatic transducers. *Ultrasonics, 34*, 111–115.

Brown, G. J., Reilly, D., & Mills, D. (1996). Development of an ultrasonic tomography system for application in pneumatic conveying. *Measurement Science and Technology, 7*, 396–405.

Challis, R. E., Povey, M. J. W., Mather, M. L., & Holmes, A. K. (2005). Ultrasound techniques for characterizing colloidal dispersions. *Reports on Progress in Physics, 68*, 1541–1637. http://dx.doi.org/10.1088/0034-4885/68/7/R01.

Cheeke, J. N. (2002). *Fundamentals and applications of ultrasonic waves*. Boca Raton: CRC Press.

Chen, Z. X., & Sanderson, M. L. (1996). Ultrasonic tomography for process measurement. In: *IEEE instrumentation and measurement technology conference, Brussels, Belgium, June 4—6*.

Contreras montes de Oca, N. I., Fairley, P., McClements, D. J., & Povey, M. J. W. (1992). Analysis of the sugar content of fruit juices and drinks using ultrasonic velocity measurements. *International Journal of Food Science and Technology, 27*, 515—529.

Deinhammer, C., Steiner, G., Sommer, M., & Watzenig, D. (2008). Electromechanical flow imaging using ultrasound and electrical capacitance data. In: *IEEE sensors conference*.

Dukhin, A. S., & Goetz, P. J. (2002). *Ultrasound for characterizing colloids: Particle sizing, zeta potential, rheology*. Oxford: Elsevier.

Ensminger, D., & Bond, J. (2012). *Ultrasonics: Fundamentals, technologies, and applications* (3rd ed.). Boca Raton, FL: Taylor and Francis.

Fazalul Rahiman, M. H., Abdul Rahim, R., Abdul Rahim, H., & Ayob, N. M. N. (2012). Design and development of ultrasonic process tomography. In Dr. Santos (Ed.), *Ultrasonic waves*.

Fazalul Rahiman, M. H., Abdul Rahim, R., Abdul Rahim, H., Muji, S. Z. M., & Mohamad, E. J. (2012). Ultrasonic tomography — image reconstruction algorithms. *International Journal of Innovative Computing, Information and Control, 8*(1B), 527—538.

Fazalul Rahiman, M. H., Abdul Rahim, R., Fazalul Rahiman, M. H., & Tajjudin, M. (2006). Ultrasonic transmission-mode tomography imaging for liquid/gas two-phase flow. *IEEE Sensors Journal, 6*, 6.

Fazalul Rahiman, M. H., Abdul Rahim, R., & Zakaria, Z. (2008). Design and modelling of ultrasonic tomography for two-component high-acoustic impedance mixture. *Sensors and Actuators A: Physical, 147*, 409—414.

Fincke, J. R. (1980). The application of reconstructive tomography to the measurement of density distribution in two phase flow. In: *Proceedings of the 26th international instrumentation symposium* (pp. 235—243). Research Triangle Park, NC: ISA.

Foldy, L. L. (1945). The multiple scattering of waves — I. General theory of isotropic scattering b randomly distributed scatterers. *Physics Review, 67*, 107.

Gai, H., Li, Y. C., Plaskowski, A., & Beck, M. S. (1989). Ultrasonic flow imaging using time-resolved transmission-mode tomography. In: *Proceedings IEE 3rd international conference on image processing and its applications* (pp. 237—241). Warwick: Warwick University Press.

Greenleaf, J. F. (1970). Introduction to computer ultrasound tomography. In: *Computed aided tomography and ultrasonics in medicine* (pp. 125—136). North-Holland.

Hay, T. R., Royer, R. L., Gao, H., Zhao, X., & Rose, J. L. (2006). A comparison of embedded sensor lamb wave ultrasonic tomography approaches for material loss detection. *Smart Material Structure, 15*, 946—951.

Holstein, P., Raabe, A., Muller, R., Barth, M., Mackenzie, D., & Starke, E. (2004). Acoustic tomography on the basis of travel-time measurement. *Measurement Science and Technology, 15*, 1420—1428.

Hoyle, B. S. (1996). Process tomography using ultrasonic sensors. *Measurement Science and Technology, 7*, 272—280.

Hoyle, B. S., Jia, X., Podd, F. J. W., Schlaberg, H. I., Tan, H. S., Wang, M., et al. (2001). Design and application of a multi-modal process tomography system. *Measurement Science and Technology, 12*, 1157—1165.

Ingleby, P., & Wright, W. M. D. (2002). Ultrasonic imaging in air using fan-beam tomography and electrostatic transdcuers. *Ultrasonics, 40*, 507—511.

Jovanovic, I. 2008. Inverse problems in acoustic tomography: Theory and applications. (Ph.D. thesis). University of Belgrade, Serbia.

Jovanovic, I., Hormati, A., Sbaiz, L., & Vetterli, M. (2007). Efficient and stable acoustic tomography using sparse reconstruction methods. In: *19th International congress on acoustics, Madrid, Spain, September 2−7*.

Kolbe, W. F., Turko, B. T., & Leskovar, B. (1986). Fast ultrasonic imaging in a liquid filled pipe. *IEEE Transactions on Nuclear Science, 33*(1), 715−722.

Krautkrämer, J., & Krautkrämer, H. (1990). *Ultrasonic testing of materials*. Berlin: Springer-Verlag.

Lasaygues, P., Mensah, S., Guillermin, R., Rouyer, J., & Franceshini, E. (2012). Non-linear inversion modeling for ultrasound computer tomography transition from soft to hard tissues imaging. *Proceedings of the SPIE 8320, Medical Imaging 2012: Ultrasonic Imaging, Tomography, and Therapy*, 832004. http://dx.doi.org/10.1117/12.911012.

Leighton, T. G., Phelps, A. D., Ramble, D. G., & Sharpe, D. A. (1996). Comparison of the abilities of eight acoustic techniques to detect and size a single bubble. *Ultrasonics, 34*, 661−667.

Liang, S., Wang, X., Wiedenbeck, J., Cai, Z., & Fu, Feng. (2007). Evaluation of acoustic tomography for tree decay detection. In: *Proceedings of the 15th international symposium on non destructive testing of wood. Duluth, Minnesota, USA. September 10−12*.

Li, W., & Hoyle, B. S. (1997). Ultrasonic process tomography using multiple active sensors for maximum real-time performance. *Chemical Engineering Science, 52*(13), 2161−2170.

Liu, L., Li, R. F., Collins, S., Wang, X. Z., Tweedie, R., & Primrose, K. (2011). Ultrasound spectroscopy and electrical resistance tomography for online characterisation of concentrated emulsions in crossflow membrane emulsifications. *Powder Technology, 213*, 123−131.

Li, Y. Q., & Zhou, H. C. (2006). Experimental study on acoustic vector tomography of 2-D flow field in an experiment-scale furnace. *Flow and Measurement Instrumentation, 17*, 113−122.

Lloyd, P., & Berry, M. V. (1967). Wave propagation through an assembly of spheres. IV. Relations between different multiple scattering theories. *Proceedings of the Physical Society, London, 91*, 678−688.

Maev, R. G. (2008). *Acoustic microscopy: Fundamentals and applications*. Weinheim: Wiley-VCH.

Martin, P. D., Beesle, M., & Myers, P. E. (1995). Ultrasound imaging in large gas and liquid processing vessels. *The Chemical Engineering Journal, 56*, 183−185.

Martini, S. (2013). Sonocrystallization of fats. In: *Springer briefs in food, health, and nutrition*. Springer.

Mazeika, L., Kazys, R., Raisutis, R., Demcenko, A., & Sliteris, R. (2006). Long-range ultrasonic testing of fuel tanks. In: *EC NDT conference, Berlin, September 25−29*.

McClements, D. J., & Povey, M. J. W. (1992). Ultrasonic analysis of edible fats and oils. *Ultrasonics, 30*(6), 383−388.

Mensah, S., & Franceschini, E. (2006). Near-field ultrasound tomography. *Journal of the Acoustical Society of America, 121*(3), 1423−1433.

Morse, P. M., & Ingard, K. U. (1968). *Theoretical acoustics*. New York: McGraw Hill.

Norton, S. J., & Linzer, M. (1979). Ultrasonic reflectivity tomography: reconstruction with circular transducer arrays. *Ultrasonic Imaging, 1*, 154−184.

Opielinski, K. J., & Gudra, T. (2006). Recognition of external object features in gas media using ultrasound transmission tomography. *Ultrasonics, 44*, 1069−1076.

Parker, N. G., & Povey, M. J. W. (2009). Scanning acoustic microscopy for mapping the microstructure of soft materials. In: *What where when multi-dimensional advances for industrial process monitoring, Leeds, UK, June 23−24*.

Pierce, A.d. (1981). Temperature and pressure dependence of the sound velocity in distilled water. In: *Acoustics: An introduction to its physical principles and applications*. New York: McGraw-Hill.

Pinfield, V. J., Povey, M. J. W., & Dickinson, E. (1995). The application of the modified forms of the Urick equation to the interpretation of ultrasound velocity is scattering systems. *Ultrasonics, 33*(3), 243−251.

Povey, M. J. W. (1997). *Ultrasonic techniques for fluids characterization*. San Diego: Academic Press.

Rose, J. L. (1999). *Ultrasonic waves in solid media*. Cambridge: Cambridge University Press.

Roy, O., Jovanovic, I., Hormati, A., Parhizkar, R., & Vetterli, M. (2010). Sound speed estimation using wave-based ultrasound tomography: theory and GPU implementation. *Proceedings SPIE 7629, Medical Imaging 2010: Ultrasonic Imaging, Tomography, and Therapy*, 76290J. http://dx.doi.org/10.1117/12.844691.

Satti, A. M. H., & Szilard, J. (July 1983). Computerised ultrasonic tomography for testing solid propellant rocket motors. *Ultrasonics, 21*, 162−166.

Schlaberg, H. I., Podd, F. J. W., & Hoyle, B. S. (2000). Ultrasound process tomography systems for hydrocyclones. *Ultrasonics, 38*, 813−816.

Schlaberg, H. I., Yang, M., & Hoyle, B. S. (1998). Ultrasound reflection tomography for industrial processes. *Ultrasonics, 36*, 297−303.

Scott, T. E., & Roegiers, J.-C. (1994). Acoustic tomographic difference imaging of dynamic stress fields. In: *SPE/ISRM rock mechanics in petroleum engineering conference. Delft, The Netherlands, August 29−31*.

Silk, M. G. (1984). *Ultrasonic transducers for non-destructive testing*. Bristol: Hilger.

Steiner, G., & Podd, F. (2006). A non-invasive and non-intrusive transducer array for process tomography. In: *XVIII IMEKO world congress, Rio de Jaeiro, Brazil, September 17−22*.

Steiner, G., & Watzenig, D. (2008). A bayesian filtering approach for inclusion detection with ultrasound reflection tomography. *Journal of Physics: Conference Series, 124*, 012049.

Uberall, H. E. (1992). *Acoustic resonance scattering*. Philadelphia: Gordon & Breach Science.

Utomo, M. B., Warsito, W., Sakai, T., & Uchida, S. (2001). Analysis of distributions of gas and TiO_2 particles in slurry bubble column using ultrasonic computed tomography. *Chemical Engineering Science, 56*, 6073−6079.

Warsito, M., Ohkawa, M., Kawata, N., & Uchida, S. (1999). Cross-sectional distributions of gas and solid holdups in slurry bubble coloumn investigated by ultrasonic computed tomography. *Chemical Engineering Science, 54*, 4711−4728.

West, R. M., Jia, X., & Williams, R. A. (2000). Parametric modelling in industrial process tomography. *Chemical Engineering Journal, 77*, 31−36.

Williams, R. A., & Beck, M. S. (1995). *Process tomography: Principles, techniques and applications*. Oxford, UK: Butterworth − Heinemann.

Wolf, J. (1988). Investigation of bubbly flow by ultrasonic tomography. *Particle and Particle Systems Characterization, 5*, 170−173.

Wood, A. B. (1941). *A textbook of sound*. London: Bell and Sons.

Wright, W. M. D., & O'Sullivan, I. J. (2003). Ultrasonic tomographic imaging of air flow in pipes using an electrostatic transducer array. *Review of Quantitative Nondestructive Evaluation, 22*, 666−673.

Wright, W. M. D., Schindel, D. W., Hutchins, D. A., Carpenter, P. W., & Jansen, D. P. (1998). Ultrasonic tomographic imaging of temperature and flow fields in gases using air-coupled capacitance transdcuers. *Journal of the Acoustical Society of America, 104*(6), 3446−3455.

Xu, L. J., & Xu, L. A. (1998). Gas/Liquid two-phase flow regime identification by ultrasonic tomography. *Flow Measurement and Instrumentation, 8*(3/4), 145−155.

Xu, L., Han, Y., Xu, L. A., & Yang, J. (1997). Application of ultrasonic tomography to monitoring gas/liquid flow. *Chemical Engineering Science, 52*(13), 2171−2183.

Yang, M., Schlaberg, H. I., Hoyle, B. S., Beck, M. S., & Lenn, C. (1999). Real-time ultrasound process tomography for two-phase flow imaging using a reduced number of transducers. *IEEE Transactions on Ultrasonics, Ferroelectrics, and Frequency Control, 46*, 3.

This page intentionally left blank

Spectro-tomography

10

B.S. Hoyle
University of Leeds, Leeds, UK

10.1 Multidimensional process measurement requirements

Industrial processes may be classified using many descriptors. Perhaps the most generic and pervasive descriptors are terms such as *efficient*, *productive* and *sustainable*. Their designers and operators must seek to achieve increasingly demanding objectives in all of these key business parameters. Processes have an almost unlimited variety of forms. Many are concerned with the transformation of raw materials into products. Here we focus on processes that operate in a defined and typically closed space, in which data on internal content and distribution are not easily accessible. If the transformation process is simple, for example where the contents are known to be homogeneous and are simply heated over a set time period, the process may be monitored at a single sampling point. Here a conventional one-dimensional sensor may be used to estimate the value of a single physical parameter, such as temperature or pressure. Even in more complex processes a single point can provide a more general insight. Thus a temperature at a critical location may be assumed to be indicative of a specific point in a process trajectory. This assumption may be based upon an explicit process model or upon empirical experience. When processes are used consistently or have broad-range characteristics that exhibit insignificant variation, such sensing and monitoring approaches can be simple and highly effective.

In many other processes models may not be universal and such assumptions may be false, for example, under extended operating parameters or with new materials and recipes. Process models may not be available, or the model range may not extend to a wide range of candidate materials or process recipes. Many industrial processes have multiple components and wide operating envelopes. In these cases an explicit recognition of the multidimensional nature of processes in the widest sense is essential in the design of process sensing technology.

10.1.1 Industrial process tomography foundations

The technology of industrial process tomography (IPT) aims to extend the limited capability of conventional one-dimensional sensors deployed for process monitoring (Hoyle, McCann, & Scott, 2005). Various detailed aspects are also described in other chapters of this book. IPT offers internal distribution data through the basic principle of injecting excitation energy into a process from a specific spatial 'projection' and sensing the resulting observable response at one or many appropriate positions.

Industrial Tomography. http://dx.doi.org/10.1016/B978-1-78242-118-4.00010-1
Copyright © 2015 Elsevier Ltd. All rights reserved.

A number of different projections are taken. Classic examples are X-ray or laser optical tomography, in which a narrow cross-section beam is applied at one peripheral projection position and a corresponding single sensor at the diametrically opposed position measures the resulting attenuated beam. In this case only one measurement is needed for each projection. Further positional attenuation measurement projections produce a raw attenuation data set. Other energy 'modes', for example the injection of electrical energy, typically require a number of measurements per projection. For example, the injection of a constant current between two points on the periphery of a process will create a distributed conduction field, whose observable peripheral distribution can be measured through the sensing of voltage at several points around the periphery. Hence in this case several measurements are typically required for each projection.

IPT 'reconstruction' is the general term for the next step, the classic 'inverse problem', which aims to estimate the corresponding unknown internal distribution of the process from the projection data set. Many methods are available for this processing task; again this topic is explored in depth in other chapters. In medical X-ray applications many thousands of projections can be taken as the subject may be practically stationary. In process applications the constraints of process dynamics typically impose severe limits.

In order to define general objectives for development it is first useful to consider the application background in which IPT typically has two application role requirements:

> *Process design and pilot stage*: confirm or develop a process model in which two-dimensional (2D) or three-dimensional (3D) spatial plus temporal process data can be used to quantify or verify model parameters; and
>
> *Process operation stage*: derive gains from the increased information arising from its tomographic data.

10.1.2 First-generation instruments

A 'first generation' of IPT instruments may be defined in which the design is based upon a singular mode and level of excitation energy, and thus requires a simple practical realisation, in terms of both electronic systems and computational capability. The excitation could, for example, be X-ray, laser or electrical, and its level is typically fixed. Thus in X-ray-based instruments a steady energy level is released from a radioactive source or from a constant-flux electrical X-ray generator. In electrical conduction-based instrumentation the excitation voltage (or current) is 'constant', which typically means the injection of a short burst of single-frequency sinusoid energy whose amplitude is controlled at the required level. Where appropriate, projection measurements are taken after any initial introduction transient has settled.

Although the projection data collection may be judged to be adequate, the sensed process data are in essence limited by the 'contrast' offered by the process space. For example, X-ray energy passes with minimal attenuation through low-density materials, but is attenuated by high-density materials, such as cartilage and bone. Thus dense objects, in a field of low-density material, have high contrast and can be easily imaged through tomography. In electrical terms, for a conduction-based instrument, objects having low conductance (high resistance) distort the conduction field, and hence have high contrast in a background of high conductance material, and can be imaged through tomography.

A number of first-generation products have been developed to support IPT applications in both design study and operation monitoring roles. A commonly used example is the Industrial Tomography Systems (ITS) P2+ product (ITS, 2014). This supports an array of up to 128 electrodes in contact with the process media, mounted around the circumference of the pipe or vessel, or on a baffle or dip-pipe. This would, for example, support data capture in a cylindrical vessel, such as a process mixer, from eight vertical planes each having 16 electrodes. Data are processed to provide a conductivity map of the sensing zone, under the assumption that this directly represents the process distribution. Figure 10.1 shows the instrument and typical results for an application in gas−liquid mixing used in this 3D mode.

A large number of applications have been supported where useful process data can be extracted using 'first-generation' IPT, which offers major and otherwise inaccessible internal distribution data, even though this may contain inaccuracies. ITS cites a wide range of application sectors for this product: biotechnology, bulk and specialty chemicals, environmental processes such as material transport, fast-moving consumer goods such as personal products, mining separation processes, nuclear processing monitoring, oil and gas in oilfield flows, pharmaceutical product monitoring and control, pulp and paper processing. There are many publications, for example in the pharmaceuticals sector by Ricard, Brechtelsbauer, Xu, and Lawrence (2005).

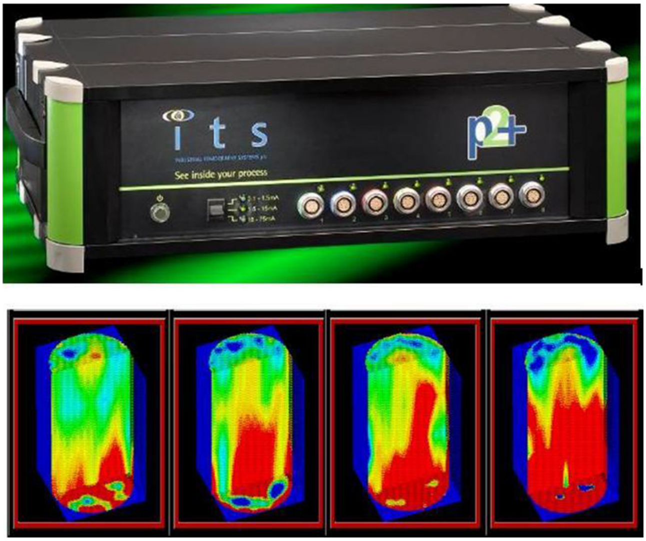

Figure 10.1 Example IPT instrument (upper); and gas−liquid mixing application example (lower) showing increasing gas injection from left to right. IPT, industrial process tomography. Courtesy of Industrial Tomography Systems plc.

10.1.3 Beyond first-generation systems

Where the ‘contrast opportunity’ does not fit the straightforward ‘first-generation tomography’ case — able to exploit a singular energy form and excitation level — results may be marginal in quality. In some cases, such IPT data are simply better than can be achieved from any other form of instrumentation able to provide ‘wide-angle’ data in ‘process real-time’. However, it is apparent that there are major distortions and ambiguities. Sparse and noisy data are likely to generate spatial errors even in simple processes. In more complex mixtures of materials there is likely to be major uncertainty in the identification of features and components, for example, when the ‘contrast’ offered by components is similar.

Improvements beyond ‘first-generation’ IPT could make the technology applicable in more complex and high-value processes, for which models may not be available, or where the model range does not extend to a wide range of candidate materials or process recipes. Increased processing to extract better information from data is clearly helpful. Significant development has been made in the refinement of inverse reconstruction processing. Iterative methods, such as that proposed by Wang (2002), offer significant improvement at modest computation cost. However, it is also clearly preferable, where possible, to enhance the process information content of the raw data. To fulfil this need in such applications requires extended or new ‘second-generation tomography’ approaches. These can be generally classified as ‘multidimensional’ IPT, in which ‘dimensionality’ can take various forms outlined below. In general there is a sensing need to seek and exploit increased ‘contrast opportunities’, so that the raw tomographic projection data are richer in terms of the intrinsic process information in regard to both temporal and spatial distribution of specific material components.

10.2 Multidimensional process sensing

The term ‘dimension’ implies classical Cartesian spatial coordinates. A further dimension is the range and modes of excitation energy used in the sensing process, and the detection of its effects, to match the physical properties of the process material(s). In engineering terms these aspects are also linked to the synchronisation, detection and processing of the sensor data. Hence, in the electrical tomography example, the energy may be applied over an energy band known to suit the ‘contrast’ response function. From this multidimensional view a summary of key engineering requirements for IPT may be expressed as:

Spatial resolution: Sufficient to yield information of interest.
Time resolution: Sufficient to reveal dynamics of interest.
Component and material identification: Sufficient to identify 3D distributions of process components of interest.

These engineering requirements may be usefully combined with the application requirements of Section 10.1.1.

10.2.1 Multidimensional data in processes

The view of IPT as a multidimensional sensing technology also implies a further requirement, concerned not with the sensing and tomographic reconstruction issues but with the opportunities and needs of the methods that allow multiple data sets to be constructively combined. In order to exploit multidimensional data a coherent method is needed to combine the various data sets from multiple sensing dimensions. The overriding aim must be to deliver information for the design or operation of the application process. For example, to deliver operational data a specific goal may be to estimate the current state in the process trajectory for a batch reactor. Figure 10.2 provides a schematic illustration of the hypothetical attributes of input data, a state estimation algorithm and a corresponding state trajectory illustrating the synthesis of product, C, from reagents A and B with a proposed optimal endpoint, before the reaction begins to reverse.

The input data of the schematic data fusion method of Figure 10.2 offer the obvious spatial and temporal data available from the sensing system. It must also include relevant information on the mode of the energy, to enable the inference of how sensed data must be interpreted to reveal estimated process states. We may represent such modes classically, for many sensing methods, in terms of the electromagnetic spectrum, as illustrated in Figure 10.3. This also shows common sensing methods: electrical impedance spectroscopy (EIS), nuclear magnetic resonance (NMR), Raman spectroscopy and their typical spectral position and range.

Data fusion methods are needed to integrate data from multiple sources that are likely to feature different sensing regions and dimensionality. Data from different

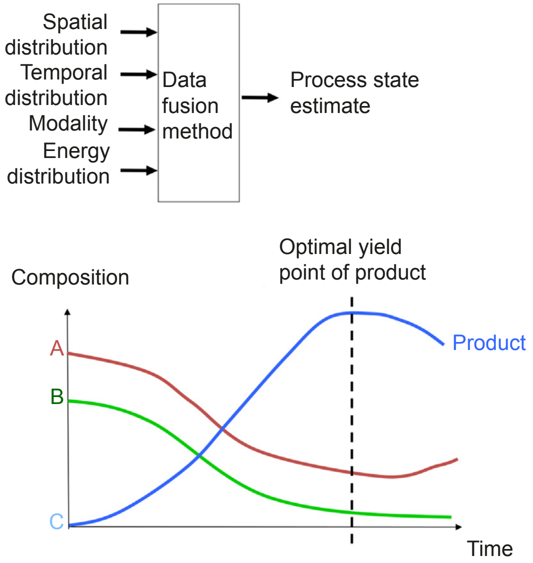

Figure 10.2 Multidimensional data and estimation of process state: (upper) attributes and data fusion; (lower) process state trajectory.

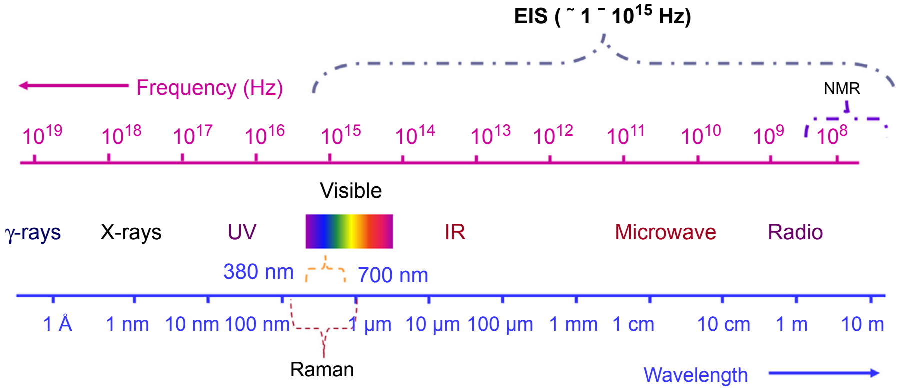

Figure 10.3 Electromagnetic energy spectrum and associated sensing methods. Courtesy of V. Ramachandran — diagram — e/m spectrum.

modalities, perhaps offering insights into different process components, may be fused through a multicomponent composition model. Second-generation IPT systems have been designed to support data collection and fusion from sensors of different energy modes. For example, a generic multimodal system design allows the selection of specific in-built fusion methods to suit various combinations of multimodal modules (Hoyle et al., 2001). This design was implemented by ITS as the M3 IPT instrument. One example description of its use features the fusion of electrical resistance and electrical capacitance mode data in the study and measurement of oil/water/gas flows (Qui, Hoyle, & Podd, 2007). Other variants in this application area have used gamma-ray sensing to locate gas structures with electrical capacitance tomography. Multimodal IPT systems are explored in depth in Chapter 15.

10.2.2 Multidimensional data fusion

The input data of the schematic data fusion method noted in Figure 10.2 offer the obvious spatial and temporal data extracted from the sensing system. It must also include relevant information on the mode of the energy to infer how the sensed data must be interpreted to reveal estimated process states. Where the excitation energy mode includes a range of levels, the specific level that relates to the sensed data is also a key factor in the data fusion interpretation method.

10.3 Spectral energy sensing dimension

10.3.1 Electrochemistry sensing opportunities

Materials typically exhibit a response to excitation in relation to an applied energy level. Here we are concerned with electrically based process estimation methods. In electrical terms the specific energy level is expressed in terms of frequency.

A characterisation across a band of frequencies is called a spectroscopic response and this presents a sensing opportunity from which a specific material identification may be inferred.

Where an industrial process features a homogeneous distribution of materials, its bulk properties can be sampled and tested from any convenient internal point. This may be carried out by exciting the sample with a range of frequency-scaled energy levels, to obtain a frequency-based impedance response characteristic. This method is commonly known as either electrical impedance spectroscopy or dielectric spectroscopy (due to the resonant energy storage in the material). Typical implementations involve a set of discrete measurement steps between which the excitation frequency is progressively increased, from an initial to a final value of interest. At each step the single-frequency response value is measured. In general materials exhibit complex impedance characteristics. Hence a set of response parameters must be described as complex quantities, representing energy dissipation (resistive) and energy storage (reactive) parts. It is convenient to illustrate characteristics as graphical frequency-based functions, either as a complex value in terms of its real and imaginary components or in 'phasor' terms of magnitude and phase (shift) components. Figure 10.4 illustrates the characteristic of a hypothetical material expressed as a complex variable in its real and imaginary components.

As would be expected, chemical compounds exhibit a variety of spectral fingerprints, based primarily upon their chemical structure. Electrical excitation produces responses arising from interaction to specific molecular and atomic features. Based upon the energy levels expressed in frequency terms, and corresponding resonance capabilities, these may be segmented into the general frequency regions illustrated in Figure 10.4. Thus ionic features in the material are likely to present spectral response

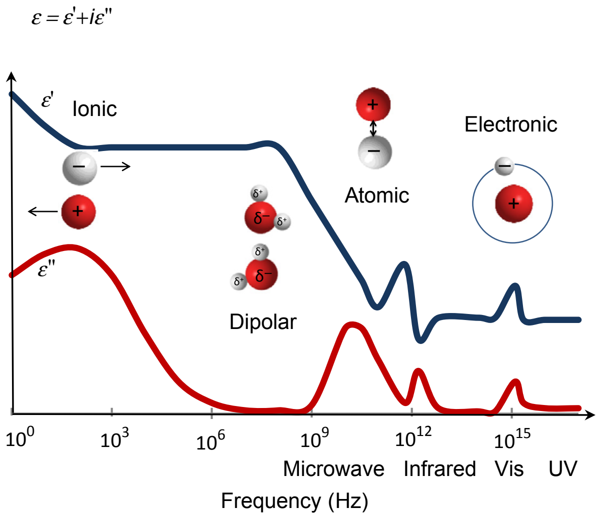

Figure 10.4 Electrochemical effects over electrical excitation spectrum. Courtesy of Q. Yuan — diagram — special interactions.

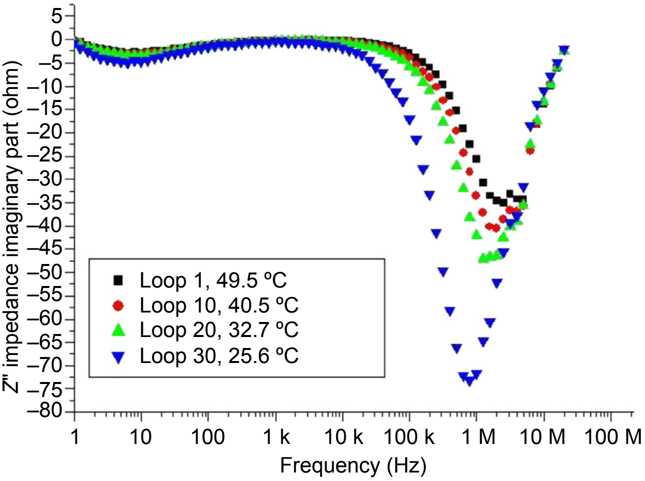

Figure 10.5 Spectral fingerprint of LGA. LGA, L-glutamic acid.
Courtesy of Y. Zhao – graph LGA spectrum.

characteristics at low frequency. At frequencies in the range of 1 MHz–1 GHz dipole structure resonances become evident. At higher frequencies atomic and electronic resonances appear.

A measured characteristic can then be considered a 'spectral fingerprint' of a specific material. Even if this is not unique, it is likely to support the discrimination of each of several distinct component materials in a specific process. For example, Figure 10.5 illustrates the spectral fingerprint of L-glutamic acid (LGA), a commonly used stimulant for pharmaceutical materials (Zhao, Wang, & Hammond, 2011).

10.3.2 Energy mode and level dimension

In many important industrial applications corresponding processes feature spatial distributions of their components. IPT offers a powerful method to gain an insight into these distributions; however, first-generation instruments are limited to a single energy mode and level. The 'contrast' provided in a resulting tomograph can then be considered as a 'grey-scale' characteristic at the corresponding energy level. Even where multimodal implementations are employed, these typically offer a small number of energy-level 'colours', which may not provide insufficient distinctive data to support reliable material identification. Hence an augmentation of IPT with a spectroscopic sensing 'dimension' has the potential to jointly estimate the spatial distribution of components explicitly identified using spectroscopic data. Hence in terms of the discussion of Section 10.1.3 this concept provides a major increase in the degrees of freedom for contrast range.

For real-time viability sensing operations must be carried out within a time window that delivers temporal data that reliably tracks the process dynamics of interest. Where there are significant process dynamics spectroscopic sensing, which relies upon a stepped set of single-frequency excitations, is likely to fail. The sensing excitation frequency range is clearly critical to explore the spectral fingerprint of the materials in a process, as illustrated for LGA in Figure 10.5, showing an overall bandwidth from 10 Hz to 50 MHz. As noted, a simple sequential sweep of the excitation over this very large range would be impractical for a dynamic process, such as a stirred vessel. Here the internal dynamics are likely faster relative to the speed at which the signal could be swept in order to gain measurements at significant frequency points. Hence a method is required that exploits a composite signal, which includes frequencies throughout the band of interest, coupled with a further method to permit the processing of the joint response set of the target process to the excitation, which then enables the spectroscopic identification of materials. We term the combination of IPT with integrated fast real-time spectroscopy and material identification *spectro-tomography*.

10.4 Spectro-tomography principles

10.4.1 Simple process model

Processes similar to that illustrated in Figure 10.1, in which reagents are combined to form a product, may be investigated using the ‘classical’ (first-generation) single-frequency IPT approach outlined in Section 10.1.2. Figure 10.2 illustrates a hypothetical example process trajectory in which reagents A and B combine to form product C. Figure 10.6 provides a pictorial view of three states from this trajectory: the initial state, when only the two reagents A and B are present; an intermediate state in which some product C has formed; and the final state when practically all the material present is product C.

Figure 10.7 provides a further hypothetical set of spectral fingerprints for the three components in the trajectory of Figure 10.2. These are not intended to represent actual materials, but to simply illustrate the effects of excitation frequency on the resulting tomographic contrast. The three components are arbitrarily colour coded for clarity.

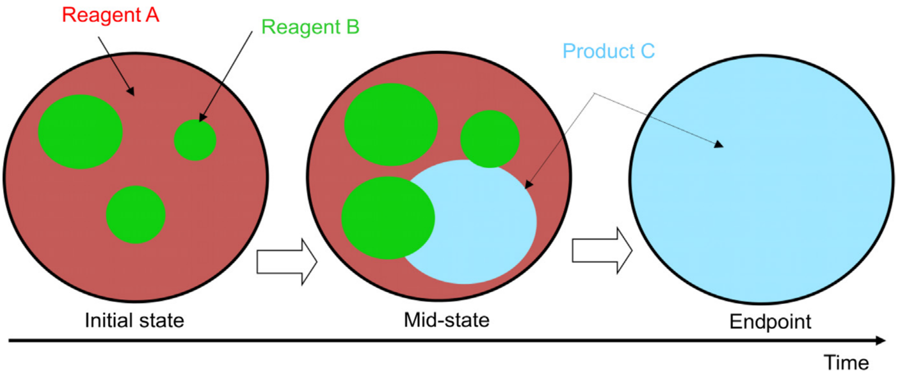

Figure 10.6 Pictorial view of three states within an example process trajectory.

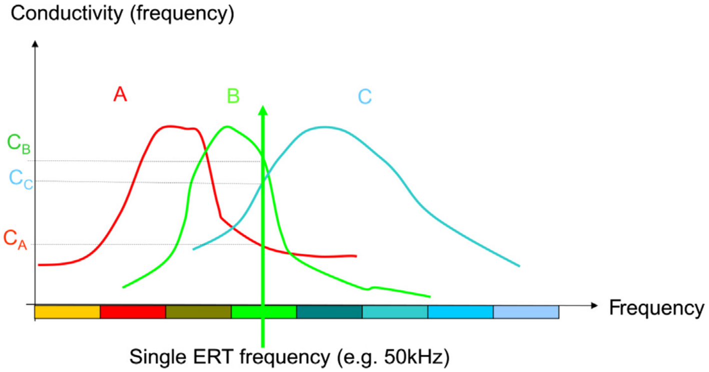

Figure 10.7 Example spectral fingerprints for reagents A and B and product C.

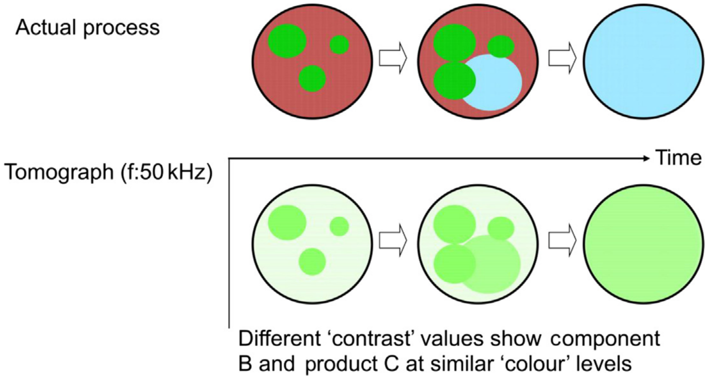
Actual process
Tomograph (f:50 kHz)
Time
Different 'contrast' values show component
B and product C at similar 'colour' levels

Figure 10.8 Tomographs for three states within an example process trajectory for 50 kHz excitation.

Figure 10.7 also shows three possible excitation frequencies of 20, 50 and 80 kHz using colours to indicate frequency steps.

If the single excitation frequency of 50 kHz is selected for an IPT investigation, from the three shown in Figure 10.7, then reagent B has the highest conductivity, followed closely by product C. Reagent A has a much lower conductivity at the single excitation frequency. In a resulting tomograph we may assume that conductivity is mapped in terms of intensity on a 'grey scale'. Since conductivities C_B and C_C are similar in value, reagent B and product C will appear at a similar value of grey-scale intensity in a synthesised tomographic image computed from the single-frequency data; reagent A will appear at a lower level of intensity. In such a multicomponent mixture, although some 'contrast' is available, it is unlikely to be possible to reliably identify specific components from each other. It is perhaps noteworthy that although major data processing efforts may deliver some improvement, it would be preferable if richer raw data were available. Figure 10.8 provides illustrative tomographs for each of the three states.

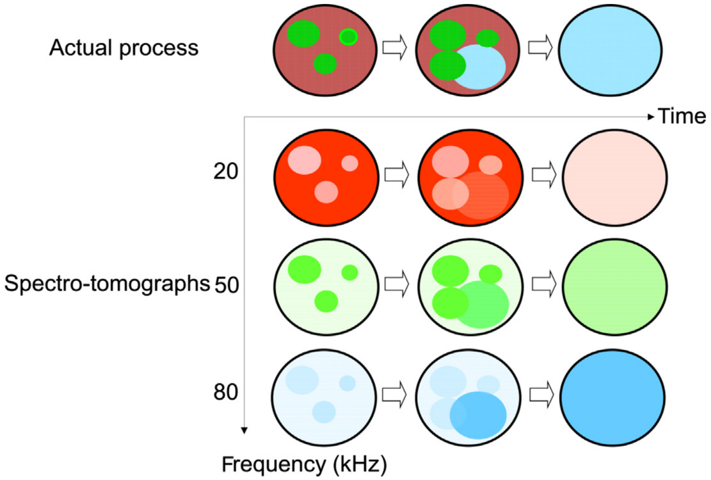

Figure 10.9 Tomographs for three states within an example process trajectory for triple excitation.

To extend the raw data available, we next explore the use of all of the three frequency excitations, at 20, 50 and 80 kHz, shown in Figure 10.7. For simplicity, we assume that the three excitations and their corresponding measurements are carried out sequentially. (In a real-world example, due to process dynamics, we may not have the requisite sample time for this sequential method.) In this illustrative example sequential IPT response data can be extracted for each of the three frequencies from which three separate, single-frequency tomographs can then be generated using conventional reconstruction methods. Figure 10.9 illustrates the corresponding set of tomographs for this set.

10.4.2 Process component identification

To complete the sensing approach to include material identification, the spectral fingerprint knowledge of process materials is required. In simple terms pixels in each of three estimated process state tomographs are compared with the data set of spectral fingerprints. An estimation process is used to select the most appropriate candidate from the possible materials to form a single 'spectro-tomograph' for each state. In some cases this can be based upon specific and well-known mathematical models. A range of such data fusion strategies can be used. Where a data model is not available or useable for a given process, experimental tests may be performed on material samples at the process operating conditions to create an empirical model (Nahvi & Hoyle, 2009a, 2009b). The specific material identification exploits these data, either from 'look-up tables' of spectral fingerprints of known materials or from the computational fitting of the sensed form to a mathematical model (Nahvi and Hoyle, 2010). The resulting 'spectro-tomograph' from this estimation process, based upon the raw tomograph data set of Figure 10.9, is shown in Figure 10.10. Here colours represent the identified materials from the three components.

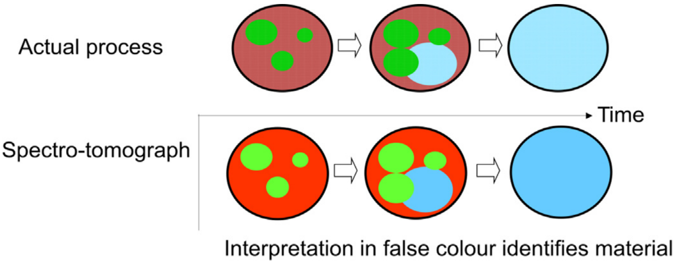

Figure 10.10 Spectro-tomograph for three states from triple excitation energy data.

10.5 Spectro-tomography system implementation

10.5.1 System requirements

The ability to estimate the location, presence and concentration of a specific material promises to overcome major barriers to effective process management. But to realise this need requires in-line sensing (rather than laboratory sampling), which satisfies real-time process trajectory constraints. The spectro-tomography method aims to offer a new approach, based upon electrical methods, to provide these data and fulfil these operational requirements. This new technology is therefore based upon the fast sensing of the wideband electrical impedance spectral fingerprint of a material. The implementation described uses an electrical impedance method, where electrodes are in contact with the process materials, and hence is directly suited to liquid-based processes. Analogous implementations could be developed using different energy modes and excitation methods suited to other process types. For example, for dry solid processes, a method based upon capacitive coupled excitation could be used.

The method implementation has two parts. Firstly, a wideband signal is injected such that the excitation spans the required frequency range. The wideband excitation may conveniently be synthesised using a compressed frequency signal format. Such signals can be designed with flexibility to suit the spectral fingerprints of the expected materials in the process. Secondly, extraction of relevant frequency bands in the resulting response characteristics provides the raw data for the computation of banded tomographs, which correspond to parts of the spectral range of interest for the same sampling interval. For an optimum solution the format of the excitation is likely to be linked to the method used in the response processing. This is followed by the third part: a data fusion process selected to suit the estimation of the material spectral fingerprint for each region of interest across the set of banded tomographs. This process will be based upon a database of spectral fingerprints for the expected materials of interest developed through either models or empirical data. For materials in solutions these data must support concentration levels.

10.5.2 Process excitation and response detection

To deliver a required real-time performance the spectro-tomography method excitation and response processing must be coherently aligned. The use of multifrequency excitation coupled with analogue or digital filtering of response processing could be used, but this is likely to lead to difficulties in effective frequency coverage and in ease of band selection. Multiscale methods hold promise in providing flexible management of real-time excitation and processing.

A wide range of possible compressed signal types are available, each having distinct properties. In terms of simplicity, ease of selection of frequency band and relatively flat spectral energy distribution, a linear frequency-modulated 'chirp' signal provides ideal properties. This signal form provides the basic design parameters expressed in Eqn (10.1):

$$\frac{B}{T} = \frac{f_2 - f_1}{T} \tag{10.1}$$

where B is the design bandwidth, between the upper frequency bound, f_2, and the lower frequency bound, f_1, and T is the duration of the signal. Based upon Eqn (10.1) the process real-time sampling regime can be designed and carefully controlled. Hence the design methodology can simply specify the frequency endpoints, leading directly to the total period, allowing the selection of an appropriate sampling interval. Figure 10.11 illustrates the general form of the 'chirp' signal scaled to 1 time value.

The wideband excitation produces a synchronised wideband response, which must be detected for all relevant physical projections on the process. In essence the wideband response must be decomposed into segments, covering specific selected bands within the total bandwidth. The specific organisation of this selection will be dependent upon the nature of the subject process. In some applications materials may have specific narrow-band spectral fingerprint features, for example, a specific oscillation at a known narrow range of frequencies. In other processes material fingerprints may present various characteristics. Each designed segment will be used to produce a separate tomograph.

To provide a multiscale match to the chirp linear compressed frequency-modulated excitation, a wavelet decomposition is selected. This exploits the wavelet transform (WT), which provides an efficient intrinsic ability to extract spectral data. By scaling a selected mother wavelet, time resolution can be traded for frequency resolution, and vice versa. The property of variable scaling provides variable time–frequency resolution and makes the WT an efficient tool to analyse

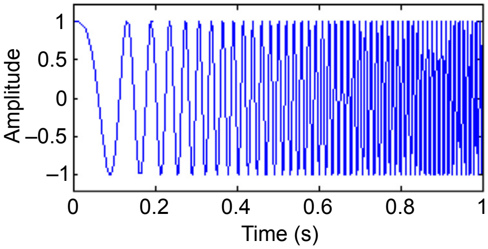

Figure 10.11 Chirp linear compressed frequency excitation.

Figure 10.12 Graph of wavelet scale to frequency—time.

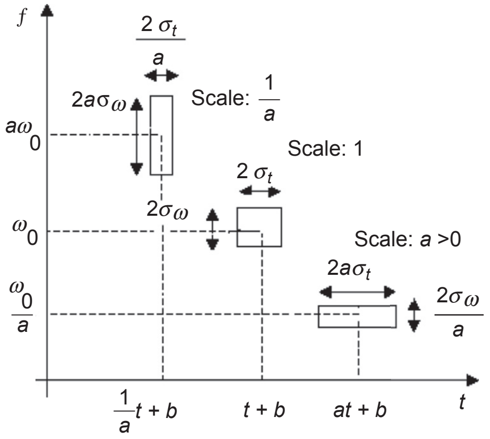

time-varying signals such as various types of the chirp form of interest. In simple terms, the width and the amplitude of the wavelet may be modified such that they can match the specific frequency component. Time and frequency resolution are also then modified. Figure 10.12 illustrates this relationship. To implement the method a mother wavelet is selected and the WT is computed to correspond to the frequency steps of interest. Where wideband data are required a set of frequency steps can be simply generated. The method is described in more detail in Nahvi and Hoyle (2007, 2008). Since the underlying response data correspond to the whole bandwidth of the excitation signal, an iterative process in which specific bands are computed in a controlled sequence is fully supported.

10.5.3 Data fusion processing

The overall aim of this final stage in the processing train is to deliver reduced and focused high-level process information useful for plant monitoring and control.

As seen from Figure 10.12, the intermediate result for each temporal sampling instant is a sequential set of spectral tomographs spanning the requisite energy frequency range. The final major processing step is to exploit these data to reveal time-domain characteristics, coupled with frequency-domain material identification, to form a complete estimation of the process trajectory, for example as shown in Figure 10.2. The temporal flow of the process state is of course provided by time-domain data, but the multitomograph data must first be fused to reveal useful process information, such as percentage composition, in terms of component C in the example. Once this reduced information is available a trend detection algorithm can be deployed to search for changes, turning points, etc.

It is important to note that the set of tomographs computed from data acquired within a given sampling interval present no relative evolution due to process dynamics. It is also the case that all tomographs share the same processing mesh. Hence for such a tomograph set, any given pixel (or voxel, for 3D tomographs) is identical in time and space to the corresponding pixel in all the other tomographs computed from data taken within a single sampling interval. If a derived subset is taken for a selected pixel across all the tomographs, the vector of contrast intensity value will vary only in terms of the extracted response to the energy frequency of each tomograph. For any such pixel such a subset vector forms a test set that may then be compared directly with a spectral fingerprint. Under the conditions outlined above, for a given sample instant, any specific pixel in all (or any subset) of the wideband tomograph set can be used to derive a test vector. This will typically offer a discrete set of points, one from each energy frequency tomogram. Hence the number of single-frequency tomographs, and their total range and frequency spacing, will define the spectral resolution of the test vector. For simplicity, all reference and test sets will have the same spectral range and discrete spacing resolution.

10.5.4 Interpretation processing

A reference spectral fingerprint data set for the expected process materials is needed to facilitate a systematic comparison. Data may be available from archives for the electrical conductance spectrum of known and classified materials, or from specific tests on materials known to be present in a process. These data may take the form of parameterised models based upon generic forms for groups of similar materials. A number of formats can be used to describe or generate a discrete reference vector for a given collection of materials, since the later comparison process must detect significant differences in an estimation. A group of look-up tables (LUT) can map the collection of materials where these exhibit large spectral feature differences. A formal model may be appropriate for materials that are similar in terms of their general spectral characteristics and feature only magnitude differences. Models based upon known materials may allow data to be fitted on a formal basis, in which the quality of estimation can be computed for each possible process component. Material estimation at a pixel involves the core operation of comparing its test vector against all possible reference vectors. Clearly this is likely to require fuzzy rules. Where component materials form physical mixtures a rule set model, or empirical data, is required to define corresponding values for the expected range of composition concentrations.

In terms of the whole 2D or 3D process space interrogated by the sensor system, a range of approaches can be taken. The simplest and obvious option is to simply extend the pixel process described above to the whole space. Although simple, this approach is potentially computationally costly. Where distributions are coarse and contain homogeneous regions, a prior data reduction process may be useful. As a set of energy frequency tomographs are synchronised in the time domain, it is straightforward to apply a segmentation process to identify spatial features that may then be used to reduce the interpretation workload. Where the process trajectory follows the example of Figure 10.2, product material may form at specific nucleation sites. If the tomograph set exhibits large uniform 'regions of interest' (ROIs) then material identification can be scheduled for their centroid pixels. The inclusive group of ROIs can then be used solely for further interpretation on the spectral set for the given time instant. At the

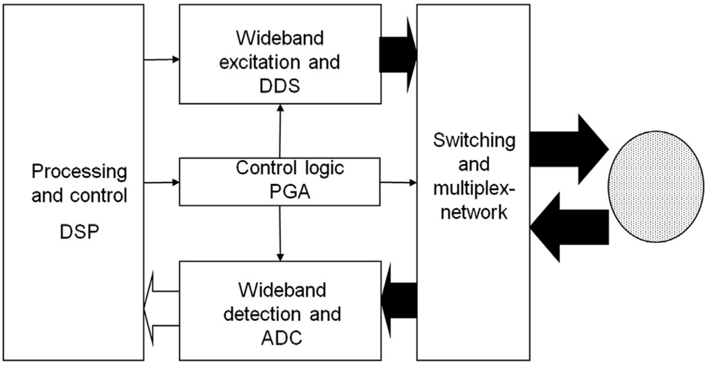
Wideband excitation and DDS
Processing and control DSP
Control logic PGA
Switching and multiplex-network
Wideband detection and ADC

Figure 10.13 System architecture.

opposite extreme, all pixels in each reconstructed image set can be used for material identification.

The result of these processes must deliver a complete material estimation within the sensing space for a given sampling instant; in image form this is a sequence of 'spectro-tomographs'. In order to deliver an overall monitoring and/or control aim, the sequence of spectro-tomographs may be tracked against application criteria, for example, to track the process state trajectory, as illustrated in Figure 10.2, and flag the endpoint.

10.5.5 Data capture and processing architecture

To support the above data acquisition and processing needs, an electronic system architecture must include appropriate control synchronisation for the wideband excitation, detection and extended signal and data fusion processing requirement. Figure 10.13 provides a schematic arrangement of a pilot trial system. The various functions are implemented through suggested hardware features: a direct digital synthesis (DDS), to produce the chirp excitation; switching and multiplexing logic to route and synchronise data streams; detection and analogue-to-digital conversion (ADC); with logic control implemented by a programmable gate array (PGA) and overall control and processing using a digital signal processor (DSP).

A multistage processing algorithm defines the key steps from the specification of the excitation signal to the interpretation of the process features, as reviewed above. This involves a set of preset and computed key steps that are ideal for execution using a DSP (Nahvi & Hoyle, 2009b, 2010).

10.6 Demonstration and implementation

Experimental trials described below demonstrate specific key steps of the composite method. For simplicity they exploit convenient physical simulants of industrial materials, pseudo-stationary physical models and computer simulation data.

10.6.1 Basic spectroscopy data extraction

This first demonstration aims to illustrate the basic method described above in Section 10.5.2. This includes excitation, using a wideband chirp signal; extraction of the wideband response function and its direct comparison with the independently measured response of the known material. In essence this focuses upon the basic spectroscopic response rather than a 2D or 3D distribution. This demonstration is also useful to illustrate the principles that would be exploited for the ROI (or pixel/voxel) interpretation processing for material identification in distributions.

The simple experimental process arrangement is shown in both schematic and image forms in Figure 10.14. The excitation port and detection port are, respectively, driven and sampled using a synchronised digital signal synthesiser and digital storage oscilloscope. As summarised in Eqn (10.1), the chirp amplitude was 5 mA, the bandwidth was 500 kHz and the signal (and test) duration was 5 ms. For each value of process conditions a measurement was also carried out using a commercial spectrum analyser, operating by means of a sequence of sinusoidal excitations and taking about 2 min to acquire data for 21 frequency steps (a measurement time ratio of ~24,500).

The material used in the small process vessel shown is the commonly used stimulant for pharmaceutical materials, LGA, as discussed above in Section 10.3.1. Following excitation and data acquisition within the 5 ms test duration, the basic method is deployed using a wavelet set giving the required number of spectral points. Figure 10.15 shows comparative data for the two methods: the 21-point spectra from the spectrum analyser, with the smooth spectra synthesised from several thousand points computed from the single 5 ms wideband response.

This demonstrates the fast identification of the electrical impedance spectroscopic characteristics of the LGA material during crystallisation. As shown, tests were carried out at each of five temperature steps. Results clearly show the expected impedance spectroscopic behaviour that crystallisation increases at lower temperatures, as illustrated from direct tests in Figure 10.5. The demonstration confirms the viability of the basic wideband excitation and wavelet frequency extraction method.

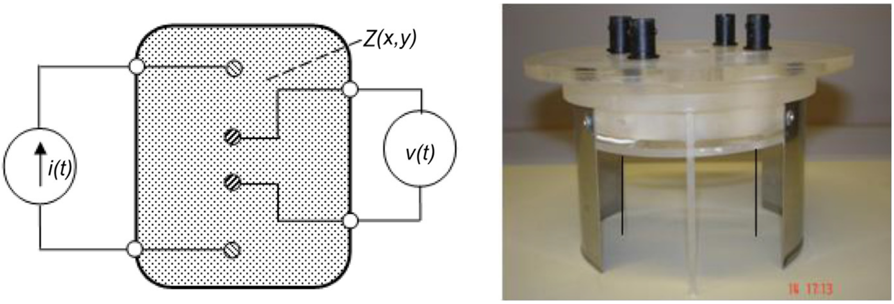

Figure 10.14 Experimental process (left) schematic; (right) physical arrangement – prior to insertion in flask with temperature-controlled water jacket.

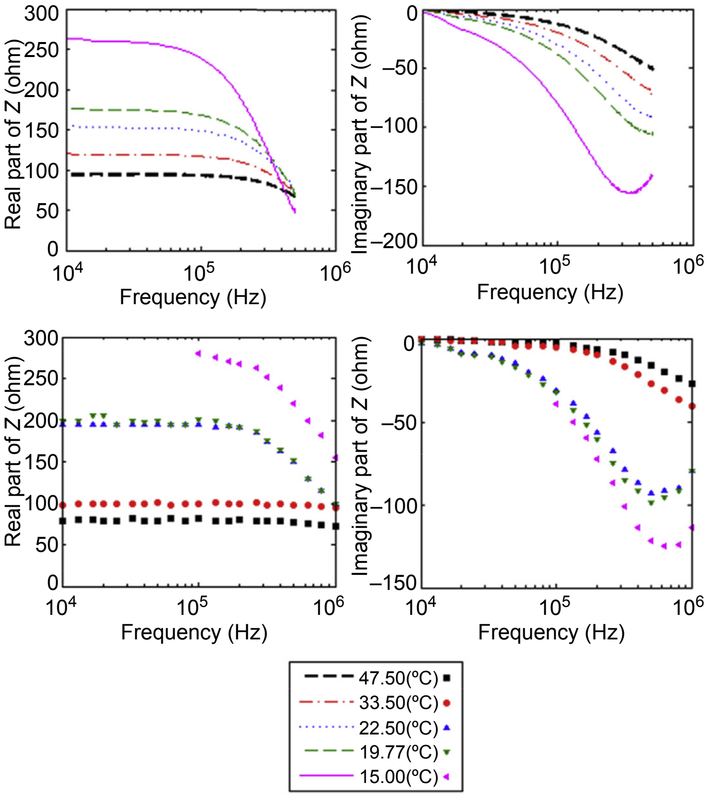

Figure 10.15 Spectroscopy results: (upper) for high-speed method (5 ms data capture); (lower) commercial spectrum analyser (2 min data capture); with temperature key.

10.6.2 Energy frequency tomograph set processing

This next demonstration aims to illustrate multiple wideband process excitation, response detection and the formation of a tomographic projection data set. This can then be used, with an appropriate wavelet set, to deliver the raw data from which to compute the corresponding set of energy frequency tomographs. This demonstrates the second key stage of the method, prior to interpretation.

In these trials time-domain issues were avoided by design, through the use of a simulated process formed of a shallow dish containing a pseudo-stationary conductive gel with two regions with fruit slices, cucumber and banana, and a third region of saline water. This was fitted with a 16-electrode sensor array as illustrated in Figure 10.16. The parallel data collection typical of an industrially scaled system was simulated for this exercise through superposition: by simply repeating the excitation for a sequence of separate measurements. Synchronised excitation and digital data acquisition units were to collect projection data sequentially in time through manual connections.

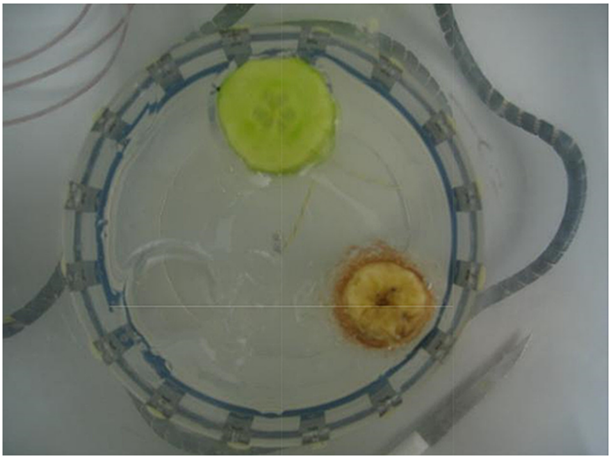

Figure 10.16 Pseudo-stationary 2D physical process simulation with a 16-electrode sensing array.

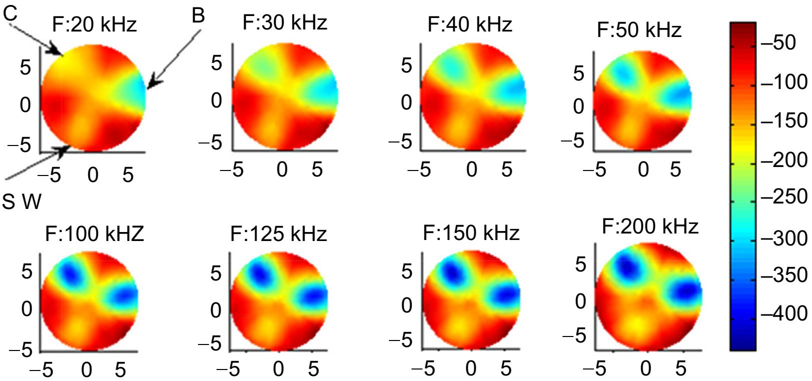

Figure 10.17 Energy frequency tomographs of cucumber (C), banana (B) and saline water (SW) objects in flat spectrum gel; for frequency steps from 20 to 200 kHz.

The data fusion method described in Section 10.5.3 is then deployed to extract a range of energy frequency response data sets, from the single wideband response data set, in the range 20—200 kHz. In this application case expected differences highlighted are at lower frequencies, as illustrated in the results shown in Figure 10.17.

The images show the spectral variations, mainly due to the complex fruit components. The demonstration confirms the viability of the formation of a set of energy frequency tomographs based upon wideband excitation, response detection and wavelet frequency extraction.

10.6.3 Overall processing with interpretation

To demonstrate the overall process from process data to interpretation, a computer-based simulated process distribution was synthesised using a distributed 2D mesh circuit model (Nahvi & Hoyle, 2008). This provides a known and fixed comparative base for evaluation, with definitive electrical impedance values at key ROIs. The simulated process is used in a standard electrical network simulation tool to perform excitation and response acquisition. The resulting data are then processed, as demonstrated in Section 10.6.2, through to the data fusion stage to produce energy frequency tomographs. These may then be explored using the interpretation processes described in Section 10.5.4.

The simulated experimental process conditions are based upon those used in Section 10.6.2 above, here using two ROIs in a background that does not exhibit major spectral variation. Figure 10.18 illustrates a range of eight energy frequency tomographs, firstly, directly from the original simulated model data; and secondly, the corresponding data generated from the method described.

As explored in Section 10.5.4, a range of interpretation variants can be applied. Where distinct regions are likely to be present, a simple image processing operation across the set can easily identify these. This variant is demonstrated here. The identified ROIs are described as R_1 — upper left side; R_2 — upper right side; R_3 — background. In this case, the two ROIs and the background area may then be compared with a selected set of spectral fingerprints to identify three materials using an LUT or an analytic model. As described, the set of tomographs represent the same sampling instant and hence there is no movement of materials across the set. Figure 10.19 illustrates the comparison process in graphical terms.

ROI R_1 is the upper curve with the marked continuous line as the known model from the original simulated data. The corresponding R_1 line reconstructed from the energy frequency tomograph set is seen as a reasonable fit. The constant R_3 model and its reconstructed form are the middle lines. The lower lines are the R_2 data. It is apparent that a spectral fingerprint fitting operation would successfully identify the three candidates.

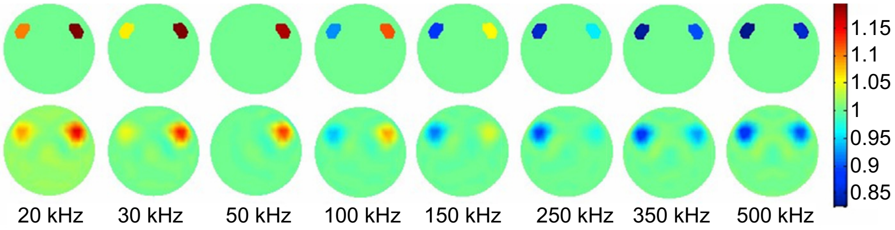

Figure 10.18 Upper row: simulation process distribution with two regions of interest in flat spectrum background; lower row: corresponding energy frequency tomographs; for frequency steps from 20 to 500 kHz.

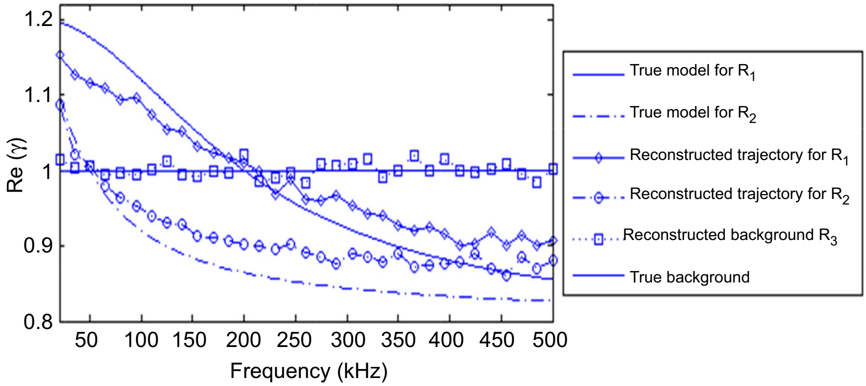

Figure 10.19 Comparison of region of interest R_1, R_2 and R_3 trajectory graphs.

10.6.4 Implementation

The implementation of the spectro-tomography system may be considered in terms of a conventional multichannel IPT instrument: excitation signal generation, response detection, tomographic reconstruction and interpretation to provide the requisite user data. These familiar IPT functional units must include extra functionality — firstly to support the wideband, multidimensional method, and secondly to support its powerful data fusion and interpretation methods. These yield the internal distribution of the process as a time series of tomograph sets from which materials are identified. In simple terms, it aims to deliver a *when* (temporal), *where* (spatial) and *what* (material) view of the process, which can be interpreted in terms of the user requirements for the process (Hoyle, Nahvi, Ye, & Wang, 2012). Some simple implementations have been demonstrated (Oguh, Hall, Bolton, Simmons, & Stitt, 2012).

10.7 Spectro-tomography application review

The paper offers a rationale for the industrial use of multidimensional IPT for multicomponent applications and identifies a number of potential application sectors that could benefit. The spectro-tomography, multidimensional method is described as a primary candidate that offers a solution that can support advanced instrumentation needs in a range of sectors.

This method has been shown via this engineering study to be capable of adding the further major dimension of '*what it is*' to the '*where it is*' information that can be obtained using conventional tomographic instrumentation. The study has also addressed the 'real-time' domain of '*when it is*' information that must also be routinely addressed for industrial applications. For this key aspect it is shown that a system can be designed that is able to capture raw data at a rate to meet this additional need with little overhead.

The paper offers a design approach, illustrated with demonstration results, to realise key aspects of the spectro-tomography method for an implementation that harnesses electrical IPT. The underlying methodology could also be applied to other IPT modes, for example using sound and ultrasound energy. At a generic level the multidimensional approach described provides a new research and development direction for IPT.

References

Hoyle, B. S., Jia, X., Podd, F. J. W., Schlaberg, H. I., Wang, M., West, R. M., et al. (2001). Design and application of a multi-modal process tomography system. *Measurement Science and Technology, 12*(8), 1157–1165.

Hoyle, B. S., McCann, H., & Scott, D. M. (2005). Process tomography. In D. M. Scott, & H. McCann (Eds.), *Process imaging for automatic control* (pp. 85–126). Taylor and Francis.

Hoyle, B. S., Nahvi, M., Ye, J., & Wang, M. (2012). Systems engineering for electrical spectro-tomography. In *6th international symposium on process tomography, Cape Town, South Africa* (pp. 1–10). ISIPT, ISBN 978-0-620-53039-2. OR19.

Industrial Tomography Systems. (2014). *P2+ IPT instrument*. Available from: http://www.itoms.com/products/p2-electrical-resistance-tomography/ Accessed 28.03.14.

Nahvi, M., & Hoyle, B. S. (2007). Process impedance spectroscopy through chirp waveform excitation. In *5th world congress on industrial process tomography, Bergen, Norway* (pp. 630–637).

Nahvi, M., & Hoyle, B. S. (2008). Wideband electrical impedance tomography. *Measurement Science and Technology, 19*, 094011–094020. http://dx.doi.org/10.1088/0957-0233/19/9/094011.

Nahvi, M., & Hoyle, B. S. (2009a). Electrical impedance spectroscopy sensing for industrial processes. *IEEE Sensors Journal, 9*(12), 1808–1816.

Nahvi, M., & Hoyle, B. S. (2009b). Data fusion for electrical spectro-tomography. In *IEEE imaging systems and techniques conference, Shenzen, China* (pp. 229–234).

Nahvi, M., & Hoyle, B. S. (2010). Spectro-tomography interpretation for integrated sensing of process component identification and distribution. *IEEE Sensors 2010 Conference*, Hawaii, US, pp. 1309–1312.

Oguh, U. I., Hall, J. F., Bolton, G. T., Simmons, M. J. H., & Stitt, E. H. (2012). Characterisation of gas/liquid/solid mixing using using tomographic electrical resistance spectroscopy. In *6th international symposium on process tomography, Cape Town, South Africa* (pp. 1–8), ISBN 978-0-620-53039-2. PO21.

Qiu, C., Hoyle, B. S., & Podd, F. J. W. (2007). Engineering and application of a dual-modality process tomography system. *Flow Measurement and Instrumentation, 18*, 247–254.

Ricard, F., Brechtelsbauer, C., Xu, X., & Lawrence, C. (2005). Monitoring of multiphase pharmaceutical processes by electrical resistance tomography. *Chemical Engineering Research and Design, 83*(A7), 794–805.

Wang, M. (2002). Inverse solutions for electrical impedance tomography based on conjugate gradient methods. *Measurement Science and Technology, 13*, 101–117.

Zhao, Y., Wang, M., & Hammond, R. B. (2011). Characterization of crystallisation processes with electrical impedance spectroscopy. *Nuclear Engineering and Design, 241*, 1938–1944.

Tomographic imaging in sensor networks

11

G. Kamath, W.-Z. Song
Georgia State University, Atlanta, GA, USA

11.1 Introduction

Over the past few decades, we have seen a tremendous advancement in industrial tomography in terms of both theory and real-world implementations. Thanks to the advancement in very large-scale integration (VLSI) technology and sensor networks, the two main ingredients for the success of industrial tomography. Current tomographic applications demand real-time and high-resolution imaging, which necessitates a large number of sensory devices to monitor the system. Typically tomography application involves collection of sensor data to a centralized monitoring system that processes the gathered data to invert the required model. Some of the applications, such as seismic tomography, network tomography, and ocean tomography, need a large number of sensors to facilitate high-resolution real-time imaging. However, adding a large number of sensors for data gathering is not compatible with the current centralized set up because wireless bandwidth or data transfer rate does not scale, unlike computing power. With the introduction of large-scale wireless devices, we are approaching the upper limit at a faster rate and collection of raw system data over a network becomes increasingly difficult due to lesser bandwidth as well as node failure, especially the centralized node. Some applications, such as seismic tomography, require high-fidelity sampling from each node, which makes it even more challenging to collect raw, real-time data from a dense sensor network (e.g., hundreds to thousands of nodes). Due to all these restrictions, many of the most threatening active volcanoes worldwide use fewer than 20 nodes (Song et al., 2009), limiting our ability to understand volcano dynamics and physical processes in real time.

In this chapter we introduce you to a new paradigm called large-scale in-network tomographic inversion, which can provide high-resolution tomography images in real time. The core idea of in-network tomography is to solve the system by exploiting the computation power at each sensor node rather than sending all the raw data to a centralized station. This chapter is structured as follows: First, we introduce tomographic imaging using large-scale sensor networks and the need for in-network tomography inversion. We then discuss the sensor network architecture required for distributed tomography imaging. Next we introduce you to some candidate distributed algorithms for in-network tomography imaging. Later, we throw some light on future trends of sensor networks in imaging. We conclude this chapter with some additional sources of information and a few pieces of advice regarding large-scale sensor network deployment and imaging. Throughout this chapter, we use seismic tomography as an

Industrial Tomography. http://dx.doi.org/10.1016/B978-1-78242-118-4.00011-3
Copyright © 2015 Elsevier Ltd. All rights reserved.

example and show how a large-scale sensor network can be used to invert the seismic image and obtain four-dimensional (4D) real-time tomography. So before we begin, let us first understand the basics about seismic tomography in general.

11.2 Seismic tomography

The basic principle behind 3D seismic tomography is to use the arrival time of the elastic waves to derive the internal velocity structure of a volcano. This approach is called travel-time seismic tomography, where the models keep evolving and are continuously refined as more earthquakes get recorded. P-wave (primary wave) and S-wave (secondary wave) are the two major elastic waves used to calculate the tomography. Generally, arrival time of the P-waves is used, as they travel faster than S-waves and reach the receiver first. Figure 11.1 shows a sample P-wave obtained at four different stations. Here we explain the three basic principles involved in travel-time seismic tomography.

1. *Event Location*: Once an earthquake occurs, seismic disturbances are detected by the nodes, which can further estimate the arrival time. Using this estimated arrival time, Geiger (1912) introduced a technique to estimate the earthquake location and origin time. This is a classic and widely used event localization scheme that uses iterative methods and Gauss–Newton optimization to determine the time and location of the event.
2. *Ray Tracing*: This is the technique used to find the ray paths between the seismic source locations and the receiver nodes with minimum travel time, following an event. Once an

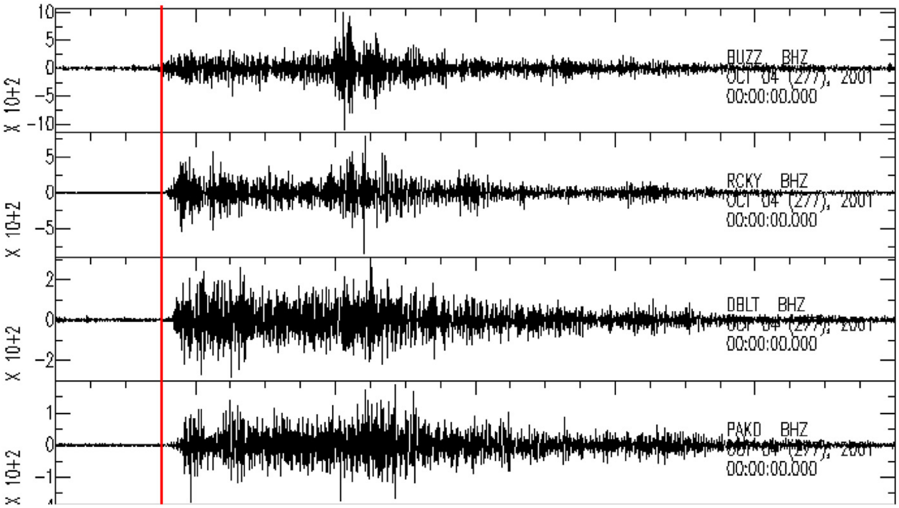

Figure 11.1 Sample of P-wave obtained at four different stations (BUZZ, RCKY, DBLT, and PAKD). X-axis represents the velocity of the wave and the red vertical line represents the first detection of the P-wave at station BUZZ.

earthquake occurs, the seismic rays originating from these events perturb and register the anomalous residuals. Given the source location of the seismic events and current velocity model of the volcano, the ray tracing method finds the ray paths from the event source locations to the nodes, as shown in Figure 11.2(b).

3. *Tomographic Inversion*: The ray paths traced in turn are used to estimate the velocity model of the volcano. Inheriting the concept from medical tomography, the volcano can be partitioned into smaller blocks, as shown in Figure 11.2(c), to form a large, sparse matrix inversion problem. We now show the formulation of travel-time seismic tomography using the perturbation model. Suppose that there are N nodes with J earthquakes and let s^* be the slowness (reciprocal of velocity) model of the volcano with resolution M (blocks). s^* can be assumed to be a reference model, s^0, plus a small perturbation s, that is, $s^* = s^0 + s$.

We can use the event location scheme introduced by Geiger (1912) to calculate the arrival times and estimate event location and origin times. Let $t_i^* = [t_{i1}^*, t_{i2}^*, \ldots, t_{iJ}^*]^T$ be a travel time measurement vector, where t_{ij}^* represents the travel time experienced by node i in the jth event. Based on the ray paths traced in step (2), the travel time of a ray is the sum of the slowness in each block times the length of the ray within that block, that is, $t_{ij}^* = A_i[j, m] \cdot s^*[m]$, where $A_i\,[j, m]$ is the length of the ray from the jth event to node i in the mth block and $s^*[m]$ is the slowness of the mth block. Let $t_i^0 = [t_{i1}^0, t_{i2}^0, \ldots, t_{iJ}^0]^T$ be the unperturbed travel times, where $t_{ij}^0 = A_i[j, m] \cdot s^0[m]$. In the rest of the chapter, we use observed travel time and predicted travel time to indicate the same meanings of t_{ij}^* and t_{ij}^0. In matrix notation we will then have the following equation:

$$A_i s^* - A_i s^0 = A_i s \tag{11.1}$$

where $A_i\,[j, m]$ represents the element at the jth row, mth column of matrix $A_i \in \Re^{J\times M}$. Let $t_i = [t_{i1}, t_{i2}, \ldots, t_{iJ}]^T$ be the travel time residual such that $t_i = t_i^* - t_i^0$ Eqn (11.1) can be rewritten as

$$A_i s = t_i \tag{11.2}$$

We now have a linear relationship between the travel time residual observation t_i and the slowness perturbation s. Since each ray path intersects with the model only at a small number of blocks compared to M, the design matrix A_i is sparse. The seismic tomography inversion problem is to solve the system

$$As = t \tag{11.3}$$

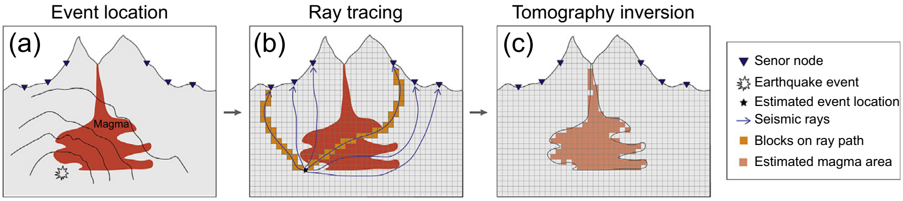

Figure 11.2 Procedures for seismic tomographic inversion.

where $A = [A_1^T, A_2^T, \ldots, A_N^T]^T$ and $t = [t_1^T, t_2^T, \ldots, t_N^T]^T$. This system is usually overdetermined and the inversion aims to fit the least-squares solution s such that

$$s = \arg\min_s \|t - As\|^2 \tag{11.4}$$

Typically the seismic tomography model shown in Eqn (11.4) is also inconsistent and contains measurement noise. Iyer and Hirahara (1993) mention some of the methods to deal with this problem. One common technique is to add some form of regularization to avoid strong, undesired influences of small singular values dominating the solutions. This can be achieved by applying a regularization parameter for determining the least square solution X_{LS}, that is,

$$s = \arg\min_s \|t - As\|^2 + \lambda^2 \|s\|^2 \tag{11.5}$$

where λ is the trade-off parameter that regulates the relative importance we assign to models that predict the data versus models that have a characteristic, a priori variance. In a centralized system, the matrix A and vector t are collected at a single server to solve the tomography imaging problem. However, our goal here is to solve this in a distributed fashion. But before we do that, we will explain the designing of sensor networks suitable for seismic tomography.

11.3 Sensor networks for volcano monitoring

Static tomographic inversion of a 3D structure using the above formulation has been widely studied since late 1970s (Iyer & Dawson, 1993) and are applied to oilfield exploration and volcanoes. Only in recent years have passive seismic data obtained from the few tens of nodes been studied to invert the volcano tomography. These centralized techniques have been implemented and studied for volcanoes such as Mount St. Helens (Lees, 1992) and Mount Rainier (Moran, Lees, & Malone, 1999). One such successful project involving sensor data collection is Optimized Autonomous Space In situ Sensor-web (OASIS) (Song et al., 2009). OASIS is a real-world deployment of a prototype system that provides scientists and decision makers a tool comprising smart ground sensors integrated with smart space-borne remote sensing assets to enable prompt assessments of evolving geophysical events in a volcanic environment.

Deploying a sensor station in an active volcanic environment proves to be very challenging for the sensor network and geophysics community. Figure 11.3 shows the aerial deployment of sensor station on Mount St. Helens and the top view of sensor network topology. The crater, which is a 3D environment, has a very rugged terrain. This area has diverse seismic and geophysical signals from rock avalanches, landslides, earthquake, and gas/steam emission. Occasional eruptions, as well as heavy rain and snowy and windy conditions, pose significant challenges and even sometimes destroy the stations. To overcome these challenges and meet some standard

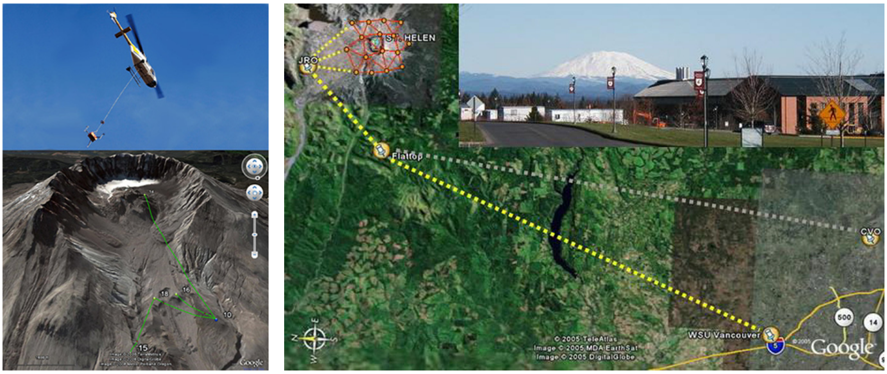
ST. HELEN
JRO
Flattop
CVO
WSU Vancouver
© 2005 TeleAtlas
Image © 2005 MDA EarthSat
Image © 2005 DigitalGlobe
Google
15
16
18
10

Figure 11.3 The aerial deployment of a sensor network in Mount St. Helens.

requirements, one should be cautious while designing system architecture, hardware, and network software, such as robust communication stacks and smart sensing algorithms.

The OASIS project mainly focused on collection of high-fidelity data using up to 20 seismic sensors in a limited-bandwidth environment. Keeping this goal in mind, a tree-based data aggregation scheme was developed to collect the data from a station deployed in a volcano to a centralized server at the base station, as shown in Figure 11.4. Although the purpose of this project was not related to tomographic imaging, it has provided us with immense knowledge about real-world systems along with technical challenges. After this project we realized that, with data collected from fewer nodes, the resolution of tomographic inversion we could achieve was typically in the tens of kilometers. Obtaining higher-resolution images from the existing sensors became difficult, as they were fewer in number and could not cover the entire region of interest.

From this real-world experience we learned that to achieve higher resolution one option was to scale the existing system by adding a greater number of nodes in strategic points. Although this seems to be a logical solution, scaling these centralized systems becomes a very tedious task and is sometimes impossible due to the sheer data load. These centralized schemes involve multiple active-source recordings spanning data over multiple years (Lees, 2007). These voluminous data accumulated over years cause bottlenecks in communication over the wireless network and also introduce huge delays due to processing time. Now, to achieve effective disaster warnings and timely

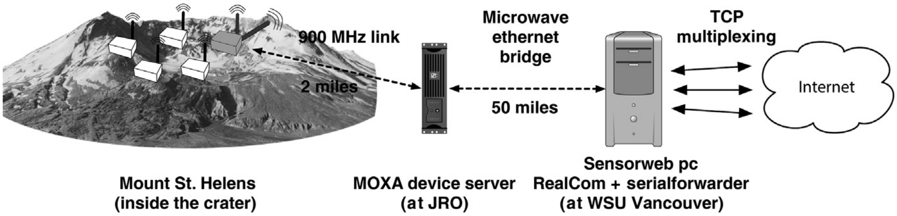
900 MHz link
2 miles
Microwave ethernet bridge
50 miles
TCP multiplexing
Internet
Mount St. Helens (inside the crater)
MOXA device server (at JRO)
Sensorweb pc RealCom + serialforwarder (at WSU Vancouver)

Figure 11.4 Data aggregation scheme used in the OASIS project.

response, new schemes and methodologies had to be developed in order to solve the real-time volcano imaging problem. This provided the motivation for researchers to develop new distributed algorithms, which we will now discuss at length in the next section.

11.4 In-network tomographic imaging

From the previous section we learned that with current centralized volcano monitoring systems it is almost impossible for us to get a real-time image of seismic tomography. In this section we will introduce you to a new approach of distributed tomographic imaging, which will enable us to obtain real-time images while performing in-network computing. This section is divided into three subsections. First we discuss some network architecture suitable for carrying out in-network computing and later we explain some of its practical restrictions in terms of computation and communication imposed by this system, especially in a harsh environment. Next, we discuss some candidate distributed algorithms. Lastly, we talk about the evaluation and testing environment for the distributed algorithms.

11.4.1 Network architecture and challenges

OASIS and several other projects gave us insight into the factors that cause limitations and bottlenecks for obtaining real-time imaging in volcanoes. We also understood that with the information obtained from a limited number of stations, it was not possible to obtain a high-resolution image, and we also learned that typical tree-based data aggregation architecture would fail miserably with increase in the nodes. For this reason, there was a need for an increase in the number of stations to monitor the seismic signals and also an efficient network topology that could scale accordingly. One available solution for efficient scalable network topology is a wireless mesh network (WMN). Here stations are organized in a mesh topology, which can provide robust and scalable solutions and also has the potential to deliver relatively high-bandwidth connectivity to a local area. The core idea involves a network of wireless stations relaying each other's packet in a multi-hop fashion. Apart from the multi-hop requirement, there is no other restriction on the design of the WMN, which makes it considerably flexible and versatile. Routing the information places a very key role in distributed networks and advancement in WMN has resulted in several competing schemes for routing packets across the mesh networks. Some of these include Ad hoc On-demand Distance Vector (AODV), Better Approach To Mobile Ad hoc Networking (B.ATM.A.N.), and Optimized Link State Routing Protocol (OSLR). All the above-mentioned features of the WMN match the requirement in terms of network topology for seismic tomography. Figure 11.5 shows the illustration of the deployment of the WMN on Latacunga, an active volcano in Ecuador, for distributed imaging.

Although the WMN seems to be a viable solution for real-time tomography inversion, there are few major technical challenges for its realization in harsh environments such as volcanoes. Below we mention a few important constraints.

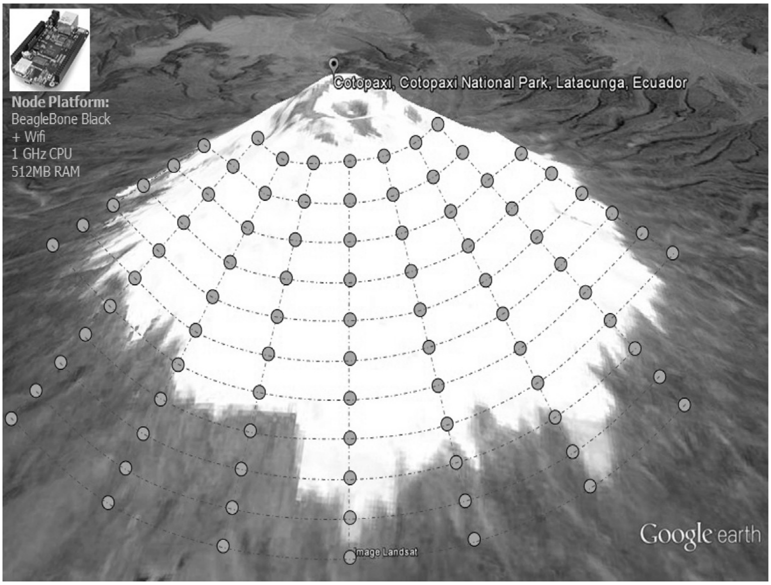

Figure 11.5 Illustration of the distributed imaging using WMN on an active volcano.

1. *Resource constraints*: The design and implementation of large-scale WMN are constrained by four types of resources: (1) energy, (2) network bandwidth, (3) processing, and (4) memory. Sensor nodes, typically small in size, deployed in remote environments, do not have access to direct power supplies. The seismic station deployed in Mount St. Helens was powered by huge batteries, which lasted for a few months (Song et al., 2009). Renewable sources like solar could be used to extend the battery life; however, sunlight in volcanic regions is mostly blocked by thick ash clouds or vegetation. Secondly, with no dedicated base station, the mesh network must rely on low-power, low-bandwidth wireless antennas. Designing and implementing these antennas must also take care of topology features such as vegetation and surrounding temperature. With the advancements in embedded systems technology, the processing power and inbuilt memory of small sensors have increased drastically. However, the processing power and increased memory could still be a bottleneck for seismic tomography inversion and has to be addressed carefully while designing the algorithms.
2. *Environmental constraints*: Harsh environments such as volcanic and tectonic regions pose a great threat for deployment, maintenance, and also the lifetime of the sensor nodes. Also, the thick vegetation and extreme temperature hinder the wireless signals. The simulation test bed must keep this in mind for effective designing of the system. The deployment of these large-scale sensor nodes on this uneven, harsh environment must be done with extreme care. Since the crater region might be inaccessible due to volcanic activity, deployment must be done in the region that is relatively safe in a geoseismic sense.

Considering these constraints and a few others, scientists from geophysics and engineering came up with a few design goals that are important for the success of distributed imaging. Some of those design goals are:

1. *Low-power and low-cost sensors*: As mentioned earlier, power is a vital constraint for this type of system, and the sensors chosen must consume very low power. Careful design of

the system is very necessary to remove some of the unnecessary sensors or reduce its power consumption by tweaking its duty cycle, etc. Cost also plays a crucial role when it comes to large-scale deployment. Selecting the sensors and other hardware and software in designing each station must be cost-effective.

2. *Scalable architecture*: The system must be designed in such a way that it could scale easily, that is, adding or removing any number of nodes must not drastically affect the performance of the system. The distributed algorithm must be robust in terms of number of nodes available.
3. *Minimal communication cost*: Solving tomography with no communication is a very ideal solution; however, this might be hard or nearly impossible due to high complexity in the algorithms involved. So the algorithms that are designed must involve limited communication and also reduced packet size.
4. *Fault tolerant*: Even with robust design, extreme conditions may cause a few nodes to fail. The distributed algorithms designed must handle this and prevent the final result from being affected.

These are several important design goals that have to be considered during the development and deployment. For further information, refer to Song et al. (2009) to gain more insight on real-world challenges faced during the OASIS project.

11.4.2 Distributed tomography algorithms

After considering the suitable architecture for distributed imaging along with the constraints and design goals, we now discuss a few candidate distributed algorithms suitable for solving distributed tomography over these architectures. But before we explain, we would like to describe the model we used and some basic assumptions we made. Consider a mesh network with N nodes $v_1,\ldots,v_N$, which are connected with wireless media. Let us assume that not every pair of nodes can talk to each other directly, but can reach others through multi-hop message relays. Without loss of generality, we assume that the diameter of the network is $\log N$ (i.e., any message can be sent from one node to another through at most log N hops). Also, let us assume that each link in the network between neighboring nodes has a unit bandwidth and each node only has one radio. In the least square problem (see eqn (11.4) formulation of the whole equation is solved in a centralized server, which contains all the required information. However, in a mesh network, there are no centralized coordinators knowing all A and t and each node v_u only knows part of the rows, while the network nodes together can compute s such that

$$s = \arg\min_{s} \|t - As\|^2$$

We now explain some of the candidate algorithms that do not require complete A and t at a centralized location. We start explaining some of the basic centralized algorithms that lay the foundation for other candidate distributed algorithms.

The first instances of iterative methods for solving linear systems involve the four well-known main stationary iterative methods: Jacobi method, Gauss–Seidel method, successive over-relaxation method (SOR), and symmetric SOR method (Hageman & Young, 1981). To parallelize the stationary iterative methods, space decomposition methods are employed to partition matrix A into blocks (block Jacobi or block SOR) as well as the original problem into smaller local problems (Frommer & Renaut, 1999). Renaut (1998) also proposed a parallel multi-splitting solution of the least-squares problem where the solutions to the local problems are recombined using weighting matrices.

Kaczmarz's row projection method (KACZ) (Kaczmarz, 1937), also known as Algebraic Reconstruction Technique (ART), was one of the first iterative methods used for large nonsymmetrical systems. Its main advantages are robustness and cyclic convergence on inconsistent systems. The block parallel versions of ART have been studied and the comparison of various methods based on their performance on graphics processing units is discussed in Elble, Sahinidis, and Vouzis (2010). Among them, Cimmino's method (Cimmino, 1938) was the first one to introduce a parallel version of ART that guaranteed convergence even in case of inconsistent- system. However, this method is slow and requires several iterations to reduce the residual error. To overcome the drawback of Cimmino's method, the component-averaging (CAV) technique was introduced by Censor, Gordon, and Gordon (2001a). CAV retains the properties of Cimmino's method in the sense that it converges in the inconsistent case. Furthermore, CAV exhibits significantly faster convergence for a large sparse system in practice. A Block-Iterative Component Average (BI-CAV) suitable for parallel architecture was introduced by Censor, Gordon, and Gordon (2001b). This algorithm is mainly suitable for parallel architectures. Further advancement in increasing the rate of convergence was achieved by the Component Average Row Projection (CARP) method introduced by Gordon and Gordon (2005). From all the above methods, CARP is more generalized and places no restriction on the system matrix or the selection of blocks. CARP does not require any preprocessing or preordering of the matrix and provides a very robust method, unlike any other block parallel algorithm, for solving large sparse linear systems. In CARP, a finite number of KACZ methods is applied in each block and the resulting point in each block is averaged to get the next iteration. It is also proved to converge for large-scale systems.

To obtain high-resolution images in seismic tomography a multiresolution evolving scheme is often used, where initially a coarse resolution model is calculated, which is then used as an initial reference for higher resolution. Solving coarser resolution is computationally less intensive and the final model obtained from this, when used to calculate higher resolution, could potentially accelerate the convergence speed. A vertical split-based multi-resolution scheme is shown in Figure 11.6.

Borrowing the above ideas, currently we have been able to develop two new algorithms to deal with seismic tomography in a distributed manner. The first algorithm, called Distributed Multiresolution Evolving Tomography (DMET) (Shi et al., 2013), falls under the category of vertical splitting, similar to multisplitting. The second algorithm, called Component-Averaged DMET (CA-DMET) (Kamath, Shi, & Song, 2013), falls under the category of horizontal splitting, similar to that of CARP. These two algorithms have been tested both in simulators and on real test beds. Below we explain these two algorithms briefly.

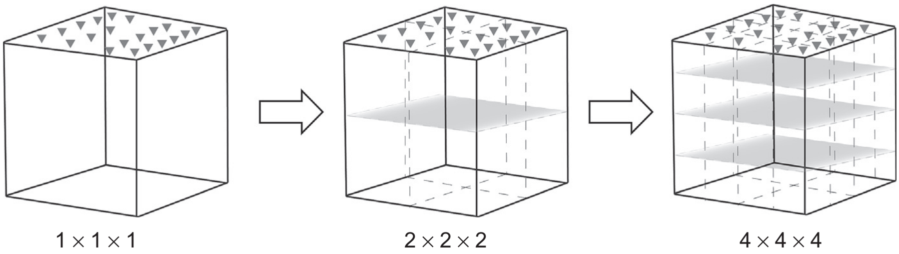

Figure 11.6 Multiresolution evolving schemes.

11.4.2.1 Distributed multiresolution evolving tomography

The core idea behind DMET is to split the least-square problem shown in Eqn (11.4) into vertical partitions aligned with the geometry of the volcano, as shown in Figure 11.6. Later some nodes in these partitions are chosen as a landlord who gathers the local information from other nodes in the partition to compute a part of tomography. The computation on each landlord is entirely local and the communication cost is bounded. Once the partial solution is obtained, it is then combined with other local solutions to obtain the entire slowness model. This algorithm follows the multiresolution scheme to obtain high-resolution images starting from coarse resolution and is also distributed in nature; thus it is called the DMET algorithm. Figure 11.7 illustrates the vertical partition of tomography, showing the landlords on the left and also the corresponding vertical partition of Eqn (11.4) on the right. For further details refer to Shi et al. (2013).

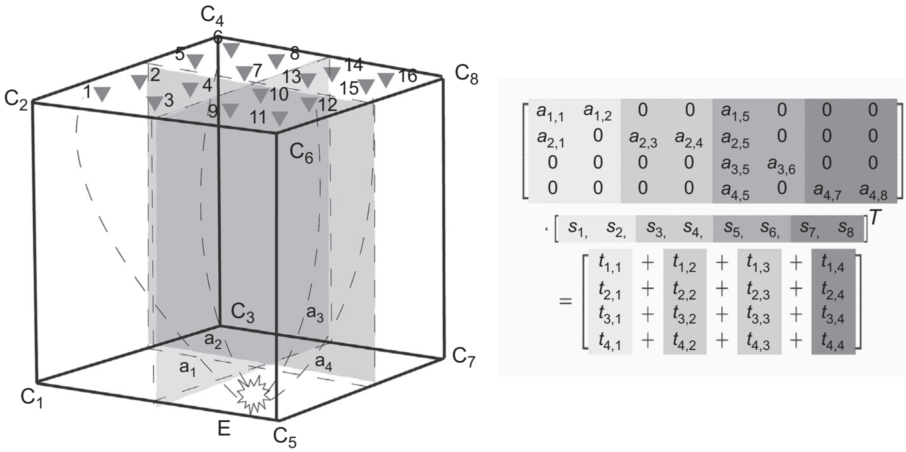

$$\begin{bmatrix} a_{1,1} & a_{1,2} & 0 & 0 & a_{1,5} & 0 & 0 & 0 \\ a_{2,1} & 0 & a_{2,3} & a_{2,4} & a_{2,5} & 0 & 0 & 0 \\ 0 & 0 & 0 & 0 & a_{3,5} & a_{3,6} & 0 & 0 \\ 0 & 0 & 0 & 0 & a_{4,5} & 0 & a_{4,7} & a_{4,8} \end{bmatrix} \cdot \begin{bmatrix} s_1, & s_2, & s_3, & s_4, & s_5, & s_6, & s_7, & s_8 \end{bmatrix}^T = \begin{bmatrix} t_{1,1} & + & t_{1,2} & + & t_{1,3} & + & t_{1,4} \\ t_{2,1} & + & t_{2,2} & + & t_{2,3} & + & t_{2,4} \\ t_{3,1} & + & t_{3,2} & + & t_{3,3} & + & t_{3,4} \\ t_{4,1} & + & t_{4,2} & + & t_{4,3} & + & t_{4,4} \end{bmatrix}$$

Figure 11.7 (left) Vertical partition of tomography geometry with landlords; (right) corresponding vertical partition of system of linear equations.

11.4.2.2 Component-average distributed multiresolution evolving tomography

Vertical partitioning in DMET using geometrical features of the volcano involved some heuristics while splitting the ray paths between the source and the receiver. This heuristic approach, although it could work with no information exchange, introduced unwanted errors that could not be removed during computation. This caused a decrease in image quality, and to overcome this we resorted to row splitting or row action methods. Row action methods like CAV and CARP are the most commonly used algorithms for parallel architecture to solve large-scale linear equations. In CA-DMET, the tomography least-squares equation is split row-wise, essentially using all the information obtained at a single node without any heuristic splitting of travel times. This algorithm also contains landlords; however, information in these landlords differs from those of DMET as we are performing row partitioning. Few iterations of stable KACZ for inconsistent systems are run on each landlord and the intermediate results are later combined with others using a technique called component average (Gordon & Gordon, 2005). The information exchanged at each iteration is less compared to what is required to transfer the raw data, and for this reason we use a tree-based aggregation scheme similar to the one used in the OASIS project. Figure 11.8 illustrates the basic communication pattern of CA-DMET. This algorithm also takes care of multiresolution and dynamic evolving schemes like DMET and uses a CAV scheme to combine the result; hence we call it CA-DMET. For further details refer to Kamath et al. (2013).

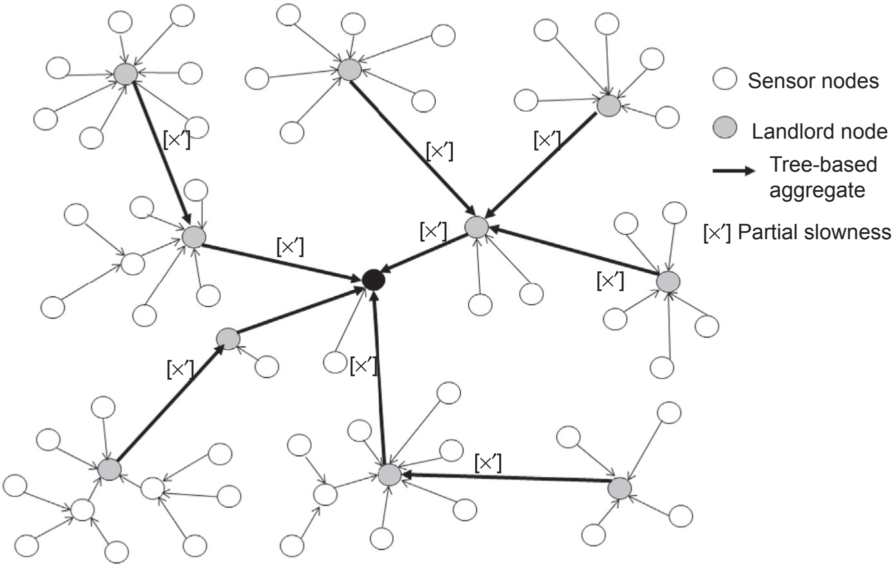

Figure 11.8 Network topology for CA-DMET.

11.4.3 Evaluation environment

The design and testing environment for developing these candidate algorithms has to be done with extreme care. Here, we offer some advice regarding this topic.

1. *Testing environment*: As we know, deployment and maintenance could be extremely hard, so a proper protocol must be developed before the actual deployment. To deal with this, an efficient testing environment could be set up that takes into account the possible real-world conditions and tests rigorously in this environment. The test bed should not be limited just to software simulation of the sensor nodes and algorithms but also should include the physical devices that will be used in actual deployment. The software simulation platform must be built in such a way that it can closely interact with the hardware and can also read, write, and monitor the behavior of each node. One such simulator platform for a WMN that we could use is CORE, which stands for Common Open Research Emulator. This is an open-source tool box developed by Naval Research Laboratories and provides lots of necessary environment to emulate distributed sensor networks. The advantage of emulating in CORE is that the code developed over this platform can be transplanted to a Linux-based device virtually without any modification. The emulation tool allocates a Linux virtual machine for each node and with Linux-powered computational units such as Android, Raspberry Pi, and Beaglebone we can directly run these codes with a very minor modification.
2. *Algorithm design*: The principle behind seismic tomography is adapted from the medical imaging domain, where the travel times of the elastic waves are used to probe the internal structure of the media. Lots of distributed and parallel methods have already been developed for medical imaging. However, there is significant difference between these two methodologies, mainly pertaining to size of the structure and event generation scheme. The relationship between the travel time and the velocity model is nonlinear and the ray path of the acoustic wave traveling in a volcano may be highly curved, mainly due to the sheer size and complexity of the volcano structure. Typically the ray source in volcano tomography is an earthquake event where the distribution of the ray path is highly nonuniform, unlike the uniform short-distance rays generated in medical imaging. These differences indicate that special care must be taken when techniques borrowed from the medical field are applied to seismic data.

11.5 In-network tomography imaging applications

Here we briefly explain the applications of distributed imaging using large-scale sensor networks. Tomography imaging has been widely used in various domains such as medical imaging, geoscience, and the oil industry. The methodology and goal in each domain might be slightly different; however, the principle behind them is essentially similar. The research in this area could benefit many communities such as oil/natural gas exploration, seismic monitoring, and also perhaps humanities.

11.5.1 Whole-earth tomography

Seismologist use tomography to infer geologic structure, such as subduction of tectonic plates into warmer mantle, etc. Whole-earth tomography is used to study the inner dynamics of earth from the lithosphere down to the core. The relationship between the lithosphere and the upper mantle is something that is not completely understood, and this technique hopes to solve some of these problems. However, to get a better understanding of the earth's deep structure, many sensors have to be installed on the surface. These are essential to obtain higher-resolution data and also data with less noise. Distributed seismic algorithms and large-scale sensor network deployment will play a vital role in development of whole-earth tomography methods.

With higher-resolution images of the earth's crust we hope to answer many questions, such as:

1. How is evolution of the continents linked to processes in the upper mantle?
2. What is the level of heterogeneity in the mid-mantle?
3. What is the relationship between the magma formation at certain areas and lower earth crust in that region?

11.5.2 Exploration geophysics

Exploration geophysics is an applied branch of geophysics that uses surface methods to determine the physical properties of earth, as well as a few anomalies in these properties, in order to detect or infer the presence of ore minerals, hydrocarbons, geothermal reservoirs, groundwater, etc. The most advanced in terms of technology and economic impact is oil and gas exploration, which uses sophisticated sensors and invests large amounts of resources for developing new technology for efficient drilling and other processes. Although the oil exploration technique in oceans and on land has matured, a centralized technique is still used to gather and process the information. Usually large companies like Shell, BP, and Chevron have their ships or vibrator trucks deployed in exploration fields such as the Pacific Ocean or sub-Saharan desert. Once these ships or trucks collect the information, they relay the massive amount of raw data gathered back to a data center located in, for example, Houston for processing and analysis. The cost of data transfer is huge and requires that a substantial amount of time be spent making the decision regarding exploration. With the introduction of distributed tomography inversion, we can imagine a few small boats or vibrator trucks collecting raw data that then work cooperatively to process this information to obtain seismic images in real time, helping make the decision-making process faster and more cost efficient. This process has its own drawbacks and challenges; however, it could certainly be used for preprocessing and preliminary exploration.

11.5.3 Mars exploration

The National Aeronautics and Space Administration (NASA), in collaboration with other space agencies, is deeply interested in the possibility of human settlement in outer space, and currently the only viable choice in the near future would be our neighboring planet Mars. While NASA has already deployed a few rovers to assess the Martian terrain and perform some exploration and experimentation, a few scientists believe that an understanding of Mars' interior will throw some light on its geographic dynamics. This could help scientists determine if this planet is active in terms of seismic activity and other inner fluid currents. Volcanoes and earthquakes, though they may seem harmful now to Earth's surface, were a boon in the past for creating the Earth that we see today, with immense resources and diverse species. Now if such activity is detected within the core of Mars, it could potentially lead to creation of an environment similar to Earth and possibly be another home for humans to settle in the future.

11.6 Future trends in in-network tomography imaging

In this section we present newly emerging trends in large-scale sensor networks to tackle some real-world challenges. With the recent advancement in VLSI technology, the size of embedded devices is growing smaller, accompanied by increases in efficiency of energy management. These systems are as small as a credit card and have the functionality of normal computers. Some systems, such as Raspberry Pi and Beaglebone, can be plugged into a TV with a keyboard and mouse and can run tasks like spreadsheets, word processing, and games (Development Board Blog, 2013). These low-power devices, which have great computing capabilities, can be essentially connected as a mesh network to form a large-scale sensor network. The future lies in in-network and distributed computing rather than centralized computing. The sensor of the future will take part in processing the data using the computational resources rather than just sending out raw information to the base station. We will see more and more distributed algorithms to perform various tasks in a more efficient and real-time manner. Most of these small embedded devices support open-source platforms like Linux, allowing people to build, modify, and port various protocols and architecture onto them. This is another reason for rapid success and widespread use in diverse domains such as seismic tomography and development.

In the future we will see more and more of these cheap devices acting as computational units connected to some external sensors to gather data. These gathered data will be either preprocessed or used completely rather than just being sent to centralized servers for calculations. In the seismic community we are already seeing this trend of using smaller and cheaper devices on a large scale for data gathering, for example, the Community Seismic Network (CSN) (About CSN, 2013) developed by Caltech. The goal of this project was to collect high-resolution ground motion intensity data before, during, and after the earthquake, using inexpensive accelerometers. By introducing cheap portable seismic sensors that could connect to any computer, a large-scale network could be set up by distributing this device for free to volunteers. With this network, researchers are able to obtain acceleration of the ground from three axes at the rate of 50 times per second, totaling about 4 MB/h. A thousand such sensors could collect up to 100 GB of data per day and relay the data to the cloud to analyze an earthquake event, identify the epicenter, etc. in real time.

The CSN project is currently deployed in the Pasadena region of southern California, where volunteers from churches, hospitals, schools, offices, and homes are encouraged to participate. This project also assumes that there is no limitation on power and bandwidth for data transfer, which is typically not true in remote regions of Ecuador or on Mount St. Helens. As mentioned before, with these resource constraints, obtaining high-resolution data for real-time processing using a centralized technique will be a challenge, and the future lies in the distributed architecture.

11.7 Other sources and advice

Deployment and maintenance of sensor nodes, especially in harsh terrain such as a volcano, is not “a walk in the park.” Requirements in such operating conditions are stringent enough to make it impossible to even consider wired sensors, leaving us no choice but to consider wireless networks. These extreme conditions can cause changes in the features and operation of the wireless devices. In this section we provide other valuable sources of information, spanning from geophysics societies to computational mathematics to distributed computing, addressing some cautions and other general guidelines that need to be followed to tackle this challenging problem.

As mentioned earlier, CSN (About CSN, 2013) is one such project which uses large-scale sensors for real-time disaster management. In the long term they also plan to develop this system to construct 3D tomographic models in the region where sensors are deployed. The OASIS project from Sensor-web Research Laboratory (Sensorweb OASIS, 2009) also provides an overview regarding the system design, field deployment, and management tools that can be used to develop network architecture for large-scale sensor networks in harsh terrains. Another community that focuses on obtaining large sets of seismic data for analysis and research is Incorporated Research Intuitions for Seismology (IRIS, 2013). This is a consortium of over 100 US universities dedicated to development of science by facilitating the data acquisition, management, and distribution of seismological data. Through this organization many research communities can obtain software and data and also contribute to the development of geophysical society and also to all of humanity. Earthscope (Earthscope Resources, 2013) is another such organization dedicated to the study of the earth in a creative way, which can provide insights into the past, present, and future of the planet we live on. The Society of Exploration Geophysicists (SEG) (SEG Resources, 2013) and United States Geological Survey (USGS) (About USGS, 2013) are some of the other important organizations that not only focus on seismology but also cover a broader area such as climate, mineral resources, energy, and protecting the earth’s ecosystem.

Lastly, having mentioned distributed computing over seismic sensor nodes, not much research is taking place regarding developing stable algorithms for distributed computation. Even today sensors are mainly used as data collection or aggregation instruments and the true potential of these powerful nodes is not being used to its full extent. Modifying existing centralized algorithms to work in distributed settings is hard and sometimes not feasible. For developing truly distributed algorithms, collaboration with different communities such as mathematics, physics, and computer science is very essential.

References

About CSN. (2013). http://csn.caltech.edu/about/.

About USGS. (2013). http://www.usgs.gov/aboutusgs/.

Censor, Y., Gordon, D., & Gordon, R. (2001a). Component averaging: an efficient iterative parallel algorithm for large and sparse unstructured problems. *Parallel Computing, 27*(6), 777−808. http://dx.doi.org/10.1016/S0167-8191(00)00100-9.

Censor, Y., Gordon, D., & Gordon, R. (2001b). BICAV: a block-iterative parallel algorithm for sparse systems with pixel-related weighting. *IEEE Transaction on Medical Imaging, 20*(10), 1050−1060. http://dx.doi.org/10.1109/42.959302.

Cimmino, G. (1938). Calcolo approssimato per le soluzioni dei sistemi di equazioni lineari. *La Ricerca Scientifica, 16*(9), 326−333.

Development Board Blog. (2013). http://developmentboards.blogspot.com/2013/04/raspberry-pi-vs-arduino-vs-beagleboard.html.

Elble, J. M., Sahinidis, N. V., & Vouzis, P. (2010). GPU computing with Kaczmarz's and other iterative algorithms for linear systems. *Parallel Computing, 36*, 215−231. http://dx.doi.org/10.1016/j.parco.2009.12.003.

Earthscope Resources. (2013). http://www.earthscope.org/resources.

Frommer, A., & Renaut, R. A. (1999). A unified approach to parallel space decomposition methods. *Journal of Computational and Applied Mathematics, 110*(1), 205−223. http://dx.doi.org/10.1016/S0377-0427(99)00235-6.

Geiger, L. (1912). Probability method for the determination of earthquake epicenters from the arrival time only. *Bulletin of St. Louis University, 8*, 60−71.

Gordon, D., & Gordon, R. (2005). Component-averaged row projections: a robust, block-parallel scheme for sparse linear systems. *SIAM Journal on Scientific Computing, 27*, 1092−1117. http://dx.doi.org/10.1016/j.parco.2010.05.004.

Hageman, L. A., & Young, D. M. (1981). *Applied iterative methods. Computer science and applied mathematics*. Academic Press.

IRIS. (2013). http://www.iris.edu/hq/programs/education_and_outreach.

Iyer, H. M., & Dawson, P. B. (1993). *Imaging volcanoes using teleseismic tomography*. Chapman and Hall.

Iyer, H. M., & Hirahara, K. (Eds.). (1993). *Seismic tomography: Theory and practice*. Springer.

Kaczmarz, S. (1937). Angenaherte Auflosung von Systemen linearer Gleichungen. *Bulletin International de l'Académie Polonaise des Sciences et des Lettres, 35*, 355−357.

Kamath, G., Shi, L., & Song, W. Z. (2013). Component-average based distributed seismic tomography in sensor networks. In *9th IEEE international conference on distributed computing in sensor systems (IEEE DCOSS)*. http://dx.doi.org/10.1109/DCOSS.2013.17.

Lees, J. M. (1992). The magma system of Mount St. Helens: non-linear high-resolution P-wave tomography. *Journal of Volcanology and Geothermal Research, 53*, 103−116. http://dx.doi.org/10.1016/0377-0273(92)90077-Q.

Lees, J. M. (2007). Seismic tomography of magmatic systems. *Journal of Volcanology and Geothermal Research, 167*(1−4), 37−56.

Moran, S. C., Lees, J. M., & Malone, S. D. (1999). P wave crustal velocity structure in the greater Mount Rainier area from local earthquake tomography. *Journal of Geophysical Research, 104*(B5), 10775−10786. http://dx.doi.org/10.1029/1999JB900036.

Renaut, R. A. (1998). A parallel multisplitting solution of the least squares problem. *Numerical Linear Algebra with Applications, 5*(1), 11−31. http://dx.doi.org/10.1002/(SICI)1099-1506(199801/02)5:1<11::AID-NLA123>3.0.CO;2-F.

SEG Resources. (2013). http://www.seg.org/resources/overview.

Sensorweb OASIS. (2009). http://sensorweb.cs.gsu.edu/?q=Oasis.

Shi, L., Song, W. Z., Xu, M., Xiao, Q., Lees, J. M., & Xing, G. (2013). Imaging volcano seismic tomography in sensor networks. In *10th annual IEEE communications society conference on sensor and ad hoc communications and networks (IEEE SECON)*.

Song, W.-Z., Huang, R., Xu, M., Ma, A., Shirazi, B., & Lahusen, R. (2009). Air-dropped sensor network for realtime high-fidelity volcano monitoring. In *The 7th annual international conference on mobile systems, applications and services (MobiSys)*. http://dx.doi.org/10.1145/1555816.1555847.

This page intentionally left blank

Part Two

Tomographic image reconstruction

This page intentionally left blank

Mathematical concepts for image reconstruction in tomography

12

S. Kim[1], A.K. Khambampati[2]
[1]School of Energy Systems Engineering, Chung-Ang University, Seoul, South Korea;
[2]Institute for Nuclear Science and Technology, Jeju National University, Jeju, South Korea

12.1 Introduction

Tomography intends to image the cross-section of an object without altering it. From the image, we want to know the internal configuration of the substances comprising the object. For this purpose, we have to use "something" that should infiltrate into the object, interact with internal substances, and escape from the object without altering the object significantly. Based on the change of "something" due to the interaction, the internal configuration is imaged. Of course, the change should be measurable.

Any particles or waves could be used for tomography if they do not alter the object significantly while passing within and interacting with the object. Tiny elementary particles such as neutrons, protons, and electrons could be considered as particles for tomography. Among these, charged particles are less attractive unless the object is very small because their range, or average penetration depth, is very short. Neutrons are electrically neutral and highly penetrative; however, their generation, treatment, and measurement are, in general, less practical. Photons are commonly used for tomography; their stream is an electromagnetic wave, which is a self-propagating transverse oscillating wave of electric and magnetic fields. Electromagnetic wave or a stream of photons is characterized according to its frequency or wavelength as shown in Figure 12.1. As its wavelength is shorter, or its frequency is larger, it becomes more energetic and penetrative. In other words, it resembles a solid particle more and its path becomes straighter. However, as its wavelength is longer, or its frequency is smaller, it resembles a wave more and behaves totally different from the high-frequency electromagnetic waves. Other types of waves for tomography are pressure or sound. For tomography, an electric (or magnetic) field can be directly applied to the object to be imaged. Electric signals are imposed on the object and the induced electric signals, which are dependent on internal distribution of the electrical properties, are measured.

The pattern of interaction between penetrating waves and the object can be classified into three groups. When the penetrating wave is strongly penetrative and behaves like a stream of particles, it can be assumed that the wave brings the information on the substances along a straight path connecting the source and the detector. However, if an electric (or magnetic) field is used for tomography, any part of the object can affect the field, namely, the entire domain of the object is the path. When the penetrating

Industrial Tomography. http://dx.doi.org/10.1016/B978-1-78242-118-4.00012-5
Copyright © 2015 Elsevier Ltd. All rights reserved.

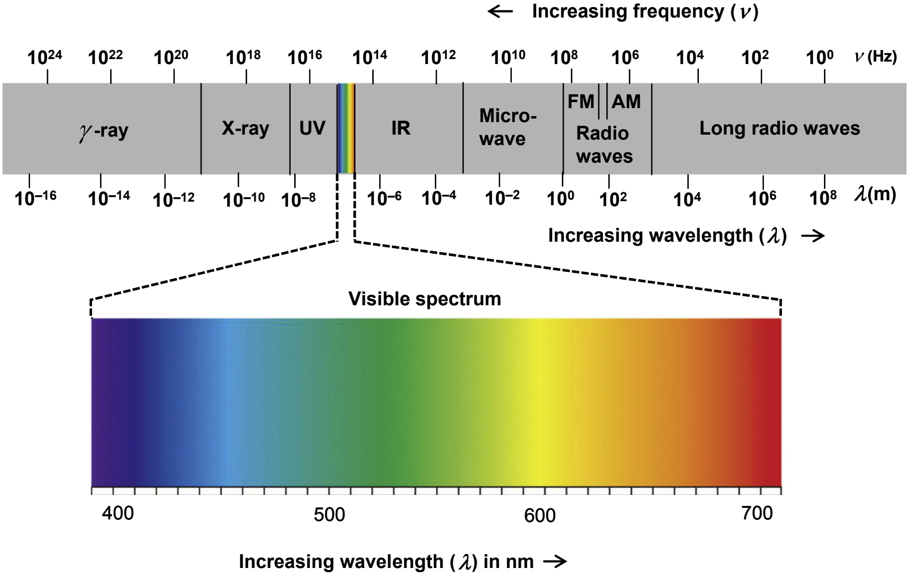
← Increasing frequency (ν)
10²⁴
10²²
10²⁰
10¹⁸
10¹⁶
10¹⁴
10¹²
10¹⁰
10⁸
10⁶
10⁴
10²
10⁰
ν (Hz)
γ-ray
X-ray
UV
IR
Micro-wave
FM
AM
Radio waves
Long radio waves
10⁻¹⁶
10⁻¹⁴
10⁻¹²
10⁻¹⁰
10⁻⁸
10⁻⁶
10⁻⁴
10⁻²
10⁰
10²
10⁴
10⁶
10⁸
λ(m)
Increasing wavelength (λ) →
Visible spectrum
400
500
600
700
Increasing wavelength (λ) in nm →

Figure 12.1 Spectrum of an electromagnetic wave.

wave behaves just as a wave, on the other hand, its path will bend due to diffraction, refraction, and reflection. Thus, the path can no longer be modeled as a straight line. Depending on the interaction pattern, the tomography can be categorized into three groups as transmission, electrical, and diffraction tomography. For each tomography, the mathematical description has a different form, and the following sections will introduce the mathematical concepts for each type of tomography.

12.2 Transmission tomography

Radiation is a stream of energetic particles or energetic electromagnetic wave. In fact, the electromagnetic wave is often regarded as a particle called a photon when it is highly energetic. Photons can have a wavelength so short as to be comparable to or less than the size of an atom, for example, X-rays and γ-rays. Radiation loses its particles or energy upon interaction with the matter. That is, radiation attenuates resulting in a decrease of intensity as it passes through matter. The ways of interaction can be roughly classified into absorption and scattering. In the case of absorption, the energy of particles is entirely absorbed by the matter (the radiation particles disappear). Often, the absorption may result in production of other radiation. On the other hand, the radiation particle may collide with matter and its momentum is altered. After the scattering, of course, the direction of the radiation is changed. The extent of attenuation depends on the sort of radiation and the matter with which it interacts; it is also a function of the radiation energy.

12.2.1 Mathematical formulation of transmission attenuation

For a mathematical formulation of the relationship between the intensity and the material property, suppose an infinite slab of thickness a is placed in a monodirectional and monoenergetic plane beam of intensity I_0 and has a detector placed behind the slab as shown in Figure 12.2. Let $I(x)$ be the intensity at x, where the intensity is defined as the power transferred per unit area or the number of radiation particles per unit time passing through a unit area. It is assumed that in traveling an additional distance dx, the intensity decrease is proportional to $I(x)$ and dx. If there is no scattering, then this assumption is exact. In this, the proportional constant μ, called the *attenuation coefficient* or *linear absorption coefficient*, is introduced:

$$\mathrm{d}I(x) = -\mu I(x)\mathrm{d}x. \tag{12.1}$$

The attenuation coefficient is a physical property of the matter for a given radiation. Strictly speaking, μ is a function of the radiation energy, but in practice the energy dependency is usually neglected. Integrating this equation gives

$$I(x) = I_0 \exp(-\mu x). \tag{12.2}$$

The intensity measured by the detector I_d is

$$I_\mathrm{d} = I(a) = I_0 \exp(-\mu a). \tag{12.3}$$

When the slab is multilayered and each layer has a different attenuation coefficient, then the intensity measured by the detector becomes

$$I_\mathrm{d} = I_0 \exp\left(-\sum_n \mu_n a_n\right), \tag{12.4}$$

where μ_n and a_n are the attenuation coefficient and the thickness of the nth layer, respectively. It should be noted that, in a one-dimensional infinite slab, the above derivation is valid even when the attenuation is solely caused by the scattering because the contribution to the detector by the scattering is uniform. However, for a point source or where the target size is finite, as the scattering contributes more the above model becomes worse.

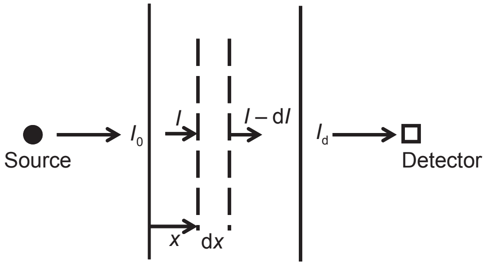

Figure 12.2 Intensity variation when radiation is passing through a slab.

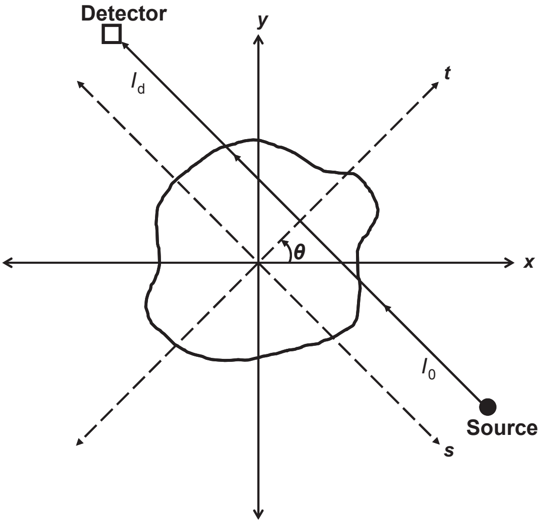

Figure 12.3 Radiation transmission through an arbitrary two-dimensional object.

For an arbitrary two-dimensional object as shown in Figure 12.3, Eqn (12.4) can be generalized to

$$I_\mathrm{d}(t;\theta) = I_0 \exp\left(- \int_{L(t;\theta)} \mu(x,y)\mathrm{d}s \right), \tag{12.5}$$

where $L(t;\theta)$ is the line (ray) connecting the source and the detector, (s,t) is the coordinate rotated by $\theta \in (0,\pi)$ from (x,y) to align s-axis parallel to the ray, and $I_\mathrm{d}(t;\theta)$ is again the intensity measured by the detector. If $I_\mathrm{d}(t;\theta)$ is measureable and distinguishable in terms of measurement uncertainty and $\mu(x,y)$ is invertible from $I_\mathrm{d}(t;\theta)$, we can expect that the radiation can be used for the reconstruction of the cross-sectional image because the attenuation coefficient distribution corresponds to the material distribution.

12.2.2 Radon transform and direct back projection

The basic idea to reconstruct the original function from a series of projected functions was given by the Austrian mathematician Johann Radon in 1917 and realized by R. N. Bracewell in 1956. When the rotated coordinate is expressed as (see Figure 12.3)

$$t = x\cos\theta + y\sin\theta, \quad s = -x\sin\theta + y\cos\theta, \tag{12.6}$$

the Radon transform of $\mu(x,y)$ along a ray parallel to the s-axis is defined as a line integral or a ray sum,

$$p(t;\theta) = \widehat{R}_s[\mu(x,y)](t;\theta) = \int_{-\infty}^{\infty} \mu(x,y)\mathrm{d}s. \tag{12.7}$$

Hence, the Radon transform of the attenuation coefficient is directly related to the intensity ratio, which can be measured:

$$p(t;\theta) = \ln\frac{I_0}{I_d(t;\theta)}. \tag{12.8}$$

12.2.2.1 Direct back projection

At each angle, the attenuated intensity is measured, and it can be readily converted to the sum of the attenuation coefficients of the pixels along a ray. However, we do not know the contribution of each pixel. The simplest assumption is that each pixel along the ray contributes equally. Hence, the simplest form of the back projection to the pixel at (*x*,*y*) will be the sum of all the projections crossing (*x*,*y*) and can be expressed as (Kak and Slaney, 1988; Natterer, 1986; Stark, Woods, Paul, & Hingorani, 1981)

$$\mu_{\mathrm{DBP}}(x,y) = \int_0^{\pi} p[t(x,y;\theta);\theta]\mathrm{d}\theta. \tag{12.9}$$

Figure 12.4 shows the back-projected image using three projections. If the contribution is expressed in a gray level, obviously, the target can be captured with the region having high brightness. However, as seen in the figure, with only a few projections, a star-like pattern around the true target remains inevitable. As the number of projections is increased, the star-like pattern is smeared out and an improved image is reconstructed. Figure 12.5(a) is reconstructed by 180 projections covering a full rotation from 0° to 180°. When increasing the number of projections, unfortunately,

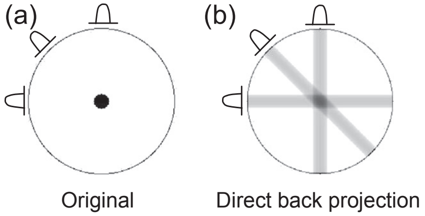

Figure 12.4 Image reconstruction using projections (a) original image (b) image from direct back projection with three projections.

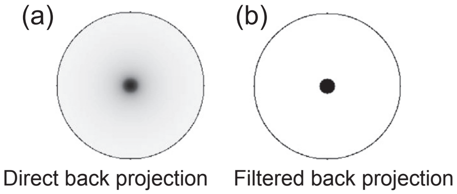

Figure 12.5 Comparison of reconstructed images from projections (a) direct back projection (b) filtered back projection.

the object image as well as the star-like pattern are blurred at the same time. Even with more projections, the spatial resolution is not further improved.

12.2.3 Fourier transform and filtered back projection

The direct back projection is not the inversion of Radon transform but just a back projection of the Radon transform of the attenuation coefficient distribution. Before proceeding to the inversion of the Radon transform, let us review the relationship between the Radon transform and Fourier transform (Bracewell, 1965; Bracewell & Riddle, 1967; Jain, 1989). The two-dimensional Fourier transform of $\mu(x,y)$ is defined as

$$M(u,v) = \widehat{F}_{(x,y)}[\mu(x,y)](u,v) = \int_{-\infty}^{\infty}\int_{-\infty}^{\infty} \mu(x,y)\exp[-j(ux+vy)]\mathrm{d}x\mathrm{d}y, \tag{12.10}$$

and its inverse is

$$\begin{aligned}\mu(x,y) &= \widehat{F}^{-1}_{(u,v)}[M(u,v)](x,y)\\ &= \frac{1}{(2\pi)^2}\int_{-\infty}^{\infty}\int_{-\infty}^{\infty} M(u,v)\exp[j(ux+vy)]\mathrm{d}u\mathrm{d}v.\end{aligned} \tag{12.11}$$

Noting that the one-dimensional Fourier transform of $p(t;\theta)$ for a given θ can be written as

$$P(\omega;\theta) = \widehat{F}_t[p(t;\theta)](\omega;\theta) = \int_{-\infty}^{\infty} p(t;\theta)\exp(-j\omega t)\mathrm{d}t, \tag{12.12}$$

introducing $(u,v) = (\omega\cos\theta, \omega\sin\theta)$ we can easily derive the relationship

$$M(\omega\cos\theta, \omega\sin\theta) = \int_{-\infty}^{\infty}\int_{-\infty}^{\infty} \mu(x,y)\exp[-j\omega(x\cos\theta + y\sin\theta)]\mathrm{d}x\mathrm{d}y$$

$$= \int_{-\infty}^{\infty}\int_{-\infty}^{\infty} \mu(x,y)\exp(-j\omega t)\mathrm{d}x\mathrm{d}y = \int_{-\infty}^{\infty}\int_{-\infty}^{\infty} \mu(x,y)\exp(-j\omega t)\frac{\partial(x,y)}{\partial(s,t)}\mathrm{d}t\mathrm{d}s,$$

$$= \int_{-\infty}^{\infty}\left[\int_{-\infty}^{\infty} \mu(x,y)\mathrm{d}s\right]\exp(-j\omega t)\mathrm{d}t = P(\omega;\theta)$$

or

$$M(\omega \cos\theta, \omega \sin\theta) = P(\omega;\theta). \tag{12.13}$$

This is called the Fourier slice theorem (or projection-slice theorem), which explains that the one-dimensional Fourier transform of a projection of a two-dimensional function onto a line, $P(\omega;\theta)$, is equal to the slice parallel to the projection line passing through an origin of the two-dimensional Fourier transform of the same function, $\mathrm{M}(\omega\cos\theta, \omega\sin\theta)$ (Bracewell, 1965; Herman, 1979, 1980; Jain, 1989; Levoy, 1992).

If $p(t;\theta)$ can be measured for all θ, $M(\omega\cos\theta, \omega\sin\theta)$ can be obtained from $P(\omega;\theta)$, the Fourier transform of $p(t;\theta)$. Finally, $\mu(x,y)$ can be reconstructed by the inverse Fourier transform of $M(\omega\cos\theta, \omega\sin\theta)$. The inversion process is as follows. At first, the inverse Fourier transform is written in a polar coordinate:

$$\begin{aligned}\mu(x,y) &= \frac{1}{(2\pi)^2}\int_{-\infty}^{\infty}\int_{-\infty}^{\infty} M(u,v)\exp[j(ux+vy)]\mathrm{d}u\mathrm{d}v \\ &= \frac{1}{(2\pi)^2}\int_{0}^{\pi}\int_{-\infty}^{\infty} M(\omega\cos\theta, \omega\sin\theta)\exp[j\omega(x\cos\theta + y\sin\theta)]|\omega|\mathrm{d}\omega\mathrm{d}\theta\end{aligned}$$

and recalling the Fourier slice theorem and $t = x\cos\theta + y\sin\theta$ we have

$$\begin{aligned}\mu(x,y) &= \frac{1}{(2\pi)^2}\int_{0}^{\pi}\int_{-\infty}^{\infty} P(\omega;\theta)\exp[j\omega(x\cos\theta + y\sin\theta)]|\omega|\mathrm{d}\omega\mathrm{d}\theta \\ &= \frac{1}{2\pi}\int_{0}^{\pi}\left[\frac{1}{2\pi}\int_{-\infty}^{\infty} P(\omega;\theta)|\omega|\exp(j\omega t)\mathrm{d}\omega\right]\mathrm{d}\theta \\ &= \frac{1}{2\pi}\int_{0}^{\pi}\widehat{F}_{\omega}^{-1}[P(\omega;\theta)|\omega|](t;\theta)\mathrm{d}\theta\end{aligned}$$

or

$$\mu(x,y) = \frac{1}{2\pi}\int_{0}^{\pi}\widehat{F}_{\omega}^{-1}[P(\omega;\theta)|\omega|](t;\theta)\mathrm{d}\theta. \tag{12.14}$$

Comparing with the direct back projection, $\frac{1}{2\pi}\widehat{F}_{\omega}^{-1}[P(\omega;\theta)|\omega|](t;\theta) = \frac{1}{2\pi}\widehat{F}_{\omega}^{-1}[|\omega|\widehat{F}_{t}[p(t;\theta)](\omega;\theta)](t;\theta)$ can be regarded as a filtered version of the projection function $p(t;\theta)$. The inverse Fourier transform of the Fourier transform of $p(t;\theta)$ multiplied by $|\omega|$ instead of $p(t;\theta)$, in practice, this implies that a high-pass filter is introduced (Kak, 1984; Pan & Kak, 1983; Schafer, Borgert, Rasche, & Grass, 2006). Figure 12.5 illustrates the comparison between the images reconstructed by a direct back projection and by a filtered back projection. Obviously, the filtered back projection reconstructs the edge of the object sharply while the direct back projection fails.

12.2.4 Algebraic reconstruction technique

In the radiation tomography mentioned above, we have seen that the main relationship between the unknowns to be imaged and the measured projection data has a form of

$$p(t;\theta) = \widehat{R}_s[\mu(x,y)](t;\theta) = \int_{-\infty}^{\infty} \mu(x,y)\mathrm{d}s, \tag{12.7a}$$

And the unknown is the attenuation coefficient $\mu(x,y)$ and the measured data are

$$p(t;\theta) = \ln\frac{I_0}{I_\mathrm{d}(t;\theta)}. \tag{12.8a}$$

This relationship in integral form will be converted to a discrete algebraic form. The ray is assumed to be a strip with a width rather than a line. In reality, the radiation detector has a finite window size, not a point. The domain to be imaged is discretized into small N pixels, and each pixel has a width approximately equal to the ray width. In each pixel, the attenuation coefficient is set to be constant. The relationship can be expressed as an algebraic form as (Bender, Gordon, & Herman, 1970; Kak & Slaney, 1988)

$$p_i = \sum_{j=1}^{N} w_{ij}\mu_j, \quad i = 1, 2, \cdots, M, \tag{12.15}$$

where p_i is the projection of the ith ray, M the number of rays or projections, μ_j the attenuation coefficient of the jth pixel, and w_{ij} the weighting factor representing the contribution of the jth pixel to the ith projection. Solving the algebraic Eqn (12.15) to reconstruct μ_j based on the projection data p_i is called the algebraic reconstruction technique (ART).

When the projection line (ray) is straight, the evaluation of the weighting factors w_{ij} is straightforward, w_{ij} is equal to the area of the jth pixel intercepted by the ith ray strip. Therefore, the matrix of w_{ij} is very sparse. Once w_{ij} are known, then the system of linear Eqn (12.15) can be solved easily using any well-known available solvers. In practice, the size of the system of linear equations is not small and direct matrix inversion methods are not feasible. In case of 1% spatial resolution, for example,

$N = 100 \times 100$ and M will have a similar size, then the size of w_{ij} is approximately $10^4 \times 10^4$, which requires iterative methods. This is why the ART is classified as an iterative method.

One of the popular methods to solve Eqn (12.15) is to apply Kaczmarz's method, which is efficient in handling sparse matrices like those in the ART. In the image reconstruction, often, Kaczmarz's method is known as ART. Kaczmarz's method is a sequence of processes to project the previous solution $\boldsymbol{\mu}^{(k-1)}$ on the hyperplane constructed by the ith Eqn (12.15) to find the updated solution $\boldsymbol{\mu}^{(k)}$, where $\boldsymbol{\mu} = (\mu_1, \mu_2, \cdots, \mu_N)^T$ and the superscript (k) denotes the kth iteration step. Hence, Kaczmarz's method is classified into a projection method for solving large linear systems of equations (Hermann 1979, 1980; Strohmer & Vershynin, 2009). This process is performed for all $i = 1, 2, \cdots, M$ in a predetermined sequence. If the solution does not converge, then other cycles are repeated until convergence. When $M = N = 2$, this process can be easily understood as shown in Figure 12.6.

This process can be expressed in a mathematical form as

$$\boldsymbol{\mu}^{(k)} = \boldsymbol{\mu}^{(k-1)} + \mathbf{d}^{(k-1)} \quad \text{and} \quad \mathbf{d}^{(k-1)} = \frac{p_i - \mathbf{w}_i \cdot \boldsymbol{\mu}^{(k-1)}}{\mathbf{w}_i \cdot \mathbf{w}_i^T}\,\mathbf{w}_i^T, \tag{12.16}$$

where $\mathbf{w}_i = (w_{i1}, w_{i2}, \cdots, w_{iN})$ is the ith row vector of matrix $[w_{ij}]$. Often, in order to control the speed of convergence, the relaxation parameter λ $(0 < \lambda < 2)$ is introduced as $\boldsymbol{\mu}^{(k)} = \boldsymbol{\mu}^{(k-1)} + \lambda \mathbf{d}^{(k-1)}$ and it can be regarded as a variant of the successive overrelaxation method.

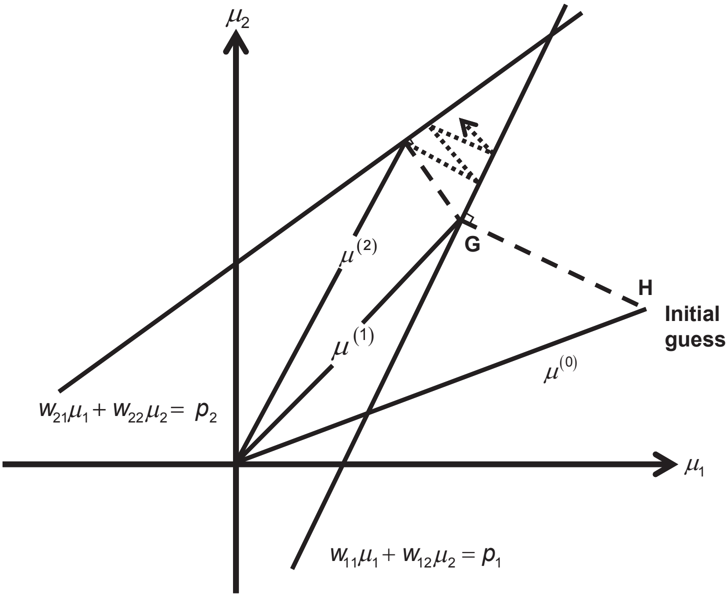
μ_2
$\mu^{(2)}$
G
H
Initial guess
$\mu^{(1)}$
$\mu^{(0)}$
$w_{21}\mu_1 + w_{22}\mu_2 = p_2$
μ_1
$w_{11}\mu_1 + w_{12}\mu_2 = p_1$

Figure 12.6 Conceptual description of Kaczmarz's method.

12.3 Electrical tomography

12.3.1 Mathematical formulation of electrical tomography

Electric field over a domain of interest depends on the geometry of the domain, the distribution of electrical properties of the medium, and the excitation sources (voltage or current) imposed on the domain boundary. For the given domain under the known boundary conditions, the measured electric signals are determined only by the electrical property distribution over the domain. Hence, if we can measure the excited electrical signals (current or voltage) on the boundary, we may consider the use of electrical signals to reconstruct the tomographic image or the electrical property distribution. In practice, when the medium is composed of substances with sufficiently distinct electrical property, it is possible to estimate the distribution of the substances using the relationship between the electric signals and the electrical property distribution. This imaging modality is called *electrical tomography* (ET).

It is well known that electric field always induces magnetic field and is also affected by it. Even when excitation sources are electrical, strictly speaking, electric field cannot exist solely and should be analyzed, simultaneously, with magnetic field. Hence, for the mathematical formulation of ET we will start from Maxwell's equations governing electromagnetic field. Maxwell's equations in matter are composed of four equations:

$$\text{Gauss's law} \quad \nabla \cdot \mathbf{D} = \rho \tag{12.17}$$

$$\text{Gauss's law for magnetism} \quad \nabla \cdot \mathbf{B} = 0 \tag{12.18}$$

$$\text{Faraday's law of induction} \quad \nabla \times \mathbf{E} = -\frac{\partial \mathbf{B}}{\partial t} \tag{12.19}$$

$$\text{Ampére's circuital law} \quad \nabla \times \mathbf{H} = \mathbf{J} + \frac{\partial \mathbf{D}}{\partial t} \tag{12.20}$$

where $\mathbf{E}$ is the electric field (V/m) = (N/C), $\mathbf{D}$ the electric displacement field (C/m^2), $\mathbf{B}$ the magnetic induction (T) = (Ns/Cm), and $\mathbf{H}$ the magnetic field (A/m). ρ and $\mathbf{J}$ are the charge density (C/m^3) and the current density (A/m^2) without any induced polarization. If the medium is linear isotropic, the following relations are valid:

$$\mathbf{D} = \varepsilon \mathbf{E}, \quad \mathbf{B} = \mu \mathbf{H}, \quad \text{and} \quad \mathbf{J}_f = \sigma \mathbf{E}, \tag{12.21}$$

where ε is the permittivity (F/m), μ the permeability (Tm/A) = (Vs/Am), and σ the electric conductivity (1/Ωm).

Combining the above relations and assuming that the injected electric signals (voltage or current) are time harmonic with an angular frequency ω, i.e., $\mathbf{E} = \mathbf{E}_0 e^{j\omega t}$,

$\mathbf{B} = \mathbf{B}_0 e^{j\omega t}$, Faraday's and Ampére's laws become (Doerstling, 1994; Sommersalo, Isaacson, & Cheney, 1992):

$$\text{Faraday's law of induction} \quad \nabla \times \mathbf{E}_0 = -j\omega\mu\mathbf{H}_0 \tag{12.22}$$

$$\text{Ampére's circuital law} \quad \nabla \times \mathbf{H}_0 = (\sigma + j\omega\varepsilon)\mathbf{E}_0. \tag{12.23}$$

Further simplification is made in ET. Due to Gauss's law for magnetism, there exists a magnetic vector potential of **B** such as

$$\mathbf{B} = \nabla \times \mathbf{A}. \tag{12.24}$$

From the vector identity, hence, the electric field can be expressed in general as

$$\mathbf{E} = -\nabla u - \frac{\partial \mathbf{A}}{\partial t}, \tag{12.25}$$

where u is the electric potential. Again, if we assume a time-harmonic field for the magnetic vector potential as $\mathbf{A} = \mathbf{A}_0 e^{j\omega t}$ and the electric potential as $u = u_0 e^{j\omega t}$,

$$\mathbf{E}_0 = -\nabla u_0 - j\omega\mathbf{A}_0. \tag{12.26}$$

Here, the magnitude of $\mathbf{A}_0$ may be estimated as

$$|\mathbf{B}_0| = |\mu\mathbf{H}_0| = |\nabla \times \mathbf{A}_0| \quad \text{and} \quad |\mathbf{A}_0| \sim \mu L_c |\mathbf{H}_0|, \tag{12.27}$$

where L_c is the characteristic length of the magnetic field. On the other hand, from Ampére's law the scale relation will be

$$|\mathbf{E}_0| = |\nabla u_0 + j\omega\mathbf{A}_0| \sim \frac{|\mathbf{H}_0|/L_c}{|\sigma + j\omega\varepsilon|}. \tag{12.28}$$

The relative contribution of the magnetic vector potential to the electric field is estimated as

$$\frac{|\omega\mathbf{A}_0|}{|\nabla u_0 + j\omega\mathbf{A}_0|} \sim \omega\mu L_c^2 |\sigma + j\omega\varepsilon|. \tag{12.29}$$

If the relative contribution is much smaller than 1, i.e.,

$$\omega\mu L_c^2 |\sigma + j\omega\varepsilon| << 1, \tag{12.30}$$

then the effect of magnetic induction inducing electric field can be neglected (Nunez, 1981). Consider a pipe of diameter 1 m filled with water. For a frequency of 100 kHz, the physical properties of water, $\varepsilon \approx 80 \times 10^{-9}/36\pi$ F/m, $\mu \approx 4\pi \times 10^{-7}$ Vs/Am, and $\sigma \approx 5.5 \times 10^{-6}$ 1/Ωm yields $\omega\mu L_c^2|\sigma + j\omega\varepsilon| \approx 3.5 \times 10^{-4} << 1$. Hence, the above simplification is valid.

Using the vector identity, readily, we have the governing equation for forward problem of the ET:

$$\nabla\cdot(\sigma + j\omega\varepsilon)\nabla u = 0 \quad \text{or} \quad \nabla\cdot\gamma\nabla u = 0. \tag{12.31}$$

Here, for simplicity the subscript "0" is dropped. The coefficient $\gamma = \sigma + j\omega\varepsilon$ is called the admittivity.

According to the ratio of $\omega\varepsilon/\sigma$, when the resistance or the capacitance term is dominant, the governing equation is simplified further (Baker, 1989; Barber & Brown, 1984):

$$\nabla\cdot\sigma\nabla u = 0 \quad \text{for} \quad \omega\varepsilon/\sigma << 1(\text{ERT}), \tag{12.32}$$

$$\nabla\cdot\varepsilon\nabla u = 0 \quad \text{for} \quad \omega\varepsilon/\sigma >> 1(\text{ECT}), \tag{12.33}$$

where electrical resistance tomography (ERT) means the resistance component is used for the tomography, while electrical capacitance tomography (ECT) uses the capacitance component. Electrical tomography combining ERT and ECT is called electrical impedance tomography (EIT). It should be noted that frequently ERT is known as EIT.

12.3.2 Image reconstruction based on transmission tomography algorithms

As can be seen from the governing equations, the electric potential satisfies Eqn (12.31) or Eqns (12.32) and (12.33). Since the governing equation is elliptic, electric potential can be altered by any variation of the electrical properties at any location within the domain by any variation of the boundary conditions. This means that the electric field may not be straight and the image reconstruction concepts for EIT should be quite different from transmission tomography. In transmission tomography, only the substances in the radiation paths can contribute to the attenuation of the radiation, and the path is assumed to be a straight line between the source and the detector. Nevertheless, if we can estimate the path of an electric current, which may be curved, for the given geometry and boundary conditions, the path can be approximated as an electric circuit unaffected by the substances that are out of the path and the use of transmission tomography concepts for EIT may be feasible. In this, the referenced electric current paths may be approximately determined with a known electrical property distribution, usually with a homogeneous medium of background substance. Whenever the distortion of the electric field due to any inclusion or anomaly against the background substance is not significant, we may adopt transmission tomography concepts for ET.

As an application of the transmission tomography concept to ET, the linear back projection algorithm in ECT is introduced. In practice, this was successfully applied to gas—solid or gas—liquid systems and extended to air—water systems (Dyakowski, Jeanmeure, & Jaworski, 2000; Warsito & Fan, 2001; Xie et al., 1992; Xie, Plaskowski, & Beck, 1989). After the discretization of the problem domain and the linearization of the relationship between the capacitance and the permittivity, we can have the expression as:

$$\mathbf{C}_{(M\times 1)} = \mathbf{S}_{(M\times N)}\mathbf{g}_{(N\times 1)}. \tag{12.34}$$

In this equation, **C** is the capacitance vector whose entities are independent capacitance data of electrode pairs, M is the number of independent capacitance data, **g** is the gray level vector that denotes the normalized permittivity distribution in a discrete number (N) of pixels, and **S** is the sensitivity matrix (or projection matrix) that represents the mapping of the gray level vector into the capacitance vector. The above expression called "forward projection" implies that the capacitance measured between a certain electrode pair is the sum of the capacitance for that particular electrode pair contributed by the permittivity in each pixel.

Xie et al. (1989) suggested a "back projection" algorithm by inverting the forward projection to obtain **g**:

$$\mathbf{g}_{(N\times 1)} = \mathbf{S}^{T}_{(M\times N)}\mathbf{C}^{*}_{(M\times 1)}. \tag{12.35}$$

Here, $C_{i,j}$ is the measured capacitance data between ith and jth electrodes, $\mathbf{C}^{*}_{(M\times 1)}$, are normalized capacitance data computed as

$$C^{*}_{i,j} = \frac{C_{i,j} - C_{i,j(\mathrm{low}-\varepsilon)}}{C_{i,j(\mathrm{high}-\varepsilon)} - C_{i,j(\mathrm{low}-\varepsilon)}}, \tag{12.36}$$

and pseudo-inverse assuming $\mathbf{S}^{-1}_{(M\times N)} = \mathbf{S}^{T}_{(M\times N)}$ is used. The sensitivity matrix is obtained as follows. At first, sensitivity areas $A_{i,j}$ are defined so that the permittivity change of the pixels in $A_{i,j}$ affects $C^{*}_{i,j}$ and the permittivity change of the pixels out of $A_{i,j}$ contributes little to $C^{*}_{i,j}$. Determining which pixel belongs to $A_{i,j}$ could be done by evaluating the change of $C^{*}_{i,j}$ due to the permittivity change of that pixel. If the change is greater than a certain threshold, then that pixel is assumed to belong to $A_{i,j}$. The change of $C^{*}_{i,j}$ could be obtained from numerical simulations or experiments by inserting a small anomaly with high permittivity into that pixel in a homogeneous domain with low permittivity. Mathematically, the gray level for the nth pixel for an eight- electrode system can be calculated as

$$g(n) = \sum_{i=1}^{7}\sum_{j=i+1}^{8} S_{i,j}(n)C^{*}_{i,j} \tag{12.37}$$

where the sensitivity matrix is evaluated as

$$S_{i,j}(n) = \frac{\delta_{i,j}(n)}{\sum\limits_{i=1}^{7}\sum\limits_{j=i+1}^{8}\delta_{i,j}(n)} \tag{12.38}$$

and the characteristic function $\delta_{i,j}(n)$ is 1 if the pixel n belongs to $A_{i,j}$, and 0 otherwise. This back projection is conceptually very simple and straightforward; however, many assumptions are engaged in the algorithm, and in fact the image reconstruction performance may not be so plausible. To improve the image quality some modifications of the sensitivity matrix have been suggested (Kim, Choi, & Kim, 2006; Reinecke & Mewes, 1997; Villares et al., 2012).

12.3.3 Linear algorithms

In the above subsection, the transmission tomography concept is applied to electrical capacitance tomography. Namely, it is assumed that the pixels influencing the capacitance between a certain electrode pair can be extracted, and the area composed of those pixels is considered as the path that radiation passes along in the transmission tomography. In reality, the change of electrical property in any pixel affects the electric signals measured at the boundary electrodes. If we abandon the transmission tomography concept, an exact expression for sensitivity matrix can be formulated. For more concrete derivation, let us start from the governing equation for the electrical capacitance tomography. The problem domain Ω enclosed by $\partial\Omega$ is filled with substances whose permittivity is $\varepsilon(x)$. Along the outer boundary $\partial\Omega$, electrodes e_l ($l = 1, 2, \cdots, L$) are mounted and the gaps between electrodes are insulated (Yang 1996). When electric potential U_l is imposed on each e_l, the electric potential distribution $u(x)$ satisfies

$$\nabla \cdot \varepsilon(x) \nabla u(x) = 0, \quad x \in \Omega, \tag{12.39}$$

subject to the boundary conditions

$$u(x) = U_l, \quad x \in e_l, \tag{12.40a}$$

and

$$\frac{\partial u(x)}{\partial \nu} = 0, \quad x \in \partial\Omega / \cup_{l=1}^{L} e_l. \tag{12.40b}$$

where ν is the outward normal unit vector. To reconstruct the permittivity distribution, the domain is discretized into small pixels Ω_n ($n = 1, 2, \cdots, N$), and in each pixel the permittivity is assumed to be constant. Namely, the number of unknowns will be the number of pixels. For the estimation of the permittivity of each pixel, we need the equations of the potential excitation and as many induced capacitances as possible. It means that for the same object we should measure capacitance data sets for a number of boundary condition sets that are independent of each other.

Assume that u^p is the potential subject to the pth boundary condition set ($p = 1, 2, \cdots, P$) for the given permittivity distribution ε, while u_0^q is the potential subject to the qth boundary condition set for a reference permittivity distribution ε_0 (Figure 12.2). Then,

$$\nabla \cdot \varepsilon \nabla u^p = 0 \quad \text{and} \quad \nabla \cdot \varepsilon_0 \nabla u_0^q = 0. \tag{12.41}$$

Upon multiplying each equation in Eqn (12.41) by u_0^q and u^p each and then subtracting, integrating over Ω, and applying the divergence theorem yields

$$\int_{\partial\Omega} \left(u_0^q \varepsilon \frac{\partial u^p}{\partial \nu} - u^p \varepsilon_0 \frac{\partial u_0^q}{\partial \nu} \right) \mathrm{d}S = \int_{\Omega} (\varepsilon - \varepsilon_0) \nabla u^p \cdot \nabla u_0^q \mathrm{d}\Omega. \tag{12.42}$$

The left-hand side collects the electrical excitations and responses on the electrodes. Recalling the boundary conditions, we have

$$\sum_{l=1}^{L} \left[U_{0,l}^q \int_{e_l} \varepsilon \frac{\partial u^p}{\partial \nu} \mathrm{d}S - U_l^p \int_{e_l} \varepsilon_0 \frac{\partial u_0^q}{\partial \nu} \mathrm{d}S \right] = \int_{\Omega} (\varepsilon - \varepsilon_0) \nabla u^p \cdot \nabla u_0^q \mathrm{d}\Omega. \tag{12.43}$$

As a simple case, consider $U_l^p = V\delta_{pl}$ and $U_{0,l}^q = V_0 \delta_{ql}$, where δ_{ij} is the Kronecker delta and $p,q = 1,2,\cdots,L$. And assuming that $V, V_0 > 0$, then we have

$$-V_0 Q_q^p + V Q_{0,p}^q = \int_{\Omega} (\varepsilon - \varepsilon_0) \nabla u^p \cdot \nabla u_0^q \mathrm{d}\Omega \quad \text{for } p \neq q \tag{12.44a}$$

or

$$C_{p,q} - C_{0,q,p} = -\int_{\Omega} (\varepsilon - \varepsilon_0) \frac{\nabla u^p}{V} \cdot \frac{\nabla u_0^q}{V_0} \mathrm{d}\Omega \quad \text{for } p \neq q \tag{12.44b}$$

where $Q_l^p = -\int_{e_l} \varepsilon \frac{\partial u^p}{\partial \nu} \mathrm{d}S$ is the charge at the lth electrode and $C_{p,q} = \frac{Q_q^p}{V}$ is the capacitance between the pth and qth electrodes when the pth electrode is activated by electric potential V while other electrodes are grounded (see Figure 12.7). Note that from the reciprocity theorem, $C_{p,q} = C_{q,p}$. Also, by applying the divergence theorem to the integration of the governing equation over Ω, we can see that $C_{p,p} = -\sum_{i \neq p}^{L} C_{p,i}$. Hence, the equation for $p = q$ is not independent of other equations for $p \neq q$ and the number of independent data is $M = L(L-1)/2$.

Let us introduce the normalized capacitance as:

$$C_{p,q}^* = \frac{C_{p,q} - C_{p,q(\text{low}-\varepsilon)}}{C_{p,q(\text{high}-\varepsilon)} - C_{p,q(\text{low}-\varepsilon)}}$$

$$= \frac{\int_{\Omega} (\varepsilon - \varepsilon_{\text{low}}) \frac{\nabla u^p}{V} \cdot \frac{\nabla u_{\text{low}}^q}{V_{\text{low}}} \mathrm{d}\Omega}{(\varepsilon_{\text{high}} - \varepsilon_{\text{low}}) \int_{\Omega} \frac{\nabla u_{\text{high}}^p}{V_{\text{high}}} \cdot \frac{\nabla u_{\text{low}}^q}{V_{\text{low}}} \mathrm{d}\Omega} \quad \text{for } p \neq q. \tag{12.45}$$

Figure 12.7 Diagram showing measurement configuration for ECT problem.

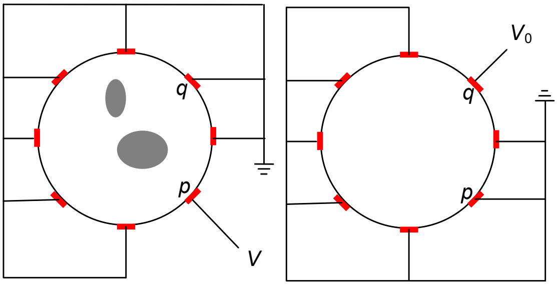

In this, the subscripts "high" and "low" mean that the problem domain is filled with "high" or "low" conductivity (or permittivity) material only, respectively. Note that $\nabla u^p_{\text{high}}/V_{\text{high}} = \nabla u^p_{\text{low}}/V_{\text{low}}$. If the domain is decomposed into N small elements as $\Omega = \cup_{n=1}^{N}\Omega_n$ and in each Ω_n the permittivity is assumed as $\varepsilon = \varepsilon_n$, then

$$C^*_{p,q} = \sum_{n=1}^{N} \varepsilon^*_n S^{p,q}_n \quad \text{for } p \neq q, \tag{12.46}$$

where ε^*_n is the normalized permittivity

$$\varepsilon^*_n = \frac{\varepsilon_n - \varepsilon_{\text{low}}}{\varepsilon_{\text{high}} - \varepsilon_{\text{low}}} \tag{12.47}$$

and $S^{p,q}_n$ is the sensitivity matrix

$$S^{p,q}_n = \frac{\int_{\Omega_n} \left(\nabla u^p/V\right)\cdot\left(\nabla u^q_{\text{low}}/V_{\text{low}}\right)\mathrm{d}\Omega}{\int_{\Omega} \left(\nabla u^p_{\text{high}}/V_{\text{high}}\right)\cdot\left(\nabla u^q_{\text{low}}/V_{\text{low}}\right)\mathrm{d}\Omega} \quad \text{for } p \neq q. \tag{12.48}$$

In an algebraic form,

$$\begin{pmatrix} C^*_{1,2} \\ C^*_{1,3} \\ \vdots \\ C^*_{2,3} \\ \vdots \\ C^*_{(L-1),L} \end{pmatrix} = \begin{bmatrix} S^{1,2}_1 & S^{1,2}_2 & \cdots & S^{1,2}_N \\ S^{1,3}_1 & S^{1,3}_2 & \cdots & S^{1,3}_N \\ \vdots & \vdots & \ddots & \vdots \\ S^{2,3}_1 & S^{2,3}_2 & \cdots & S^{2,3}_N \\ \vdots & \vdots & \ddots & \vdots \\ S^{(L-1),L}_1 & S^{(L-1),L}_2 & \cdots & S^{(L-1),L}_N \end{bmatrix} \begin{pmatrix} \varepsilon^*_1 \\ \varepsilon^*_2 \\ \vdots \\ \vdots \\ \vdots \\ \varepsilon^*_N \end{pmatrix} \tag{12.49a}$$

or

$$\mathbf{C}^* = \mathbf{S}\varepsilon^*, \tag{12.49b}$$

where $\mathbf{C}^* \in \Re^{L(L-1)/2\times 1}$ is the normalized capacitance vector, $\boldsymbol{\varepsilon}^* \in \Re^{N\times 1}$ is the normalized permittivity vector, and $\mathbf{S} \in \Re^{L(L-1)/2\times N}$ is the sensitivity matrix. The normalized capacitance vector is a measurable quantity, therefore, the permittivity distribution can be reconstructed if the sensitivity matrix is available. Recalling the definition of the sensitivity matrix, unless ∇u^p under the given $\boldsymbol{\varepsilon}$ is known in advance, $\mathbf{S}$ cannot be evaluated. If there are only two substances with $\varepsilon_{\text{high}}$ and ε_{low}, it is possible to evaluate the sensitivity matrix exactly. Consider a domain with $\varepsilon(x) = \varepsilon_{\text{low}} + (\varepsilon_{\text{high}} - \varepsilon_{\text{low}})\chi_{\Omega_n}(x)$, where $\chi_{\Omega_n}(x)$ is the characteristic function defined as

$$\chi_{\Omega_n}(x) = \begin{cases} 1 & \text{for } x \in \Omega_n \\ 0 & \text{otherwise} \end{cases}.$$

Then, we have

$$S_n^{p,q} = \frac{C_{p,q}^{(n)} - C_{p,q(\text{low}-\varepsilon)}}{C_{p,q(\text{high}-\varepsilon)} - C_{p,q(\text{low}-\varepsilon)}} = C_{p,q}^{*(n)} \quad \text{for } p \neq q. \tag{12.50}$$

In this, $C_{p,q}^{(n)}$ is the capacitance for $\varepsilon(x) = \varepsilon_{\text{low}} + (\varepsilon_{\text{high}} - \varepsilon_{\text{low}})\chi_{\Omega_n}(x)$. These can be obtained by solving the governing equation.

It should be noted that the above formulation is valid for the ERT when the conductivity and the conductance are substituted for the permittivity and the capacitance, respectively.

12.3.4 Gradient-based algorithms

In general, the problem domain may contain more than two substances with distinct electrical properties or miscible mixture with continuously varying electrical property. Then, the above linear algorithms may not be feasible since the electric field for a given electrical property distribution cannot be known in advance. However, if the deviation of the electrical property distribution from the reference is less, one can try a linearization about the reference. For example, if the permittivity is perturbed as $\varepsilon(x) = \varepsilon_{\text{low}} + (\delta\varepsilon)\chi_{\Omega_n}(x)$, then both the potential field and the capacitance are perturbed and we have

$$\delta C_{p,q}^* = \delta\varepsilon^* \frac{\displaystyle\int_{\Omega_n} \left(\nabla u_{\text{low}}^p / V_{\text{low}}\right) \cdot \left(\nabla u_{\text{low}}^q / V_{\text{low}}\right) \mathrm{d}\Omega}{\displaystyle\int_{\Omega} \left(\nabla u_{\text{high}}^p / V_{\text{high}}\right) \cdot \left(\nabla u_{\text{low}}^q / V_{\text{low}}\right) \mathrm{d}\Omega} + O\left(\delta\varepsilon^{*2}\right) \quad \text{for } p \neq q \tag{12.51}$$

or the Jacobian, the partial derivative of $C^*_{p,q}$ with respect to the permittivity of the nth subdomain Ω_n, can be expressed as

$$J_n^{p,q} = \frac{\partial C^*_{p,q}}{\partial \varepsilon^*_n} = \frac{\displaystyle\int_{\Omega_n} \left(\nabla u^p_{\text{low}}/V_{\text{low}}\right)\cdot\left(\nabla u^q_{\text{low}}/V_{\text{low}}\right)\mathrm{d}\Omega}{\displaystyle\int_{\Omega} \left(\nabla u^p_{\text{high}}/V_{\text{high}}\right)\cdot\left(\nabla u^q_{\text{low}}/V_{\text{low}}\right)\mathrm{d}\Omega} \quad \text{for } p \neq q. \tag{12.52}$$

Linearizing the normalized capacitance about the homogeneous configuration with ε_{low}, it can be approximated as

$$\mathbf{C}^* = \mathbf{J}\boldsymbol{\varepsilon}^*, \tag{12.53}$$

in which the evaluation of the Jacobian $\mathbf{J}$ requires much less computations as compared with the previous one. However, since this is a first-order approximation, it is expected that the more the permittivity distribution deviates from ε_{low} the worse the reconstruction performance becomes.

Now, let us find general approaches to arbitrary situations. For a given domain, if we know the electrical property (conductivity and/or permittivity) distribution and the imposed boundary conditions, then the potential distribution can be calculated by solving the governing equation, Eqn (12.31) or Eqns (12.32) and (12.33). Also, the measured electric signals should be very close to the calculated ones with the known information. Note that they cannot be exactly the same since the measurement error and the modeling error cannot be avoided. Hence, the EIT image reconstruction can be regarded as a process to properly assume the electrical property distribution such that the difference between the measured electric signals and the calculated ones with the assumed distribution is minimized. In other words, EIT is an optimization problem to find the electrical property distribution by minimizing the difference between the measured and the calculated electric signals (Vauhkonen, 1997; Yorkey, Webster, & Tompkins, 1987).

Let us consider EIT, more strictly ERT problem. In this, it is common to inject electric currents through the electrodes attached along the boundary discretely for excitation and to measure excited voltages on the electrodes. The domain is discretized into small pixels as $\Omega = \cup_{n=1}^{N}\Omega_n$, and the conductivity distribution is assumed to be a pixel-wise constant function such that $\sigma(x) = \sum_{n=1}^{N}\sigma_n\chi_{\Omega_n}(x)$, where the conductivity vector $\boldsymbol{\sigma} = [\sigma_1, \sigma_2, \cdots, \sigma_N]^T \in \Re^{N\times 1}$ is the unknown to be estimated by minimizing the cost functional that is the sum of squares of the voltage difference, $\mathbf{f}(\boldsymbol{\sigma}) = \mathbf{U}(\boldsymbol{\sigma}) - \mathbf{V}$

$$\Phi(\boldsymbol{\sigma}) = \frac{1}{2}[\mathbf{U}(\boldsymbol{\sigma}) - \mathbf{V}]^T[\mathbf{U}(\boldsymbol{\sigma}) - \mathbf{V}] = \mathbf{f}^T\mathbf{f}. \tag{12.54}$$

The measured voltage vector is denoted as $\mathbf{V} \in \Re^{LM\times 1}$ and the calculated voltage vector based on the assumed conductivity vector $\boldsymbol{\sigma}$ is $\mathbf{U}(\boldsymbol{\sigma}) \in \Re^{LM\times 1}$ (Vauhkonen 1997; Woo, Hua, Webster, & Tompkins, 1994). In this, it is assumed that voltages are measured at all the electrodes e_l ($l = 1, 2, \cdots, L$) and the number of current injection patterns, or the boundary condition sets, is M. According to the data collection strategy, the voltages may be measured at some selected electrodes and not at all the electrodes. Let the number of voltage data be P, i.e., $\mathbf{f}, \mathbf{V}, \mathbf{U}(\boldsymbol{\sigma}) \in \Re^{P\times 1}$. The calculated voltage $\mathbf{U}(\boldsymbol{\sigma})$ can be obtained by solving the governing equation:

$$\nabla \cdot \sigma \nabla u = 0 \tag{12.55}$$

subject to the boundary conditions

$$\int_{e_l} \frac{\partial u(x)}{\partial \nu} \, \mathrm{d}S = I_l, \quad x \in e_l, \tag{12.56a}$$

and

$$\frac{\partial u(x)}{\partial \nu} = 0, \quad x \in \partial\Omega / \cup_{l=1}^{L} e_l. \tag{12.56b}$$

Also, two more constraints should be imposed:

$$\sum_{l=1}^{L} I_l = 0 \quad \text{and} \quad \sum_{l=1}^{L} U_l = 0. \tag{12.57}$$

The former is to satisfy Kirchhoff's law and the latter is introduced to fix the potential distribution since only the Neumann conditions are given along the boundary (Somersalo, Cheney, & Isaacson, 1992). For the latter, the other form of constraint is possible as long as the potential can be fixed, e.g., $U_1 = 0$. For the current injection boundary condition, the current itself, as given in Eqn (12.56a), cannot be used as the boundary condition. The current density instead of the current should be specified. A simple approach is to assume a uniform current density:

$$\frac{\partial u(x)}{\partial \nu} = \frac{I_l}{|e_l|}, \quad x \in e_l, \tag{12.58}$$

which is called the average gap model (Cheng, Isaacson, Newell, & Gisser, 1989). On the other hand, we need to compute the electrode voltages from the potential distribution. As an electrode material, high conductive metals are used, and thus the potential distribution within an electrode can be assumed to be a constant, which will be the electrode voltage. Hence, an approximation can be considered such that the potential of the substance at the points contacting the electrode may be set to electrode voltage. This is called the shunt model:

$$u(x) = U_l, \quad x \in e_l, \tag{12.59}$$

However, in reality, the current density may not be uniform and there is contact impedance between the electrode and the substance. As a more realistic model, the complete electrode model considers the contact impedance and the shunt effect at the same time (Cheng et al., 1989; Vauhkonen, 1997):

$$u(x) + z_l \sigma \frac{\partial u(x)}{\partial \nu} = U_l, \quad x \in e_l, \tag{12.60}$$

where z_l is the effective contact impedance at the lth electrode. Disadvantages of the complete electrode model are that z_l is unknown in general and should be estimated in advance through separate experiments or simultaneously estimated along with the conductivity distribution, which increases the number of unknowns and degrades the image reconstruction performance. For the solution of the governing equation with the boundary conditions, the constraints, and the complete electrode model, usually, the finite element method is preferred since it can easily handle the pixel-wise conductivity distribution (Brenner & Scott, 1994; Hinton & Owen, 1979; Vauhkonen 1997). The finite element formulation is well established, and many references and computer programs are available (Adler et al., 2009; Kim, Choi, & Kim, 2006; Vauhkonen, 1997).

One of the most common approaches used to solve the above nonlinear least squares problems is the Gauss–Newton algorithm. It can be regarded as a modification of Newton's method for finding a minimum of a function. The Gauss–Newton algorithm iteratively finds the minimum of the sum of squares (Adler, Dai, & Lionheart, 2007; Kohn & McKenney, 1990; Polydorides, Lionheart, & McCann, 2002; Vauhkonen, 1997; Yorkey et al., 1987). To find the minimum, the derivative of the cost functional with respect to $\boldsymbol{\sigma}$, denoted by prime $'$, is set to zero:

$$\Phi'(\boldsymbol{\sigma}) = \mathbf{J}^T(\boldsymbol{\sigma})\mathbf{f}(\boldsymbol{\sigma}) = 0,$$

and from the first-order Taylor series expansion its recurrence relation is written as

$$\mathbf{0} = \Phi'\left(\boldsymbol{\sigma}^k\right) + \Phi''\left(\boldsymbol{\sigma}^k\right)\left(\boldsymbol{\sigma}^{k+1} - \boldsymbol{\sigma}^k\right)$$

or

$$\boldsymbol{\sigma}^{k+1} = \boldsymbol{\sigma}^k - \left[\Phi''\left(\boldsymbol{\sigma}^k\right)\right]^{-1}\Phi'\left(\boldsymbol{\sigma}^k\right).$$

Here, $\mathbf{J}(\boldsymbol{\sigma})$ is the Jacobian matrix of $\mathbf{U}(\boldsymbol{\sigma})$ defined as

$$[\mathbf{J}(\boldsymbol{\sigma})]_{ij} = [\mathbf{f}'(\boldsymbol{\sigma})]_{ij} = \left[\frac{\partial \mathbf{f}(\boldsymbol{\sigma})}{\partial \boldsymbol{\sigma}}\right]_{ij} = \left[\frac{\partial \mathbf{U}(\boldsymbol{\sigma})}{\partial \boldsymbol{\sigma}}\right]_{ij} = \frac{\partial U_i(\boldsymbol{\sigma})}{\partial \sigma_j} \in \Re^{P \times N}, \tag{12.61}$$

and $\Phi''(\boldsymbol{\sigma})$ is called the Hessian matrix $\mathbf{H}$ of Φ expressed as

$$\begin{aligned}\Phi''(\boldsymbol{\sigma}) &= \mathbf{H}(\boldsymbol{\sigma}) = [\mathbf{f}']^T[\mathbf{f}'] + [\mathbf{f}'']^T[\mathbf{I}_{n\times n}\otimes\mathbf{f}] \\ &= \mathbf{J}^T\mathbf{J} + \left[\nabla^2_{N\times N}\otimes\mathbf{f}^T\right]\left[\mathbf{I}_{N\times N}\otimes\mathbf{f}\right]\in\Re^{N\times N}.\end{aligned} \tag{12.62}$$

$\nabla^2_{N\times N}$ is the second-order partial differential operator whose entity is $[\nabla^2_{N\times N}]_{ij} = \frac{\partial^2}{\partial\sigma_i\partial\sigma_j}$, $\mathbf{I}_{N\times N}\in\Re^{N\times N}$ is the identity matrix, and $\otimes$ is the Kronecker product. In the Gauss–Newton method, the second-order derivative terms $\frac{\partial^2 f_k}{\partial\sigma_i\partial\sigma_j}f_k$ are ignored. That is, the Hessian is approximated as

$$\Phi''\left(\boldsymbol{\sigma}\right) = \mathbf{H}\approx\mathbf{J}^T\mathbf{J}\in\Re^{N\times N}. \tag{12.63}$$

Convergence of the Gauss–Newton method may not be guaranteed in all cases unless

$$\left|\frac{\partial^2 f_k}{\partial\sigma_i\partial\sigma_j}f_k\right| << \left|\frac{\partial f_k}{\partial\sigma_i}\frac{\partial f_k}{\partial\sigma_j}\right|,$$

This approximation is valid if the voltage difference f_k is small in magnitude, at least around the minimum, or the nonlinearity is not severe so that $\frac{\partial^2 f_k}{\partial\sigma_i\partial\sigma_j}$ is relatively small in magnitude. Consequently, the rate of convergence of the Gauss–Newton algorithm is at most quadratic.

In general, the number of unknowns in EIT is larger than the number of the current–voltage data sets, i.e., $N > M$, which means that the problem is ill-posed. In addition, the sensitivity of the boundary voltages with respect to the change of the conductivity in a certain pixel may be highly nonuniform and this leads to an ill-conditioning of the Hessian matrix. Hence, in practice, regularization is introduced to mitigate the ill-posed and ill-conditioned nature of the problem. The regularized cost functional is expressed as

$$\Phi(\boldsymbol{\sigma}) = \frac{1}{2}[\mathbf{U}(\boldsymbol{\sigma}) - \mathbf{V}]^T[\mathbf{U}(\boldsymbol{\sigma}) - \mathbf{V}] + \frac{\alpha}{2}[\mathbf{R}(\boldsymbol{\sigma} - \boldsymbol{\sigma}^*)]^T[\mathbf{R}(\boldsymbol{\sigma} - \boldsymbol{\sigma}^*)], \tag{12.64a}$$

where α is the regularization parameter and $\mathbf{R}\in\Re^{N\times N}$ is the regularization matrix; $\boldsymbol{\sigma}^*\in\Re^{N\times 1}$ is the prior information for the conductivity distribution if available (Hua, Webster, & Tompkins, 1988; Hua, Woo, Webster, & Tompkins, 1991; Vauhkonen, 1997).

Starting with an initial guess $\boldsymbol{\sigma}^0$ for the minimum, the Gauss–Newton method proceeds by the iterations

$$\boldsymbol{\sigma}^{k+1} = \boldsymbol{\sigma}^k - \left[\mathbf{J}^T\mathbf{J} + \alpha\mathbf{R}^T\mathbf{R}\right]^{-1}\left[\mathbf{J}^T(\mathbf{U}(\boldsymbol{\sigma}^k) - \mathbf{V}) + \alpha\mathbf{R}^T\mathbf{R}(\boldsymbol{\sigma} - \boldsymbol{\sigma}^*)\right] \tag{12.65}$$

with $[\mathbf{J}(\boldsymbol{\sigma}^k)]_{ij} = \frac{\partial U_i(\boldsymbol{\sigma}^k)}{\partial \sigma_j^k}$.

The Jacobian matrix can be obtained from the following identity:

$$\sum_{l=1}^{L}\left[U_{0,l}^{q}\int\limits_{e_l}\sigma\frac{\partial u^p}{\partial \nu}\,\mathrm{d}S - U_l^p\int\limits_{e_l}\sigma_0\frac{\partial u_0^q}{\partial \nu}\,\mathrm{d}S\right] = \int\limits_{\Omega}(\sigma-\sigma_0)\nabla u^p\cdot\nabla u_0^q\,\mathrm{d}\Omega, \tag{12.66}$$

which can be derived in a similar way used for Eqn (12.42) in ECT. From the boundary condition of the current injection, (Eqn 12.66) becomes

$$\sum_{l=1}^{L}\left[U_{0,l}^{q}I_l^p - U_l^pI_l^q\right] = \int\limits_{\Omega}(\sigma-\sigma_0)\nabla u^p\cdot\nabla u_0^q\,\mathrm{d}\Omega. \tag{12.67}$$

Note that even with the complete electrode model the above identity is the same. Assume that the same boundary condition is applied for both electric fields $u_0(x)$ under $\sigma_0(x)$ and $u(x)$ under $\sigma(x)$. If the conductivity $\sigma(x) = \sigma_0(x) + \delta\sigma_n\chi_{\Omega_n}(x)$ is perturbed, the potential and the electrode voltages are perturbed as $u^p = u_0^p + \delta u^p$ and $U_l^p = U_{0,l}^p + \delta U_l^p$. The perturbed equation is written as

$$\sum_{l=1}^{L}\left[U_{0,l}^{q}I_l^p - U_{0,l}^pI_l^q - \delta U_l^pI_l^q\right] = \delta\sigma_n\int\limits_{\Omega_n}\nabla u_0^p\cdot\nabla u_0^q\,\mathrm{d}\Omega + O\left(\delta\sigma_n^2\right).$$

Considering $\sum_{l=1}^{L}[U_{0,l}^qI_l^p - U_{0,l}^pI_l^q] = 0$, an equation for the Jacobian matrix can be formulated as

$$\sum_{l=1}^{L}\frac{\partial U_l^p}{\partial \sigma_n}I_l^q = -\int\limits_{\Omega_n}\nabla u_0^p\cdot\nabla u_0^q\,\mathrm{d}\Omega. \tag{12.68}$$

The right-hand side can be calculated for the reference conductivity distribution or the conductivity distribution at the previous iteration step. In practice, the right-hand side is calculated during the process of the finite element calculation for solving the governing equation, so that extra computations are not required.

12.3.5 Dynamic algorithms

For EIT image reconstruction, a number of boundary condition sets are applied and resulting electric signals are measured sequentially. To get one frame of image, this sequential process of data collection is needed, and it consumes time. If the internal configuration is stationary during the data collection, the measured data sets are for the same object. In process imaging, however, the internal configuration may be varying during the data collection since the process may proceed. Then, the measured data at each boundary condition cannot be assumed for the same internal configuration, and it is expected that the image reconstruction performance becomes worse as the characteristic time of the process becomes shorter than the data collection time (Bar-Shalom & Li, 1993; Kaipio & Somersalo, 1999; Kim et al., 2001). Compared to static imaging where the internal configuration is stationary during the data collection time required to acquire a frame of image, the dynamic imaging where the internal configuration is time-varying requires different approaches.

For the dynamic imaging, the Kalman filter algorithm and its variants are plausible (Khambampati, Rashid, Kim, Soleimani, & Kim, 2009; Kim et al., 2001, 2006; Trigo, Gonzalez-Lima, & Amato, 2004; Vauhkonen, Karjalainen, & Kaipio, 1998). The Kalman filter well known in the control theory was devised to estimate the state of a discrete-time-controlled process governed by the linear stochastic difference equation with measurements. The Kalman filter provides a recursive procedure to estimate the state based on the previous states and the measurements (Kim et al., 2001, 2006). In the sense of dynamic process, the conductivity (or permittivity) is considered as a state variable and evolving with time. And, at each time step (or data collection) a new set of measured data is available. Hence, the state transition model for the conductivity $\boldsymbol{\sigma} \in \Re^{N\times 1}$ in EIT can be written as (Kaipio, Karjalainen, Somersalo, & Vauhkonen, 1999; Kim et al., 2001; Seppanen, Vauhkonen, Somersalo, Kaipio, 2001)

$$\boldsymbol{\sigma}_k = \mathbf{F}_{k-1}\boldsymbol{\sigma}_{k-1} + \mathbf{w}_{k-1}, \tag{12.69}$$

with the measurement vector, or measured electrode voltage vector, $\mathbf{V} \in \Re^{P\times 1}$ such that

$$\mathbf{V}_k = U_k(\boldsymbol{\sigma}_k) + \mathbf{v}_k. \tag{12.70}$$

The subscript "k" denotes the time step. The state transition model $\mathbf{F}_k \in \Re^{N\times N}$ and the observation model U_k are determined from the physics of the problem considered. In the EIT problem, the conductivity evolution is governed by the motion of the substances within the problem domain. If we are imaging multiphase flows or mixing process, the flow field or the concentration distribution evolves according to physical laws, and proper physical models describing the evolution can be used as the transition model (Seppanen, Vauhkonen, Vauhkonen, Somersalo, Kaipio, 2001). In case such a model is not available, a so-called random work model is used; $\mathbf{F}_k$ is set to the identity matrix, which means that the state evolves randomly. The observation model can be the numerical solution of the governing equation. The random variables $\mathbf{w}_k \in \Re^{N\times 1}$ and $\mathbf{v}_k \in \Re^{P\times 1}$ denote the process and the measurement noise, respectively. They are assumed to be independent of each other, white, and with normal probability distributions:

$$p(\mathbf{w}_k) \sim N(0, \boldsymbol{Q}_k) \quad \text{and} \quad p(\mathbf{v}_k) \sim N(0, \overline{\mathbf{R}}_k), \tag{12.71}$$

where $\mathbf{Q}_k \in \Re^{N\times N}$ and $\overline{\mathbf{R}}_k \in \Re^{P\times P}$ are the process and the measurement noise covariance, respectively. Usually it is assumed that both state variables and measured data are independent of each other and both covariance matrices are diagonal matrices. Now, let us derive a recursive procedure to estimate $\boldsymbol{\sigma}_k$ with the previous states $\boldsymbol{\sigma}_1,\cdots,\boldsymbol{\sigma}_{k-1}$ and the measurements $\mathbf{V}_1,\cdots,\mathbf{V}_k$. Set $\boldsymbol{\sigma}_{k|k-1}\in\Re^{N\times 1}$ to be a priori state estimate at step k given the knowledge of the process up to step $k-1$, and $\boldsymbol{\sigma}_{k|k}\in\Re^{N\times 1}$ to be a posteriori state estimate at step k given the measurement $\mathbf{V}_k$. We linearize the observation model about a priori state estimate at step k, $\boldsymbol{\sigma}_{k|k-1}\in\Re^{N\times 1}$:

$$\begin{aligned}\mathbf{V}_k &= U_k\left(\boldsymbol{\sigma}_{k|k-1}\right) + \frac{\partial U_k\left(\boldsymbol{\sigma}_{k|k-1}\right)}{\partial\boldsymbol{\sigma}_k}\left(\boldsymbol{\sigma}_k - \boldsymbol{\sigma}_{k|k-1}\right) + \mathbf{v}_k + \mathbf{HOT} \\ &= \mathbf{V}_{k|k-1} + \mathbf{J}_k\left(\boldsymbol{\sigma}_k - \boldsymbol{\sigma}_{k|k-1}\right) + \mathbf{v}_k + \mathbf{HOT},\end{aligned} \tag{12.72}$$

where **HOT** denotes higher order terms. Let us define the pseudo-measurement $\mathbf{y}_k\in\Re^{P\times 1}$:

$$\mathbf{y}_k \equiv \mathbf{V}_k - U_k\left(\boldsymbol{\sigma}_{k|k-1}\right) + \mathbf{J}_k\boldsymbol{\sigma}_{k|k-1} = \mathbf{J}_k\boldsymbol{\sigma}_k + \tilde{\mathbf{v}}_k, \tag{12.73}$$

where $\tilde{\mathbf{v}}_k\in\Re^{P\times 1}$ is the pseudo-measurement noise $\tilde{\mathbf{v}}_k = \mathbf{v}_k + \mathbf{HOT}$ with zero mean and known covariance $\tilde{\mathbf{R}}_k\in\Re^{P\times P}$:

$$E\left[\tilde{\mathbf{v}}_k\right] = 0 \quad \text{and} \quad \tilde{\mathbf{R}}_k = \operatorname{cov}\left(\mathbf{v}_k + \mathbf{HOT}\right). \tag{12.74}$$

The Jacobians $\mathbf{J}_k\in\Re^{P\times N}$ will be defined as

$$\mathbf{J}_k = \frac{\partial U_k\left(\boldsymbol{\sigma}_{k|k-1}\right)}{\partial\boldsymbol{\sigma}_k}. \tag{12.75}$$

The *a priori* state estimate at step k, $\boldsymbol{\sigma}_{k|k-1}$, and the pseudo-measurement estimate at step k, $\mathbf{y}_{k|k}$, will be

$$\begin{aligned}\boldsymbol{\sigma}_{k|k-1} &= E\left[\boldsymbol{\sigma}_k\middle|\mathbf{y}_{k-1}\right] = E\left[\mathbf{F}_{k-1}\boldsymbol{\sigma}_{k-1} + \mathbf{w}_k\middle|\mathbf{y}_{k-1}\right] \\ &= \mathbf{F}_{k-1}\boldsymbol{\sigma}_{k-1|k-1}, = \mathbf{F}_{k-1}E\left[\boldsymbol{\sigma}_{k-1}\middle|\mathbf{y}_{k-1}\right]\end{aligned} \tag{12.76}$$

$$\mathbf{y}_{k|k} = E\left[\mathbf{y}_k\middle|\boldsymbol{\sigma}_k\right] = E[\mathbf{J}_k\boldsymbol{\sigma}_k + \tilde{\mathbf{v}}_k|\boldsymbol{\sigma}_k] = \mathbf{J}_k\boldsymbol{\sigma}_{k|k}. \tag{12.77}$$

The predicted error $\mathbf{e}_{k|k-1}\in\Re^{N\times 1}$ and its covariance $\mathbf{C}_{k|k-1}\in\Re^{N\times N}$ will be

$$\mathbf{e}_{k|k-1} = \boldsymbol{\sigma}_k - \boldsymbol{\sigma}_{k|k-1} = \mathbf{F}_{k-1}\mathbf{e}_{k-1|k-1} + \mathbf{w}_{k-1}, \tag{12.78}$$

$$\mathbf{C}_{k|k-1} = \operatorname{cov}\left(\mathbf{e}_{k|k-1}\right) = \mathbf{F}_{k-1}\mathbf{C}_{k-1|k-1}\mathbf{F}_{k-1}^T + \mathbf{Q}_{k-1}. \tag{12.79}$$

Let the updated state estimate $\boldsymbol{\sigma}_{k|k}$ be the state maximizing the probability density $\boldsymbol{\sigma}_k$ given $\mathbf{y}_k$

$$p\left(\boldsymbol{\sigma}_k \middle| \mathbf{y}_k\right) \sim p\left(\boldsymbol{\sigma}_k \middle| \mathbf{y}_{k-1}\right) p\left(\mathbf{y}_k \middle| \boldsymbol{\sigma}_k\right) \tag{12.80}$$

or minimizing the following cost functional that corresponds to the exponent of the probability density function

$$\Phi(\boldsymbol{\sigma}_k) = \|\boldsymbol{\sigma}_k - \boldsymbol{\sigma}_{k|k-1}\|_{\mathbf{C}_{k|k-1}^{-1}} + \left\|\mathbf{y}_k - \mathbf{J}_k\boldsymbol{\sigma}_k\right\|_{\tilde{\mathbf{R}}_k^{-1}}, \tag{12.81}$$

where $\|x\|_R = x^T Rx$. In case the regularization is considered, the cost functional will be of the form

$$\Phi(\boldsymbol{\sigma}_k) = \|\boldsymbol{\sigma}_k - \boldsymbol{\sigma}_{k|k-1}\|_{\mathbf{C}_{k|k-1}^{-1}} + \left\|\mathbf{y}_k - \mathbf{J}_k\boldsymbol{\sigma}_k\right\|_{\tilde{\mathbf{R}}_k^{-1}} + \alpha\|\mathbf{R}(\boldsymbol{\sigma}_k - \boldsymbol{\sigma}^*)\|, \tag{12.82}$$

where α is the regularization parameter and $\mathbf{R} \in \Re^{N \times N}$ is the regularization matrix; $\boldsymbol{\sigma}^* \in \Re^{N \times 1}$ is the prior information for the conductivity distribution if available. If we define the augmented pseudo-measurement $\tilde{\mathbf{y}}_k \in \Re^{(P+N) \times 1}$ and the augmented pseudo-observation matrix $\mathbf{H}_k \in \Re^{(P+N) \times N}$ as

$$\tilde{\mathbf{y}}_k = \begin{pmatrix} \mathbf{y}_k \\ \sqrt{\alpha}\mathbf{R}\boldsymbol{\sigma}^* \end{pmatrix} \quad \text{and} \quad \mathbf{H}_k = \begin{pmatrix} \mathbf{J}_k\left(\boldsymbol{\sigma}_{k|k-1}\right) \\ \sqrt{\alpha}\mathbf{R} \end{pmatrix}, \tag{12.83}$$

then the cost functional can be rearranged as

$$\Phi(\boldsymbol{\sigma}_k) = \left\|\boldsymbol{\sigma}_k - \boldsymbol{\sigma}_{k|k-1}\right\|_{\mathbf{C}_{k|k-1}^{-1}} + \left\|\tilde{\mathbf{y}}_k - \mathbf{H}_k\boldsymbol{\sigma}_k\right\|_{\boldsymbol{\Gamma}_k^{-1}}. \tag{12.84}$$

The augmented measurement model can be written as

$$\tilde{\mathbf{y}}_k = \mathbf{H}_k\boldsymbol{\sigma}_k + \gamma_k, \tag{12.85}$$

where the augmented measurement noise $\gamma_k \in \Re^{(P+N) \times 1}$ is assumed to have zero mean and its covariance $\boldsymbol{\Gamma}_k \in \Re^{(P+N) \times (P+N)}$ is a block diagonal matrix if the pseudo-measurement noise covariance $\tilde{\mathbf{R}}_k$ is a diagonal matrix:

$$E\left[\gamma_k\right] = 0 \quad \text{and} \quad \boldsymbol{\Gamma}_k \equiv \operatorname{cov}\left(\gamma_k\right) = \operatorname{Blockdiag}\left[\tilde{\mathbf{R}}_k, \mathbf{I}_{N \times N}\right]. \tag{12.86}$$

Then, by differentiating $\Phi(\boldsymbol{\sigma}_k)$ with respect to $\boldsymbol{\sigma}_k$ and setting it to zero,

$$\frac{\partial\Phi(\boldsymbol{\sigma}_k)}{\partial\boldsymbol{\sigma}_k} = \mathbf{C}_{k|k-1}^{-1}\left(\boldsymbol{\sigma}_k - \boldsymbol{\sigma}_{k|k-1}\right) - \mathbf{H}_k^T\boldsymbol{\Gamma}_k^{-1}\left(\tilde{\mathbf{y}}_k - \mathbf{H}_k\boldsymbol{\sigma}_k\right) = 0, \tag{12.87}$$

the updated state estimate $\boldsymbol{\sigma}_{k|k}$ is obtained as

$$\boldsymbol{\sigma}_{k|k} = \left(\mathbf{H}_k^T \boldsymbol{\Gamma}_k^{-1} \mathbf{H}_k + \mathbf{C}_{k|k-1}^{-1}\right)^{-1} \left(\mathbf{H}_k^T \boldsymbol{\Gamma}_k^{-1} \tilde{\mathbf{y}}_k + \mathbf{C}_{k|k-1}^{-1} \boldsymbol{\sigma}_{k|k-1}\right). \tag{12.88}$$

On the other hand, the augmented measurement error $\boldsymbol{\varepsilon}_k \in \Re^{P\times 1}$ and its covariance $\mathbf{S}_k \in \Re^{P\times P}$ are

$$\boldsymbol{\varepsilon}_k = \tilde{\mathbf{y}}_k - \tilde{\mathbf{y}}_{k|k-1} = \tilde{\mathbf{y}}_k - \mathbf{H}_k \boldsymbol{\sigma}_{k|k-1} = \mathbf{H}_k \mathbf{e}_{k|k-1} + \boldsymbol{\gamma}_k, \tag{12.89}$$

$$\mathbf{S}_k = \operatorname{cov}(\boldsymbol{\varepsilon}_k) = \mathbf{H}_k \mathbf{C}_{k|k-1} \mathbf{H}_k^T + \boldsymbol{\Gamma}_k. \tag{12.90}$$

If we set the posterior estimate as a linear combination of the prior estimate $\boldsymbol{\sigma}_{k|k-1}$ and the weighted measurement residual of $\boldsymbol{\varepsilon}_k$

$$\boldsymbol{\sigma}_{k|k} = \boldsymbol{\sigma}_{k|k-1} + \mathbf{K}_k \boldsymbol{\varepsilon}_k = \boldsymbol{\sigma}_{k|k-1} + \mathbf{K}_k \left(\tilde{\mathbf{y}}_k - \mathbf{H}_k \boldsymbol{\sigma}_{k|k-1}\right), \tag{12.91}$$

where $\mathbf{K}_k \in \Re^{N\times P}$ is the Kalman gain. The Kalman gain can be determined by minimizing the a posteriori error covariance of the a posteriori estimate error:

$$\begin{aligned} \mathbf{e}_{k|k} &= \boldsymbol{\sigma}_k - \boldsymbol{\sigma}_{k|k} = \boldsymbol{\sigma}_k - \boldsymbol{\sigma}_{k|k-1} - \mathbf{K}_k \left(\tilde{\mathbf{y}}_k - \tilde{\mathbf{y}}_{k|k-1}\right) \\ &= \mathbf{e}_{k|k-1} - \mathbf{K}_k \left(\mathbf{H}_k \mathbf{e}_{k|k-1} + \boldsymbol{\gamma}_k\right) = \left(\mathbf{I} - \mathbf{K}_k \mathbf{H}_k\right) \mathbf{e}_{k|k-1} - \mathbf{K}_k \boldsymbol{\gamma}_k. \end{aligned} \tag{12.92}$$

Its covariance will be

$$\begin{aligned} \mathbf{C}_{k|k} &= \left(\mathbf{I} - \mathbf{K}_k \mathbf{H}_k\right) \mathbf{C}_{k|k-1} (\mathbf{I} - \mathbf{K}_k \mathbf{H}_k)^T + \mathbf{K}_k \boldsymbol{\Gamma}_k \mathbf{K}_k^T \\ &= \left(\mathbf{I} - \mathbf{K}_k \mathbf{H}_k\right) \mathbf{C}_{k|k-1}, \end{aligned} \tag{12.93}$$

so that from $\frac{\partial \mathbf{C}_{k|k}}{\partial \mathbf{K}_k} = 0$ we can have the Kamlan gain as

$$\mathbf{K}_k = \mathbf{C}_{k|k-1} \mathbf{H}_k^T \left(\mathbf{H}_k \mathbf{C}_{k|k-1} \mathbf{H}_k^T + \boldsymbol{\Gamma}_k\right)^{-1} = \mathbf{C}_{k|k-1} \mathbf{H}_k^T \mathbf{S}_k^{-1}. \tag{12.94}$$

With the Kalman gain the covariance becomes

$$\mathbf{C}_{k|k} = \left(\mathbf{I} - \mathbf{K}_k \mathbf{H}_k\right) \mathbf{C}_{k|k-1}, \tag{12.95}$$

Finally, a full set of recursive equations to estimate the state variable is as follows:

Time update equations

$$\text{Predicted } (\textit{a priori}) \text{ state : } \boldsymbol{\sigma}_{k|k-1} = \mathbf{F}_{k-1}\boldsymbol{\sigma}_{k-1|k-1} \tag{12.96}$$

$$\text{Predicted } (\textit{a priori}) \text{ error covariance : } \mathbf{C}_{k|k-1} = \mathbf{F}_{k-1}\mathbf{C}_{k-1|k-1}\mathbf{F}_{k-1}^{T} + \mathbf{Q}_{k-1} \tag{12.97}$$

$$\text{Jacobian : } \mathbf{J}_k = \frac{\partial U_k\left(\boldsymbol{\sigma}_{k|k-1}\right)}{\partial \boldsymbol{\sigma}_k} \tag{12.98}$$

$$\text{Augmented observation model} \quad \tilde{\mathbf{y}}_k = \begin{pmatrix} \mathbf{y}_k \\ \sqrt{\alpha}\mathbf{R}\boldsymbol{\sigma}^* \end{pmatrix}, \quad \mathbf{H}_k = \begin{pmatrix} \mathbf{J}_k\left(\boldsymbol{\sigma}_{k|k-1}\right) \\ \sqrt{\alpha}\mathbf{R} \end{pmatrix} \tag{12.99}$$

$$\text{Augmented measurement noise covariance : } \boldsymbol{\Gamma}_k = \text{Blockdiag}\left[\tilde{\mathbf{R}}_k, \mathbf{I}_{N\times N}\right] \tag{12.100}$$

$$\text{Predicted measurement error : } \boldsymbol{\varepsilon}_k = \tilde{\mathbf{y}}_k - \mathbf{H}_k\boldsymbol{\sigma}_{k|k-1} \tag{12.101}$$

$$\text{Predicted measurement error covariance : } \mathbf{S}_k = \mathbf{H}_k\mathbf{C}_{k|k-1}\mathbf{H}_k^{T} + \boldsymbol{\Gamma}_k \tag{12.102}$$

Measurement update equations

$$\text{Kalman gain : } \mathbf{K}_k = \mathbf{C}_{k|k-1}\mathbf{H}_k^{T}\mathbf{S}_k^{-1} \tag{12.103}$$

$$\text{Updated } (\textit{a posteriori}) \text{ state : } \boldsymbol{\sigma}_{k|k} = \boldsymbol{\sigma}_{k|k-1} + \mathbf{K}_k\boldsymbol{\varepsilon}_k \tag{12.104}$$

$$\text{Updated } (\textit{a posteriori}) \text{ error covariance : } \mathbf{C}_{k|k} = \left(\mathbf{I} - \mathbf{K}_k\mathbf{H}_k\right)\mathbf{C}_{k|k-1} \tag{12.105}$$

12.4 Diffraction tomography

12.4.1 Mathematical formulation of diffraction tomography

Diffraction is related to spreading of waves upon interaction with an object in the medium. Diffraction tomography is an inverse scattering technique to reconstruct the object characteristics from the scattered field data measured at the receiver locations. Diffraction tomography considers both scattering as well as absorption effects, whereas in transmission tomography absorption effect is assumed to be dominant. The power or energy of X- or γ-ray used in transmission tomography techniques is very high; therefore, the ray path can be regarded as a straight line. Ultrasound and microwave imaging involves transmitting low power, nonionizing waves to propagate through the medium; therefore, the path may not be straight and they come under the category of diffraction tomography (Figure 12.8). Ultrasound imaging uses a transducer that converts the excited electrical signal into mechanical disturbance (pressure wave), and vice versa. In ultrasound imaging, attenuation coefficient, sound speed, and reflection coefficient are estimated from the measured scattered field at the receivers. On the other hand, microwave imaging consists of an antenna that converts the electrical signal into low power electromagnetic microwaves, and vice versa. Complex permittivity distribution is reconstructed from the received scattered microwaves that give us the spatial distribution within the medium. As ultrasound and microwaves get refracted and diffracted while passing through the objects, more sophisticated algorithms as compared to transmission tomography are required. Here, the reconstruction algorithms that are usually used in diffraction tomography are discussed.

If the object is relatively large and has a small refractive index, then it can be assumed that the waves generated from ultrasound or microwave travel in a straight line after interaction with the object. In that case, the Fourier slice theorem that was discussed in Section 12.2.3 can be used to reconstruct the refractive index (Greenleaf, Johnson, Lee, Herman, & Wood, 1974). However, for the case when the transmitted waves undergo refraction and diffraction, methods based on ray tracing (Andersen & Kak, 1982; Mueller, Kaveh, & Wade, 1979) and solving wave equations are usually employed. Ray tracing methods that consider only refraction of waves are not so accurate, especially when the change in refractive index is more than 10% (Andersen & Kak, 1984). Methods based on solving wave equations are more accurate and are considered in solving the diffraction tomography problem.

Consider a plane wave insonified on the object such that the propagation of waves can be modeled with Helmholtz's wave equation. For a loss-free object, with a

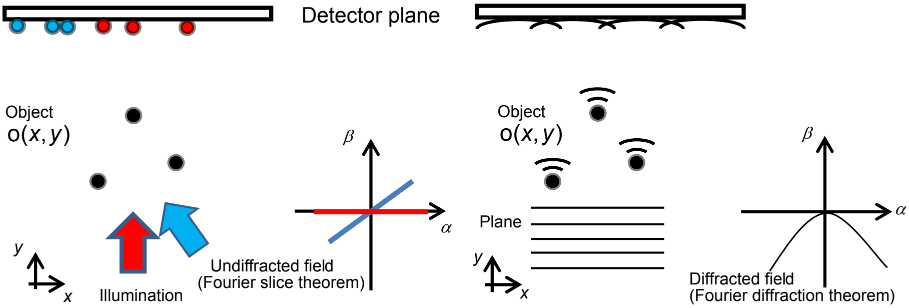

Figure 12.8 Schematic diagram that explains the difference between transmission and diffraction tomography.

constant density, the waves transmitted with field magnitude $u(\mathbf{r})$ and wave number $k(\mathbf{r})$ satisfies Helmholtz's equation:

$$\left[\nabla^2 + k^2(\mathbf{r})\right]u(\mathbf{r}) = 0, \tag{12.106}$$

where the wave number $k(\mathbf{r})$ with respect to position $\mathbf{r}$ is defined as

$$k(\mathbf{r}) = \frac{2\pi}{\lambda} = \frac{2\pi\omega}{c}, \tag{12.107}$$

where ω is the temporal frequency, λ, c, are the field wavelength and velocity, respectively. For acoustic or ultrasound tomography, the field $u(\mathbf{r})$ is the pressure field, and for microwave tomography, it is the complex amplitude of electric field. In homogeneous conditions, the complex wave number is constant, i.e., $k(\mathbf{r}) = k_0$, therefore, the wave Eqn (12.106) becomes

$$\left[\nabla^2 + k_0^2\right]u(\mathbf{r}) = 0. \tag{12.108}$$

rewriting Eqn (12.106) as

$$\left[\nabla^2 + k_0^2\right]u(\mathbf{r}) = -\left[k^2(\mathbf{r}) - k_0^2\right]u(\mathbf{r}). \tag{12.109}$$

In the propagation of electromagnetic waves, if the polarization effects are neglected, the wave number is related to complex refractive index $n(\mathbf{r})$ given by

$$k(\mathbf{r}) = k_0 n(\mathbf{r}) = k_0[1 + n_\delta(\mathbf{r})], \tag{12.110}$$

where $n_\delta(\mathbf{r})$ is the deviation from the average refractive index. The electromagnetic refractive index is defined as (Kak, 1984)

$$n(\mathbf{r}) = \sqrt{\frac{\mu(\mathbf{r})\varepsilon(\mathbf{r})}{\mu_0\varepsilon_0}}, \tag{12.111}$$

where $\mu(\mathbf{r})$ and $\varepsilon(\mathbf{r})$ are the spatially varying magnetic permeability and permittivity inside the object and μ_0, ε_0 correspond to the homogeneous medium. Also, in ultrasound, the complex refractive index is defined as the ratio of propagation velocity of the medium in which an object is immersed to the spatially varying velocity in the object $c(\mathbf{r})$, i.e., (Kak, 1984)

$$n(\mathbf{r}) = \frac{c_0}{c(\mathbf{r})}. \tag{12.112}$$

The general wave equation that can be modeled for both ultrasound and microwave tomography can be written as

$$\left[\nabla^2 + k_0^2\right] u(\mathbf{r}) = -k_0^2 \left[n(\mathbf{r})^2 - 1\right] u(\mathbf{r}). \tag{12.113}$$

Substituting, $n(\mathbf{r}) = [1 + n_\delta(\mathbf{r})]$ in the right-hand side of Eqn (12.113) and neglecting the higher order terms, considering $n_\delta(\mathbf{r}) << 1$, we have

$$\left[\nabla^2 + k_0^2\right] u(\mathbf{r}) = -2k_0^2 n_\delta(\mathbf{r}) u(\mathbf{r}). \tag{12.114}$$

Defining, the object function, $o(\mathbf{r}) = -2k_0^2 n_\delta(\mathbf{r})$, the above equation is simplified as

$$\left[\nabla^2 + k_0^2\right] u(\mathbf{r}) = -o(\mathbf{r}) u(\mathbf{r}). \tag{12.115}$$

Let us consider the field $u(\mathbf{r})$ is composed of incident field $u_0(\mathbf{r})$ without any inhomogeneities and scattered field $u_s(\mathbf{r})$ due to the presence of inhomogeneities:

$$u(\mathbf{r}) = u_0(\mathbf{r}) + u_s(\mathbf{r}). \tag{12.116}$$

Substituting Eqn (12.116) into Eqn (12.115) we have the inhomogeneous wave equation for scattered field:

$$\left[\nabla^2 + k_0^2\right] u_s(\mathbf{r}) = -o(\mathbf{r}) u(\mathbf{r}). \tag{12.117}$$

The inhomogeneous Helmholtz wave equation given above cannot be solved directly for scattered field, rather its solution can be obtained in terms of Green's function (Morse & Feshbach, 1953):

$$\left[\nabla^2 + k_0^2\right] g(\mathbf{r}|\mathbf{r}') = -\delta(\mathbf{r} - \mathbf{r}'). \tag{12.118}$$

The solution of two-dimensional Helmholtz equation can be expressed in terms of zero-order Henkel function of first kind, i.e.,

$$g(\mathbf{r}|\mathbf{r}') = \frac{j}{4} H_0^1(k_0 R). \tag{12.119}$$

with

$$R = |\mathbf{r} - \mathbf{r}'|. \tag{12.120}$$

The forcing function on the right-hand side of Eqn (12.117) can be considered as summation of an array of impulses:

$$o(\mathbf{r})u(\mathbf{r}) = \int o(\mathbf{r}')u(\mathbf{r}')\delta(\mathbf{r} - \mathbf{r}')\mathrm{d}\mathbf{r}'. \tag{12.121}$$

Performing simple convolution, the total radiation from all sources on the right-hand side of Eqn (12.115) is given by the following superposition:

$$u_{\mathrm{s}}(\mathbf{r}) = \int g(\mathbf{r} - \mathbf{r}')o(\mathbf{r}')u(\mathbf{r}')\mathrm{d}\mathbf{r}'. \tag{12.122}$$

The solution to the scattered field given in Eqn (12.122) is not straightforward as it is nonlinear. Approximation methods based on perturbation methods are usually used and are discussed in the following subsections.

12.4.2 Born and Rytov approximations for weakly scattered objects

In this section, approximation methods called Born and Rytov are formulated that provide the solution for the scattered field (Iwata & Nagata, 1974; Kaveh, Soumekh, & Muller, 1982). They serve the basis for the Fourier diffraction theorem that will be discussed in the next subsection. First, we will formulate the solution for the scattered field using the Born approximation. Recalling that the definition of total field, which is the sum of incident field and scattered field, and substituting in Eqn (12.122), we have (Born & Wolf, 1999; Kak & Slaney, 1988; Oppengeim & Schafer, 1975):

$$u_{\mathrm{s}}(\mathbf{r}) = \int g(\mathbf{r} - \mathbf{r}')o(\mathbf{r}')u_0(\mathbf{r}')\mathrm{d}\mathbf{r}' + \int g(\mathbf{r} - \mathbf{r}')o(\mathbf{r}')u_{\mathrm{s}}(\mathbf{r}')\mathrm{d}\mathbf{r}'. \tag{12.123}$$

If the scattered field effect is very small as compared to the incident field, then the above equation for scattered field is called as Born scattered field, which is given by

$$u_{\mathrm{s}}(\mathbf{r}) \cong u_{\mathrm{B}}(\mathbf{r}) = \int g(\mathbf{r} - \mathbf{r}')o(\mathbf{r}')u_0(\mathbf{r}')\mathrm{d}\mathbf{r}'. \tag{12.124}$$

This Born approximation is valid when the magnitude of scattered field is less as compared to incident field (Born & Wolf, 1999; Newton, 1966).

In formulating a solution using Rytov approximation, first let us consider that the total field is represented by complex phase Ψ (Ishimaru, 1978):

$$u(\mathbf{r}) = e^{\Psi(\mathbf{r})}, \tag{12.125}$$

and the total phase is equal to incident phase function and scattered phase function

$$\Psi(\mathbf{r}) = \Psi_0(\mathbf{r}) + \Psi_{\mathrm{s}}(\mathbf{r}), \tag{12.126}$$

where

$$u_0(\mathbf{r}) = e^{\Psi_0(\mathbf{r})}. \tag{12.127}$$

Using the above relation in the wave equation, we can get

$$\left[\nabla^2 + k_0^2\right] u_0 \Psi_s = -u_0\left[(\nabla\Psi_s)^2 - o(\mathbf{r})\right]. \tag{12.128}$$

The solution to this equation can be represented in terms of Green's function, similar to before:

$$u_0\Psi_s = \int g(\mathbf{r}-\mathbf{r}')u_0\left[(\nabla\Psi_s)^2 - o(\mathbf{r}')\right]\mathrm{d}\mathbf{r}'. \tag{12.129}$$

Using the Rytov approximation, the terms in the brackets are approximated as

$$(\nabla\Psi_s)^2 - o(\mathbf{r}) \cong -o(\mathbf{r}). \tag{12.130}$$

Under the above approximation, the first-order Rytov approximation for scattered phase is

$$\Psi_s(\mathbf{r}) = \frac{1}{u_0(\mathbf{r})}\int g(\mathbf{r}-\mathbf{r}')u_0(\mathbf{r}')o(\mathbf{r}')\mathrm{d}\mathbf{r}'. \tag{12.131}$$

From the Born approximation for scattered field, Eqn (12.124), the above equation can have the form

$$\Psi_s = \frac{u_B(\overrightarrow{\mathbf{r}})}{u_0(\overrightarrow{\mathbf{r}})}. \tag{12.132}$$

Although, it appears that both Born and Rytov solutions look similar, they are obtained using different approximations.

Note that the Born approximation produces a better estimate of the scattered amplitude for large deviations in the refractive index for objects small in size. On the other hand, the Rytov approximation gives a more accurate estimate of the scattered phase for large-sized objects with small deviations in refractive index (Andersen and Kak, 1984; Keller, 1969). If the object is small and the refractive index of the object has less deviation from background, both Born and Rytov approximations result in same solution.

12.4.3 Fourier diffraction theorem

The Fourier diffraction theorem relates the measured diffracted projections to the Fourier transform of the object function. Fourier diffraction theorem serves as the main basis for the formulation of the reconstruction methods in diffraction tomography. The theorem states that when an object is illuminated with a plane wave, the Fourier transform of the forward-scattered data measured at receiver plane TT′ gives us 2D Fourier transform of object function $O(\omega_1,\omega_2)$ over a semicircular arc in frequency domain. The object function can then be recovered from the Fourier inversion. It is only valid for weakly scattering objects. Next, theoretical procedure to formulate the Fourier diffraction theorem is discussed.

First, let us consider the scattered field of the object due to incidence of plane wave from the Born approximation, which is given by

$$u_{\mathrm{s}}(\mathbf{r}) \cong u_{\mathrm{B}}(\mathbf{r}) = \int g(\mathbf{r}-\mathbf{r}')o(\mathbf{r}')u_0(\mathbf{r}')\mathrm{d}\mathbf{r}'. \tag{12.124a}$$

Let us define the Fourier transform pairs for terms in the above equation.

$$\widehat{F}[o(\mathbf{r})] = O(\boldsymbol{\Lambda}), \quad \widehat{F}[g(\mathbf{r})] = G(\boldsymbol{\Lambda}), \text{ and } \widehat{F}[u(\mathbf{r})] = U(\boldsymbol{\Lambda}). \tag{12.133}$$

The scattered field from the first-order Born equation can be considered as convolution of Green's function $g(\mathbf{r}-\mathbf{r}')$ and the product of object function $o(\mathbf{r}')$ and incident field $u_0(\mathbf{r}')$. The Born equation for scattered field can be written in terms of the Fourier transform pairs as

$$U_{\mathrm{S}}(\boldsymbol{\Lambda}) = G(\boldsymbol{\Lambda})\{O(\boldsymbol{\Lambda}) * U_0(\boldsymbol{\Lambda})\}, \tag{12.134}$$

where $\boldsymbol{\Lambda} = (\alpha,\gamma)$, and (α,γ) are the spatial frequencies along x and y directions, respectively. Considering a plane wave of incident field $u_0(\mathbf{r}) = e^{j\mathbf{K}\cdot\mathbf{r}}$ and recalling

$$G(\boldsymbol{\Lambda}|\mathbf{r}') = \frac{e^{-j\boldsymbol{\Lambda}\cdot\mathbf{r}'}}{\Lambda^2 - k_0^2}, \tag{12.135}$$

the scattered field in Eqn (12.135) becomes

$$U_{\mathrm{S}}(\boldsymbol{\Lambda}) = 2\pi\frac{O(\boldsymbol{\Lambda}-\mathbf{K})}{\Lambda^2 - k_0^2}. \tag{12.136}$$

From Eqn (12.119), it can be noticed that Green's function has singularity at the origin in the space domain, therefore the function is approximated by two-dimensional average of values near the singularity. Also, the Fourier transform representation of Green's function can be interpreted such that the point scatter acts as both source and sink waves. If only the outgoing waves are considered, then it is considered as transmission diffraction tomography; in other cases, the waves traveling inward are related with reflection diffraction tomography.

To evaluate the measured scattered field at the receiver line l_0, let us consider a plane wave traveling along the positive y direction, i.e., $\mathbf{K} = (0,k_0)$. The scattered field measured at receiver line $y = l_0$ is computed from the inverse Fourier transform:

$$u_s(x, y = l_0) = \frac{1}{4\pi^2} \int_{-\infty}^{\infty} \int_{-\infty}^{\infty} U_s(\mathbf{\Lambda}) e^{j\mathbf{\Lambda}\cdot\overrightarrow{\mathbf{r}}} \mathrm{d}\alpha \mathrm{d}\gamma$$
$$= \frac{1}{4\pi^2} \int_{-\infty}^{\infty} \int_{-\infty}^{\infty} \frac{O(\alpha, \gamma - k_0)}{\alpha^2 + \gamma^2 - k_0^2} e^{j(\alpha x + \beta l_0)} \mathrm{d}\alpha \mathrm{d}\gamma. \tag{12.137}$$

The integration of the above expression with γ for a given α has singularity at

$$\gamma = \pm\sqrt{k_0^2 - \alpha^2}. \tag{12.138}$$

Performing contour integration along the circular arc with respect to γ results in

$$u_s(x, y) = \frac{1}{2\pi} \int \Gamma_1(\alpha, y) e^{j\alpha x} \mathrm{d}\alpha + \frac{1}{2\pi} \int \Gamma_2(\alpha, y) e^{j\alpha x} \mathrm{d}\alpha, \tag{12.139}$$

where

$$\Gamma_1(\alpha, y) = \frac{jO\left(\alpha, \sqrt{k_0^2 - \alpha^2} - k_0\right)}{2\sqrt{k_0^2 - \alpha^2}} e^{j\sqrt{k_0^2 - \alpha^2} l_0}, \tag{12.140}$$

$$\Gamma_2(\alpha, y) = \frac{-jO\left(\alpha, \sqrt{k_0^2 - \alpha^2} - k_0\right)}{2\sqrt{k_0^2 - \alpha^2}} e^{-j\sqrt{k_0^2 - \alpha^2} l_0}. \tag{12.141}$$

Note that only the waves that satisfy the condition $\alpha^2 + \gamma^2 = k_0^2$ are considered. In the above expression, the solution $\Gamma_1(\alpha,y)$ represents the solution for transmission diffraction tomography for outgoing waves:

$$u_s(x, y) = \frac{1}{2\pi} \int \Gamma_1(\alpha, y) e^{j\alpha x} \mathrm{d}\alpha, \quad y > \text{object}. \tag{12.142}$$

If the receiver location is less than the y coordinates of the object, then the solution $\Gamma_2(\alpha,y)$ represents the solution for reflection diffraction tomography:

$$u_s(x, y) = \frac{1}{2\pi} \int \Gamma_2(\alpha, y) e^{j\alpha x} \mathrm{d}\alpha, \quad y < \text{object}. \tag{12.143}$$

This is called the Fourier diffraction theorem or generalized Fourier slice theorem (Devaney, 2012; Kak & Slaney, 1988; Mueller, Kaveh, & Wade, 1979; Soumekh, Kaveh, & Mueller, 1984). Using the Fourier diffraction theorem, it is possible to estimate the object function distribution from the measured scattered field. In the following subsection, some reconstruction methods using the Fourier diffraction theorem are discussed.

12.4.4 Image reconstruction methods for weakly scattering objects

Using the Fourier diffraction theorem the diffracted projections are related to the Fourier transform of the object along the semicircular arc $(\gamma = \pm\sqrt{k_0^2 - \alpha^2})$. To estimate the object function from the measured scattered fields, there are two interpolation methods using frequency and space domain. Frequency domain methods are fast and use direct Fourier inversion to estimate the object function (Devaney, 1982; Mueller et al., 1979; Pan & Kak, 1983; Soumekh et al., 1984). Space domain methods are similar to back projection techniques for transmission tomography but they are computationally intensive (Devaney, 1982; Pan & Kak, 1983; Rouseff & Winters, 1994).

12.4.5 Image reconstruction methods for highly scattering objects

Diffraction tomography, which involves diffraction mostly, provides good reconstruction using first-order Born or Rytov approximations for weakly scattering objects. The use of first-order Born or Rytov approximations based on perturbation theory is not plausible when the size of the object and change in refractive index are large. Methods based on perturbation only can be used when the change in refractive index is less than 10%. However, in general, for industrial and medical applications the contrast between the objects may be high, therefore involving more scattering than diffraction. Hence, the problem of reconstructing the properties for a high scattering object is termed as an inverse scattering problem. Formulation of a direct method to solve for the exact Helmholtz wave equation could allow imaging of objects with large attenuation and change in index of refraction. The relationship between the scattered field and the scattering object is nonlinear, and, moreover, multiple scattering increases the nonlinearity of the problem.

Let us consider again the expression of the field:

$$u(\mathbf{r}) = u_0(\mathbf{r}) + \int g(\mathbf{r} - \mathbf{r}')o(\mathbf{r}')u(\mathbf{r}')\mathrm{d}\mathbf{r}'. \tag{12.144}$$

To solve the above equation for high scattering problem, usually numerical methods are employed and the method of moment (MOM) is commonly used (Colton & Kress, 1998; Conte & de Boor, 1980; Gibson, 2008). In MOM, the unknowns are approximated as a linear combination of known basis functions $f_n(\mathbf{r})$ with unknown coefficients such as (Gibson, 2008; Harrington, 1968):

$$u(\mathbf{r}) = \sum_{n=1}^{N} u_n f_n(\mathbf{r}) \quad \text{and} \quad o(\mathbf{r}) = \sum_{n=1}^{N} o_n f_n(\mathbf{r}). \tag{12.145}$$

Two known functions, $u_0(\mathbf{r})$ and $u_s(\mathbf{r})$, are also approximated in the same way. Usually, due to the nonlinearity, the solution is obtained in two steps, and in each step the equation is assumed to be linear:

$$\begin{aligned} u_0(\mathbf{r}) &= u(\mathbf{r}) - \int g(\mathbf{r}-\mathbf{r}')o(\mathbf{r}')u(\mathbf{r}')\mathrm{d}\mathbf{r}', \\ u_s(\mathbf{r}) &= \int g(\mathbf{r}-\mathbf{r}')o(\mathbf{r}')u(\mathbf{r}')\mathrm{d}\mathbf{r}'. \end{aligned} \tag{12.146}$$

Evaluating the above equations at discrete M locations, we can construct two sets of linear equations (Devaney, 2012; Haddadin & Ebbini, 1998; Wang & Chew, 1989):

$$\mathbf{u}_0 = \mathbf{P}\mathbf{u} \quad \text{and} \quad \mathbf{u}_s = \mathbf{Q}\mathbf{o} \tag{12.147}$$

where

$$P_{m,n} = \delta_{mn} - \int g(\mathbf{r}_m - \mathbf{r}')o(\mathbf{r}')f_n(\mathbf{r}')\mathrm{d}\mathbf{r}', \quad m,n = 1,\cdots,N, \tag{12.148}$$

$$Q_{m,n} = \int g(\mathbf{r}_m - \mathbf{r}')f_n(\mathbf{r}')u(\mathbf{r}')\mathrm{d}\mathbf{r}, \quad m = 1,2,\cdots,M; \; n = 1,2,\cdots,N. \tag{12.149}$$

One of the simplest ways to solve the incident and scattered field is the Born iterative method (Chew & Wang, 1990; Haddadin & Ebbini, 1998; Tsihrintzis & Devaney, 2000; Wang & Chew, 1989), in which with the initial guess for the total field $u(\mathbf{r}) = u_0(\mathbf{r})$ and the object function $o(\mathbf{r})$ is evaluated by solving $\mathbf{u}_s = \mathbf{Q}\mathbf{o}$, then $\mathbf{P}$ and $\mathbf{u}$ are computed. This procedure is repeated until convergence. Also, the problem can be converted into a minimization problem by defining the cost function as

$$\Phi = \frac{1}{2}\|\mathbf{Q}\mathbf{o} - \mathbf{u}_s\|^2 \tag{12.150}$$

and any optimization algorithms used for ET can be used to solve the field (Caorsi, Gragnani, & Pastorino, 1990; Franchois & Pichot, 1997; Haddadin & Ebbini, 1998; Joachimowicz, Pichot, & Hugonin, 1991; Tsihrintzis and Devaney, 2000; Wang & Chew, 1989).

12.5 Future trends

Tomography helps us to know about the distribution of the substance properties in the domain of interest, thus it provides valuable information about the actual process. Various tomography technologies use different interaction phenomena between penetrating wave and medium to generate tomograms. For the same physical process, using different tomography techniques would result in distribution of different properties, which depend on the type of interaction. The different property distributions combined together would give us better understanding of the process. Fusion of two or more different techniques has attracted the scientific community and is the current hot topic for imaging. However, the application of these systems requires efficient mathematical formulations that depict the process phenomenon.

In imaging objects that are varying in space with respect to time, if their kinematic behavior can be represented using available constraints and used in the mathematical formulation this can give us additional prior information about the process. Also, in tomography reconstruction problems there is a lot of prior information needed to get satisfactory results. However, in real situations, the prior information available is limited, therefore there is still the need to develop efficient inverse algorithms that can tackle the ill-posed nature. Moreover, the existing tomography systems that are developed for industry-use static image reconstruction algorithms. Although data acquisition is very fast with the current measurement hardware, in some applications that involve fast transient behavior such as two- or multiphase flows, there is a need for dynamic algorithms that use limited data to reconstruct the image. Although the dynamic algorithms have been studied for many years, they are not used in image reconstruction in real-time monitoring due to the challenges they pose in computational complexity.

In most of the tomography methods, the forward and inverse problem is associated with nonlinear behavior. To solve the nonlinear forward problem, numerical methods such as finite element method and boundary element method are usually employed to solve the partial differential equations and the MOMs for integral equations. All these numerical techniques involve discretizing the domain, and the level of discretization has a significant effect on the image quality. Also, these domain or boundary discretization methods are of high computational complexity, especially, for 3D cases. Meshless methods that do not require any mesh or boundary integration can be an alternative. Mathematical formulation using meshless methods can improve the computational complexity and also be applicable in a number of applications where a complex-shaped boundary or moving boundary is involved.

12.6 Further useful information

This chapter primarily contains mathematical concepts for three modes of tomography techniques. Radon transform forms the main idea in realizing the tomography imaging (Radon, 1917). Fourier transform is used to reconstruct the projected data

(Bracewell & Riddle, 1967). Fourier slice theorem relates the projected data to the unknown field (Kak & Slaney, 1988). Computerized tomography is also discussed in Natterer (1986). Filtered back projection method offers better reconstruction performance compared to direct projection (Natterer 1986; Kak & Slaney, 1988). Matrix-based methods known as algebraic reconstruction technique are used to solve large sets of linear equations (Bender et al., 1970; Herman, 1980; Strohmer & Vershynin, 2009).

Maxwell equations are used to derive the governing equations for ET (Holder, 2004; Webster, 1990). Different electrode models used in ET are discussed in Cheng et al. (1989). Forward problem is usually solved using finite element method (Vauhkonen, 1997). Various kinds of regularization methods are used to reduce the ill-posedness (Vauhkonen, 1997). Static imaging is done using whole frame of data (Yorkey et al., 1987) and in dynamic imaging, only a few measurements are available (Khambampati et al., 2009; Kim et al., 2001; Vaukhonen et al., 1998).

In diffraction tomography, wave equations are solved using perturbation methods based on Born and Rytov for weakly scattered media (Born & Wolf, 1999; Iwata & Nagata, 1974). Fourier diffraction theorem and filtered back propagation theorem are similar in concept to transmission tomography (Devaney, 1982). For a highly scattering medium, numerical methods based on MOM are used (Gibson, 2008; Harrington, 1968). The inverse scattering problem is formulated and solved in the same way as ET problem (Chew & Wang, 1990).

References

Adler, A., Arnold, Bayford, Borsic, Brown, & Dixon. (2009). GREIT: a unified approach to 2D linear EIT reconstruction of lung images. *Physiological Measurement, 30*, S35.

Adler, A., Dai, T., & Lionheart, W. R. B. (2007). Temporal image reconstruction in electrical impedance tomography. *Physiological Measurement, 28*, S1−S11.

Andersen, A. H., & Kak, A. C. (1982). Digital ray tracing in two dimensional refractive fields. *Journal of Acoustical Society of America, 72*, 1593−1606.

Andersen, A. H., & Kak, A. C. (1984). *The application of ray tracing towards a correction for refracting effects in computed tomography with diffracting sources*. School of Electrical Engineering, Purdue University. TR-EE 84−14.

Baker, L. E. (1989). Principles of the impedance technique. *IEEE Engineering in Medicine and Biology Magazine, 8*, 11−15.

Barber, D. C., & Brown, B. H. (1984). Applied potential tomography. *Journal of Physics E: Scientific Instruments, 17*, 723−733.

Bar-Shalom, Y., & Li, X. R. (1993). *Estimation and Tracking: Principles, Techniques and Softwares*. Artech House.

Bender, R., Gordon, R., & Herman, G. T. (1970). Algebraic reconstruction techniques (ATR) for three-dimensional electron microscopy and X-ray photography. *Journal of Theoretical Biology, 29*, 471−481.

Born, M., & Wolf, E. (1999). *Principles of optics: Electromagnetic theory of propagation, interference and diffraction of light* (7th ed.). Cambridge: Cambridge University Press.

Bracewell, R. N. (1956). Strip integration in radio astronomy. *Australian Journal of Physics, 9*, 198–217.

Bracewell, R. N. (1965). *The Fourier transform and its applications*. New York: McGraw-Hill.

Bracewell, R. N., & Riddle, A. C. (1967). Inversion of fan-beam scans in radio astronomy. *Astrophysical Journal, 150*, 427–434.

Brenner, S. C., & Scott, L. R. (1994). *The mathematical theory of finite element methods*. Springer.

Caorsi, S., Gragnani, G. L., & Pastorino, M. (1990). Two-dimensional microwave imaging by a numerical inverse scattering solution. *IEEE Transactions on Microwave Theory and Techniques, 38*(8), 980–981.

Cheng, K. S., Isaacson, D., Newell, J. C., & Gisser, D. J. (1989). Electrode models for electric current computed tomography. *IEEE Transactions on Biomedical Engineering, 36*, 918–924.

Chew, W. C., & Wang, Y. M. (1990). Reconstruction of two-dimensional permittivity distribution using the distorted Born iterative method. *IEEE Transactions on Medical Imaging, 9*(2), 218–225.

Colton, D., & Kress, R. (1998). *Inverse acoustic and Electromagnetic Scattering Theory* (2nd ed.). New York: Springer Verlag.

Conte, S. D., & de Boor, C. (1980). *Elementary Numerical Analysis: An Algorithmic Approach*. New York: McGraw-Hill.

Devaney, A. J. (1982). A filtered backpropagation algorithm for diffraction tomography. *Ultrason Imaging, 4*, 336–350.

Devaney, A. J. (2012). *Mathematical foundations of imaging, tomography and wavefield inversion*. Cambridge: Cambridge Press.

Doerstling, B. H. (1994). *A 3-D reconstruction algorithm for the linearized inverse boundary value problem for Maxwell's equations* (Ph.D. thesis). Troy, New York: Rensselaer Polytechnic Institute.

Dyakowski, T., Jeanmeure, L. F. C., & Jaworski, A. J. (2000). Applications of electrical tomography for gas–solids and liquid–solids flows — a review. *Powder Engineering, 112*, 174–192.

Franchois, A., & Pichot, C. (1997). Microwave imaging-complex permittivity reconstruction with a Levenberg-Marquardt method. *IEEE Transactions on Antennas and Propagation, 45*(2), 203–214.

Gibson, W. C. (2008). *The method of moments in electromagnetics*. London: Chapman & Hall/CRC.

Greenleaf, J. F., Johnson, S. A., Lee, S. L., Herman, G. T., & Wood, E. H. (1974). Algebraic reconstruction of spatial distributions of acoustic absorption within tissue from their two dimensional acoustic projections. In *Acoustical holography* (pp. 591–603). Plenum Press.

Haddadin, O. S., & Ebbini, E. S. (1998). Imaging strongly scattering media using a multiple frequency distorted Born iterative method. *IEEE Transactions on Ultrasonics, Ferroelectrics, and Frequency Control, 45*(6), 1485–1496.

Harrington, R. F. (1968). *Field Computation by Moment Methods*. New York: Macmillan.

Herman, G. T. (Ed.), (1979). *Topics in applied physics: Vol. 32. Image reconstruction from projections: Implementation and applications*. Berlin: Springer-Verlag.

Herman, G. T. (1980). *Image reconstruction from projections — The fundamentals of computerised tomography*. New York: Academic Press.

Hinton, E., & Owen, D. R. (1979). *An introduction to finite element computations*. Wales: Pineridge Press.

Holder, D. S. (Ed.). (2004). *Electrical impedance tomography: Methods, history and applications*. CRC Press.

Hua, P., Webster, J. G., & Tompkins, W. J. (1988). A regularized electrical impedance tomography reconstruction algorithm. *Clinical Physics and Physiological Measurement, 9*(Suppl. A), 137−141.

Hua, P., Woo, E. J., Webster, J. G., & Tompkins, W. J. (1991). Iterative reconstruction methods using regularization and optimal current patterns in electrical impedance tomography. *IEEE Transactions on Medical Imaging, 10*, 621−628.

Ishimaru, A. (1978). *Wave propagation and scattering in random media*. New York: Academic Press.

Iwata, K., & Nagata, R. (1974). Calculation of refractive index distribution from interferograms using the Born and Rytov's approximation. *Japanese Journal of Applied Physics, 14*, 379.

Jain, A. K. (1989). *Fundamentals of digital image processing, chapter: Image reconstruction from projections*. New York: Prentice-Hall, 431−475.

Joachimowicz, N., Pichot, C., & Hugonin, J. P. (1991). Inverse scattering: An iterative numerical method for electromagnetic imaging. *IEEE Transactions on Antennas and Propagation, 39*(12), 1742−1753.

Kaipio, J. P., Karjalainen, P. A., Somersalo, E., & Vauhkonen, M. (1999). State estimation in time-varying electrical impedance tomography. *Annals of New York Academy of Sciences, 873*, 430−439.

Kaipio, J. P., & Somersalo, E. (1999). Nonstationary inverse problems and state estimation. *Journal of Inverse and Ill-posed Problems, 7*, 273−282.

Kak, A. C. (1984). Tomographic imaging with diffracting and non-diffracting sources. In A. Metherell (Ed.), *Acoustical imaging*. New York: Plenum Press.

Kak, A. C., & Slaney, M. (1988). *Principles of computerized tomographic imaging*. New York: IEEE.

Kaveh, M., Soumekh, M., & Muller, R. K. (1982). Tomographic imaging via wave equation inversion. *ICASSP, 82*, 1553−1556.

Keller, J. B. (1969). Accuracy and validity of the Born and Rytov approximation. *Journal of Optical Society of America, 59*, 1003.

Khambampati, A. K., Rashid, A., Kim, S., Soleimani, M., & Kim, K. Y. (2009). Unscented Kalman filter approach to track moving interfacial boundary in sedimentation process using three-dimensional electrical impedance tomography. *Philosophical Transactions of the Royal Society A, 367*, 3095−3120.

Kim, K. Y., Kim, B. S., Kim, M. C., Lee, Y. J., & Vauhkonen, M. (2001). Image reconstruction in time-varying electrical impedance tomography based on the extended Kalman filter. *Measurement Science and Technology, 12*, 1032.

Kim, J. H., Choi, B. Y., & Kim, K. Y. (2006). Novel iterative image reconstruction algorithm for electrical capacitance tomography: direct algebraic reconstruction technique. *IEICE Transactions on Fundamentals, 89*, 1578−1584.

Kohn, R. V., & McKenney, A. (1990). Numerical implementation of a variational method for electrical impedance tomography. *Inverse Problems, 6*, 389−414.

Levoy, M. (1992). *Volume rendering using the Fourier projection-slice theorem* (Vol. 94). California: Computer Systems Laboratory, Departments of Electrical Engineering and Computer Science Stanford University Stanford, 305−405.

Morse, P. M., & Feshbach, H. (1953). *Method of theoretical physics*. New York: McGraw Hill Book Company.

Mueller, R. K., Kaveh, M., & Wade, G. (1979). Reconstructive tomography and applications to ultrasonics. *Proceedings of the IEEE, 67*, 567.

Natterer, F. (1986). *The mathematics of computerized tomography*. New York: Wiley.

Newton, R. G. (1966). *Scattering theory of waves and particles*. New York: McGraw-Hill.

Nunez, P. L. (1981). *Electric fields of the brain: The neurophysics of EEG*. New York: Oxford University Press.

Oppengeim, A. V., & Schafer, R. W. (1975). *Digital signal processing*. Englewood Cliffs, NJ: Prentice-Hall.

Pan, S. X., & Kak, A. C. (1983). A computational study of reconstruction algorithms for diffraction tomography: Interpoltion versus filtered backpropagation. *IEEE Transactions on Acoustics, Speech, and Signal Process, 10*, 1262−1275.

Polydorides, N., Lionheart, W. R. B., & McCann, H. (2002). Krylov subspace iterative techniques: on the detection of brain activity with electrical impedance tomography. *IEEE Transactions on Medical Imaging, 21*, 596−603.

Radon, J. (1917). On the determination of functions from their integral values along certain manifolds. English translation 1986 *IEEE Transactions on Medical Imaging, 5*, 170−176.

Reinecke, N., & Mewes, D. (1997). Investigation of the two-phase flow in trickle-bed reactors using capacitance tomography. *Chemical Engineering Science, 52*, 2111−2138.

Rouseff, D., & Winters, K. B. (1994). Two-dimensional vector flow inversion by diffraction tomography. *Inverse Problems, 10*(3), 687.

Schafer, D., Borgert, J., Rasche, V., & Grass, M. (2006). Motion-compensated and gated cone beam filtered back-projection for 3-D rotational X-ray angiography. *IEEE Transactions on Medical Imaging, 25*, 898−906.

Seppanen, A., Vauhkonen, M., Somersalo, E., & Kaipio, J. P. (2001). State space models in process tomography—approximation of state noise covariance. *Inverse Problems in Engineering, 9*, 561−585.

Seppanen, A., Vauhkonen, M., Vauhkonen, P. J., Somersalo, E., & Kaipio, J. P. (2001). State estimation with fluid dynamical evolution models in process tomography— an application to impedance tomography. *Inverse Problems, 17*, 467.

Somersalo, E., Cheney, M., & Isaacson, D. (1992). Existence and uniqueness for electrode models for electric current computed tomography. *SIAM Journal of Applied Mathematics, 52*, 1023−1040.

Sommersalo, E., Isaacson, D., & Cheney, M. (1992). A linearized inverse boundary value problem for Maxwell's equations. *Journal of Computational and Applied Mathematics, 42*, 123−136.

Soumekh, M., Kaveh, M., & Mueller, R. K. (1984). Fourier domain reconstruction methods with application to diffraction tomography. *Acoustical Imaging, 13*, 17−30.

Stark, H., Woods, J. W., Paul, I., & Hingorani, R. (1981). An investigation of computerized tomography by direct Fourier inversion and optimum interpolation. *IEEE Transactions on Biomedical Engineering, 28*, 496−505.

Strohmer, T., & Vershynin, R. (2009). A randomized Kaczmarz algorithm for linear systems with exponential convergence. *Journal of Fourier Analysis and Applications, 15*, 262−278.

Trigo, F. C., Gonzalez-Lima, R., & Amato, M. B. P. (2004). Electrical impedance tomography using the extended Kalman filter. *IEEE Transactions on Biomedical Engineering, 51*, 72−81.

Tsihrintzis, G. A., & Devaney, A. J. (2000). Higher-order (nonlinear) diffraction tomography: Reconstruction algorithms and computer simulation. Image Processing. *IEEE Transactions on, 9*(9), 1560−1572.

Vauhkonen, M. (1997). *Electrical impedance tomography and prior information* (Ph.D thesis).

Vauhkonen, M., Karjalainen, P. A., & Kaipio, J. P. (1998). A Kalman filter approach to track fast changes in electrical impedance tomography. *IEEE Transactions on Biomedical Engineering, 45*, 486–493.

Villares, G., Begon-Lours, L., Margo, C., Oussar, Y., Lucas, J., & Holé, S. (2012). Non-linear model of sensitivity matrix for electrical capacitance tomography. In *Electrostatic joint conference* (p. R4).

Wang, Y. M., & Chew, W. C. (1989). An iterative solution of the two-dimensional electromagnetic inverse scattering problem. *International Journal of Imaging Systems and Technology, 1*(1), 100–108.

Warsito, W., & Fan, L. S. (2001). Measurement of real-time flow structures in gas–liquid and gas–liquid–solid flow systems using electrical capacitance tomography (ECT). *Chemical Engineering Science, 56*, 6455–6462.

Webster, J. G. (1990). *Electrical impedance tomography*. Adam Hilger.

Woo, E. J., Hua, P., Webster, J. G., & Tompkins, W. J. (1994). Finite element method in electrical impedance tomography. *Medical & Biological Engineering & Computing, 32*, 530–536.

Xie, C. G., Huang, S. M., Hoyle, B. S., Thron, R., Lenn, C., Snowden, D., et al. (1992). Electrical capacitance tomography for flow imaging-system model for development of image reconstruction algorithms and design of primary sensors. *IEEE Proceedings G, 139*, 89–98.

Xie, C. G., Plaskowski, A., & Beck, M. S. (1989). 8-electrode capacitance system for two component flow identification. Part 1: tomographic flow imaging. *IEEE Proceedings A, 136*, 173–183.

Yang, W. Q. (1996). Hardware design of electrical capacitance tomography systems. *Measurement Science and Technology, 7*, 233–246.

Yorkey, T. J., Webster, J. G., & Tompkins, W. J. (1987). Comparing reconstruction algorithms for electrical impedance tomography. *IEEE transactions on Biomedical Engineering, 34*, 843–852.

Image reconstruction for hard field tomography

13

U. Hampel
Helmholtz-Zentrum Dresden-Rossendorf, Dresden, Germany; Technische Universität Dresden, Dresden, Germany

13.1 Introduction and basic considerations

In many tomographic imaging modalities the signal carrier propagates straight through the object of investigation. This holds for tomography with X-rays, gamma rays, and neutrons, and also for tomography with visible or infrared light as well as sound, as long as signal formation is based on pure radiation absorption or emission and not on direction changes due to changing refractive index or acoustic impedances in the object. That is, the propagation of the signal carrier is independent of the material distribution in the object, and hence tomographic imaging modalities are frequently being referred to as hard field tomography. For theoretical treatment it is useful to provide a very abstract view on such modalities. Therefore we will first make some simplified assumptions, which should ideally hold for hard field tomography and which are the basis for analytical and algebraic image reconstruction introduced in this chapter. In the following sections we shall introduce, discuss, and exemplify three such assumptions. Note that these assumptions are idealizations that facilitate the process of image reconstruction. They are mostly violated by different counteracting physical effects and technical limitations, and hence a great deal of effort must be spent to account for them in real applications.

13.1.1 Assumption 1: the signal carrier propagates straight within the object

Straight propagation of the signal carrier particularly holds for ionizing electromagnetic and particle radiation. Therefore computed tomography (CT) with X-rays, gamma rays, and neutrons, but also with electrons, falls into this category. Moreover it holds for visible and infrared light tomography in gases, liquids, or semitransparent solids with purely absorbing constituents. Also low-frequency electromagnetic waves, such as microwaves or radar waves and sound waves, do in principle propagate straight. But they produce interference patterns when they are deflected, scattered and refracted at impedance discontinuities. Therefore, tomography methods based on wave−material interaction require different reconstruction schemes, such as diffraction tomography approaches. The interested reader may find further information on such approaches in other textbooks, such as Kak and Slaney (1988).

Industrial Tomography. http://dx.doi.org/10.1016/B978-1-78242-118-4.00013-7
Copyright © 2015 Elsevier Ltd. All rights reserved.

With the assumed straight propagation of the signal carrier we can understand the measurement process in transmission tomography as attenuation of rays. For emission tomography we would rather speak of thin measurement channels through which emitted radiation propagates towards external detectors.

13.1.2 Assumption 2: the tomographic data represent integral values of an object function along lines

When radiation passes an object it is attenuated. The attenuation law was already derived in Chapter 6 as:

$$I_D = I_0 \exp\left(-\int_0^L \mu(l)\,\mathrm{d}l \right) \tag{13.1}$$

for the radiation intensity and

$$E = -\log\frac{I_D}{I_0} = \int_0^L \mu(l)\,\mathrm{d}l \tag{13.2}$$

for the radiation extinction. It turns out that the total extinction E of an X-ray is just the integral value of the local attenuation coefficient along its path of total length L between source and detector. Without this linearity assumption a solution of the inverse problem would be very intractable. While in transmission tomography (Figure 13.1(a)) the Lambert law provides the linearity, in emission tomography the measured parameter (the incident photon count rate in single-photon emission computed tomography (SPECT) or the coincidence rate in positron emission tomography (PET)) is in a first approximation directly linear to the measured radiation intensities. This is illustrated in Figure 13.1(b) for two detectors in a PET configuration. All gamma radiation that emerges due to radioactive decay along the ray is received by detectors 1 and 2. Hence the detectors measure a line integral of the local activity a given by

$$A \propto \int_0^L a(l)\mathrm{d}l. \tag{13.3}$$

This expression has the same integral form as Eqn (13.2). In reality, of course, the geometry of sources and detectors used in the tomography systems defines spatial channels of transmission or emission, in which radiation is received. These channels may have quite complicated spatial structures. Thus, in transmission tomography they are defined by the geometric extension and emission profile of the source and the geometry as well as the spatial sensitivity distribution of the detector. In PET,

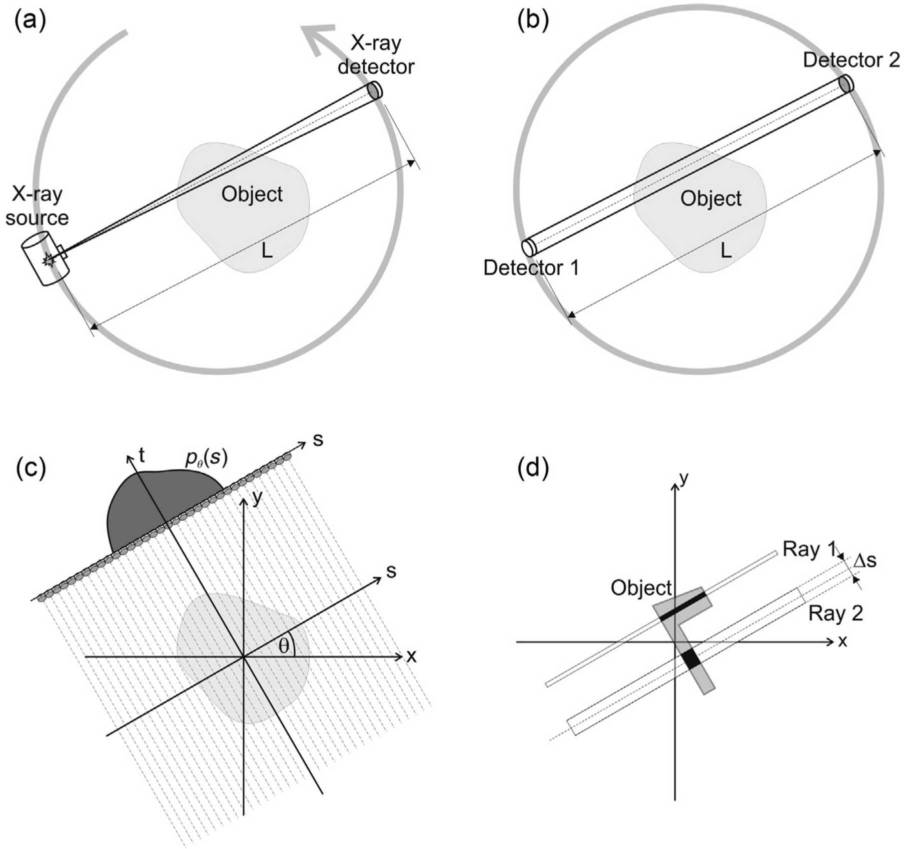

Figure 13.1 Exemplary ray geometry for (a) a transmission tomography setup and (b) an emission tomography setup. (c) Parallel projection geometry. (d) Intersection areas of two rays of different thickness Δs with an object.

for instance, the channels are defined by the acceptance cones of the respective detector pairs with respect to the point of radiation emission. For mathematical treatment it is convenient to assume that radiation propagates only along an infinitely thin ray or within an infinitely thin channel, which for instance connects the center points of source and detector in an X-ray setup. As is shown in Figure 13.1(c), this assumption is supported by the concept of spatial sampling. Thus, acquiring measurement data for a set of spatial channels, which are parallel to each other, can be seen in an abstract sense as a sampling of the parallel projection function $p_\theta(s)$. Considering the sampling values as integral values along infinitely thin rays or lines is first of all helpful in a mathematical sense. The sampling density and the real width of the channels are then related to the sampling bandwidth and hence recoverable spatial resolution. However, for transmission tomography the concept of infinitely thin rays also has a more practical background. Consider the example shown in Figure 13.1(d). For an infinitely thin ray the intensity at the detector is given by Eqn (13.1). That is, in ray direction the line integral of the attenuation coefficient is a logarithmic function of intensity. In lateral direction, however, a broader ray would linearly integrate the intensity, that is,

$$I_D = I_0 \frac{1}{\Delta s} \int_{s_0-\Delta s/2}^{s_0+\Delta s/2} \exp\left(-\int_0^L \mu(t)\,\mathrm{d}t \right) \mathrm{d}s. \tag{13.4}$$

This leads to an uncorrectable ambiguity, as illustrated in Figure 13.1(d). Here two measurement channels intersect with an object. Though both channels have the same intersection area with the object, they produce different extinction values. For emission tomography, such as SPECT and PET, this problem does not occur due to the fact that here the line integrals are strict linear spatial integrals over the radioactive source distribution in the respective channels. Hence, for transmission tomography having thin rays is generally preferential.

13.1.3 Assumption 3: the line integral measurements densely and homogeneously populate the Radon space of the object

As we will see later, an object distribution, let us say the two-dimensional (2D) distribution $\mu(x,y)$ of the linear attenuation coefficient of an object, can be recovered from all line integrals of this distribution. It is now important to clarify what “all” means. First of all we note that a line in 2D space is described by two parameters. As is illustrated in Figure 13.1(c), we may uniquely define a line by its inclination angle θ against the x-axis of the coordinate system and the lateral distance s the line has from the origin of the coordinate system. Under a given inclination angle θ all line integrals form a parallel projection $p_\theta(s)$. This continuous projection function is sampled by thin rays, all with the same angle θ but with different offsets s. While in a strict mathematical sense the projection consists of a twofold infinite number of values (infinite with respect to $|s| \rightarrow \infty$ and with respect to the density of values within a given interval), in reality $|s|$ is bound by the object size and number of sampling values by the number of rays (respectively, detectors). The sampling theorem applies and with f_S being the sampling frequency in line pairs per unit lengths, it is clear that the real projection can be recovered up to the Nyquist frequency $f_s/2$. Thus, with respect to the single projections, tomographic imaging requires that projections be sampled dense enough such that the highest wanted spatial frequency is below the Nyquist frequency. Moreover, projection sampling should be preferably equidistant. In order to be able to reconstruct a certain spatial frequency, the angular sampling must also be sufficiently dense. It requires, however, some more dedicated analysis to translate the sampling density into spatial resolution due to the fact that the inverse problem is a transformation from polar to Cartesian coordinates. A quantitative analysis is possible via the central slice theorem, which is introduced later. Moreover, the angular range from $0° \leq \theta < 180°$ should be sampled rather homogeneously. Note, that for each line a symmetry relation holds, that is, a line defined by parameters (s,θ) is identical to a line ($-s$,$\theta + \pi$), such that sampling over 180° in θ is sufficient. Higher sampling frequency in both coordinates s and θ secure, in principle, higher image resolution, and it should be further noted here that nonuniform or incomplete sampling leads to image artifacts.

13.2 The forward problem: projections and the Radon space

Within this chapter we will continue the discussion of the last section and derive mathematical formulae for the description of the so-called forward problem, that is, the generation of projections from an object. Equations (13.2) and (13.3) describe in a general way how line integral values are obtained in transmission and emission tomography. However, this description is not suited for describing the generation of projection data as a mathematical transformation. Therefore we will first derive an equation for a line in 2D space. For the parallel projection illustrated in Figure 13.1(c) we may define a new (rotated) Cartesian coordinate system (s,t). The parallel X-rays are then described in this coordinate system by s = constant and t = arbitrary. The transformation from the (x,y) coordinates to (s,t) coordinates is given by

$$\begin{pmatrix} s \\ t \end{pmatrix} = \begin{pmatrix} \cos\theta & \sin\theta \\ -\sin\theta & \cos\theta \end{pmatrix} \begin{pmatrix} x \\ y \end{pmatrix}. \tag{13.5}$$

Hence, with s = constant and t = arbitrary it follows that

$$s = x\cos\theta + y\sin\theta \tag{13.6}$$

defines the ray line in (x,y) coordinates. Note that Eqn (13.6) is the Hessian normal form of the line in 2D space. It is to be understood as follows: a point (x,y) lies on the line given by (s,θ) if and only if Eqn (13.6) holds. Next we have to derive a mathematical formula that describes a line integral in 2D space. Therefore we revert to the concept of the Dirac distribution $\delta(z)$, which is defined as $\delta(z) = 0$ if $z \neq 0$ and

$$\int_{-\infty}^{+\infty} \delta(z)\mathrm{d}z = 1. \tag{13.7}$$

Reshaping Eqn (13.6) to $z = s - x\cos\theta - y\sin\theta$ and inserting it into Eqn (13.7) gives

$$p(s,\theta) = \int_{-\infty}^{+\infty}\int_{-\infty}^{+\infty} \delta(s - x\cos\theta - y\sin\theta)\mu(x,y)\mathrm{d}y\mathrm{d}x. \tag{13.8}$$

With Eqn (13.8) we have not only an elegant formulation of a line integral over the object distribution $\mu(x,y)$ but also a 2D transformation of the object distribution into another space, the so-called Radon space of the line parameters (s,θ). Hence, Eqn (13.8) is also referred to as the Radon transformation of $\mu(x,y)$, or in operator notation

$$p(s,\theta) = \mathscr{R}\{\mu(x,y)\}. \tag{13.9}$$

We note that the Radon space is the space of line integral values of an object distribution. The kernel of this integral transformation is just the spatial line function $\delta(s - x\cos\theta - y\sin\theta)$. Now it should be more clear what it means that tomography requires a homogeneously sampled Radon space of the object distributions. It means that sufficiently dense and homogeneously distributed projection values $p(s,\theta)$ must be acquired by a practical line integration process. The Radon transformation has the following elementary properties, as can easily be shown:

1. The Radon transformation is periodic in θ, that is, $p(s,\theta) = p(s,\theta + 2n\pi)$, with n being integer.
2. The Radon transformation is symmetric with respect to $p(s,\theta) = p(-s,\theta + \pi)$.
3. A point (s,θ) in Radon space corresponds to a line $s = x\cos\theta + y\sin\theta$ in object space.
4. A point (x,y) in object space corresponds to a sinusoidal curve $s = x\cos\theta + y\sin\theta$ in Radon space.

13.3 The inverse problem and two-dimensional analytic image reconstruction with parallel beams

Having an analytical description of the forward problem, we can now give a general formulation of the inverse problem. It can be stated as follows: given the forward problem $p(s,\theta) = \mathscr{R}\{\mu(x,y)\}$, find an inverse transformation $\mu(x,y) = \mathscr{R}^{-1}\{p(s,\theta)\}$, which restores the object distribution from its (parallel) projections. Since Eqn (13.8) is a linear integral transformation, we can hope that the inverse transformation is another integral transformation

$$\mu(x,y) = \int_{0}^{\pi} \int_{-\infty}^{+\infty} K(x,y,s,\theta)p(s,\theta)\mathrm{d}s\mathrm{d}\theta \tag{13.10}$$

with a kernel $K(x,y,s,\theta)$, which has yet to be determined.

From the statements above we can see that the Radon transformation is an integral transformation that maps line integrals of an object distribution in a Cartesian coordinate system into values, which are in a polar system. Unfortunately the involved coordinate transformation hampers an elegant mathematical treatment of the problem. Deriving an analytical inverse according to Eqn (13.10) requires a rather cumbersome analysis. This was achieved in 1917 by Radon (1917), and his solution reads in polar coordinates

$$\mu(r,\varphi) = \frac{1}{2\pi^2}\int_0^{\pi}\int_{-\infty}^{+\infty}\frac{1}{r\cos(\theta-\varphi)}\frac{\partial p(s,\theta)}{\partial s}\,\mathrm{d}s\mathrm{d}\theta. \tag{13.11}$$

Particularly the singularity at $r = 0$ brings in some practical difficulties if one would use this inverse in a numerical scheme. A more convenient way to solve the inverse problem is to first transform the projection data from polar Radon space back to Cartesian object space and then to solve the inverse problem in object space. Though many different linear back-transformations could be applied, the most reasonable is the one called *simple back-projection*. What we know about a single ray measurement is that the obtained value is only from the area of the corresponding line in the object space. What we do not know is how the value was distributed along the line. Hence the fairest back-transformation is to smear the projection values homogeneously across the respective ray areas. The mathematical notation of this back-projection is then

$$b(x,y) = \int_0^{\pi}\int_{-\infty}^{+\infty}\delta(s - x\cos\theta - y\sin\theta)p(s,\theta)\mathrm{d}s\mathrm{d}\theta \tag{13.12}$$

or in operator notation

$$b(x,y) = \mathscr{B}\{p(s,\theta)\}. \tag{13.13}$$

Figure 13.2 shows results of the back-projection operation for a complex object distribution as well as for a single point in object space. For the complex object we can see that the back-projection operation produces an image that somewhat resembles the original object distribution, though not very sharply. The smaller the structures in the image, the worse they are recovered. We could say for our back-projection that partly we did right by smearing the data along their corresponding lines, and this gives us back the coarse structures of the original object distributions. But partly we did not do right, because we smeared the data homogeneously along the lines (having no better idea), and this leads to a lack of structural information.

After having introduced the back-projection operation $\mathscr{B}\{\cdot\}$ we will proceed on the mathematical side to derive some interesting properties of the above transformations. Assume our object distribution is a very small absorber, for example, in the very center of our coordinate system (Figure 13.2(d)). It could be a lead bead of a few microns diameter scanned by an X-ray CT scanner. This punctual absorber will produce a data set in Radon space with nonzero value at $s = 0$ and at any angle θ. That is, in the Radon space data image we see a kind of "vertical line" at $s = 0$. Mathematically we get

$$\mathscr{R}\{\delta(x,y)\} = \int_{-\infty}^{+\infty}\int_{-\infty}^{+\infty}\delta(s - x\cos\theta - y\sin\theta)\delta(x,y)\mathrm{d}x\mathrm{d}y = \delta(s). \tag{13.14}$$

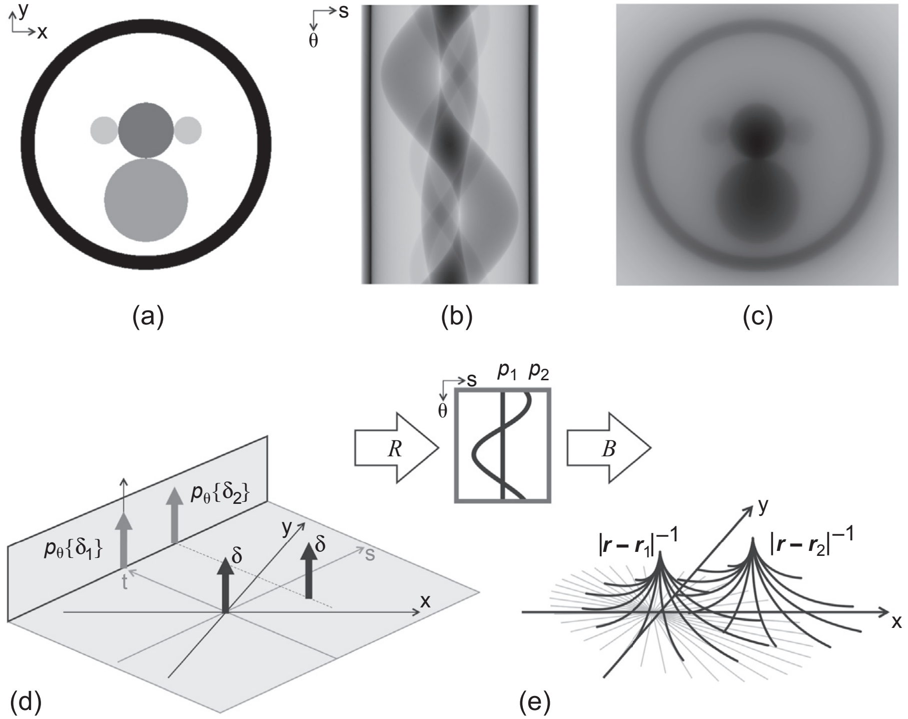

Figure 13.2 A simple object as a gray value image (a) and its Radon transformation (b). Due to the rotation and parallel projection the objects' structures map to sinusoidal structures in Radon space. Therefore the Radon space data set is frequently called a sinogram. A simple back-projection along the projection lines yields an image (c) that resembles the original object in its coarse structures, but fine structures are blurred. The reason for that can be explained by considering the point response function. Two point-like structures are projected in direction t and create point-like projections (d). Back-projecting these projections for all angles θ, that is, cumulatively smearing the projection data along the projection lines, gives a $1/|\boldsymbol{r}|$-function for each point absorber (e). Hence the points are smeared in object space to $1/|\boldsymbol{r}|$-functions, which explains the blurring (loss of resolution). Since the operations are linear and shift invariant, the combined operation $\mathscr{B}\{\mathscr{R}\{\cdot\}\}$ is a 2D convolution and the inverse solution can be constructed in 2D Fourier space (see text).

Doing a back-projection of these data, we have to smear the nonzero value along all lines with $s = 0$ and these are only lines that run through the position of the point absorber, which is the coordinate center in this case. Doing the back-smearing additively for many angles θ produces an object distribution with successively higher values towards the location of the point absorber. If we consider a ring of distance r and width dr around the point absorber, then the line density on that ring is const/r. Hence the back-projection of the Radon transformation of a point in the center of the object space is

$$\begin{aligned} b_\delta(x,y) &= \mathscr{B}\{\delta(s)\} = \mathscr{B}\{\mathscr{R}\{\delta(x,y)\}\} \\ &= \int_0^{\pi}\int_{-\infty}^{+\infty}\int_{-\infty}^{+\infty}\int_{-\infty}^{+\infty} \delta(s - x\cos\theta - y\sin\theta)\delta(s - x\cos\theta - y\sin\theta)\delta(x,y)\mathrm{d}x\mathrm{d}y\mathrm{d}s\mathrm{d}\theta \\ &= \frac{\text{const}}{|\boldsymbol{r}|} = \frac{\text{const}}{\sqrt{x^2+y^2}}. \end{aligned} \tag{13.15}$$

The result can be summarized as follows: The back-projection of the Radon space data from a point distribution produces a back-projection image $b_\delta(x,y) = 1/|\boldsymbol{r}|$. We call the distribution b_δ the point response function of the operation sequence $\mathscr{B}\{\mathscr{R}\{\cdot\}\}$.

Next we will take notice of two important properties of the combined transformation $\mathscr{B}\{\mathscr{R}\{\cdot\}\}$, but we will not give formal mathematical proofs here. First we note that the transformation is shift-invariant. If the point absorber was off the origin, the transformation $\mathscr{B}\{\mathscr{R}\{\cdot\}\}$ would produce the same $1/|\boldsymbol{r}|$ distribution, but shifted to the position of the point. This is illustrated in Figure 13.2(d) and (e). That is, in mathematical terms

$$b_\delta(x-\Delta x, y-\Delta y) = \frac{1}{\sqrt{(x-\Delta x)^2 + (y-\Delta y)^2}}. \tag{13.16}$$

It is easy to see that this must be so, because the back-projection smears the nonzero data values along all lines that run through the point's coordinates. Hence the resulting back-projection distribution has the same shape regardless of the position of the point. Next we may note that the transformation of Eqn (13.15) is fully linear and hence the superposition principle can be applied. The back-projection of the data from two point absorbers is the same as the sum of the back-projection images of two single point absorbers. Thus let $\delta_1 = \delta(x - \Delta x_1, y - \Delta y_1)$ denote a point absorber at $(\Delta x_1, \Delta y_1)$ and $\delta_2 = \delta(x - \Delta x_2, y - \Delta y_2)$ another point absorber at $(\Delta x_2, \Delta y_2)$; then

$$\mathscr{B}\{\mathscr{R}\{c_1\delta_1 + c_2\delta_2\}\} = c_1\mathscr{B}\{\mathscr{R}\{\delta_1\}\} + c_2\mathscr{B}\{\mathscr{R}\{\delta_2\}\} \tag{13.17}$$

with any constants c_1 and c_2. Of course we can extend Eqn (13.17) to even more point absorbers. Eventually we can think of the object distribution $\mu(x,y)$ just as a dense set of point functions, each with a constant value given by $\mu(x,y)$. Extending Eqn (13.17) to this set then reads

$$\begin{aligned} b(x,y) &= \mathscr{B}\{p(s,\theta)\} = \mathscr{B}\{\mathscr{R}\{\mu(x,y)\}\} \\ &= \int_{-\infty}^{+\infty}\int_{-\infty}^{+\infty} b_\delta(x-x', y-y')\mu(x',y')\mathrm{d}x'\mathrm{d}y'. \end{aligned} \tag{13.18}$$

That is, $\mathscr{B}\{\mathscr{R}\{\cdot\}\}$ is a linear convolution transformation and, as such, there exists a beautiful generalized inverse solution. Recall the correspondences of the Fourier transformation and remember that the rather complex convolution operation turns into a simple frequency-wise multiplication in Fourier space. Hence, taking the 2D Fourier transforms

$$M(\omega_x, \omega_y) = \mathcal{F}\{\mu(x,y)\} = \int\limits_{-\infty}^{+\infty}\int\limits_{-\infty}^{+\infty} \mu(x,y)\exp(-\mathrm{i}[\omega_x x + \omega_y y])\, dxdy$$

$$B_\delta(\omega_x, \omega_y) = \mathcal{F}\{b_\delta(x,y)\} = \int\limits_{-\infty}^{+\infty}\int\limits_{-\infty}^{+\infty} b_\delta(x,y)\exp(-\mathrm{i}[\omega_x x + \omega_y y])\, dxdy \tag{13.19}$$

Eqn (13.18) becomes in the Fourier domain

$$B(\omega_x, \omega_y) = B_\delta(\omega_x, \omega_y)\cdot M(\omega_x, \omega_y). \tag{13.20}$$

The inverse problem, that is, the search for an object distribution $\mu(x,y)$ that produces the data $p(s,\theta)$ and back-projection $b(x,y)$, can then be solved in Fourier space by the frequency-wise division

$$M(\omega_x, \omega_y) = \frac{B(\omega_x, \omega_y)}{B_\delta(\omega_x, \omega_y)}. \tag{13.21}$$

Practically, this leads to the following inversion procedure:

1. Take the projection data $p(s,\theta)$ and project them back to object space, giving $b(x,y)$;
2. Transform the recovered back-projection distribution $b(x,y)$ into Fourier space, giving $B(\omega_x,\omega_y)$;
3. Apply Eqn (13.21);
4. Transform the Fourier space object distribution $M(\omega_x,\omega_y)$ back to object space by inverse Fourier transformation.

It is beautifully simple, however, there is one thing to note – Equation (13.21) involves a division operation and whenever the denominator is zero, there will be no inverse solution for this particular spatial frequency. Practically, even if the denominator is close to zero, the solution at this spatial frequency tends to be less reliable and there is the danger that noisy measurement data will dominate the solution in this frequency range. It means that whenever the denominator is very small, the transfer function tells us that this mode is badly transferred and hence cannot easily be recovered. We then call it an illposedness in this spatial frequency band.

13.4 The central slice theorem

Now from the above we have a method to solve the inverse problem. We do have an analytical form of the point response function of $\mathscr{B}\{\mathscr{R}\{\cdot\}\}$. What we do not have analytically yet is its 2D Fourier transform. Deriving analytically closed Fourier transforms in 2D is somewhat more difficult than for 1D Fourier transforms, but an interesting theorem can be used for this particular case, which can be again derived by pure common sense without many mathematical formulae.

To understand the *central slice theorem* it is first of all helpful to have a clear view of how 2D Fourier transforms are being carried out. According to Eqn (13.19) we first have to solve the inner integral. That is, we first do a 1D transformation along the x-dimension while keeping y fixed. Subsequently, we do the same in the y-dimension with fixed x. From Eqn (13.19) it becomes immediately clear that if we were to interchange the order of integration nothing would change in the result. But we can even go further. Assume we have a rotation of the coordinate system as given in Eqn (13.5). If we were to do the Fourier transform in the (s,t) coordinate system the result would be the same as if we were to do it in the (x,y) system. This is known as rotational invariance of the 2D Fourier transformation; a mathematical proof is given in Appendix A.1. What does it tell us? The 2D Fourier transformation is invariant against rotation. We can do the Fourier transformation in the (s,t) system and first transform along the t-coordinate and then along the s-coordinate. No matter under which angle θ the (s,t) system is rotated, the result will always be the same as in the (x,y) system.

Consider the parallel projection shown in Figure 13.3. For this setting we will now do a Fourier transformation of the object distribution $\mu(x,y)$, however, not in (x,y)-coordinates but in (s,t)-coordinates. We start by transforming in the s-dimension, that is

$$M(\omega_s, t) = \int_{-\infty}^{+\infty} \mu(s,t)\exp(-\mathrm{i}\omega_s s)\mathrm{d}s. \tag{13.22}$$

Figure 13.3(b) illustrates the result. Now we do the second part of the 2D Fourier transform, that is,

$$M(\omega_s, \omega_t) = \int_{-\infty}^{+\infty} M(\omega_s, t)\exp(-\mathrm{i}\omega_t t)\mathrm{d}t. \tag{13.23}$$

Note, that Eqn (13.23) holds for any ω_s, that is, the transformation is done for values along lines given by a fixed ω_s. We will now focus our attention on the spatial frequency $\omega_t = 0$. For this particular frequency Eqn (13.23) reads

$$M(\omega_s, 0) = \int_{-\infty}^{+\infty} M(\omega_s, t)\mathrm{d}t. \tag{13.24}$$

We know this as a fundamental property of the Fourier transform: The Fourier coefficient belonging to frequency zero ($\omega_t = 0$) is just the (infinite) integral over the transformed function. It requires some effort to understand this concept in the 2D case, but it is worth spending this effort. Figure 13.3(c) gives an illustrative explanation of the usefulness of this fact. For any spatial frequency ω_s it holds that the value $M(\omega_s,\omega_t = 0)$

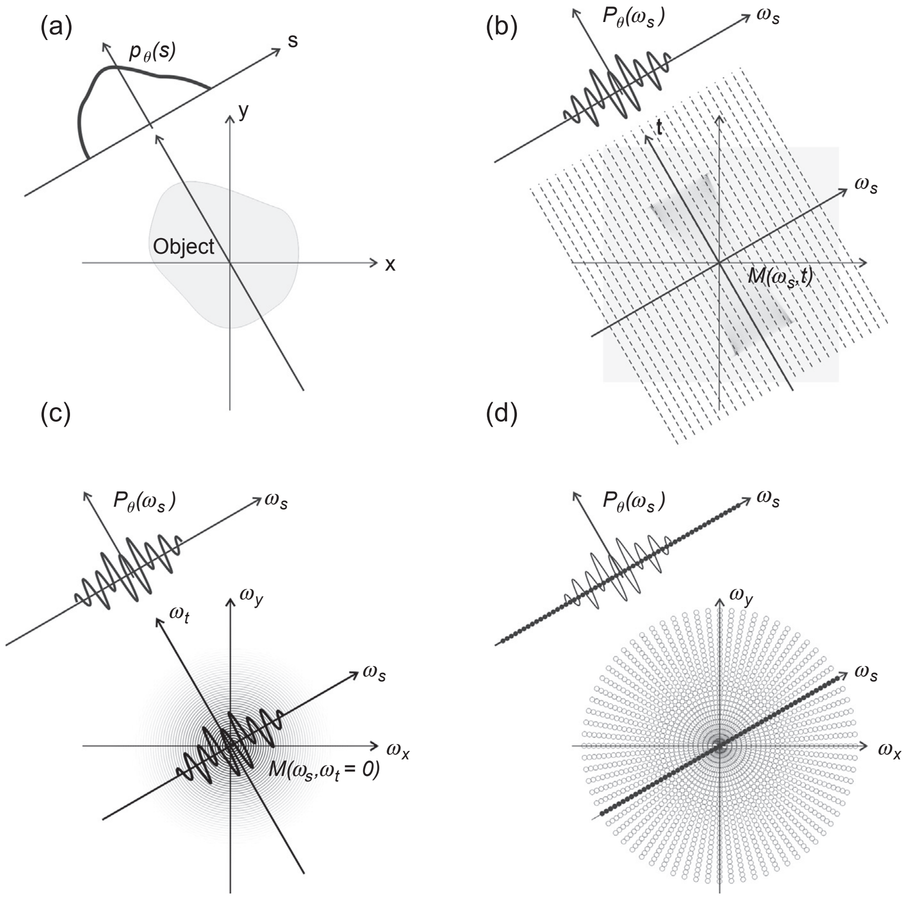
(a)
$p_\theta(s)$
s
y
x
Object
(b)
$P_\theta(\omega_s)$
ω_s
t
ω_s
$M(\omega_s,t)$
(c)
(d)
$P_\theta(\omega_s)$
ω_s
ω_y
ω_t
ω_s
ω_x
$M(\omega_s,\omega_t = 0)$
$P_\theta(\omega_s)$
ω_s
ω_y
ω_s
ω_x

Figure 13.3 The central slice theorem: (a, b) For the parallel projection $p_\theta(s)$ of an object distribution $\mu(x,y)$ it holds that for each ω_s the 1D Fourier transform $P_\theta(\omega_s)$ is equal to the line integral (dashed lines) through $M(\omega_s,t)$ along t. (c) Because the infinite line integral along t corresponds to the zero-frequency value of the 1D Fourier transform of $M(\omega_s,t)$ along t, we get $P_\theta(\omega_s) = M(\omega_s,\omega_t = 0)$. (d) Hence $M(\omega_s,\omega_t)$ can be recovered by populating the 2D Fourier space with the values $P_\theta(\omega_s)$ for each angle θ (hollow circles).

is equal to the line integral value of the function $M(\omega_s,t)$ along t. This line integral value is a parallel projection value along the t-dimension of the half-transformed object space distribution $M(\omega_s,t)$. Because this is so, we can note that

$$M(\omega_s, \omega_t = 0) = \int_{-\infty}^{+\infty} M(\omega_s, t)\mathrm{d}t = P_\theta(\omega_s) = \int_{-\infty}^{+\infty} p(s,\theta)\exp(-\mathrm{i}\omega_s s)\mathrm{d}s. \tag{13.25}$$

Note that the third term in Eqn (13.25) represents a parallel projection of the function $M(\omega_s,t)$ in t-direction and the fourth term the 1D Fourier transform of the parallel projection at angle θ. Now we can state that the Fourier transform $P_\theta(\omega_s)$ of the projection $p_\theta(s)$ is equal to the values $M(\omega_s,\omega_t = 0)$ of the 2D Fourier transform of the object distribution. Figure 13.3(d) illustrates the consequences and gives rise to another algorithm to solve the inverse problem. This algorithm would read as follows:

1. Do a 1D Fourier transformation of each parallel projection $p_\theta(s)$;
2. Populate the 2D Fourier space $M(\omega_s,\omega_t)$ with those values along the line $\omega_t = 0$;
3. Do an inverse 2D Fourier transformation of $M(\omega_s,\omega_t)$.

For any angle θ the line $\omega_t = 0$, which is to be populated with values, goes through the origin of the coordinate system and is orthogonal to the projection direction. Due to the first property, Eqn (13.25) is referred to as the *central slice theorem.*

The above-derived algorithm is, however, not the most efficient one. The population of the object's Fourier space is still done in polar coordinates giving the nonuniform sampling shown in Figure 13.3(d). It requires subsequent remapping of the data into Cartesian coordinates, which is a complex operation. But the central slice theorem readily answers a question we have raised above and which lets us derive the final algorithm. This is the question of the 2D Fourier transform $B_\delta(\omega_x,\omega_y)$ of the point spread function $b_\delta(x,y)$. The central slice theorem tells us that $B_\delta(\omega_x,\omega_y)$ is in fact the same as the back-projection of Fourier-transformed projections

$$p_\delta(s,\theta) = \int\limits_{-\infty}^{+\infty} p_\delta(s,\theta)\exp(-\mathrm{i}\omega_s s)\mathrm{d}s. \tag{13.26}$$

Now since $p_\delta(s,\theta) = \delta(s)$, its Fourier transform is $P_\delta(\omega_s,\theta) = 1$. Hence, to obtain the 2D Fourier transform of the function $b_\delta(x,y) = b_\delta(s,t) = 1/|\boldsymbol{r}|$ we have to populate the line $\omega_t = 0$ with values 1 and repeat this additively for all angles θ. As is illustrated in Figure 13.4, this is in fact the same action we have done with the standard simple back-projection in object space, that is, back-projecting the functions $p_\delta(\theta,s)$ in object space. The only difference: the back-projection (smearing of 1 s) is done under an angle of 90° compared to object space back-projection. Doing it for all angles gives the same result and we note that the 2D Fourier transform of the point response function is

$$B_\delta(\omega_x,\omega_y) = \frac{\text{const.}}{|\boldsymbol{\omega}|} = \frac{\text{const.}}{\sqrt{\omega_x^2 + \omega_y^2}}. \tag{13.27}$$

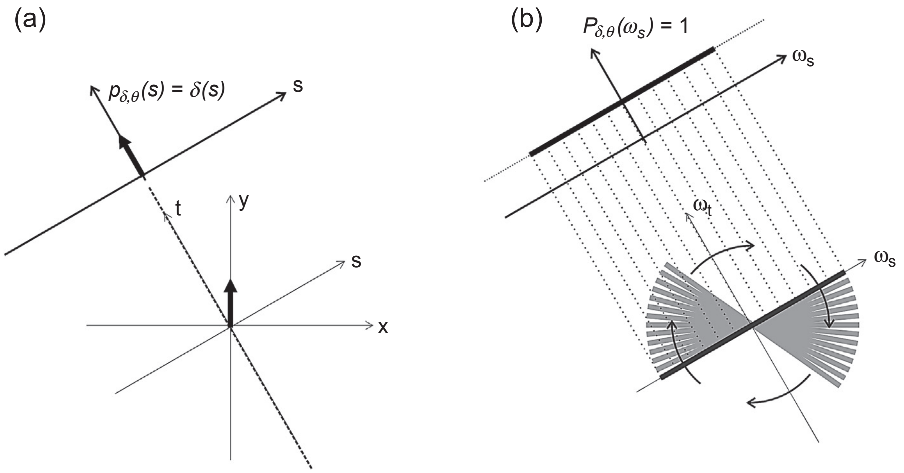
(a)
$p_{\delta,\theta}(s) = \delta(s)$
s
t
y
s
x
(b)
$P_{\delta,\theta}(\omega_s) = 1$
ω_s
ω_t
ω_s

Figure 13.4 The central slice theorem is useful to derive the 2D Fourier transform of the $1/|\boldsymbol{r}|$ point response function. (a) The central point produces projections $p_{\delta,\theta}(s) = \delta(s)$ with 1D Fourier transforms $P_{\delta,\theta}(\omega_s) = 1$. (b) Back-projecting (smearing) $P_{\delta,\theta}(\omega_s)$ along the t-direction is, according to the central slice theorem, the same as populating the 2D Fourier space along lines with $\omega_t = 0$ (dark line). Doing this for all projection angles θ (as indicated by the gray lines) produces, in the same way, a $1/|\boldsymbol{\omega}|$-profile as the back-projection of $\delta(s)$ in object space produces a $1/|\boldsymbol{r}|$-profile. The only difference: the lines in 2D Fourier space are 90° to the lines in object space.

This is indeed a very interesting finding: that the 2D Fourier transform of the point spread function of $\mathscr{B}\{\mathscr{R}\{\cdot\}\}$ has the same shape in object space and Fourier space. Now we can easily derive the inverse integral kernel, which is in Fourier space:

$$B_\delta^{-1}(\omega_x, \omega_y) = |\boldsymbol{\omega}| = \sqrt{\omega_x^2 + \omega_y^2}. \tag{13.28}$$

Remembering our earlier statements about ill-posedness, we can see that $B_\delta(\omega_x,\omega_y)$ approaches zero for $|\boldsymbol{\omega}| \rightarrow \infty$. That is, higher spatial frequencies are less recoverable and high-frequency noise may lead to corruption of reconstructed images. Furthermore, we can see that at $|\boldsymbol{\omega}| = 0$ the inverse solution will always be zero. In other words: the average object value (average attenuation, average activity) cannot be recovered. This fact results formally from the infinite angular integration, which gives an infinite average in the back-projection and which in turn is consequently canceled by the inverse kernel (note the constant term in Eqn (13.15), which we have subsequently omitted). Practically, the loss of average can be compensated by proper calibration and image scaling.

All the mathematics above give rise to the following variants of 2D tomographic image reconstruction algorithms for parallel beams:

(I) Filtered back-projection (and correction in 2D Fourier space)

1. Take all projection data $p(s,\theta)$ and back-project it in object space according to $b(x,y) = \mathscr{B}\{p(s,\theta)\}$.
2. Correct the back-projected image in Fourier space by
   a. Fourier transformation $B(\omega_x,\omega_y) = \mathcal{F}\{b(x,y)\}$
   b. Correction $M(\omega_x,\omega_y) \approx \frac{B(\omega_x,\omega_y)}{B_\delta(\omega_x,\omega_y)} = |\boldsymbol{\omega}|B(\omega_x,\omega_y)$
   c. Fourier back-transformation $\mu(x,y) = \mathcal{F}^{-1}\{M(\omega_x,\omega_y)\}$

(II) Filtered back-projection (and correction in object space)

1. As above…
2. Correct the back-projected image in object space by the 2D convolution $\mu(x,y) \approx b(x,y) * \mathcal{F}^{-1}\{|\boldsymbol{\omega}|\}$

(III) Back-projection of filtered projections (and correction in 1D Fourier space of Radon space)

1. Correct each projection in the following way:
   a. Fourier transformation $P_\theta(\omega_s) = \mathcal{F}\{p_\theta(s)\}$
   b. Correction $\widehat{P}_\theta(\omega_s) = \omega_s P_\theta(\omega_s)$
   c. Fourier back-transformation $\widehat{p}_\theta(s) = \mathcal{F}^{-1}\{\widehat{P}_\theta(\omega_s)\}$
2. Back-project each projection $\mu(x,y) \approx \mathscr{B}\{\widehat{p}(s,\theta)\}$

(IV) Back-projection of filtered projections (and correction in 1D Radon space)

1. Correct each projection by deconvolution according to $\widehat{p}_\theta(s) = p_\theta(s) * \mathcal{F}^{-1}\{\omega_s\}$
2. Back-project each projection $\mu(x,y) \approx \mathscr{B}\{\widehat{p}(s,\theta)\}$

In the case of *Filtered Back-projection* the central slice theorem was useful to derive the correction functions $1/B_\delta(\omega_x,\omega_y)$ analytically. In case of the *Back-projection of Filtered Projections* it was useful to derive that correction can be made in Radon space before back-projecting the values. Note that the difference of algorithms I/III and II/IV is whether the correction step is done by deconvolution in object/Radon space or by division in the respective Fourier spaces. The *Back-projection of Filtered Projections* (III, IV) is in general the faster procedure and has the advantage that correction can be made immediately after acquisition of a single projection. Whether correction is less complex via deconvolution or via 1D Fourier transformation depends on the structure of the correction function. A closer look shows that the inverse kernel for deconvolution can be kept small with respect to nonzero values and hence the deconvolution can be faster than the Fourier transform solution. But in general one should say that with today's strong computer powers such questions are no longer of importance, at least for 2D image reconstruction.

13.5 Implementation

In the last section we derived the basic theoretical formulations of the inverse problem of parallel beam hard field tomography and its analytical solution. A practical implementation on a computer requires further considerations, such as proper discretization and application of numerical procedures. All the details of this are far beyond the scope of this book. Therefore we will touch on these things only briefly here and refer the interested reader to other textbooks, such as Herman (1980), Kak and Slaney (1988), and Natterer (1986).

13.5.1 Sampling and discretization

Since computers can only handle finite sets of numbers we have to discretize the problem. Formally, as we will see in the next section, this means that functions become vectors, operators become matrices, and operations become matrix multiplications. Practically, one proceeds in the following way. The object space is commonly discretized into pixels, that is, a regular set of mutually disjoint square regions (Figure 13.5). Within each pixel the object value (attenuation, activity) is considered as being constant. After assigning indices (i,j) to the pixels, the object is then represented by a matrix or image with discrete values $\mu_{i,j}$. A projection $p_\theta(s)$, which is a continuous function, is now considered as being discretely sampled, as shown in Figure 13.5. Discretizing both the s-dimension and the θ-dimension gives discrete Radon space representation by a matrix with values $p_{k,l}$. The measurement channels or rays may be considered as either infinitely small lines or channels of finite width. The choice is somewhat dependent on the conditions how pixel values contribute to ray integrals (compare the discussion in Section 13.1). The fundamental principle is to discretize the infinitely small contributions $\mu(l)\mathrm{d}l$, respectively $a(l)\mathrm{d}l$ in Eqns (13.2) and (13.3). For transmission tomography the contribution of a pixel to a ray integral is $\mu_{i,j}\Delta l_{i,j}$, that is, pixel attenuation value times ray length within the pixel. For emission tomography it is $a_{i,j}\Delta A$, that is, pixel activity value times area contribution of the pixel to the measurement channel. In general we may say that each pixel (i,j) contributes to the integral value in a measurement channel (k,l) with a weight $a_{i,j,k,l}$.

There are many ways to obtain the weights $a_{i,j,k,l}$. Primarily they are derived from geometric considerations of the tomography scanner design, that is, the spatial positions and extensions of sources and detectors relative to the defined object. However, some simplified weight calculations have also been developed, which are less geometry based but more computationally efficient. In the following we will, with reference to Figure 13.5, give four examples of how weight functions may be calculated, but omit derivation of mathematical formulae or algorithm descriptions.

Binary pixel weights (I): In this most simple and computationally efficient procedure, a pixel binary weight is determined by answering the question of whether the center of the pixel is within or outside a finite-width ray. If rays are considered as infinitely thin, a threshold distance between ray and pixel center may be used for consideration.

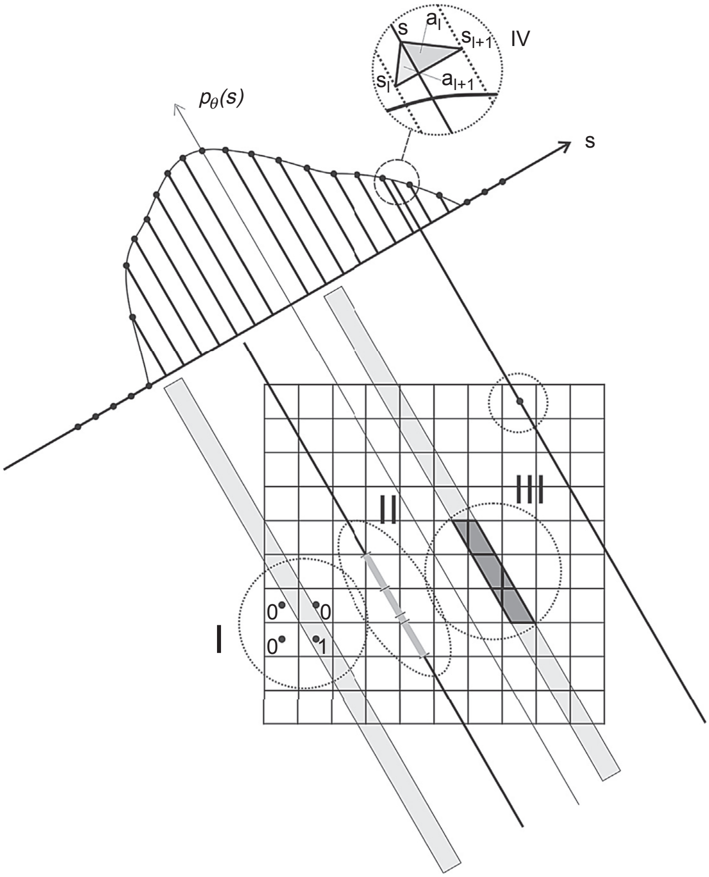

Figure 13.5 Discretization. The object space is a matrix of pixels and the projection is discretely sampled. The contribution of pixels to projection values is given by weights. For the computation of their values, different schemes (I—IV) exist. Further explanation is given in the text.

Length of ray (II): For a thin ray, represented mathematically by a line, the length of the ray in the pixel is determined and taken as weight. This corresponds to the physical principle of ray attenuation in transmission tomography. The calculation is more expensive than for (I).

Area of ray and pixel (III): For a ray of finite width, represented mathematically by a polygon, the intersection area of the ray with the pixel is determined and taken as weight. This corresponds to the physical principle of measurements in emission tomography. The calculation is more expensive than for (II).

Weighted assignment (IV): This method is less accurate in a geometrical sense but highly computationally efficient. For each pixel center one determines the s-value in a parallel projection; see Eqn (13.6). This value is typically in between two sampling points s_l and s_{l+1}. Hence the ray is being considered as contributing to both projection samples with weights $a_{i,j,k,l} = (s_{l+1} - s)/\Delta s$ and $a_{i,j,k,l+1} = (s - s_l)/\Delta s$.

Having done this discretization, the elementary transformations derived above can be carried out as tensor operations (double matrix summations) according to the following equations:

Projection (equivalent to Eqn (13.8)):

$$p_{k,l} = \sum_{i=0}^{N_p-1} \sum_{j=0}^{N_p-1} a_{i,j,k,l} \mu_{i,j}. \tag{13.29}$$

Simple back-projection (equivalent to Eqn (13.12)):

$$b_{i,j} = \sum_{k=0}^{N_\theta-1} \sum_{l=0}^{N_s-1} a_{i,j,k,l} p_{k,l}. \tag{13.30}$$

1D Fourier transformation and inverse Fourier transformation:

$$F_k = \sum_{m=0}^{N_m-1} \exp\left(-2\pi \mathrm{i} \frac{m \cdot k}{N_m}\right) f_m \tag{13.31}$$

$$f_m = \frac{1}{N_k} \sum_{k=0}^{N_k-1} \exp\left(2\pi \mathrm{i} \frac{m \cdot k}{N_k}\right) F_k \tag{13.32}$$

2D Fourier transformation and inverse Fourier transformation:

$$F_{k,l} = \sum_{n=0}^{N_n-1} \sum_{m=0}^{N_m-1} \exp\left(-2\pi \mathrm{i}\left[\frac{n \cdot l}{N_l} + \frac{m \cdot k}{N_k}\right]\right) f_{m,n} \tag{13.33}$$

$$f_{m,n} = \frac{1}{N_k N_l} \sum_{k=0}^{N_k-1} \sum_{l=0}^{N_l-1} \exp\left(2\pi \mathrm{i}\left[\frac{n \cdot l}{N_l} + \frac{m \cdot k}{N_k}\right]\right) F_{k,l}. \tag{13.34}$$

13.5.2 Noise and apodization of the inverse kernel

Typically measurement data are corrupted by noise. In transmission and emission tomography noise is mostly attributed to the photon statistics in the measurement process. Particularly for fast tomography modalities with short sampling time windows, statistical variations of the photon flux at the detector are an unavoidable source of noise. But also uncorrected fluctuations in emissivity of an X-ray source as well as detector electronics noise contribute to the total noise. Furthermore, there are always some systematic deviations between the assumed and real geometry in the projection process, which introduces errors. Hence, a critical reassessment of the restoration multiplier in Eqn (13.28) is necessary. Remember that reconstruction requires that either the 2D Fourier-transformed back-projection image or the 1D Fourier-transformed

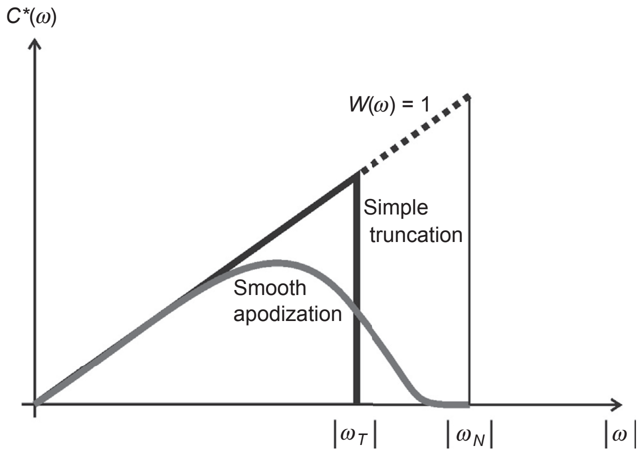

Figure 13.6 Spectral filtering of the correction function $C(\boldsymbol{\omega}) = |\boldsymbol{\omega}|$. The highest recoverable spatial frequency is the Nyquist frequency ω_N. Spatial frequencies above ω_T maybe simply truncated. However, as this introduces visible wave patterns, a smooth apodization is commonly used. The type and shape of the frequency filter function can be freely chosen case by case to obtain images of good quality.

projections need frequency-wise multiplication with the respective correction function $C(\boldsymbol{\omega}) = |\boldsymbol{\omega}|$ and $C(\omega_s) = \omega_s$. As $|\boldsymbol{\omega}|$ or ω_s increases, (backprojected) values will be more amplified by the multiplication. If the data contain additive noise, it will also be amplified. Using the unmodified frequency space correction function is mathematically correct but may lead to image degradation by noise amplification. Hence some band limitation of the kernel is of advantage. This is done by spectral filtering with a window function $W(|\boldsymbol{\omega}|)$, which truncates higher spatial frequencies more or less smoothly, as illustrated in Figure 13.6. The modified correction function is then

$$C^*(\boldsymbol{\omega}) = W(|\boldsymbol{\omega}|)\cdot C(\boldsymbol{\omega}). \tag{13.35}$$

Note that the choice of the apodizing filter function is by no means physically justified. It simply serves the adequate suppression of noise. Its effect on quantitative information in the reconstructed image must be assessed case by case and, if required, accounted for by proper calibration of the imaging process.

13.5.3 Tomography with fan beams and other projection geometries

Eventually some comments shall be made to the fact that most projection geometries are not parallel projection geometries. In fact this holds only for very few arrangements, for instance synchrotron X-ray tomography or some type of SPECT cameras. A more typical projection geometry is fan-beam geometry (Figure 13.7). Examples here are transmission tomography with a single source and an opposite

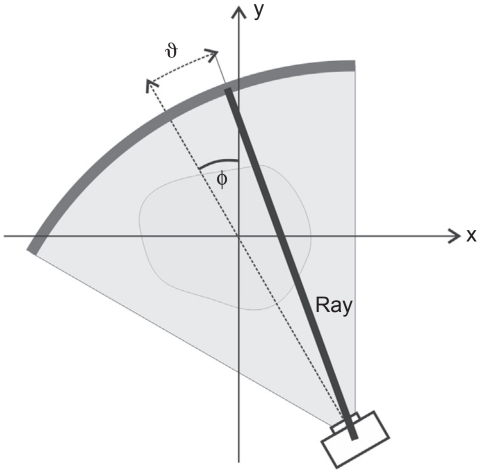

Figure 13.7 Parameters of a fan-beam geometry.

detector arc as well as, to some degree, emission tomography with circular detector arrangements. However, also fan-beam geometry, though widely used in medical CT, is only one particular projection arrangement. Hence we shall say that the most common way to do image reconstruction in the frame of parallel backprojection, as derived above, involves a step of transforming the projection data into a parallel beam geometry. This concept is referred to as *rebinning* and is illustrated in Figure 13.7.

Assume that we obtain an X-ray projection in a fan-beam geometry, with the X-ray source being in rotational position ϕ. The detector arc then acquires samples of a projection, which is a function of the detection angle ϑ. Once we have completed a full rotation of the setup we need an interpolative mapping $p(\vartheta, \phi) \mapsto p(s, \theta)$ within Radon space. For a point (s,θ), applying some rules of geometry, we find that $\theta = \phi + \vartheta$ and $s = R \sin \vartheta$, with R being the distance of the source from the center of rotation.

13.6 Algebraic image reconstruction

As we have seen in Section 13.5, a proper discretization leads to an algebraic formulation of forward and inverse problem. This algebraic formulation can be further condensed into the subsequent set of linear algebra equations. Here it should be noted that a direct solution of the algebraic equation system for most hard field tomography problems is far beyond today's computer powers. However, this framework is useful to derive iterative solution procedures, which may be of some advantage in particular cases, for example, for inverse problems with incompletely or nonhomogeneously sampled Radon space, such as *Limited Angle Tomography*.

In the last section we have derived the discrete representation of object and Radon space as matrices and the operations as weighted double summations over matrices (Eqns (13.29) and (13.30)). For algebraic treatment it is more convenient to lump 2D object and projection data into vectors. That is, we define an object vector $\boldsymbol{\mu} = [\mu_{0,0}, \ldots, \mu_{0,N_p-1}, \ldots, \mu_{N_p-1,0}, \ldots \mu_{N_p-1,N_p-1}]^T$ with N_p^2 values and the same for the projection data $\boldsymbol{p} = [p_{0,0}, \ldots, p_{,0,N_s-1}, \ldots, p_{N_\theta-1,0}, \ldots p_{N_\theta-1,N_s-1}]^T$ with $N_s \cdot N_\theta$ values. The weights are lumped in a matrix:

$$\boldsymbol{A} = \begin{bmatrix} a_{0,0} & \cdots & a_{N_p^2-1,0} \\ \vdots & \ddots & \vdots \\ a_{0,N_sN_\theta-1} & \cdots & a_{N_p^2-1,N_sN_\theta-1} \end{bmatrix}. \tag{13.36}$$

Then we get the following equivalent algebraic operations:

Projection (equivalent to Eqns (13.8) and (13.29)):

$$\boldsymbol{p} = \boldsymbol{A}\boldsymbol{\mu}. \tag{13.37}$$

Simple back-projection (equivalent to Eqns (13.12) and (13.30)):

$$\boldsymbol{b} = \boldsymbol{A}^{\boldsymbol{T}}\boldsymbol{p}. \tag{13.38}$$

Combined projection and simple back-projection (equivalent to Eqn (13.15)):

$$\boldsymbol{b} = \boldsymbol{A}^{\boldsymbol{T}}\boldsymbol{A}\boldsymbol{\mu}. \tag{13.39}$$

Inverse solution via back-projection:

$$\boldsymbol{\mu} \approx \boldsymbol{C}\boldsymbol{A}^{\boldsymbol{T}}\boldsymbol{p} = \left(\boldsymbol{A}^{\boldsymbol{T}}\boldsymbol{A}\right)^{-1}\boldsymbol{A}^{\boldsymbol{T}}\boldsymbol{p}. \tag{13.40}$$

So far these are interesting properties. If we call $\boldsymbol{A}$ the system matrix, then back-projection is multiplying with the transposed system matrix and the inverse correction via the point response function is given by the matrix $\boldsymbol{C} = (\boldsymbol{A}^{\boldsymbol{T}}\boldsymbol{A})^{-1}$. By introducing further matrix operations we may complete the story in algebraic terms. Thus, let $\boldsymbol{F}_s$ denote the transformation coefficient matrix for a 1D Fourier transform along the s-dimension of the projections, $\boldsymbol{F}$ the transformation coefficient matrix of a 2D Fourier transform, and $\boldsymbol{R}$ the apodizing spatial filter coefficient matrix; then we find the following equivalents:

Filtered back-projection solution in Fourier space with apodization:

$$\boldsymbol{\mu} \approx \boldsymbol{F}^{-1}\boldsymbol{R}\left(\boldsymbol{A}^{\boldsymbol{T}}\boldsymbol{A}\right)^{-1}\boldsymbol{F}\boldsymbol{A}^{\boldsymbol{T}}\boldsymbol{p}. \tag{13.41}$$

Back-projection of filtered projections via projection Fourier space and apodization:

$$\boldsymbol{\mu} = \boldsymbol{A}^T \boldsymbol{F}_s^{-1} \boldsymbol{R}_s \boldsymbol{C}_s \boldsymbol{F}_s \boldsymbol{p}. \tag{13.42}$$

In the sense of compact notation, these algebraic operator equations are wonderful. However, practically they are of no use. Consider an X-ray tomography system with, let us say, only 100 projections, 100 detectors, and an image space with 100 × 100 pixels. For this system the system matrix would be of dimension $10^4 \times 10^4$. Note that computation of the inverse is of computational order $O(N^3)$. Besides the impossibility to compute $(\mathbf{A}^{\mathrm{T}}\mathbf{A})^{-1}$, the ill-posedness of $\boldsymbol{A}$ would require a spectral decomposition approach to avoid numerical difficulties. Hence, the only way of inverting Eqn (13.37) is to use an iterative algorithm. At this point it should be noted that there is quite a large number of existing iterative reconstruction schemes and a concise treatment is far beyond the scope of this book. Therefore we will only give a brief description here, introduce the correction formula for the algebraic reconstruction technique (ART), and leave the reader with references to other textbooks and publications, for example, Viergever (1988).

A general concept of solving an algebraic inverse problem considers the fact that only an approximate solution can be obtained. That is, we have to extend Eqn (13.37) in the following way:

$$\boldsymbol{p} = \boldsymbol{A}\boldsymbol{\mu} + \boldsymbol{r}. \tag{13.43}$$

Here, $\boldsymbol{p}$ represents the measured projection data and $\boldsymbol{A}\boldsymbol{\mu}$ the ideal projection data coming from our projection model. There will inevitably be some difference between model and real data and this is accounted for by the residue vector $\boldsymbol{r}$. Now, as in regression analysis, we seek an optimal solution $\boldsymbol{\mu}$ that minimizes some distance criterion on $\boldsymbol{r}$. Commonly the L_2 norm is chosen to be minimized, or in other words, we look for a least-squares solution

$$||\boldsymbol{r}||^2 = ||\boldsymbol{p} - \boldsymbol{A}\boldsymbol{\mu}||^2 \overset{!}{\rightarrow} \mathrm{Min}. \tag{13.44}$$

If we were to follow now the conventional way to solve the above optimization problem, we would after a few steps of algebraic math arrive at Eqn (13.40). This is quite interesting, because it tells us that the back-projection-correction approach solves the inverse problem in a least-squares sense. However, we will not do this here, but instead will continue with Eqn (13.43) to derive an iterative solution procedure.

The basic principle of an iterative algorithm is as follows: choose an arbitrary initial solution $\boldsymbol{\mu}^{(0)}$ and correct this solution in subsequent steps denoted by τ until Eqn (13.44) is sufficiently satisfied. In the subsequently derived ART algorithm the correction is done on a per-projection base, but this is specific to ART. Thus, let us assume that we are somewhere in such an algorithm, let us say in step τ. The solution $\boldsymbol{\mu}^{(\tau)}$ is already quite good but not perfect. Hence we get a residue for the projection number i in that very step, which is

$$r_i^{(\tau)} = p_i^{(\tau)} - \boldsymbol{A_i}\boldsymbol{\mu}^{(\tau)}. \tag{13.45}$$

Note that $r_i^{(\tau)}$ and $p_i^{(\tau)}$ are scalar values for projection value i , $\boldsymbol{A_i}$ is a row vector and $\boldsymbol{A_i}\boldsymbol{\mu}^{(\tau)}$ is the forward projection of the whole iterated object values $\boldsymbol{\mu}^{(\tau)}$ onto this single projection value. Now we would like to provide a correction to $\boldsymbol{\mu}^{(\tau)}$ to account for the fact that $r_i^{(\tau)} \neq 0$. Hence, we need to add some correction vector $\boldsymbol{c}^{(\tau)}$ in the form

$$\boldsymbol{\mu}^{(\tau+1)} = \boldsymbol{\mu}^{(\tau)} + \boldsymbol{c}^{(\tau)}. \tag{13.46}$$

How to choose $\boldsymbol{c}^{(\tau)}$? It should be chosen such that the correction leads to a match with the projection value; hence:

$$\boldsymbol{A_i}\left(\boldsymbol{\mu}^{(\tau)} + \boldsymbol{c}^{(\tau)}\right) = p_i^{(\tau)}. \tag{13.47}$$

Rearranging this gives

$$\boldsymbol{A_i}\boldsymbol{c}^{(\tau)} = p_i^{(\tau)} - \boldsymbol{A_i}\boldsymbol{\mu}^{(\tau)} = r_i^{(\tau)}. \tag{13.48}$$

If we had an inverse of $\boldsymbol{A_i}$, we would have a correction vector

$$\boldsymbol{c}^{(\tau)} = \mathrm{Inv}(\boldsymbol{A_i})r_i^{(\tau)}. \tag{13.49}$$

However, such an inverse does not exist, since $\boldsymbol{A_i}$ is not square. In fact, $\boldsymbol{A_i}$ is a vector. However, its closest inverse is the Moore–Penrose inverse

$$\mathrm{Inv}(\boldsymbol{A_i}) = \frac{\boldsymbol{A}_i^T}{\|\boldsymbol{A_i}\|}, \tag{13.50}$$

since it produces the identity $\boldsymbol{A}_\mathbf{i}\ \mathit{Inv}(\boldsymbol{A_i}) = \mathbf{1}$. Now combining Eqns (13.46), (13.49), and (13.50) gives the sought correction term and leads to the corrector for the *Algebraic Reconstruction Technique* (Gordon, Bender, & Herman, 1970):

$$\boldsymbol{\mu}^{(\tau+1)} = \boldsymbol{\mu}^{(\tau)} + \frac{\boldsymbol{A}_i^T\left(p_i^{(\tau)} - \boldsymbol{A_i}\boldsymbol{\mu}^{(\tau)}\right)}{\|\boldsymbol{A_i}\|}. \tag{13.51}$$

There are, as said before, derivatives of this algorithm. Correcting for several projections instead of a single projection leads to the so-called Block-ART algorithm. Correcting all projections in one step leads to a group of algorithms referred to as *Simultaneous Iterative Reconstruction Techniques*. Providing a multiplicative corrector in Eqn (13.46) leads to so-called multiplicative reconstruction techniques, such as the multiplicative ART (De Piero, 1991). Eventually in some cases the least-squares solution is not appropriate. This is the case in emission tomography. There the photon statistics obeys a Poisson law with probability density functions, which are for low photon numbers no longer symmetric about the expectation value. Here expectation maximization techniques, such as maximum likelihood expectation maximization (Shepp & Vardi, 1982), are a proper choice. Moreover, other iterative correction schemes, such as the *Landweber Method* (Landweber, 1951), *Projection onto Convex Sets* (Bauschke & Borwein, 1996), or *Gradient Descent Algorithms* (Snyman, 2005) should be mentioned to complete the view on this particular solution strategy.

13.7 3D analytic image reconstruction

The standard fan-beam tomography can be extended towards 3D tomographic imaging in different ways. In the simplest case, 2D images from different slices are stacked to a 3D data set. This approach can be improved by optimizing the scanning procedure for volumetric imaging, as is being done in helical CT, where the X-ray source follows a spiral path around the object. Another option is to gather projections from different planes simultaneously by increasing the aperture angle of the X-ray beam from a fan towards a cone and measuring the X-ray intensity by a 2D detector array. This method reduces the data acquisition time significantly, compared to the aforementioned techniques.

The standard cone-beam setup comprises an X-ray source with a cone-shaped beam and a 2D flat panel detector (Figure 13.8). Assume that the source–detector compound is rotated around the object such that the source moves along a circular path. It should be noted that in this configuration the 3D Radon space is not as completely sampled as required for analytic reconstruction. Hence this configuration produces some kind of a 3D limited-angle tomography problem. However, this configuration is the most practical one and is today established in many applications. It has been shown that the accuracy in the reconstructed data is acceptable as long as cone-beam angles are small. The Radon transform in three dimensions can be written in general as

$$P(\theta,\gamma,s,r) = \int_{-\infty}^{+\infty} \mu(\theta,\gamma,s,r,t)\mathrm{d}t, \tag{13.52}$$

where μ is the 3D distribution of the linear attenuation coefficient and P are parallel projections defined by the azimuthal and polar angles θ and γ, respectively, as well as the distances s and r (Figure 13.8(a)). According to the central slice theorem, the distribution μ can be reconstructed exactly, if the Radon space is completely sampled,

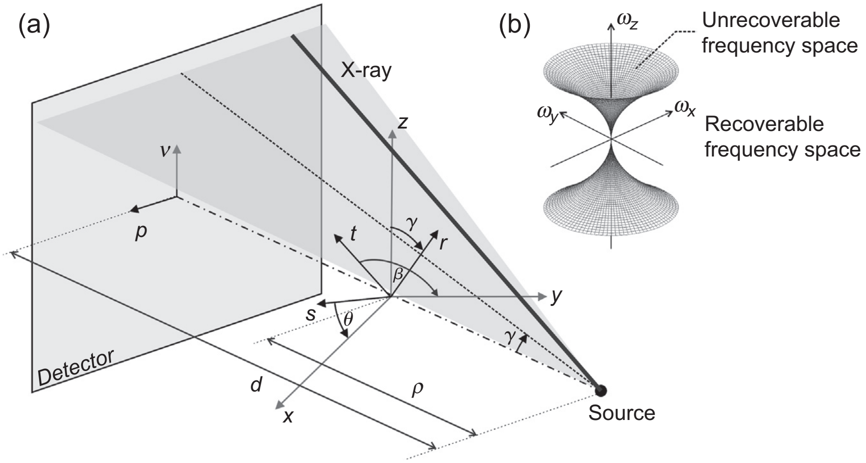

Figure 13.8 Cone-beam tomography with a source-detector rotating in a plane: geometryrecoverable regions in frequency space.

comprising all values for θ,γ,s, and r. With just a rotation of the source and usage of a flat panel detector, radiographic projections $R(p,v,\beta)$, in which p and v are the coordinates of the pixels on the detector and β is the angle of rotation of the source, can be acquired.

The part of the 3D frequency space that can be recovered with this kind of setup is depicted in Figure 13.8(b). From this drawing it is apparent that during reconstruction of the object space, an exact solution can only be achieved in the plane of the source path. With growing tilting angle the uncertainty increases, which should be considered in practical measurements. There are approaches for other scanning modalities that cover a larger region of the frequency space, but in turn require far more complicated scanning procedures (Tuy & June, 1981).

3D image reconstruction can be performed in different ways. Although there exist approaches for a direct inversion of the Radon transformation (Minerbo, 1979), which could provide an exact solution, they are not feasible in practical applications. Instead, different approximate solutions have been proposed. The most practical one is the algorithm introduced by Feldkamp (Feldkamp, Davis, & Kress, 1984). It is based on a convolution−back-projection. In this algorithm, the coordinates of the corresponding parallel projections are calculated from the cone-beam projections by geometrical considerations as

$$t = p\frac{\rho}{d\sqrt{1+\frac{p^2}{d^2}}}; \quad \theta = \beta + \arctan\left(\frac{p}{d}\right); \quad r = v\frac{\rho}{d\sqrt{1+\frac{v^2}{d^2}}}; \quad \gamma = \arctan\left(\frac{v}{d}\right) \tag{13.53}$$

with ρ and d being the distance between the X-ray source and the center of rotation and the distance between the X-ray source and the detector, respectively. The object distribution is then reconstructed by

$$\mu(x,y,z) = \frac{1}{2}\int_{0}^{2\pi} \frac{\rho^2}{(\rho-s)^2} \int_{-\infty}^{\infty} R(p,\xi,\beta)\, c\left(\frac{\rho t}{\rho-s}-p\right) \frac{\rho}{\sqrt{\rho^2+p^2+\xi^2}}\, \mathrm{d}p\mathrm{d}\beta. \tag{13.54}$$

The function c is the reconstruction filter kernel, which is equivalent to the 2D case. It has been proven that this algorithm is accurate in the xy-plane, but causes some blurring in the z-direction, and here only for the varying part of the object in this direction. Also, iterative reconstruction techniques such as ART have been proposed for cone-beam CT (Colsher, 1977). However, for 3D reconstruction iterative schemes are computationally very expensive.

13.8 Local tomography, limited-angle tomography, and limited-data tomography

It should be mentioned that, particularly in nonmedical tomography applications, it can happen that a full 180° sampling of the Radon space is technically not feasible (Quinto, 1988). This concerns problems where the object cannot be surrounded by the source–detector setup due to space constraints. Such situations happen frequently in nondestructive testing of objects with critical aspect ratios. A good example is inspection of printed circuit board assemblies with X-ray CT. Here, projections are missing and hence we speak of a *limited-angle tomography* (Figure 13.9(a)). In other cases it may be difficult to provide a homogeneous sampling of the Radon space, either with respect to the angle or with respect to the projections. Again, this is mostly due to restricted access to the object of investigation. An example of this is tomography on Tokamak plasmas. Another frequently encountered problem is that tomography is to be applied on objects that are too large to fully fit into the beam arrangement. In this case some areas of the object are only partly contributing to the projection generation, and we then speak of *limited-data tomography* (Figure 13.9(b)).

For limited-angle and limited-data problems it can be generally stated that reconstructed images will contain artifacts. For limited angle problems such artifacts constitute themselves as cushion-like distortions of the object shapes. For limited-data problems the artifacts can have various appearances. If the Radon space is rather homogeneously but not very densely sampled, then object structures appear blurred and of low resolution. Inhomogeneous sampling, which means that larger angular or lateral projection regions are spared from the data, cause streak and cushion artifacts. Analytic reconstruction techniques, which rely on a fully sampled Radon space, are more prone to image distortions, and even for already moderate missing data ratios the images may become largely corrupt. The reason is that steep gradients from

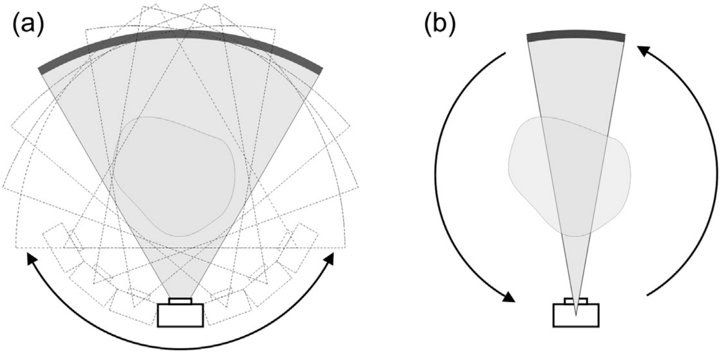

Figure 13.9 Limited-angle tomography (a) and local tomography (b).

measured values to zero nonmeasured values in the projection data are amplified and back-projected in the reconstruction. A work-around may be to extrapolate data from the missing regions, which is, however, not straightforward. Iterative reconstruction techniques are much better suited to account for missing data, since they do not erroneously incorporate data into reconstruction. Moreover, iterative schemes can in principle incorporate a priori knowledge, for example, on object shape or object value ranges, which facilitates reconstruction from limited data. There are a number of overview articles on that problem, but eventually it must be stated that for limited-angle and limited-data tomography no coherent solution strategy exists and assessment must be made on a case-by-case basis. For local tomography things are somewhat better. In this case some object structures that are outside the reconstructed region, that is, the region fully covered in all projections, will in some way give an additive contribution to the local regions in the reconstruction process. This will first of all corrupt the quantitative reconstruction. However, the distortion of structural details is only significant if external structures have large spatial gradients and are being close to the inner reconstructed region. The farther away are such structures, the smaller is their influence on the final image. But again, it is not possible to make general assessments for this case; rather, once again a case-by-case consideration is required.

13.9 Future trends

Image reconstruction for hard field tomography is a continuously developing field. While the basic mathematics of the Radon transformation and its inverse in two or more dimensions is a solved problem, the practical aspects of image reconstruction of noisy, corrupted, or limited tomographic data is a major driver for current developments. Reconstruction of noisy data is fostered by recent developments in fast low-dose X-ray CT systems. Limited-data and limited-angle problems are of highest interest in process analysis and nondestructive testing, where often process components, machines, and other objects are too large for a full coverage with projections, as required from the inverse problem solution. Here, particularly, iterative image reconstruction schemes are of great importance. Since iterative algorithms are commonly computationally expensive, we see more and more applications of novel computer architectures, such as massive parallel and graphics processing unit systems. The latter are even important for fast tomography modalities, which can generate thousands of images per second, such as ultrafast X-ray tomography introduced earlier in this book. Solving an inverse problem under incorporation of a priori knowledge or with inherent nonlinearity, as for instance introduced by data corruption due to beam hardening or scattering, is yet another challenge. Moreover, data and image fusion of multiple tomographic modalities gains a stronger focus today in process tomography. All in all, inverse problems and their efficient solution remain a challenging mathematical, computational, and engineering problem in the coming years.

13.10 Sources of further information and advice

The fundamentals of image reconstruction for hard field tomography have been concisely described in many textbooks, particularly for medical imaging. Some are more focused on the mathematical and computational points, while others are more related to technical principles. This chapter provides an extract of the most common reconstruction techniques and their mathematical background. Throughout the text references to other literature have been given.

Appendix A.1: proof of rotational invariance of the 2D Fourier transform

We would like to prove the following: If $G(\omega_x,\omega_y)$ is the 2D Fourier transform of a 2D function $g(x,y)$, then for any rotation

$$\begin{pmatrix} s \\ t \end{pmatrix} = \begin{pmatrix} \cos\theta & \sin\theta \\ -\sin\theta & \cos\theta \end{pmatrix} \begin{pmatrix} x \\ y \end{pmatrix}$$

of the coordinate system also $G(\omega_s,\omega_t)$ is the 2D Fourier transform of $g(\omega_s,\omega_t)$ with

$$\begin{pmatrix} \omega_s \\ \omega_t \end{pmatrix} = \begin{pmatrix} \cos\theta & \sin\theta \\ -\sin\theta & \cos\theta \end{pmatrix} \begin{pmatrix} \omega_x \\ \omega_y \end{pmatrix}.$$

This effectively means that the 2D Fourier transform is rotationally invariant and that it is of no matter under which rotation of the coordinate system the two-step integration is performed.

Proof:

$$\mathcal{F}\{g(s,t)\} = \int_{-\infty}^{+\infty}\int_{-\infty}^{+\infty} g(s,t)\exp\left(-i\left[\omega_x x + \omega_y y\right]\right)\mathrm{d}x\mathrm{d}y$$

$$\mathcal{F}\{g(s,t)\} = \int_{-\infty}^{+\infty}\int_{-\infty}^{+\infty} g(s,t)\exp\left(-i\left[\omega_x(s\cos\theta - t\sin\theta)\right.\right.$$
$$\left.\left. + \omega_y(s\sin\theta + t\cos\theta)\right]\right)\mathrm{d}x\mathrm{d}y$$

$$\mathcal{F}\{g(s,t)\} = \int_{-\infty}^{+\infty}\int_{-\infty}^{+\infty} g(s,t)\exp\left(-i\left[s(\omega_x\cos\theta + \omega_y\sin\theta)\right.\right.$$
$$\left.\left. + t(\omega_x\sin + \omega_y\cos\theta)\right]\right)\mathrm{d}x\mathrm{d}y$$

$$\mathcal{F}\{g(s,t)\} = \int_{-\infty}^{+\infty}\int_{-\infty}^{+\infty} g(s,t)\exp\left(-i\left[s(\omega_x\cos\theta + \omega_y\sin\theta)\right.\right.$$
$$\left.\left. + t(\omega_x\sin\theta + \omega_y\cos\theta)\right]\right)\mathrm{d}s\mathrm{d}t$$

$$\mathcal{F}\{g(s,t)\} = G(\omega_x\cos\theta + \omega_y\sin\theta, \omega_x\sin\theta + \omega_y\cos\theta)$$

Note that $\mathrm{d}x\mathrm{d}y = \mathrm{d}s\mathrm{d}t$.

References

Bauschke, H. H., & Borwein, J. M. (1996). On projection algorithms for solving convex feasibility problems. *SIAM Review, 38*, 367−426.

Colsher, J. G. (1977). Iterative three-dimensional image reconstruction from tomographic projections. *Computer Graphics and Image Processing, 6*, 513−537.

De Piero, A. R. (1991). Multiplicative iterative methods in computed tomography. In G. T. Hermann, A. K. Louis, & F. Natterer (Eds.), *Mathematical methods in tomography* (pp. 167−186). Berlin-Heidelberg: Springer.

Feldkamp, L. A., Davis, L. C., & Kress, J. W. (1984). Practical cone-beam algorithm. *Journal of the Optical Society of America A, 1*, 612−691.

Gordon, R., Bender, R., & Herman, G. T. (1970). Algebraic reconstruction techniques (ART) for three-dimensional electron microscopy and X-ray photography. *Journal of Theoretical Biology, 29*, 471−481.

Herman, G. T. (1980). *Image reconstruction from projections: Fundamentals of computerized tomography*. New York: Academic Press.

Kak, A. C., & Slaney, M. (1988). *Principles of computerized tomographic imaging*. New York: IEEE Press.

Landweber, L. (1951). An iteration formula for Fredholm integral equations of the first kind. *American Journal of Mathematics, 73*, 615−624.

Minerbo, G. N. (1979). Convolutional reconstruction from cone-beam projection data. *IEEE Transactions on Nuclear Science, NS-26*, 2682−2684.

Natterer, F. (1986). *The mathematics of computerized tomography*. New York: Wiley-Teubner.

Quinto, T. E. (1988). Exterior and limited-angle tomography in non-destructive evaluation. *Inverse Problems, 14*, 339−353.

Radon, J. (1917). Über die Bestimmung von Funktionen durch ihre Integralwerte längs gewisser Mannigfaltigkeiten, Berichte über die Verhandlungen der Königlich-Sächsischen Gesellschaft der Wissenschaften zu Leipzig. *Mathematisch-Physische Klasse, 69*, 262−277.

Shepp, L. A., & Vardi, Y. (1982). Maximum likelihood reconstruction for emission tomography. *IEEE Transactions on Medical Imaging, 1*, 113−122.

Snyman, J. A. (2005). *Practical mathematical optimization: An introduction to basic optimization theory and classical and new gradient-based algorithms*. New York: Springer Publishing.

Tuy, H. K. (June 1981). *An inversion formula for cone-beam reconstruction*. Department of Computer Science Tech. Rep. MIPG57. Buffalo, NY: State University of New York at Buffalo.

Viergever, M. A. (1988). Introduction to discrete reconstruction methods in medical imaging. In M. A. Viergever, & A. E. Todd-Prokropek (Eds.), *Medical imaging, NATO ASI series, mathematics and computer science F39* (pp. 43−65). Berlin: Springer.

Direct methods for image reconstruction in electrical capacitance tomography

14

Z. Cao, L. Xu
Beihang University, Beijing, China

14.1 Introduction

Electrical capacitance tomography (ECT) has been developed to reconstruct the spatial permittivity distribution of dielectric materials by using the measured capacitances. Compared with X-ray tomography, ECT possesses the advantages of no radiation, fast response, robustness, and simple structure. It is considered as a promising technology for many industrial applications, such as multiphase flow measurement in pipelines (Ismail, Gamio, Bukhari, & Yang, 2005), choking transition in gas−solid risers (Du, Warsito, & Fan, 2006a), flames in porous media (Liu, Chen, Xiong, Zhang, & Lei, 2008), mass flow measurement of pneumatically conveyed solids (Sun, Liu, Lei, & Li, 2008), solids distribution measurement in a cyclone separator (Wang, Liu, Jiang, & Yang, 2004), and the analysis of dynamic processes in fluidized beds (Du, Warsito, & Fan, 2006b). The key issue of ECT is to reconstruct the permittivity distribution from a set of electrical capacitances measured on the boundary of the region of interest (ROI).

Unlike the so-called "hard field" property of the X-ray, the distribution of the electrical field can be distorted by the objects placed inside. The distortion stems from the "soft field" property of the electromagnetic field. The property indicates that any of the electrodes has the ability to collect the information of changes in any part of the whole sensing region, so the ability of information capture for any electrode is global, while that of the sensing unit in X-ray tomography is local, as only the information along the X-ray radiation lines can be detected. As a result, besides the image reconstruction algorithms that can be inherited from the X-ray tomography, such as the sensitivity matrix-based algorithms, the ECT has its own boundary map-based algorithms, which are also termed direct algorithms (Calderon, 2006; Bikowski & Mueller, 2008; Cao & Xu, 2013a,b). There usually exist two different boundary maps, that is, the Dirichlet-to-Neumann map and the Neumann-to-Dirichlet map, which can be physically interpreted as the voltage-to-current density map and the current density-to-voltage map, respectively (Cao & Xu, 2013c). The discretized form of the maps can be constructed from the measured mutual capacitances.

In the literature, most of the image reconstruction algorithms of ECT were implemented based on the sensitivity theorem (Geselowitz, 1971; Lehr, 1972), which is a kind of linearization method through using the perturbation principle (Soleimani

Industrial Tomography. http://dx.doi.org/10.1016/B978-1-78242-118-4.00014-9
Copyright © 2015 Elsevier Ltd. All rights reserved.

& Lionheart, 2005). However, ECT possesses the "soft" field property, as the sensing field is distorted by objects in the imaging area. The sensitivity distribution changes with the spatial permittivity distribution. In recent years, iterative image reconstruction with an updated sensitivity matrix has been investigated (Fang, 2004; Li & Yang, 2008; Smolik, Mirkowski, Olszewski, & Szabatin, 2006), but they are very time-consuming and the property of convergence of the iteration has not been reported. Some existing noniterative methods are usually simplifications of the iterative ones, for example, preiteration method (Wang, Wang, & Yin, 2004) and linear back-projection (LBP) (Yang & Peng, 2003). These noniterative methods, based on the sensitivity/Jacobi matrix, are not direct algorithms. The permittivity perturbations at all positions in the ROI can only be reconstructed simultaneously.

In recent years, several direct algorithms have been introduced to electrical tomography by using Calderon's method (Bikowski & Mueller, 2008; Boverman, Kao, Isaacson, & Saulnier, 2009; Cao, Xu, & Wang, 2009), the dbar method (Cao, Xu, Fan, & Wang, 2010; Isaacson, Mueller, Newell, & Siltanen, 2004; Mueller, Siltanen, & Isaacson, 2002; Murphy & Mueller, 2009), the complex geometrical optics method (Astala, Mueller, Paivarinta, & Siltanen, 2010), and the factorization method (Cao et al., 2011b; Hyvönen, Hakula, & Pursiainen, 2007; Hyvöen, 2007; Schmitt, 2009). Both the dbar method and the complex geometrical optics method originate from Calderon's method (Calderon, 2006), which is practically suitable for low-contrast material distribution (Cao et al., 2009). However, the factorization method is suitable to reconstruct the disturbed distributions with a high-contrast background, as it is a method based on the principle of the value range identification. The factorization method is usually suitable to reconstruct the disturbed distributions with a connected background, for example, multi-rods. If the region to be reconstructed is of a ring shape, for example, the factorization method fails to work (Schmitt, 2009). The dbar method has no such requirement on the shape of the ROI. However, the sensor configurations used in electrical impedance tomography (EIT) are different from those applied in ECT. The dbar method that was reported and implemented in EIT requires a sinusoidal wave-like current pattern, in which all the values of the current injected at each electrode generates a discrete approximation of the sine function (Isaacson et al., 2004). As the ECT sensor has an earthed screen and each electrode is usually either excited or grounded for hardware implementation, the dbar method successfully implemented in EIT cannot be directly applied to ECT.

Moreover, the sensors and associated reconstruction techniques in ECT are often of and for circular shapes. There exists a demand for noncircular sensors, for example, the cross sections of the pipes in the power industry or chemical reactors are square or rectangular (Liu et al., 2008; Wang, Lv, & Li, 2008). However, direct calculation of the scattering transform from measured capacitances in the case of a noncircular sensor, for example, an elliptical region, is very complicated (Murphy, Mueller, & Newell, 2007). Also, the factorization method requires the calculation of the Neumann-to-Dirichlet map, that is, the current density-to-voltage map. The test function was constructed directly for the noncircular region (Hakula & Hyvönen, 2009), which is very computationally complicated.

In this chapter, we also provide a new treatment to the direct methods, for example, Calderon's method, dbar method, and factorization method, when applied to the noncircular sensors by using the conformal transformation after the reconstruction. The direct methods summarized here can also be applied to a circular sensor, which is a simplified case of noncircular sensors. A square sensor was constructed and experiment results were carried out.

14.2 Three typical direct algorithms for ECT

14.2.1 Conformal transformation and governing equation

Figure 14.1 shows that a simply connected region of any shape, for example, E, can be mapped onto a unit disk, termed as Ω according to Riemann's theorem (Ahlfors, 2004). Assume that $f(z)$ defines a conformal mapping of a region E onto another region Ω. If a point in Ω is represented by w, then there exists a unique conformal map that transforms a point denoted by z in E onto w, which satisfies

$$w = f(z) \tag{14.1}$$

Accordingly, the subregions of E, that is, e_1, e_2, and e_3, are conformally mapped onto subregions of Ω, Ω_1, Ω_2, and Ω_3, respectively. Meanwhile, any continuous function defined in E holds its values after the conformal mapping onto Ω. The Laplace equations associated with the piece-wise constant coefficients in E can be solved in Ω by using a unique conformal transformation (Gong & Gong, 2007). Therefore, the reconstruction in E can be first performed in the unit disk Ω, then finalized by conformally transforming the results onto E to obtain the solution in E. As a result, direct calculations on the noncircular region can be avoided for image reconstruction in noncircular sensors.

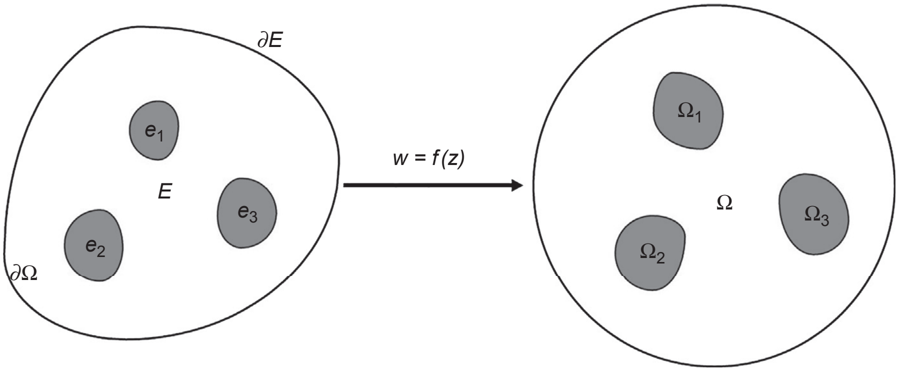

Figure 14.1 Conformal map from a simply connected region to a unit disk.

Since the positions of pixels in the reconstructed image are transformed from the unit disk to the noncircular region in advance, the image reconstruction is performed in two steps. First, the image data are calculated using the reconstruction method of the circular sensor. Secondly, the data are displayed in the noncircular region in a point-to-point mapping manner from the circular region to the noncircular region through the conformal transformation. In the two steps, the scattering transform only needs to be calculated for the circular sensor before the conformal transformation that transforms the points in the noncircular region onto those in the unit disk (Cao et al., 2010).

The governing equation of the circular sensing field that denoted as Ω in ECT is

$$\nabla \cdot \varepsilon(z)[\nabla \phi_{\varepsilon}(z)] = 0 \tag{14.2}$$

where $\varepsilon(z)$ and $\phi_{\varepsilon}(z)$ are permittivity and associated electric potential at z, respectively. $z = x + \mathrm{i}y$ is a complex number that represents the position with coordinates (x, y), and i is the imaginary unit.

If the permittivity distribution is $\varepsilon(z)$, denote the voltage-to-current density map, that is, the Dirichlet-to-Neumann map, as

$$\Lambda_{\varepsilon}: \quad \phi(z)|_{\partial\Omega} \rightarrow \varepsilon(z) \frac{\partial \phi(z)}{\partial n}\bigg|_{\partial\Omega} \tag{14.3}$$

Here, $\Lambda_{\varepsilon}(\cdot)$ denotes the voltage-to-current density map when the sensing field Ω contains the permittivity distribution $\varepsilon(z)$. In particular, $\Lambda_1(\cdot)$ denotes the voltage-to-current density map when Ω contains constant permittivity of 1. The functional $\Lambda_{\delta\varepsilon}(\cdot)$ represents the difference between the two Dirichlet-to-Neumann maps $\Lambda_{\varepsilon}(\cdot)$ and $\Lambda_1(\cdot)$, namely,

$$\Lambda_{\delta\varepsilon}(\cdot) = (\Lambda_{\varepsilon} - \Lambda_1)(\cdot) \tag{14.4}$$

where $\varepsilon = 1 + \delta\varepsilon$.

Similarly, if the permittivity distribution is $\varepsilon(z)$, the current density-to-voltage map, that is, the Neumann-to-Dirichlet map, can be denoted as

$$R_{\varepsilon}: \quad \varepsilon(z) \frac{\partial \phi(z)}{\partial n}\bigg|_{\partial\Omega} \rightarrow \phi(z)|_{\partial\Omega} \tag{14.5}$$

The functional $R_{\delta\varepsilon}(\cdot)$ represents the difference between the two Neumann-to-Dirichlet maps R_{ε} and R_1, namely,

$$R_{\delta\varepsilon}(\cdot) = (R_{\varepsilon} - R_1)(\cdot) \tag{14.6}$$

where $\varepsilon = 1 + \delta\varepsilon$.

For the same sensor configuration, the Dirichlet-to-Neumann maps $\Lambda_\varepsilon(\cdot)$ and the Neumann-to-Dirichlet map $R_\varepsilon(\cdot)$ satisfies

$$\begin{cases} \Lambda_\varepsilon R_\varepsilon(\cdot) = I(\cdot) \\ R_\varepsilon \Lambda_\varepsilon(\cdot) = I(\cdot) - P(\cdot) \end{cases} \tag{14.7}$$

where $I(\cdot)$ and $P(\cdot)$ means the identity operator and a nonzero projection operator, respectively (Siltanen, Mueller, & Isaacson, 2001). It should be noted that $\Lambda_\varepsilon(\cdot)$ and $R_\varepsilon(\cdot)$ are not the inverse operator of each other, as the dimension of the operator is $N - 1$ if there exist N electrodes in a sensor. In the following sections, the symbols for the operators are rewritten for convenience, for example, $\Lambda_\varepsilon(\cdot)$ and $R_\varepsilon(\cdot)$ are denoted by Λ_ε and R_ε, respectively.

14.2.2 Calderon's method in circular ECT sensor

Calderon's method is a linearized method to deal with the inverse problem in the form of the conductivity equation. The main idea of Calderon's method can be simply expressed into two steps. First, assume that the permittivity distribution is nearly constant, for example, one. The distribution of electrical potential can be approximated analytically in this case. Secondly, the two-dimensional Fourier transform can be applied to reconstruct the perturbations of the permittivity distribution.

The divergence theorem relates integrals of the spatially varying permittivity to voltage and current measurements on the boundary, that is,

$$\int_\Omega v(z)\nabla\cdot\varepsilon(z)\nabla\phi(z)\,\mathrm{d}z = \int_{\partial\Omega} v(z)\varepsilon(z)\frac{\partial\phi(z)}{\partial n}\mathrm{d}l - \int_\Omega \nabla v(z)\cdot\varepsilon(z)\nabla\phi(z)\,\mathrm{d}z = 0 \tag{14.8}$$

where $v(z)$ is an arbitrary continuous function in L^2-Space. $\mathrm{d}L = |\mathrm{d}z|$ denotes the measured length of arc on $\partial\Omega$.

Equation (14.8) can be rewritten as

$$\int_\Omega \varepsilon(z)\nabla v(z)\cdot\nabla\phi(z)\,\mathrm{d}z = \int_{\partial\Omega} v(z)\Lambda_\varepsilon[\phi(z)]\mathrm{d}L \tag{14.9}$$

For a disturbed permittivity $\varepsilon = 1 + \delta\varepsilon$, if the perturbation is strictly within the whole domain Ω, we obtain

$$\int_\Omega \nabla v(z)\cdot[1+\delta\varepsilon(z)]\nabla\phi_{1+\delta\varepsilon}(z)\,\mathrm{d}z = \int_{\partial\Omega} v(z)\Lambda_{1+\delta\varepsilon}[\phi_1(z)]\mathrm{d}L \tag{14.10}$$

and

$$\int\limits_{\Omega} \nabla v(z) \cdot \nabla \phi_1(z)\ \mathrm{d}z = \int\limits_{\partial\Omega} v(z)\Lambda_1[\phi_1(z)]\mathrm{d}L \tag{14.11}$$

As the excitation voltage is applied to an electrode or several electrodes of the ECT system, $\phi_\varepsilon(z) = \phi_1(z)$ strictly holds on the boundary of the whole domain Ω. If we assume $\phi_\varepsilon(z) \approx \phi_1(z)$ in the whole sensing field, subtracting Eqn (14.10) from Eqn (14.11) results in

$$\int\limits_{\partial\Omega} v(z)\Lambda_\varepsilon[\phi_1(z)]\mathrm{d}L - \int\limits_{\partial\Omega} v(z)\Lambda_1[\phi_1(z)]\mathrm{d}L \approx \int\limits_{\Omega} \delta\varepsilon(z)\ \nabla v(z) \cdot \nabla \phi_1(z)\ \mathrm{d}L \tag{14.12}$$

that is,

$$\int\limits_{\partial\Omega} v(z)(\Lambda_\varepsilon - \Lambda_1)[\phi_1(z)]\mathrm{d}L \approx \int\limits_{\Omega} \delta\varepsilon(z) \nabla v(z) \cdot \nabla \phi_1(z)\ \mathrm{d}L \tag{14.13}$$

The approximation in Eqn (14.13) holds when the disturbed permittivity is small. Let $\phi_1(z) = \mathrm{e}^{\mathrm{i}kz}$ and $v(z) = \mathrm{e}^{\mathrm{i}\overline{kz}}$. The upper bar notation denotes the conjugate, $k = k_1 + \mathrm{i}k_2$ is a complex number, while k_1 and k_2 are real numbers. $\phi_1(z)$ and $v(z)$ can be treated as a linear combination of the trigonometric functions, for example, sine and cosine functions. They are real-valued functions and can be realized on the hardware system using different voltage excitation patterns. Denote the left-hand side of Eqn (14.13) as $t(k)$, that is,

$$t(k) = \int\limits_{\partial\Omega} \mathrm{e}^{\mathrm{i}\overline{kz}} \Lambda_{\delta\varepsilon}(\mathrm{e}^{\mathrm{i}kz})\mathrm{d}L \tag{14.14}$$

Then, Eqn (14.13) can be rewritten as

$$t(k) \approx -2\left(k_1^2 + k_2^2\right) \iint_{\Omega} \delta\varepsilon\ \mathrm{e}^{-\mathrm{i}(-2k_1, 2k_2)\cdot(x,y)}\ \mathrm{d}x\mathrm{d}y \tag{14.15}$$

Using the inverse Fourier transform (Cao et al., 2009), we obtain the distribution of the disturbed permittivity as follows:

$$\delta\varepsilon(x, y) = \delta\varepsilon(z) \approx \frac{1}{2\pi^2} \iint_{R^2} \frac{t(k_1 + \mathrm{i}k_2)}{k_1^2 + k_2^2}\ \mathrm{e}^{\mathrm{i}\left(-2k_1, 2k_2\right)\cdot(x,y)^{\mathrm{T}}} \mathrm{d}k_1 \mathrm{d}k_2 \tag{14.16}$$

where $k = k_1 + \mathrm{i}k_2$ is a complex number, while k_1 and k_2 are real numbers, and $(x,y)^{\mathrm{T}}$ is the transpose of (x,y).

It has been proved that the reconstruction error of $\delta\varepsilon(x,y)$ approaches zero when $\delta\varepsilon(x,y)$ is close to zero (Bikowski & Mueller, 2008). Since Calderon's method is a simplification of the dbar method (Knudsen, Lassas, Mueller, & Siltanen, 2008), the theoretical scattering transform $t(k)$ has a general form

$$t(k) = \int_{\partial\Omega} \mathrm{e}^{\mathrm{i}\overline{kz}} \Lambda_{\delta\varepsilon}[\psi(\cdot,k)]\mathrm{d}L \tag{14.17}$$

where $\psi(\cdot,k)$ is the exponentially growing solution to Eqn (14.17), the upper bar notation denotes conjugate, and $\mathrm{d}L = |\mathrm{d}z|$ the measured arc length on boundary $\partial\Omega$. On the boundary, the following equation holds:

$$A_{\delta\varepsilon}[\psi(\cdot,k)]|_{\partial\Omega} = \mathrm{e}^{\mathrm{i}kz} \tag{14.18}$$

where

$$A_{\delta\varepsilon}(\cdot) = [I + S_0\Lambda_{\delta\varepsilon}](\cdot) \tag{14.19}$$

Here, $I(\cdot)$ means the identity operator. The Green function S_{o} satisfies

$$(S_0\phi)(z_0) = -\frac{1}{2\pi}\int_{\partial\Omega} \log|z_0 - z|\phi(z)\mathrm{d}L, z_0 \in \partial\Omega. \tag{14.20}$$

When the sensing field Ω is circular, Eqn (14.16) can be rewritten in the polar coordinates of parameters r and θ, namely,

$$\delta\varepsilon(x,y) \approx \frac{1}{2\pi^2}\int_0^{R_0}\int_{-\pi}^{\pi} \frac{t(r\mathrm{e}^{\mathrm{i}\theta})}{r}\mathrm{e}^{\mathrm{i}2r(-\cos\theta,\sin\theta)\cdot(x,y)^{\mathrm{T}}}\mathrm{d}\theta\mathrm{d}r \tag{14.21}$$

where R_0 is the radius of the region defined in the numerical integration.

14.2.3 Dbar method in circular ECT sensor

When the distribution of permittivity is varied from a uniformly distributed permittivity, as $\varepsilon(z) = 1$, the scattering transform $t(k)$ is defined as

$$t(k) = \int_{\partial\Omega} \mathrm{e}^{\mathrm{i}\overline{kz}} \Lambda_{\delta\varepsilon}(\mathrm{e}^{\mathrm{i}kz})\mathrm{d}L \tag{14.22}$$

where $k = k_1 + ik_2$ represents a complex number, as k_1 and k_2 are real numbers. The values of $\varepsilon(z)$ can be obtained as it satisfies

$$\sqrt{\varepsilon(z)} = \lim_{k \to 0} \mu(z, k) \tag{14.23}$$

where $\mu(z, k)$ is the solution of the weakly singular Fredholm integral equation of the second kind (Nachman, 1996), that is,

$$\mu(z, s) = 1 + \frac{1}{(2\pi)^2} \iint_{R^2} \frac{t(k)}{(s-k)\bar{k}} \, e^{-i\left(kz + \overline{kz}\right)} \overline{\mu(z, k)} \mathrm{d}k_1 \mathrm{d}k_2 \tag{14.24}$$

In image reconstruction for noncircular sensors, direct calculations on the noncircular region can be avoided through using the conformal transformation (Cao et al., 2010).

14.2.4 Factorization method in a circular ECT sensor

The factorization method (Kirsch & Grinberg, 2008) is based on a characterization using the range of difference between two Neumann-to-Dirichlet maps (Harrach & Seo, 2009). If the subdomain, for example, Ω_1 contains a different material other than the background in Ω, then we have the following results:

$z \in \Omega_1$ if and only if $\Phi_z|_{\partial\Omega_1}$ is in the range of the operator $|R_\varepsilon - R_1|^{1/2}$, where R_1 corresponds to Neumann-to-Dirichlet map when the conductivity $\varepsilon(x) = 1$ and Φ_z is the solution of

$$\begin{cases} \Delta_x \Phi_z(x) = d \bullet \nabla_x \delta_z(x) \\ \left. \dfrac{\partial}{\partial \nu} \Phi_z \right|_{\partial B} = 0 \\ \displaystyle\int_{\partial\Omega} \Phi_z(x) \; \mathrm{d}x = 0 \end{cases}, \tag{14.25}$$

where $\boldsymbol{d}$ is a unit vector and $\delta_z(x)$ is the Dirac delta function at z. Especially for the unit circle in the two dimensions, the test function Φ_z can be written as

$$\Phi_z(x) = \frac{1}{\pi} \frac{(z - x) \cdot d}{|z - x|^2} \text{ for all } x \in \partial\Omega. \tag{14.26}$$

Since there exists only a limited number of electrodes in a real ECT sensor, we have an approximate to the map, that is, $|R_\varepsilon - R_1|^{1/2}$ that denoted by A. Let $Av_k = \lambda_k v_k$ be the spectral decomposition of the operator A; then it is yielded according to the Picard criterion that

$$\Phi_z|_{\partial\Omega_1} \in \mathrm{Range}\left(A^{1/2}\right), \tag{14.27}$$

if and only if

$$f(z) := \frac{1}{\left\|\Phi_z|_{\partial\Omega}\right\|}\sum_{k=1}^{\infty}\frac{\left\|\left(\Phi_z|_{\partial\Omega}, v_k\right)\right\|^2}{\lambda_k} \tag{14.28}$$

is in the range of the operator $|R_\varepsilon - R_1|^{1/2}$.

Using the singular value decomposition of the discrete approximation $A_d \in \mathrm{C}^{N-1\times N-1}$,

$$A_d v_k^d = \lambda_k^d u_k^d, \quad k = 1, 2, \ldots, N-1, \tag{14.29}$$

where N denotes the number of electrodes. With nonnegative $\{\lambda_k^d\} \subset \mathrm{R}$ (sorted in descending order) and orthonormal bases $\{u_k^d\}, \{v_k^d\} \subset \mathrm{C}^N$, the function $f(z)$ can be approximated by

$$f_d(z) := \left(\sum_{k=1}^{m}\frac{\left|\Phi_{dz}^{*}v_k^d\right|^2}{\lambda_k^d}\right)\Bigg/\left(\sum_{k=1}^{m}\left|\Phi_{dz}^{*}v_k^d\right|^2\right) \tag{14.30}$$

where $\Phi_{dz} \in \mathrm{C}^N$ is the values of $\Phi_z|_{\partial\Omega_1}$ on each electrode.

To obtain a numerical criterion telling whether a point z belongs to the unknown inclusion Ω or not, one now has to decide whether the approximate value $f_d(z)$ is greater than a large positive number, for example, a threshold denoted by C_∞. The following indicator function can be used:

$$\mathrm{Ind}(z) := \log(f_d(z))^{-1}. \tag{14.31}$$

Then a reconstruction of the whole sensing region is obtained by evaluating $f_d(z)$ and saying that all points with $f_d(z) < C_\infty$ belong to the inclusion (Hyvönen et al., 2007; Schmitt, 2009).

14.3 Constructions of the Dirichlet-to-Neumann/Neumann-to-Dirichlet maps

For the direct algorithms mentioned above, the construction of the map on the boundary links the measurement to the reconstructed gray values. The maps can be obtained by several methods, for example, the capacitance matrix, matrix transformation methods, and the inner product method. In this section, the first two methods will be described; more details on other methods can be found in the literature (Cao & Xu, 2013a,b,c; Isaacson et al., 2004).

14.3.1 Construction of the Dirichlet-to-Neumann map

As the ECT sensor has an earthed screen that introduces stray capacitances, the voltage patterns required by Eqn (14.14) cannot be directly implemented on the electrodes. However, the electric charge on each electrode is given by the general expression $q = C\,V$, in matrix form as (Yang, Spinkz, Gamioy, & Beck, 1997)

$$\begin{bmatrix} q_1 \\ q_2 \\ q_3 \\ \vdots \\ q_N \end{bmatrix} = \begin{bmatrix} C_{1,1} & -C_{1,2} & -C_{1,3} & \cdots & -C_{1,N} \\ -C_{2,1} & C_{2,2} & -C_{2,3} & \cdots & -C_{2,N} \\ -C_{3,1} & -C_{3,2} & C_{3,3} & \cdots & -C_{3,N} \\ \vdots & \vdots & \vdots & \vdots & \vdots \\ -C_{N,1} & -C_{N,2} & -C_{N,3} & \cdots & C_{N,N} \end{bmatrix} \begin{bmatrix} V_1 \\ V_2 \\ V_3 \\ \vdots \\ V_N \end{bmatrix} \tag{14.32}$$

where q_s is the electric charge on the sth electrode, V_t the voltage applied to the tth electrode, and $C_{s,t}$ the capacitance between electrode pair s—t ($s \neq t$). The self-capacitance of the sth electrode, that is, $C_{s,s}$, is defined as the sum of the capacitances between this electrode and all other electrodes plus the capacitance between the electrode and the earthed screen, that is,

$$C_{s,s} = \sum_{\substack{t=1 \\ t \neq s}}^{N} C_{s,t} + C_s^e \tag{14.33}$$

where C_s^e is the stray capacitance between the sth electrode and the earthed screen and $C_{s,t}$ the capacitance between electrodes s and t ($s \neq t$).

When the interval between each two neighboring electrodes is small, the effect of the variation in capacitance caused by the earthed screen can be neglected (Cao, Wang, & Xu, 2008). The relationship between $\Delta C_{s,s}$ and variations in capacitance on all N electrodes can be given by

$$\Delta C_{s,s} = \sum_{\substack{j=1 \\ j \neq s}}^{N} \Delta C_{s,j} \tag{14.34}$$

where $\Delta C_{s,s}$ is the variation of the self-capacitance of the sth electrode and $\Delta C_{s,j}$ the variation of the mutual capacitance between the electrode pair s—j ($s \neq j$). When the voltage V_j^t in the tth voltage pattern is applied to the jth electrode, the variations of the electric charge Δq_j^t ($j = 1, 2, \ldots, N$) on each of the N electrodes can be expressed as

$$\Delta q_j^t = \Delta C_{j,j} V_j^t - \sum_{s \neq j}^{N} \Delta C_{s,j} V_s^t \tag{14.35}$$

$\Delta C_{s,j}$ can be measured through the traditional excitation scheme, that is, the sth electrode is excited with all other electrodes grounded. The N variations of the electric charge, that is, Δq_j^t ($j = 1, 2, \ldots, N$) under the tth voltage pattern are obtained by using the transformation described in Eqn (14.35). Finally, the discretized form of the voltage-to-current density map, that is, the Dirichlet-to-Neumann map $\Lambda_{\delta\varepsilon} = \Lambda_\varepsilon - \Lambda_1$, can be constructed as follows:

$$\Lambda_{\delta\varepsilon} = \begin{bmatrix} \Delta C_{1,1} & -\Delta C_{1,2} & -\Delta C_{1,3} & \cdots & -\Delta C_{1,N} \\ -\Delta C_{2,1} & \Delta C_{2,2} & -\Delta C_{2,3} & \cdots & -\Delta C_{2,N} \\ -\Delta C_{3,1} & -\Delta C_{3,2} & \Delta C_{3,3} & \cdots & -\Delta C_{3,N} \\ \vdots & \vdots & \vdots & \vdots & \vdots \\ -\Delta C_{N,1} & -\Delta C_{N,2} & -\Delta C_{N,3} & \cdots & \Delta C_{N,N} \end{bmatrix} \tag{14.36}$$

According to Eqn (14.34), $\Delta C_{i,j}$ can be measured from the traditional scheme, that is, the ith electrode is excited while all other electrodes are grounded. The resulted electric charges of the voltage patterns described by Eqn (14.35) can be obtained by multiplying the matrix given in Eqn (14.36) with the voltages on the electrodes.

14.3.2 Construction of the Neumann-to-Dirichlet map

There is another method to construct the Dirichlet-to-Neumann map as well as the Neumann-to-Dirichlet map. The Neumann-to-Dirichlet map $R_{\delta\varepsilon} = R_\varepsilon - R_1$ can be constructed by using the inner product through a method similar to adjacent excitation measurement (Mueller et al., 2002). Here we provide an alternative to calculate the Neumann-to-Dirichlet map.

If the excitation voltage on the jth electrode during the ith scanning can be denoted as $V_{i,j}$, the varied electric charges after the distribution is distorted from one to $\varepsilon(z)$ at the same electrode is $\Delta q_{i,j}(1 \leq i \leq N - 1, 1 \leq j \leq N - 1)$, then the excitations and measurements can be constructed in the forms of matrices,

$$\begin{bmatrix} V_{1,1} & V_{1,2} & V_{1,3} & \cdots & V_{1,N-1} \\ V_{2,1} & V_{2,2} & V_{2,3} & \cdots & V_{2,N-1} \\ V_{3,1} & V_{3,2} & V_{3,3} & \cdots & V_{3,N-1} \\ \vdots & \vdots & \vdots & \vdots & \vdots \\ V_{N-1,1} & V_{N-1,2} & V_{N-1,3} & \cdots & V_{N-1,N-1} \end{bmatrix}$$

$$= \begin{bmatrix} \Delta q_{1,1} & -\Delta q_{1,2} & -\Delta q_{1,3} & \cdots & -\Delta q_{1,N-1} \\ -\Delta q_{2,1} & \Delta q_{2,2} & -\Delta q_{2,3} & \cdots & -\Delta q_{2,N-1} \\ -\Delta q_{3,1} & -\Delta q_{3,2} & \Delta q_{3,3} & \cdots & -\Delta q_{3,N-1} \\ \vdots & \vdots & \vdots & \vdots & \vdots \\ -\Delta q_{N-1,1} & -\Delta q_{N-1,2} & -\Delta q_{N-1,3} & \cdots & \Delta q_{N-1,N-1} \end{bmatrix} \frac{R_{\delta\varepsilon}}{A_{\mathrm{E}}} \tag{14.37}$$

Here, the values of $V_{i,j}$ in each excitation are normalized to have a zero mean, in order to obtain a unique expression of $R_{\delta\varepsilon}$ without loss of generality. It should be noted that the rank of the operator is only $N - 1$ for a sensor with N electrode.

Equation (14.37) can be rewritten as

$$V = q\frac{R_{\delta\varepsilon}}{A_{\mathrm{E}}} \tag{14.38}$$

According to Eqn (14.32), the values of electric charges in Eqn (14.38) can be obtained. Using Gram—Schmidt orthonormalization, we have a set of orthonormalized bases for V, for example, denoted by V_o, which satisfies

$$V = V_o G_s \tag{14.39}$$

where G_s is the transfer matrix resulting from the orthonormalization $V_o^T V_o = I$. Inserting Eqn (14.38) into Eqn (14.37) leads to the discretized form of the Neumann-to-Dirichlet map, that is,

$$R_{\delta\varepsilon} = A_{\mathrm{E}}\left(G_s^{-1} V_o^T q\right)^{-1} \tag{14.40}$$

14.4 Calculation of the scattering transforms

Theoretically, the ideal scattering transform $t(k)$ in Eqns (14.14) and (14.17) requires an infinite number of electrodes. However, only a limited number of electrodes are available in a real ECT system. Two approximations of the scattering transform $t(k)$ can be used. One is the approximation referred to as $t^{\mathrm{exp}}(k)$, when $\psi(\cdot, k)$ is replaced by the exponential solution (Knudsen et al., 2008). The other is deduced from the famous Fadeev Green function that is widely used in the inverse scattering theory (Nachman, 1996). It is termed as $t^{\mathrm{b}}(k)$, which needs to solve a weakly singular Fredholm integral equation of the second kind on the boundary. In view of the fact that through a linear conformal transformation any simply connected region is equivalent to the unit disk, we assume that the radius of the sensor is one.

14.4.1 Approximation of t(k) *using* $\mathrm{t^{exp}(k)}$

Expand $\mathrm{e}^{\mathrm{i}kz}$ into a Fourier series with $z = \mathrm{e}^{\mathrm{i}\theta}$ to obtain

$$\mathrm{e}^{\mathrm{i}kz} = \sum_{n=-\infty}^{\infty} a_n(k)\mathrm{e}^{\mathrm{i}n\theta} \tag{14.41}$$

where $a_n(k) = \frac{(ik)^n}{n!}$.

If we assume $A_{\delta\varepsilon}(\cdot)$ to be the identity operator, then the scattering transform in Eqn (14.5) can be simplified as

$$\mathrm{t}(k) = \int_{\partial\Omega} \mathrm{e}^{\mathrm{i}\overline{kz}}(\Lambda_\varepsilon - \Lambda_1)\left(\mathrm{e}^{\mathrm{i}n\theta_j}\right)\mathrm{d}L \tag{14.42}$$

According to Eqn (14.41), the scattering transform can be rewritten as

$$t^{\mathrm{exp}}(k) = t(k) = \sum_{m=0}^{\infty} a_m(\bar{k}) \sum_{n=0}^{\infty} a_n(k) \int_{\partial\Omega} \mathrm{e}^{-\mathrm{i}m\theta_l}\Lambda_{\delta\varepsilon}\left(\mathrm{e}^{\mathrm{i}n\theta_j}\right)\mathrm{d}L \tag{14.43}$$

Let A_{E} denote the area of an electrode and N the number of the electrodes in the ECT sensor. Assume that the sth electrode is centered at angle $\theta_s = \frac{2\pi s}{N}$ (Isaacson et al., 2004). In the case of N discrete electrodes, the integral in Eqn (14.43) can be approximated by a finite summation and can be rewritten as

$$t^{\mathrm{exp}}(k) = \frac{\Delta\theta}{A_{\mathrm{E}}} \sum_{m=1}^{N/2} a_m(\bar{k}) \sum_{n=1}^{N/2} a_n(k) \sum_{s=1}^{N} \left[\mathrm{e}^{-\mathrm{i}m\theta_s} A_{\mathrm{E}}\Lambda_{\delta\varepsilon}\left(\mathrm{e}^{\mathrm{i}n\theta_s}\right)\right] \tag{14.44}$$

where $\Delta\theta = \frac{2\pi}{N}$, $\Lambda_{\delta\varepsilon}(\mathrm{e}^{\mathrm{i}n\theta_s})$ is the electric current density.

Finally, Eqn (14.44) turns to

$$t^{\mathrm{exp}}(k) = \frac{\Delta\theta}{A_{\mathrm{E}}} \sum_{m=1}^{N/2} a_m(\bar{k}) \sum_{n=1}^{N/2} a_n(k) \sum_{s=1}^{N} \left(\mathrm{e}^{-\mathrm{i}m\theta_s}\Delta q_s^n\right) \tag{14.45}$$

where Δq_s^n represents the changes of electric charge caused by the excitation voltage $\mathrm{e}^{\mathrm{i}n\theta_s}$ on the sth electrode, if the homogeneous dielectrics distribution with permittivity value of 1 is distorted to a new distribution $\varepsilon(z)$.

14.4.2 *Approximation of* t(k) *using* t^{b}(k)

If we use $A_{\delta\varepsilon}(\cdot)$ defined in Eqns (14.18), (14.19), and (14.20), then

$$\psi(\cdot,k)|_{\partial\Omega} = [I + S_0\Lambda_{\delta\varepsilon}]^{-1}\left(\mathrm{e}^{\mathrm{i}kz}\right) \tag{14.46}$$

For an N-electrode square ECT sensor, $t^{\mathrm{b}}(k)$ can be obtained using the following equation:

$$t^{\mathrm{b}}(k) = \Delta\theta\sum_{m=1}^{N/2} a_m(\overline{k})\sum_{n=1}^{N/2} a_n(k)\sum_{j=1}^{N}\left\{\mathrm{e}^{-\mathrm{i}m\theta_j}\Lambda_{\delta\varepsilon}[I + S_0\Lambda_{\delta\varepsilon}]^{-1}\left(\mathrm{e}^{\mathrm{i}n\theta_j}\right)\right\} \tag{14.47}$$

Apparently, if $S_0\Lambda_{\delta\varepsilon} \approx 0$, then $t^{\mathrm{b}}(k) = t^{\exp}(k)$. From this point of view, $t^{\exp}(k)$ is a simplification of $t^{\mathrm{b}}(k)$. Meanwhile, Eqn (14.46) is ill posed and theoretically solvable; the operator that must be inverted to solve the equation needs to be regularized. In particular, $t^{\exp}(k)$ is a regularized form of $t^{\mathrm{b}}(k)$, and the reconstructed images by using $t^{\exp}(k)$ are similar to those by using $t^{\mathrm{b}}(k)$ (Cao et al., 2011). In the following sections, only $t^{\exp}(k)$ will be used to calculate the scattering transforms.

14.5 Reconstructed results and discussion

To evaluate the performance of the direct methods and the conformal transformation, a square ECT sensor was constructed and used as an example to implement and validate the methods for a noncircular sensor.

The implementation of the direct methods can be depicted in Figure 14.2. It can be summarized in three steps. Firstly, the traditional excitation and measurement scheme was applied to the N-electrode sensor in order to obtain the $N\ (N-1)/2$ independent measurements of capacitance changes, that is, $\Delta C_{i,j}$, from which the $N \times N$ transform matrix ΔC was constructed and the change of electric charge on each electrode, that is, $\Delta q_{i,j}$ that is associated with the applied voltage excitations, that is, $V_{i,j}$. Secondly, the discretized form of the Neumann-to-Dirichlet map or Dirichlet-to-Neumann map was obtained. Finally, the values of the indicator function at each pixel were calculated by using a direct algorithm and conformally transformed to the associated point in the simply connected region for reconstructed images.

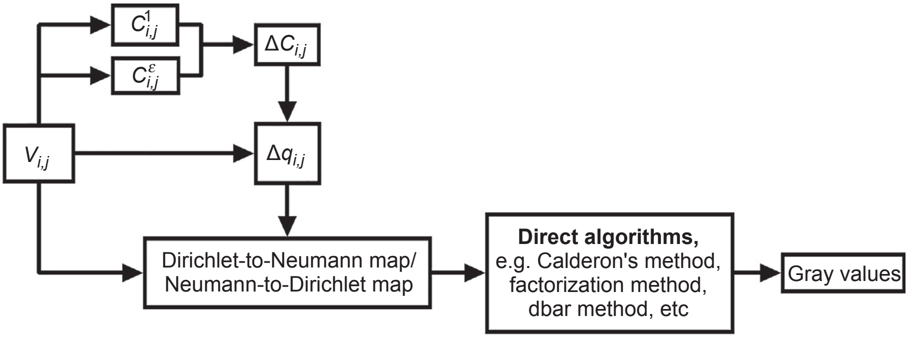
$C^1_{i,j}$
$C^\varepsilon_{i,j}$
$\Delta C_{i,j}$
$V_{i,j}$
$\Delta q_{i,j}$
Dirichlet-to-Neumann map/ Neumann-to-Dirichlet map
Direct algorithms, e.g. Calderon's method, factorization method, dbar method, etc
Gray values

Figure 14.2 Implementation process of the direct methods in ECT.

14.5.1 Conformal mapping from a square to the unit disk

The conformal transformation from a square to the unit disk in the complex plane is

$$w = \frac{sn\left(\sqrt{2}z, \frac{1}{\sqrt{2}}\right)}{\sqrt{2}dn\left(\sqrt{2}z, \frac{1}{\sqrt{2}}\right)} \tag{14.48}$$

where $sn(\cdot, \cdot)$ and $dn(\cdot, \cdot)$ are the Jacobi elliptic functions. z and w are the complex numbers that represent the locations in the unit disk and the square, respectively. In the calculations, the precise integration method was used to calculate the elliptic functions, as it generated the results in the machine precision (Cao et al., 2008; Zhong & Yao, 2004).

The square sensor used here was optimized in the sense of information entropy. The size and interval of each electrode in the square sensor were associated with those of the evenly positioned electrode configuration in the circular sensor through a unique conformal transformation (Cao et al., 2008); see Figure 14.3.

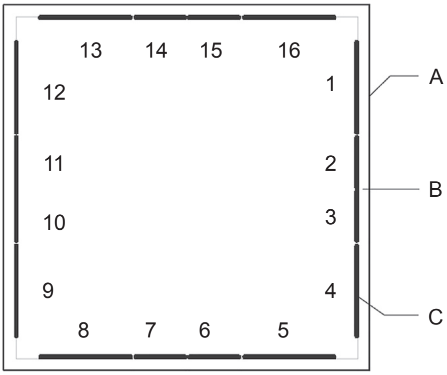
13
14
15
16
1
12
A
11
2
B
10
3
9
4
8
7
6
5
C

Figure 14.3 Cross-section of the optimized square sensor with 16 electrodes. A, copper shielding; B, plastic frame; C, measurement electrode.

14.5.2 Simulation results and discussions

Six phantoms with different permittivity distributions were constructed as shown in Figure 14.4. The distributions of permittivity were of binary values. The electrical permittivity in the gray and white regions are one (representing air) and three (representing solids), respectively. The phantoms are designed to represent three typical distributions, that is, one disturbed region (phantoms a and f), two disturbed regions (phantoms b, c, and e), and more than two disturbed regions (phantom d). In the case of one disturbed region, phantoms (a) and (f) represent a simply connected and a multiply connected region, respectively. Phantoms (b), (c), and (e) provide the comparisons of different locations and shapes. Phantom (d) can be used to test the performance of the proposed method for multi-rod distributions. The configuration of 16 electrodes is depicted in Figure 14.3. The forward problem was solved using the finite element analysis software package ANSYS.

For the convenience of comparison, the gray values of pixels in all the reconstructed images are normalized to a range from one to three. The reconstructed results in Figure 14.5, Figure 14.6, and Figure 14.7 show the reconstructed images by using Calderon's method, the dbar method, and the factorization method, respectively. In Calderon's method, the a priori information of the distributions was used to minimize the artefacts, that is, all the negative real parts of $\delta\varepsilon(x,y)$ were set to be zero (Cao et al., 2009). The image quality in Figure 14.5 appears to be better than that of images in Figure 14.6, which were produced using the dbar method. However, it should be noted that the results produced using the dbar method are all positive; as a result, no a priori information was used. Figure 14.7 shows that factorization method fails to work when

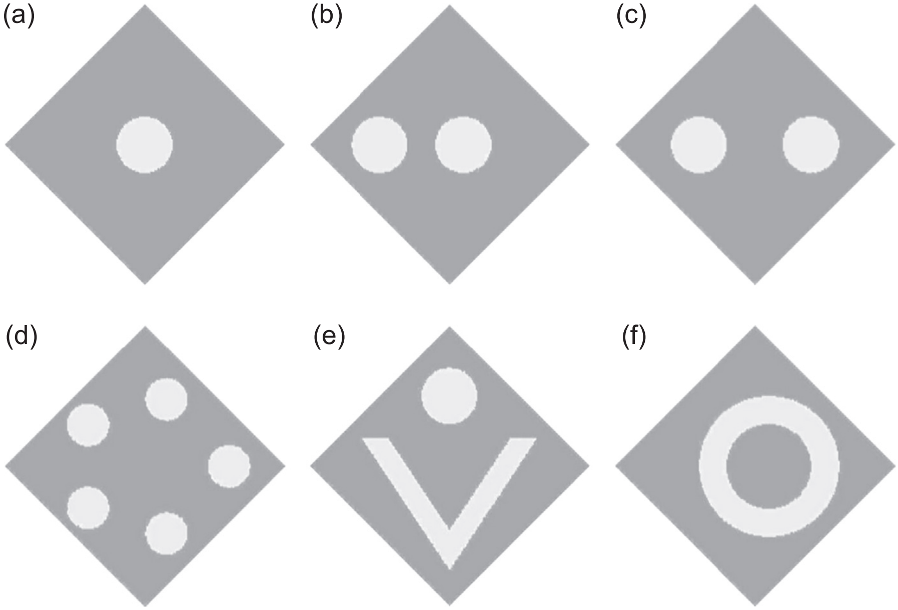

Figure 14.4 Six phantoms of binary-value distribution of electrical permittivity.

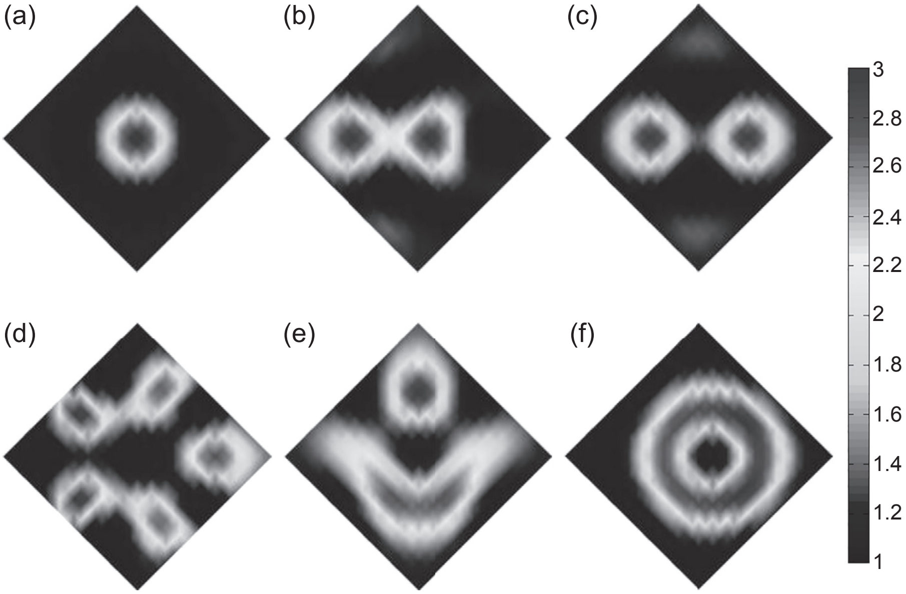

Figure 14.5 Images reconstructed using Calderon's method.

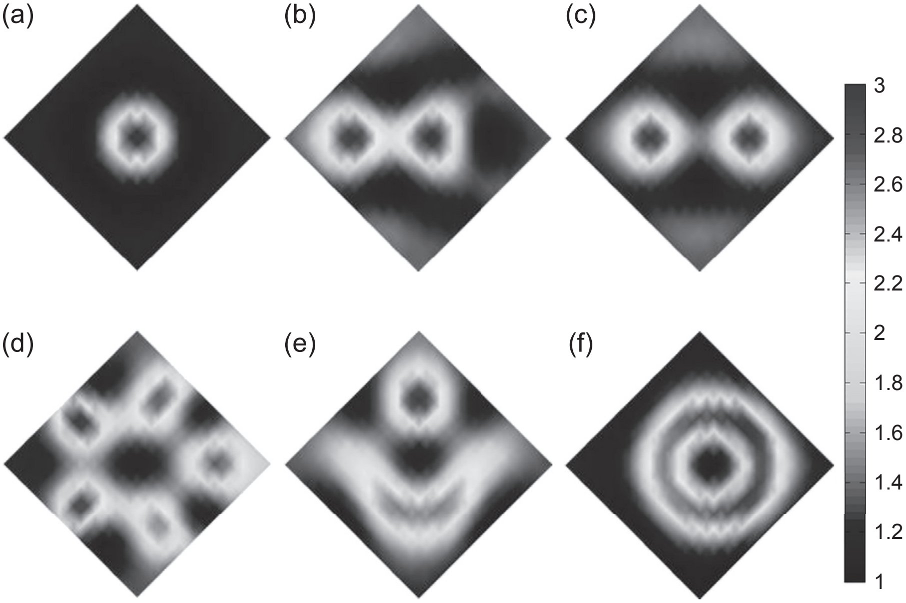

Figure 14.6 Images reconstructed using the dbar method.

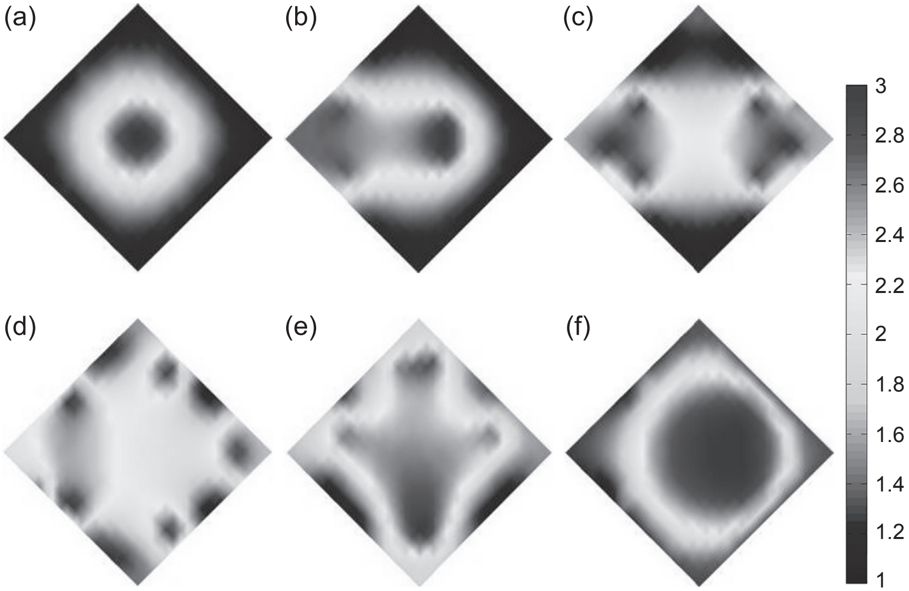

Figure 14.7 Images reconstructed using the factorization method.

the background is not a connected region, for example, Figure 14.7(f). Compared with the results shown in Figures 14.5 and 14.6, the spatial resolution of reconstructed images in Figure 14.7 was low. However, the factorization method takes about 0.03 s to reconstruct one image, while the time spent for one image using Calderon's method and the dbar method were about 0.7 s and 56.8 s, respectively. Moreover, the reconstructed value at each pixel of the images was obtained directly and independently.

14.5.3 Experiment results and discussion

Two cases of permittivity distributions were constructed for experimental test, that is, two plastic rods and one plastic pipe. The reconstructed images of the two plastic rods in the square sensor are depicted in Figure 14.8(c), (e), and (g). With the same process, the reconstructed images of a ring-shaped plastic pipe (see Figure 14.8(b)) were also obtained, as shown in Figure 14.8(d), (f), and (h). Similar to the results from simulated data, the reconstructed images from experiment data using both Calderon's method and the dbar method are of high contrast in the sense of visual appearance. The factorization method produced images with low resolution, as it is a kind of sampling method (Gebauer, Hanke, & Schneider, 2008).

14.6 Conclusions

Currently, most algorithms are based on a simplified linear mathematical model that is deduced from the sensitivity theorem. It should be noted that in the algorithms based

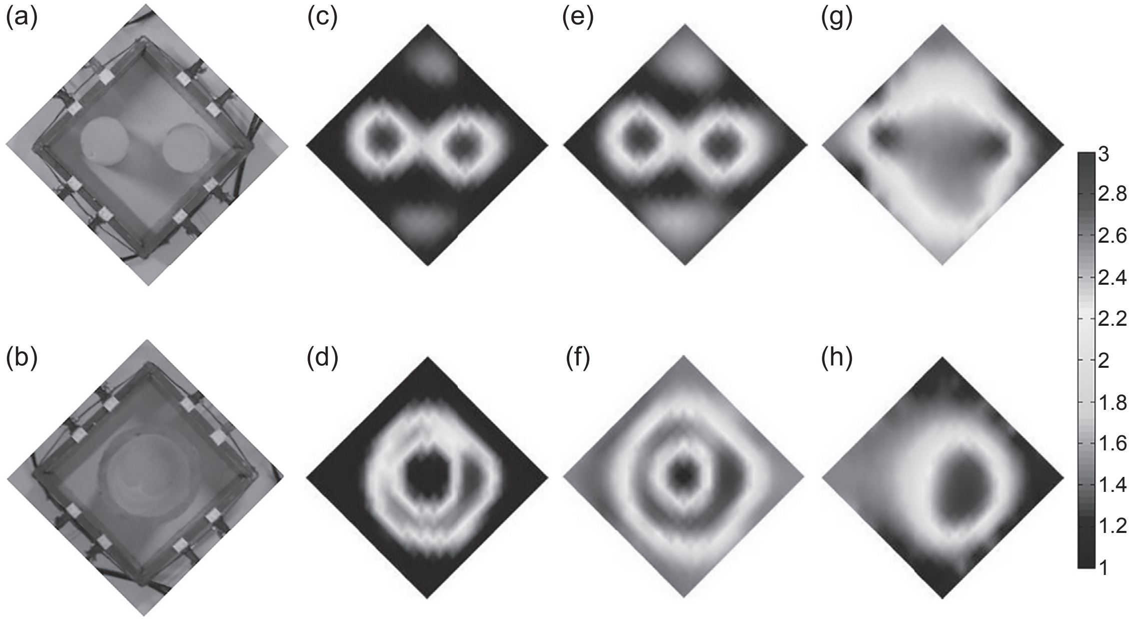

Figure 14.8 Experiment results using direct methods. (a and b) Phantoms of two plastic rods and a ring-shaped plastic pipe, respectively. (c and d) Reconstructed images of (a) and (b), respectively, using Calderon's method. (e and f) Reconstructed images of (a) and (b), respectively, using the dbar method. (g and h) Reconstructed images of (a) and (b), respectively, using the factorization method.

on the sensitivity/Jacobi matrix, the permittivity perturbations for the whole domain must be reconstructed simultaneously. The direct methods mentioned here provide a new view for image reconstruction in ECT, as it has the following advantages:

1. Is able to reconstruct only a part of the ROI without information on the other parts.
2. Can be generalized to the case of sensors of noncircular cross sections by using conformal transformations.
3. Provides a new view of the linearization methods for ECT.

Most of all, it provides a promising direct method to ECT as the values of permittivity usually change from 1 to 3 in gas/oil two-phase flows.

14.7 Future trends

There exist three major trends for the direct algorithms. First, the methods are generalized from the two-dimensional distributions to the three-dimensional case, which is very time-consuming for the nondirect algorithms. Secondly, these methods are also developed to deal with the multimodality reconstruction in an integrated way, in which the sensitivity matrix-based methods have to reconstruct each modality separately. Last but not least, partial boundary measurements will be required to retrieve the material distribution by using the direct methods, as in some applications, only measurements on part of the boundary can be available.

14.8 Further information

For more information about the advances of the inverse problems in the aspect of the mathematician, the readers can refer to the work of Gunther Uhlmann, Kirsch, Andreas and Samuli Siltanen et al. The authors gratefully acknowledge the financial support from the National Natural Science Foundation of China (61,001,135, 61,370,016).

References

Ahlfors, L. V. (2004). *Complex analysis*. Beijing, China: China Machine Press.

Astala, K., Mueller, J. L., Paivarinta, L., & Siltanen, S. (2010). Numerical computation of complex geometrical optics solutions to the conductivity equation. *Applied and Computational Harmonic Analysis, 29*, 2−17. http://dx.doi.org/10.1016/j.acha.2009.08.001.

Bikowski, J., & Mueller, J. L. (2008). 2D EIT reconstructions using Calderon's method. *Inverse Problems and Imaging, 2*, 43−61. http://dx.doi.org/10.3934/ipi.2008.2.43.

Boverman, G., Kao, T., Isaacson, D., & Saulnier, G. J. (2009). An implementation of Calderon's method for 3-D limited-view EIT. *IEEE Transactions on Medical Imaging, 28*, 1073−1082. http://dx.doi.org/10.1109/TMI.2009.2012892.

Calderon, A. P. (2006). On an inverse boundary value problem (reprint). *Computational & Applied Mathematics, 25*, 133−138.

Cao, Z., Wang, H., & Xu, L. (2008). Electrical impedance tomography with an optimized calculable square sensor. *Review of Scientific Instruments, 79*, 103710−103717. http://dx.doi.org/10.1063/1.3006388.

Cao, Z., & Xu, L. (2013a). 2D image reconstruction of a human chest by using Calderon's method and the adjacent current pattern. *Journal of Instrumentation, 8*, P3004. http://dx.doi.org/10.1088/1748−0221/8/03/P03004.

Cao, Z., & Xu, L. (2013b). Direct recovery of the electrical admittivities in 2D electrical tomography by using Calderon's method and two-terminal/electrode excitation strategies. *Measurement Science and Technology, 24*, 74007. http://dx.doi.org/10.1088/0957-0233/24/7/074007.

Cao, Z., & Xu, L. (2013c). Direct image reconstruction for 3-D electrical resistance tomography by using the factorization method and electrodes on a single plane. *IEEE Transactions on Instrumentation and Measurement, 62*, 999−1007. http://dx.doi.org/10.1109/TIM.2012.2232475.

Cao, Z., Xu, L., Fan, W., & Wang, H. (2010). Electrical capacitance tomography with a non-circular sensor using the dbar method. *Measurement Science and Technology, 21*, 15502−15506. http://dx.doi.org/10.1088/0957-0233/21/1/015502.

Cao, Z., Xu, L., Fan, W., & Wang, H. (2011a). Electrical capacitance tomography for sensors of square cross sections using Calderon's method. *IEEE Transactions on Instrumentation and Measurement, 60*, 900−907. http://dx.doi.org/10.1109/TIM.2010.2045255.

Cao, Z., Xu, L., Fang, W., & Wang, H. (2011b). 2D electrical capacitance tomography with sensors of non-circular cross sections using the factorization method. *Measurement Science and Technology, 22*, 114003−114008. http://dx.doi.org/10.1088/0957-0233/22/11/114003.

Cao, Z., Xu, L., & Wang, H. (2009). Image reconstruction technique of electrical capacitance tomography for low-contrast dielectrics using Calderon's method. *Measurement Science and Technology, 20*, 104012−104027. http://dx.doi.org/10.1088/0957-0233/20/10/104027.

Du, B., Warsito, W., & Fan, L. (2006a). Imaging the choking transition in gas−solid risers using electrical capacitance tomography. *Industrial & Engineering Chemistry Research, 45*, 5384−5395. http://dx.doi.org/10.1021/ie051401w.

Du, B., Warsito, W., & Fan, L. (2006b). Behavior of the dense-phase transportation regime in a circulating fluidized bed. *Industrial & Engineering Chemistry Research, 45*, 3741−3751. http://dx.doi.org/10.1021/ie0513548.

Fang, W. (2004). A nonlinear image reconstruction algorithm for electrical capacitance tomography. *Measurement Science and Technology, 15*, 2124−2132. http://dx.doi.org/10.1088/0957-0233/15/10/023.

Gebauer, B., Hanke, M., & Schneider, C. (2008). Sampling methods for low-frequency electromagnetic imaging. *Inverse Problems, 24*, 15007−15018. http://dx.doi.org/10.1088/0266-5611/24/1/015007.

Geselowitz, D. B. (1971). An application of electrocardiographic lead theory to impedance plethysmography. *IEEE Transactions on BME Biomedical Engineering, 18*, 38−41. http://dx.doi.org/10.1109/TBME.1971.4502787.

Gong, S., & Gong, Y. (2007). *Concise complex analysis* (revised edition). Singapore: World Scientific Publishing Company.

Hakula, H., & Hyvönen, N. (2009). On computation of test dipoles for factorization method. *BIT Numerical Mathematics, 49*, 75−91. http://dx.doi.org/10.1007/s10543-008-0205-9.

Harrach, B., & Seo, J. K. (2009). Detecting inclusions in electrical impedance tomography without reference measurements. *SIAM Journals on Applied Mathematics, 69*, 1662−1681. http://dx.doi.org/10.1137/08072142X.

Hyvöen, N. (2007). Application of the factorization method to the characterization of weak inclusions in electrical impedance tomography. *Advances in Applied Mathematics, 39*, 197–221. http://dx.doi.org/10.1016/j.aam.2006.12.004.

Hyvönen, N., Hakula, H., & Pursiainen, S. (2007). Numerical implementation of the factorization method within the complete electrode model of electrical impedance tomography. *Inverse Problems and Imaging, 1*, 299–317.

Isaacson, D., Mueller, J. L., Newell, J. C., & Siltanen, S. (2004). Reconstructions of chest phantoms by the D-bar method for electrical impedance tomography. *IEEE Transactions on Medical Imaging, 23*, 821–828. http://dx.doi.org/10.1109/TMI.2004.827482.

Ismail, I., Gamio, J. C., Bukhari, S. F. A., & Yang, W. Q. (2005). Tomography for multi-phase flow measurement in the oil industry. *Flow Measurement and Instrumentation, 16*, 145–155. http://dx.doi.org/10.1016/j.flowmeasinst.2005.02.017.

Kirsch, A., & Grinberg, N. (2008). The factorization method for inverse problems. *Oxford Lecture Series in Mathematics and its Applications*. USA: Oxford University Press.

Knudsen, K., Lassas, M., Mueller, J., & Siltanen, S. (2008). Reconstructions of piecewise constant conductivities by the D-bar method for electrical impedance tomography. *Journal of Physics: Conference Series, 124*, 12029. http://dx.doi.org/10.1088/1742-6596/124/1/012029.

Lehr, J. (1972). A vector derivation useful in impedance plethysmographic field calculations. *IEEE Transactions on BME Biomedical Engineering, 19*, 156–157. http://dx.doi.org/10.1109/TBME.1972.324058.

Liu, S., Chen, Q., Xiong, X., Zhang, Z., & Lei, J. (2008). Preliminary study on ECT imaging of flames in porous media. *Measurement Science and Technology, 19*, 94017. http://dx.doi.org/10.1088/0957-0233/19/9/094017.

Li, Y., & Yang, W. Q. (2008). Image reconstruction by nonlinear Landweber iteration for complicated distributions. *Measurement Science and Technology, 19*, 94014–94018. http://dx.doi.org/10.1088/0957-0233/19/9/094014.

Mueller, J. L., Siltanen, S., & Isaacson, D. (2002). A direct reconstruction algorithm for electrical impedance tomography. *IEEE Transactions on Medical Imaging, 21*, 555–559. http://dx.doi.org/10.1109/TMI.2002.800574.

Murphy, E. K., & Mueller, J. L. (2009). Effect of domain shape modeling and measurement errors on the 2-D d-bar method for EIT. *IEEE Transactions on Medical Imaging, 28*, 1576–1584. http://dx.doi.org/10.1109/TMI.2009.2021611.

Murphy, E. K., Mueller, J. L., & Newell, J. C. (2007). Reconstructions of conductive and insulating targets using the D-bar method on an elliptical domain. *Physiological Measurement, 28*, S101–S114. http://dx.doi.org/10.1088/0967-3334/28/7/S08.

Nachman, A. I. (1996). Global uniqueness for a two-dimensional inverse boundary value problem. *The Annals of Mathematics, 143*, 71–96.

Schmitt, S. (2009). The factorization method for EIT in the case of mixed inclusions. *Inverse Problems, 25*, 65012–65020. http://dx.doi.org/10.1088/0266-5611/25/6/065012.

Siltanen, S., Mueller, J., & Isaacson, D. (2001). An implementation of the reconstruction algorithm of A Nachman for the 2D inverse conductivity problem. *Inverse Problems, 17*, 1561–1563.

Smolik, W., Mirkowski, J., Olszewski, T., & Szabatin, R. (2006). Verification of image reconstruction algorithm with sensitivity matrix updating for real data in electrical capacitance tomography. In: *Proceedings of fourth international symposium on process tomography* (pp. 85–89). Warsaw, Poland.

Soleimani, M., & Lionheart, W. R. B. (2005). Nonlinear image reconstruction for electrical capacitance tomography using experimental data. *Measurement Science and Technology, 16*, 1987–1996. http://dx.doi.org/10.1088/0957-0233/16/10/014.

Sun, M., Liu, S., Lei, J., & Li, Z. (2008). Mass flow measurement of pneumatically conveyed solids using electrical capacitance tomography. *Measurement Science and Technology, 19*, 45503−45506. http://dx.doi.org/10.1088/0957-0233/19/4/045503.

Wang, H. G., Liu, S., Jiang, F., & Yang, W. Q. (2004). Using electrical capacitance tomography for measuring the solids distribution in cyclone separator. *Proceedings of the Chinese Society of Electrical Engineering, 24*, 174−179.

Wang, C., Lv, Z., & Li, D. (2008). Experimental study on gas-solids flows in a circulating fluidised bed using electrical capacitance tomography. *Powder Technology, 185*, 144−151. http://dx.doi.org/10.1016/j.powtec.2007.10.007.

Wang, H., Wang, C., & Yin, W. (2004). A pre-iteration method for the inverse problem in electrical impedance tomography. *IEEE Transactions on Instrumentation and Measurement, 53*, 1093−1096. http://dx.doi.org/10.1109/TIM.2004.831180.

Yang, W. Q., & Peng, L. (2003). Image reconstruction algorithms for electrical capacitance tomography. *Measurement Science and Technology, 14*, R1−R13. http://dx.doi.org/10.1088/0957-0233/14/1/201.

Yang, W. Q., Spinkz, D. M., Gamioy, J. C., & Beck, M. S. (1997). Sensitivity distributions of capacitance tomography sensors with parallel field excitation. *Measurement Science and Technology, 8*, 562−569. http://dx.doi.org/10.1088/0957-0233/8/5/016.

Zhong, W. X., & Yao, Z. (2004). Precise integration method for elliptic functions. In Y. S. Hong (Ed.), *Advances in applied mechanics(in Chinese)* (pp. 106−111). Beijing: Science press.

This page intentionally left blank

Statistical image reconstruction

15

R.G. Aykroyd
University of Leeds, Leeds, UK

15.1 Introduction

This chapter considers the use of statistical modelling approaches and stochastic estimation algorithms for the reconstruction of images from data. A key distinguishing feature of statistical image reconstruction, compared to classical deterministic approaches, is the explicit use of statistical descriptions and probability models. This provides an intuitive and flexible framework within which the whole modelling and reconstruction process can be described. In essence, the relationship between data and parameters is described by a likelihood and relationships between parameters described by prior distributions. These are combined using Bayes theorem to produce a posterior distribution that is used as the basis for reconstruction. The resulting estimation task is now too complicated to admit explicit solution, and so numerical algorithms, designed using the Markov chain Monte Carlo (MCMC) method, are often used. As well as leading to image reconstruction, these techniques also allow a fuller investigation, in terms of estimation reliability and uncertainty, than other approaches.

In the next section, general motivating and historical background is given. In Section 15.3 the general approach to statistical image reconstruction will be introduced including basic notation and definitions. Then, in Section 15.4, different types of data models will be discussed and corresponding definitions of likelihood functions given. Prior modelling will be the theme of Sections 15.5−15.7. In the first two, pixel-based models are considered, whereas in the third, some comments on feature-based approaches are made. Numerical estimation methods, in particular the MCMC approach, are described in Section 15.8 with examples in Section 15.9. Finally, discussion of future directions and some concluding remarks are given in Section 15.10, followed by references.

15.2 Background

Image reconstruction usually refers to the process of converting a hard-to-interpret set of data into an easier-to-interpret target image − where the target image represents some physical property that may be a proxy for function or form − and although tomography is a good example, it is only one example. A review of statistical methods in electrical tomography can be found in Watzenig and Fox (2009) and a mathematical treatment of inverse problems in general in Stuart (2010). Image reconstruction problems can, broadly, be divided into two types. The first type is where the data

Industrial Tomography. http://dx.doi.org/10.1016/B978-1-78242-118-4.00015-0
Copyright © 2015 Elsevier Ltd. All rights reserved.

are simply a noisy version of the target image, but there are variations according to whether there is also blurring of the image. Blurring has the effect of combining, or superimposing, information from spatially close locations. In these problems an image of the data often resembles the target image and can sometimes be interpreted usefully by experienced experts without the need for further processing. In these cases, image reconstruction is used to remove, or at least reduce, the effects of noise and blur, making image interpretation more reliable and any quantitative summary more precise. The second type of imaging problem is also likely to involve noise in the data collection process, but more importantly there is also a projective transformation — as in tomography — which is the main focus here. In contrast to the blurring mentioned above, projection has the effect of combining, or superimposing, information from locations that are spatially far apart. This makes direct interpretation of the data much more difficult, or even impossible, and hence undoing the projection, along with denoizing and deblurring, is essential.

A good illustration of this is in medical imaging. Figure 15.1 shows an example of single photon emission computed tomography (SPECT) data of the human head where a radioactively tagged chemical was injected into the bloodstream to highlight areas of high blood flow. Multiple projections are recorded by a gamma camera at equally spaced angles around the patient.

A single projection is shown in Figure 15.1(a) and (b) shows all data corresponding to a particular horizontal slice — known as a sinogram — with the full dataset analysed in Aykroyd and Zimeras (1999). Clearly, only limited information can be recovered directly from the projections, and so there is a real need to reconstruct the spatial variation of the tagged chemical within the patient before any medical diagnosis can start.

Another good example, involving information from spatially distant locations, is electrical capacitance tomography (ECT), which has applications in industrial process monitoring and medical imaging (see e.g. Kaipio, Kolehmainen, Vauhkonen, & Somersalo (1999) and West, Aykroyd, Meng, & Williams (2004), West, Meng, Aykroyd, & Williams (2005) and references therein). Figure 15.2 shows a synthetic

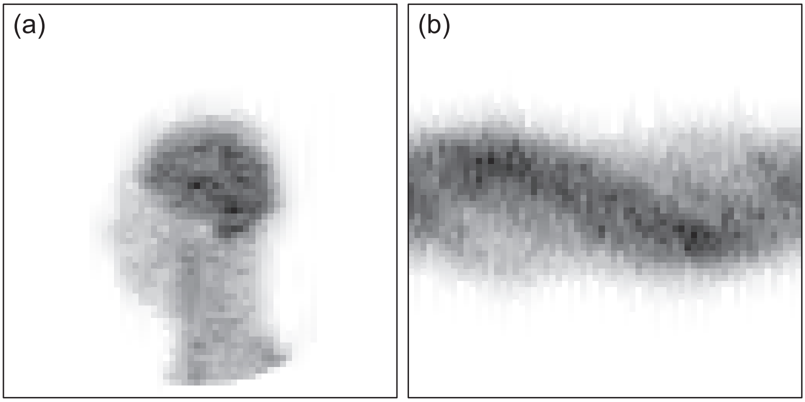

Figure 15.1 An example of SPECT data: (a) shows a single projection and (b) a sinogram for a single horizontal slice.

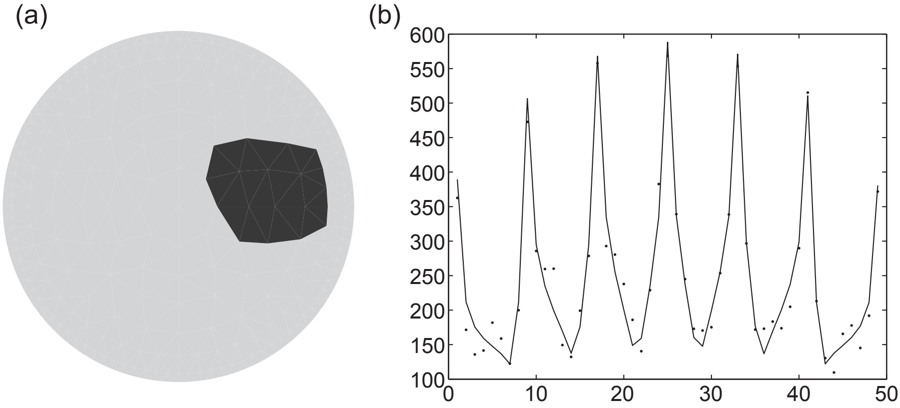

Figure 15.2 Synthetic electrical tomography example: (a) shows the true conductivity distribution and (b) shows calculated exact voltages (line) with noisy data (points).

example using ECT. Panel (a) shows the true conductivity distribution of a small low-conducting object within a circular region of uniform higher-conducting background. Electrodes are fixed on the boundary of the circular region at equally spaced intervals. Panel (b) shows typical recorded values where a known current is passed between a pair of drive electrodes and voltages are measured between other electrode pairs. To produce a full dataset, different electrode drive pairs and several measurement pairs are used (see Somersalo, Cheney, & Isaacson (1992) and Vauhkonen, Lionheart, Heikkinen, Vauhkonen, & Kaipio (2001) for modelling and computational details). The exact values of these voltages depend on what is inside the region, as well as the exact configuration of the electrodes used for the measurement. For this picture, calculations use the finite element method (FEM) implemented in Matlab using the EIDORS library (Polydorides & Lionheart, 2002).

In general, statistical image reconstruction has taken one of two broad approaches, which are sometimes called low-level and high-level. Low-level approaches are usually based on pixel representations and on a simple expectation that the physical quantity varies smoothly. In the high-level approach, it is assumed that the target image contains distinct features, or objects, and that these should be modelled explicitly. There are also intermediate approaches, in particular, the low-level approach can be modified to include abrupt changes, which might occur at region or feature boundaries, or it can be in terms of region labels that naturally lead to a segmentation, or it can incorporate assumptions of sparseness. In each of these situations, the choice of model should be made carefully and appropriately. It is important to remember that all models can only capture some elements of the truth, but it seems inappropriate to use a model that we know has unappealing properties. In addition, the choice of model may be influenced by the aims of any analysis. Therefore, a model that works well in some applications may not work well elsewhere.

In the statistical approach, the relationship between data and model parameters is described in a hierarchical way through a series of conditional distributions, and

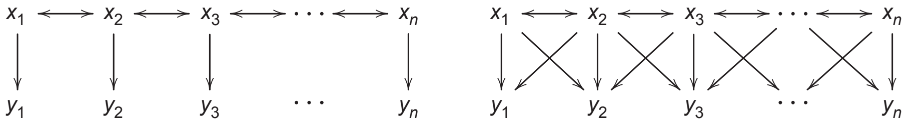

Figure 15.3 Directed graphs showing the hierarchical relationships between model variables.

at the end the relative plausibility of any remaining parameters is described in terms of unconditional distributions. For a complete description, and to allow estimation, the various distributions are combined. In classical statistics, the data are described by random variables but the unknown values would be considered as fixed parameters, and hence it is impossible to talk about the relative plausibility. In addition, artificial arguments are needed to provide explanations of confidence intervals, etc. In contrast, in the Bayesian approach all values, both known and unknown, are considered as random variables, making hierarchical modelling a natural approach and construction of credible intervals an intuitive consequence.

The relationships between modelled variables can usefully be illustrated in terms of a directed graph to show the hierarchical structure and to allow consideration of the implied conditional independences between variables. Figure 15.3 shows two example directed graphs made up of nodes representing variables and lines that indicate which variables are related — a single arrow indicates a causal relationship, whereas a double arrow indicates a symmetric correlation.

If there is no line between variables, then there is no direct dependence, but if there is some indirect route, then the variables are not independent. On the left, the diagram shows that each y-value depends on exactly one x-value, and that each x-value depends on its adjacent x-value(s). On the right, each y-value depends on more than one x-value. Such graphs, and how they relate to conditional independence, will be discussed later.

Early examples of statistical approaches to image reconstruction were based around maximum likelihood (ML) (e.g. Shepp & Vardi (1982) and Vardi, Shepp, & Kaufman (1985) in SPECT). The problems being tackled, however, were ill conditioned and ill posed, meaning that reliable estimation was not possible. Hence, these attempts had only partial success as iterative algorithms needed to be artificially truncated to avoid uncontrollable instability. The first recommendations for the use of prior information in image processing was by Besag (1983). The ideas were developed substantially by Geman and Geman (1984), who set out all the main ideas for pixel-based methods. Progress then focussed on model details, such as the choice of pixel-prior distribution. Early work on feature-based modelling began with Grenander (1970, 1973) who pioneered the aim of automated image understanding (Grenander & Keenan, 1989). This approach uses deformable templates with a hierarchical description of feature components. An excellent starting point for historical background are two supplements to the *Journal of Applied Statistics*, Mardia and Kanji (1993) and Mardia (1994), which contain republished versions of many of the above papers along with previously unpublished papers.

The next phase of research was on the development of estimation algorithms. Initially, deterministic methods were used to find posterior estimates, such as iterated conditional modes (ICM) (Besag, 1983) and the one-step-late (OSL) algorithm (Green, 1990b). Also, Geman and Geman (1984) proposed simulated annealing, which is a stochastic optimization method. The earliest stochastic sampling algorithms were the Metropolis algorithm (Metropolis, Rosenbluth, Rosenbluth, Teller, & Teller, 1953) and its generalization, the Metropolis–Hastings algorithm (Hastings, 1970), and the latter even used Markov chain and Monte Carlo in the title of the paper. It was not until the 1990s, however, that theoretical and practical advances led to the now ubiquitous MCMC method. An early review is given by Besag, Green, Higdon, and Mengersen (1995) and practical uses in Gilks, Richardson, and Spiegelhalter (1995) with more recent updates in Lui (2001), Gamerman and Lopes (2006) and Voss (2013). An interesting historical review of the development of MCMC methods is given in Robert and Casella (2011).

15.3 Bayesian paradigm

The overall aim of image reconstruction, and tomography in particular, is to estimate an unknown function, $\mathbf{x}(\mathbf{s})$, $\mathbf{s} \in \Omega$, within some domain, $\boldsymbol{\Omega} \subset \boldsymbol{R}^d$ with $d = 2, 3$, from a finite set of measurements $\mathbf{y} = \{y_i : i = 1,\ldots,n\}$ taken at locations $\mathbf{t} = \{t_i : i = 1,\ldots,n\}$ on the domain boundary $\boldsymbol{T} = \partial\boldsymbol{\Omega}$ or outside the domain $\boldsymbol{T} \subset \boldsymbol{R}^d/\boldsymbol{\Omega}$. In many examples the domain will be partitioned into disjoint pixels and the function correspondingly discretized to give unknowns $\mathbf{x} = \{x_j : j = 1,\ldots,m\}$; other approaches are possible and some examples will be discussed in Section 15.7. Figure 15.4 shows three example domains (top row) and corresponding discretizations (bottom row). In (a) the target and study domains are equal rectangular regions. In (b), although the target is irregular, a regular rectangular study domain in used. This latter case occurs in medical tomography where the target domain would be the unknown shape of a patient. In (c) the domains are equal circles. Discretizations (d) and (e) are intended to be applied to the rectangular study domains. The rectangular grid is more common, but the hexagonal can give a natural alternative when linear features are not aligned with the vertical/horizontal. For the circular domain, it is more usual to choose a triangular grid as shown in (f).

The data are measurements, $\mathbf{y}$, which depend on $\mathbf{x}$ though a deterministic function $\mathbf{g}$, as well as stochastic noise $\boldsymbol{\varepsilon}$. Often the noise is assumed to be additive so that $\mathbf{y} = \mathbf{g}(\mathbf{x}) + \boldsymbol{\varepsilon}$. Further, if the relationship is linear then this can be written as $\mathbf{y} = \boldsymbol{G}\mathbf{x} + \boldsymbol{\varepsilon}$. These, and other models, will be discussed in detail in the next section.

The key ingredients in the Bayesian approach are the likelihood function and prior distribution, and the resulting posterior distribution. The basic ideas of each of these distributions will now be discussed with further details and examples given in later sections. The likelihood is the conditional distribution of the data given the unknowns, denoted as $f(\mathbf{y}|\mathbf{x})$. It is usual to assume that the data values follow the same distribution and are conditionally independent given knowledge of the unknowns. The idea of conditional independence was mentioned in the previous section and illustrated by the directed graphs in Figure 15.3. Notice that in Figure 15.3, if the value of y_2, say, is fixed and hence removed from the graphs, then there is no change in the remaining

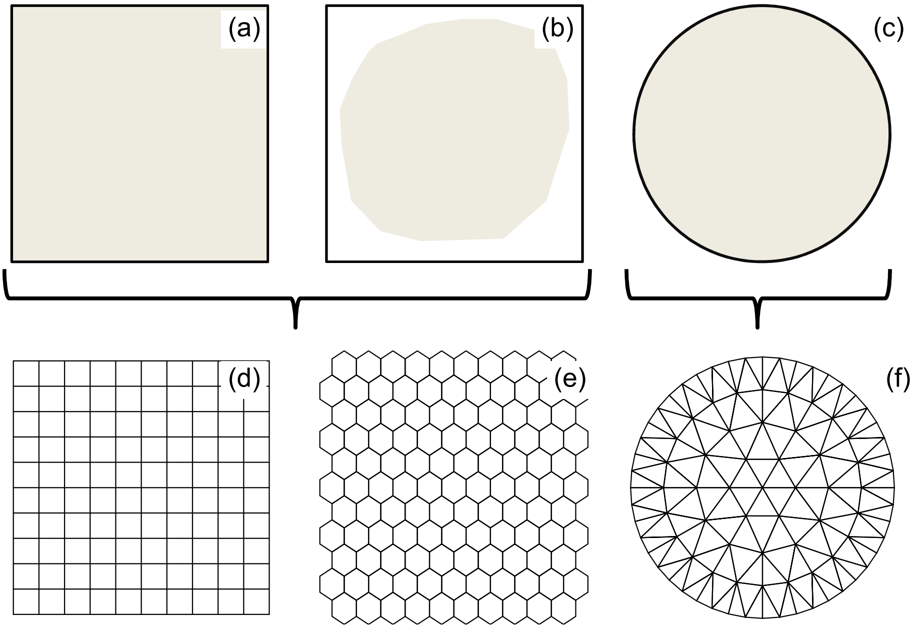

Figure 15.4 Study domains (top) with target domains (grey) partitioned into pixel images (bottom). In (a) the rectangular study and target domains coincide, in (b) the irregular target domain is contained within a rectangular study domain, and in (c) the circular study and target domains coincide. In (d) the image is partitioned into regular square pixels, in (e) the pixels are regular hexagons, and in (f) the circular image is made of differently sized triangular pixels.

dependence structure. If, however, x_2 is fixed, then in the left-hand diagram the graph is split into two subgraphs, and hence the variables in the subgraphs are said to be conditionally independent given x_2. In the right-hand diagram, however, knowledge of x_2 and x_3, say, would be needed to split the graph and create conditionally independent subgraphs. Also, if the values of all x-variables are fixed, then the y-variables are conditionally independent. Hence, the likelihood, the joint multivariate distribution of the data given the unknowns, can now be rewritten as a product of the component univariate distributions — as the y-variables are conditionally independent given the x-variables:

$$f(\mathbf{y}|\mathbf{x}) = \prod_{i=1}^{n} f(y_i|\mathbf{x}). \tag{15.1}$$

This will be a discrete probability mass function, if the data are discrete counts or a continuous probability density function if the data are continuous measurements. The most common examples of this are the discrete Poisson distribution and the continuous Gaussian, or normal, distribution. The prior distribution, denoted $p(\mathbf{x})$, quantifies detailed expert knowledge or general beliefs about the unknown function. The choice of the exact form of this distribution is much more subjective than is the choice of likelihood.

For estimation, evidence from the data and from prior beliefs are brought together by combining the likelihood and prior distribution, using Bayes theorem, to form the posterior distribution, defined as

$$p(\mathbf{x}|\mathbf{y}) = \frac{f(\mathbf{y}|\mathbf{x})p(\mathbf{x})}{f(\mathbf{y})}, \tag{15.2}$$

where $f(\mathbf{y})$ is a normalizing constant that is given by

$$f(\mathbf{y}) = \begin{cases} \sum f(\mathbf{y}|\mathbf{x})\, p(\mathbf{x}) & \text{if } \mathbf{x} \text{ is discrete} \\ \int f(\mathbf{y}|\mathbf{x})\, p(\mathbf{x}) d\mathbf{x} & \text{if } \mathbf{x} \text{ is continuous.} \end{cases} \tag{15.3}$$

Note that since these involve an n-fold integration, or summation, it may be unacceptably time-consuming to perform the calculation in all but the simplest cases. Fortunately, the normalizing constant contains no information about the unknown function $\mathbf{x}$ and hence is often dropped giving the key statement

$$p(\mathbf{x}|\mathbf{y}) \propto f(\mathbf{y}|\mathbf{x})\, p(\mathbf{x}), \tag{15.4}$$

that is 'posterior' is proportional to 'likelihood' times 'prior'. This distribution incorporates evidence from the data and knowledge from the prior distribution allowing an estimation process that balances the two types of information.

In classical statistics the likelihood function, more usually denoted $\mathscr{L}(\mathbf{x}) = f(\mathbf{y}|\mathbf{x})$, alone would be the basis for estimation and a point estimate found using the ML estimate

$$\widehat{\mathbf{x}}_{\text{ML}} = \arg\max_{\mathbf{x}} \mathscr{L}(\mathbf{x}),$$

and then, either using exact knowledge of the distribution or relying on asymptotic normality, creating confidence statements. In the Bayesian setting, a similar approach can be followed using the posterior distribution as the basis for estimation. Hence, the equivalent would be to calculate a point estimate using the value that corresponds to the maximum of the posterior distribution, called the maximum a posteriori (MAP) estimate

$$\widehat{\mathbf{x}}_{\text{MAP}} = \arg\max_{\mathbf{x}} p(\mathbf{x}|\mathbf{y}).$$

In addition, the joint posterior distribution can be used, for example, to construct marginal posterior distributions and to calculate Bayesian credible intervals.

In practice, it is only in simple problems where this maximization can be performed explicitly. In many low-dimensional problems deterministic approaches, such as gradient-accent methods, are possible, but it has become increasingly popular, especially in high-dimensional problems, for stochastic sampling methods to be used.

One such approach is based on the MCMC algorithm. This will be discussed in Section 15.8, but in brief the algorithm is used to simulate a sample path from a Markov chain that has the required posterior distribution as its equilibrium distribution. The resulting correlated sample is then studied and used for estimation.

15.4 Data models

The data model incorporates descriptions of two aspects of the measurement process: (1) the deterministic relationship between the unknown function and the data, and (2) a stochastic component quantifying sources of measurement error and natural random variation. It is important to realize, however, that this describes an idealized situation. In practice, it is unlikely that we will have modelled the process perfectly, and hence the stochastic component will also be expected to account for any model miss-specification.

Description of the deterministic relationship is usually based on the physical data collection process. It defines the expected values of the data, denoted

$$E[\mathbf{y}|\mathbf{x}] = g(\mathbf{x}) = \{g_i(\mathbf{x}) : i = 1, \ldots, n\},$$

that is it defines the values of noise-free data. This relationship can be written $g(\mathbf{x}) = \boldsymbol{G}\mathbf{x}$ for linear problems. The calculation of $g(\mathbf{x})$ is sometimes referred to as the forward problem, and in many applications the efficient and accurate solution of the forward problem requires substantial mathematical care and computational effort. In this chapter, however, it will be assumed that there is a suitable method for determining $g(\mathbf{x})$, at least to a sufficient level of accuracy.

The stochastic component describes how the data vary around these expected values. The most usual assumption is that the error, denoted $\boldsymbol{\varepsilon}$, will have an additive effect, then

$$\mathbf{y} = g(\mathbf{x}) + \boldsymbol{\varepsilon}.$$

When the data are continuous measurements it is often assumed that the random variability can be well modelled by a multivariate Gaussian distribution with independent components, that is, $\mathbf{y}|\mathbf{x} \sim \mathrm{MVN}(g(\mathbf{x}), \sigma^2 I)$, with corresponding likelihood

$$f(\mathbf{y}|\mathbf{x}) = \frac{1}{(2\pi\sigma^2)^{n/2}} \exp\left\{ -\frac{1}{2\sigma^2} \sum_{i=1}^{n} (y_i - g_i(\mathbf{x}))^2 \right\}. \tag{15.5}$$

Another common situation is where the data are discrete counts, in such cases, one possible model for the random variability is the multivariate Poisson distribution with independent components, that is, $\mathbf{y}|\mathbf{x} \sim \mathrm{Po}(g(\mathbf{x}))$, with corresponding likelihood

$$f(\mathbf{y}|\mathbf{x}) = \prod_{i=1}^{n} \frac{g_i(\mathbf{x})^{y_i} \mathrm{e}^{-g_i(\mathbf{x})}}{y_i!}. \tag{15.6}$$

A common example of this is in medical imaging were radioactive compounds are used to highlight function within the body (see Weir & Green (1994) and references therein).

The above data models, and their corresponding likelihood functions, are likely to cover many practical examples, but it is important to realize that should a nonstandard situation be encountered, then it is possible to simply switch this part of the model accordingly — it is not the case that 'one size fits all'.

15.5 Pixel-based continuous prior models

The prior distribution, $p(\mathbf{x})$, quantifies the relative plausibility of different configurations of $\mathbf{x}$. It is often difficult to design suitable distributions from first principles using this full multivariate representation directly. Also, it is often impossible to check that a particular arbitrary function defines a valid probability function because of unobvious consistency conditions. Instead it is helpful to consider the univariate conditional distribution of a single pixel x_i given all the other pixel values $\mathbf{x}_{\boldsymbol{\Omega}/i}$, that is $p(x_i|\mathbf{x}_{\boldsymbol{\Omega}/i})$. It is a usual assumption that there is only local dependence and in particular that

$$p(x_i|\mathbf{x}_{\Omega/i}) \equiv p(x_i|\mathbf{x}_{\partial(i)}),$$

where $\partial(i)$ is the set of pixels close to pixel i, which are called the neighbours. This is a version of the Markov property and leads to the multivariate distribution being referred to as a locally dependent Markov random field (full background on Markov random fields can be found in Kinderman & Snell (1992)). These results lead to a recipe for defining valid multivariate distributions for $\mathbf{x}$. That is: (1) define a neighbourhood system and (2) choose a conditional distribution. The resulting function is guaranteed to be consistent and lead to a valid probability distribution.

The most common approach to describe a neighbourhood system is to consider each pixel as the node on a regular lattice and the neighbourhood structure being defined by edges — see Figure 15.5. A good starting point is to say that pixels are neighbours if they have edges in common. In the rectangular discretization, this leads to four neighbours, compared to six in the triangular case. This however is considered to be too simple in many situations and is not capable of describing all common situations. Instead, it is usual to also include pixels with corners in common. Figure 15.6 shows examples of first-order and second-order neighbourhood systems for a rectangular lattice. In the first-order system each pixel has four neighbours, whereas in the second-order each has eight neighbours.

For the boundary pixels there are several options on the action to take, with the most common being: (1) to only take the neighbours that are present and (2) to 'wrap' the lattice onto the surface of a torus so that nodes on the top row are neighbours of those along the bottom, and those on the left are neighbours of those on the right. The first option is often the safest unless it is reasonable to assume that the image has similar properties at extreme edges when this periodic boundary assumption is reasonable. However, a periodic assumption makes calculations for linear inverse problems

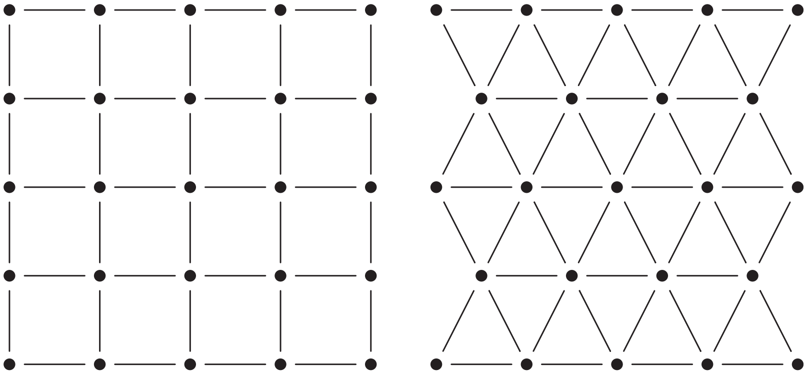

Figure 15.5 Examples of regular square (left) and triangular (right) lattices with nodes representing pixels.

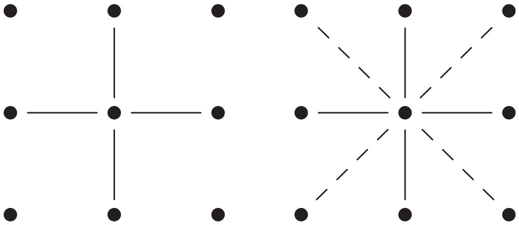

Figure 15.6 Neighbourhood structure for first-order (left) and second-order (right) systems for a square lattice.

much easier as the blurring convolution can be performed efficiently using fast Fourier transforms.

The first statisticians to work on image reconstruction, in the 1980s (e.g. Geman & Geman (1984)), noted common structure with previous work on statistical mechanics and the modelling of thermodynamic systems from the 1950s (e.g. Metropolis et al. (1953)). These models were shown to be equivalent to Markov random fields (Besag, 1974). This led to the adoption of models described in terms of energy systems. A common class of prior distribution is the Gibbs distribution (see e.g. Geman & McClure (1985, 1987)), which is defined as

$$p(\mathbf{x}) = \frac{1}{Z(\beta)}\exp\{-\beta \mathrm{V}(\mathbf{x})\}, \quad \beta > 0, \tag{15.7}$$

where $V(\mathbf{x})$ is called the energy and $Z(\beta)$ is a normalizing constant. The parameter β controls the variation between neighbours: for $\beta \to \infty$ the image is constant, for small β there is little spatial structure and as $\beta \to 0$ the values are spatially independent. The energy is often rewritten in terms of a summation of potentials, such as

$$V(\mathbf{x}) = \sum_{<i,j>} \phi\left(x_i - x_j\right) \tag{15.8}$$

where the sum is over all pairs of neighbours, this is denoted by the symbols $<i,j>$, and

$$V(\mathbf{x}) = \sum_i \phi(x_i - \bar{x}_{\partial(i)}), \tag{15.9}$$

where the sum is over all pixels, and $\bar{x}_{\partial(i)}$ is the mean of the neighbours of pixel i. There are few theoretical restrictions on the form of ϕ except that it must be symmetric about zero and $\phi(u)$ should increase monotonically with $|u|$.

The first potential function to be used was the quadratic function, $\phi(u) = u^2$, which leads to a Gaussian prior. Figure 15.7 shows the quadratic potential in (a) along with the corresponding Gaussian prior in (b). This, however, results in very smooth reconstructions as all but the smallest changes are discouraged. Examples from the Gaussian model are shown in Figure 15.8. From (a) to (c) the variance between pixel values is reduced, and in the limit there would be a constant value.

A natural alternative is the absolute value or modulus, $\phi(u) = |u|$, which gives a double exponential or Laplace prior distribution (see Figure 15.7). In some ways this has the opposite problem of forcing larger changes, sometimes leading to a staircase effect. There was then a multitude of suggestions for alternative potential functions that balanced smoothness. For example, Green (1990a) suggested the 'logcosh', $\phi(u) = \log\cosh(u/\delta)$, which gives an inverse-cosh, or hyperbolic secant, distribution. This is quadratic near zero, but becomes linear for large values (see Figure 15.7) with the value of δ determining where the type of behaviour changes. This potential function is an example of an edge-preserving, or implicit discontinuity, model, as such functions tend to leave abrupt changes in value but do not model edges explicitly. The use of such edge-preserving potentials has been compared using

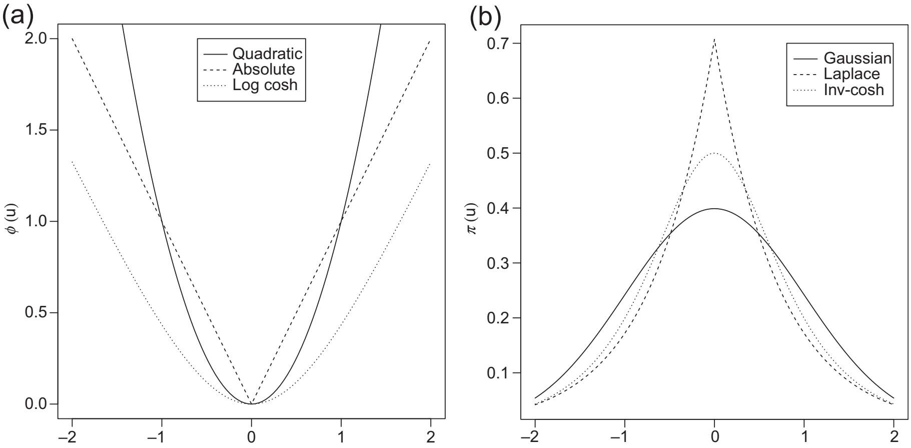

Figure 15.7 Common examples of potential functions are shown in (a) with corresponding prior distributions in (b).

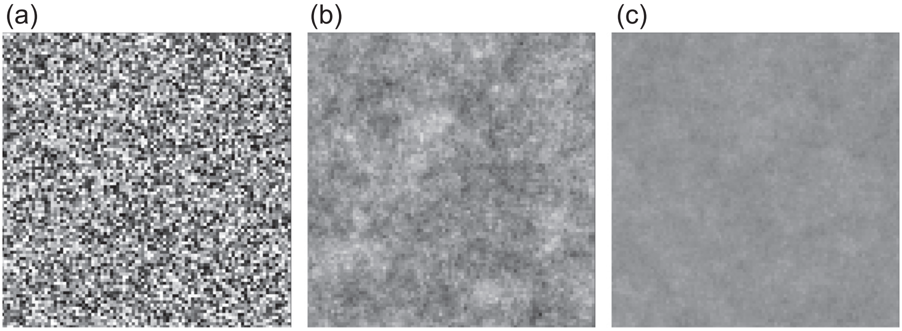

Figure 15.8 Example images from the Gaussian prior model with parameters: (a) $\beta = 0.01$, (b) $\beta = 0.1$, and (c) $\beta = 1.0$.

simulations by Weir (1997) who found that the logcosh generally leads to better reconstructions for medical tomography data.

Figure 15.9 shows example MAP reconstructions using these three prior models for the ECT problem described in Section 15.2 using the data shown in Figure 15.2. Prior parameters have been chosen to produce representative reconstructions. In panel (a), using the Gaussian prior, the reconstruction shows the general location of the object, but its outline is indistinct. For this value of the prior parameter the spatial distribution is over smoothed. If a lower value is used, however, the effect of the noise is too great and stable reconstruction is not possible. From this reconstruction it would be hard to get reliable estimates of background and object conductivity, or to obtain useful estimates of object size. When using the Laplace prior distribution, panel (b), there is greater contrast between object and background, but there is greater spatial variability. Even if the prior parameter is increased moderately, there will be no great change. Clearly, there is greater contrast between object and background. Although not with complete confidence, it would now be much easier to suggest an object outline and estimate its size. For the inverse-cosh prior, panel (c), the reconstruction is much improved with relatively constant background and good contrast between object and background. Here a fixed

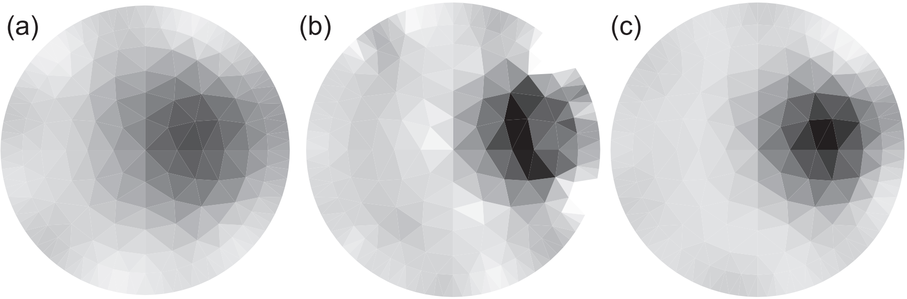

Figure 15.9 MAP image reconstructions using various prior distributions: (a) Gaussian with $\alpha = 0.5$, (b) Laplace with $\alpha = 0.5$, and (c) Inv-cosh with $\alpha/\delta = 1.0$.

value of $\delta = 400$ was used to represent the maximum difference expected between object and background, and then a prior parameter of $\alpha = 400$ was chosen.

The reconstructions shown in Figure 15.9 use a relatively coarse domain discretization containing about 300 pixels. The forward solution was evaluated using the FEM on a finer mesh to achieve good reliability. The MAP estimates were obtained using simulated annealing, a modified version of a MCMC algorithm, which will be discussed in Section 15.8. It is important to note that such methods require the forward problem to be solved many thousands of times and hence usually consume substantial computer time. For some applications, such as finding an object within a background, there may be alternatives to the pixel-based approach that allow faster algorithms and even produce more interpretable results – these issues will be considered in Section 15.7. Examples where pixel-based approaches have been applied to, essentially, object identification problems can be found in Bera and Nagaraju (2011) and Borsic, Graham, Adler, and Lionheart (2010).

15.6 Other pixel-based prior models

In the previous section models for continuous values were considered, but for other situations other types of prior models might be appropriate. Two such examples will now be considered, but many more are possible (see e.g. Cross & Jain (1983), Geman & Geman (1984), Besag (1986) and Dubes & Jain (1989)).

The most famous model for binary spatial processes, much used to model thermodynamic and magnetic systems, is the Ising model (Ising, 1925). This is a special case of the Gibbs distribution with first-order neighbourhood, $x \in (-1, +1)$ and $\phi(u) = 1$ if $u = 0$ and $\phi(u) = 0$ otherwise. The energy of the system, $V(\mathbf{x})$, is the Hamiltonian and the parameter β is related to the inverse temperature – then the energy simply counts the number of adjacent pixel pairs that are unequal. If β is positive, then equal valued adjacent pairs will have high probability (ferromagnetism), whereas if β is negative, then discordant pairs will have high probability (antiferromagnetism).

As a final example of pixel-based models, consider a situation where the image contains disjoint homogeneous subregions. Further suppose that there are small, smoothly varying changes between neighbours within regions but large, abrupt changes between neighbours in different regions. Even though the edge-preserving potentials aim to be robust to such situations, they are not likely to be able to fully deal with this structure. As a solution to this, pixel-based models are combined with edge variables (Geman & Geman, 1984) to explicitly produce disjointed regions, eliminating neighbourhood correlation between regions.

15.7 Feature-based prior models

Many authors proposed the move away from the use of pixel-based prior models, which are only able to describe local dependency structure and hence limit the type of prior information that can be included. When the expert knowledge is in the form of long-range structural information, then a different approach is needed that uses high-level information directly. Resulting models often take the form of hierarchical geometric descriptions (see e.g. Phillips & Smith (1993)). In many applications the results also allow for direct interpretation and image understanding, compared to the blind image processing style of pixel-based methods. By their very nature, however, it is not possible to give a general model that will work well. Each application requires a new model to be defined. This is in contrast to pixel-based approaches where one model will do, at least, a reasonable job for a wide range of applications. A simple illustrative example will now be given and the general mathematical framework will be discussed.

Suppose that it is known that the region of interest contains one or more objects, such as solid ball-shaped masses in air or bubbles in some liquid, but that their positions and sizes are unknown; Figure 15.10 illustrates three simple feature-based models for this type of situation. Further suppose, for simplicity here, that a single object has known value x_O and that the background has value x_B. A suitable parametric model, in two dimensions, for this situation might include the object's centre, (ζ_x, ζ_y), and radius r, giving a vector of unknown parameters $\boldsymbol{\theta} = (\zeta_x, \zeta_y, r)$. Alternatively, the detailed shape may be unknown, but might be parametrized as star shaped in terms of n radii, $r_1,\ldots,r_n$, at equally spaced angles around the centre of the object giving unknown parameter vector $\boldsymbol{\theta} = (\zeta_x, \zeta_y, r_1, \ldots, r_n)$. It is now possible to directly calculate the expected data values $g(\boldsymbol{\theta})$, or through $\mathbf{x}$ if appropriate as $g(\mathbf{x}(\boldsymbol{\theta}))$ and the corresponding likelihood $f(\mathbf{y}|\boldsymbol{\theta})$.

It is important to note that in some examples, such as the case of a single circular object, it may now be possible to estimate the model parameters without prior information, corresponding to ML estimation. However, it might have been that the pixel-based model is linear but that the problem is now nonlinear. If this is the case, then an ill-posed linear inverse problem has been re-parameterized into a well-posed nonlinear problem. In many cases, however, there will be important prior information about likely values of the model parameters that can be quantified in a prior distribution $p(\boldsymbol{\theta})$.

Even though the dimensions of the problem may now be orders of magnitude fewer than the pixel-based approach, there will still be advantages in using stochastic sampling methods such as the MCMC algorithm. Estimation is the theme of the next

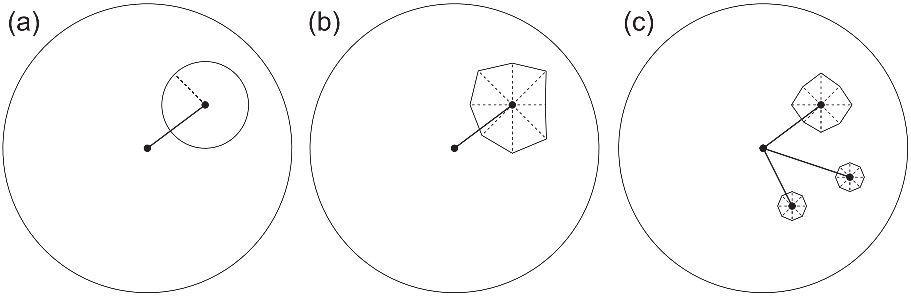

Figure 15.10 Examples of simple feature-based models: (a) circular object, (b) star-shaped object, and (c) multiple objects.

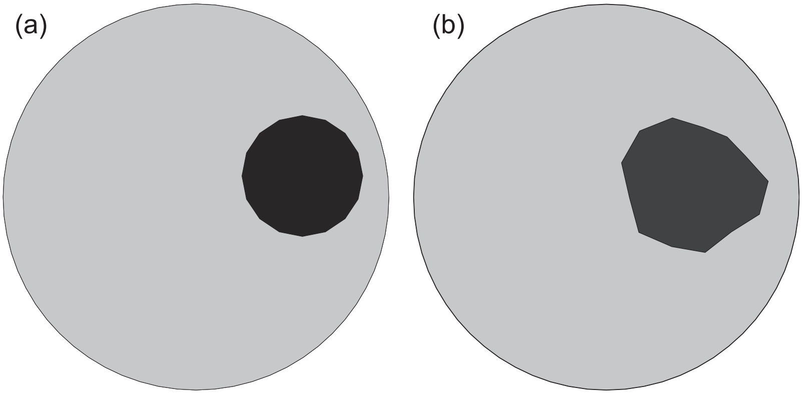

Figure 15.11 MAP image reconstructions using geometric models: (a) circular model and (b) star-shaped model.

section, but discussion will be limited to the use of pixel-based prior models. For feature-based models the general approach of the estimation method is unchanged, but it is common for greater care and thought to be needed in order to produce an efficient algorithm. For the synthetic ECT example considered earlier, it is now possible to solve the underlying system of governing partial differential equations using the boundary element method (BEM) rather than the computationally expensive FEM. For application of the BEM to electrical tomography data, see Aykroyd and Cattle (2007) and Khambampati, Hong, Kim, and Kim (2013). This allows a huge reduction in computational time and can produce reconstructions with greater spatial resolution.

Figure 15.11 shows reconstructions based on a circular model in (a) and a star-shaped model in (b) using the data shown in Figure 15.2. In each case the location and size are well estimated, though in (b) the true shape of the object is evident. By the very nature of the model there is great contrast between object and background, and it is very straightforward to estimate background and object conductivity, and to reliably estimate the object size. Also, although the circle model in (a) does not attempt to reproduce the detailed shape of the object, if this level of detail is sufficient, then reconstruction can be very fast, even making real-time applications possible.

15.8 Estimation methodology

The aim of image reconstruction is to estimate the value of an unknown function at a set of points that often form some regular grid. This may be done directly, through a pixel-based approach, by estimating the values, $\mathbf{x}$, at the grid points. Alternatively, this can be done indirectly through some alternative parameterization, such as in a feature-based approach, by estimating the corresponding model parameters, $\boldsymbol{\theta}$. In this section all equations and definitions will be in terms of unknowns $\mathbf{x}$, but all will also apply for the feature-based models simply by replacing $\mathbf{x}$ by $\boldsymbol{\theta}$.

For data measurements $\mathbf{y} = \{y_j : j = 1,\ldots,n\}$ and unknown parameter values $\mathbf{x} = \{x_i : i = 1,\ldots,m\}$, estimation is based on the posterior distribution

$$p(\mathbf{x}|\mathbf{y}) = \frac{f(\mathbf{y}|\mathbf{x})p(\mathbf{x})}{f(\mathbf{y})},$$

where $f(\mathbf{y}|\mathbf{x})$ is the likelihood and $p(\mathbf{x})$ is a prior distribution. Since the denominator is not a function of $\mathbf{x}$ it is not needed for estimation, hence the key equation is

$$p(\mathbf{x}|\mathbf{y}) \propto f(\mathbf{y}|\mathbf{x})p(\mathbf{x}).$$

Typically, the unknown parameter vector, $\mathbf{x}$, will be high dimensional and the posterior distribution will be complex, making analytic solution impossible and even numerical algorithms require careful design and must be implemented efficiently.

The MCMC approach is now widely used for many statistical estimation problems; for theoretical details see Gamerman and Lopes (2006) and Brooks, Gelman, Jones, and Meng (2011), and for practical examples see Gilks et al. (1995). In particular, it provides a feasible approach when model complexity and parameter dimensionality make deterministic gradient-based algorithms infeasible. More importantly, however, even in situations were deterministic algorithms are feasible, it also allows the posterior distribution to be investigated more deeply and a greater range of statistical questions to be considered in a rigorous way.

The MCMC method is not, in itself, an estimation algorithm, but it provides a framework that can be used to design tailor-made iterative algorithms to explore the properties of a given probability distribution. In particular, the resulting algorithm is used to produce a correlated sample from some target statistical distribution, commonly the posterior distribution in a Bayesian analysis. The method is based on two basic statistical techniques: Markov chains and rejection sampling. The former is use to provide ‘candidate’ values and the latter to ‘test’ the candidate values. Specifically, the transitions in the Markov chain are designed so that an equilibrium distribution exists and is equal to the target distribution. If the transitions are designed well, then after an initial transient period, referred to as burn-in, values pass the test in the same proportions as would be obtained by direct simulation. Hence, the sample will have the same statistical properties as a sample obtained directly from the posterior distribution. The only exception is that, by the very nature of a Markov chain, there will be serial correlation within the sample that must be taken into account when the algorithm output is summarized. If transitions are badly designed, however, then the initial transient period could be long and the within sample correlation could be high. This means that the algorithm is inefficient and larger samples would be required to achieve acceptable accuracy and precision.

The Markov chain can start at any feasible point in the parameter space; let this arbitrary value be denoted $\mathbf{x}^0$. From this starting value a discrete time Markov chain is simulated to produce values $\mathbf{x}^1$, $\mathbf{x}^2,\ldots,\mathbf{x}^K$. The algorithm will now be defined and is also summarized in Figure 15.12.

```
Set an initial value for $\mathbf{x}$, call this $\mathbf{x}^0$
Repeat the following steps for $k = 1,...,K$
    Generate a propose new value $\mathbf{x}^*$ with proposal kernel $q(\mathbf{x}^*|\mathbf{x}^{k-1})$
    Evaluate
        $\alpha = \alpha(\mathbf{x}^k|\mathbf{x}^*) = \min\left\{1, \frac{p(\mathbf{x}^*|\mathbf{y})\,q(\mathbf{x}^*|\mathbf{x}^{k-1})}{p(\mathbf{x}^{k-1}|\mathbf{y})\,q(\mathbf{x}^{k-1}|\mathbf{x}^*)}\right\}$
    Generate $u$ from a uniform distribution, $U(0, 1)$
    If $\alpha > u$ then accept the proposal and set $\mathbf{x}^k = \mathbf{x}^*$, otherwise $\mathbf{x}^k = \mathbf{x}^{k-1}$
End repeat
Discard initial values and use the remainder to make inference
```

Figure 15.12 A generic MCMC algorithm.

Consider the Markov chain transition from state $\mathbf{x}^{k-1}$ at time $k-1$ to state $\mathbf{x}^k$ at time k, with probability $\pi(\mathbf{x}^k|\mathbf{x}^{k-1})$. For the Markov chain to have the required posterior distribution as its equilibrium distribution, then detailed balance must hold, that is

$$\pi\left(\mathbf{x}^k|\mathbf{x}^{k-1}\right)p\left(\mathbf{x}^{k-1}|\mathbf{y}\right) = \pi\left(\mathbf{x}^{k-1}|\mathbf{x}^k\right)p\left(\mathbf{x}^k|\mathbf{y}\right).$$

In the MCMC algorithm the transition is broken down into two stages, introducing an intermediate variable, $\mathbf{x}^*$, that is: a proposal is made, with probability $q(\mathbf{x}^*|\mathbf{x}^{k-1})$, and it is accepted, with probability $\alpha(\mathbf{x}^k|\mathbf{x}^*)$, or it is rejected. So, for detailed balance to hold, the transition probability is similarly broken down into two parts as

$$\pi\left(\mathbf{x}^k|\mathbf{x}^{k-1}\right) = \alpha\left(\mathbf{x}^k|\mathbf{x}^*\right)q\left(\mathbf{x}^*|\mathbf{x}^{k-1}\right),$$

and the condition for detailed balance becomes

$$\alpha(\mathbf{x}^k|\mathbf{x}^*)q(\mathbf{x}^*|\mathbf{x}^{k-1})p(\mathbf{x}^{k-1}|\mathbf{y}) = \alpha(\mathbf{x}^{k-1}|\mathbf{x}^*)q(\mathbf{x}^*|\mathbf{x}^k)p(\mathbf{x}^k|\mathbf{y}).$$

Hence, the acceptance probability $\alpha(\mathbf{x}^k|\mathbf{x}^*)$ must be chosen so that

$$\alpha(\mathbf{x}^k|\mathbf{x}^*) = \frac{q(\mathbf{x}^*|\mathbf{x}^k)p(\mathbf{x}^k|\mathbf{y})}{q(\mathbf{x}^*|\mathbf{x}^{k-1})p(\mathbf{x}^{k-1}|\mathbf{y})}\alpha(\mathbf{x}^{k-1}|\mathbf{x}^*).$$

A reasonable approach is to make $\alpha(\mathbf{x}^k|\mathbf{x}^*)$ as large as possible, but noting that it is a probability and hence it cannot be greater than 1. This is achieved either by setting $\alpha(\mathbf{x}^{k-1}|\mathbf{x}^*) = 1$ or by making it so large that $\alpha(\mathbf{x}^k|\mathbf{x}^*) = 1$, hence

$$\alpha(\mathbf{x}^k|\mathbf{x}^*) = \min\left\{1, \frac{q(\mathbf{x}^*|\mathbf{x}^k)p(\mathbf{x}^k|\mathbf{y})}{q(\mathbf{x}^*|\mathbf{x}^{k-1})p(\mathbf{x}^{k-1}|\mathbf{y})}\right\}.$$

Although the derivation is complicated, the statement and implementation of the algorithm are usually straightforward. The only consideration left is the choice of proposal scheme, which although almost arbitrary can greatly affect the efficiency of the algorithm. The only formal requirement is that all parts of sample space can be reached infinitely often by the chain and that there is no periodic pattern to the number of steps between returns. These conditions make the Markov chain irreducible, positive recurrent and aperiodic, which guarantees eventual convergence to the equilibrium distribution.

One of the simplest proposal schemes, which works well for many applications, is based on separate single variable updates based on a random walk (see Figure 15.13). That is, at each step only the value of a single variable is proposed and further that the proposal is a perturbation of the previous value. Suppose that a new value for x_i is being proposed, then $x_i^* = x_i^{k-1} + \varepsilon$ and an obvious choice is $\varepsilon \sim N(0, \tau^2)$. When considering more complex estimation problems, extra care may be needed; Lui (2001) gives an in-depth catalogue of basic approaches that are likely to cover a range of situations.

When choosing a value for τ^2, it is important to realize that both low and high values lead to long transient periods and highly correlated samples and hence unreliable estimation. A reasonable proposal variance can be chosen adaptively during the early burn-in period, and it has been proven theoretically that for a wide variety of high-dimensional problems an acceptance rate of 23.4% (Gelman, Gilks, & Roberts, 1997) is optimal.

If the algorithm is designed carefully, then as the iterations progress the current parameter set does not depend on the starting values, and the subsequent values can be treated as a correlated sample from the posterior distribution. Key issues then become how to judge when this initial transient behaviour has ended, and the chain

```
Set an initial value for $\mathbf{x}$, call this $\mathbf{x}^0$
Repeat the following steps for $k = 1,\ldots,K$
    Repeat the following steps for $i = 1,\ldots,m$
        Generate $\varepsilon$ from a Gaussian distribution $N(0, \tau^2)$
        Generate a propose new value $x_i^* = x_i^k + \varepsilon$
        Evaluate
            $\alpha = \alpha(\mathbf{x}^k|\mathbf{x}^*) = \min\left\{1, \frac{p(x_1^k,\ldots,x_{i-1}^k,x_i^*, x_{i+1}^{k-1},\ldots,x_m^{k-1}|\mathbf{y})}{p(x_1^k,\ldots,x_{i-1}^k,x_i^{k-1}, x_{i+1}^{k-1},\ldots,x_m^{k-1}|\mathbf{y})}\right\}$
        Generate $u$ from a uniform distribution, $U(0,1)$
        If $\alpha > u$ then accept the proposal and set $x_i^k = x_i^*$, otherwise $x_i^k = x_i^{k-1}$
    End repeat
End repeat
Discard initial values and use remainder to make inference
```

Figure 15.13 A single-variable random walk MCMC algorithm.

is in equilibrium, and how many iterations to perform to have a sufficiently large sample for reliable estimation. Further, it is wise to also check Markov chain paths and to calculate sample autocorrelation functions. For good estimation, the paths should look 'random' and the autocorrelation functions be close to zero for all except small lags. A variety of more formal convergence diagnostics are available (see e.g. Raftery & Lewis (1995), Cowles & Carlin (1996) and Geyer (2011)).

Once the sample has been generated from the posterior distribution, a number of possible estimators are available. Let $\mathbf{x}^1, \mathbf{x}^2, \ldots, \mathbf{x}^N$ be the MCMC sample collected after equilibrium of the Markov chain has been declared, then the pixel-wise posterior mean and variances are estimated by the sample mean and variance

$$\widehat{x}_i = \frac{1}{N}\sum_{k=1}^{N} x_i^k \quad \widehat{\sigma}_i^2 = \frac{1}{N-1}\sum_{k=1}^{N}(x_i^k - \widehat{x}_i)^2 \quad i = 1, \ldots, m.$$

Also, sample percentiles can be used to estimate confidence bounds, for example, a symmetric 95% credible interval is given by $\left(x_i^{(0.025N)}, x_i^{(0.975N)}\right)$ where $x_i^{(k)}$ is the kth order statistics – that is the kth observation in the ordered sample. It is also possible to inspect low-dimensional marginal distributions and functions of the simulated values with

$$\widehat{g(\mathbf{x})} = \frac{1}{N}\sum_{k=1}^{N} g(\mathbf{x}^k) \quad \mathrm{var}(\widehat{g(\mathbf{x})}) = \frac{1}{N-1}\sum_{k=1}^{N}\left(g(\mathbf{x}^k) - \widehat{g(\mathbf{x})}\right)^2.$$

The whole MCMC sampling ethos encourages the investigation of a variety of summary measures, and not only mean and variance. Also, it is usual not to assume normality of the sampling distributions of the various quantities being estimated, but instead the sample histograms are used to estimate the unknown distributions. To illustrate estimation using the MCMC sampling approach, the ECT example described in Section 15.2 will be considered again in the next section.

Before finishing this section, it is worth mentioning that any MCMC algorithm can be converted into a simulated annealing algorithm (Geman & Geman, 1984), though not vice versa, by making a small modification. This gives a more efficient algorithm when the goal is only to obtain the MAP estimate, and has been used to find the MAP estimates in the previous sections. In particular a temperature, T_k, is included that decreases as the iterations progress, with $T_k = 2/\log(1+k)$ being one choice of annealing schedule, and α in the acceptable step is replaced by α^{T_k}. Clearly, there is no burn-in, and the MAP estimate is taken as the final iteration, $\widehat{\mathbf{x}}_{\mathrm{MAP}} = \mathbf{x}^K$. Simulated annealing algorithms usually provide an answer more quickly than a sampling algorithm, but at the expense of not producing a posterior sample for further investigation. Clearly, this approach should produce the same answer at a deterministic algorithm, but it has the added advantage that it should not get caught in local optima and it requires only function evaluations.

15.9 Estimation examples

To illustrate estimation using the MCMC sampling approach, the ECT example described in Section 15.2 will be considered again. It is important to note, however, that these are intended as illustration, and in general great care must be taken when designing synthetic experiments so as not to produce results that are overly optimistic (a good discussion of such issues can be found in Lionheart (2004)). Further examples of statistical output can be seen in West et al. (2004) and Aykroyd and Cattle (2006).

The MCMC algorithm output shown in Figure 15.14 is based on the same Gaussian pixel-based model used to produce the MAP estimate in Figure 15.9. In (a) the posterior mean is a slight improvement on the MAP estimate and provides a good general impression of the conductivity distribution. The posterior variance, in (b), with dark areas indicting low variance, shows that estimation is least reliable around the edge, and there is a single pixel in the centre of the object with almost zero posterior variance. The image in (c) shows the posterior probability that the pixel value exceeds some arbitrarily chosen fixed value. It is interesting to see that, although the posterior mean does not give a high contrast between object and background, there is a clear ordering, which means that a carefully thresholded version does locate the object well.

Figure 15.15 is based on a binary model, as described in Section 15.6, where the conductivity of the object and background have been assumed known. Hence, the MCMC algorithm has been used to estimate whether each pixel is object or background with an Ising model ($\beta = 0.1$) describing the spatial pattern. The MAP estimate, in (a), shows the single most likely configuration. This clearly locates the object with only a slight error. Similarly, in (b), the posterior mean reconstructs the true conductivity distribution well. It can be seen, however, that there are some pixel values spread around the background and at the boundary of object and background, where the posterior mean is somewhere between the two fixed values. This reflects the uncertainty in the estimated values — in essence this is a posterior estimate that the pixel belongs to the object with darker shading indicating that the probability is greater. It is important to note that for these two image reconstructions the model has led to single, well-defined regions of object, but that there is no part of the model

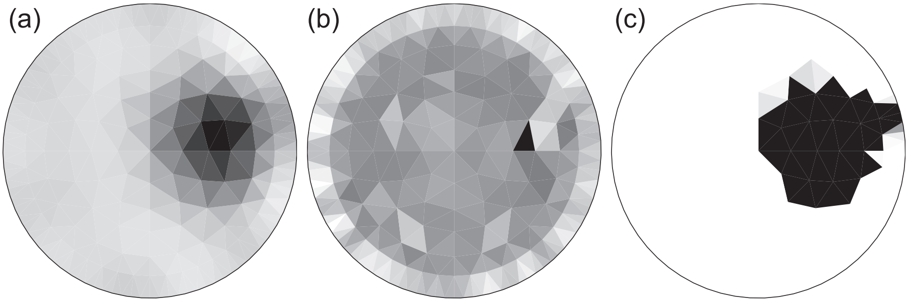

Figure 15.14 Posterior summary using the Gaussian model: (a) posterior mean, (b) posterior variance, and (c) exceedance probability.

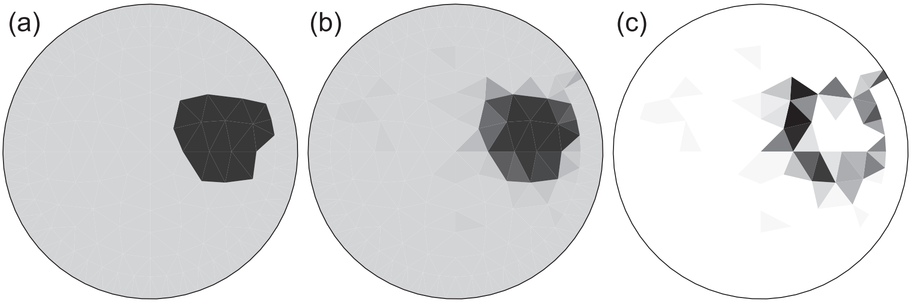

Figure 15.15 Posterior summary using an Ising model: (a) MAP estimate, (b) posterior mean, and (c) posterior variance.

that makes this certain. The posterior variance, in (c), again reflects the uncertainty in the estimation of pixel values.

As a final example of the MCMC method, Figure 15.16 shows selected output when using a feature-based model with a single star-shaped object. Again, this has been applied to data shown in Figure 15.2. Note that here the parameters include the unknown conductivity contrast between object and background, the centre of the object and multiple radii parameters of a star-shaped object. The image reconstruction corresponding to the MAP parameter estimates has already been shown in Figure 15.11(b).

Figure 15.16 (a) shows an estimate of the univariate marginal distribution of the contrast in conductivity of the object relative to the background − note that the true value is 10. Clearly, this is a very skewed distribution, which has a posterior mode close to the true value. Also shown, as a thick horizontal bar, is a 95% credible interval that contains the true value but extends a long way above. The centre of the object is described in (b) as a contour plot of the bivariate joint distribution of the two centre parameters. The thicker contour defines a 95% credible region. Panels (c) and (d) summarize the uncertainty in the location of the object outline. In (c) a random selection of 20 sampled outlines are shown, whereas (d) shows a ribbon that contained half the sampled outlines.

15.10 Discussion and future trends

Image reconstruction tasks appear throughout applied science, from archaeology to zoology. In some cases the aim is humble denoizing or deblurring, but in others the aim is more challenging. The most obvious area where substantial mathematical manipulation is required is in tomography, and medical and industrial applications are archetypal examples. Not only is the collected data noisy but it is also subject to a complex transformation that must be undone before reliable analysis is possible. The combination of noisy data and mathematical inversion make such applications very demanding.

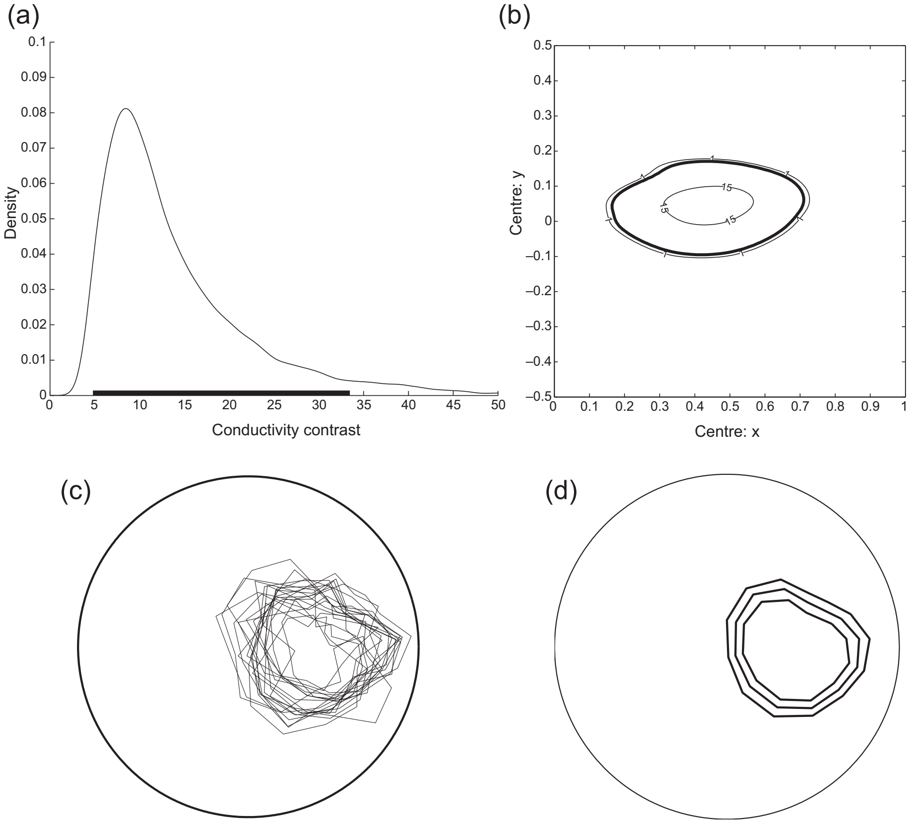

Figure 15.16 Posterior summary for star-shaped object model: (a) marginal distribution of the conductivity contrast, (b) bivariate distribution of centre location, (c) sample of outlines, and (d) 50% credible ribbon.

The statistical approach to image reconstruction is based on the use of statistical modelling principles to describe the stochastic properties of data collection, and to quantify expert knowledge and prior belief. In many cases the resulting procedures are closely related to classical deterministic algorithms, but the statistical approach leads to natural description and intuitive interpretation. This approach is sometimes referred to as Bayesian, because of the central role of Bayes theorem, but in practice it simply exploits the natural causal and conditional independence structure of the given application − Bayes theorem is used purely to perform the correct probability accounting.

To highlight the link with deterministic algorithms consider the log of Bayes theorem, as defined in Eqn (15.2), to give

$$\log p(\mathbf{x}|\mathbf{y}) = \log f(\mathbf{y}|\mathbf{x}) + \log p(\mathbf{x}) - \log f(\mathbf{y}). \tag{15.10}$$

Assuming a Gaussian likelihood, as defined in Eqn (15.5), and Gaussian prior distribution, using Eqns (15.7) and (15.9), gives

$$\log p(\mathbf{x}|\mathbf{y}) = -\frac{1}{2\sigma^2}\sum_i \left(y_i - g_i(\mathbf{x})\right)^2 - \beta\sum_i \left(x_i - \bar{x}_{\partial(i)}\right)^2 + \text{Constant.} \quad (15.11)$$

Then, after a little further rewriting, the following objective function is obtained:

$$\varphi(\mathbf{x}) = ||\mathbf{y} - g(\mathbf{x})||^2 + \lambda||\boldsymbol{R}\mathbf{x}||^2, \quad (15.12)$$

for some regularizing matrix $\boldsymbol{R}$. This is, of course, the classical regularized sum of squares whose minimum gives the regularized least-squares solution. Although the two approaches coincide for such particular choices of likelihood and prior distribution, the aim of classical regularization is still to find a single solution. Hence, the Bayesian approach has classical techniques as special cases, however, it makes explicit use of statistical descriptions and probability models and encourages a richer set of modelling options. It also provides a descriptive framework in terms of intuitive and interpretable components. The resulting statistical analysis is based around a probability distribution, the posterior distribution and so a wide range of possible summaries are available that are far beyond a single point estimate. Linked with the use of MCMC methods, a fuller investigation of the posterior distribution is relatively easy. This allows measures of estimation reliability and uncertainty that are not possible with other approaches.

Until recently, the majority of applications have been limited to the use of prior distributions that either smooth or shrink. As discussed in Section 15.5, a Gaussian prior on local differences produces very smooth reconstructions. This leads to the introduction of a total variation measure (Rudin, Osher, & Fatemi, 1992), corresponding to a Laplace prior distribution. The most famous shrinkage method is Tikhonov regularization, which corresponds to a Gaussian prior distribution on the pixel values. This method is effective in regularizing the least-squares problem but will not always be appropriate. Instead, there is scope to select a prior model that correctly describes what is expected rather than using something that is computationally convenient.

In some applications the unknown image may be mainly zeros with a few isolated significantly nonzero values — it is said to be sparse. In this case, neither smoothing nor shrinkage is appropriate. A key property of the Laplace prior when combined with a Gaussian likelihood is that it favours sparseness. The MAP estimation has a thresholding action, in that values close to zero become exactly zero, whilst the others are shrunk toward zero. When applied to pixel values isolated features appear against a zero background, and when applied to differences a staircase (Liu, Huang, Xu, & Lv, 2013) effect will be produced. Liu et al. (2013) suggest a higher order modification, which could also be accommodated in the Bayesian setting modifying Eqn (15.9). This highlights the flexibility of the Bayesian approach, and there is substantial scope for work identifying the most appropriate type of prior distribution for each application.

Wavelets methods are a natural approach to the reconstruction of a function from noisy data (for general details, see Donoho & Johnstone (1994) and Nason (2008)). These methods have also started to be applied to inverse problems through the so-called wavelet-vaguelete transform (see e.g. Donoho, 1995 and Abramovich & Silverman, 1998). Such an approach should allow for denoizing and provides a sparse representation. This too has an interpretation within the Bayesian framework and so can be accommodated into the approach described in this chapter without too many modifications.

Most applications of image reconstruction use pixel-based models, and the only output is an image. In Section 15.7, however, an alternative approach was considered where models are in terms of hierarchical geometric representations. The unknowns are then parameters of the geometric model. Typically, the number of unknowns is then orders of magnitude fewer than in an equivalent pixel-based model. Further, it is common for the geometric parameters to have physical meaning allowing direct interpretation. Such models, however, must be designed individually for each application. Further, when dealing with nonlinear inverse problems computational aspects of the forward solution are crucial, and it may also be possible to match the numerical method to the style of model. There is, perhaps, a natural link between pixel-based models and FEM, and between feature-based models and boundary BEM. This is another area of ongoing research.

In all applications of Bayesian modelling there are various hyper-parameters. Here they have been fixed using some trial and error. In many investigations, however, these are also part of the posterior distribution with their own hyper-prior distributions. The use of such approaches is currently uncommon in inverse problems, and hence there are no standard recommendations. Further research on this aspect would make the reconstruction process fully automatic and remove subjective concerns.

The aim of this chapter is to give an introduction to the basic principles of statistical image reconstruction. The two approaches of pixel-based and feature-based were described and illustrated. A great benefit of the statistical modelling approach when linked with MCMC estimation is the great flexibility over the choice of prior distributions and output summaries. This means that all components of the model can be selected separately to accurately reflect current knowledge and to address questions of interest, without any need to follow a mathematically or computationally convenient path. Hence, the statistical approach provides an ideal framework within which many new and important applications can be examined.

References

Abramovich, F., & Silverman, B. W. (1998). Wavelet decomposition approaches to statistical inverse problems. *Biometrika, 85*, 115−129.

Aykroyd, R. G., & Cattle, B. A. (2006). A flexible statistical and efficient computational approach to object location applied to electrical tomography. *Journal of Statistics and Computing, 16*, 363−375.

Aykroyd, R. G., & Cattle, B. A. (2007). A boundary-element approach for the complete-electrode model of EIT illustrated using simulated and real data. *Inverse Problems in Science and Engineering, 15*, 441−461.

Aykroyd, R. G., & Zimeras, S. (1999). Inhomogeneous prior models for image reconstruction. *Journal of the American Statistical Association, 94*, 934−946.

Bera, T. K., & Nagaraju, J. (2011). Resistivity imaging of a reconfigurable phantom with circular inhomogeneities in 2d-electrical impedance tomography. *Measurement, 44*, 518−526.

Besag, J. (1974). Spatial interaction and the statistical analysis of lattice systems (with discussion). *Journal of the Royal Statistical Society. Series B, 36*, 192−236.

Besag, J. (1983). Discussion of paper by P. Switzer. *Bulletin of the International Statistical Institute, L-3*, 422−425.

Besag, J. (1986). On the statistical analysis of dirty pictures (with discussion). *Journal of the Royal Statistical Society. Series B, 48*, 259−302.

Besag, J., Green, P. J., Higdon, D., & Mengersen, K. (1995). Bayesian computation and stochastic systems. *Statistical Science, 10*, 1−41.

Borsic, A., Graham, B., Adler, A., & Lionheart, W. (2010). In vivo impedance imaging with total variation regularization. *IEEE Transactions on Medical Imaging, 29*, 11−54.

Brooks, S., Gelman, A., Jones, G., & Meng, X.-L. (2011). *Handbook of Markov chain Monte Carlo*. Chapman & Hall/CRC.

Cowles, M. K., & Carlin, B. P. (1996). Markov chain Monte Carlo convergence diagnostics: a comparative review. *Journal of the American Statistical Association, 91*, 883−904.

Cross, G. R., & Jain, A. K. (1983). Markov random field texture models. *IEEE Transactions on PAMI, 5*, 25−39.

Donoho, D. L. (1995). Nonlinear solution of linear inverse problems by wavelet vaguelette-decomposition. *Applied and Computational Harmonic Analysis, 2*, 101126.

Donoho, D. L., & Johnstone, I. M. (1994). Ideal spatial adaptation by wavelet shrinkage. *Biometrika, 81*, 425−455.

Dubes, R. C., & Jain, A. K. (1989). Random field models in image analysis. *Journal of Applied Statistics, 16*, 131−164.

Gamerman, D., & Lopes, H. F. (2006). *Markov chain Monte Carlo: Stochastic simulation for Bayesian inference* (2nd ed.). Chapman & Hall/CRC Texts in Statistical Science.

Gelman, A., Gilks, W. R., & Roberts, G. O. (1997). Weak convergence and optimal scaling of random walk Metropolis algorithms. *Annals of Applied Probability, 7*, 110−120.

Geman, S., & Geman, D. (1984). Stochastic relaxation, Gibbs distributions and the Bayesian restoration of images. *IEEE Transactions on PAMI, 6*, 721−741.

Geman, S., & McClure, D. E. (1985). Bayesian image analysis: an application to single photon emission tomography. In *Proceedings of the American Statistical Association, Statistical Computing Section* (pp. 12−18).

Geman, S., & McClure, D. E. (1987). Statistical methods for tomographic image reconstruction. *Bulletin of the International Statistical Institute, 52*, 5−21.

Geyer, C. J. (2011). Introduction to Markov chain Monte Carlo. In S. Brooks, A. Gelman, G. L. Jones, & X.-L. Meng (Eds.), *Handbook of Markov chain Monte Carlo*. Chapman and Hall/CRC.

Gilks, W., Richardson, S., & Spiegelhalter, D. (1995). *Markov chain Monte Carlo in practice*. Chapman & Hall/CRC Interdisciplinary Statistics Series.

Green, P. J. (1990a). Bayesian reconstructions from emission tomography data using a modified EM algorithm. *IEEE Transactions on Medical Imaging, 9*, 84−93.

Green, P. J. (1990b). On the use of the EM algorithm for penalised likelihood. *Journal of the Royal Statistical Society. Series B, 52*(3), 443−452.

Grenander, U. (1970). A unified approach to pattern analysis. *Advances in Computers, 10*, 175−216.

Grenander, U. (1973). Statistical geometry: a tool for pattern analysis. *Bulletin of the American Mathematical Society, 79*, 829−856.

Grenander, U., & Keenan, D. M. (1989). Towards automated image understanding. *Journal of Applied Statistics, 16*, 207−221.

Hastings, W. K. (1970). Monte Carlo sampling methods using Markov chains, and their applications. *Biometrika, 57*, 97−109.

Ising, H. (1925). Beitrag zur theorie des ferromagnetismus. *Zeitschrift für Physik, 31*, 253−258.

Kaipio, J., Kolehmainen, V., Vauhkonen, M., & Somersalo, E. (1999). Inverse problems with structural prior information. *Inverse Problems, 15*, 713729.

Khambampati, A. K., Hong, Y. J., Kim, K. Y., & Kim, S. (2013). A boundary element method to estimate the interfacial boundary of two immiscible stratified liquids using electrical resistance tomography. *Chemical Engineering Science, 95*, 161−173.

Kinderman, R., & Snell, J. L. (1992). *Markov random fields and their applications*. American Mathematical Society.

Lionheart, W. R. (2004). EIT reconstruction algorithms: pitfalls, challenges and recent developments. *Physiological Measurement, 25*, 125−142.

Liu, J., Huang, T.-Z., Xu, Z., & Lv, X.-G. (2013). High-order total variation-based multiplicative noise removal with spatially adapted parameter selection. *Journal of the Optical Society of America A, 30*, 1956−1966.

Lui, J. (2001). *Monte Carlo strategies in scientific computing*. Berlin: Springer-Verlag.

Mardia, K. V. (1994). *Advances in Applied statistics: Statistics and Images: 2*. Carfax Publishing Company.

Mardia, K. V., & Kanji, G. K. (1993). *Advances in Applied statistics: Statistics and images: 1*. Carfax Publishing Company.

Metropolis, N., Rosenbluth, A., Rosenbluth, M., Teller, A., & Teller, E. (1953). Equations of state calculations by fast computing machines. *Journal of Chemical Physics, 21*, 1087−1091.

Nason, G. P. (2008). *Wavelet methods in statistics with R*. New York: Springer.

Phillips, D. B., & Smith, A. F. M. (1993). Dynamic image analysis using Bayesian shape and texture models. In K. V. Mardia, & G. K. Kanji (Eds.), *Statistics and Images* (Vol. 1, pp. 299−322). Oxford: Carfax.

Polydorides, N., & Lionheart, W. R. B. (2002). A Matlab toolkit for three-dimensional electrical impedance tomography: a contribution to the electrical impedance and diffuse optical reconstruction software project. *Measurement Science and Technology, 13*, 1871.

Raftery, A., & Lewis, S. (1995). The number of iterations, convergence diagnostics and generic Metropolis algorithms. In W. R. Gilks, S. Richardson, & D. J. Spiegelhalter (Eds.), *Practical Markov chain Monte Carlo*. Chapman and Hall.

Robert, C., & Casella, G. (2011). A short history of Markov chain Monte Carlo: subjective recollections from incomplete data. *Statistical Science, 26*, 102−115.

Rudin, L., Osher, S., & Fatemi, E. (1992). Nonlinear total variation based noise removal algorithms. *Physics D, 60*, 259−268.

Shepp, L. A., & Vardi, Y. (1982). Maximum likelihood reconstruction in positron emission tomography. *IEEE Transactions on Medical Imaging, 1*, 113−122.

Somersalo, E., Cheney, M., & Isaacson, D. (1992). Existence and uniqueness for electrode models for electric current computed tomography. *SIAM Journal on Applied Mathematics, 52*, 1023−1040.

Stuart, A. M. (2010). Inverse problems: a Bayesian perspective. *Acta Numerica, 19*, 451−559.

Vardi, Y., Shepp, L. A., & Kaufman, L. (1985). A statistical model for positron emission tomography. *Journal of the American Statistical Association, 80*, 8−37.

Vauhkonen, M., Lionheart, W. R. B., Heikkinen, L. M., Vauhkonen, P. J., & Kaipio, J. P. (2001). A MATLAB package for the EIDORS project to reconstruct two-dimensional EIT images. *Physiological Measurements, 22*, 107−111.

Voss, J. (2013). *An introduction to statistical computing: A simulation-based approach*. Wiley.

Watzenig, D., & Fox, C. (2009). A review of statistical modelling and inference for electrical capacitance tomography. *Measurement Science and Technology, 20*, 22, 052002.

Weir, I. S. (1997). Fully Bayesian SPECT reconstructions. *Journal of the American Statistical Association, 92*, 49−60.

Weir, I. S., & Green, P. J. (1994). Modelling data from single photon emission computed tomography. In K. V. Mardia (Ed.), *Statistics and images* (Vol. 2). Abingdon: Carfax.

West, R. M., Aykroyd, R. G., Meng, S., & Williams, R. A. (2004). Markov chain Monte Carlo techniques and spatial-temporal modelling for medical EIT. *Physiological Measurements, 25*, 181−194.

West, R., Meng, S., Aykroyd, R., & Williams, R. (2005). Spatial-temporal modeling for electrical impedance imaging of a mixing process. *Review of Scientific Instruments*, *76*, 073703.

This page intentionally left blank

Part Three

Tomography applications

This page intentionally left blank

Applications of tomography in mineral transportation

16

C. Tan, F. Dong
Tianjin University, Tianjin, China

16.1 Introduction

Slurry flows, gas—solid two-phase flows, and oil—gas—water multiphase flows are the frequently encountered flow phenomena in the processes of mineral transportation in industries. Measurement of these flow parameters has been a popular research and engineering topic, which also involves safety and fiscal issues that have been discussed worldwide for the past several decades.

Parameters of each phase are required in order to fully describe the process hydrodynamics of custody transportation. These parameters include phase distribution, concentration, and transport velocity of each individual phase. Most of the problems encountered in multiphase-flow measurements are due to the increased number of the characteristic flow parameters as compared to those in single-phase flows, because multiphase flow always involves the interactions between phases, for example mass transfer, momentum transfer, and heat transfer. In addition, all the changes and interactions are simultaneous and transient, which makes the flow process more complicated. For example, measuring a typical flow phenomenon in mineral transportation, the slurry flow, requires information about phase concentration and velocity to study its behavior in transportation. Thus the slurry concentration profile is an important factor to predict the pressure drop and the frictional pressure losses in pipeline transportation, as well as to understand the hydrodynamics and predict the performance of chemical conversion and heat transfer in chemical reactors. Another phenomenon of rheological change of a multiphase mixture in mineral transportation is called flow regime or flow pattern, which dominates the governing fluid dynamic and consequently the means of measurements conducted.

The difficulty of measuring/monitoring a multiphase fluid is that both the phase distribution and the velocity profile vary significantly with flow patterns in temporal and spatial coordinates. Lots of flow measuring techniques are employed to solve this problem; however, no one individual method could accomplish this task to fully satisfy the field application so far. That is because in these cases, the issue is the availability of reliable and nonintrusive measurement methods to obtain concentration and velocity profiles required to design and scale up mineral transportation processes (Giguere, Fradette, Mignon, & Tanguy, 2009).

To fully understand the multiphase flow phenomena and to consequently establish the description models, a comprehensive, nonintrusive, and visualized detecting method is required, which falls in the scope of capability of industrial process

Industrial Tomography. http://dx.doi.org/10.1016/B978-1-78242-118-4.00016-2
Copyright © 2015 Elsevier Ltd. All rights reserved.

tomography (IPT). IPT can provide information regarding mineral flow transportation by integrating multisource information at different positions of the measured cross section of the pipeline. It also can provide visual monitoring on the phase distribution within the pipe line in a two-dimensional (2D) or three-dimensional (3D) manner. Therefore, IPT is widely studied in the field of mineral pipe flow due to its capability of "looking" inside the flow region where the local flow information such as phase fraction and velocity can be extracted. In this way, a more accurate means of calculating flow rate and eliminating the uncertainty in measurement will be available, overcoming the inability to predict flow profile associated with existing flow measurement methods. Due to the virtues a tomography system possesses, it gains wide applications in mineral transportation for flow measurement/monitoring, such as petroleum transportation in the oil industry (Ismail, Gamio, Bukhari, & Yang, 2005), fluidized beds (Yang, Du, & Fan, 2007), and slurry flow transportation (Wang, Jones, & Williams, 2003).

This chapter will give an overview on how to apply IPT in measuring the multiphase pipe flow in mineral transportation. These applications include process parameter measurement and flow process monitoring, along with flow process analysis based on either the reconstructed cross-sectional (or volumetric) images or raw data. The multiphase flow studied in this chapter includes oil—gas—water multiphase flow (in oil industry transportation) and solid—liquid flow (especially slurry flow in mineral transportation concerning particles). Definition of flow pattern in multiphase flow is introduced in Section 16.2 along with flow pattern identification methods with IPT. Then flow parameter measurement, mainly the phase fraction and flow velocity, with IPT is discussed in Section 16.3, also covering the topics of flow process monitoring and characterization. Because of the complexity of multiphase flow, one individual sensor may not be able to conduct a comprehensive monitoring or measurement alone, so IPT in the frame of multisensor fusion is discussed in Section 16.4, covering the topics of multimodality IPT, and IPT with other sensors. A closing remark is given in Section 16.5.

16.2 Flow pattern and flow pattern identification with industrial process tomography

16.2.1 Flow patterns in mineral transportation

Flow pattern (flow regime in some literature) of a multiphase fluid system is the temporally and spatially geometrical distribution of each individual phase; it reflects the flow conditions and governs nearly all the flow parameters that are of interest to field applications. The characterization of flow patterns in mineral transportation is useful not only for the design, optimization, and control of a transportation process, but also for research purposes by providing experimental data needed to develop, tune, and validate empirical and numerical multiphase models. Flow pattern changes with the fluid property, pipe diameter, pipe inclination, and operation conditions. Therefore, only the horizontal flow patterns are discussed herein as an example demonstrating the application of IPT in flow pattern identification and characterization. The horizontal flow patterns are usually asymmetric in the pipes, because gravity acts perpendicular to flow, and separation of the fluid might occur, which makes the flow asymmetric and hence more complex.

Four typical flow patterns that are commonly seen in a horizontal slurry flow can be classified with solid phase concentration, where the density of the solid phase is usually higher than the density of the carrier fluid. They are flow with a stationary bed, flow with a moving bed, heterogeneous flow (asymmetric), and pseudo-homogenous flow (symmetric) (Giguere, Fradette, Mignon, & Tanguy, 2008). In petroleum transportations, air or oil usually occurs within the slurry flow, making the flow more complicated and potentially classified as three- or even four-phase flow.

For the oil—gas—water multiphase flow, usually the oil—gas—water three-phase flow is studied based on the understanding of gas—liquid (water or oil) two-phase flow and liquid—liquid (oil—water) two-phase flow. Due to gravity and buoyancy that simultaneously occur to gas—liquid two-phase flow, the gas phase flows more likely on the top of the pipe. Slug flow and elongated bubble flows can be jointly classified as “intermittent”; stratified flow and annular low are the “separated” flow and dispersed bubble flow is the “homogeneous” flow. The flow regime of oil—water flows is quite different from that of gas—liquid two-phase flows. The different flow structure is mainly caused by the large liquid/liquid momentum transfer capacity and small buoyancy effects. The lower free energy at the interface allows the formation of shorter interfacial waves and smaller dispersed phase droplet size.

The flow patterns of three-phase flow were once investigated by considering the two liquid phases as a mixture, which simplified the models and analysis but also confined their applications within only particular conditions (Taitel, Barnea, & Brill, 1995). One widely accepted flow regime categorization is given by Acikgoz and associates (Acikgoz, Franca, & Lahey, 1992). They observed and also named six different flow regimes, which can be classified into two major groups, oil-based flow and water-based flow, according to the distinct formation of which phase dominates. In addition, the solid phase involving three-phase flow is also a research area regarding sand transportation, usually a gas—liquid—solid multiphase-flow (usually oil and water are together called liquid phase) system, making the flow pattern much more complicated.

16.2.2 Flow pattern identification with industrial process tomography

Radiation-based tomographies, such as computed tomography (CT), have been successfully applied on solid—liquid two-phase flow pattern identification (Karim, Varma, Vesvikar, & Al-Dahhan, 2004), because of the linearized projections of CT that reduce the uncertainty of solving inverse problems. However, most other tomography techniques are subject to fluid properties, particularly electrical tomography, which is thriving in this field due to its simple structure and low environmental hazard. For instance, in gas—oil flow, usually the electrical capacitance tomography (ECT) systems are employed (Wang & Zhang, 2009); when conductive liquid is the continuous phase, such as gas—water two-phase flow, usually electrical resistance tomography (ERT) does the job (Tan, Dong, & Wu, 2007).

Obviously, the flow regimes can be visually identified either by stacking the reconstructed 2D images or by 3D reconstructions. However, these observations are highly restricted by the image reconstruction speed and artifacts of the reconstructed images. Therefore, a more rapid method of identifying flow regimes by extracting flow features from tomographic measurements was developed. In this way, the flow features at a certain time interval are further processed with a classification algorithm (or pattern recognition) to separate the features of one individual flow regime from others. This method does not need an image reconstruction procedure, and thus is a time-saving way of identifying flow regimes in a practical application (Tan et al., 2007). The classification algorithms usually adopted in flow regime recognition include support vector machine, neural network, and dynamic clustering.

16.3 Mineral transportation process measurement and monitoring with industrial process tomography

In mineral transportation, the most important process parameters of interest are the phase fraction (by volume, cross section, or mass) and the flow rate (by volume or mass) of each individual phase. Variations of either parameter will bring changes to flow conditions in terms of flow patterns and hydrodynamic models. Therefore precise estimates of these two parameters without flow disturbance are required.

16.3.1 Phase fraction measurement

Phase fraction of a multiphase fluid is a key parameter that reflects flow conditions, and is indispensable in all the flow models and correlations. IPT is capable of reconstructing the phase distribution of the cross section of interest in a visualizing manner. Therefore, it offers a great perspective in measuring the phase concentration of multiphase flow. In general, phase concentration is calculated from the ratio of the area occupied by one phase to the whole cross section in a reconstructed image. However, the precision is restricted by the gray-level threshold, i.e., how to define the gray level representing a dispersed phase in a reconstructed image. It is also restricted by the spatial resolution of the system, i.e., how small a pixel of the reconstructed image could be. Thus, the method that directly processes the data to extract the phase concentration information without image reconstruction was presented and is still being developed (Dong, Qiao, Jiang, & Xu, 2003).

The two most popularly adopted tomographic principles for phase fraction estimation in slurry flows are based on radiation and electrical techniques. Because the radiation beams do not bend at the interaction of phases, the accurate phase distribution and, furthermore, the phase concentration in the field can be obtained (Suzuki, Tsuchitani, Iimura, & Hirota, 2004). Because the field of electrical tomography is vulnerable to phase interactions, it is always difficult to get results of phase distribution as precise as those from radioactive tomography. But electrical tomography is simple in structure and reliable in operation, and the mean error rate could reach less than 5% (Huang, Wang, & Li, 2003).

The radioactive wave, e.g., X-ray or γ-ray, attenuates when transmitted in fluids; its attenuation varies with fluid properties. Usually a single-energy γ-ray is able to measure a two-phase flow system. However, for a three-phase flow system, two independent measurements of the phase fractions are usually required; the fraction of the third phase will be obtained from their relation that the summation of the three-phase fractions is unity. A different technology is needed, such as capacitance measurements; furthermore, if only a radiation-based method is preferred, then two independent measurements can be obtained using the dual-energy technique (Frøystein, Kvandal, & Aakre, 2005). One typical example of measuring the phase fraction of a three-layered oil—gas—water three-phase flow by a two-beam (one vertical and one horizontal) X-ray CT is shown in Figure 16.1. Two 160-keV X-ray sources are used to penetrate a 4-inch-diameter pipeline. The measurement data are obtained and processed with the calibration data when the pipe is full of either oil, gas, or water. The results are normalized to reduce the influence of noise and systematic error (Hu et al., 2005). Figure 16.2 shows that the phase fraction measured could track the ideal phase fraction well by using such an X-ray system and the corresponding data processing method.

As with all radiation measurement techniques, a trade-off between measurement speed and accuracy must be made due to the statistical nature of the radiation source. The greater the accuracy required, the longer will be the measurement period. Stronger radiation sources will shorten the measurement period, but much greater safety precautions have to be taken. Besides, the vessel size is not always large, and hence wall effects usually influence the process measurement. Therefore new X-ray hardware and image processing software have been developed to measure vessels of up to 32 cm in diameter and temporal resolutions of up to 60 frames per second, providing a good compromise between temporal and spatial resolutions (Heindel, Gray, &

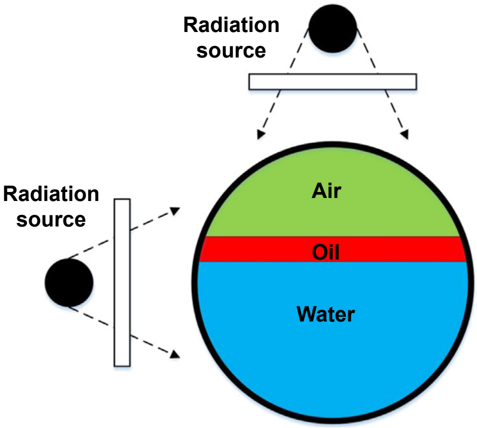

Figure 16.1 Phase distribution to generate the phase fraction test data. Oil holdup = 0.11 (red); water holdup = 0.63 (blue); air holdup = 0.26 (green).
Adapted from Hu et al. (2005).

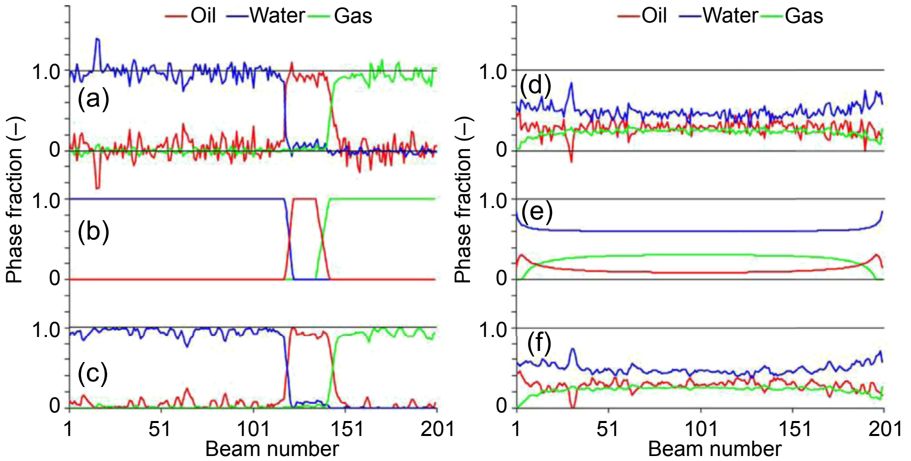

Figure 16.2 Experimental and computed phase fraction data from horizontal beams (a—c) and vertical beams (d—f) for the three-layered stratified flow in Figure 16.1: (a), (d) measured phase fraction data; (b), (e) ideal phase fraction data; (c), (f) measured phase fraction data, after processing and filtering. Sodium iodide (5 g/l) is added to the water phase (Hu et al., 2005).

Jensen, 2008). An ultrafast electron beam X-ray tomography has also been developed for the visualization and measurement of a gas—liquid two-phase flow. The electron beam is produced by an electron gun, as shown in Figure 16.3. An acceleration voltage of 150 kV and a beam current of 5—10 mA is projected by the electron gun through a beam-centering electromagnetic lens system to a focal spot of a tungsten block to generate an X-ray. This scanning can be performed very fast and a frame rate of 5 kHz can be achieved (Fischer et al., 2008).

Radioactive tomography usually utilizes a single radiation source, and the measurement of tomographic data is acquired by rotating the source mechanically. The multibeam system is more complex and expensive, and yet the component concentration can be measured with an accuracy of a few percent; thus they are being increasingly used in multicomponent flow measurement (Sætre, Johansen, & Tjugum, 2012).

Other radiation-based tomography techniques for tracking the particle movement, local or cross-sectional averaged phase holdups, and velocities include positron emission tomography and single-photon emission computed tomography to obtain dynamic 3D images of radioactive tracer concentrations (Barigou, 2004), and nuclear magnetic resonance or magnetic resonance imaging for the investigation of the hydrodynamics in trickle bed reactors (Marashdeh et al., 2010).

ERT has been successfully applied in reconstructing the phase distribution of slurry flow. Through certain reconstruction algorithms, such as the back-projection algorithm and generalized iterative algorithm, the conductivity distribution within the target pipeline could be reconstructed; then the phase fraction can be estimated based on the area each phase occupies, as shown in Figure 16.4. However, artifacts within reconstructed images are always troublesome. To alleviate these artifacts, several options are available, including decreasing the intensity of electrical current injected,

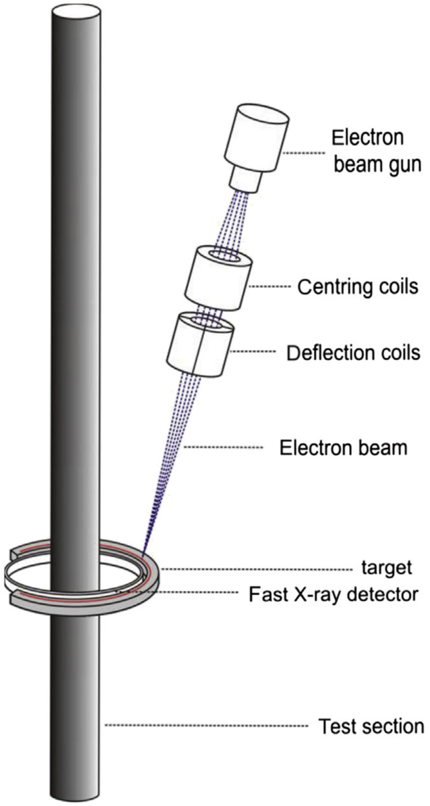
Electron beam gun
Centring coils
Deflection coils
Electron beam
target
Fast X-ray detector
Test section

Figure 16.3 Operation principle of ultrafast electron beam X-ray CT (Fischer et al., 2008).

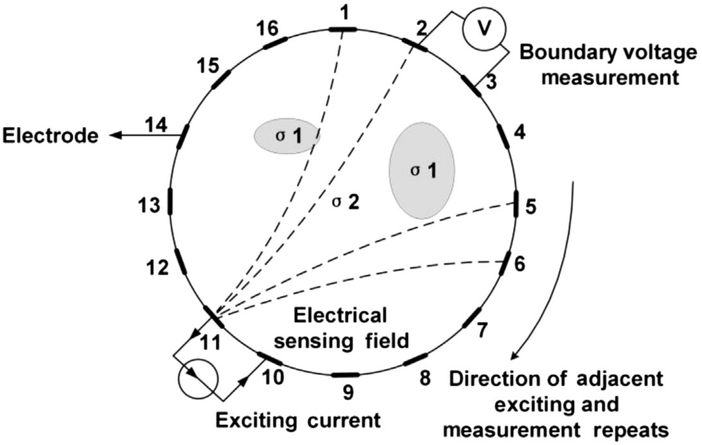
1
2
3
4
5
6
7
8
9
10
11
12
13
14
15
16
V
Boundary voltage measurement
Electrode
σ 1
σ 1
σ 2
Electrical sensing field
Exciting current
Direction of adjacent exciting and measurement repeats

Figure 16.4 Phase fraction measurement with ERT.

increasing the absolute electrical conductivity of the water phase, or modifying the gain used by the hardware for the resistance measurements. Any of these methods will increase the definition of image reconstruction, but will decrease the quality of ERT reference measurements.

Another methodology of utilizing ERT measurement on phase fraction estimation is directly processing the measurement data to determine the phase fraction without image reconstruction. For sphere particles evenly distributed within a slurry flow, their volume fraction α_c can be converted from the conductivity distributions with the Maxwell equation, as given below:

$$\alpha_c = \frac{2\sigma_1 - 2\sigma_{mc}}{\sigma_{mc} + 2\sigma_1} \tag{16.1}$$

where σ_1 is the conductivity of the first phase, σ_{mc} is from the local mixture conductivity distribution.

Razzak used ERT and the Maxwell relationship to obtain the solid fraction distribution of slurry flow (Razzak, Barghi, & Zhu, 2009). The reconstructed phase fraction distribution at superficial liquid velocity, $u_l = 11.2$ cm/s and superficial solid velocity $u_s = 0.75$ cm/s is shown in Figure 16.5, where the solid concentration was higher near the wall regions and decreased toward the central region. A 3D topographic view of the cross-sectional solids holdup in Figure 16.5(b) shows the distribution more clearly.

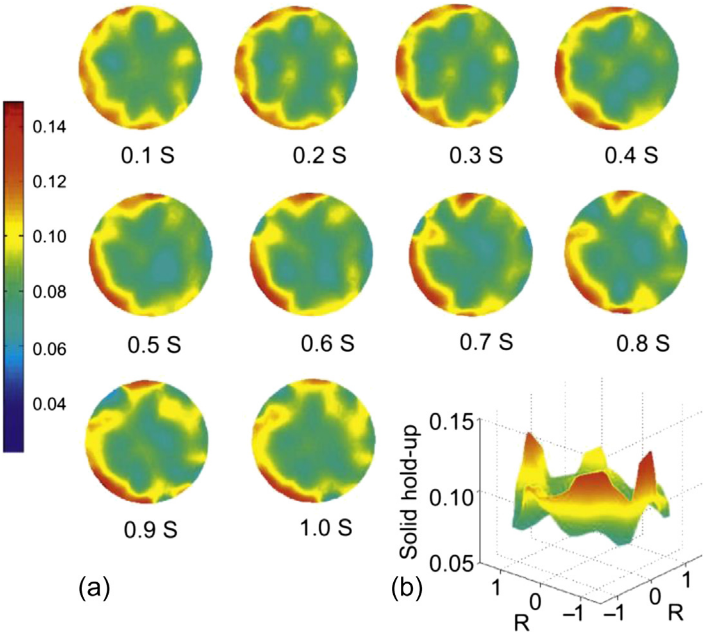

Figure 16.5 (a) Two-dimensional topographic view from 0.1 to 1 s frame and (b) three-dimensional topographic view of the cross-sectional solid holdup at superficial liquid velocity, $u_l = 11.2$ cm/s, superficial solid velocity $u_s = 0.75$ cm/s (Razzak et al., 2009).

Since the water temperature, and consequently the conductivity, normally varies during the operation of the flow, the reference profile needs temperature compensation for phase fraction estimate.

16.3.2 Flow velocity measurement

Flow velocity can be measured in many ways and the accurate measurement is broadly needed in science, engineering, industry, and daily life. However, in slurry transportation processes, due to the intrinsic complexity of fluid in both temporal and spatial domains, as well as the industrial requirement on nonintrusive and low energy loss, it is becoming an area in which process tomography is of practical value. Combined with the measurement of phase fraction, process tomography can obtain the mixture velocity, local individual phase velocity, and even radial or rotating velocity (Dai, Wang, Panayotopoulos, Lucas, & Williams, 2005).

Generally, the method that a process tomography system adopts for flow velocity measurement is cross-correlation. The basic idea of this method is to seek the time delay of the flow structure passing from upstream sensors to downstream sensors (Beck & Plaskowski, 1987). When applying cross-correlation to process tomography techniques, the upstream and downstream sensors are referred to as the tomographic sensor planes and are mounted on the cross sections or slices of interest of a pipe, as shown in Figure 16.6.

This system structure is usually named the “dual-plane tomography system,” and its extended version is multiplane tomography, which, by definition, employs more than two sensor planes on the target pipeline. A multiplane ERT usually has four or eight electrode planes, depending on the scale and the range of interest for flow investigations—for instance, an 8 × 16 array of resistance tomography sensors for the visualization of the mixing process of a gas–liquid two-phase flow (Wang, Dorward, Vlaev, & Mann, 2000).

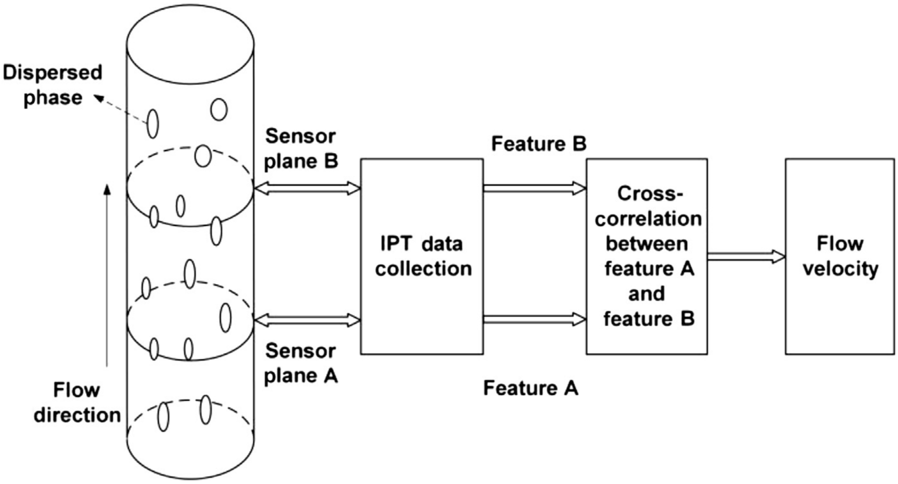

Figure 16.6 Flow velocity measurement with cross-correlation and an IPT.

Basically two methods of tomography-based cross-correlation are employed. One is to correlate the corresponding pixels of reconstructed images on each plane for local velocity measurement (Lucas, Cory, Waterfall, Loh, & Dickin, 1999). In this way, the axial velocity profile within one cross section can be reconstructed, as shown in Figure 16.7.

The pixel-based cross-correlation method can also reconstruct the radial velocity distribution (Wang, Lucas, Dai, Panayotopoulos, & Williams, 2006). A dual-plane ERT system is used for measuring local air volume fraction and 3D velocity distribution in gas—liquid flows. A "best-correlated pixels" method was developed for the axial, angular, and radial velocity profile measurement of swirling flow. A pixel from the upstream sensing plane (plane X) is correlated with an axially corresponding pixel and its neighbor's pixels from the downstream sensing plane (plane Y) through the following correlation:

$$R_{x[n,m]y[n+i,m+j]}[p] = \sum_{k=0}^{T-1} x_{[n,m]}[k]y_{[n+i,m+j]}[k+p] \tag{16.2}$$

where T is the number of images for which the cross-correlation is calculated; $p = -(T-1),\ldots 0, 1, 2, 3\ldots T-1$; $k = 0, 2, 3, 4\ldots T-1$; n and m are the coordinates of the pixel; x and y are the values of the pixels on plane X and plane Y, respectively; $(i, j) \in B$ is the group of neighboring pixels on plane Y. After calculation of the corresponding cross-correlation functions between each pixel, the highest correlation value will be selected as the best-correlated pixel, and thus the velocity between these two pixels is obtained:

$$u_{nm} = \frac{d}{\tau} \tag{16.3}$$

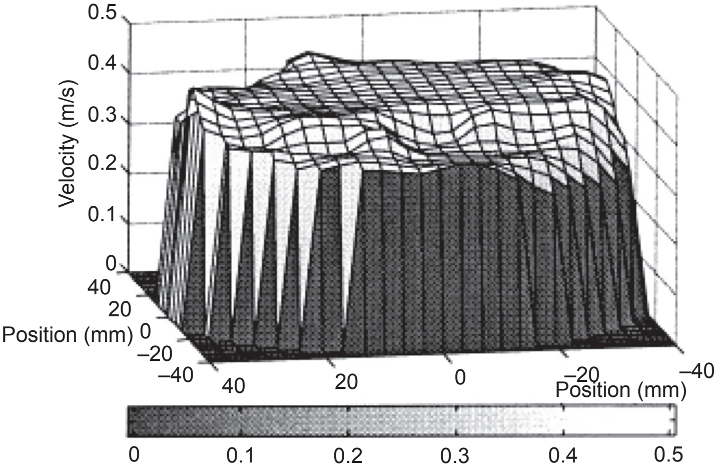

Figure 16.7 Axial velocity profile of vertical upward slurry flow reconstructed by ERT ($Q_s = 1.11$ m^3/h, $Q_w = 6.84$ m^3/h, and $\alpha_m = 0.16$) (Lucas, Cory, Waterfall, Loh, & Dickin, 1999).

where d is the separation distance between the corresponding pixels at the upstream and downstream plane X and plane Y; τ is the transit time of the flow through the two sensing planes and is calculated from the frame number delayed, corresponding to the highest correlation value and the known data collection speed. One typical reconstructed velocity profile is shown in Figure 16.8, where the swirling velocity profile can be clearly observed.

The other cross-correlation method is to correlate the features that are directly extracted from the raw measurement data without image reconstruction (Tan & Dong, 2010). The velocity obtained is the overall flow velocity; it is faster in calculation than the pixel-based cross-correlation but loses details on the velocity profile, and

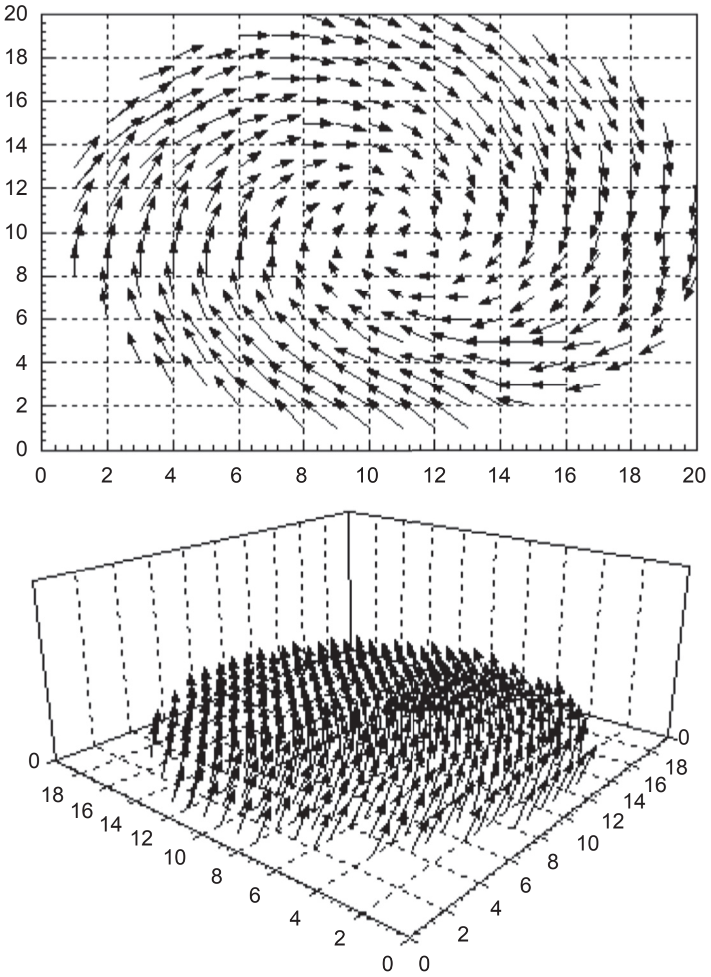

Figure 16.8 Velocity distributions in both 2D and 3D at flow condition of $u_w = 0.41$ m/s and $u_g = 0.068$ m/s (where w and g represent water and gas, respectively) (Wang et al., 2006).

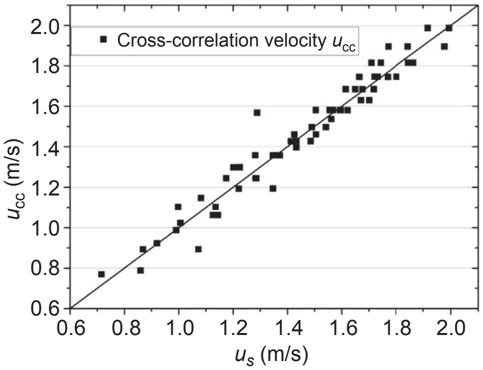

Figure 16.9 Oil—water two-phase flow velocity u_{cc} prediction with cross-correlation method at superficial mixture velocity u_s ranging from 0.7 m/s to 2.1 m/s.

thus can be used in fast industrial process measurement. The model of tomography feature cross-correlation is flow regime dependent, and needs a priori knowledge on velocity field. Therefore, a priori knowledge of both the flow pattern and the phase concentration is required. An example of using ERT cross-correlation for oil—water two-phase flow velocity estimation is shown in Figure 16.9, where the cross-correlation velocity is in line with the reference velocity with a scatter caused by the flow patterns.

The accuracy of the cross-correlation technique in slurry flow velocity measurement is jointly determined by the data acquisition rate and the separation between two sensors (arrays). A large separation increases the velocity measurement while maintaining the time resolution, but the similarity of the signals captured by the two sensing planes decreases due to the transient and complex character of two-phase flow. Therefore the separation should be carefully selected to match the flow velocity and acquisition rate of the sensor system (Beck, 1981).

16.3.3 Flow process analysis and characterization

Characterization of flow process in mineral transportation is helpful to the understanding and thus modeling of multiphase flow. IPT is an ideal tool for flow process analysis owing to the multiple information simultaneously provided by the sensors implemented at different locations of the target vessel. Similar to flow pattern identification, the methods of flow process analysis and characterization can also be categorized into image-based analysis and time series-based analysis.

The image-based analysis is used to analyze flow behavior through the reconstruction of a cross-sectional (or 3D) image. For example, the phase distribution of a horizontal swirling slurry flow is studied with image-based analysis of a dual-plane ERT (Wang et al., 2003). ERT has practical potential to analyze the swirling flow conditions and also identify the areas of erosion in pipes. Two-dimensional solids volume fraction distributions of slurry with and without the swirl-inducing pipe are shown in

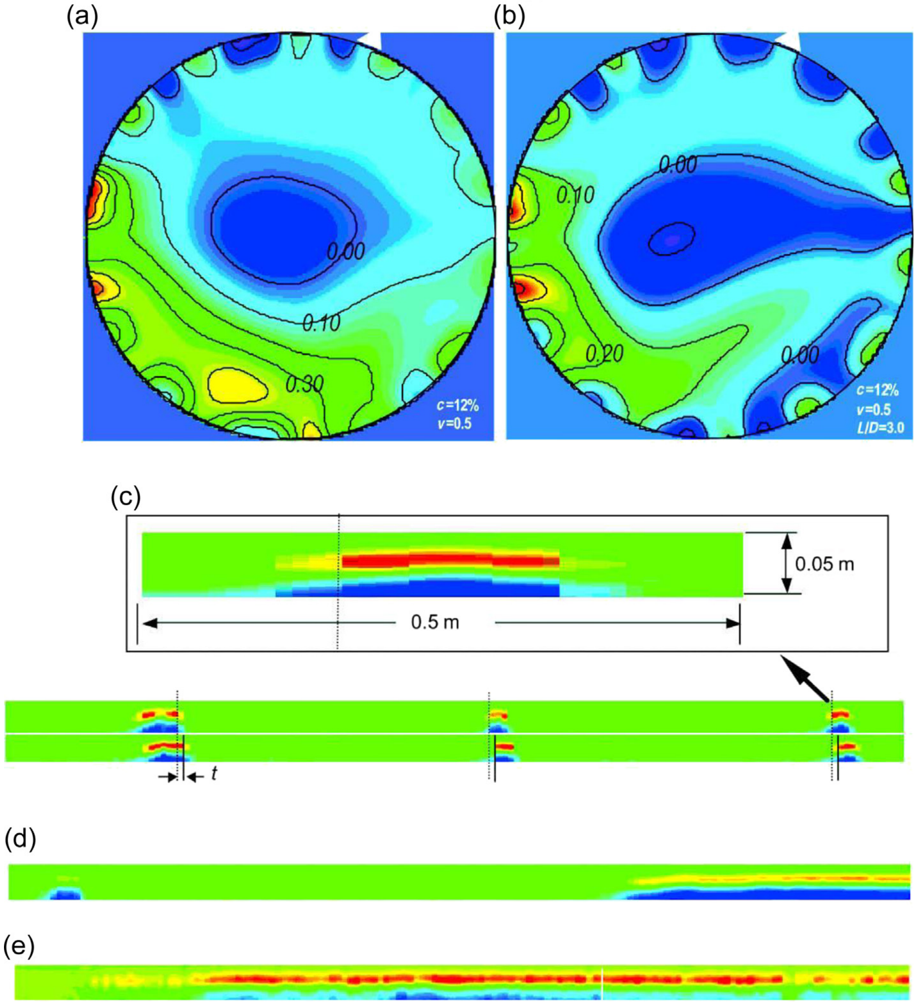

Figure 16.10 Axial solids volume fraction distributions from nonswirling flows with estimated concentrations of 2.1% (a and c) and 8.6% (d), and a swirling flow with a concentration of 8.6% (b and e). The water flow velocities in all cases are 0.5 m/s (Wang et al., 2003).

Figure 16.10(a) and (b). The longitudinal stacked views of nonswirling flow phase distributions are shown in Figure 16.10(c) and (d). These stacked views are formed by projecting the 2D cross-sectional images of 150 frames of time, so that the flow history can be observed in a side view. The two side views in Figure 16.10(c) are reconstructed by the two electrode planes, the time delay of the same solid volumes can be clearly observed, and the velocity of the solid volumes can be calculated with the cross-correlation method discussed in the previous section.

A similar work of examining the swirling slurry flow with a four-plane ERT has been done by Stevenson (Stevenson, Harrison, Miles, & Cilliers, 2006): a 3D tomogram

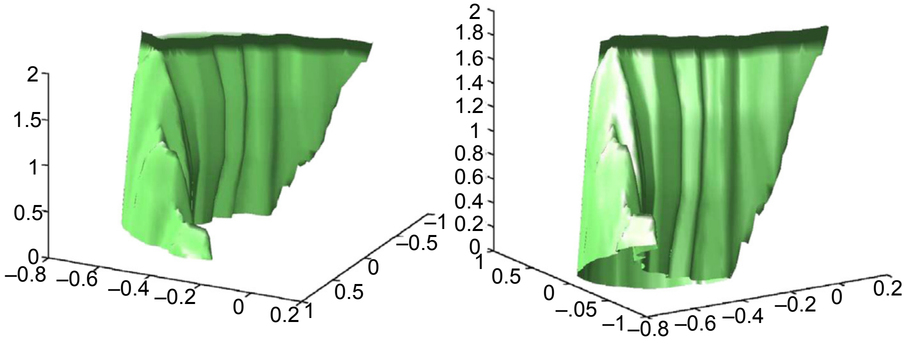

Figure 16.11 3D view of upward vertical swirling flow at a linear velocity of 1.5 m/s and 3% mass solids where the green twisting section represents the bulk fluid—solid interface (Stevenson et al., 2006).

is constructed from the four tomograms by interpolation and by choosing a threshold conductivity that defined the bulk—particle/bulk—fluid interface. The reconstructed 3D tomograms of different orientations are shown in Figure 16.11, where the slurry flows upward vertically. These 3D-like stacked side views are not really 3D reconstructions, but are usually referred to as 2.5D. A real 3D reconstruction is computationally expensive and time-consuming, and thus is by far not a practical option for the transient flow reconstruction. With the development of computing technologies, 3D reconstruction has become more popular in academic researches for the dynamic reconstructions. It is an intrinsic method utilizing the distinct advantages of IPT to provide visualized flow conditions. However, it suffers from the spatial and temporal resolution of image reconstruction as mentioned above, and thereby is suitable for off-line analysis.

The time series-based analysis method treats the measurement data of one cross section as a matrix containing spatial information about phase distribution. With certain matrix dimension reductions or compressions, the data matrix is reduced to a set of feature vectors or a feature value. A multivariate/univariate time series is formed if the time history of the feature vector/value is considered. The formed time series contains rich information regarding the flow process, and can be analyzed with a variety of time series analysis methods — for example, principal component analysis, independent component analysis (ICA), and other statistical methods; wavelet transform and other time — frequency methods; and other methods including nonlinear time series analysis, such as chaos and wavelet package network. An example of analyzing the gas—liquid two-phase flow using ICA is shown in Figure 16.12 (Xu, Cui, et al., 2009), along with the side view of the reconstructed images of plug/bubble flow ($u_{\mathrm{sw}} = 1.09$ m/s, $u_{\mathrm{sg}} = 0.02$ m/s). The measurement data history of an ERT is decomposed into different independent components (ICs) by using ICA; different levels of ICs can represent the fluctuation characteristics of the gas—liquid two-phase flow. Comparison of the ICs with the reconstructed images shown in Figure 16.12 indicates that IC1 corresponds to the light blue interface in (c); IC2 and IC3 reflect the lighter

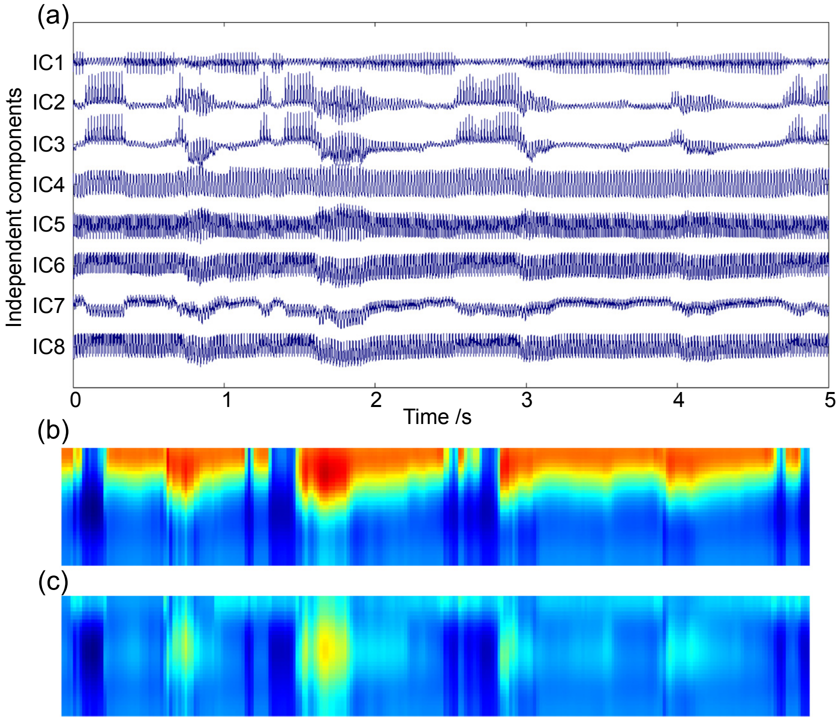

Figure 16.12 Comparison between the estimated ICs and the reconstructed images by ERT for a plug/bubble flow. (a) Estimated ICs. (b) Reconstructed image serials for 5 s from the side view. (c) Reconstructed image serials for 5 s from the top view (Xu, Cui, et al., 2009).

impulsive motion; and IC4—IC8 are the high-frequency noises. By using such analysis, the flow process of different fluctuation scales could be separated for further analysis.

16.4 Industrial process tomography in multiphase-flow measurement with multisensory fusion

16.4.1 Multimodality industrial process tomography

In mineral transportation, the mixture fluid is not always an ideal combination of two phases, but sometimes three phases are mixed together. In this case, one modality tomography might not work properly as expected or tested in the laboratory scale, and a multimodality tomography that combines tomographies based on different sensing principles is more favorable to work in this scenario.

A typical multimodality tomography that easily comes to mind is the combination of ERT and ECT. It is an ideal application that the ECT and ERT are combined into one set of electrodes to achieve more comprehensive observations on phase distributions.

An attempt has been made by considering the capacitance and power character of an ERT electrode array to image two-phase flow (Marashdeh, Warsito, Fan, & Teixeira, 2007). The iterative linear back-projection is adopted, along with a dual-sensitivity map method (two sensitivity maps of capacitance matrix and conductivity matrix, respectively), for the forward and inverse problem solution.

Strictly speaking, the combination of ERT and ECT is an intramodality tomography, because the resistance and capacitance all belong to the dielectric property of the medium. The combination of intermodality tomography to introduce tomographies based on the different properties of the medium, such as electrical impedance tomography and gamma-densitometry tomography measurements, is presented to simultaneously measure the solid, liquid, and gas radial distributions in a vertical three-phase flow (George, Shollenberger, Torczynski, O'Hern, & Ceccio, 2001). Another example is that ECT is fused with gamma-ray tomography on a pixel-to-pixel fusion procedure to separately reconstruct tomograms based on the Landweber reconstruction algorithm for oil—gas—water three-phase-flow imaging (Hjertaker, Maad, & Johansen, 2011). This pixel-to-pixel fusion is carried out by setting up a threshold of 256 gray levels of the separately reconstructed images by ECT and gamma-ray tomography, respectively. Then the material of oil, gas, and water could be determined by the gray value of each pixel, as, for example, the gray level 0 (oil) to 127 (water) to 255 (gas). The results of three-phase distribution are shown in Figure 16.13. An extension of this combination is to introduce ERT into the combined method to form an ERT/ECT/gamma-ray multimodality Nowakowski et al. (2010).

Apart from radiation-based tomography, a dual-mode ultrasound (URT) and ECT for monitoring of gas—solid two-phase material distributions are presented (Deinhammer, Steiner, Sommer, & Watzenig, 2008): data fusion are performed through a sequential coupling of URT and ECT, where the reconstructed ultrasound image is used as prior knowledge for the subsequent ECT inversion algorithm (Steiner, 2006).

16.4.2 Industrial process tomography combined with other sensors

Similar to the problem that multimodality tomography faces, multiple sensors are required to solve the multiple parameter measurement problem. When combined with other sensors, e.g., flow meters, IPT will provide rich information regarding the flow conditions to facilitate the process diagnosis and modeling. One example is the combination of ERT with electromagnetic flow meters (EFM) to obtain the actual solid flow rate in a vertical slurry flow (Xu, Wu, et al., 2009); another similar combination was also presented in Deng, Li, Wei, Yan, & Yang (2011). ERT is in charge of providing phase distribution information and flow pattern change, while EFM is for flow velocity estimation.

The combination of ERT with a Venturi meter was presented for individual flow rate estimation of two-phase flow, where ERT provides flow pattern and void fraction estimation, and Venturi provides the overall flow rate of two-phase flow (Meng et al., 2010). Another application is the combination of ERT with a cone meter for flow

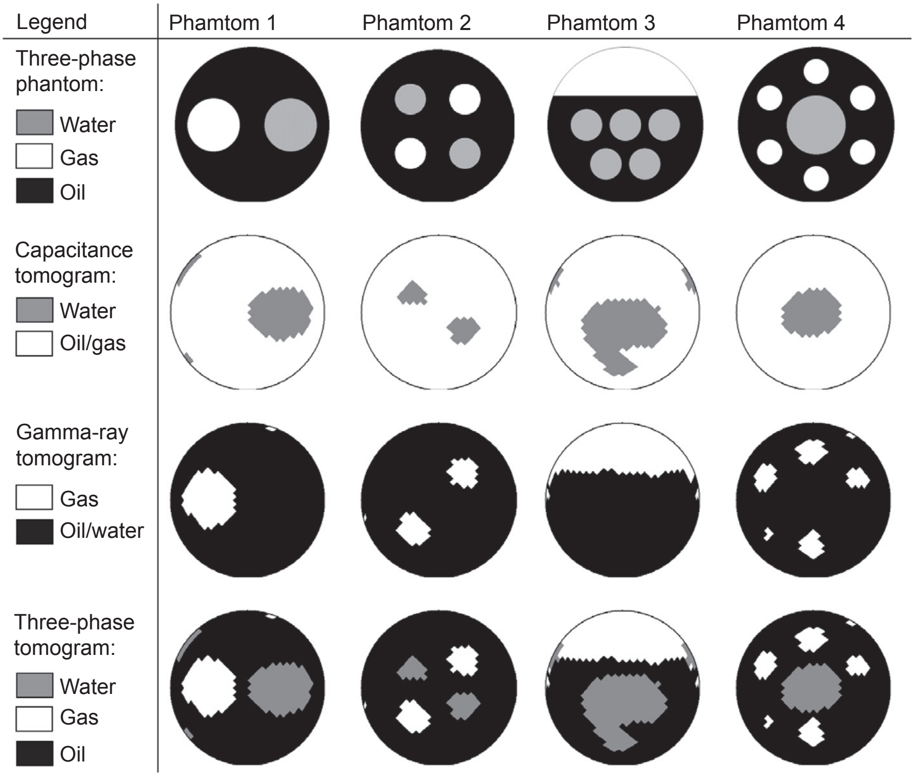
Legend
Phamtom 1
Phamtom 2
Phamtom 3
Phamtom 4
Three-phase phantom:
Water
Gas
Oil
Capacitance tomogram:
Water
Oil/gas
Gamma-ray tomogram:
Gas
Oil/water
Three-phase tomogram:
Water
Gas
Oil

Figure 16.13 Three-phase dual-mode phantoms and acquired tomograms using a gamma-ray tomograph integration time of 1 s and 37 averaged capacitance tomograph sensor measurement frames (Hjertaker et al., 2011).

regime identification, where the phase fraction information provided by ERT is combined with flow velocity information provided by the cone meter at feature level to present a simple and effective way of flow pattern identification (Tan & Dong, 2009).

Theoretically, IPT is capable of being combined with any flow meters, if they provide complementary information to each other. Therefore, such combinations are almost countless, but the main issue is how to design an appropriate fusion architecture and, correspondingly, a proper fusion scheme/algorithm in order to process the heterogeneous information provided by IPT and flow meters. Typical methods for data fusion include statistics-based methods such as Monte Carlo method and Bayesian methods, state estimation methods such as Kalman filter, machine learning methods such as artificial neural network and support vector machine, and other methods such as fuzzy set method. Regression methods can also be used for the purpose of parameter measurement, such as partial least squares regression to achieve a jointly optimized estimation on the target parameter. In sum, the combination of tomography with other sensors will provide sufficient space for investigation and improvement of data fusion and, thus, comprehensive measurement of multiphase flow.

16.5 Conclusions

This chapter reviews the applications of IPT on mineral transportation, specifically focusing on slurry flow and oil—gas—water multiphase flow. The flow pattern identification methods and flow process parameter measurements with IPT from different disciplines are covered. The issue of flow process monitoring and analysis with IPT is discussed. Finally, multimodality IPT for multiphase-flow measurement and analysis is introduced, and the sensor fusion of IPT with other flow meters is also investigated, with examples reported.

IPT is capable of providing not only visual observations on the internal phase distribution of multiphase flow, but also rich information regarding flow process and parameter modeling through the multiple sensors installed on the target vessel. The future trend of applying IPT in mineral transportation will be how to fuse information from multimodality IPT and also to fuse such information with information provided by other flow meters.

Acknowledgements

The authors would like to gratefully acknowledge the support provided by the National Natural Science Foundation of China (61227006; 61104207; 51176141) and National Key Scientific Instrument and Equipment Development Projects of China (2011YQ120048). Chao Tan is also supported by the Elite Scholar Program of Tianjin University.

References

Acikgoz, M., Franca, F., & Lahey, R. T. (1992). An experimental study of three-phase flow regimes. *International Journal of Multiphase Flow, 18*(3), 327—336.

Barigou, M. (2004). Particle tracking in opaque mixing systems: an overview of the capabilities of PET and PEPT. *Chemical Engineering Research & Design, 82*(A9), 1258—1267.

Beck, M. S. (1981). Correlation in instruments: cross correlation flowmeters. *Journal of Physics E: Scientific Instruments, 14*(1), 7—19.

Beck, M. S., & Plaskowski, A. (1987). *Cross-correlation flowmeters: their design and application*. Bristol, England: IOP Publishing Ltd.

Dai, Y., Wang, M., Panayotopoulos, N., Lucas, G., & Williams, R. A. (2005). In: *3-D visualisation of a swirling flow using electrical resistance tomography, 4th World Congress on industrial process tomography* (pp. 362—367).

Deinhammer, C., Steiner, G., Sommer, M., & Watzenig, D. (2008). Electromechanical flow imaging using ultrasound and electrical capacitance data. In: *Proceeding of sensors, 2008 IEEE* (pp. 160—163).

Deng, X., Li, G., Wei, Z., Yan, Z., & Yang, W. (2011). Theoretical study of vertical slug flow measurement by data fusion from electromagnetic flowmeter and electrical resistance tomography. *Flow Measurement and Instrumentation, 22*(4), 272—278.

Dong, F., Qiao, X. T., Jiang, Z. X., & Xu, L. A. (2003). Application of electrical resistance tomography to two-phase flow and void fraction measurement. In: *Proceeding of 3rd World Congress on industrial process tomography, Banff, Canada* (pp. 299–304).

Fischer, F., Hoppe, D., Schleicher, E., Mattausch, G., Flaske, H., Bartel, R., et al. (2008). An ultra fast electron beam X-ray tomography scanner. *Measurement Science and Technology, 19*(9), 94002.

Frøystein, T., Kvandal, H., & Aakre, H. (2005). Dual energy gamma tomography system for high pressure multiphase flow. *Flow Measurement and Instrumentation, 16*(2–3), 99–112.

George, D. L., Shollenberger, K. A., Torczynski, J. R., O'Hern, T. J., & Ceccio, S. L. (2001). Three-phase material distribution measurements in a vertical flow using gamma-densitometry tomography and electrical-impedance tomography. *International Journal of Multiphase Flow, 27*(11), 1903–1930.

Giguere, R., Fradette, L., Mignon, D., & Tanguy, P. A. (2008). Characterization of slurry flow regime transitions by ERT. *Chemical Engineering Research & Design, 86*(9A), 989–996.

Giguere, R., Fradette, L., Mignon, D., & Tanguy, P. A. (2009). Analysis of slurry flow regimes downstream of a pipe bend. *Chemical Engineering Research & Design, 87*(7A), 943–950.

Heindel, T. J., Gray, J. N., & Jensen, T. C. (2008). An X-ray system for visualizing fluid flows. *Flow Measurement and Instrumentation, 19*(2), 67–78.

Hjertaker, B. T., Maad, R., & Johansen, G. A. (2011). Dual-mode capacitance and gamma-ray tomography using the Landweber reconstruction algorithm. *Measurement Science and Technology, 22*(10), 104002.

Huang, Z., Wang, B., & Li, H. (2003). Application of electrical capacitance tomography to the void fraction measurement of two-phase flow. *IEEE Transactions on Instrumentation and Measurement, 52*(1), 7–12.

Hu, B., Stewart, C., Hale, C., Lawrence, C., Hall, A. W., Zwiens, H., et al. (2005). Development of an X-ray computed tomography (CT) system with sparse sources: application to three-phase pipe flow visualization. *Experiments in Fluids, 39*(4), 667–678. http://dx.doi.org/10.1007/s00348-005-1008-2.

Ismail, I., Gamio, J. C., Bukhari, S. F., & Yang, W. Q. (2005). Tomography for multi-phase flow measurement in the oil industry. *Flow Measurement and Instrumentation, 16*(2–3), 145–155.

Karim, K., Varma, R., Vesvikar, M., & Al-Dahhan, M. H. (2004). Flow pattern visualization of a simulated digester. *Water Research, 38*(17), 3659–3670.

Lucas, G. P., Cory, J., Waterfall, R. C., Loh, W. W., & Dickin, F. J. (1999). Measurement of the solids volume fraction and velocity distributions in solids–liquid flows using dual-plane electrical resistance tomography. *Flow Measurement and Instrumentation, 10*(4), 249–258.

Marashdeh, Q., Holland, D. J., Wang, F., Chandrasekera, T. C., Pore, M., Dennis, J. S., et al. (2010). Cross-validation of ECVT and MRI measurements with applications to gas–solid fluidized bed. In: *Proceeding of 6th World Congress on industrial process tomography, Beijing, China* (pp. 285–291).

Marashdeh, Q., Warsito, W., Fan, L., & Teixeira, F. L. (2007). A multimodal tomography system based on ECT sensors. *IEEE Sensors Journal, 7*(3), 426–433.

Meng, Z., Huang, Z., Wang, B., Ji, H., Li, H., & Yan, Y. (2010). Air–water two-phase flow measurement using a Venturi meter and an electrical resistance tomography sensor. *Flow Measurement and Instrumentation, 21*(3), 268–276.

Nowakowski, J., Hammer, E., Sankowski, D., Styra, D., Wajman, R., Banasiak, R., et al. (2010). Application of ECT/ERT/gamma ray image reconstruction algorithm for multiphase flow measurements. In: *Proceeding of 6th World Congress on industrial process tomography, Beijing, China* (pp. 231−255).

Razzak, S. A., Barghi, S., & Zhu, J. X. (2009). Application of electrical resistance tomography on liquid−solid two-phase flow characterization in an LSCFB riser. *Chemical Engineering Science, 64*(12), 2851−2858.

Steiner, G. (2006). Sequential fusion of ultrasound and electrical capacitance tomography. *International Journal of Information and Systems Sciences, 2*(4), 484−497.

Stevenson, R., Harrison, S., Miles, N., & Cilliers, J. J. (2006). Examination of swirling flow using electrical resistance tomography. *Powder Technology, 162*(2), 157−165.

Suzuki, M., Tsuchitani, T., Iimura, K., & Hirota, M. (2004). Measurement of Voidage distribution in particle packed bed using X-ray micro computed tomography. In: *Proceeding of 4th World Congress on industrial process tomography, Aizu, Japan* (pp. 930−935).

Sætre, C., Johansen, G. A., & Tjugum, S. A. (2012). Tomographic multiphase flow measurement. *Applied Radiation and Isotopes, 70*(7), 1080−1084.

Taitel, Y., Barnea, D., & Brill, J. P. (1995). Stratified three phase flow in pipes. *International Journal of Multiphase Flow, 21*(1), 53−60.

Tan, C., & Dong, F. (2009). Gas−water two-phase flow regime identification with feature fusion from an ERT system and a V-cone meter. In: *Proceeding of imaging systems and techniques, 2009. IST '09. IEEE International Workshop on* (pp. 307−312).

Tan, C., & Dong, F. (2010). Cross correlation velocity of oil−water two-phase flow by a dual-plane electrical resistance tomography system. In: *Proceeding of international instrumentation and measurement technology conference, Austin, TX, USA* (pp. 766−770).

Tan, C., Dong, F., & Wu, M. M. (2007). Identification of gas/liquid two-phase flow regime through ERT-based measurement and feature extraction. *Flow Measurement and Instrumentation, 18*(5−6), 255−261.

Wang, M., Dorward, A., Vlaev, D., & Mann, R. (2000). Measurements of gas−liquid mixing in a stirred vessel using electrical resistance tomography (ERT). *Chemical Engineering Journal, 77*, 93−98.

Wang, M., Jones, T. F., & Williams, R. A. (2003). Visualization of asymmetric solids distribution in horizontal swirling flows using electrical resistance tomography. *Chemical Engineering Research & Design, 81*(A8), 854−861.

Wang, M., Lucas, G., Dai, Y., Panayotopoulos, N., & Williams, R. A. (2006). Visualisation of bubbly velocity distribution in a swirling flow using electrical resistance tomography. *Particle & Particle Systems Characterization, 23*(3−4), 321−329. http://dx.doi.org/10.1002/ppsc.200601063.

Wang, H. X., & Zhang, L. F. (2009). Identification of two-phase flow regimes based on support vector machine and electrical capacitance tomography. *Measurement Science and Technology, 20*(11), 114007.

Xu, Y. B., Cui, Z. Q., Wang, H. X., Dong, F., Chen, X. Y., & Yang, W. Q. (2009). Independent component analysis of interface fluctuation of gas/liquid two-phase flows—experimental study. *Flow Measurement And Instrumentation, 20*(6), 220−229.

Xu, J., Wu, Y., Zheng, Z., Wang, M., Munir, B., Oluwadarey, H. I., et al. (2009). Measurement of solid slurry flow via correlation of electromagnetic flow meter, electrical resistance tomography and mechanistic modelling. *Journal of Hydrodynamics, 21*(4), 557−563.

Yang, G. Q., Du, B., & Fan, L. S. (2007). Bubble formation and dynamics in gas−liquid−solid fluidization—a review. *Chemical Engineering Science, 62*(1−2), 2−27.

X-ray tomography of fluidized beds

17

A. Kantzas
University of Calgary, Calgary, AB, Canada

17.1 Introduction

Nondestructive, nonintrusive flow visualization techniques have been extensively used in understanding fluid flow phenomena in porous media since the early 1980s (Kantzas, 1990, 1994). The term *process tomography* has been used to describe all the techniques used for monitoring and visualizing physical and chemical processes at the laboratory, pilot plant, or plant scale (Williams and Beck, 1995). The techniques used are grouped into two major classes: electrical and electromagnetic. The utilization of X-ray tomography (CT) for monitoring the fluid and solid distribution in laboratory gas–solid fluidized beds was studied extensively by the Kantzas group as illustrated in this chapter. This technique was used as the basis for determining bubble diameter, volumetric flow rate, and linear velocity of descending solids. The objective of their work is to determine the limits of X-ray tomography for such predictions and define the boundaries of overlapping of the different electromagnetic techniques used in our laboratory flow visualization and imaging of flow phenomena in fluidized beds. Several other approaches, including radioactive particle tracking (RPT) and particle image velocimetry (Chen & Fan, 1992; Yates & Simons, 1994) were also used for similar purposes.

CT provides a 2-D image of X-ray absorption by an object by manipulating a series of one-dimensional projections of the X-ray absorption measured through different angles. This is done through a series of data that is acquired and manipulated using sophisticated reconstruction algorithms. When dealing with chemical reactors, the reconstructed images are further interpreted to provide information that is useful to chemical engineers. The property that describes the X-ray absorption is called the linear attenuation coefficient, and it is a function of density and atomic number (Kantzas, 1990). In the experiments described in this chapter, the atomic number of the system is constant and the density is the main variable. In the cases where polymer beds are evaluated, the measured density is actually the bulk density of the voxel, which is the volume average of the polymer particle density and the surrounding gas density. If the density of the polymer is known, then the voidage can be calculated with good accuracy at a predefined resolution.

The voidage measured by the X-ray CT scanner is different from what is usually defined as voidage in the literature. In the common definition of voidage, only interspace was considered. With the CT scanner, the sum of the interspace and the intraspace voidage of particles can be mapped. This is especially important when the

Industrial Tomography. http://dx.doi.org/10.1016/B978-1-78242-118-4.00017-4
Copyright © 2015 Elsevier Ltd. All rights reserved.

solid particles are porous as in the case of polyethylene resins. In the cases of nonporous particles, the intraspace voidage is zero. Therefore, for a dense phase, the voidage measured by the X-ray CT scanner would be higher than the voidage measured with conventional liquid displacement techniques.

Fluidization is the process by which solid particles are brought into a fluid-like state through suspension in a gas or liquid. Fluidized beds were first used in the coal gasification industry in 1926 (Kunii & Levenspiel, 1991). Fluidized beds are very important to the chemical industry because fluidization provides an excellent mixing ability, high heat and mass transfer rates, and typically low pressure drop. Most gas–solid fluidized bed reactors operate at high temperatures, and some, such as those used in the production of polyolefins, also operate at elevated pressures. Due to the multiphase nature of fluidized beds, multiregion models (Behie & Kehoe, 1973) were required to properly account for the hydrodynamics of flow. Since the early 1990s, significant strides have been made on the modeling front. Current models range from the classical approaches (Behie & Kehoe, 1973; Davidson & Harrison, 1963; Kunii & Levenspiel, 1991) to multiphase Eulerian models that are based on the assumption of interpenetrating continuum (Gidaspow, 1994), to discrete particle simulations (Hoomans, Kuipers, & van Swaaij, 1998; Kaneko, Shiojima, & Horio, 1999; Tsuji, Kawaguchi, & Tanaka, 1993). Because of computational limitations (Ranade, 2002), the Eulerian models are preferred over discrete particle simulations even though the latter treat particle dynamics more rigorously, which results in better predictions. Computational fluid dynamics (CFD) simulation becomes more and more popular in chemical reactor design, scale-up, and modeling, however, reliable experimental data are rare to validate the CFD simulation. It is necessary to carry out experimental measurements of flow behavior in fluidized beds at elevated temperature and pressure. In this chapter, most of the examples presented are based on fluidization of sand or polyethylene.

Many researchers have indicated that the performance of a fluidized bed reactor is strongly influenced by the specific characteristics and behavior of the bubbles. These bubbles are nothing but regions of lower solid density. The main characteristics of a bubble that affect a fluidized bed are size, rising velocity, and frequency (Cheremisinoff & Cheremisinoff, 1984). Another parameter used by researchers to infer the state of a fluidized bed and which is the only means of obtaining detailed data on an industrial scale are pressure fluctuation measurements (Johnsson, Zijerveld, Schouten, van den Bleek, & Leckner, 2000; Peirano, Delloume, Johnsson, Lechner, & Simonin, 2002; Schober, Hulme, Chandrasekaran, & Kantzas, 2003). Pressure fluctuations are believed to be caused by the passage of bubbles in the column and are therefore also measures of the dynamics of a fluidized bed. Results from the study indicate sensitive variations in the pressure fluctuations with the coefficient of restitution. In the last 20 years, researchers started using pressure fluctuations as another important parameter to evaluate model predictions (Lyczkowski et al., 1993; Peirano et al., 2002). In this chapter, pressure fluctuation analysis is often referred to as a means to either complement or verify modeling data. Also because of the noninvasive nature of the pressure transducers, the pressure fluctuation analysis can be a complementary tool for tomographic measurements.

Fluidization characteristics detection and fluidization state monitoring are very important for the operation and control of fluidized bed reactors. Statistics of triboelectric current were used to detect the local fluidization characteristics (Briens et al., 1999). Coefficient of variation and fractal dimension of conductivity measurements were used to characterize channeling in a liquid fluidized bed (Briens, Briens, Margaritis, Cooke, & Bergougnou, 1997). Hurst's analysis of signals from various measurement probes was used to detect minimum fluidization and gas maldistribution in fluidized beds (Briens, Briens, Hay, Hudson, & Margaritis, 1997). However, among the sensors used in previous investigations, only pressure fluctuation measurements are commonly used in industrial fluidized beds systems. More recently, pressure fluctuations were proposed to monitor and control the state of fluidized bed (Croxford & Gilbertson, 2006; Gheorghiu, Van Ommen, & Coppens, 2003; Schouten & Van Den Bleek, 1998; Van Ommen, Coppens, & Van Den Bleek, 2000). Due to the global characteristic of pressure fluctuation measurement, local flow behavior needs to be measured and compared to pressure measurements, though some local flow behavior can be extracted using statistical or other mathematical methods (Gheorghiu et al., 2003). X-ray CT measurements are known to provide detailed flow patterns of fluidized beds and can be used to monitor fluidization characteristics (Kantzas & Kalogerakis, 1996). It is necessary to investigate fluidized beds using both pressure fluctuation and X-ray CT measurement. If a correlation between pressure fluctuation and tomographic data can be found, then pressure fluctuation measurements can be another scale-up tool that will help decipher large column hydrodynamics, where tomography with any reasonable resolution will be unattainable.

17.2 Imaging of fluid beds

Bubble imaging with X-rays goes back to the pioneering work of Rowe, MacGillivray, and Cheesman (1979). However, the recent use of digital fluoroscopy (DF) offers a very powerful option that can accumulate and process massive amounts of data that can be used in fluid bed characterization. X-ray fluoroscopy in conjunction with an image acquisition system provides a means of viewing moving objects. Figure 17.1 shows a single black-and-white frame from a series of images captured using the X-ray camera. Some recent studies are included as examples only and are by no means exhaustive.

Although X-ray CT is well developed for medical application, the application to fluidized bed only started in the 1990s (Kantzas, 1994). It was first applied to determine the time-average gas holdup in a gas–solid bed (Kantzas, Wright, & Kalogerakis, 1997; Wright et al., 2001). Most of the fluidization experiments in this group's work were conducted using lab-scale Plexiglas columns. Figure 17.2 shows the experimental setup used to collect column wall pressure measurements. Either tomography or direct imaging was complemented by pressure fluctuation analysis. Pressure transducers were used to sample the pressure oscillations at a frequency of 500 Hz. In later studies, columns made out of aluminum were utilized to run tests at elevated pressures.

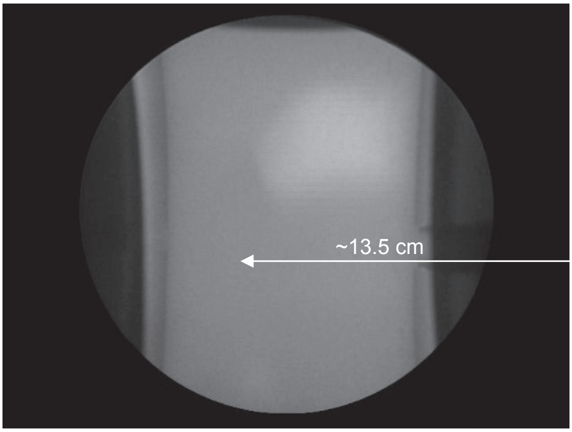

Figure 17.1 A rising bubble acquired with X-ray imaging.
Chandrasekaran (2005).

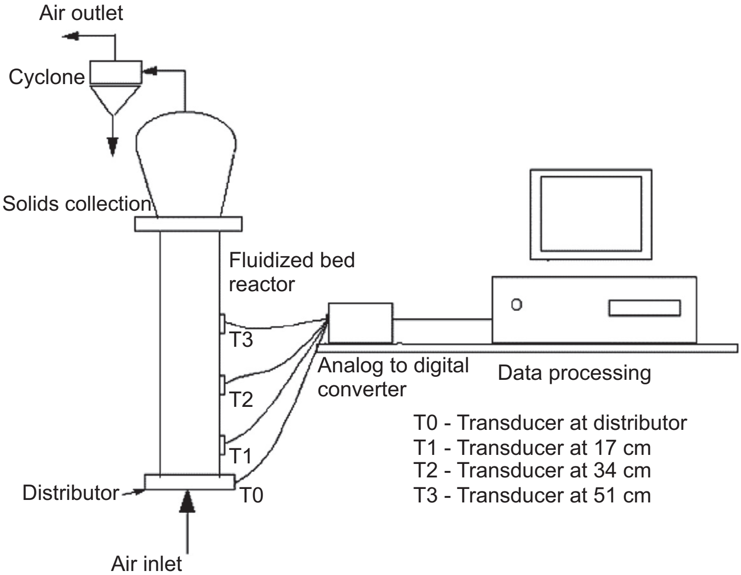
Air outlet
Cyclone
Solids collection
Fluidized bed reactor
T3
T2
T1
T0
Distributor
Air inlet
Analog to digital converter
Data processing
T0 - Transducer at distributor
T1 - Transducer at 17 cm
T2 - Transducer at 34 cm
T3 - Transducer at 51 cm

Figure 17.2 Laboratory fluid bed system with pressure fluctuation sensors, as used in X-ray imaging and X-ray CT experimental work at the University of Calgary.
Hulme (2003).

More recently, an X-ray imaging system was developed by Heindel, Gray, and Jensen (2008) to achieve 3-D visualization for fluidized beds, which can also provide time-averaged CT imaging for the fluidized beds (Drake & Heindel, 2012a,b). All the early applications faced a practical limit of X-ray CT: the scanning time of traditional

X-ray CT is too long to record the dynamics of the flow of a fluidized bed (Heindel, 2011). Time-averaged data are rather limited when analyzing the dynamic phenomena of fluidized beds.

For a fluidized bed reactor, the intensity of the X-ray beam after attenuation is calculated based on the Beer—Lambert law, which implies that the bubbles in a fluidized bed appear as bright regions due to less attenuation of the beam compared to the beam that passes through the emulsion. Denser materials, such as glass beads, attenuate X-rays more when compared to polyethylene particles. In other words, glass beads yield a high contrast image compared to that of a bed of polyethylene particles due to the higher density of the former.

17.3 Computational models and their experimental validation

However, measurement alone is not enough. Since the experiments cannot be scaled up to reactor sizes, an intermediate approach must be followed. This is done by CFD modeling. The models can be used to match the images obtained from the experiments, and then the models can be scaled up to reactor conditions.

Most of the computational models currently available are extended versions of the Navier—Stokes equations for multiphase flow. The various governing equations and constitutive relations used in closing these equations have been a subject of debate for many years. The closure laws range from empirical formulations to the kinetic theory of granular flow (Syamlal, Rogers, & O'Brien, 1993). Because of these reasons many researchers highlight the importance of the validation of these models before application for a specific purpose (Boemer, Qi, & Renz, 1998; Kantzas, Wright, Bhargava, Li, & Hamilton, 2001; Kuipers, Duin van, Beckum van, & Swaaij van, 1993; McKeen & Pugsley, 2003; Van Wachem et al., 1999).

The validation of these models poses significant problems, as it is imperative that the experimental data available have to be obtained in a nonintrusive fashion. Most experimental methods for tracking bubbles are either intrusive in nature or do not represent a complete picture of the full dynamics of the column.

17.4 Experimental studies

17.4.1 *Fluid bed characterization using computer tomography*

In order to study fluidization behavior, scanners capable of scanning large vertical objects have to be designed. Until recently, this presented a challenge. Instead, many of the presented studies were run using third- or fourth-generation medical X-ray CT scanners that have been modified to perform scans on vertically placed objects. The spatial resolution was as low as 0.2 mm × 0.2 mm in cross-section and the temporal resolution as low as 2 s. Data were acquired by scanning the bed using a slice thickness of up to 1 cm at various heights usually spaced 1 cm along the column and at various superficial velocities.

Zarabi and Kantzas (1998, 2000) tomographically quantified solid and gas distributions as a function of position with high resolution in a series of laboratory fluid beds containing air and polyethylene particles. The resolution used was 0.4 mm × 0.4 mm × 3 mm. The laboratory models were Plexiglas columns of 10 cm in diameter and the settling bed L/D ratios varied between one and three. Large particles (up to 1.5 mm in diameter) of high density polyethylene and linear low density polyethylene were used. The superficial gas velocities varied from the minimum fluidization velocity to 50 cm/s. The analysis of fluid bed CAT scanner images was extended to show bubble, emulsion, and dense phase distribution. The analysis was also used to determine bubble diameters and to predict the flow direction of solid particles as well as the velocity of descending solids. The voidage frequency distributions of a bed at different gas flow rates were compared to each other, and the voidage threshold values corresponding to gas, emulsion, and dense phases were determined. These threshold values were used to prepare ternary images that clearly showed the parts of the bed cross-section corresponding to bubble, emulsion, and dense phases.

Hydrodynamic properties of a three-phase laboratory fluidized bed were characterized using X-ray CT, RPT, and pressure fluctuation analysis (Song et al. (1999)). Solid–liquid mass transfer measurements were done using benzoic acid as a tracer. Columns 12.7 cm in diameter and 160–200 cm in length were used. The fluids used were water and air, and the solids were spherical polycarbonate particles 0.65 cm in diameter.

The combination of the above techniques provided a unique opportunity to integrate several tools into a single apparatus. Thus, a comprehensive characterization of the transport phenomena in this three-phase fluid bed system was obtained. The application of X-ray CAT scanning was extended in the qualitative and quantitative analysis of fluidized beds. The lower and higher threshold values were introduced for deconvolution of voidage frequency distribution by Gaussian curves. From deconvolution, the area fractions of three distinct phases were calculated (i.e., dense, emulsion, and gas phases). The lower and higher threshold values were defined as the voidage value for minimum fluidization and minimum bubbling, respectively.

These threshold values were used for constructing ternary images showing the phase distributions across the cross-section. Also, from the images, the bubble diameters and number of bubbles could be determined. These images are a powerful tool for visualizing the flow pattern and explaining the behavior of fluidized bed. Moreover, it was found that the particle morphology and its size distribution are important parameters in hydrodynamics of the fluid bed. The analysis was extended to determine the average solid flow rate and solid linear velocity at any height. The results pertaining to the bubble diameters were quite satisfactory when compared with some correlations. For calculating the solid velocity, the two-phase model and some correlations from the literature were used.

Grassler and Wirth (2000) performed a tomographic measurement to determine the solid concentration in a fluidized bed filled with glass beads of 70 mm. The measuring system consisted of a 60 keV X-ray source and a linear X-ray detector with 1024 sensitive elements and signal resolution of 8 bit. The integration time was 15 s for each projection and 30 min for a radial concentration pattern. The system had a capacity to measure the solid concentration up to 20% vol and a minimum spatial resolution of 0.2 mm. The superficial gas velocity was in the range of 2−7 m/s.

The tomography results of the upflow fluidized bed showed a decrease in solid concentration at higher elevation of the bed. The solid concentration was maximum 45% vol near the wall of the tube at any gas superficial flow and elevation of the bed. The solid concentration profile at different elevation changed in the downflow bed. Higher concentration of solids in the tube center was observed in the downflow bed. More homogeneous distribution of solid was observed at the lower elevations from the solid−gas distributor.

Bhargava, Kabir, Vaisman, Langford, and Kantzas (2004) used X-ray tomography to study hydrodynamics of an annular dual function photocatalytic reactor operating in absorption (fixed bed) and regeneration (fluid bed) modes. This was a unique application in solid−liquid fluidized bed columns. Degradation experiments of model pollutant (phenol) were conducted with a pilot scale reactor to evaluate its effectiveness. Adsorption of pollutant to the catalyst and pollutant degradation with respect to various catalyst loadings was investigated.

Wu B. et al. (2007) used pressure fluctuations, X-ray DF, and X-ray computed tomography (CT) to characterize the flow behavior of gas−solid fluidized bed using polyethylene particles in three Plexiglas columns with diameters of 10, 20, and 30 cm. The particles were linear-low-density polyethylene resins with same mean particle size (750 μm) and particle size distribution (140−1500 μm). The static bed height was 40 cm. Experiments were carried out using air as the gas phase under ambient conditions and at different superficial gas velocities. Pressure fluctuation measurements were obtained from four pressure transducers (Schlumberger Solartron, model 8000 DPD). Dynamic flow behavior of the gas−solids was analyzed using both chaos and wavelet analysis. Characteristics of the flow behavior caused by bubble and particle movement at different scales were extracted from wavelet decomposition of the pressure fluctuation time series. Statistical and chaos analysis methods were further used to distinguish the dynamics behavior at different scales. CT technique was also used to visualize the bubbling behavior of the polyethylene powder. CT images at different bed heights were obtained over a broad range of gas velocities. Based on the processed images, the time-average voidage distribution, bubble phase area fraction, bubble diameter, and bubble number distribution varying with the bed heights and the superficial velocities were extracted for all three scales of operation. In addition to pressure fluctuation and CT measurements, an X-ray DF system was also used. The bubble diameter, bubble velocity, bubble number distribution, and bubble diameter distribution varying with the bed heights and the superficial velocities were obtained and analyzed in conjunction to that obtained from other techniques to evaluate the effect of particle size distribution and scale of operation on the fluidization behavior of polyethylene powder. The results extracted from their analysis can be used to validate models and can facilitate implementation of changes for further improvement of hydrodynamic modeling and simulation of gas—solid fluidized bed system. The results also contribute to the theoretical basis of the design, scale-up, operation optimization, and assessment of new processes.

Particles with different shapes will affect the bed packing properties, the granular flow, and the hydrodynamics of fluidized beds. Zhang, Wu, Li, Bellehumeur, and Kantzas (2007) used a CT scanner to investigate the effect of particle shape on the behavior of gas—solid fluidized beds in a 20-cm-diameter column. Particles with different shapes were used as solid phase, and air was used as the gas phase. An algorithm verified by bed height measurements was developed to remove the artifacts that existed in the CT images. The processed CT images were then used to analyze the time-averaged voidage, voidage distribution, and bubble behavior under different superficial gas velocities and bed heights with different particles.

17.4.2 Fluid bed characterization by X-ray fluoroscopy and pressure measurements

The X-ray fluoroscopy unit used in these studies was a GE RFXII (which consists of the X-ray tube and the image intensifier) with a GE MPX100 generator. The voltage and current for the experiments conducted in the study were 100 kV and 6 mA, respectively. The apparatus was complemented by software that could analyze the X-ray fluoroscopy images. The program identifies the bubble boundaries and an excel macro tracked the bubbles from frame to frame. The original image is processed using different techniques to enhance contrast, change to grayscale, remove noise, and get a binary image to obtain area, centroid, equivalent diameter, and boundaries.

Chandrasekaran, Van der Lee, Hulme, and Kantzas (2005) used power spectral analysis of pressure fluctuations in conjunction with bubble properties obtained from an advanced experimental technique to validate the CFD simulations of an air/polyethylene-fluidized bed. The current Eulerian models based on the kinetic theory of granular flow have been studied extensively for systems that have ideal characteristics for the solid phase. However, the models need to be investigated for particles such as polyethylene that do not have ideal characteristics with respect to shape, size distribution, and elastic character from a simulation standpoint. Unlike previous works, which mostly use average bubble properties for validation, this work utilizes both pressure fluctuations and bubble properties of a high temporal and spatial resolution for the validation process. Results have indicated that significant work is required to adapt the solid phase model CFD code for particles such as polyethylene.

Wu, Briens, and Zhu (2006) worked with nonintrusive techniques to characterize the hydrodynamics in gas—solids bubbling fluidized bed using polyethylene powder and glass beads with comparable mean diameter. Pressure fluctuations and X-ray fluoroscopy measurements were performed on a pseudo 2-D fluidized bed. Statistical, wavelet, and chaos analyses were applied to the nonstationary pressure signal series to extract and characterize the intrinsic features of the gas—solids fluidized bed. Dominant cycle time was calculated from approximate coefficient of scale 6 decomposed from cleaned pressure fluctuation. The global bubbling behavior of the glass bead system was greatly affected by changes in the superficial gas velocity while polyethylene powder only significantly varied with the distance from the distributor. Average cycle time, dominant cycle time, Kolmogorov entropy, and wavelet energy were also calculated from detail coefficients of scale 1—6 decomposed from cleaned pressure fluctuation to investigate flow dynamics at micro- and mesoscales. Similarities and differences of bubbling behavior at different scales for glass beads and polyethylene powder systems from pressure fluctuations were verified from X-ray fluoroscopy measurements. Results showed that polyethylene particle systems have quite different bubble properties compared with glass beads particle systems under comparable operating conditions. The combination of statistical, chaos, and wavelet analyses proved to be an effective method to characterize multiscale flow behavior in the gas—solids fluidized bed.

Orta et al. (2011) studied hydrodynamics of a polyethylene-fluidized bed at different operating pressures (191—2908 kPa) and constant temperature of 30 °C. In order to extract measurements in systems that can operate in temperatures up to 100 °C and pressures up to 3.1 MPag, under X-ray transparent conditions, an aluminum-body column was designed and built. Polyethylene particles (Geldart B) were used as the bed material. Minimum fluidization velocity (U_{mf}) decreased with increasing of operating pressures. Power spectral density of pressure fluctuation series indicated similar frequency distribution of the bubbling behavior at different superficial velocities. Bubble diameter and bubble velocities were estimated from X-ray fluoroscopy images. Bubble diameter and bubble velocity increase with increasing bed height and superficial gas velocity (Hulme and Kantzas, 2004). At ambient conditions, bubble diameter and bubble velocity increase while increasing bed height and superficial gas velocity due to coalescence and more gas flowing upward under the multiple bubbling regimes in study. The effect of pressure over the U_{mf} indicates that while increasing the pressure, the minimum fluidization velocity decreases for polyethylene particles (530 μm and 918 kg/m^3).

17.5 Data evaluation

Once the images from the experiments and simulations are obtained, separate image processing algorithms can be used to identify the bubbles and calculate the bubble properties such as bubble diameters and velocities. The important step in this process is bubble identification and tracking. The first step was to select a threshold to define bubble boundaries. For most of the work referenced in this chapter, the bubbles were defined as regions with a void fraction greater than 0.8. The definition was obtained by comparing the predicted bubble diameters with experimentally observed bubble diameters. Extra steps were required during the bubble identification procedure to remove noise. Furthermore, a concept called “local thresholding” was incorporated to identify the bubbles. This is necessary for bubbles in experimental images that do not have well-defined boundaries and are affected by background noise as well as noise created by the X-ray beam.

When this is done, comparisons between bubble properties of simulation and experiment can be done. Standardization is required and needs to be explicitly stated. Ensemble averaging is sometimes used.

A successful match will imply that both image shapes and pressure fluctuation analysis spectra between experiment and simulation should match. The presented literature work indicates that when comparing simulated and experimental pressure drop across the bed, at different gas superficial velocities almost 10% deviation from the experimental results can be achieved. The simulated and experimental pressure drop decreases to the same extent for increases in gas superficial velocity.

Snapshots of the simulated and experimental polyethylene beds presented by Chandrasekaran (2005) demonstrate that the simulation results often did not show a major change in the size distribution of the bubbles. However, there were specific cases where the opposite was observed. Thus the argument that the simulation matches experiment invariably cannot (unfortunately) be made.

Figure 17.3 shows a comparison of the experimental and simulated bubble frequency distributions with height above the distributor at a gas superficial velocity of 3 (Hulme, 2003). It can be seen that there were more bubbles in the experiment than the simulation except at lower bed heights. This is quite surprising because it was expected that the experiment should mask smaller bubbles in the wake of larger bubble streams. The figure illustrates that if bubble behavior is to be used as a yardstick for fluid bed reactor performance, then precise and accurate bubble tracking will have to be an important parameter.

Figure 17.4 (Hulme, 2003) shows that the bubble diameters were distributed similarly for both the experiments and the simulation, with smaller bubbles being more than larger bubbles. It should be noted that all the bubble properties from simulation and experiments are time averaged.

In literature, the average bubble size is invariably used to validate model predictions. As can be observed in Figure 17.5 there is considerable deviation between the

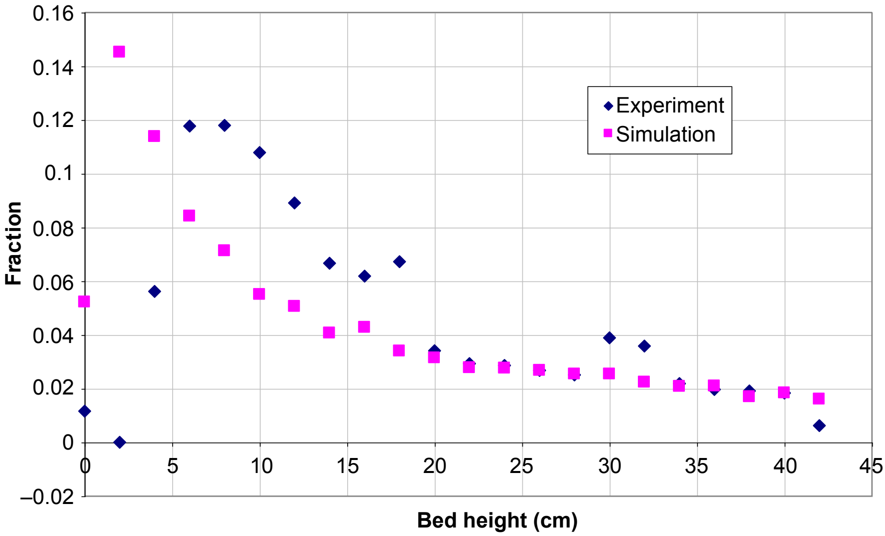

Figure 17.3 Comparison of experimental and simulated bubble frequency distribution as a function of bed height.
Hulme (2003).

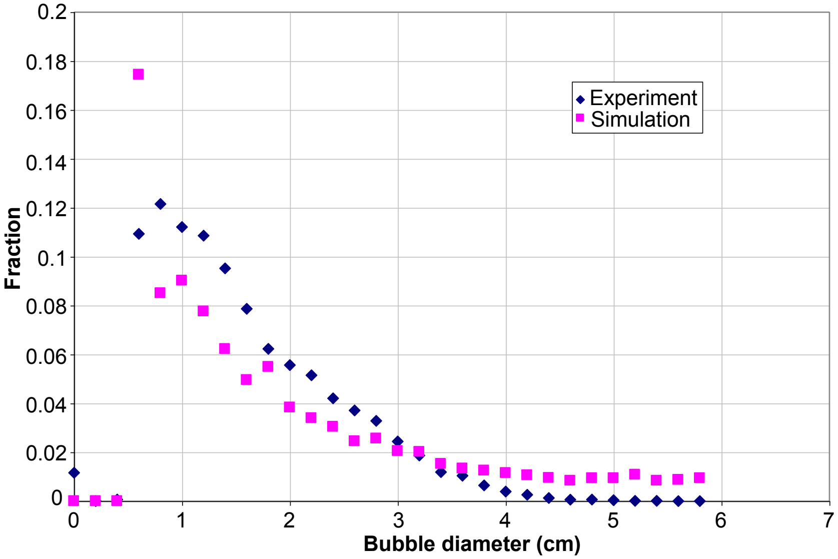

Figure 17.4 Comparison of experimental and simulated bubble diameter distribution in a polyethylene-fluidized bed operating at $3U_{mf}$.
Hulme (2003).

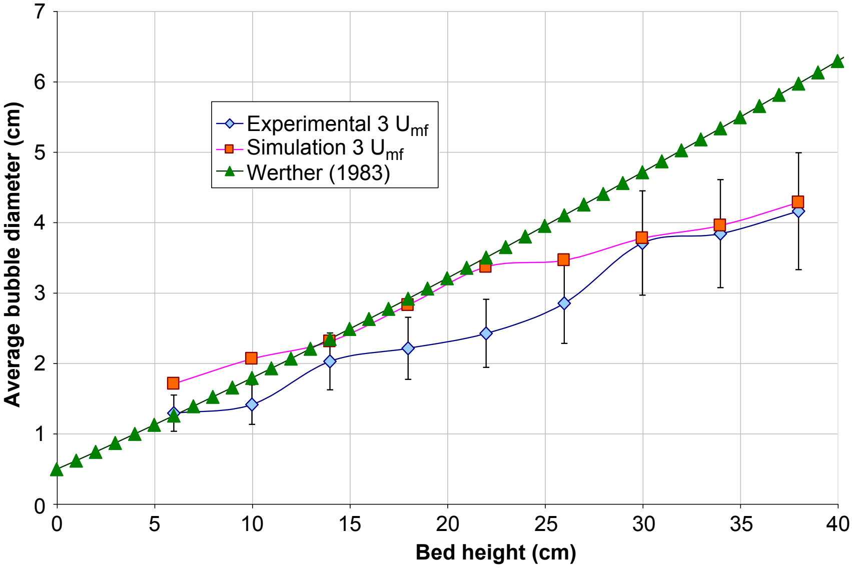

Figure 17.5 Bubble size as a function of height in a polyethylene bed operating at $3U_{mf}$.
Hulme (2003).

simulated bubble diameters and experimental results at lower heights. However, at higher bed heights it appears that the simulations were able to closely predict the experimentally observed results. Similar results were reported consistently by Hulme (2003), Chandrasekaran (2005), and Orta et al. (2011), among others. There was no consistent correlation that matched experimentally derived bubble properties. That adds value to the need for accurate and precise experimental measurements.

17.6 Validation experiments for narrow and wide particle size distribution

One of the major assumptions of multiphase CFD codes is the assumption of a uniform particle size and shape. In polymerization processes the size is not controlled, hence there is a wide particle size distribution. Because of this there is difficulty in capturing the bubble properties with a change in operating conditions. Therefore, to assess the effect of particle size distribution, simulations and experiments of a narrow particle size distribution of polyethylene were conducted.

The simulation bubble diameter predictions for the wide particle size sample showed larger deviations than the narrow size distribution sample, which showed excellent agreement with the experimental average bubble sizes. However, a comparison of the experimental power spectra with the simulation predictions showed significant differences in power spectra magnitude, frequency distribution, and dominant frequencies for both the wide and narrow particle size samples. Subsequent analyses showed that the differences in the bubble size distributions between the simulation and experimental results contributed to the differences in the power spectra.

However, the presence of high frequency energy in the simulations could not be explained from that study. It is speculated that oscillations in the numerical solution of the governing equations can be one of the contributing factors but remains to be investigated. Typically, in validation studies the average size distribution is used for evaluation of the simulation results. This might lead to erroneous conclusions. Various factors contribute to the deviations between the simulation and experiment for the air/polyethylene-fluidized bed. Parallel studies with an ideal particle system, such as glass beads with a narrow size distribution and nearly spherical particles, have shown excellent predictions in both the power spectral and bubble property analyses using CFD packages.

Chandrasekaran et al. (2005) have shown that the bubble diameters and pressure fluctuations are very sensitive to the coefficient of restitution for polyethylene particles. This sensitivity increased dramatically for larger particles and almost disappeared for smaller particles. Typically, the bubble diameters were found to increase with a decrease in the restitution coefficient or an increase in the angle of internal friction. Hence, there will be an error introduced in the simulation results for polyethylene-fluidized bed systems, as experimental values of the solid parameters are currently absent in literature. This will be vital to further development of the current granular flow model. The same investigations also highlighted issues with modeling the solid phase stress tensor. The sensitivity of the model to the restitution coefficient is not understood at this time. Preliminary results (Fan, Marchisio, & Fox, 2004; Goldschmidt, Kuipers, & Van Swaaji, 2001) suggest that a consistent and tested formulation for the solid phase stress tensor will make the difference in understanding nonideal particle fluidization systems such as polyethylene. Multiple solid phases representative of the various size fractions are currently available for polydisperse powders.

17.7 Comparison between different validation approaches

Hulme (2003) conducted simulation using CFD software and experiments were conducted on a scaled-down cold flow model of a gas−solid fluidized bed reactor used for the production of polyethylene. Using a Eulerian−Eulerian multiphase model based on the two-phase model of Anderson and Jackson (1967), Jackson (2000) simulations were conducted to determine the effect of several parameters—time step, differencing scheme, frictional stress, and closing equations—on the bubble properties (predominantly bubble diameter). Once the model flexibility was accessed, the next step was to compare these results with those from experiments conducted using X-ray fluoroscopy (Hulme, 2003). X-ray fluoroscopy was used to create a statistically significant data set. Preliminary experiments comparing the bubble diameter and axial bubble velocity were conducted using glass beads. The results demonstrated that, for glass beads, the average bubble diameters were comparable for CFD and experiments.

Figure 17.6 (Van der Lee, Shepperson, & Kantzas, 2005) shows the experimental bubble diameters for the polyethylene bed (wide particle size distribution: 165−1500 μm) at three superficial gas velocities and a static bed height of 40 cm. Figure 17.6 also shows the bubble diameters predicted from a correlation developed by Cai, Schiavetti, De Michele, Grazzini, and Miccio (1994) and those predicted from pressure measurements taken at 17 and 34 cm above the distributor (indicated by "PF" on the legend). The correlation by Cai et al. (1994) overpredicts bubble diameters at 2.5 times minimum fluidization and underpredicts at 3.5 times minimum fluidization, however, at 3.0 times minimum fluidization, the bubble diameter predictions match quite closely with the experimental values. The comparison of bubble diameters predicted by pressure fluctuations and those measured experimentally changes with measurement height as well as superficial gas velocity.

From the comparison of correlations it was quite evident that an incorrect choice of correlation for bubble diameter prediction for polyethylene fluidized beds would result in deviant fluidized bed behavior. For instance, it was found that most correlations grossly overpredicted bubble diameters at a given superficial gas velocity. Such an error could translate into a difficulty such as agglomeration inside an operational fluidized bed.

The average bubble diameters measured while fluidizing the two narrow particle size distributions (<425 μm and 425−707 μm) were also compared with published correlations, and it was found that correlations by Darton, LaNauze, Davidson, and

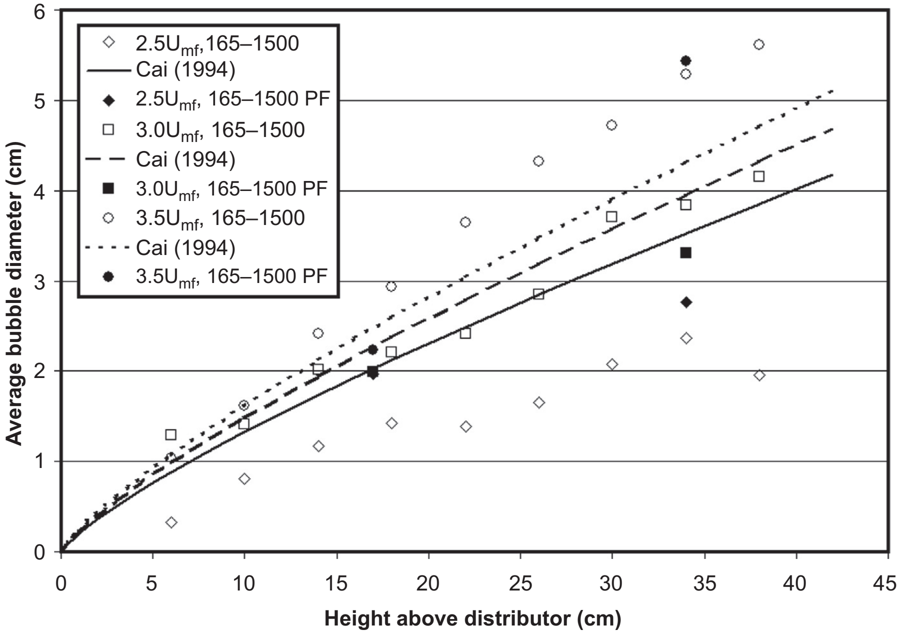

Figure 17.6 Average bubble diameter versus height above the distributor for a wide particle size distribution of polyethylene at various superficial gas velocities.
Van der Lee, Shepperson, and Kantzas (2005).

Harrison (1977) and Yasui and Johanson (1958) were most suited to predict bubble diameters for the low (<425 μm) and medium (425−707 μm) particle size distributions, respectively. In addition to this, the bubble diameters predicted from pressure fluctuations matched well with the medium (425−707 μm) particle size distribution. Axial velocities were also compared, and it was found that a correlation by Geldart (1973) (using calculated bubble diameters from Cai et al. (1994)) predicted the data most closely, except for the smallest particle size distribution (less than 425 μm) where correlations by Wallis and Grace (as cited in Kunii and Levenspiel (1991)) were found to fit best.

17.8 Validation for reactor scale-up

The scale-up of the fluidized bed reactors is difficult due to complexity of hydrodynamics and chemical kinetics (Rudisuli, Schildhauer, Biollaz, & Van Ommen, 2012). The fluidized bed performance is linked to particle interactions, chemical kinetics, and heat and mass transfer in the reactors. As a result, the mathematical modeling of hydrodynamics becomes challenging. Lab-scale cold models are able to predict the hydrodynamics of the hot scaled-up reactors. But, still the scaling-up of the cold models is challenging.

The most common procedures in scaling-up the fluidized bed use dimensionless numbers such as Gliksman, which is a function of Reynolds number, Froude number, gas-to-particle density ratio, sphericity, and size distribution of the particles and bed geometry. Dimensionless scaling-up can be validated using spectral analysis and CFD. However, some of the fluidization phenomena such as wall effect and particle interactions are neglected in dimensionless scaling-up.

Over the past few years, the Kantzas group has focused on developing nonintrusive measurement techniques for cold laboratory-scale polymerization reactors to provide statistically significant data for comparison with CFD models for the production of polyethylene. This is illustrated by the multiple references of this chapter. To model the behavior of these reactors they have chosen commercial CFD packages. They used the combination of experiment and simulation to study the effect of certain model parameters on the predicted bubble properties. These parameters in simulation include the time step, differencing scheme, solid stress closure equations, and frictional stress. The geometric configuration and conditions specified for these simulations were based on a case run by Syamlal and O'Brien (1987) and Laux and Johansen (1998), which provided a means for quantitative comparison. In addition, simulation results were compared with results from a statistically significant data set obtained from X-ray fluoroscopy experiments, using relatively monosized glass beads as the solid phase.

Owing to the difficulty in solving the momentum and continuity equations for every particle in the gas—solid fluidized bed reactor, much effort has been focused on reducing the number of equations to describe this system. The most common method is to apply an averaging technique to the Navier—Stokes equations. In this manner, the two fluids (gas and solid) are treated as two fully interpenetrating continua. The development of the equations used for the continuum models, or two-fluid models, can be found in Anderson and Jackson (1967) and Jackson (2000).

In recent years, due to the controversy surrounding the governing and closing equations used for the simulations, many researchers have been validating proposed models. Of particular note is the work by Boemer, Qi, and Renz (1997), Boemer et al. (1998), Van Wachem, Schouten, Krishna, and Van D Bleek (1999), and Van Wachem, Van Der Schaaf, Schouten, Krishna, and Van Den Bleek (2001). Boemer's work (1997) determined the closing equation that best predicted spontaneous bubble formation in a fluidized bed. In addition, Boemer et al. (1998) conducted experiments and simulations to verify properties using a 2-D bed. Among the properties studied were the bubble wake angle, voidage and pressure distribution, bubble size, and velocity. In general, these properties found good agreement with experiments. It should be noted that while their work gave positive results, the amount of data studied for bubble properties is limited. Van Wachem et al. (1999) also conducted a validation of Eulerian simulated dynamic behavior of gas—solid fluidized beds. They studied the behavior of Geldart B particles to determine if the dynamic behavior matched experiments. The choice of closing equations was based on fast numerical convergence and accurate physical results. The closing equation chosen followed the work of

Syamlal et al. (1993), Boemer, Qi, and Renz (1995), Ding and Gidaspow (1990), and Lun, Savage, Jeffrey, and Chepurnity (1984) with the interphase exchange being that of Syamlal et al. (1993). Van Wachem et al. (1999) mainly examined the power spectral density of the pressure and voidage fluctuations, which they found matched correlations. The paper by Van Wachem et al. (2001) succinctly summarizes the governing and closing equations that are more commonly used. Showing results both qualitatively and quantitatively, they were able to get a feel for the range of applicability of simulating the behavior of a bed with glass beads. They also concluded that the choice of solids stress models, or radial distribution functions, plays little role in the final simulation result.

Very little open literature discusses simulations of large commercial-scale or even pilot-scale reactors for the polymerization process. Gobin et al. (2001) is one of the only groups, in open literature, studying large-scale polymerization reactors. They describe their simulator's ability to predict the gross flow patterns of a large-scale reactor. Their numerical code, ESTET-ASTRID, developed by Electricité de France for CFB boilers and based on the two fluids model, is used for these simulations. They were able to determine the pressure drop across a fluid bed and determine some of the gross flow patterns, such as solid flow rate and solid volume fraction. They also conducted some preliminary work to examine the credibility of modeling a 3-D reactor in two dimensions. While there were some variations, they concluded that for industrial use they were comparable. An additional study by Lettieri, Cammarata, Micale, and Yates (2003) concluded that a 2-D model provided sufficient accuracy.

Many of the authors agree that CFD will be a powerful tool in determining the macro- and microscopic phenomena associated with gas—solid fluidized bed reactors. Yet, it is generally accepted that the next step necessary in providing a reliable, fully predictable model is experimental validation (Gobin et al., 2001). A set of experiments and simulations that were conducted on a glass-bead fluidized bed system were performed by He, Wu, Bellehumeur, and Kantzas (2007). Although polyethylene systems are the focus of their research, the nonideality of the particles makes it difficult to access the applicability of the CFD model and effect of its parameters. By initially using an "ideal" and much-studied system, such as glass beads, they determined the value of simulation results as well as the effect of various parameters by comparison with literature and the experimental data. The glass bead system was also used to validate the image processing software that was developed to analyze the statistically significant amount of quantitative experimental data produced with X-ray fluoroscopy. The glass bead data were used to compare experimental results with correlations presented in literature (Hulme, 2003; Hulme & Kantzas, 2004). A simple parametric study was conducted to determine the effect of parameters such as time step, differencing scheme, closing equations, and frictional stress.

The vessel was a scaled down cold-model reactor used for the production of polyethylene, with a diameter of 0.1 and 1 m in height. Images showing bubble movement were captured at a frequency of 30 Hz and then analyzed using in-house software to determine the bubble properties. The particles used in this study were glass beads with a narrow particle size distribution (150—250 μm). Two minutes (3600 frames) of data were captured at each set of fluidization conditions. Experiments were repeated three times and found to be statistically valid. More details on the experimental procedure and data analysis can be found in Hulme (2003) and Hulme and Kantzas (2004) with a summary provided above.

Experimental results using glass bead as the solid phase were compared with the results obtained from the simulation. The simulation of the cylindrical laboratory reactor was performed assuming it could be modeled in two dimensions (Gobin et al. 2001; Lettieri et al. 2003). The first parameter examined was the average fluidized bed height and pressure drop across the bed. The average height for the experimental bed was found to be approximately 42 cm. For the simulations, the average bed height was closer to 46 cm, or approximately 10% greater. Other authors have noted the same discrepancy, and in the case of Gobin et al. (2001) the simulated bed height was 15% higher.

Examination of the distribution of the bubble diameters throughout the bed indicates similarities between the experimental and simulation results. Once the distribution of the bubbles and bubble diameters was deemed comparable, the effort shifted to examining the bubble diameter and axial velocity for binned bed heights.

The diameters of the bubbles for the simulations were determined using a modified version of the program developed for the experiments. The simulation output images show the volume fraction of solids. To analyze the images, a void fraction of solids had to be chosen as a cutoff (similar to the thresholding for experimental images) for determining the bubble boundaries. While some authors have chosen the value of 0.3 (Guenther & Syamlal, 2001) others have chosen void fractions of 0.2 (Boemer et al., 1997; Gidaspow, 1994) and 0.15 (Kuipers, 1990). After comparing with experimental results, a cutoff of 0.2 was chosen. The conclusion by most authors listed above is that an exact definition of the bubble boundary is not necessary. However, after examining the effect of varying the volume fraction cutoff, it becomes apparent that the definition of the bubble boundary is important.

After comparing the simulation results with a statistically significant amount of experimental data, it becomes apparent that the simulations are able to reasonably predict average bubble diameters. However, the bubble distribution near the top of the bed did not match well and the absolute axial velocities were off by approximately 10 cm/s. However, they both followed the same trend, which is encouraging.

17.9 Ultrafast X-ray computer tomography

Fast moving objects typically produce poor quality images and motion artifacts in CT scans. The imaging of bubbling gas—solid fluidized beds, where many bubbles may pass through the sensing cross-section in a tomographic measurement, gives such a problem. Previously, one method of dealing with this problem was to remove artifacts from the reconstructed image itself through low-pass filtering. However, this method leads to lost information from the images. When the concentration of bubbles is low, and their shape is close to cylindrically symmetric, analysis of consecutive scans in the raw data sinogram can also provide valuable information about the frequency of bubbles passing, and about their individual size, shape, and position (Bennet, Kryuchkov, & Kantzas, 2006). Then, utilizing the inverse Abel transform, this information can also be used to contribute to time-averaged properties of the bed's behavior such as voidage distribution, bubble phase area fraction, and spatial bubble number distribution. The approach is simple but has uncertainties.

There are uncertainties for bubble definition using pressure fluctuation and X-ray tomography methods (Dantas, Melo, & dos Santos, 2008). Measurement of pressure fluctuations due to wall effect causes large inaccuracy. Application of X-ray single projection for bubble distribution measurement will be inaccurate at the presence of several bubbles at one cross-section area of reactor and wall effects (Grassler & Wirth, 1999).

Insufficient X-ray projections cause limited data in tomography, which is a problem in conventional CT algorithm. Instantaneous tomographic measurements of fluidized beds provide an alternative approach that has great merit and potential.

A high-speed X-ray tomography system has been developed for measuring the bubbling flow in a fluidized bed by Mudde et al. (2008). Three X-ray sources are set up at equal angles around the bed to generate projections simultaneously, so that detector arrays receive the attenuated X-ray signals at the same time. A time resolution of 2500 frames/s can be reached. Meanwhile, another fast X-ray system was built by Bieberle et al. (2007) for gas liquid flow. The frame rate can be as high as 10,000 frames/second (Bieberle et al., 2010). It later was also applied in a fluidized bed measurement (Bieberle, Barthel, & Hampel, 2012). Both of these fast X-ray CT systems have high enough time resolution to study multiphase fluid flow. The time resolution is improved but the spatial resolution changed from millimeter-scale to centimeter-scale for a 25-cm diameter fluidized with the current hardware controlled by the limited number of detectors or limited angle.

Mudde, Schulte, and Van Den Akker (1994) have developed a fast CT system consisting of three X-ray sources to measure bubble rise velocity in a bubble bed with 23-cm ID. The system is able to acquire data with 100 frame/s rate. However, small bubbles with less than 3-cm ID were not detected by this system due to signal noise. By increasing the number of X-ray sources to 5, better accuracy could be obtained (Mudde, 2010).

Kai, Misawa, Takahashi, Tiseanu, and Ichikawa (2005) were able to produce high quality images with pixels of 0.15 mm^2 and shorter measuring time of 4 ms using 18 X-ray sources and 122 detectors.

Measurements of size and velocity of bubbles were also performed using X-ray computer tomography by Brouwer, Wagner, van Ommen, and Mudde (2012). They used CT scans to study the effect of fine concentration and operating pressure on bubble size in fluidized bed. Three X-ray sources with YXLON Y.TU 160-D06 tubes were mounted at 120° around the fluidized bed. Maximum voltage and current were 160 V and 12 mA. The velocity of detected phantom between the planes has been measured using a high-speed (500 fps) camera.

Bieberle et al. (2012) have applied an ultrafast X-ray tomography technique to assess the gas phase and the particulate structure in fluidized bed columns. An X-ray beam of 150 kV, 12 mA, and maximum 10 kW power has been used rotating the object to have limited-angle and full-angle imaging in two heights of 30 and 70 cm. The X-ray tomography result was validated as performing the experiments in columns with the diameter of 50 and 94 mm filled with ellipsoidal shape polyoxymethylene particles with 3 × 2 mm size. The result of ultrafast X-ray CT at the 50-mm-diameter column showed that as the gas flow rate increases the bubble fraction increases. Increase in bubble fraction changed the flow regime from bubble flow to slug flow. The bubbles and slugs were in similar shape and centered at different heights in the 50-mm column. Formation of gas channels close to the wall was observed in the 94-mm column. They observed that bubbles coalescence in the center at upper regions.

Although virtually all reconstruction problems in CT are ill-posed, this problem in high-speed X-ray CT is particularly serious in high-speed X-ray CT; the number of data points depends on the number of detectors, which is restricted by space and detector size. The traditional CT algorithms such as filtered back projection are seriously influenced by the ill-posed problem. It is easy to produce unknown errors when the order of the image matrix is much larger than the order of the raw data matrix (Natterer, 1986). The simultaneous algebraic reconstruction technique (SART) (Andersen & Kak, 1984) was firstly applied to solve such a problem. Alternatively, the genetic algorithm (GA) (Holland, 1992) is introduced to tomographic image reconstruction (Abdoli, Ay, Ahmadian, Dierckx, & Zaidi, 2010; Di Gesu, Boscoa, Millonzi, & Valenti, 2010; Kihm et al., 1996; Valenti, 2008; Venere, Liao, & Clausse, 2000; Wu et al., 2007). Although it is proved that GA performed well in reconstructing images from ill-posed and noisy data, a comparison between SART and GA has not been made.

17.10 Future trends

In this chapter it was demonstrated that CT can play an important role in characterizing laboratory- and pilot-scale fluidized bed systems. New designs in ultrafast scanning can make this vision a reality in the very near future. It was also demonstrated that without supplementary methods such as CFD and pressure fluctuation analysis it will be impossible to provide information on plant-scale systems. Thus CT becomes one tool for process monitoring and process design in fluid bed columns (reactors or not). There are numerous problems to be tackled and numerous types of reactors where tomography will be invaluable from dryers to spouted beds to fixed beds. What needs to be addressed in earnest is how this information will translate into real-world information.

Acknowledgements

The author acknowledges the contributions of all the graduate students, postdoctoral fellows, technologists, and research associates that have worked hard over the years to materialize the vision of the tomography and imaging of fluid bed systems. This work would never have been done without the financial contributions of Nova Chemicals, the Natural Sciences and Engineering Research Council of Canada (NSERC), and the Canada Foundation for Innovation (CFI).

References

Abdoli, M., Ay, M., Ahmadian, A., Dierckx, R., & Zaidi, H. (2010). Reduction of dental filling metallic artifacts in CT-based attenuation correction of PET data using weighted virtual sinograms optimized by a genetic algorithm. *Medical Physics, 37*, 6166–6177.

Andersen, A. H., & Kak, A. C. (May 1984). *The application of ray tracing towards a correction for refraction effects in computed tomography with diffracting sources*. Purdue University Research Rep. TR-EE84–14. West Lafayette, Ind: Purdue University.

Anderson, T. B., & Jackson, R. (1967). A fluid mechanical description of fluidized beds equations of motion. *Industrial & Engineering Chemistry Fundamentals,, 6*(1), 527–538.

Behie, L. A., & Kehoe, P. (1973). The grid region in a fluidized bed reactor. *AIChE Journal, 19*(5), 1070–1072.

Bennett, M., Kryuchkov, S., & Kantzas, A. (2006). Interpretation of CT-Scan sinograms to study the dynamic flow properties of a fluidized bed. In *Multiphase flow: The ultimate measurement challenge, proceedings 5th ISMTMF/IWPT-2, Macau, China, December 10-13*.

Bhargava, A., Kabir, M., Vaisman, E., Langford, C. H., & Kantzas, A. (2004). A novel technique to characterize hydrodynamics and analyze performance of a fluidized bed photocatalytic reactor for wastewater treatment. *Industrial & Engineering Chemistry Research, 43*, 980–989.

Bieberle, M., Barthel, F., & Hampel, U. (2012). Ultrafast X-ray computed tomography for the analysis of gas-solid fluidized beds. *Chemical Engineering Journal, 189*, 356–363.

Bieberle, M., Fischer, F., Schleicher, E., Hampel, U., Koch, D., Aktay, K. S. D. C., et al. (2007). Ultrafast limited-angle-type X-ray tomography. *Applied Physics Letters, 91*.

Bieberle, M., Schleicher, E., Fischer, F., Koch, D., Menz, H.-J., Mayer, H.-G., & Hampel, U. (2010). Dual-plane ultrafast limited-angle electron beam X-ray tomography. *Flow Measurement and Instrumentation, 21*(3), 233–239.

Boemer, A., Qi, H., & Renz, U. (1995). Eulerian computation of fluidized bed hydrodynamics – A comparison of physical models. In *Proceedings of the 13th international conference on fluidized bed combustion, Orlando, FL., USA* (pp. 775–786).

Boemer, A., Qi, H., & Renz, U. (1997). Eulerian simulation of bubble formation at a Jet in a two-dimensional fluidized bed. *International Journal of Multiphase Flow, 23*(5), 927–944.

Boemer, A., Qi, H., & Renz, U. (1998). Verification of Eulerian simulation of spontaneous bubble formation in a fluidized bed. *Chemical Engineering Science, 53*(10), 1835–1846.

Briens, C. L., Briens, L. A., Barthel, E., Le Blevec, J. M., Tedoldi, A., & Margaritis, A. (1999). Detection of local fluidization characteristics using the V statistic. *Powder Technology, 102*, 95–103.

Briens, C. L., Briens, L. A., Hay, J., Hudson, C., & Margaritis, A. (1997). Hurst's analysis to detect minimum fluidization and gas maldistribution in fluidized beds. *AIChE Journal, 43*(7), 1904–1908.

Briens, L. A., Briens, C. L., Margaritis, A., Cooke, S. L., & Bergougnou, M. A. (1997). Characterization of channeling in multiphase systems. Application to a liquid fluidized bed of angular biobone particles. *Powder Technology, 91*, 1–9.

Brouwer, G., Wagner, E., van Ommen, J., & Mudde, R. (2012). Effects of pressure and fines content on bubble diameter in a fluidized bed studied using fast X-ray tomography. *Chemical Engineering Journal, 207208*, 711–717.

Cai, P., Schiavetti, M., De Michele, G., Grazzini, G. C., & Miccio, M. (1994). Quantitative estimation of bubble size in PFBC. *Powder Technology, 80*, 99−109.

Chandrasekaran. A. (2005). *Verification of the hydrodynamics of a polyethylene fluidized bed reactor using CFD and imaging experiments* (M. Sc. thesis). Calgary, Alberta: University of Calgary.

Chandrasekaran, B., Van der Lee, L., Hulme, I., & Kantzas, A. (2005). A simulation and experimental study of the hydrodynamics of a bubbling fluidized bed of linear low density polyethylene using bubble properties and pressure fluctuations. *Macromolecular Materials and Engineering, 290*, 592−609.

Chen, R. C., & Fan, L.-S. (1992). Particle image velocimetry for characterizing the flow structure in three-dimensional gas-liquid-solid fluidized beds. *Chemical Engineering Science, 47*(13/14), 3615−3622.

Chereminsinoff, N. P., & Cheremisinoff, P. N. (1984). *Hydrodynamics of gas-solids fluidization*. Houston, Texas: Gulf Publishing Company.

Croxford, A. J., & Gilbertson, M. A. (2006). Control of the state of a bubbling fluidized bed. *Chemical Engineering Science, 61*, 6302−6315.

Dantas, C. C., Melo, S. B., & dos Santos, V. A. (September 3−5, 2008). A study of uncertainty evaluation in transmission measurement in gamma ray tomography. In *12th IMEKO TC1 & TC7 joint symposium on man science & measurement* (Annecy, France).

Darton, R. C., LaNauze, R. D., Davidson, J. F., & Harrison, D. (1977). Bubble growth due to coalescence in fluidized beds. *Transactions of the Institution of Chemical Engineers, 55*, 274−280.

Davidson, J. F., & Harrison, D. (1963). *Fluidized particles*. New York: Cambridge University Press.

Di Gesù, V., Boscoa, G. L., Millonzi, F., & Valenti, C. (2010). A mimetic approach to discrete tomography from noisy projections. *Pattern Recognition, 43*(9), 3073−3082.

Ding, J., & Gidaspow, D. (1990). A bubbling fluidization model using kinetic theory of granular flow. *AIChE Journal, 36*, 523−538.

Drake, J. B., & Heindel, T. J. (2012a). Comparisons of annular hydrodynamic structures in 3D fluidized beds using X-ray computed tomography imaging. *Journal of Fluids Engineering-Transactions of the ASME, 134*.

Drake, J. B., & Heindel, T. J. (2012b). Local time-average gas holdup comparisons in a cold flow fluidized beds with side-air injection. *Chemical Engineering Science, 68*, 157−165.

Fan, R., Marchisio, D. L., & Fox, R. O. (2004). Gas-solid fluidized beds. *Powder Technology, 139*, 7−20.

Geldart, D. (1973). Types of gas fluidization. *Powder Technology, 7*, 285−292.

Gheorghiu, S., Van Ommen, J. R., & Coppens, M. O. (2003). Power law distribution of pressure fluctuations in multiphase flow. *Physical Review E, 67*, 041305-1−041305-7.

Gidaspow, D. (1994). *Multiphase flow and fluidization*. Boston: Academic Press Inc.

Gobin, A., Neau, H., Simonin, O., Llinas, J., Reiling, V., & Selo, J. (2001). Numerical simulation of a gas phase polymerisation reactor. In *European congress on computational methods in applied sciences and engineering ECCOMAS computational fluid dynamics conference 20012; Wales*.

Goldschmidt, M. J. V., Kuipers, J. A. M., & Van Swaaji, W. P. M. (2001). Hydrodynamic modeling of dense gas-fluidized beds using the kinetic theory of granular flow: effect of coefficient of restitution on bed dynamics. *Chemical Engineering Science, 56*(2), 571.

Grassler, T., & Wirth, K. E. (1999). Computerized tomography and image processing. In *DGZfP proceedings, BB 67-CD*.

Grassler, T., & Wirth, K. E. (2000). X-ray computer tomography potential and limitation for the measurement of local solids distribution in circulating fluidized beds. *Chemical Engineering Journal, 77*, 65−78.

Guenther, C., & Syamlal, M. (2001). The effect of numerical diffusion on simulation of isolated bubbles in a gas-solid fluidized bed. *Powder Technology, 116*(2−3), 142−154.

Heindel, T. J. (2011). A review of X-ray flow visualization with applications to multiphase flows. *Journal of Fluids Engineering-Transactions of the ASME, 133*.

He, Z., Wu, B., Bellehumeur, C., & Kantzas, A. (2007). In *"X-ray fluoroscopy measurements and CFD simulation of hydrodynamics in a two-dimensional gas-solids fluidized bed", fluidization XII, Harrison Hot Springs, Vancouver, B.C., May 13-17*.

Heindel, T. J., Gray, J. N., & Jensen, T. C. (2008). An X-ray system for visualizing fluid flows. *Flow Measurement and Instrumentation, 19*, 67−78.

Holland, J. H. (1992). Genetic algorithms. *Scientific American, 267*, 44−50.

Hoomans, B. P. B., Kuipers, J. A. M., & van Swaaij, W. P. M. (1998). Discrete particle simulation of segregation phenomena in dense gas-fluidized beds. In *fluidization IX, proceedings of the ninth engineering foundation conference on fluidization, Durangeo, Colorado* (pp. 485−492).

Hulme. I. (2003). *Verification of the hydrodynamics of a polyethylene fluidized bed reactor using CFD and imaging experiments* (M. Sc. thesis). Calgary: University of Calgary.

Hulme, I., & Kantzas, A. (2004). Determination of bubble diameter and axial velocity for a polyethylene fluidized bed using X-ray fluoroscopy. *Powder Technology, 147*(1−3), 20−33.

Jackson, R. (2000). *The dynamics of fluidized bed particles*. New York: Cambridge University Press.

Johnsson, F., Zijerveld, R. C., Schouten, J. C., van den Bleek, C. M., & Leckner, B. (2000). Characterization of fluidization regimes by time-series analysis of pressure fluctuations. *International Journal of Multiphase Flow, 26*, 663−715.

Kai, T., Misawa, M., Takahashi, T., Tiseanu, I., & Ichikawa, N. (February 2005). Observation of 3-D structure of bubbles in a fluidized catalyst bed. *The Canadian Journal of Chemical Engineering, 83*(1), 113−118.

Kaneko, Y., Shiojima, T., & Horio, M. (1999). DEM simulation of fluidised beds for gas-phase olefin polymerization. *Chemical Engineering Science, 54*, 5809−5821.

Kantzas, A. (1990). Investigation of physical properties of porous rocks and fluid flow phenomena in porous media using computer assisted tomography. *In Situ, 14*(1), 77−132.

Kantzas, A. (1994). Computation of holdups in fluidized beds and trickle beds by computer assisted tomography. *AIChE Journal, 40*(7), 1254−1261.

Kantzas, A., & Kalogerakis, N. (1996). Monitoring the fluidization characteristics of polyolefin resins using X-ray computer assisted tomography scanning. *Chemical Engineering Science, 51*(10), 1979, 14th international symposium on chemical reactor engineering (ISCRE 14), Brugge, Belgium, May 5-8.

Kantzas, A., Wright, I., & Kalogerakis, N. (1997). Quantification of channeling in polyethylene resin fluid beds using X-ray computer assisted tomography (CAT). *Chemical Engineering Science, 52*(13), 2023−2035.

Kantzas, A., Wright, I., Bhargava, A., Li, F., & Hamilton, K. (2001). Measurement of hydrodynamic data of gas phase polymerization reactors using non-intrusive methods. *Catalysis Today, 64*(3−4), 189−203.

Kihm, K. D., & Lyons, D. P. (1996). Optical tomography using a genetic algorithm. *Optics Letters, 21*(17), 1327−1329.

Kuipers, J.A.M. (1990). A two-fluid micro Balance model of fluidized bed (Ph.D. thesis). Enschede, The Netherlands: Twente University.

Kuipers, J. A. M., Duin, van, K. J., Beckum, van, F. P. H., & Swaaij, van, W. P. M. (1993). Computer simulation of the hydrodynamics of a two-dimensional gas-fluidized bed. *Computers & Chemical Engineering, 17*(8), 839−858.

Kunii, D., & Levenspiel, O. (1991). *Fluidization engineering* (2nd ed.). Newton: Butterworth-Heinemann.

Laux, H., & Johansen, S. T. (1998). Computer simulation of bubble formation in a gas-solid fluidized bed. In *Fluidization IX, proceedings of the ninth engineering foundation conference on fluidization, Durangeo, Colorado* (pp. 517−524).

Lettieri, P., Cammarata, L., Micale, G., & Yates, J. (2003). CFD simulation of gas fluidized beds using alternative Eulerian−Eulerian modelling approaches. *International Journal of Chemical Reactor Engineering, 1*.

Lun, C., Savage, S., Jeffrey, D., & Chepurnity, N. (1984). Kinetic theories for granular flow: inelastic particles in Couette flow and slightly inelastic particles in a general flow-field. *Journal of Fluid Mechanics, 140*, 233−256.

Lyczkowski, R. W., Gamwo1, I. K., Dobran, F., Ai, Y. H., Chao, B. T., Chen, M. M., et al. (1993). Validation of computed solids hydrodynamics and pressure oscillations in a bubbling atmospheric fluidized bed. *Powder Technology, 76*, 65−77.

McKeen, T., & Pugsley, S. T. (2003). Simulation and experimental validation of a freely bubbling bed of FCC catalyst. *Powder Technology, 129*, 139−152.

Mudde, R. F. (2010). Time-resolved X-ray tomography of a fluidized bed. *Powder Technology, 199*, 55−59.

Mudde, R. F., Alles, J., & van der Hagen, T. H. J. J. (2008). Feasibility study of a time-resolving X-ray tomographic system. *Measurement Science and Technology, 19*.

Natterer, F. (1986). *The mathematics of computerized tomography*. John Wiley & Sons and B.G. Teubner. Reprint SIAM 2001.

Orta, A., Wu, B., Guerrero, A., Ghods, M., Bellehumeur, C., & Kantzas, A. (2011). Pressure effect on hydrodynamics of a high pressure X-ray transparent polyethylene fluidized bed. *IJCRE, 9*(1).

Peirano, E., Delloume, V., Johnsson, F., Lechner, B., & Simonin, O. (2002). Numerical simulation of the fluid dynamics of a freely bubbling fluidized bed: influence of the air supply system. *Powder Technology, 122*, 69−82.

Ranade, V. V. (2002). *Computational flow modeling for chemical reactor engineering* (Vol. 5). San Diego, California: Academic Press.

Rowe, P. N., MacGillivray, H. J., & Cheesman, D. J. (1979). Gas discharge from an orifice into a gas fluidized bed. *Transactions of the Institution of Chemical Engineers E, 57*, 194−199.

Rudisuli, M., Schildhauer, T. J., Biollaz, S. M. A., & Van Ommen, J. R. (2012). Scale-up of bubbling fluidized bed reactors − a review. *Powder Technology, 217*, 21−38.

Schober, L., Hulme, I., Chandrasekaran, B., & Kantzas, A. (2003). An experimental and simulation study of the hydrodynamics of linear low density polyethylene. In *3rd world congress on industrial process tomography, Banff, Alberta, September 2-5*.

Schouten, J. C., & Van Den Bleek, C. M. (1998). Monitoring the quality of fluidization using the short-term predictability of pressure fluctuation. *AIChE Journal, 44*(1), 48−60.

Song, J., Hyndman, C. L., Jakher, R. K., Hamilton, K., Kryuchkov, S., & Kantzas, A. (1999). Fundamentals of hydrodynamics and mass transfer in a three-phase fluidized bed system, 4th international conference on gas–liquid and gas–liquid–solid reactor engineering, Delft, The Netherlands, August 23–25. *Chemical Engineering Science, 54*(21), 4967–4973

Syamlal, M., O'Brien, T.J. (1987). *A generalized drag correlation for multiparticle systems*. Unpublished Report U.S. Department of Energy, Office of Fossil Energy, Morgantown Energy Technology Center, Morgantown, WV.

Syamlal, M., Rogers, W., & O'Brien, T. J. (1993). *MFIX documentation: Volume 1, theory guide*. Springfield, VA: National Technical Information Service.

Tsuji, Y., Kawaguchi, T., & Tanaka, T. (1993). Discrete particle simulation of two-dimensional fluidized bed. *Powder Technology, 77*, 79–87.

Valenti, C. (2008). A genetic algorithm for discrete tomography reconstruction. *Genet Programming Evolvable Machines, 9*(1), 85–96.

Van der Lee, L., Shepperson, J., & Kantzas, A. (2005). A comparison of experimental and predicted bubble characteristics of a linear low density polyethylene. In *Proceedings, 3rd European conference on the reaction engineering of polyolefins, Lyon, France, June 20–24*.

Van Ommen, J. R., Coppens, M. O., & Van Den Bleek, C. M. (2000). Early warning of agglomeration in fluidized beds by attractor comparison. *AIChE Journal, 46*(11), 2183–2197.

Van Wachem, B. G., Schouten, J. C., Krishna, R., & Van D Bleek, C. M. (1999). Validation of the Eulerian simulated dynamic behavior of gas-solid fluidized beds. *Chemical Engineering Science, 54*, 2141–2149.

Van Wachem, B. G. M., Van Der Schaaf, J., Schouten, J. C., Krishna, R., & Van Den Bleek, C. M. (2001). Experimental validation of Lagrangian–Eulerian simulations of fluidized beds. *Powder Technology, 116*, 155–165.

Venere, M., Liao, H., & Clausse, A. (July 2000). A genetic algorithm for adaptive tomography of elliptical objects. *IEEE Signal Processing Letters, 7*(7), 176–178.

Williams, R. A., & Beck M. S. (Ed.). (1995). *Process tomography: Principles, techniques and applications*. Butterworth-Heinemann.

Wright, I., Hamilton, K., Kruychkov, S., Chen, J., Li, F., & Kantzas, A. (2001). On the measurement of hydrodynamic properties of an air–polyethylene fluidized bed system. *Chemical Engineering Science, 56*(13), 4085–4097.

Wu, B. Y., Briens, L., & Zhu, J.-X. (2006). Multi-scale flow behaviors in gas-solids two-phase flow systems. *Chemical Engineering Journal, 117*, 187–195.

Wu, B., Kantzas, A., Bellehumeur, C., He, Z., & Kryuchkov, S. (2007). Multiresolution analysis of pressure fluctuations in a gas-solids fluidized bed: application to glass beads and polyethylene powder systems. *Chemical Engineering Journal, 131*(1–3), 23–33.

Wu, C., Cheng, Y., Ding, Y., Wei, F., & Jin, Y. (2007). A novel X-ray computed tomography method for fast measurement of multiphase flow. *Chemical Engineering Science, 62*, 4325–4335.

Yasui, G., & Johanson, L. N. (1958). Characteristics of gas pockets in fluidized beds. *AIChE Journal, 4*, 445–452.

Yates, J. G., & Simons, S. J. R. (1994). Experimental methods in fluidization research. *International Journal of Multiphase Flow, 20*, 297–330.

Zarabi, T., & Kantzas, A. (October 1998). Predictions on bubble and solids movement in laboratory polyethylene fluid beds as visualized by X-ray computer assisted tomography (CAT) scanning. *Canadian Journal of Chemical Engineering, 76*(5), 853–865.

Zarabi, T., & Kantzas, A. (October 2000). Analysis of gamma-ray imaging data to describe hydrodynamic properties of gas−polyethylene fluidized beds. *Canadian Journal of Chemical Engineerig, 78*(5), 849−857.

Zhang, Q., Wu, B., Li, Y., Bellehumeur, C., & Kantzas, A. (2007). Effect of particle shape on fluidized bed hydrodynamics using X-ray tomography and pressure measurement. In *5th world congress on industrial process tomography, Bergen, Norway, September 3−6*.

This page intentionally left blank

Applications of tomography in bubble column and trickle bed reactors

18

D.J. Holland
University of Canterbury, Christchurch, New Zealand

18.1 Introduction

Many chemical reactions of industrial interest require contacting of gases, liquids and solids. Two of the most common reactor configurations used for these reactions are bubble column and trickle bed reactors. Some examples of industrial reactions commonly using bubble column or trickle bed reactors include oxidation, hydrogenation, polymerization, fermentation, hydrodesulphurization and Fischer—Tropsch synthesis of liquid fuels (Deckwer, 1992; Dudukovic, Larachi, & Mills, 1999; Gianetto & Specchia, 1992; Kantarci, Borak, & Ulgen, 2005; Satterfield, 1975). The efficient design and operation of these systems requires understanding the interaction of the gas and liquid phases. For example, the reaction rate is frequently determined not by the kinetics of the reaction but rather by the rate at which the gas and liquid come into contact, often with a solid catalyst as well. For many years the design of these reactors has been based on empirical correlations derived from measurements of the inlet and outlet conditions of the reactor, including pressure, temperature and concentration. However, these conventional measurements provide little insight into the internal operations of the reactor and therefore can be adversely affected by, for example, maldistribution of the fluid entering the reactor, imperfect mixing of the continuous phase or changes in the flow regime. Without detailed knowledge of these factors, it is necessary to assume that the reactor behaves as if it were following an ideal model whereby each phase is treated as being either in plug flow or well mixed. It is well known that such models are only approximate descriptors of industrial reactors. Indeed, it is common for full-scale industrial reactors designed using these approaches to fail to achieve their design objectives, leading to significant increases in production costs and loss of efficiency (Dudukovic, 2010).

Computational fluid dynamic techniques potentially provide significantly improved insight into the design and operation of bubble column and trickle bed reactors, and many researchers are actively exploring these techniques (Jakobsen, 2008; Kuipers & van Swaaij, 1998; Monahan, Vitankar, & Fox, 2005; Olmos, Gentric, Vial, Wild, & Midoux, 2001; Sanyal, Vasquez, Roy, & Dudukovic, 1999; Selma, Bannari, & Proulx, 2010; Sokolichin, Eigenberger, & Lapin, 2004; Van Sint Annaland, Dijkhuizen, Deen, & Kuipers, 2006). However, such numerical models of multiphase reactors require closure laws to describe the interaction of the gas

Industrial Tomography. http://dx.doi.org/10.1016/B978-1-78242-118-4.00018-6
Copyright © 2015 Elsevier Ltd. All rights reserved.

and liquid phases. These closure laws are typically derived from simplified phenomenological models or experimental measurements of bulk properties such as the holdup and their accuracy is questionable (Dudukovic, 2010). Accurate specification of closure laws becomes even more complex in the presence of a solid phase. Detailed noninvasive measurements of local characteristics of the hydrodynamics are required to improve our understanding of multiphase flows and to validate the predictions of numerical models. Such information is not available using conventional measurement techniques. Tomographic imaging techniques can provide noninvasive measurements of the local phase fraction, velocity and composition. Such measurements can be used to develop new science-based approaches to modelling industrial-scale chemical reactors and therefore will lead to improved designs and increased efficiency of operation.

This chapter explores some recent studies of bubble column and trickle bed reactors using tomographic imaging techniques. The theoretical bases for these techniques are covered elsewhere in this book and therefore will not be further described here. This chapter focuses on describing some of the key properties of the two reactor types considered, and how tomographic techniques have been used to investigate these properties. Owing to the wealth of literature on the topic, this review cannot summarize all of the work in the area. The interested reader is referred to earlier reviews for further discussion of the importance of tomography in understanding multiphase reactors (Joshi, Tabib, Deshpande, & Mathpati, 2009; Al-Dahhan, Larachi, Dudoković, & Laurent, 1997; Boyer, Duquenne, & Wild, 2002; Chaouki, Larachi, & Dudukovic, 1997; Dudukovic, 2002; Dudukovic, 1999; Heindel, 2011; Mudde, 2010a; Reinecke & Mewes, 1996; Schubert, Bieberle, Barthel, Boden, & Hampel, 2011). The chapter concludes with an outlook for expected future developments of tomographic imaging in these systems and some sources of further information.

18.2 Bubble column reactors

Bubble column reactors consist of a vessel containing a liquid or a liquid–solid suspension with a gas distributor at the bottom. Gas is injected into the column through the distributor to form bubbles. A schematic illustration of a bubble column is shown in Figure 18.1. They are used throughout the chemical and biochemical industries especially for reactions involving oxidation, chlorination, alkylation, polymerization, hydrogenation, Fischer–Tropsch synthesis, fermentation and wastewater treatment. Bubble columns are an attractive choice owing to their excellent heat and mass transfer characteristics, low operating costs and durability of any solid material present (Kantarci, et al., 2005). A further advantage is the relative ease with which catalyst can be added or removed from the column. However, there are several significant challenges associated with using bubble column reactors.

One of the characteristics of industrial bubble column reactors is their large size. Bubble column reactors used for commodity products typically have a volume on the order of 100 m^3; when used as fermenters or in waste treatment applications, the volumes can be two orders of magnitude larger. Owing to the complex interaction of the gas and liquid phases, small changes in the column geometry, internals,

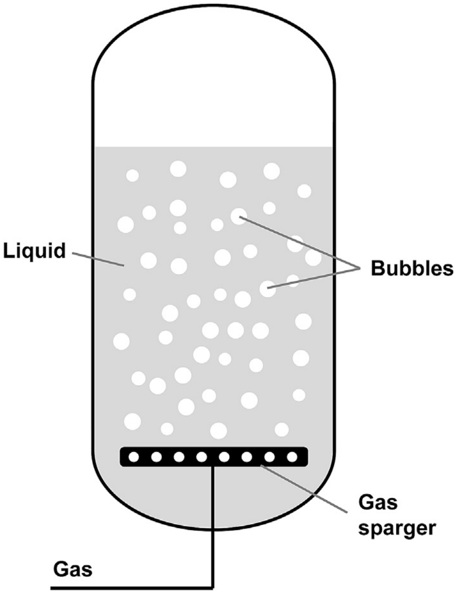

Figure 18.1 Schematic diagram illustrating a bubble column reactor. Gas enters the column through a gas distributor or sparger in the base of the column. Once in the column gas forms discrete bubbles that rise due to their buoyancy and induce motion of the continuous liquid phase.

distributor, gas flow rate and solid or liquid phase properties can lead to dramatic changes in the flow regime in a bubble column reactor. The scale of these systems and their sensitivity to the operating conditions makes accurate design and scale-up of bubble columns challenging. There is therefore a need to obtain measurements of the key parameters that determine the operation of bubble column reactors including local gas and liquid fraction, bubble size and gas and liquid velocity (Kantarci, et al., 2005). The following sections describe some of the advanced tomographic measurement techniques that are used to provide such measurements.

18.2.1 Fluid phase fraction measurements

Perhaps the simplest measurement obtainable from tomographic techniques is a local phase fraction or hold-up measurement. A variety of techniques have been used to characterize the hold-up including electrical capacitance tomography (ECT) (Bennett, West, Luke, Jia, & Williams, 1999; Cai, Shen, Shen, & Dai, 2010; Warsito & Fan, 2001, 2003; Warsito, Ohkawa, Kawata, & Uchida, 1999), electrical resistance tomography (Fransolet, Crine, Marchot, & Toye, 2005; Ishkintana & Bennington, 2010; Toye et al., 2005; Vijayan, Schlaberg, & Wang, 2007), ultrasonic tomography (Supardan, Masuda, Maezawa, & Uchida, 2007; Utomo, Warsito, Sakai, & Uchida, 2001; Warsito et al., 1999), X-ray or γ-ray computed tomography (CT) (Chen et al., 1998; Fischer & Hampel, 2010; Gulati, Behling, Munshi, Luke, & Mewes, 2010; Hubers, Striegel, Heindel, Gray, & Jensen, 2005; Nedeltchev, Shaikh, & Al-Dahhan, 2006, 2007; Ong, Gupta, Youssef, Al-dahhan, & Dudukovic, 2009; Patel & Thorat, 2008; Rabha, Schubert, & Wagner, 2013a,b; Rabha, Schubert, Wagner, Lucas, & Hampel, 2013; Shaikh & Al-dahhan, 2005); and magnetic resonance imaging (MRI) (Daidzic, Schmidt, Hasan, & Altobelli, 2005; Sankey, Yang, et al., 2009; Tayler, Holland, Sederman, & Gladden, 2012a). These measurements have been used to explore a variety of characteristics of bubble column reactor performance. Flow in bubble column reactors is divided into up to five different regimes including homogeneous, slugging, churn, semi-annular and annular flow (Spedding, Woods, Raghunathan, & Watterson, 1998). The hold-up in bubble column reactors is most frequently used to track changes in the flow regime; however, if the temporal and spatial resolution are sufficiently great, tomography can also be used to estimate the bubble size distribution and interfacial area, which are perhaps the most important characteristics required to predict the performance of a bubble column reactor.

CT techniques have high spatial resolution, but typically a low temporal resolution, and therefore have mostly been used to measure time-averaged voidage distributions (Chen, Kemoun, et al., 1999; Shaikh & Al-dahhan, 2005). CT techniques have been used to characterize changes in the flow structure from different sparger designs (Ong et al., 2009; Varma & Al-dahhan, 2007), internals (Chen, Kemoun, et al., 1999; Chen, Li, et al., 1999) and composition (Hubers et al., 2005; Patel & Thorat, 2008) and have also been explored as a means to characterize the flow regime using ideas from chaos analysis (Nedeltchev, 2009; Nedeltchev et al., 2006, 2007). However, these studies have been limited to time-averaged measurements owing to the long time taken to acquire conventional CT measurements.

An exciting development of CT techniques has been the advent of fast CT scanners (Bieberle & Hampel, 2006; Mudde, Alles, Hagen, & Van Der, 2008). The ultrafast electron beam X-ray tomography system developed in Dresden promises to be particularly beneficial for high resolution, dynamic imaging (Bieberle & Hampel, 2006; Bieberle, Barthel, Menz, Mayer, & Hampel, 2011; Bieberle et al., 2010; Bieberle et al., 2007; Fischer & Hampel, 2010). This facility is used to obtain two-dimensional images at a rate of up to 7000 frames/s with a spatial resolution of about 1 mm, though in practice a slower frame rate is often used owing to the large quantity of data produced (Rabha et al., 2013a, 2013). Figure 18.2 shows an example of the quality of data that can be produced using this facility (Rabha et al., 2013). A clear demarcation between the gas and liquid phases is obtained. The measurements have been used to extract an apparent bubble size distribution and interfacial area distribution — both of which are key parameters required to predict the performance of bubble column reactors. In this case, solids were also present in the flow, though these are not resolved as the particles were smaller than the resolution of the scanner. Figure 18.2 shows a clear change in the flow regime as the solid fraction increases from 0.05 through to 0.36, with significantly fewer and larger bubbles being found at higher solid fractions. Such a change in flow regime is consistent with the solid particles acting to stabilize the gas—liquid interface leading to a reduction in the break-up of bubbles. However, it is known that the presence of solids can lead to either an increase or decrease in bubble size. Measurements such as those obtained by Rabha et al. (2013) provide detailed information on the void structure and will

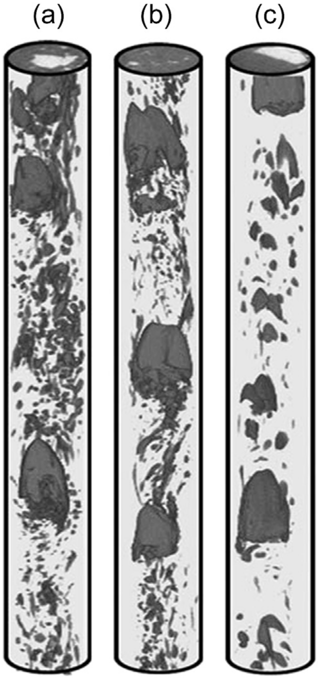

Figure 18.2 Ultrafast X-ray images of bubbles in a slurry bubble column. Images shown are a virtual projection of the pseudo-three-dimensional gas phase structure obtained from a time series of two-dimensional images of the cross-section of the column. The images shown were obtained for an air–water mixture at a superficial gas velocity of 0.05 m s^{-1} at a height of 950 mm above the distributor. The water contained spherical glass particles at concentrations of (a) 0.05, (b) 0.10 and (c) 0.36.

Adapted from Rabha, S., Schubert, M., Wagner, M., Lucas, D., Hampel, U. (2013c). Bubble size and radial gas hold-up distributions in a slurry bubble column using ultrafast electron beam X-ray tomography. *American Institute of Chemical Engineers Journal*, *59*, 1709–1722. doi: 10.1002/aic. Copyright © 2012 American Institute of Chemical Engineers (AIChE).

in the future lead to more advanced models of bubble size, coalescence and break-up than has hitherto been possible. Already these measurements are being used to test CFD simulations of two-phase flow (Rabha, et al., 2013b). However, a particular strength of this facility is that it will be integrated into the TOPFLOW facility at Dresden (Fischer & Hampel, 2010), which will permit the characterization of flows at up to 7 MPa and 286 °C (Prasser et al., 2006). Such measurements will provide invaluable data for improving our understanding of bubble column reactor hydrodynamics at industrially relevant conditions. One limitation of this ultrafast X-ray system is the diameter of the column that can be studied. This limitation has been partially overcome by the design used in TUDelft (Mudde, 2010b), though the increase in scale that is achievable comes at the cost of a decrease in the spatial and temporal resolution. The system at TU Delft has been extensively used to study gas–solid fluidised beds, but has not yet been applied to study bubble column reactors.

MRI presents another promising technique for the characterization of bubble column reactors (Daidzic et al., 2005; Sankey et al., 2009b; Tayler et al., 2012a). Conventional MRI is too slow to resolve the structure of gas—liquid flows and thus was initially confined to time-averaged measurements (Daidzic et al., 2005; Sankey et al., 2009b). Ultrafast MRI techniques such as EPI (Stehling, Turner, & Mansfield, 1991) are available; however, they are sensitive to turbulent motion in the fluid phase and therefore are not well suited to study gas—liquid flows. However, recently spiral MRI techniques have been adapted to study gas—liquid flows (Tayler et al., 2012a, 2011) at a spatial resolution of ~500 μm and a temporal resolution of 55 frames/s. The spatial resolution of these images has since been further increased through the introduction of compressed sensing (Tayler, Holland, Sederman, & Gladden, 2012b), which is a new image reconstruction approach recently adapted to MRI measurements of multiphase flow (Holland, Malioutov, Blake, Sederman, & Gladden, 2010). Spiral MRI is advantageous as it is robust to motion artefacts and therefore can be used to provide quantitative measurements of the bubble size distribution in bubble columns for a gas hold-up of up to 0.2, and potentially higher using compressed sensing (Tayler et al., 2012a). MRI measurements of bubbles columns were used to explore the variation in bubble size distribution and interfacial area with radial and axial position in the column. A particular advantage of MRI-based imaging is that it is possible to acquire a two-dimensional image at any orientation. Thus, Tayler et al. (2012a) demonstrate the acquisition of vertical images in the centre of a bubble column and use these to study bubble break-up and coalescence. In the future, measurements such as these will be used to derive kernel functions for the population balance models used to simulate industrial bubble column reactors. Although spiral MRI shows significant promise for characterizing bubble columns, there are some limitations. MRI generally requires the use of a superconducting magnet and therefore is restricted typically to columns <50 mm in diameter. An interesting approach that could potentially overcome this limitation is the use of Bayesian analysis (Holland, Blake, Tayler, Sederman, & Gladden, 2012, Holland, Blake, Tayler, Sederman, Gladden, 2011). This approach has been shown to provide measurements of the bubble size distribution in a bubble column from very simple measurements. Further, the technique has been adapted for use on a low-field permanent magnet system for characterizing the grain size distribution in rock samples at a resolution an order of magnitude or more better than could be achieved with conventional MRI techniques (Holland, Mitchell, Blake, & Gladden, 2013). In the future such an approach could be used with other low-field instrumentation, for example (Leblond, Javelot, Lebrun, & Lebon, 1998), to permit the measurement of bubble size distributions under conditions of relevance to industrial bubble columns.

Industrial process tomography requires sensors that can be operated on large-scale processes and under industrially relevant conditions. MRI and ultrafast X-ray measurements are typically limited to small-scale systems (perhaps <50 mm diameter) and relatively benign conditions. Whilst some progress is being made to overcome these limitations as noted above, perhaps a more promising approach for industrial process monitoring is to use the electrical and ultrasonic tomography techniques. ECT and ERT have both been used to study bubble column systems for some time. An early

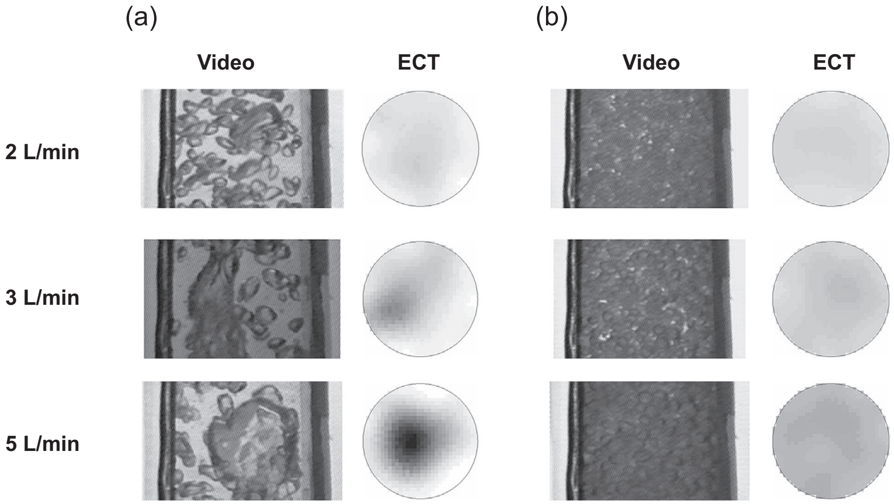

Figure 18.3 These images show a comparison of high speed video (left) and electrical capacitance tomography measurements (right) of gas—liquid flow when the liquid has either (a) no surfactant or (b) 32 ppm of a surfactant frother. In the absence of the surfactant, the column undergoes a regime transition where large bubbles or slugs are formed at high gas flow rates. The presence of the surfactant ensures a homogeneous flow regime and no large bubbles are formed regardless of the flow rate.
Adapted from Bennett, M. A., West, R. M., Luke, S. P., Jia, X., Williams, R. A. (1999). Measurement and analysis of flows in a gaseliquid column reactor. *Chemical Engineering Science,* 54, 5003—5012 with permission.

example is the work of Bennett et al. (1999) who were able to distinguish between churn flow and homogeneous flow by comparing the differences between ECT measurements of a gas—water flow with and without a surfactant present, as shown in Figure 18.3. In their work, the homogeneous flow produced in the presence of the surfactant resulted in a uniform decrease in the permittivity throughout the tomogram as the gas fraction increased. By contrast, when no surfactant was present, large bubbles and slugs were formed that were visible in the tomograms. Similarly, Fransolet et al. (2005) observed a transition from homogeneous flow with small bubbles through to heterogeneous flow with large bubbles as the viscosity of the water was increased through the addition of xanthan gum.

In general, ECT, ERT and ultrasonic tomography techniques are all characterized by a relatively low spatial resolution. Therefore, the major benefit of these types of tomographic imaging techniques is in the extension to larger-scale processes, industrial process conditions and the characterization of macroscopic heterogeneity arising from, for example, sparger malfunctioning, drift in operating conditions or flow regime transitions. Full-scale industrial processes are still challenging to access with these techniques owing to limitations of signal to noise and practicality, though several studies of pilot-scale facilities have been presented (Wang, Dorward, Vlaev, & Mann, 2000; Wang, Marashdeh, Fan, & Warsito, 2010). Linear sensor arrays have

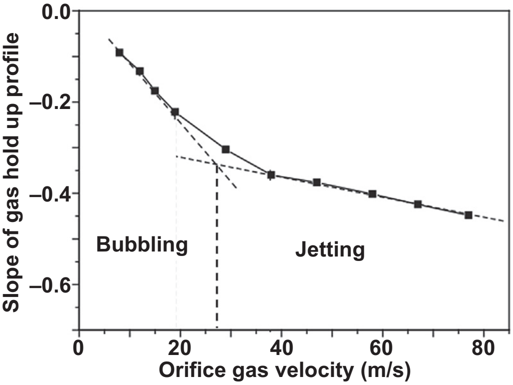

Figure 18.4 Electrical capacitance tomography measurements near a single orifice distributor show linear increases in the gas hold-up profile as the orifice velocity increases, within a single flow regime. However, a clear change in the slope of the gas hold-up curve occurs as the flow transitions from bubbling to jetting.
Adapted from Cai, Q., Shen, X., Shen, C., Dai, G. (2010). A simple method for identifying bubbling/jetting regimes transition from large submerged orifices using electrical capacitance tomography (ECT). *Canadian Society for Chemical Engineering,* 88, 340−349. Copyright © 2010 Canadian Society for Chemical Engineering.

been proposed to permit measurements on full-scale processes (Schlaberg et al., 2006); however, these have not yet been applied to study bubble column reactors. One interesting study of bubble column reactors using electrical tomography mapped the transition from bubbling to jetting at an orifice (Cai et al., 2010). In this case, the local void fraction and the standard deviation of the void fraction were shown to be linearly related to the gas flow rate in both the bubbling and jetting flow regimes, as shown in Figure 18.4. However, a sharp transition in the slope of this relationship was exhibited, indicating a simple mechanism for characterizing the change in flow regime. Measurements such as these potentially provide a model for future exploitation of the robustness of these industrial process tomography sensors. For example, measurements of the local void fraction might be obtained using small electrodes located in the vicinity of the object of interest, for example, the nozzle. The limiting case of this approach could perhaps be considered to be the wire mesh sensor.

Wire mesh sensors consist of a network of wires that are placed inside the column to be imaged (Prasser, Böttger, & Zschau, 1998). Initially, the conductivity of the fluid between pairs of these wires was measured; however, more recently measurements of the local capacitance have also been used (Silva, Da, Schleicher, & Hampel, 2007). Wire mesh sensors are advantageous as they are robust and can readily be applied to study systems at high pressure and temperature (Pietruske & Prasser, 2007). Wire mesh sensors also do not require the solution of an ill-posed, nonlinear inverse problem, as is required for other electrical tomography techniques. Of course, the disadvantage of wire mesh sensors is that they are inherently invasive, and therefore the application of these devices in certain processes may be problematic. The intrusive effects of wire mesh sensors have been studied by comparison with high speed camera measurements in transparent systems (Fuangworawong, Kikura, Aritomi, & Komeno, 2007; Ito, Prasser, Kikura, & Aritomi, 2011; Wangjiraniran et al., 2003). These studies revealed that the wire mesh can cause bubbles to break up and to either slow or accelerate, depending on the liquid velocity. However, despite this limitation, wire mesh sensors have been used successfully to study the transition between flow regimes, bubble size distribution, and bubble flow patterns (Fuangworawong et al., 2007; Lucas, Krepper, & Prasser, 2005; Pietruske & Prasser, 2007; Prasser, Krepper, & Lucas, 2002; Richter, Aritomi, Prasser, & Hampel, 2002; Wangjiraniran, Aritomi, Kikura, Motegi, & Prasser, 2005). Wire mesh sensors have also been used extensively in validation studies of other tomographic imaging techniques including ultrafast X-ray, ECT and ERT (Azzopardi et al., 2010; Olerni, Jia, & Wang, 2013; Prasser, Misawa, & Tiseanu, 2005).

Up to this point, the discussion has focused on the characterization of the distribution of the gas and liquid phases within the bubble column. In the following section, the discussion will consider a second critical parameter in the characterization of bubble column reactors, the velocity of each phase.

18.2.2 Fluid velocity measurements

Measurements of the velocity are more difficult to obtain than measurements of the voidage. Wire mesh sensors, ECT, ERT, radioactive particle tracking (known as computer-aided radioactive particle tracking, CARPT, or positron emission particle tracking, PEPT, depending on the exact technique used) and MRI have all been used to measure the velocity of one or both phases in bubble column reactors.

Wire mesh sensors, ECT and ERT have been used to obtain measurements of the velocity of the discrete phase (Gumery, Ein-Mozaffari, & Dahman, 2011; Jin, Wang, & Williams, 2007; Richter et al., 2002; Warsito & Fan, 2003). In these examples, the distribution of the two phases is measured by sensors separated by a known distance. A cross-correlation of the phase fraction is obtained from a time series of images, and from this the time-averaged velocity distribution is obtained. Wang et al. (2006) modified the standard cross-correlation approach by calculating a 'best-correlated' pixel to allow for the transverse motion of the bubbles in between the two measurement planes. This approach was validated using point measurements obtained with a four-sensor ERT probe and enabled the measurement of the horizontal velocity in a swirling pipe flow. Jin et al. (2007) validate the cross-correlation approach by comparison of estimates of the bubble velocity from ERT and a drift-flux model. Their results demonstrate excellent agreement, provided that the bubble column is operated in a regime consisting of relatively isolated swarms of bubbles, that is, below the transition to slugging flow. However, these techniques are not sensitive to the motion of the continuous phase. Such a limitation can be overcome through the introduction of a tracer molecule (Gumery et al., 2011; Hamood-ur-rehman, Dahman, & Ein-mozaffari, 2012), although this increases the invasiveness of the measurement.

An alternative method of tracking the motion of the continuous phase is to use radioactive particle tracking. These techniques measure the flow field by tracing the position of a single radioactive tracer particle over time. By assuming ergodicity, that is that a long time average of a single particle is equivalent to a spatial average of many particles, and that the motion of the tracer particle is determined by the motion of the continuous phase, it is then possible to extract a map of the distribution of the velocity of the continuous phase (Chen, Kemoun, et al., 1999; Karim, Varma, Vesvikar, & Al-dahhan, 2004; Rados, Shaikh, & Al-Dahhan, 2005; Upadhyay, Pant, & Roy, 2013; Varma & Al-dahhan, 2007). A benefit of these radioactive particle tracking techniques is that they are capable of measuring the velocity and velocity fluctuations of the continuous phase of opaque flows at high pressure and temperature, and thus are able to probe operations at industrially relevant conditions (Karim et al., 2004; Rados et al., 2005). Such experiments have proven particularly beneficial when combined with CT measurements of the same system, as in this case it is possible to extract both time-averaged density and velocity information. In one study, CARPT and CT were combined to examine the effect of changing the gas distribution in an airlift bioreactor (Varma & Al-dahhan, 2007). These measurements demonstrate that a multi-orifice distributor improves the gas distribution, as expected. However, in addition, the multi-orifice distributor was found to provide enhanced liquid recirculation for the same power input and therefore improved mixing. CARPT and CT have also been combined to demonstrate the importance of tomographic measurements for scale-up studies. Shaikh and Al-dahhan (2010) studied bubble columns operating in the same flow regime and with similar overall hold-up, but with different radial distributions of the hold-up as measured by CT. CARPT was then used to study the mixing patterns in the bubble columns. Shaikh and Al-dahhan demonstrate that when the radial distribution of the hold-up is the same, similar mixing patterns are established and the columns exhibit hydrodynamic similarity. However, when the radial distribution of the hold-up is not consistent, the mixing patterns are also dissimilar and the reactors are not hydrodynamically similar, even though the overall hold-up and flow regime are similar. These results demonstrate the need for detailed tomographic measurements of multiphase flows in order to develop fundamental scale-up criteria for bubble column reactors.

One disadvantage of radioactive particle tracking techniques for measuring the velocity is that it is necessary to assume that the long-time-averaged motion of the tracer particle provides an accurate estimate of the map of the time-averaged velocity in the continuous phase. This approximation is likely valid in most situations. However, in a bubble column it is possible that the particle may become trapped at the interface of the gas and liquid and therefore travel with the discrete phase for a period of time. The long-time-averaged velocity of the tracer particle may then represent a combination of the velocity of the continuous and discrete phases.

MRI is able to measure the motion of the continuous phase directly, overcoming any limitations associated with the long time average required for CARPT. In early work, such measurements were confined to obtaining the time average of the liquid velocity (Sankey et al., 2009b). However, recently the adaptation of spiral MRI to study gas−liquid flows has enabled the characterization of the liquid velocity at an acquisition rate of up to 188 frames per second (Tayler et al., 2012a; Tayler, Holland, Sederman, & Gladden, 2012b, 2011). Figure 18.5 provides an example of an MRI

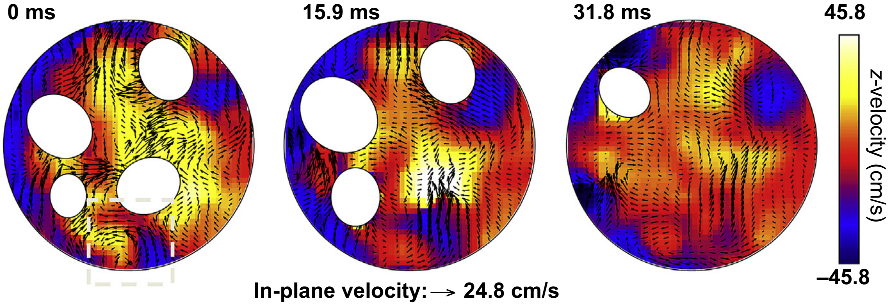

Figure 18.5 MRI measurements of the velocity of the water around freely rising air bubbles. The grey-scale gives the through-plane velocity, whilst the arrows indicate the direction and speed of the in-plane velocity. Three-component velocity images were acquired at a rate of 63 frames per second and a spatial resolution of 390 × 390 μm.
Adapted from Tayler, A. B., Holland, D. J., Sederman A. J., Gladden L. F. (2012). Exploring the origins of turbulence in multiphase flow using compressed sensing MRI. *Physical Review Letter,* 108, 264505.

image of the liquid velocity distribution in a bubble column (Tayler et al., 2012b). These images were obtained at a rate of 188 frames per second for each velocity component, or 63 frames per second for all three velocity components. The measurements were used to study the onset of turbulence in the continuous liquid phase in bubble columns. It is well known that rising gas bubbles can lead to the formation of turbulent structures in multiphase flows (Balachandar & Eaton, 2010), and indeed this is one of the reasons why bubble columns are desirable as industrial reactors as it leads to high heat and mass transfer. However, it is still unclear how this turbulence arises and is difficult to simulate numerically. Tayler et al. (2012b) used MRI to measure the velocity in the wake of single and multiple rising bubbles. They demonstrated that the formation of a pair of secondary vortices in the wake of a single bubble drives the horizontal motion of the bubble as it rises. When multiple bubbles rise together, these vortices were observed to join together to form ‘vorticity chains’: large-scale structures that extend over multiple bubble-length scales. These vorticity structures are hypothesized to be significant in the formation of multiphase induced turbulence.

The research described above presents an introduction to some of the measurements of bubble column reactors performed using tomographic imaging techniques. Low-resolution measurements of the local phase fraction have been obtained using CT, MRI and electrical tomography techniques, as well as direct imaging of the individual bubbles using high speed CT, MRI and wire mesh sensors. Measurements of the velocity of the discrete phase have been obtained using electrical tomography, ultrafast CT and MRI, whilst radioactive particle tracking and MRI have been used to measure the velocity of the continuous phase. These measurements characterize the key parameters of bubble column reactors and hence will lead to improved design and operation of industrial reactors. The potential for tomography to influence reactor design and modelling will be discussed further below.

18.3 Trickle bed reactors

Trickle bed reactors consist of a vessel filled with solid catalyst particles over which gas and liquid flow. In classic trickle bed operation, the gas and liquid flow co-currently downward over the particles; however, upward flow of the gas or both liquid and gas is also used. A schematic illustration of a trickle bed reactor is shown in Figure 18.6. Trickle bed reactors are used throughout the chemical industry, but especially for hydrogenation and oxidation reactions in the petrochemicals industry. A recent high-profile example of the use of a trickle bed reactor is at the Pearl Gas-to-Liquid plant that recently came online in Ras Laffan, Qatar. Trickle beds are attractive reactors as liquid flow patterns tend to produce high conversions, catalyst losses are minimal, they can be operated at high temperature and pressure, and are scaled up with relative ease. However, there are also several drawbacks of trickle bed reactors. For example, the catalyst effectiveness in trickle bed reactors is low owing to the large particle size needed to achieve a reasonable pressure drop, liquid maldistribution can lead to decreased performance, side reactions can lead to fouling, and heat transfer is

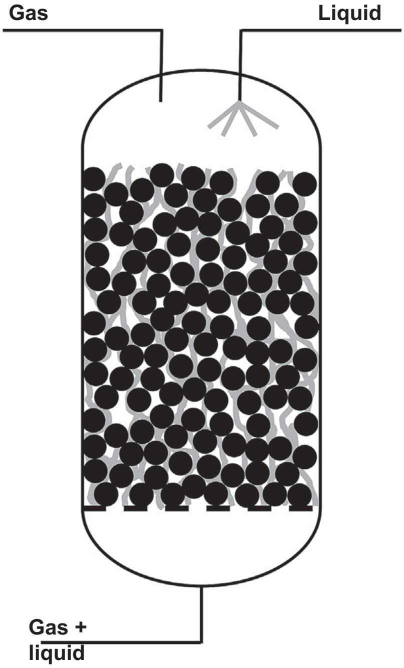

Figure 18.6 Schematic diagram of a trickle bed reactor. Gas and liquid enter the column at the top and flow co-currently over a fixed bed of solid particles. The solid particles typically contain a catalyst, and the reaction between the gas and liquid occurs inside the particles. A two-phase mixture containing the products and any unreacted material is withdrawn from the bottom of the column. Gas and liquid flow may be stable or unstable depending on the operating conditions of the reactor.

poor (Gianetto & Specchia, 1992). Industrial trickle bed reactors tend to be large, on the order of 10-m diameter. However, scale-up of these reactors can be achieved using parallel small diameter columns contained in a single process vessel and hydrodynamic features tend to be dominated by particle-scale phenomena that are largely scale invariant. As a result, the challenge for tomographic measurements of trickle bed reactors is not so much to determine how best to scale up these reactor designs but rather to identify how to operate the reactors most efficiently, regardless of scale. Research has tended to focus on either hydrodynamic studies in cold-model trickle beds or on the interaction of operating conditions with the chemical conversion.

18.3.1 Hydrodynamic studies

MRI measurements of trickle bed reactors have proven beneficial owing to the high spatial and temporal resolution that can be achieved (Anadon, Sederman, & Gladden, 2006; Gladden et al., 2010; Gladden, Lim, Mantle, Sederman, & Stitt, 2003; Sederman & Gladden, 2001, 2005). MRI can extract the distribution of gas and liquid within the three-dimensional structure of the packing. These measurements provide quantitative, local measurements of the hold-up, wetting efficiency and velocity (Gladden et al., 2003, 2010; Sankey, Holland, Gladden, & Sederman, 2009). MRI is particularly valuable for dynamic studies of, for example, the transition from trickle to pulsing flow. Using real-time measurements of the liquid hold-up in a trickle bed, Anadon et al. (2006) were able to identify the characteristics of the onset of the pulsing regime. Figure 18.7 shows an example of 3D images of the standard deviation of the liquid distribution as a function of increasing liquid flow rate. At low liquid flow rates, the bed is stable with a uniformly low standard deviation. As the liquid flow rate increases, isolated pulsing events occur at the pore scale. As the liquid flow rate increases further, these isolated events merge until the entire cross-section of the bed is pulsing. Thus, the transition to pulsing flow occurs over a range of flow rates. In a subsequent study, they compared MRI results with measurements of the pressure and conductance in a trickle bed (Anadon, Sederman, & Gladden, 2008). These results demonstrate that conductance identifies the onset of the macroscopic pulsing regime, whereas pressure fluctuations are sensitive to the onset of isolated pulsing and the point at which the maximum number of liquid pulses occurs. Together, conductance and pressure fluctuations were able to fully characterize the transition from trickle to pulsing flow. Thus, using insights from MRI they demonstrate that an accurate characterization of the transition from trickle to pulsing flow can be obtained using conventional instrumentation, such as could be installed on many industrial trickle bed reactors.

Hydrodynamic effects have long been known to affect the chemical conversion in trickle bed reactors. One approach that has been proposed to improve the performance of a trickle bed reactor is to operate in a periodic regime, whereby the flow rate of the gas or liquid feed is increased periodically (Silveston, Hudgins, & Renken, 1995). Numerical models have been presented to describe this periodic operation (Dietrich, Grünewald, & Agar, 2005; Kouris, Neophytides, Vayenas, & Tsamopoulos, 1998); however, such models require an accurate description of the dynamic behaviour of flow of liquid and gas over the catalyst particles. MRI studies of periodic operation

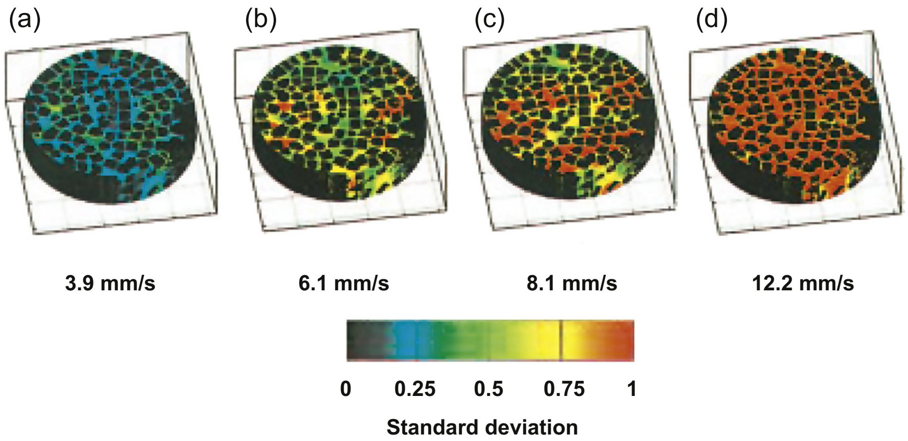

Figure 18.7 MRI measurements of the transition from stable, trickle flow to pulsing flow in a trickle bed reactor. Pulsing events are identified by the change in signal intensity in the pixels within the images over time. To characterize the change in intensity, the standard deviation of the liquid intensity is shown. Bright colours correspond to higher standard deviation and hence more unstable flow. For these images, a transition from stable to pulsing flow occurs as the liquid velocity is increased from 3.9 mm/s to 12.2 mm/s at a fixed gas velocity of 300 mm/s. The height of the bed section shown is 9 mm.

Adapted from Anadon, L. D., Sederman, A. J., Gladden, L. F. (2006). Mechanism of the trickle-to-pulse flow transition in fixed-bed reactors. *American Institute of Chemical Engineers Journal*, 52, 1522–1532. Copyright © 2005 American Institute of Chemical Engineers (AIChE).

demonstrate that periodic operation leads to a heterogeneous distribution of liquid contacting in the pores of the reactor (Anadon, 2006; Lim, Sederman, Gladden, & Stitt, 2004). Anadon (2006) was able to identify three characteristic pore-scale draining events, each of which was associated with a number of different time scales for the draining events. Using the experimentally measured heterogeneity of the liquid contacting, reactor models can be used to explore changes in operation to improve reactor performance. In one study, the reaction rate was demonstrated to almost double if the distribution of pores that rapidly fill and empty could be increased (Dietrich, Anadon, Sederman, Gladden, & Agar, 2012). These results demonstrate the importance of understanding the local hydrodynamic phenomena, or mesoscale structure, in order to predict the overall behaviour of the reactor.

One drawback of MRI measurements of trickle bed reactors is that they are restricted to narrow diameter columns made of nonconducting materials. Thus, the application of MRI to reactors with metallic internals has been challenging. X-ray and γ-ray CT are potentially advantageous in this regard (Bazer-Bachi, Haroun, Augier, & Boyer, 2013; Bieberle et al., 2013; Boyer & Fanget, 2002; Schubert et al., 2011). CT techniques have also been used in an analogous manner to the MRI techniques discussed above to characterize the distribution of gas and liquid in structured packing materials such as Katapak-SP 12 (Aferka, Crine, Saroha, Toye, & Marchot, 2007) and Mellapak 752Y (Roy et al., 2005). These measurements provide

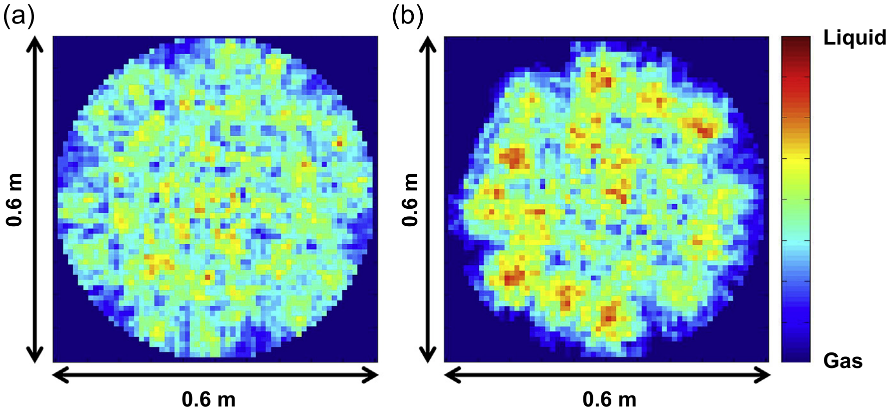

Figure 18.8 γ-Ray tomography measurements of the distribution of liquid in a trickle bed reactor with (a) tray or (b) gas-lift distributor designs. The liquid phase was heptane and the gas phase was nitrogen and the column was operated at low pressure (0.1—0.4 bar gauge) and room temperature. The images are shown for a superficial liquid velocity of 2 mm/s and a superficial gas velocity of 20 mm/s.

Adapted with permission from Bazer-Bachi, F., Haroun, Y., Augier, F., Boyer, C. (2013). Experimental evaluation of distributor technologies for trickle-bed reactors. *Industrial and Engineering Chemical Research* 52, 11189—11197. Copyright 2013 American Chemical Society.

the specific surface area and gas/liquid interfacial area within the packing materials. CT techniques have also been used to explore the distribution of liquid at the entrance of packed bed columns and catalytic beds (see e.g. Bazer-Bachi et al., 2013; Fourati, Roig, & Raynal, 2012; Kalaga et al., 2009; Merwe, Nicol, & Beer, 2007; Roy et al., 2005 and references therein). For example, Figure 18.8 illustrates the distribution of liquid in a trickle bed reactor of diameter 0.6 m with two types of distributors: a chimney tray with deflectors and a gas-lift distributor. Commercial literature suggests that gas-lift distributors are beneficial for achieving a homogeneous distribution of liquid in the trickle bed. However, the experimental measurements shown in Figure 18.8 indicate that the chimney tray gives superior liquid distribution, with no obvious bias of the liquid flow in the vicinity of the drip points.

Although CT techniques can potentially be used on large, metallic vessels, typical CT hardware systems are difficult to apply to industrial processes owing to the hazards of ionizing radiation and the bulk and power requirements of the source of radiation. Therefore, instruments used to study industrial processes typically obtain only very limited measurements and do not reconstruct entire images. However, Kuzeljevic, Dudukovic, and Stitt (2011) note that industrial measurements require only simple diagnostic information, and that such information can be extracted from far fewer measurements than a complete tomographic reconstruction would require. Thus, even these relatively simple devices can provide significant insight into optimizing the operation of industrial reactors. Alternatively, it is possible to devise portable CT systems that can achieve relatively high spatial resolution and full tomographic reconstructions, though these may have other restrictions regarding the size of the equipment on which they can be applied (Bieberle et al., 2013; Kim et al., 2012).

Electrical tomography techniques have also proven beneficial for studying trickle bed reactors owing to the high time resolution that can be achieved (Bieberle et al., 2010; Häfeli, Hutter, Damsohn, Prasser, & Rudolf von Rohr, 2013; Llamas et al., 2008; Matusiak, Jose, Hampel, & Romanowski, 2010; Reinecke & Mewes, 1997). Measurements of the conductivity require the conductive phase to be continuous, which is not often the case in a trickle bed. For this reason, electrical measurements in trickle beds have primarily used invasive wire mesh sensors or capacitance measurements. Wire mesh sensors provide a higher spatial resolution than capacitance tomography measurements; however, they are invasive so not suitable for all applications. In one recent study, wire mesh sensors were compared with capacitance tomography (Matusiak et al., 2010). Both techniques were shown to yield very similar measurements of the average liquid hold-up and were able to identify macroscopic heterogeneity of the liquid distribution. Additionally, the wire mesh sensor was able to measure local variations in the liquid hold-up around individual particles. Such measurements demonstrate the potential for electrical tomography techniques to characterize flow within trickle bed reactors and indicate they will provide a valuable tool for testing models of these reactors in the future.

18.3.2 Reaction studies

One of the major challenges in optimizing the performance of trickle bed reactors is to understand the interplay between the chemical reaction kinetics and hydrodynamic phenomena. MRI is the only tomographic imaging technique that can be used to map the local chemical concentration, distribution of phases, and their velocity (Gladden et al., 2010; Lysova, Koptyug, & Weckhuysen, 2010). One of the first examples to demonstrate the importance of understanding the interaction of flow and reaction was a study of the liquid phase esterification of methanol and acetic acid (Yuen, Sederman, & Gladden, 2002). Previous work had illustrated that the velocity of fluid flowing through a fixed bed reactor does not follow an ideal plug flow model, but rather that there are variations in the local fluid velocity of up to an order of magnitude (Sederman, Johns, Alexander, & Gladden, 1998). However, it had been assumed that dispersion over the length of the reactor would lead to a relatively homogeneous distribution of concentration. The study of Yuen et al. (2002) showed fractional variations in the steady-state conversion of approximately 20% arising from the heterogeneity in flow. This study was for single-phase flow in a fixed bed reactor; however, similar effects are expected in trickle bed reactors as well.

In the past, MRI studies of catalytic reactors have largely been confined to reactions that can be performed at close to ambient conditions. However, recently there has been a move toward studying reactions at conditions of industrial relevance (Gladden et al., 2010; Koptyug, Khomichev, Lysova, & Sagdeev, 2008). ^{13}C NMR has been used to explore changes in selectivity and conversion in trickle bed reactors operating at up to 5 barg and 120 °C (Akpa, Mantle, Sederman, & Gladden, 2005;

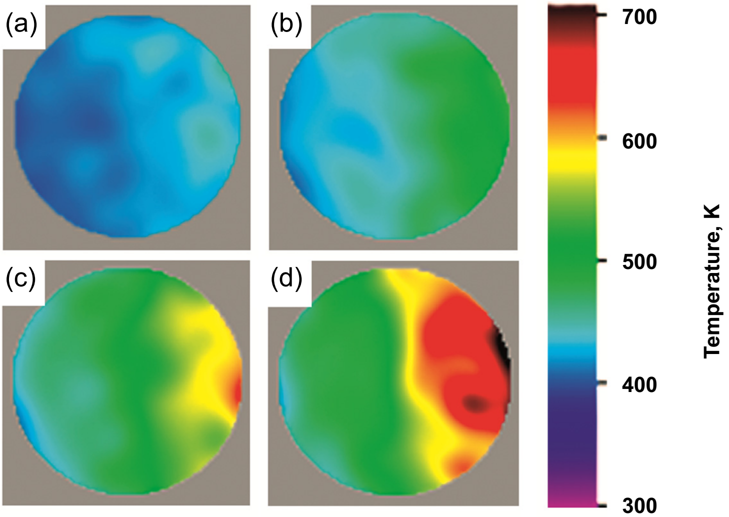

Figure 18.9 MRI measurements of the temperature of a catalyst pellet during oxidation of H_2. The temperature of the catalyst was obtained from the ^{27}Al NMR signal intensity, which is a function of the local temperature of the pellet. Images were detected for hydrogen flow rates of (a) 0.8, (b) 1.4, (c) 2.0, and (d) 2.5 mL/s.

Adapted from Lysova, A.A., Kulikov, A. V, Parmon, V.N., Sagdeev, Z., Koptyug, I. V. (2012). Quantitative temperature mapping within an operating catalyst by spatially resolved 27Al NMR. *Chemical Communication* 48, 5763–5765 with permission from The Royal Society of Chemistry.

Gladden et al., 2010; Sederman, Mantle, Dunckley, Huang, & Gladden, 2005). Koptyug et al. have developed NMR thermometry techniques to permit the quantification of the temperature of catalyst pellets during reaction (Koptyug et al., 2008; Koptyug, Sagdeev, Gerkema, Van As, Sagdeev, 2005; Lysova, Kulikov, Parmon, Sagdeev, & Koptyug, 2012). For example, Figure 18.9 shows the temperature distribution in a Pt/γ-Al_2O_3 catalyst pellet when contacted on one side with a mixture of hydrogen and air. The temperature in this system approached 700 K, whilst a temperature difference of up to 150 K was observed across the catalyst pellet. These studies represent a significant advance in our ability to study phenomena occurring inside chemical reactors at industrially relevant conditions.

Recently, the conditions at which reactions can be monitored have been pushed even further with the introduction of a novel reactor designed to operate within an MRI system at up to 350 °C and 30 barg (Roberts et al., 2013). This reactor system opens entirely new possibilities for MRI measurements of trickle bed reactors including studies of, for example, the effect of catalyst formulation and operating conditions on catalyst performance. In the first study reported using this reactor, MRI was used to study an ethene oligomerization reaction performed at 110 °C and 28 barg (Roberts et al., 2013). By monitoring the changes in the NMR spectrum, the authors were able to track the conversion and product distribution within the operating reactor. In this system, the conversion of ethene was found to rapidly reach a steady value of around 6%; however, the product distribution was found to shift from a mixture of high-molecular-weight species at short times to a relatively narrow distribution of low-molecular-weight species with increasing time on stream. This change in product distribution may be related to a deactivation of the catalyst. In the future, measurements such as these will help design improved catalyst formulations and lead to new reactor start-up and catalyst reactivation processes.

The results discussed here present some of the detailed studies of the characteristics of trickle bed reactors that have been performed using tomography. CT, MRI and ECT have all been used to study the distribution of liquid and gas within trickle bed reactors, though CT and MRI are the only noninvasive techniques that are able to provide the high spatial resolution required to measure the liquid distribution around individual particles. MRI is the only technique that can provide direct measurements of the interaction of flow and reaction. The measurements presented above have already provided significant advances in our understanding of the operation of trickle bed reactors, for example, regarding the liquid distribution during periodic operation. The next section considers how these measurements will lead to further improvements in trickle bed reactor performance.

18.4 Future trends

The literature covered in the previous sections has demonstrated the significant potential for tomographic imaging techniques for studying bubble column and trickle bed processes. Tomographic techniques have been shown to provide detailed measurements of the local phase fraction and interfacial area, as well as the velocity distribution of both the continuous and discrete phases. Furthermore, various tomographic techniques have been cross-validated against each other to ensure that the measurements obtained are reliable. Thus, tomographic imaging is already influencing the design and operation of industrial-scale processes. Recently, tomographic imaging has begun to be applied at close to industrial conditions, which promises to provide another step change in our understanding of the phenomena that govern the operation of these complex reactors. In the future, such studies will likely influence the design of catalyst pellets, the composition of the reactant mixture and the geometry of the reactors themselves.

In addition to such fundamental studies, tomographic imaging techniques will also be used to develop computational models of industrial-scale reactors. As noted earlier, the design of industrial reactors has traditionally been based on correlations derived from measurements of the inlet and outlet of small-scale reactors and simple assumptions of the flow patterns in the reactor. Now, increasingly advanced computational fluid dynamic (CFD) models of reactors are being used to describe the flow patterns in more detail (Alopaeus, Hynynen, Aittamaa, & Manninen, 2006; Atta, Roy, & Nigam, 2007; Delnoij, Kuipers, & van Swaaij, 1997; Jiang, Khadilkar, Al-dahhan, & Dudukovic, 1999, 2002; Kuipers & van Swaaij, 1997; Kuzeljevic & Dudukovic,

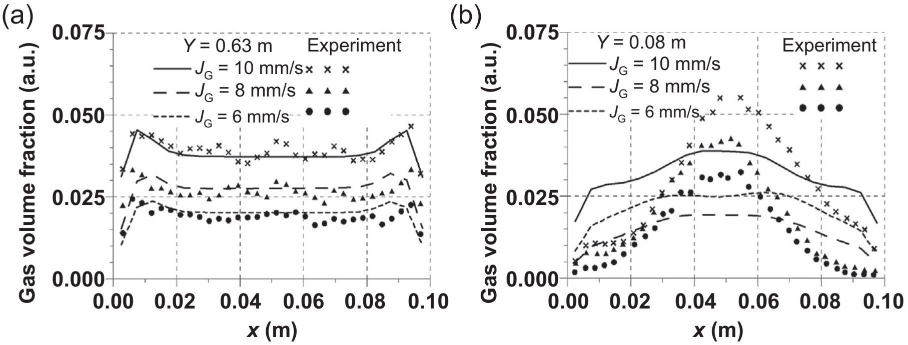

Figure 18.10 Profiles of the gas volume fraction are shown in a rectangular bubble column reactor (a) high in the column and (b) near the distributor. Gas volume fraction profiles are obtained from either experimental measurements using a wire mesh sensor or numerical simulations of the column. The gas was introduced through a stone sparger 0.02 m in width by 0.01 m in depth. The column was 0.10 m in width and 0.02 m in depth. Comparisons are shown for superficial gas velocities of 10, 8 and 6 mm/s.
This figure is adapted from Krepper, E., Reddy Vanga, B. N., Zaruba, A., Prasser, H.-M., Lopez de Bertodano, M. A. (2007). Experimental and numerical studies of void fraction distribution in rectangular bubble columns. *Nuclear Engineering Design* 237, 399–408 with permission.

2012; Lappalainen, Manninen, & Alopaeus, 2009; Lopes and Quinta-Ferreira, 2009; Mahr & Mewes, 2008); however, closure models are needed in these models to describe, for example, the interaction between fluid phases. Therefore, such simulations need to be validated before they can be used to design industrial systems with confidence (Dudukovic, 2010). Tomographic imaging techniques can provide the validation studies required for these CFD models (Atta, Hamidipour, Roy, Nigam, & Larachi, 2010; Atta, Schubert, Nigam, Roy, & Larachi, 2010b; Bazmi, Hashemabadi, & Bayat, 2012; Boyer, Koudil, Chen, & Dudukovic, 2005; Gunjal, Kashid, Ranade, & Chaudhari, 2005; Hamidipour, Chen, & Larachi, 2013; Krepper, Reddy Vanga, Zaruba, Prasser, & Lopez de Bertodano, 2007; Lopes & Quinta-Ferreira, 2010; Lopes, Quinta-ferreira, & Larachi, 2012; Rabha et al., 2013b; Robbins, El-bachir, Gladden, Cant, & von Harbou, 2012). In one of these studies, summarized in Figure 18.10, an Euler–Euler computational model was compared with wire mesh sensor measurements of the time-averaged voidage in the bubble column (Krepper et al., 2007). The computational model was shown to describe the distribution of the average voidage accurately high in the column, where the fluid phase turbulence was not too severe. The model was even able to predict the sharp rise in void fraction at the wall that was seen experimentally. However, in the region near the distributor, the model performed poorly, significantly underestimating the heterogeneity of the voidage distribution. The poor performance of the model near the distributor was attributed to the simple turbulence model used in the numerical study. These results highlight the need to incorporate detailed turbulence models for the fluid phase when predicting the dynamics of bubble column reactors. Advanced measurement techniques are now becoming available that will permit the direct characterization of the closure models required to describe some of the phenomena occurring in these systems. For example, in a recent MRI study, simultaneous measurements of the gas and liquid velocity distribution in a trickle bed reactor have been presented (Sankey, Holland, et al., 2009). Such measurements will provide a means for testing directly the assumptions that underpin the closure models used for gas–liquid interaction in trickle bed reactors (Attou, Boyer, & Ferschneider, 1999; Iliuta, Larachi, & Al-Dahhan, 2000; Iliuta, Larachi, & Grandjean, 1998; Sáez & Carbonell, 1985). Future developments of numerical models of bubble column and trickle bed reactors will depend on detailed experimental investigations, such as those described above, in order to establish the correct methods for modelling these complex systems.

18.5 Sources of further information

The literature cited in this chapter primarily focuses on recent publications. Significant publications describing tomographic imaging of bubble column and trickle bed reactors are not included here as they have been included in earlier review articles (Al-Dahhan, et al., 1997; Boyer et al., 2002; Chaouki et al., 1997; Dudukovic, 2002; Dudukovic et al., 1999; Heindel, 2011; Mudde, 2010a; Reinecke & Mewes, 1996; Schubert et al., 2011a). The reader is referred to these articles and the references contained therein for further information. Additionally, the articles cited within this chapter contain relevant background information; the reader is encouraged to explore these for further information.

For details of the fundamental principles of the tomographic techniques discussed in this chapter, the reader is referred to the earlier chapters in this book, as well as the seminal text by Williams, and Beck entitled *Process Tomography: Principles, Techniques and Applications*. Butterworth Heinemann, 1995.

For further information regarding the fundamentals of the operation of bubble column and trickle bed reactors and how to estimate the performance of these, the reader is referred to the following material:

Akita, K., & Yoshida, F. (1974). Bubble size, interfacial area, and liquid-phase mass transfer coefficient in bubble columns. *Industrial & Engineering Chemistry Process Design and Development*s, 13(1), 84–91.

Al-Dahhan, M., Larachi, F., Duduković, M. P., & Laurent, A. (1997). High-pressure trickle-bed reactors: a review. *Industrial & Engineering Chemistry Research*, 36(8), 3292–3314.

Deckwer, W. (1992). *Bubble column reactors*. Chichester: Wiley.

Gianetto, A., & Specchia, V. (1992). Trickle-bed reactors: state of art and perspectives. *Chemical Engineering Science*, 47, 3197–3213.

Kantarci, N., Borak, F., & Ulgen, K. O. (2005). Bubble column reactors. *Process Biochemistry*, 40(7), 2263–2283.

Satterfield, C. N. (1975). Trickle-bed reactors. *American Institute of Chemical Engineers Journal*, 21(2), 209–228.

Shah, Y. T., Kelkar, B. G., Godbole, S. P., & Deckwer, W.-D. (1982). Design parameters estimations for bubble column reactors. *American Institute of Chemical Engineers Journal*, 28(3), 353–379.

For details of the techniques available for numerical modelling of bubble column and trickle bed reactors, the reader is referred to the following material.

Deen, N. G., Mudde, R. F., Kuipers, J. A. M., Zehner, P., Kraume, M., 2010. *Bubble columns*. In: Ullmann's encyclopedia of industrial chemistry. Wiley Online Library.

Deen, N. G., van Sint Annaland, M., & Kuipers, J.A. M. (2004). Multi-scale modeling of dispersed gas–liquid two-phase flow. *Chemical Engineering Science*, 59(8–9), 1853–1861. doi:10.1016/j.ces.2004.01.038

Jakobsen, H. A. (2008). *Chemical reactor modeling* (vol. 3). Berlin, Heidelberg: Springer Berlin Heidelberg.

Joshi, J. B. (2001). Computational flow modelling and design of bubble column reactors. *Chemical Engineering Science*, 56, 5893–5933.

Kuipers, J. A. M., & van Swaaij, W. P. M. (1997). Application of computational fluid dynamics to chemical reaction engineering. *Reviews in Chemical Engineering*, 13, 1–118.

Rafique, M., Chen, P., & Duduković, M. P. (2004). Computational modeling of gas-liquid flow in bubble columns. *Reviews in Chemical Engineering*, 20, 225–375.

Sokolichin, A., Eigenberger, G., & Lapin, A. (2004). Simulation of buoyancy driven bubbly flow: established simplifications and open questions. *American Institute of Chemical Engineers Journal*, 50(1), 24–45.

References

Aferka, S., Crine, M., Saroha, A. K., Toye, D., & Marchot, P. (2007). In situ measurements of the static liquid holdup in Katapak-SP12 packed column using X-ray tomography. *Chemical Engineering Science, 62*, 6076–6080. http://dx.doi.org/10.1016/j.ces.2007.06.025.

Akpa, B. S., Mantle, M. D., Sederman, A. J., Gladden, L. F. (2005). In situ 13 C DEPT-MRI as a tool to spatially resolve chemical conversion and selectivity of a heterogeneous catalytic reaction occurring in a fixed-bed reactor. *Chemical Communications,* 2741–2743. doi:10.1039/b501698c.

Al-Dahhan, M., Larachi, F., Duduković, M. P., & Laurent, A. (1997). High-pressure trickle-bed reactors: a review. *Industrial & Engineering Chemistry Research, 36*, 3292–3314. http://dx.doi.org/10.1021/ie9700829.

Alopaeus, V., Hynynen, K., Aittamaa, J., & Manninen, M. (2006). Modeling of gas-liquid packed-bed reactors with momentum equations and local interaction closures. *Industrial & Engineering Chemistry Research, 45*, 8189–8198.

Anadon, L. D. (2006). *Transient hydrodynamics and reaction in trickle-bed reactors using NMR and MRI.* University of Cambridge.

Anadon, L. D., Sederman, A. J., & Gladden, L. F. (2006). Mechanism of the trickle-to-pulse flow transition in fixed-bed reactors. *American Institute of Chemical Engineers Journal, 52*, 1522–1532. http://dx.doi.org/10.1002/aic.

Anadon, L. D., Sederman, A. J., & Gladden, L. F. (2008). Rationalising MRI, conductance and pressure drop measurements of the trickle-to-pulse transition in trickle beds. *Chemical Engineering Science, 63*, 4640–4648. http://dx.doi.org/10.1016/j.ces.2007.10.033.

Atta, A., Hamidipour, M., Roy, S., Nigam, K. D. P., & Larachi, F. (2010a). Propagation of slow/fast-mode solitary liquid waves in trickle beds via electrical capacitance tomography and computational fluid dynamics. *Chemical Engineering Science, 65*, 1144–1150. http://dx.doi.org/10.1016/j.ces.2009.09.069.

Atta, A., Roy, S., & Nigam, K. D. P. (2007). Investigation of liquid maldistribution in trickle-bed reactors using porous media concept in CFD. *Chemical Engineering Science, 62*, 7033–7044. http://dx.doi.org/10.1016/j.ces.2007.07.069.

Atta, A., Schubert, M., Nigam, K. D. P., Roy, S., & Larachi, F. (2010b). Co-current descending two-phase flows in inclined packed beds: experiments versus simulations. *The Canadian Journal of Chemical Engineering, 88*. http://dx.doi.org/10.1002/cjce.20340.

Attou, A., Boyer, C., & Ferschneider, G. (1999). Modelling of the hydrodynamics of the cocurrent gas–liquid trickle flow through a trickle-bed reactor. *Chemical Engineering Science, 54*, 785–802. http://dx.doi.org/10.1016/S0009-2509(98)00285-1.

Azzopardi, B. J., Abdulkareem, L. A., Zhao, D., Thiele, S., da Silva, M. J., Beyer, M., et al. (2010). Comparison between electrical capacitance tomography and wire mesh sensor output for air/silicone oil flow in a vertical pipe. *Industrial & Engineering Chemistry Research, 49*, 8805–8811. http://dx.doi.org/10.1021/ie901949z.

Balachandar, S., & Eaton, J. K. (2010). Turbulent dispersed multiphase flow. *Annual Review of Fluid Mechanics, 42*, 111–133. http://dx.doi.org/10.1146/annurev.fluid.010908.165243.

Bazer-Bachi, F., Haroun, Y., Augier, F., & Boyer, C. (2013). Experimental evaluation of distributor technologies for trickle-bed reactors. *Industrial & Engineering Chemistry Research, 52*, 11189–11197.

Bazmi, M., Hashemabadi, S. H., & Bayat, M. (2012). CFD simulation and experimental study of liquid flow mal-distribution through the randomly trickle bed reactors. *International Communications in Heat and Mass Transfer, 39*, 736–743. http://dx.doi.org/10.1016/j.icheatmasstransfer.2012.03.005.

Bennett, M. A., West, R. M., Luke, S. P., Jia, X., & Williams, R. A. (1999). Measurement and analysis of flows in a gas–liquid column reactor. *Chemical Engineering Science, 54*, 5003–5012.

Bieberle, A., Nehring, H., Berger, R., Arlit, M., Härting, H.-U., Schubert, M., et al. (2013). Compact high-resolution gamma-ray computed tomography system for multiphase flow studies. *Review of Scientific Instruments, 84*, 033106. http://dx.doi.org/10.1063/1.4795424.

Bieberle, A., Schubert, M., da Silva, M. J., & Hampel, U. (2010). Measurement of liquid distributions in particle packings using wire-mesh sensor versus transmission tomographic imaging. *Industrial & Engineering Chemistry Research, 49*, 9445–9453.

Bieberle, M., Barthel, F., Menz, H.-J., Mayer, H.-G., & Hampel, U. (2011). Ultrafast three-dimensional X-ray computed tomography. *Applied Physics Letter, 98*, 034101. http://dx.doi.org/10.1063/1.3534806.

Bieberle, M., Fischer, F., Schleicher, E., Hampel, U., Koch, D., Aktay, K. S. D. C., et al. (2007). Ultrafast limited-angle-type X-ray tomography. *Applied Physics Letter, 91*, 123516. http://dx.doi.org/10.1063/1.2787879.

Bieberle, M., & Hampel, U. (2006). Evaluation of a limited angle scanned electron beam X-ray CT approach for two-phase pipe flows. *Measurement Science and Technology, 17*, 2057–2065. http://dx.doi.org/10.1088/0957-0233/17/8/001.

Bieberle, M., Schleicher, E., Fischer, F., Koch, D., Menz, H.-J., Mayer, H.-G., et al. (2010b). Dual-plane ultrafast limited-angle electron beam X-ray tomography. *Flow Measurement and Instrumentation, 21*, 233–239. http://dx.doi.org/10.1016/j.flowmeasinst.2009.12.001.

Boyer, C., Duquenne, A., & Wild, G. (2002). Measuring techniques in gas–liquid and gas–liquid–solid reactors. *Chemical Engineering Science, 57*, 3185–3215.

Boyer, C., & Fanget, B. (2002). Measurement of liquid flow distribution in trickle bed reactor of large diameter with a new gamma-ray tomographic system. *Chemical Engineering Science, 57*, 1079–1089.

Boyer, C., Koudil, A., Chen, P., & Dudukovic, M. P. (2005). Study of liquid spreading from a point source in a trickle bed via gamma-ray tomography and CFD simulation. *Chemical Engineering Science, 60*, 6279–6288. http://dx.doi.org/10.1016/j.ces.2005.03.049.

Cai, Q., Shen, X., Shen, C., & Dai, G. (2010). A simple method for identifying bubbling/jetting regimes transition from large submerged orifices using electrical capacitance tomography (ECT). *The Canadian Journal of Chemical Engineering, 88*, 340–349. http://dx.doi.org/10.1002/cjce.20295.

Chaouki, J., Larachi, F., & Dudukovic, M. P. (1997). Noninvasive tomographic and velocimetric monitoring of multiphase flows. *Industrial & Engineering Chemistry Research, 36*, 4476–4503.

Chen, J., Gupta, P., Degaleesan, S., Al-Dahhan, M. H., Duduković, M. P., & Toseland, B. A. (1998). Gas holdup distributions in large-diameter bubble columns measured by computed tomography. *Flow Measurement and Instrumentation, 9*, 91–101. http://dx.doi.org/10.1016/S0955-5986(98)00010-7.

Chen, J., Kemoun, A., Al-dahhan, M. H., Dudukovic, M. P., Lee, D. J., & Fan, L. (1999). Comparative hydrodynamics study in a bubble column using computer-automated radioactive particle tracking (CARPT)/computed tomography (CT) and particle image velocimetry (PIV). *Chemical Engineering Science, 54*, 2199–2207.

Chen, J., Li, F., Degaleesan, S., Gupta, P., Al-Dahhan, M. H., Dudukovic, M. P., et al. (1999). Fluid dynamic parameters in bubble columns with internals. *Chemical Engineering Science, 54*, 2187–2197. http://dx.doi.org/10.1016/S0009-2509(99)00003-2.

Daidzic, N., Schmidt, E., Hasan, M., & Altobelli, S. (2005). Gas–liquid phase distribution and void fraction measurements using MRI. *Nuclear Engineering and Design, 235*, 1163–1178. http://dx.doi.org/10.1016/j.nucengdes.2005.02.024.

Deckwer, W. (1992). *Bubble column reactors*. Chichester: Wiley.

Delnoij, E., Kuipers, J. A. M., & van Swaaij, W. P. M. (1997). Computational fluid dynamics applied to gas-liquid contactors. *Chemical Engineering Science, 52*, 3623–3638. http://dx.doi.org/10.1016/S0009-2509(97)00268-6.

Dietrich, W., Anadon, L., Sederman, A. J., Gladden, L. F., & Agar, D. W. (2012). Simulation studies on the performance enhancement in periodically operated trickle-bed reactors based on experimental local liquid distribution measurements. *Industrial & Engineering Chemistry Research, 51*, 1672–1679. http://dx.doi.org/10.1021/ie200827c.

Dietrich, W., Grünewald, M., & Agar, D. W. (2005). Dynamic modelling of periodically wetted catalyst particles. *Chemical Engineering Science, 60*, 6254–6261. http://dx.doi.org/10.1016/j.ces.2005.03.054.

Dudukovic, M. (2002). Opaque multiphase flows: experiments and modeling. *Experimental Thermal and Fluid Science, 26*, 747–761. http://dx.doi.org/10.1016/S0894-1777(02)00185-1.

Dudukovic, M. P. (2010). Reaction engineering: status and future challenges. *Chemical Engineering Science, 65*, 3–11. http://dx.doi.org/10.1016/j.ces.2009.09.018.

Dudukovic, M. P., Larachi, F., & Mills, P. L. (1999). Multiphase reactors – revisited. *Chemical Engineering Science, 54*, 1975–1995. http://dx.doi.org/10.1016/S0009-2509(98)00367-4.

Fischer, F., & Hampel, U. (2010). Ultra fast electron beam X-ray computed tomography for two-phase flow measurement. *Nuclear Engineering and Design, 240*, 2254–2259. http://dx.doi.org/10.1016/j.nucengdes.2009.11.016.

Fourati, M., Roig, V., & Raynal, L. (2012). Experimental study of liquid spreading in structured packings. *Chemical Engineering Science, 80*, 1–15.

Fransolet, E., Crine, M., Marchot, P., & Toye, D. (2005). Analysis of gas holdup in bubble columns with non-Newtonian fluid using electrical resistance tomography and dynamic gas disengagement technique. *Chemical Engineering Science, 60*, 6118–6123. http://dx.doi.org/10.1016/j.ces.2005.03.046.

Fuangworawong, N., Kikura, H., Aritomi, M., & Komeno, T. (2007). Tomographic imaging of counter-current bubbly flow by wire mesh tomography. *Chemical Engineering Science, 130*, 111–118. http://dx.doi.org/10.1016/j.cej.2006.08.033.

Gianetto, A., & Specchia, V. (1992). Trickle-bed reactors: state of art and perspectives. *Chemical Engineering Science, 47*, 3197–3213.

Gladden, L. F., Abegao, F. J. R., Dunckley, C. P., Holland, D. J., Sankey, M. H., & Sederman, A. J. (2010). MRI: operando measurements of temperature, hydrodynamics and local reaction rate in a heterogeneous catalytic reactor. *Catalysis Today, 155*, 157–163.

Gladden, L. F., Lim, M. H. M., Mantle, M. D., Sederman, A. J., & Stitt, E. H. (2003). MRI visualisation of two-phase flow in structured supports and trickle-bed reactors. *Catalysis Today, 79-80*, 203–210. http://dx.doi.org/10.1016/S0920-5861(03)00006-3.

Gulati, S., Behling, M., Munshi, P., Luke, A., & Mewes, D. (2010). Tomographic KT-1 signature of phase-fraction distributions in multiphase bubble columns. *Flow Measurement and Instrumentation, 21*, 249–254. http://dx.doi.org/10.1016/j.flowmeasinst.2009.12.005.

Gumery, F., Ein-Mozaffari, F., & Dahman, Y. (2011). Macromixing hydrodynamic study in draft-tube airlift reactors using electrical resistance tomography. *Bioprocess and Biosystems Engineering, 34*, 135–144. http://dx.doi.org/10.1007/s00449-010-0454-2.

Gunjal, P. R., Kashid, M. N., Ranade, V. V., & Chaudhari, R. V. (2005). Hydrodynamics of trickle-bed reactors: experiments and CFD modeling. *Industrial & Engineering Chemistry Research, 44*, 6278–6294. http://dx.doi.org/10.1021/ie0491037.

Häfeli, R., Hutter, C., Damsohn, M., Prasser, H.-M., & Rudolf von Rohr, P. (2013). Dispersion in fully developed flow through regular porous structures: experiments with wire-mesh sensors. *Chemical Engineering and Processing: Process Intensification, 69*, 104–111. http://dx.doi.org/10.1016/j.cep.2013.03.006.

Hamidipour, M., Chen, J., & Larachi, F. (2013). CFD study and experimental validation of trickle bed hydrodynamics under gas, liquid and gas/liquid alternating cyclic operations. *Chemical Engineering Science, 89*, 158–170. http://dx.doi.org/10.1016/j.ces.2012.11.041.

Hamood-ur-rehman, M., Dahman, Y., & Ein-mozaffari, F. (2012). Investigation of mixing characteristics in a packed-bed external loop airlift bioreactor using tomography images. *Chemical Engineering Science, 213*, 50–61. http://dx.doi.org/10.1016/j.cej.2012.09.106.

Heindel, T. J. (2011). A review of X-Ray flow visualization with applications to multiphase flows. *Journal of Fluids Engineering, 133*, 074001. http://dx.doi.org/10.1115/1.4004367.

Holland, D. J., Blake, A., Tayler, A. B., Sederman, A. J., & Gladden, L. F. (2011). A Bayesian approach to characterising multi-phase flows using magnetic resonance: application to bubble flows. *Journal of Magnetic Resonance, 209*, 83–87. http://dx.doi.org/10.1016/j.jmr.2010.12.003.

Holland, D. J., Blake, A., Tayler, A. B., Sederman, A. J., & Gladden, L. F. (2012). Bubble size measurement using Bayesian magnetic resonance. *Chemical Engineering Science, 84*, 735–745.

Holland, D. J., Malioutov, D. M., Blake, A., Sederman, A. J., & Gladden, L. F. (2010). Reducing data acquisition times in phase-encoded velocity imaging using compressed sensing. *Journal of Magnetic Resonance, 203*, 236–246. http://dx.doi.org/10.1016/j.jmr.2010.01.001.

Holland, D. J., Mitchell, J., Blake, A., & Gladden, L. F. (2013). Grain sizing in porous media using bayesian magnetic resonance. *Physics Review Letters, 110*, 018001. http://dx.doi.org/10.1103/PhysRevLett.110.018001.

Hubers, J. L., Striegel, A. C., Heindel, T. J., Gray, J. N., & Jensen, T. C. (2005). X-ray computed tomography in large bubble columns. *Chemical Engineering Science, 60*, 6124–6133. http://dx.doi.org/10.1016/j.ces.2005.03.038.

Iliuta, I., Larachi, F., & Al-Dahhan, M. H. (2000). Double-slit model for partially wetted trickle flow hydrodynamics. *American Institute of Chemical Engineers Journal, 46*, 597–609. http://dx.doi.org/10.1002/aic.690460318.

Iliuta, I., Larachi, F., & Grandjean, B. P. A. (1998). Pressure drop and liquid holdup in trickle flow reactors: Improved Ergun constants and slip correlations for the slit model. *Industrial & Engineering Chemistry Research, 37*, 4542–4550. http://dx.doi.org/10.1021/ie980394r.

Ishkintana, L. K., & Bennington, C. P. J. Ã. (2010). Gas holdup in pulp fibre suspensions: Gas voidage profiles in a batch-operated sparged tower. *Chemical Engineering Science, 65*, 2569–2578. http://dx.doi.org/10.1016/j.ces.2009.12.040.

Ito, D., Prasser, H.-M., Kikura, H., & Aritomi, M. (2011). Uncertainty and intrusiveness of three-layer wire-mesh sensor. *Flow Measurement and Instrumentation, 22*, 249–256. http://dx.doi.org/10.1016/j.flowmeasinst.2011.03.002.

Jakobsen, H. A. (2008). Chemical Reactor Modeling (Vol. 3). Berlin, Heidelberg: Springer Berlin Heidelberg.

Jiang, Y., Khadilkar, M. R., Al-Dahhan, M. H., & Dudukovic, M. P. (1999). Two-phase flow distribution in 2D trickle-bed reactors. *Chemical Engineering Science, 54*, 2409–2419.

Jiang, Y., Khadilkar, M. R., Al-Dahhan, M. H., & Dudukovic, M. P. (2002). CFD of multiphase flow in packed-bed Reactors: I. K-fluid modeling Issues. *American Institute of Chemical Engineers Journal, 48*, 701–715.

Jin, H., Wang, M., & Williams, R. A. (2007). Analysis of bubble behaviors in bubble columns using electrical resistance tomography. *Chemical Engineering Journal, 130*, 179–185. http://dx.doi.org/10.1016/j.cej.2006.08.032.

Joshi, J. B., Tabib, M. V., Deshpande, S. S., & Mathpati, C. S. (2009). Dynamics of Flow Structures and Transport Phenomena, 1. Experimental and Numerical Techniques for Identification and Energy Content of Flow Structures. *Industrial & Engineering Chemistry Research, 48*, 8244–8284.

Kalaga, D. V., Kulkarni, A. V., Acharya, R., Kumar, U., Singh, G., & Joshi, J. B. (2009). Some industrial applications of gamma-ray tomography. *Journal of the Taiwan Institute of Chemical Engineers, 40*, 602–612. http://dx.doi.org/10.1016/j.jtice.2009.05.012.

Kantarci, N., Borak, F., & Ulgen, K. O. (2005). Bubble column reactors. *Process Biochemistry, 40*, 2263–2283. http://dx.doi.org/10.1016/j.procbio.2004.10.004.

Karim, K., Varma, R., Vesvikar, M., & Al-Dahhan, M. H. (2004). Flow pattern visualization of a simulated digester. *Water Research, 38*, 3659–3670. http://dx.doi.org/10.1016/j.watres.2004.06.009.

Kim, J., Jung, S., Moon, J., Guen Park, J., Jin, J., & Cho, G. (2012). Development of transportable gamma-ray tomographic system for industrial application. *Nuclear Instruments and Methods in Physics Research Section A: Accelerators, Spectrometers, Detectors and Associated Equipment, 693*, 203–208. http://dx.doi.org/10.1016/j.nima.2012.07.046.

Koptyug, I. V., Khomichev, A. V., Lysova, A. A., & Sagdeev, R. Z. (2008). Spatially resolved NMR thermometry of an operating fixed-bed catalytic reactor. *Journal of the American Chemical Society, 130*, 10452–10453. http://dx.doi.org/10.1021/ja802075m.

Koptyug, I. V., Sagdeev, D. R., Gerkema, E., Van As, H., & Sagdeev, R. Z. (2005). Solid-state 27Al MRI and NMR thermometry for catalytic applications with conventional (liquids) MRI instrumentation and techniques. *Journal of Magnetic Resonance, 175*, 21–29. http://dx.doi.org/10.1016/j.jmr.2005.03.005.

Kouris, C., Neophytides, S., Vayenas, C. G., & Tsamopoulos, J. (1998). Unsteady state operation of catalytic particles with constant and periodically changing degree of external wetting. *Chemical Engineering Science, 53*, 3129—3142. http://dx.doi.org/10.1016/S0009-2509(98)00090-6.

Krepper, E., Reddy Vanga, B. N., Zaruba, A., Prasser, H.-M., & Lopez de Bertodano, M. A (2007). Experimental and numerical studies of void fraction distribution in rectangular bubble columns. *Nuclear Engineering and Design, 237*, 399—408. http://dx.doi.org/10.1016/j.nucengdes.2006.07.009.

Kuipers, J. A. M., & van Swaaij, W. P. M. (1997). Application of computational fluid dynamics to chemical reaction engineering. *Reviews in Chemical Engineering, 13*, 1—118. http://dx.doi.org/10.1515/REVCE.1997.13.3.1.

Kuipers, J. A. M., & van Swaaij, W. P. M. (1998). Computational fluid dynamics applied to chemical reaction engineering. *Advances in Chemical Engineering, 24*, 227—328.

Kuzeljevic, Z. V., & Dudukovic, M. P. (2012). Computational modeling of trickle bed reactors. *Industrial & Engineering Chemistry Research, 51*, 1663—1671. http://dx.doi.org/10.1021/ie2007449.

Kuzeljevic, Z., Dudukovic, M., & Stitt, H. (2011). From laboratory to field tomography: data collection and performance assessment. *Industrial & Engineering Chemistry Research, 50*, 9890—9900. http://dx.doi.org/10.1021/ie101759s.

Lappalainen, K., Manninen, M., & Alopaeus, V. (2009). CFD modeling of radial spreading of flow in trickle-bed reactors due to mechanical and capillary dispersion. *Chemical Engineering Science, 64*, 207—218. http://dx.doi.org/10.1016/j.ces.2008.10.009.

Leblond, J., Javelot, S., Lebrun, D., & Lebon, L. (1998). Two-phase flow characterization by nuclear magnetic resonance. *Nuclear Engineering and Design, 184*, 229—237. http://dx.doi.org/10.1016/S0029-5493(98)00199-X.

Lim, M. H. M., Sederman, A. J., Gladden, L. F., & Stitt, E. (2004). New insights to trickle and pulse flow hydrodynamics in trickle-bed reactors using MRI. *Chemical Engineering Science, 59*, 5403—5410. http://dx.doi.org/10.1016/j.ces.2004.07.096.

Llamas, J.-D., Pérat, C., Lesage, F., Weber, M., D'Ortona, U., & Wild, G. (2008). Wire mesh tomography applied to trickle beds: a new way to study liquid maldistribution. *Chemical Engineering and Processing: Process Intensification, 47*, 1765—1770. http://dx.doi.org/10.1016/j.cep.2007.09.017.

Lopes, R. J. G., & Quinta-Ferreira, R. M. (2009a). CFD modelling of multiphase flow distribution in trickle beds. *Chemical Engineering Journal, 147*, 342—355. http://dx.doi.org/10.1016/j.cej.2008.11.048.

Lopes, R. J. G., & Quinta-ferreira, R. M. (2009b). Volume-of-fluid-based model for multiphase flow in high-pressure trickle-bed reactor: Optimization of numerical parameters. *American Institute of Chemical Engineers Journal, 55*. http://dx.doi.org/10.1002/aic.

Lopes, R. J. G., & Quinta-Ferreira, R. M. (2010). Evaluation of multiphase CFD models in gas—liquid packed-bed reactors for water pollution abatement. *Chemical Engineering Science, 65*, 291—297. http://dx.doi.org/10.1016/j.ces.2009.06.039.

Lopes, R. J. G., Quinta-ferreira, R. M., & Larachi, F. (2012). ECT imaging and CFD simulation of different cyclic modulation strategies for the catalytic abatement of hazardous liquid pollutants in trickle-bed reactors. *Chemical Engineering Journal, 211—212*, 270—284. http://dx.doi.org/10.1016/j.cej.2012.09.050.

Lucas, D., Krepper, E., & Prasser, H.-M. (2005). Development of co-current air—water flow in a vertical pipe. *International Journal of Multiphase Flow, 31*, 1304—1328. http://dx.doi.org/10.1016/j.ijmultiphaseflow.2005.07.004.

Lysova, A. A., Koptyug, I. V., & Weckhuysen, B. M. (2010). Magnetic resonance imaging methods for in situ studies in heterogeneous catalysis. *Chemical Society Reviews, 39*, 4585–4601. http://dx.doi.org/10.1039/b919540h.

Lysova, A. A., Kulikov, A. V., Parmon, V. N., Sagdeev, Z., & Koptyug, I. V. (2012). Quantitative temperature mapping within an operating catalyst by spatially resolved 27Al NMR. *Chemical Communications, 48*, 5763–5765. http://dx.doi.org/10.1039/c2cc31260c.

Mahr, B., & Mewes, D. (2008). Two-phase flow in structured packings: modeling and calculation on a macroscopic scale. *American Institute of Chemical Engineers Journal, 54*, 614–626. http://dx.doi.org/10.1002/aic.

Matusiak, B., Jose, M., Hampel, U., & Romanowski, A. (2010). Measurement of dynamic liquid distributions in a fixed bed using electrical capacitance tomography and capacitance wire-mesh sensor. *Industrial & Engineering Chemistry Research, 49*, 2070–2077.

Merwe, W. Van Der, Nicol, W., & Beer, F. De (2007). Trickle flow distribution and stability by X-ray radiography. *Chemical Engineering Journal, 132*, 47–59. http://dx.doi.org/10.1016/j.cej.2007.01.015.

Monahan, S. M., Vitankar, V. S., & Fox, R. O. (2005). CFD predictions for flow-regime transitions in bubble columns. *AIChE Journal, 51*, 1897–1923.

Mudde, R. F. (2010a). Advanced measurement techniques for GLS reactors. *The Canadian Journal of Chemical Engineering, 88*, 638–647. http://dx.doi.org/10.1002/cjce.20315.

Mudde, R. F. (2010b). Double X-ray tomography of a bubbling fluidized bed. *Industrial & Engineering Chemistry Research, 49*, 5061–5065. http://dx.doi.org/10.1021/ie901537z.

Mudde, R. F., Alles, J., Van Der Hagen, T. H. J. J., 2008. Feasibility study of a time-resolving X-ray tomographic system *Measurement Science and Technology 19,* 85501. doi:10.1088/0957-0233/19/8/085501.

Nedeltchev, S. (2009). Application of chaos analysis for the investigation of turbulence in heterogeneous bubble columns. *Chemical Engineering & Technology, 32*, 1974–1983. http://dx.doi.org/10.1002/ceat.200900336.

Nedeltchev, S., Shaikh, A., & Al-Dahhan, M. (2006). Flow regime identification in a bubble column based on both statistical and chaotic parameters applied to computed tomography data. *Chemical Engineering & Technology, 29*, 1054–1060. http://dx.doi.org/10.1002/ceat.200600162.

Nedeltchev, S., Shaikh, A., & Al-Dahhan, M. (2007). Prediction of the Kolmogorov entropy derived from computed tomography data in a bubble column operated under the transition regime and ambient pressure. *Chemical Engineering & Technology, 30*, 1445–1450. http://dx.doi.org/10.1002/ceat.200700053.

Olerni, C., Jia, J., & Wang, M. (2013). Measurement of air distribution and void fraction of an upwards air–water flow using electrical resistance tomography and a wire-mesh sensor. *Measurement Science & Technology, 24*, 035403. http://dx.doi.org/10.1088/0957-0233/24/3/035403.

Olmos, E., Gentric, C., Vial, C., Wild, G., & Midoux, N. (2001). Numerical simulation of multiphase flow in bubble column reactors. Influence of bubble coalescence and break-up. *Chemical Engineering Science, 56*, 6359–6365.

Ong, B. C., Gupta, P., Youssef, A., Al-Dahhan, M. H., & Dudukovic, M. P. (2009). Computed tomographic investigation of the influence of Gas sparger design on Gas holdup distribution in a bubble column. *Industrial & Engineering Chemistry Research, 48*, 58–68.

Patel, A. K., & Thorat, B. N. (2008). Gamma ray tomography — an experimental analysis of fractional gas hold-up in bubble columns. *Chemical Engineering Journal, 137*, 376–385. http://dx.doi.org/10.1016/j.cej.2007.05.014.

Pietruske, H., & Prasser, H.-M. (2007). Wire-mesh sensors for high-resolving two-phase flow studies at high pressures and temperatures. *Flow Measurement and Instrumentation, 18*, 87−94. http://dx.doi.org/10.1016/j.flowmeasinst.2007.01.004.

Prasser, H., Beyer, M., Carl, H., Manera, A., Pietruske, H., Schütz, P., et al. (2006). The multipurpose thermal hydraulic test facility TOPFLOW: an overview on experimental capabilities, instrumentation and results. *Kernteknik, 71*, 163−173.

Prasser, H., Böttger, A., & Zschau, J. (1998). A new electrode-mesh tomograph for gas−liquid flows. *Flow Measurement and Instrumentation, 9*, 111−119.

Prasser, H.-M., Krepper, E., & Lucas, D. (2002). Evolution of the two-phase flow in a vertical tube—decomposition of gas fraction profiles according to bubble size classes using wire-mesh sensors. *The International Journal of Thermal Sciences, 41*, 17−28. http://dx.doi.org/10.1016/S1290-0729(01)01300-X.

Prasser, H.-M., Misawa, M., & Tiseanu, I. (2005). Comparison between wire-mesh sensor and ultra-fast X-ray tomograph for an air−water flow in a vertical pipe. *Flow Measurement and Instrumentation, 16*, 73−83. http://dx.doi.org/10.1016/j.flowmeasinst.2005.02.003.

Rabha, S., Schubert, M., & Hampel, U. (2013a). Intrinsic flow behavior in a slurry bubble column: a study on the effect of particle size. *Chemical Engineering Science, 93*, 401−411. http://dx.doi.org/10.1016/j.ces.2013.02.034.

Rabha, S., Schubert, M., & Hampel, U. (2013b). Hydrodynamic studies in slurry bubble columns: experimental and numerical study. *Chemie Ingenieur Technik, 85*, 1092−1098.

Rabha, S., Schubert, M., Wagner, M., Lucas, D., & Hampel, U. (2013). Bubble size and radial gas hold-up distributions in a slurry bubble column using ultrafast electron beam X-ray tomography. *American Institute of Chemical Engineers Journal, 59*, 1709−1722. http://dx.doi.org/10.1002/aic.

Rados, N., Shaikh, A., & Al-Dahhan, M. H. (2005). Solids flow mapping in a high pressure slurry bubble column. *Chemical Engineering Science, 60*, 6067−6072. http://dx.doi.org/10.1016/j.ces.2005.04.087.

Reinecke, N., & Mewes, D. (1996). Tomographic imaging of trickle-bed reactors. *Chemical Engineering Science, 51*, 2131−2138.

Reinecke, N., & Mewes, D. (1997). Investigation of the two-phase flow in trickle-bed reactors using capacitance tomography. *Chemical Engineering Science, 2509*, 2111−2127.

Richter, S., Aritomi, M., Prasser, H., & Hampel, R. (2002). Approach towards spatial phase reconstruction in transient bubbly flow using a wire-mesh sensor. *International Journal of Heat and Mass Transfer, 45*, 1063−1075.

Robbins, D. J., El-bachir, M. S., Gladden, L. F., Cant, R. S., & von Harbou, E. (2012). CFD modeling of single-phase flow in a packed bed with MRI validation. *American Institute of Chemical Engineers Journal, 58*, 3904−3915. http://dx.doi.org/10.1002/aic.

Roberts, S. T., Renshaw, M. P., Lutecki, M., McGregor, J., Sederman, A. J., Mantle, M. D., et al. (2013). Operando magnetic resonance: monitoring the evolution of conversion and product distribution during the heterogeneous catalytic ethene oligomerisation reaction. *Chemical Communication (Cambridge), 49*, 10519−10521. http://dx.doi.org/10.1039/c3cc45896b.

Roy, S., Kemoun, A., Al-Dahhan, M. H., Dudukovic, M. P., Skourlis, T. B., & Dautzenberg, F. M. (2005). Countercurrent flow distribution in structured packing via computed tomography. *Chemical Engineering Process, 44*, 59−69. http://dx.doi.org/10.1016/j.cep.2004.03.010.

Sáez, A. E., & Carbonell, R. G. (1985). Hydrodynamic parameters for gas-liquid cocurrent flow in packed beds. *American Institute of Chemical Engineers Journal, 31*, 52−62. http://dx.doi.org/10.1002/aic.690310105.

Sankey, M. H., Holland, D. J., Gladden, L. F., & Sederman, A. J. (2009). Magnetic resonance velocity imaging of liquid and gas two-phase flow in packed beds. *Journal of Magnetic Resonance, 196*, 142−148. http://dx.doi.org/10.1016/j.jmr.2008.10.021.

Sankey, M. H., Yang, Z., Gladden, L., Johns, M. L., Lister, D., & Newling, B. (2009). SPRITE MRI of bubbly flow in a horizontal pipe. *Journal of Magnetic Resonance, 199*, 126−135. http://dx.doi.org/10.1016/j.jmr.2009.01.034.

Sanyal, J., Vasquez, S., Roy, S., & Dudukovic, M. P. (1999). Numerical simulation of gas-liquid dynamics in cylindrical bubble column reactors. *Chemical Engineering Science, 54*, 5071−5083.

Satterfield, C. N. (1975). Trickle-bed reactors. *American Institute of Chemical Engineers Journal, 21*, 209−228. http://dx.doi.org/10.1002/aic.690210202.

Schlaberg, H. I., Baas, J. H., Wang, M., Best, J. L., Williams, R. A., & Peakall, J. (2006). Electrical resistance tomography for suspended sediment measurements in open channel flows using a novel sensor design. *Particle & Particle Systems Characterization, 23*, 313−320. http://dx.doi.org/10.1002/ppsc.200601062.

Schubert, M., Bieberle, A., Barthel, F., Boden, S., & Hampel, U. (2011). Advanced tomographic techniques for flow imaging in columns with flow distribution packings. *Chemie Ingenieur Technik, 83*, 979−991. http://dx.doi.org/10.1002/cite.201100022.

Sederman, A., Johns, M., Alexander, P., & Gladden, L. F. (1998). Structure-flow correlations in packed beds. *Chemical Engineering Science, 53*, 2117−2128.

Sederman, A. J., & Gladden, L. F. (2001). Magnetic resonance imaging as a quantitative probe of gas-liquid distribution and wetting efficiency in trickle-bed reactors. *Chemical Engineering Science, 56*, 2615−2628.

Sederman, A. J., & Gladden, L. F. (2005). Transition to pulsing flow in trickle-bed reactors studied using MRI. *American Institute of Chemical Engineers Journal, 51*, 615−621. http://dx.doi.org/10.1002/aic.10317.

Sederman, A. J., Mantle, M. D., Dunckley, C. P., Huang, Z., & Gladden, L. F. (2005). In situ MRI study of 1-octene isomerisation and hydrogenation within a trickle-bed reactor. *Catalysis Letters, 103*, 1−8. http://dx.doi.org/10.1007/s10562-005-7522-2.

Selma, B., Bannari, R., & Proulx, P. (2010). Simulation of bubbly flows: comparison between direct quadrature method of moments (DQMOM) and method of classes (CM). *Chemical Engineering Science, 65*, 1925−1941. http://dx.doi.org/10.1016/j.ces.2009.11.018.

Shaikh, A., & Al-Dahhan, M. (2005). Characterization of the hydrodynamic flow regime in bubble columns via computed tomography. *Flow Measurement and Instrumentation, 16*, 91−98. http://dx.doi.org/10.1016/j.flowmeasinst.2005.02.004.

Shaikh, A., & Al-Dahhan, M. (2010). A new methodology for hydrodynamic similarity in bubble columns. *The Canadian Journal of Chemical Engineering, 88*, 503−517. http://dx.doi.org/10.1002/cjce.20357.

Da Silva, M. J., Schleicher, E., & Hampel, U. (2007). Capacitance wire-mesh sensor for fast measurement of phase fraction distributions. *Measurement Science and Technology, 18*, 2245−2251. http://dx.doi.org/10.1088/0957-0233/18/7/059.

Silveston, P., Hudgins, R., & Renken, A. (1995). Periodic operation of catalytic reactors—introduction and overview. *Catalysis Today, 25*, 91−112.

Sokolichin, A., Eigenberger, G., & Lapin, A. (2004). Simulation of buoyancy driven bubbly flow: established simplifications and open questions. *AIChE Journal, 50*(1), 24−45.

Spedding, P. L., Woods, G. S., Raghunathan, R. S., & Watterson, J. K. (1998). Vertical two-phase flow. Part I: flow regimes. *Transactions of the Institution Chemical Engineers, 76*, 612−619.

Stehling, M. K., Turner, R., & Mansfield, P. (1991). Echo-Planar imaging: magnetic resonance imaging in a fraction of a second. *Science, 254*, 43−50.

Supardan, M. D., Masuda, Y., Maezawa, A., & Uchida, S. (2007). The investigation of gas holdup distribution in a two-phase bubble column using ultrasonic computed tomography. *Chemical Engineering Journal, 130*, 125−133. http://dx.doi.org/10.1016/j.cej.2006.08.035.

Tayler, A. B., Holland, D. J., Sederman, A. J., & Gladden, L. F. (2011). Time resolved velocity measurements of unsteady systems using spiral imaging. *Journal of Magnetic Resonance, 211*, 1−10. http://dx.doi.org/10.1016/j.jmr.2011.03.017.

Tayler, A. B., Holland, D. J., Sederman, A. J., & Gladden, L. F. (2012a). Applications of ultra-fast MRI to high voidage bubbly flow: measurement of bubble size distributions, interfacial area and hydrodynamics. *Chemical Engineering Science, 71*, 468−483.

Tayler, A. B., Holland, D. J., Sederman, A. J., & Gladden, L. F. (2012b). Exploring the origins of turbulence in multiphase flow using compressed sensing MRI. *Physics Review Letters, 108*, 264505.

Toye, D., Fransolet, E., Simon, D., Crine, M., L'Homme, G., & Marchot, P. (2005). Possibilities and limits of application of electrical resistance tomography in hydrodynamics of bubble columns. *The Canadian Journal of Chemical Engineering, 83*, 4−10.

Upadhyay, R. K., Pant, H. J., & Roy, S. (2013). Liquid flow patterns in rectangular air-water bubble column investigated with radioactive particle tracking. *Chemical Engineering Science, 96*, 152−164. http://dx.doi.org/10.1016/j.ces.2013.03.045.

Utomo, M. B., Warsito, W., Sakai, T., & Uchida, S. (2001). Analysis of distributions of gas and TiO2 particles in slurry bubble column using ultrasonic computed tomography. *Chemical Engineering Science, 56*, 6073−6079.

Van Sint Annaland, M., Dijkhuizen, W., Deen, N. G., & Kuipers, J. A. M. (2006). Numerical simulation of behavior of gas bubbles using a 3-D front-tracking method. *American Institute of Chemical Engineers Journal, 52*, 99−110. http://dx.doi.org/10.1002/aic.10607.

Varma, R., & Al-Dahhan, M. (2007). Effect of sparger design on hydrodynamics of a gas recirculation anaerobic bioreactor. *Biotechnology and Bioengineering, 98*, 1146−1160. http://dx.doi.org/10.1002/bit.

Vijayan, M., Schlaberg, H. I., & Wang, M. (2007). Effects of sparger geometry on the mechanism of flow pattern transition in a bubble column. *Chemical Engineering Journal, 130*, 171−178. http://dx.doi.org/10.1016/j.cej.2006.06.024.

Wang, F., Marashdeh, Q., Fan, L.-S., & Warsito, W. (2010). Electrical capacitance volume tomography: design and applications. *Sensors, 10*, 1890−1917. http://dx.doi.org/10.3390/s100301890.

Wang, M., Dorward, A., Vlaev, D., & Mann, R. (2000). Measurements of gas − liquid mixing in a stirred vessel using electrical resistance tomography (ERT). *Chemical Engineering Journal, 77*, 93−98.

Wang, M., Lucas, G., Dai, Y., Panayotopoulos, N., & Williams, R. A. (2006). Visualisation of bubbly velocity distribution in a swirling flow using electrical resistance tomography. *Particle & Particle Systems Characterization, 23*, 321−329. http://dx.doi.org/10.1002/ppsc.200601063.

Wangjiraniran, W., Aritomi, M., Kikura, H., Motegi, Y., & Prasser, H.-M. (2005). A study of non-symmetric air water flow using wire mesh sensor. *Experimental Thermal and Fluid Science, 29*, 315−322. http://dx.doi.org/10.1016/j.expthermflusci.2004.05.004.

Wangjiraniran, W., Motegi, Y., Richter, S., Kikura, H., Aritomi, M., & Yamamoto, K. (2003). Intrusive effect of wire mesh tomography on gas-liquid flow measurement. *Journal of Nuclear Science and Technology, 40*, 932−940.

Warsito, W., & Fan, L. S. (2003). 3D-ECT velocimetry for flow structure quantification of gas-liquid-solid fluidized beds. *The Canadian Journal of Chemical Engineering, 81*, 875−884.

Warsito, W., & Fan, L. S. (2001). Measurements of real-time flow structures in gas-liquid and gas-liquid-solid flow systems using electrical capacitance tomography (ECT). *Chemical Engineering Science, 56*, 6455−6462.

Warsito, W., Ohkawa, M., Kawata, N., & Uchida, S. (1999). Cross-sectional distributions of gas and solid holdups in slurry bubble column investigated by ultrasonic computed tomography. *Chemical Engineering Science, 54*, 4711−4728.

Yuen, E. H. L., Sederman, A. J., & Gladden, L. F. (2002). In situ magnetic resonance visualisation of the spatial variation of catalytic conversion within a fixed-bed reactor. *Applied Catalysis A: General, 232*, 29−38. http://dx.doi.org/10.1016/S0926-860X(02)00064-9.

This page intentionally left blank

Applications of tomography in reaction engineering (mixing process)

19

V. Mosorov
Institute of Applied Computer Science, Lodz University of Technology, Lodz, Poland

19.1 Introduction

Mixing processes are general operations in industrial process engineering. The main goal of these processes is to make a heterogeneous physical system homogeneous by using manipulating operations. Generally, efficient mixing can be challenging to achieve, especially on an industrial scale. Sometimes industrial mixing is done in batches, in which case one can call it dynamic mixing. However, many industrial applications use static mixers, that is the reactor position is fixed. Segregation is the opposite operation to mixing. An example of such an operation is particle segregation, that is the segregation of particles according to their size, density, shape and other properties.

There are two types of patterns produced by a typical mixer simultaneously: radial mixing and flow division. In the first case, rotational circulations of a processed material around its own centre cause its radial mixing. Processed material is intermixed to reduce or eliminate radial gradients in temperature, velocity and material composition. In the case of flow division, a processed material divides at the leading edge of each element of the mixer and follows the channels created by the element shape.

Nowadays, static mixers are used for a wide range of different applications in many different industrial areas, such as pharmaceutical, chemical, agricultural and food industries. A general application is mixing *n*-component powders and particles. Other applications include many different chemical processes, for instance wastewater treatment. Static mixers are also widely used in oil and gas refineries, for example for desalting crude oil. Another example of mixing processes in chemistry is polymer production, where mixers are applied to facilitate polymerization reactions.

Mixing phenomena also have a place in multiphase flows, which are widely found in the petroleum and petrochemical industries. In many numerous types of reactors, such as airlift loop reactors, bubble columns, packed columns and vessels with combined mechanical agitation, there occur multiphase flow reactions, which can be named mixing. Examples of parameters describing mixing processes in

Industrial Tomography. http://dx.doi.org/10.1016/B978-1-78242-118-4.00019-8
Copyright © 2015 Elsevier Ltd. All rights reserved.

reactors are phase volume fractions, mixing parameters and mass transfer coefficients. In many cases these parameters are the critical ones, because they allow understanding of the operational, geometrical and physicochemical nature of the reactor and improvement of its work. Therefore, the mixing operations should be taken into account in terms of process efficiency and, ultimately, product quality.

Besides process tomography, there exist several other techniques for monitoring and controlling of mixing processes. We will briefly discuss several examples of such techniques. Determining the degree of mixing between components in a mixing process can be done by adding luminescent materials to the mixture (see, e.g. Kraft, Launikonis, & Swiegers, 2005). Such a luminescent material has a uniquely detectable luminescence emission wavelength. Monitoring of mixing is performed by measuring the emitted luminescence waves coming from the mixture. Then, the ratio of luminescence intensities and/or the absolute or relative intensities of luminescence are indicative of the degree of mixing between the components.

Another technique is radioactive particle tracking (RPT), which is based on tracking the motion of a single radioactive particle in the three-dimensional (3D) volume of interest. The radioactive particle should have physical properties identical to the ones of the investigated flow. Nowadays such radioactive chemical elements as Sc-46, Co-60 or other isotopes emitting gamma-rays are widely used to track the motion in single-phase or multiphase systems (Mosorov, 2013). The instantaneous particle positions are identified by monitoring the radiation intensities measured by the detectors arranged in different positions around the reactor. In order to reconstruct the position of the particle, a calibration procedure is needed. The calibration relates the intensities measured at the detector as a function of coordinates of the particle. It is not feasible to carry out the calibration procedure by direct experimental measurements, because of the large number of positions that must be considered. Generally, this number depends on the number of detectors, the dimensions of the vessel and requirement accuracy. Even a simple RPT system requires more than several thousand points for a calibration procedure.

However, the methods mentioned above, compared with process tomography, have serious disadvantages that limit their use in practice. Thus, they need invention into mixing processes by adding other components. Besides, these techniques do not allow good understanding of the underlying mechanisms and principles of the particular mixing processes, which are often largely dependent on the properties of the components.

Therefore, monitoring based on analysis of the cross-sectional distribution of the material enables us to ‘look through’ inside the internal behaviour of the processes and may be used to improve the economy of operation and stability of technological processes, measuring the degree of mixing between components in commercial mixing processes so as to enable the mixing processes to be monitored or optimized.

The objective of the chapter is to show how tomographic techniques can be used to monitor and control mixing processes in order to improve technologies and reduce power consumption.

19.2 Review of tomographic techniques utilized for different kinds of mixing processes

Obviously, the type of sensor that can be used to monitor mixing processes depends on the nature of the mixing materials. For instance, since electrical resistance tomography (ERT) can detect local changes in conductivity/resistivity, the technique is usually used for hydrodynamic studies of the unsteady mixing dynamics of miscible liquids if the fluids to be blended have different conductivities.

Table 19.1 presents the known sensing principles that can be used to study/monitor mixing processes. As can been seen from Table 19.1 the following kinds of tomography have been utilized for monitoring/control of gas—solids mixing: electrical capacitance tomography (ECT), position emission technique and optical/near-infrared (NIR) tomography; whereas two kinds of electrical tomography are generally applied for gas—liquid mixing monitoring.

One of the tomography types that can be successfully utilized for monitoring of different gas—solids mixing processes is ECT. During the mixing process, the measured capacitance data are changed that could be correlated with the changes in the particle size distribution and the power consumption of the mixer device (see Rimpiläinen et al., 2010). Next, the mixing indexes or, generally, mixing parameters can be calculated from tomograms.

Another kind of electrical tomography is electrical impedance tomography (EIT). The example of using EIT for investigation of the mixing of chemicals in a turbulent flow is described in Kourunen et al., 2007. The EIT system (KIT4 system) developed at the Department of Physics, University of Kuopio, consists of 16 independent current injection channels and 80 simultaneously sampled measurement channels, a real-time controller and a host PC.

Table 19.1 **Sensing principles for study/monitor of mixing processes**

Mixing process	**Sensing principle**		
Gas—solid mixing	ECT tomography (Du, Fan, Wei, & Warsito, 2002)	Position emission particle tracking technique (Laurent, Bridgwater, & Parker, 2001)	Optical tomography/ near-infrared spectroscopy (Rantanen, Wikstro Turner, & Taylor et al., 2005)
Gas—liquid mixing	Electrical resistance tomography (Kagoshima & Mann, 2005; Wang & Yin, 2001)	Electrical impedance tomography (West, Meng, Aykroyd, & Williams, 2003)	Ultrasonic transducers (Dyakowski et al., 2003; Huang & Xie, 2013)

An alternative tomographic technique is the positron emission particle tracking technique, which is similar to the above-mentioned RPT. The technique is based on detection of gamma-rays emitted by positron-emitting tracers. The particle injection unit introduces suspended tracers into the reactor. 2D/3D images of tracer concentration within the reactor are then constructed by computer analysis. Such a technique can be utilized for the study of gas–solid mixing in the case of powder flows, that is in the case when material density is relatively low. The mentioned technique allows the macroscopic solids behaviour to be analysed. It can be used to estimate the particle velocity fluctuations at both radial and axial positions (Ding, Wang, Wen, & Ghadiri, 2005). The main disadvantage of the technique is that time data acquisition in relation to ECT is higher. This limits application of the technique in the case of rapid flows.

Another technique is NIR tomography, also known as diffuse optical tomography, where NIR light (650–900 nm) is injected through the optical fibres positioned on the surface of the imaging volume of interest and the emergent light is measured at other locations on the same tissue surface using either other fibres or a detector array, such as a charge-coupled device. Such a system will provide a time-varying concentration profile, which will then be cross-correlated to provide a velocity profile over the measurement cross-section. The profile will relate to axial velocities; however, information relating to swirl is available too. For instance, process analysis of three separate phases of high-shear wet granulation (mixing, spraying and wet massing) using the NIR technique was described in Rantanen et al. (2005). There are no generally accepted online tools to gain insight into such a process in practice; therefore, NIR tomography can be a successful technique to provide corresponding chemical information including the homogeneity of the formulation and the amount of water in wet mass. Thus, NIR spectroscopy could be used to determine the end points of the three subphases of high-shear wet granulation and also provide a fast in-line quality control tool.

Another technique is ultrasonic tomography. The use of the thick-film ultrasonic transducers for deployment within an oil and gas extraction plant to measure the composition of heterogeneous mixtures has been reported in Dyakowski et al., 2003. The technology of manufacturing the transducers is described therein, and the preliminary measurements, conducted for mixtures of vegetable oil and saline water, using time-of-flight principle are presented.

19.3 How to extract information about mixing from tomographic images

One of the main problems of using of any tomographic technique for the investigation of mixing processes is how to extract from the tomographic image series information concerning the mixing process.

The tomograms represent temporal images of material distribution in the cross-section only. Moreover, in the case of the application of a one-plane sensor system,

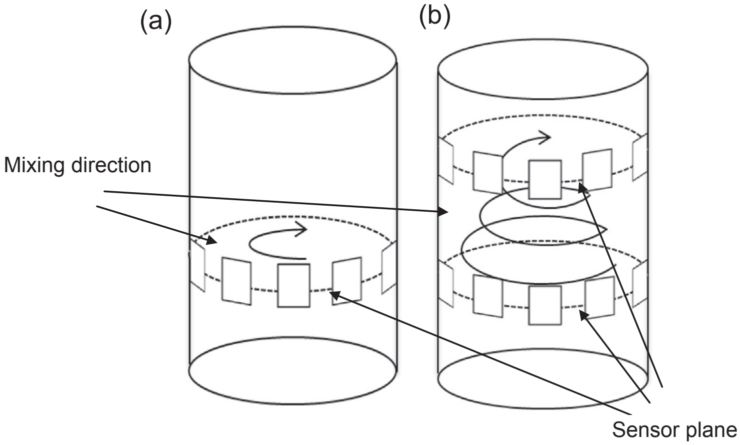

Figure 19.1 One-plane sensor system for monitoring mixing process in radial direction only (a); twin-plane sensors system for monitoring mixing process in radial and axial direction (b).

we should assume that the material moves in a radial direction with the angular velocity (see Figure 19.1(a)). That means that axial moves of material will be ignored.

However, in a general case the material moves in 3D volume. Therefore, analysis of a mixing process in 3D volume needs to have at least a twin-plane sensor system. Then such a solution will be allowed to analyse the motion of the material in both axial and radial direction (see Figure 19.1(b)). Angular velocity profiles of a rotating rod measured with two sets of electrodes in a displaced angle (Etuke & Bonnecaze, 1998) and axial velocity profiles of solid—liquid flow obtained with a dual-plane sensor system (Lucas, Cory, Waterfall, Loh, & Dickin, 1999) have been reported.

In the next sections the use of tomography for two aforementioned cases, radial mixing and flow division, will be considered separately.

19.4 Application of one-plane tomography in mixing processes

The idea of how to analyse a mixing process from the series of tomographic images utilizing a one-plane tomographic system is based on an assumption of a strong correlation between neighbouring images. The similar idea of applying a cross-correlation technique to calculate the velocity profiles has already been widely demonstrated in previous chapters. The cross-correlation technique can also be employed for the implementation of mixing analysis (Pląskowski et al., 1995). Due to all the data coming from one set of sensors, an autocorrelation method was employed for the implementation of the angular velocity. The basic method to obtain the angular velocity from autocorrelation is the same as the cross correlation, which is to find the transition time between two profiles with a certain angle where the similarities are most obvious. According to a mathematical description, it intends to find a transition time τ that can make the difference $\varepsilon(\tau)$ minimum. This can be achieved using the least squares criterion, as given by Eqn (19.1):

$$\varepsilon^2(\tau) = \int_0^T (X_{\alpha 1}(t) - X_{\alpha 2}(t-\tau))^2 \mathrm{d}t \tag{19.1}$$

where $X_{\alpha 1}(t)$ and $X_{\alpha 2}(t)$ are two reconstructed images in a T imaging sequence with starting angle α_1 and α_2, respectively.

Expanding Eqn (19.1) and then taking the average values away, the autocorrelation for extracting the angular velocity can be expressed in discrete terms, as shown below:

$$R_{k\cdot\Delta\alpha}(n) = \sum_{m=0}^{M-n} X_{k\cdot\alpha_1}(m) X_{k\cdot\alpha_2}(m-n) \tag{19.2}$$

where $R_{k\cdot\Delta\alpha}$ is the autocorrelation function at a k discrete radius with an angular difference $\Delta\alpha$, where ($\Delta\alpha = \alpha_1 - \alpha_2$), M is a sample length, n is correlated sample ($n = 1,\ldots,M - 1$).

Unlike the rotated rod in a mixing phantom or the flow regime in a pipeline, where the moving feature has no change or little change during a short transition time, the mixing dynamics of the concentration profile will be diluted or dispersed quickly to a homogeneous distribution. In order to extract the dynamic velocity feature in the miscible liquid mixing, a normalization procedure was applied to data at each imaging ring shown in Figure 19.2, which gives the same weight factor to all ring profiles.

Applying the normalization procedure and the autocorrelation method to a data set of 300 tomographic images acquired from the slow stirred mixing phantom, a strong correlation was found, as given in Figure 19.3. It should be noted that the reason for having different correlation angles at these rings in Figure 19.2 was due to the limited

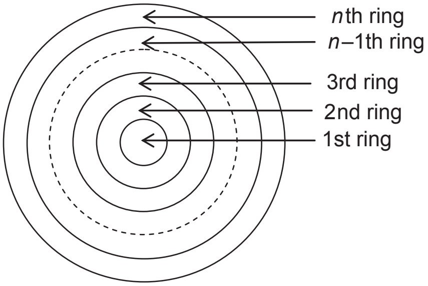

Figure 19.2 Example of a mesh with *n* rings to determine angular velocities along the radius of a reactor.

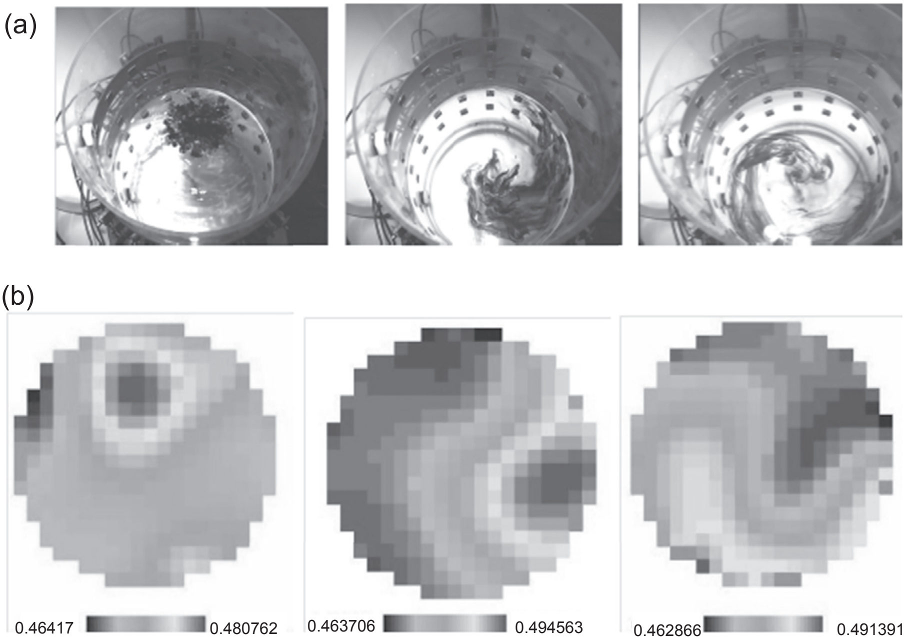

Figure 19.3 Visualization of concentration distribution with the photographic dye distribution (a); the tomographic conductivity distribution (b) (Wang & Yin, 2001).

and different pixel numbers at each ring in the finite element mesh. The conversion from the results to angular velocities is given in Eqn (19.3):

$$\omega = \frac{2\pi}{N_{\text{ring}}} \cdot \frac{N_{\text{corr}}}{\Delta_{\text{time}} \cdot M}; \quad (\text{rad/s}) \tag{19.3}$$

where ω denotes angular velocity, N_{ring} is the number of pixels per ring, N_{corr} the number of pixels between a correlated angle, M is the distance (number of images) between two correlated images and Δ_{time} is the time for collecting each frame of data.

19.5 Mixing process monitoring by twin-plane tomographic system

The example demonstrating the opportunity to use a twin-plane ECT system to monitor solid mixing processes is further discussed. Such a process, for instance, has a place in pneumatic conveying systems where solid and gas phases are mixed. A twin-plane ECT system in such an analysis is used to measure concentration profiles at two axially separated locations on the section of a pipe. Jaworski and

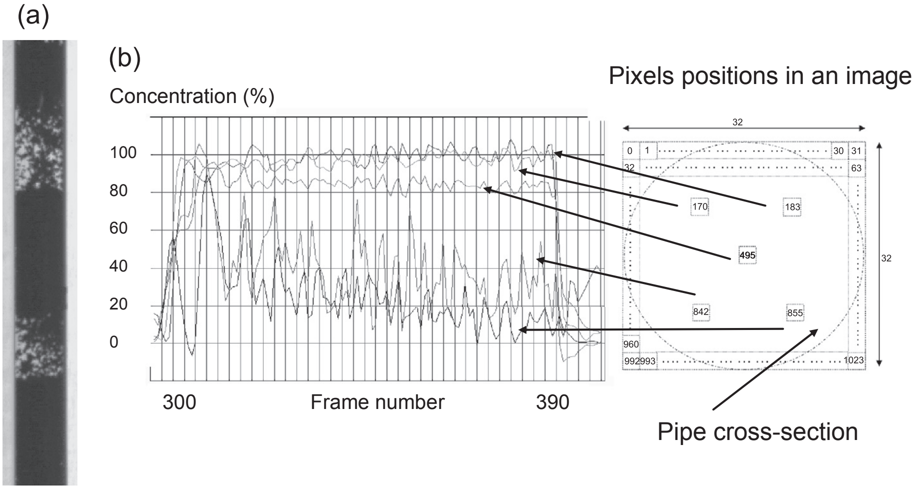

Figure 19.4 Solid concentration changes: (a) high-speed camera photographs of plug propagation in vertical pipe; (b) within chosen pixels of the cross-section.

Dyakowski (2001) reported that a predominant mechanism for solid transport in a vertical pipe of the dense pneumatic conveying is due to flow instabilities referred to as ‘plugs’, and a sequence of a number of plugs appeared with some periodicity. When the velocity of a gas increases, the successive plugs create one plug and then the flow has the form of a non-axis-symmetrical discrete plug (see Figure 19.4).

As previously mentioned, the tomograms represent physical parameters measured in each pixel of a cross-section. Individual instantaneous images of material distribution are not useful to analyse any process, including mixing. Only analysis of a series of images allows one to extract data relating to mixing processes. Therefore, for mixing process descriptions a hierarchical model is proposed, which is based on the series of tomographic images. Such a model includes two levels: a function level and a level of structural components. On the function level, a flow $\boldsymbol{X}(t)$ is defined by n-dimensional image vector $\boldsymbol{X}(t) = [X_i(t),\ i = 0, \ldots N - 1$, where N is the number of pixel elements into a cross-section area. Mathematically, the vector element $X_i(t)$ is a stochastic process that is determined by probabilistic values of the ith pixel and is called an elementary process (EP) (Mosorov et al., 2004).

On the components level, real relationships among EPs allow determination of flow components by connecting of processes (grouping) with similar properties according to a chosen criterion. In the concrete example of solid flow there are similar changes of material concentration. In this way an obtained group of EPs determines a flow component. The result of grouping has been represented as an image called an image of groups (see Figure 19.5).

Since the grouping procedure is performed periodically, sequences of images of groups can be obtained. The marked groups correspond to variable flow components determined in the volume of interest, that is in the space between two cross-sections.

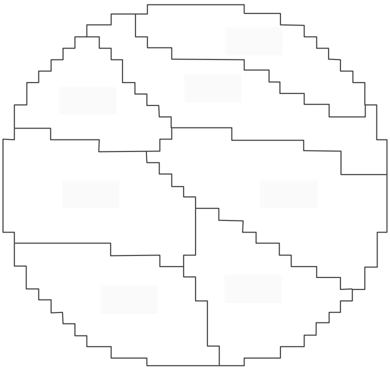

Figure 19.5 An example of grouping regions in a reactor cross-section.

Next, the behaviour of the mixing process during pneumatic conveying will be described by observing the motion of its components. The motion of each group can be defined by the displacement of a group's centre, which was determined as its centre of 'gravity'. The mixing process is then represented by a 2D group motion image, where each line determines a movement direction of the components. The basic idea of the proposed approach is shown in Figure 19.6.

Statistical information concerning the probabilistic relationships between EP in time interval Δt can be described by a covariance matrix $C_X^{\Delta t}$ of size $N \times N$. If the number of EPs is in practice equal to 1024, then the number of matrix elements is equal to 1024 × 1024. The example of fragment of the covariance matrix $C_{ki,}$ $i = 0,\ldots,1023$ for a solid–gas flow is shown in Figure 19.7.

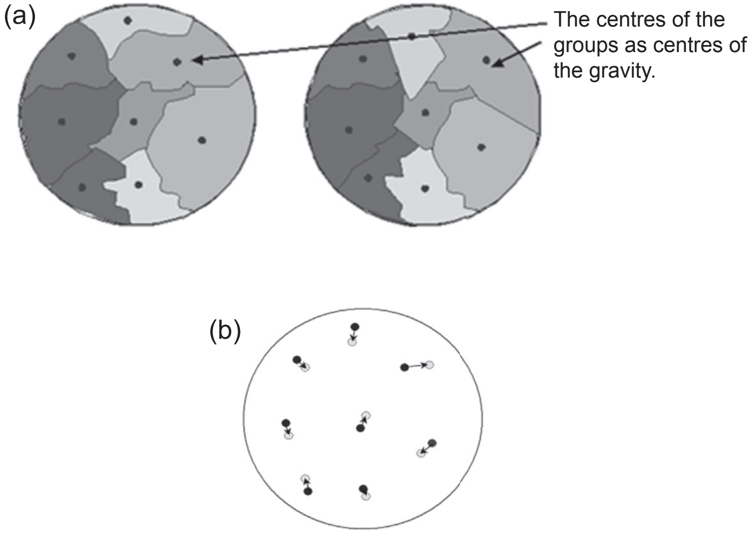

Figure 19.6 Examples of a cross-section decomposition based on EP process grouping (b) group motion changes for examples in (a); each vector is perpendicular to a cross-section.

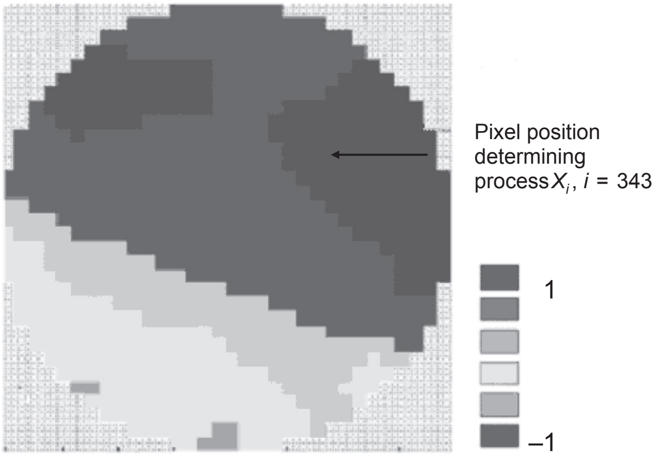

Figure 19.7 The fragment of covariance matrix C_X for a solid mass flow (the colours correspond to the values of matrix elements).

For groupings of EPs, it is proposed to use the principal component analysis (Krzanowski, 2000) of a covariant matrix and a k-means clustering (Hartigan & Wong, 1979), which allows creation of k possible different groups from the cloud of data points.

In principal component analysis, the perpendicular axes (called eigenvectors), which are defined by the dimensions of a covariance matrix of size 1024 × 1024 elements, should be determined. The principal components are the eigenvectors obtained from an eigenvector–eigenvalue decomposition of the covariance matrix of the EPs. The eigenvalue corresponding to an eigenvector represents the amount of variability explained by that eigenvector. The eigenvector of the largest eigenvalue is the first principal component. The eigenvector of the second-largest eigenvalue is the second principal component, and so on. There will be the same number of axes as variables/dimensions; the longest axis is the first principal component (PC1), and the next major axis is the second principal component (PC2). We make a slice through the cloud of EPs using the n-dimensional space defined by PCi, $i = 1,\ldots,n$ and project all of the EPs onto this space, then obtain an n-dimensional representation of the EPs, retaining the maximum variation (information) contained in the multivariate tomographic data Rodriguez and Tobias (2001).

In our case, it is assumed that this is the best n-dimensional representation of the multidimensional data, which contains multiple separate clusters of points called groups, and the space of PCi, $i = 1,\ldots,n$ provide a view of the maximum n-dimensional separation between them. Each EP in the analysed tomographic data is assessed concerning its contribution to the overall distribution of the data.

The percentage of the variability explained by the ith principal component can be calculated as follows:

$$\frac{\lambda_i}{\lambda_1 + \lambda_2 + \ldots + \lambda_n} * 100\% \tag{19.4}$$

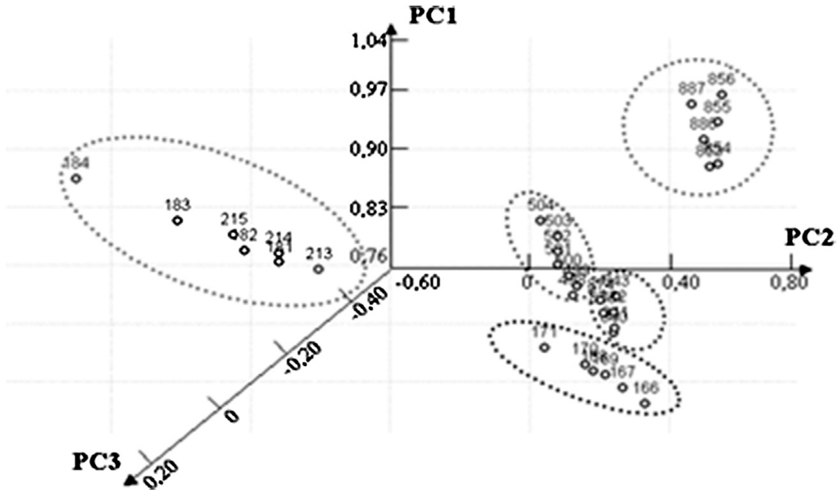

Figure 19.8 An example of grouping based on three principal components (PC1−3) for chosen EPs.

Figure 19.8 presents an example of a 3-D representation of the relationship between EP, where P_i is the ith EP.

The first $n = 8$ principal components, representing most of the variance of the multivariate data, are taken as latent variables. The eigenvectors and the eigenvalue give information about the dimensionality of the data and how the variables are related to each other (Figure 19.9).

The example of usage of the proposed analysis was carried out for tomographic images obtained from a pneumatic conveying flow rig at the Department of Chemical Engineering, UMIST, in the United Kingdom. Details concerning the above-mentioned system are described in Jaworski and Dyakowski (2001). All investigations were made for reconstructed images of a vertical pipe of a dense pneumatic conveying system.

The ECT sensors are mounted on a 60 mm outer diameter, 50 mm inner diameter perspex tube. Two planes of electrodes are adjacent to each other, and spacing between the centre line of the planes is equal to 3 cm. Each plane sensor includes eight electrodes, 3 cm in length. The centre of the ECT sensor is located approximately 87 cm below the neck of the hopper funnel. Dielectric material consists of polypropylene beads. Electrodes are numbered anti-clockwise when viewed from the funnel end of the flow rig. Injected air is swirled clockwise when viewed from the funnel end of the flow rig. Data were captured using a modified PTL ECT system controlled by an embedded PC. Approximate data capture rates are equal to 200 frames per second.

The grouping of processes based on principal component analysis was carried out for a time window when the material appeared in the space between two sensor planes (number of images in the sequence $M = 60$, number of time delay $\Delta t = 0.03$ s). The

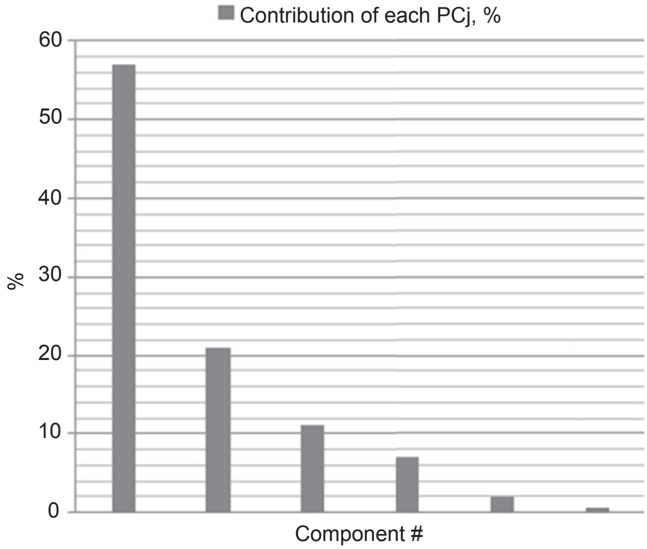

Figure 19.9 Percentage of variability explained by the first six principal components.

examples of the results obtained by the proposed approach are presented in Figures 19.10 and 19.11. Figures 19.10(b) and 19.11(b) show groups motion of Figures 19.10(a) and 19.11(a), respectively.

As one can see from Figures 19.10(b) and 19.11(b) a groups motion image distinctly indicates directions of relocating groups into the plug. The material is dispersed from an area with higher concentration to a part of the area with the lowest concentration. It is caused by the fact that the material is transported on one part of the pipe and influenced by gravitation dispersion of the material to the pipe centre as well as to the opposite wall of the pipe.

The estimation of the group velocity (perpendicular to the direction of a main flow) v_i can be calculated as follows:

$$v_i = \frac{d_i}{\Delta t}.$$

where d_i is the length of the velocity vector from an image flow, and Δt is the time between two serial groupings.

Tables 19.2 and 19.3 comprise the calculated velocities of marked groups for two examples of plugs. Displacement of groups into plug cases is shown in Figure 19.12.

Summing up, the proposed approach is based on a model of flow wherein tomographic measurement is presented as stochastic processes. The statistical analysis of such processes permits the decomposition of a flow into separated components. The components of the flow are defined as an area, in which changes in the material concentration are very similar. Changes in the position of individual components permit

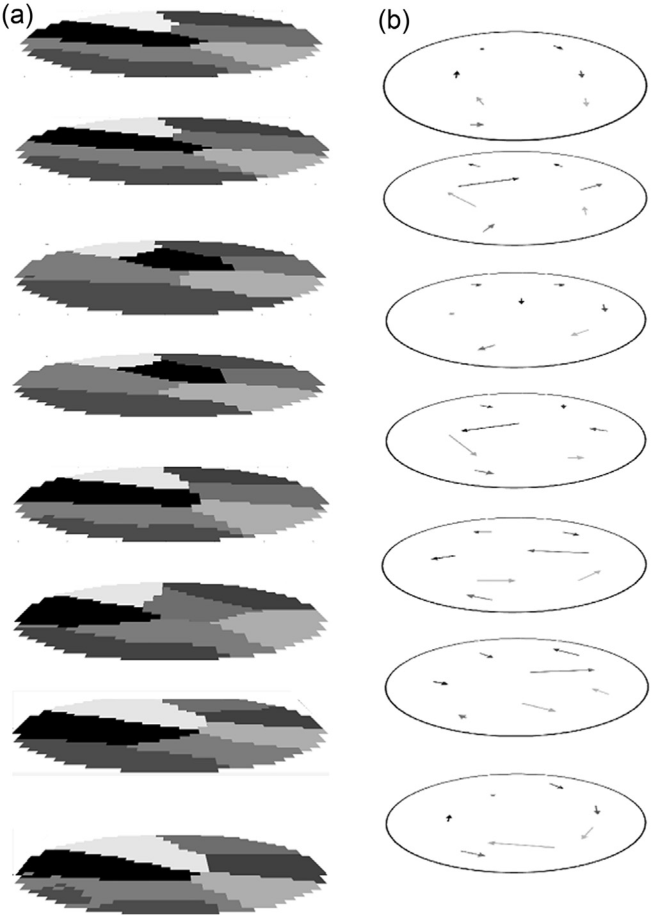

Figure 19.10 Examples of the grouping and image flow during plug 1: groups image, (b) groups motion image.

one to investigate the dynamics of the process, its monitoring and the measurement of flow parameters. Definition of such parameters as group velocities allows investigation of mixing processes.

19.6 Other applications of tomography for mixing processes

Although tomography provides new opportunities to study/monitor the mixing processes inside the reactors, it has some limitations to use in practice. Thus tomographic techniques can apply when there are at least two phases/mixtures inside the volume of interest, whose physical properties will allow observation of a distinction by means of measurement unit. Otherwise, if materials have similar physical properties, using

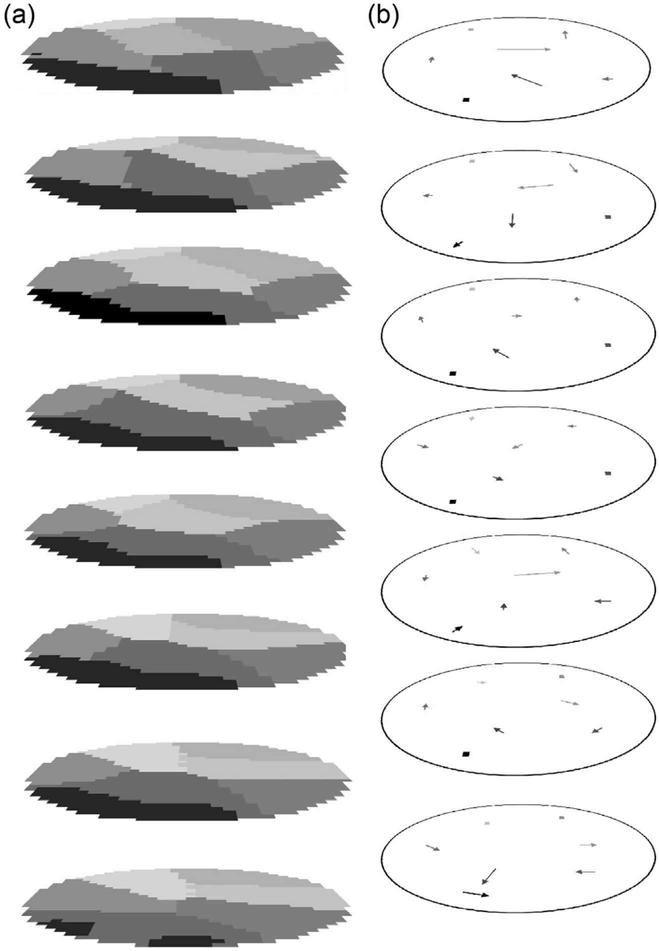

Figure 19.11 Examples of the grouping and image flow during plug 2: (a) groups image, (b) groups motion image.

tomographic techniques becomes not useful, because it will be impossible to determine the distribution of the materials. On the other hand, the number of phases/mixtures may not be significant because of the weak quality of the reconstructed images.

Consider the examples of the tomographic techniques in specified applications. One of them is the utilization of tomography to quantify the degree of homogeneity of multiphase mixtures in pharmaceutical industry and related application areas. Tomography provides useful information about the chemical composition, physical shapes or general status of manufacturing. The use of ECT to study the solid−gas mixing has been described in detail in Section 19.5.

However, electrical tomography can be successfully used for other types of phases. Solid−liquid mixing is another case of mixing that occurs in different industry fields. For instance, monitoring dispersion of dry powders into solution or the suspension of

Table 19.2 The group velocities (Figure 19.10)

Frame number	v_1 (m/s)	v_2 (m/s)	v_3 (m/s)	v_4 (m/s)	v_5 (m/s)	v_6 (m/s)	v_7 (m/s)
1320–1323	0.06	0.13	0.06	0.06	0.08	0.00	0.06
1323–1325	0.20	0.57	0.18	0.76	0.13	0.20	0.32
1325–1330	0.08	0.00	0.10	0.04	0.04	0.04	0.07
1330–1333	0.13	0.48	0.06	0.50	0.06	0.13	0.13
1333–1335	0.28	0.45	0.38	0.28	0.20	0.18	0.72
1335–1338	0.08	0.27	0.08	0.13	0.30	0.17	0.54
1338–1340	0.40	0.72	0.40	0.09	0.25	0.00	0.27

Table 19.3 The group velocities (Figure 19.11)

Frame number	v_1 (m/s)	v_2 (m/s)	v_3 (m/s)	v_4 (m/s)	v_5 (m/s)	v_6 (m/s)	v_7 (m/s)
5408–5411	0.00	0.30	0.06	0.06	0.42	0.00	0.18
5411–5413	0.08	0.24	0.00	0.06	0.3	0.00	0.19
5413–5416	0.00	0.17	0.00	0.13	0.06	0.00	0.06
5416–5419	0.00	0.08	0.00	0.08	0.13	0.06	0.06
5419–5422	0.08	0.06	0.06	0.06	0.36	0.13	0.13
5422–5425	0.00	0.08	0.08	0.06	0.13	0.06	0.00
5425–5428	0.19	0.24	0.12	0.17	0.12	0.00	0.00

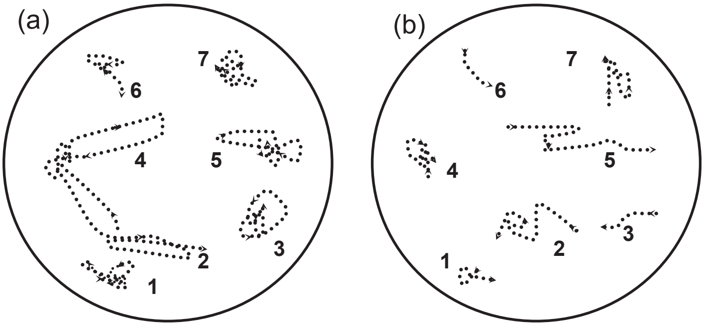

Figure 19.12 Displacement of groups during: (a) first plug; (b) second plug. *k*-number of group.

denser solids in a fluid remains a big challenge. Electrical resistance tomography can visualize the solids distribution in specified cross-sections of the reactor. In this case, the sensors are the linear probes, which are inserted into the reactor. These probes are connected to a tomography system, for instance ITS p2000, which is designed to measure resistance data and display reconstructed images. The probe measures conductivities perpendicular to its position and reflects the conductivity profile inside the reactor. Next, the degree of mixing throughout the vessel can be calculated based on the conductivity profiles.

Another application where electrical tomography can be successfully utilized, is liquid—liquid mixing. The number of sensor planes and electrode plane configuration can be different, for instance four plane sensor systems where each plane includes eight electrodes. These *n*-electrode sensors will allow one to obtain the online conductivity maps of the cross-sections. The map will represent mixing patterns in specified planes from the top to the bottom of the reactor. This provides the opportunity to have full observation of liquid—liquid mixing process in time. An example of conductivity maps after high-conductivity injection on the right side is shown in Figure 19.13. Next, an analysis of reconstructed images should be applied. The velocity profiles can be calculated using the similar idea based on principal component analysis as described in Section 19.5.

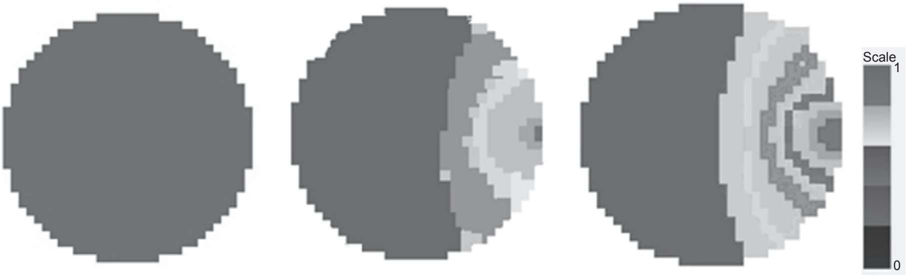

Figure 19.13 Conductivity maps after high-conductivity injection at right side.

Electrical tomography can also be utilized in gas—liquid mixing. The basic idea is the same as has been shown in previous applications. The $n \times m$-electrode sensor system, where n is the number of planes and m is the number of electrodes connected to a tomograph, is mounted around the reactor. The tomograph measures and displays resistance/conductivity value data. The reconstructed images present corresponding profiles. To get more clarity, information about mixing 3D image reconstruction algorithms can be applied.

It is obvious that the possible frame rate of a tomograph is dependent on process speed. Because most chemical processes have a slow nature, the frame rate of modern multisensor tomograph systems is enough to provide online monitoring of processes. The problem can be in cases of use of 3D visualization.

An interesting case of the use of process tomography for mixing processes is detection of grotto formations, which can occur in the mixing of fluids, for instance production of shampoos, pastes and sauces. The grotto patterns (regions) often occur in reactors during non-Newtonian fluid mixing. These weakly mixed regions should be detected because their presentation degrades the quality of the output product. Therefore, process tomography can be an effective tool for detecting of such artifacts inside reactors. More details concerning the grotto detection can be found, for instance, in Simmons et al. (2009).

19.7 Future trends

The problem of determining the parameters of mixing processes for different types of materials based on the analysis of images capturing corresponding tomographic systems remains a significant challenge. The main difficulty is not the manner of obtaining the tomograms but the development of efficient processing algorithms that extract information about the mixing process. The known algorithms are based on the use of correlation techniques in the analysis of mixing processes. However, their common drawback is that correlation methods impose certain restrictions on the input data. Thus, for example, input data should be cross-correlated and have significant value changes. Otherwise, the use of the correlation method is not possible.

Also, the main problem is the question of how to validate whether the obtained data relating to mixing processes corresponds to reality. One of the possible solutions is to carry out the verification procedure for a tomographic system. The procedure can be carried out by the addition of materials like tracers, which are easily identifiable during the mixing. Comparing the results obtained by observing the movement of tracers to results obtained from the tomographic system, one can estimate the correctness of its performance. Developing such a methodology to estimate the correctness can be a main priority in future work.

Another important issue is the question whether 3D tomography can be used to analyse the mixing processes. At present there is no single answer to this question, since such a tomography exists in laboratory versions only.

Acknowledgement

The author wishes to express gratitude to Prof D. Sankowski and Dr K. Grudzien; without their knowledge and assistance this chapter would not have been successful.

References

Ding, Y., Wang, Z., Wen, D., & Ghadiri, M. (2005). Solids motion in a gas-solid two-phase mixture flowing through a packed bed. In *4th world congress on industrial process tomography, aizu, Japan* (pp. 368−374).

Du, B., Fan, L.-S., Wei, F., & Warsito, W. (2002). Gas and solids mixing in a turbulent fluidized bed. *AIChE Journal, 48*(9), 1896−1909.

Dyakowski, T., Hale, J., Jaworski, A., White, N., Harris, N., Nowakowski, A., et al. (2003). Characterisation of heterogeneous mixtures by using thick-film ultrasonic transducers. In *3rd world congress on industrial process tomography, Banff, Canada* (pp. 761−767).

Etuke, E., & Bonnecaze, R. (1998). Measurement of angular velocities using electrical impedance tomography. *Journal of Flow Measurement and Instrumentation, 9*(3), 159−169.

Hartigan, J. A., & Wong, M. A. (1979). A k-means clustering algorithm. *Applied Statistics, 28*(1), 100−108.

Huang, S., & Xie, C. (2013). Ultrasound imaging and measurement of swirling gas-liquid multiphase flow. In *7th world congress on industrial process tomography, WCIPT7, Krakow, Poland* (pp. 1−9).

Jaworski, A. J., & Dyakowski, T. (2001). Tomographic measurements of solids mass flow in dense pneumatic conveying. What do we need to know about the flow physics?. In *2nd world congress on industrial process tomography. Hannover, Germany* (pp. 353−361).

Kagoshima, M., & Mann, R. (2005). Tomographic visualisation of semi-batch precipitation with multizone mixing model validation. In *4th world congress on industrial process tomography, Aizu, Japan* (pp. 788−793).

Kourunen, J., Heikkinen, L. M., Vauhkonen, M., Käyhkö, R., Matula, J., & Käyhkö, J. (2007). Imaging of mixing of two miscible liquids using electrical impedance tomography. In *5th world congress on industrial process tomography, Bergen, Norway* (pp. 803−809).

Kraft, J., Launikonis, A. L., & Swiegers, G. F. (August 22, 2005). *Method of monitoring and controlling of mixing processes*. CA 2619702 A1.

Krzanowski, W. J. (2000). *Principles of multivariate analysis: A user's perspective*. Oxford University Press.

Laurent, B. F. C., Bridgwater, J., & Parker, D. J. (2001). Structure of transaxial flow in a powder mixer. In *2nd world congress on industrial process tomography, Hannover, Germany* (pp. 346−352).

Lucas, G. P., Cory, J., Waterfall, R., Loh, W. W., & Dickin, F. J. (1999). Measurement of the solids volume fraction and velocity distributions in solids-liquid flows using dual-plane electrical resistance tomography. *Journal of Flow Measurement and Instrumentation, 10*(4), 249−258.

Mosorov, V. (2013). An iterative position reconstruction algorithm for radioactive particle techniques. *Applied Radiation and Isotopes, 79*, 56−61.

Mosorov, V., Sankowski, D., Grudzien, K., & Romanowski, A. (2004). Characterizing solids mixing process within a plug body. *Bulletin De la Societe Des Sciences Et Des Letters De Lodz,* 45−56. Poland, 2004.

Pląskowski, A., Beck, M. S., Thorn, R., & Dyakowski, T. (1995). *Imaging industrial flows*. Bristol: Institute of Physics Publishing.

Rantanen, J., Wikström, H., Turner, R., & Taylor, L. S. (2005). Use of in-line near-infrared spectroscopy in combination with chemometrics for improved understanding of pharmaceutical processes. *Analytical Chemistry, 77*, 556−563.

Rimpiläinen, V., Poutiainen, S., Heikkinen, L. M., Savolainen, T., Vauhkonen, M., & Ketolainen, J. (2010). Monitoring of high shear mixing and granulation with capacitive measurements and tomography. In *6th world congress on industrial process tomography, Beijing, China* (pp. 44−51).

Rodriguez, R. N., Tobias, R. D. (2001). *Multivariate methods for process knowledge discovery: The power to know your process*. Cary, NC: SAS Institute Inc., paper 252−26. http://www.sas.com.

Simmons, M., Edwards, I., Hall, J., Xiangfeng, F., Parker, D. J., & Stitt, E. (2009). Techniques for visualisation of cavern boundaries in opaque industrial mixing systems. *AIChE Journal, 55*(11), 2765−2772.

Wang, M., & Yin, W. (2001). Measurements of the angular velocity distribution in miscible liquid mixing using electrical resistance tomography. In *2nd world congress on industrial process tomography, Hannover, Germany* (pp. 146−150).

West, R. M., Meng, S., Aykroyd, R. G., & Williams, R. A. (2003). Spatial-temporal modelling for electrical impedance imaging of a mixing process. In *3rd world congress on industrial process tomography, Banff, Canada* (pp. 226−232).

Applications of capacitance tomography in gas–solid fluidized bed systems

20

A. Wang[1], *Q. Marashdeh*[2], *F.L. Teixeira*[1], *L.-S. Fan*[1]
[1]The Ohio State University, Columbus, OH, USA; [2]Tech4Imaging LLC, Columbus, OH, USA

20.1 Introduction to fluidized bed systems

20.1.1 The principle of fluidization

Fluidization is the process of stationary solid particles brought into a dynamic "fluid-like" state by an upward stream of fluid (gas or liquid) (Fan & Zhu, 2005). In this chapter, only gas–solid fluidization will be discussed. The basic components required for a fluidized bed are a container, a gas distributor, solid powder, and gas. When a gas flow is introduced into the bottom of a bed packed with solid particles, the gas will move upwards through the gaps between the particles. When the gas velocity is low, the drag force on each individual particle is small, and the bed remains in a packed configuration. When the gas velocity exceeds a certain threshold velocity U_{mf} (where mf denotes "minimum fluidization"), the upward aerodynamic drag force becomes large enough to counteract the particle gravity minus buoyancy. In this case, the particles will move away from each other and become suspended within the fluid, causing the bed to expand in volume and exhibit some fluid behavior. As the gas velocity is further increased, the bed will keep expanding and the bulk density will keep dropping, and finally the particles cannot form a bed anymore and will be blown away by the gas.

In a fluidized bed, as the particles are held suspended by the gas stream, the pressure drop Δp of the gas passing through the fluidized bed is constant and equal to the difference between solids weight minus buoyancy over the unit surface of the bed cross-section (if no particle is conveyed away from the bed):

$$\Delta p = H_{fb}(1-\varepsilon)(\rho_s - \rho_g)g \tag{20.1}$$

in which H_{fb} is height of the fluidized bed; the porosity ε is the voidage fraction defined by the volume of the fluidized bed divided by the total bed volume; ρ_s and ρ_g are the densities for the solids and for the gas, respectively; and g is the gravitational constant.

When fully fluidized, the solid particles will float and move chaotically; in this case, the bed will behave as a fluid. The bed surface will always be horizontal, with objects with lower density floating up and objects with higher density sinking down. The fluidic character permits the particles to be transported freely, akin to a fluid in a pipe.

Industrial Tomography. http://dx.doi.org/10.1016/B978-1-78242-118-4.00020-4
Copyright © 2015 Elsevier Ltd. All rights reserved.

20.1.2 Fluidization regimes

Geldart (1973) classified particulate powders into four groups according to their mean particle size d_p and the difference between the solid and gas phase densities $\rho_p - \rho_g$, as Figure 20.1 shows. The most salient features of each group can be summarized as follows: Group A, the bed can exhibit dense phase expansion after minimum fluidization and before minimum bubbling velocity; Group B, no dense phase expansion, the gas bubbles appear at minimum fluidization velocity; Group C, powders are cohesive and very difficult to be fluidized; Group D, coarse particles can form stable sported beds, and the mixing is not as good as Group A and B.

Fluidization regimes can be generally classified into two categories: homogeneous and heterogeneous (Harrison, Davidson, & De Kock, 1961). In homogeneous fluidization, solid particles are uniformly dispersed in the fluid material without observable bubbles. Most liquid fluidized beds are homogeneous. For gas—solid systems, the fluidization regimes are more complex. Based on different Geldart particle groups and gas velocities, several different fluidization regimes can be observed: fixed bed, homogeneous fluidization, bubbling fluidization, slugging fluidization, turbulent fluidization, and entrainment process.

When the gas velocity is lower than the minimum fluidization velocity U_{mf}, no particle moves with the gas and the bed is in a fixed bed situation. When the gas velocity is higher than U_{mf}, different particles will have different fluidization regimes. For Geldart's Group A powders, no bubbles will be observed and the bed will expand homogeneously. Only when the gas velocity is higher than the minimum bubbling velocity U_{mb}, bubbles will appear in Group A particles. For Geldart's Group B and D particles, as soon as the gas velocity is larger than U_{mf}, virtually solids-free gas bubbles will begin to form. Bubbles that form near the gas distributor rise up and coalesce and the local mean bubble size increases rapidly with increasing height above the distributor. As they reach the bed surface, the bubbles burst, ejecting any particles

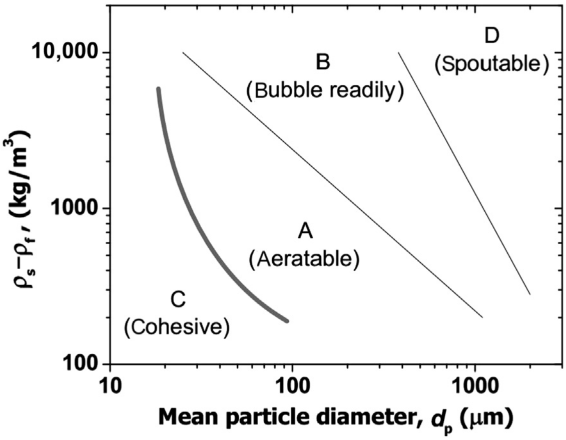

Figure 20.1 Geldart classification of particles.
Figure produced based on Geldart (1973), with permission from Elsevier.

into the empty chamber of the reactor. Behind the rising bubbles there are wakes or tails dragging particles upwards. Bubble movement promotes intense particle circulation and gas−solid mixing in the fluidized bed. The bed can be treated as if it consists of two phases: (1) the bubble phase, in which there are virtually no particles; and (2) the emulsion phase, constituting the remaining of the bed with a much higher solids density compared with the bubble phase, which is in a condition similar to the state of the bed at the minimum fluidization velocity U_{mf}.

If gas velocity is further increased, the bubble size may become large enough to cover the whole cross-section of the column, thus inducing the slugging regime. Slugging often occurs in a fluidized bed with a small diameter or large height/diameter ratio. With an even further increase in the gas velocity, the bed will change to a turbulent regime where the bubble and emulsion phases may become indistinguishable and the surface of the bed becomes diffused. When the gas velocity is high enough, particles will be transported out of the bed, and the bed will have no surface but a dense phase region at bottom and a dilute phase on top. In such case, the particles need to be replaced or recycled to operate the bed. If the gas velocity is very high, all particles fed into the reactor will be transported out in dilute phase, comprising a pneumatic conveying. Spouting occurs when high-velocity gas is injected through a small opening into the bed, normally with Group D particles. At the center of the spouting bed, a dilute flow core region exists and the gas jet penetrates the whole bed. Channeling will happen if the bed particles are cohesive (Group C) or the gas distribution is not uniform enough across the distributor.

20.1.3 Industry applications of gas−solid fluidized bed reactors

Based on the principle of fluidization, gas−solid fluidized beds may exhibit some distinct advantages compared to other types of reactors:

1. The reactor structure is relatively simple and the handling of solids is very easy, due to the liquid-like behavior of solids particles under fluidization conditions. The solids can be continuously added or discharged from the system without shutting down the units.
2. Very good temperature uniformity occurs due to the intense solids mixing. Hot spots can be avoided even with strongly exothermic reactions such as combustions.
3. High-heat-transfer coefficients are present between the bed and reactor walls and any immersed heating/cooling surfaces.
4. A large gas−solid contact area is enabled by virtue of the small size of particles.

At the same time, certain limitations and disadvantages of fluidized beds should be recognized:

1. Low conversion as a consequence of high solids mixing rate, nonuniform residence time, substantial back-mixing of both solids and gas, and bypassing of gas via bubbles or through channels in the beds. Such properties may also contribute to an unfavorable selectivity.
2. Solids separation devices, such as cyclones, as well as gas purification equipments are required, which increases the capital cost. Without these equipments, solid materials or products may be lost, due to the solids entrainment by fluidizing gas, and may pollute the atmosphere.

3. Attrition of solids (especially significant with catalysts), erosion of internal surfaces, and agglomeration of solids may cause serious operational problems.
4. Due to the inherent complexity of the fluidization phenomenon, it is not easy to make precise predictions for reactor design and scale-up.

Although gas—solid fluidized bed reactors have limitations, they are extensively applied in industry. These processes can be generally categorized into three types:

1. Catalytic gas phase reactions. Solid particles serve as catalyst and gas phases react inside the reactor. Solid catalyst materials often combine favorable activity and selectivity characteristics along with acceptable physical properties such as size, density, and rigidity. The most important application for such kind of reactions is the fluidized catalytic cracking (FCC) process used in petroleum refineries. This process converts the high-molecular-weight hydrocarbon fractions of crude oils into gasoline and other products.
2. Gas—solid reactions. In this type of reaction, fluidized particles react with gas to provide useful products such as thermal energy or other types of gas and solids. Typical applications include: ore-roasting, which was one of the first usages of fluidized beds; fluidized bed combustion, which can burn coal at lower temperature compared to traditional pulverized coal combustion, units thus reducing nitrogen oxide emissions; and coal gasification process, which is used for producing “syngas” composed primarily of CO and H_2.
3. Other noncatalytic processes. In these processes, the solid particles are inert. The solids can be used as uniform heat medium, or nuclei of product vapor. And very often, the fluidized beds can be used for drying the particulate materials, as well as for agglomeration and granulation of solid particles. These processes are widely used in food and pharmaceutical industries.

20.2 Electrical capacitance characterization of gas—solid fluidized beds

20.2.1 Tomography techniques for fluidized beds

Since gas—solid fluidized beds are very important for industry, many experimental techniques have been developed for such beds. For example, tracers can be used to study the solids residence time; pressure transducers and pilot tubes are employed to monitor pressure fluctuations; and thermal couples are irreplaceable for temperature controlling. In this chapter, those of interest are tomography techniques. Photography and tomography are the main noninvasive techniques used to investigate bubble behaviors, particle motions, and phase distributions in fluidized beds. Below are listed several such types of experimental techniques:

1. Photography. Used in 2D or 3D columns with the aid of transparent reactor walls and external light sources; good for observing near-wall behaviors but difficult to clearly see through the inside of the column.
2. X-ray, gamma-ray, and positron emission tomography. Accurate methods yielding high resolution, but with very high capital costs, and potential environmental and health hazards.
3. Magnetic resonance imaging (MRI). High resolution, but the imaging scale is very limited and also has a high capital cost. Relatively slow acquisition times can also be an issue.

4. Electrical tomography techniques, including electrical capacitance tomography (ECT), electrical impedance tomography (EIT), and electromagnetic inductance tomography (EMT). ECT monitors the permittivity distributions of nonconductive phases; EIT is useful for the reactor with conductive phases inside; and EMT is mainly applied for high conductive fluids that could induce measurable current under a magnetic field, which is not suitable for gas—solid systems. Electrical tomography techniques have been much used in recent years because of their low cost, high imaging speeds, noninvasive design, and safe nature. The most significant drawback for the tomography system is its relatively low spatial resolution. Currently, the most advanced electrical tomography system can have a linear resolution of about 3% of the reactor's characteristic length. ECT will be the focus of our discussion in what follows.

20.2.2 Electrical capacitance tomography applications in gas—solid fluidization

ECT is a promising imaging technique with high potential in multiphase flow measurements. Besides the merits shared above with other electrical tomography systems, the ECT system has its unique advantages as well. Below is a list of additional attractive features of ECT for gas—solid applications:

1. Fast imaging speed. The frame rate (FPS, frames per second) of ECT could be as high as 1000 FPS. As gas—solid fluidization systems often have very turbulent flow behaviors, the high-speed imaging ECT is a highly desirable characteristic to capture transient flows inside the vessel.
2. Suitable for nonconductive materials. Unlike EIT, ECT does not require a continuous phase of conductive material for providing a measuring path between sender and receiver plates. Most gas—solid applications involve nonconductive solids, thus making ECT a natural choice for such applications.
3. Reasonable permittivity difference range between gas and solid. To differentiate the various phases, ECT requires a noticeable permittivity difference between the two phases. At the same time, this difference should not to be too large as it might then impact the reconstruction results (based on linearization approximations) through "soft-field effects" (nonlinearities). The permittivity difference between common gas and solids is more favorable than some gas—liquid or liquid—solid applications. For example, the relative permittivity of dry air at standard condition is close to 1; the relative permittivity of FCC catalyst powder at the same condition is about 3—5; in the meantime, the relative permittivity of pure water at similar conditions is more than 80. Because of this, ECT image reconstruction techniques are typically more accurate for an air—FCC system than for an air—water system.

20.2.3 Validation with conventional instruments

The first investigations on capacitance measuring techniques can be traced back to the 1980s in the Morgantown Energy Technology Center (METC) of the US Department of Energy (Halow & Nicoletti, 1992). Starting from the early 1990s, ECT systems have been used to investigate multiphase flow phenomena (Halow, Fasching, Nicoletti, & Spenik, 1993; Huang, Plaskowski, Xie, & Beck, 1989). Since then, more advanced

ECT systems have been applied in fluidization phenomenon research (Makkawi & Wright, 2004). Besides traditional 2D ECT systems, advanced 3D ECT systems and electrical capacitance volume tomography (ECVT) systems have been devised and implemented to further expand the capabilities of capacitance tomography.

For any novel measurement technique, the first and maybe the most important feature is the reliability of the technology. For fluidization phenomena, by directly comparing the measured results between ECT systems and some traditional experimental methods, it has been verified that the ECT can be successfully used to measure fluidization phenomena.

In 2003, Pugsley et al. (2003) compared the results from ECT with those of a fiber optic probe in an operating fluidized bed. Figure 20.2 shows the diagram of the circulating fluidized bed (CFB) system used in that experiment. The riser is 7 m in height

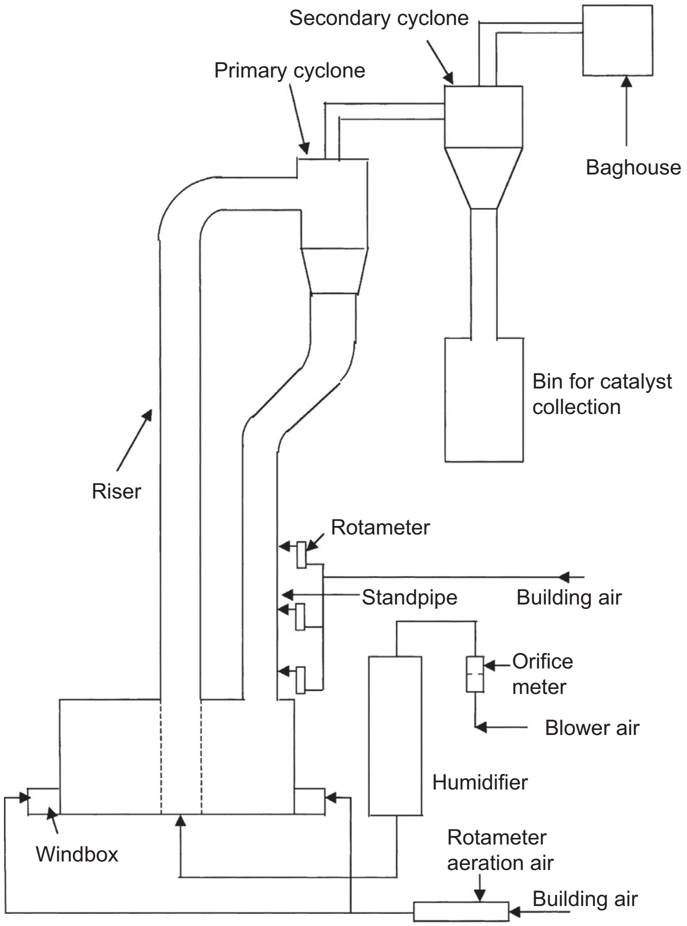
Secondary cyclone
Primary cyclone
Baghouse
Bin for catalyst collection
Riser
Rotameter
Standpipe
Building air
Orifice meter
Blower air
Humidifier
Windbox
Rotameter aeration air
Building air

Figure 20.2 Diagram of the CFB system. CFB, circulating fluidized bed.
Figure reproduced from Pugsley et al. (2003), with permission from Elsevier.

with an inner diameter (ID) of 0.14 m. The CFB riser consists of several interchangeable flanged Plexiglas sections 1.6 m above the riser inlet. One section is equipped with an ECT sensor and the other has an optical fiber probe mounted. By carefully controlling the air and solid flux, flow conditions can be reestablished for comparison. FCC catalyst is used as the solid phase with an average diameter of 89 μm. The particle density is 1550 kg/m^3. The twin-plane ECT system used in the experiment consisted of eight electrode plates in each layer and an iterative linear back-projection (ILBP) algorithm was employed to perform the image reconstruction from the ECT data.

Figure 20.3 shows the time-averaged radial voidage profiles from both ECT and fiber optic probe measurements under various solid flux conditions. The differences between the two curves from ECT and optical fiber probe are smaller than 10%. In the center core region of the riser, the difference is less than 1%, becoming progressively larger near the wall region. This may be explained by the nonuniformity of the sensitivity distribution and the bias of boundary effect in the ECT system. Basically, the results show good agreement between the ECT data and optical fiber probe results.

Recently, Rautenbach, Mudde, Yang, Melaaen, and Halvorsen (2013) compared the ECT system with an X-ray tomography system on a fluidized bed with wide particle size distributions. They compared bubble volume and found good agreement. Chandrasekera et al. (2012) compared the ECVT system with an MRI tomography system on a spouting bed, and also found satisfactory agreement between the two techniques.

All these results corroborate the fact that ECT technique is a reliable experimental technique for fluidization investigations.

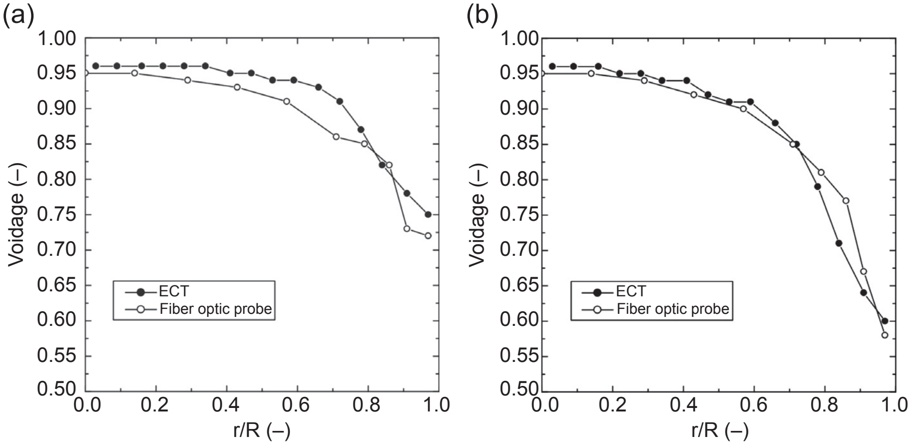

Figure 20.3 Comparison of radial voidage profiles measured with ECT and fiber optic probe in the CFB riser containing FCC catalyst: (a) riser solids mass flux = 148 kg/(m^{2}s), superficial gas velocity = 4.7 m/s; (b) riser solids mass flux = 264 kg/(m^{2}s), superficial gas velocity = 4.7 m/s. CFB, circulating fluidized bed; ECT, electrical capacitance tomography; FCC, fluidized catalytic cracking.
Figure reproduced from Pugsley et al. (2003), with permission from Elsevier.

20.3 Examples and discussion for electrical capacitance tomography applications in conventional fluidized beds

In this section, further examples of ECT measurements, in particular 3D ECVT applications to fluidization systems, will be discussed to illustrate the suitability of ECT techniques.

20.3.1 Circulating fluidized bed

A gas—solid CFB is a device in which particles are carried upwards by gas in a riser and then separated by a cyclone to return back to the bottom through a downer, forming a recirculation loop for the particles. Major commercial applications of CFBs include fluid catalytic cracking, Fischer—Tropsch synthesis, coal combustion and gasification, and ore processing. ECT techniques can be used to image flow behaviors and solids distributions in CFBs. Traditional ECT systems have all electrodes placed in one plane and can generate cross-sectional slice images. On the other hand, fully volumetric images can be directly produced using ECVT with several longitudinal layers of sensor plates interacting simultaneously (Wang, Marashdeh, Fan, & Warsito, 2010). Researchers in the Ohio State University have constructed a CFB cold model with ECVT sensors mounted around it. In this section, some experimental results will be

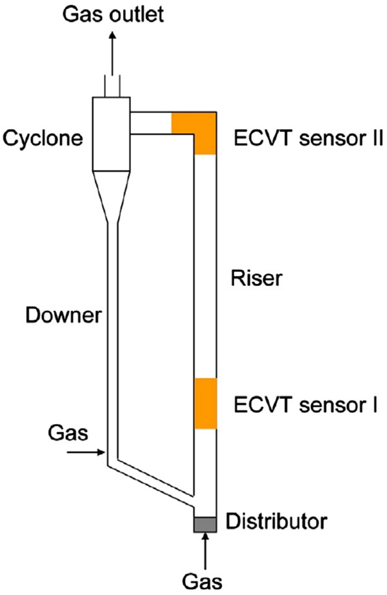

Figure 20.4 Schematic diagram of the gas—solid CFB mounted with ECVT sensors. CFB circulating fluidized bed; ECVT, electrical capacitance volume tomography.
Figure reproduced from Wang et al. (2012) with permission from American Chemical Society.

discussed to illustrate the application of ECVT to CFBs (Wang, Marashdeh, Wang, & Fan, 2012).

Figure 20.4 shows the schematic diagram of the CFB system. The Plexiglas CFB consists of a 5 cm ID riser with a height of 2.6 m, a 90° bend exit, a cyclone, a 3.8 cm ID downer, and an L-valve. A porous plate with a mean pore size of 20 μm and 60% fractional free area is used as the gas distributor. FCC particles (Geldart group A, mean diameter 60 μm, density 1400 kg/m^3) are used as the solid phase and the fluidization gas is air. A cylinder and a bend shape ECVT sensor are installed at the riser and bend exit region of the CFB, respectively. Figure 20.5 is an actual photograph of the CFB system and the ECVT sensors.

From ECVT sensor I, the solids distribution images in the riser are obtained as shown in Figure 20.6, where time-averaged solids distribution in the riser under different gas superficial velocities can be visualized.

The left figure in each image is the solids distribution along the axial direction, whereas the right image represents three horizontal cross-sectional distributions. The results clearly indicate the core-annular shape lean phase flow in the riser. Most solids are distributed near the wall. In the center of the riser, gas is the dominating phase. The thickness of the annulus and the concentration in the annulus near the wall decrease with the superficial fluidization gas velocity.

The ECVT sensor II mounted at the riser exit is used to monitor the solids distribution at the bend section connecting the riser and the cyclone. Figure 20.7 illustrates the theoretical prediction that solids move upward through the riser with the fluidization gas, and that, in the bend exit, most solids will turn their moving directions into

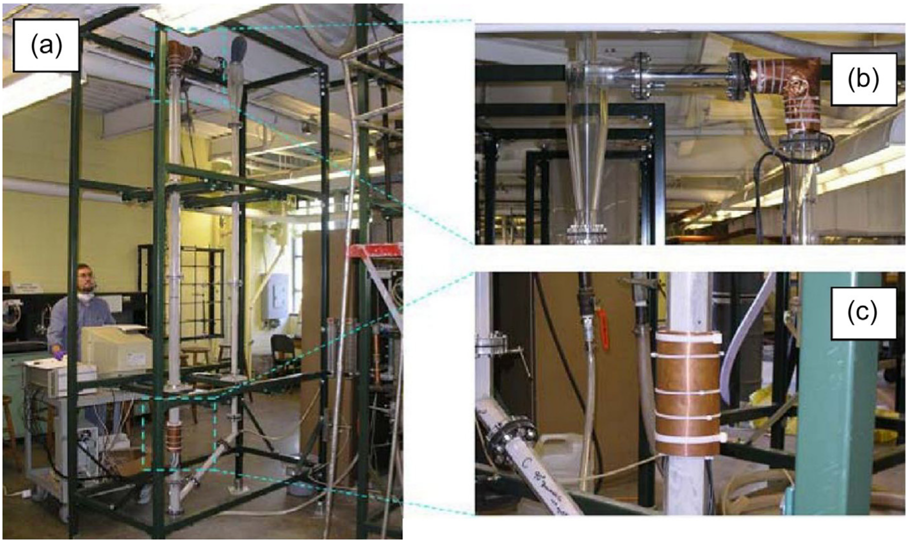

Figure 20.5 Photograph of the 0.05 m ID gas–solid CFB mounted with ECVT sensors: (a) CFB; (b) ECVT bend sensor; (c) ECVT riser sensor. CFB, circulating fluidized bed; ECVT, electrical capacitance volume tomography; ID, inner diameter.
Figure reproduced from Wang et al. (2012) with permission from American Chemical Society.

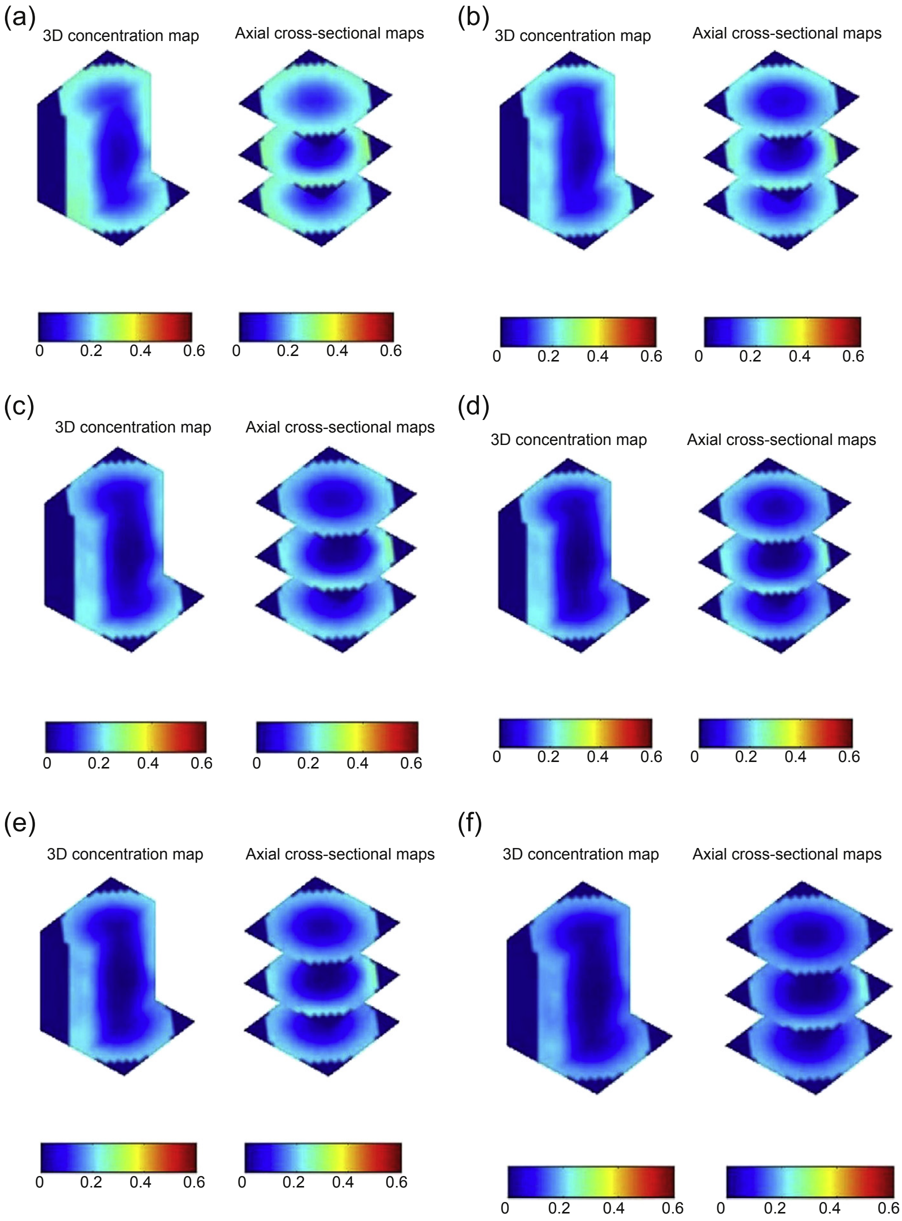

Figure 20.6 Time-averaged solids holdup distribution in the riser at $U\mathrm{g}$ = (a) 0.97; (b) 1.16; (c) 1.36; (d) 1.55; (e) 1.75; (f) 1.94 m/s.
Figure reproduced from Wang et al. (2012) with permission from American Chemical Society.

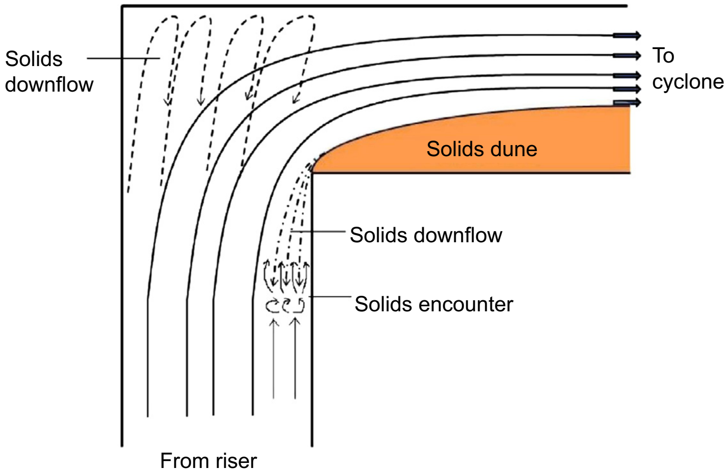

Figure 20.7 Theoretic illustration of the solids distribution in the bend section.
Figure reproduced from Wang et al. (2012) with permission from American Chemical Society.

horizontal and go into the cyclone. Due to the high upwards gas velocity, some solids will be carried to the top corner of the bend and fall back into the riser. Some solids in the horizontal pipe will fall down by gravity and a solids dune will appear as indicated.

Figure 20.8 shows the solids distributions under different gas velocities at the riser bend exit from ECVT sensor II. The solids dune and the entrained solids at the top corner of the bend can be clearly seen from the images. Figure 20.9 shows the quantitative results of the solids concentrations at the corner of the bend. The solids concentration will increase with the superficial gas velocities.

From these results, the solids distributions in the CFB can be observed directly, which can offer a better understanding of the flow behavior inside the CFB system. The solids distribution information from the bend riser exit section can be used to

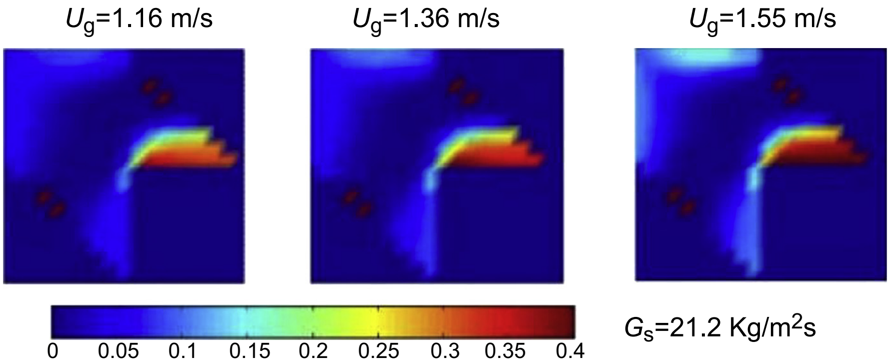

Figure 20.8 Time-averaged solids holdup distribution in the axial plane of the bend.
Figure reproduced from Wang et al. (2012) with permission from American Chemical Society.

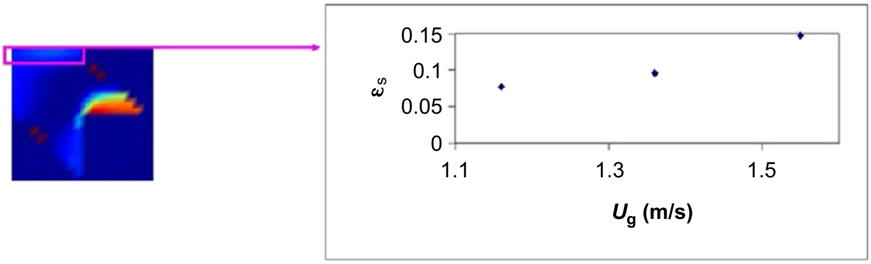

Figure 20.9 Quantitative time-averaged solids holdup distribution in the axial plane of the bend at $G_s = 21.2$ kg/(m^2 s): top wall area of the horizontal section.
Figure reproduced from Wang et al. (2012) with permission from American Chemical Society.

improve the bending design to reduce the erosion and attrition for the reactor wall as well as the solid particles.

20.3.2 Gas and gas/solid jet penetration in a gas—solid fluidized bed

Gas—solid fluidized beds are extensively employed in industry. One of the advantages of fluidized beds is that under a fluidization situation, solid particles can behave like liquid and the solid feedstock can be continuously added without suspending the reactor. In some scenarios, solid particles are transported into the reactor by the carrier gas as horizontal jets at a certain height above the bed bottom to enhance the mixing of the phases. Wang, Yu, Marashdeh, and Fan (2010) have studied the jets' penetration inside a gas—solid fluidized bed using an ECVT system. Figure 20.10 shows the schematic diagram of the gas—solid fluidized bed with a horizontal gas/solid jet penetration system. The column has an ID of 0.3 m and above the column there is a 0.5 m ID disengagement section. A two-stage cyclone is employed at the top of the unit to recycle the solids. A porous plate with 20 μm mean pore size and 60% fractional free area is mounted at the bottom gas inlet as the gas distributor. The height of the unit is about 2.4 m. The 2.54 cm ID horizontal jet inlet is 0.3 m above the distributor. FCC particles (Geldart group A, mean diameter 60 μm, density 1400 kg/m^3) are used as the solid phase inside the bed and horizontal jet; the fluidization and carrier gas is air. ECVT sensors are mounted around the penetration area.

Figure 20.11 shows the penetration process of a pure gas jet in 3D format. The fluidization gas velocity is 0.064 m/s, the horizontal carrier gas jet velocity is 15 m/s, and the cut-off boundary concentration is set at 0.5 (0 for empty bed and 1 for packed bed). Initially, the gas jet is narrow and straight. During the penetration, the gas jet slowly migrates upward due to the upward fluidization gas and the buoyancy force. The width of the gas jet expands during the penetration due to the increasing gas volume and decreasing penetration momentum.

A similar study for horizontal gas—solid mixture jet penetration shows that the maximum penetration length of the gas—solid mixture is larger than that of a pure gas jet, due to the higher momentum of the former. These instantaneous 3D results are very useful to reveal the mixing behavior inside the fluidized bed.

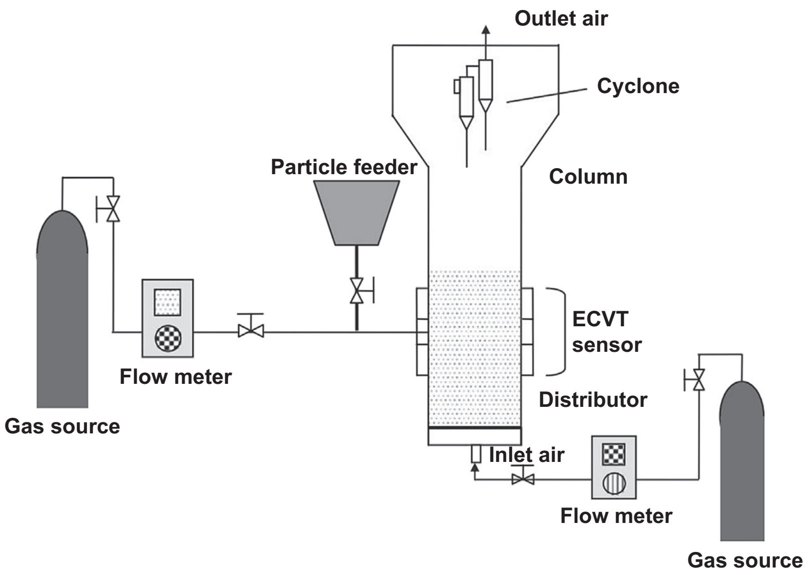
Outlet air
Cyclone
Particle feeder
Column
ECVT sensor
Flow meter
Gas source
Distributor
Inlet air
Flow meter
Gas source

Figure 20.10 Schematic diagram of the gas–solid fluidized bed with a horizontal gas/solid jet penetration system.
Figure reproduced from Wang, Yu, et al. (2010), with permission from Elsevier.

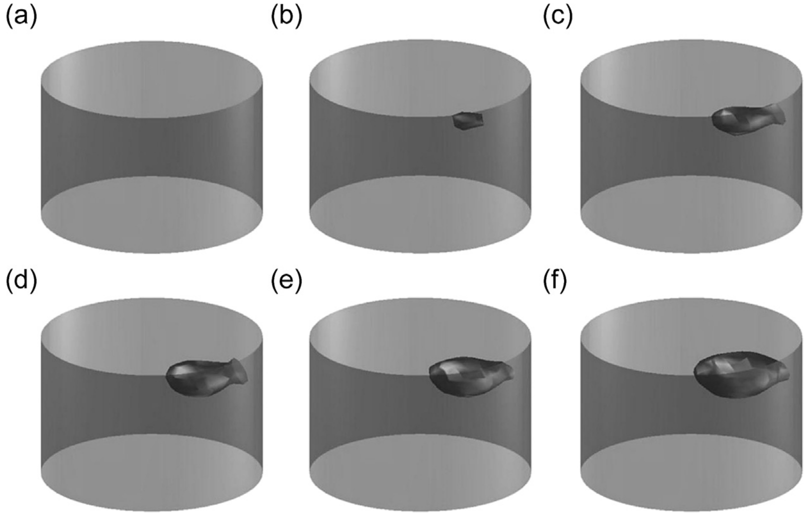

Figure 20.11 Three-dimensional shape of a horizontal gas jet in the 0.3 m gas–solid fluidized bed obtained by ECVT: (a) $t = 0$; (b) $t = 12.5$ ms; (c) $t = 25.0$ ms; (d) $t = 37.5$; (e) $t = 50.0$ ms; and (f) $t = 62.5$ ms. $U_g = 0.064$ m/s, $U_0 = 15$ m/s. ECVT, electrical capacitance volume tomography.
Figure reproduced from Wang, Yu, et al. (2010), with permission from Elsevier.

20.4 Applications of capacitance tomography in the pharmaceutical industry

In the pharmaceutical industry, a series of steps are involved to make tablets and capsules in large quantities from a given tablet/capsule chemical formula and dosage. These steps include chemical/biological synthesis, drying, purification, milling, granulation, and coating (Muzzio, Shinbrot, & Glasser, 2002). Obviously, such manufacturing process is akin to that of powder and particle systems and fluidized beds are intensively used in the pharmaceutical industry as well. Because of this, ECT is a novel technique of interest to the pharmaceutical field. All ECT system applications for fluidized beds mentioned in the previous sections can be adapted for use in the pharmaceutical industry. In this section, some examples of the applications of capacitance tomography technology in the pharmaceutical field will be illustrated.

20.4.1 Solids distribution profile and visualization

Wang and Yang (2011) reported the construction of several pharmaceutical fluidized beds mounted with ECT sensors from lab scale to production scale to research the gas—solid hydrodynamic behaviors, as shown in Figure 20.12. Table 20.1 shows the capacity of such fluidized beds.

Figure 20.13 shows the reconstructed results for fluidized beds with different scales. These images provide some qualitative indicators of the flow behavior inside the beds.

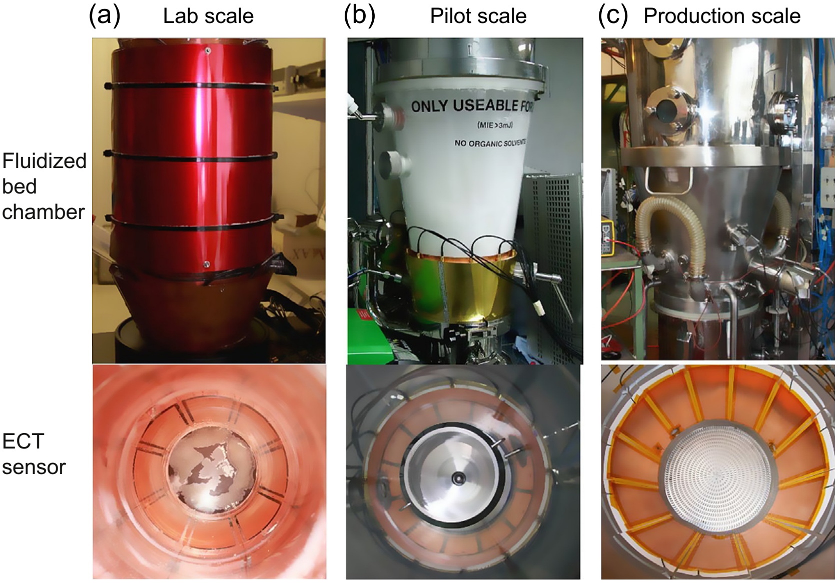

Figure 20.12 Fluidized beds and ECT sensors. ECT, electrical capacitance tomography. Figure reproduced from Wang and Yang (2011), with permission from IOP Publishing.

Table 20.1 **Fluidized beds parameters for tests**

Parameter	Lab scale	Pilot scale	Production scale
Diameter (mm)	160	296	960
Height (mm)	500	1500	3000
Capacity (kg)	0.5—1.0	1.0—2.5	50—100
Fluidization velocity (m/s)	0.5—3.5	0.5—5.5	0.5—5.5
Material	Rice powder	Placebo pellets	Chlorpheniramine pellets
Median particle diameter (D50) (μm)	500	750	750
ECT senssor	8 electrodes	12 electrodes	12 electrodes
Electrodes (width × height) (cm)	2 × 6	5 × 10	25 × 35

ECT, electrical capacitance tomography.
Table reproduced from Wang and Yang (2011), with permission from IOP Publishing.

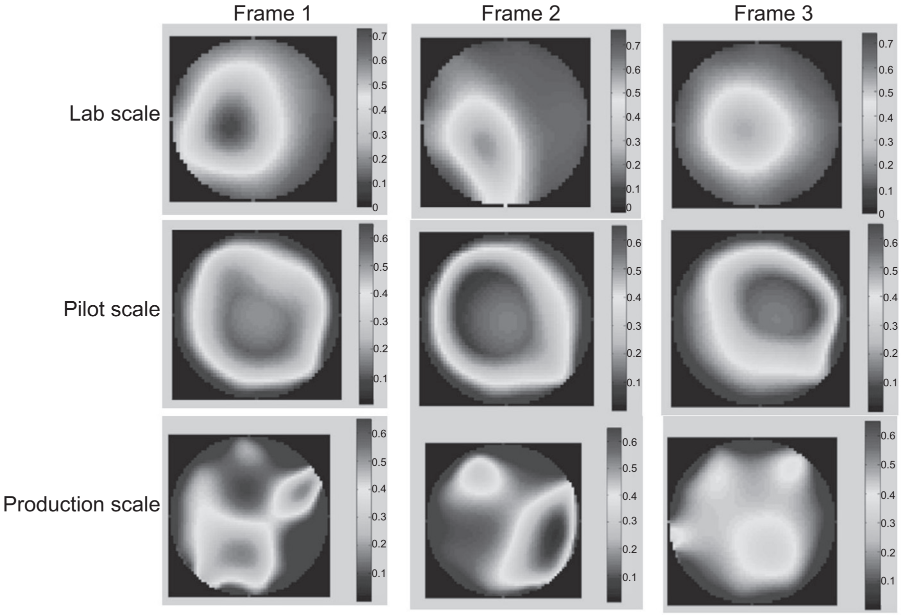

Figure 20.13 Images reconstructed from different scales of different fluidized beds. Figure reproduced from Wang and Yang (2011), with permission from IOP Publishing.

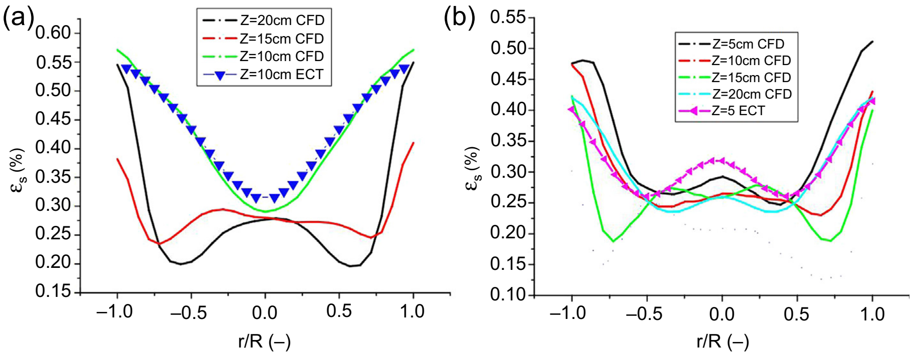

Figure 20.14 Average solid concentration at different positions above the air distributor: (a) lab scale, (b) pilot scale.

Figure reproduced from Wang and Yang (2011), with permission from IOP Publishing.

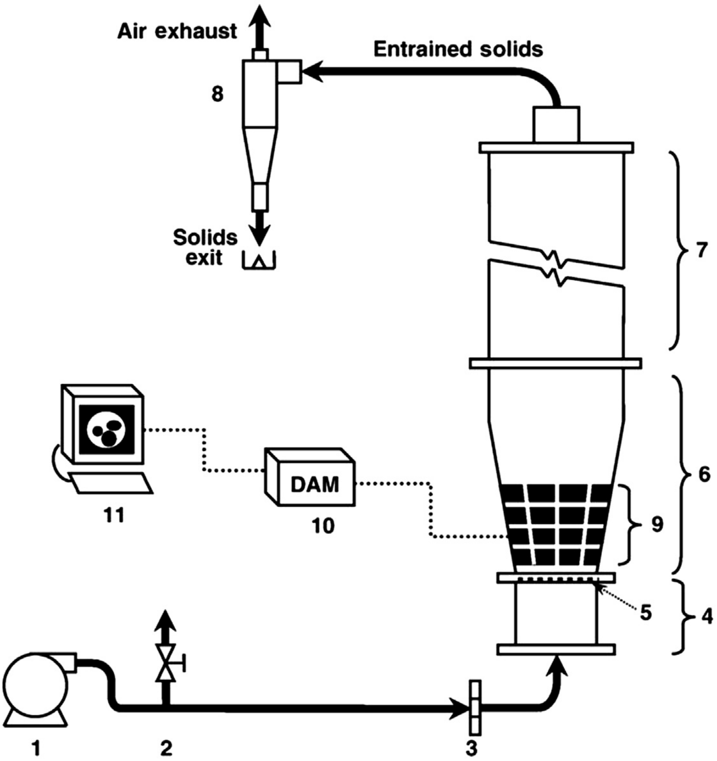

Figure 20.15 Fluidized bed apparatus components and instrumentation: blower (1), air bypass (2), orifice (3), wind box (4), distributor (5), product bowl (6), freeboard (7), cyclone (8), electrical capacitance tomography sensor (9), ECT data acquisition module (10), data acquisition computer (11). ECT, electrical capacitance tomography.

Figure reproduced from Wiens and Pugsley (2006), with permission from Elsevier.

It can be seen that the flow in the production-scale reactor is much more complex compared with the lab-scale and pilot-scale units.

They also reported average solid concentration profiles in the radial directions, as shown in Figure 20.14. It is observed that the solids concentration is low in the center of the reactor and high near the wall, which can well be expected for traditional fluidized beds.

Similar average solids distribution profiles from ECT systems have also been reported by Wiens and Pugsley (2006) using a lab-scale facility. The facility used is depicted in Figure 20.15.

The voidage distributions are reported in Figure 20.16. It can be seen that the voidage profile is similar to that of Wang and Yang (2011) work.

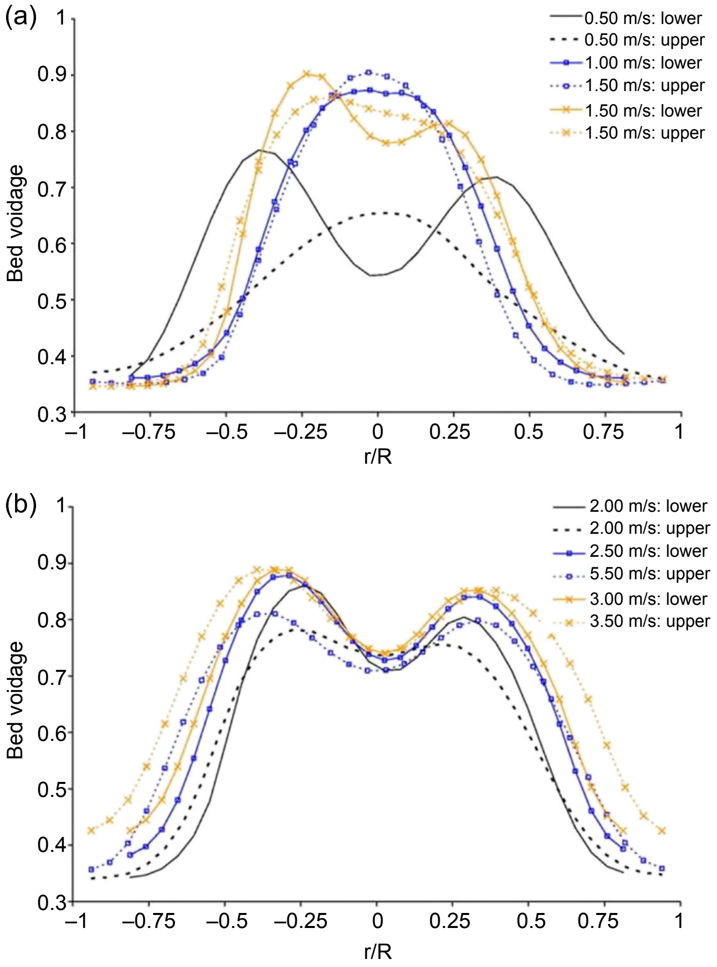

Figure 20.16 Time-averaged radial bed voidage profiles for PSD0: (a) gas velocities 0.50, 1.00, and 1.50 m/s, (b) gas velocities 2.00, 2.50, and 3.00 m/s.
Figure reproduced from Wiens and Pugsley (2006), with permission from Elsevier.

20.5 Effective permittivities of mixtures and phase distributions

The dielectric permittivity distribution is the essential information captured by ECT systems. In particular, ECT systems can measure the *macroscopic* effective dielectric permittivity distribution of solid materials as a function of position; however, it is how the effective dielectric permittivity distribution relates to the real phase's distribution of a mixture that is of main interest for gas—solid applications. This section provides a brief discussion on the relationship between the phase distribution of mixtures and their macroscopic dielectric properties.

Due to the inherent complexity, it is impossible to exactly capture the microscopic electromagnetic behavior of a multiphase mixture system. For example, complex interfacial polarization phenomena occur when two phases with different dielectric permittivities are put into contact. In addition, the presence of conductivities of the materials further increases the complexity of the problem. Several mixing rules can be employed to reduce the complexity of this problem. Dielectric mixing rules express the effective (macroscopic) permittivity of a mixture as a function of the permittivity for each material (phase) in the mixture, their respective fractional volumes, and some other geometrical parameters characterizing the structure of the mixture. In a fluidized bed system, when a solid material is composed of large particles, the mixture can be considered as discrete, whereas when fine powders are encountered, the mixture can be treated as continuous. The concept of macroscopic effective permittivity presumes that a heterogeneous mixture responds to electromagnetic excitations as if it were a homogeneous medium. From an electromagnetic point of view, the effective permittivity concept is meaningful only if the particles inside the mixture are very small compared to the wavelength of the excitation field, corresponding to a not-too-high frequency. This is often referred to as a quasi-static regime. Fortunately, most ECT and fluidization systems fit this criterion.

Among all mixing rules, the simplest one is to express the effective dielectric permittivity ε_e of a mixture as a function of the concentrations (particle volume fraction q) and respective permittivities of each, as proposed by Gladstone and Dale (1863). In the case of a mixture with two phases (viz., background and single type of particle), this simply reads as

$$\varepsilon_e = (1-q)\varepsilon_1 + q\varepsilon_2 \tag{20.2}$$

where ε_1 denotes background permittivity and ε_2 the particles' permittivity. After rearranging, one can calculate the volume fraction q as

$$q = \frac{\varepsilon_e - \varepsilon_1}{\varepsilon_2 - \varepsilon_1} \tag{20.3}$$

If ε_1 and ε_2 are comparable and q is small (i.e., low-contrast and tenuous mixtures), this approximation provides good results (Tretyakov & Sihvola, 2000).

This simple model ignores many factors, such as the local polarization fields surrounding solid particles. In a mixture, especially when the particles are dense and large, one cannot assume that the field in the presence of a certain particle distribution would remain the same as the external field. The surrounding polarization can affect the field's acting on a certain particle, and it is also dependent on the shape of the "particle" (Kittel & McEuen, 1976). For spherical particles, based on the concept of local polarization, the well-known Maxwell Garnett formula can be used (Maxwell Garnett, 1904):

$$\varepsilon_e = \varepsilon_1 + 3q\varepsilon_1 \frac{\varepsilon_2 - \varepsilon_1}{\varepsilon_2 + 2\varepsilon_1 - q(\varepsilon_2 - \varepsilon_1)} \tag{20.4}$$

which also takes an equivalent form as the Rayleigh mixing rule (Rayleigh, 1892):

$$q = \frac{\varepsilon_2 + 2\varepsilon_1}{\varepsilon_e + 2\varepsilon_1} * \frac{\varepsilon_e - \varepsilon_1}{\varepsilon_2 - \varepsilon_1} \tag{20.5}$$

Under the Rayleigh mixing rule, the volume fraction q is no longer proportional to the effective permittivity ε_e. It should be pointed out that in this model the spheres need not be of the same size as long as all of them are small compared to the wavelength (Sihvola, 2000).

But even Rayleigh's formula is too idealistic for many real scenarios. This approximation works well for dilute phase mixtures with spherical shapes; however, many fluidization systems do not obey these assumptions, so more complex and general models are necessary. The particles' shape is an important parameter because it can significantly affect the polarization. We next consider the important case of ellipsoidal particles, which can serve as a better approximation in many cases. For ellipsoid particles, the alignment or packing format significantly affects the effective permittivity. If the particles are regularly aligned, then the mixture will be anisotropic, and along the principal axis of the ellipsoid, the permittivity tensor will be a diagonal tensor with entries expressed by the modified Maxwell Garnett formula:

$$\varepsilon_{e,x} = \varepsilon_1 + q\varepsilon_1 \frac{\varepsilon_2 - \varepsilon_1}{\varepsilon_2 + (1-q)N_x(\varepsilon_2 - \varepsilon_1)} \tag{20.6}$$

in which N_x is the depolarization factor along the x-axis of the ellipsoid, and similar expressions for the y and z components. For a sphere particle the above formula applies with $N_x = N_y = N_z = 1/3$.

If the ellipsoid particles are randomly packed, the mixture will be isotropic and the effective permittivity can be expressed as estimated by the average of the permittivities along the three directions, that is,

$$\varepsilon_e = \varepsilon_1 + \varepsilon_1 \frac{\frac{q}{3}\sum_{i=x,y,z} \frac{\varepsilon_2 - \varepsilon_1}{\varepsilon_2 + N_j(\varepsilon_2 - \varepsilon_1)}}{1 - \frac{q}{3}\sum_{i=x,y,z} \frac{N_j(\varepsilon_2 - \varepsilon_1)}{\varepsilon_2 + N_j(\varepsilon_2 - \varepsilon_1)}} \tag{20.7}$$

If the particles follow an orientation distribution, the sum terms in Eqn (20.6) should be weighted by the distribution function.

Many other mixing rules exist, each emphasizing different properties. Among them, we can cite the Polder—van Santen formula (Polder & van Santeen, 1946), Birchak formula (Birchak, Gardner, Hipp, & Victor, 1974), and Looyenga formula (Looyenga, 1965). The presence of certain components, such as water, can significantly affect the effective permittivity. For a more detailed discussion, please refer to Sihvola's work (Sihvola, 2000).

20.6 Future trends and conclusion

The widespread use of gas—solid flow systems in industrial settings and the complex flow dynamics they obey demand the adoption of advanced flow measurement techniques. The majority of probes used for this purpose have been based on intrusive techniques that can obstruct or interfere with solids flow. Reluctance to using such invasive probes has been on the rise, especially in conjunction with advanced gas—solid systems that may be significantly impacted by any flow intrusion. The present trend in industry is to explore global measurement methods that can be deployed noninvasively. In this regard, ECT systems are excellent candidates for future widespread deployment.

Electrical noninvasive imaging modalities are highly desirable for gas—solid flow imaging applications as they exhibit favorable features such as safety, high speed, low-profile sensor geometry, and relatively lower capital requirements. Among available electrical imaging modalities, ECT is especially attractive because it can image phase distributions from capacitance signals while relaxing the condition of continuous phase required, observed in other modalities.

ECT has been used in various applications in the gas—solid industry, including side injections, exit regions, riser sections, and tapered columns. It is very likely that future hardware and software development will make ECT even more attractive and cost effective for gas—solid applications.

References

Birchak, J. R., Gardner, C. G., Hipp, J. E., & Victor, J. M. (1974). High dielectric constant microwave probes for sensing soil moisture. *Proceedings of the IEEE, 62*(1), 93—98.

Chandrasekera, T. C., Wang, A., Holland, D. J., Marashdeh, Q., Pore, M., Wang, F., et al. (2012). A comparison of magnetic resonance imaging and electrical capacitance tomography: an air jet through a bed of particles. *Powder Technology, 227*, 86—95.

Fan, L. S., & Zhu, C. (2005). *Principles of gas—solid flows*. Cambridge University Press.

Geldart, D. (1973). Types of gas fluidization. *Powder Technology, 7*(5), 285—292.

Gladstone, J. H., & Dale, T. P. (1863). Researches on the refraction, dispersion, and sensitiveness of liquids. *Philosophical Transactions of the Royal Society of London, 153*, 317—343.

Halow, J. S., Fasching, G. E., Nicoletti, P., & Spenik, J. L. (1993). Observations of a fluidized bed using capacitance imaging. *Chemical Engineering Science, 48*(4), 643−659.

Halow, J. S., & Nicoletti, P. (1992). Observations of fluidized bed coalescence using capacitance imaging. *Powder Technology, 69*(3), 255−277.

Harrison, D., Davidson, J. F., & De Kock, J. W. (1961). On the nature of aggregative and particulate fluidization. *Transactions of the Institution of Chemical Engineers, 39*, 202−211.

Huang, S. M., Plaskowski, A. B., Xie, C. G., & Beck, M. S. (1989). Tomographic imaging of two-component flow using capacitance sensors. *Journal of Physics E: Scientific Instruments, 22*(3), 173.

Kittel, C., & McEuen, P. (1976). *Introduction to solid state physics*. New York: Wiley.

Looyenga, H. (1965). Dielectric constants of heterogeneous mixtures. *Physica, 31*(3), 401−406.

Makkawi, Y. T., & Wright, P. C. (2004). Electrical capacitance tomography for conventional fluidized bed measurements—remarks on the measuring technique. *Powder Technology, 148*(2), 142−157.

Maxwell Garnett, J. C. (1904). Colours in metal glasses and metal films. *Philosophical Transactions of Royal Society of London, Section A, 3*, 385−420.

Muzzio, F. J., Shinbrot, T., & Glasser, B. J. (2002). Powder technology in the pharmaceutical industry: the need to catch up fast. *Powder Technology, 124*(1), 1−7.

Polder, D., & van Santeen, J. H. (1946). The effective permeability of mixtures of solids. *Physica, 12*(5), 257−271.

Pugsley, T., Tanfara, H., Malcus, S., Cui, H., Chaouki, J., & Winters, C. (2003). Verification of fluidized bed electrical capacitance tomography measurements with a fibre optic probe. *Chemical Engineering Science, 58*(17), 3923−3934.

Rautenbach, C., Mudde, R. F., Yang, X., Melaaen, M. C., & Halvorsen, B. M. (2013). A comparative study between electrical capacitance tomography and time-resolved X-ray tomography. *Flow Measurement and Instrumentation, 30*, 34−44.

Rayleigh, L. (1892). On the influence of obstacles arranged in rectangular order upon the properties of a medium. *The London, Edinburgh, and Dublin Philosophical Magazine and Journal of Science, 34*(211), 481−502.

Sihvola, A. (2000). Mixing rules with complex dielectric coefficients. *Subsurface Sensing Technologies and Applications, 1*(4), 393−415.

Tretyakov, S. A., & Sihvola, A. H. (2000). On the homogenization of thin isotropic layers. *IEEE Transactions on Antennas and Propagation, 48*(12), 1858−1861.

Wang, F., Marashdeh, Q., Fan, L. S., & Warsito, W. (2010). Electrical capacitance volume tomography: design and applications. *Sensors, 10*(3), 1890−1917.

Wang, F., Marashdeh, Q., Wang, A., & Fan, L. S. (2012). Electrical capacitance volume tomography imaging of three-dimensional flow structures and solids concentration distributions in a riser and a bend of a gas−solid circulating fluidized bed. *Industrial & Engineering Chemistry Research, 51*(33), 10968−10976.

Wang, H., & Yang, W. (2011). Scale-up of an electrical capacitance tomography sensor for imaging pharmaceutical fluidized beds and validation by computational fluid dynamics. *Measurement Science and Technology, 22*(10), 104015.

Wang, F., Yu, Z., Marashdeh, Q., & Fan, L. S. (2010). Horizontal gas and gas/solid jet penetration in a gas−solid fluidized bed. *Chemical Engineering Science, 65*(11), 3394−3408.

Wiens, J., & Pugsley, T. (2006). Tomographic imaging of a conical fluidized bed of dry pharmaceutical granule. *Powder Technology, 169*(1), 49−59.

This page intentionally left blank

Process tomography and estimation of velocity fields

21

J.P. Kaipio[1,2,3], *A. Seppänen*[2], *M. Vauhkonen*[2,3], *A. Lipponen*[2], *A. Voutilainen*[3], *A. Lehikoinen*[2,3], *V. Rimpiläinen*[1]
[1]The University of Auckland, Auckland, New Zealand; [2]University of Eastern Finland, Kuopio, Finland; [3]Rocsole Ltd, Kuopio, Finland

21.1 Introduction

Process tomography is primarily used to obtain images related to process phenomena such as monitoring mixing and chemical reactions, applications of which are comprehensively covered in other chapters in this book. On the other hand, most phenomena are also related to flows in the process vessels or pipelines. Process tomography has been applied to imaging of mixers (George, Torczynski, Shollenberger, O'Hern, & Ceccio, 2000; Kourunen et al., 2008; Pakzad, Ein-Mozaffari, & Chan, 2008), separators (Ismail, Gamio, Bukhari, & Yang, 2005; Liu et al., 2005; Williams, 1995; York, Davidson, Mazurkiewich, Mann, & Grieve, 2005), chemical reactors (Hampel, Hristov, Bieberle, & Zippe, 2007; Stanley, 2006; Vilar, Williams, Wang, & Tweedie, 2008), and industrial pipelines and vessels (Henningsson, Ã—stergren, & Dejmek, 2006; Reinecke, Petritsch, Boddem, & Mewes, 1998; Wang, 2005), see the other chapters in this book for further information. Several imaging modalities have been used in process tomography, with the most common modalities having been related to electromagnetic probing, that is, capacitance tomography and impedance tomography (Williams & Beck, 1995).

One often faces the following dual problem. If the flows are not interesting, they are a nuisance parameter in the overall models that describe the evolution of the interesting (indirectly measurable) variables, such as conductivity, concentration, density or void fraction. For example, in a convection—diffusion or advection—diffusion models, the flow fields appear as a distributed parameter. The (usually time-varying) flow fields, on the other hand, are not known except in rare circumstances. Using incorrect nominal flow fields in the transport models may or may not induce significant errors in the estimates for the primary variables. If, on the other hand, the flow is another interesting, or even primary, variable, then it needs to have a significant effect on the overall model predictions — otherwise it cannot be estimated from the measurements in practice.

The above seems to suggest that accurate estimation of the primary variable necessitates that either the flow is known or it has to be estimated simultaneously with the primary variable. In the vast majority of process tomography applications, however, the flow fields are not known and are not estimated directly. This is often possible when the flows are slow when compared to the time required to carry out one

Industrial Tomography. http://dx.doi.org/10.1016/B978-1-78242-118-4.00021-6
Copyright © 2015 Elsevier Ltd. All rights reserved.

set of measurements, often called a frame, that allows for the reconstruction of the primary variable. As described in the other chapters, in most measurement modalities the measurements that are needed to compute a single reconstruction are carried out sequentially with respect to time. For example, in 3D electrical impedance tomography (EIT), say, 60 current patterns are used to probe the target, and the demodulation time (used to compute the resulting electrode voltages from the raw measurements) is 5 ms, and the target needs to be essentially temporally constant for 300 ms. If, on the other hand, the length of the imaged segment in a pipeline is 30 cm and the target is allowed to move 3 cm during the frame, it means that the maximum flow can be around 0.1 m/s. If this condition can be assumed, it is then possible to consider the sequence of snapshot estimates to infer characteristics of the flow, given that there is adequate contrast in the primary variable.

On the other hand, if the transport (and the flow) is also modelled as a variable, it is possible to employ the state estimation approach for the reconstruction of the primary variable (and the flow) since in this approach the target needs to be (approximately) constant only over the duration of a single measurement — not over the entire frame. In the example above, this means that, in principle, the maximum flows speed could be around 6 m/s.

Below, we give a brief review of existing approaches to infer flows. We prefer to refer to inference and estimation rather than measurement of flows since tomographic problems are commonly ill-posed inverse problems and measurement and modelling errors may induce significant errors in any computed values. Especially when significant modelling errors and/or uncertainties are present, the Bayesian framework for inverse problem is usually adopted. For general information related to Bayesian inverse problems, see for example, Kaipio and Somersalo (2004), Tarantola (2004) and Calvetti and Somersalo (2007).

21.1.1 Indirect methods

In this section, we review indirect approaches to infer the fluid velocity. In indirect methods, information on the velocity field is obtained via the change of some other quantity, such as concentration distribution under the influence of the velocity field. A well-known indirect method in process tomography is the cross-correlation velocimetry (Beck & Plaskowski, 1987). In the simplest form of a cross-correlation flowmeter, the inference of the fluid velocity is based on cross-correlation between signals measured at different positions (upstream and downstream) of a pipeline. Beck and Plaskowski (1987) suggested a cross-correlation flowmeter based on tomographic imaging. Here, sequences of tomographic images from two or more sensor arrays are collected and the velocity is inferred based on cross-correlations between the pixel values in two images.

The cross-correlation flowmeters based on EIT and electrical capacitance tomography (ECT) have been used for measurement of multiphase flows (Dyakowski, 1996; Dyakowski, Jeanmeure, & Jaworski, 2000; Lucas, Cory, Waterfall, Loh, & Dickin, 1999). In these studies, dual plane EIT/ECT systems were used.

In a standard cross-correlation method based on dual plane tomography, the direction of the velocity is assumed to be known a priori. This limitation can be, to some extent, avoided by the 'best-correlated pixels' method proposed in Mosorov, Sankowski, Mazurkiewicz, and Dyakowski (2002). Different modifications of EIT-based cross-correlation method have also been used for estimation of angular velocities (Etuke & Bonnecaze, 1998) and radial flows (Bolton, Hooper, Mann, & Stitt, 2004). Another electrically based cross-correlation flowmeter uses electrodynamic tomography to estimate the flow of electrically charged particles (Green et al., 1997).

The above listed cross-correlation flowmeters were based on electrical measurements. Cross-correlation and other indirect methods have been developed also using various other imaging modalities. In the following, a brief review of a few commonly used approaches is given.

21.1.1.1 Optical flow meters

In particle image velocimetry (PIV) (Adrian, 2005; Raffel, Willert, Wereley, & Kompenhans, 2007), tracer particles are inserted into the flow field. A layer of fluid is sequentially illuminated with a (2D) light sheet, and images of the illuminated fluid layer at different times are recorded. The inference of the velocity field is based on displacements of the particles between two instants of time. For tomographic (3D) PIV, see Elsinga, Scarano, Wieneke, and Oudheusden (2006).

Laser speckle velocimeter (LSV) (Shibata et al., 1996; Takai, Iwai, & Asakura, 1980) is basically the same method as PIV, but in LSV the particle concentration is so high that it is difficult to observe individual particles in an image.

An obvious limitation of the optical flow meters is that they are only applicable for measuring velocities in transparent or semitransparent fluids, or on surfaces of opaque fluids. Hence, optical flow meters are used mostly in laboratory studies.

21.1.1.2 X-ray and γ-ray CT

X-ray computed tomography (CT) is one of the classical choices for tomographic imaging. The X-ray CT principle can be adopted to visualize stationary flow field distributions. Such work has been reported, for example, in Wu, Orta, and Kantzas (2011) in which a modified medical CT scanner was used to study flow regimes in a fluidized bed. Similar works for studying structured packings have been reported in Janzen et al. (2013) and Toye, Crine, and Marchot (2005). In Grudzien, Niedostatkiewicz, Adrien, Tejchman, and Maire (2011), an X-ray CT system was used to investigate granular flows in silos.

Frame rate is a critical factor when applying tomographic techniques for flow imaging. A fast X-ray CT system with 60 independent switchable X-ray sources has been suggested in Hori, Fujimoto, and Kawanishi (1998) and a similar system with 18 X-ray sources having the frame rate of 250 frames/s in Kai et al. (2000) and Misawa, Tiseanu, Prasser, and Ichikawa (2003). A slightly different approach enabling dual plane measurements with the speed of 100 frames/s has been introduced in Mudde (2011) and Saayman, Nicol, van Ommen, and Mudde (2013). The system has been used, for example, to determine the velocities of voids in fluidized beds. An X-ray CT system based on electron beam scanning was introduced in Bieberle et al. (2009), Fischer and Hampel (2010) and Bieberle, Barthel, and Hampel (2012). The system reaches frame rates of up to 8000 frames/s and can also be operated in dual plane mode. Other X-ray systems have been reported also in Morton et al. (1999), Banholzer, Spiro, Kosky, and Maylotte (1987), Wu, Cheng, Ding, Wei, and Jin (2007) and Heindela, Grayb, and Jensenb (2008).

An alternative to X-ray CT is γ-ray CT. The working principle of γ-ray CT is similar to X-ray CT with the difference that the X-ray tube is replaced by an isotopic γ-ray source. Systems of this type have been developed and applied by several groups, see for example, Kumar, Moslemian, and Dudukovic (1995), Al-Dahhan et al. (2007), Hampel et al. (2007), Bieberle, Hoppe, Schleicher, and Hampel (2011), Bieberle, Schleicher, and Hampel (2007), Johansen, Hjertaker, Froystein, and Olsen (1996), Johansen, Hampel, and Hjertaker (2010), and Maad and Johansen (2008). The actual velocity field estimation in X-ray and γ-ray imaging modalities is done indirectly by analysing a sequence of images with, for example, cross-correlation techniques explained above.

21.1.1.3 Positron emission tomography

Positron emission tomography (PET), better known from diagnostic medical applications, has also been used in tomographic flow imaging. In flow experiments the approach is to track radioactive tracer particles inserted into the flow (Dechsiri, Van der Zwan, Dehling, & Hoffmann, 2005; Devanathan, Dudukovic, Lapin, & L'ubbert, 1995; Parker & McNeil, 1996). The spatial resolution of PET is about 5 mm as shown in Parker et al. (2008). One of the major advantages of PET is that small particles can be tracked in fluid flows, which gives information, for example, on fluid velocities, disperse particle velocities and dispersion parameters in the scale, which cannot be obtained with other techniques.

21.1.1.4 Magnetic resonance imaging

Magnetic resonance imaging (MRI) is also a medical imaging technique that has been used in imaging of industrial process flows. The first MRI flow images were suitable only for a limited number of applications due to the long measurement times (Daidzic, Schmidt, Hasan, & Altobelli, 2005; Elkins, Markl, Pelc, & Eaton, 2003; Newling et al., 2004; Sederman, Johns, Alexer, & Gladden, 1998). The temporal resolution of the MRI technique has been improved dramatically in recent years through the introduction of new measurement protocols and advanced image reconstruction techniques (Anadon, Sederman, & Gladden, 2006; Gladden et al., 2006; Holland, Malioutov, Blake, Sederman, & Gladden, 2010; Muller et al., 2007; Sankey, Holl, Sederman, & Gladden, 2009; Sederman, Mantle, Buckley, & Gladden, 2004; Tayler, Holl, Sederman, & Gladden, 2010; Tayler, Holl, Sederman, & Gladden, 2012). With these advances it is now possible to acquire MRI measurements at a spatial resolution of better than 400 μm and a temporal resolution of 5 ms. One of the advantages of

MRI is that direct measurement of the fluid velocity is possible (Elkins & Alley, 2007). MRI has also been used to characterize the structure of the interparticle pore space and the single-phase flow field in a packed bed of alumina catalyst particles (Mantle, Sederman, & Gladden, 2001).

21.1.2 Direct methods, other than state estimation

While in indirect methods the inference of the velocity field is based on postprocessing tomographic images, in direct methods the imaging problems are formulated so that the velocity field is the estimated parameter distribution.

Examples of direct methods are laser (Albrecht, 2003) and acoustic (Mori, Suzuki, & Kakuno, 2007) Doppler velocimetry. Further, a method for tomographic reconstruction of the fluid velocity based on differential ultrasonic time-of-flight measurements has been proposed in Braun and Hauck (1991). In addition, certain modes of MRI allow for direct measurement of the fluid velocity (Elkins & Alley, 2007).

One of the latest techniques for measuring the flow velocity fields is based on electromagnetic induction, similar to the technique used in standard electromagnetic flow meters. Two types of approaches have recently been developed: the inductive flow tomography (IFT) was developed for measuring the flow velocity distributions in pipe flows (Leeungculsatien & Lucas, 2013; Lucas & Leeungculsatien, 2010), and contactless inductive flow tomography (CIFT) is suited for contactless flow measurements of molten metal flows (Stefani & Gerbeth, 2000; Stefani, Gudrum, & Gerbeth, 2004; Wondrak et al., 2010, 2011). These techniques are based on the fact that a magnetic field applied to a conductive flowing liquid causes an induced voltage and thus a current flow inside a pipe or vessel. By creating such a magnetic field with coils and measuring the corresponding voltages on the surface of the pipe with electrodes (IFT) or by measuring the perturbation of the applied magnetic field with magnetic field sensors distributed around the melt (CIFT), the flow velocity distribution inside the object can be estimated.

21.1.3 Estimation of primary variables and flows using the state space approaches

State space estimation approaches are sequential Bayesian methods in which the estimates for the unknowns are based on modelling the sequence of measurements explicitly. In applications and specific problems in which there are significant measurement errors and/or model uncertainties, the Bayesian framework for inverse problems is usually adopted. In this framework, the modelling of the measurement process and the explicit modelling of the primary (interesting) uncertainties as well as the secondary unknowns and uncertainties are carried out separately. The separation of the problem into observation and evolution models is called the state space representation of a dynamical system. This is appealing since our understanding of how the unknowns behave should not depend on how the measurements are carried out.

Nonstationary inverse problems are a special class of Bayesian inverse problems in which the primary unknown can be modelled with a stochastic evolution model, typically a stochastic partial differential equation equipped with (partially unknown) initial and boundary conditions (Kaipio & Somersalo, 1999, 2004; Vauhkonen, Karjalainen, & Kaipio, 1998). These problems can be tackled with sequential Bayesian estimation methods (Doucet, de Freitas, & Gordon, 2001) and, in special cases, recursive algorithms such as the Kalman filter (Kalman, 1960) and its variants (Anderson & Moore, 1979; Kaipio & Somersalo, 2004). The sequential Bayesian estimation in the context of inverse problems, and in particular, tomographic problems, is discussed, for example, in Kaipio and Somersalo (2004).

The most common class of problems that induces nonstationary inverse problems is the one related to transport phenomena such as diffusion, advection and convection in fluids, solids and porous materials, as well as chemical reactions. In particular, problems that are governed by stochastic convection-diffusion (CD) models in fluids have served as standard examples for sources of nonstationary inverse problems (Seppänen, Vauhkonen, Vauhkonen, Somersalo, & Kaipio, 2001b; Seppänen, Heikkinen et al., 2007; Seppänen, Vauhkonen, Vauhkonen, Voutilainen, and Kaipio, 2008; Voutilainen & Kaipio, 2009). Here, the temporally and spatially varying concentration of some substance is typically the physical entity of primary interest. In these problems, the stochasticity of the models is typically due to unknown boundary data for the CD model or the fluid dynamics model (Seppänen, Vauhkonen, Somersalo, & Kaipio, 2001; Seppänen, Vauhkonen, Vauhkonen, Somersalo, & Kaipio, 2001a; Voutilainen et al., 2007), unknown velocity field (Lipponen, Seppänen, & Kaipio, 2010a,b; Seppänen et al., 2001a), and highly approximate reduced-order models for the primary unknowns (Huttunen & Kaipio, 2007; Huttunen, Kaipio, & Somersalo, 2007; Lipponen, Seppänen, & Kaipio, 2011).

With the stochastic CD problems, we face the dual problem that is related to the associated velocity fields: these (unknown) velocity fields may either have the role of a nuisance parameter, or it may be one of the interesting unknowns. In the latter case, of course, the velocity field could be considered as the primary unknown, while the usual tomographic imaging target, such as concentration, acts as a nuisance parameter. In the general case, however, the most tomographic modalities carry such vague indirect information on the velocity field that the simultaneous estimation of both the time-varying concentration (or other tomographic variable) distribution and the (entire) time-varying velocity field is a challenging problem. This is especially the case when model uncertainties are present, which is practically always the case. For quantitative estimation of any unknowns, the effect of uncertainties needs to be accounted for. With quantitative estimation, we refer to feasible error estimates, that is, the actual value of the unknown should be supported by the error bounds. On the other hand, in the Bayesian framework, the uncertainties are marginalized by integrating the associated posterior distribution over the uncertainties. Marginalization refers to the procedure in which the effects of the uninteresting unknowns to the probability distribution of the interesting variables are determined. The structure of the nonstationary inverse problems, however, is such that exact marginalization can seldom be carried out in practice.

Partial solutions to the stochastic CD problems with EIT as the observation modality, and treating the velocity field as a nuisance parameter, have been studied earlier. In the case of conducting fluids and substances, there is a nonlinear mapping between conductivity and concentration. The state estimation problem governed by a convection—diffusion model under uncertainties in boundary data was discussed in Seppänen, Vauhkonen, Somersalo, et al. (2001) and Seppänen, Vauhkonen, Vauhkonen et al. (2001b). In Seppänen, Vauhkonen, Somersalo, et al. (2001) and Seppänen, Vauhkonen, Vauhkonen et al. (2001b), the related velocity field was assumed to be stationary (Navier—Stokes flow) and known. The tolerance of the state estimation approach to mismodelling of the flow rate was studied in Seppänen et al. (2001a), and it was found out that slight mismodelling of the rate induced tolerable errors to the estimation of the primary unknown, the conductivity of the target. The estimation of rotating two-phase flows using a single-phase fluid dynamics model with laboratory data was considered in Seppänen et al. (2007a). In Seppänen et al. (2008), the state estimation scheme was verified in a 3D pipeline flow and further, in Seppänen, Peltola, Heikkinen, Kourunen, and Kaipio (2007) and Lipponen et al. (2011), this problem was verified with real data. In Lipponen et al. (2010a), a systematic approach for the approximate marginalization over nonstationary velocity fields was proposed. In this work, the mean flow was used in the CD equation, but the time variability of the flow was embedded in the statistics of the stochastic CD equation.

The problem of simultaneously estimating partial information on the flow was considered in Seppänen, Voutilainen, and Kaipio (2009). In Seppänen et al. (2009), the velocity field was modelled as translationally invariant so that the field could be parameterized with a velocity profile across the pipeline. A low-dimensional (1—3 parameters) approximation of the velocity profile was then considered, and the profile was estimated as a time-varying quantity. Such low-dimensional approximations are in this context often referred to as reduced-order models. It was found that such a reduced-order model could be identified simultaneously with the concentration. The reduced-order subspaces were, however, ad hoc choices, and a nonphysical random walk model was used as the model for the evolution of the projection coefficients. In Lipponen et al. (2010a), the velocity field was not estimated simultaneously with the conductivity, while the actual flow exhibited vortices. Based on these, it seems evident that in the case of significantly nonstationary flows, mere approximative marginalization over the flow is not adequate for high quality reconstructions of the concentration.

Thus, in the case of nonstationary flows, it seems that it is mandatory to estimate the velocity field simultaneously with the tomographic variable — irrespective of whether the velocity field is a nuisance parameter or the primary variable.

21.2 Nonstationary inverse problems and state estimation

21.2.1 Nonstationary inverse problems

Nonstationary inversion refers to problems in which the unknown is a time-varying quantity and the measurements are obtained sequentially. With a nonstationary inverse problem, the measurements that are obtained at a time often do not allow for reasonable reconstructions of the unknown target. If a feasible stochastic evolution model for the target, however, can be constructed, the reconstruction problem can be recast as a statistical state estimation problem. For a general description of the state estimation formulation of nonstationary inverse problems, see Kaipio and Somersalo (2004, 1999). The main difference between ordinary state estimation problems and nonstationary inverse problems is that the latter are unstable with respect to measurement and model uncertainties, as is the case with stationary inverse problems. As discussed below, the evolution models related to nonstationary inverse problems typically exhibit a number of significant uncertainties. In fact, if all these uncertainties were known, no measurements would be needed to infer about the unknowns!

The difference between stationary and nonstationary inverse problems is that (in Bayesian terminology) with stationary inverse problems the unknowns do not depend on time and the prior models are written in terms of the unknowns and uncertainties. With nonstationary inverse problems, the prior models are generated by the associated evolution models, that is, the temporal rate of change in the unknowns, and possibly also the uncertainties. The simplest evolution models are usually of the random walk type. But even such a seemingly simple model is not trivial, since a feasible covariance structure of the associated state noise might not be trivial.

The majority of nonstationary inverse problems are related to transport phenomena, such as fluid flows in process industry (process tomography) (Ijaz et al., 2007; Seppänen et al., 2001b), unsaturated flows in hydrology (Lehikoinen, Finsterle, Voutilainen, Kowalsky, & Kaipio, 2009; Lehikoinen, Huttunen, Finsterle, Kowalsky, & Kaipio, 2010; Vrugt, Robinson, & Vesselinov, 2005; Vrugt, Diks, Gupta, Bouten, & Verstraten, 2005) and transport of environmental substances (Voutilainen et al., 2007; Voutilainen & Kaipio, 2009). For problems that are related to process tomography, we refer to the other chapters in this book as well as the references cited in the Introduction of this chapter.

21.2.2 State estimation: general formulation

The state space representation of a dynamical system consists of *the evolution model* for the state variables (time-varying unknowns) and *the observation model* that links the observations to the state variables. In the state space theory, the state variables and observations are modelled to be stochastic (random) processes. The standard state space theory is based on first order Markov models as evolution models. For higher order Markov models, it is, however, a straightforward task to augment the state variable and convert the state evolution model to a first-order model. In the following, we state the general state estimation problem.

Let X_t be the unknown *state variable* and $t = 1,2,\ldots$ be the discrete time index. Let the sequence of measurements be Y_t. We denote probability distributions (density functions) with $\pi(\cdot)$ and conditional distributions with $\pi(\cdot|\cdot)$. In general, in sequential Bayesian estimation, the task is to model the posterior distribution $\pi(X_t|D)$ where $D = \{Y_\ell,\ \ell \in I\}$, and where I is a set of time indices. In the *filtering problem*, we set $I = \{1,\ldots,t\}$ and denote $D_t = \{Y_\ell,\ \ell = 1,\ldots,t\}$. Thus, in the filtering problem, the task is to model the distribution of the state at time t given all the data up to the same time.

Let the discrete-time (state) evolution model and the observation model be

$$X_{t+1} = F_t(X_t, W_t) \tag{21.1}$$

$$Y_t = G_t(X_t, E_t) \tag{21.2}$$

respectively. In Eqns (21.1) and (21.2), F_t and G_t are deterministic models and W_t and E_t are the *state noise* and *observation noise* processes, respectively. We note that the terminology 'noise' is a misleading one especially for the state evolution model. The model for the processes W_t and E_t should account for the uncertainties in predicting the evolution of the state and the measurements. The Eqns (21.1) and (21.2) together with the specification of the associated mappings and probabilistic models for W_t and E_t and the initial distribution of the state variable specify the state space representation of the dynamical system.

For the actual point estimates $\widehat{X}_t$, the *mean square criterion* is usually aspired. This amounts to the minimization of the expectation of the squared estimate error norm, that is, min $\mathbb{E}\|X_t - \widehat{X}_t\|_2^2$ where $\mathbb{E}$ denotes expectation and $\widehat{X}_t$ can be shown to be the conditional mean $\widehat{X}_t = \mathbb{E}(X\_t|D)$. In the sequel, we adopt the standard notation for estimates and write $\mathbb{E}(X_t|D_k) = X_{t|k}$. A closed form for the mean square estimate only exists for state space models that are linear and in which all related variables are normally distributed. Thus, usually, one only can compute approximations for the mean square estimate.

If the state and observation noise processes can be modelled as sequentially uncorrelated processes, Eqn (21.1) defines a first-order Markov process and we can write:

$$\pi(X_{t+1}|D_{t+1}) \propto \pi(Y_{t+1}|X_{t+1})\pi(X_{t+1}|X_t) \tag{21.3}$$

which allows for recursive estimation schemes, see, for example, Anderson and Moore (1979), Doucet et al. (2001) and Kaipio and Somersalo (2004).

With linear models for F_t and G_t and Gaussian models for W_t and E_t, all related (conditional) distributions are Gaussian, and full inference necessitates the computation of the (conditional) means and covariances only. These are obtained by the *Kalman filtering recursions* (Kalman, 1960). In particular, the conditional means $X_{t|t} = \mathbb{E}(X_t|D_t)$ are also the *minimum mean square estimates*, that is, the best estimates in the sense of minimizing the estimation error $\mathbb{E}\|X_t - X_{t|t}\|^2$, as noted above.

With nonlinear non-Gaussian problems, the computation of the conditional distributions and related inference can be accomplished using general sequential Bayesian procedures such as particle filtering (Doucet et al., 2001). Approximative recursive schemes, such as *extended*, *unscented* or *ensemble Kalman filters* usually have to be resorted to, see Anderson and Moore (1979), Julier and Uhlmann (1997) and Evensen (2007). These variants of the Kalman filter do not possess any optimality properties of the Kalman filter estimates. They have, however, proved to yield feasible estimates for many large dimensional nonlinear nonstationary inverse problems, given that the uncertainties have been modelled properly.

Typical uncertainties that are related to the evolution and/or the observation model include unknown boundary data (Lehikoinen et al., 2007; Seppänen et al., 2001b), uninteresting distributed parameters (Kolehmainen et al., 2011), and the geometry of the domain (Nissinen, Heikkinen, & Kaipio, 2008; Nissinen, Heikkinen, Kolehmainen, & Kaipio, 2009). Naturally, the formulation of such problems could be done so that parameterizations of these uncertainties are taken as unknowns to be estimated simultaneously with the primary interesting unknowns. This approach will, however, often lead to a computationally significantly more complex problem.

21.2.3 Linear Gaussian problems, recursions and Kalman filter

We restate the linear (affine) state space model:

$$X_{t+1} = F_t X_t + S_t + W_t \tag{21.4}$$

$$Y_t = G_t X_t + E_t \tag{21.5}$$

Let $\mathcal{N}(\mu, \Gamma)$ denote the normal (Gaussian) distribution with mean μ and covariance $\Gamma = \mathrm{cov}(\cdot)$. We make the following assumptions:

1. The initial state obeys the Gaussian distribution $X_0 \sim \mathcal{N}(\overline{X}_0, \Gamma_0)$.
2. The matrices F_t, G_t and the vector S_t are known at respective times.
3. The state and observation noise processes are Gaussian, have zero mean and (known) covariances Γ_{W_t} and Γ_{E_t}, respectively. Furthermore, both are serially uncorrelated vector valued processes so that $\mathrm{cov}(W_t, W_k) = \delta_{tk}\Gamma_{W_t}$ and $\mathrm{cov}(E_t, E_k) = \delta_{tk}\Gamma_{E_t}$, where δ_{tk} is the Kronecker delta.
4. We make the additional assumption of $\mathrm{cov}(W_t, E_k) = 0$ for all t, k. This assumption is not essential; see, for example, Anderson and Moore (1979) for Kalman filter recursions without this assumption.

Since X_0, W_t and E_t are Gaussian and the mappings are linear (affine), Y_t and X_t are also Gaussian for all t. Thus it follows that the conditional probability distributions $\pi(X_t|Y_1, \ldots, Y_k) = \pi(X_t|D_k)$ are also Gaussian and it is sufficient to compute only the means and covariances for these distributions. Denote the related covariances by $\mathrm{cov}(X_{t|k}) = \Gamma_{t|k}$. The standard *innovation form* Kalman filter and (one-step) predictor recursions take the form

$$X_{t|t-1} = F_{t-1} X_{t-1|t-1} + S_{t-1} \tag{21.6}$$

$$\Gamma_{t|t-1} = F_{t-1}\Gamma_{t-1|t-1}F_{t-1}^{\mathrm{T}} + \Gamma_{\mathrm{W}_{t-1}} \tag{21.7}$$

$$K_t = \Gamma_{t|t-1}G_t^{\mathrm{T}}\left(G_t\Gamma_{t|t-1}\, G_t^{\mathrm{T}} + \Gamma_{E_t}\right)^{-1} \tag{21.8}$$

$$\Gamma_{t|t} = (I - K_t G_t)\Gamma_{\mathrm{t|t-1}} \tag{21.9}$$

$$X_{t|t} = X_{t|t-1} + K_t(Y_t - G_t X_{t|t-1}) \tag{21.10}$$

where $X_{t|t}$ and $X_{t|t-1}$ are the conditional means of the filtering and prediction densities, respectively, and K_t is the so-called Kalman gain.

The recursions Eqns (21.6—21.10) are often interpreted as follows. Once an estimate $X_{t|t}$ is available, the evolution equation is propagated to time $t+1$ to obtain the predictor estimate $X_{t+1|t}$. When the observation Y_t is obtained, the predicted state is corrected based on the predicted measurement $Y_{t+1|t} = G_{t+1}X_{t+1|t}$ and the respective prediction error $Y_{t+1} - Y_{t+1|t}$.

21.2.4 Recursive and nonrecursive smoothers

If the state estimates are used for automatic control, the filter and predictor estimates are used to determine the control input, see Ruuskanen, Seppänen, and Kaipio (2006), Ruuskanen, Seppänen, Duncan, Somersalo, and Kaipio (2006), and Duncan, Kaipio, Ruuskanen, Malinen, and Seppänen (2005). If (automatic) control is not employed, however, the estimates can be computed offline, or at least online but not real time. The two relevant schemes for these two cases are the *fixed-lag smoother* and the *fixed-interval smoother*.

The fixed lag-smoother is derived as follows. The problem is to obtain an estimate for $X_{t-q|t}$ $q > 0$. The Kalman filter provides the optimal estimate for the state X_t at time t after observing Y_t. We can define the state variable X_t in any way we like as long as we can write the corresponding state and observation models. Now, assume that Eqns (21.4 and 21.5) are a valid model and define an augmented state vector $Z_t^{\mathrm{T}} = (X_t^{\mathrm{T}}, X_{t-1}^{\mathrm{T}}, \ldots, X_{t-q}^{\mathrm{T}})$.

By adding the identities $X_{t-k} = X_{t-k}$, $k = 1,\ldots,q$ to the state evolution model Eqn (21.4), we have the augmented state space model:

$$Z_{t+1} = \begin{pmatrix} F_t & & & \\ I & & & \\ & \ddots & & \\ & & I & 0 \end{pmatrix} Z_t + \begin{pmatrix} S_t \\ 0 \\ \vdots \\ 0 \end{pmatrix} + \begin{pmatrix} W_t \\ 0 \\ \vdots \\ 0 \end{pmatrix} \tag{21.11}$$

$$Y_t = (G_t, 0, \ldots, 0)Z_t + E_t \tag{21.12}$$

The representation Eqns (21.11) and (21.12) is clearly equal to Eqns (21.4) and (21.5) — with straightforward associations and modifications to the variables of the state space representation, including the initial state mean and covariance, and the state noise covariance. If we apply the Kalman filter to the system of

Eqns (21.11) and (21.12), the last block of the Kalman filtered estimate $Z_{t|t}$ equals $X_{t-q|t}$ as desired.

Exploiting the sparse structure of the evolution and observation matrices and the covariances yields the recursion:

$$X_{t-i|t} = X_{t-i|t-1} + K_{t-i}(Y_t - G_t X_{t|t-1}), \quad i = 0, \ldots, q \tag{21.13}$$

$$K_{t-i} = \Gamma^{(i,0)}_{t|t-1} G_t^{\mathrm{T}} (G_t \Gamma_{t|t-1} G_t^{\mathrm{T}} + \Gamma_{v_t})^{-1}, \quad i = 0, \ldots, q \tag{21.14}$$

$$\Gamma^{(i+1,0)}_{t+1|t} = \Gamma^{(i,0)}_{t|t-1} (I - K_t G_t)^{\mathrm{T}} F_t^{\mathrm{T}}, \quad i = 0, \ldots, q \tag{21.15}$$

where the covariance matrices $\Gamma^{(i,0)}_{t|t-1}$ are defined as $\Gamma^{(i,0)}_{t|t-1} = \mathbb{E}\{(\mathrm{X}_{t-i} - \mathrm{X}_{t-i|t-1})(\mathrm{X}_t - \mathrm{X}_{t|t-1})^{\mathrm{T}}\}$, and thus $\Gamma^{(0,0)}_{t|t-1} = \Gamma_{t|t-1}$ is obtained from the filter Eqn (21.7). Note that depending on q we may have a very large number of matrices and vectors that we have to store. For further details of the fixed-lag smoother, see Anderson and Moore (1979), and in the context of nonstationary inverse problems, see Vauhkonen, Vauhkonen, and Kaipio (2001) and Seppänen et al. (2001b).

The fixed-interval smoother consists of two recursions: first, the conventional Kalman filter and predictor estimates are computed (the forward iteration) and the estimates as well as the backward gain matrices A_t are stored:

$$A_{\mathrm{t}} = \Gamma_{t|t} F_t \Gamma^{-1}_{t+1|t}, \quad t = 1, \ldots, T-1 \tag{21.16}$$

Then, the following backward iteration is carried out:

$$X_{t-1|T} = X_{t-1|t-1} + A_{t-1}(X_{t|T} - X_{t|t-1}), \quad t = T, \ T-1, \ldots, 2 \tag{21.17}$$

$$\Gamma_{t-1|T} = \Gamma_{t-1|t-1} + A_{t-1}(\Gamma_{t|T} - \Gamma_{t|t-1}) A^{\mathrm{T}}_{t-1} \tag{21.18}$$

The storage requirement can be significant for large dimensional states and long total observation/experiment lengths T.

How much better the smoothed estimates are when compared to the real-time Kalman filtered estimates depends on the overall state space model in a complex manner. It is, however, intuitively obvious and mathematically provable that estimates that are based on a set of measurements cannot be worse than those based on a subset of these measurements. In particular, it can be shown that $\Gamma_{t|k} \geq \Gamma_{\mathrm{t}|\ell}$ for all $\ell > k$ in the sense that $\Gamma_{t|k} - \Gamma_{t|\ell}$ is a positive semidefinite matrix. For further considerations of using smoothers in process tomography, see Kaipio, Duncan, Seppanen, Somersalo, and Voutilainen (2005) and Duncan et al. (2005).

21.3 Approximate nonlinear and non-Gaussian state estimation and handling modelling errors

Many observation modalities that are used in process tomography are nonlinear. This applies also to some evolution models. Some models may be linear in the way the problems are usually viewed. In the presence of model uncertainties, it may, however, turn out that the observation model is not linear with respect to *both* the primary unknown and the auxiliary unknowns (uncertainties). Furthermore, the associated noise processes are often not Gaussian but are approximated as such.

Note also that even in the case of evolution models that are linear with respect to the primary unknown, say temperature, an unconventional choice for state variables may render the state evolution model highly nonlinear. See Kolehmainen, Voutilainen, and Kaipio (2001) for an example in which the state variables comprise a parametric representation for the boundary of a temporally varying inclusion in a vessel, or Tossavainen, Vauhkonen, Kolehmainen, and Kim (2006) and Tossavainen, Vauhkonen, and Kolehmainen (2007) in which a kinematic evolution model was used for estimating the velocity and acceleration of phase interfaces in sedimentation processes.

In this section, we review briefly the *extended Kalman filter*, which is the most commonly used algorithm to compute approximations for the mean square estimates.

21.3.1 Extended Kalman filters

In this section we treat only the additive state and observation noise case. Let the (nonlinear) state space model be of the form

$$X_{t+1} = F_t(X_t) + W_t \tag{21.19}$$

$$Y_t = G_t(X_t) + E_t \tag{21.20}$$

where $F_t : \mathbb{R}^N \rightarrow \mathbb{R}^N$ is the state (evolution) operator and $G_t : \mathbb{R}^N \rightarrow \mathbb{R}^M$ is the observation (forward) model. The extended Kalman filter can also be derived for more complex models.

The idea in extended Kalman filters is straightforward: the nonlinear mappings are approximated with the affine mappings given by the first two terms of the Taylor expansion. We refer to the approximation of the mappings with their first-order Taylor series as linearization and denote the associated Jacobian mappings by J. The notion of extended Kalman filter is not completely fixed, and there are three main levels of refinement. The state in which the linearizations are computed will be denoted with X_t^*, which may or may not depend on time.

In the *global linearization* approach, the mappings F_t and G_t are linearized in some time-invariant point $X_t^* \equiv X^*$ so that we have $F_t(X_t) \approx F_t(X^*) + J_{F_t}\big|_{X^*}(X_t - X_*) = B_t + J_{F_t}\big|_{X^*} X_t$ and similarly for G_t. In the global linearization approximation, the Jacobian does not have to be recomputed during the iteration. It is clear that a feasible linearization point X^* is a prerequisite for this approximation to be successful. Furthermore, it is clear that this approximation works well only when the expected variation in the actual X_t is small.

The most commonly used version of extended Kalman filter is the *local linearization version* in which the mappings are linearized in the best available state estimates, that is, either the predicted or the filtered state. This necessitates the recomputation of the Jacobians at each time instant. Note that the linearization is usually not used when the prediction $X_{t|t-1}$ is computed, but it is used for the computation of the associated prediction covariance. This applies also for the measurement update. The recursions take the form:

$$X_{t|t-1} = F_{t-1}(X_{t-1|t-1}) + S_t \tag{21.21}$$

$$\Gamma_{t|t-1} = J_{F_{t-1}}\Gamma_{t-1|t-1}J_{F_{t-1}}^{\mathrm{T}} + \Gamma_{W_{t-1}} \tag{21.22}$$

$$K_t = \Gamma_{t|t-1}J_{G_t}^{\mathrm{T}}(J_{G_t}\Gamma_{t|t-1}J_{G_t}^{\mathrm{T}} + \Gamma_{E_t})^{-1} \tag{21.23}$$

$$\Gamma_{t|t} = (I - K_t J_{G_t})\Gamma_{t|t-1} \tag{21.24}$$

$$X_{t|t} = X_{t|t-1} + K_t(Y_t - G_t(X_{t|t-1})) \tag{21.25}$$

The linearizations are also needed for the computation of the Kalman gain K_t.

We shall only mention the idea of the third version, the *iterated extended Kalman filter* here. In this variant, at each time, another (inner) iteration is performed. This iteration computes the *maximum* a posteriori estimate of the approximate model for $\pi(\mathrm{X_t}|\mathrm{D_t})$. Since G_t is nonlinear, the respective maximizer does not generally have an analytical form and leads to the inner iteration. See, for example, Kaipio et al. (2005) for further discussion. In all cases it must be noted that the above recursions in this section are not optimal with respect to any simple criteria.

21.3.2 Modelling errors: Bayesian approximation error approach

For approximate marginalization over auxiliary unknowns, as well as handling discretization and other model reduction related errors, the *approximation error approach* was proposed in Kaipio and Somersalo (2004, 2007) in which, for example, EIT was considered. The approximation error approach has also been successfully applied to optical tomography and model reduction (discretization) (Arridge et al., 2006), anisotropy (Heino, Somersalo, & Kaipio, 2005), handling unknown boundary data (Lehikoinen et al., 2007), and has also been verified with real EIT data under model reduction, geometry related uncertainties and unknown contact impedances (Nissinen et al., 2008, 2009, 2011). The extension of the approximation error approach to nonstationary inverse problems was developed in Huttunen and Kaipio (2007), Huttunen et al. (2007), Huttunen and Pikkarainen (2007) and Huttunen and Kaipio (2009) in which the model reduction, long-time stepping and other computational problems were under particular consideration.

In the context of state estimation problems, consider the following state space model:

$$X_{t+1}^a = F_t^a\left(X_t^a; \beta\right) + W_t \tag{21.26}$$

$$Y_t = G_t(X_t, \beta) + E_t \tag{21.27}$$

where β are parameters that are poorly known but for which a probabilistic model $\pi(\beta)$ is available, and where X_t^a and F_t^a correspond to a (numerically) accurate representation of the state evolution model. For computational reasons, we would prefer to use a possibly drastically reduced-order state variable and model, X_t^r and F_t^r, and, furthermore, we would not attempt to estimate β simultaneously but set $\beta = \beta_*$. Then, attempting to use, say, Kalman recursions for the reduced-order model, might yield meaningless or at least infeasible estimates.

The Bayesian approximation error (BAE) approach is a systematic way in which the system of Eqns (21.26) and (21.27) is replaced by the system:

$$X_{t+1}^r = F_t^r\left(X_t^r; \beta_*\right) + W_t + Q_t \tag{21.28}$$

$$Y_t = G_t\left(X_t^r, \beta_*\right) + E_t + D_t \tag{21.29}$$

where the processes Q_t and D_t are the approximation error processes; see, for example, Huttunen and Kaipio (2007), Huttunen et al. (2007), Huttunen and Pikkarainen (2007), Huttunen and Kaipio (2009) and Lipponen et al. (2011). The BAE is a systematic, albeit often tedious, approach to compute the second-order statistics of the processes Q_t and D_t. We note that the means of these processes are seldom zero and any estimator is to be modified to account for this. The numerical examples later in this chapter are based on adopting the BAE approach.

21.4 Approaches with auxiliary parameters

In practical problems one or more of the state space terms is often at least partially unknown. While careful analysis and numerical modelling of the measurement system usually pins the observation model down relatively accurately, the state evolution model is typically subject to uncertainties. There are basically four alternatives depending on the type of the uncertainties and/or other auxiliary parameters.

The first is the subjective ‘manual tuning’ approach, which means that the parameters are tuned manually or by ‘previous experience’. The other three approaches are more objective ones. In the batch-type optimization approaches, the task is to estimate the best *time-invariant* parameters typically by the maximum likelihood method.

However, if the unknown parameters are assumed to be *time-varying*, it is possible to augment the state variable to include the unknown (time-varying) parameters. The fourth approach is the BAE approach mentioned above, in which the auxiliary unknowns are not estimated but the effects of their uncertainty in the state space model are computed.

21.4.1 Batch-type optimization: (a few) time-invariant parameters

The estimation of unknown parameters in a state space model is often called *state space identification*. Denote the unknown parameters by $\beta\in\mathbb{R}^s$. Several parameters of the state space representation might depend on the parameters β. A typical example would be to postulate the model $\Gamma_{W_t}\equiv\sigma_W^2 I$ for the state noise covariance but with an unknown σ_W^2.

The idea is to compute the likelihood L of the observations $D_T=(Y_1,\ldots,Y_T)$ given the parameters β and maximize the likelihood with respect to β, that is, $\max_\beta L(D_T|\beta)$.

The likelihood depends on the unknown parameters. Let the initial state $X_0\in\mathbb{R}^M$ be known. Then the log-likelihood $\log L(D_T)$ can be written in the form (Durbin & Koopman, 2001):

$$\log L(D_T|\beta)=-\frac{MT}{2}\log 2\pi-\frac{1}{2}\sum_{t=1}^{T}(\log|\Gamma_{t|t-1}|+R_t^{\mathrm{T}}\Gamma_{t|t-1}R_t|\beta)\qquad(21.30)$$

where $|\cdot|$ denotes determinant, $R_t=Y_t-G_tX_{t|t-1}$ is the prediction error (residual) and the notation $(\cdot|\beta)$ on the left-hand side refers to all terms being calculated with parameters β.

Most often it is necessary to use Newton or quasi-Newton methods such as the BFGS (Broyden–Fletcher–Goldfarb–Shanno) algorithm with numerically approximated gradients to compute the maximum of Eqn (21.30). For more details, see, for example, Durbin and Koopman (2001) and Nocedal and Wright (1999). See also Shumway (1988) for the application of the expectation-maximization (EM) algorithm to this problem.

21.4.2 Augmented state models: time-varying parameters

Often, the unknown parameters β_t are time-varying and occur in the state evolution model. The unknown boundary conditions for the convection–diffusion transfer model serve as a standard example. If the parameters were known, we could employ the state evolution model $X_{t+1}=F_t(X_t;\beta_t)+S_t+W_t$.

The straightforward approach to account for an unknown β_t is to augment the state to include the unknown parameters so that we write $Z_t=(X_t,\beta_t)$. The usual choice would be to postulate a random walk model for $\beta_{t+1}=\beta_t+W_t^\beta$.

Thus, for example, we would write:

$$Z_{t+1} = \begin{pmatrix} X_{t+1} \\ \beta_{t+1} \end{pmatrix} = \begin{pmatrix} F_t(X_t; \beta_t) \\ \beta_t \end{pmatrix} + \begin{pmatrix} S_t \\ 0 \end{pmatrix} + \begin{pmatrix} W_t \\ W_t^\beta \end{pmatrix} \tag{21.31}$$

where the associated state noise covariance can be written as

$$\operatorname{cov}\begin{pmatrix} W_t \\ W_t^\beta \end{pmatrix} = \begin{pmatrix} \Gamma_{W_t} & 0 \\ 0 & \Gamma_{W_t^\beta} \end{pmatrix} \tag{21.32}$$

and where the tracking speed of β_t is controlled by $\Gamma_{W_t^\beta}$. Then, in this case, the extended Kalman filter would be employed.

This is the approach taken in the sections below where β_t corresponds to a reduced-order representation of the time-varying Navier−Stokes flow. In this case, however, the evolution model $\beta_{t+1} = F_t^\beta(\beta_t) + W_t^\beta$ is a nonlinear (quadratic) model, and the construction of the covariance structure and nonzero mean of the process W_t^β is based on the BAE approach.

21.5 Tomographic state space estimation of velocity fields

Even with single-phase flows, the actual velocity field may exhibit a complex spatiotemporal structure with, for example, vortices. The estimation of the entire time-varying velocity field with a spatiotemporal resolution that the modelling of vortices would require is beyond the capability of all practical tomographic modalities. It is, however, possible to attempt to use reduced-order models for the flows that may be constructed so that they exhibit all the characteristics of, say, vortex flows.

In this section, we restrict to the EIT as the imaging modality and assume (for notational simplicity) that we are imaging a spatiotemporally varying solution of strong electrolytes with concentration c_t, which distribution induces the spatial distribution of the conductivity σ_t. We take the flows to be so fast that only the measurements corresponding to a single current pattern can be considered to correspond to a stationary target.

In Section 5.1, we review the complete electrode model (CEM) as the observation model. In Section 5.2 we formulate the velocity field as a translationally invariant profile flow with few parameters. This is a very simple example of a reduced-order model for the velocity field. In Section 5.3, we formulate the reduced-order model for the velocity field such that it is based on a quadratic optimality criterion, and derive the related stochastic evolution model and, further, its computational realization. In Section 5.4, we construct the numerical stochastic model for the related convection−diffusion transport problem and present the resulting form of the extended Kalman filter. In the following, we give only limited details to the extent that allows for an overview of the steps needed to set up the overall state space model and the Kalman estimators.

21.5.1 Electrical impedance tomography

For quasi-stationary EIT measurements (frequency less than about 140 kHz), the complete electrode model (CEM) (Cheng, Isaacson, Newell, & Gisser, 1989) is the usual measurement model choice. The CEM is a mixed boundary value problem:

$$\nabla \cdot (\sigma \nabla u) = 0, \quad \vec{r} \in \Omega \tag{21.33}$$

$$u + z^{(\ell)} \sigma \frac{\partial u}{\partial \vec{n}} = U^{(\ell)}, \quad \vec{r} \in e^{(\ell)}, \quad \ell = 1, 2, \ldots, L \tag{21.34}$$

$$\sigma \frac{\partial u}{\partial \vec{n}} = 0, \quad \vec{r} \in \partial\Omega / S_{\Omega,e} \tag{21.35}$$

$$\int_{e^{(\ell)}} \sigma \frac{\partial u}{\partial \vec{n}} \mathrm{d}S = I^{(\ell)}, \quad \ell = 1, 2, \ldots, L \tag{21.36}$$

where $\sigma = \sigma(\vec{r})$ is the conductivity distribution, $u = u(\vec{r})$ is electrical potential in the target domain Ω and L is the number of the electrodes. The terms $U^{(\ell)}$, $I^{(\ell)}$ and $z^{(\ell)}$, respectively, are the electric potential, current and contact impedance corresponding to the ℓ^{th} electrode $e^{(\ell)}$. Furthermore, $S_{\Omega,e} = \bigcup_{\ell=1}^{L} e^{(\ell)}$ is the union of boundary patches covered by the electrodes. In addition, the injected currents must satisfy the current conservation law and a reference level of the potential u:

$$\sum_{\ell=1}^{L} I^{(\ell)} = 0, \quad \sum_{\ell=1}^{L} U^{(\ell)} = 0 \tag{21.37}$$

The conditions of Eqn (21.37) ensure the uniqueness and existence of the (weak) solution of the CEM (Somersalo, Cheney, & Isaacson, 1992).

Let the kth current pattern be $I = (I^{(1)}, \ldots, I^{(L)})$ with respective electrode potentials $U = (U^{(1)}, \ldots, U^{(L)})$. The relationship between the noiseless measurements U, the conductivity σ and the current pattern I can be written as $U = R(\sigma)I$. Here, we consider only the additive measurement noise model:

$$V = R(\sigma)I + E \tag{21.38}$$

For numerical approximation, the finite element method would typically be applied to the variational form of CEM; see, for example, Somersalo et al. (1992) and Vauhkonen, Vauhkonen, Savolainen, and Kaipio (1999). Since we have a time-depending conductivity distribution, we write:

$$V_t = R(\sigma_t)I_t + E_t \tag{21.39}$$

In the sequel, the evolution model will be formulated in terms of concentration $c(\overrightarrow{r}, t)$ of an electrically conducting target. The observation model in terms of concentration is the composite map:

$$V_t = (R \circ \sigma)(c_t)I_t + E_t = \overline{G}_t^c(c_t) + E_t \tag{21.40}$$

where $\sigma_t = \sigma(c_t)$ is typically a nonlinear function and the time-dependence is only through the temporal dependence of c_t. For more details, see Vauhkonen et al. (1999) and Lipponen et al. (2010b).

Using an accurate numerical model for the CEM is not feasible resource-wise for most practical applications. Therefore, a possibly drastic numerical approximation usually has to be used. For example, this could be carried out by constructing a finite element mesh that is very sparse. Using a sparse mesh and a resulting poor forward solver induces errors that are often much larger than the observation errors E_t. As explained above, to cope with this and to make the observation model feasible, the BAE approach can be employed, which yields the model:

$$V_t = G_t^c\left(c_t\right) + E_t + D_t^c \tag{21.41}$$

where the noise process D_t^c is induced by a probabilistic model of c_t. Typically, simulations would be carried out to compute the second-order statistics of D_t^c. We note that almost invariably, $\mathbb{E}(D_t^c) \neq 0$. For more details on computing the approximation error statistics for the reduced-order EIT, see, for example, Kaipio and Somersalo (2004) and Lipponen et al. (2011).

21.5.2 Flow profile model

If we can assume that the (two-dimensional) flow is almost stationary (slowly varying) and vortex free, we could approximate it as

$$\overrightarrow{v}(\overrightarrow{r}, t) = \sum_{i=1}^{p} \beta_i(t)\overrightarrow{v_i}(x_2) \tag{21.42}$$

where $\overrightarrow{r} = (x_1, x_2)$, x_1 is the coordinate along the pipeline so that $\{\overrightarrow{v_i}(x_2),\ i = 1, \ldots, p\}$ is a basis for the flow profile across the pipeline. Furthermore, the basis vectors are time independent and we write $\beta_t = (\beta_1(t),\ldots,\beta_p(t))^{\mathrm{T}}$, which, once the basis is fixed, are the unknown variables. The representation (21.42) would then be inserted in the convection–diffusion model as in Section 5.4.

We note that a representation such as Eqn (21.42) does not relate directly to any physical (partial differential) model for a flow. It is merely an (small dimensional) ad hoc representation that may be a feasible model, for example, for horizontal fluid conveyors with a multiphase (solid and fluid) flow. See Seppänen et al. (2009) for further details.

21.5.3 Reduced-order Navier–Stokes evolution model

In Section 5.2, we posed an ad hoc model for the flow. In this section, we consider the stochastic Navier–Stokes flow and build such a basis for it that it is an optimal one with respect to a quadratic optimality criterion over time and space. Furthermore, we outline the construction of the associate numerical evolution model and the stochastic driving (state noise) process, which is based on the nonstationary BAE approach. For any further details, we refer to Lipponen et al. (2010b).

The Navier–Stokes (NS) equations can be written in the form

$$\rho \frac{\partial \vec{v}}{\partial t} + \rho \vec{v} \cdot \nabla \vec{v} - \mu \Delta \vec{v} + \nabla p = 0 \text{ in } \Omega \tag{21.43}$$

$$\nabla \cdot \vec{v} = 0 \tag{21.44}$$

where ρ is the density, μ is the viscosity, p is the pressure, and where we have assumed that no external forces are present. Furthermore, we take the density as a constant.

Eventually, we aim to derive the stochastic version of the flow, and the unknown initial values will be absorbed in the driving stochastic process. The same applies for the unknown boundary data on the truncation boundaries of the computational domain. On the pipe walls, we set the no slip conditions.

For the numerical approximation of the NS equation, one would usually use a semi-discrete approach with locally supported basis such as in finite element or finite volume method. In the reduced-order modelling of the NS equations, however, the velocity field is approximated in the form

$$\vec{v}(\vec{r}, t) \approx \vec{v}_0(\vec{r}) + \sum_{i=1}^{N} \beta_i(t) \vec{v}_i(\vec{r}) \tag{21.45}$$

where the *mean flow* $\vec{v}_0(\vec{r})$ is a fixed vector field. Furthermore, none of the fields $\vec{v}_i(\vec{r})$, $i = 0, \ldots, N$ is locally supported. To achieve adequate accuracy with a semidiscrete scheme, the number of basis vectors would typically have to be very high, in particular, to capture vortices. With the reduced-order approach that will be discussed below, one might only need a few basis vectors.

Let us write

$$\vec{v}(\vec{r}, t) \approx \vec{v}_o(\vec{r}) + \sum_{i=1}^{p} \beta_i(t) \vec{v}_i(\vec{r}) + \sum_{i=p+1}^{N} \beta_i(t) \vec{v}_i(\vec{r}) = \vec{v}_0 + \vec{v}^p + \vec{v}^{\tilde{p}} \tag{21.46}$$

In reduced-order Navier–Stokes, the velocity field is considered as a stochastic flow and the basis $\{\vec{v}_i\}$ is chosen so that $\mathbb{E}_{\vec{r},t} \|\vec{v} - (\vec{v}_0 + \vec{v}^p)\|^2$ is minimized over all $p+1$-dimensional bases (including $\vec{v}_0$), where

$$\mathbb{E}_{\vec{r},t}\|\vec{v}-(\vec{v}_0+\vec{v}^p)\|^2 \approx \frac{1}{T}\int\limits_0^T\int\limits_\Omega \|\vec{v}(\vec{r},t)-(\vec{v}_0(\vec{r})+\vec{v}^p(\vec{r},t))\|^2_{\mathbb{R}^2}\mathrm{d}\vec{r}\,\mathrm{d}t \tag{21.47}$$

Such a basis and the respective representation is variably referred to as the *proper orthogonal decomposition* (POD), Karhunen–Loeve decomposition, Hotelling transform or *principal component (analysis)* (PCA), see, for example, Jolliffe (2002). The POD basis of dimension p is obtained as the p eigenvectors of the covariance of the stochastic flow, which correspond to the p largest eigenvectors.

In practice, simulation of the NS equation over a distribution of parameter uncertainties, boundary and initial conditions is performed. This will give an ensemble of stochastic realizations of the flow, from which ensemble the mean flow and covariance can be estimated as sample averages. Further, the POD theory states that the optimal $\vec{v}_i,\quad i=1,\ldots,p$ are given by the mean and the eigenvectors $\vec{v}_i(\vec{r})$ corresponding to the p largest eigenvalues λ_i of the covariance.

The reduced-order model is then obtained by inserting the approximation $\vec{v}\approx\vec{v}_0+\vec{v}^p$ into the NS equation, which gives

$$\dot{\beta}^p(t) = F(\beta^p(t)) = \begin{pmatrix} \beta^p(t)^{\mathrm{T}}A_1^p\beta^p(t) \\ \vdots \\ \beta^p(t)^{\mathrm{T}}A_p^p\beta^p(t) \end{pmatrix} + B\beta^p(t)+d \tag{21.48}$$

where A_k^p, B and d are matrices and vectors arising (in our case) from the finite element approximation of the NS equation.

The system of ODEs Eqn (21.48) usually has only a few equations and is not a stiff system. Therefore, we can use, for example, a second-order explicit Runge–Kutta method:

$$\beta_{t+1}^p = \beta_t^p + \Delta t\widetilde{F}\left(\beta_t^p + \frac{1}{2}\Delta t\widetilde{F}\left(\beta_t^p\right)\right) \tag{21.49}$$

The next step is to use the BAE to compute the error structure of the POD approximation and equip Eqn (21.48) with a stochastic driving term so that we can write

$$\beta_{t+1}^p = F^\beta\left(\beta_t^p\right) + W_t^\beta \tag{21.50}$$

for the evolution model of the coefficients β_t^p.

21.5.4 Stochastic convection–diffusion model

As noted above, we consider only the case of convection and diffusion under a single-phase flow. The uncertainties here are related to the unknown boundary conditions, especially on the input boundary where the flow enters the (computational) domain. Further errors are induced by using approximate forward solvers in the semidiscrete scheme. We refer to Seppänen et al. (2001b, 2008) for the details of how to construct a stochastic convection-diffusion model and its computational approximation.

The CD equation is of the form

$$\frac{\partial c}{\partial t} = \nabla \cdot \kappa \nabla c - \vec{v} \cdot \nabla c \tag{21.51}$$

where $\kappa = \kappa(\vec{r})$ is the diffusion coefficient. Our domain is a segment of a pipeline and we have the following boundary conditions:

$$c = c_{\text{in}}, \quad \vec{r} \in \Gamma_{\Omega,\text{in}} \tag{21.52}$$

$$\frac{\partial c}{\partial \vec{n}} = 0, \quad r \in (\partial\Omega / S_{\Omega,\text{in}}) \tag{21.53}$$

where $c_{\text{in}} = c_{\text{in}}(\vec{r}, t)$ is an unknown time-varying function (which will be modelled as a stochastic process on $S_{\Omega,\text{ in}}$) and where $S_{\Omega,\text{ in}}$ is the input boundary where the flow enters the domain Ω. Note that if the velocity field $\vec{v}$ and the boundary condition c_{in} were known, and if a very accurate solver was used, we would not need any (EIT or other) measurements to infer the state of the system.

For the computational approximation of the CD equation, we use the semidiscrete Petrov–Galerkin FEM scheme, which yields the stiff system of differential equations:

$$M_1 \dot{c} + K_1(\vec{v})c + L_1 c = -M_2 \dot{c}_{\text{in}} - K_2(\vec{v})c_{\text{in}} - L_2 c_{\text{in}} \tag{21.54}$$

where $M_{1,2}$ are mass-type matrices, $K_{1,2}$ are stiffness-type matrices, and their elements are functions of the velocity field, and $L_{1,2}$ are further matrices arising from the FEM scheme.

For the derivation of the stochastic evolution model for c_t, we proceed as follows. We insert the decomposition $\vec{v} = \vec{v}_0 + \vec{v}^p + \vec{v}^{\tilde{p}}$, write $c_{\text{in}} = \bar{c}_{\text{in}} + \tilde{c}_{\text{in}}$, where $\bar{c}_{\text{in}}$ is the time average of the input boundary process. Next, we rearrange the terms in the system of equations so that all the unknowns and the terms that are not included in the estimated variables (such as the remainder of the velocity field $\tilde{\beta}$ and $\tilde{c}_{\text{in}}$) are embedded in additive (approximation) error terms. Since the system is stiff, we use an implicit Runge–Kutta scheme and obtain

$$c_{t+1} = F^c\left(c_t, \beta_t^p\right) + Q_t^c + W_t^c \tag{21.55}$$

where the stochastic processes Q_t^c and W_t^c are induced by (1) numerical approximations, (2) a stochastic model for $\tilde{c}_{\text{in}}$ and (3) the statistics for the variables $\tilde{\beta}$ that were obtained when the POD decomposition for the Navier–Stokes flow was determined. For more details, we refer to Lipponen et al. (2010b).

21.5.5 The overall state space model and realization of the extended Kalman filter

The state variable is now $X_t = (\beta_t^p, c_t)$ and state evolution and observation operators are now of the form

$$F(X_t) = \begin{pmatrix} F^\beta\left(\beta_t^p\right) \\ F^c\left(c_t, \beta_t^p\right) \end{pmatrix} \tag{21.56}$$

$$G_t\left(X_t\right) = G_t^c(c_t) \tag{21.57}$$

that is, the observations do not directly depend on the velocity field.

As noted above, the uncertainties, omitted terms and modelling errors are modelled as random variables or stochastic processes, and they in turn induce the state and evolution noise processes, whose second-order statistics are computed by employing the nonstationary BAE approach. Thus, we have the overall state space model (for the measurements, we have $Y_t = V_t$):

$$X_{t+1} = F(X_t) + W_t + Q_t \tag{21.58}$$

$$Y_t = G_t\left(X_t\right) + E_t + D_t = G_t^c(c_t) + E_t + D_t \tag{21.59}$$

Here, the approximation error term D_t includes contributions from the approximation of the CEM (D_t^c), but also contributions from the approximation of the evolution model. We note that the structure of the covariances of all noise processes is generally highly nontrivial. Furthermore, with the possible exception of E_t (measurement noise), the means of the processes are not zero. This means that the (extended) Kalman filter (EKF) recursions have to be modified accordingly, as follows.

As above, let $X_{t|t}$ and $X_{t|t-1}$ denote the EKF filter and predictor estimates, respectively, and let $\Gamma_{\mathrm{t|t}}$ and $\Gamma_{\mathrm{t|t-1}}$ denote the (approximate) EKF filter and predictor covariances, respectively. The recursive EKF algorithm now takes the form

$$X_{t|t-1} = F(X_{t-1|t-1}) + \mathbb{E}Q_t + \mathbb{E}W_t \tag{21.60}$$

$$\Gamma_{t|t-1} = J_{F_t}\Gamma_{t-1|t-1}\, J_{F_t}^{\mathrm{T}} + \Gamma_{W_t} + \Gamma_{Q_t} \tag{21.61}$$

$$K_t = (\Gamma_{t|t-1}J_{G_t^c}^{\mathrm{T}})(J_{G_t^c}\Gamma_{t|t-1}J_{G_t^c}^{\mathrm{T}} + \Gamma_{E_t} + \Gamma_{D_t})^{-1} \tag{21.62}$$

$$\Gamma_{t|t} = (I - K_tJ_{G_t^c})\Gamma_{t|t-1} \tag{21.63}$$

$$X_{t|t} = X_{t|t-1} + K_t(V_t - G_t(X_{t|t-1}) - \mathbb{E}D_t - \mathbb{E}E_t) \tag{21.64}$$

21.6 Computational case studies

First, we consider the estimation of a flow profile with an ad hoc basis for the reduced-order model. For more details for this case, see Seppänen et al. (2009). Then, we consider two cases of the POD-type model reduction, with both cases corresponding to a vortex flow situation. In the first case, we have a stationary flow with fully developed von Karman street vortex structure. In the second case, we have a nonstationary situation in which the von Karman street first does not exist but emerges later. This is to assess the robustness of the overall approach; while the overall approach can detect and estimate a vortex flow, this should not occur when the vortex is not present. For more details for these cases, see Lipponen et al. (2010b).

21.6.1 Estimation of a flow profile

In the first example case, we consider a flow profile model discussed in Section 5.2. The actual velocity profile is parabolic, and the mean flow velocity is time-varying, starting from 200 cm s^{-1} and increasing smoothly to 550 cm s^{-1} at the end of the measurement set. In state estimation, we assume that the velocity profile is known to be parabolic, and hence, only a single unknown (time-varying) parameter β_t, the mean flow, needs to be inferred based on the EIT data. We write a random walk model for the mean flow β_t and estimate the state variable $X_t = (\beta_t, c_t)$ based on a sequence of EIT observations using EKF, as described above in Section 5.5. The reconstructed concentration distributions and velocity profiles are shown in Figure 21.1. The true mean velocity and the evolution of the estimated mean flow velocity are shown in Figure 21.2. The estimated concentration distributions are clearly feasible estimates for the true distributions, and their accuracy reflects the accuracy that can be obtained with EIT measurements in general. Furthermore, the EKF can track the transient in the mean flow with a delay, which is typical for all filtering approaches. This is due to the fact that in filtering, the estimates are based on the past observations only. Smoothing-type approaches tend not to exhibit any delays, but they are not real-time algorithms. On the other hand, only a few lags might be needed for a fixed-lag smoother, which could exhibit an estimation lag of only a few milliseconds. We also note that the 'noisiness' of estimates is a trade-off with the tracking speed of the EKF. We can reduce the noisiness by simply adjusting (reducing) the variance of state noise component of β_t. As a result of this, the delay in tracking would increase.

21.6.2 POD model reduction with a stationary flow

We consider the benchmark case of the so-called von Karman street, which involves flow past a cylinder with an appropriate Reynolds number (Williamson, 1996). The von Karman street is an oscillating time-varying flow (vortex) on the downstream side of the cylinder, which occurs with Reynolds numbers between about 80 and 170. We study the case in two spatial dimensions. For the estimation of reduced-order representation of the velocity field, we estimate two components only, that is, we set $p = 2$ and estimate β_t^2 together with the time-varying concentration c_t. This choice was based

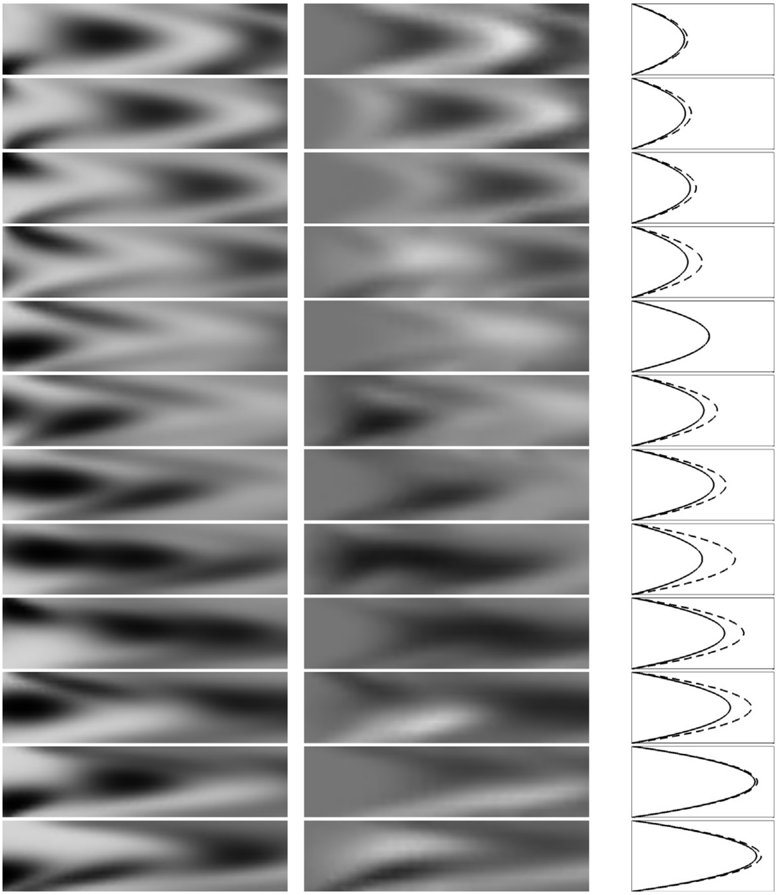

Figure 21.1 Estimation of a flow profile. Left column: The true concentration distributions. Middle column: estimated concentration distributions. Right column: the true (dashed line) and the estimated velocity profile (solid line). The figures correspond to time instants $t = 16,20,\ldots,60$. All the images on left and middle columns are on the same scale.

on an analysis of the eigenvalues of the associated covariance: with $p = 2$, the average (relative) velocity field approximation error that is due to the model reduction falls to a level of 4%.

The Reynolds number is 100 here, which will result in a stationary von Karman street. For reference, we restate at this stage that (assuming that we were first hand interested in the evolution of the concentration) there are three possibilities to handle the (unknown) velocity field: (1) to use the mean field only in the CD model, (2) embed the entire time-varying flow in the approximation error processes and (3) estimate (a reduced-order representation of the) velocity fieldly with the concentration. In Lipponen et al. (2010a), it was shown that (2) is a much better strategy than (1) in the case of time-varying flows. On the other hand, the estimates using (2) were clearly

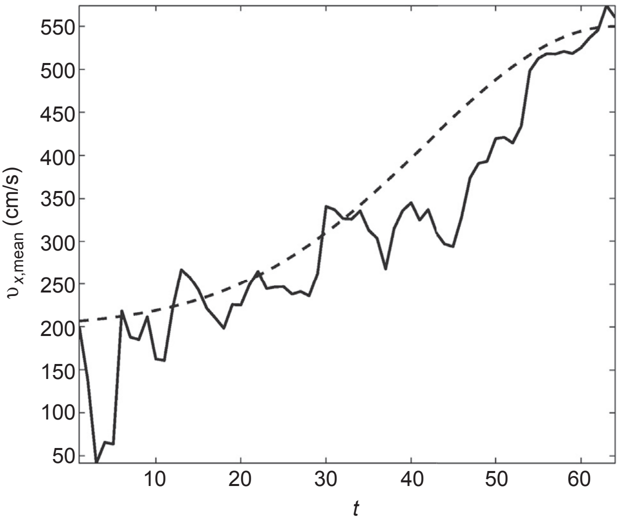

Figure 21.2 Estimation of a flow profile. Estimated mean flow velocity at different time instants (solid line) and the true mean velocity (dashed line).

inferior to estimates using the actual velocity field. This was also evident in the residual processes, which inferentially suggests that the measurements carry information that (in principle) allow for (3), which was carried out in Lipponen et al. (2010b) and has been reviewed above.

The actual evolutions and the respective estimates for the coefficients β_t^2, the velocity field $\overrightarrow{v}_t^2$ and the concentration distribution are shown in Figures 21.3–21.5, respectively. The errors in the estimates for the coefficients are due to the initial settling time of the Kalman filter: the initial state was set as $\beta_0^2(1) = \beta_0^2(2) = 0$. After about 100 time steps (which may be of the order of a few seconds), the filter estimates have settled quite accurately on the actual coefficient evolution. The concentration estimates are also good, although in view of the topic of this chapter, the estimation of the concentration is a secondary objective. It should, however, be kept in mind that due to the coupled nature of the evolution of the velocity field and concentration, it is not plausible to expect accurate estimates for one variable and very inaccurate estimates for the other variable. Also, it is worth noting that the observations carry explicit information on the concentration only.

21.6.3 POD model reduction with a nonstationary flow

Here, we carry out an artificial temporal modulation of the velocity field so that the vortex structure is first (almost) absent and then emerges smoothly. Qualitatively, this corresponds to a temporal change in the viscosity.

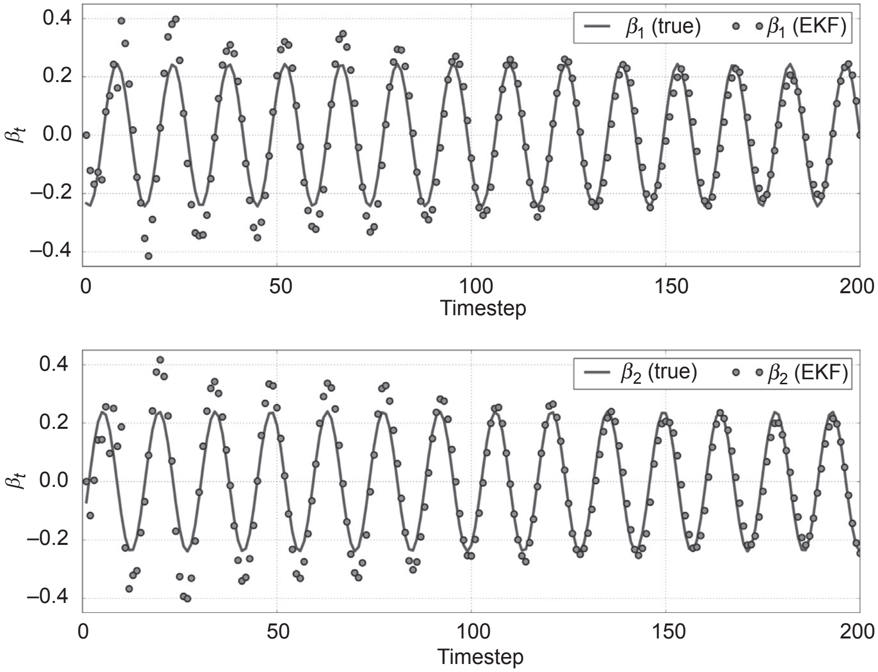

Figure 21.3 Estimation of a fully developed stationary von Karman street. True and estimated coefficients $\beta_{1,t}$ and $\beta_{2,t}$.

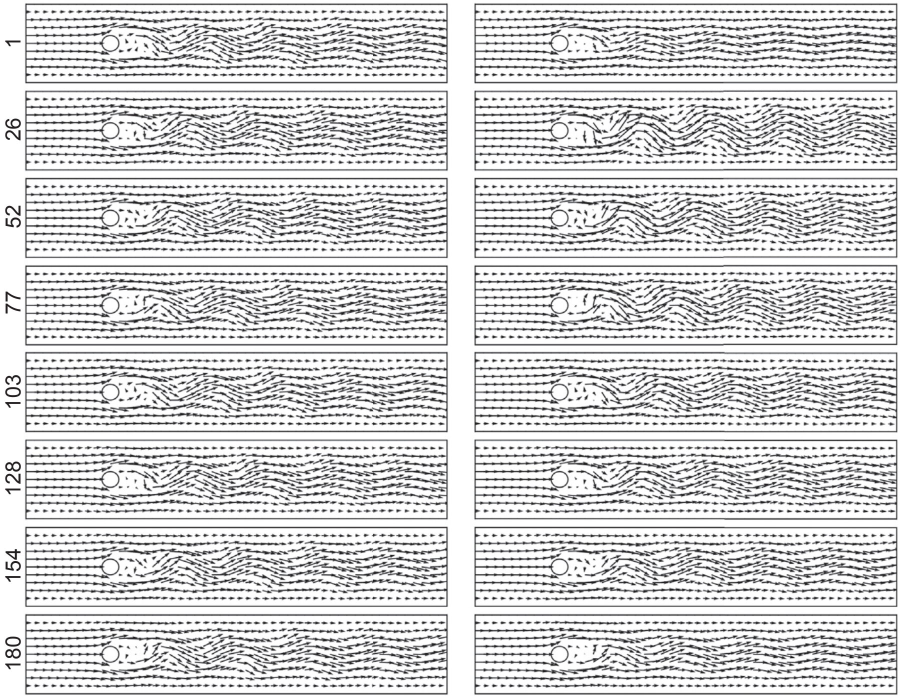

Figure 21.4 Estimation of a fully developed stationary von Karman street. True (left column) and estimated (right column) velocity fields at selected times.

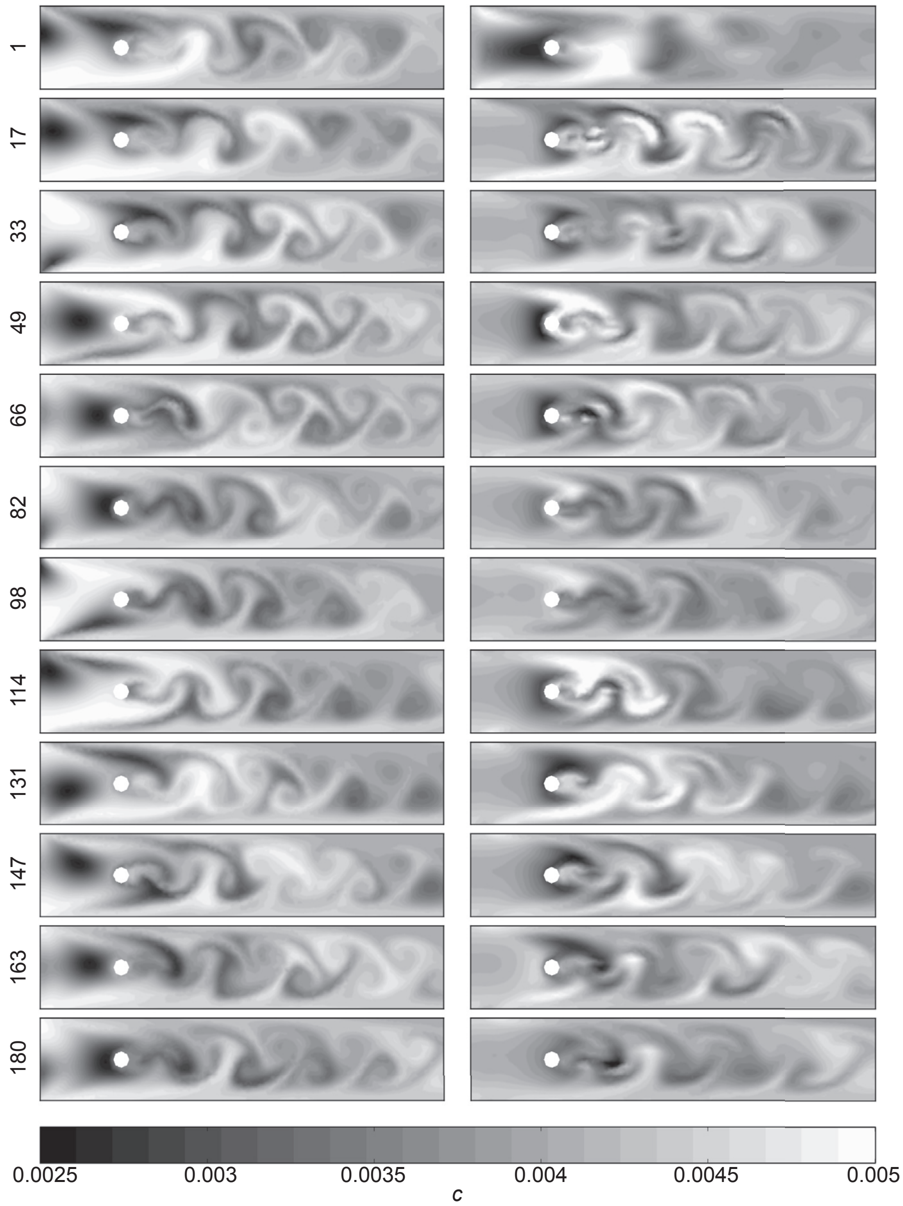

Figure 21.5 Estimation of a fully developed stationary von Karman street. True (left column) and estimated (right column) concentration distributions at selected times.

Again, the actual evolutions and the respective estimates for the coefficients β_t^2, the velocity field $\overrightarrow{v}_t^2$ and the concentration distribution are shown in Figures 21.6–21.8, respectively. In this case, the extended Kalman filter had been running over some time so that the tracking behaviour is due to the changes in the actual velocity field only.

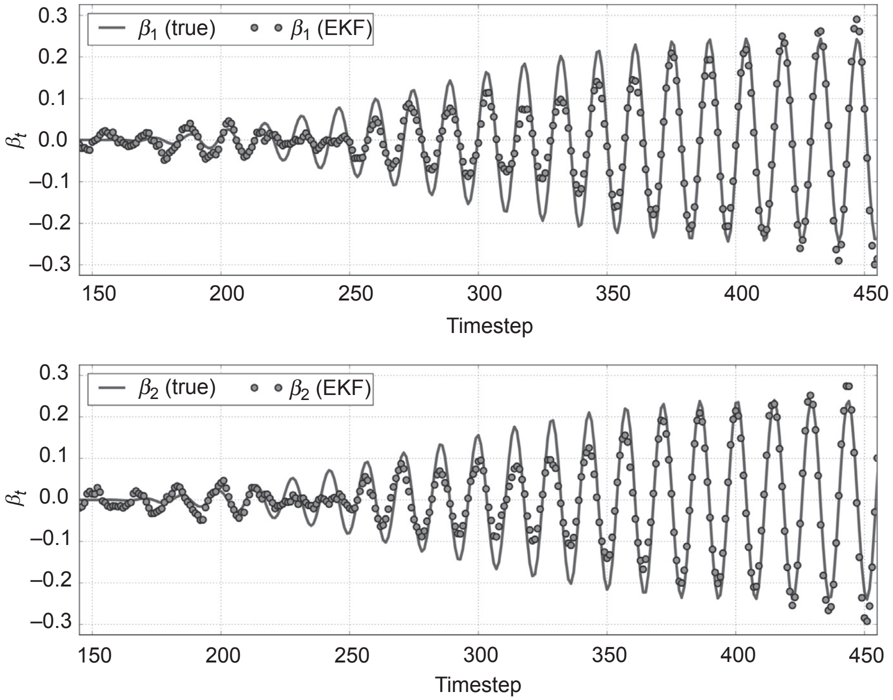

Figure 21.6 Estimation of a nonstationary flow. True and estimated coefficients $\beta_{1,t}$ and $\beta_{2,t}$.

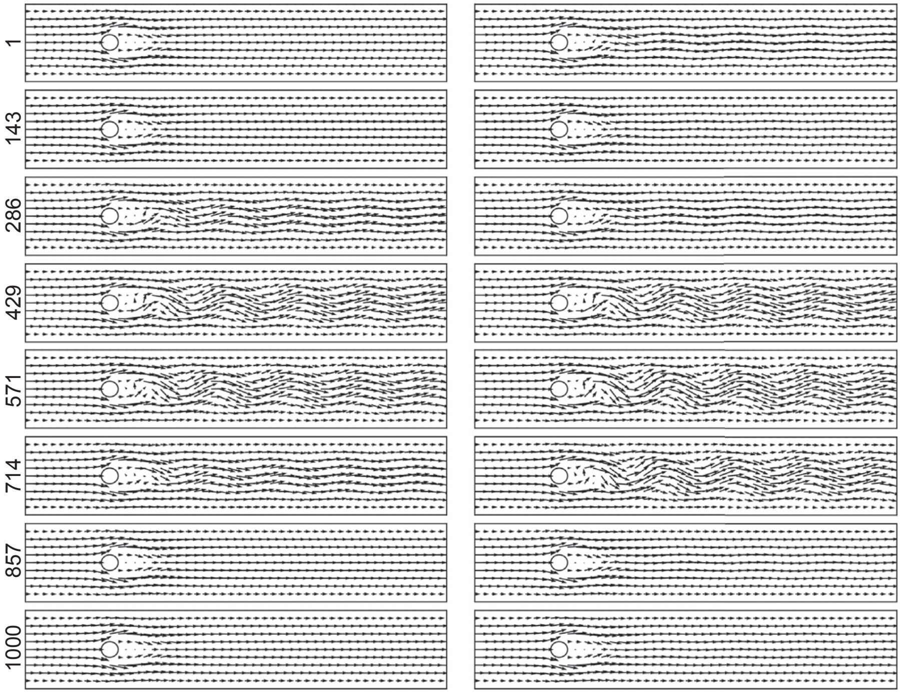

Figure 21.7 Estimation of a nonstationary flow. True (left column) and estimated (right column) velocity fields at selected times.

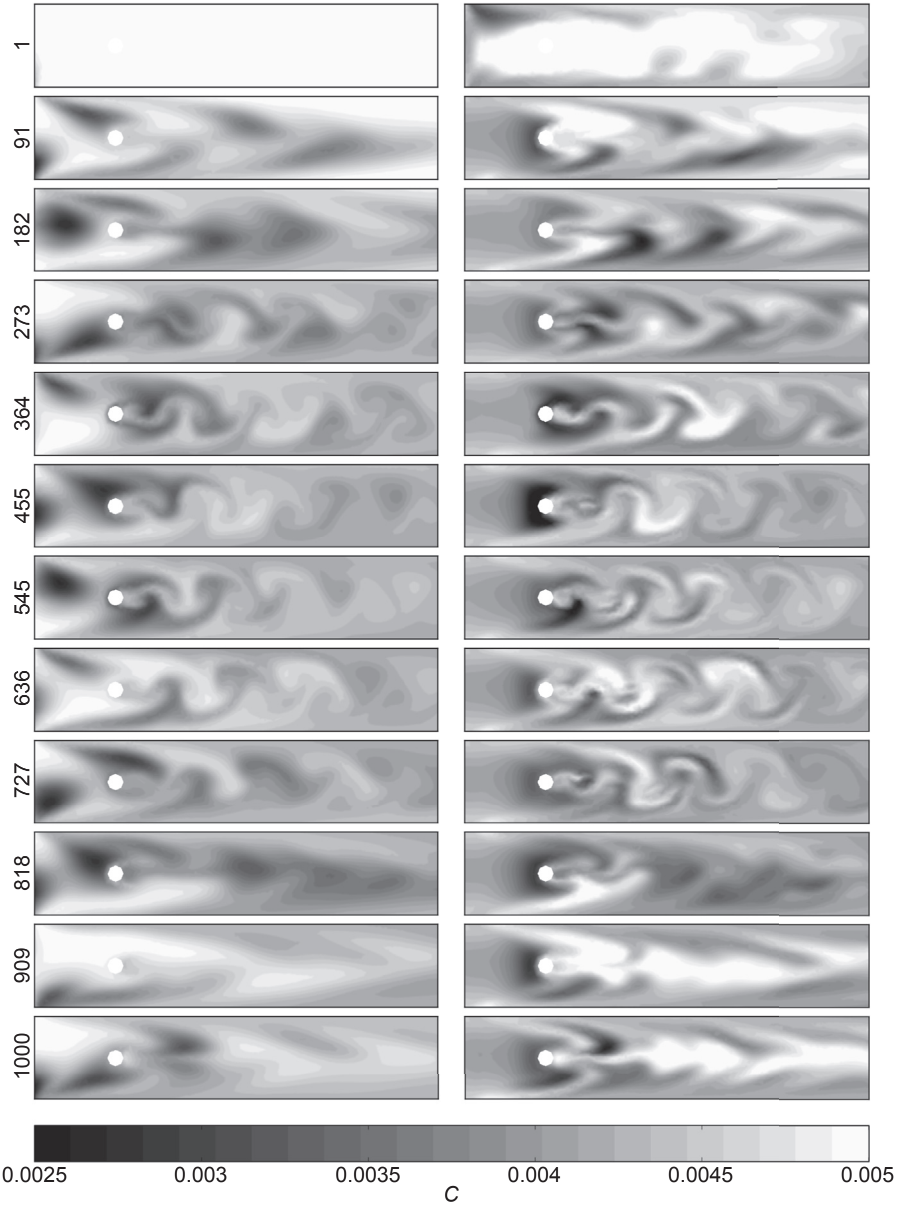

Figure 21.8 Estimation of a nonstationary flow. True (left column) and estimated (right column) concentration distributions at selected times.

We note that around time 150, there are small residual oscillations in the β_t^2 estimates. When viewing the corresponding velocity fields at the same time in Figure 21.7, these oscillations can be judged to be insignificant. This is an important test for the robustness: When the distribution models for all variables were laid down and the POD approximation was fixed, the model did not explicitly include vortex-free velocity fields. Despite this, the EKF estimates for the flow field do not exhibit significant vortice structure when the actual flow is vortex-free.

The evolution of the concentration and the estimates in Figure 21.8 are shown over a longer time period than the coefficients. In Figure 21.8, we see later stages of the simulation when the vortices die down again. We see that the estimates again follow the actual flow with a delay.

21.7 Discussion

Inference on the velocity field of a flow can be accessed either by direct or indirect approaches using tomographic data, when there is spatiotemporal contrast in the variable(s) for which the tomographic modality is sensitive. In direct approaches, the flow field is modelled explicitly in the overall formulation of the problem, and it is estimated directly based on the measurement data. Indirect approaches are two-stage methods, in which a sequence of snapshot estimates is first computed, and subsequently (typically) correlation analysis of the sequence is carried out.

The indirect methods are used more commonly than the direct methods, largely due to the modelling and computational complexities that are related to the direct approaches. In indirect approaches, no explicit model for the (stochastic) flow is needed. The downside of correlation type estimates is, however, that it is difficult to take into account material (and contrast) transfer in any other direction than along the pipeline. In most process applications, the flow is time-varying and in three dimensions. An exact correlation analysis would have to be carried out along the flow lines at each time or, more precisely, along the path of an infinitesimal fluid element. Furthermore, since the relationship between the measurements, the contrast variable and the flow is generally a nonlinear one, all two-stage approaches are likely to exhibit a bias in any estimates in the second stage. For this reason, any estimates that are derived from the inferred flow field are also bound to be biased.

The direct approaches suffer from the above-mentioned modelling and computational complexity. The potential of direct approaches is clearly greater than that of indirect approaches but, at least currently and according to the authors' knowledge, no practical online industrial application is running. The required computational complexity of the approach that was given above is still more than an order of magnitude too complex for practical implementation.

21.7.1 Future trends

To make the direct approaches practically applicable, the main effort is to push the computational complexity further down. In the above example, the (representation for the) velocity field was reduced from hundreds of thousands of variables to just two. If the flow is assumed and allowed to vary more, one would need to use more variables to represent the flow field, but based on preliminary analyses, one would typically need only around 10 variables to represent the flow field. A POD type approach, however, can be used also to parameterize the primary tomographic variable (such as the conductivity) as well as the measurement variable. Such model reduction approaches are currently widely investigated. In this context, see, for example, Lipponen, Seppänen, and Kaipio (2013) for addressing the stationary EIT with an approach in which both the conductivity and the measurements are written in a reduced-order basis. For POD-type model reduction approaches, see also, for example, Lieberman, Willcox, and Ghattas (2010), Banks and Kepler (2003) and Jin (2008). For compressed sensing approaches, which are most commonly used in problems with a very high number of measurements, see, for example, Candes and Wakin (2008).

In general, the trend with inverse problems, including nonstationary problems, is to focus on the modelling of uncertainties. Unless the modelling uncertainties, errors and approximations are treated properly, any estimates can only be treated as qualitative ones, which are mainly valid for visualization. A quantitative estimate consists of the estimate together with reliable well-defined estimate for the related accuracy. It is currently widely agreed that without feasible modelling of the underlying uncertainties, all estimates for the accuracy are bound to be unrealistically optimistic. In the above example, the main effort was in the modelling of the state and measurement noise processes that were related to the model approximations (model reduction by POD) and uncertainties (unknown boundary data).

21.8 Sources of further information and advice

For further information on correlation-based approaches, see, for example, Beck and Plaskowski (1987). For a review of PIV, see Adrian (2005). For a general text in Kalman filtering and state estimation, we refer to Anderson and Moore (1979), and for these topics in relation to nonstationary inverse problems, we refer to Kaipio and Somersalo (2004). State estimation and related (optimal stochastic) control problems in the context of process tomography were treated in Kaipio et al. (2005) and Duncan et al. (2005), respectively.

The above example on using POD in direct estimation of the velocity field was described in more detail in Lipponen et al. (2010a). Modelling uncertainties in the context of inverse problems, and the so-called BAE approach, have been discussed, for example, in Kaipio and Somersalo (2004), Kolehmainen, Tarvainen, Arridge, and Kaipio (2011) and Kaipio and Kolehmainen (2013). These references describe a general approach to constructing computationally feasible (reduced order) models in the context of inverse problems. For Bayesian modelling of modelling errors in a more general context, see Kennedy and O'Hagan (2003).

Acknowledgement

This study was supported by the Academy of Finland (Project numbers 213476 and 250215, Finnish Programme for Centres of Excellence in Research 2012-2017, and projects 270174 and 273536), Finnish Graduate Schools in Computational Sciences (FICS) and Inverse Problems, and University of Auckland, Faculty of Science FDRF project 9844/3700389.

References

Adrian, R. J. (2005). Twenty years of particle image velocimetry. *Experiments in Fluids, 39*, 159−169.

Al-Dahhan, M. H., Kemoun, A., Cartolano, R., Roy, S., Dobson, R., & Williams, J. (2007). Measuring gas-liquid distribution in a pilot scale monolith reactor via an industrial tomography scanner (ITS). *Chemical Engineering Journal, 130*, 147−152.

Albrecht, H. E. (2003). *Laser doppler and phase doppler measurement techniques*. Berlin: Springer-Verlag.

Anadon, L. D., Sederman, A. J., & Gladden, L. F. (2006). Mechanism of the trickle-to-pulse flow transition in fixed-bed reactors. *AIChE Journal, 52*, 1522−1532.

Anderson, B. D. O., & Moore, J. B. (1979). *Optimal filtering*. Englewood Cliffs, NJ: Prentice-Hall.

Arridge, S. R., Kaipio, J. P., Kolehmainen, V., Schweiger, M., Somersalo, E., Tarvainen, T., et al. (2006). Approximation errors and model reduction with an application in optical diffusion tomography. *Inverse Problems, 22*, 175−195.

Banholzer, W. F., Spiro, C. L., Kosky, P. G., & Maylotte, D. H. (1987). Fluidized reactor using X-ray computed tomography. *Industrial & Engineering Chemistry Research, 26*, 763−767.

Banks, H. T., & Kepler, G. M. (2003). Reduced order computational methods for electromagnetic material interrogation using pulsed signals and conductive reflecting interfaces. *Journal of Inverse and Ill-posed Problems, 11*, 343−370.

Beck, M. S., & Plaskowski, A. (1987). *Cross correlation flowmeters − their design and application*. Bristol: Adam Hilger.

Bieberle, M., Barthel, F., & Hampel, U. (2012). Ultrafast X-ray computed tomography for the analysis of gas-solid fluidized beds. *Chemical Engineering Journal, 189−190*, 355−363.

Bieberle, M., Fischer, F., Schleicher, E., Koch, D., Menz, H.-J., Mayer, H.-G., et al. (2009). Experimental two-phase flow measurement using ultra fast limited-angle-type electron beam X-ray computed tomography. *Experiments in Fluids, 47*, 369−378.

Bieberle, A., Hoppe, D., Schleicher, E., & Hampel, U. (2011). Void measurement using high-resolution gamma-ray computed tomography. *Nuclear Engineering and Design, 241*, 2086−2092.

Bieberle, A., Schleicher, E., & Hampel, U. (2007). Data acquisition system for angle synchronized gamma-ray tomography of rapidly rotating objects. *Measurement Science and Technology, 18*, 3384−3390.

Bolton, G. T., Hooper, C. W., Mann, R., & Stitt, E. H. (2004). Flow distribution and velocity measurement in a radial flow fixed bed reactor using electrical resistance tomography. *Chemical Engineering Science, 59*, 1989−1997.

Braun, H., & Hauck, A. (1991). Tomographic reconstruction of vector fields. *IEEE Transactions on Signal Processing, 39*, 464−471.

Calvetti, D., & Somersalo, E. (2007). *An introduction to Bayesian scientific computing − ten lectures on subjective computing*. Springer.

Candes, E. J., & Wakin, M. B. (2008). An introduction to compressive sampling. *IEEE Signal Processing Magazine, 25*, 21−30.

Cheng, K. S., Isaacson, D., Newell, J. C., & Gisser, D. G. (1989). Electrode models for electric current computed tomography. *IEEE Transactions on Biomedical Engineering, 36*, 918−924.

Daidzic, N., Schmidt, E., Hasan, M., & Altobelli, S. (2005). Gas-liquid phase distribution and void fraction measurements using MRI. *Nuclear Engineering and Design, 235*, 1163−1178.

Dechsiri, C., Van der Zwan, E. A., Dehling, H. G., & Hoffmann, A. C. (2005). Dispersion of particle pulses in fluidized beds measured by positron emission tomography. *AIChE Journal, 51*, 791−801.

Devanathan, N., Dudukovic, M. P., Lapin, A., & L'ubbert, A. (1995). Chaotic flow in bubble column reactors. *Chemical Engineering Science, 50*, 2661−2667.

Doucet, A., de Freitas, J. F. G., & Gordon, N. J. (2001). *Sequential Monte Carlo methods in practice*. Springer Verlag.

Duncan, S., Kaipio, J. P., Ruuskanen, A. R., Malinen, M., & Seppänen, A. (2005). Control systems. In D. M. Scott & H. McCann (Eds.), *Process imaging for automatic control*. Taylor & Francis Group: CRC Press.

Durbin, J., & Koopman, S. J. (2001). *Time series analysis by state space methods*. Oxford University Press.

Dyakowski, T. (1996). Process tomography applied to multi-phase flow measurement. *Measurement Science and Technology, 7*, 343−353.

Dyakowski, T., Jeanmeure, L. F. C., & Jaworski, A. J. (2000). Applications of electrical tomography for gas-solids and liquid-solids flows − a review. *Powder Technology, 112*, 174−192.

Elkins, C. J., & Alley, M. T. (2007). Magnetic resonance velocimetry: applications of magnetic resonance imaging in the measurement of fluid motion. *Experiments in Fluids, 43*, 823−858.

Elkins, C. J., Markl, M., Pelc, N., & Eaton, J. K. (2003). 4D magnetic resonance velocimetry for mean velocity measurements in complex turbulent flows. *Experiments in Fluids, 34*, 494−503.

Elsinga, G. E., Scarano, F., Wieneke, B., & Oudheusden, B. W. (2006). Tomographic particle image velocimetry. *Experiments in Fluids, 41*, 933−947.

Etuke, E. O., & Bonnecaze, R. T. (1998). Measurement of angular velocities using electrical impedance tomography. *Flow Measurement and Instrumentation, 9*, 159−169.

Evensen, G. (2007). *Data assimilation − the ensemble Kalman filter*. Springer.

Fischer, F., & Hampel, U. (2010). Ultra fast electron beam X-ray computed tomography for two-phase flow measurements. *Nuclear Engineering and Design, 240*, 2254−2259.

George, D. L., Torczynski, J. R., Shollenberger, K. A., O'Hern, T. J., & Ceccio, S. L. (2000). Validation of electrical-impedance tomography for measurements of material distribution in two-phase flows. *International Journal of Multiphase Flow, 26.4*, 549−581.

Gladden, L. F., Akpa, B. S., Anadon, L. D., Heras, J. J., Holl, D. J., Mantle, M. D., et al. (2006). Dynamic MR imaging of single- and two-phase flows. *Chemical Engineering Research and Design, 84*, 272−281.

Green, R. G., Rahmat, M. F., Dutton, K., Evans, K., Goude, A., & Henry, M. (1997). Velocity and mass flow rate profiles of dry powders in a gravity drop conveyor using an electrodynamic tomography system. *Measurement Science and Technology, 8*, 429.

Grudzien, K., Niedostatkiewicz, M., Adrien, J., Tejchman, J., & Maire, E. (2011). Quantitative estimation of volume changes of granular materials during silo flow using X-ray. *Chemical Engineering and Processing, 50*, 59−67.

Hampel, U., Hristov, H. V., Bieberle, A., & Zippe, C. (2007). Application of high-resolution gamma ray tomography to the measurement of gas hold-up distributions in a stirred chemical reactor. *Flow Measurement and Instrumentation, 18*, 184−190.

Heindela, T. J., Grayb, J. N., & Jensenb, T. C. (2008). An X-ray system for visualizing fluid flows. *Flow Measurement and Instrumentation, 19*, 67−78.

Heino, J., Somersalo, E., & Kaipio, J. P. (2005). Compensation for geometric mismodelling by anisotropies in optical tomography. *Optics Express, 13*, 296−308.

Henningsson, M., Ã−stergren, K., & Dejmek, P. (2006). Plug flow of yoghurt in piping as determined by cross-correlated dual-plane electrical resistance tomography. *Journal of Food Engineering, 76*, 163−168.

Holland, D. J., Malioutov, D. M., Blake, A., Sederman, A. J., & Gladden, L. F. (2010). Reducing data acquisition times in phase-encoded velocity imaging using compressed sensing. *Journal of Magnetic Resonance, 203*, 236−246.

Hori, K., Fujimoto, T., & Kawanishi, K. (1998). Development of ultra-fast X-ray computed tomography scanner system. *IEEE Transactions on Nuclear Science, 45*, 2089−2094.

Huttunen, J. M. J., & Kaipio, J. P. (2007). Approximation error analysis in non-linear state estimation with an application to state-space identification. *Inverse Problems, 23*, 2141−2157.

Huttunen, J. M. J., & Kaipio, J. P. (2009). Model reduction in state identification problems with an application to determination of thermal parameters. *Applied Numerical Mathematics, 59*, 877−890.

Huttunen, J. M. J., Kaipio, J. P., & Somersalo, E. (2007). Approximation errors in nonstationary inverse problems. *Inverse Problems and Imaging, 1*, 77−93.

Huttunen, J. M. J., & Pikkarainen, H. K. (2007). Discretization error in dynamical inverse problems: one-dimensional model case. *Journal of Inverse and Ill-posed Problems, 15*, 365−386.

Ijaz, U. Z., Kim, J.-H., Khambampati, A. K., Kim, M.-C., Kim, S., & Kim, K.-Y. (2007). Concentration distribution estimation of fluid through electrical impedance tomography based on interacting multiple model scheme. *Flow Measurement and Instrumentation, 18*, 47−56.

Ismail, I., Gamio, J. C., Bukhari, S. F. A., & Yang, W. Q. (2005). Tomography for multi-phase flow measurement in the oil industry. *Flow Measurement and Instrumentation, 16*, 145−155.

Janzen, A., Steube, J., Aferka, S., Kenig, E., Crine, M., Marchot, P., et al. (2013). Investigation of liquid flow morphology inside a structured packing using X-ray tomography. *Chemical Engineering Science, 12*, 451−460.

Jin, B. (2008). Fast Bayesian approach for parameter estimation. *International Journal for Numerical Methods in Engineering, 76*, 230−252.

Johansen, G. A., Hampel, U., & Hjertaker, B. T. (2010). Flow imaging by high speed transmission tomography. *Applied Radiation and Isotopes, 68*, 518−524.

Johansen, G. A., Hjertaker, B. T., Froystein, T., & Olsen, O. (1996). A dual sensor flow imaging tomographic system. *Measurement Science and Technology, 6*, 297−307.

Jolliffe, I. T. (2002). *Principal component analysis*. Springer-Verlag.

Julier, S. J., & Uhlmann, J. K. (1997). A new extension of the Kalman filter to nonlinear systems. *International Symposium on Aerospace/Defense Sensing, Simulation and Controls, 3*, 26.

Kai, T., Misawa, M., Takahashi, T., Tiseanu, I., Ichikawa, N., & Takada, N. (2000). Application of fast X-ray CT scanner to visualization of bubbles in fluidized bed. *Journal of Chemical Engineering of Japan, 33*, 906−909.

Kaipio, J. P., Duncan, S., Seppanen, A., Somersalo, E., & Voutilainen, A. (2005). State estimation. In D. M. Scott & H. McCann (Eds.), *Process imaging for automatic control*. Taylor & Francis Group: CRC Press.

Kaipio, J. P., & Kolehmainen, V. (2013). Approximate marginalization over modeling errors and uncertainties in inverse problems. In P. Damien, N. Poslon, & D. Stepehns (Eds.), *Bayesian theory and applications*. Oxford University Press.

Kaipio, J. P., & Somersalo, E. (1999). Nonstationary inverse problems and state estimation. *Journal of Inverse and Ill-Posed Problems, 7*, 273−282.

Kaipio, J. P., & Somersalo, E. (2004). *Statistical and computational inverse problems*. New York: Springer.

Kaipio, J. P., & Somersalo, E. (2007). Statistical inverse problems: discretization, model reduction and inverse crimes. *Journal of Computational and Applied Mathematics, 198*, 493−504.

Kalman, R. E. (1960). A new approach to linear filtering and prediction problems. *Transactions of the ASME − Journal of Basic Engineering, 82D*, 35−45.

Kennedy, M. C., & O'Hagan, A. (2003). Bayesian calibration of computer models. *Journal of the Royal Statistical Society: Series B, 63*, 425−464.

Kolehmainen, V., Tarvainen, T., Arridge, S. R., & Kaipio, J. P. (2011). Marginalization of uninteresting distributed parameters in inverse problems - application to diffuse optical tomography. *International Journal for Uncertainty Quantification, 1*, 1−17.

Kolehmainen, V., Voutilainen, A., & Kaipio, J. P. (2001). Estimation of nonstationary region boundaries in EIT - state estimation approach. *Inverse Problems, 17*, 1937−1956.

Kourunen, J., Käyhkö, R., Matula, J., Käyhkö, J., Vauhkonen, M., & Heikkinen, L. M. (2008). Imaging of mixing of two miscible liquids using electrical impedance tomography and linear impedance sensor. *Flow Measurement and Instrumentation, 19*, 391−396.

Kumar, S. B., Moslemian, D., & Dudukovic, M. P. (1995). A Î^{3}-ray tomographic scanner for imaging voidage distribution in two-phase flow systems. *Flow Measurement and Instrumentation, 6*, 61−73.

Leeungculsatien, T., & Lucas, G. P. (2013). Measurement of velocity profiles in multiphase flow using a multielectrode electromagnetic flow meter. *Flow Measurement and Instrumentation, 31*, 86−95.

Lehikoinen, A., Finsterle, S., Voutilainen, A., Heikkinen, L. M., Vauhkonen, M., & Kaipio, J. P. (2007). Approximation errors and truncation of computational domains with application to geophysical tomography. *Inverse Problems and Imaging, 1*, 371−389.

Lehikoinen, A., Finsterle, S., Voutilainen, A., Kowalsky, M. B., & Kaipio, J. P. (2009). Dynamical estimation of geophysical ERT data: state estimation in the vadoze zone. *Inverse Problems in Science and Engineering, 17*, 715−736.

Lehikoinen, A., Huttunen, J. M. J., Finsterle, S., Kowalsky, M. B., & Kaipio, J. P. (2010). Dynamic inversion for hydrological process monitoring under model uncertainties. *Water Resources Research, 46*, W04513.

Lieberman, C., Willcox, K., & Ghattas, O. (2010). Parameter and state model reduction for large-scale statistical inverse problems. *SIAM Journal on Scientific Computing, 32*, 2523−2542.

Lipponen, A., Seppänen, A., & Kaipio, J. P. (2010a). Nonstationary inversion of convection-diffusion problems − recovery from unknown nonstationary velocity fields. *Inverse Problems and Imaging, 4*, 463−483.

Lipponen, A., Seppänen, A., & Kaipio, J. P. (2010b). Reduced-order estimation of nonstationary flows with electrical impedance tomography. *Inverse Problems, 26*, 074010.

Lipponen, A., Seppänen, A., & Kaipio, J. P. (2011). Nonstationary approximation error approach to imaging of three-dimensional pipe flow: experimental evaluation. *Measurement Science and Technology, 22*, 104013.

Lipponen, A., Seppänen, A., & Kaipio, J. P. (2013). Electrical impedance tomography imaging with reduced-order model based on proper orthogonal decomposition. *Journal of Electronic Imaging, 22*, 023008.

Liu, S., Chen, Q., Wang, H. G., Jiang, F., Ismail, I., & Yang, W. Q. (2005). Electrical capacitance tomography for gas-solids flow measurement for circulating fluidized beds. *Flow Measurement and Instrumentation, 16*, 135−144.

Lucas, G. P., Cory, J., Waterfall, R. C., Loh, W. W., & Dickin, F. J. (1999). Measurement of the solids volume fraction and velocity distribution in solids-liquid flows using dual-plane electrical resistance tomography. *Flow Measurement and Instrumentation, 10*, 249−258.

Lucas, G., & Leeungculsatien, T. (2010). A new method of measuring velocity profiles using a multielectrode electromagnetic flow meter. In *6th World Congress on industrial process tomography, 6−9 September 2010, Beihang University, China* (pp. 1016−1025).

Maad, R., & Johansen, G. A. (2008). Experimental analysis of high-speed gamma-ray tomography performance. *Measurement Science and Technology, 19*, 085502.

Mantle, M. D., Sederman, A. J., & Gladden, L. F. (2001). Single- and two-phase flow in fixed-bed reactors: MRI flow visualisation and lattice-Boltzmann simulations. *Chemical Engineering Science, 56*, 523−529.

Misawa, M., Tiseanu, I., Prasser, H.-M., & Ichikawa, N. (2003). Ultra-fast X-ray tomography for multi-phase flow interface dynamic studies. *Kerntechnik, 68*, 85−89.

Mori, N., Suzuki, T., & Kakuno, S. (2007). Noise of acoustic doppler velocimeter data in bubbly flows. *Journal of Engineering Mechanics, 133*, 122−125.

Morton, E. J., Luggar, R. D., Key, M. J., Kundu, A., Tgvora, L. M. N., & Gilboy, W. B. (1999). Development of a high speed X-ray tomography system for multiphase flow imaging. *IEEE Transactions on Nuclear Science, 46*, 380−384.

Mosorov, V., Sankowski, D., Mazurkiewicz, L., & Dyakowski, T. (2002). The 'best-correlated pixel' method for solid mass flow measurements using electrical capacitance tomography. *Measurement Science and Technology, 13*, 1810.

Mudde, R. F. (2011). Bubbles in a fluidized bed: a fast X-ray scanner. *AIChE Journal, 57*, 2684−2690.

Muller, C. R., Holl, D. J., Gladden, L. F., Davidson, J. F., Dennis, J. S., Hayhurst, A. N., et al. (2007). Rapid two-dimensional imaging of bubbles and slugs in a three-dimensional, gas-solid, two-phase flow system using ultrafast magnetic resonance. *Physical Review E, 75*, 020302(R).

Newling, B., Poirier, C., Rioux, J., Zhi, Y., Coristine, A., Balcom, B., et al. (2004). Velocity imaging of highly turbulent gas flow. *Physical Review Letters, 93*, 154503.

Nissinen, A., Heikkinen, L. M., & Kaipio, J. P. (2008). The Bayesian approximation error approach for electrical impedance tomography experimental results. *Measurement Science and Technology, 19*, 015501.

Nissinen, A., Heikkinen, L. M., Kolehmainen, V., & Kaipio, J. P. (2009). Compensation of errors due to discretization, domain truncation and unknown contact impedances in electrical impedance tomography. *Measurement Science and Technology, 20*, 105504.

Nissinen, A., Kolehmainen, V., & Kaipio, J. P. (2011). Compensation of modelling errors due to unknown domain boundary in electrical impedance tomography. *IEEE Transactions on Medical Imaging, 30*, 231−242.

Nocedal, J., & Wright, S. J. (1999). *Numerical optimization*. New York: Springer Verlag.

Pakzad, L., Ein-Mozaffari, F., & Chan, P. (2008). Using electrical resistance tomography and computational fluid dynamics modeling to study the formation of cavern in the mixing of pseudoplastic fluids possessing yield stress. *Chemical Engineering Science, 63*, 2508−2522.

Parker, D. J., Leadbeater, T. W., Fan, X., Hausard, M. N., Ingram, A., & Yang, Z. (2008). Positron imaging techniques for process engineering: recent developments at Birmingham. *Measurement Science and Technology, 19*, 094004.

Parker, D. J., & McNeil, P. A. (1996). Positron emission tomography for process applications. *Measurement Science and Technology, 7*, 287−296.

Raffel, M., Willert, C., Wereley, S., & Kompenhans, J. (2007). *Experimental fluid mechanics − particle image velocimetry: a practical guide*. Berlin: Springer.

Reinecke, N., Petritsch, G., Boddem, M., & Mewes, D. (1998). Tomographic imaging of the phase distribution in two-phase slug flow. *International Journal of Multiphase Flow, 24*, 617−634.

Ruuskanen, A. R., Seppänen, A., & Kaipio, J. P. (2006). Optimal actuator placement for controlling concentration profiles via process tomography. *Inverse Problems in Science and Engineering, 14*, 819−836.

Ruuskanen, A. R., Seppänen, A., Duncan, S., Somersalo, E., & Kaipio, J. P. (2006). Using process tomography as a sensor for optimal control. *Applied Numerical Mathematics, 56*, 37−54.

Saayman, J., Nicol, W., van Ommen, J. R., & Mudde, R. F. (2013). Fast X-ray tomography for the quantification of the bubbling-, turbulent- and fast fluidization-flow regimes and void structures. *Chemical Engineering Journal, 234*, 437−447.

Sankey, M. H., Holl, D. J., Sederman, A. J., & Gladden, L. F. (2009). Magnetic resonance velocity imaging of liquid and gas two-phase flow in packed beds. *Journal of Magnetic Resonance, 196*, 142−148.

Sederman, A. J., Johns, M. L., Alexer, P., & Gladden, L. F. (1998). Structure-flow correlations in packed beds. *Chemical Engineering Science, 53*, 2117−2128.

Sederman, A. J., Mantle, M. D., Buckley, C., & Gladden, L. F. (2004). MRI technique for measurement of velocity vectors, acceleration, and autocorrelation functions in turbulent flow. *Journal of Magnetic Resonance, 166*, 182−189.

Seppänen, A., Heikkinen, L., Savolainen, T., Voutilainen, A., Somersalo, E., & Kaipio, J. P. (2007). An experimental evaluation of state estimation with fluid dynamical models in process tomography. *Chemical Engineering Journal, 127*, 23−30.

Seppänen, A., Peltola, A., Heikkinen, L., Kourunen, J., & Kaipio, J. P. (2007). State estimation in process tomography − experimental study in 3D multi-phase flow case. In *Proceedings of the 5th World Congress on industrial process tomography, Bergen, Norway*.

Seppänen, A., Vauhkonen, M., Somersalo, E., & Kaipio, J. P. (2001). State space models in process tomography − approximation of state noise covariance. *Inverse Problems in Science and Engineering, 9*, 561−585.

Seppänen, A., Vauhkonen, M., Vauhkonen, P. J., Somersalo, E., & Kaipio, J. P. (2001a). State estimation with fluid dynamical evolution models in process tomography − an application to impedance tomography. *Inverse Problems, 17*, 467−483.

Seppänen, A., Vauhkonen, M., Vauhkonen, P., Somersalo, E., & Kaipio, J. P. (2001b). Fluid dynamical models and state estimation in process tomography: effect due to inaccuracies in flow fields. *Journal of Electronic Imaging, 10*, 630−640.

Seppanen, A., Vauhkonen, M., Vauhkonen, P. J., Voutilainen, A., & Kaipio, J. P. (2008). State estimation in process tomography − three-dimensional impedance imaging of moving fluids. *International Journal for Numerical Methods in Engineering, 73*, 1651−1670.

Seppänen, A., Voutilainen, A., & Kaipio, J. P. (2009). State estimation in process tomography — reconstruction of velocity fields using EIT. *Inverse Problems, 25*, 085009.

Shibata, T., Shinohara, S., Ikeda, H., Yoshida, H., Sawaki, T., & Sumi, M. (1996). Laser speckle velocimeter using self-mixing laser diode. *IEEE Transactions on Instrumentation and Measurement, 45*, 499—503.

Shumway, R. H. (1988). *Applied statistical time series analysis*. Prentice-Hall.

Somersalo, E., Cheney, M., & Isaacson, D. (1992). Existence and uniqueness for electrode models for electric current computed tomography. *SIAM Journal on Applied Mathematics, 52*, 1023—1040.

Stanley, S. J. (2006). Tomographic imaging during reactive precipitation in a stirred vessel: mixing with chemical reaction. *Chemical Engineering Science, 61*, 7850—7863.

Stefani, F., & Gerbeth, G. (2000). A contactless method for velocity reconstruction in electrically conducting fluids. *Measurement Science and Technology, 11*, 758—765.

Stefani, F., Gudrum, T., & Gerbeth, G. (2004). Contactless inductive flow tomography. *Physical Review E, 70*, 056306.

Takai, N., Iwai, T., & Asakura, T. (1980). Real-time velocity measurement for a diffuse object using zero-crossings of laser speckle. *Journal of the Optical Society of America, 70*, 450—455.

Tarantola, A. (2004). *Inverse problem theory and methods for model parameter estimation*. Philadelphia: SIAM.

Tayler, A. B., Holl, D. J., Sederman, A. J., & Gladden, L. F. (2010). Exploring the origins of turbulence in multiphase flow using compressed sensing MRI. *Physical Review Letters, 108*, 264505.

Tayler, A. B., Holl, D. J., Sederman, A. J., & Gladden, L. F. (2012). Applications of ultra-fast MRI to high voidage bubbly flow: measurement of bubble size distributions, interfacial area and hydrodynamics. *Chemical Engineering Science, 71*, 468—483.

Tossavainen, O.-P., Vauhkonen, M., & Kolehmainen, V. (2007). A three-dimensional shape estimation approach for tracking of phase interfaces in sedimentation processes using electrical impedance tomography. *Measurement Science and Technology, 18*, 1413.

Tossavainen, O.-P., Vauhkonen, M., Kolehmainen, V., & Kim, K. Y. (2006). Tracking of moving interfaces in sedimentation processes using electrical impedance tomography. *Chemical Engineering Science, 61*, 7717—7729.

Toye, D., Crine, M., & Marchot, P. (2005). Imaging of liquid distribution in reactive distillation packings with a new high-energy X-ray tomograph. *Measurement Science and Technology, 16*, 2213—2220.

Vauhkonen, M., Karjalainen, P. A., & Kaipio, J. P. (1998). A Kalman filter approach to track fast impedance changes in electrical impedance tomography. *IEEE Transactions on Biomedical Engineering, 45*, 486—493.

Vauhkonen, P. J., Vauhkonen, M., & Kaipio, J. P. (2001). Fixed-lag smoothing and state estimation in dynamic electrical impedance tomography. *International Journal for Numerical Methods in Engineering, 50*, 2195—2209.

Vauhkonen, P. J., Vauhkonen, M., Savolainen, T., & Kaipio, J. P. (1999). Three-dimensional electrical impedance tomography based on the complete electrode model. *IEEE Transactions on Biomedical Engineering, 46*, 1150—1160.

Vilar, G., Williams, R. A., Wang, M., & Tweedie, R. J. (2008). On line analysis of structure of dispersions in an oscillatory baffled reactor using electrical impedance tomography. *Chemical Engineering Journal, 141*, 58—66.

Voutilainen, A., & Kaipio, J. P. (2009). Model reduction and pollution source identification from remote sensing data. *Inverse Problems and Imaging, 3*, 711—730.

Voutilainen, A., Pyhälahti, T., Kallio, K. Y., Pulliainen, J., Haario, H., & Kaipio, J. P. (2007). A filtering approach for estimating lake water quality from remote sensing data. *International Journal of Applied Earth Observations and Geoinformation, 9*, 50−64.

Vrugt, J. A., Robinson, B. A., & Vesselinov, V. V. (2005). Improved inverse modeling for flow and transport in subsurface media: combined parameter and state estimation. *Geophysical Research Letters, 32*, L18408.

Vrugt, J. A., Diks, C. G. H., Gupta, H. V., Bouten, W., & Verstraten, J. M. (2005). Improved treatment of uncertainty in hydrologic modeling: combining the strengths of global optimization and data assimilation. *Water Resources Research, 41*.

Wang, M. (2005). Impedance mapping of particulate multiphase flows. *Flow Measurement and Instrumentation, 16*, 183−189.

Williams, R. A. (1995). Tomographic imaging for modelling and control of mineral processes. *Chemical Engineering Journal, 59*, 71−85.

Williams, R. A., & Beck, M. S. (1995). *Process tomography: principles, techniques and applications*. Oxford: Butterworth-Heinemann.

Williamson, C. H. K. (1996). Vortex dynamics in the cylinder wake. *Annual Review of Fluid Mechanics, 28*, 477−539.

Wondrak, T., Eckert, S., Gerbeth, G., Klotsche, K., Stefani, F., Timmel, K., et al. (2011). Combined electromagnetic tomography for determining two-phase flow characteristics in the submerged entry nozzle and in the mold of a continuous casting model. *Metallurgical and Materials Transactions B, 42*, 1201−1210.

Wondrak, T., Galindo, V., Gerbeth, G., Gundrum, T., Stefani, F., & Timmel, K. (2010). Contactless inductive flow tomography for a model of continuous steel casting. *Measurement Science and Technology, 21*, 045042.

Wu, C., Cheng, Y., Ding, Y., Wei, F., & Jin, Y. (2007). A novel X-ray computed tomography method for fast measurement of multiphase flow. *Chemical Engineering Science, 62*, 4325−4335.

Wu, B., Orta, A., & Kantzas, A. (2011). Experimental flow measurements of a spout bed using pressure transducer and X-ray CT scanner. *International Journal of Chemical Reactor Engineering, 9*, A32.

York, T. A., Davidson, J. L., Mazurkiewich, L., Mann, R., & Grieve, B. D. (2005). Towards process tomography for monitoring pressure filtration. *IEEE Sensors Journal, 5*, 139−152.

Applications of tomography in oil-gas industry – Part 1

22

C.-G. Xie
Singapore Well Testing Centre (SWTC), Schlumberger Oilfield (S) Pte Ltd, Singapore; Schlumberger Gould Research Centre, Cambridge, UK; Schlumberger Oilfield PetroTechnical Services, Richmond, CA, USA

22.1 Introduction

Applications of tomography in the upstream oil-gas industry are widespread, covering from kilometre reservoir-scale, sub-metre borehole scale, to sub-mm rock-core pore scale. This chapter illustrates the use of different seismic tomography modalities in hydrocarbon exploration, reservoir monitoring and production monitoring.

In Section 22.1, the range of physical parameters of reservoir rocks and fluids that can be explored by different tomographic-sensing methods, such as seismic velocity, resistivity (conductivity) and density, will be introduced.

The basic principle of seismic (traveltime) tomography and depth imaging, widely used for hydrocarbon exploration, is briefly described in Section 22.2.

The potential of multicomponent time-lapse (space-time four-dimensional) seismic surveys in monitoring reservoir changes during production and some typical enhanced oil recovery (EOR) processes is then discussed in Sections 22.3 and 22.4.

In Section 22.5, various borehole seismic imaging techniques are introduced. Some application examples of time-lapse cross-borehole seismic imaging for reservoir EOR monitoring are given.

In Section 22.6, we will make some remarks of the future trend of seismic tomography imaging in oil-gas industry.

22.2 Seismic tomography in hydrocarbon exploration and reservoir characterization

A petroleum reservoir is a subsurface body of rock having sufficient porosity and permeability to store and transmit fluids. Sedimentary rocks are the most common reservoir rocks because they have more porosity than most igneous and metamorphic rocks. A reservoir is a critical component of a complete petroleum system. Subsurface rocks containing hydrocarbon oil and/or gas and connate waters are composed of grains, pores and cementing materials. Porosity (the percentage of pore volume or void space) provides the fluids storage capacity of the rock. Permeability is a rock's

Industrial Tomography. http://dx.doi.org/10.1016/B978-1-78242-118-4.00022-8
Copyright © 2015 Elsevier Ltd. All rights reserved.

ability to transmit fluids, typically measured in darcies or millidarcies (mD). Porosity and permeability influence a reservoir's ability to accumulate and produce hydrocarbons. A petroleum trap is a configuration of rocks suitable for containing hydrocarbons and is sealed by a relatively impermeable formation (a barrier) through which hydrocarbons will not migrate laterally or upward, allowing oil-gas to accumulate. A trap is an essential component of a petroleum system, and may be a structural trap (in deformed strata such as folds and faults, Figure 22.1) or a stratigraphic trap (in areas where rock types change, such as unconformities, pinch-outs and reefs).

Various geophysical exploration techniques have been used in the upstream oil-gas industry to help identify petroleum reservoir prospects and plan drilling operations, such as the gravity method and the seismic method. The gravity method measures local gravity-field differences due to variations in density (ρ) in the subsurface; the effects of such density variations are very small ($\sim 0.1-1$ part per million) compared with those of the earth's (global) gravity field (Seidel & Lindner, 2007, p. 185). A gravity survey may be used to detect, for example, lithological and structural changes and fractures in consolidated rock, or lithology in unconsolidated rock. However, the use of the measurements from the gravity (potential) field alone, due to the principle of equivalence, cannot yield unique information about the depth, size and/or density of a subsurface gravity anomaly. An integrated geophysical survey including additional data (such as seismic velocity data) can reduce the ambiguity when interpreting gravity survey data.

In the quest to find hydrocarbon resources, electromagnetic surveys are also used to identify subsurface features by electrical resistivity contrast. Near-surface (shallow) electromagnetic surveys may be conducted by deploying an inductive loop at the earth's surface (Dawoud, Hallinan, Hermann, & van Kleef, 2009). Two different deep-reading EM technologies, magnetotelluric (MT) and controlled-source electromagnetic (CSEM), provide distinctly different insights into the earth subsurface that

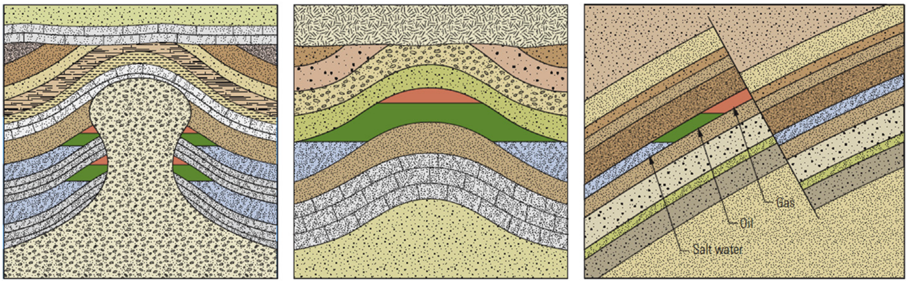

Figure 22.1 Structural traps. The weight of overlying sediments causes salt layers to plastically deform, creating diapirs. As diapirs evolve, sediments onlap their margins, forming traps that typically accommodate hydrocarbons (left). Where the strata have deformed to form an anticline (centre), oil (green) and gas (red) may become trapped under a seal. Faulting may also trap hydrocarbons (right) by sealing the undip margin of a reservoir.
From Barriol, Y., Glaser, K.S., Pop, J., Bartman, B., Corbiell, R., Eriksen, K.O., et al. (Autumn 2005). The pressure of drilling and production. Oilfield Review, 17(3), 22–41. Graphic copyright Schlumberger. Used with permission.

are complementary to seismic data. The MT fields generated by passive (atmospheric, plane-wave vertically incident) sources are sensitive to large (basin-scale) conductive features and are used to detect structure and lithology, such as large salt, basalt and carbonate bodies due to their contrasts with the conductive surroundings (Brady et al., 2009). The complex electrical impedance (Z) of the subsurface formation (hence the bulk formation resistivity ρ_a) can be obtained by taking the ratio of the horizontal electric field in one direction (E_x) to the horizontal magnetic field in orthogonal direction (H_y), i.e. $Z = E_x/H_y = (i \cdot \rho_a \cdot \omega\mu)^{1/2}$ (where ω is the angular frequency, μ the magnetic permeability). Recent interest in MT measurements has focused on evaluation of marine or subsea environments, driven by the increasing cost of deep-water drilling and the complexity of imaging below salt and basalt.

However, the attenuation of the MT fields with depth makes them insensitive to resistivity contrasts of thin reservoir formations. The marine CSEM method imposes an appropriate EM signal from a transmitter source comprising a long horizontal dipole, making it more sensitive in detecting resistivity layers (possibly hydrocarbon-bearing formations) against a conductive background (water-bearing formations). The same receivers can be used for both CSEM and MT measurements. The typical frequency range of the CSEM signal is between 0.05 and 5 Hz; the effective upper limit for marine MT is 1 Hz. Major obstacles to marine MT and CSEM surveys are the high cost and the low data collection efficiency. Seismic measurements covering large three-dimensional areas can be performed efficiently by deploying vessel-towed multiple receiving streamers and source array (Brady et al., 2009).

The seismic exploration industry was revolutionized in the early 1990s by the transition of imaging from two to three dimensions, from time to depth, and from poststack to prestack. The industry replaced interactive normal moveout (NMO) velocity analysis with efficient methods that can meet the new challenges in large data volume and in growing spatial resolution expectations. (In Section 22.2.3, the meanings of poststack, prestack and NMO will be described.) By the late 1990s, the industry was implementing ray-based, prestack depth migration tomography methods to perform full migration velocity analysis (Woodward, Nichols, Zdraveva, Whitfield, & Johns, 2008). Over the last decade, ray-based postmigration grid tomography has become the standard model-building tool for seismic depth imaging. The problems it can solve have become bigger, driven by seismic exploration demands and enabled by 1000-fold increases in computing power. The three main areas of change are (Woodward et al., 2008):

- Standard model spatial resolution has improved 10-fold, from a few thousand meters to a few hundred meters. This has been attributed to high-quality multiple-parameter residual-moveout data picked as densely as 25—50 m vertically and horizontally, and to a strategy of working down from long-wavelength to short-wavelength solutions.
- More seismic data sets are being acquired along multiple azimuths for improved illumination and suppression of multiples. In order to prevent short-wavelength velocity heterogeneity from being mistaken for azimuthal anisotropy, high-resolution velocity tomography must solve for all azimuths simultaneously.
- Models have shifted from largely isotropic to largely anisotropic, both vertical transverse isotropic (VTI) and TTI (tilted TI). With four-component data, anisotropic grid tomography can be used to build models that tie PZ and PS images in depth (see Section 22.3).

22.2.1 Basics of seismic waves

The basic principle of all seismic methods is the controlled generation of elastic waves by a seismic source to obtain an image of the subsurface properties. Surface and/or borehole seismic energy sources (e.g. explosives, vibrators, airguns) produce the following type of strain-energy wave pulses that propagate in solids and fluids (Schuck & Lange, 2007, p. 337):

- Body wave that travels in all directions, and
- surface wave that travels along/near the surface (usually considered a source of noise). (Dispersion of surface waves has been used to solve for near-surface velocity variations, Bagaini, Bunting, El-Emam, Laake, & Strobbia, 2010; Strobbia et al., 2009.)

There are two types of body waves:

- *P*-waves (primary, longitudinal or compressional waves) with particle motion parallel to the direction of propagation, and
- *S*-waves (secondary, shear or transverse waves) with particle motion perpendicular to the direction of propagation (and referred to as *SV*-waves and *SH*-waves with particle motion in the vertical plane and in the horizontal plane, respectively).

In marine seismic surveys, hydrophones are often used to record pressure (stress) P directly. In a medium of density ρ and compressibility (or bulk modulus) κ, the following wave equation can be derived based on the theory of elastic continua, which relates deformation (strain) and stress (Chapman, 2004, p. 104):

$$\frac{\nabla^2 P}{\partial t^2} = \kappa\nabla\cdot\left(\frac{1}{\rho}\,\nabla P\right) - \kappa\nabla\cdot\left(\frac{1}{\rho}\mathbf{F}\right). \tag{22.1}$$

For a medium of constant density, the above is reduced to

$$\frac{\nabla^2 P}{\partial t^2} = c^2\nabla^2 P - c^2\nabla\cdot\mathbf{F}, \tag{22.2}$$

where the acoustic wave velocity c is defined by

$$c = \sqrt{\kappa/\rho} \tag{22.3}$$

The source is modelled as a force distribution $\mathbf{F}$ (e.g. representing an underwater airgun explosion ‘equivalent force’, Chapman, 2004, p. 104). Outside the source region $F = 0$, Eqn (22.2) is reduced to the Helmholtz wave equation. For a wave of harmonic time dependence of the form $P(\mathbf{r}, t) = P(\mathbf{r}, \omega)\, e^{-\mathrm{i}\omega t}$, the frequency-domain solution for homogeneous media is

$$c^2\nabla^2 P + \omega^2 P = 0. \tag{22.4}$$

The general solution is of the form $g(|\mathbf{r}| - ct)$. A special wave is the harmonic wave where g is a sine, cosine or more generally:

$$P(\mathbf{r}, t) = P(\mathbf{k}, \omega) e^{i(\mathbf{k} \cdot \mathbf{r} - \omega t)}, \tag{22.5}$$

where $P(\mathbf{k}, \omega)$ is the amplitude of the harmonic wave; the wavenumber vector **k** in the direction of wave propagation and angular frequency ω are related by the dispersion relationship $|\mathbf{k}| = \omega/c$. A more general wave shape can be formed by summing up individual harmonic waves in a Fourier series. For a system of homogeneous layers, the homogeneous solution can still be applied within each layer. Ray approximation can be used to predict wave propagation in smoothly varying inhomogeneous media (Nolet, 2008, p. 20).

For a homogeneous isotropic elastic medium of very small deformations, according to Hooke's law, strain (change of volume and shape) is proportional to stress (force per unit area). For anisotropic media, a general elastic tensor containing up to 21 independent elastic constants is used to describe the relations between stress and strain. In Table 22.1, these elastic constants are listed versus each other, *P*- and *S*-wave velocities (V_p and V_s), and bulk density ρ. For the simplest case of seismic wave propagation in an isotropic medium, there exist only two elastic constants, Lamé's constant λ (lambda constant) and μ (shear modulus); the wave equation solution results in two different velocities $V_p = \sqrt{(\lambda + 2\mu)/\rho}$ and $V_s = \sqrt{\mu/\rho}$ (Nolet, 2008, p. 28). Because fluids do not support shear stress, *S*-waves cannot propagate in fluids. The velocities of seismic waves are the most fundamental attributes in the seismic method (obviously $V_s < V_p$); they vary with lithology, mineral content (Table 22.2), porosity, pore fluid saturation and degree of compaction.

As an illustrative example of the dependence of velocity on lithology, we consider shaly sandstones and shales, which are a major component of sedimentary basins and of prime relevance to oil reservoirs. Experimental studies of 80 saturated shaly sandstone samples (at confining pressure 40 MPa and pore pressure 1 MPa) have found that both *P*-wave velocity (V_p) and *S*-wave velocity (V_s) decrease with increasing porosity (ϕ). A clay volumetric content term (C_{clay}) is also needed in order to fit the experimental data (Nur, 1987, p. 205):

$$V_p(\text{km/s}) = 5.59 - 6.93\phi - 2.18C_{\text{clay}},$$

$$V_s(\text{km/s}) = 3.52 - 4.91\phi - 1.89C_{\text{clay}}.$$

The velocity ratio V_p/V_s is a useful seismic attribute in the determination of rock properties. For water-saturated shaly sandstones, the increase of V_p/V_s with increasing porosity and/or increasing clay content was found by least-square regression (Nur, 1987, p. 207):

$$V_p/V_s = 1.55 + 0.56\phi + 0.43C_{\text{clay}}.$$

Table 22.1 **Relationships between elastic constants, *P*- and *S*-wave velocities, and bulk density ρ for isotropic media**

		λ, μ	κ, μ	E, σ	V_p^2, V_s^2
Lamé's constant	λ	λ	$\kappa - \frac{2}{3}\mu$	$\frac{E\sigma}{(1+\sigma)(1-2\sigma)}$	$\rho(V_p^2 - 2V_s^2)$
Shear modulus	μ	μ	μ	$\frac{E}{2(1+\sigma)}$	ρV_s^2
Bulk modulus	κ	$\lambda + \frac{2}{3}\mu$	κ	$\frac{E}{3(1-2\sigma)}$	$\rho\left(V_p^2 - \frac{4}{3}V_s^2\right)$
Young's modulus	E	$\mu\left(\frac{3\lambda+2\mu}{\lambda+\mu}\right)$	$\frac{9\kappa\mu}{3\kappa+\mu}$	E	$\rho V_p^2\left(\frac{3V_p^2-4V_s^2}{V_p^2-V_s^2}\right)$
Poisson's ratio	σ	$\frac{\lambda}{2(\lambda+\mu)}$	$\frac{3\kappa-2\mu}{6\kappa+2\mu}$	σ	$\frac{\frac{V_p^2}{V_s^2}-2}{2\frac{V_p^2}{V_s^2}-2}$
P-wave velocity	V_p^2	$\frac{\lambda+2\mu}{\rho}$	$\frac{\kappa+\frac{4}{3}\mu}{\rho}$	$\frac{E(1-\sigma)}{\rho(1+\sigma)(1-2\sigma)}$	V_p^2
S-wave velocity	V_s^2	$\frac{\mu}{\rho}$	$\frac{\mu}{\rho}$	$\frac{E}{2\rho(1+\sigma)}$	V_s^2
P- to *S*-wave velocity ratio	$\left(\frac{V_p}{V_s}\right)^2$	$\frac{\lambda+2\mu}{\mu}$	$\frac{\kappa+\frac{4}{3}\mu}{\mu}$	$\frac{2(1-\sigma)}{1-2\sigma}$	$\left(\frac{V_p}{V_s}\right)^2$

Adapted from Table 4.6-1 of Schuck, A., & Lange, G. (2007). Seismic methods. In J. Knodel, Lange G., & Voigt H.-J. (Eds.), Environmental geology – handbook of field methods and case studies, (p. 344). Berlin: Springer, with kind permission from Springer Science + Business Media.

Table 22.2 **Typical densities and resistivities of selected sedimentary, metamorphic and igneous rocks, and fluids**

	Density ρ (g/cm^3)	Resistivity (Ω m)	P-wave velocity V_p (m/s)	S-wave velocity V_s (m/s)
Sediments				
Fine sand, dry	1.5 (1.3–1.7)	$>10^4$	100–600	100–500 (sand)
Fine sand, wet	1.8 (1.7–2.0)	50 (water saturated)	200–2000; 1300–1800 (saturated); 1740 (fine)	
Medium sand	1.7 (1.5–2.0)		1835 (coarse)	
Gravel, dry	1.7 (1.7–2.0)	$>10^4$	180–1250; 750–1250 (wet)	
Gravel, wet	2.0 (1.8–2.3)	50 (water saturated)		
Silt	1.7 (1.2–2.0)	20–50		
Clay, dry	1.7 (1.3–1.8)	>1000	500–2800	110–1500 (clay)
Clay, wet	1.9 (1.7–2.2)	5–30		
Sandstone	2.35 (1.6–2.7);	<50 (wet, jointed); $>10^5$ (compact)	800–4500	320–2700
Loose	1.80–2.40;		1500–2500	575–1101
Compacted	2.22–2.69		1800–4300	672–1023
Siliceous			2200–2400	
Limestone	2.55 (1.9–2.8)	100 (wet, jointed); $>10^5$ (compact)	2000–6250	1800–3800
Dolomite	1.75–2.88		2000–6250	2900–3740
Gypsum	2.31–2.33		1500–4600	750–2760
Anhydrite	2.15–2.44		4500–6500	750–3600
Halite (rock salt)	2.2 (2.1–2.6)	30 (wet); $>10^6$ (compact)	4500–6500	2250–3300

Continued

Table 22.2 Continued

	Density ρ (g/cm^3)	Resistivity (Ω m)	*P*-wave velocity V_p (m/s)	*S*-wave velocity V_s (m/s)
Metamorphic and igneous rocks				
Granite	2.65 (2.5–2.7)	<100 (weathered, wet); $>10^6$ (compact)	4500–6000[a]	2500–3300[a]
Granodiorite	2.7 (2.6–2.7)	-ditto-		
Basalt	3.1	-ditto-	5000–6000[a]	2800–3400[a]
Gneiss	2.7 (2.6–2.8)	-ditto-	4400–5200[a]	2700–3200[a]
Fluids				
Air (gas)	1.29×10^{-3}		310–340	
Water	0.98–1.01	10–300	1430–1590	
Sea water	1.02	0.25	1400–1600	
Brine	Up to ∼1.2	<0.15	1400–1600	
Petroleum	0.92–1.07	$>10^5$	1035–1370	

[a] https://pangea.stanford.edu/courses/gp262/Notes/8.SeismicVelocity.pdf (accessed 6 August 2013).

Adapted from Table 4.2-1 of Seidel, K., & Lindner, H. (2007), Gravity methods, In J. Knodel, Lange G., & Voigt H.-J. (Eds.), Environmental geology – handbook of field methods and case studies, (p. 188). Berlin: Springer; Table 4.3-2 of Seidel, K., & Lange, G. (2007). Direct current resistivity methods, In J. Knodel, Lange G., & Voigt H.-J. (Eds.), Environmental geology – handbook of field methods and case studies, (p. 213). Berlin: Springer; Table 4.6-2 of Schuck, A., & Lange, G. (2007). Seismic methods. In J. Knodel, Lange G., & Voigt H.-J. (Eds.), Environmental geology – handbook of field methods and case studies (p. 346). Berlin: Springer. With kind permission from Springer Science + Business Media.

Sandstones with high clay content have velocity ratios and Poisson's ratios similar to those of carbonate rocks. The combined use of velocity and velocity ratio may provide discrimination of lithology.

Seismic waves are reflected, refracted or diffracted at subsurface boundaries between layers of different properties. Reflection seismology is the most important method to prospect for oil and gas at great depths. The recording of seismic waves returning from the subsurface to surface and/or borehole receivers (e.g. geophones, hydrophones) and subsequent processing allow inference of structures and lithological composition of the subsurface. With measurements of traveltimes and amplitude attenuations of seismic waves, velocities of subsurface layers can be determined and a geological model of the subsurface reservoir can be constructed.

For a planar wave incident normal to a reflecting interface, the contrast in acoustic impedance (ρV) across the interface is expressed as the reflection coefficient or reflectivity R:

$$R = (\rho_2 V_2 - \rho_1 V_1)/(\rho_2 V_2 + \rho_1 V_1). \tag{22.6}$$

The corresponding transmission coefficient T is

$$T = 1 - R = 2\rho_1 V_1/(\rho_2 V_2 + \rho_1 V_1). \tag{22.7}$$

In general, incidence angle-dependent reflection and transmission coefficients for elastic plane waves at a horizontal boundary are given by the Zoeppritz equations (see references in Schuck & Lange, 2007, p. 349). The angle of the reflected and transmitted wave at oblique incidence can be easily obtained from Snell's law:

$$p = \sin(i_\alpha)/V_\alpha = \text{constant}, \tag{22.8}$$

where p is the ray parameter (slowness), i_α the angle of the incident, reflected or transmitted ray and V_α is the P- or S-wave velocity of the wave-propagating medium. The transmitted wave is refracted with a change in its propagation direction if there is a velocity contrast at the interface; the reflection and refraction angles are independent of bulk density.

For the case of P-wave propagation shown in Figure 22.2, four waves will be generated: reflected P-wave and SV-wave, transmitted (refracted) P-wave and SV-wave. The angles of reflected and refracted rays can be calculated as follows by using Snell's law:

$$\sin\left(i_{p1}\right)/V_{p1} = \sin\left(i_{p2}\right)/V_{p2} = \sin\left(i_{s1}\right)/V_{s1} = \sin\left(i_{s2}\right)/V_{s2} = p = \text{constant}$$

The above calculations are applicable only to planar and relatively large interfaces, and are not valid for regions around faults or fracture zones if the scale of such a structure is equal to or less than the wavelength ($= 2\pi V/\omega$); at such interfaces, the wave energy will be diffracted instead (as a secondary spherical source according to

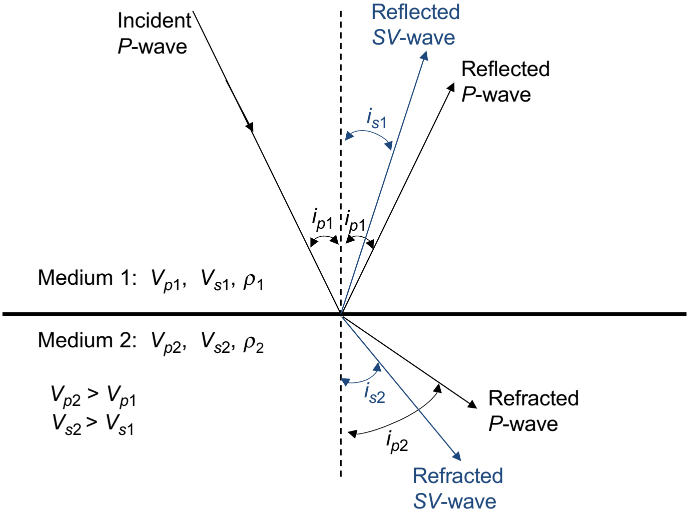
Incident
P-wave
Reflected
SV-wave
Reflected
P-wave
i_{s1}
i_{p1}
i_{p1}
Medium 1: V_{p1}, V_{s1}, ρ_1
Medium 2: V_{p2}, V_{s2}, ρ_2
$V_{p2} > V_{p1}$
$V_{s2} > V_{s1}$
i_{s2}
i_{p2}
Refracted
P-wave
Refracted
SV-wave

Figure 22.2 Reflection, refraction and mode conversion of a *P*-wave incident at a planar interface between Medium 1 and Medium 2 with different *P*- and *S*-wave velocities V_p and V_s (and bulk densities ρ).

Huygens' principle). Since the reflected, refracted and diffracted waves interfere with each other, identifying diffracted waves on seismic record may be a challenge (Wielandt, 1987).

22.2.2 Traveltime tomography

In Eqn (22.8), the (horizontal) slowness $p = \mathrm{d}T/\mathrm{d}X$ (measured in s/m) is known as the ray parameter. At an extended interface with a discontinuity in seismic velocity V, the slowness remains constant, implying a jump in incidence angle i by refraction. The horizontal distance X travelled by a ray with slowness p is (Nolet, 2008, pp. 22,23):

$$\begin{aligned} X(p) &= \int \mathrm{d}x = \int \tan i \, \mathrm{d}z = \int \sin i \Big/ \sqrt{1 - (\sin i)^2} \, \mathrm{d}z \\ &= \int V \cdot p \Big/ \sqrt{1 - V^2 p^2} \, \mathrm{d}z, \end{aligned} \tag{22.9}$$

and the corresponding traveltime is

$$T(p) = \int \mathrm{d}t = \int V^{-1} \mathrm{d}s = \int V^{-1} \Big/ \sqrt{1 - V^2 p^2} \, \mathrm{d}z \tag{22.10}$$

For a general three-dimensional geological model, the traveltime for a ray is a function of the velocity profile $V(\mathbf{r})$ and the ray path trajectory S. For a number of seismic sources ($j = 1, \ldots, M$) placed at the surface, the classical problem of 'traveltime tomography' is to derive the velocity model $V(\mathbf{r})$ of the interior of the earth from a number of traveltimes measured by a number of receivers ($i = 1,\ldots, N$) at the surface (Nolet, 1987, p. 9):

$$T_{i,j} = \int_{S_{i,j}} V^{-1}(\mathbf{r})\, \mathrm{d}s \quad i = 1,\ldots,N; \quad j = 1,\ldots,M. \tag{22.11}$$

If there are a sufficient number of ray paths, analytic solutions to $V(\mathbf{r})$ are available (Chapman, 1987). In general this is not the case and more general numerical methods have to be used (Nolet, 1987).

To solve a traveltime tomography problem numerically, the image domain can be partitioned into pixels with the slowness p specified pixel-wise. The resulting matrix-equation is

$$\mathbf{t} = \mathbf{S}\,\mathbf{p} \tag{22.12}$$

where $\mathbf{t}$ is the traveltime vector for each ray path, $\mathbf{p}$ the slowness vector for each pixel, and $\mathbf{S}$ the ray path matrix with S_{ij} = arc length of segment of ray path i in pixel j.

Traveltime tomography can be obtained by solving Eqn (22.12) using, for example, simultaneous iterative reconstructive technique (SIRT) (van der Sluis & van der Vorst, 1987), with ray path information obtained from ray tracing (with Snell's law obeyed at interfaces) through the current estimate of the seismic-velocity field (Červeny, 1987).

The intrinsic amplitude attenuation when a wave propagates through a rock medium can be expressed in terms of effective Q, defined as the integration of the Q effects along the propagation ray path S. If the amplitude attenuation varies linearly with frequency f and if Q effects are frequency independent, the log ratio between a propagated signal of amplitude A and the reference A_o may be approximated as (Cavalca & Fletcher, 2008)

$$\ln(A/A_o) = -\pi f \int_S Q^{-1}(S)\, V^{-1}(S)\, \mathrm{d}s = -\pi f\, T/Q_{\mathrm{eff}} + c \tag{22.13}$$

where T is the propagating-wave traveltime; c captures remaining elastic effects such as geometrical spreading or transmission losses and is assumed frequency independent.

For attenuated traveltime tomography, an equivalent absorption coefficient α can be deduced from Eqn (22.13) as

$$\alpha = -\pi f/(QV) \tag{22.14}$$

Equation (22.13) can then be rewritten in the following discretized form for a varying α:

$$-\ln(A_i/A_o) = \sum_j \alpha_j S_{ij} \tag{22.15}$$

A_i is the measured amplitude after traversing ray path i, α_j the absorption coefficient in pixel j, and S_{ij} the length of ray path i within pixel j. Leggett, Goulty, and Kragh (1993) applied an appropriate correction to the amplitude A_i in Eqn (22.15) to account for the effects of directivity, geometric spreading and elastic transmission losses (source–receiver coupling factors).

Traveltimes or amplitudes of propagating waves can be inverted to obtain a distribution of seismic velocity V or absorption coefficient α of the surveyed domain (Tarantola, 1987). For example, in Leggett et al. (1993), the resulting attenuated traveltime tomography locates the waterflood zone in a simulated EOR process. Time-lapse 'cross-well' seismic amplitude tomography showed the flood zone as a region of higher absorption. Amplitude absorption tomograms are found to complement velocity tomograms in imaging heterogeneous reservoirs because absorption and velocity respond differently to changes in liquid or gas saturations in reservoir rocks.

22.2.3 Seismic depth imaging: stacking and migration

In structurally complex reservoirs, especially where faulting and salt intrusions necessitate complicated seismic-velocity models, conventional (travel) time-domain processing gives misleading results. Seismic depth imaging reveals the true location and shape of subsurface structures and hence improves the success rates of oil-gas companies in challenging exploration and reservoir-delineation projects (Albertin et al., 2002).

Similar to time-domain imaging, depth imaging consists of two main processing aspects: stacking and migration. *Stacking* increases the signal-to-noise ratio (SNR) by summing records obtained from several seismic shots reflecting at the same point (Figure 22.3). Traces from several source–receiver pairs, centred on a common midpoint (CMP, at the same reflection point but with different offsets), are gathered together. The shape of the two-way traveltimes (T_x) plotted against the offset (X) defines a hyperbola (Dutta, 2002):

$$(T_x)^2 = (T_0)^2 + (X/V)^2, \tag{22.16}$$

where T_0 is the time at zero offset ($X = 0$), the normal-incidence reflection time, V the (stacking) velocity of the layer.

The variation of reflected wave traveltime with offset due to an oblique wave path, in comparison with the normal-incidence trace, is called normal moveout (NMO). So from Eqn (22.16):

$$\mathrm{NMO} = T_x - T_0 = \sqrt{(T_0)^2 + (X/V)^2} - T_0 \tag{22.17}$$

For any sample in a trace in the CMP gather, T_0 and the offset X are known. If V is also known, NMO can be calculated for each trace, and the reflections can be shifted backward in time (from recorded time T_x to T_0 at zero offset) and then stacked

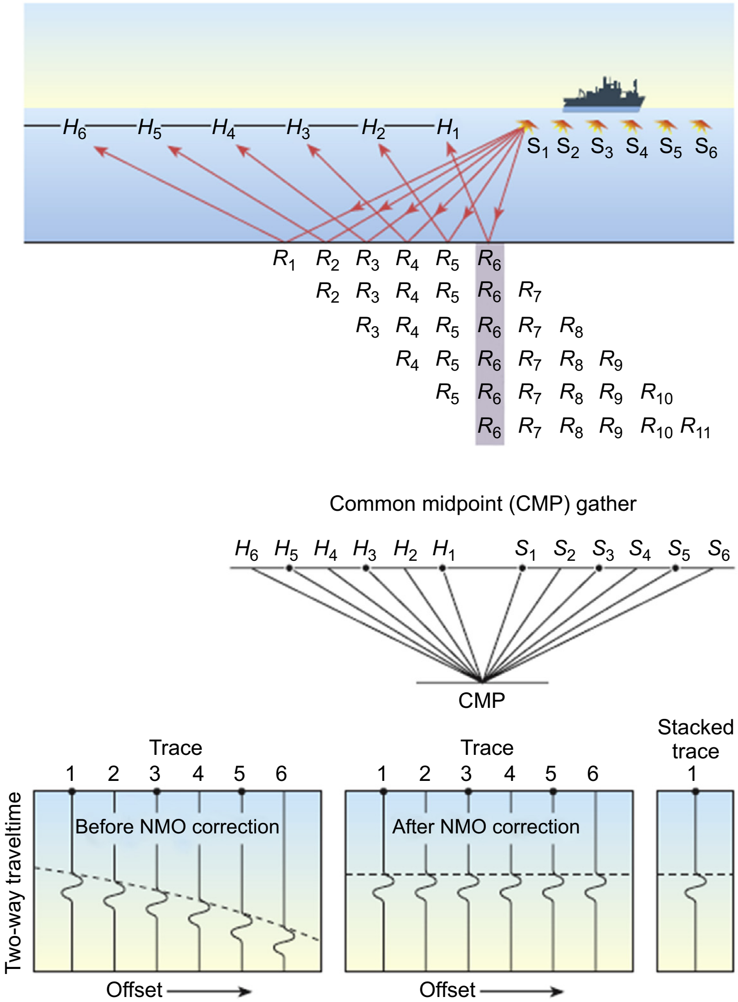
H6 H5 H4 H3 H2 H1
S1 S2 S3 S4 S5 S6
R1 R2 R3 R4 R5 R6
R2 R3 R4 R5 R6 R7
R3 R4 R5 R6 R7 R8
R4 R5 R6 R7 R8 R9
R5 R6 R7 R8 R9 R10
R6 R7 R8 R9 R10 R11
Common midpoint (CMP) gather
H6 H5 H4 H3 H2 H1 S1 S2 S3 S4 S5 S6
CMP
Trace
1 2 3 4 5 6
Before NMO correction
Trace
1 2 3 4 5 6
After NMO correction
Stacked trace
1
Two-way traveltime
Offset
Offset

Figure 22.3 Stacking basics. Stacking enhances signal and reduces noise by adding several traces together. In this example, a marine seismic vessel acquires traces at many offsets from every source (top). *S* numbers represent sources, *R* numbers represent reflection points, and *H* numbers represent hydrophones. Stacking first gathers traces from all available source–receiver offsets that reflect at a common midpoint (CMP) (middle). Because arrivals from longer offsets have traveled farther, a time correction, called normal moveout (NMO) correction, is applied to each gather to flatten the arrivals (bottom left). The flattened traces are averaged (bottom right) to produce one stacked trace that represents the normal-incidence (zero-offset) trace, with improved signal-to-noise ratio.
From Barclay, F., Bruun, A., Rasmussen, K. B., Alfaro, J. C., Cooke, A., Cooke, D., et al. (Spring 2008). Seismic inversion: reading between the lines. Oilfield Review. 20(1), 42–63. Graphic copyright Schlumberger. Used with permission.

(summed) across the gather to form a single enhanced trace with an improved SNR (by a factor of $\sqrt{n}$ if n traces are stacked). In stacking, the trace amplitude is increased (by a factor of n if n traces are summed).

The velocity V in Eqn (22.17) is initially unknown; a process can be used to find the particular velocity value (called the stacking velocity V_{stack}) that makes the best NMO correction for each reflection and stacks the reflection to maximum amplitude. An approximation of the NMO is as follows (Ashcroft, 2011; Dutta, 2002, p. 44):

$$\mathrm{NMO} \approx X^2 \Big/ \left(2V_{\mathrm{stack}}^2\, T_0\right). \tag{22.18}$$

For flat-lying strata comprising m layers, stacking velocity at short range (called V_{NMO}) is a good approximation to the root-mean-square velocity V_{rms}:

$$V_{\mathrm{rms}} = \sqrt{\sum\left(V_i^2 t_i\right) \Big/ \sum\left(t_i\right)}, \quad (i = 1, \ldots \mathrm{m}) \tag{22.19}$$

with the ith layer interval time and interval velocity being:

$$t_i = (T_{i+1} - T_i)/2,$$

$$V_i = 2(D_i - D_{i-1})/(T_i - T_{i-1}),$$

where D_i is the depth of the ith layer from the surface.

Importantly, V_{rms} can be used to derive the desired interval velocity V_i from the following Dix equation (Ashcroft, 2011; Dutta, 2002, p. 42):

$$V_i = \sqrt{\left(V_2^2 T_2 - V_1^2 T_1\right)/(T_2 - T_1)}, \tag{22.20}$$

where V_1, T_1, V_2 and T_2 are the V_{rms} and TWT (two-way time) values for the reflections at the top and the bottom of a layer. For strata that are not flat, the Dix velocity of Eqn (22.20) may be used to establish a rough velocity structure of an area with moderate dips.

Once the interval velocity is obtained, it is straightforward to calculate the layer thicknesses (and thus the depths and average velocities) for key reflections in the seismic section. From CMP stacking, usable velocities can hence be derived from the seismic data alone. The suppression of troublesome surface multiple reflections also benefits from the process of CMP stacking (Ashcroft, 2011, p. 44).

Migration, the second aspect in depth imaging, uses a velocity model to redistribute reflected seismic energy from its assumed position at the midpoint to its true position (lateral reposition of the reflection, Figure 22.4). The horizontal shift X_{m} is (Ashcroft, 2011, p. 46)

$$X_{\mathrm{m}} = \frac{1}{4} V^2 T(\mathrm{d}T/\mathrm{d}X), \tag{22.21}$$

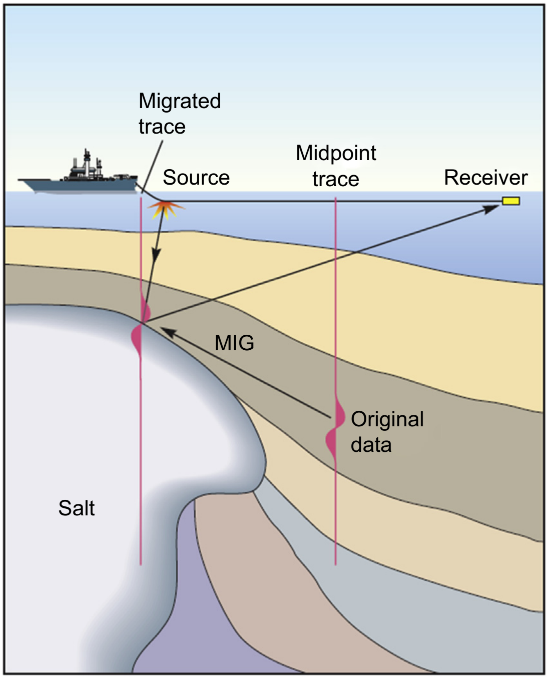

Figure 22.4 Migration of reflected seismic energy. For this simplified two-dimensional example, migration repositions the data trace from its recorded position at the source—receiver midpoint to its true position (MIG) using a velocity model. In 3D cases, reflections may be redistributed to and from positions outside the plane containing the sources and receivers. From Albertin, U., Kapoor, J., Randall, R., Smith, M., Brown, G., Soufleris, et al. (Spring 2002). The time for depth imaging. Oilfield Review, 14(1), 2—15. Graphic copyright Schlumberger. Used with permission.

where V is the velocity down to the reflector, $T = \text{TWT}$ at the CMP location and $\mathrm{d}T/\mathrm{d}X$ is the gradient of the reflection at the CMP location (on the unmigrated time section). It can be observed that lateral shift is much bigger for deep reflections (at greater T and V^2).

Migration can be performed by solutions to elastic wave propagation equations (Ashcroft, 2011, p. 48), in time or in depth, and either before or after stacking (Figure 22.5). Time migration can be used to solve certain imaging problems, but more complex ones need depth migration. Time migration is applicable to most sedimentary basins worldwide, where the seismic velocity increases with traveltime (depth) and varies gradually horizontally. For a velocity model having large horizontal or vertical contrasts, depth migration is applied when steeply dipping faults, folds or intrusions juxtapose layers with significantly different elastic properties (Albertin et al., 2002).

Stacking reduces the number of processed traces typically by an order of magnitude; migration-applied poststacking is much faster than applied prestacking.

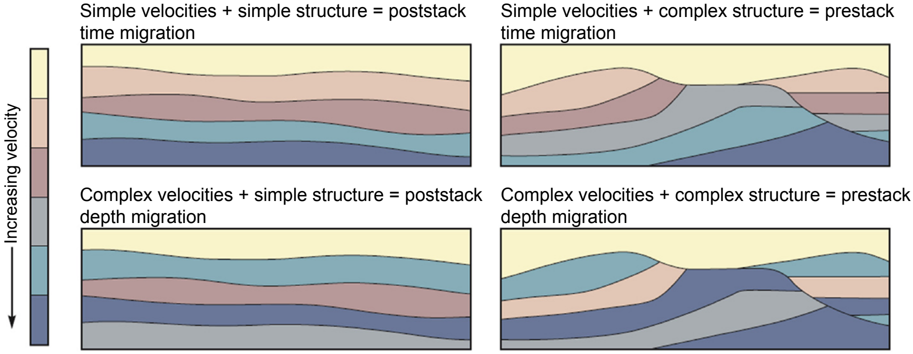
Simple velocities + simple structure = poststack time migration
Simple velocities + complex structure = prestack time migration
Complex velocities + simple structure = poststack depth migration
Complex velocities + complex structure = prestack depth migration
Increasing velocity

Figure 22.5 Simple and complex seismic velocity models (with two-way traveltime TWT as vertical axis) and structures treated by four seismic migration classes — time (top), depth (bottom), prestack (right) and poststack (left). For time migration, the velocity model may have smooth variations, but only with depth, and only monotonically increasing with depth. Depth migration is required for more complex velocity models, such as those with lateral variation or decreases of velocity with depth. Poststack migration works with models with low structure complexity. Prestack can handle the most complex models.
From Albertin, U., Kapoor, J., Randall, R., Smith, M., Brown, G., Soufleris, et al. (Spring 2002). The time for depth imaging. Oilfield Review, 14(1), 2—15. Graphic copyright Schlumberger. Used with permission.

Prestack migration requires fewer assumptions than poststack in the variations in the lithology and fluid content over the span of the gathered traces; prestack migration is hence used to handle complex structures and velocity fields, thanks to high-performance computing (Vesnaver, 2008).

The data processing workflow for prestack depth migration (such as for subsalt depth imaging) is a complex interplay of several steps. Building the velocity model itself requires iterations of prestack depth migration to define the velocity and the geometric boundaries of each layer (Albertin et al., 2002). The key step of updating the velocity model is mostly based on *tomographic* inversion that uses traveltime information derived from seismic data to refine velocity models (Dutta, 2002). Classical reflection tomography uses the differences between the predicted and observed reflection traveltimes. Ray tracing is used to predict the arrival times of reflections on CMP gathers at control points. On each gather, the actual arrival time of the shallowest reflector is compared with the predicted arrival times, and the velocity that best flattens the actual arrival times is used to update the model. This time-consuming step derives a final velocity model that optimally satisfies the data at all control points (Albertin et al., 2002). The next step applies depth migration using the updated velocity model. The migrated traces are gathered again and arrival flatness checked. For subsalt imaging, if the preliminary time migration shows that the top of salt is smooth (or structurally simple), the velocities of the overburden can be used in a poststack depth migration to obtain an image of the top of the salt. If this image is rough (or structurally complex), prestack depth migration should be applied. After the top of the salt is interpreted from the image, the velocity model is updated by filling the volume below the salt top with a uniform salt velocity. With this new velocity model, the volume is again prestack depth migrated; the image of the bottom of the salt comes into focus (Figure 22.6) (Albertin et al., 2002).

In reality, much of the subsurface is anisotropic in some physical property, such as in elasticity, permeability or electromagnetic properties (for the effect of kerogen on the elastic anisotropy of organic-rich shales, see Sayers, 2013). Elastic anisotropy is one of the factors that can complicate the seismic-velocity model-building process, and it can be incorporated into the prestack depth-migration process. Ignoring anisotropy can lead to vertically and horizontally unfocussed and mispositioned structures. The effects of anisotropy can be seen as a non-hyperbolic shape in the arrivals from a flat reflector (Figure 22.7). Traces from long offsets arrive earlier than predicted by an isotropic velocity model as they travel longer in the faster, horizontal direction (Albertin et al., 2002).

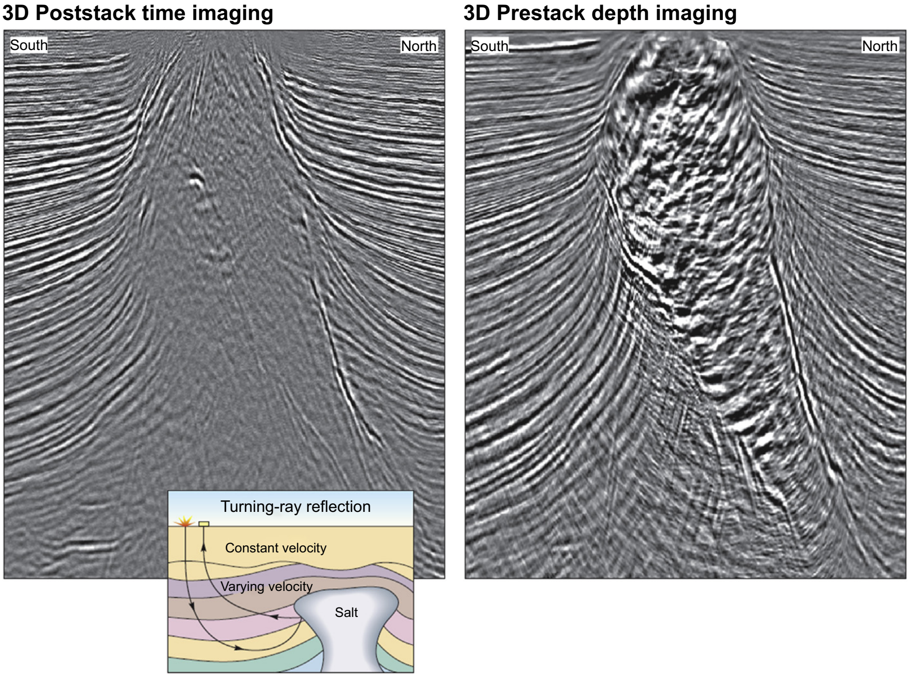

Figure 22.6 Seismic imaging under a Gulf of Mexico salt overhang with time and depth migration. Poststack time migration (left) manages to image the north side of a salt diapir, but the southern side is lost in a shadow created by an overhang. By including turning rays (inset) and rays that pass through the salt, prestack depth migration (right) images the steeply dipping layers and the overhang on the south side of the intrusion.
From Albertin, U., Kapoor, J., Randall, R., Smith, M., Brown, G., Soufleris, et al. (Spring 2002). The time for depth imaging. Oilfield Review, 14(1), 2—15. Graphic copyright Schlumberger. Used with permission.

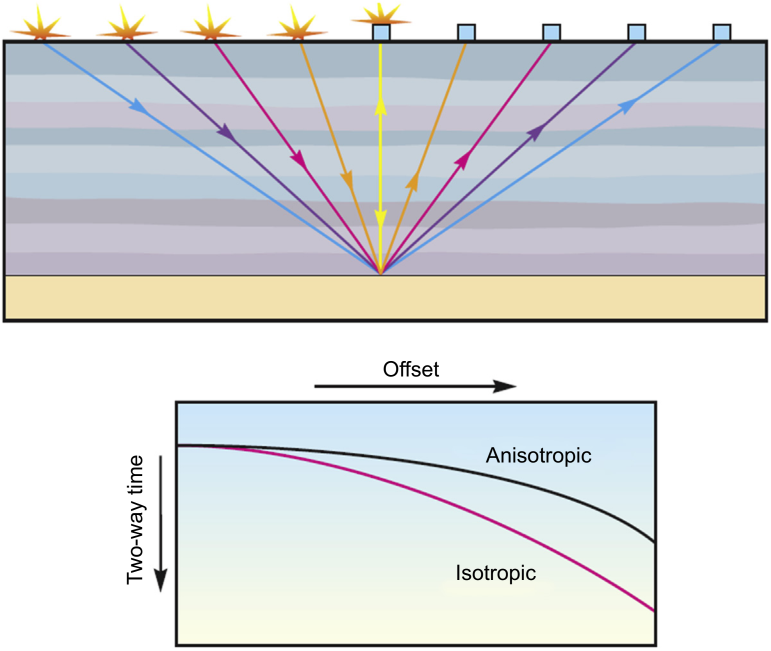

Figure 22.7 Comparison of arrival times versus offset for an isotropic layer (red curve) and an anisotropic layer (black curve).
From Albertin, U., Kapoor, J., Randall, R., Smith, M., Brown, G., Soufleris, et al. (Spring 2002). The time for depth imaging. Oilfield Review, 14(1), 2–15. Graphic copyright Schlumberger. Used with permission.

The use of *P*- and *PS* converted-wave reflection moveout for estimating vertical transverse isotropic (VTI) parameters has been reviewed by Li and Zhang (2011).

22.3 Multicomponent seismic data for reservoir characterization

In some cases, the acoustic impedance contrast at the interface between two lithologies may be too small to generate a normal-incidence reflection. For example, a shale with low density and high *P*-wave velocity might have nearly the same acoustic impedance as an oil-filled sandstone with high density and low *P*-wave velocity. Without an acoustic impedance contrast, such oil reservoirs are extremely difficult to detect using traditional *P*-wave surface seismic acquisition and processing.

Multicomponent seismic data from both *P*-waves and *S*-waves can improve reservoir characterization and reduce exploration risk (Barkved et al., 2004; Landrø & Kvam, 2002). Hydrocarbon reservoirs formed from subtle lithological changes, such as stratigraphic traps, may be delineated from changes in *P*- and *S*-wave velocities and impedances. Variations in the seismic attributes derived from multicomponent data can provide vital information about fluid type and distribution (Li & Zhang, 2011).

From Table 22.1, the velocities of *P*-waves and *S*-waves are

$$V_p = \sqrt{\left(\kappa + \frac{4}{3}\mu\right) \Big/ \rho} \tag{22.22}$$

$$V_s = \sqrt{\mu/\rho} \tag{22.23}$$

The rock density (ρ) can be expressed as a function of the porosity (ϕ), fluid and rock-matrix densities (ρ_{fluid}, ρ_{matrix}), viz,

$$\rho = \phi\, \rho_{\text{fluid}} + (1 - \phi)\, \rho_{\text{matrix}} \tag{22.24}$$

Bulk modulus (κ) is sensitive to fluid compressibility; this makes *P*-waves highly sensitive to fluid content in a rock. The dependence on both fluid compressibility and shear modulus (μ) allows *P*-waves to propagate in both solids and liquids. A shear wave is almost insensitive to fluid content in a rock; its velocity and reflectivity remain unchanged whether a rock formation contains gas, oil or water. *S*-waves can originate and propagate only in solids.

Lithology can be determined more readily from both *P*- and *S*-wave velocities (V_p, V_s) than from *P*-wave data alone. The V_p/V_s ratio, the common seismic attribute derived from multicomponent seismic data, can be used to predict rock type. Typically, different lithologies may give rise to different velocity ratios. As shown in Figure 22.8, hydrocarbon-bearing rocks are often characterized by a low-velocity ratio (Li & Zhang, 2011).

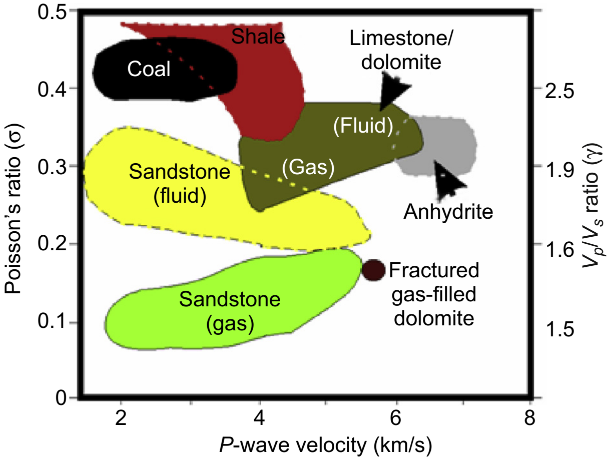

Figure 22.8 V_p/V_s ratio and lithology.
From Li, X. -Y., & Zhang, Y. -G. (2011). Seismic reservoir characterization: how can multicomponent data help? Journal of Geophysics and Engineering, 8, 128. Copyright IOP Publishing. Used with permission.

Comparison of *P*-wave with *S*-wave behaviour at a reflector can distinguish lithology changes from fluid changes: a lateral change in *P*-wave reflection amplitude along a layer boundary may indicate either a lithology change or a fluid change, but if *S*-wave reflection amplitude at the same boundary also changes, the variation is more likely due to a lithology change. Consistent *S*-wave reflectivity at the same reflector indicates a change in the fluid type is more probable (Barkved et al., 2004).

In *P*-waves, particle motion is parallel to the direction of propagation, while in *S*-waves, particle motion is perpendicular to the direction of propagation (Figure 22.9, top). In land-based surface seismic data acquisition, *P*-waves can be recorded by single-component geophones that detect vertical motion in the rock formation. In typical marine seismic surveys, *P*-waves can also be detected by towed-streamer hydrophones (or pressure sensors) surrounded by water. The field of *S*-waves is three-dimensional; therefore, three-component sensors (with three geophone-accelerometers in orthogonal orientation in each sensor) are required to fully characterize it (Figure 22.9, bottom). Processing of land multicomponent *S*-wave surveys is often problematic because inhomogeneity of near-surface layers causes large traveltime variations for the *S*-waves (Barkved et al., 2004).

Recording *S*-waves in a marine survey requires deployment of multicomponent sensors on the seafloor. It still is impractical to deploy a shear-wave source on seabed; in a multicomponent survey, the surface-source generated *P*-waves undergo partial conversion to *S*-waves at subsurface interfaces, and the resulting converted *PS*-waves (or *C*-waves) can be detected by ocean-bottom cables (OBCs) (De Freitas, 2011). These cables contain an array of four component sensors – three geophones and a hydrophone – spaced at intervals determined by the survey requirements (Figure 22.9, bottom). The geophones detect the multicomponents of *S*-wave motion; the hydrophone detects *P*-wave signals, designated as *PP* arrivals. The *P*-wave is also detected by the geophones, mainly on the vertical component, giving rise to *PZ* signals.

The combination of *P*- and *S*-waves improves development drilling. For example, in a gas-condensate field in the UK sector of the North Sea, delineating the major reservoir fault is difficult because migrated gas above the structural crest disturbs *P*-wave propagation. A *PP*-image from the conventional 3D-towed-streamer survey indicates the imaging problems typical of low-velocity gas clouds (Figure 22.10, left). Converted *PS*-waves recorded by a 3D-multicomponent survey gave a clear picture of the gas-condensate field structure (Figure 22.10 right). The clearly resolved fault on the *PS*-image made it possible to locate development wells and to guide the drilling of a good production well (Barkved et al., 2004).

In addition to the velocity ratio, *P*- and *S*-wave impedances are also commonly used seismic attributes and may be derived from *P*-wave data using prestack amplitude variation with offset (AVO) (Figure 22.11) inversion. However, the inversion can be better constrained using multicomponent data (Li & Zhang, 2011; Mathewson et al., 2012).

The AVO for a reservoir interface can be calculated theoretically. The amplitude is defined by the reflection coefficient *R* of the interface; it depends on the angle of incidence at the interface and on the contrast in the *P*-wave velocity, *S*-wave velocity and density across the interface (Figure 22.2). For angles of incidence no more than 50°,

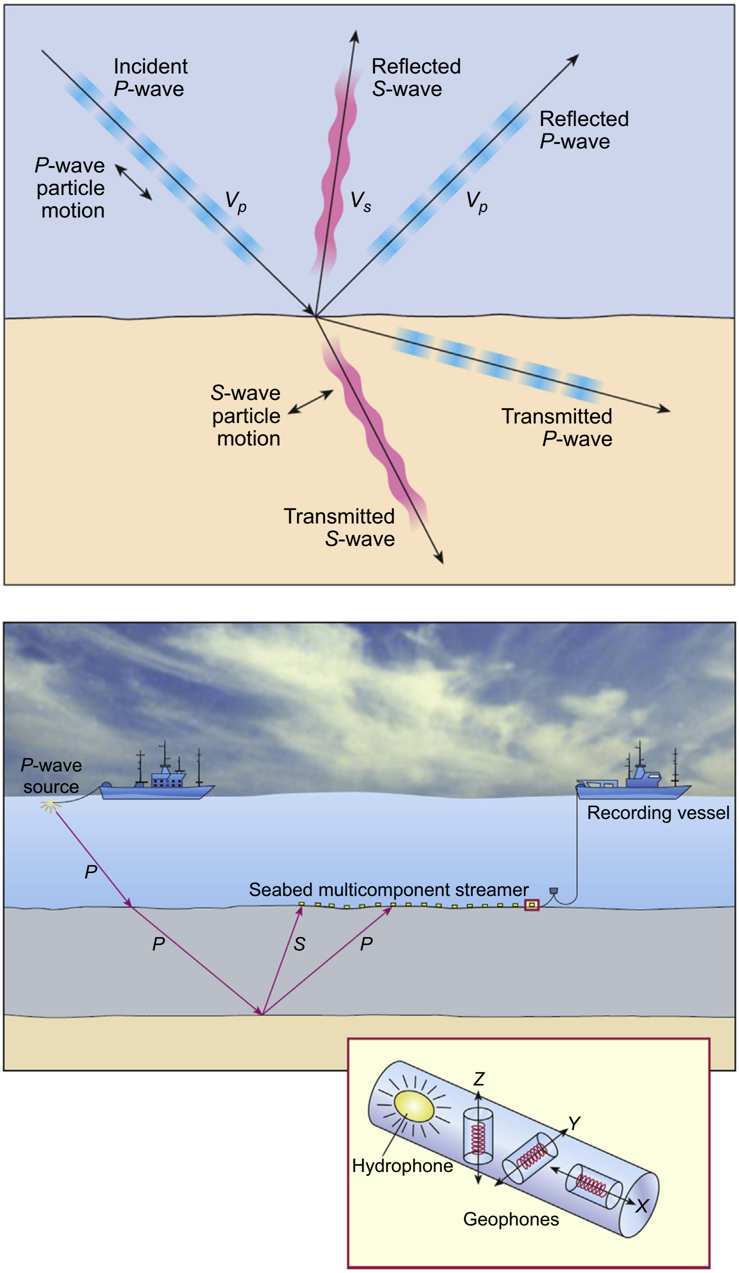
Incident
P-wave
Reflected
S-wave
Reflected
P-wave
P-wave
particle
motion
V_p
V_s
V_p
S-wave
particle
motion
Transmitted
P-wave
Transmitted
S-wave
P-wave
source
Recording vessel
P
Seabed multicomponent streamer
P
S
P
Z
Y
Hydrophone
X
Geophones

Figure 22.9 Top: Particle motion and propagation of compressional *P*-waves and shear *S*-waves. Bottom: Detecting converted waves by seabed sensors. At a subsurface interface, incident *P*-waves reflect and transmit as *P*-waves and also are partially converted to *S*-waves. Upgoing *S*-waves can be detected by seabed receivers sensitive to multiple components of motion. The four receiver components consist of one hydrophone and three orthogonally oriented geophones or accelerometers – *X*, *Y* and *Z* (inset).
From Barkved, O., Bartman, B., Compani, B., Gaiser, J., Van Dok, R., Johns, T., et al. (Summer 2004). The many facets of multicomponent seismic data. Oilfield Review, 16(2), 42–56. Graphic copyright Schlumberger. Used with permission.

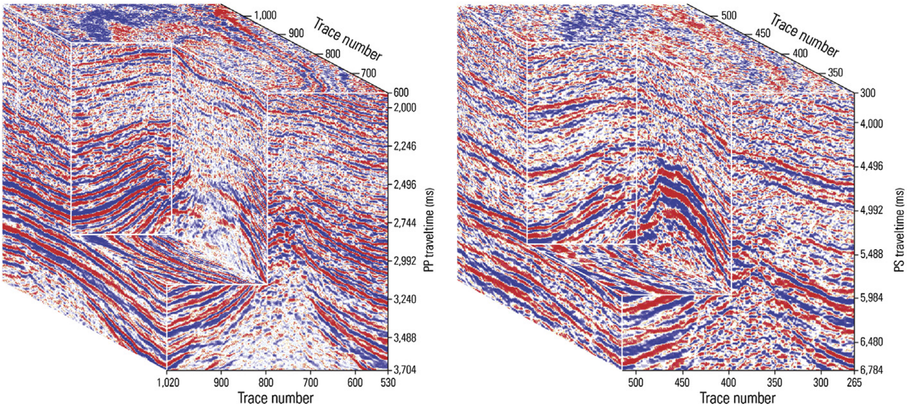

Figure 22.10 Comparison of 3D data from towed-marine survey and a seabed survey. In the *PP* image from the towed survey (left), reflections at the crest of a North Sea gas-condensate field structure are obscured by shallow (low-velocity) gas. The *PS*-converted wave image from the seabed survey (right) clearly resolves the large fault passing through the structure at its crest, and fully illuminates the structure with high-amplitude reflections.
From Barkved, O., Bartman, B., Compani, B., Gaiser, J., Van Dok, R., Johns, T., et al. (Summer 2004). The many facets of multicomponent seismic data. Oilfield Review, 16(2), 42–56. Graphic copyright Schlumberger. Used with permission.

the *PP*- and *PS*-wave reflection coefficients are derived as follows (Ashcroft, 2011, p. 131; Li & Zhang, 2011):

$$R_{pp}(\theta) \approx \frac{1+(\tan\theta)^2}{2}R_p - 4\gamma^2(\sin\theta)^2 R_s - \left(\frac{1}{2}(\tan\theta)^2 - 2\gamma^2(\sin\theta)^2\right)R_d \tag{22.25}$$

$$\begin{aligned} R_{ps}(\theta,\varphi) \approx \frac{\tan\varphi}{2\gamma}\Big[&\left(4(\sin\varphi)^2 - 4\gamma\cos\theta\cos\varphi\right)R_s \\ &- \left(1+2(\sin\varphi)^2 - 2\gamma\cos\theta\cos\varphi\right)R_d\Big] \end{aligned} \tag{22.26}$$

where:

$\theta = \frac{\theta_2+\theta_1}{2}$, average of *P*-wave angles of incidence and transmission across the interface;

$\varphi = \frac{\varphi_2+\varphi_1}{2}$, average of *S*-wave angles of reflection and transmission across the interface;

$\gamma = V_s/V_p$, velocity ratio;

$V_p = \frac{V_{p2}+V_{p1}}{2}$, $\Delta V_p = V_{p2} - V_{p1}$, *P*-wave average velocity and velocity contrast;

$V_s = \frac{V_{s2}+V_{s1}}{2}$, $\Delta V_s = V_{s2} - V_{s1}$, *S*-wave average velocity and velocity contrast;

$\rho = \frac{\rho_2+\rho_1}{2}$, $\Delta\rho = \rho_2 - \rho_1$, average density and density contrast;

$R_d = \frac{\Delta\rho}{\rho}$, density (reflection) coefficient;

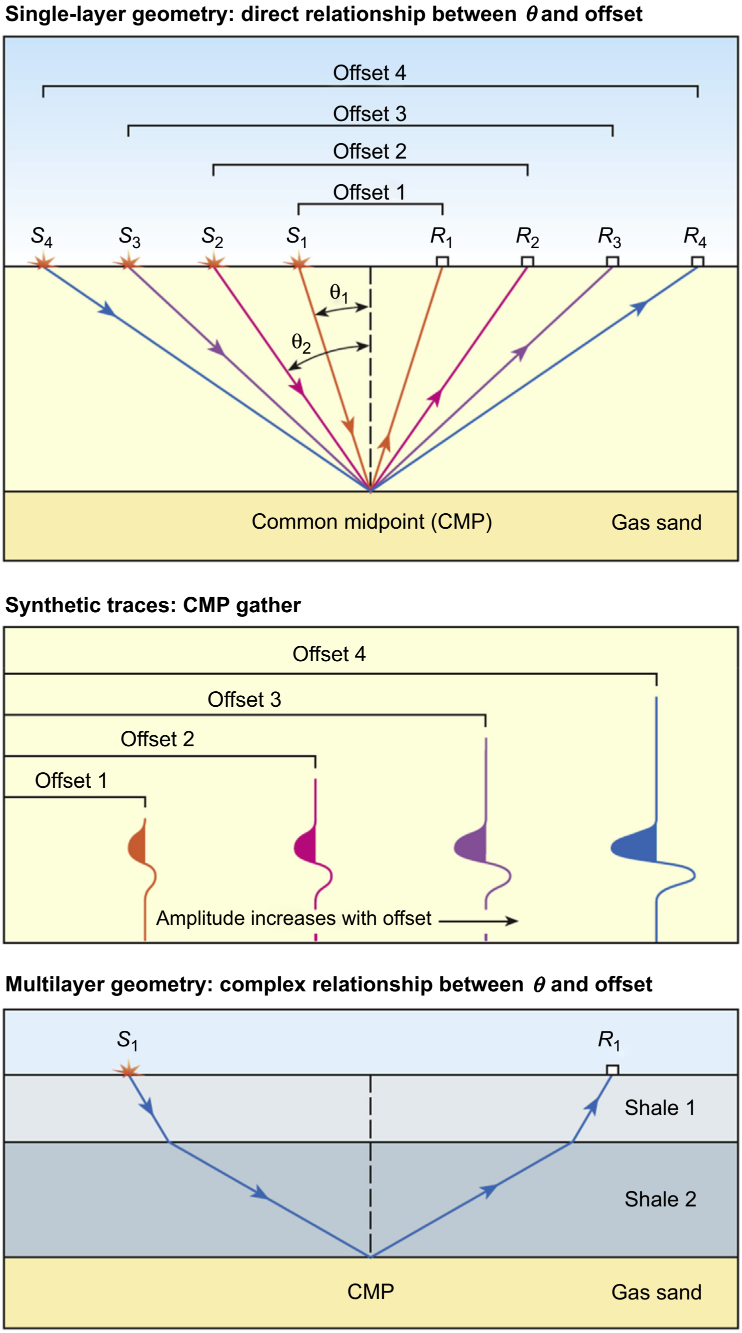
Single-layer geometry: direct relationship between θ and offset
Offset 4
Offset 3
Offset 2
Offset 1
S_4
S_3
S_2
S_1
R_1
R_2
R_3
R_4
θ_1
θ_2
Common midpoint (CMP)
Gas sand
Synthetic traces: CMP gather
Offset 4
Offset 3
Offset 2
Offset 1
Amplitude increases with offset
Multilayer geometry: complex relationship between θ and offset
S_1
R_1
Shale 1
Shale 2
CMP
Gas sand

Figure 22.11 Amplitude variation with offset (AVO). In steps similar to preparation for stacking, traces reflecting at a common midpoint are gathered and sorted by offset (top), then the arrivals are flattened using a normal moveout velocity model while preserving the amplitude information (middle). Clearly, in this case, averaging the four traces would produce a trace that does not resemble the zero-offset trace; in other words, stacking would not preserve amplitudes. The offset versus angle (θ) relationship is determined by ray tracing (bottom).
From Barclay, F., Bruun, A., Rasmussen, K. B., Alfaro, J. C., Cooke, A., Cooke, D., et al. (Spring 2008). Seismic inversion: reading between the lines, Oilfield Review, 20(1), 42−63. Graphic copyright Schlumberger. Used with permission.

$$R_p = \frac{\rho_2 V_{p2} - \rho_1 V_{p1}}{\rho_2 V_{p2} + \rho_1 V_{p1}} \approx \frac{1}{2}\left(\frac{\Delta V_p}{V_p} + \frac{\Delta\rho}{\rho}\right), \text{ P-wave normal-incidence reflection coefficient;}$$

$$R_s = \frac{\rho_2 V_{s2} - \rho_1 V_{s1}}{\rho_2 V_{s2} + \rho_1 V_{s1}} \approx \frac{1}{2}\left(\frac{\Delta V_s}{V_s} + \frac{\Delta\rho}{\rho}\right), \text{ S-wave normal-incidence reflection coefficient.}$$

From multicomponent seismic data, *PP* and *PS* reflectivities (R_{pp}, R_{ps}) are assumed to be known, and density is assumed to follow Gardner's relation ($\rho = 0.23V^{1/4}$). For a given velocity model, Eqns (22.25) and (22.26) can be used to solve the two unknowns R_p and R_s. This process is often called joint *PP*- and *PS*-wave AVO inversion. The resulting attributes can then be used directly for lithological interpretation (Li & Zhang, 2011).

Figure 22.12 demonstrates the three-parameter AVO inversion workflow applied to a case study in one area of the central North Sea (Barclay et al., 2008). An operating company intended to distinguish the clean sands from the surrounding shales by improving seismic characterization of injected reservoir sands in the Balder interval that were particularly difficult to image from the existing surface seismic data. A new marine seismic survey was designed to map the distribution and thickness of the reservoir pay zone, delineate the geometry of individual sand wings and assess reservoir connectivity. Data acquisition with the new marine seismic survey system enabled accurate streamer cable positioning, fine spatial sampling and calibration of sources and receivers. These capabilities are all important for achieving a successful inversion, facilitated by precision imaging, improved noise attenuation, increased bandwidth and preservation of amplitude and phase information.

The prestack seismic input data were divided into seven angle stacks, each containing reflections in a 7° range of incidence angles out to 49°. Three-parameter AVO inversion generated estimates of *P*- and *S*-wave reflectivities and density contrast. These data volumes were inverted for *P*- and *S*-wave impedances and density, leading to determination of rock constants such as $\mu\rho = (\rho V_s)^2$, $\lambda/\mu = (V_p/V_s)^2 - 2$ (see Table 22.1).

Log data from three wells intersecting the reservoir were analysed for correlations between *P*- and *S*-wave velocities, ρ, μ, λ, lithology and fluid saturation. For example,

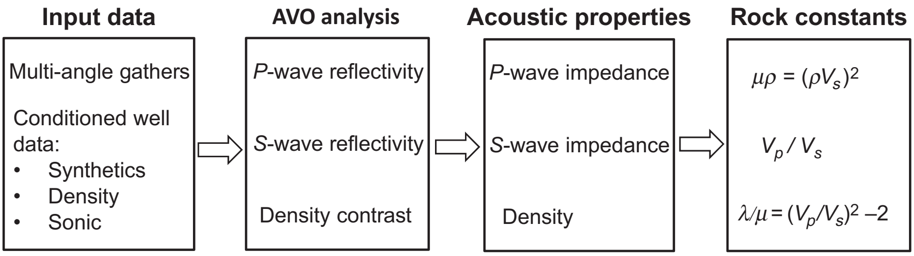

Figure 22.12 AVO inversion workflow. The input data consisted of prestack AVO gathers in e.g. 7° offset ranges, along with sonic and density well logs (left). The first step, three-parameter AVO inversion, produced estimates of *P*-wave and *S*-wave reflectivities and density contrast. These volumes were inverted for *P*-wave and *S*-wave impedances and density. The final step extracted rock properties, in the form of $\mu\rho$, V_p/V_s and λ/μ.
Adapted from Barclay, F., Bruun, A., Rasmussen, K. B., Alfaro, J. C., Cooke, A., Cooke, D., et al. (Spring 2008). Seismic inversion: reading between the lines, Oilfield Review, 20(1), 42–63.

cross-plotting V_p/V_s with the product $\mu\rho$, and colour-coding by lithology showed that high sand probability correlated with low V_p/V_s and high $\mu\rho$ values. These relationships were then applied to V_p/V_s calculated from seismic inversion to map high sand content throughout the seismic volume. This characterization of the extent and quality of the injected sand bodies helped optimize development of these complex features (Barclay et al., 2008).

In Figure 22.13, to further illustrate the value of the *PS* data from multicomponent OBC sensors, simultaneous inversion (see next Section 22.4) of the *PZ* data alone is compared with simultaneous inversion of the combined *PZ* and *PS* data sets. The acoustic impedance and density derived from the *PZ* and *PS* reflection amplitudes are much better resolved and match the well-logging values better than those calculated from *PZ* arrivals alone.

22.4 Simultaneous inversion of time-lapse seismic surveys for reservoir monitoring

Most of the examples shown so far are the results from inversion techniques based on trace-by-trace reflectivity methods. A simultaneous inversion method has been developed to examine all traces at once to invert for a model of rock properties, globally optimized based on simulated annealing (Barclay et al., 2008). Simultaneous inversion enhances resolution and accuracy by making use of the full bandwidth (low and high frequencies) of the seismic signal. The underlying global-optimization cost function has four penalty terms that are collectively minimized to deliver the best solution. Modification of these terms can be made to incorporate requirements of more complex data types into the simultaneous inversion algorithm (Table 22.3), such as time-lapse surveys to highlight time-lapse changes in rock and fluid properties (Albright et al., 1994; Aronsen et al., 2004) and shear-wave multicomponent data (Figure 22.13).

In an attempt to help increase oil recovery factor, advanced time-lapse (or 4D) marine seismic surveys have been tested on the Norne field in the North Sea operated by Statoil (Barclay et al., 2008). The Norne field has high-quality sandstone reservoirs, with porosities ranging from 25% to 32% and permeabilities from 200 to 2000 mD; changes in fluid saturation and pressure result in noticeable differences in seismic amplitudes and elastic impedances. The Norne field is therefore conducive to successful time-lapse monitoring. Its first advanced marine seismic survey was acquired in 2001, forming the baseline for the 2003, 2004 and 2006 subsequent monitor surveys. Early time-lapse monitoring delivered vital information for optimizing field development. Differences in the AVO inversions of the 2001 and 2003 surveys revealed changes in acoustic impedance that were interpreted as increases in water saturation; the trajectory of a planned well was modified to avoid a high water saturation zone (Barclay et al., 2008).

To optimize reservoir drainage and injection strategies and to understand the effects of continued field production on changes in effective stress, a simultaneous inversion project incorporated all available seismic data, log data from seven wells and production

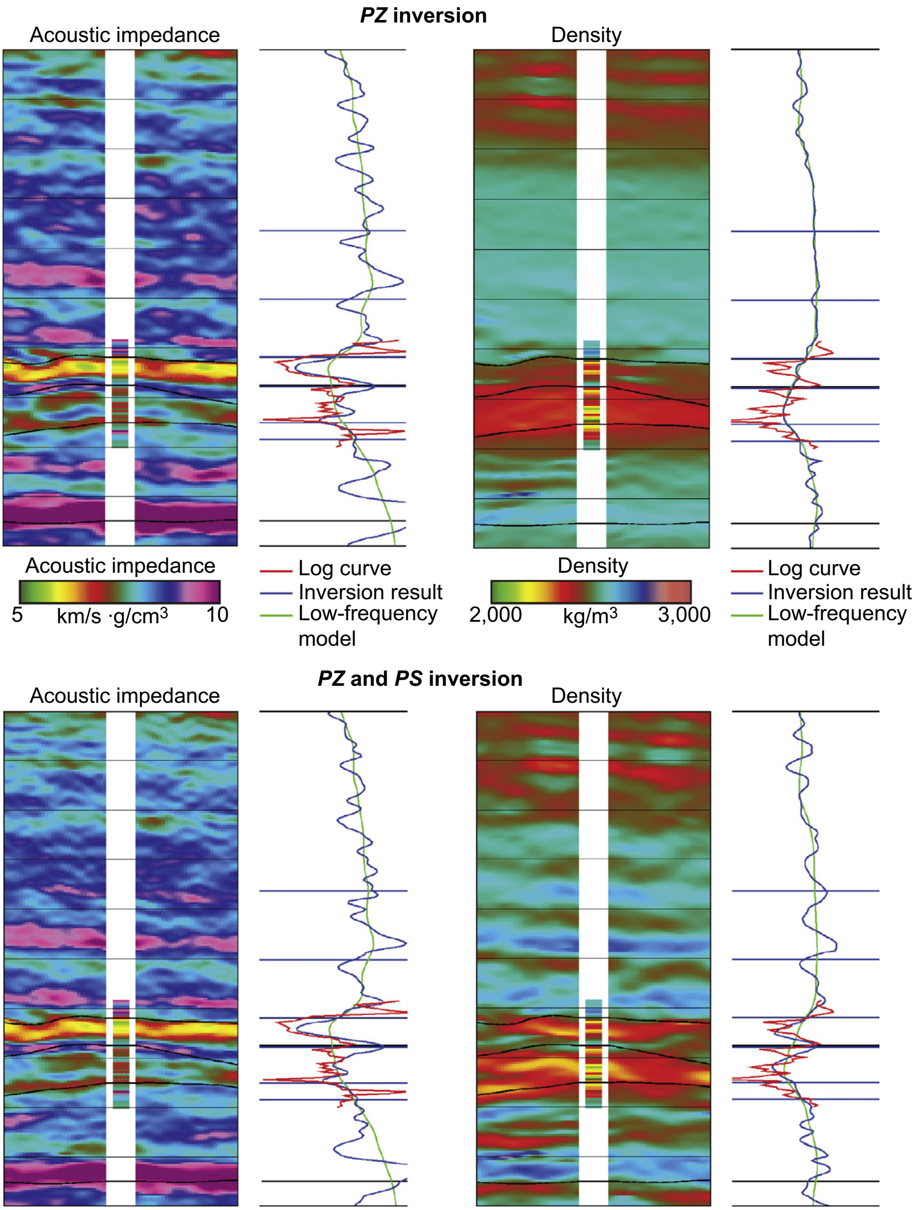

Figure 22.13 Simultaneous inversion of multicomponent data from seabed sensors. Acoustic impedance (left) and density (right) from inversion using only *PZ* data (top) lack the resolution and continuity of the results of inversion using *PZ* and *PS* data (bottom). In particular, compared with *PZ* inversion, the densities predicted by inversion of *PZ* and *PS* data showed much better correlation with log values. In the panels showing inversion results, the nearly horizontal black lines are interpreted horizons.

From Barclay, F., Bruun, A., Rasmussen, K. B., Alfaro, J. C., Cooke, A., Cooke, D., et al. (Spring 2008). Seismic inversion: Reading between the lines, Oilfield Review, 20(1), 42–63. Graphic copyright Schlumberger. Used with permission.

Table 22.3 **Applications of simultaneous inversion**

Data type	Physical properties
Full-stack data	*P*-wave impedance
Partial-stack AVO data	*P*-wave impedance, V_p/V_s (or *S*-wave impedance) and density, from which Poisson's ratio, λ and μ can be estimated.
Intercept and gradient AVO data	Acoustic impedance from the intercept data; shear impedance from shear seismic data calculated from the intercept and gradient data
Multicomponent full-stack data (*P*-to-*P* and *P*-to-*S* conversions)	*P*-wave impedance and *S*-wave impedance
Multicomponent partial-stack AVO data	*P*-wave impedance, V_p/V_s (or *S*-wave impedance) and density
Borehole seismic (VSP) data	Acoustic impedance from the *PP* data; shear impedance from the *PS* data
Time-lapse full-stack data (which may include multicomponent full-stack data)	Simultaneous time-lapse inversion for baseline *P*-wave impedance and the changes in *P*-wave impedance for each time interval: for multicomponent data, inversion will also output baseline *S*-wave impedance and changes in *S*-wave impedance over the time interval.
Time-lapse partial-stack AVO data (which may include multicomponent partial-stack AVO data)	Simultaneous time-lapse inversion for baseline properties and the changes: for example, for partial-stack data, inversion can determine baseline *P*-wave impedance, V_p/V_s (or *S*-wave impedance) and density and the changes in these properties over the time interval.

Adapted from Barclay, F., Bruun, A., Rasmussen, K. B., Alfaro, J. C., Cooke, A., Cooke, D., et al. (Spring 2008). Seismic inversion: reading between the lines, Oilfield Review, 20(1), 42—63.

data from the reservoir model. The simultaneous inversion estimated baseline values and changes in acoustic impedance and Poisson's ratio from the time-lapse seismic data (Figure 22.14). To compensate for the lack of low-frequency information in the seismic bandwidth — needed to determine absolute elastic properties — background models were constructed. For the (time-lapse) baseline survey, the background model was derived by propagating borehole (sonic logging) values of elastic properties throughout the zone of interest, constrained by key interpreted horizons and the seismic interval velocities.

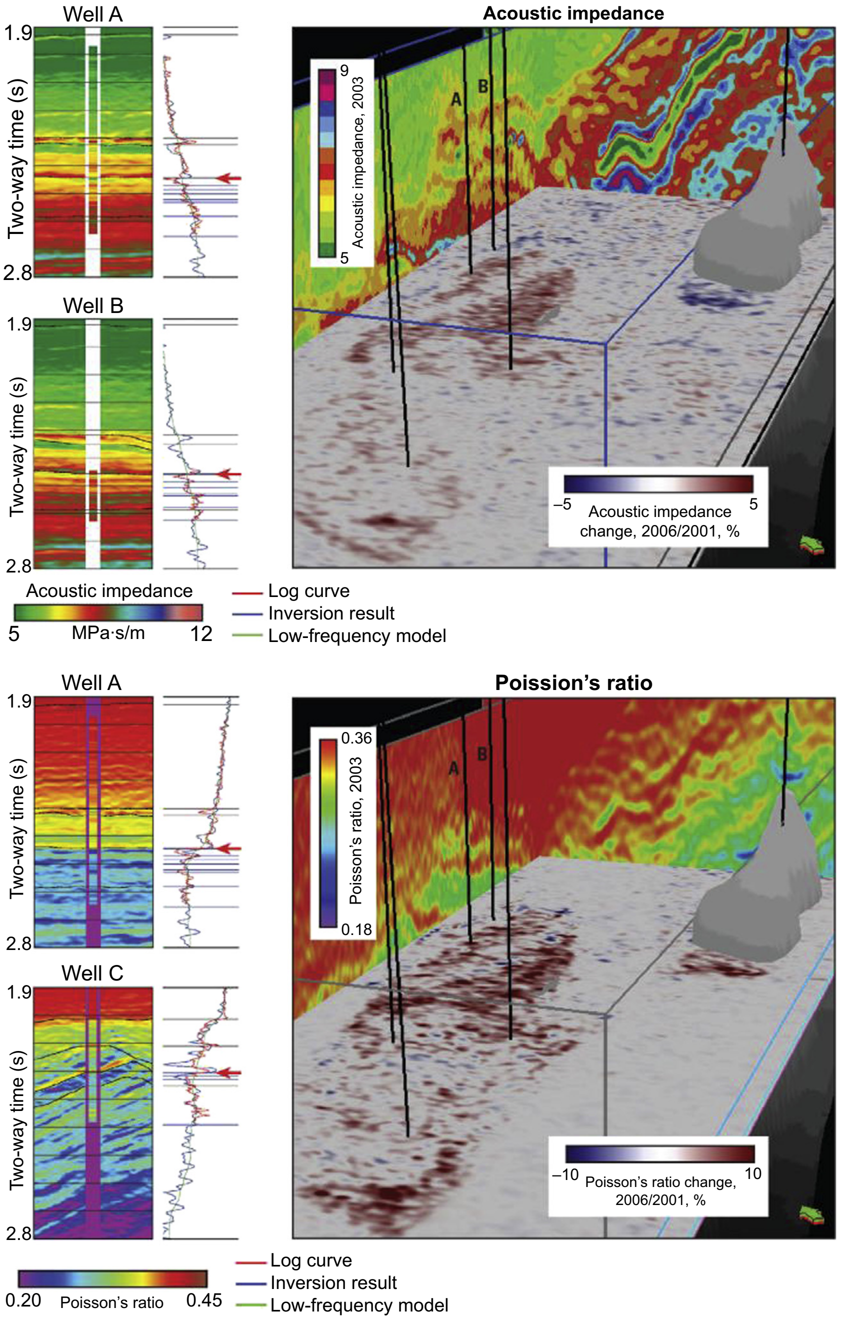

Figure 22.14 Time-lapse inversion. Results for acoustic impedance (top) and Poisson's ratio (bottom) use a low-frequency model based on simulation results. In the 3D volume (top right), the back and side panels show acoustic impedance values from the 2003 survey. The horizontal

For the time-lapse low-frequency models, estimates of elastic properties were obtained from the reservoir simulator in three steps: First, reservoir properties were converted from depth to time using the velocity model, then converted to elastic-property changes using rock-physics models. Finally, the spatial and temporal distributions of the property changes were constrained by seismic-velocity changes observed in time-lapse traveltime differences. This unique combination of time-converted reservoir properties with seismic-derived traveltime changes delivered accurate changes in elastic properties consistent with the reservoir simulation (Barclay et al., 2008).

The reservoir management team can use these time-lapse results to track the movement of the waterflood front, evaluate the progress of water and gas injection, estimate the pressure distribution and update the reservoir model.

22.5 Borehole seismic surveys

Borehole seismic surveys have an advantage over their surface seismic counterparts in that they record direct signals in a low-noise environment. Traditional vertical seismic profiles (VSPs) consisted of receivers deployed in a vertical borehole to record the most basic signals from a seismic source at the surface to perform time—depth correlation analysis (Figure 22.15).

Modern VSPs delivered innovations by recording more information and expanding survey geometries (Figure 22.16) with improved acquisition tools, including 3D VSPs (Figure 22.17), VSPs acquired while drilling (Figure 22.18) and walkaround VSP (Figure 22.19). From these data, exploration and production companies derive important information about reservoir depth, extent and heterogeneity, as well as fluid content, rock-mechanical properties, pore pressure, enhanced oil-recovery progress, elastic anisotropy, induced-fracture geometry and natural-fracture orientation and density (Blackburn et al., 2007).

The main types of waves generated and recorded in borehole seismic surveys are body waves emitted by point sources or frequency-sweep sources (airguns, vibrating trucks or dynamite sources), and consist of *P*-waves (and *PP*, *PZ*) and *S*-waves (and *PS*). Most modern downhole hardware for recording VSPs consists of clamped, calibrated three-component (3C) geophones.

surface is a time-slice of the ratio of acoustic impedance in 2006 to that in 2001. The increase (red) has been interpreted as replacement of oil by water. Absolute acoustic impedance comparisons at two wells (top left) show good correlation between well measurements and the 2003 acoustic impedance values. The red arrows in each log track point to the top of the horizon of interest. The log tracks display well data (red), seismically derived values (blue) and the low-frequency model (green). Results for Poisson's ratio (bottom) are plotted similarly. Well C is outside the 3D volume.

From Barclay, F., Bruun, A., Rasmussen, K. B., Alfaro, J. C., Cooke, A., Cooke, D., et al. (Spring 2008). Seismic inversion: reading between the lines, Oilfield Review, 20(1), 42—63. Graphic copyright Schlumberger. Used with permission.

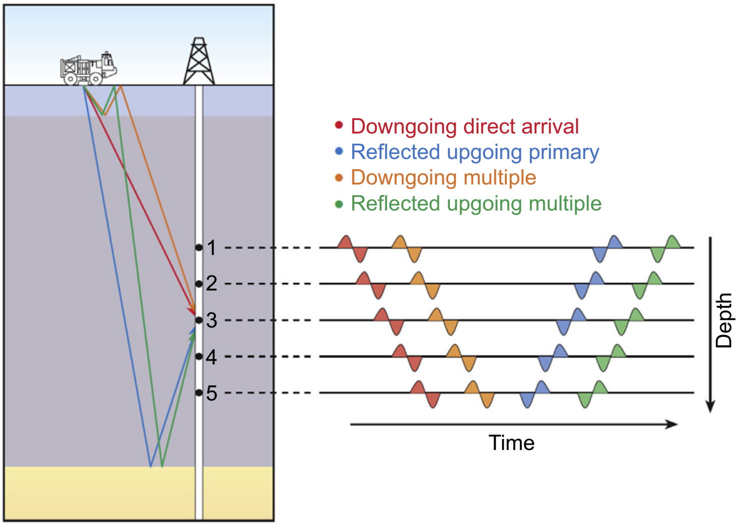
• Downgoing direct arrival
• Reflected upgoing primary
• Downgoing multiple
• Reflected upgoing multiple
1
2
3
4
5
Depth
Time

Figure 22.15 Upgoing, downgoing, primary and multiple arrivals. Upgoing waves reflect at interfaces below the receiver and then travel upward to be recorded (blue and green). Downgoing waves arrive at the receivers from above (red and orange). A wave that arrives at the receiver without reflecting is called the direct arrival (red). Waves that reflect only once are called primaries. The reflected upgoing primary (blue) is the arrival that is desired for imaging reflections. Both upgoing and downgoing signals can contain interfering multiples. Downgoing signals can be used to distinguish multiples from (multiples-free) primary arrivals and to enable more reliable processing of the surface seismic upgoing wavefield. Together with *P*- and *S*-waves propagating from a near-surface source to the receiver, source-generated noise tube waves also arise. Another form of noise that sometimes contaminates recordings is casing ringing.
From Blackburn, J., Daniels, J., Dingwall, S., Hampden-Smith, G., Leaney, S., Le Calvez, J., et al. (Autumn 2007). Borehole seismic surveys: beyond the vertical profile. Oilfield Review, 19(3), 20−35. Graphic copyright Schlumberger. Used with permission.

Hydraulically induced fractures can also be monitored using borehole seismic methods. While the fracture is being created in the treatment well, a multicomponent receiver array in a monitor well records the microseismic activity generated by the fracturing process (Figure 22.20). Locating hydraulically induced microseismic events requires an accurate velocity model (Blackburn et al., 2007). Mapping in real time the extent of the fracture with time helps monitor the progress of well stimulation treatments, allows comparison between actual and planned fractures, and optimizes reservoir treatments by allowing engineers to modify pumping rates when observed fractures differ from plan.

Another borehole seismic technology, called *passive seismic monitoring*, characterizes fractures by recording microseismic signals generated when fluid is produced from or injected into a naturally fractured reservoir. When fluid injection and production modify the stress state enough to cause seismic events, the resulting acoustic emissions can be recorded for long periods of time in nearby monitoring wells by arrays of multicomponent borehole receivers. The microseismic events can be plotted in space

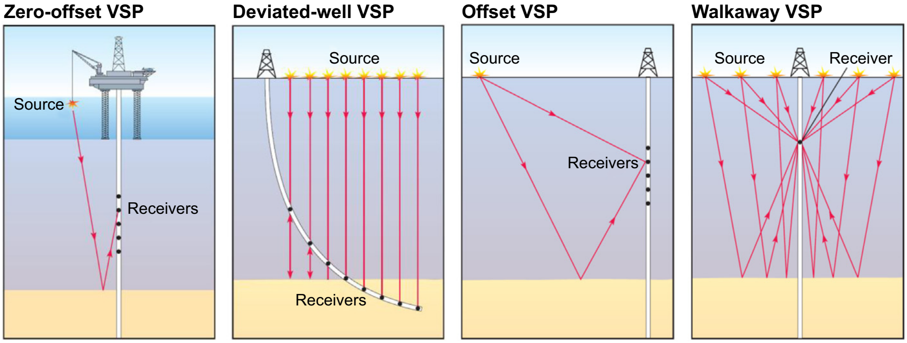

Figure 22.16 Variations on a theme of VSPs. The original acquisition geometry, with no offset between source and wellbore, creates a zero-offset VSP. Seismic waves travel essentially vertically down to a reflector and up to the receiver array. Processing yields velocities of formations at different depths, which can be tied to well log properties and interpreted for detection and prediction of overpressured zones. The velocity model can also be used to generate synthetics to identify multiples in surface seismic processing. Another normal-incidence or vertical-incidence VSP is acquired in deviated wells with the source always vertically above each receiver tool. This is known as a deviated-well, or walkabove, VSP; this survey acquires a 2D image of the region below the borehole. The additional benefits of a walkabove VSP are good lateral coverage and fault and dip identification beneath the well. In an offset VSP, an array of seismic receivers is clamped in the borehole at a wide range of depths, and a seismic source is placed some distance away, producing a 2D image. The nonvertical incidence can give rise to *P*-to *S*-wave conversion. The offset increases the volume of subsurface imaged and maps reflectors at a distance from the borehole that is related to the offset and subsurface velocities. The added volume of illumination enhances the usefulness of the image for correlation with surface seismic images, and for identification of faulting and dip laterally away from the borehole. In addition, because the conversion of *P*-waves to *S*-waves increases with offset, an offset VSP allows shear-wave, AVO and anisotropy analysis. In walkaway VSPs, a seismic source is activated at numerous positions in a line on the surface. The range of offsets acquired in a walkaway VSP is particularly useful for studying shear-wave, AVO and anisotropy effects. In addition, because they can illuminate a large volume of subsurface, offset and walkaway VSPs are useful elements in the design of surface seismic surveys. All these survey types may be acquired onshore or offshore.
From Blackburn, J., Daniels, J., Dingwall, S., Hampden-Smith, G., Leaney, S., Le Calvez, J., et al. (Autumn 2007). Borehole seismic surveys: beyond the vertical profile. Oilfield Review, 19(3), 20–35. Graphic copyright Schlumberger. Used with permission.

and time to identify the fractures that are responding to the change in stress state. Receiver arrays may be installed permanently to record for extended periods (Blackburn et al., 2007).

In *crosswell seismic surveys* (Figures 22.21–22.23), downhole seismic sources, such as downhole vibrators, are deployed at selected depths in one borehole, shooting to a receiver array in another borehole (Hu, Abubakar, & Habashy, 2008; Rao & Wang, 2011). Deep-reading crosswell seismic survey technology can combine traveltime tomography with reflection imaging between wells (Dong, Marion, Meyer, Xu, & Xu, 2005).

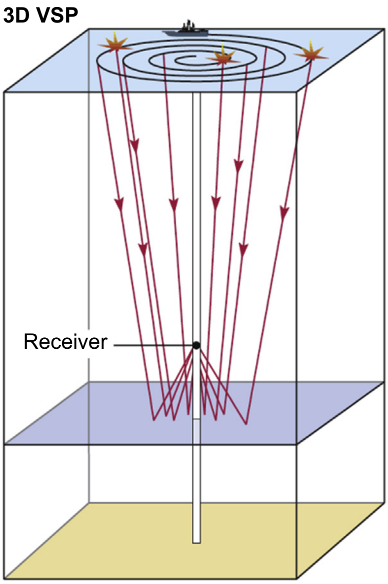

Figure 22.17 Three-dimensional VSPs. Onshore and offshore, 3D VSPs tend to borrow surface seismic acquisition geometries. On land, source positions usually follow lines in a grid. Offshore, source positions can be laid out in lines or in a spiral centred near the well. Ray-trace modelling prior to acquisition ensures proper coverage and illumination of the target. 3D VSPs deliver high-resolution subsurface imaging for exploration and development applications, and require detailed pre-job modelling and planning. 3D VSPs can fill in areas that cannot be imaged by surface seismic surveys because of interfering surface infrastructure or difficult subsurface conditions, such as shallow gas, which disrupts propagation of *P*-waves.
From Blackburn, J., Daniels, J., Dingwall, S., Hampden-Smith, G., Leaney, S., Le Calvez, J., et al. (Autumn 2007). Borehole seismic surveys: beyond the vertical profile. Oilfield Review, 19(3), 20−35. Graphic copyright Schlumberger. Used with permission.

Figure 22.24 is an example of utilization of such reflection imaging data, based on shooting ray paths above the reservoir as shown in the dotted paths of Figure 22.22. Recorded data are processed to extract information about the velocities in the interwell region. A limitation of the crosswell method is the maximum allowable distance between boreholes—a few thousand feet is typical—which varies with rock type, attenuation, and source strength and frequency content (Blackburn et al., 2007).

Many of the borehole seismic surveys mentioned above can be acquired at different stages in the life of a reservoir. Offset VSPs, walkaways, 3D VSPs and crosswell surveys can also be acquired in time-lapse fashion, before and after production. Time-lapse surveys can reveal changes in the position of fluid contacts (Albright et al., 1994, p. 8), changes in fluid content and/or front movement, such as in steam flooding (Figure 22.23) and in CO_2 flooding (Figure 22.24) in an EOR process, and other variations, such as pore pressure (Figure 22.25), rock stress (Cook et al., 2007) and temperature.

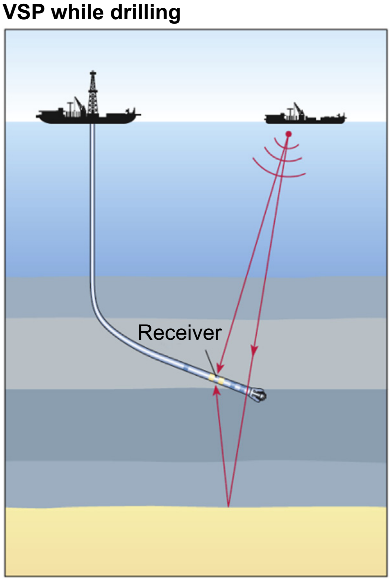

Figure 22.18 A VSP while drilling. A seismic-while-drilling tool positioned near the drill bit receives signals generated by a seismic source at the surface. Signals are transmitted to the surface for real-time, time-depth information. A seismic-while-drilling process can help reduce uncertainty in time-depth correlation without having to stop the drilling process. This technology uses a conventional seismic source at the surface, a logging-while-drilling (LWD) tool containing seismic sensors in the drill string, and a high-speed mud-pulse telemetry system to transmit data to the surface. Availability of real-time seismic waveforms allows operators to look thousands of feet ahead of the bit to safely guide well drilling. Seismic source activation and signal measurement must take place during quiet periods, when drilling has paused for making drill pipe connections. The drill bit can act as a downhole source, generating vibrations that are detected by sensors deployed at the surface or on marine cables. The processed recordings can provide critical answers in time for decisions to be made while drilling, such as changing mud weight or setting casing.
From Blackburn, J., Daniels, J., Dingwall, S., Hampden-Smith, G., Leaney, S., Le Calvez, J., et al. (Autumn 2007). Borehole seismic surveys: beyond the vertical profile. Oilfield Review, 19(3), 20—35. Graphic copyright Schlumberger. Used with permission.

The detection of high pore pressure (geopressure) zones is important in oil-gas exploration, especially for early detection ahead of the drill bit to prevent blowout due to insufficient mud weight (Dutta, 2002). Both *P*-wave velocity (V_p) and *S*-wave velocity (V_s) have been shown to be anomalously low in a zone of high pore pressure, in sharp contrast with a gas-bearing zone where there is a marked low velocity in V_p but not in V_s (Nur, 1987, p. 232). Anomalous pore pressure detection can hence be realized by the combined use of compressional and shear-wave velocity data by discriminating between a gas zone and an overpressured zone.

Conventional seismic data smooth out velocity fluctuations and have velocity resolution too coarse for accurate pore-pressure prediction for well-planning purposes

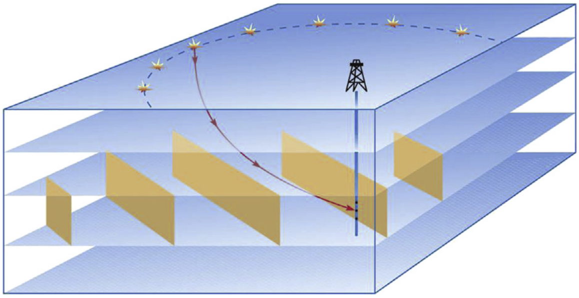

Figure 22.19 A walkaround VSP. With offset source locations spanning a large circular arc to probe the formation from a wide range of azimuths, this survey can be used to characterize direction and magnitude of anisotropy caused by aligned natural fractures. Walkaround VSPs can help understand fractures and fracture systems, both natural and hydraulically induced. From Blackburn, J., Daniels, J., Dingwall, S., Hampden-Smith, G., Leaney, S., Le Calvez, J., et al. (Autumn 2007). Borehole seismic surveys: beyond the vertical profile. Oilfield Review, 19(3), 20−35. Graphic copyright Schlumberger. Used with permission.

(Barriol et al., 2005). Seismic reflection tomography based on a ray-tracing modelling-based approach refines the velocity model, leading to a better understanding of the amplitude and spatial distribution of pore pressure, reducing the uncertainty in its predictions (Figure 22.25).

Discovered hydrocarbon reservoirs have increasing complexity in spatial heterogeneity. We have established some understanding of the complex relation between the seismic properties of reservoir and related rocks, and their petrophysical properties

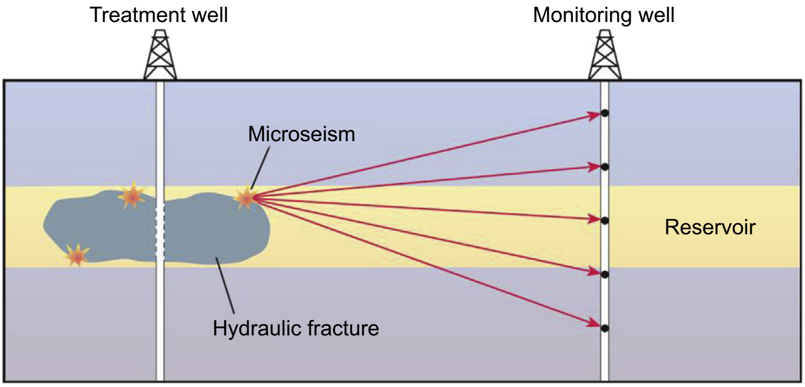

Figure 22.20 Microseismic method of hydraulic fracture monitoring. Sensitive multicomponent sensors in a monitoring borehole record microseismic events, or acoustic emissions, caused by hydraulic fracturing. Data processing determines event location, and visualization allows engineers to monitor the progress of stimulation operations.
From From Blackburn, J., Daniels, J., Dingwall, S., Hampden-Smith, G., Leaney, S., Le Calvez, J., et al. (Autumn 2007). Borehole seismic surveys: beyond the vertical profile. Oilfield Review, 19(3), 20−35. Graphic copyright Schlumberger. Used with permission.

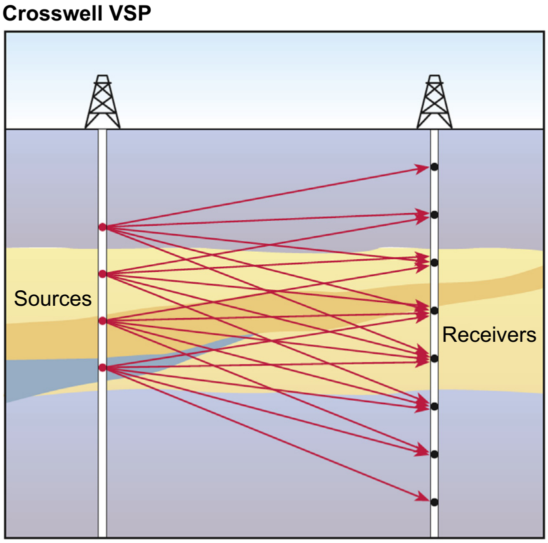

Figure 22.21 Crosswell seismic surveys, with sources in one borehole and receivers in another. Because ray paths are at large angles to any formation interfaces, little energy is reflected; most energy recorded by the receivers comes from direct arrivals. These data reveal information about formation velocities in the interwell volume. The repeatable survey geometry makes crosswell seismic surveys useful for time-lapse monitoring of steam injection, for example.
From From Blackburn, J., Daniels, J., Dingwall, S., Hampden-Smith, G., Leaney, S., Le Calvez, J., et al. (Autumn 2007). Borehole seismic surveys: beyond the vertical profile. Oilfield Review, 19(3), 20–35. Graphic copyright Schlumberger. Used with permission.

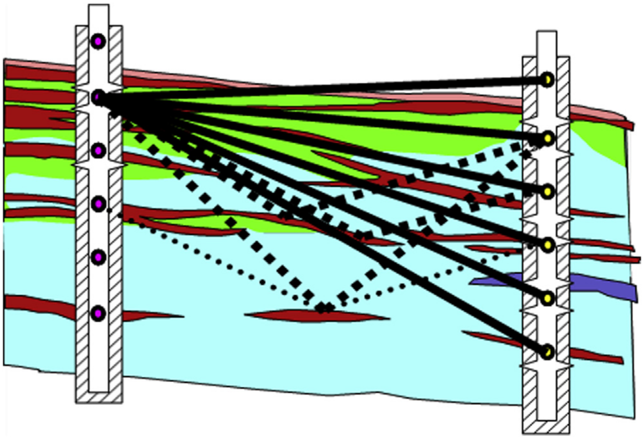

Figure 22.22 Crosswell seismic survey includes also a reflection section between wells, a stack of precritical reflection energy, based on shooting ray paths above the reservoir as shown in the dotted paths.

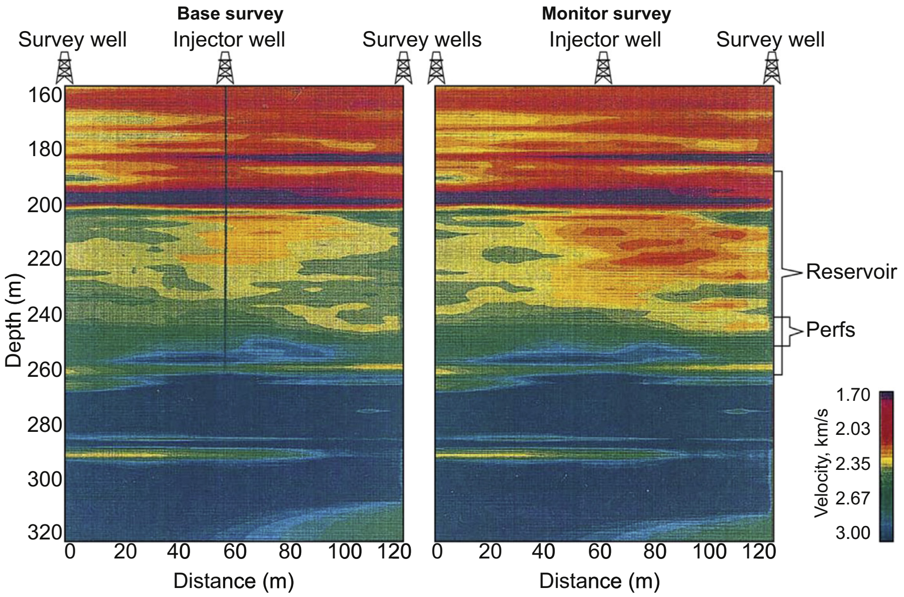

Figure 22.23 Crosswell seismic velocity images before and after steam injection in the Athabasca tar sands, Alberta, Canada. The base survey (left) was acquired before steam injection. The injection well is halfway between the survey wells. The monitor survey (right) was run three months after steam injection began. The reservoir interval is 190—260 m, with a gas cap from 197 to 205 m. Perforation interval is 240—250 m. As seen from the velocity decrease — more orange and red — the steam has risen and taken off to the right.
From Albright, J., Cassell, B., Dangerfield, J., Deflandre, J. -P., Johnstad, S., & Withers, R. (January 1994). Seismic surveillance for monitoring reservoir changes. Oilfield Review, 6(1), 4—14. Graphic copyright Schlumberger. Used with permission.

in relation to production (porosity, permeability) and state (mineralogy, saturation, pore pressure). The unlocking of the interconnections between seismic attributes and petrophysical parameters is of key importance for the evaluation of stratigraphic traps, fracture detection and the spatial distribution of porosity and permeability (Grochau, 2009; Grochau & Gurevich, 2008; Nur, 1987; Scott, Zaman, & Roegiers, 1998; Shapiro & Gurevich, 2002). Some applications of seismic velocity (and attenuation) imaging in the description of reservoirs and the monitoring of reservoir recovery (Nur, 1987, p. 235) have been demonstrated over the years. Some related references are given in Table 22.4.

22.6 Future trends

There have been new developments in full azimuth (FAZ) marine seismic imaging. A new data acquisition technique, in which a single vessel acquires full azimuth (FAZ) 3D seismic data by sailing in circles, can deliver for better illumination and

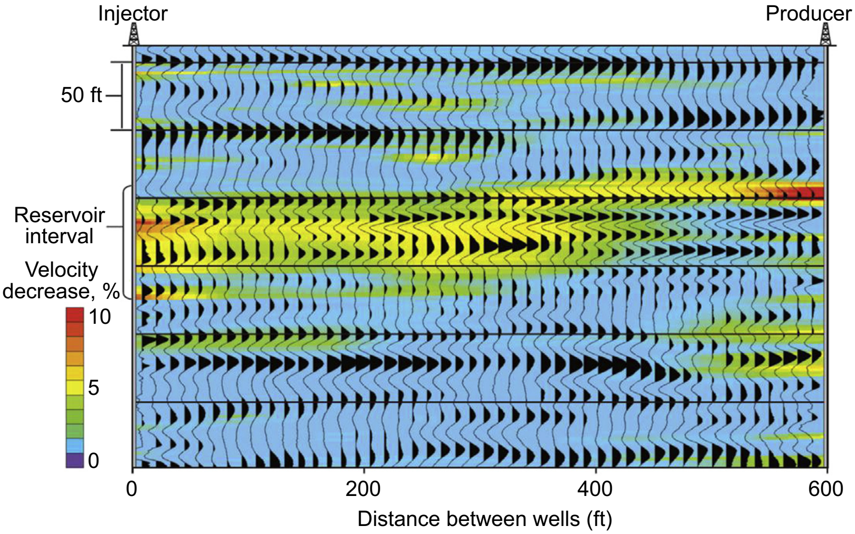

Figure 22.24 Time-lapse crosswell seismic monitoring. Crosswell seismic tomography was used for mapping miscible CO_2 between an injector and producer in an EOR program. The display shows high-resolution crosswell seismic reflection data (black traces) overlying colour-coded velocity-difference data. This colour scale helps geoscientists track changes in seismic velocity between a baseline preinjection survey and a later survey conducted nine months after CO_2 injection commenced. The zone in the centre (yellow and red) experienced a greater velocity decrease than surrounding layers (blue and green), indicating a potential CO_2 accumulation. In this case, the operator concluded the CO_2 sweep was not uniform between the injector and producer wells.
From Al-Ali, Z.A., Al-Buali, M.H., AlRuwaili, S., Ma, S.M., Marsala, A.F., Alumbaugh, D., et al. (Summer 2009). Looking deep into the reservoir. Oilfield Review, 21(2), 38—47. Graphic copyright Schlumberger. Used with permission.

more accurate and reliable subsurface images than conventional 3D methods in areas of complex geology. Recently, a multi-vessel implementation of the new technique has been developed to address subsalt imaging challenges in deepwater areas. A typical FAZ tomography workflow is illustrated in Figure 22.26 (Brice et al., 2013).

Further improvements are expected from the implementation of innovative acquisition configurations, advanced processing technologies and new workflows that will extract more information from seismic measurements to enhance our understanding of the subsurface.

Improving seismic imaging resolution requires extending the range of usable signal frequencies at both high and low ends. The preservation of lower frequencies is important not only for imaging deep or steep targets but also for building high-resolution velocity models using full waveform inversion (FWI) (ten Kroode et al., 2013; Robertsson, Ronen, Singh, & van Borselen, 2013; Vigh, Jiao, & Watts, 2012).

New processing including 3D prestack acoustic full waveform inversion (FWI) uses a two-way wave equation method to build high-resolution velocity models.

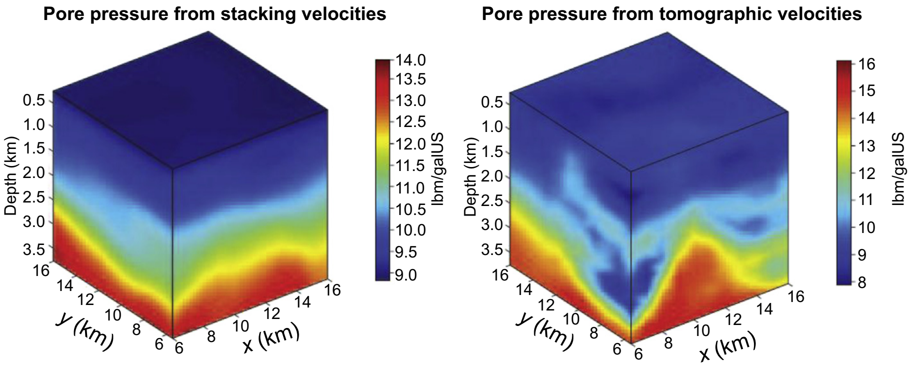

Figure 22.25 Seismic pore pressure tomography. In previous (conventional) methods, interpreters stacked seismic velocities to improve resolution; from this they generated a pore-pressure cube representing pore pressures across a given area (left). Now, tomographic techniques dramatically improve pore-pressure resolution (right), reducing uncertainty and increasing accuracy in well planning.
From Barriol, Y., Glaser, K.S., Pop, J., Bartman, B., Corbiell, R., Eriksen, K.O., et al. (Autumn 2005). The pressure of drilling and production. Oilfield Review, 17(3), 22–41 Graphic copyright Schlumberger. Used with permission.

Full waveform inversion performs forward modeling to compute the differences between the acquired seismic data and the current model and carries out a process similar to reverse time migration (RTM) on the residual data set to compute a gradient volume and to update the velocity model (RTM is a prestack two-way wave equation migration algorithm suited to accurate imaging in and below areas with structural and velocity complexities). When combined with imaging using RTM, model building with FWI

Table 22.4 Applications of seismic imaging in reservoir description and the monitoring

Applications listed (Nur 1987, p. 235)	Some references
Porosity and permeability mapping	Barclay et al. (2008)
Anomalous pore pressure detection	Landrø and Kvam (2002)
Fracture detection	Blackburn et al. (2007)
Tracking thermal fronts	Zadeh, Srivastava, Vedanti, and Landrø (2010)
Gap cap movement	Albright et al. (1994), Barkved (2004)
Water flooding	Leggett et al. (1993)
Steam reservoir boundaries	Justice et al. (1989), Albright et al. (1994), Brzostowski and McMechan (1995)
Distribution of permafrost	

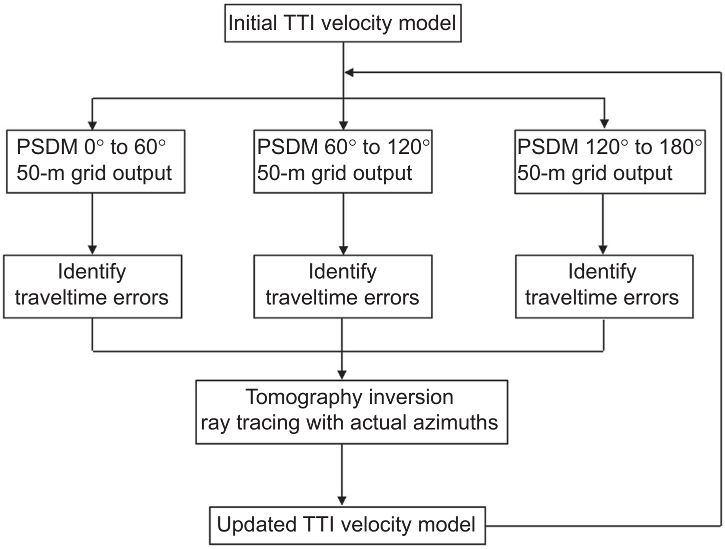
Initial TTI velocity model
PSDM 0° to 60°
50-m grid output
PSDM 60° to 120°
50-m grid output
PSDM 120° to 180°
50-m grid output
Identify
traveltime errors
Identify
traveltime errors
Identify
traveltime errors
Tomography inversion
ray tracing with actual azimuths
Updated TTI velocity model

Figure 22.26 Azimuthal tomography workflow. A tilted transverse isotropic (TTI) velocity model derived from time-domain processing formed the starting model. The new marine seismic acquisition data set was divided into three azimuthal groups for prestack depth migration (PSDM). Traveltimes from the PSDM are compared with those predicted by the model using tomography inversion and ray-tracing techniques, leading to an updated velocity model. Adapted from Brice, T., Buia, M., Cooke, A., Hill, D., Palmer, E., Khaled, N., et al. (Spring 2013). Developments in full azimuth marine seismic imaging, Oilfield Review, 25(1), 42—55. Used with Schlumberger permission.

improved the final product because consistent wavefield solutions were applied throughout the depth imaging workflow (Brice et al., 2013).

Deep-reading resistivity tomography obtained through electromagnetic (EM) induction crosswell surveys described in Chapter 23 can provide better petrophysical control in building reservoir models than surface seismic surveys. The capability to identify and monitor fluid fronts using crosswell EM measurements can be complemented by the crosswell seismic imaging technique, which can delineate structure and monitor fluid movement in the reservoir. The detailed reservoir-level information obtained from combined deep-reading measurements gives petrophysicists and reservoir engineers greater insight into how fluids move and interact, which will ultimately determine the decision-making of oilfield management and production (Al-Ali et al., 2009).

22.7 Sources of further information and advice

- The Society of Exploration Geophysicists (SEG) journals:
  Geophysics
  The Leading Edge

- The European Association of Geoscientists and Engineers (EAGE) journals:
  Geophysical Prospecting First Break
- Other journals:
  Petroleum Geoscience
  Journal of Petroleum Geology

Acknowledgements

I would like express my gratitude to Schlumberger for permission to publish this book chapter, and to several Schlumberger clients for permission to reuse some figures containing their data. Thanks to Lisa Stewart, executive editor of Schlumberger *Oilfield Review*, for her help in the preparation of this chapter. Bruce Marion, Schlumberger advisor, reviewed the draft of the manuscript and provided invaluable suggestions for improving the section related to crosswell seismic imaging.

References

Al-Ali, Z. A., Al-Buali, M. H., AlRuwaili, S., Ma, S. M., Marsala, A. F., Alumbaugh, D., et al. (Summer 2009). Looking deep into the reservoir. *Oilfield Review, 21*(2), 38−47.

Albertin, U., Kapoor, J., Randall, R., Smith, M., Brown, G., Soufleris, C., et al. (Spring 2002). The time for depth imaging. *Oilfield Review, 14*(1), 2−15.

Albright, J., Cassell, B., Dangerfield, J., Deflandre, J.-P., Johnstad, S., & Withers, R. (January 1994). Seismic surveillance for monitoring reservoir changes. *Oilfield Review, 6*(1), 4−14.

Aronsen, H. A., Osdal, B., Dahl, T., Eiken, O., Goto, R., Khazanehdari, J., et al. (Summer 2004). Time will tell: new insights from time-lapse seismic data. *Oilfield Review, 16*(2), 6−15.

Ashcroft, W. (2011). *A petroleum geologist's guide to seismic reflection*. Chichester: Wiley-Blackwell.

Bagaini, C., Bunting, T., El-Emam, A., Laake, A., & Strobbia, C. (Summer 2010). Land seismic techniques for high-quality data. *Oilfield Review, 22*(2), 28−39.

Barclay, F., Bruun, A., Rasmussen, K. B., Alfaro, J. C., Cooke, A., Cooke, D., et al. (Spring 2008). Seismic inversion: reading between the lines. *Oilfield Review, 20*(1), 42−63.

Barkved, O., Bartman, B., Compani, B., Gaiser, J., Van Dok, R., Johns, T., et al. (Summer 2004). The many facets of multicomponent seismic data. *Oilfield Review, 16*(2), 42−56.

Barriol, Y., Glaser, K. S., Pop, J., Bartman, B., Corbiell, R., Eriksen, K. O., et al. (Autumn 2005). The pressure of drilling and production. *Oilfield Review, 17*(3), 22−41 (2006).

Blackburn, J., Daniels, J., Dingwall, S., Hampden-Smith, G., Leaney, S., Le Calvez, J., et al. (Autumn 2007). Borehole seismic surveys: beyond the vertical profile. *Oilfield Review, 19*(3), 20−35.

Brady, J., Campbell, T., Fenwick, A., Ganz, M., Sandberg, S. K., Buonora, M. P. P., et al. (Spring 2009). Electromagnetic sounding for hydrocarbons. *Oilfield Review, 21*(1), 4−19.

Brice, T., Buia, M., Cooke, A., Hill, D., Palmer, E., Khaled, N., et al. (Spring 2013). Developments in full azimuth marine seismic imaging. *Oilfield Review, 25*(1), 42−55.

Brzostowski, M. A., & McMechan, G. A. (1995). Tomographic imaging of 3D seismic low-velocity anomalies to simulate monitoring of enhanced oil recovery. *International Journal of Imaging Systems and Technology, 5*(1), 62−72.

Cavalca, M., & Fletcher, R. P. (2008). Deriving 3D Q models from surface seismic data using attenuated traveltime tomography. In *70th EAGE conference & exhibition, Rome, Italy, 9−12 June 2008*. Paper H003.

Červeny, V. (1987). Ray tracing algorithms in three-dimensional laterally varying layered structures. In G. Nolet (Ed.), *Seismic tomography* (pp. 99−133). D. Reidel Publishing Co.

Chapman, C. (1987). The Radon transform and seismic tomography. In G. Nolet (Ed.), *Seismic tomography* (pp. 25−47). D. Reidel Publishing Co.

Chapman, C. (2004). *Fundamentals of seismic wave propagation*. Cambridge: Cambridge University Press.

Cook, J., Frederiksen, R. A., Hasbo, K., Green, S., Judzis, A., Martin, J. W., et al. (Autumn 2007). Rock matters: ground truth in geomechanics. *Oilfield Review, 19*(3), 36−55.

Dawoud, M., Hallinan, S., Hermann, R., & van Kleef, F. (Spring 2009). Near-surface electromagnetic surveying. *Oilfield Review, 21*(1), 20−25.

De Freitas, J. M. (2011). Recent developments in seismic seabed oil reservoir monitoring applications using fibre-optic sensing networks. *Measurement Science and Technology, 22*, 052001.

Dong, Q., Marion, B., Meyer, J., Xu, Y., & Xu, D. (2005). Imaging complex structure with crosswell seismic in Jianghan oil field. *The Leading Edge, 24*, 18.

Dutta, N. C. (2002). Geopressure prediction using seismic data: current status and the road ahead. *Geophysics, 67*(6), 2012−2041.

Grochau, M. H. (2009). *An integrated approach to improve time-lapse seismic interpretation: investigation of pressure and saturation effects on elastic parameters*. Lambert Academic Publishing.

Grochau, M. H., & Gurevich, B. (2008). Investigation of core data reliability to support time-lapse interpretation in Campos Basin, Brazil. *Geophysics, 3*(2), E59−E65.

Hu, W., Abubakar, A., & Habashy, T. (2008). A local contrast source inversion algorithm for cross-well time-lapse seismic applications. In *SEG Las Vegas 2008 annual meeting*.

Justice, J. H., Vassiliou, A. A., Singh, S., Logel, J. D., Hansen, P. A., Hall, B. R., et al. (1989). Acoustic tomography for monitoring enhanced oil recovery. *The Leading Edge, 8*(2), 12−19.

ten Kroode, F., Bergler, S., Corsten, C., de Maag, J., Strijbos, F., & Tijhof, H. (2013). Broadband seismic data — The importance of low frequencies. *Geophysics, 78*(2), WA3−WA14.

Landrø, M., & Kvam, Ø. (September 2002). Pore pressure estimation − what can we learn from 4D? *CSEG Recorder*, 82−87.

Leggett, M., Goulty, N. R., & Kragh, J. E. (1993). Study of traveltime and amplitude time-lapse tomography using physical model data. *Geophysical Prospecting, 41*(5), 599−619.

Li, X.-Y., & Zhang, Y.-G. (2011). Seismic reservoir characterization: how can multicomponent data help? *Journal of Geophysics and Engineering, 8*, 123−141.

Mathewson, J. C., Evans, D., Leone, C., Leathard, M., Dangerfield, J., & Tonning, S. A. (2012). Improved imaging and resolution of overburden heterogeneity by combining amplitude inversion with tomography. In *SEG Las Vegas 2012 annual meeting*.

Nolet, G. (1987). Seismic wave propagation and seismic tomography. In G. Nolet (Ed.), *Seismic tomography* (pp. 1−23). D. Reidel Publishing Co.

Nolet, G. (2008). *A breviary of seismic tomography − Imaging the interior of the Earth and Sun*. Cambridge: Cambridge University Press.

Nur, A. (1987). Seismic rock properties for reservoir description and monitoring. In G. Nolet (Ed.), *Seismic tomography* (pp. 203−237). D. Reidel Publishing Co.

Rao, Y., & Wang, Y. (2011). Crosshole seismic tomography including the anisotropy effect. *Journal of Geophysics and Engineering, 8*, 316−321.

Robertsson, J. O. A., Ronen, S., Singh, S., & van Borselen, R. (2013). Broadband seismology in oil and gas exploration and production – Introduction. *Geophysics, 78*(2), WA1–WA2.

Sayers, C. (2013). The effect of kerogen on the elastic anisotropy of organic-rich shales. *Geophysics, 78*(2), D65–D74.

Schuck, A., & Lange, G. (2007). Seismic methods. In J. Knodel, G. Lange, & H.-J. Voigt (Eds.), *Environmental geology – handbook of field methods and case studies* (pp. 337–402). Berlin: Springer.

Scott, T. E., Jr, Zaman, M. M., & Roegiers, J.-C. (1998). Acoustic-velocity signatures associated with rock-deformation processes. *Journal of Petroleum Technology, 50*(6), 70–74.

Seidel, K., & Lange, G. (2007). Direct current resistivity methods. In J. Knodel, G. Lange, & H.-J. Voigt (Eds.), *Environmental geology – handbook of field methods and case studies* (pp. 205–237). Berlin: Springer.

Seidel, K., & Lindner, H. (2007). Gravity methods. In J. Knodel, G. Lange, & H.-J. Voigt (Eds.), *Environmental geology – handbook of field methods and case studies* (pp. 185–204). Berlin: Springer.

Shapiro, S. A., & Gurevich, B. (2002). Seismic signatures of fluid transport—Introduction. *Geophysics, 67*(1), 197–198.

van der Sluis, A., & van der Vorst, H. A. (1987). Numerical solution of large, sparse linear algebraic systems arising from tomographic problems. In G. Nolet (Ed.), *Seismic tomography* (pp. 49–83). D. Reidel Publishing Co.

Strobbia, C. L., Glushchenko, A., Laake, A., Vermeer, P., Papworth, S., & Ji, U. (2009). Arctic near surface challenges: the point receiver solution to coherent noise and statics. *First Break, 27*(2), 69–76.

Tarantola, A. (1987). Inversion of travel times and seismic waveforms. In G. Nolet (Ed.), *Seismic tomography* (pp. 135–157). D. Reidel Publishing Co.

Vesnaver, A. (2008). Yardsticks for industrial tomography. *Geophysical Prospecting, 56*, 457–465.

Vigh, D., Jiao, K., & Watts, D. (2012). Elastic full-waveform inversion using 4C data acquisition. In *SEG Las Vegas 2012 annual meeting*.

Wielandt, E. (1987). On the validity of the ray approximation for interpreting delay times. In G. Nolet (Ed.), *Seismic tomography* (pp. 85–98). D. Reidel Publishing Co.

Woodward, M. J., Nichols, D., Zdraveva, O., Whitfield, P., & Johns, T. (2008). A decade of tomography. *Geophysics, 73*(5), VE5–VE11.

Zadeh, H. M., Srivastava, R. P., Vedanti, N., & Landrø, M. (2010). Seismic monitoring of in situ combustion process in a heavy oil field. *Journal of Geophysics and Engineering, 7*(1), 16–29.

Applications of tomography in the oil-gas industry − Part 2

23

C.-G. Xie[1,2,3], M. Wilt[2,3]
[1]Singapore Well Testing Centre (SWTC), Schlumberger Oilfield (S) Pte Ltd, Singapore;
[2]Schlumberger Gould Research Centre, Cambridge, UK; [3]Schlumberger Oilfield
PetroTechnical Services, Richmond, CA, USA

23.1 Introduction

Applications of tomography in the upstream oil-gas industry are widespread, covering from kilometre reservoir scale, sub-metre borehole scale to sub-mm rock-core pore scale. Continuing with the theme of Chapter 22 on the applications of seismic tomography in the oil-gas industry, this chapter illustrates the use of other tomography modalities in hydrocarbon exploration, reservoir monitoring and production monitoring.

In Section 23.2, cross-well (cross-borehole) tomography for reservoir monitoring is demonstrated by way of electromagnetic (EM) (induction) resistivity imaging of water-flood and steam-flood processes.

Complex oil-gas-water multiphase flows are often encountered in hydrocarbon production pipelines, and the accurate measurement of their flow rates over a wide range of flow regimes is still a challenge facing the oil-gas industry. In Section 23.3, some tomography modalities investigated for multiphase flow imaging and measurement will be described, and some results from electrical capacitance tomography (ECT) demonstrated.

In Section 23.4, we will make some remarks about the future trend of industrial tomography in the oil-gas industry.

23.2 Cross-well electromagnetic tomography in hydrocarbon reservoir monitoring

Seismic surveys described in the last chapter can image reservoir volumes but tend to lack sufficient vertical resolution and sensitivity to fluid type and fluid distribution within a reservoir (seismic surveys are more sensitive to the rock matrix). To better monitor movements of hydrocarbon fluid lying between wells at a reservoir scale, fluid-saturation surveys based on cross-well EM induction tomography have been performed (Alumbaugh & Morrison, 1995; Wilt et al., 1995; DePavia et al., 2008; Wilt, Donadille, AlRuwaili, Ma, & Marsala, 2008; Marsala et al., 2008. Surface-to-borehole EM uses an array of borehole receivers and a movable surface

Industrial Tomography. http://dx.doi.org/10.1016/B978-1-78242-118-4.00023-X
Copyright © 2015 Elsevier Ltd. All rights reserved.

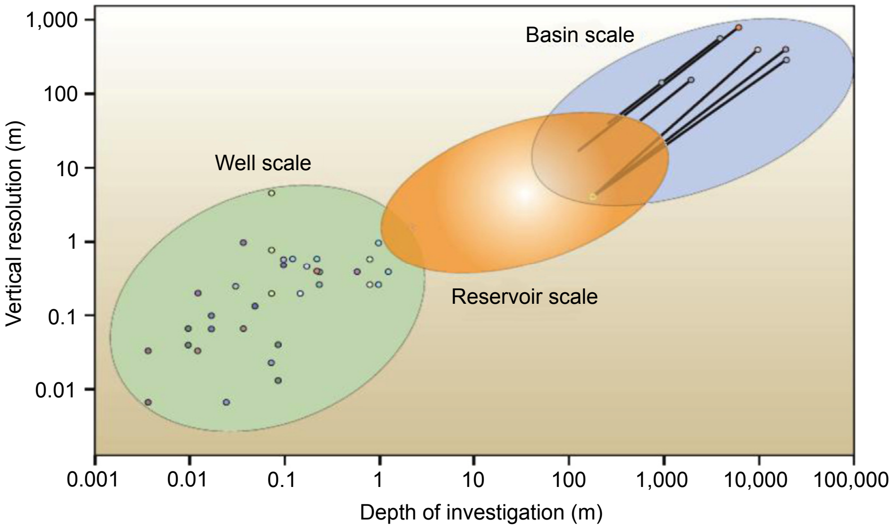

Figure 23.1 Bridging the resolution gap. Most oilfield measurements fall at the ends of a spectrum; they are obtained by probing either the near-wellbore vicinity at high resolution or a basin-wide area at lower resolution. Cross-well measurements sample at an intermediate depth of investigation and resolution to help geoscientists characterize and image the reservoir within the inter-well region.

From Al-Ali et al., 2009. Graphic copyright Schlumberger. Used with permission.

source, Pardo, Torres-Verdín, & Zhang, 2008; Marsala et al., 2011). The cross-well EM induction tomography approach produces a resistivity distribution between wells and offers a better resolution than surface seismic surveys (Al-Ali et al., 2009). As indicated in Figure 23.1, cross-well EM surveys investigating the inter-well region fill an intermediate role between high-resolution near-wellbore logs (e.g. nuclear magnetic resonance logging, Allen et al., 2000) and lower resolution surface seismic or electrical resistivity surveys (Ramirez, Daily, Owen, Chesnut, & LaBrecque, 1992; Seidel & Lange, 2007; Tsourlos, Ogilvy, Papazachos, & Meldrum, 2011). High-resolution analyses of rock core samples are carried out in laboratories by using magnetic resonance imaging (Mitchell, Chandrasekera, Holland, Gladden, & Fordham, 2013, Mitchell, Staniland, et al., 2013), X-ray tomography (Figure 23.2) or micro X-ray tomography (Kayser, Knackstedt, & Ziauddin, 2006; Ziauddin & Bize, 2007; Iglauer, Wang, & Rasouli, 2011; Feali et al., 2012).

Induction measurements respond primarily to electrical conductivity (the reciprocal of resistivity); in the downhole environment, high conductivity values generally indicate the presence of salt water. The presence of hydrocarbons may be indicated by low conductivity (high resistivity) values. However, the measurement is influenced by temperature, porosity, pore-fluid resistivity and fluid saturations. Cross-well EM resistivity imaging is used to distinguish the electrical contrast between resistive oil and conductive saline water. Inter-well resistivity data are also useful for mapping variations in reservoir properties (see Table 22.2 in Chapter 22) for heterogeneity or connectivity between wells.

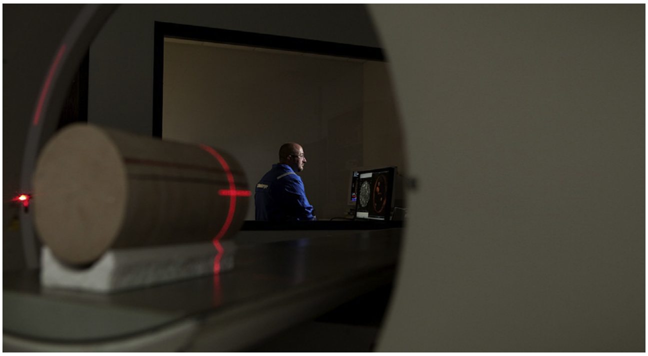

Figure 23.2 Computed tomography (CT) scans of a rock core indicate heterogeneity. Graphic copyright Schlumberger. Used with permission.

23.2.1 Principles of EM induction cross-well tomography

Illustrated in Figure 23.3, in a cross-well EM survey, a magnetic dipole transmitter is placed in one well and an array of magnetometer receivers in another well to investigate the inter-well area. By transmitting from one well to another at frequencies in the Hz to kHz range, signals over a distance up to 1 km can be propagated, depending on wellbore casing and formation characteristics (Table 23.1) (Wilt & Alumbaugh, 2014).

EM cross-well data are collected for tomographic resistivity imaging by lowering the receiver array into a wellbore to a specified depth. While this receiver array remains stationary, the EM transmitter in the other well continuously broadcasts as it is moved between selected depths. Once the signals from a complete transmitter traverse are obtained at a depth, the receiver tool is repositioned (typically uphole) to another depth, and the process is repeated. Thus, as the transmitter and receivers are moved across the logging interval, the inter-well target zone is interrogated from multiple angles (Figure 23.3).

The EM transmitter generates a magnetic field that is sent into the formation at frequencies between 5 Hz and 1 kHz. This magnetic field, known as the primary field, attenuates with increasing distance from the transmitter. The primary field induces a current in conductive formations (Figure 23.4). This current generates an opposing secondary EM field, such that the total field decreases in amplitude with decreasing formation resistivity. An array of sensitive induction-coil receivers can be stationed in the receiver well to detect the primary EM field generated by the transmitter and the secondary EM field generated by the induced currents.

For a vertically oriented (z-direction) magnetic dipole source in homogeneous isotropic earth, Maxwell's equations can be combined to yield a second-order equation for the vertical magnetic field H_z (Wilt & Alumbaugh, 2014):

$$\frac{\partial^2 H_z}{\partial x^2} + \frac{\partial^2 H_z}{\partial y^2} + \frac{\partial^2 H_z}{\partial z^2} + k^2 H_z = m_z \tag{23.1}$$

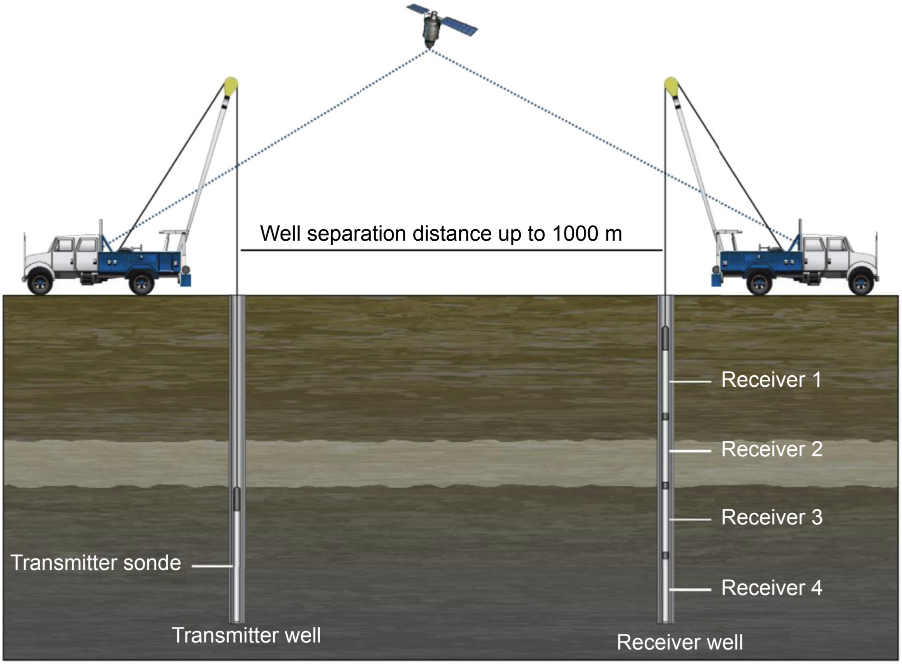
Well separation distance up to 1000 m
Receiver 1
Receiver 2
Receiver 3
Receiver 4
Transmitter sonde
Transmitter well
Receiver well

Figure 23.3 Cross-well EM acquisition system. A magnetic dipole transmitter is lowered into the first well (left). In the second well (right), an array of four receivers is deployed. Magnetometers in the receiver array can measure magnetic fields ten orders of magnitude smaller than the earth's static magnetic field. The transmitter and receiver components are linked wirelessly between wells and spaced up to 1 km apart.
From Al-Ali et al. (2009). Graphic copyright Schlumberger. Used with permission.

Table 23.1 **Distance versus casing. EM induction cross-well surveys are constrained by casing type and formation conditions**

Transmitter well	Receiver well	Maximum well spacing
Open hole	Open hole	1000 m
Fibreglass casing	Fibreglass casing	1000 m
Open hole	Chromium steel casing	500 m
Open hole	Carbon steel casing	450 m
Chromium steel casing	Chromium steel casing	350 m

Adapted from Al-Ali et al. (2009).

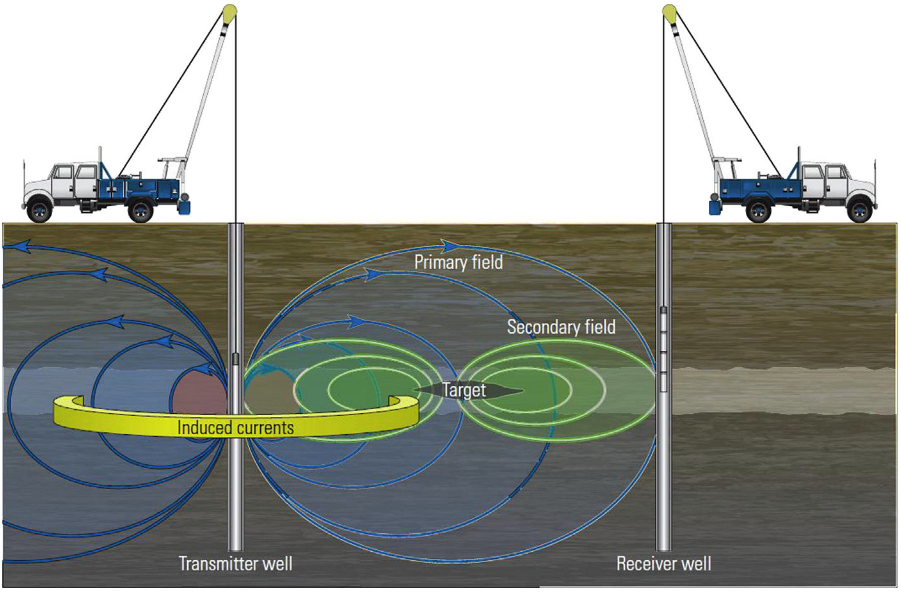

Figure 23.4 Primary and secondary fields. An alternating current excites the magnetic dipole transmitter coil to send an electromagnetic field into the formation. This primary field induces eddy currents that, in turn, generate a secondary alternating electromagnetic field whose strength is inversely proportional to formation resistivity. The secondary electromagnetic field is detected at the receiver array along with the primary field.
From Al-Ali et al. (2009). Graphic copyright Schlumberger. Used with permission.

For a multiturn loop (or coil), the magnetic dipole moment in the preceding equation is $m = \mu_r NAI$, representing the strength of the source (where A is the cross-sectional area, N is the number of windings, I is the current flowing in the windings and $\mu_r = \mu/\mu_0$ is the effective magnetic permeability of the core relative to free space).

Equation (23.1) is the Helmholtz wave equation commonly associated with a propagating energy field such as a seismic field (Eqn (22.4)). For low-frequency EM waves where the dielectric constant can be essentially ignored, the propagation wavenumber, $k = \sqrt{i\sigma\omega\mu}$, is complex, leading to the diffusive nature of the fields (here, $\sigma = 1/\rho$ is the formation conductivity, $\omega = 2\pi f$ is the angular frequency (with frequency f), μ is the magnetic permeability and $i = \sqrt{-1}$). The diffusive nature means that the waveform changes in shape and amplitude as it propagates through the medium, with higher frequency fields attenuating more rapidly than the lower ones, and the phase shifts as the energy moves away from the source.

For a receiver at the same depth level as the source, the solution to Eqn (23.1) is given by the sum of primary and secondary fields (Wilt & Alumbaugh, 2014):

$$H_z = H_{z,\mathrm{primary}} + H_{z,\mathrm{secondary}} = \frac{m}{4\pi \mathrm{r}^3}\left(k^2\mathrm{r}^2 - ik\mathrm{r} - 1\right)\mathrm{e}^{-ik\mathrm{r}} \tag{23.2}$$

The total field is, thus, a function of the complex propagation constant k. To illustrate how the earth conductivity affects the field, we need to separate the in-phase (real) and out-of-phase (imaginary or quadrature) field components and combine terms. The quantity of plane-wave skin depth, $\delta = \sqrt{2/(\sigma\omega\mu)}$, can be used to represent the distance that a propagating plane wave attenuates to$1/e$ of its initial value and experiences a phase-shift of one radian (57.3°). Equation (23.2) can be written in terms of the induction number r/δ as follows:

$$H_z = H_{z,\text{primary}} + H_{z,\text{secondary}} = \frac{m}{4\pi \mathrm{r}^3}\left(2i\frac{\mathrm{r}^2}{\delta^2} - (1+i)\frac{\mathrm{r}}{\delta} - 1\right)\mathrm{e}^{-\mathrm{i}\mathrm{r}/\delta}\,\mathrm{e}^{-\mathrm{r}/\delta} \tag{23.3}$$

At low frequency, low conductivity or close well spacing (i.e. $\mathrm{r}/\delta < 0.01$), the last term in the brackets dominates, and Eqn (23.3) yields the primary field. Data collected under these conditions are useful for determining the positions of the transmitters and receivers but insensitive to the formation conductivity. At high frequency, high conductivity or large well spacing ($\mathrm{r}/\delta > 10$), the exponential decay function ($e^{-\mathrm{r}/\delta}$) dominates, and the field is attenuated to below system noise levels. In this case, the induced currents shield the transmitter, and the fields are invisible to the receiver.

The intermediate range ($0.4 < \mathrm{r}/\delta < 10.0$) is where cross-well EM measurements are most useful (the sweet spot). At the low end of this range, the formation signal is roughly 10% of the total received signal; but at the high end, the fields are exponentially decaying due to the formation conductivity and, thus, very sensitive to the inter-well conductivity structure. In cross-well EM tomography, it is a general rule to operate at the highest frequency where one can still achieve a good signal/noise ratio.

In addition to the attenuation term ($\mathrm{e}^{-\mathrm{r}/\delta}$), Eqn (23.3) also has the oscillatory component given in the complex exponential $\mathrm{e}^{-\mathrm{i}\mathrm{r}/\delta} = \cos(\mathrm{r}/\delta) + i\sin(\mathrm{r}/\delta)$. The field, therefore, changes in phase as a function of the formation conductivity, a very useful attribute for inter-well imaging (e.g. $\mathrm{r}/\delta = \pi/2$ means the phase of the signal has changed by 90° during inter-well propagation, a very significant change if we can detect phase to within 1°).

Figure 23.5 (Wilt & Alumbaugh, 2014) shows the cross-well vertical magnetic field in-phase and out-of-phase (or quadrature) with respect to the transmitter current as a function of the induction number for a source and receiver at the same depth level. Note that here we plot the total field (primary plus secondary) and that the primary field is in-phase with the transmitter. The shaded region is the sweet spot for cross-well EM surveys, where the fields are sensitive to the formation conductivity but still large enough to be accurately measured.

The conductivity of subsurface ground with fully or partially saturated sediments (σ_m) is determined by their porosity (ϕ), conductivity of the pore fluid (σ_w) and water saturation (S), and it is defined by the following Archie's law (for shale-free, clean, sandy sediments):

$$\sigma_\mathrm{m} = (\phi^m/a)\,\sigma_\mathrm{w}\,S^n \tag{23.4}$$

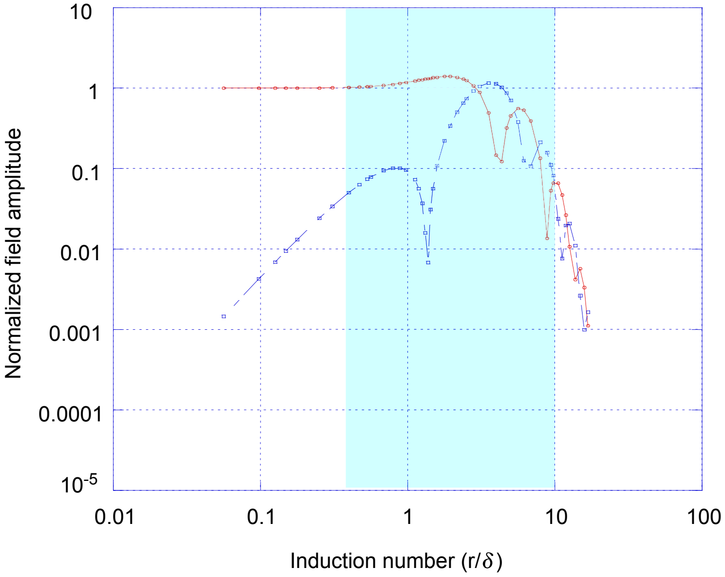

Figure 23.5 The in-phase (real) (red) and quadrature (imaginary) (blue) cross-well field in a homogeneous whole space.

where n is the saturation exponent ($n \cong 2$), m is the cementation exponent (for most sedimentary rocks $1.3 < m < 2.5$) and a is an empirical parameter ($0.5 < a < 1$, depending on the type of sediment) (Lange & Seidel, 2007).

An EM cross-well tomography survey can help map variations in the resistivity distribution within a reservoir, hence reflecting changes in the underlying resistivity-dependent properties such as porosity, fluid saturations and temperature. The detection of these changes can be valuable for hydrocarbon reservoir management. For instance, changes in porosity may be indicative of subsidence within a reservoir. Changes in saturation often suggest the advancing front of a water flood, whereas static saturation measurements may indicate bypassed pay. Temperature variations can help evaluate the effectiveness of a steam flood. During fluid injection, differences in resistivity distribution over time provide information about fluid movement, which in turn may provide clues to permeability distribution. EM cross-well tomography surveys can, hence, be utilized for a variety of oilfield applications, such as monitoring reservoir sweep efficiency, identifying bypassed pay, planning infill drilling locations and improving effectiveness of reservoir simulations (Al-Ali et al., 2009).

An EM survey dataset often constitutes several thousand measurements spanning about 50 logging depths at various transmitter—receiver view angles. To increase the signal/noise ratio of the weak secondary signal, the received signals are stacked and averaged over several hundred cycles per logging depth. Transmitter logging speeds may range from 600 to 1520 m/h, and it may require 12—30 h of field recording for a vertical section of 300 m. The distance covered by the multiple evenly spaced coils in the receiver array helps reduce logging times by spanning a wide interval for each logging depth.

Once the actual field survey data are acquired after careful pre-job planning (Al-Ali et al., 2009; Wilt & Alumbaugh, 2014), an image of the resistivity distribution between wells is generated through a nonlinear data-inversion process. This process employs an iterative procedure to update and minimize the differences between the measured data and the modelled responses in a least-squares sense (Abubakar et al., 2005; Al-Ali et al., 2009; Li, Abubakar, Li, Pan, & Habashy, 2010; Wilt & Alumbaugh, 2014). The resulting resistivity distributions are used to track inter-well fluid movements (Mieles et al., 2009; Wilt et al., 2012).

23.2.2 EM cross-well tomography case 1: imaging fluid flow on a reservoir-scale

To understand how uneven sweep of injected water was affecting production, an operator in UAE needed to monitor subsurface water flood movements between wells to help improve reservoir modelling in predicting water-front dimensions. The monitoring method should provide better lateral coverage than well logging and a higher vertical resolution than seismic surveys (Al-Ali, Al-Buali, et al., 2009; Al-Ali, Vahrenkamp, et al., 2009).

Deep-reading EM cross-well profiles of well pairs were obtained among three dedicated observer wells having chromium steel completions (with maximum inter-well distance being 350 m for such casings, Table 23.1). The EM survey conducted before injection established the baseline to enable tracking of changes in the inter-well reservoir space. Time-lapse survey images obtained 6 months after the baseline indicated effective water flooding from the horizontal injector well in the direction of observer Wells 1 and 3, with a large volume of water swept along a preferential flow direction (Figure 23.6), confirmed by well logs from a downhole reservoir saturation tool. The results of subsequent time-lapse EM surveys provided more details on the advancement of the water flood. From this information, engineers and geologists developed an improved reservoir-engineering flow-simulation model and devised strategy for placement of new injectors and infill development wells whilst fine-tuning performance of existing injectors for optimal recovery.

23.2.3 EM cross-well tomography case 2: water flood monitoring

In an oil field in Saudi Arabia, seawater was pumped into peripheral water injectors for several years to maintain reservoir pressure. The injected water replaces produced oil and has broken through in some of the producer wells. The distribution of injected water is variable, because of heterogeneities in this carbonate reservoir (Wilt et al., 2008). In one part of this giant field, resistivity measurements obtained by conventional wireline logs indicated two producing wells were nearly watered out. Because the resistivity distribution between the wells was unknown, the fluid saturation in the inter-well region could not be determined.

Water-cut measurements at the producer wells have been used to track the progression of the water front over time; but this method does not delineate the shape

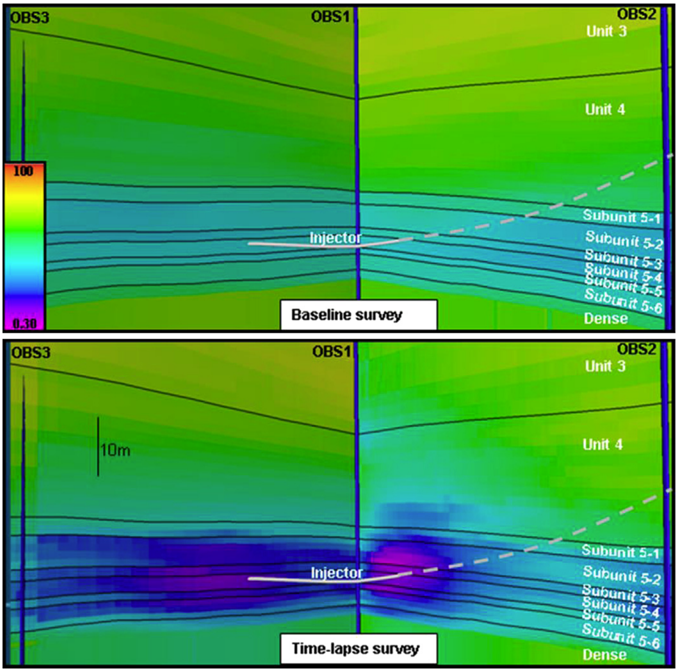

Figure 23.6 EM induction cross-well time-lapse survey images. Imaging foldout section among three dedicated observer wells (OBS1, OBS2 and OBS3) from water injection pilot at reservoir depths where the flooding occurred. The plots show baseline resistivity (upper) and the resistivity after six months of water flooding (lower).
From Al-Ali et al. (2009). Reproduced with permission of SPE.

of the front between the wells. The injected water is obtained from seawater or recycled produced water, with salinity being around 60 k-ppm. Fluid-swept zones can exhibit a drastic change in formation resistivity, from 30 to 50 Ω m to less than 2 Ω m, depending on the saturation and porosity. There are also corresponding changes in density but only minor changes in seismic velocity. A high resistivity contrast between injected water and oil in the reservoir would be apparent in deep-reading EM imaging profiles. Cross-well survey results would also facilitate the interpretation of formation resistivity to fluid saturation (Marsala et al., 2008).

A deep-reading EM cross-well survey was, therefore, conducted between producing wells 845 m apart on the west flank of the reservoir (Marsala et al., 2008), yielding several thousand data points at an operating frequency of 100 Hz. The processed survey indicated that the resistivity distribution differs significantly from the interpolated baseline cross-section based solely on pre-survey well logs (Figure 23.7). Although conventional resistivity logs indicated the near-wellbore section was essentially watered out, a deep-reading EM survey revealed areas of variable sweep efficiency between the wells (Al-Ali et al., 2009). The final results of this pilot field study have been described by Marsala et al. (2008).

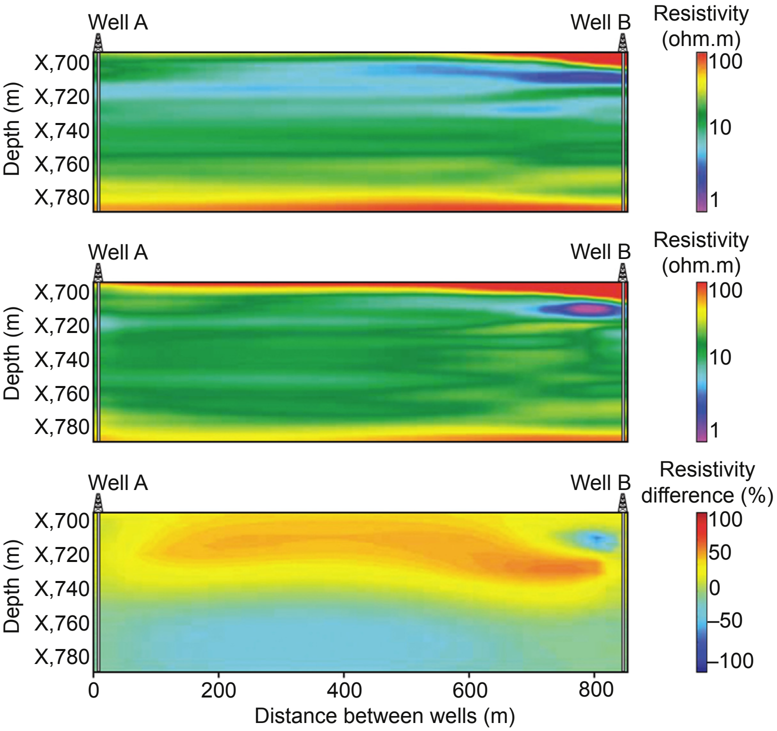

Figure 23.7 A big difference. The baseline model (top panel) inferred from conventional resistivity logs seems to indicate the reservoir interval between the wells is watered out, and the conductive injected fluid (blue area, top of the section) is sweeping the reservoir. By contrast, the inverted deep-reading EM resistivity image (middle panel) shows a higher resistivity range (green to yellow) in the same section, indicative of oil. The resistivity differences between the baseline and inverted data (bottom panel) indicate the efficiency of the water flood is variable in an area known for higher porosity.

From Al-Ali et al. (2009). Graphic copyright Schlumberger. Used with permission.

23.2.4 EM cross-well tomography case 3: imaging steam fronts

In a heavy-oil field in the San Joaquin Valley of California, cyclic steam injection technique is used to enhance production in several reservoirs. The steam-injected well is shut in for several days to allow hot steam to disperse and thin the oil by reducing its viscosity. The well is then opened and the thinned oil is produced.

The steeply dipping and complex geology of this large field (52 km^2) made it a challenging task for the operator to determine the vertical and radial distributions of steam around each injector and, hence, to have an overall better understanding of how heat is distributed through the reservoir after steam injection.

The proposed approach was to image the reservoir's resistivity response to steam injection. Induction well logging data show that reservoir resistivity values typically decrease by 35—80% after steam injection. This response is due to the fact that as temperature increases, rocks become less resistive; the response will also be seen when lower resistivity salt water replaces high-resistivity oil. The sensitivity to resistivity changes made deep-reading EM cross-well tomography an obvious candidate technique for tracking the injected-steam distribution and identifying swept zones in the reservoirs. Using cross-well EM resistivity tomography, the operator would be able to infer structure, temperature distribution and residual saturation of steam-affected reservoir volumes.

During the planning stage a baseline model for EM tomographic inversion was constructed. This model incorporated conventional resistivity logs obtained before the wells were cased or subjected to steam injection. Deep-reading EM transmitters and receivers were deployed in two wells once the feasibility of the survey had been determined for mapping the steam-affected zone between wells. The resulting resistivity image from the survey clearly revealed depleted and unswept zones within the reservoir (Figure 23.8). Data from this cross-well survey enabled the operator to map the effects of steam injection, guide field development plans and improve reserves estimates (Al-Ali et al., 2009).

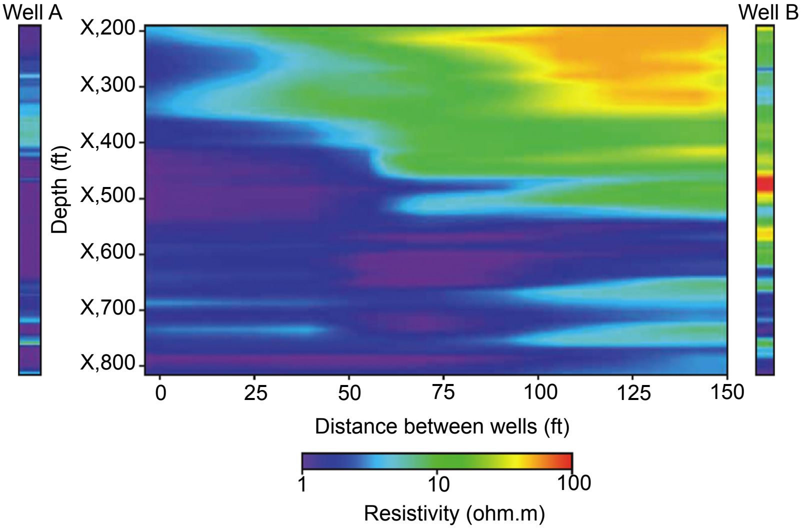

Figure 23.8 Resistivity profile between wells. Low resistivity (blue shading) is a typical characteristic of shale layers and steam-swept zones; at the other end of the spectrum, higher resistivities (orange to red) are a characteristic of unswept oil sands. Intermediate resistivities (green) represent transition zones between steam and oil. This deep-reading EM survey imaged an abrupt boundary midway between wells — the resistivity changes from 2 Ω m in the depleted zone to more than 50 Ω m in the unswept zone. The low resistivity most probably results from replacement of oil by formation of water and steam condensate injected from a well to the left of this survey.

From Al-Ali et al. (2009). Graphic copyright Schlumberger. Used with permission.

23.3 Potential of tomography in hydrocarbon production monitoring

The previous section focused on the oilfield use of EM tomographic techniques for reservoir fluid-movement monitoring on a large scale (~100 m to 1 km). In this section, the status on the research and development of various process tomography techniques relevant to the understanding of multiphase flows in pipes (diameter < 1 m) and to the online measurement of oil-gas production will be described.

The advent of new surface multiphase flowmeter (MPFM) technology is fundamentally changing the production monitoring of complex flows from oil-gas production wells. This transformation is driven by new technology that accurately measures rapid variations in oil-water-gas multiphase flows that previously were difficult to quantify. The capability to measure multiphase flow in real time increases operational efficiency, saving both time and cost. It is now possible to allocate hydrocarbon production without conventional phase separation and to overcome processing bottlenecks in surface facilities (Figure 23.9). Accurately quantifying individual fluid phases in a production stream allows operators to make more informed decisions about well performance, to better identify, understand and remediate problematic wells, optimize artificial lift operations and build dynamic reservoir models (Xie, Atkinson, & Lenn, 2007; Pinguet, 2012).

Unlike conventional test separators, an MPFM continuously measures gas, oil and water flow rates without physically separating the flow-stream into individual fluid phases, giving measurements within minutes of being placed in operation. The pressure drop across an MPFM is significantly less than for conventional separators, allowing wells to be tested close to actual producing conditions. In permanent metering applications, these devices have minimal footprints at surface locations or on offshore platforms.

In the subsea environment, an MPFM provides substantial cost savings through downscaling or elimination of surface well testing facilities and subsea test lines. Continuous measurement with an MPFM can also help identify potential flow assurance risks – blockages in the subsea production systems (e.g. hydrates, asphaltenes, wax, sand, scale) or breakthrough of first formation or injection water. This MPFM capability enables oil-gas operators to make appropriate risk mitigation decisions, for example, injection of hydrate and/or corrosion inhibitors in time and at an appropriate injection rate (Couput, 2011; Pinguet et al., 2013).

Oil-gas-water multiphase flows produced from oil-gas wells are very complex in nature. The accurate measurement of the individual phase flow rates demands a flowmeter with a combination of multiple measurement principles for phase fraction and phase velocity measurements (Figure 23.10), such as EM, single- or dual-energy gamma ray and Venturi differential pressure (for recent modelling and flow visualization work of multiphase flow through a Venturi, see Gajan, Salque, Couput, & Berthiaud, 2013; Paladinoa & Maliska, 2011). To reduce the uncertainty of flow-regime variations in the accuracy of multiphase flow rate measurements, most commercial MPFMs are installed vertically to tackle flow regimes with more axi-symmetry than horizontal flows (Figure 23.11, Dahl, 2005). MPFM measurement

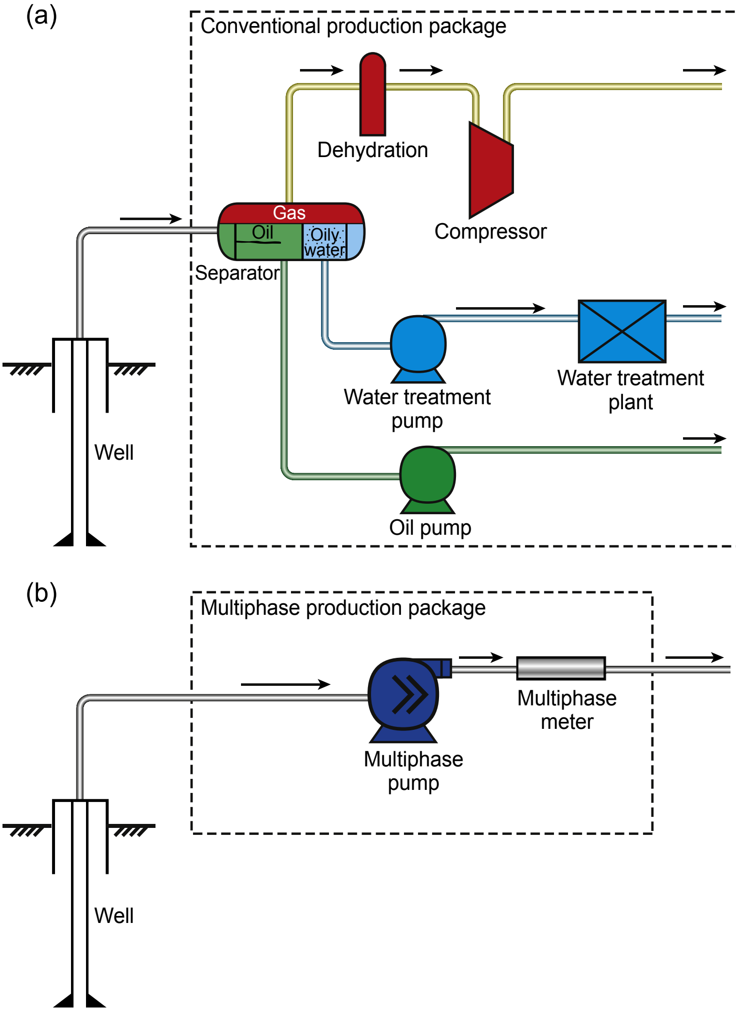
(a)
Conventional production package
Dehydration
Compressor
Gas
Oil
Oily water
Separator
Water treatment pump
Water treatment plant
Oil pump
Well
(b)
Multiphase production package
Multiphase pump
Multiphase meter
Well

Figure 23.9 Comparison of the conventional permanent production scenario with a separator, associated equipment and pipelines (a) with the cost-saving scenario (b) that only needs a multiphase pump and meter.
From Pinguet, 2012, *Fundamentals of Multiphase Metering*, 2nd Edition, Schlumberger, p. 11; used with permission.

accuracy of individual phase volumetric flow rates is generally within ±5 to ±10% of reading for gas volume fractions (GVFs) up to about 95%. Higher GVF wet-gas flow metering often requires different techniques to achieve good accuracy in liquid as well as gas flow rate measurements (Xie et al., 2007). Further descriptions of various commercial MPFMs and the measurement strategies can be found in an industrial monograph (Pinguet, 2012), text book (Falcone, Hewitt, & Alimonti, 2010) or review paper (Thorn, Johansen, & Hjertaker, 2012).

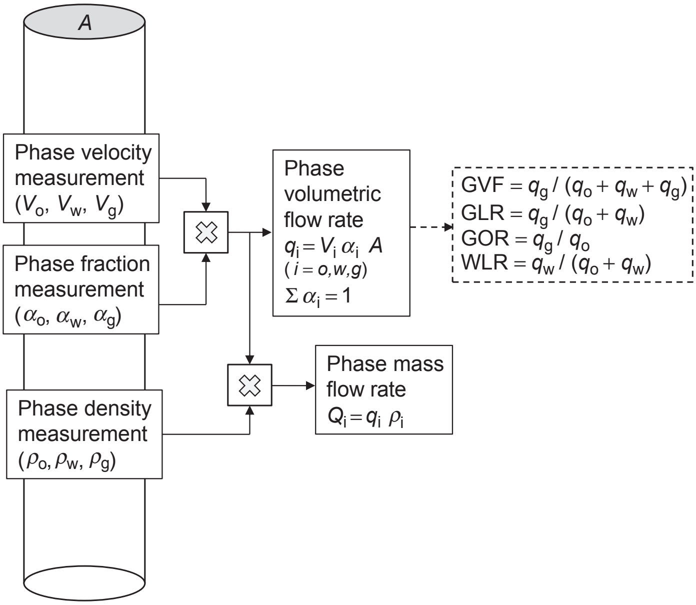
A
Phase velocity measurement (V_o, V_w, V_g)
Phase fraction measurement (α_o, α_w, α_g)
Phase density measurement (ρ_o, ρ_w, ρ_g)
Phase volumetric flow rate
$q_i = V_i\,\alpha_i\,A$
($i = o,w,g$)
$\Sigma\,\alpha_i = 1$
$GVF = q_g / (q_o + q_w + q_g)$
$GLR = q_g / (q_o + q_w)$
$GOR = q_g / q_o$
$WLR = q_w / (q_o + q_w)$
Phase mass flow rate
$Q_i = q_i\,\rho_i$

Figure 23.10 Inline oil-water-gas multiphase flow measurement problem. Phase volumetric flow rate is inferred from phase fraction and phase velocity measurements; further measurement of phase density is needed to determine phase mass flow rate (pressure and temperature sensors are often needed for the determination of phase density; not shown here). Multiphase flow parameters such as gas volume fraction (GVF), gas—liquid ratio (GLR), gas oil ratio (GOR) and water liquid ratio (WLR) can be derived. In some of the multiphase flow meters, WLR is measured together with the total liquid flow rate $q_L = q_w + q_o$; the oil and water flow rates are then derived from $q_w = WLR\ q_L$ and $q_o = (1 - WLR)\ q_L$.

Process tomography has been conceived to have the potential of measuring dynamic multiphase processes such as multiphase flows of complex regimes through a pipeline (Thorn et al., 1990; Plaskowski, Beck, Thorn, & Dyakowski, 1995; Williams & Beck, 1995; Chaouki, Larachi, & Dudukovic, 1997). The basic concept is to mathematically reconstruct the phase holdup and phase velocity profiles at a sufficient spatial and temporal resolution from appropriate multiple measurements made at a pipe's periphery. The individual phase volumetric flow rates are then derived by appropriately integrating phase holdup and phase velocity profiles over the pipe cross-section (individual mass rates are derived given the phase densities). The challenge with multiphase flow measurement is that both the phase distribution and the phase velocity profile vary significantly in time and space, as manifested by various flow regimes mapped for vertical and horizontal pipe inclinations (Figure 23.11, Dahl, 2005).

Process tomography, either as a standalone system or as an add-on to an existing MPFM, has the potential to improve multiphase metering accuracy by reducing flow-regime dependency. With this being achieved, it would enable an MPFM to

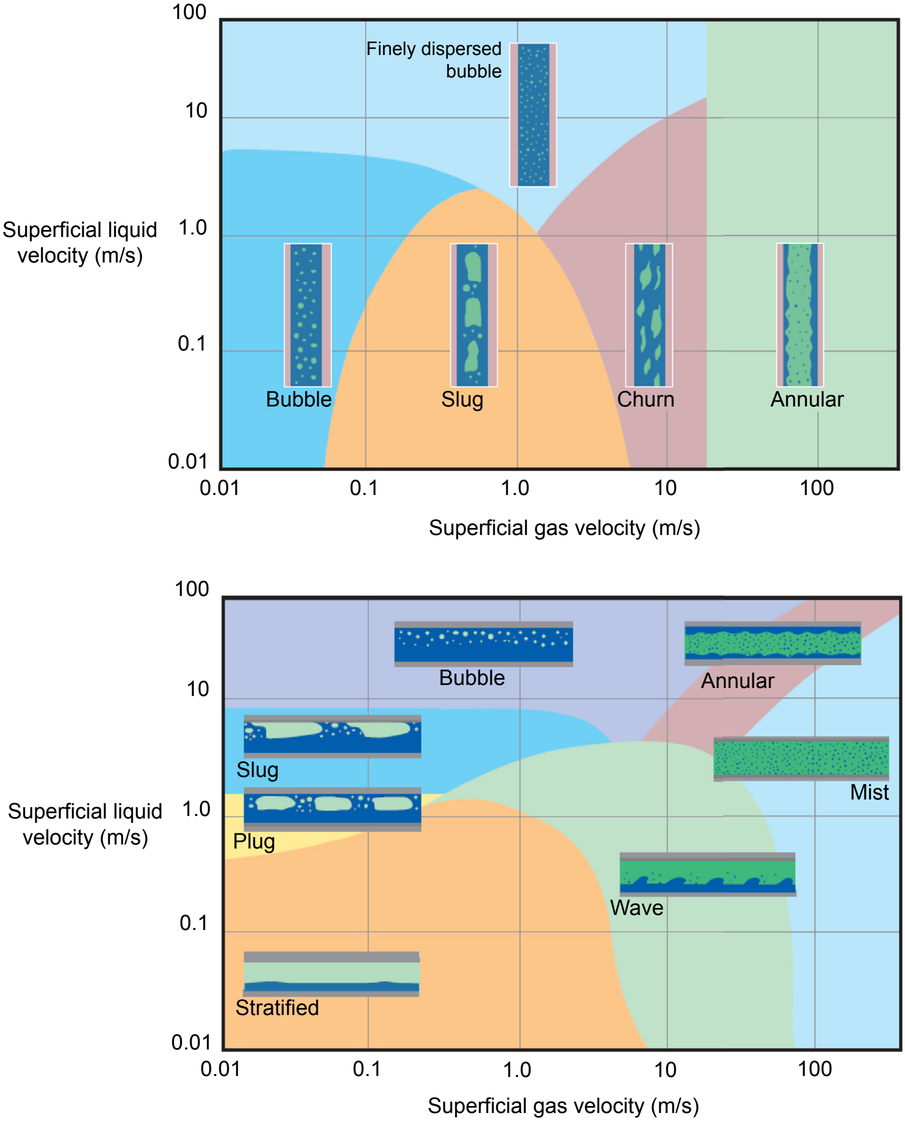

Figure 23.11 Vertical (top) and horizontal (bottom) flow patterns.
From NFOGM and Tekna, 2005, *Handbook of Multiphase Metering*; used with permission.

operate over much wider flow conditions, with less dependency on flow models. Some level of tomographic (phase-fraction) measurements based on multiview microwave, electrical impedance or electrical capacitance sensing have appeared in surface MPFMs (Scheers & Wee, 2011; Brandt, Tol, & Lars, 2009) and in downhole production logging tools (Xie et al., 2005, 2007; Hallundbaek & Kjærsgaard-Rasmussen, 2010; Kjærsgaard-Rasmussen & Meyer, 2011).

It is yet to be demonstrated that tomography-based techniques can measure individual phase flow rates more accurately than the existing commercially available MPFMs. Magnetic resonance is the only technique that can map the 3D flow field (fraction and velocity) of relatively slow-moving fluid in complex geometries. Considerable developments are needed to apply magnetic resonance to oilfield multiphase flow measurement in terms of enhancement in system response time, velocity range and of reduction in weight and cost. A few prototypes are under development (Appel, Freeman, & Pusiol et al., 2011; Pusiol et al., 2012; Ong, Chen, & Bussear, 2012; Fordham, 2013).

Most of the academic and industrial research efforts have been devoted to more accurately profiling multiphase flow phase fraction, based on electrical tomography (RF/microwave, impedance, capacitance, resistance, magnetic, electrostatic, wire-mesh sensors; Table 23.2(a)), gamma-ray and X-ray tomography (Table 23.2(b)) or their combinations. Dispersed phase velocity profiling is done mainly by cross-correlating axially spaced dual-plane phase-fraction segment images, using fast X-ray, electrical capacitance and conductance tomographic sensors (Table 23.2(a) and (b)). EM flowmeters using single- or multiple-pair of potential-sensing electrodes have been investigated for (water) continuous phase velocity measurement or profiling (Wang, Tian, & Lucas, 2007; Leeungculsatien & Lucas, 2013). Other tomography modalities, such as ultrasound, optical and thermal have also been investigated (Table 23.2(c)). Cross-validation of the accuracy of tomography-based multiphase-flow measurement system is also examined (Table 23.2(d)).

The key technical challenges are to demonstrate the capability of determining accurately individual phase holdups and phase velocities, for both oil- and water-continuous flows, over a wide range of flow regimes, water and gas cuts and fluid properties. Spatial and/or temporal resolutions inherent with different physical measurement principles can pose limitations to measuring fast varying multiphase flows (sometimes limited by the accuracy and speed in the image reconstruction); further development is continuing (Wang, Hu, Wang, & Wang, 2012; Kim, Khambampati, Kim, & Kim, 2013; Liu, Lei, Wang, & Liu, 2013; Liu, Yang, He, & Tan, 2013; Sun & Yang, 2013). Cost, robustness and reliability are also issues to be addressed in transferring technology to industrial applications.

Coined as ‘tomometry’ (Thorn et al., 2012), the information output from a process tomography system can be a few key process parameters, such as multiphase-flow pattern, phase fraction and water/liquid ratio (Section 23.3.1 below). A MPFM based on multiple-electrode impedance measurements and three gamma-ray beams (for flow-regime identification to reduce fraction-sensing error) has been used in oilfield downhole applications (Johansen et al., 2012).

23.3.1 Case study: ECT for multiphase-flow WLR and liquid fraction measurement

In this section, the measurement results of oil-continuous multiphase flows from a research prototype eight-electrode ECT sensor (Figure 23.12) are briefly described (for further details see Li et al., 2013). In the prototype, to minimize the variation

Table 23.2(a) **Electrical tomography techniques for multiphase flow measurement and research**

Modality	Physics parameter(s)	Phase fraction	Phase velocity	References
RF/microwave tomography	Complex permittivity $\varepsilon^* = \varepsilon' - j\sigma/(\varepsilon_0\omega)$ profile from amplitude-attenuation and/or phase-shift data	Gas-, oil- and water-continuous flows: water fraction, WLR (with γ-ray liquid fraction input)	(1) Venturi	(1) MPFM based on parametric tomography Scheers and Wee (2011), Taherian and Habashy (1996), Wu et al. (2009)
Electrical impedance tomography (EIT)	Complex permittivity $\varepsilon^* = \varepsilon' - j\sigma/(\varepsilon_0\omega)$ profile from $Y = G + j\omega C$ data (capacitance C; conductance G)	Gas-, oil- and water-continuous flows: (1) water fraction, WLR, (2) and with γ-ray liquid fraction input	(3) $V_{\text{dispersed-phase}}$ by cross-correlation, (4) Venturi	(2)(4)(3) Brandt et al. (2009) (MPFM with six-electrode rotating near-wall regions sensing), (1)(4) Xie (2013b)
Electrical capacitance tomography (ECT)	Permittivity ε profile from capacitance (C) data	Gas- or oil-continuous flows: water fraction, (2) WLR and liquid fraction, (3) solids fraction (in gas)	(1) Venturi (4) $V_{\text{dispersed-phase}}$ (profile) by dual-plane cross-correlation	Yang, Stott, Beck, and Xie (1995), Yang et al. (2004), Hasan and Azzopardi (2007), (1) Huang, Xie, Zhang, and Li (2005); (2) Li et al. (2013); (1)(2) Xie (2013a); (3)(4) Yang and Liu (2000), Hunt, Pendleton, and Byars (2004)
Electrical resistance tomography (ERT)	Conductivity σ profile from conductance (G) data	Water-continuous flows: water fraction, (4) insulated electrode sensor design, (5) flow-regime identification	(1) $V_{\text{dispersed-phase}}$ (profile) by dual-plane cross-correlation, (2) Venturi, (3) $V_{\text{continuous-phase}}$ by (two-electrode) electromagnetic flow meter	(1) Li et al. (2009), Dong, Xu, Xu, Hua, and Qiao (2005), (2) Meng et al. (2010), (3) Deng, Li, Wei, Yan, and Yang (2011), (4) Wang, Zhang, Huang, Ji, and Li (2013), (5) Tan, Dong, and Wu (2007)

Continued

Table 23.2(a) **Continued**

Modality	**Physics parameter(s)**	**Phase fraction**	**Phase velocity**	**References**
ERT and ECT dual modality	Composite permittivity ε and conductivity σ profiles from conductance and capacitance data	Oil- and water-continuous flows: water fraction, WLR (separate C and G electrodes)		Qiu, Hoyle, and Podd (2007), Glen and Ross (2010), Primrose, et al. (2010)
Electrical magnetic tomography (EMT) Magnetic induction tomography (MIT)	Conductivity σ profile from water-induced eddy-current data (magnetic coils excitation and pick-up)	Oil- and water-continuous flows: water fraction		Liu et al. (2013)
Electromagnetic velocity profiler (multielectrode)	Flow-velocity induced potential−difference profile measured by electrodes at boundary	Water-continuous flows: (liquid fraction input from ERT)	$V_{\text{continuous-phase}}$ (profile)	Wang et al. (2007), Leeungculsatien and Lucas (2013)
Electrostatic charge tomography and ECT dual modality	Electrostatic-charge-induced voltage profile at boundary	Solids fraction profile (in gas)	($V_{\text{dispersed-phase}}$ by cross-correlation)	Zhou and Zhang (2013), Zhou et al. (2013), Zhang, Hu, Dong, and Yan (2012)
Wire-mesh sensor (WMS) − capacitance	Direct mapping of permittivity ε profile	Gas fraction (profile) bubble size distribution		Da Silva, Thiele, Abdulkareem, Azzopardi, and Hampel (2010)
Wire-mesh sensor (WMS) − conductance	Direct mapping of conductivity σ profile	Gas fraction (profile)	(1) Gas velocity profiles by auto-/cross-correlation (2) Gas velocity (profile) by cross-correlation with fast X-ray	(1) Hoppe, Grahn, and Schütz (2010), (1) Beyer, Lucas, and Kussin (2010), (2) Zhang, Xu, Wu, Li, and Li (2013), Hampel et al. (2009)

Table 23.2(b) Nucleonic tomography techniques for multiphase flow measurement and research

Modality	Physics parameter(s)	Phase fraction	Phase velocity	References
γ-ray tomography	High-energy mass/linear attenuation coefficient μ	Liquid (or gas) fraction	(1) Venturi (2) Cross-correlation	(1)(2) Chen, Li, Ye, and Yu (2011), Johansen, Hampel, and Hjertaker (2010), Sætre et al. (2010), Bruvik, Hjertaker, and Hallanger (2010), Johansen et al. (2012), Sætre, Johansen, and Tjugum (2012), Xue, Wang, Yang, and Cui (2013)
Dual-energy γ-ray tomography	Dual-energy mass/linear attenuation coefficient μ	Liquid (oil, water) and gas fractions, WLR		Frøystein, Kvandal, and Aakre (2005)
X-ray tomography	Mass/linear attenuation coefficient μ	Liquid (or gas) fraction	(1) Cross-correlation	(1) Bieberle et al. (2010), Johansen et al. (2010), Hu, Nuland, and Lawrence (2011)
Positron tomography	Absorption coefficient (from positron radiation source and γ-ray detector array)	Gas/oil/water fractions	Cross-correlation	Li and Chen (2013)

Table 23.2(c) **Other tomography techniques for multiphase flow measurement and research**

Modality	Physics parameter(s)	Phase fraction	Phase velocity	References
Ultrasound tomography	Reflection (acoustic impedance) and/or transmission attenuation	Gas fraction, flow-regime identification, gas—liquid interface detection	Liquid velocity from range-gated Doppler	Xu and Xu (1998), Murai, Tasaka, Nambu, Takeda, and Roberto Gonzalez (2010), Huang and Xie (2013)
Optical tomography	Transmission attenuation	Solids fraction (in gas)		Rahim, Yunos, Rahiman, and Rahim (2010), Muji et al. (2013)
Thermal tomography	Thermal conductivity profile	Water fraction profile (of oil-water flow)		Hoffmann, Amundsen, Schulkes, & Schüller (2012)

in horizontal flow regime over a wide range of GVFs (Figure 23.11), a novel flow-conditioning device is used at the upstream of the ECT sensor (not shown) to form predominantly a gas—liquid annular flow.

Figure 23.13 shows the data and image inversion steps developed to determine the water/liquid ratio (WLR) from the raw capacitance measurements C_m by: (i) converting the measured normalized capacitance C_n to mixture-permittivity ε_m, and (ii) converting ε_m to WLR and liquid fraction for a gas—liquid flow based on the dielectric mixing laws shown. The outcome of the key step (i) also permits a more quantitative reconstruction of the mixture-permittivity image (Figure 23.14) based on multiview ε_m data (rather than based on the normalized capacitance C_n) for transient gas—liquid flows.

Working in the mixture-permittivity parameter domain also permits the use of appropriate dielectric mixing models (as shown in Figure 23.13) for the determination WLR and/or liquid fraction of gas—liquid flows. The purpose of using a

Table 23.2(d) Cross-validation of tomography techniques for multiphase flow measurement and research

Modality 1	Modality 2	Comparative measurement	References
X-ray tomography	ECT	Solids (or gas) fraction	Rautenbach, Mudde, Yang, Melaaen, and Halvorsen (2013)
X-ray tomography	Wire-mesh sensor (conductance)	Gas fraction profile Gas velocity profile (by cross-correlation of X-ray and WMS)	Zhang et al. (2013)
X-ray tomography	Thermal sensor array	Water fraction profile (of oil-water flow)	Hoffmann et al. (2012)
Dual-energy γ-ray (traversable)	Single-energy γ-ray (stationary) — non-tomographic	Oil-water-gas three-phase fraction profiles (at 100 bar), flow pattern identification	Hoffmann and Johnson (2011), Kaku Arvoh, Hoffmann, and Halstensen (2012)
Wire-mesh sensor (WMS) — conductance	Air—water flow-loop reference	Time-averaged integrated gas flow rate (from gas fraction and velocity profiles)	Beyer et al. (2010)
Electrical tomography	Pressure drop	Oil—water flow liquid fraction	Zhang et al. (2013)

flow-conditioning device upstream of the ECT sensor is to create a gas-core and a liquid annulus at the ECT measurement section. As can be seen from the instantaneous permittivity images illustrated in Figure 23.14, a more steady gas core (or smoother liquid-layer) is formed at a relatively low GVF ($\sim$25%) than at a relatively high GVF ($\sim$63%). As expected, the permittivity of an oil/water mixture near the pipe wall region increases when the WLR increases. The real-time images reconstructed by the linear back-projection method (shown in Figure 23.13) are also useful to indicate gas—liquid flow regimes. Figure 23.15 shows that the near-wall measurement (1-electrode apart) at low GVFs preferentially measures the liquid-layer mixture-permittivity, especially during the time intervals with the liquid-rich slugs passing (see Figure 23.14, GVF $\leq$ 0.4).

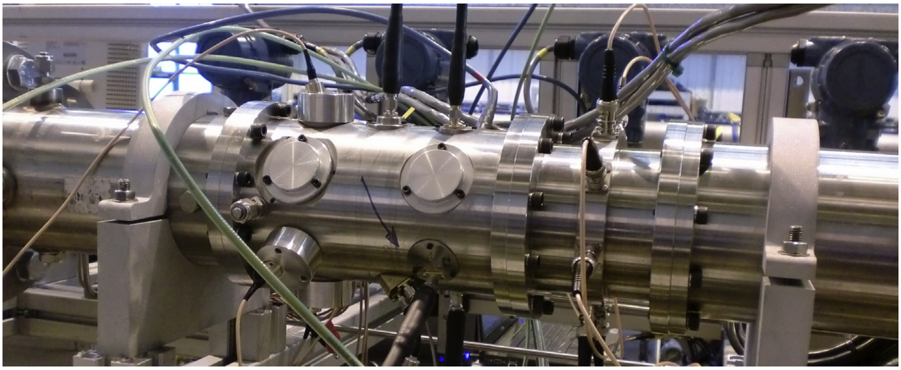

Figure 23.12 The eight-electrode ECT sensor tested on TUV-NEL multiphase flow facility. The experimental section instrumented with (from left to right, flow direction) ultrasound and electrical tomography sensors.

In multiphase flows, the WLR of the (oil/water) liquid is generally much more stable than the liquid fraction over a short measurement interval (say $\Delta T = 10$ s, with one or more liquid-rich slugs passing the sensors); this feature of near-wall localized sensing (in space) and/or dynamic liquid-rich slug mixture-permittivity data capturing (in time, at a fast rate say $\Delta t = 10$ ms) can yield a rolling estimate (within each ΔT interval) of a short time-average permittivity of liquid $\varepsilon_{\text{liquid}(\Delta T)}$. This then results in a rolling estimate of the liquid WLR by using an oil/water (uniform) mixing model for an oil-continuous flow:

$$\text{WLR}_{(\Delta T)} = \frac{\varepsilon_{\text{liquid}(\Delta T)} - \varepsilon_{\text{oil}}}{\varepsilon_{\text{liquid}(\Delta T)} + 2\varepsilon_{\text{oil}}} \tag{23.5}$$

From Figure 23.16 (left), it can be seen that by capturing and analyzing the mixture-permittivity data of a near-wall liquid-rich slug, the WLR can be estimated to ±5% for GVF up to about 90%, WLR up to ~40% (largely within the permittivity linearity range of near-wall electrode pairs). With respect to liquid fraction estimates, Figure 23.15 indicates that, at the same WLR and GVF, the mixture-permittivity from cross-pipe (i.e. opposite-electrode) measurement (which interrogates the entire gas-rich core) is much lower than that of the near-wall one. From instantaneous gas–liquid mixture-permittivity measured cross-pipe, an instantaneous and time-average liquid fraction can be obtained by using an appropriate gas–liquid mixing model as below, with near-wall sensed liquid-permittivity as input, viz:

$$\alpha_{\text{liquid}}(t) = \left(\frac{\varepsilon_{\text{mixture}}(t) - \varepsilon_{\text{gas}}}{\varepsilon_{\text{liquid}(\Delta T)} - \varepsilon_{\text{gas}}}\right)^{\frac{1}{x}} = \left(\frac{\varepsilon_{\text{mixture(cross-pipe)}}(t) - \varepsilon_{\text{gas}}}{\varepsilon_{\text{mixture(near-wall, liquid-slug)}(\Delta T)} - \varepsilon_{\text{gas}}}\right)^{\frac{1}{x}} \tag{23.6}$$

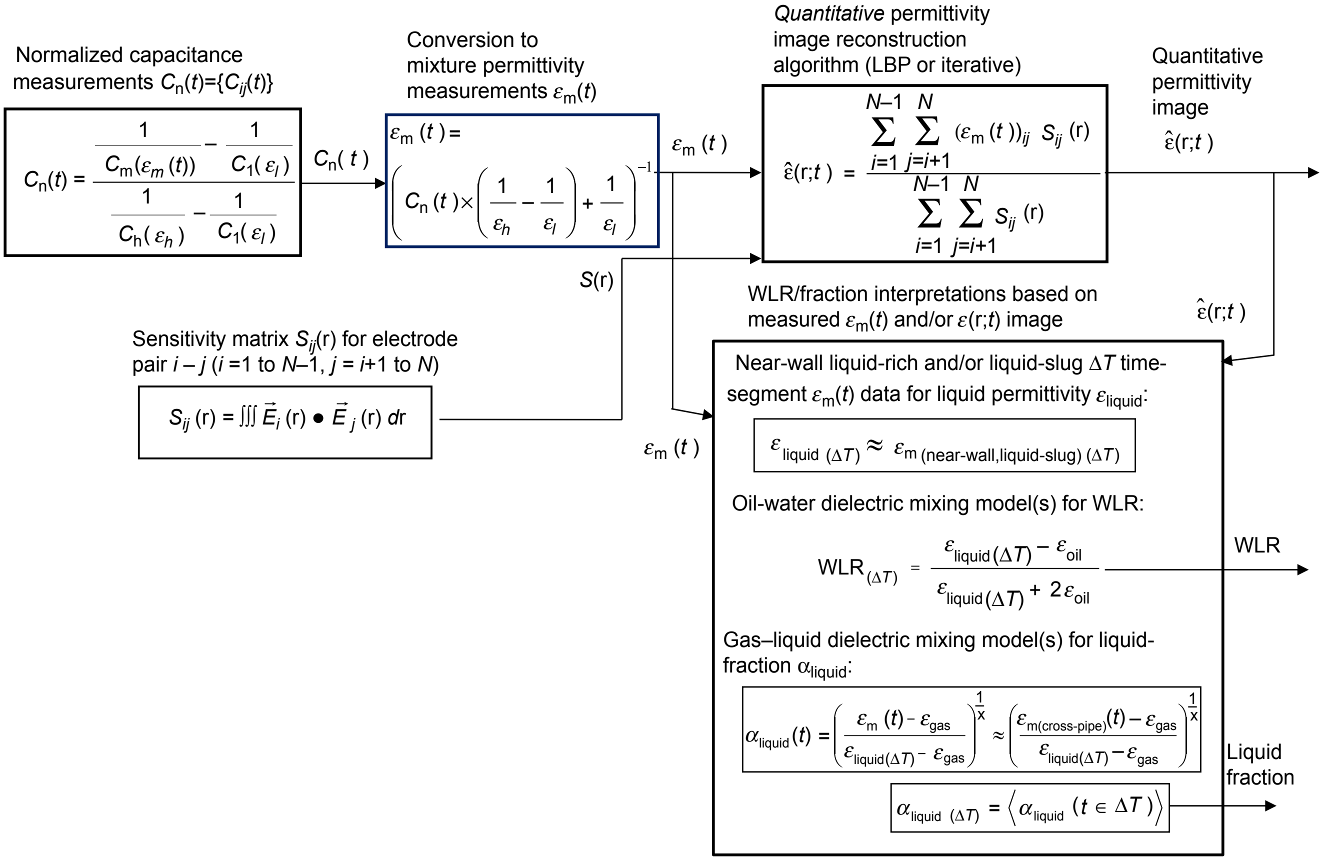
Normalized capacitance measurements $C_n(t)=\{C_{ij}(t)\}$
$C_n(t) = \dfrac{\frac{1}{C_m(\varepsilon_m(t))} - \frac{1}{C_1(\varepsilon_l)}}{\frac{1}{C_h(\varepsilon_h)} - \frac{1}{C_1(\varepsilon_l)}}$
$C_n(t)$
Conversion to mixture permittivity measurements $\varepsilon_m(t)$
$\varepsilon_m(t) = \left(C_n(t)\times\left(\frac{1}{\varepsilon_h}-\frac{1}{\varepsilon_l}\right)+\frac{1}{\varepsilon_l}\right)^{-1}$
$\varepsilon_m(t)$
Quantitative permittivity image reconstruction algorithm (LBP or iterative)
$\hat{\varepsilon}(r;t) = \dfrac{\sum_{i=1}^{N-1}\sum_{j=i+1}^{N}(\varepsilon_m(t))_{ij}\, S_{ij}(r)}{\sum_{i=1}^{N-1}\sum_{j=i+1}^{N} S_{ij}(r)}$
Quantitative permittivity image $\hat{\varepsilon}(r;t)$
$S(r)$
Sensitivity matrix $S_{ij}(r)$ for electrode pair $i-j$ ($i=1$ to $N-1$, $j=i+1$ to N)
$S_{ij}(r) = \iiint \vec{E}_i(r) \bullet \vec{E}_j(r)\, dr$
$\varepsilon_m(t)$
WLR/fraction interpretations based on measured $\varepsilon_m(t)$ and/or $\varepsilon(r;t)$ image
$\hat{\varepsilon}(r;t)$
Near-wall liquid-rich and/or liquid-slug ΔT time-segment $\varepsilon_m(t)$ data for liquid permittivity ε_{liquid}:
$\varepsilon_{liquid\ (\Delta T)} \approx \varepsilon_{m\ (near\text{-}wall,liquid\text{-}slug)\ (\Delta T)}$
Oil-water dielectric mixing model(s) for WLR:
$WLR_{(\Delta T)} = \dfrac{\varepsilon_{liquid(\Delta T)} - \varepsilon_{oil}}{\varepsilon_{liquid(\Delta T)} + 2\varepsilon_{oil}}$
WLR
Gas–liquid dielectric mixing model(s) for liquid-fraction α_{liquid}:
$\alpha_{liquid}(t) = \left(\dfrac{\varepsilon_m(t) - \varepsilon_{gas}}{\varepsilon_{liquid(\Delta T)} - \varepsilon_{gas}}\right)^{\frac{1}{x}} \approx \left(\dfrac{\varepsilon_{m(cross\text{-}pipe)}(t) - \varepsilon_{gas}}{\varepsilon_{liquid(\Delta T)} - \varepsilon_{gas}}\right)^{\frac{1}{x}}$
$\alpha_{liquid\ (\Delta T)} = \langle \alpha_{liquid}(t \in \Delta T) \rangle$
Liquid fraction

Figure 23.13 Inversion steps of permittivity image reconstruction and derivation of WLR and liquid fraction.

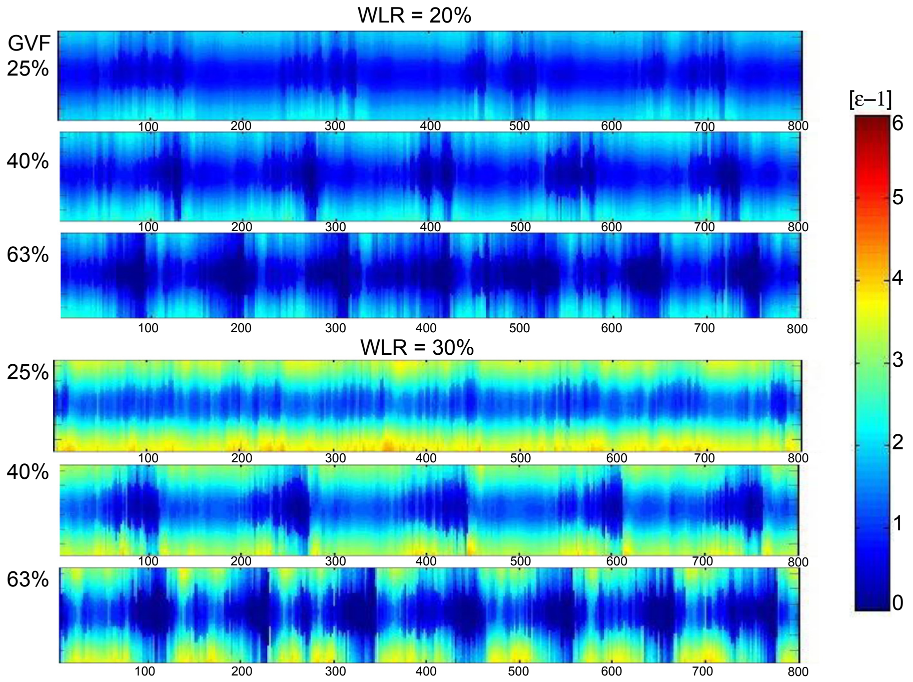

Figure 23.14 Instantaneous longitudinal cross-sectional images stacked with over 8 s (imaging frame rate at 100 frames per second). Permittivity-change colour scale $\varepsilon - 1 = 0\text{–}6$ as shown on the far right. Image reconstruction based on instantaneous permittivity of gas–liquid mixture for horizontal gas–liquid conditioned flows with total liquid rate $Q_l = 30\ \text{m}^3/\text{h}$, WLR = 20% and 30%, and GVF = 25%, 40% and 63%.

$$\alpha_{\text{liquid}(\Delta T)} = \overline{\alpha_{\text{liquid}}(t \in \Delta T)} \tag{23.7}$$

where x is an empirical factor for gas–liquid annular-type distribution (including GVF = 0).

The time-averaged liquid fractions derived from the cross-pipe mixture-permittivity data given in Figure 23.16 (right) show a good agreement with some of the liquid fractions measured by ultrasound sensors (Huang & Xie, 2013).

23.4 Future trends

Deep-reading resistivity tomography obtained through EM induction cross-well surveys can provide better petrophysical control in building reservoir models than surface seismic surveys. The capability to identify and monitor fluid fronts using cross-well EM measurements can be complemented by cross-well seismic imaging technique, which can delineate structure and monitor gas movement in the reservoir (Yu et al., 2008, Göktürkler, 2011). The detailed reservoir-level information obtained from

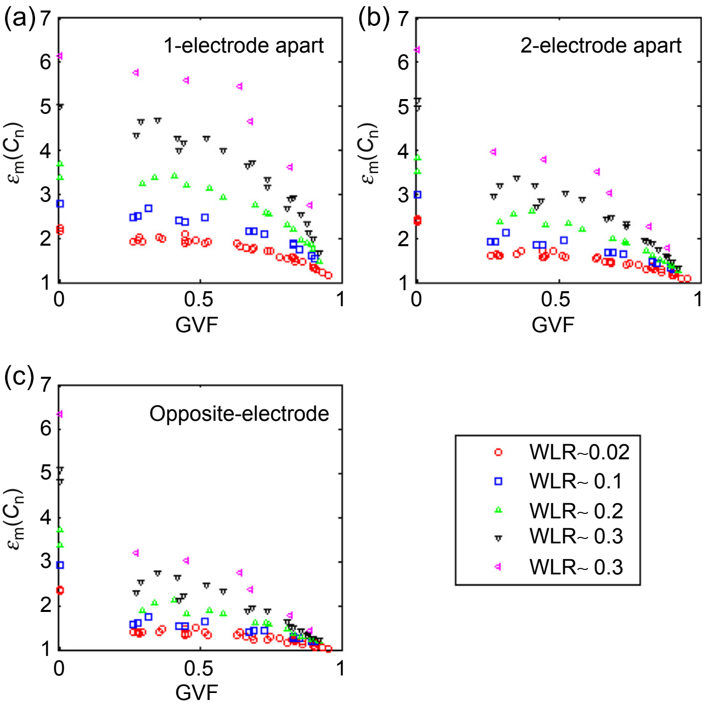

Figure 23.15 Plotted vs. GVF of gas–liquid horizontal conditioned flows with WLR up to ∼40%, with permittivity of mixture $\boldsymbol{\varepsilon}_{\mathbf{m}}$ calculated from normalized capacitance $\boldsymbol{C}_{\mathbf{n}}$ in Figure 23.13, for (a) 1-electrode apart, (b) 2-electrode-apart and (c) opposite-electrode. Note some $\boldsymbol{\varepsilon}_{\mathbf{m}}$ of 1-electrode apart are close to saturation for WLR > ∼40%.

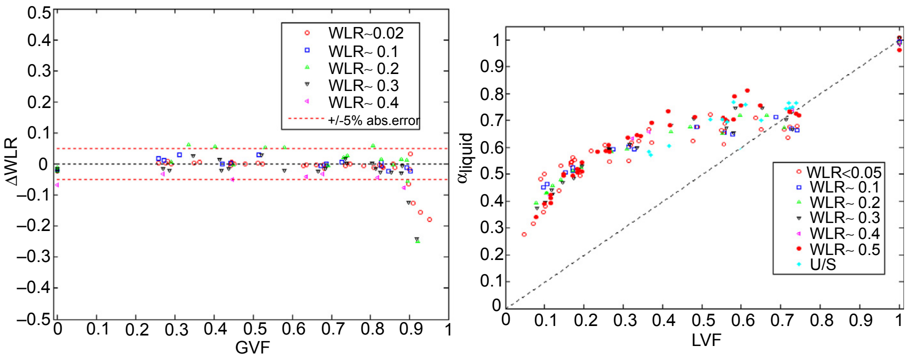

Figure 23.16 Left: Plotted vs GVF, absolute error in WLR estimated by ECT from permittivity of near-wall liquid-slug mixture by using Eqn (23.5) (∼60 s data acquisition interval). Right: Plotted vs. LVF (=1 − GVF), time-average liquid fraction α_{liquid} estimated by opposite-electrode mixture-permittivity data using Eqns (23.6) and (23.7). Ultrasound (U/S) sensor measured liquid fraction data also shown.

combined deep-reading measurements gives petrophysicists and reservoir engineers greater insight into how fluids move and interact, which will ultimately determine the decision-making of oilfield management and production (Al-Ali et al., 2009).

On the oil-gas production monitoring front, with technological innovations, multiphase flow meters are likely to be deployed in higher pressure and temperature environments. This could significantly expand subsea applications for MPFM technology, with additional applications onshore in heavy-oil thermal recovery (Pinguet et al., 2010) and natural gas production (Pinguet et al., 2013).

For permanent-metering applications, MPFMs with minimal calibration requirements are desirable. Research in a novel microwave measurement interpretation has demonstrated a potential multiphase flow WLR measurement system that is robust to changes in water salinity (Xie, 2006). It is shown feasible to characterize the salinity of multiphase flow from a combination of transmission and scattering gamma-radiation measurements (Sætre, Johansen, & Tjugum, 2010). This potentially has well-monitoring, flow assurance or diagnosis applications, such as detection of formation or injection water breakthrough and salinity-independent multiphase flow measurement.

Process tomography has the potential to improve MPFM accuracy by reducing flow regime dependency, identifying (and correcting for the effects of) flow regimes and measuring directly the individual phase fractions and phase velocities. This improvement would enable accurate measurement of multiphase flow rates, at surface and downhole, over a broader range of flow regimes, water and gas cuts and fluid properties with less dependency on flow models than current methods have. Continued collaborative research and joint industrial projects are needed to demonstrate that a process tomography-based MPFM can outperform existing MPFMs, ideally without using a radioactive source and at an acceptable cost.

23.5 Sources of further information and advice

- The Society of Exploration Geophysicists (SEG) journals: *Geophysics* and *The Leading Edge*
- The European Association of Geoscientists and Engineers (EAGE) journals: *Geophysical Prospecting* and *First Break*
- Other journals: *Petroleum Geoscience*, *Journal of Petroleum Geology*, *Flow Measurement and Instrumentation*, *Measurement Science and Technology* and *International Journal of Multiphase Flow*

Acknowledgements

We would like express our gratitude to Schlumberger for permission to publish this book chapter, and to several Schlumberger clients for permission to re-use some figures containing their data. Lisa Stewart, executive editor of Schlumberger *Oilfield Review* is thanked for her help in the preparation of this chapter. The work described in Section 23.3.1 was co-funded by the UK Technology Strategy Board (TSB); the project team consisted of Schlumberger, the University of Manchester and TUV-NEL.

References

Abubakar, A., Habashy, T., Druskin, V., Alumbaugh, D., Zhang, P., Wilt, M., et al. (2005). A fast and rigorous 2.5D inversion algorithm for cross-well EM data. *SEG Extended Abstracts, 24*, 534—537.

Al-Ali, Z. A., Al-Buali, M. H., AlRuwaili, S., Ma, S. M., Marsala, A. F., Alumbaugh, D., et al. (Summer 2009). Looking deep into the reservoir. *Oilfield Review, 21*(2), 38—47.

Al-Ali, M., Vahrenkamp, V., Elsembawy, S., Bhatti, Z., Reeder, S. L., Clerc, N., et al. (2009). Constraining inter-well water flood imaging with geology and petrophysics: an example from the Middle East. In: *SPE Middle East oil and gas show and conference, 15—18 March 2009*. Bahrain: SPE 120558.

Allen, D., Flaum, C., Ramakrishnan, T. S., Bedford, J., Castelijns, K., Fairhurst, D., et al. (Autumn 2000). Trends in NMR logging. *Oilfield Review, 12*(3), 2—19.

Alumbaugh, D. L., & Morrison, H. F. (1995). Monitoring subsurface changes over time with cross-well electromagnetic tomography. *Geophysical Prospecting, 43*(7), 873—902.

Appel, M., Freeman, J. J., & Pusiol, D. (2011). Robust multi-phase flow measurement using magnetic resonance technology. In: *Proceedings SPE Middle East oil and gas show (Manama, Bahrain, September 2011) SPE 141465*.

Beyer, M., Lucas, D., & Kussin, J. (2010). Quality check of wire-mesh sensor measurements in a vertical air/water flow. *Flow Measurement and Instrumentation, 21*, 511—520.

Bieberle, M., Schleicher, E., Fischer, F., Koch, D., Menz, H.-J., Mayer, H.-G., et al. (2010). Dual-plane ultrafast limited-angle electron beam X-ray tomography. *Flow Measurement and Instrumentation, 21*, 233—239.

Brandt, M., Tol, M., & Lars, A. R. (2009). Improving measurement quality and meeting changing operator challenges with the multiphase meter. Paper 8.2. In: *8th South East Asia hydrocarbon flow measurement workshop (Kuala Lumpur, Malaysia, 4—6 March 2009).*

Bruvik, E. M., Hjertaker, B. T., & Hallanger, A. (2010). Gamma-ray tomography applied to hydrocarbon multi-phase sampling and slip measurements. *Flow Measurement and Instrumentation, 21*, 240—248.

Chaouki, J., Larachi, F., & Dudukovic, M. P. (1997). Noninvasive tomographic and velocimetric monitoring of multiphase flows. *Industrial and Engineering Chemistry Research, 36*, 4476—4503.

Chen, J., Li, H., Ye, J., & Yu, H. (2011). *Gamma ray section imaging device, multiphase flow detecting device and detecting method*. Lanzhou Haimo Technologies. PCT patent application WO2012100385A1. March 28, 2011.

Couput, J.-P. (2011). Subsea multiphase measurements: where are we and what's next from an oil and gas operator perspective. In: *Proceedings 29th int. North Sea flow measurement workshop (Tønsberg, Norway, October 2011).*

Da Silva, M. J., Thiele, S., Abdulkareem, L., Azzopardi, B. J., & Hampel, U. (2010). High-resolution gas—oil two-phase flow visualization with a capacitance wire-mesh sensor. *Flow Measurement and Instrumentation, 21*, 191—197.

Dahl, E. (Ed.). (2005). *Handbook of multiphase flow metering* (2nd ed.) (Oslo: Norwegian Society for Oil and Gas Measurement/Norwegian Society of Chartered Technical and Scientific Professionals) www.nfogm.no Accessed January 2012.

Deng, X., Li, G., Wei, Z., Yan, Z., & Yang, W. (2011). Theoretical study of vertical slug flow measurement by data fusion from electromagnetic flowmeter and electrical resistance tomography. *Flow Measurement and Instrumentation, 22*, 272—278.

DePavia, L., Zhang, P., Alumbaugh, D., Levesque, C., Zhang, H., & Rosthal, R. (2008). *Next-generation cross-well EM imaging tool*. SPE 116344.

Dong, F., Xu, Y. B., Xu, L. J., Hua, L., & Qiao, X. T. (2005). Application of dual-plane ERT system and cross-correlation technique to measure gas—liquid flows in vertical upward pipe. *Flow Measurement and Instrumentation, 16*, 191—197.

Falcone, G., Hewitt, G. F., & Alimonti, C. (2010). *Multiphase flow metering: Principles and applications*. Amsterdam: Elsevier.

Feali, M., Pinczewski, W. V., Cinar, Y., Arns, C. H., Arns, J.-Y., Turner, M., et al. (2012). Qualitative and quantitative analyses of the three-phase distribution of oil, water, and gas in Bentheimer sandstone by use of micro-CT imaging. *SPE Reservoir Evaluation and Engineering, 15*(6), 706—711.

Fordham, E. (2013). *NMR flowmeter with superconducting polarizer*. Schlumberger Technology. PCT patent application WO2013/024456 2013-February 21.

Frøystein, T., Kvandal, H., & Aakre, H. (2005). Dual energy gamma tomography system for high pressure multiphase flow. *Flow Measurement and Instrumentation, 16*, 99—112.

Gajan, P., Salque, G., Couput, J. P., & Berthiaud, J. (2013). Experimental analysis of the behaviour of a Venturi meter submitted to an upstream air/oil annular liquid film. *Flow Measurement and Instrumentation, 33*, 160—167.

Glen, N., & Ross, A. (2010). Use of dual modality tomography for complex flow visualization. Paper 7.3. In: *28th international North Sea flow measurement workshop, 26—29 October 2010*.

Göktürkler, G. (2011). A hybrid approach for tomographic inversion of crosshole seismic first-arrival times. *Journal of Geophysics and Engineering, 8*(1), 99—108.

Hallundbaek, J., & Kjærsgaard-Rasmussen, J. (2010). *Logging tool*. Welltec AS. US patent application 2011/0101983 A1, May 5, 2011.

Hampel, U., Otahal, J., Boden, S., Beyer, M., Schleicher, E., Zimmermann, W., et al. (2009). Miniature conductivity wire-mesh sensor for gas-liquid two-phase flow measurement. *Flow Measurement and Instrumentation, 20*, 15—21.

Hasan, N. M., & Azzopardi, B. J. (2007). Imaging stratifying liquid—liquid flow by capacitance tomography. *Flow Measurement and Instrumentation, 18*, 241—246.

Hoffmann, R., Amundsen, L., Schulkes, R., & Schüller, R. B. (2012). Measuring phase distribution using external thermal excitation. *Flow Measurement and Instrumentation, 26*, 55—62.

Hoffmann, R., & Johnson, G. W. (2011). Measuring phase distribution in high pressure three-phase flow using gamma densitometry. *Flow Measurement and Instrumentation, 22*, 351—359.

Hoppe, D., Grahn, A., & Schütz, P. (2010). Determination of velocity and angular displacement of bubbly flows by means of wire-mesh sensors and correlation analysis. *Flow Measurement and Instrumentation, 21*, 48—53.

Huang, S. M., & Xie, C. G. (2013). Ultrasound imaging and measurement of swirling gas-liquid multiphase flow. In: *7th world congress on industrial process tomography, 2—5 September 2013, Krakow, Poland*.

Huang, Z., Xie, D., Zhang, H., & Li, H. (2005). Gas—oil two-phase flow measurement using an electrical capacitance tomography system and a Venturi meter. *Flow Measurement and Instrumentation, 16*, 177—182.

Hunt, A., Pendleton, J., & Byars, M. (2004). Non-intrusive measurement of volume and mass using electrical capacitance tomography. In: *7th Biennial ASME conference on engineering system design and analysis, Manchester, UK. (July 19—22, 2004)*. ESDA 2004-58398.

Hu, B., Nuland, S., & Lawrence, C. (2011). *A method of conducting X-ray tomography measurements of petroleum-containing multiphase flows through a pipe*. Institutt for Energiteknikk. PCT patent application WO2011119045 September 29, 2011.

Iglauer, S., Wang, S., & Rasouli, V. (2011). X-ray micro-tomography measurements of fractured tight sandstone. In: *SPE Asia Pacific oil and gas conference and exhibition, 20—22 September, Jakarta, Indonesia: SPE 145960.*

Johansen, G. A., Hampel, U., & Hjertaker, B. T. (2010). Flow imaging by high speed transmission tomography. *Applied Radiation and Isotopes, 68*, 518—524.

Johansen, G. A., Hjertaker, B. T., Tjugum, S.-A., Bruvik, E. M., Maad, R., Sætre, C., et al. (2012). Industrial applications of tomographic gamma-ray methods. In: *Proceedings 6th international symposium on process tomography (Cape Town, South Africa, March 2012).*

Kaku Arvoh, B., Hoffmann, R., & Halstensen, M. (2012). Estimation of volume fractions and flow regime identification in multiphase flow based on gamma measurements and multivariate calibration. *Flow Measurement and Instrumentation, 23*, 56—65.

Kayser, A., Knackstedt, M., & Ziauddin, M. (Spring 2006). A closer look at pore geometry. *Oilfield Review, 18*(1), 4—13.

Kim, B. S., Khambampati, A. K., Kim, S., & Kim, K. Y. (2013). Improving spatial resolution of ERT images using adaptive mesh grouping technique. *Flow Measurement and Instrumentation, 31*, 19—24.

Kjærsgaard-Rasmussen J. (2010), *Inside-out electrical capacitance tomography for downhole multiphase flow evaluation* (PhD thesis), Technical University of Denmark.

Kjærsgaard-Rasmussen, J., & Meyer, K. E. (2011). Inside-out electrical capacitance tomography. *Flow Measurement and Instrumentation, 22*, 104—109.

Lange, G., & Seidel, K. (2007). Electromagnetic methods. In J. Knodel, G. Lange, & H.-J. Voigt (Eds.), *Environmental geology — Handbook of field methods and case studies* (pp. 239—281). Berlin: Springer.

Leeungculsatien, T., & Lucas, G. P. (2013). Measurement of velocity profiles in multiphase flow using a multi-electrode electromagnetic flow meter. *Flow Measurement and Instrumentation, 31*, 86—95.

Li, M., Abubakar, A., Li, J., Pan, G., & Habashy, T. (2010). Three-dimensional regularized Gauss—Newton inversion algorithm using a compressed implicit Jacobian calculation for EM applications. *SEG Extended Abstracts, 29*, 4.

Li, H., & Chen, J. (2013). *Positron tomography imaging apparatus and method for multiphase flow*. Lanzhou Haimo Technologies. US Patent application US20130313437.

Liu, S., Lei, J., Wang, X. Y., & Liu, Q. B. (2013). Generalized multi-scale dynamic inversion algorithm for electrical capacitance tomography. *Flow Measurement and Instrumentation, 31*, 35—46.

Liu, Z., Yang, G., He, N., & Tan, X. (2013). Landweber iterative algorithm based on regularization in electromagnetic tomography for multiphase flow measurement. *Flow Measurement and Instrumentation, 27*, 53—58.

Li, H., Wang, M., Wu, Y. X., & Lucas, G. (2009). Volume flow rate measurement in vertical oil-in-water pipe flow using electrical impedance tomography and a local probe. *Multiphase Science and Technology, 21*, 81—93.

Li, Y., Yang, W. Q., Xie, C. G., Huang, S. M., Wu, Z., Tsamakis, D., et al. (2013). Gas/oil/water flow measurement by electrical capacitance tomography. *Measurement Science and Technology, 24*(074001), 12.

Marsala, A. F., Al-Buali, M., Ali, Z., Ma, S. M., He, Z., Tang, B., et al. (2011). First borehole to surface electromagnetic survey in KSA: reservoir mapping and monitoring at a new scale. In: *SPE Annual technical conference and exhibition, 30 October—2 November 2011, Denver, Colorado, USA*. 146348-MS.

Marsala, A. F., Ruwaili, S., Ma, S. M., Ali, Z., Buali, M., Donadille, J. M., et al. (2008). Crosswell electromagnetic tomography: From resistivity mapping to inter-well fluid distribution.

In: *International petroleum technology conference, 3–5 December 2008, Kuala Lumpur, Malaysia*. 12229-MS.

Meng, Z., Huang, Z., Wang, B., Ji, H., Li, H., & Yan, Y. (2010). Air-water two-phase flow measurement using a Venturi meter and an electrical resistance tomography sensor. *Flow Measurement and Instrumentation, 21*, 268–276.

Mieles, L., Darnet, M., Popta, J. V., Singh, M., Wilt, M., & Levesque, C. (2009). *Experience with cross-well electromagnetics (EM) for waterflood management in Oman*. IPTC 14080.

Mitchell, J., Chandrasekera, T. C., Holland, D. J., Gladden, L. F., & Fordham, E. J. (2013). Magnetic resonance imaging in laboratory petrophysical core analysis. *Physics Reports, 526*, 165–225.

Mitchell, J., Staniland, J., Chassagne, R., Mogensen, K., Frank, S., & Fordham, E. J. (2013). Mapping oil saturation distribution in a limestone plug with low-field magnetic resonance. *Journal of Petroleum Science and Engineering, 108*, 14–21.

Muji, S. Z. M., Goh, C. L., Ayob, N. M. N., Rahim, R. A., Rahiman, M. H. F., Rahim, H. A., et al. (2013). Optical tomography hardware development for solid gas measurement using mixed projection. *Flow Measurement and Instrumentation, 33*, 110–121.

Murai, Y., Tasaka, Y., Nambu, Y., Takeda, Y., & Roberto Gonzalez, S. A. (2010). ‘Ultrasonic detection of moving interfaces in gas–liquid two-phase flow’. *Flow Measurement and Instrumentation, 21*, 356–366.

Ong, J. T., Chen, S., & Bussear, T. R. (August 16, 2012). *Multiphase meter to provide data for production management*. Baker Hughes. US patent application 2012/0209541.

Paladinoa, E. E., & Maliskab, C. R. (2011). Computational modeling of bubbly flows in differential pressure flow meters. *Flow Measurement and Instrumentation, 22*(4), 309–318.

Pardo, D., Torres-Verdín, C., & Zhang, Z. (2008). Sensitivity study of borehole-to-surface and cross-well electromagnetic measurements acquired with energized steel casing to water displacement in hydrocarbon-bearing layers. *Geophysics, 73*(6), F261–F268.

Pinguet, B. (2012). *Fundamentals of multiphase metering*. 09-TS-0022 (2nd ed.) Schlumberger.

Pinguet, B., Gaviria, F., Kemp, L., Graham, J., Coulder, C., Damas, C., et al. (2010). First ever complete evaluation of a multiphase flow meter in SAGD and demonstration of the performance against conventional equipment. In: *Proc. 28th int. North Sea flow measurement workshop (St Andrews, UK, October 2010).*

Pinguet, B., Smith, M. T., Vagen, N., Merete Alendal, G., Rustad, R., & Xie, C. G. (2013). A step change in the water detection and redundancy measurement in wet gas subsea business. In: *The Americas flow measurement conference, Houston, 1–2 may 2013*. Paper 4.1.

Plaskowski, A., Beck, M. S., Thorn, R., & Dyakowski, T. (1995). *Imaging industrial flows: Applications of electrical process tomography*. Bristol: Institute of Physics Publishing.

Primrose, K. M., Qiu, C., Bolton, G. T., Talmon, A. M., Glen, N., Ross, A., et al. (2010). Visualisation and measurement of 3 phase (air water oil) flow and 2 phase flow (sand water) with electrical tomography. In: *Proc. 6th world congress on industrial process tomography (Beijing, China, September 2010)* (pp. 108–118).

Pusiol, D., Carpinella, M., Albert, G., Osán, T. M., Ollé, J. M., Freeman, J. J., et al. (2012). *Method for analyzing a multi-phase fluid*. Shell Oil Company. US patent US8212557B2. July 03.

Qiu, C., Hoyle, B. S., & Podd, F. J. W. (2007). Engineering and application of a dual-modality process tomography system. *Flow Measurement and Instrumentation, 18*, 247–254.

Rahim, R. A., Yunos, Y. Md, Rahiman, M. H. F., & Rahim, H. A. (2010). Mathematical modelling of gas bubbles and oil droplets in liquid media using optical linear path projection. *Flow Measurement and Instrumentation, 21*, 388–393.

Ramirez, A. L., Daily, W., Owen, E. W., Chesnut, D. A., & LaBrecque, D. J. (1992). Electrical resistance tomography used to monitor subsurface steam injection. In: *SEG annual meeting, October 25—29, New Orleans, Louisiana, USA*. Paper ID: 1992-0492.

Rautenbach, C., Mudde, R. F., Yang, X., Melaaen, M. C., & Halvorsen, B. M. (2013). A comparative study between electrical capacitance tomography and time-resolved X-ray tomography. *Flow Measurement and Instrumentation, 30*, 34—44.

Scheers, L., & Wee, A. (2011). Solutions for reliable and accurate measurement of water production in subsea wet gas fields. In: *Subsea controls downunder, 17—19 October 2011, Perth, Australia*. http://www.mpm-no.com/company/papers—publications/ Accessed in August 2013.

Seidel, K., & Lange, G. (2007). Direct current resistivity methods. In J. Knodel, G. Lange, & H.-J. Voigt (Eds.), *Environmental geology — Handbook of field methods and case studies* (pp. 205—237). Berlin: Springer.

Sun, J., & Yang, W. Q. (2013). Fringe effect of electrical capacitance and resistance tomography sensors. *Measurement Science and Technology, 24*, 074002.

Sætre, C., Johansen, G. A., & Tjugum, S. A. (2010). Salinity and flow regime independent multiphase flow measurements. *Flow Measurement and Instrumentation, 21*, 454—461.

Sætre, C., Johansen, G. A., & Tjugum, S. A. (2012). Tomographic multiphase flow measurement. *Applied Radiation Isotope, 70*, 1080—1084.

Taherian, R., & Habashy, T. (1996). *Microwave device and method for measuring multiphase flows*. Schlumberger Technology. US patent number 5485743A. 1996—January-23.

Tan, C., Dong, F., & Wu, M. (2007). Identification of gas/liquid two-phase flow regime through ERT-based measurement and feature extraction. *Flow Measurement and Instrumentation, 18*, 255—261.

Thorn, R., Huang, S. M., Xie, C. G., Salkeld, J. A., Hunt, A., & Beck, M. S. (1990). Flow imaging for multi-component flow measurement. *Flow Measurement and Instrumentation, 1*, 259—268.

Thorn, R., Johansen, G. A., & Hjertaker, B. T. (2012). Three-phase flow measurement in the petroleum industry. *Measurement Science and Technology, 24*(012003), 17.

Tsourlos, P., Ogilvy, R., Papazachos, C., & Meldrum, P. (2011). Measurement and inversion schemes for single borehole-to-surface electrical resistivity tomography surveys. *Journal of Geophysics and Engineering, 8*, 487—497.

Wang, H., Hu, H., Wang, L., & Wang, H. X. (2012). Image reconstruction for an electrical capacitance tomography (ECT) system based on a least squares support vector machine and bacterial colony chemotaxis algorithm. *Flow Measurement and Instrumentation, 27*, 59—66.

Wang, J. Z., Tian, G. Y., & Lucas, G. P. (2007). Relationship between velocity profile and distribution of induced potential for an electromagnetic flow meter. *Flow Measurement and Instrumentation, 18*, 99—105.

Wang, B., Zhang, W., Huang, Z., Ji, H., & Li, H. (2013). Modeling and optimal design of sensor for capacitively coupled electrical resistance tomography system. *Flow Measurement and Instrumentation, 31*, 3—9.

Williams, R. A., & Beck, M. S. (1995). *Process tomography, principles, techniques and applications*. Oxford: Butterworth-Heinemann.

Wilt, M., & Alumbaugh, D. (2014). Fundamental concepts in cross-well electromagnetic induction. In K. M. Strack, & K. Vozoff (Eds.), *Hydrocarbon applications of electromagnetics*. Publisher Society of Exploration Geophysicists (SEG) (working title).

Wilt, M. J., Alumbaugh, D. L., Morrison, H. F., Becker, A., Lee, K. H., & Deszcz-Pan, M. (1995). Cross-well electromagnetic tomography: system design considerations and field results. *Geophysics, 60*, 871—885.

Wilt, M., Donadille, J. M., AlRuwaili, S., Ma, S. M., & Marsala, A. (2008). Cross-well electromagnetic tomography in Saudi Arabia: from field surveys to resistivity mapping. In: *Presented at the 70th EAGE conference and exhibition, Rome, June 9−12, 2008.*

Wilt, M., Zhang, P., Maeki, J., Netto, P., Queiroz, J., Santos, J., et al. (2012). *Monitoring water flood of moderate saturation changes with cross-well EM: A case study from Dom Joao Brazil*. Las Vegas: SEG.

Wu, Z., McCann, H., Davis, L. E., Hu, J., Fontes, A., & Xie, C. G. (2009). Microwave tomographic system for oil and gas multiphase flow imaging. *Measurement Science and Technology, 20*(104026), 8.

Xie, C. G. (2006). Measurement of multiphase flow water fraction and water-cut. In: *Proceedings 5th international symposium on measurement techniques for multiphase flows, 10−13 December 2006, Macau, China: vol. 914*. *AIP conference proceedings* (pp. 232−239).

Xie, C. G. (2013a). *Tomography of multiphase mixtures*. Schlumberger Technology. US patent application 20130144548. June 6, 2013.

Xie, C. G. (2013b). *Multiphase flowmeter*. Schlumberger Technology. PCT patent application WO2013084183. June 13, 2013.

Xie, C. G., Atkinson, I., & Lenn, C. (2007). Multiphase flow measurement in oil and gas production. In: *5th world congress on industrial process tomography, Bergen, Norway, 3−6 September 2007*. pp. 723−736 (ISBN 978 0 85316 265 0).

Xie, C. G., North, R., Wilt, M., Zhang, P., Denaclara, H., & Levesque, C. (2005). Imaging technologies in oilfield applications. *Journal Zhejiang University SCIENCE, 6A*(12), 1394−1400.

Xue, Q., Wang, H. X., Yang, C. Y., & Cui, Z. Q. (2013). Experimental research on two-phase flow visualization using a low-energy gamma CT system with sparse projections. *Measurement Science and Technology, 24*(074008), 8.

Xu, L. J., & Xu, L. A. (1998). Gas/liquid two-phase flow regime identification by ultrasonic tomography. *Flow Measurement and Instrumentation, 8*, 145−155.

Yang, W. Q., Chondronasios, A., Nattrass, S., Nguyen, V. T., Betting, M., Ismail, I., et al. (2004). Adaptive calibration of a capacitance tomography system for imaging water droplet distribution. *Flow Measurement and Instrumentation, 15*, 249−258.

Yang, W. Q., & Liu, S. (2000). Role of tomography in gas/solids flow measurement. *Flow Measurement and Instrumentation, 11*, 237−244.

Yang, W. Q., Stott, A. L., Beck, M. S., & Xie, C. G. (1995). Development of capacitance tomographic imaging systems for oil pipeline measurements. *Review Scientific Instruments, 66*, 4326−4332.

Yu, G., Marion, B., Bryans, B., Carrillo, P., Guo, W., Pang, Y., et al. (2008). 'Crosswell seismic imaging for deep gas reservoir characterization'. *Geophysics, 73*(6), B117−B126.

Zhang, Z., Bieberle, M., Barthel, F., Szalinski, L., & Hampel, U. (2013). Investigation of upward cocurrent gas−liquid pipe flow using ultrafast X-ray tomography and wire-mesh sensor. *Flow Measurement and Instrumentation, 32*, 111−118.

Zhang, J., Hu, H., Dong, J., & Yan, Y. (2012). Concentration measurement of biomass/coal/air three-phase flow by integrating electrostatic and capacitive sensors. *Flow Measurement and Instrumentation, 24*, 43−49.

Zhang, J., Xu, J., Wu, Y. X., Li, D., & Li, H. (2013). Experimental validation of the calculation of phase holdup for an oil−water two-phase vertical flow based on the measurement of pressure drops. *Flow Measurement and Instrumentation, 31*, 96−101.

Zhou, H., Yang, Y., Dong, K., Wu, J., Yan, Y., Qian, X., et al. (2013). Investigation of two-phase flow mixing mechanism of a swirl burner using an electrostatic sensor array system. *Flow Measurement and Instrumentation, 32*, 14—26.

Zhou, B., & Zhang, J. Y. (2013). A novel ECT—EST combined method for gas—solids flow pattern and charge distribution visualization. *Measurement Science and Technology, 24*, 074003.

Ziauddin, M., & Bize, E. (2007). The effects of pore-scale heterogeneities on carbonate stimulation treatments. In: *15th SPE Middle East oil & gas show and conference, Bahrain, 11—14 March 2007. SPE 104627.*

This page intentionally left blank

Application of tomography in microreactors

24

N. Ali Othman[1,2], *M. Takei*[2]
[1]Universiti Kebangsaan Malaysia, Bangi, Selangor, Malaysia; [2]Chiba University, Inage, Chiba, Japan

24.1 Introduction

This chapter focuses on engineering processes involved in microreactors, generally defined as devices with the internal structural features, most conveniently measured in microns, that are capable of performing, controlling, and processing chemical or biological reactions in a continuous-flow manner. A typical microfluidic platform has a lab-on-chip configuration and can manipulate small volumes (from femtoliter to microliter) of fluids constrained within microfluidic channels. A basic microreactor may include enclosed microchannels, simple mixing units, a heat source, and a pumping system to control fluid or gas flow. Devices have been fabricated from a variety of materials including glass, metals, silicon, quartz, polymers, plastics, and ceramics. Fluid pumping and manipulation in the devices can be achieved by hydrodynamic pumping, most commonly using an external syringe or diaphragm pumps to generate flow or electrokinetic flow, which relies on the application of an electric field along the microreactor to induce bulk flow in aqueous or suitable polar solvent systems. Fluid flow in the microreactors is characteristically different from fluid flow in bulk systems and provides a unique environment in which to perform chemical reactions. Microreactors are capable of controlling and transferring small amounts of gases/liquids/particles that allow chemical processes and biochemical assays to be integrated and carried out on a microscale.

A microfluidic platform has been widely used in the fields of biology and chemistry; it plays an important role in the chemical and process industries. Handling systems involving two or more phases are commonplace in areas from processing of fuels and chemicals to the production of feed, food, pharmaceuticals, and specialty materials. Many applications are aimed at improving aspects of critical basic biologic analyses and clinical diagnosis. For example, in biology, applications using microreactors include immunoassays, polymerase chain reaction amplification, DNA analyses, chemical gradient formation, cell manipulation, separation, and patterning. On the chemistry side, many examples have demonstrated that microreactors are extremely useful in performing a wide variety of chemical reactions with purer products, higher yields, greater selectivities, and shorter reaction times than those obtained in batch-scale reactions. As one of the major attributes of the microfluidic technology, more benign and milder reaction conditions can be found for certain reactions within

Industrial Tomography. http://dx.doi.org/10.1016/B978-1-78242-118-4.00024-1
Copyright © 2015 Elsevier Ltd. All rights reserved.

microreactors. Manufacturing processes to fabricate microreactors are relatively inexpensive and easily amenable to mass production, even with highly elaborate, complicated device designs. Besides, biology and chemistry carried out in integrated microfluidic chips have great promise as a foundation for new chemical technology and processes.

Additionally, microreactors have a series of generic components for introducing and removing multiple reagents and samples within microfluidic channels; efficient mixing of separate reagents; performing reactions with precise temperature control; and carrying out other functionalities, such as purification for chemical syntheses or detection for product characterization. At the microscale, heat and mass transfer are very rapid owing to high-surface area-to-volume ratio and a large heat exchange coefficient; hence the reaction conditions within such an environment can be precisely controlled. As a consequence, the yield and selectivity of many biological reactions and chemical syntheses carried out in microfluidic channels can be dramatically improved, whereas the consumption of reagents and reaction or process time is significantly reduced. In addition, unlike devices used in the macroscale chemical and biological reactions, microreactors exhibit a high degree of scalability, reproducibility, modularity, and automaticity. The dominance of viscous forces over inertial forces for moving fluids in microreactors generally results in the existence of laminar flow regimes with Reynolds numbers typically less than 10^2.

Although laminar flow is achieved in most microreactors, mixing can in fact be an extremely fast process, provided that the channel diameters (diffusion distances) are less than 100 μm. Consequently, the rates of chemical reactions can be significantly improved compared with standard laboratory methods. The consequence of increased surface area-to-volume ratio is the enhancement of mass transport via rapid diffusion time scales and significantly improved heat transfer either into or out of the microreactor. Furthermore, it is important to note that from concept to working chip, each microreactor takes less than three working days to construct because of the use of soft lithography. When a new reaction protocol is selected, a chip can be rapidly designed by a computer-aided design program on a personal computer, as well as a standardized production scheme, to meet the new conditions. The reconfiguration of microreactors is more flexible and can meet the diverse needs of producing many different types of compounds. Applications of tomography imaging techniques used with microreactor systems are described and summarized in Table 24.1.

24.2 X-ray and γ-ray tomography

The main factors to determine the imaging capabilities of a computed tomography (CT) scanner used in engineering applications are its achievable spatial, temporal, and density resolution. Spatial resolution is the minimum distance that two high-contrast point objects can be separated; temporal resolution refers to the frequency with which the images can be obtained; and density resolution refers to the smallest difference in the mass attenuation coefficients that the system is able to distinguish. The transmission of X-rays or γ-rays through the heterogeneous medium is

Table 24.1 **Summary of the tomography techniques in microreactors**

General measurement	Sensor installed	Size of microreactor/ microchannel tested system	Phase condition	Ref for more details
X-ray microtomography/ transmission CT	Tungsten or molybdenum sources/ionization chamber type or scintillation type detectors	$D = 3.54 \times H = 3.54 \times V = 2.36\ \text{mm}^3$	Gas−solid	Grunwaldt and Schroer (2010); Schroer et al. (2003); Smit et al. (2008)
X-ray absorption spectroscopy	Placing a two-dimensional position-sensitive X-ray camera behind the reactor	Quartz glass capillary microreactor ($D = 1$ mm, $W = 20$ mm)	Gas−solid	Hannemann et al. (2006)
X-ray radiography	Sources same as in X-ray CT; detector, sheet of film, or image intensifier camera		Gas−solid	Jamal et al. (1997)
NMRI	External magnetic field gradient and radiofrequency pulses	186 nm, $D = 85$ nm, and $W = 100$ nm	Liquid	Bouchard et al. (2008)
PET	Positron emitter tracers/position camera as detector	Flat disk shape ($D = 5$ mm, $H = 255$ mm)	Gas−solid	Elizarov, Meinhart et al. (2010)
			Liquid−gas−solid	Gillies, Prenant, Chimon, Smethurst, Perrie, Dekker, et al. (2006); Gillies, Prenant Chimon, Smethurst, Perrie, Hamblett, et al. (2006); Watts and Wiles (2007); Elizarov, Michael et al. (2010)

Continued

Table 24.1 Continued

General measurement	Sensor installed	Size of microreactor/ microchannel tested system	Phase condition	Ref for more details
		Ring-shaped channel ($W = 100\ \mu m$)		Lee et al. (2005)
		T-shaped channel ($W = 220\ \mu m \times D = 60\ \mu m \times L = 14$ mm; $V = \sim 0.2$ mL)		Lu et al. (2004)
		Capillary reactor ($D = 300\ \mu m$, $L = 0.7$ m)		Wester et al. (2009)
		$W = 200\ \mu m$ and $H = 45\ \mu m$		Cheng-Lee et al. (2005)
		$D = 100\ \mu m$, $L = 4.0$ m, $V = 31.4\ \mu L$		Lu and Pike (2010)
		$D = 100\ \mu m$, $L = 4.0$ m, $V = 31.4\ \mu L$		Chun et al. (2010)
		$D = 100\ \mu m$, $L = 2.0$ m, $V = 15.6\ \mu L$		Pascali et al. (2012)
		Glass microreactor ($W = 200\ \mu m \times D = 75\ \mu m \times L = 5$ m		Miller et al. (2007)
		Glass microreactor: $V = 100\ \mu L$, $W = 600\ \mu m$, $D = 500\ \mu m$ and $L = 360$ mm		Van den Broek et al. (2012)
Electrical capacitance tomography	Electrodes energized sequentially	$H = 700\ \mu m$ and $L = 20$ mm	Liquid−solid	Choi et al. (2010); Ali Othman et al. (2013)

Inner diameter = D, Height = H, Length = L, Volume = V.

accompanied by attenuation of the incident radiation, and the measurement of this attenuation provides a measure of the line integral of the local mass density distribution along the path traversed by beam. The measurement of several such beams at different spatial and angular orientations with respect to test section or volume, followed by an image reconstruction procedure, provides density distribution of phases to a high degree of spatial resolution. Scanners for transmission tomography employ radiation sources, such as an X-ray tube or an encapsulated γ-ray source, positioned on one side of the object to be scanned and a set of collimated detectors arranged on the other side. With X-ray and γ-ray tomography, the data obtained for the concentration distribution of the phases are almost always time-averaged, since a significant period of time is required to obtain the photon count rates for all the projections (necessary to rotate the sensors and the source). Depending on the design of the scanner, the period can range from a few minutes to close to 1 h. This is a basic limitation of these techniques in studies of the time-evolving flow phenomena. However, dynamic information can be obtained when the dispersion rate or flow velocities are sufficiently slow.

For example, a tomographic study of a Cu/ZnO catalyst in a microreactor (ex situ in a closed capillary: after a reduction−oxidation−reduction cycle) was investigated (Hannemann et al., 2006). In this way, a series of absorption tomograms for all energies in the absorption spectrum were obtained. Each of the tomograms was reconstructed individually, yielding a reconstruction of the distribution of the attenuation at a given energy. Together, the reconstructions provided a full X-ray absorption near-edge structure (XANES) spectrum at each location in the tomographic reconstruction. By fitting the spectra of different copper species at every location in the tomographic reconstruction, the distributions of metallic, monovalent, and bivalent copper can be determined together with the distribution of other elements. The Cu(I):Cu(II) ratio is very different within the microreactor. Although this study was not performed in situ, it was done on a sealed capillary after several reduction/reoxidation cycles; thus, it is straightforward to extend this approach to an in situ analysis. Full-field X-ray spectroscopic tomography could be performed, for example, in an alternative approach: not the X-ray absorption spectroscopic data but the X-ray diffraction (XRD) patterns were acquired by the so-called tomographic energy-dispersive diffraction imaging technique. It used an approach to image in three dimensions the distribution and composition in the catalyst bodies. The sample is scanned in the beam by an energy-dispersive detector. The signal contains both the diffraction and the fluorescence peaks from the defined volume element and thus a full scan results in XRD and X-ray fluorescence datasets. In this way, both concentration in a pellet and the individual phases can be identified. The impregnation of alumina pellet with $(NH_4)_6Mo_7O_{244}H_2O$, after calcination at 500 °C MoO_3 is found with the resolution in the 100-μm range. Their method (Hannemann et al., 2006) is related to tomographic X-ray absorption spectroscopic imaging of catalysts applied by Schroer et al. (2003). Figure 24.1 shows in detail the tomographic reconstruction of copper in (a) the metallic (Cu), (b) the monovalent $[Cu(I)_2O]$, and (c) the bivalent state $[Cu(I)_2O]$ on a virtual section through a reactor capillary filled with a Cu/ZnO catalyst. The results show that the bivalent copper is not present in the sample within the detection limit, while the metallic and monovalent copper are distributed slightly differently, as shown in

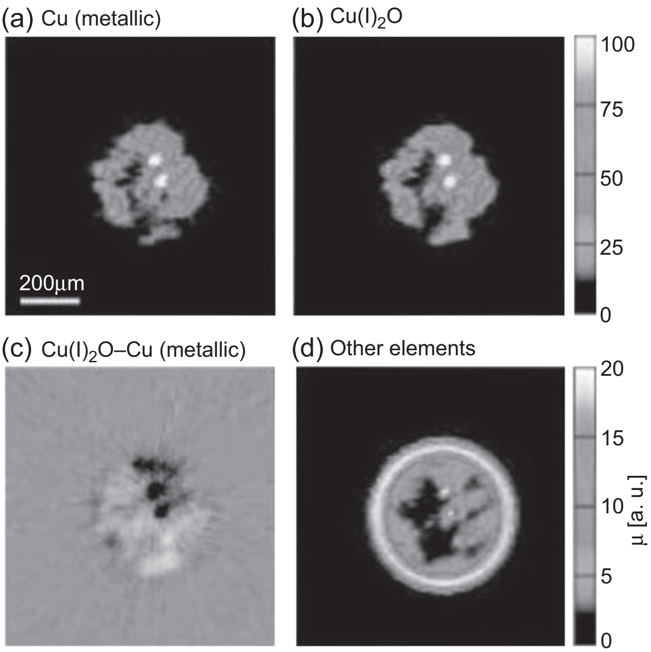

Figure 24.1 Tomographic reconstruction of copper in (a) the metallic (Cu) and (b) the monovalent [$Cu(I)_2O$] on a virtual section through a reactor capillary filled with a Cu/ZnO catalyst. Metallic and monovalent copper are distributed slightly differently, as shown in the difference map in (c). The shade of gray outside the specimen corresponds to zero difference. While brighter areas depict a higher concentration of $Cu(I)_2O$, darker regions show a higher concentration of metallic copper. (d) Attenuation due to other elements.
Reprinted with permission from Schroer et al. (2003). Copyright 2003, AIP Publishing LLC.

the difference map in (d). The shade of gray outside the specimen corresponds to zero difference. Brighter areas depict a higher concentration of $Cu(I)_2O$, and darker regions show a higher concentration of metallic copper.

Also, Hannemann et al. (2006) investigated the distinct spatial changes of catalyst structure inside a fixed-bed microreactor during partial oxidation of methane over Rh/Al_2O. The experiment results are shown in Figure 24.2, where the amount of oxidized Rh-species and the distribution of other elements show a featureless absorption spectrum in the given energy range. Selected examples demonstrate the application of X-ray microscopy and tomography to monitor structural gradients in the catalytic reactors and catalyst preparation with micrometer resolution but also the possibility to follow structural changes in the sub-100 nm regime. In addition, Smit et al. (2008) investigated the nanoscale chemical imaging of a working catalyst by scanning transmission X-ray microscopy. The detailed strategy of their experiment for two-dimensional (2D) mapping of samples on the microscale, experimental setup, and data acquisition method for soft X-ray scanning microscopy is shown in Figure 24.3. In order to improve their situation for X-ray absorption spectroscopy, either a

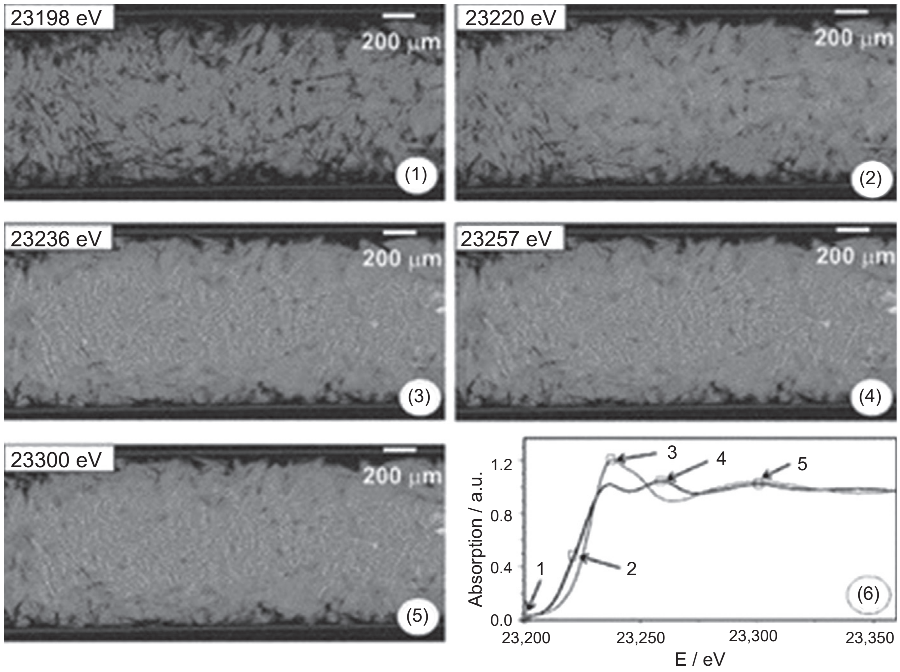

Figure 24.2 Absorption extracted from transmission images (recorded by the CCD camera; flat- and dark-field corrected) of Rh/Al_2O_3 inside the microreactor at 362 C during the CPO of methane at the energies indicated in the corresponding images; centre position is 1.8 mm for image (1)—(5); (6) shows the extracted XANES spectra from the flat- and dark-field corrected transmission images at about 0.3 and 3.3 mm at 362 C.
Reprinted with permission from Hannemann et al. (2006). Copyright 2006, Catalyst Today Publishing. http://dx.doi.org/10.1016/j.cattod.2006.08.065.

continuously scanning monochromator in the so-called QEXAFS mode or dispersive EXAFS is used. In their experiment, by using the QEXAFS mode, the X-rays were focused onto the sample by parabolic refractive X-ray lenses made of beryllium. The sample was scanned through the focus in translation and rotation, recording at each position of the tomographic scan a full near-edge absorption (XANES) spectrum at the Cu K-edge by means of a fast monochromator (sampling frequency 100 kHz, 10 spectra per sample point). In total, about 101 projections over 3601 were recorded, each consisting of 90 translational steps of 10 mm each.

Espinosa-Alonso et al. (2009) approached the real in situ measurements and investigated in a specially designed environmental cell the changes of impregnated $[Ni(en)^3](NO_3)^2/g\text{-}Al_2O_3$ and $[Ni(en)^3]Cl_2/g\text{-}Al_2O_3$ treated in N_2. Despite that the profile was uniform after impregnation with $[Ni(en)^3](NO_3)^2/g\text{-}Al_2O_3$ already during drying at 20 °C, the crystallization of large $[Ni(en)^3](NO_3)^2$ was observed, especially at the outer part of the pellet. In situ 1D scans applied during the calcination process showed the decomposition of the precursor at 190 °C. The egg-shell distribution was

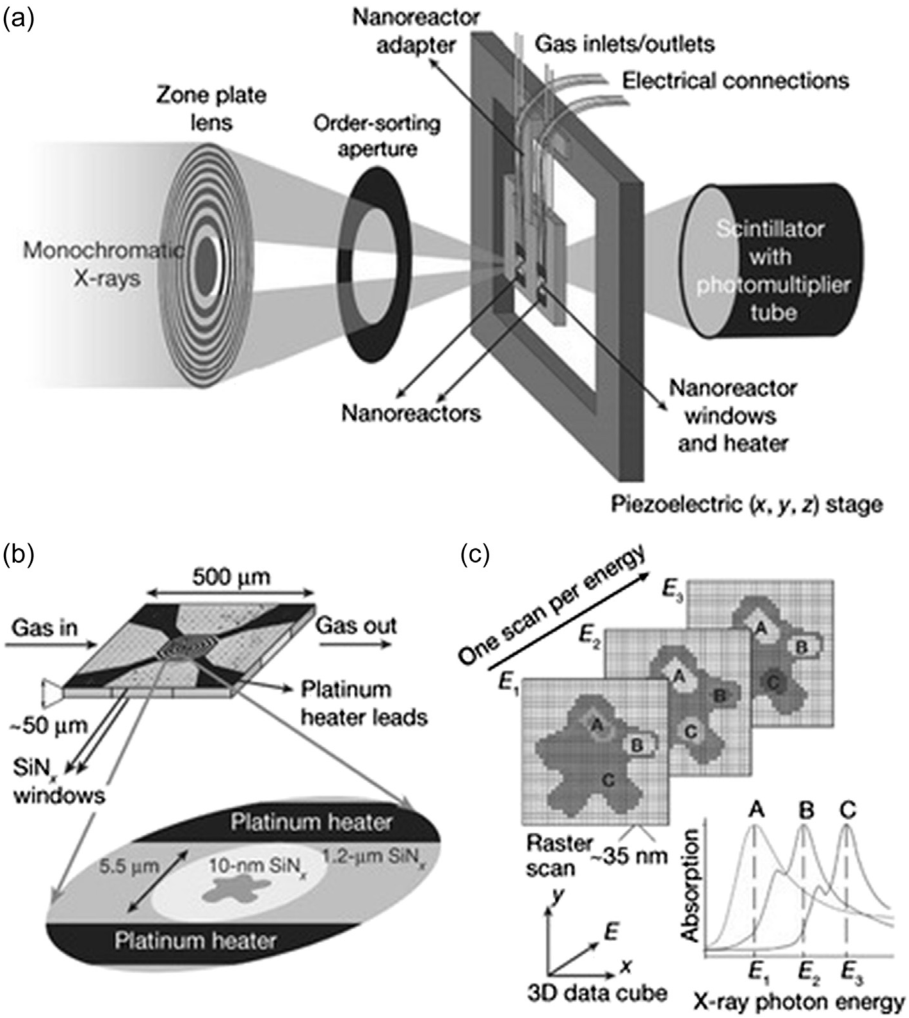
(a)
Nanoreactor adapter
Gas inlets/outlets
Electrical connections
Zone plate lens
Order-sorting aperture
Monochromatic X-rays
Scintillator with photomultiplier tube
Nanoreactors
Nanoreactor windows and heater
Piezoelectric (x, y, z) stage
(b)
500 µm
Gas in
Gas out
Platinum heater leads
~50 µm
SiN$_x$ windows
Platinum heater
5.5 µm
10-nm SiN$_x$
1.2-µm SiN$_x$
Platinum heater
(c)
One scan per energy
E$_1$
E$_2$
E$_3$
A
B
C
Raster scan
~35 nm
y
E
x
3D data cube
Absorption
A B C
E$_1$ E$_2$ E$_3$
X-ray photon energy

Figure 24.3 Experimental setup and data acquisition method for soft X-ray scanning microscopy. (a) Diagram of the in situ STXM technique. Soft X-ray light is focused on the sample using a Fresnel-type zone plate lens. An order-sorting aperture filters out higher-order diffraction orders. The nanoreactor containing the sample is placed in an adaptor that holds up to two nanoreactors at the same time. The adaptor can be translated with nanometer precision by an interferometrically controlled (*x, y, z*) piezoelectric stage, allowing the acquisition of raster scans. (b) Close-up of the nanoreactor, showing the windows and the embedded heater spiral. The reactor dimensions are ~500 × 500 × 50 μm^3. The platinum heater has four electronic connections for simultaneous power supply and resistive temperature measurement. The sample itself is supported on the SiN_x windows. The measurements are performed in the circular areas (5.5-mm diameter) where the 1.2-µm-thick SiN_x windows are etched down to a thickness of ~10 nm. (c) Diagram of a typical STXM data acquisition method. By acquiring images at different X-ray photon energies (for example, *E1*, *E2*, and *E3*), a three-dimensional (3D) data cube with full spectral information at every pixel is obtained. These data can be used to image and distinguish between specific chemical species (for example, species A, B, and C). Reprinted with permission from Smit et al. (2008). Copyright 2008, Nature Publishing.

maintained, after calcinations at 500 °C, where 5-nm large particles were detected. These examples demonstrate the importance of imaging the catalyst structure under working conditions and the preparation of catalysts in the millimeter-to-centimeter length scale, where hard X-rays are the optimal choice. Grunwaldt and Schroer (2010) investigated the spatial changes of catalyst structure inside a fixed-bed microreactor during the partial oxidation of methane by using in situ X-ray absorption spectroscopy tomography. They found that in certain cases a variation of catalyst structure can occur inside a catalytic reactor, as a result of temperature or concentration gradients, by using a position-sensitive X-ray camera to record XANES spectra of the catalytic reactor with a spatial resolution on the scale of a few micrometers. Moreover, they also investigated the hard and soft X-ray microscopy and tomography in catalysis, bridging the different time and length scales. They reported that a particularly important aspect is to study catalysts during their preparation and activation and under operating conditions, where X-rays have an inherent advantage due to their good penetration length, especially in a hard X-ray regime. While reaction cell design for hard X-rays is straightforward, smart in situ cells were also reported for the soft X-ray regime. In their study, the axial temperature distribution over a 5.0% Rh/Al_2O_3 catalyst is observed in a quartz microreactor (length 10 mm) upon heating from 300 °C to 400 °C. The inset gives the thermographic views at furnace temperatures of 300 and 400 °C. After ignition, a strong hot spot can be found, connected to strong structural changes.

24.3 X-ray and γ-ray absorption/radiography tomography

X-ray absorption or radiography is a technique based on the same principle as X-ray tomography, but the attenuation of the beam emitted by the X-ray source is registered by sheets of film or an image-intensifier camera. The registered images are recorded on a cine camera or a video recorder and transferred to a computer for processing and analysis. X-ray absorption or radiography has been used for many years to probe the interior of microreactors and enable direct observations of motion. Impregnation of preshaped metal oxide particles is one of the most applied preparation procedures of industrial heterogeneous catalysts. Therefore, different mathematical descriptions of the impregnation step have been developed. For example, Jamal, Larachi, and Dudukovic (1997) reported on the application of X-ray absorption tomography to identify the oxidation state distribution inside a catalytic microreactor. Its nondestructively yields information on the microstructure, e.g., grain size structure, of the preshaped catalyst pellets, and the element contrast can be achieved if the X-ray absorption is different. To demonstrate the perspective of their approach, they determined the microstructure of a commercial 0.5% Pd/Al_2O_3 catalyst successfully applied in the alcohol oxidation in supercritical fluids where a Cu-based catalyst with different impregnation depths was prepared using different impregnation times and a similar kind of Al_2O_3 pellet.

Moreover, Elizarov (2009) studied functionalized inorganic monolithic microreactors for high productivity in fine chemical catalytic synthesis. In their study, two striking features of Monosil are a uniform radial distribution of voids and struts by X-ray tomography and a very narrow size distribution of windows and diffusion pores. These characteristics guarantee an extremely flat flow profile and the same residence time for all reactant molecules, as well as a very short diffusion path of 3 μm in the struts. Compared to a microreactor packed with 50 μm particles, the typical diffusion time scale is then 200 times smaller in Monosil. The schematic setup and picture for mapping the oxidation state inside a catalytic reactor in two dimensions under reaction conditions are shown in Figure 24.4 (Hannemann et al., 2006), and Figure 24.5 shows the experimental result of the extracted components from the analysis of the 160 dark and flat-field corrected transmission images.

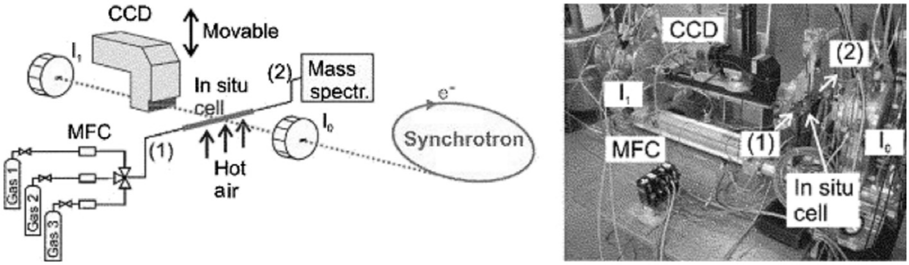

Figure 24.4 Schematic setup and picture for mapping the oxidation state inside a catalytic reactor in two dimensions under reaction conditions; CCD-detector (position sensitive detection of the X-ray absorption), ionization chambers ("integral" X-ray absorption spectra) as well as microreactor (in situ cell), oven and gas supply including MFCs (mass flow controllers) are depicted; (1) denotes the inlet of the in situ cell and (2) the outlet connected to a mass spectrometer. Reprinted with permission from Hannemann et al. (2006). Copyright 2006, Catalyst Today Publishing.

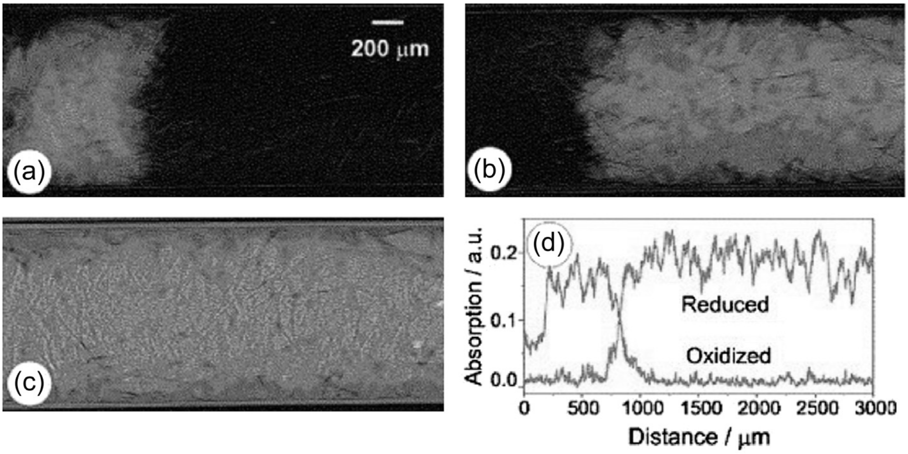

Figure 24.5 Extracted components from the analysis of the 160 dark- and flat-field corrected transmission images: (a) oxidized Rh-species; (b) reduced Rh-species; (c) featureless background; (d) relative concentration of the oxidized (red) and reduced (blue) Rh-particles in the axis of the fixed-bed (conditions: 362 8C, space velocity 1.9 105 h1).
Reprinted with permission from Hannemann et al. (2006). Copyright 2006, Catalyst Today Publishing.

24.4 Nuclear magnetic resonance imaging

Nuclear magnetic resonance imaging (NMRI) has received a great deal of attention, particularly due to the remarkable advances that have been made in the field of medical imaging. The NMRI is a noninvasive method based on the paramagnetic properties of the nuclei. Atomic nuclei are characterized by states that are quantum mechanical in their behavior. Each nucleus has a spin quantum number associated with it and a fixed quantity characterizing its stable ground state. An angular momentum and a magnetic dipole moment, proportional to the angular momentum, are associated with the spin of the nucleus. The constant of proportionality relating the angular momentum and the magnetic dipole moment is known as the gyromagnetic ratio. In NMRI experiments, signals are obtained by having radiofrequency pulses (Callaghan & Xia, 1991) and magnetic field gradient pulses interact with the spin system positioned in a static magnetic field. Imaged velocity and liquid diffusion profiles in laminar flow were investigated through an abrupt contraction and expansion and in capillary flows using spin-echo technique.

The NMRI technique is also applied for catalyst application in microreactor systems. It has proven challenging to correlate the active regions in the heterogeneous catalyst beds with morphology and to monitor multistep reactions within the catalyst bed. Previous applications of NMRI to heterogeneous catalysis included studies of the hydrogenation processes without parahydrogen (pH_2), catalyst morphologies and synthesis technique, and fluid flow through the catalyst bed, as well as monitoring of esterification reactions in situ. All of these applications were based on the nuclear magnetic resonance signal detection of the liquid phase and thus offer a sensitivity that is three orders of magnitude larger as compared with gases, resulting from the difference in density. The sensitivity enhancement offered by pH_2-induced polarization (PHIP) is essential for the application of NMRI to the heterogeneous chemical reactions in the gas phase. From the previous studies, techniques using magnetic resonance imaging and pH_2 polarization were demonstrated that allow direct visualization of gas-phase flow and the density of active catalyst in the packed-bed microreactor, as well as control over the dynamics of the polarized state in space and time to facilitate the study of the subsequent reactions. These procedures are suitable for characterizing reactors and reactions in microreactors; low sensitivity of the conventional magnetic resonance would otherwise be the limiting factor.

To demonstrate the effectiveness of heterogeneously catalyzed PHIP in microreactors, two model catalytic reactors are used. Bouchard et al. (2008) reported that at time, $T = 0$ ms, no isotropic mixing with the polarized product is observed in the catalyst layer. Meanwhile, during $T = 10$ ms after isotropic mixing, the polarized product travels about 5 mm and at $T = 40$ ms after isotropic mixing the product has traveled 10 mm. The schematic of the microreactors, consisting of catalyst layers sandwiched between layers of glass beads for stability, is shown in Figure 24.6(a), and the result of the density of active catalyst and flow map imaging by NMRI is shown in Figure 24.6(b).

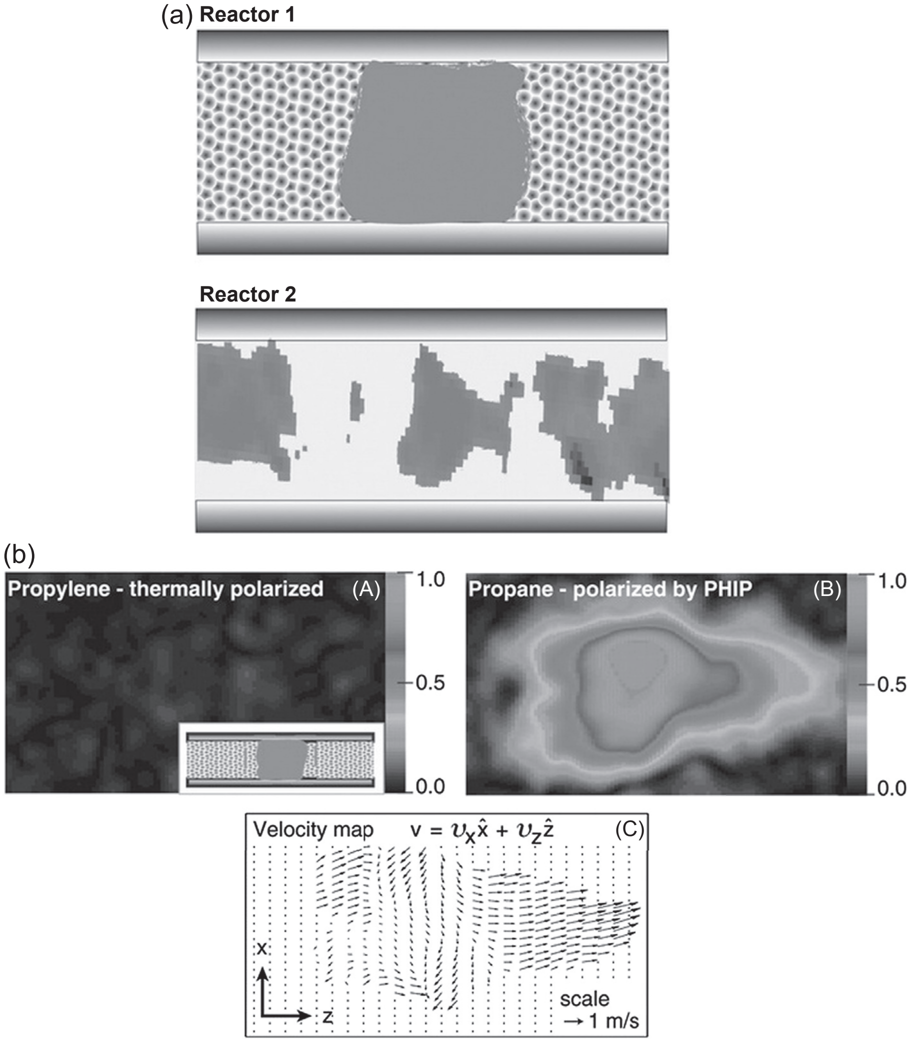
(a) Reactor 1
Reactor 2
(b)
Propylene - thermally polarized
(A)
1.0
0.5
0.0
Propane - polarized by PHIP
(B)
1.0
0.5
0.0
Velocity map $v = \upsilon_x\hat{x} + \upsilon_z\hat{z}$
(C)
x
z
scale
→ 1 m/s

Figure 24.6 (a) Experiment results: Schematic of the microreactors, consisting of catalyst layers sandwiched between layers of glass beads for stability. (b) Experiment results: Density of active catalyst and flow map imaging by magnetic resonance imaging.

Reprinted with permission from Bouchard et al. (2008). Copyright 2008, Science Publishing.

24.5 Positron emission tomography

Positron emission tomography (PET) is a very powerful diagnostic technique; it can be used in a wide range of medical applications including oncology, neurology, and cardiology. The basic principle of PET relies on the incorporation of short-lived positron-emitting radioisotopes, most commonly ^{18}F (half-life of 110 min) or ^{11}C (half-life of 20 min), into the radiopharmaceutical; other isotopes that are sometimes used include ^{13}N, ^{15}O, and ^{124}I. The fact that ^{18}F and ^{11}C radioisotopes have such short half-lives is a significant challenge for the synthetic chemist, as the organic reactions used to prepare the molecule of interest must be relatively fast chemical transformations, with the goal being to prepare, purify, and isolate the desired product in one to two half-lives; consequently, for ^{11}C, this means that the chemist must synthesize and isolate the pure target in less than 30 min. The enhanced mass transport and heat transfer in such microreactors should result in shorter reaction times and better radiochemical yields (RCYs) and radiochemical purities (RCP). As PET radionuclides in the tracer molecules decay, the emitted positrons travel a short distance in a range of about 1−5 mm in tissue, depending on the radionuclide, and collide with the nearby electrons. Widely expected benefits included a superior reaction control, enhanced product yields, enhanced reaction kinetics, production reliability, safety, and facile automation and integration with downstream processing, all essential for good manufacturing practices in production of PET tracers.

The miniaturization of the PET radiosynthesis devices has the potential to address many of the current issues associated with PET probe production. This is because the microfluidic radiochemistry microreactor platforms can offer several advantages, such as reliable production of PET probes with high RCP and RCY, stand-alone and self-shielded devices without the full-sized hot cells, production of various probes using custom-designed microfluidic chips, use of lower starting activity and less probe precursor, and a significant reduction in separation challenge during purifications. Typically, the PET uses radioactive tracers that decay via the emission of a positron. The radioactive decay occurs when the nucleus of these tracers, rich in protons, converts one proton into an uncharged neutron, expelling a positron and the antiparticle of the electron. Any positron expelled from the nucleus will combine with an electron and these can annihilate each other, and their total rest mass energy is converted into two 511-keV back-to-back γ-rays. By detecting γ-rays simultaneously with the positron-sensitive detectors, a line of sight along which the decay must have taken place can be inferred. By detecting many such decays, the distribution of tracer activity can be determined (Benton & Parker, 1997).

In the case of [^{11}C] methylation application in microreactors, Lu et al. (2004) synthesized ^{11}C-labeled carboxylic ester via [^{11}C] methylation using a simple hydrodynamically driven microreactor. It was composed of two inlet ports for reagent delivery: a microfluidic channel for mixing and radiolabeling (with dimensions of 220 μm [width] × 60 μm [height] × 14 mm [length] and total volume of approximately 0.2 μL), and one outlet port for product collection. Precise control of flow rate was attained by syringe pumps, delivering [^{11}C]CH_3I and 3-(3-pyridinyl) propionic acid accurately into the microchannel. From their study, the best RCY, where the RCY is decay-corrected of the corresponding [^{11}C]methyl ester, was 88% when the infusion rate of the reagents was set at 1 μL/min at room temperature. The average residence time of the reagents on the chip device was approximately 12 s and gave a total processing time of 10 min for the whole reaction, which is commensurate with the time scale of PET radiolabeling reactions. Their microreactor was further applied to prepare the compound of brain peripheral benzodiazepine receptor ligand via [^{11}C] methylation and the highest RCY was 65% when the infusion rate was at 1 μL/min.

Cheng Lee et al. (2005) reported the synthesis of [^{18}F]FDG in a polydimethylsiloxane (PDMS) microreactor consisting of a complex array of channels, typically 200 μm wide and 45 μm deep. Their microreactor was designed to have different temperature zones; the fluorination reaction was conducted at 100 °C for 30 s followed by 120 °C for 50 s, while acid hydrolysis was conducted at 60 °C. Using their approach, [^{18}F]FDG was obtained in 38% RCY but in very high purity; 97%. The total processing time was reduced to 14 min compared with the typical 50 min for current batch protocol. They also designed a chemical reaction circuit with the capacity to synthesize large [^{18}F]FDG doses. The chip has a coin-shaped reactor with a volume of 5 mL equipped with a vacuum vent. It was used to synthesize 1.74 mCi of [^{18}F]FDG, an amount sufficient for several mouse experiments. From the purified and sterilized product, two doses (375 and 272 mCi) were used for micro-PET molecular imaging of two mouse models of cancer. They concluded that a proof of principle for automated multistep syntheses at the nanogram to microgram scale may be generalized to a range of radiolabeled substrates.

In the case of radiohalogenation of small- and large-molecular-weight molecules with a microfluidic device, Gillies, Prenant, Chimon, Smethurst, Perrie, Dekker, et al. (2006) and Gillies, Prenant, Chimon, Smethurst, Perrie, Hamblett, et al. (2006) used two microreactor devices in series to achieve two steps ([^{18}F] fluorination + deprotection) required for [^{18}F]FDG synthesis. These reactions involved direct radioiodination of apoptosis marker annexin V using ^{124}I, the indirect radioiodination of the anticancer drug doxorubicin from a tinbutyl precursor, and the radiosynthesis of [^{18}F]FDG from a mannose triflate precursor and ^{18}F. They demonstrated the rapid radioiodination of the protein annexin V (40% RCY within 1 min) and the rapid radiofluorination of [^{18}F]FDG (60% RCY within 4 s) using a polymer microreactor chip. In addition, Gillies, Prenant, Chimon, Smethurst, Perrie, Dekker, et al. (2006) and Gillies, Prenant, Chimon, Smethurst, Perrie, Hamblett, et al. (2006) reported on a three-layer polycarbonate microreactor for radiolabeling the PET isotopes ^{18}F and ^{124}I, and SPECT (single-photon emission CT) isotope ^{99m}Tc. In their study, the top plate of their device contains three inlets for reagents; the middle plate is a disc-shaped cavity with a simple vortex mixer, which also acts as an outlet to the bottom disc cavity containing an outlet port. Three separate syringes were respectively loaded with annexin V protein in buffer solution, [^{124}I]NaI in buffer solution and iodogen (an oxidizing agent necessary to convert I^- to I^+ for electrophilic oxidation) in acetonitrile, and pumped through the microreactor simultaneously. As a result, after 2 min, the labeling efficiency was about 40% and was comparable with conventional methods over the same time frame. The microreactor was used to conduct the fluorination of mannose triflate, followed by acid hydrolysis of an intermediate to synthesize [^{18}F]FDG; 50% incorporation of the radiolabel was achieved with a residence time of just 4 s.

In other research, Miller et al. (2007) described a simple, low-cost, and effective microreactor employing a reusable silica-supported palladium catalyst packed into a standard Teflon tube for rapid multiphase [^{11}C] carbonylation reactions. It combined three phases: gaseous [^{11}C]CO, substrates in the solution, and a solid-phase catalyst in the [^{11}C] labeling process. The main component of the microreactor is the catalyst-immobilized Teflon microtube with a diameter of 1 mm and a length 45 cm, connected with precision syringe pumps or injectors and a mass flow controller to meter the flow of [^{11}C]CO through a mixing of a T-shaped connector. The active catalyst within the microtube is a palladium phosphine complex attached to the silica support material, where the surface area-to-volume ratio is drastically increased. It is estimated to be about 20,000 times larger than that produced by coating only the catalyst inside the surface of the microchannel. A feature such as this has dual properties in contributing to the improved yields of [^{11}C]-labeled amides: it provides a large active surface area (coated with palladium catalyst) for the catalytic reaction to occur; and, as well, it increases the turbulence of [^{11}C]CO and substrate solution, enhancing the mixing efficiency.

Meanwhile, Steel, O'Brien, Luthra, and Brady (2007) reported the use of a two-stage glass-fabricated microreactor for the automated synthesis of [^{18}F]FDG where a solution of mannose triflate in the anhydrous acetonitrile is reacted with a premade complex from [^{18}F]KF, Kryptofix, and K_2CO_3 in acetonitrile. They reported about 40% conversion for the radiolabeling reaction when a residence time of 2 min was used. A total run time of 10 min was reported from dilute [^{18}F]fluoride ion processed macroscopically to crude [^{18}F]FDG. The automated single device presents a significant advantage, in terms of total processing time, over the two-device method reported; it took about 30–60 min for the same [^{18}F] fluorination/acetyl deprotection steps. Improved RCYs of 40% for [^{18}F]FDG synthesis were reported using different structured microfluidic devices enabling fast-flow rates and [^{18}F] processing within a total processing time of 10 min. In another case, Wester, Schoultz, Hultsch, and Henriksen (2009) used a capillary reactor (inner diameter 300 μm, length 0.7 m) for the production of [^{18}F]FDG. They reported that the reaction had optimum performance at a temperature of 105 °C and a residence time of 40 s. The group subsequently conducted a NaOH hydrolysis, to afford [^{18}F]FDG in 88% RCY within a processing time of 7 min. In another instance, Lu and Pike (2007) reported the synthesis and reaction of [^{18}F]XeF_2 in a microreactor. They conducted a detailed study that indicated that the optimum method for the synthesis was to react xenon difluoride with cyclotron-produced [^{18}F]fluoride in either dichloromethane (DCM) at room temperature or acetonitrile at 80 °C, with a residence time of about 1.5 min. With the optimum conditions for generation of [^{18}F]XeF_2 in hand, they subsequently investigated the reaction of the complex. Also, the reaction of a solution of trimethylsilyl (TMS) silyl enol ether in acetonitrile with [^{18}F]XeF_2 at 80 °C for 3.1 min afforded the radiolabeled ketone in 78% RCY.

Also, Lu, Giamis, and Pike (2009) synthesized [^{18}F]fallypride in a microreactor for rapid optimization and multiple production in small doses. A commercial coiled-tube microreactor (NanoTek; Advion) was used as a convenient platform for synthesis of [^{18}F]fallypride in small doses (0.5–1.5 mCi) of brain dopamine subtype-2 receptors in rodents. Each radiosynthesis used low amounts of tosylate precursor and [^{18}F]fluoride ion. Optimization of the labeling reaction in their apparatus, with respect to the effects of precursor amount, reaction temperature, flow rate, and [^{18}F]fluoride ion-to-precursor ratio was achieved rapidly and the decay-corrected RCY of [^{18}F]fallypride up to 88% was reproducible. From their study, in a 2-m-long reactor, the decay-corrected RCY of [^{18}F]fallypride increased from 0% to 65% over the temperature between 100 and 170 °C. The RCYs of [^{18}F]fallypride were quite reproducible and independent of laboratory setting and method of analysis. Each radiosynthesis used 20 or 40 μg (38.7 or 77.4 nmol) of precursor, only 1 or 2% of that used conventionally, and a whole run required only 4 min. By using two of 2-m-long reactors (total length 4 m) connected in series, RCYs reached 88%. In a single 4-m reactor, a longer residence time, achieved by using a slower flow rate from each reactant syringe, moreover increased the RCY. When the volume ratio of [^{18}F]fluoride ion to precursor solution was increased, RCY increased slightly and when this ratio was decreased RCY decreased slightly with flow rate on the RCYs of [^{18}F]fallypride at 140 °C in a 4-m microreactor. The product fraction eluting between 10.9 and 11.9 min was collected for formulation.

Moreover, Chun, Lu, Lee, and Pike (2010) investigated fast and high-yield microreactor syntheses of *ortho*-substituted [^{18}F]fluoroarenes from the reactions of [^{18}F]fluoroarene ion with diaryliodonium salts. In their study, a microreactor was applied to produce the *ortho*-substituted [^{18}F]fluoroarenes from reactions of cyclotron-produced [^{18}F]fluoride ion with $t_{1/2} = 109.7$ min with diaryliodonium salts. The microreactor provided a very convenient means for running sequential reactions rapidly with small amounts of the reagents under well-controlled conditions, thus allowing reaction kinetics to be followed and Arrhenius activation energies to be measured. The schematic of the experimental setup for the synthesis of a PET-tracer (FMISO) is shown in Figure 24.7. As well, Elizarov et al. (2010) investigated the flow optimization of a batch microfluidics PET-tracer synthesizing device with a coin-shaped microfluidic chip. They used fluorescent imaging techniques for mixing and elution optimization inside a fabricated reaction chamber. For the mixing quality evaluation tests, the reactor was partially filled with an aqueous dye solution (Alexa-Fluor4 fluorophore dye; 0.1 mg/mL) followed by dead-end injection of pure water and monitoring the quality of mixing over time. Total fluorescence emission within the reactor was monitored to record elution efficiency. As a result, the elution process was considered complete when the total reactor fluorescence measure had decreased by 95% of initial value. Also, Keng et al. (2011) investigated the microchemical synthesis of molecular probes on an electronic microfluidic device. Figures 24.8 and 24.9 show the electrowetting on dielectric (EWOD) microchip with four concentric heaters with a maximum volume and the sequence of photographic images with corresponding Carenkov images and synthetic scheme of multistep radiosynthesis performed on EWOD.

24.6 Electrical impedance tomography

Electrical impedance tomography (EIT) is a noninvasive technique for imaging the distribution of an electrical property within a medium using electrical measurements from a series of electrodes flush-mounted with the medium surface. Electrical properties employed in EIT include capacitance, resistance, inductance, and eddy current. For example,

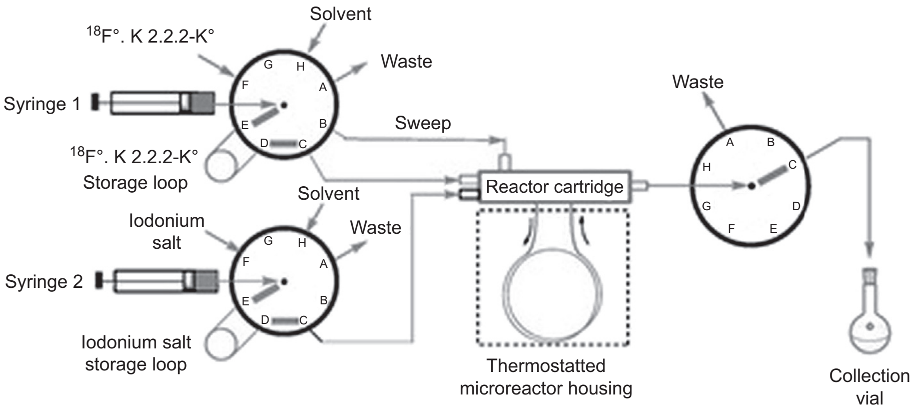
Solvent
^{18}F°. K 2.2.2-K°
G
H
Waste
F
A
Syringe 1
E
B
Sweep
D
C
^{18}F°. K 2.2.2-K°
Storage loop
Solvent
Iodonium
salt
G
H
Waste
F
A
Syringe 2
E
B
D
C
Iodonium salt
storage loop
Reactor cartridge
Thermostatted
microreactor housing
Waste
A
B
H
C
G
D
F
E
Collection
vial

Figure 24.7 Experiment setup: Schematic setup for the synthesis of a PET tracer (FMISO). Reprinted with permission from Chun et al. (2010). Copyright 2010, J. Org. Chem Publishing.

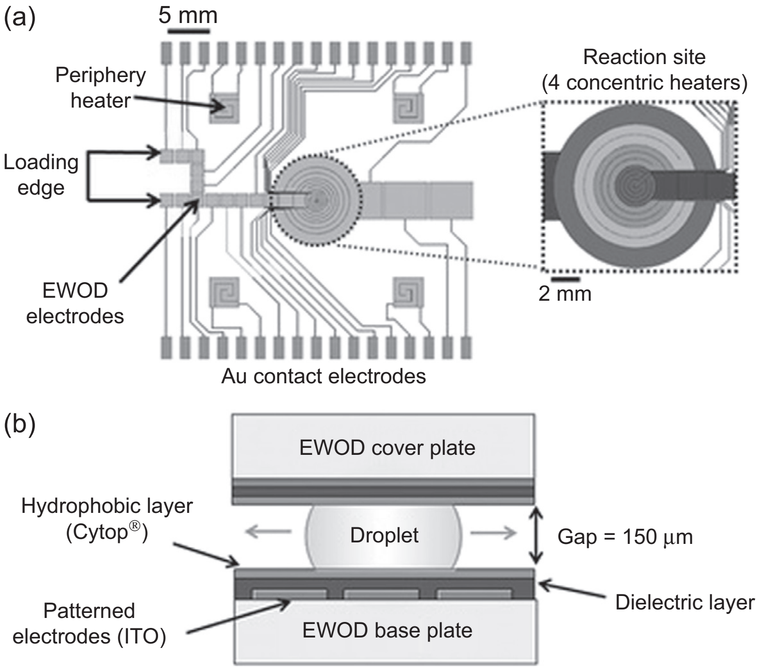
(a)
5 mm
Periphery
heater
Loading
edge
EWOD
electrodes
Reaction site
(4 concentric heaters)
2 mm
Au contact electrodes
(b)
EWOD cover plate
Hydrophobic layer
(Cytop®)
Droplet
Gap = 150 µm
Dielectric layer
Patterned
electrodes (ITO)
EWOD base plate

Figure 24.8 (a) EWOD microchip with four concentric heaters (dashed circle) with a maximum volume of 17 µL. Inset shows magnified area of the heater with four concentric individually controlled resistive heating rings. (b) Schematic side view of the EWOD chip sandwiching a reaction droplet between two plates coated with ITO electrodes, a dielectric layer, and a hydrophobic layer of Cytop (not to scale).
Reprinted with permission from Keng et al. (2011). Copyright 2011, Proceedings of the National Academy of Sciences of the United States of America Publishing.

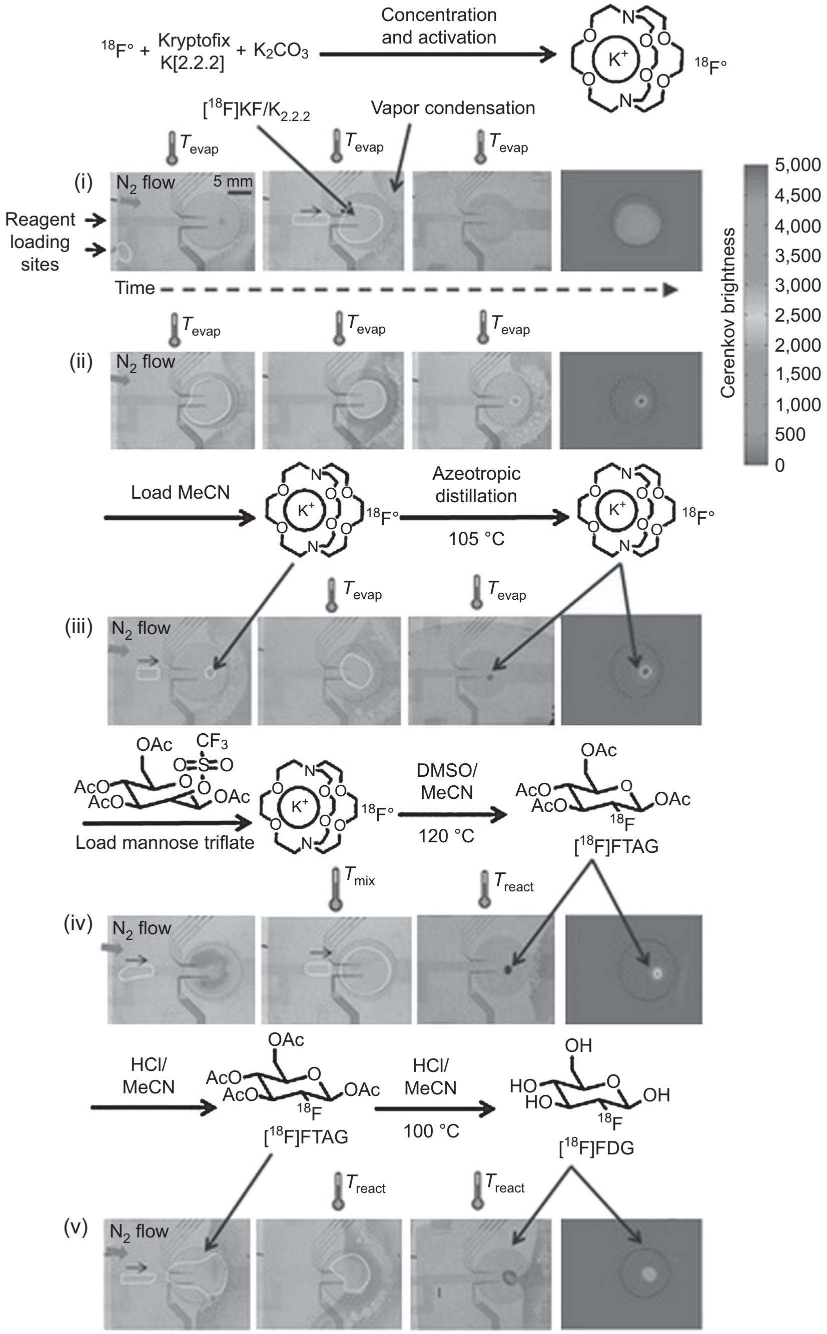

$^{18}F^{\circ}$ + Kryptofix K[2.2.2] + K_2CO_3
Concentration and activation
K+
N
O
$^{18}F^{\circ}$
[^{18}F]KF/$K_{2.2.2}$
Vapor condensation
T_{evap}
(i)
N_2 flow
5 mm
Reagent loading sites
Time
(ii)
Cerenkov brightness
5,000
4,500
4,000
3,500
3,000
2,500
2,000
1,500
1,000
500
0
Load MeCN
Azeotropic distillation
105 °C
(iii)
OAc
CF_3
O=S=O
AcO
Load mannose triflate
DMSO/ MeCN
120 °C
^{18}F
[^{18}F]FTAG
T_{mix}
T_{react}
(iv)
HCl/ MeCN
100 °C
OH
HO
[^{18}F]FDG
(v)

Figure 24.9 Experiment results: Sequence of photographic images with corresponding Carenkov images and the synthetic scheme of the multistep radiosynthesis performed on EWOD.

Reprinted with permission from Keng et al. (2011). Copyright 2011, Proceedings of the National Academy of Sciences of the United States of America Publishing.

capacitance sensing is suitable for electrically insulating multiphase systems, while resistance and inductance sensing are useful for detecting electrically conducting materials or for materials that generate eddy currents or affect magnetic permeability. Among EIT techniques, electrical capacitance tomography (ECT) is better developed in chemical reactor applications. In the applications and principles of resistivity-based EITs, ECT uses a contrasting property for imaging the electrical capacitance (or the dielectric constant), which is a function of the volume fraction of the materials. In point measurement devices, capacitance sensors usually consist of two or more electrodes placed on the opposite sides of the section to be imaged. For tomographic measurements, an array of electrodes around the boundary of the process stream is required. Each measurement can be used to determine the capacitance value in one region or pixel in sensed volume.

In general, electrical sensing techniques such as ECT have the advantage of being faster and safer than hard-field shorter-wavelength nuclear-based tomographies. Also, since the primary signal issued from electrical sensing techniques is itself of an electrical nature, these techniques are easily amenable to automation and digital computer control. As well, the cheaper commercial implementation of ECT, and electrical imaging techniques in general, accommodate large- and small-vessel geometries with greater flexibility than nuclear-based tomographies. However, even though ECT is powerful in tracing evanescent phenomena and fast-flowing streams exhibiting intense composition fluctuations, the spatial resolution of ECT images is considerably poorer than that of the nuclear-based tomographies. The spatial resolution corresponds to voxels of 1 $\text{cm}^2 \times 2.54$ cm (METC ECT, 32 electrodes) and 3.4 $\text{cm}^2 \times 10$ cm (UMIST ECT, 12 electrodes) and is limited by uniformity, alignment, and electrode size used to contain and shape electrical flux lines.

Additionally, the fluid flow in a microchannel has emerged as an important area of research that has been motivated by various applications in medical and biomedical use, computer chips, and chemical separations. Usually, the ECT is visualized into the cross-sectional image representing the distribution of density. ECT is a recently developed imaging technique, where the images of conductivity or permittivity of the subject can be rapidly collected with channels of external electrodes. Recently, Takei's group considered application of ECT to the microchannel (Ali Othman, Obara, & Takei, 2013). As a first step, we developed the ECT measurement technique to determine nanoparticle concentration in the microchannel with 60 sensor electrodes. Using ECT in the microchannel, a particle distribution image can be obtained. Based on the reconstructed image, it is easy to estimate the particle diffusion/migration behaviors in a fluid flow.

In addition, we also investigated the sorting of embryonic stem (ES) cells using dielectrophoresis and electro-osmosis (Choi, Takei, & Doh, 2010). From that, we were able to separate a group of small-cell and large-cell populations from large populations of mixed cells. A miniature sensor system is designed for electrical tomography comprising many sensor electrodes, which are distributed around the microchannel with a rectangular cross section, where the rectangular cross section has 12 sensor electrodes. Our microchannel was fabricated by Covalent Materials Corporation, Japan, and consisted of 60 multilayered sensor electrodes attached around the microchannel to measure the particle distribution of five different positions. Figure 24.10 shows the microchannel device with cross-sectional configuration and a position of vertical cross sections (Ali Othman et al., 2013). Figure 24.10(a)

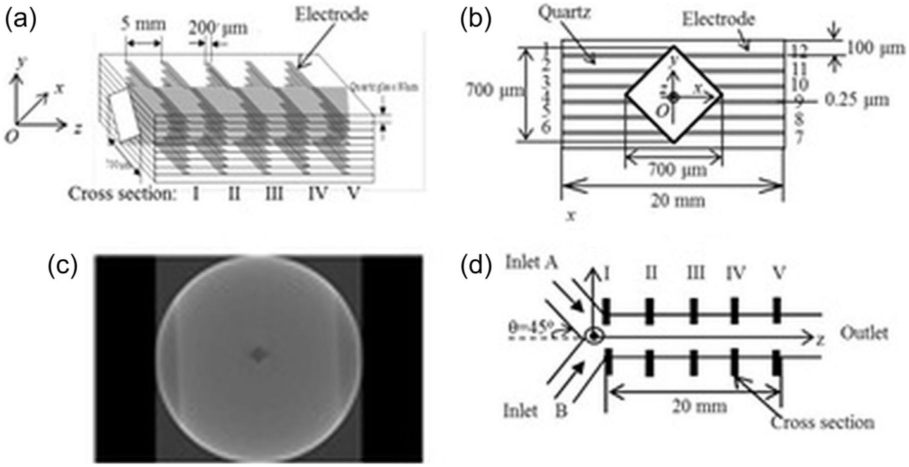

Figure 24.10 Microchannel with cross-sectional configuration and top view of cross-section position: (a) 3D microchannel, (b) cross-sectional microchannel, (c) micro image of diamond-shaped cross-sectional microchannel, and (d) position of five cross sections.
Reprinted with permission from Ali Othman et al. (2013). Copyright 2013, Flow Measurement and Instrumentation Publishing.

illustrates a 3D cross-sectional microchannel with five cross sections and multilayered electrodes embedded at each cross section. The length of the microchannel from origin to outlets is 20 mm, and the distance between cross sections is 5 mm, as shown in Figure 24.10(d). The electrode has a diameter of 75 μm, and the electrode interval in the cross section is 200 μm. The total size of the microchannel is 4 × 2 cm. Figure 24.10(b) shows the cross-sectional microchannel in a diamond-shaped groove with 12 multilayered electrode positions; electrodes are numbered in a counterclockwise manner from the top left position 1–12. The diamond-shaped groove width and height is 700 μm in x-axis and y-axis. In the case of 12 electrodes, the total number of electrode pairs in the capacitance measurement, n, is 66 pairs. Figure 24.11 shows an example of the experimental results of the reconstruction image of particle concentration distribution at three vertical cross sections in the microchannel (Choi et al., 2010). In our latest research, ECT is applied for 3D particle concentration, monitoring, and particle or cell manipulation using a dielectrophoresis technique.

In addition, Yonghong, Xiantao, and Takei (2013) investigated solid–liquid phase flow image reconstruction using electrical resistance tomography (ERT) in a microchannel. On a quartz-glass-made framework with 570 μm width, five cross sections are separated from each other by 4.5 mm. In each cross section, 16 resistance-sensing electrodes are embedded, separated from each other by 80 μm, as shown in Figure 24.12. Figure 24.13 shows the experimental result of the predicted equipotential in the cross section from finite element modeling. It gives representative results for the 16-electrode in microchannel, a single particle with 5 μm diameter located near the top right of the diagram, suggesting that the invading solid phase can result in

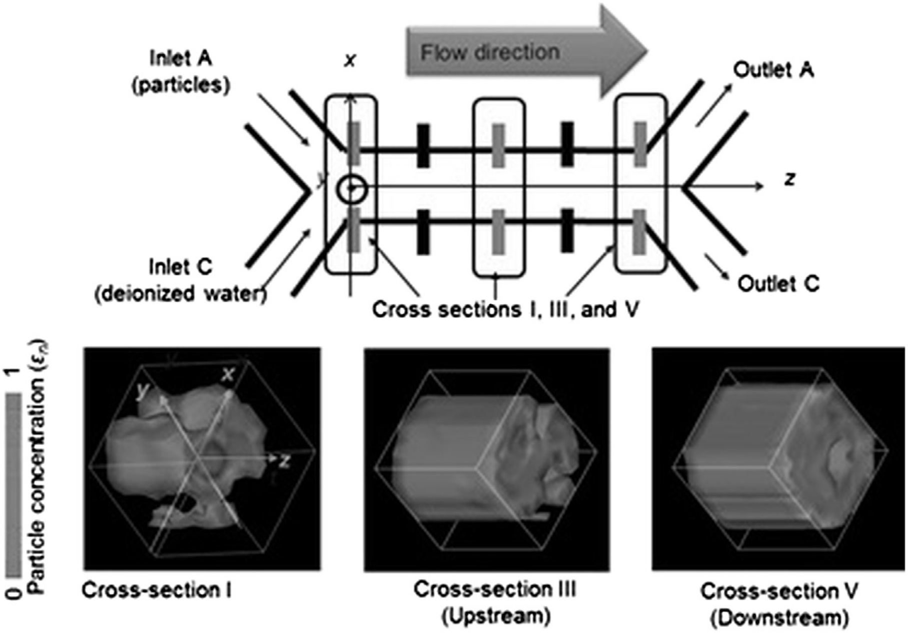

Flow direction
Inlet A
(particles)
x
Outlet A
z
Inlet C
(deionized water)
Outlet C
Cross sections I, III, and V
1
0
Particle concentration (ε_p)
y
x
z
Cross-section I
Cross-section III
(Upstream)
Cross-section V
(Downstream)

Figure 24.11 Experiment results: Particle concentration distribution at vertical cross sections. Reprinted with permission from Choi et al. (2010). Copyright 2010, Flow Measurement and Instrumentation Publishing.

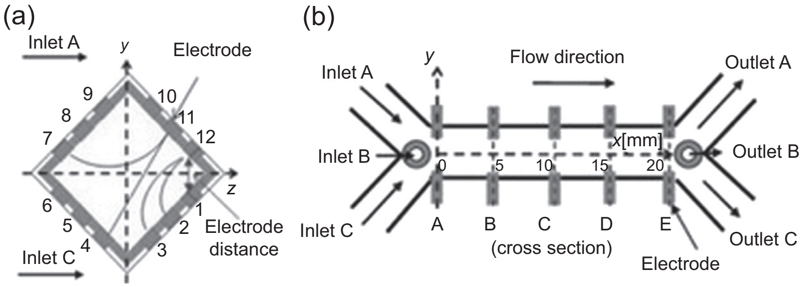

(a)
Inlet A
y
Electrode
9
10
8
11
7
12
z
6
1
5
2
Electrode
distance
4
3
Inlet C
(b)
y
Flow direction
Inlet A
Outlet A
Inlet B
x[mm]
Outlet B
0
5
10
15
20
Inlet C
A
B
C
D
E
(cross section)
Outlet C
Electrode

Figure 24.12 (a) Positions of electrodes in the cross section. (b) Geometry of the microchannel. Reprinted with permission from Choi et al. (2010). Copyright 2010, Flow Measurement and Instrumentation Publishing.

the change of equipotentials distribution. Figure 24.14 shows voltages measured in the experiment; Figure 24.14(a), (b), and (c) are corresponding voltages measured on cross sections I, III, and V. From these results, it has shows the change with the controlled two-phase flow inside a microchannel with the highest voltage level about 3.5 mV. The results prove that contact resistance can be effectively suppressed, and measured boundary voltages are sensitive to the changes of resistivity distribution in the microchannel under the experimental conditions.

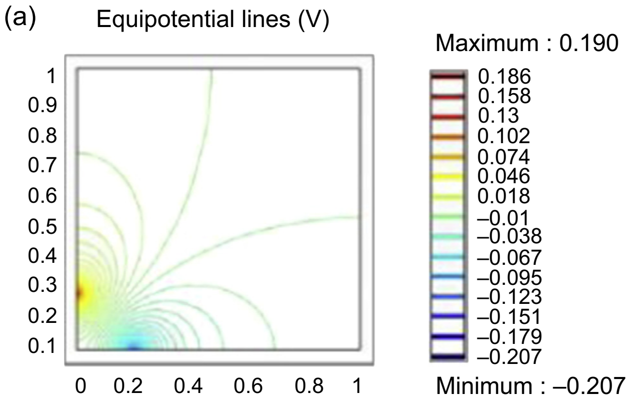

No disturbance

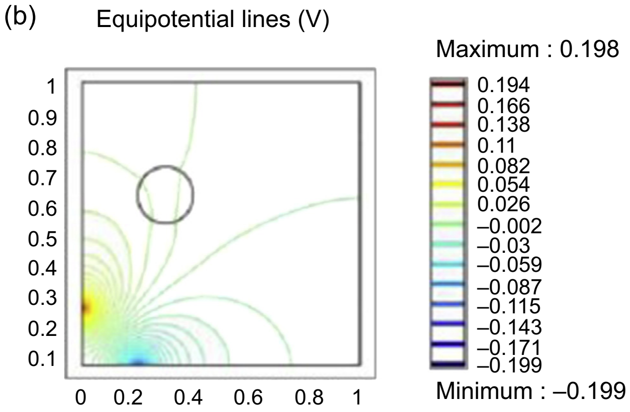

5μm diameter solid particle as disturbance

Figure 24.13 Predicted equipotential in the cross section from finite element modeling. Reprinted with permission from Yonghong et al. (2013). Copyright 2013, TELKOMNIKA Publishing. http://dx.doi.org/10.1016/j.flowmeasinst.2010.03.006

24.7 Future trends

Microreactor and microchannel technology is a powerful tool and has become indispensable over a wide application range, from organic synthesis to enzymatic controlled reactions. A miniaturization with the possibility of reaction tomography, and thus a significant reduction in costs, will be the next step in the foreseeable future. Many chemical reactions, especially organic and fine chemical synthesis, could already be transferred to continuous microreaction processes. The small geometric dimensions result in an intensified mass and heat transfer, which often leads to increased yield and selectivity compared to the classical batch approach. However, microreaction

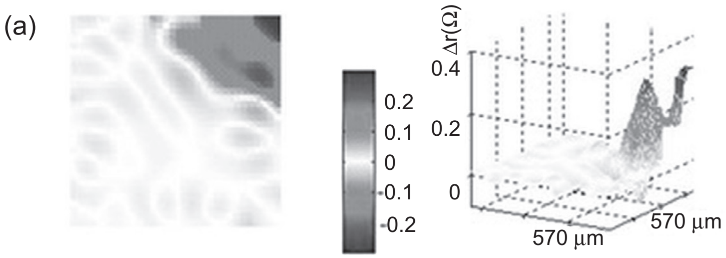

Reconstructed image on cross-section I

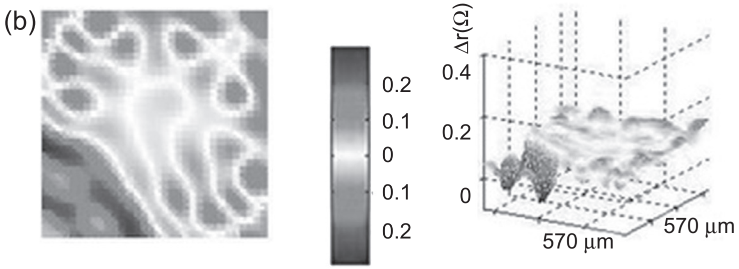

Reconstructed image on cross-section III

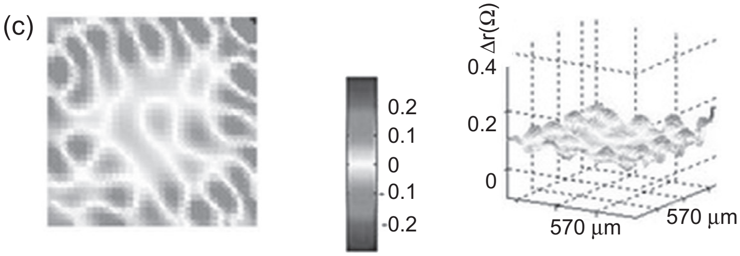

Reconstructed image on cross-section V

Figure 24.14 2D and 3D distribution on some sample cross sections. It shows the changes of resistivity distribution in all of the five cross-sections in the microchannel. It can see that along the flow direction from cross section I (a) to cross-section III (b) and cross-section V (c), Polymer microsphere suspension and NaCl solution resolve into each other gradually except in cross-section I, NaCl solution just meet each other. The test result also reveals that under certain flow rate, polymer micro particles have already dispersed evenly near cross-section V. Reprinted with permission from Yonghong et al. (2013). Copyright 2013, TELKOMNIKA Publishing.

technology today is still at the threshold between academia and industry. A crucial factor for the successful implementation of microstructured production processes in industry is a suitable process analytical technology. Time and spatially resolved online analysis must be implemented directly in the microfluidic channels. Thus, parallel and multiplexed measurement technologies are needed to reduce costs and increase the robustness of information. To date, no commercially available solutions exist. Typical state-of-the-art procedures to study chemical processes use flow cells positioned after microstructured environments or off-line methods.

Moreover, no information about the actual reaction process inside the microreactor and microchannel is generated. However, a disadvantage for the industry is the increasing costs for analytical devices required to assure constant product quality. The production of high-added-value chemicals by means of a microstructured process requires several hundred microreactors in order to produce sufficiently large amounts of final product. Thus, large numbers of flow cells, each attached to a separate spectrometer, are needed to meet these unique requirements. An alternative technology is to analyze several microchannels simultaneously or to analyze a single microchannel spatially resolved along the reaction path using push-broom imaging technology. This type of optical online spectroscopy is an ideal tool to characterize chemical reactions in a fast and reliable way, even on a molecular level. Transmission or reflectance spectra are registered through fixed prism—grating—prism optics with a 2D charge-coupled device (CCD) camera attached to it. Thereby, the *x*-axis of the CCD array corresponds to the spatial resolution, and the *y*-axis of the camera provides the full spectrum of the sample.

References

Ali Othman, N. T., Obara, H., & Takei, M. (2013). Cross-sectional capacitance measurement of particles concentration in a microchannel with multi-layered electrodes. *Flow Measurement and Instrumentation, 31*, 47—54. http://dx.doi.org/10.1016/j.flowmeasinst.2012.12.003.

Benton, D. M., & Parker, D. J. (1997). Non-medical applications of positron emission tomography. In J. Chaouki', F. Larachi, & M. P. Duduković (Eds.), *Non-invasive monitoring of multiphase flows* (Vol. 5, p. 161). Amsterdam, the Netherlands: Elsevier.

Bouchard, L.-S., Burt, S. R., Anwar, M. S., Kovtunov, K. V., Koptyug, I. V., & Pines, A. (2008). NMR imaging of catalytic hydrogenation in microreactors with the use of para-hydrogen. *Science, 319*, 442.

Callaghan, P. T., & Xia, Y. (1991). Velocity and diffusion imaging in dynamic NMR microscopy. *Journal of Magnetic Resonance, 91*, 326.

Cheng-Lee, C., Sui, G., Elizarov, A., Shu, C. J., Shin, Y.-S., Dooley, A. N., et al. (2005). Multistep synthesis of a radiolabeled imaging probe using integrated microfluidics. *Science, 310*, 1793—1796.

Choi, J., Takei, M., & Doh, D. H. (2010). Fabrication of microchannel with 60 electrodes and resistance measurement. *Flow Measurement and Instrumentation, 21*(3), 178—183. http://dx.doi.org/10.1016/j.flowmeasinst.2010.03.006.

Chun, J.-H., Lu, S., Lee, Y.-S., & Pike, V. W. (2010). Fast and high-yield microreactor syntheses of ortho-substituted [^{18}F]fluoroarenes from reactions of [^{18}F]fluoride ion with diaryliodonium salts. *Journal of Organic Chemistry, 75*, 3332—3338.

Elizarov, A. M. (2009). Microreactors for radiopharmaceutical synthesis. *Lab Chip, 9*, 1326—1333.

Elizarov, A. M., Meinhart, C., Miraghaie, R., Michael, R., Huang, J., Daridon, A., et al. (2010). Flow optimization study of a batch microfluidics PET tracer synthesizing device. *Biomedical Microdevices, 13*, 231—242.

Elizarov, A. M., Michael, R., Shik Shin, Y., Hartmuth, C. K., Henry, C. P., Stout, D., et al. (2010). Design and optimization of coin-shaped microreactor chips for PET radiopharmaceutical synthesis. *Journal of Nuclear Medicine, 51*, 282−287.

Espinosa-Alonso, L., O'Brien, M. G., Jacques, S. B. M., Beale, A. M., de Jong, K. P., Barnes, P., et al. (2009). Tomographic energy dispersive diffraction imaging to study the genesis of Ni nanoparticles in 3D within γ-Al_2O_3 catalyst bodies. *Journal of the American Chemical Society, 131*, 16932.

Gillies, J. M., Prenant, C., Chimon, G. N., Smethurst, G. J., Perrie, W., Dekker, B. A., et al. (2006). Microfluidic technology for PET radiochemistry. *Journal of Applied Radiation and Isotopes, 64*, 333−338.

Gillies, J. M., Prenant, C., Chimon, G. N., Smethurst, G. J., Perrie, W., Hamblett, I., et al. (2006). Microreactor for the radiosynthesis of PET radiotracers. *Journal of Applied Radiation and Isotopes, 64*, 325−332.

Grunwaldt, J.-D., & Schroer, C. G. (2010). Hard and soft X-ray microscopy and tomography in catalysis: bridging the different time and length scales. *Chemical Society Reviews, 39*, 4741−4753.

Hannemann, S., Grunwaldt, J.-D., Vegten, N., Baiker, A., Boye, P., & Schroer, Christian G. (2006). Distinct spatial changes of the catalyst structure inside a fixed-bed microreactor during the partial oxidation of methane over Rh/Al_2O_3. *Catalyst today, 126*, 54−63.

Jamal, C., Larachi, F., & Dudukovic, M. P. (1997). Noninvasive tomographic and velocimetric monitoring of multiphase flows. *Industrial and Engineering Chemistry Research, 36*, 4476−4503.

Keng, P. Y., Chen, S., Ding, H., Sadeghi, S., Shah, G. J., Dooraghi, A., et al. (2011). Micro-chemical synthesis of molecular probes on an electronic microfluidic device. *Proceedings of the National Academy of Sciences of the United States of America*, v1−6. Pnas 1117566109.

Lee, C. C., Sui, G. D., Elizarov, A., Shu, C. J., Shin, Y. S., Dooley, A. N., et al. (2005). Multistep synthesis of a radiolabeled imaging probe using integrated microfluidics. *Science, 310*, 1793−1796.

Lu, S. Y., Giamis, A. M., & Pike, V. W. (2009). Synthesis of [^{18}F]fallypride in a micro-reactor: rapid optimization and multiple-production in small doses for micro-PET studies. *Current Radiopharmaceuticals, 2*, 49−55.

Lu, S. Y., & Pike, V. W. (2007). Micro-reactors for PET tracer labeling. In A. Schubiger, L. Lehmann, & M. Friebe (Eds.), *PET chemistry: The driving force in molecular imaging* (Vol. 62, pp. 271−287). Berlin: Springer.

Lu, S. Y., & Pike, V. W. (2010). Synthesis of [^{18}F]xenon difluoride as a radiolabeling reagent from [^{18}F]fluoride ion in a micro-reactor and at production scale. *Journal of Fluorine Chemistry, 131*, 1032−1038.

Lu, S. Y., Watts, P., Chin, F. T., Hong, J., Musachio, J. L., Briard, E., et al. (2004). Syntheses of ^{11}C- and ^{18}F-labeled carboxylic esters within a hydrodynamically driven micro-reactor. *Lab Chip, 4*, 523−525.

Miller, P. W., Long, N. J., de Mello, A. J., Vilar, R., Audrain, H., Bender, D., et al. (2007). Rapid multiphase carbonylation reactions by using a microtube reactor: applications in positron emission tomography ^{11}C-radiolabeling. *Angewandte Chemie, International Edition, 46*, 2875−2878.

Pascali, G., Nannavecchia, G., Pitzianti, S., & Salvadori, P. A. (2011). Dose-on-demand of diverse ^{18}F-fluorocholine derivatives through a two-step microfluidic approach. *Nuclear Medicine and Biology, 38*, 37−644.

Schroer, C. G., Kuhlmann, M., Günzler, T. F., Lengeler, B., Richwin, M., Griesebock, B., et al. (2003). Mapping the chemical states of an element inside a sample using tomographic X-ray absorption spectroscopy. *Applied Physics Letters, 82*, 3360−3362.

Smit, E.de, Swart, I., Creemer, J. F., Hoveling, G. H., Gilles, M. K., Tyliszczak, T., et al. (2008). Nanoscale chemical imaging of a working catalyst by scanning transmission X-ray microscopy. *Nature, 456*, 222−225.

Steel, C. J., O'Brien, A. T., Luthra, S. K., & Brady, F. (2007). Automated PET radiosyntheses using microreactor. *Journal of Labelled Compounds and Radiopharmaceuticals, 50*, 308−311.

Van den Broek, S. A. M., Becker, R., Koch, K., & Nieuwland, P. J. (2012). Microreactor technology: real-time flow measurements in organic synthesis. *Micromachines, 3*, 244−254. http://dx.doi.org/10.3390/mi3020244.

Watts, P., & Wiles, C. (2007). Recent advances in synthetic micro reaction technology. *Chemical Communications, 5*, 443−467.

Wester, H. J., Schoultz, B. W., Hultsch, C., & Henriksen, G. (2009). Fast and repetitive incapillary production of F-18 FDG. *European Journal of Nuclear Medicine and Molecular Imaging, 36*, 653−658.

Yonghong, L., Xiantao, W., & Takei, M. (2013). Solid-liquid two-phase flow image reconstruction based on ERT technique in microchannel. *TELKOMNIKA, 11*, 173−180. http://dx.doi.org/10.11591/telkomnika.v11i1.1885.

Applications of tomography in food inspection

25

M.A. Del Nobile, J. Laverse, V. Lampignano, B. Cafarelli, A. Spada
University of Foggia, Foggia, Italy

25.1 Introduction

To aid understanding of the physical and rheological behaviour as well as the mechanical and sensory attributes of foods, processing focus and emphasis have shifted to the microstructure level. This chapter, therefore, deals in the application of X-ray microtomography to food inspection. Microstructure elements such as air bubbles or cells, starch granules, protein assemblies and food biopolymer matrices contribute greatly to the identity and quality of foods (Aguilera, 2005). The microstructure of food has an influence over the main attributes of a product as evaluated by consumers. Advances in the last decade in microscopy techniques, along with an improvement in computing capabilities, have made it possible to understand a food's structure, its relation to physical properties (so-called structure—property relationships) and how to engineer and control these properties (Aguilera, 2005). Although a wide range of imaging techniques exists, they are mostly invasive, as they require sample preparation, hence, formation of artefacts or are restricted to certain types of food products. X-ray microtomography (μCT), on the other hand, is a noninvasive technique that has several advantages over other methods, including the ability to image low-moisture materials. Given the enormous success of X-ray computed tomography (μCT) in medical applications and material science, it is not surprising that in recent years much attention has been focused on extending this imaging technique to food science as a useful technique to aid in the study of food microstructure. This chapter uses four case studies to prove how X-ray microtomography can be used in food inspection and also to help understand the correlation between the physical aspect and microstructural properties of food products. These studies also demonstrate how the application of X-ray microtomography can aid in the study of cellular food microstructure such as breads, wheat and coffee beans by imaging and visualizing the internal structure.

25.2 Description of testing method used in X-ray microtomography

X-ray microtomography (μCT) uses the differences in X-ray attenuation arising, principally, from differences in density within the specimen. A series of X-ray projections are recorded at a number of angles around the specimen (usually over a range of either

Industrial Tomography. http://dx.doi.org/10.1016/B978-1-78242-118-4.00025-3
Copyright © 2015 Elsevier Ltd. All rights reserved.

180 or 360°). In μCT, unlike medical CT, the specimen is usually rotated, rather than the X-ray source and detector. If the projections are taken through a single plane in the specimen, it is possible to reconstruct a cross-sectional image of that plane. In most μCT scanners today, 2D images are recorded, making it possible to reconstruct a complete 3D map of X-ray attenuation. A complete μCT analysis is normally made by acquiring a number of radiographs (typically about 1000) of the same sample under different viewing angles (one orientation for each radiograph). A series of 2D X-ray images are obtained as a sample is rotated. A final computed reconstruction step is required to produce a 3D map of the linear attenuation coefficients in the material. This 3D map indirectly gives a picture of the structure density. In μCT, the X-ray source and the detector are placed at the opposite sides of the sample. The spatial resolution of the attenuation map depends on the characteristics of both the detector and the number of X-ray projections. Differences in the linear attenuation coefficients within a material are responsible for the X-ray image contrast. The main contrast formation in μCT is due to absorption contrast. Manipulation and analyses of μCT data using special software also allow reconstruction of cross-sections at depth increments as low as 15 μm and along any desired orientation of the plane of cut. A series of noninvasive μCT slices of the same sample in any direction can provide much more information than just one scanning electron microscopy (SEM) or optical imaging picture, for example. The true 3D shape of the cells can also be visualized from its 2D slices (Trater, Alavi, & Rizvi, 2005). Through μCT image analysis, it is possible to obtain the following average and/or individual quantitative microstructural properties for the food product under investigation: object volume (OV), object surface (OS), percent object volume (POV), object surface/volume ratio (OSVR), fragmentation index (FI), structure thickness (St.Th), structure separation (St.Sp), structure model index (SMI), and degree of anisotropy (DA).

Where, (1) OV is the total volume of each individual binarized 3D object present within the volume of interest (VOI); (2) OS is the total surface of each individual binarized 3D object present within the VOI measured for each sample; (3) POV is the proportion of the VOI occupied by binarized solid objects; (4) OSVR is the basic parameter in characterizing the average complexity of the structures and is also the basis of model-dependent estimates of thickness; that is, average size and distribution of the object/structure present in each sample; (5) FI is the average index of connectivity of the structures; (6) St.Th calculates or estimates the average structure diameter of the object from 2D measurements; (7) St.Sp is essentially the average thickness (average distance) of the structure separating the object under investigation; (8) SMI estimates the characteristic form of which the structure is composed, that is, whether it is more plate-like, rod-like or even sphere-like (0 = ideal plate, 3 = cylinder and 4 = sphere) and (9) DA is a measure of preferential alignment of the object under investigation.

As stated above, with μCT image analysis, it is possible to obtain the average and/or individual quantitative microstructural properties for the objects under investigation, for example, pore/air spaces or fat. Previous studies by Cafarelli, Spada, Laverse, Lampignano, and Nobile (2014) have shown that the average quantitative microstructural data obtained can indeed be used to characterize and classify samples under investigation. Although, there is a large dataset generated by the individual microtomographic parameters, for example, a dataset produced for each individual pore present in a bread sample can be up to a 100,000 for each parameter; this could be solved by the use of advanced statistical analysis for data elaboration.

25.3 To date: food products studied

To date, X-ray microtomography has been successfully used to observe the stability of gas bubbles in dough during bread making process (Whitworth & Alava, 1999), the microstructure of foams (Lim & Barigou, 2004) and ice crystals within frozen foods (Mousavi, Miri, Cox, & Fryer, 2005). X-ray microtomography has also proven to be a very useful technique for the noninvasive visualization and measurement of the internal microstructure of cellular food products, such as porous rice kernels and whipped cream (Van Dalen, Blonk, Van Aalst, & Hendriks, 2003), bread (Falcone et al., 2004, 2005; Lassoued, Babin, Della Valle, Devaux, & Réguerre, 2007), cornflakes (Chaunier, Della Valle, & Lourdin, 2007), dough (Lampignano et al., 2012), extruded starches (Babin, Della Valle, Dendievel, Lourdin, & Salvo, 2007), biopolymer foams (Trater et al., 2005) and to study the microstructure, textural and sensorial properties of durum wheat bread as affected by yeast content (Lampignano et al., 2012).

The fat content in food products is a very important compound, and nowadays, lots of meat, dairy and emulsion products with different fat contents and different physical and chemical features (protein network, moisture content, ingredients, additives and so on) are being manufactured. Consumers of today require some of this information (e.g. total fat content, types of fat, ingredients, additives, etc.) to be stated. Therefore, the total fat content of these types of food products (e.g. salami, steak, mayonnaise, yoghurt, etc.) is an important quantity used in numerous studies. Thus, reliable methods for the quantitative analysis of fat from these types of food products are of critical importance. There are several methods to analyse fat content quantitatively (Monin, 1998). Although the method (AOAC, 1995) that is commonly used is based on chemical analysis, it is quite expensive and time-consuming. Furthermore, this technique is destructive to the sample; as a result, the same sample cannot be measured more than once and sometimes uses harmful, flammable solvents with health and environmental hazards. X-ray microtomography is nondestructive and provides in-depth information on the microstructure of the food product being tested; therefore, a better understanding of the physical structure of the product and, from an engineering perspective, knowledge about the microstructure of foods can be used to identify the important processing parameters that affect the quality of a product. In addition, to date X-ray microtomography has also been successfully used to study the fat contents in meat, yoghurt and mayonnaise food products (Frisullo, Laverse, Marino, & Del Nobile, 2009; Frisullo, Marino, Laverse, Albenzio, & Del Nobile, 2010; Laverse et al., 2011; Laverse, Mastromatteo, Frisullo, & Del Nobile, 2012).

With regard to porous food products, characteristics such as cell wall thickness, cell size and uniformity of cell size do not only affect the texture of the product (Kamman, 1970) but also its appearance, taste perception and stability of the final product (Autio & Laurikainen, 1997). Although microstructure parameters like size and number density of air cells and their contribution to mechanical properties of solid food foams have been studied before (Barrett, Cardello, Lesher, & Taub, 1994; Barrett & Peleg, 1992; Gao & Tan, 1996; Van Hecke, Allaf, & Bouvier, 1995), the underlying mechanism relating cellular structure to the mechanics of these products is still not well understood. The limitations of traditional imaging techniques like SEM and optical microscopy, which are two-dimensional and destructive in nature and also provide poor contrast, make it difficult to characterize cellular structure accurately. As stated above, X-ray tomography in recent years has proven to be particularly well suited for the 3D investigation of cellular materials. The studies to date show that tomographic images can accurately demonstrate in three dimensions the complexity of the morphology of cellular food products.

25.4 Case studies of food products studied to date

The aim of the following four case studies, as previously stated, is to prove the application of X-ray microtomography in food inspection and to demonstrate how the application of this technique can aid in the quantitative analysis of fat and in the study of cellular microstructure in foods such as wheat, coffee and bread that have different porosity by imaging and visualizing the internal structure.

25.4.1 Case study 1: meat

The aim of this case study was to demonstrate the capability of X-ray microtomography as a useful technique to quantify intramuscular fat content and to study fat distribution in different types of meat.

25.4.1.1 Sample preparation and analysis

The meat slices analysed (150) came from 30 animals of two different breeds, Podolian (P) versus Charolaise (CH), provided by two farms situated in the Gargano National Park, 50 km northwest of Foggia, Southern Italy. Immediately after slaughter the carcasses were chilled to 2 °C and samples excised 7 days postmortem. Five different commercial joints were collected to exhibit variability in terms of the visible structure of fat: tenderloin (TL), top sirloin (TS), top side (TSi), chuck tender (CT) and eye of round (ER). These were removed with their respective muscles: psoas major, biceps femoris, semimembranosus, supraspinatus and semitendinosus. Three samples were prepared for each type of meat, each 28 mm in diameter and a thickness of 18 mm. Each sample used for X-ray microtomography (μCT) analysis was wrapped with parafilm to avoid dispersion of moisture; the parafilm does not interfere with the X-rays. The same samples used for μCT analysis were also used for chemical analysis.

25.4.1.2 Image acquisition, processing and data analysis

The Skyscan 1172 high-resolution desktop X-ray microtomography system and the Skyscan software, CT-Analyser (CTAn) (Skyscan, Belgium), was used for image acquisition, processing and analysis. The following seven geometric parameters were measured using the CTAn software (Skyscan); percent object volume (POV), object surface/volume ratio (OSVR), fragmentation index (FI), structure model index (SMI), structure separation (St.Sp) and degree of anisotropy (DA).

25.4.1.3 Fat content determination using extraction method

Analysis of intramuscular fat content was performed according to AOAC (1995) method using the FOSS SoxCap 2047 System in combination with Soxtec extraction systems.

25.4.1.4 Discussion

Figure 25.1(a) and (b) shows the grey level reconstructed cross-sectional images acquired by X-ray microtomography for the CT samples for the CH and P meat, respectively. As reported beforehand, the contrast in these images is produced by a variation of density and a change in composition of the sample and is based exclusively on the detection of an amplitude variation of X-rays transmitted through the sample itself. It can be assumed from these figures that the dark grey areas represent fat as it has a lower absorption coefficient with respect to protein. Further information cannot be acquired from these images, as these are only 2D representations of the samples. Figure 25.2(a) and (b) shows as an example the three-dimensional reconstructions of the CT samples for both breeds from which the geometrical parameters were calculated using the CTAn software (Skyscan). The percentage fat volume, that is, the geometric parameter POV, was calculated for each image as a representation of the percentage total fat content within the sample. In order to assess the validity of X-ray microtomography, the fat content of the examined muscles were also determined by chemical analysis.

Pearson correlation coefficients (CORR procedure) were calculated to examine the relationship between percentage fat content and all μCT parameters (table not shown). It was noted that the POV is highly correlated with the fat determined by chemical

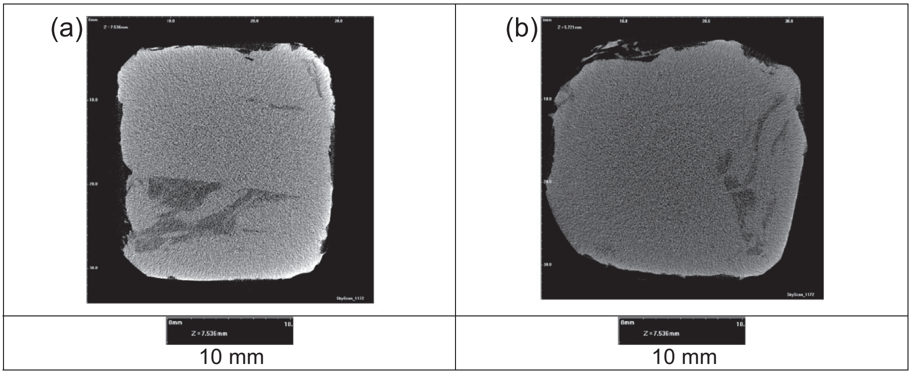

Figure 25.1 (a) and (b) show the grey-scale reconstructed cross-section images acquired by X-ray microtomography for the Charolaise (CH) and Podolian (P) breeds, respectively.

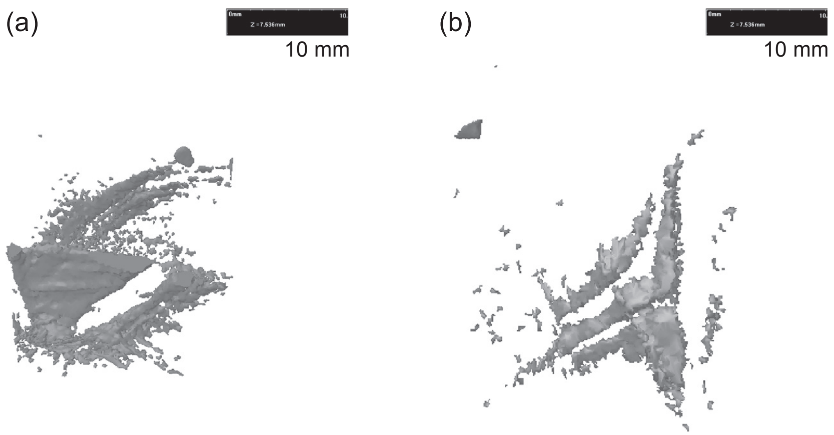

Figure 25.2 (a) and (b) show an example of the 3D reconstructions of the CT samples for both the Charolaise (CH) and Podolian (P) breeds, respectively.

analysis in both genotype and in all joints analysed in a range of $r = 0.92-0.99$ ($P < 0.001$). The high correlations between the two methods for determination of fat percentage highlight the validity of X-ray microtomography; therefore, this analysing technique allows an accurate quantification of the visual appearance of fat in meat. Previous research (Pipeck, Jelenikova, & Sarnovsky, 2004) found positive correlation between fat and fat content determined by video image analysis. However, that analysis showed some inaccuracies in fat determination as a consequence of interfering influence of connective tissue and bones. On the contrary, this case study verified the high level of reliability and accuracy of the X-ray microtomography technique. In addition, it could also be used to determine the spatial distribution of muscular fat.

Quantitative analysis was also carried out on the images obtained by μCT for the five different commercial joints of the meat from Podolian and Charolaise breeds. No significant differences were found for the SMI index in the different commercial joints of two different breeds. It is known that intramuscular fat penetrates into the core of the muscle as a vein, but to our knowledge, no information is available on the typical shape of intramuscular fat in the meat. The SMI values calculated for both the Podolian and Charolaise breeds ranged from 2.03 to 2.40 and from 2.17 to 2.40, respectively; these values are fairly close to 3, suggesting that the characteristic shape of the fat in the meat is cylindrical, as expected.

The fat content, expressed as POV, of the tenderloin, chuck tender, top sirloin, top side and eye round is similar to the values reported by Jeremiah, Dugan, Aalhus, and Gibson (2003), comparing different muscles. Tenderloin and chuck tender in both breeds had the highest POV ($P < 0.001$) values and the lowest OSVR ($P < 0.01$) with respect to the other commercial joints. OSVR indicates the fat distribution within the sample: the higher the value, the more finely distributed is the fat present in the sample. Therefore tenderloin and chuck tender have a higher fat content and the fleck of fat is largely distributed within these samples. This information could be very useful, because, if fat is finely distributed within a sample, higher fat content penetrates the meat sample without being negatively perceived by consumers, as they appreciate the taste of fat but not its appearance (Fernandez, Monin, Talmant, Mourot, & Lebret, 1999). In addition, the tenderloin had the lowest values of St.Sp ($P < 0.001$) in both breeds; St.Sp indicates the distance between flecks of fat within the samples: this result shows that tenderloin has flecks of fat that are close to each other. The DA is a measure of the 3D structural symmetry, that is, in this case it indicates the presence or absence of preferential alignment of the fat present along a particular direction (Lim & Barigou, 2004). A value of 0 would correspond to total isotropy, whereas a value of one would indicate total anisotropy. According to the quantitative results obtained for the DA parameter, the fleck of fat present in all the different commercial joints is isotropic, and there were no statistical differences among the samples. The FI parameter is the index of connectivity and is a measure of relative convexity or concavity of the total solid surface, based on the principle that concavity indicates connectivity, and convexity indicates isolated, disconnected structures (Lim & Barigou, 2004). A low FI signifies better connected, solid lattices; whereas, a high FI indicates a more disconnected, solid structure. The results showed a great variability of this index.

With regard to breed, Podolian is a rustic breed with low intramuscular fat content, as reported by Marino et al. (2006), whilst the Charolaise is a breed specialized in meat production with a higher visual appearance of intramuscular fat. The results of μCT analysis showed that the fat content, which is expressed as POV, was higher ($P < 0.01$) in the Charolaise breed, therefore reflecting the characteristics of this breed. The meat from the Charolaise breed has higher St.Sp ($P < 0.01$) values than Podolian. St.Sp is the average distance between the fat structures in the samples, the higher the value the more distant are the fat structures from one another.

This case study proves that X-ray microtomographic analysis seems to be suitable for rapid estimation of intramuscular fat of meat. The comparison of this method with the classical Soxhlet extraction showed a high correlation between fat contents obtained by both methods in all samples. X-ray microtomography allows a more accurate inspection of the fat in meat, more than the visual appearance; it shows the microstructure of fleck of fat measuring the size, shape, networking/connectivity and distribution of various phases.

25.4.2 Case study 2: wheat

The granary weevil *Sitophilus granarius* (L.) (*Coleoptera*, *Curculionidae*) is one of the most damaging primary pests of stored cereals and derived products worldwide. Infestation by this pest is generally difficult to detect because the immature stages (from egg to pupa) develop inside the grains. Given the enormous success of X-ray microtomography in medical applications, material science, chemical engineering, geology and biology, it is not surprising that in recent years this analysing technique has assumed an increased importance in entomological research as a new method for the noninvasive imaging of insects at a microscopic level. Therefore, the aim of this study is to evaluate the use of X-ray microtomography in detecting immature life stages of *S. granarius* in wheat grains in view of its application to study the development of internal-feeding insects and to detect hidden infestation in wheat samples.

25.4.2.1 Sample preparation and analysis

Adults of *S. granarius* were collected from a wild population occurring in traditional storage facilities near Campobasso (central Italy) and reared for several generations on wheat grains in cylindrical glass containers (15 cm diameter × 15 cm height) closed by a nylon mesh. Colonies were maintained in the dark in a climatic chamber set at 25 ± 2 °C and 60% ± 5% RH.

Wheat grains from rearing containers at different time intervals from initial infestation with adult weevils were used for detection analysis by X-ray microtomography. A batch sample was prepared by placing 88 wheat grains in a cylindrical tube that included two infested grains. The two infested grains (larval stage) were first identified by X-ray microtomography before added to the noninfested grains.

X-ray microtomographic analysis (μCT) was performed on three types of samples: (1) batch samples each containing four wheat grains from rearing containers glued to a metallic circular support to check for the presence of pre-imaginal stages of the granary weevil; (2) infested wheat samples from experiment 1 periodically analysed to assess the effect of X-ray exposure on the insect survival, and (3) a larger wheat sample obtained by mixing noninfested kernels with two infested grains collected from rearing containers and checked for infestation by X-ray analysis before sample preparation. All wheat samples were imaged under the same conditions, using the Skyscan 1172 high-resolution desktop X-ray microtomography system (Skyscan, Belgium).

25.4.2.2 Discussion

Figure 25.3 shows the cross-section of a wheat grain with an elliptical object enclosed in a cavity, which correspond to the typical granary weevil egg infestation. It is known that during the oviposition process an adult female first bores a hole into a grain; then she deposits a single elliptical egg into the cavity and finally seals in the egg with a gelatinous secretion forming a protective egg plug (Kirkpatrick, 1962; Robinson, 2005). Microstructural quantitative parameters measured on these images showed that the size of the object within the grain is 0.564 mm, which is consistent with the egg dimension of *S. granarius* reported in the literature (Cotton, 1921; Kirkpatrick, 1962).

Figure 25.4 shows a cross-section of wheat grains infested by a granary weevil larva. Larvae can be distinguished from the egg because they have a different shape (semicircular instead of elliptical) and are surrounded by a clearly visible dark tunnel. In fact, after hatching, the larva tunnelled from the egg cavity towards the centre of the grain, where it turned at right angles and continued lengthwise along the grain (Kirkpatrick, 1962). The tunnel and the accumulation of the frass beneath the dark line around the larva in Figure 25.4 confirms that the object within the grain image is indeed the larva of *S. granarius* (Kirkpatrick, 1962).

Finally, Figure 25.5 shows clearly the image of the pupa inside an infested grain. The pupa is recognized by the head with a snout, the thorax with wing pads and legs, and a definite abdomen (Kirkpatrick, 1962).

Although 2D X-ray imaging techniques have been used to this aim, they are not capable of producing high-quality images such as those produced by X-ray

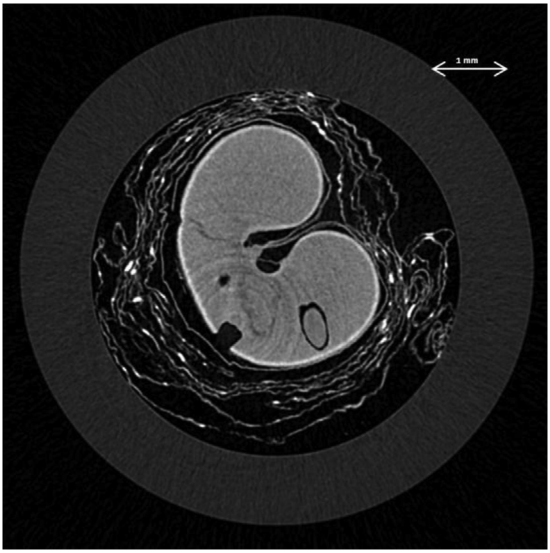

Figure 25.3 Cross-sections of a wheat grain with an elliptical object (egg stage of the *Sitophilus granarius*) enclosed in a cavity.

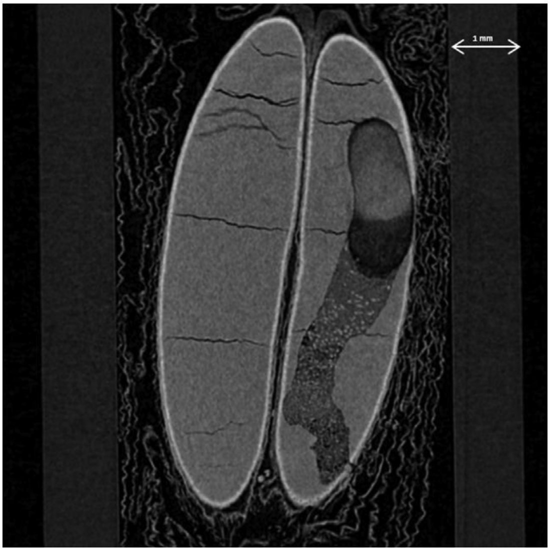

Figure 25.4 Images of a large larva inside a grain, as demonstrated by the almost completed tunnel.

microtomography. Also, they do not always make it possible to distinguish all the eggs on a radiograph, not only because of their small size but because of blemishes on the kernel and because of the angle at which the eggs were X-rayed (Kirkpatrick, 1962).

X-ray microtomography does not only allow visualization of the images in 2D but also in 3D. Although all the images above have been of single grain, X-ray

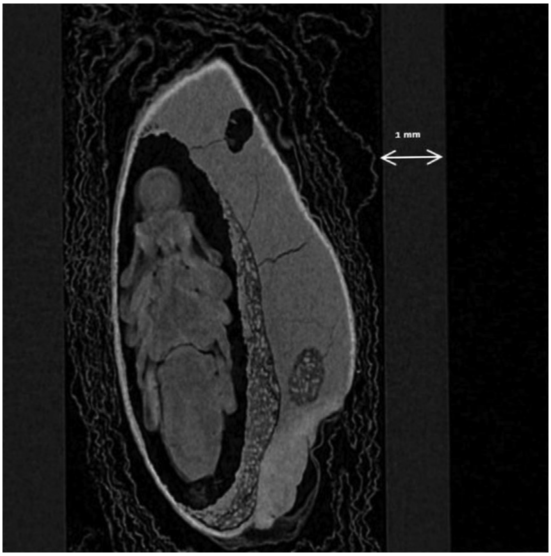

Figure 25.5 Images of a granary weevil at its pupa stage inside an infested grain.

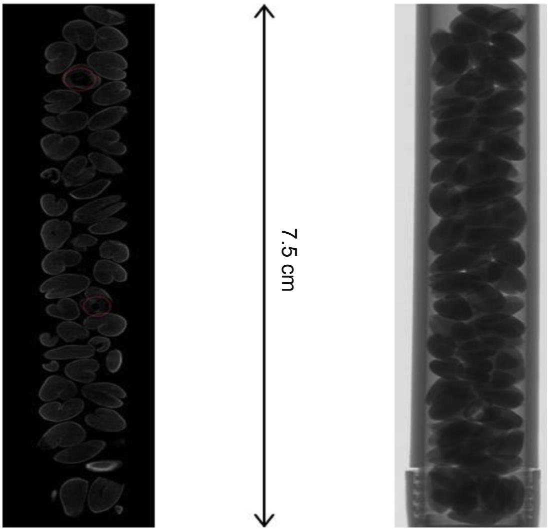

Figure 25.6 These images show a scanned cylindrical tube containing 88 wheat grains and two infested grains, which can easily be identified.

microtomography does have the ability to inspect larger quantities; this can be seen in Figure 25.6. The image shows a scanned cylindrical tube containing 88 wheat grains, and the two infested grains that were added to the noninfested grains can easily be identified.

The granary weevil *S. granarius* is one of the most damaging primary pests of stored cereals and derived products worldwide, and its infestation is generally difficult to detect because the immature stages (from egg to pupa) develop inside grains. The results of this study confirm that X-ray microtomography does allow the inspection and detection of all the immature developmental stages (from egg to pupa) of *S. granarius* in wheat grains. Also, other imaging techniques have been used to this aim, but they are not capable of producing high-quality images such as that produced by X-ray microtomography nor always able to distinguish all the eggs.

25.4.3 Case study 3: coffee bean

This case study demonstrates the capability of μCT as a useful tool for the quantitative analysis of the microstructure of different processed coffee beans (Arabica, Robusta, Arabica monsooned and Robusta monsooned coffee) before and after roasting, as well as the effect on the coffee bean microstructure by cultivation processing. The results from this study show that μCT is a suitable technique for microstructural analysis of roasted foods such as coffee beans, as it was able to quantify the structural alterations of the microstructure of the coffee bean before and after the roasting process.

25.4.3.1 Sample preparation and analysis

Four different types of coffee beans were used in this study: *Coffea arabica* (Arabica) var. S-795 from India, crop 2008–2009 (Ar), Arabica monsooned (Arabica mons), *Coffea canephora* var. *Robusta* (Robusta) and Robusta monsooned (Robusta mons). These varieties are from different geographic origin and were kindly provided by Illy (Illycaffè s.p.a, Trieste, Italy). Five coffee beans for each variety, green and roasted, were chosen for this experiment. The green coffee beans were roasted (time = 5 min, $T = 220$ °C, 100 g starting sample) with a laboratory-scale coffee roaster, Probat model BR74. The roasting degree corresponding to a medium roast was determined from the total weight loss (15% ± 1%). Each coffee bean was weighed on a digital precision balance (±0.1 g) (Gibertini Europe, Italy) to calculate the density of the sample.

With regard to tomographic analysis, each sample was placed vertically on a metal plate using modelling clay, which is a material irrelevant to X-ray. The samples were imaged under the same conditions using the Skyscan 1172 high-resolution desktop X-ray microtomography system (Skyscan, Belgium). A sample was placed on a round metal plate; the source and the detector were fixed, while the sample was rotated during measurement.

25.4.3.2 Discussion

With regard to μCT analysis, the percentage object (pore) volume, that is, the geometric parameter POV obtained by μCT analysis, was calculated for each sample as a representation of the percentage total pore content within the sample. Figure 25.7(a) and (b) shows the graph for the percentage POV values of the pores present for all the coffee bean samples before and after roasting, respectively. The percentage total pore volume represented in the graph does not take into account the large central pore of the coffee bean, as this structure is excluded in this microstructural study. It can be noted

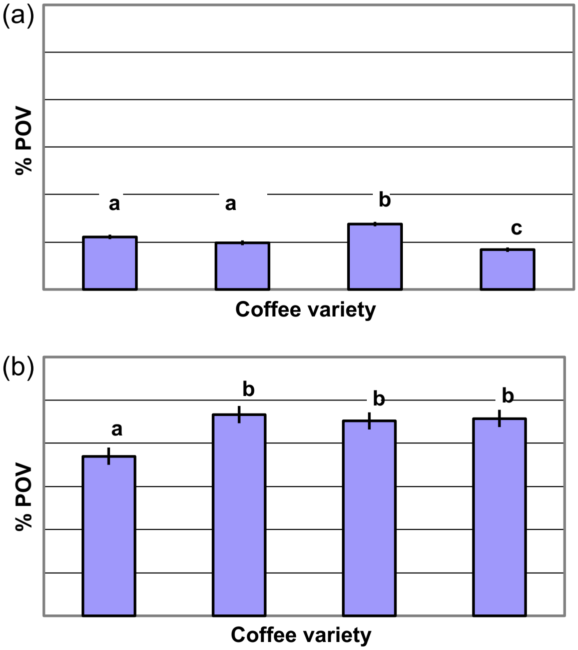

Figure 25.7 (a) and (b) show the percentage POV values of the pores present for all the coffee bean samples before and after roasting, respectively.

from Figure 25.7(a) that the coffee bean Arabica mons has the highest percentage volume of pores present before roasting; whereas the variety Robusta mons has the lowest percentage volume of pores. With regard to the two main varieties Arabica and Robusta, there are no statistical differences among the percentage volume of pores present within these samples. It can also be noted from this figure that Arabica mons has a higher percentage of pores with respect to the main variety Arabica in its green state, whereas the contrary is true for the Robusta and Robusta mons green samples. As no work has been done to date on the discrimination of coffee bean varieties according to their microstructure, there is a lack of reference to support these findings.

It can be noted from Figure 25.7(b), the total percentage pore volume increases for all the bean samples, which was expected after roasting. This is in accordance with Schenker et al. (2000), who found an increase in cumulated pore volume with roasting. This could be due to the rupture of bonds in the internal structure of the coffee beans during roasting, as expected. It can also be seen from the graph that the Arabica coffee variety has the lowest percentage volume of pores after roasting. Statistical analysis performed on the results of this graph confirmed that there are no statistical differences for the total volume among the other varieties after roasting.

Due to the wide range of pore sizes present in the coffee bean, the probability of the pore size distribution was also studied in this work to give a better understanding of the microstructure of the coffee beans studied. Figure 25.8(a) is a graph of the probability of pore size distribution for all the coffee bean samples before roasting, t_before, that plots the probability density versus the natural log of the OV indicating the probability

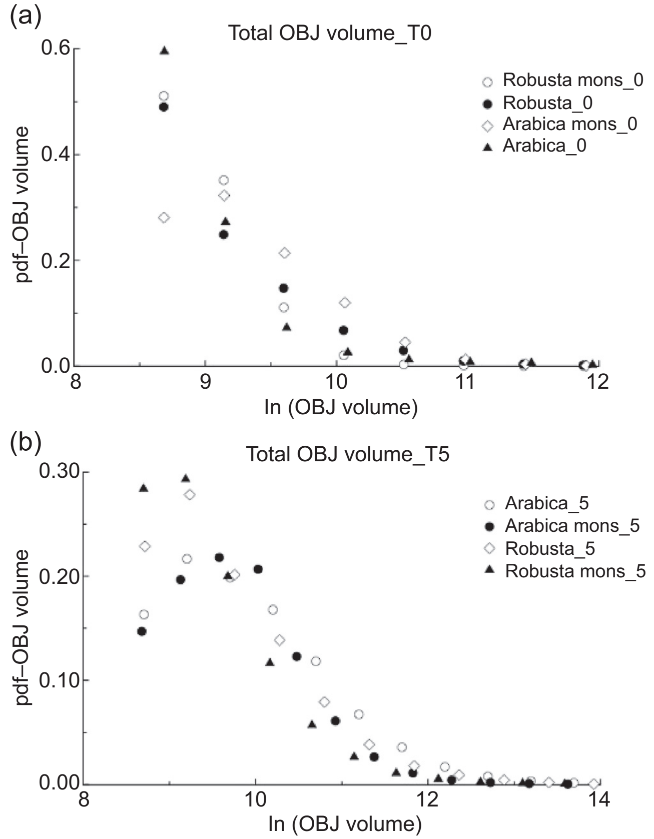

Figure 25.8 (a) and (b) show the probability of pore size distribution for all the coffee bean samples before roasting (T0) and after roasting (T5), respectively.

of the volume size distribution. With respect to the two main varieties, Arabica and Robusta, the Arabica coffee bean variety has a higher probability of having smaller pores and, consequently, a lower probability of having larger pores with respect to the Robusta coffee bean. Alternatively, the Robusta mons with respect to Arabica mons has a much higher probability of having a higher volume of small pores and, consequently, a lower probability of having larger pores. Note that among the different cultivars of Arabica, Arabica mons has a much higher probability of having a higher volume of small pores and, consequently, a lower probability of having larger pores. Robusta mons, with respect to Robusta, has a much higher probability of having a higher volume of smaller pores but a lower probability of having larger pores. In general, this figure portrays that there is a high probability of the pore size distribution being dominated by a high volume of small pores in a very narrow diameter range.

Figure 25.8(b) is the graph of the probability of pore size distribution for all the coffee bean samples after roasting, t_after. As previously stated, this graph is simply a plot of the probability density versus the natural log of the OV which basically indicates the probability of the volume size distribution. In general, at t_after, the probability of having a high volume of small pores drops to less than half of what it was at t_before. Consequently, the probability of having a high volume of large pores with respect to t_before doubles. This is due to the rupture of bonds in the internal structure of the coffee beans, as expected. With respect to the two main varieties, Arabica and Robusta, unlike t_before, the Robusta coffee bean has a higher probability of having a higher volume of small pores and a lower probability of having larger pores with respect to the Arabica coffee bean at t_after. Note that the Robusta mons at t_before, with respect to Arabica mons, still has a much higher probability of having a higher volume of small pores but a lower probability of having larger pores. Considering the different cultivars after roasting, t_after for Arabica and Arabica mons displays a probability distribution of pore volume more or less the same between these two samples. Whereas, the Robusta mons, with respect to Robusta, has a much higher probability of having a higher volume of smaller pores.

With regard to the total average number of pores present in the samples of coffee beans before roasting (data not shown), excluding the large central hole as before, the Arabica mons and Robusta mons samples had the highest number of holes that were also statistically equal, and the Arabica sample had the lowest number of holes present. After roasting, there was an increase in the number of holes for all the samples, although Arabica, Arabica mons and Robusta mons had the highest number of holes present that were also statistically equal. As stated previously, no work has been done to date on the discrimination of coffee bean varieties according to their microstructure; therefore, there is a lack of references to support these findings.

The total volume of pores for each coffee bean sample before and after roasting was also calculated (data not shown). It was noted that at t_before, the processed coffee beans (Arabica mons and Robusta mons) had the highest total pore volume compared to the natural coffee beans (Arabica and Robusta) because monsooned coffees contain a higher moisture content (13−14%) compared to that of regular coffee (10−12%) (Murthy & Manonmani, 2009). After roasting, there was a significant increase in total pore volume for all samples because internal gas formation leads to the rupture of bonds in the structure of the coffee beans. This was expected and is in accordance with Dutra, Oliveira, Franca, Ferraz, and Afonso (2001), who found a significant decrease in bean density due to an increase in total pore volume after roasting. As demonstrated in this case study, X-ray microtomography is a useful and sophisticated tool to provide detailed information on the microstructure, that is, pore structure of green and roasted coffee beans. In fact, this technique was able to quantify the structural alteration of the microstructure of the coffee beans after roasting.

25.4.4 Bread

In this case study, breads varying in yeast content, which have distinct cellular structures, are investigated. X-ray microtomography is used to characterize not only the final cellular structure, but also the process of development of microstructure during the fermentation stage. Microtomographic analysis was carried out on the bread dough at 30 (T30) and 105 (T105) minutes of fermentation to analyse the effect of the yeast content on bubble growth. With μCT, image analysis of the full 3D microstructure, measuring the size, shape, networking/connectivity and distribution of various phases was possible. These measurements represent the full 3D microstructure, which is not always possible by 2D image analysis using statistical techniques.

25.4.4.1 Sample preparation and analysis

Dough mixing, processing and baking were performed on laboratory-scale equipment. A double dough fermentation process was used. The dough, based on durum wheat (100%), was obtained with a pre-mixture of 2.9 L of water, 100 g of salt, 1.5 kg of flour and 100 mL of extra virgin olive oil and was stirred at high speed for 10 min in a mixer (Conti, Bussolengo, Verona, Italy). Once a homogeneous mixture was obtained, it was transferred to a mixer with a higher capacity (Bernardi Impastatrici, Cuneo, Italy). At this point, a mixture of yeast, 100 g of dry sourdough and 3.0 kg of durum wheat flour were added and mixed at the average speed for 25 min. The amounts of yeast used to make the bread are the following: 20 g (sample Br-y20), 50 g (sample Br-y50), 100 g (sample Br-y100), 300 g (sample Br-y300), 400 g (sample Br-y400) and 500 g (sample Br-y500). Afterwards, the dough was left to rest for 15 min before adding another 100 mL of extra virgin olive oil. After mixing was complete, the dough rested in bulk in the incubator (Thermogel, Varese, Italy) for a time of 15 min at a temperature of 30 °C and 85% relative humidity. Subsequently, portions of 1500 g were made; they were manually rounded and placed above a baking tray in the incubator at the same conditions for the final fermentation that lasted 75 min. Following fermentation, the samples were baked at 270 °C for 55 min in an electric oven (Europa Forni, Vicenza, Italy).

For tomographic analysis, the dough and bread samples were determined using a Skyscan 1172 high-resolution desktop X-ray microtomography system (Skyscan, Belgium). The bread samples were cylindrical in shape with a diameter of 2.8 cm. The dough samples, each weighing 1.5 g, were analysed at two different times of leavening (30 and 105 min). In particular, immediately after the leavening period, the dough samples were put in a cooling cell at 4 °C for 20 min in order to stop the fermentation process during scanning. Five replicates were carried out for each sample.

25.4.4.2 Discussion

Tables 25.1–25.3 show the average values obtained for the microstructural parameters using the CTAn software (Skyscan) and the results of the statistical analysis that were carried out as reported for the dough (T30 and T105) and baked bread samples, respectively. With regard to the POV parameter, the standard deviation values in some cases are very large because of variations in this bread's structure that are not homogeneous. At leavening time (T30), there was an increase in the POV value up to BR-y50, after which the POV values were statistically equal. However, at T105, the POV values were statistically equal regardless of the quantity of yeast added. With regard to the POV of the bread samples (Table 25.3), it can be noted that an increase in the yeast content up to 300 g (sample Br-y300) causes an increment in the POV value, after which the POV stabilizes regardless of the increment in the quantity of yeast added.

Table 25.1 Values of the geometric parameters for the dough T30 samples.

	POV	SMI	FI	OSVR	DA
Br-y20	0.04±0.03^{a}	2.68±0.11^{a,b}	0.02±0.007^{a}	0.06±0.022^{a}	0.18±0.05^{a}
Br-y50	1.94±0.59^{a,b}	2.79±0.70^{a}	0.02±0.00^{b}	0.08±0.00^{b}	0.21±0.03^{a}
Br-y100	3.77±1.52^{b}	2.56±0.35^{b}	0.01±0.005^{b}	0.03±0.002^{b,c}	0.26±0.06^{a}
Br-y300	5.13±0.64^{b}	3.30±0.04^{b}	0.01±0.001^{b}	0.02±0.003^{b,c}	0.19±0.03^{a}
Br-y400	3.97±3.28^{b,c}	3.99±0.33^{b}	0.01±0.005^{a,b}	0.01±0.007^{c}	0.25±0.05^{a}
Br-y500	4.23±0.80^{c}	2.60±0,12^{b}	0.00±0.010^{b}	0.01±0.002^{c}	0.18±0.02^{a}

$^{a\text{-}c}$Mean in the same column followed by different superscript letters differs significantly ($p<0.05$).

Table 25.2 Values of the geometric parameters for the dough T105 samples.

	POV	SMI	FI	OSVR	DA
Br-y20	2.74±1.06^{a}	2.28±0.43^{a,b}	0.008±0.007^{a}	0.03±0.005^{a}	0.25±0.03^{a}
Br-y50	4.70±2.77^{a}	2.07±0.52^{a}	0.006±0.00^{a}	0.03±0.007^{a}	0.24±0.04^{a}
Br-y100	4.11±0.71^{a}	2.26±0.37^{a,b}	0.006±0.005^{a}	0.03±0.002^{a}	0.27±0.04^{a}
Br-y300	6.81±4.59^{a}	2.56±0.29^{a,b}	0.008±0.001^{a}	0.025±0.007^{a}	0.22±0.028^{a}
Br-y400	4.11±3.25^{a}	2.79±0.09^{b}	0.011±0.005^{a}	0.031±0.009^{a}	0.17±0.01^{a}
Br-y500	3.64±3.60^{a}	2.79±0.13^{b}	0.013±0.01^{a}	0.034±0.010^{a}	0.19±0.06^{a}

$^{a\text{-}b}$Mean in the same column followed by different superscript letters differs significantly ($p<0.05$).

Table 25.3 Values of the geometric parameters for the bread samples.

	POV	SMI	FI	OSVR	DA
Br-y20	37.16±7.7^{a}	2.90±0.3^{a}	0.002±0.002^{a}	0.012±0.001^{a}	0.642±0.079^{a}
Br-y50	42.79±9.3^{a,b}	2.25±0.5^{a}	0.001±0.001^{a,b}	0.009±0.002^{a,b}	0.654±0.068^{a}
Br-y100	44.85±9.6^{a,b}	2.82±9.6^{a}	0.001±0.001^{a,b}	0.008±0.001^{b}	0.698±0.046^{a}
Br-y300	58.16±9.1^{b}	2.36±0.58^{a}	0.000±0.001^{b}	0.005±0.001^{c}	0.631±0.048^{a}
Br-y400	56.01±6.9^{b}	2.29±0.3^{a}	0.000±0.001^{b}	0.006±0.002^{c}	0.615±0.058^{a}
Br-y500	57.13±4.8^{b}	2.22±0.6^{a}	0.000±0.000^{c}	0.006±0.001^{c}	0.617±0.055^{a}

$^{a\text{-}c}$Mean in the same column followed by different superscript letters differs significantly ($p<0.05$).

This is due to the CO_2 production rate that is strictly related to the metabolism of the yeast as it consumed the simple sugars present in the flour (Romano, Toraldo, Cavella, & Masi, 2007). In this case, as the flour quantity is kept constant, the water content and the amount of simple sugars present in the flour also stay constant. Therefore, it is not surprising that the POV, which describes the percentage pore volume expansion, reaches a maximum value even though the yeast amount increases. These results confirm that the yeast content does play an important role in bread porosity. For dough samples T30 and T105 (Tables 25.1 and 25.2), the SMI values calculated for all the samples range from almost 2 to 4, suggesting that the characteristic shape of the pores present in all the dough samples can be described as being anything from cylindrical to a sphere, and the shape is not affected by the yeast content. For the baked bread samples (Table 25.3), the SMI values are all statistically equal and have a narrow range of 2.2−2.9. Therefore, they are almost cylindrical in shape.

With regard to the FI parameter, Tables 25.1−25.3 (i.e. from dough to bread) show that the FI is positive for all samples. Therefore, the pores present in all the dough (T30 and T105) and bread samples have very thin to disconnected solid lattices. They are, thus, convex in structure. In the dough samples, this could be due to the cells becoming larger during proofing and, therefore, having thinner cell walls. This in turn leads to an increase in the possibility for cell wall failure during baking, hence, the disconnected lattices in the bread cell structure. The results show that there is an overall decrease of the OSVR from dough to the baked bread samples. This is due to coalescence during baking that causes a decrease in surface area as a result of the rupture of thin films, which separate gas cells, thereby causing them to combine (Campbell, 2003) and leading to a structure formed by larger pores. According to the results obtained for DA for the dough samples at T30 and T105 (see Tables 25.1 and 25.2), the pores present are almost isotropic in nature, and there are no statistical differences among the samples. This shows that during the period of leavening of the dough, the samples have structures that are equally spaced and have a consistent thickness. However, the DA values for the all the bread samples are statistically equal and closer to 1. Therefore, the cells present in the baked bread samples are anisotropic in nature and have an irregular shape, which concurs with Zghal, Scanlon, and Sapirstein (2001), who also showed that the cells present in bread are anisotropic in nature. As this case study has demonstrated, X-ray microtomography (μCT) is a very useful tool for the investigation of the microstructure characteristics of dough and baked bread.

These case studies have shown that with μCT, image analysis of the full 3D microstructure and measurement of the size, shape, networking/connectivity and distribution of various phases is possible.

25.5 Future trends

X-ray microtomography is nondestructive and provides in-depth information on the microstructure of the food product being tested. Therefore, a better understanding of the physical structure of the product and (from an engineering perspective) knowledge about the microstructure of foods can be used to identify the important processing parameters that affect the quality of a product. Structure—property relationships can strongly affect the physiochemical, functional, technological and even nutritional properties of foods. For example, with regard to solid food foams like bread, extruded cereals, biscuits and cakes, the consumer appreciation of these products is strongly linked to the texture. For texture, sensory properties of solid food foams are related to both mechanical properties and cellular structure. In this context, determining the relationships between a given mechanical property and the cellular structure is of prime importance. Processes are no longer designed from a macroscopic level; knowing the properties of foods on the microscale determines the process specification. Hence, X-ray microtomography is quickly becoming a very useful tool to aid in the study of food microstructure and nanostructure, which is the future trend.

25.6 Further information

For further information, please see the references listed below.

Bruker microtomography is available in a range of easy-to-use desktop instruments, which generate 3D images of your sample's morphology and internal microstructure with resolution down to the submicron level.

References

Aguilera, J. M. (2005). Why food microstructure. *Journal of Food Engineering, 67*, 3—11.

AOAC. (1995). *Official methods of analysis* (16th ed.). Washington, DC: AOAC International.

Autio, K., & Laurikainen, T. (1997). Relationships between flour/dough microstructure and dough handling and baking properties, review. *Trends in Food Science and Technology, 8*, 181—185.

Babin, P., Della Valle, G., Dendievel, R., Lourdin, D., & Salvo, L. (2007). X-ray tomography study of the cellular structure of extruded starches and its relations with expansion phenomenon and foam mechanical properties. *Carbohydrate Polymers, 68*, 329—340.

Barrett, A. H., Cardello, A. V., Lesher, L. L., & Taub, I. A. (1994). Cellularity, mechanical failure and texture perception of corn meal extrudates. *Journal of Texture Studies, 25*, 77—95.

Barrett, A. H., & Peleg, M. (1992). Extrudate cell structure—texture relationships. *Journal of Food Science, 57*(5), 1253—1257.

Cafarelli, B., Spada, A., Laverse, J., Lampignano, V., & Del Nobile, M. A. (2014). X-ray microtomography and statistical analysis: tools to quantitatively classify bread microstructure. *Journal of Food Engineering, 124*, 64—71.

Campbell, G. M. (2003). Bread aeration. In S. P. Cauvain (Ed.), *Breadmaking: Improving quality* (pp. 352—374). Cambridge: Woodhead.

Chaunier, L., Della Valle, G., & Lourdin, D. (2007). Relationships between texture, mechanical properties and structure of cornflakes. *Food Research International, 40*, 493—503.

Cotton, R. T. (1921). Four *Rhychophora* attacking corn in storage. *Journal of Agricultural Research, 20*, 605—614.

Dutra, E. R., Oliveira, L. S., Franca, A. S., Ferraz, V. P., & Afonso, R. J. C. F. (2001). A preliminary study on the feasibility of using the composition of coffee roasting exhaust gas for the determination of the degree of roast. *Journal of Food Engineering, 47*(3), 241−246.

Falcone, P. M., Baiano, A., Zanini, F., Mancini, L., Tromba, G., Dreossi, D., et al. (2005). Three-dimensional quantitative analysis of bread crumb by X-ray microtomography. *Journal of Food Science, 70*(3), 265−272.

Falcone, P. M., Baiano, A., Zanini, F., Mancini, L., Tromba, G., Montanari, F., et al. (2004). A novel approach to the study of bread porous structure: phase-contrast X-ray microtomography. *Journal of Food Science, 69*(1), 38−43.

Fernandez, X., Monin, G., Talmant, A., Mourot, J., & Lebret, B. (1999). Influence of intramuscular fat content on the quality of pig meat − 2. Consumer acceptability of *m. longissimus lumborum*. *Meat Science, 53*, 67−72.

Frisullo, P., Laverse, J., Marino, R., & Del Nobile, M. A. (2009). X-ray computer tomography to study processed meat micro-structure. *Journal of Food Engineering, 94*, 283−289.

Frisullo, P., Marino, R., Laverse, J., Albenzio, M., & Del Nobile, M. A. (2010). Assessment of intramuscular fat level and distribution in beef muscles using X-ray microcomputed tomography. *Meat Science, 85*, 250−255.

Gao, X., & Tan, J. (1996). Analysis of expanded-food texture by image processing, Part II: Mechanical properties. *Journal of Food Process Engineering, 19*, 445−456.

Jeremiah, L. E., Dugan, M. E. R., Aalhus, J. L., & Gibson, L. L. (2003). Assessment of the relationship between chemical components and palatability of major beef muscles and muscle groups. *Meat Science, 65*, 1013−1019.

Kamman, P. W. (1970). Factors affecting the grain and texture of white bread. *Baker's Digest, 44*(2), 34−38.

Kirkpatrick, R. L. (1962), The development and habits of the granary weevil, *Sitophilus granarius* (L.) within the kernel of wheat (Master thesis). Manhattan, Kansas: Department of Entomology, Kansas State University.

Lampignano, V., Laverse, J., Mastromatteo, M., & Del Nobile, M. A. (2012). Microstructure, textural and sensorial properties of durum wheat bread as affected by yeast content. *Food Research International, 50*(2013), 369−376.

Lassoued, N., Babin, P., Della Valle, G., Devaux, M. F., & Réguerre, A. L. (2007). Granulometry of bread crumb grain: contributions of 2D and 3D image analysis at different scale. *Food Research International, 40*, 1087−1097.

Laverse, J., Mastromatteo, M., Frisullo, P., Albenzio, M., Gammariello, D., & Del Nobile, M. A. (2011). Fat microstructure of yogurt as assessed by X-ray microtomography. *Journal of Dairy Science, 94*(2).

Laverse, J., Mastromatteo, M., Frisullo, P., & Del Nobile, M. A. (2012). X-ray microtomography to study the microstructure of mayonnaise. *Journal of Food Engineering, 108*, 225−231.

Lim, K. S., & Barigou, M. (2004). X-ray microtomography of cellular food products. *Food Research International, 37*, 1001−1012.

Marino, R., Albenzio, M., Girolami, A., Muscio, A., Sevi, A., & Brughieri, A. (2006). Effect of forage to concentrate ratio on growth performance, and on carcass and meat quality of Podolian young bulls. *Meat Science, 72*, 415−424.

Monin, G. (1998). Recent methods for predicting quality of whole meat. *Meat Science, 49*, 231−243.

Mousavi, R., Miri, T., Cox, P. W., & Fryer, P. J. (2005). A novel technique for ice crystal visualization in frozen solids using X-ray microcomputed tomography. *Journal of Food Science, 70*(7), 437−442.

Murthy, P. S., & Manonmani, H. K. (2009). Physico-chemical, antioxidant and antimicrobial properties of Indian monsooned coffee. *European Food Research and Technology, 229*, 645−650.

Pipeck, P., Jelenikova, J., & Sarnovsky, L. (2004). The use of video image analysis for fat content. *Czech Journal of Animal Science, 49*(3), 115−120.

Robinson, W. H. (2005). *Handbook of urban insects and arachnids*. Cambridge: Cambridge University Press, 472 pp.

Romano, A., Toraldo, G., Cavella, S., & Masi, P. (2007). Description of leavening of bread dough with mathematical modelling. *Journal of Food Engineering, 83*, 142−148.

Schenker, S., Handschin, S., Frey, B., Perren, R., & Escher, F. (2000). Pore structure of coffee beans affected by roasting conditions. *Journal of Food Science, 65*(3), 452−457.

Trater, A. M., Alavi, S., & Rizvi, S. S. H. (2005). Use of non-invasive X-ray microtomography for characterizing microstructure of extruded biopolymer foams. *Food Research International, 38*, 709−719.

Van Dalen, G., Blonk, H., Van Aalst, H., & Hendriks, C. L. (2003). 3D imaging of foods using X-ray microtomography. *G.I.T. Imaging and Microscopy, 3*, 18−21.

Van Hecke, E., Allaf, K., & Bouvier, J. M. (1995). Texture and structure of crispy-puffed food products, I: Mechanical properties in bending. *Journal of Texture Studies, 26*, 11−25.

Whitworth, M. B., & Alava, J. M. (1999). The imaging and measurement of bubble in bread doughs. In G. M. Campbell, C. Webb, S. S. Pandiella, & K. Niranjan (Eds.), *Bubbles in foods* (pp. 221−231). St. Paul, MN: Eagan Press.

Zghal, M. C., Scanlon, M. G., & Sapirstein, H. D. (2001). Effects of flour strength, baking absorption and processing conditions on the structure and mechanical properties of bread crumb. *Journal of Cereal Science, 78*, 1−7.

Application of process tomography in nuclear waste processing

26

K. Primrose
Industrial Tomography Systems plc, Manchester, UK

26.1 Introduction

Since the 1940s, there have been defence and civil nuclear programmes applied to the processing of nuclear material. This has necessarily produced waste products, and it is estimated that there are millions of gallons of contaminated liquids and thousands of tonnes of spent nuclear fuel and other materials around the world.

As yet, there is no widely accepted method for the long-term storage or permanent disposal of nuclear waste, so much of it is in temporary storage facilities – either in storage tanks in alkaline or acid solution or as solids.

A number of governments – notably the UK and US – have moved their policies for the care and maintenance of waste in the form it has been stored over the last 50+ years to processing the waste into low, medium and high levels of radioactivity and then treating these accordingly for more stable long-term storage. This is typically in the form of grouted concrete material in drums or vitrified in highly durable containers.

The processing of these liquid waste streams involves a variety of unit processes based on mobilising slurries, mixing methods, separation techniques and reactions to move the waste between solid and liquid forms to make it more efficiently managed.

The overall cost of decommissioning in the UK is estimated to be nearly £100 billion, whilst the worldwide costs, including the rest of Europe, the US, Russia (including Chernobyl) and Japan (including Fukushima) are estimated to be £250 billion.

The range and complexity of the processes, the costs and technical challenges mean that nuclear waste management has been an area where many early process tomography applications have been developed.

26.1.1 Process measurement requirements

Process tomography provides information on the spatial variation of a volume based on a particular detection technology. Discrimination is typically based on resolving bulk materials in multiphase processes where they are mixed, separated or being transported.

Industrial Tomography. http://dx.doi.org/10.1016/B978-1-78242-118-4.00026-5
Copyright © 2015 Elsevier Ltd. All rights reserved.

Electrical resistance tomography (ERT) is the most widely established technique in the nuclear sector, where the electrical conductivity of aqueous systems is measured. The first section of this chapter deals with ERT; the second addresses other modalities.

Process tomography applications tend to fall into three groups:

- Improving process understanding
- Measuring critical process characteristics
- Providing process control information

These have particular significance in the context of nuclear waste management due to the nature of the materials involved, the restricted or nonaccessibility of the processes being monitored because of their radioactivity, the environment in which sensors and instruments are sited and the timescale over which processes are required to operate.

For example, improving process understanding is typically performed under controlled laboratory conditions, so there is no need for precautions to be taken over radioactive materials. However, it can often be very challenging to prepare surrogate materials that exhibit the same performance characteristics as those found in the actual process.

As measurements move from lab/pilot conditions to an active process, it is necessary to take into account the following:

- Material effects (radiation and chemical) on sensors in contact or close proximity to the process
- Construction of sensors at appropriate scales to match the process
- Siting of electronics – at sufficient distance or under sufficient protection to ensure that sensitive circuitry is not affected by radiation
- Ergonomic design of sensors to allow safe, remote manipulation through radiation shielding and/or whilst operators are wearing appropriate personal protection
- Simplicity of software interfaces to allow use by personnel with minimal training
- Long-term performance of software and maintainability of hardware over extended periods
- Simple replacement of wetted components

Engineers in the nuclear sector have sought to use process tomography in a wide range of application areas. Among the most prevalent are the following:

- Homogeneity measurement of slurries
- Transportation of slurries
- Effectiveness of ion-exchange columns and packed bed filters
- Effectiveness of solvent extraction processes
- Drying of slurries
- Calcination
- CFD validation

In addition to these, ERT has been used as a virtual sensor to determine air/liquid interface in a heavily stirred continuous crystallisation process.

The most advanced technique in terms of range of applications in the field is ERT, which will be the primary topic of this chapter.

26.2 Applications of resistance tomography

ERT is currently the most advanced technique in terms of actual implementation in active installations. This is due to a number of factors. First, its fit with process conditions – much of nuclear waste requiring treatment is in the form of aqueous slurries, and furthermore, a number of other processes involved treatment in aqueous systems. Second, the commercial availability of measurement systems simplifies its deployment.

The case studies discussed next demonstrate the utility, benefits, challenges and opportunities of resistance tomography in nuclear waste management.

26.2.1 Solid–liquid mixing

A significant number of ERT applications are based on the characterisation and optimisation of mixing. This includes gas–liquid, liquid–liquid and solid–liquid systems.

In the case of the Washington River Protection Program at the Hanford nuclear site in the USA (Townson, Wright, Jensen, & Vanatta, 2011; Townson, 2011), a high-level waste slurry is formed through mixing approximately 720,000 L of settled solids on the bottom of double-shelled storage tanks (DSTs) with the remaining tank volume – up to 3,407,000 L (approximately 1 M gallons).

There is some uncertainty surrounding the ability of the mixer pump system to adequately suspend and homogeneously distribute the solid particles within the tank. The design basis assumes each staged HLW feed tank is homogeneously mixed and delivered in consistent feed delivery batches of 570,000 L (150,000 gallons). Consistent, as used here, is intended to mean that the first 570,000 L batch has the same solids composition as the last 570,000 L batch (i.e. approximately eight batches).

26.2.1.1 Measurement objective

The primary objectives of this phase of demonstrations were to test scale models of the large mixing tanks and the scale up methodologies such that there was confidence in the overall mixing programme.

The detailed objectives were the following:

- Demonstrate that equivalent tank mixing behaviour can be achieved in the two sizes of scaled tanks by the following:
  - Demonstrate equipment performance and the ability of the scaled tanks to meet performance objectives.
  - Demonstrate instrumentation performance and the ability to measure particulate movement within the tank.
  - Collect fluid velocity measurements for input into a computational fluid dynamic (CFD) model. Data were used to calibrate and validate the model.
- Demonstrate a range of tank operating parameters that define the edges of mixing performance to include:
  - Mixer pump flow rate
  - Mixer pump rotation rate

- Provide a framework to move forward to the next phase of batch transfer and sampling testing:
    - Support the batch transfer testing by identifying the range of parameters, simulants and instrumentation to be used during that testing.

A range of test equipment was deployed including the ITS p2+ resistance tomography system, and the test vessels were equipped with radial tomography arrays and linear probes. This provided real time, 3D visualisation of the solids distribution within the vessels, so areas of good and not as good mixing could be identified qualitatively.

In addition, a Coriolis flow metre, FBRM (fixed beam reflection microscopy for studying chord lengths of suspended particles), video and visual observations and direct sampling were also used.

26.2.1.2 Design considerations

The main components of the platform (Figure 26.1) are the flush vessel (11,000 L), test vessel TK-201 (110 cm diameter, 420 L) and test vessel TK-301 (305 cm diameter, 8877 L); both test vessels were fitted with four circular 16-electrode tomography arrays.

26.2.1.3 Implementation

The circular tomography arrays were hitherto the largest deployed in a mixing rig, and whilst calculations had been carried out, it was not certain how these would perform.

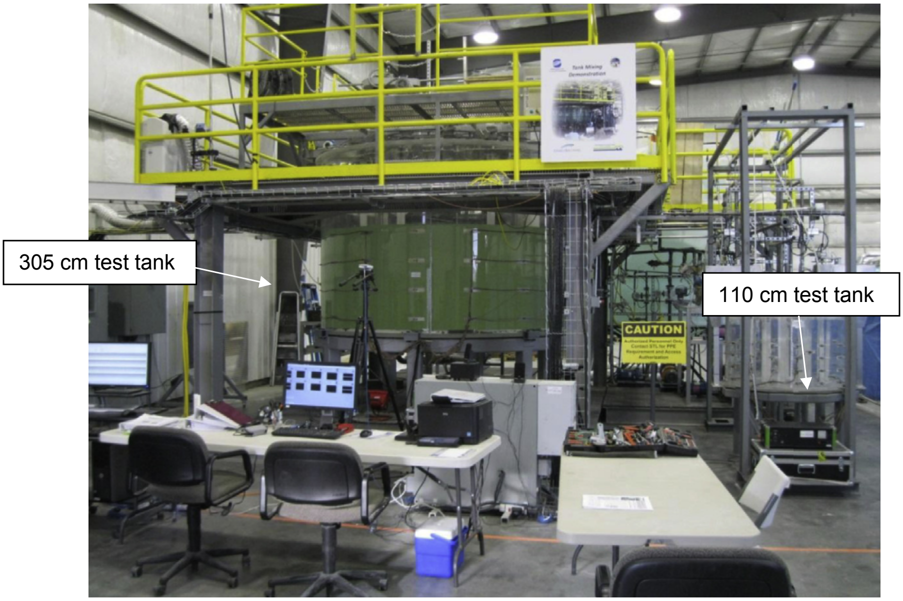

Figure 26.1 Mixing tank, in addition linear tomography probes were used to study mixing in the z-axis (i.e. solids concentration as a function of height).

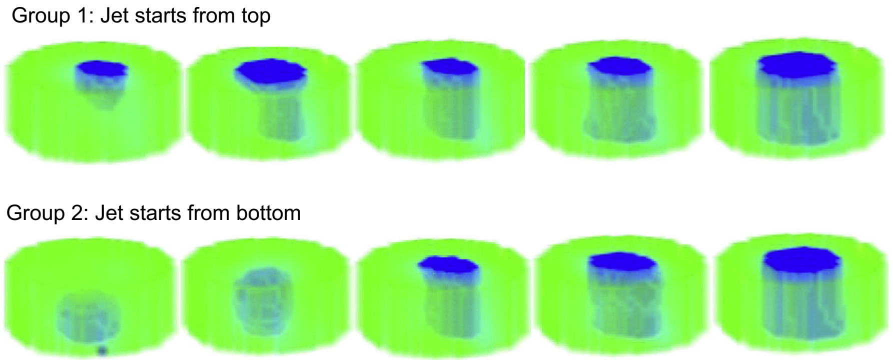

Figure 26.2 Large tank tomograms, ERT – Bi-Modal $Al(OH)_3$ and SiC Planes (110 cm tank).

As it transpired, the circular arrays performed beyond expectations and were able to characterise the full mixing of the vessel such that the linear probes were not required. Preliminary results are set out in Figure 26.2.

Using this instrument on both test vessels allowed each vessel to be set up so that the mixing in each was equivalent, and this information, combined with later testing, was used to derive scaling correlations for this type of fluidically mixed system. The testing demonstrated that the two scales of test vessel could be set up to show almost identical mixing patterns as observed via the ERT system. It is also possible that a linear probe–based ERT system will be deployed on the full-scale DSTs to monitor mixing during full-scale mixing demonstrations scheduled for approximately 2015.

It should also be noted that the v5r instrument was not available from ITS when this work was carried out (in 2009). This instrument has been designed to deliver a higher current and, consequently, can provide better quality data for large diameter vessels using circular arrays.

26.2.2 Hydraulic conveying of slurries

Closely related to mobilisation of slurries through effective mixing is their subsequent transportation.

Efficient solid slurry transportation is particularly important in the nuclear plant decommissioning process to move radioactive waste between unit processes. An important aspect of such transportation is the continued mobility of all solids, ensuring, for example, that heavy metals do not preferentially build up at any particular location.

It had been proposed that helically formed pipes could be used to keep solids in suspension, and these should be applied to enhance the distribution of solids in piped slurries.

To test this, in situ measurement methods based on electrical impedance tomography were used to gain an understanding of the effect of particle suspension resulting from using swirl-inducing geometries, and these experiments are described next (Pachowko, Wang, Poole, & Rhodes, 2004).

The experiments were carried out on a 50-mm-diameter hydraulic conveying pipe loop composed of transparent 1-m flanged horizontal sections in a vertical plane.

The pumped medium was a mixture of water and cylindrical nonconductive beads (diameter 2 mm and specific gravity 1.45).

The swirling pipe section measured was 1 m long and had a 900° of spiral.

The EIT sensor was made of three sensing planes with gaps of 30 and 50 cm between them. Each plane was fitted with 16 electrodes, evenly distributed along the inner wall of the pipe.

Experiments were taken with the sensing unit fitted at 150, 370, 885 and 1150 mm downstream of the outlet of swirl section.

This corresponds to downstream distances in the length to the pipe diameter ratios (L/D) of 3.0, 7.4, 17.7 and 23.0.

A series of experiments were carried out at mean in situ particle concentrations of 3%, 6%, 9% and 12% by weight (2.1%, 4.0%, 6.4% and 8.6% by volume). The flow velocities used were 0.5, 1.0, 1.5, 2.0 and 2.5 m/s.

Through the application of SCG algorithm and other analysis tools, the asymmetric solids concentration distribution in horizontal swirling flows was quantified. Particle trajectories and concentration regimes are reported as a function of the water axial flow velocity and the downstream distance from the swirl-inducing pipe section. The nature of the solids distribution at a typical cross-section is reproducible and takes the form of a crescent region of a higher solids concentration, re-orientated in the direction of swirl by approximately $\pi/2$ rad from the normal settling position. Low concentration areas in a crescent shape appear on the opposite side of the pipe. These appear to develop into a ring structure as the mean axial velocity increases.

At a high flow velocity, the mode of particle dispersion along the length of the pipeline appears to take the form of a group of ellipses. Larger ellipses were observed near the swirl-inducing pipe. The work demonstrated that in the absence of accurate predictive models for such complex flows, EIT enables direct visualisation and quantitative analysis of the solids concentration profiles in such pipes.

Images in Figure 26.3 show solid volume fraction distribution in a pipeline at downstream positions of L/D = 3.0, 7.4, 17.7 and 23.0 for water flow velocities of 1.0, 1.5, 2.0 and 2.5 m/s at a fixed particle volumetric concentration of 8.6% (L/D: the ratio of downstream length to pipe diameter).

26.2.3 Solvent extraction

The three generic areas of ERT are often characterised as mixing, separation and flow. Having covered mixing and flow of slurries, the next example covers separation.

Solvent extraction is used to selectively transfer a specific material between an aqueous and organic (or solvent) phase. It generally consists of vigorous mixing of the two liquid phases followed by a quiescent period of gravity-based separation. The solvent phase, containing the material of interest, can then be decanted away from the aqueous phase so that the material can be recovered, normally by a second phase transfer back into a new aqueous phase. As well as nuclear waste management, solvent extraction is used in a range of different process industries including pharmaceuticals, mineral processing and flavour extraction for food and beverages.

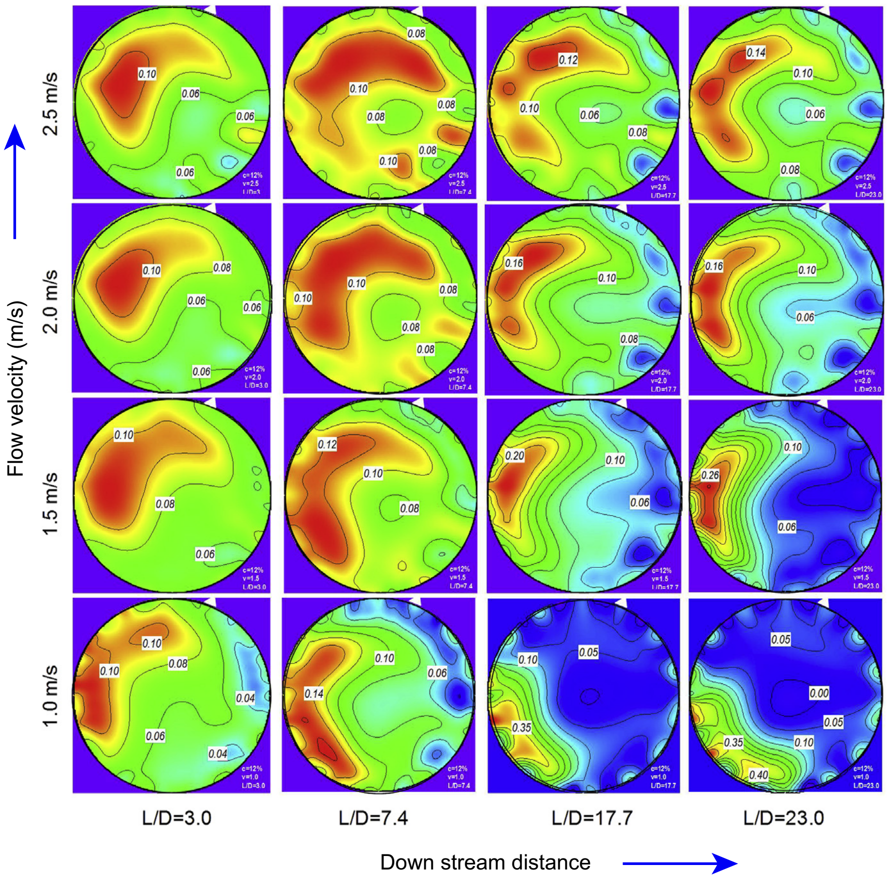

Figure 26.3 SCG tomograms of swirling flow.

26.2.3.1 *Measurement objectives*

1. In this case, the objective was to determine the interface between organic and aqueous liquid levels in underground storage tanks so that a precise estimate of the volume of each phase could be determined.
2. The required accuracy of the probe was to be ±0.5% at full scale.
3. Interface height was to be monitored at a frequency of 1 Hz.

26.2.3.2 *Design considerations*

1. As stated, it was necessary to fabricate the system in materials that would withstand radiation fields over a protracted period.
2. The use of significant volumes of volatile organics necessitated the equipment to be certified as safe in an explosive atmosphere.
3. The sensor location is underground, and access is through a duct that has bends to prevent direct radiation exposure.
4. The facility has an operating lifetime of 40 years, so there is a requirement for the unit to be fit for long-term use and serviceable remotely.

26.2.3.3 Implementation

As well as selecting suitable materials for extended exposure in radiation fields, the design considerations were implemented through the use of the following:

1. Segmented linear tomography array that allowed the sensor to be lowered through curved ducting
2. Certified Zenner barriers to clamp safe voltages within safe energy limits
3. Vortex finder for monitoring of semicontinuous crystallisation

26.2.4 Precipitation process

A further application of resistance tomography is worthy of more detailed coverage as it represented an early example of implementation of ERT for the monitoring and improved performance of precipitation process under extremely challenging conditions (Bolton et al., 2006).

26.2.4.1 Process

The process is based on the precipitation of radioactive salts contained in a glass vessel with two overhead feeds and an overflow at the side.

The first feed contains a metal salt in nitric acid (typically 3.5 M) and the other contains an organic acid. The contents of the vessel (from the two feeds) are continuously mixed using a rotating magnetic stirrer bar at the base of the vessel to maintain a reaction. The reaction products leave the vessel through the overflow at the side. The effect of the magnetic stirrer bar is to swirl the fluids and create a vortex at the centre of the vessel and produce a centrifugal force to enable the precipitate to leave through the overflow.

The size and shape of the vortex depend upon the rotational speed of the stirrer bar.

Access to the vessels is restricted, and visual inspection is difficult due to the opaque nature of the tanks contents and the presence of a heating jacket.

Prior to the installation of tomographic monitoring, the status of the vessel was monitored by means of a conductivity probe located in the central air space caused by the vortex.

Under normal operation, the conductivity probe should not be in contact with the process liquor. If the vortex fails, the liquid level will rise until it reaches the level of the overflow, and the liquors make contact with the conductivity probe; then an alarm is signalled.

However, false alarms were created due to splashing of liquor onto the conductivity probe. In addition, very little can be deduced about the internal flow structure within the precipitator vessel (such as size and shape of the vortex).

26.2.4.2 Measurement objective

The measurement objective was to develop an alternate method of determining the vortex that was not vulnerable to false positives should a leak form in the vessel (resulting in the conductivity probe being in air, but process conditions are faulty); nor false negatives, when the conductivity probe is splashed (resulting in an apparently faulty condition when the process is actually running to specification).

A linear tomography probe was proposed that would be sensitive to the vortex depth and free of the limitations of the single probe.

26.2.4.3 Design considerations

The design considerations were as follows:

- Process environment was acidic.
- The acidity limited the selection of materials. In addition, the high acidity also meant the continuous medium was highly conducting (in excess of brine at 600 mS/cm). The high conductivity had an impact on electrode size and also meant that a high current would be required to achieve the necessary signal–noise ratio required to reconstruct images.
- Process environment was radioactive.
- This consideration carries across all applications in nuclear waste management and limits the selection of materials.
- Process unit was remote (operating in the glove box in a different location from the control room).
- The impact of the remote siting of the glove box was there would need for long cables from the sensor to the instrument; in addition, it limits the access to the sensor/process, making installation more demanding.
- The process itself was a technically validated operation.
- This consideration arises in a number of different sectors (e.g. pharmaceuticals). It means that the sensor should not alter process operations, either through the hydrodynamic impact of the probe or through changing operating procedures (such as through taking an online reference).

26.2.4.4 Implementation

In 2003, Industrial Tomography Systems plc was asked to provide instrumentation to address this challenge, and a solution was developed using the p2000 ERT instrument. The University of Leeds was asked to validate the instrumentation with project management provided through BNFL Research (now the UK's National Nuclear Laboratory).

The successful implementation of the sensor was achieved addressing each of the above requirements. Key aspects of this included the following:

- Signal amplification was developed to optimise sensitivity. Performance was measured with and without amplifier. The measurements without the amplifier are below zero (−3.5 mA), which is below the minimum threshold necessary for effective reconstruction.
  With the amplified signal, all measurements are positive, and the data set can be reconstructed.
  In addition, the injection current was optimised at 75 mA, and measurement frequencies of 1200, 2400, 4800, 9800 and 19,600 Hz were tested.
  These test results showed that the stability of the voltage signature in the absence of a vortex deteriorated with increasing frequency. However, the tests at injection current frequencies of 1200 and 2400 Hz failed to effectively discriminate between the absence and presence of a

vortex. On this basis, the best results were obtained with a frequency of 4800 Hz, and this value was recommended for all future work.

- A thin, blade-like probe was designed and hydrodynamically tested to have minimal impact on the vortex. The main body of the sensor was constructed from polyvinylidene fluoride (PVDF), which possesses good chemical resistance and offers good properties in terms of radiological resistance. The electrodes were manufactured from stainless steel grade 316L, and the design was such that only PVDF and stainless steel were in contact with the process liquor.
- A virtual referencing methodology was developed to enable references to be taken in the presence of the vortex. A method of processing the raw image was used to provide an image to characterise the vortex. This was achieved by the average of the pixel values in each of the 10 columns of imaging pixels being calculated, and these are plotted as a bar chart. Due to the presence of the vortex, the average pixel value for each column decreases from left to right across the image. This average value (which is normalised between 0 and 1) was assumed to be proportional to the volume fraction of liquor and then used to define the interface of the liquor and gas. It is assumed that liquor exists below this point and gas exists above this point.

A mirror image is used to produce a representation of the V-shaped vortex, which was familiar to plant operatives.

A software user interface was developed to acquire the measurements, analyse the data and display the results, as shown in Figure 26.4. The user interface displays the processed image of the vortex and a historical trace of the vortex depth. Lower and upper thresholds can be defined for the vortex depth, and an alarm is registered if the depth reaches either of these values.

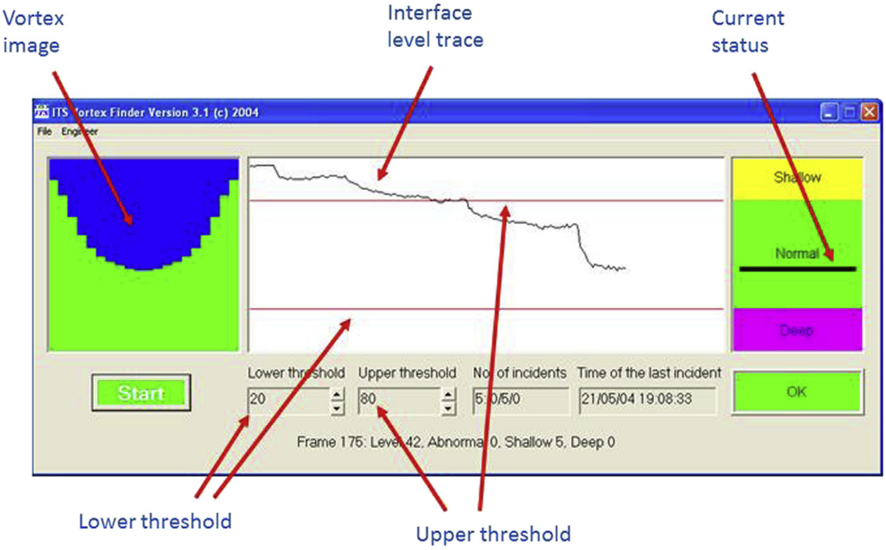

Lower threshold: 20
Upper threshold: 80
No of incidents: 5/0/5/0
Time of the last incident: 21/05/04 19:08:33

Frame 175: Level 42, Abnormal 0, Shallow 5, Deep 0

Figure 26.4 ITS vortex monitor.

A simplified start-up routine was programmed so a user could initiate operations with a single mouse click (based on established reference).

Acceptance tests were carried out at University of Leeds in May 2004, and the system was installed at the Thermal Oxide Reprocessing Plant (THORP) at the Sellafield, UK nuclear site THORP in autumn 2004 and switched on for use in November of the same year.

26.2.5 Other applications of ERT in nuclear waste processing

Other ERT applications in nuclear waste management include the following:

- A submersible ERT scanner to determine buried objects that are either more or less conducting than the surrounding slurry
- Determination of flow fields through packed beds (similar to work published by Johnson Matthey, ITS and University of Manchester)
- Characterisation of settled slurries and sedimentation through use of a linear probe (Wang, Rhodes, Young, Primrose, & Takei, 2007)
- Monitoring of crystallisation and dissolution of salts (Wang et al., 2007).

26.3 Applications of other tomographic modalities

A range of other tomography modalities have also been reported in the literature. However, interestingly, whilst electrical capacitance tomography has been proposed to monitor pneumatic transport, there are few citations of its actual use in the sector.

26.3.1 Waste characterisation X-ray computed tomography

X-ray tomography has been particularly applied to the inspection of nuclear waste containers. Such applications have primarily been at the research and demonstration stage and have shown a capability to detect cracks, voids and other structures (Rizo et al., 2000).

26.3.2 Waste characterisation gamma tomography

As several categories of nuclear waste inherently emit gamma radiation, a number of tomographic techniques have been deployed to make use of this property (Richard, Bernardi, Harry, & Martz, 1995).

This approach was started in the 1990s – not long after the development of electrical process tomography. The most commercially advanced application of gamma tomography has been developed by AN Technology for use in the nondestructive evaluation of waste drums.

A further application of utilising natural gamma radiation of nuclear waste is a device that detects the direction of incoming radiation to map radiation sources within a large space. This has been commercialised through the National Nuclear Laboratories in the UK.

26.3.3 Waste characterisation using photo-fission tomography

Similar to detection of gamma rays, the alpha-activity due to the presence of actinides inside the packages can be determined using nondestructive active methods (Jeanneau, Lainé, & Poumarè et al., 2006).

Being able to characterise and classify nuclear waste packages is helpful for an appropriate mode of storage. CEA-LIST has developing instrumentation, based on fission and induced by photons, that allows quantification of the global mass of actinides in large concrete packages and determination of its position by the means of a tomography using delayed particles emitted after the fission process.

26.3.4 Waste imaging by muon tomography

Naturally occurring cosmic rays have been proposed to image large-scale structures such as waste ponds, nuclear reactor cores and other large structures. Recently (2013), it was proposed to apply the technique to imaging the structures within the Fukushima Dai-ichi (Miyadera et al., 2013) power plant site in order to remotely assess the internal complexities of the damage done to the reactors cores.

26.4 Future trends

The applicability of process tomography to measure complex multiphase processes, such as mixing, separation, flow and reactions and to describe the spatial distribution of different materials means that it will certainly become more widely applicable in the processing of nuclear waste.

The main limitation of process tomography's usage in the sector is experience and awareness of the technology, and these will be addressed over time.

In addition, applications will become more widespread through the following:

- The use of techniques that obviate the need for in-line references
- A track record of installations demonstrating robustness and reliability
- A wider range of applications of different modalities that demonstrate the usefulness in solving particular challenges in the sector

Over time, it is hoped that the tomography technology will be advanced through addressing new challenges in nuclear waste processing and also that nuclear waste processing will be carried out more efficiently and more safely through the application of process tomography.

26.5 Sources of further information and advice

Industrial Tomography Systems plc www.itoms.com.

On-line Instrumentation Laboratory, University of Leeds www.leeds.ac.uk/olil/

Energy Solutions Inc. www.energysolutions.com.

Nuclear Decommissioning Authority www.nda.gov.uk.
National Nuclear Laboratory www.nnl.co.uk.
US Nuclear Regulatory Commission www.nrc.gov.
International Atomic Energy Association www.iaea.org.

Acknowledgement

The author gratefully acknowledges the advice and support of Prof. M. Wang of the University of Leeds and Mr. C. Phillips of Energy Solutions Inc., Dr. G. Bolton of National Nuclear Laboratories and Ms. C. Qiu of Industrial Tomography Systems plc.

References

Bolton, G., Bennett, M., Qiu, C., Wang, M., Wright, M., Primrose, K., et al. (2006). In *Development of an electrical tomographic system for operation in a remote, acidic and radioactive environment, to be published in Chemical Engineering Journal in October 2006, on-line on 20th August 2006*.

Jeanneau, F., Lainé, F., & Poumarède, B. (June 23, 2006). *Nuclear Instruments and Methods in Physics Research Section a: Accelerators, Spectrometers, Detectors and Associated Equipment, 562*(2), 1089−1092. Proceedings of the 7th international conference on accelerator applications.

Miyadera, H., Borozdin, K. N., Greene, S. J., Lukić, Z., Masuda, K., Milner, E.. C., et al. (2013). Imaging Fukushima Daiichi reactors with muons. *AIP Advances, 3*(052133).

Pachowko, A. D., Wang, M., Poole, C., & Rhodes, D. (2004). Measurement of slurry density profiles in horizontal pipes by using electrical resistance tomography. In *Proceedings of the sixteenth international conference on the hydraulic transport of solids in pipes, BHRA, Santiago, Chile* (pp. 481−495).

Bernardi, Richard T., & Martz, Harry E. (1995). Nuclear waste drum characterization with 2 MeV X-ray and gamma-ray tomography. In *Proc. SPIE 2519, X−ray and ultraviolet sensors and applications* (vol. 140).

Rizo, Ph, Robert-Coutant, Ch, Moulin, V., Sauze, R., & Antonakios, M. (October 2000). Application of transmission tomography to nuclear waste management. In *15th world conference on nondestructive testing Roma (Italy)* (pp. 15−21).

Townson, P., & Thien, M. (2011). In *Design and fabrication of test facilities for the demonstration of jet mixer performance in the Hanford double shell tanks WM2011 conference, February 27−March 3* (Phoenix, AZ).

Townson, P., Wright, S., Jensen, J., & Vanatta, M. (2011). In *Instrumentation for real time monitoring of the 3-Dimensional particulate distribution in the Hanford double shell tank small scale mixing demonstration platform; WM2011 conference, February 27−March 3* (Phoenix, AZ.).

Wang, M., Rhodes, D., Young, J., Primrose, K., & Takei, M. (2007). Electrical impedance tomography for nuclear engineering. In *15th international conference on nuclear engineering Nagoya, Japan, April 22−26*. ICONE15.

This page intentionally left blank

Index

Note: Page numbers followed by “f” and “t” indicate figures and tables respectively.

A
Abel transform, inverse, 467–468
Abel’s integral equation, 146
Absorption spectroscopy, 136–141
  Beer–Lambert law, 136–137
  direct (DAS), 140–141
  dual wavelength ratio (DWR) technique, 140
  Heisenberg’s uncertainty principle, 138–139
  schematic, 137f
  simulated H_2O absorption spectra, 139f
  suitable features, 140
  transmission spectrum of iso-octane/air mixture, 141f
  tunable diode laser (TDLAS), 136–137
Acoustic impedance, 239, 618f–619f
Acoustic propagation wave theory, 237–239
  attenuation of wave, 238–239
  propagating pressure wave, 238
  wave descriptors, 237f
Ad hoc on-demand distance vector (AODV), 290
Adaptive electrical capacitance volume tomography (AECVT), 18–20
Advanced 3D ECT systems, 533–534
ALARA (as low as reasonably achievable) philosophy, 200, 209–210, 220–221
Algebraic reconstruction technique (ART), 6–7, 145, 312–313, 368–369. *See also* Kaczmarz’s row projection method (KACZ)
  Landweber algorithm, 7–8
  multiplicative, 369–370
  simultaneous (SART), 469
Alternating current (AC) coupling circuits, 27
Ampére’s circuital law, 314–315
Amplitude variation with offset (AVO) inversion, 610
  of P- and S-waves, 613f
  workflow, 614, 614f
Analogue-to-digital conversion (ADC), 278
  for ECT, 10
  for EIT, 45–46
ANSYS (software package), 392
Approximate nonlinear and non-Gaussian state estimation, 563–565
  extended Kalman filters, 563–564
  modeling errors, 564–565
Approximation error approach, 564–565
  Bayesian, 564–566, 569–570, 573, 582
Archie’s law, 51, 638–639
Attenuation coefficient, 307
Auger effect, 202
Augmented state models, 566–567
Automotive in-cylinder hydrocarbon imaging, 162–165
  CST images, 164f
  optical access layer (OPAL) and beam configuration, 163f
  pre-ignition hydrocarbon imaging, 162–163
  temporal and spatial behaviours of images, 165, 165f
  wavelet denoising (WD) step, 164
Axial gradiometer, 95–96, 96f
Azimuthal tomography workflow, 626–627, 629f

B
Back projection algorithm, 192–193, 317, 436–438
Ballistic photon techniques, 156. *See also* Time-of-flight (TOF) techniques

Basic imaging techniques, MRI, 121–123
  gradient echo and spin echo imaging sequences, 122–123
  signal relaxation measurement, 123
  velocity imaging, 123
Batch-type optimization, 566
Bayes theorem, 422
Bayesian analysis, 416
Bayesian approximation error (BAE) approach, 564–566, 569
  nonstationary, 570, 573
Bayesian methods, 447
  sequential, 555
Bayesian paradigm, 405–408
  continuous Gaussian distribution, 406
  discrete Poisson distribution, 406
  example domains, 405, 406f
  maximum a posteriori (MAP) estimate, 407
  maximum likelihood (ML) estimate, 407
Beer–Lambert law, 136–137
Better Approach To Mobile Ad hoc Networking (B.ATM.A.N.), 290
BFGS (Broyden–Fletcher–Goldfarb–Shanno) algorithm, 566
Binary pixel weights, s0055
Bipolar gradient pulse sequence, 121f
Birchak formula, 548
Block-iterative component average (BI-CAV), 293
Boltzmann distribution, 110
Borehole seismic surveys, 619–626
  wave arrivals, 620f
Born and Rytov approximations for weakly scattered objects, 335–336
  Born scattered field, 335–336
Born iterative method (BIM), 340
Boundary element method (BEM), 414–415
Bread studies, X-ray microtomography, 706–709
  discussion, 707–709
  sample preparation and analysis, 707
Bubble column reactors, 478–487
  fluid phase fraction measurements, 479–485, 483f
  fluid velocity measurements, 485–487
  schematic of, 479f
Bubble columns, applications of tomography in, 477–478
  bubble column reactors, 478–487. *See also* Bubble column reactors
  future trends, 494–496
Bubbles, 452
  data evaluation, 459–460
  frequency distribution, 460f–461f
  in fluidized bed, 455
  size, 461f
  in ultrafast X-ray computer tomography, 467–469
Bubbling beds, 3–4
Bulk modulus, 594, 596t, 609

C

Cadmium zinc telluride (CZT), 207
Calderon's method, 378–379
  circular electrical capacitance tomography sensor, 381–383
  images reconstructed using, 393f
Capacitance sensors, 4–5, 11–12
  in conventional ECT applications, 10
  in point measurement devices, 682–685
Capacitance tomography, in gas–solid fluidized bed systems
  effective permittivities of mixtures and phase distributions, 546–548
  fluidization principle, 529
  fluidization regimes, 530–531
  future trends, 548
Capacitance tomography, in pharmaceutical industry, 542–545
  solids distribution profile and visualization, 542–545, 545f
[^{11}C] labeling process, 680–681
Carenkov images, 682, 684f
Cartesian coordinates, 350–351, 359
Central slice theorem, 356–361, 358f
  2D Fourier transform, 360f
  2D tomographic image reconstruction algorithms, 361t
Chemical species tomography (CST), 135–136
  absorption spectroscopy for, 136–141
  beam array design and optimization, 150–151
  design of systems, 151–162, 153f. *See also* CST system design

  future trends, 168–170
  in-cylinder HC fuel vapour distribution, 165f
  low beam–count systems, 143–150
  radio-frequency CST, 135
  rank-deficient problem, 147f
Chirp signal, 275
  linear compressed frequency excitation, 275f
Cimmino's method, 293
Circular electrical capacitance tomography sensor
  Calderon's method, 381–383
  dbar method, 383–384
  factorization method, 384–385
Circulating fluidized bed (CFB) system, 3–4, 534–540, 534f
  gas–solid CFB, 536f–537f
  theoretic illustration of solids distribution, 539f
  time-averaged solids holdup distribution, 538f–540f
Coffee bean studies, X-ray microtomography, 703–706, 704f–705f
  discussion, 703–706
  sample preparation and analysis, 703
Collimation lenses, 157–158
Combustion, 3–4, 531
  air-fuel mixing, 162
  carbon dioxide (CO_2) at, 137–138
  coal combustion, 536–537. *See* Circulating fluidized bed (CFB) system
  iso-octane/air mixture at, 141f
  laboratory combustion studies, 166–168
Common mode voltage (CMV), 41–42
Common mode voltage feedback (CMFB), 41–42
Community Seismic Network (CSN), 298–299
Complete electrode model (CEM), 568–569
Component average row projection (CARP) method, 293
Component-averaged DMET (CA-DMET), 293
  network topology for, 295f
Component-averaging (CAV) technique, 293
Compressed sensing, 126–127
  principle of, 127
Compton scattering, 202–203
Computational case studies, 574–581
  estimation of flow profile, 574, 575f–576f
  POD model reduction with stationary flow, 574–576
  POD model reduction with nonstationary flow, 576–581, 579f–580f
  stationary von Karman street, 577f–578f
Computational fluid dynamics (CFD), 452, 469, 477–478
  codes, 458, 462
  computational models, 455
  simulations, 458
  software, 463, 465–466
Computed tomography (CT), 175. *See also* X-ray computed tomography
  fluid bed characterization using, 455–458
  generations and categories, 198–199
  measurement geometries, 198f
Computer automated radioactive particle tracking (CARPT), 231, 485–487
  disadvantage of, 486
  vorticity chains, 486–487
Concept of local polarization, 547
Conductivity contrast, 47
Conductivity resolution, 47
Cone-beam tomography, 371f
Cone-beam X-ray computed tomography, 190–193
  beam hardening, 191–193
  gas holdup, 190, 191f
  scatter correction, 190–191
Conformal mapping, 391
Conformal transformation and governing equation, 379–381
Contactless inductive flow tomography (CIFT), 65, 555
Controlled-source electromagnetic (CSEM) technology, 592–593
Convection diffusion (CD) models, 556
Cross-well electromagnetic tomography
  acquisition system, 636f
  distance versus casing, 636t
  EM induction cross-well tomography, principles of, 635–640
  in hydrocarbon reservoir monitoring, 633–643

Cross-well electromagnetic tomography (*Continued*)
  - imaging fluid flow on reservoir-scale, 640
  - imaging steam fronts, 642–643
  - primary and secondary fields, 637f
  - resistivity profile between wells, 643f
  - water flood monitoring, 640–641
  - well time-lapse survey images, 639f

Crosswell seismic surveys, 621–622, 625f–626f

CST system design, 151–162, 153f
  - achieving optical access, 157–159
  - lens–detector combination, 161f
  - optical propagation and scattering, 154–157, 155f
  - optoelectronic considerations, 160–162

CTAn software (Skyscan), 696–697, 701f–702f

D

Data acquisition system (DAS)
  - capacitance normalization, 10
  - charge–discharge and AC-based designs, 9
  - for ECT, 3, 5, 9–10
  - for EIT, 23–25, 45–47, 45f

Data models, 408–409

Dbar method, 379
  - circular electrical capacitance tomography sensor, 383–384
  - images reconstructed using, 393f

De la Rue and Tobias correlation function, 50t

Deep-reading resistivity tomography, 629

Diffraction tomography
  - Born and Rytov approximations for weakly scattered objects, 335–336
  - difference between projection and, 332f
  - Fourier diffraction theorem, 336–339
  - image reconstruction methods. *See* Image reconstruction
  - mathematical formulation of, 331–335

Diffractive optical elements (DOEs), 158

Diffuse optical tomography (DOT), 135. *See also* Near-infrared (NIR) tomography

Digital fluoroscopy (DF), 457–458

Digital signal processor (DSP) modules, 46, 91, 278

Direct absorption spectroscopy (DAS), 140–141

Direct back projection, 309–310, 309f

Direct digital synthesis/synthesiser (DDS), 33, 89–90, 278

Direct methods for image reconstruction, 377–379
  - conformal mapping, 391
  - direct algorithms for, 379–385
  - experiment results and discussion, 394, 395f
  - future trends, 381–382
  - reconstructed results and discussion, 390–394
  - scattering transforms, calculation of, 388–390
  - simulation results and discussions, 392–394

Dirichlet-to-Neumann map, 377, 380
  - construction of, 385–388

Discovery™ (nonintrusive inspection tool), 212–213, 213f–214f

Discretization and image reconstruction, 362–364, 363f, 388–390
  - area of ray and pixel, 363
  - binary pixel weights, 362
  - length of ray, 363
  - weighted assignment, 363

Distinguish-ability, 48
  - performance of EIT, 49f

Distributed multiresolution evolving tomography (DMET), 293, 294f
  - component-average. *See* Component-averaged DMET (CA-DMET)

Distributed tomography algorithms, 292–295
  - distributed multiresolution evolving tomography, 294. *See also* Distributed multiresolution evolving tomography (DMET)
  - multiresolution evolving schemes, 294f

Dix equation, 604

Dynamic algorithms, 326–331
  - augmented measurement model, 329–330
  - for EIT image reconstruction, 326–327
  - Jacobians, 328
  - Kalman filter algorithm, 327
  - Kalman gain, 330

E
ECAH (mathematical inversion models), 243
Echo planar techniques, 124–125
Eddy current tomography. *See* Electromagnetic induction tomography (EIT)
Eigenvectors, 518
Electrical capacitance tomography (ECT), 3–4, 61, 316, 377–379, 402–403, 433–434, 511, 533, 552
  in comparison with ERT and MIT, 62t, 64–65
  components, 5f
  conventional fluidized beds, , 536–540. *See* Circulating fluidized bed (CFB) system
  data acquisition system, 3, 5, 9–10. *See also* Data acquisition system (DAS)
  direct algorithms for, 379–385
  disadvantage, 18
  experiment results and discussion, 394, 395f
  features of, 17
  fluidized beds and ECT sensors, 542f
  for multiphase-flow WLR and liquid fraction measurement, 648–656
  future trends, 19–20, 381–382, 656–658
  gas–solid fluidization, 533
  image reconstruction algorithms, 6–8. *See also* Image reconstruction algorithms, for ECT
  measurements, 320f, 484f
  principles of operation, 4–6
  reconstructed results and discussion, 390–394
  scattering transforms, calculation of, 388–390
  simulation results and discussions, 392–394
  volume tomography. *See* Electrical capacitance volume tomography (ECVT)
Electrical capacitance volume tomography (ECVT) systems, 10–12, 533–535
  computational fluid dynamics (CFD) simulations versus, 15, 15f–17f
  conventional, 19f
  isosurface volume images, 14f
  resolution quality comparison, 13f
  sensor regions, 11f
Electrical impedance spectroscopy (EIS), 267, 269
Electrical impedance tomography (EIT), 23–25, 316, 511, 533, 552, 568–569, 682–687, 686f–689f
  for biomedical research and development for process engineering, 24t
  data acquisition systems, 45–47. *See also* Data acquisition system (DAS)
  data for process application, 49–51
  electrode modelling, 28–32. *See* Electrode modeling, EIT
  future trends, 51–52
  imaging capability, 47–48
  performance of, 48f–49f
  sensing strategies, 36–38, 37f, 39f
  sensor, 25–28, 26f
  signal sources, 33–36. *See also* Signal sources, for EIT
  two-port impedance system, 38f
Electrical permittivity
  binary-value distribution of, 392f
  effective permittivity, 546–548
Electrical resistance tomography (ERT), 23, 61, 316, 511, 686–687, 715–723
  in comparison with ECT and MIT, 62t, 64–65
  hydraulic conveying of slurries, 717–718
  independent component analysis (ICA), 444–445
  independent components (ICs), 444–445, 445f
  other application, 723
  phase fraction measurement with, 437f
  precipitation process, 720–723
  solid–liquid mixing, 715–717
  solvent extraction, 718–720
  with Venturi meter, 446–447
Electrical tomography. *See also* Electrical resistance tomography (ERT)
  dynamic algorithms, 326–331
  gradient-based algorithms, 321–326
  image reconstruction, 316–318
  linear algorithms, 318–321
  mathematical formulation of, 314–316
  measurement update equations, 331
  time update equations, 331

Electrode modeling, EIT
  electrode-electrolyte impedance, 31f–32f
  overpotential and current density, 29f
Electromagnetic energy spectrum, 268f
Electromagnetic flow meters (EFM), 446
Electromagnetic induction tomography (EIT), 61–65, 533
  in comparison with ECT and MIT, 62t, 64–65
  concept of, 63f
  forward problem, solution for, 72–82. *See* Forward problem, solution for
  inverse problem, solution for, 82–89. *See* Inverse problem, solution for
  principle of operation and governing equations, 65–72
  system hardware. *See* System hardware, for MIT
  typical system, 64f
Electromagnetic sensor, applications, 101–103
  biomedical, 102–103
  conductivity profiling, 102
  hot metal processing, 101–102
  medical detection, 103
Electromagnetic wave, 305
  spectrum of, 306f
Electronic collimation, 225
Electrowetting on dielectric (EWOD) microchip, 682, 683f
Emission tomography setup, 349f
Enhanced oil recovery (EOR) processes, 591, 622
ESTET-ASTRID (numerical code), 466
Euclidean norm, 146–147, 166
Euler–Euler computational model, 494–496
Exploration geophysics, 297
Explosive remnants of war (ERW), 93
Extended Kalman filter (EKF), 559–560, 563–564
  iterated EKF, 564
  local linearization version, 564
  realization of, 573
  recursions, 573
Extended X-ray absorption fine structure (*EXAFS*) mode, 672–673

F
Factorization method, 379
  images reconstructed using, 394f
Faraday’s law of induction, 65, 314–315
Fast imaging techniques, MRI, 123–128
  full *k*-space fast sampling, 124–126
  sparse and nonlinear sampling, 126–128
Fast tomography, 181
Feature-based prior models, 413–415, 414f
Field programmable gate array (FPGA), 91
Filtered back projection, 144, 309f, 310–312
Finite difference time domain (FDTD) technique, 78
Finite element methods/modeling (FEM), 8, 413
  predicted equipotential in, 688f
First order Markov models, 558–559
Fischer–Tropsch synthesis, 477–478
FLASH, 126
Flow process analysis and characterization, 442–445
  axial solids volume fraction distributions, 443f
  upward vertical swirling flow, 444f
Flow profile model, 569
Flow regime, 431
Flow velocity measurement, 439–442
  axial velocity profile, 440f
  with cross-correlation and IPT, 439f
  oil–water two-phase flow velocity, 442f
  velocity distributions, 441f
Fluid beds
  bubble frequency distribution, 460f–461f
  bubble size, 461f
  characterization by X-ray fluoroscopy and pressure measurements, 458–459
  characterization using computer tomography, 455–458
  imaging of, 453–455
Fluidization, 452–453. *See also* Gas–solid fluidized bed systems
  principle of, 529
  regimes, 530–531
Fluidized beds, tomography techniques for, 3–4, 532–533
  apparatus components and instrumentation, 544f
  average solid concentration, 544f
  comparison of radial voidage profiles, 535f

  and ECT sensors, 542f
  images reconstructed from, 543f
  parameters for tests, 543t
  validation with conventional instruments, 532–533
[^{18}F]FDG synthesis, 680–681
FMISO, 682
  synthesis of, 683f
Food inspection, application of tomography in, 693
  bread studies, 706–709
  coffee bean studies, 703–706
  food products studied, 695–696
  future trends, 709–710
  meat studies, 696–699
  wheat studies, 699–703
Forward problem, solution for, 72–82
  analytical approach, 75, 76f
  boundary element method (BEM), 77–78, 78f
  dipole approximation, 80–82, 81f
  finite element method (FEM), 75–77, 77f
  full wave solutions, 78
  impedance method, 79–80, 79f–80f
  linear approximation, 73–75, 75f
Fourier diffraction theorem, 336–339
Fourier slice theorem, 311
Fourier transform(ation), 112, 337–338, 356, 382–383
  –based reconstruction, 144f
Fredholm integral equation, 143, 390
Full azimuth (FAZ) marine seismic imaging, 626–627
Full data tomography, 145
Full waveform inversion (FWI), 627–629

G
Gamma camera, 223f, 224
Gamma ray attenuation in matter
  build-up, 204
  counting statistics and measurement errors, 205
  transmission, 201–204
Gamma (γ) ray CT, 553–554. *See also* Gamma (γ) ray tomography
Gamma ray system engineering, 209–212
  detector technology, 211
  energy and isotope, 210
  image reconstruction algorithms and software, 212
  read-out electronics and computer interface, 211–212
  shielding and collimation, 211, 211f
  source activity, 210
  system design, 209–210
  system geometry, 210–211
Gamma (γ) ray tomography, 197–199, 447f, 532, 668–675
  absorption tomography, 675–676, 676f
  attenuation in matter. *See* Gamma-ray attenuation in matter
  detector and read-out systems, 206–209
  fundamental principle of, 197–198
  future trends, 220–221
  measurement modes used in, 198f
  scatter tomography, 198
  system engineering and geometry, 209–212. *See also* Gamma ray system engineering
GammaScorpion, 213–214, 215f
Gas volume fraction (GVF), 219–220, 495f, 644–645, 648–653
  flows, plotted vs, 657f
Gas–liquid mixing, 526
  monitoring, 511
  principles, 511t
Gas–solid fluidized bed systems
  electrical capacitance characterization of, 532–535
  fluidization regimes, 530–531
  gas and gas/solid jet penetration in, 540, 541f
  industry applications of, 531–532
  principle, 529
  schematic diagram of, 541f
Gas–solid mixing, 511
  principles, 511t
Gas–solid two-phase flows, 431
Gasoline direct injection (GDI) engine, 164
Gauss–Newton algorithm/method, 85, 324–326
Gauss–Seidel method, 292–293
Gauss's law, 66–67, 314
Gaussian curves, 456
Gaussian distribution, 408, 559
Gaussian likelihood, 423

Gaussian model, 412f
  posterior summary, 420f
  prior model, 412f
Geldart particle groups, 530–531
  B particles, 465–466
  classification of particles, 530f
Gibbs distribution, 410–411, 413
Gouy–Chapman diffuse model, 30–31
Gradient-based algorithms, 321–326
Gram-Schmidt orthonormalization, 388
Green’s function, 336–337
Grotto formations, 526

H
Hamiltonian parameter, 413
Hard-field of tomography, 135
Heisenberg’s uncertainty principle, 138–139
Helmholtz double layer capacitance, 30–31
Helmholtz’s wave equation, 332–334, 339, 594
Hessian matrix, 325
High-speed gamma-ray tomography for pipe flow imaging, 214–218, 216f
HITRAN (database), 138
  CO_2 line strengths based on, 138f
Hooke’s law, 595
Hotelling transform, 571
Hydraulic conveying of slurries, 717–718
Hydraulically induced fractures, 620
  microseismic method of, 624f
Hydrocarbon exploration and reservoir characterization, seismic tomography in, 591–608
  basics of seismic waves, 594–600
  seismic depth imaging, 602–608
  seismic exploration industry revolution, 593
  structural traps, 592f
  traveltime tomography, 600–602
Hydrocarbon production monitoring, 644–656
  case study, 648–656
  conventional permanent production scenario, 645f
  flow patterns, 647f
  gas volume fractions (GVF), 644–645
  inline oil-water-gas multiphase-flow measurement problem, 646f
  magnetic resonance, 648
  process tomography, 646–647
  technical challenges, 648
  tomometry, 648

I
Image contrast, MRI
  flow and diffusion, 118–121. *See* Phase-shift velocity imaging; Time-of-flight (TOF) techniques
  signal relaxation, 116–118. *See also* Spin echo
Image reconstruction
  diffraction tomography. *See* Diffraction tomography
  electrical tomography. *See* Electrical tomography
  future trends, 341
  for highly scattering objects, 339–340
  for low beam–count systems, 143–150
  mathematical concepts, 305–306
  transmission tomography, 306–313. *See also* Transmission tomography
  for weakly scattering objects, 339
Image reconstruction algorithms, ECT, 6–8
  first-order Born approximation, 7
  linear back projection (LPB), 7–8
  soft-field effect, 6–8
Image reconstruction, for hard field tomography, 347–351
  algebraic image reconstruction, 366–370. *See also* Algebraic reconstruction technique (ART)
  assumptions, 347–351
  central slice theorem, 356–361, 358f, 360f
  forward problem, projections and Radon space, 351–352
  future trends, 373–374
  inverse problem and parallel beams, 352–356
  limited-angle tomography, 372–373, 373f
  limited-data tomography, 372–373
  local tomography, 372–373, 373f
  noise and apodization of inverse kernel, 364–365
  sampling and discretization, 362–364, 363f, 388–390. *See also* Discretization and image reconstruction
  3D analytic image reconstruction, 370–372
  tomography with fan beams and other projection geometries, 365–366, 366f

Impedance camera, 23
Inductive flow tomography (IFT), 555
Industrial process tomography (IPT), 147–148, 263–266, 431–432, 434–445, 482–483
  combined with other sensors, 446–447
  example instruments, 265f
  first generation, 265
  flow process analysis and characterization, 442–445
  flow velocity measurement, 439–442. *See also* Flow velocity measurement
  multimodality IPT, 445–446
  phase fraction measurement, 434–439, 436f, 438f. *See also* Phase fraction measurement
Industrial Tomography Systems (ITS), 38, 265, 268
In-network tomographic imaging, 290–296
  applications, 296–298
  distributed tomography algorithms, 292–295. *See also* Distributed tomography algorithms
  evaluation environment, 296
  future trends, 298–299
  network architecture and challenges, 290–292
Integral values of object function along lines, 348–350
Internal combustion (IC) engines, 162
International Commission on Radiological Protection (ICRP), 200
Inv-cosh, 412f
Inverse problem, solution for, 82–89
  iterative solutions, 83–85
  linear case, 82–83
  sensitivity formulations, 85–89
Ising model, 413, 420–421
  posterior summary, 421f
Iterative algorithm, 189, 368, 436–438
  principles, 368–369
Iterative linear back-projection (ILBP) algorithm, 534–535

J
Jacobi elliptic functions, 391
Jacobi method, 292–293
Jacobian matrix, 324–326

K
Kaczmarz's method, 313
  conceptual description of, 313f
Kaczmarz's row projection method (KACZ), 293, 295
Kalman filter, 447, 560–561
  algorithm, 327
  ensemble Kalman filters, 559–560
  innovation form, 560–561
  recursions, 559, 565
  unscented, 559–560
Kalman gain, 330
Karhunen–Loeve decomposition, 571
Kirchhoff's law, 323
Kronecker product, 325

L
Laboratory combustion studies, 166–168
  OH* chemiluminescence in, 167f–168f
Lambert law, 348
Lambert–Beers law, 204
Lamé's constant, 595, 596t
Landweber algorithm, 7–8
Landweber iteration, 147–148, 369–370, 412f
Laplace equation, 4–5, 67, 379
Laplace prior distribution, 411–412
Large-scale in-network tomographic inversion, 285–286
Laser speckle velocimeter (LSV), 553
Leeds FICA system, 46, 46f
Level set method (LSM), 148–149
Limited-angle tomography, 366, 372–373, 373f
Limited-data tomography, 372–373
Line integral measurements, 350–351
Linear absorption coefficient, 307
Linear algorithms, 318–321
Linear back-projection (LBP) method, 7–8, 248–249
  and hybrid binary reconstruction techniques, 255f
Linear Gaussian problems, 560–561
Liquid–liquid mixing, 525
Lithology, 609, 609f
Local thresholding concept, 459
Local tomography, 372–373, 373f
Look-up tables (LUT), 277

Looyenga formula, 548
Lorentzian line shape, 138–139

M
Magnetic induction tomography (MIT), 61. *See also* Electromagnetic induction tomography (EIT)
  circular MIT arrays, 90f
  in comparison with ECT and ERT, 62t, 64–65
  inversion algorithm, 83f
  main elements of, 63–64, 64f
  multiple interacting resonances on, 100f
  phasor response of different objects in, 71f
  receiver channel, 91f
  receiver coil input connections, 100f
  sensitivity map in, 75f
  sensor array configurations, 93f
  16 transmitter and 16 receiver channel system, 92, 92f
  system hardware. *See* System hardware, for MIT
  transmitter channel, 90f
Magnetic materials, 68–71
  effects of diffusion with frequency, 70f
Magnetic resonance applications, 128–130
  non-spatially resolved measurement, 128–129
  phase-shift velocity imaging, 130
  and time of flight, 129
Magnetic resonance imaging (MRI), 109–116, 436, 532, 554–555
  advantages of, 127–128
  fast imaging approaches. *See* Fast imaging techniques, MRI
  frequency and phase encoding, 113
  future trends, 131–132
  image contrast. *See* Image contrast, MRI
  imaging techniques. *See* Basic imaging techniques, MRI
  magnetic field gradients and imaging, 111–112
  precessing magnetisation vector, 110
  simple 1D and 2D imaging sequences, 113–115, 114f
  slice selection, 115–116, 115f
Magnetotelluric (MT) technology, 592–593
Manual tuning approach, 565–566
Maximum a posteriori (MAP) estimate, 407, 413, 419–421, 423
  reconstructions, 412–413, 412f, 415f
Marginalization, 556
Markov chain Monte Carlo (MCMC) method, 401, 416
  generic algorithm, 417f
  single-variable random walk algorithm, 418f
Markov random fields, 410–411
Mars exploration, 297–298
Maximum likelihood (ML) estimate, 407
Maxwell equationss, 65–67, 314, 438, 635
Maxwell–Garnett equation/formula, 50t, 547
Maxwell–Wagner equation, 50t
Measurement update equations, 331
Meat studies, X-ray microtomography, 696–699, 697f–698f
  discussion, 697–699
  fat content determination using extraction method, 697
  image acquisition, processing and data analysis, 696–697
  sample preparation and analysis, 696
Medical imaging, 402
Method of moment (MOM), 339
Microchannel system, 669t–670t, 680–681, 685–687
  configuration of, 687f
  with cross-sectional configuration, 686f
  future of, 688–690
Microfluidic technology, 667–668
  channel, 668, 688–690
  devices, 685
  radiochemistry, 679
Microreactors, application of tomography in, 667–668
  electrical impedance tomography, 682–687. *See also* Electrical impedance tomography (EIT)
  future trends, 688–690
  γ-ray absorption tomography, 675–676
  γ-ray tomography, 668–675
  nuclear magnetic resonance imaging, 677, 678f. *See also* Nuclear magnetic resonance imaging

- positron emission tomography, 678–682. *See also* Positron emission tomography (PET)
- tomographic reconstruction of copper, 672f
- tomography techniques in, 669t–670t
- X-ray absorption radiography, 675–676
- X-ray tomography, 668–675

Mineral transportation, applications of tomography, 431–432
- flow pattern identification with, 433–434
- flow pattern in, 432–433
- industrial process tomography. *See* Industrial process tomography (IPT)

MiniGamma, 218–219, 219f

Minimum mean square estimates, 559

Mixing process, applications of tomography, 509–510
- conductivity maps, 525f
- displacement of groups, 525f
- extracting information about mixing, 512–513
- future trends, 526
- group velocities, 523t–524t
- one-plane sensor system, 513f
- one-plane tomography in, 513–515
- sensing principles for, 511t
- static mixers, 509
- tomographic techniques utilised for, 511–512
- by twin-plane tomographic system, 515–521

Model reduction, 564–565, 574
- with nonstationary flow, 576–581, 579f–580f
- with stationary flow, 574–576

Modelling errors
- Bayesian approximation error approach, 564–565
- extended Kalman filters, 563–564

Monte Carlo integration, 150, 447

Moore–Penrose inverse, 82, 369

Multidimensional data
- data and estimation of process state, 267f
- in fusion, 268
- in processes, 267–268

Multimodality industrial process tomography, 445–446

Multiphase flow meter (MPFM) technology, 214, 218f, 644–645, 658

Multiphase flow systems, 3

Multiphase flow WLR, 648–656
- cross-validation of tomography techniques, 653t
- eight-electrode ECT sensor, 654f
- nucleonic tomography techniques for, 651t
- tomography techniques for, 649t–650t

Multisensor fusion. *See* Industrial process tomography (IPT); Multimodality industrial process tomography

N

National Aeronautics and Space Administration (NASA), 297–298

Navier–Stokes equations, 455

Navier–Stokes flow, 557, 567

Near-infrared (NIR) tomography, 511–512

Neumann conditions, 323

Neumann-to-Dirichlet (NtD) map, 377–378, 380
- construction of, 385–388

Neural-network multicriteria optimization image reconstruction technique (NNMOIRT), 8

Newton method, 566

Nondestructive testing (NDT) applications, 93

Nonmagnetic materials
- effects of diffusion with frequency, 70f
- electrical conductivity, 69f
- magnetic permeability, 69f

Nonrecursive smoothers, 561–562

Nonstationary inverse problems, 556–558

Normal moveout (NMO) velocity analysis, 593

Norne field sandstone reservoirs, 615

Nuclear magnetic resonance (NMR), 96, 109, 267, 436, 677

Nuclear medicine imaging
- positron emission tomography, 224–226. *See also* Positron emission tomography (PET)
- single photon emission computed tomography, 223–224. *See also* Single photon emission computed tomography (SPECT)

Nuclear waste processing, application of process tomography in, 713–714
  future trends, 724
  other tomographic modalities, 723–724
  process measurement requirements, 713–714
  resistance tomography, 715–723. *See also* Electrical resistance tomography (ERT)
Nucleonic tomography techniques, for multiphase-flow WLR, 651t
Nyquist frequency, 350–351

O

Observation noise processes, 559
Ohm's law, 27, 29–30
Oil–gas industry, application of tomography, 591, 633
  borehole seismic surveys, 619–626
  bridging resolution gap, 634f
  cross-well electromagnetic tomography, 633–643
  future trends, 656–658
  hydrocarbon exploration and reservoir characterization, 591–608
  in hydrocarbon production monitoring, 644–656
  multicomponent seismic data for reservoir characterization, 608–615
  reservoir monitoring, simultaneous inversion, 615–619. *See* Reservoir monitoring, simultaneous inversion of time-lapse seismic surveys for
Oil–gas–water multiphase flows, 431
One-plane tomography, in mixing process, 513–515
  photographic dye distribution, 515f
  tomographic conductivity distribution, 515f
Operational amplifier (op-amp)
  common mode voltage rejection ratio (CMRR), 41–42
  in ECT, 32
  in EIT, 33–34
OPtical Access Layer (OPAL), 162–163
  and beam configuration used in IMAGER project, 163f
Optical flow meters, 553
Optical tomography, 652t
Optimization techniques, 6–7
Optimized Autonomous Space In situ Sensor-web (OASIS), 288–289
  data aggregation scheme used, 289f
Optimized Link State Routing Protocol (OSLR), 290
Overall state space model, 573
Over-zero switching (OZS) scheme, 41

P

Parallel projection geometry, 349f
Particle image velocimetry (PIV), 51, 553
Passive seismic monitoring, 620–621
Petrov–Galerkin FEM scheme, 572
pH_2-induced polarization (PHIP), 677
Phase fraction measurement, 434–439, 436f, 438f
  with ERT, 437f
  phase distribution, 435f
Phase-sensitive demodulators (PSDs), 42
  based on matched filter theory, 43
  drawback of, 44
  Fourier series expansion, 42
  input and output signals of, 43f
  principle, 42f
  reference sequences, 44
Phase-shift velocity imaging, 119–120, 121f, 130
Photo multiplier tube (PMT), 206–207
Photography, 532
Pixel-based continuous prior models, 409–413, 410f–411f
Pixel-based prior models, 413
Planar gradiometer, 96f
Planar laser-induced fluorescence (PLIF), 162
Plexiglas columns, 453
Pneumatic conveying systems, 3–4
Poisson distribution, 408
Poisson equation, 67
Poisson's ratio, 596t
Polder–Van Santen formula, 548
Pollutant, 457
Polyvinylidene fluoride (PVDF), 722
Porosity, 591–592
Position emission technique, 511
Positron camera, 227–228
Positron emission particle tracking (PEPT), 231–233, 231f, 512

Positron emission tomography (PET), 224–226, 348–350, 436, 532, 554, 678–682
  advantages over SPECT, 225
  industrial applications, 227–229
  scanner, schematic, 226f
Positron projection images, 228f
Precipitation process, 720–723
  design considerations, 721
  implementation, 721–723
  ITS vortex monitor, 722f
  measurement objectives, 720–721
  process, 720
Pressure fluctuation
  analysis, 456
  measurements, 457–458
  sensors, 454f
Principal component analysis (PCA), 518, 571
  for chosen EPs, 519f
  percentage of variability in, 520f
Process applications, of tomographic techniques
Process measurement requirements, spectro-tomography, 263–266
  beyond first-generation systems, 266
  first-generation instruments, 264–265
  industrial process tomography foundations, 263–264
Process tomography, 451, 510, 551–557, 646–647. *See* Velocity fields, estimation of
  approaches with auxiliary parameters, 565–567
  direct methods, 555
  future trends, 582
  indirect methods, 552–555
  state space approaches, 555–557
Programmable gain amplifiers (PGAs), 10, 91
Programmable gate array (PGA), 278
Projection slice theorem, 143–144. *See also* Fourier slice theorem
Proper orthogonal decomposition (POD), 571
P-waves (primary waves), 594–595, 596t, 609
  amplitude variation with offset (AVO) inversion, 610, 613f
  behaviour at reflector, 610
  particle motion and propagation of, 611f
  reflection, refraction and mode conversion of, 600f

Q
Quantum cascade lasers (QCLs), 160
Quasi-Newton method, 566
Quasi-Poynting vector, 85–86
Quick scanning extended X-ray absorption fine structure (*QEXAFS*) mode, 672–673

R
Radiation detector technologies, 206–207
  intensity measurements, 208–209
  pulse height analyser, 208
Radiation transmission, 308f
Radiation-based tomographies, 433–434
Radioactive particle tracking (RPT), 230–231, 456, 510
Radioactive tomography, 436
Radiochemical purities (RCP), 678–680
Radiochemical yields (RCY), 678–682
Radioisotope sources, 199–201
  collimation, 201
  gamma ray sources, 199–200
  safety and regulations, 200–201
Radioisotope tracer techniques
  nuclear medicine imaging, 223–226. *See also* Nuclear medicine imaging
  particle tracking, 230–233. *See also* Positron emission particle tracking (PEPT); Radioactive particle tracking (RPT)
  single photon imaging, 227
Radon space, 350–351
Radon transform(ation), 143–144, 308, 310, 352–355
  gray value image and, 354f
Raman spectroscopy, 267
RARE (rapid acquisition with relaxation enhancement) technique, 125, 125f
Ray approximation, 595
Ray tracing, 286–287, 332
Rayleigh correlation function, 50t
Rayleigh mixing rule, 547
Rayleigh scattering, 185–186, 203f

Reaction engineering, applications of tomography, 509–528. *See* Mixing process, applications of tomography
Read-out electronics, 207–208
  for gamma-ray detectors, 207f
Reciprocity theorem, 37–38
Recursions, 560–561
Recursive smoothers, 561–562
Reduced order Navier–Stokes evolution model, 570–571
Reflection seismology, 599
Regions of interest (ROI), 277, 377–378
Reservoir characterization
  hydrocarbon exploration and, 591–608
  multicomponent seismic data for, 608–615
Reservoir monitoring, 633–643
  imaging fluid flow on reservoir-scale, 640
  imaging steam fronts, 642–643
  principles of EM induction cross-well tomography, 635–640
  water flood monitoring, 640–641
Reservoir monitoring, simultaneous inversion of time-lapse seismic surveys for, 615–619
  ISIS simultaneous inversion, 617t
  from seabed sensors, 616f
  time-lapse inversion, 618f–619f
Reverse time migration (RTM), 627–629
Reynolds numbers, 574–576, 668
Riemann’s theorem, 379
Root mean square error (RMSE), 216–217
Roxar down-hole multibeam gamma sensor, 218–220, 220f
Runge–Kutta method, 571–572
Rytov approximation, 336
Röntgen, William Conrad, 197

S
Scattering transforms, calculation of, 388–390
SCG algorithms, 718
  tomograms of swirling flow, 719f
Seismic depth imaging, 602–608, 607f
  migration, 604–605, 605f
  seismic velocity models, 606f
  stacking, 602, 603f
  tomographic inversion, 606–607
Seismic imaging in reservoir description and monitoring, 628t
Seismic pore pressure tomography, 628f
Seismic tomography, 286–288
  sample P-wave, 286f
Seismic waves, basics of, 594–600
  reflection seismology, 599
  sedimentary, metamorphic and igneous rocks, 597t–598t
Semiconductor optical amplifiers (SOAs), 160
Sensitivity theorem, 377–378
Sensor electronics
  and demodulation, 40–44
  one excitation and measurement channel, 40f
  sensing strategies, 36–38, 37f, 39f
Shear modulus, 596t
Shunt model, 323
Signal sources, for EIT
  dual operational amplifier positive-feedback VCCS, 34f
  one amplifier negative feedback current source, 34f
  voltage-controlled bipolar current source, 35f
Signal-to-noise ratio (SNR), 8, 91
Silica-based optical glasses, 159
Simultaneous iterative reconstructive technique (SIRT), 369–370, 601
Single photon emission computed tomography (SPECT), 223–224, 348, 402, 436
  example data, 402f
Single photon imaging, 227
Single-electrode sensor, 25–27
Sinogram, 354f
Slurry flows, 431–432, 446, 448
  axial velocity profile of, 440f
  cross-correlation technique, 442
  flow patterns, 433, 436–438
  phase fraction estimation in, 434–435
  solid fraction distribution of, 438
  swirling flow, 442–444
Smooth basis function minimization (SBFM) method, 148–149
Snell’s law, 599
Society of Exploration Geophysicists (SEG), 299
Soft X-ray scanning microscopy (STXM), 674f

Soft-field effect, 6–8
Soft-field modality, 135
Solid–liquid mixing, 522–525, 715–717
  design considerations, 716
  implementation, 716–717
  large tank tomograms, 717f
  measurement objectives, 715–716
  mixing tank, 716f
Solvent extraction, 718–720
  design considerations, 719
  implementation, 720
  measurement objectives, 719
Sonogram, 402
Sound, speed of, 240
  and attenuation of water, 241f
  in common materials, 240t
Spatial resolution, 47, 252
Spatial sampling, concept of, 348–350
Spectral energy sensing dimension
  electrochemical effects over electrical excitation spectrum, 269f
  electrochemistry sensing, 268–270
  energy mode and level dimension, 270–271
  spectral fingerprint, 270f, 272f
Spectral filtering, 364–365, 365f
Spectro-tomography
  application review, 283–284
  data capture and processing architecture, 278
  data fusion processing, 276–277
  energy frequency tomograph set processing, 280–281, 281f
  energy sensing. *See* Spectral energy sensing dimension
  implementation, 283
  interpretation processing, 277–278
  multidimensional process measurement requirements, 263–266. *See also* Process measurement requirements; spectro-tomography
  multidimensional process sensing, 266–268
  overall processing with interpretation, 282, 282f
  process component identification, 273
  process excitation and response detection, 274–276
  simple process model, 271–273, 271f–274f
  spectroscopy data extraction, 279, 279f–280f
  system requirements, 274
Spin echo, 118
  imaging sequences, 122–123
Star-shaped object model, 414f, 421
  MAP image reconstructions using, 415f
  posterior summary, 422f
State estimation, general formulation, 558–560
State noise processes, 559
State space estimation approaches, 555–557
State space identification, 566
Static mixers, 509
Statistical image reconstruction, 401
  Bayesian paradigm, 405–408
  data models, 408–409
  estimation examples, 420–421
  estimation methodology, 415–419
  feature-based prior models, 413–415, 414f
  future trends, 421–424
  pixel-based continuous prior models, 409–413, 410f
  pixel-based prior models, 413
Stefan–Boltzmann law, 179–181
Stochastic convection-diffusion model, 571–572
Straight propagation of signal carriers, 347–348
Successive over-relaxation (SOR) method, 292–293, 313
S-waves (secondary waves), 594–595, 596t, 609
  amplitude variation with offset (AVO) inversion, 610, 613f
  behaviour at reflector, 610
  particle motion and propagation of, 611f
  reflection, refraction and mode conversion of, 600f
Symmetric successive over-relaxation method, 292–293
Synthetic electrical tomography, 403f
System hardware, for MIT, 89–100
  coil design, 94–96
  electrostatic screening, 96–98, 98f
  overlapping transmitter and receiver coils, 97f

System hardware, for MIT (*Continued*)
  resonance, 98–100
  resonant versus nonresonant detection schemes, 99t
  system configurations, 89–94

T

Taylor expansion, 563
Taylor series expansion, 324
Technetium generator, 224
Temporal resolution, 252
Thermal tomography, 652t
3D analytic image reconstruction, 370–372
3D capacitance tomography, 11–12
Tikhonov regularization, 146, 148
  first-order, 150
Tilted transverse isotropy (TTI), 593, 629f
Time update equations, 331
Time-lapse crosswell seismic monitoring, 627f
Time-of-flight (TOF) techniques
  for CST, 156
  velocity imaging, 118–119, 119f
Tomographic energy-dispersive diffraction imaging (TEDDI) technique, 671–672
Tomographic imaging in sensor networks, 285–286
  in-network, 290–296. *See also* In-network tomographic imaging
  seismic tomography, 286–288
  for volcano monitoring, 288–290
Tomographic inversion, 287
  procedure, 287f
Tomometry, 212, 218–219, 221
Tracerco discovery pipe integrity scanner, 212–213
Transmission line matrix (TLM) method, 78
Transmission tomography, 306–313
  algebraic reconstruction technique, 312–313
  algorithms, 316–318
  direct back projection, 309–310, 309f
  filtered back projection, 309f, 310–312
  setup, 349f
Trickle bed reactors, applications of tomography in, 3–4, 477–478, 488–494
  future trends, 494–496
  gamma-ray tomography measurements, 491f
  hydrodynamic studies, 489–492
  MRI measurements of, 490f, 493f
  reaction studies, 492–494
  schematic of, 488f
Tunable diode laser absorption spectroscopy (TDLAS), 136–137
Twin-plane tomographic system, 515–521
  elementary process (EP), 516, 517f
  fragment of covariance matrix, 518f
  grouping and image flow, 521f–522f
  image of groups, 516, 517f
  solid concentration changes, 516f
2D Fourier transform, 374–375

U

Ultrafast electron beam X-ray tomography (Ultrafast electron beam X-ray CT), 193–194, 480–481
  helical static mixer, 194f
  images, 481f
  operation principle of, 437f
  TOPFLOW facility, 480–481
Ultrafast X-ray computer tomography, 467–469
Ultrasonic tomography, 512
Ultrasound theory, 244–252
  acoustic impedance, 239
  acoustic propagation wave theory, 237–239
  in industrial process, 241–244. *See also* Wave propagation
  speed of sound, 240
Ultrasound tomography, 235–236, 652t
  benefits of, 236
  equipment, 244–252. *See also* Ultrasound tomography techniques
  future trends, 254–256
  linked with additional techniques, 250
  multiphase system, characterisation, 253
  single-phase system, characterisation, 253
  techniques, 236–244. *See also* Ultrasound tomography techniques
  theory, 236–244. *See also* Ultrasound theory
Ultrasound tomography techniques, 244–252
  image reconstruction, 248–250, 251f, 253f
  pulser, receiver and signal processing, 247

  system resolution calculation, 250–252
  system types, 247–248
  transducers, 244–247
Ultrasound velocity
  limitations on, 244
  of oil in water margarine, 243f
Unexploded remnants of war, 80
United States Geological Survey (USGS), 299
University of Bergen (UiB), 214–215
  high-speed gamma-ray tomography for pipe flow imaging, 214–218, 216f

V
Velocimetry, 130
Velocity fields, estimation of, 551–557. *See also* Process tomography
  future trends, 582
  tomographic state space estimation of, 567–573
Vertical seismic profiles (VSPs), 619
  while drilling, 623f
  variations on theme of, 621f
  walkaround, 624f
Vertical transverse isotropy (VTI), 593, 608
Very large-scale integration (VLSI) technology, 285
Voigt profile, 138–139
Volcano monitoring, sensor networks for, 288–290
  aerial deployment of, 289f

W
Walk-through metal detectors (WRMDs), 78, 80, 82, 93
Waste characterization
  gamma tomography, 723
  by muon tomography, 724
  using photo-fission tomography, 724
  X-ray computed tomography, 723
Water/liquid ratio (WLR), 652–656, 658. *See also* Multiphase flow WLR
  instantaneous longitudinal cross-sectional images, 656f
  inversion steps of permittivity image reconstruction and derivation of, 655f
Wave propagation
  from fan-based transducer, 245f
  at interface in multiphase system, 242–244
  in single phase, 241–242
  tradeoff in spatial resolution and attenuation, 246f
Wavelength modulation spectroscopy (WMS), 141, 142f
Wavelet, 279–281
  denoising (WD), 164
  scale to frequency-time, 276f
  transform (WT), 275–276
Wheat studies, X-ray microtomography, 699–703
  discussion, 700–703
  sample preparation and analysis, 700
Whole-earth tomography, 296–297
Wideband excitation, 274–275, 278–279, 281
Wiener's rule, 50t
Wireless mesh network (WMN), 290–291
  distributed imaging using, 291f
  resource constraints, 291

X
X-ray absorption near edge structure (XANES) spectrum, 671–673
X-ray absorption radiography, 675–676, 676f
X-ray attenuation, 176–177
  derivation of law, 187f
  mass attenuation coefficient, 185f
  measurement, 185–188
X-ray computed tomography, 175–177, 553–554
  beam hardening and radiation scattering, 188–190
  cone beam. *See* Cone-beam X-ray computed tomography
  future trends, 194–195
  scanning principles, 177f
  ultrafast. *See* Ultrafast electron beam X-ray tomography (Ultrafast electron beam X-ray CT)
  variants of, 177–178
  X-ray detectors, 183–185. *See also* X-ray detectors
  X-ray sources for process tomography, 178–182
X-ray CT, 456–458. *See also* Computed tomography (CT)
  scanner, 451–452

X-ray detectors, 183–185
  electronics, 184f
  principles, 183f
  scintillator materials, 183
  semiconductor detectors, 183–184
X-ray diffraction (XRD) patterns, 671–672
X-ray fluorescence (XRF) datasets, 671–672
X-ray imaging, 454f
  in food inspection, 693
  testing method, 693–695
  volume of interest (VOI), 694
X-ray tomography, 135, 532, 668–675
X-ray tomography, of fluidized beds, 451–453
  comparison between different validation approaches, 463–464, 464f
  computational models, 455
  data evaluation, 459–462
  fluid bed characterization by X-ray fluoroscopy and pressure measurements, 458–459
  fluid bed characterization using computer tomography, 455–458
  future trends, 469
  imaging of, 453–455
  narrow and wide particle size distribution, 462–463
  reactor scale-up, validation for, 464–467
  ultrafast X-ray computer tomography, 467–469
X-ray tubes, 179–181, 180f
  energy spectrum, 179f
  for tomography applications, 181

Y

Young's modulus, 596t
YXLON Y.TU 160-D06 tubes, 468

Z

Zoeppritz equations, 599